International Conference on Advances and Innovations in Engineering

2.ICAIE

Conference Date
21-23 September 2023

www.icaie.org.tr

Fırat University, Atatürk Culture and Congress Center

15 June 2023
Deadline for abstract submission

1 August 2023
Deadline for full-text submission

SPONSORLAR

arslanlı

MİRYILDIZ
MÜH.İNŞ.TİC.İTH.VE İHR.LTD.ŞTİ.

MEGA
Insulation Solutions

ALKEN İNŞAAT

2.ICAIE

2. International Conference on Advances and Innovations in Engineering

Volume 1: Engineering

ISBN: 978-975-394-095-5

Full-Texts Submissions Book

21-23th SEPTEMBER 2023

Fırat University Engineering Faculty /
ELAZIĞ

Editor in Chief
Erkut YALÇIN

Editor
M. Sefa ÇETİN

Fırat University

Honour Committee of the ICAIE

Prof. Dr. Fahrettin GÖKTAŞ, Rector

Prof. Dr. Mehmet YILMAZ, Vice Rector

Prof. Dr. Ebru AKPINAR, Dean

Commıttee Members of the ICAIE

Chair of Conference

Prof. Dr. Ebru AKPINAR

Abdulkadir GÜL, Fırat University(Bioengineering)

Ahmet ÇINAR, Fırat University (Computer Engineering)

Akın ODABAŞI, Fırat University (Metallurgical and Materials Engineering)

Alper K. TANYILDIZI, Fırat University (Mechatronics Engineering)

Belkız TORĞUL, Fırat University (Computer Engineering)

Beyza Furtana YALÇIN, Fırat University (Civil Engineering)

Bircan ÇALIŞIR, Fırat University (Electrical and Electronics Engineering)

Çağrı KAYMAK, Fırat University (Mechatronics Engineering)

Erkut YALÇIN, Fırat Universit (Civil Engineering)

M. Barbaros DURMUŞ, Fırat University (Environmental Engineering)

M. Gökhan ALBAYRAK, Fırat University (Metallurgical and Materials Engineering)

M. Sefa ÇETİN, Fırat University (Electrical and Electronics Engineering)

Mehmet Erbil ÖZCAN, Fırat University (Mechanical Engineering)

Mesut GÖR, Fırat University (Civil Engineering)

Mukaddes KARATAŞ, Fırat University (Chemical Engineering)

Mustafa KANIK, Fırat University (Geological Engineering)

Özge Erdoğan YAMAÇ, Fırat University (Civil Engineering)

Özge HANAY, Fırat University (Environmental Engineering)

Sertaç Emre KARA, Fırat University (Mechanical Engineering)

Sinem AKYOL, Fırat University (Software Engineering)

Şeyda TAŞAR, Fırat University (Chemical Engineering)

Veyis SELEN, Fırat University (Bioengineering)

Yılmaz AYDIN, Fırat University (Software Engineering)

Yusuf KARGINOĞLU, Fırat University (Geological Engineering)

Scıentıfıc Commıttee

A. Didem KILIÇ, Fırat University
A. Erçin ERSUNDU, Yıldız Technical University
A. Garcia HERNANDEZ, RWTH Aachen University
A. Münir ÖZDEMİR, Bursa Technical University
A. Şükran DEMİRKIRAN, Sakarya University
A. Tevfik BİLDİK, Fırat University
Abayhan BURAN, Fırat University
Abdulkadir GÜL, Fırat University
Abdullah Hilmi LAV, İstanbul Technical University
Abdullah SAR, Fırat University
Abdülcelil KÜLEKÇİOĞLU, Fırat University
Abdülhakim ZEYBEK. Muş Alparslan University
Abuzer ÇALIŞKAN, Fırat University
Adem ATMACA, Gaziantep University
Ahmet Arif AYDIN, İnönü University
Ahmet Bedri ÖZER, Fırat University
Ahmet Burak TATAR, Adıyaman University
Ahmet Can ALTUNIŞIK, Karadeniz Technical University
Ahmet ÇINAR, Fırat University
Ahmet ORHAN, Fırat University
Ahmet ÖZER, Fırat University
Ahmet ŞAŞMAZ, Fırat University
Ahmet TÜRK, Manisa Celal Bayar University
Ahmet YILDIZ, Fırat University
Akın ODABAŞI, Fırat University
Ali ARI, İnönü University
Ali TAŞKIRAN, Fırat University
Ali TOPAL, Dokuz Eylül University
Alper BAŞTÜRK, Erciyes University
Alper K. TANYILDIZI, Fırat University
Arif GÜLTEN, Fırat University
Arijit DE, The University of Manchester
Arkadiusz DOBRZYCKI, Poznan University of Technology
Arzu Fırat ERSOY, Karadeniz Technical University

Arzu Yadigar DURSUN, Fırat University

Aslı GİRAY, Alanya Alaaddin Keykubat University

Atike NAZİK, Çukurova University

Ayberk KAYA, Recep Tayyip Erdoğan University

AYÇA AK, Marmara University

Aydın ÇITLAK, Fırat University

Ayhan AKBAL, Fırat University

Ayhan ÜNLÜ, Fırat University

Aykut TOPDEMİR, Fırat University

Ayla ÖZER, Mersin University

Aynur UÇAR, Fırat University

Ayşe Erdoğan YILDIRIM, Fırat University

Ayşe Ruşen DURUCAN,Fırat University

Ayşe Vildan BEŞE, Atatürk University

Ayşe BİÇER, Turgut Özal University

Ayşegül AŞKIN, Eskişehir Osman Gazi University

Ayşegül UÇAR, Fırat University

Aytekim ÇELİK, Fırat University

Aziz AKSOY, Turgut Özal University

Baha Vural KÖK, Fırat University

Bahadır YILMAZ, Bursa Technical University

Bahtiyar ÖZTÜRK, Ondokuz Mayıs University

Banu TAŞKAN, Fırat University

Barbaros DURMUŞ, Fırat University

Barış KARAKAYA, Fırat University

Belkız TORĞUL, Fırat University

Betül AY, Fırat University

Beyda TAŞAR, Fırat University

Beyza Furtana YALÇIN, Fırat University

Bilal ALATAŞ, Fırat University

Bircan ÇALIŞIR, Fırat University

Burak ŞENGÖZ, Dokuz Eylül University

Burak YILDIRIM, Aarhus University

Burçak EBİN, Chalmers University

Burhan ERGEN, Fırat University

Bünyamin AKGÜL, Fırat University

C. Fahir ARISOY, İstanbul Technical University

Calibe Koç TAŞGIN, Fırat University

Canan DÜLGER, İzmir University of Economics

Canan KOÇ, Fırat University

Celal KISTAK, Fırat University

Cemal BÖLÜCEK, Balıkesir University

Cengiz YILDIZ, Fırat University

Cenk YANEN, Fırat University

Cevdet AKOSMAN, Fırat University

Cihan ÖZEL, Fırat University

Çağla DANACI, Fırat University

Çağrı KAYMAK, Fırat University

Davut HANBAY, İnönü University

Deniz ÜNER, Middle East Technical University

Dicle Bal AKKOCA, Fırat University

Dursun BAKIR, Fırat University

Dursun ÖZER, Fırat University

Duygu EVİN, Turgut Özal University

Duygu KAYA, Fırat University

E. Sabri KAYALI, Haliç University

Ebru AKPINAR, Fırat University

Ebubekir ERDEM, Fırat University

Elif AKGÜN, Fırat University

EMİNE CENGİL, Bitlis Eren University

Emine Işıl TOPAL, Fırat University

Emrah ÇELİK, Fırat University

Emre GÜÇLÜ, Fırat University

Emrehan YAVŞAN, Tekirdağ Namık Kemal University

Ender SUVACI Eskişehir Technical University

Engin GÜRTEKİN, Fırat University

Enis GÜNAY, Erciyes University

Ercan AKSOY, Fırat University

Ercan AYDOĞMUŞ, Fırat University

Erdal ÖBEK, Fırat University

Erdal ÖZBAY, Fırat University

Ergin TAŞKAN, Fırat University

Erhan AKIN, Fırat University

Erkan DUMAN, Fırat University

Erkin EREN, Fırat University

Erkut SAYIN, Fırat University

Erkut YALÇIN, Fırat University

Ertan BÜTÜN, Fırat University

Ertan EVİN, Malatya Turgut Özal University

Ertuğrul ÇAMBAY, Bitlis Eren University

Ertuğrul GÜL, Hakkari University

Eser SERT, Malatya Turgut Özal University

Esra İNCE, Fırat University

Esra Tuğrul TUNÇ, Fırat University

Esra YILDIRIM, Fırat University

Esra YÜZGEÇ, Fırat University

F. Rumeysa KÜLEKÇİOĞLU, Fırat University

Fatih ÖZYURT, Fırat University

Fatih KAYA, Fırat University

Fatih TOPALOĞLU, Malatya Turgut Özal University

Fatma MURAT DURANAY, Fırat University

Ferkan SİPAHİ, Gümüşhane University

Fethi KAMIŞLI, Fırat University

Feyza ALTUNBEY ÖZBAY, Fırat University

Figen BALO, Fırat University

Filiz KAR, Fırat University

Fulvio PARISI, University of Naples Federico II

Galip AYDIN, Fırat University

Gamze BİLGEN, Zonguldak Bülent Ecevit University

Gizem ARSLAN, Fırat University

Gökay BAYRAK, Bursa Technical University

Gökhan ALBAYRAK, Fırat University

Gökhan BAŞMAN, Eti Krom Elazığ

Gökhan ERGÜVEN, Munzur University

Gökhan KURNAZ, Fırat University

Gökhan ÖZER, Fatih Sultan Mehmet Vakıf University

Gökmen TAYFUR, İzmir Institute of Technology

Gülbeyi DURSUN, Fırat University

Gülşad Uslu ŞENEL, Fırat University

Gülşah ÇAKMAK, Fırat University

Gülşah KARADUMAN, Fırat University

Gültekin GÖLLER, İstanbul Technical University

Güngör YILDIRIM, Fırat University

H. Lütfi YÜCEL, Fırat University

H. Suha AKSOY, Fırat University

H.Soner ALTUNDOĞAN, Fırat University

Hakan ÇELİK, Fırat University

Halil HASAR, Fırat University

Halil GÖR, Hakkari University

Hande Yüksel BAYRAM, Fırat University

Hanzade AÇMA, İstanbul Technical University

Hasan ÇELİK, Fırat University

Hasan GÜLER, Fırat University

Hasan YETİŞ, Fırat University

Haşim PIHTILI, Fırat University

Hatice KARA, Fırat University

Haydar EREN, Fırat University

Hayrettin CAN, Fırat University

Hediye AYDIN, Kütahya Dumlupınar University

Hossein MOAYEDI, Duy Tan University

Hülya BİÇER, Kütahya Dumlupınar University

Hümeyra ŞAHİN, Fırat University

Hüseyin ÇİMENOĞLU, İstanbul Technical University

Hüseyin KARACA, İnönü University

Hüseyin YAĞLI, Gaziantep University

İbrahim BERKAN AYDİLEK, Harran University

İbrahim TÜRKMEN, Balıkesir University

İhsan DAĞTEKİN, Fırat University

İlhan AYDIN, Fırat University

İnanç ÖZGEN, Fırat University

İrem GÖRGÖZ, Fırat University

İrem MERTYÜZ, Fırat University

İsmail YILDIRIM, Fırat University

Kazım TÜRK, İnönü University

Kelami ŞEŞEN, İstanbul Technical University
Kıvanç DOĞAN, Fırat University
Kübra ARSLANOĞLU, Fırat University
Kübra KOÇAK, Fırat University
Kübra ŞİŞLİOĞLU, Fırat University
Kürşat Esat ALYAMAÇ, Fırat University
Latif ÖZLER, Fırat University
Levent TAŞÇI, Fırat University
Leyla KALENDER, Fırat University
Loke Kok FOONG, Duy Tan University
M. Cihat TUNA, Fırat University
M. Deniz TURAN, Fırat University
M. Emin EMİROĞLU, Fırat University
M. Erbil ÖZCAN, Fırat University
M. Salih KESKİN, Dicle University
Mahmut PALUTOĞLU, Fırat University
Mahmut Temel ÖZDEMİR, Fırat University
Mansour MOSALLANEZHAD, Shiraz University
Mediha İPEK, Sakarya University
Mehmet Ali ERTÜRK, Fırat University
Mehmet ALTUNBEY, Fırat University
Mehmet ARSLAN, Karadeniz Technical University
Mehmet CEBECİ, Fırat University
Mehmet DAŞ, Fırat University
Mehmet DURANAY, Fırat University
Mehmet EROĞLU, Fırat University
Mehmet KALENDER, Fırat University
Mehmet KARAKÖSE, Fırat University
Mehmet KARATAŞ, Fırat University
Mehmet KAYA, Fırat University
Mehmet KÖKÜM, Fırat University
Mehmet ÖZDEMİR, Fırat University
Mehmet POLAT, Fırat University
Mehmet Sait SÖYLEMEZ, Gaziantep University
Mehmet Sinan BİLGİLİ, Yıldız Technical University
Mehmet ŞAHİN, Fırat University

Mehmet YILMAZ, Fırat University

Mehtap MURATOĞLU, Fırat University

Mehtap ÜLKER, Fırat University

Melahat BEYARSLAN, Fırat University

Melek Ural, Fırat University

Melek YILGIN, Fırat University

Melike AVER, Fırat University

Melike ESEN GÜNGÖR, Fırat University

Meltem ÇAKMAK KALKAN, Fırat University

Meral ÖZEL, Fırat University

Merve YILDIRIM, Fırat University

Mesut GÖR, Fırat University

Mete KALYONCU, Konya Technical University

Mete Onur KAMAN, Fırat University

Metin GÜRÜ, Gazi University

Mevlüt ALATAŞ, Munzur University

Miray Çelikbilek ERSUNDU, Yıldız Technical University

Mohammed Abdullahi Mu'azu, University of Hafr Al-Batin

Muammer TÜRKOĞLU, Samsun University

Muhammad Masood RAFIi NED University of Engineering and Technology

Muhammed ATAR, Fırat University

Muhammed Emre ÇOLAK, Fırat University

Muhammed Fatih TALU, İnönü University

Muhammed Furkan KÜÇÜK, Fırat University

Muhammed Sefa ÇETİN, Fırat University

Muhammed TALO, Fırat University

Muhammed ULUCAN, Fırat University

Muhammed YILDIRIM, Malatya Turgut Özal University

Muhammet AYDIN, Fırat University

Muhammet KARATON, Fırat University

Muharrem AKGÜL, Balıkesir University

Muhsin Tunay GENÇOĞLU, Fırat University

Mukaddes KARATAŞ, Fırat University

Murat BAYDOĞAN, İstanbul Technical University

Murat DOĞAN, Gazi University

Murat ELİBOL, Ege University

Murat KARACASU, Eskisehir Osmangazi University

Murat ŞEN, Fırat University

Murat Yavuz SOLMAZ, Fırat University

Musa ÇIBUK, Bitlis Eren University

Musa YETKİN, Fırat University

Musharraf ZAMAN, University of Oklahoma

Mustafa BOYRAZLI, Fırat University

Mustafa Can BİNGÖL, Burdur Mehmet Akif Ersoy University

Mustafa Eren RİZELİ, Fırat University

Mustafa GÜR, Fırat University

Mustafa İNALLI, Fırat University

Mustafa KANIK, Fırat University

Mustafa KAPTANOĞLU, Fırat University

Mustafa Selman AYDOĞAN, Balıkesir University

Mustafa TUNCER, Kütahya Dumlupınar University

Mustafa TUNÇ, Fırat University

Mustafa TÜRK, Fırat University

Mustafa ULAŞ, Fırat University

Müslüm ARKAN, İnönü University

Müslün Sara TUNÇ, Fırat University

Namık AYSAL, İstanbul University

Necip ÜNLÜ, İstanbul Technical University

Neslihan DURANAY, Fırat University

Neslihan DURMUŞ, Fırat University

Nevin ÇELİK, Fırat University

Nevin KONAKÇI, Fırat University

Nicola TARQUE, Pontifical Catholic University of Peru

Nigar ÖZBEY, Fırat University

Nihat KAYA, Fırat University

Nihat TOSUN, Fırat University

Nilüfer KOÇER, Fırat University

Niyazi Furkan BAR, Fırat University

Nizamettin ÖZDOĞAN, Zonguldak Bülent Ecevit University

Nuno MENDES, University of Minho

Nurhan ARSLAN, Fırat University

Oğuz YAKUT, Fırat University

Oğuzhan HASANÇEBİ, Middle East Technical University

Onur ALKAÇ, Fırat University

Onuralp YÜCEL, İstanbul Technical University

Orhan ÇAKAR, Fırat University

Osman YİĞİD, Fırat University

Ozan İNCE, Fırat University

Ö. Faruk DURSUN, İnönü University

Ömer ARAL, Ankara Yıldırım Beyazıt University

Ömer Faruk OSMANLI, Fırat University

Ömer Faruk TAŞ, Fırat University

Ömer GÜLER, Munzur University

Ömer Sinan ŞAHİN, Konya Technical University

Ömer ŞAHİN, İstanbul Technical University

Ömer Yavuz BOZKURT, Gaziantep University

Özge Erdoğan YAMAÇ, Fırat University

Özge HANAY, Fırat University

Özgür AVŞAR, Eskişehir Technical University

Özgür KARADUMAN, Fırat University

Özgür YILDIZ, Malatya Turgut Özal University

Özkan ÖZDEMİR, Sakarya University of Applied Sciences

Özlem Öztekin OKAN, Fırat University

Özlem TEPE, Fırat University

Paki TURGUT, İnönü University

Pranshoo SOLANKI, Illinois State University

Ragıp İNCE, Fırat University

Ramazan ORHAN, Fırat University

Recep ARTIR, Marmara University

Remzi TÜNTAŞ, Van Yüzüncü Yıl University

Rouzbeh GHABCHI, South Dakota State University

S. Emre KARA, Fırat University

Saadettin KAPUCU, Gaziantep University

Said ERAY, Sivas Technical University

Salih AYDOĞAN, Konya Technical University

Sanjay MISRA, Atılım University

Seda ARSLAN TUNCER, Fırat University

Sedat SAVAŞ, Fırat University

Selçuk ALEMDAĞ, Gümüşhane University

Selçuk KARATAŞ, Fırat University

Selen GÜRBÜZ, Fırat University

Sencer ÜNAL, Fırat University

Serap Çolak EROL, Fırat University

Serdar Ethem HAMAMCI, İnönü University

Serkan ERDEM, Fırat University

Servet SOYGÜDER, Ankara Yıldırım Beyazıt University

Seval GÜLER, Munzur University

Sevcan KÜRÜM, Fırat University

Sibel ASLAN, Fırat University

Sibel KAYGILI, Fırat University

Sinan KAPAN, Fırat University

Sinem AKYOL, Fırat University

Soheil GHAREH, Payame Noor University

Şaban TANYILDIZI, Fırat University

Şeyda ÖZDEMİR, Fırat University

Şeyda TAŞAR, Fırat University

Şule KAYA, Fırat University

Taha TAŞKIRAN, Ankara Yıldırım Beyazıt University

Tahsin BOYRAZ, Sivas Cumhuriyet University

Taner ALATAŞ, Fırat University

Taner TUNCER, Fırat University

Taylan SANÇAR, Munzur University

Tevfik YİĞİT, Fırat University

Turgay KAYA, Fırat University

Tülay YILDIRIM, Yıldız Technical University

Utku KÖSE, Süleyman Demirel University

Vedat ÇELİK, Fırat University

Vedat TANYILDIZI, Fırat University

Venhar ÇELİK, Fırat University

Veyis SELEN, Fırat University

Yakup DEMİR, Fırat University

Yasemin Didem AKTAŞ, University College London

Yasemin TOPÇUOĞLU,i Fırat University

Yaşar NUHOĞLU, Yıldız Technical University

Yavuz EROL, Fırat University

Yılmaz AYDIN, Fırat University

Yılmaz YILDIRIM, Zonguldak Bülent Ecevit University

Yunus AKSOY, Fırat University

Yunus Emre BENKLİ, Atatürk University

Yusuf CALAYIR, Fırat University

Yusuf DONAT, Fırat University

Yusuf KARGINOĞLU, Fırat University

Z. Fuat TOPRAK, Dicle University

Zeki ÇİZMECİOĞLU, İstanbul Ticaret University

Zülfü Çınar ULUCAN, Fırat University

Zülfü GÜROCAK,i Fırat University

Zümriye AKSU, Hacettepe University

Session Chairmans

Bedri ÖZER

H. Soner ALTUNDOĞAN

Muhammet KARATON

İhsan DAĞTEKİN

M. Emin EMİROĞLU

Oğuz YAKUT

Güngör YILDIRIM

M. Temel ÖZDEMİR

Zülfü GÜROCAK

Bilal ALATAŞ

Nevin ÇELİK

Akın ODABAŞI

Murat KARACASU

M. Yavuz SOLMAZ

Leyla KALENDER

Mehmet EROĞLU

Ayşegül UÇAR

Ahmet ÇINAR

M. Onur KAMAN

Özge HANAY

Erkut SAYIN

Filiz KAR

Ragıp İNCE

Cevdet AKOSMAN

Nihat TOSUN

Barış KARAKAYA

Mustafa KANIK

Murat ŞEN

Mustafa ULAŞ

Fatih ÖZYURT

INTRODUCTION

Dear Distinguished Delegate,

The second edition of the International Conference on Advances and Innovations in Engineering (ICAIE) was held between 21-23 September 2023 at Fırat University Faculty of Engineering, Elazığ.

International Conference on Advances and Innovations in Engineering is an international scientific forum of distinguished scholars engaged in scientific, engineering and technological research, dedicated to the furtherance of science, engineering and technology. The academic research conference since its inception is at the cutting edge of international nonprofit scientific, engineering and technological progress to promoting excellence in science.

The conference plays an influential role in science and promotes developments in science, engineering and technology in a wide range of ways. The conference aims to foster research in the area of science and technology and its impact to mainstream human activities. Specifically, it serves as a venue for discussions and exchange of ideas in current issues in science and technology.

All full paper and abstract submissions to the conference are peer reviewed and refereed and evaluated based on originality, research content and correctness, relevance to contributions, and readability. In this content the full paper and abstract submissions are chosen based on technical merit, interest, applicability and how well they fit a coherent and balanced technical program. The accepted papers after rigorous peer reviewing process have been published in the refereed international conference proceedings

Chair of ICAIE Committee
Prof. Ebru AKPINAR

CONTENTS

A Review on Physical Unclonable Function(PUF)-based Security Solutions in Cryptography 1

A Deepfake Image Detection Approach Based on YOLOv3 10

Crowd Analysis by Using Image Processing and Deep Learning Methods 19

Design of Optimal and Combinational Logic Circuit Using Karnaugh Method in Quantum Circuits 26

A seq2seq based approach for generation of quantum circuits using deep learning 34

Fault Detection Method Using Truth Table in Quantum Circuits 41

Quantum Neural Network Models: Literature Review and Application Analysis 50

Unet With Layer-based Hybrid Convolution For Retinal Vessel Segmentation 59

Development of the Tool that Converts Machine Readable Format to OpenQASM and Quirk for Quantum Computing: tfc2OpenQASM and tfc2Quirk 65

Optimization of Supply Chain Management for Medical Drug Warehouses using Genetic Algorithms 74

Fine Tuning and Comparative Performance Analysis of Pre-trained Transformers for Dialogue Texts Abstractive Summarization 81

Mask R-CNN Based Video Segmentation ın Smart Campus Areas 90

A New Approach to Reduce False Detections in Deepfake Detection 98

Current Technologies for Bioethanol Production 105

The Main Pivot For Resilient City Versus Disaster: Geographic Knowledge 113

The Effects of Pesticides on Aquatic Ecosystems 122

Heavy Metal Pollution and Risks in Aquatic Environments 129

Green Buildings and Environmental Problems 136

A Peroxyelectrocoagulation Method Application to Remove Chemical Oxygen Demand from Tannery Wastewater 143

Effect of Titanium on High Temperature Properties of NiAl-34Cr Eutectic Alloy Produced by Electric Current Assisted Sintering 148

Health Classification for Plants by Using Computer-Aided Deep Learning Methods 166

Harmonics generated during the electric vehicle charging process 173

Sliding mode control of liquid level trainer system 178

G-GLOVE: A VR/AR Glove That Sensates at Your Fingertips 187

FPGA Implementation of Fractional Order Volta’s Chaotic System 192

Forecasting Wind Speed Measured From Nacelle Anemometer: Integrating Empirical Mode Decomposition, Convolutional Neural Network and Gated Recurrent Unit 198

Fractional-Order High-Pass Filter Using Operational Transresistance Amplifier 205

Intelligent Advert Insertion into Videos Using YOLOv4 Object Detection Method and Centroid Tracking Algorithm 211

Speed Control of Single Phase Induction Motor Using Asymmetric PWM with PI Controller 217
Determination of conventional binder properties of bitumen modified with activated carbon from olive pomace and vinasse 224
Seismic Site Effects of Elazığ-Sürsürü District 229
Drought evaluation of Elazığ in Turkey using SPI and SPEI 237
Assessment of the Mechanical Properties of a Masonry Church in Malatya by Non-Destructive Testing 249
Mitigating the out-of-plane seismic vulnerability of unreinforced masonry façades with viscoelastic devices 257
A study on lost time coefficient in determining optimum cycle time 267
at signalized intersections 267
A random forest model optimized with genetic algorithm for cantilever retaining walls 277
Comparison of Flow Trends of The Eastern Mediterranean Basin with Mann Kendall and Innovative Trend Analysis Methods 282
Optimizing Post-Conflict Building Reconstruction in Iraq: A Multi- Criteria Decision-Making Approach in Public Projects 290
An overview of the global land water storage data set release 2 (GLWS2.0) 299
Evaluation of Library Buildings in Terms of Lighting: 305
The Production of Durable Precast Concrete Using Reactive Powder Concrete at Various Mixing Ratios in High-Rise Structures 314
Determination of Flood Risk Areas by AHP and Frequency Ratio Method; A Case Study for Fatsa (Ordu) 320
Location and Seasonal Evaluation of Major Flood Hazards in Rize Province 329
Evaluation of Ceramic Cake Waste in Asphalt Concrete 337
2023 Kahramanmaraş and Hatay earthquakes: Structural seismic performance, 347
Investigation of doleritic rocks around Konakalmaz (Elazig) by Confocal Raman Spectroscopy 354
Changes in the unconfined compressive strength of high plasticity clay with basalt fiber reinforcement 360
Risk Analysis and Risk Assessment in Limestone Quarry: L Matrix Method 366
Degradation of Amoxicillin in the Presence of Metal-free Composite Photocatalysts 372
Selection of ore for boric acid production: Why must use the colemanite ore 381
Numerical Simulation of Ballistic Impact on Layered Kevlar Armor 384
Investigation of Convective Heat Transfer Coefficient in Air Solar Collector Assisted Greenhouse Dryer by Experimental and Artificial Intelligence Methods 391
SEM and EDS Analysis Reviews of Wear Behaviors of Carbon Nanotube Reinforced AZ91 and AZ80 Alloys 399
Thermohydraulic performance analysis of a crossflow finned tube heat exchanger 405
Numerical ınvestigation of flow and heat transfer in hybrid corrugated channels with different winglet forms 411
Meso-Mechanic Analysis of Laminated Composites Reinforced with Aluminum Mesh 420
A Review on Heat Shields 426
Comparison crushing performance of various types of 2-D auxetic structures by using topology optimization 431

Transport by Land and Air Vehicles, Advantages, Literature Review and Classification of Flying Cars 443
NOx emission reduction in a biodiesel-powered diesel engine with adiabatic humidification technique 450
Influence of welding tool advance speed on weld tensile strength in friction stir lap welding of 7075-T651 aluminum alloy plates 459
Development Of Hybrid (Metal & Plastic) Brake Pedal For 465
Investigation of Heat Storage Capacities of Organic and Inorganic Phase Change Materials in a Heat Exchanger 472
Investigation of the Effect of Nozzle Diameter and Collision Distance on Resultant Momentum in an Active Protection System 481
Experimental analysis of impinging circular jet on a moving plate 488
The tensile properties of three- dimensional (3D) textile reinforced composites 496
Numerical Analysis of A Pulsating Nanofluid Impinging Jet 500
Energy Efficiency in Public Buildings 509
Modeling the Hourly Distillation Volume of a Distillation Machine with a Parabolic Dish-Type Collector Using a Support Vector Machine 515
Receptance Based Dynamic Structural Modification of an Unmanned Combat Aerial Vehicle (UCAV) Model 523
Investigation of the effects on support amounts of changing the coefficients in the YEKDEM formulation 532
Design of Spin Coating Unit and Parameters Affecting the System 538
Numerical Analysis of Battery Thermal Management System Include Phase Change Material at Temperatures Lower than Normal Conditions 545
Retrogression and Reaging of a Flow Formed 7075 Aluminum Alloy 555
Confocal Raman Studies on mafic volcanics north of Fahribey (Elazığ) 560
Production and Characterization of Graphene Nanohseets+Boron Nitride Nanosheets-doped CdS by Sol-Gel Method 568
The leaching behavior of copper slags in presence of hydrochloric acid and acetone 576
Comparison of photoelectric conversion efficiencies of DSSCs sensitized with velvet red rose and ivy rose dye 580
Characterization of Activated Carbon Produced by Hydrothermal Carbonization Method Using Tea Plant Wastes 586
Design of Pellet Extrusion System for 3D Printers 595
Synchronous Reluctance Motor Design for Washing Machine 602
Harnessing AI and NLP Techniques for Combatting Racism and Xenophobia on Online 609
Classification of Alzheimer's disease using ADNI dataset with deep learning techniques 619
Comparative Study of Deep Learning and Machine Learning Algorithms to Predict Hospitalization to Cardiology on Patients Who Applied Emergency Department with Chest Pain 625
A Cloud GIS Based Street Food Recommender Web App 635
Weather Analysis and Renewable Energy Sources 640

A Novel Dynamometer Design for Bogie Suspension Balancement on Trams: Finite Elements and Statistical Approach 649
Effect of welding tool rotation speed on weld tensile strength in friction stir lap welding of 7075-T651 aluminum alloy sheets 658
High Temperature Oxidation and Hot Corrosion Behavior of NiAl-34Cr Eutectic Alloys With Different Fe Contents 664
Investigation of Short Column Damages After 6 February 2023 Kahramanmaraş Earthquakes 682

International Conference on Advances and Innovations in Engineering

A Review on Physical Unclonable Function(PUF)-based Security Solutions in Cryptography

Seyfullah KANER[1] , Ali Murat GARİPCAN [2], Ebubekir ERDEM [3]
[1]Muş Alparslan University, Department of Distance Education Application and Research Center, Muş-Türkiye,
[2]Fırat University, Department of Computer Engineering, Elazığ-Türkiye,
[3]Fırat University, Department of Computer Engineering, Elazığ-Türkiye
[1]s.kaner@alparslan.edu.tr, [2]agaripcan6223@gmail.com, [3]aberdem@firat.edu.tr

[1](ORCID: 0000-0001-5576-0582), [2](ORCID: 0000-0002-9659-8785),[3](ORCID: 0000-0001-7093-7016)

Abstract

In this study, a compilation and analysis of Physical Unclonable Functions (PUFs) are presented. PUFs play an important role in various applications in the field of information security, such as secure key generation and identity authentication. PUFs provide a unique set of features based on physical properties that are primarily used as hardware components. Particularly, due to their ability to generate unique output bits specific to the physical hardware they operate on and their unclonability, PUFs are frequently used in authentication mechanisms that employ cryptographic protocols. The study addresses different PUF architectures based on various design principles, their implementation forms, security vulnerabilities, and advantages against advanced cryptographic attacks. In addition to fundamental design paradigms, the study also provides explanatory information about the cryptographic purposes and statistical verification methods of PUFs. The aim of the study is to contribute to the development of protocols aimed at enhancing electronic design security by focusing on the current status of PUF technologies and their future potential in terms of information security. Furthermore, we believe that understanding the potential of PUF technologies will guide security researchers and application developers. In light of technological advancements, PUF technologies will play a significant role in the development of effective cryptographic solutions against advanced attacks, both in terms of quantity and effectiveness, for information security.

Keywords: cryptographic protocols, electronic design security, information security, physical unclonable functions (PUFs)

1. Introduction

In today's world, a significant and crucial portion of information is constituted by messages and data transmitted over publicly accessible digital networks. The transfer of these data, which are central to communication, via these networks brings forth the necessity of ensuring their absolute protection due to potential security issues that may arise during transmission. Cryptographic methods, employed to ensure the security of communication between recipients and senders, play a significant role in information security [1].

Modern cryptographic protocols can be implemented on various integrated circuit devices such as Field-Programmable Gate Arrays (FPGAs), Application-Specific Integrated Circuits (ASICs), Digital Signal Processors (DSPs), and others. While these protocols provide a secure computation enclave and easy implementation capabilities, the security of integrated circuits has become a significant issue due to high information security requirements. Authentication, identification, and key generation are crucial security risks associated with integrated devices. Therefore, the confidentiality of a stored key on an integrated circuit, without proper protection, does not ensure an adequate level of cryptographic security against attackers. Moreover, ensuring the security of a key throughout the usage lifespan of an integrated circuit is not trivial without specialized protection. For instance, even if a key stored in non-volatile memory (NVM) without specialized protection is physically assigned to a unique key entity, it remains vulnerable to copying. The continuous presence of such critical information within the system occasionally creates security vulnerabilities. Furthermore, the generation and distribution of keys are also highly

[1]Corresponding author

critical for system security. Hence, for device security, processes such as authentication and key generation should encompass the creation and identification of unique IDs for embedded devices [1-2].

Due to their advantages such as resistance to physical attacks, low cost, and resistance to cloning, PUFs have emerged as a prominent alternative security approach. PUFs can be utilized for generating secure identification information by producing environment-specific values and being inherently non-copyable. Unlike keys, PUFs are not assigned from an external source; instead, they are intrinsic to the PUF itself. During production, PUFs can generate unique identification information by utilizing actual random variations present on the device. While these variations, which are attempted to be minimized during the production of integrated circuits, might be measurable, creating a physical copy of them remains infeasible. This is because it is considered impossible to fully control micro and nano-scale manufacturing variations. Easily obtainable yet difficult to predict, this identification information also represents a unique signature or biometric data akin to a fingerprint of the integrated device. By utilizing these functions capable of generating hardware-specific outputs, robust authorization protocols can be established, potentially providing solutions to the challenges of key generation and storage [3].

Due to the distinctive physical characteristics of circuits, it is impossible for the device-specific identification information generated by a PUF to belong to a different IC or to be reproduced by an attacker. The PUFs produce output responses by receiving challenge inputs in the form of (challenge-response), as illustrated in Fig. 1. Thus, during the characterization of these functions, challenge-response are used together. The challenge is typically an externally applied stimulus to the circuit, while the response is the corresponding device-specific identification information generated in reaction to this stimulus [2-4].

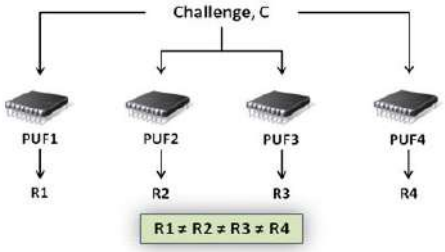

Figure 1. Functional description of PUFs

PUFs are utilized in various domains requiring security, such as intellectual property protection (IP), authentication, chip tracking, personal data and private communication security, Radio Frequency Identification (RFID) technology, and the Internet of Things (IoT). In the literature, numerous PUF architectures have been proposed for these purposes, employing different design paradigms.

Singh et al. [5] proposed a novel PUF design using a three-input arbiter-based approach. Initially, they designed a priority arbiter using a simple arbiter, two 2:1 multiplexers, and an exclusive-OR (XOR) gate. Through their conducted tests and the application of error correction techniques, they demonstrated achieving 100% reliability and 49.63% uniqueness. In another study, Wisiol and Pirnay [6] revealed that XOR Arbiter PUFs with an even number of arbiter chains exhibit inherently biased responses, even when all arbiter chains are perfectly unbiased. Siddhanti et al. [7] employed arbiter PUFs for runtime secure key generation. They implemented their design on an Artix-7 FPGA and measured a reliability level of 92% using error correction mechanisms. Hazari et al. [8] analyzed the vulnerability of the XOR Random Output PUF (ROPUF) to machine learning attacks. They examined the XOR-Inverter ROPUF trained with different machine learning models using the Challenge-Response Pairs (CRPs) data. According to their analysis, Artificial Neural Network models were able to train on XOR-inverter based PUF CRPs with nearly 99% training accuracy and predict around 69.41% of the CRPs. Alsulami and Niamat [9] conducted a performance analysis of an AND-Inverter based RO-PUF. They determined that a 3-stage AND-Inverter RO-PUF exhibited higher uniqueness 47.5% and ideal bit mismatch 50% rates. On the other hand, a 7-stage AND-Inverter RO-PUF achieved the best homogeneity 50.07% and ideal bit mismatch 50% values. Chauhan et al. [10] introduced a study involving a RO-PUF-based Random Number Generator (RNG) design named C-RO-PUF. Their proposed C-RO-PUF design comprises a cascaded RO-PUF design using Linear Feedback Shift Register (LFSR). They demonstrated that the suggested C-RO-PUF design exhibits reliability-enhancing features by increasing the number

of CRPs. In their study, Aung et al. [11] investigated the use of Static Random Access Memory (SRAM) PUFs for the security of IoT devices. Using the data remanence method, they derived a 128-bit SRAM PUF from initially 512-bit SRAM values. They measured an error rate of $3 \cdot 77 \times 10^{-8}$ and a stability rate of 99.98% for the derived SRAM PUF. Shifman et al. [12] have proposed a more reliable SRAM PUF in their study. This suggested PUF was manufactured using the TSMC $65 - nm$ process and is more reliable compared to previous-generation SRAM PUFs. In these PUF arrays, a new pre-selection test was conducted, demonstrating its effectiveness in eliminating all unstable cells $20 - 25\%$. Silverio et al. [13] presented a low-cost and semi-compact 128-bit key encryption optical system by combining a PUF identifier used in optical authentication with the use of an organic-inorganic hybrid structure. They utilized identity verification decisions based on Hamming distances to determine threshold values for optimal decryption and highlighted it as a promising approach for secure and robust encryption systems. Lee et al. [14] proposed optical authentication for spin-orbit torque (SOT) devices. They emphasized the potential of SOT devices for secure key generation due to their durability and high repeatability. They presented a simple optical method based on magneto-optical Kerr effect to authenticate the suggested SOT PUF device, and calculated its reliability as $97.8 \pm 1.03\%$.

In this review informative insights and evaluations regarding the types of PUFs and their application methods on reconfigurable integrated circuits such as FPGAs and ASICs. Within this study, elucidation is given to the fundamental randomness processes of each PUF architecture, as well as their design methodologies, cryptographic purposes including key management, authentication, and design security. Furthermore, acomparative analysis is presented, covering both the cryptographic utility purposes and potential vulnerabilities, along with possible attack and defense strategies related to these weaknesses. The primary objective of this study is to establish a foundational comprehension of essential concepts and principles concerning PUF design for the readers, aiming to facilitate their understanding. This aspect will also assist readers in accurately comprehending future academic endeavors and potential contributions in the field of PUF, thereby fostering a more comprehensive understanding of the literature.

The remaining sections of the study are organized as follows: The second section provides explanatory information about typical PUF architectures and their application areas. In the third section, the cryptographic purposes of PUFs are addressed. The fourth section delves into attack and defense strategies concerning PUFs, along with security risks. Concluding with the summary of the study, the final section encapsulates the outcomes while also incorporating prospects for future research endeavors.

2. Typical PUF Methodologies and Basic Areas of Usage

PUFs, hardware-based security mechanisms used in applications such as secure identity authentication and key generation. This technology relies on the unique characteristics of the physical world to enable differentiation between any two objects, forming an irreproducible and non-replicable foundation. PUFs operate by creating a "challenging question" based on these distinctive features. Each PUF instance generates an output value derived from the unique attributes of a physical object, which is exclusive to that object alone. This output value reflects a statistical aspect of the physical object's specific attribute, making it impossible for any other object to produce the same output. Similarity between PUF responses is measured by Hamming Distance (HD). The Hamming distance is used to quantify the similarity between PUF responses. For two binary vectors of equal length, the HD is calculated as the number of changes needed to transform one vector into the other. The calculation involves performing XOR operation on the bits of the vectors:

$$\boldsymbol{HD}(\boldsymbol{u},\boldsymbol{v}) = \sum_{\boldsymbol{b=0}}^{\boldsymbol{N-1}} (\boldsymbol{u}[\boldsymbol{b}] \oplus \boldsymbol{v}[\boldsymbol{b}]) \quad (1)$$

where in this context $u[b]$ represents the b_{th} bit of vector u.
PUFs can come in various types based on design principles and physical attributes. For instance, among the physical attributes, there can be electrical, optical, or magnetic characteristics. These attributes ensure that each object possesses a unique PUF instance. The primary purpose of PUFs is to provide reliable identity authentication and secure key generation by producing distinct output values. PUFs mitigate the risk of security vulnerabilities by preventing counterfeit identities and copied keys. Furthermore, they serve as a decentralized identity verification method, ensuring secure communication and data transfer.

The equation representing the basic operation of an Arbiter PUF is as follows:

$$\boldsymbol{R = f(C')} \quad (2)$$

Here:

R, represents the output of the PUF (response).

The function f illustrates the internal operation of the Arbiter PUF. This function represents the comparison of external bit paths determined by the input challenge (C').

2.1. Ring Oscillator Based PUF (RO-PUF)

RO-PUF is a silicon PUF that generates a response based on the frequencies of digital ring oscillators on the chip. As the precise frequency of such oscillators is significantly affected by process variations, their exact measurement will contain unpredictable and device-specific information. The initial concept of ROPUF was proposed by Gassend and colleagues [15], and it relies on a single reconfigurable oscillator foundation.

An RO-PUF consists of a series of ring oscillators, each composed of a single number of inverters, forming a closed loop. The oscillation frequency of the RO is approximately calculated as follows:

$$\boldsymbol{f_{RO} = \frac{1}{2} \cdot n_{\text{stages}} \cdot \tau_{INV}} \quad (3)$$

Here, n_{stages} represents the number of stages in the RO, and τ_{INV} is the nominal time delay of each inverter. The total delay in an RO loop should also include the delays caused by the paths connecting the active devices to each other. Therefore, two ROs with the same number of stages and the same configuration should have the same characteristic frequency. However, the variability in the production processes of Complementary Metal-Oxide-Semiconductor (CMOS) integrated circuits leads each RO to have a unique operating frequency. This enables the individual identification of different instances of the circuit. Typically, an inverter in the chain is replaced with a not-AND (NAND) gate to enable or disable the oscillation [16]. The RO structure in an RO-PUF is depicted in Fig. 2.

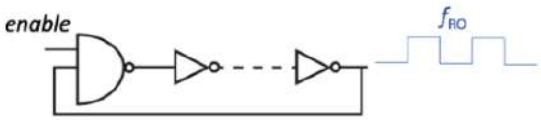

Figure 2. Structure of one RO in an RO-PUF

2.2. Arbiter PUF

Arbiter PUF were initially introduced in the articles [17-18]. These functions consist of k stages, such as multiplexers for instance. Two electrical signals compete simultaneously and in parallel through these stages. Precise paths are determined by k external bits $b_1 \ldots . b_k$ applied to the stages, where the i_{th} bit is applied to the stage. After the final stage, a memory cell called an "arbiter element" determines whether the upper or lower signal arrived first and produces a corresponding output of zero or one. The external bits are generally considered as the challenge C of this PUF, so $C = b_1 \ldots . b_k$, and the output of the arbiter element is interpreted as the response. The Arbiter PUF structure is depicted in Fig. 3.

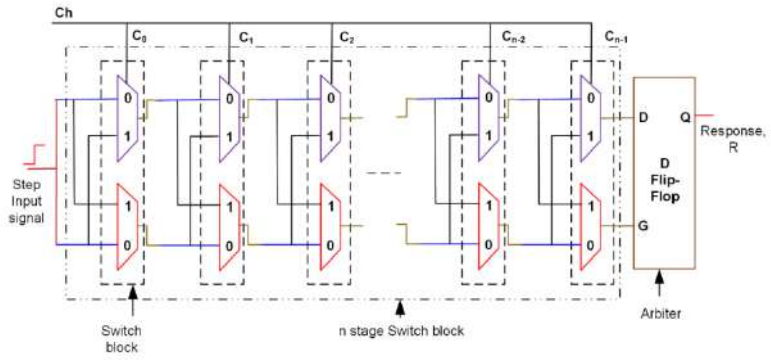

Figure 3. Arbiter PUF

2.3. Static Random Access Memory (SRAM) PUF

As the name suggests, the stable structure of two consecutive inverters is utilized to increase the trip point difference, with an equal probability of logical states $'1'$ or $'0'$. Previous SRAM PUFs used the power-up state of $6T$ SRAM cells, while some recent works added specialized pull-up/pull-down transistors to allow multiple evaluations of cells without the need to toggle the entire supply for each evaluation. An example of such an implementation is shown in Fig. 4. Prior to evaluation, when the $'En'$ signal is low, the internal nodes are held at $'O'$ and $'OB'$ at the Vdd level, preventing the cell's access transistor from conducting. Once 'En' is activated, the access transistor becomes conductive, and $'O'$ / $'OB'$ begins to discharge towards $Vdd/2$. The mismatch-induced trip point difference between the two inverters is amplified by a positive feedback loop, causing the cell to approach a state where one internal node is $'0'$ and the other is $'1'$ [19]. The SRAM-based PUF cell is illustrated in Fig. 4.

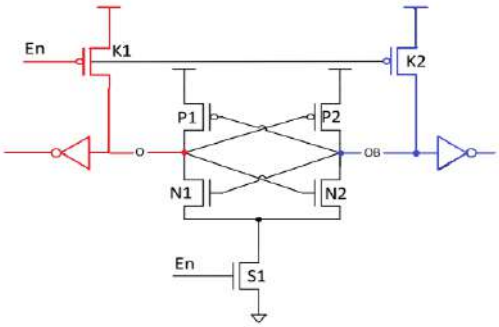

Figure 4. SRAM-based PUF cell

2.4. Optical PUF

A precursor to PUFs based on utilizing unclonable physical irregularities is referred to as the Unique Object (UNO). During the Cold War era, for instance, a thin layer of light-reflecting particles was sprayed onto the surface of nuclear weapons, forming a structure where particles were randomly distributed. Consequently, the interference pattern that emerges after illumination becomes unique and unpredictable based on the viewing angle. Among the earliest known PUFs, the optical PUF stands out as a physically one-way function. The goal here was to create a one-way function using physical methods rather than number theory. Particularly, when illuminated at a specific angle, a complex interference-based two-dimensional dot pattern is generated within a heterogeneous transparent plastic token, and this pattern is recorded using a high-capacity device camera. In Fig. 5a, a photography of the PUF token is shown with its respective sample holder that was idealized to block most of the external light sources, having only a small orifice for the laser to illuminate the sample. Moreover, in Fig. 5b, an example image of the speckle produced is shown where it is noticeable the granular profile of the pattern [13], [2].

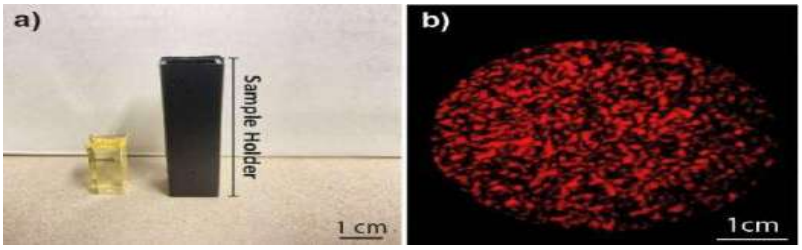

Figure 5. Photography of a) organic-inorganic hybrid, and its respective sample holder, used as a PUF device and b) the speckle pattern produced upon the laser incidence on the token.

Cryptographic Applications of PUFs

PUFs play a significant role in cryptographic protocols within the field of information security. The unique attributes of PUFs can be harnessed for secure identity authentication, key generation, and other cryptographic applications. In this section, the cryptographic purposes of PUFs will be discussed in detail.

3.1. Secure Key Generation

When used for secure key generation, the output values derived from the unique attributes of each object in PUFs can serve as strong and unpredictable cryptographic keys. This simplifies key management systems and prevents the physical copying of keys. Unlike traditional key generation methods, where keys might be generated algorithmically or stored centrally, PUFs harness the individual characteristics of each device. This uniqueness greatly enhances security, as it renders keys virtually impossible to predict or replicate.

3.2. Identity Verification and Authorization

PUFs are employed in identity verification mechanisms, enabling users to securely prove their identities by utilizing the unique attributes of their physical objects. This helps prevent the use of counterfeit identities and unauthorized access attempts. In the realm of identity verification and authorization, PUFs present a stark contrast to traditional methods. While conventional approaches often rely on passwords, PINs, or knowledge-based authentication, PUFs harness the inherent physical uniqueness of electronic components to provide a new level of security. Traditional methods are susceptible to various attacks, including brute force, password cracking, and phishing, while PUFs bolster security, making it exceptionally challenging for attackers to impersonate legitimate users. PUFs strengthen Two-Factor Authentication (2FA) with hardware tokens, increasing the effectiveness of online account protection. Furthermore, they play a pivotal role in decentralized identity systems, empowering users with self-sovereign, privacy-preserving identities while reducing the dependence on centralized authorities.

3.3. Usage in Cryptographic Protocols

PUFs can be utilized to enhance the security of cryptographic protocols. In the realm of cryptographic protocols, PUFs have emerged as a versatile and robust tool with numerous applications. These innovative devices find application in various critical aspects of cryptographic security, including key generation, where PUFs leverage the unique physical characteristics of individual chips or hardware to generate cryptographic keys that are inherently resistant to cloning or replication. PUFs also play a pivotal role in authentication by providing a secure means to verify the authenticity of devices or users, ensuring that only authorized entities gain access. Additionally, PUFs contribute significantly to data encryption, enhancing the security of data by generating and managing encryption keys in a manner that is highly resistant to tampering or unauthorized access. Thereby bolstering the overall security of cryptographic protocols in a wide range of applications.

When employed in cryptographic protocols, PUF technology can enhance hardware-based security. Thanks to their unique and unclonable attributes, PUFs can effectively contribute to areas such as key management, identity verification, and secure communication. Table 1 demonstrates how PUF technology can be integrated into various cryptographic protocols and the security domains in which it can be utilized.

Table 1. Integration of cryptographic protocols with PUFs

Cryptographic Protocol	PUF Integration	Purpose and Usage Areas	Security Contribution
Key Generation	Powerful key generation from PUF	Encryption, Authentication	Key Security
Authentication	PUF-based authentication	Secure Sessions over the Internet, Physical Access Control	Identity Security, Authorization
Data Encryption	Encryption key generation with PUF	Data Security, Privacy	Data Encryption Security
Message Verification	Digital signature verification with PUF	Data Integrity, Authorization	Message Integrity and Authentication
Token Based Security	PUF-based secure authentication	Multi-Factor Authentication, Data Access Control	Identity and Data Security
Distributed Key Management	Secure Key Distribution with PUF	Multi-Device Key Sharing	Key Security and Distribution

PUF Security and Defense Against Attacks

The PUF stands out as a significant component of modern information security. PUF is a security mechanism based on generating random and unique keys through the measurement of unique physical attributes in electronic devices. Thanks to these distinctive characteristics, PUFs are utilized in a range of applications, from device authentication to encryption key generation. However, it's crucial to remember that PUFs are inherently sensitive and require defense against various attacks. PUF security aims to prevent attackers from modeling, emulating, or manipulating PUF responses. In this context, different strategies and defense approaches have been developed to enhance security.

Table 2 summarizes some important works in PUF security and defense against attacks. These works include innovative methods developed to enhance PUF security and resist various attack types. The information in the table reflects a broad spectrum of research in PUF security, aiding our understanding of advancements in this field.
This table presents only a snapshot of PUF security and defense against attacks research. In the future, the development of new strategies and defense mechanisms in the battle between more complex and robust PUF technologies and more sophisticated attack methods will continue to be a crucial step in the field of information security.

Table 2. PUF security and defense against attacks studies

Title of Study	Purpose	Type of PUF Used	Attack Types	Defense Approaches	Results
Efficient Transfer Learning on Modeling Physical Unclonable Functions [20]	Transfer learning in modeling attacks on physical unclonable functions (PUFs)	Arbiter PUF	Modeling attacks machine learning model	Transfer learning techniques	The study demonstrates the effectiveness of transfer learning in modeling attacks on PUFs
Physical Unclonable Functions-based Linear Encryption against Code Reuse Attacks [21]	Defend against code reuse attacks (CRA)	Silicon physical unclonable functions (PUF)	Code reuse attacks (CRA)	PUF-based key generation and management with an XOR-based lightweight linear encryption architecture (LEA)	Protection against malicious code injection type attacks with low hardware and increased uptime
Defending against model extraction attacks with physical unclonable function [22]	To protect DNN models from being stolen by attackers	Arbiter PUF	Black-box model extraction attacks, Known plaintext attacks	Training a corresponding PUF model at the service provider side	Attacker's ability to extract an effective model is limited
On the Effectiveness of the Remanence Decay Side-Channel to Clone Memory-Based PUFs [23]	Introducing fault injection via remanence decay for memory-based PUFs non-invasive exploitation.	Memory-based PUFs	Differential template attacks on PUF-enabled cryptographic devices, Data remanence experiment-based attacks.	Controlling the remanence decay in the SRAM. Using accurate equipment for precise control of remanence decay.	Showing attack feasibility via experimental validation; noting setup limitations, proposing performance-enhancing improvements.
Initial tamper tests of novel tamper-indicating optical physical unclonable functions [24]	To test the tamper-indicating ability of Optical PUFs	Optical physical unclonable functions	Mechanical, thermal, and chemical attacks	Wavefront-shaping controlled reflection	The material/method showed robust tamper-indicating ability.

4. Conclusions

PUFs play a significant role in fields such as reliable identity authentication, key generation, and hardware security, with expectations for further growth and development in the future. The future potential of PUF technology is quite exciting, offering various possibilities in different areas. Some of these areas include the IoT, Biometric and Medical Applications, Data Security and Encryption, and Application and Hardware Security. This review and analysis on PUFs have addressed the role of PUF technology in critical areas like secure identity authentication, key generation, and hardware security. PUFs have the potential to provide reliability and security by utilizing the unique attributes of physical objects.

In today's world, the constantly increasing threats and attacks in information security require stronger and more effective security solutions. PUFs play a crucial role in addressing this gap across various application areas. The use of PUF technology in secure key generation, identity verification, electronic design security, and many other fields enables the creation of more robust and reliable systems from a security standpoint. The significance of PUF technology lies in addressing fundamental security concerns like reliability, authenticity, and protection against counterfeiting. PUFs are particularly important in critical areas such as secure data transmission, identity authentication, and hardware security in today's rapidly evolving digital age.

In conclusion, the potential and future role of PUF technology are promising. The aim of this study is to explain the fundamental principles of PUF technology, its design architectures, cryptographic application areas, and security potential, while raising awareness in this field. Expanding the reliability and application areas of PUF technology will be a crucial step in providing more effective and robust solutions against future security challenges.

5. References

[1] Hatti, K., & Paramasivam, C. (2022). Design and implementation of enhanced PUF architecture onFPGA. *International Journal of Electronics Letters*, *10*(1), 57-70.

[2] Gao, Y., Al-Sarawi, S. F., & Abbott, D. (2020). Physical unclonable functions. *Nature Electronics*, *3*(2), 81-91.

[3] Bernard, F., Fischer, V., Costea, C., & Fouquet, R. (2012). Implementation of ring-oscillators-based physical unclonable functions with independent bits in the response. *International Journal of Reconfigurable Computing*, *2012*, 13-13.

[4] El-Hajj, M., Fadlallah, A., Chamoun, M., & Serhrouchni, A. (2021). A taxonomy of PUF Schemes with a novel Arbiter-based PUF resisting machine learning attacks. *Computer Networks*, *194*, 108133.

[5] Singh, S., Bodapati, S., Patkar, S., Leupers, R., Chattopadhyay, A., & Merchant, F. (2022, October). Pa-puf: A novel priority arbiter puf. In *2022 IFIP/IEEE 30th International Conference on Very Large Scale Integration (VLSI-SoC)* (pp. 1-6). IEEE.

[6] Wisiol, N., & Pirnay, N. (2020). Short paper: XOR arbiter PUFs have systematic response bias. In Financial Cryptography and Data Security: 24th International Conference, FC 2020, Kota Kinabalu, Malaysia, February 10–14, 2020 Revised Selected Papers 24 (pp. 50-57). Springer International Publishing.

[7] Siddhanti, A. A., Bodapati, S., Chattopadhyay, A., Maitra, S., Roy, D., & Stănică, P. (2019). Analysis of the strict avalanche criterion in variants of arbiter-based physically unclonable functions. In *Progress in Cryptology–INDOCRYPT 2019: 20th International Conference on Cryptology in India, Hyderabad, India, December 15–18, 2019, Proceedings 20* (pp. 556-577). Springer International Publishing.

[8] Hazari, N. A., Oun, A., & Niamat, M. (2019, August). Analysis and machine learning vulnerability assessment of XOR-inverter based ring oscillator PUF design. In *2019 IEEE 62nd International Midwest Symposium on Circuits and Systems (MWSCAS)* (pp. 590-593). IEEE.

[9] Alsulami, F., & Niamat, M. (2020, July). Performance study of FPGA based AND-inverter ring oscillator PUFs. In *2020 IEEE International Conference on Electro Information Technology (EIT)* (pp. 194-199). IEEE.

[10] Chauhan, A. S., Sahula, V., Mandal, A. S., & Dutta, A. (2020, January). Intensifying Challenge Obfuscation by Cascading FPGA RO-PUFs for Random Number Generation. In *2020 33rd International Conference on VLSI Design and 2020 19th International Conference on Embedded Systems (VLSID)* (pp. 195-200). IEEE.

[11] Aung, P. P., Mashiko, K., Ismail, N. B., & Yee, O. C. (2020). Evaluation of SRAM PUF characteristics and generation of stable bits for IoT security. In *Emerging Trends in Intelligent Computing and Informatics: Data Science, Intelligent Information Systems and Smart Computing 4* (pp. 441-450). Springer International Publishing.

[12] Shifman, Y., Miller, A., Keren, O., Weizmann, Y., & Shor, J. (2018). A method to improve reliability in a 65-nm SRAM PUF array. *IEEE Solid-State Circuits Letters*, *1*(6), 138-141.

[13] Silvério, T., Dias, L., Ferreira, R. A., & André, P. S. (2021, October). Optical Authentication of Physically Unclonable Functions Using Flexible and Versatile Organic-Inorganic Hybrids. In *2021 SBMO/IEEE MTT-S International Microwave and Optoelectronics Conference (IMOC)* (pp. 1-3). IEEE.

[14] Lee, J. K., Lee, J., Yoon, S. I., Lee, M. H., Lee, J. S., Jang, Y., ... & Kim, Y. K. (2023). Optical Verification of Physically Unclonable Function Devices Based on Spin-Orbit Torque Switching. *Advanced Electronic Materials*, 2300056.

[15] Gassend, B., Clarke, D., Van Dijk, M., & Devadas, S. (2002, November). Silicon physical random functions. In *Proceedings of the 9th ACM Conference on Computer and Communications Security* (pp. 148-160).

[16] Martinez-Rodriguez, M. C., Camacho-Ruiz, E., Brox, P., & Sánchez-Solano, S. (2021). A configurable RO-PUF for securing embedded systems implemented on programmable devices. *Electronics*, *10*(16), 1957.

[17] Gassend, B., Lim, D., Clarke, D., Van Dijk, M., & Devadas, S. (2004). Identification and authentication of integrated circuits. *Concurrency and Computation: Practice and Experience*, *16*(11), 1077-1098.

[18] Lee, J. W., Lim, D., Gassend, B., Suh, G. E., Van Dijk, M., & Devadas, S. (2004, June). A technique to build a secret key in integrated circuits for identification and authentication applications. In *2004 Symposium on VLSI Circuits. Digest of Technical Papers (IEEE Cat. No. 04CH37525)* (pp. 176-179). IEEE.

[19] Shifman, Y., & Shor, J. (2022). Preselection methods to achieve very low BER in SRAM-based PUFs—a tutorial. *IEEE Transactions on Circuits and Systems II: Express Briefs*, *69*(6), 2551-2556.

[20] Wang, Q., Aramoon, O., Qiu, P., & Qu, G. (2020, March). Efficient transfer learning on modeling physical unclonable functions. In *2020 21st International Symposium on Quality Electronic Design (ISQED)* (pp. 1-6). IEEE.

[21] Qiu, P., Lyu, Y., Zhang, J., Wang, X., Zhai, D., Wang, D., & Qu, G. (2016, June). Physical unclonable functions-based linear encryption against code reuse attacks. In *Proceedings of the 53rd Annual Design Automation Conference* (pp. 1-6).

[22] Li, D., Liu, D., Guo, Y., Ren, Y., Su, J., & Liu, J. (2023). Defending against model extraction attacks with physical unclonable function. *Information Sciences*, *628*, 196-207.

[23] Oren, Y., Sadeghi, A. R., & Wachsmann, C. (2013). On the effectiveness of the remanence decay side-channel to clone memory-based PUFs. In *Cryptographic Hardware and Embedded Systems-CHES 2013: 15th International Workshop, Santa Barbara, CA, USA, August 20-23, 2013. Proceedings 15* (pp. 107-125). Springer Berlin Heidelberg.

[24] Anderson, B. R., Gunawidjaja, R., & Eilers, H. (2017). Initial tamper tests of novel tamper-indicating optical physical unclonable functions. *Applied Optics*, *56*(10), 2863-2872.

International Conference on Advances and Innovations in Engineering

A Deepfake Image Detection Approach Based on YOLOv3

YOLOv3'e Dayalı Deepfake Görüntü Algılama Yaklaşımı

Mert ÇEÇEN[1] , Mehmet KARAKÖSE [2]
[1] Computer Engineering Department, Engineering Faculty, Fırat University, Elazığ, Türkiye.
[2] Computer Engineering Department, Engineering Faculty, Fırat University, Elazığ, Türkiye.
[1]mert.cecen23@gmail.com, [2]mkarakose@firat.edu.tr

[1](ORCID: 0009-0008-3658-047X), [2](ORCID: 0000-0002-3276-3788)

Abstract

Increasing use of social and digital media and facilitating data sharing make it very easy to access users' voices, videos and images. Deepfake technology is a technology used to produce fake images or sounds from real images or sounds with deep learning and artificial intelligence techniques. Deepfake technology can produce fake videos or images by learning from large amounts of data with artificial neural networks. Today, it is used in the entertainment, games and film industry, but it is also used in situations such as creating malicious fake news and discrediting individuals. In order not to encounter these situations in the literature, studies have been carried out to detect deepfake images and videos. In this study, real and fake images were collected manually from different datasets or videos with a comprehensive literature search, labeling was performed, and a data set was made by applying the necessary preprocessing steps. With the created data set, YOLO technology, which can detect objects in images quickly and with high accuracy by using Convolutional Neural Networks, is used. Contrary to traditional detection methods, a training was conducted with the YOLOv3 version, which can handle all operations as a single regression problem by calculating class probabilities, and the modeling process was explained. In order to validate the designed model, the performance of the model was tested using different images. As a result of the tests, a model that can detect fake images produced with deepfake technology with an accuracy rate of 95% was obtained.

Keywords: convolutional neural networks, deepfake image detection, deep learning, yolov3

1. Introduction

Today, the increase in the use of the internet environment and the increase in the use of social media and digital media by the users have made it very simple to access the personal information, videos and images of the users in these environments. As a result, the opportunity to use these images has become quite easy by gaining access to the personal images of government officials, business people, celebrities and many others. Deepfakes are a widely used technology for fabricating fake content from real images and sounds using deep learning techniques. It is frequently used in the process of changing human faces using deep learning techniques. Deepfake images are created from artificial neural networks that can learn with large amounts of data. Deepfake images produced using deepfake technology allow a new image to be created as a result of using a person's face on another body. Deepfakes are fake media content created using artificial intelligence to make fake news agendas, fake agendas in the policy area, or personal attacks. If deepfakes are used for malicious purposes, they can damage the reputation of individuals by sabotaging personal data security. Since there is no law to ban deepfakes today, detection of deepfakes is an important element in separating and securing real images and fake image data. Convolutional Neural Networks have started to be preferred especially in studies on facial manipulation in deepfake images. Karras et al proposed a Contested generative network model called StyleGAN to generate images of faces that never existed before [1]. In yet another

[1]Corresponding author

study, Zhu et al. proposed a GAN-based face swapping method based on a generative adversarial network called CycleGAN [2]. Choi et al. have proposed a technique called StarGAN that can be used to change some characteristics of a face such as hair or skin color, gender, age, wearing glasses, and so on[3]. Thies et al. used a productive competitor network-based technique called Face2Face to manipulate facial expressions of people in images [4]. With the widespread use of creating such fake images and the large-scale development of deepfake technology, the methods used to detect images created using this technology have also begun to be developed. For the detection of deepfake images, models were trained using datasets and with the created models, certain signs and anomalies were tried to be detected in order to distinguish fake images from real images. Deepfake Detection technology is used to detect fake images or videos. Deepfake Detection is the process of identifying deepfake content developed for use in detecting fake or modified media content using deep learning techniques and artificial intelligence. There are different studies in the literature on the detection of deepfake images. An open source online platform that can integrate Deepfake detection methods called DeepFake-o-meter has been created by Yuezun Li et al.[5]. Users using this platform choose one of the methods that can upload any video that meets the requirement of not exceeding 50 Mb file size and use it based on the advanced Inception modules, which is one of the deepfake detection methods offered by the system. These methods are MesoInception4 [6], FWA [7], VA-MLP, Xception-c23, ClassNSeg [8], Capsule [9], DSP-FWA, CNNDetection [10] Upconv [11], WM, Selim methods. After the uploaded video passes through Docker containers, the faces in the video are extracted. After the received images go through various preprocessing steps, it is indicated whether the face is fake or not. Sara Concas et al. aimed to design a deepfake detector that is resistant to background and image size variability, which can properly detect images that have been resized and compressed [12]. While performing this operation, firstly OpenForensics dataset [13] divided the input data into 8x8 blocks and processed them with Discrete Cosine Transform. When they tested the CNN architecture they designed, they achieved 99.2% accuracy. Ashifur Rahman et al. have trained a Convolutional neural network that detects deepfakes in low-resolution and short-term video data in the Kaggle Deepfake Detection Challenge (DFDC) and Face Forensics++ datasets [14]. As a result of the training, they obtained an accuracy value of 94.93% in detecting fake videos for the DFDC dataset, while they obtained an accuracy value of 93.2% for the FaceForensics++ Dataset. Shan Jia et al. created a new dataset from DeepFakes with different models at the top. In this set, they created five valid categories for Deepfake videos using Facewap[20] software and Autoencoder models with examples in encoder, decoder, middleware and input data. Over 70% accuracy got in identifying high quality Deepfakes by designing DMA-STA, a simple and effective Deepfakes model no-hold method based on spatial and temporal attention, and evaluated on the DFDM dataset[16]. In these study, a model training was carried out, which is used to determine whether your deepfake viewing is real or fake.

A deep learning and deepfake image detection

In the literature, different deep learning methods have been used for detecting deepfake images and videos within the scope of these studies. Deep learning is a subset of machine learning that uses classification operations and learning methods to represent data in specific formats. The basis of deep learning is based on creating a model capable of predicting outputs using artificial intelligence with a data set as input. While classifying with deep learning, the preprocessing steps significantly strengthen the inputs and irrelevant variations are suppressed significantly [18]. Convolutional Neural Network (CNN), Recurrent Neural Network (RNN), Deep Belief Network, Deep Boltzmann Machine and Deep Auto-Encoder techniques are used in deep learning. Convolutional Neural Networks have achieved great success in areas such as image processing, object detection, face recognition, and video analysis [19]. It is a neural network that contains one or more convolutional layers, subsampling layers and standard multi-layers in Convolutional Neural Networks. Although neural networks are not a new technology, they are based on Alexnet[20] and Imagenet[21] technologies used in the classification of large-scale data. In the working principle of Convolutional Neural Networks, there is a structure consisting of layers that can automatically extract and represent the complex features of the data. YOLO is a technology for taking the entire image at once and estimating the bounding box coordinates and class probabilities. The training process of YOLO technology ensures that it has a better generalization ability in general, as it is created using a large dataset. In addition, it can achieve better results as it offers users the opportunity to use various data augmentation techniques. In this study, YOLOv3 technology using Convolutional Neural Networks was used. YOLOv3 consists of 106 layers in total[22]. The YOLOv3 architecture consists of 3 different layers. This architecture is shown in Figure 1.

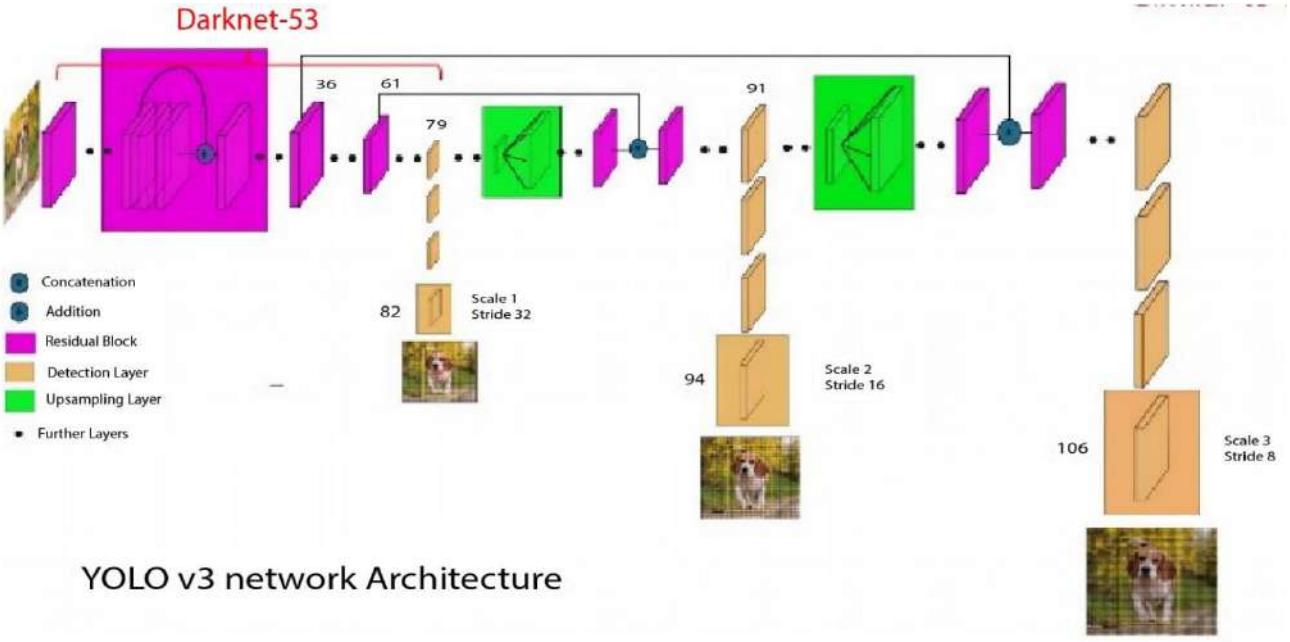

Figure 1. Architecture of YOLOv3 [22]

YOLOv3, three different estimation scales are used when estimating. The detection layer is used to detect feature maps of three different dimensions, consisting of 32, 16, and 8 steps, respectively. The deepfake images included in the dataset used in the study were resized to 416 x 416. In order to train the model quickly and with high accuracy, the training process was carried out using YOLOv3 technology.

2. Proposed Method

Deepfake is a technology that uses a person's face to be mounted on another person's body to obtain a different image. Internet users first encountered the images produced by this technology in 2017. The first studies to produce deepfakes occurred in 2014 by training the Artificial Neural Networks (GAN) with very large data sets. Deepfakes, a type of artificial media that uses artificial intelligence to transform a person's image into a manipulated photo or video, can make people appear to be saying or doing things they're not actually doing. Research reports state that the images, sounds or videos produced with this technology can be used to facilitate crime in the coming years. Within the scope of preventing these events from occurring, a study was carried out to detect the images produced by deepfake in this study. The original images of the people and the fake images produced with deepfake technology from these original images were collected manually and turned into a dataset. The generated dataset is divided into training, validation and test data. The validation data was used to measure the accuracy of the model, while the test data was used to test the model after the model was created. The operations performed are shown in the block diagram in Figure 2.

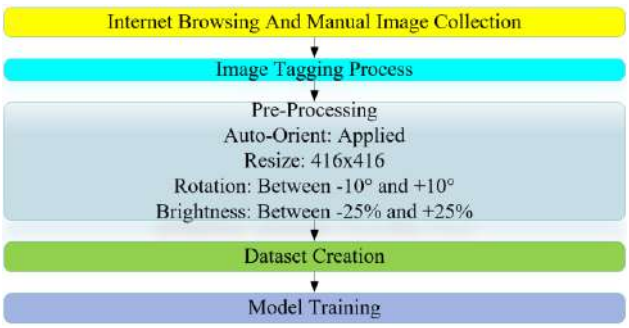

Figure 2. Model training block diagram

In the block diagram in Figure 2, the process of manually displaying the dataset to create, image creation, preprocessing and model development is given step by step in the block diagram.

Dataset creation and preprocessing

Real and fake images produced with deepfake technology, different from the images or videos on the internet, were collected manually in image format. The collected images were then labeled using the bounding box labeling method. In order to enrich the collected images before transfer, automatic orientation process was applied to the existing images. The input format of all image data was resized to 416x416 to make it ready for the training process using YOLOv3. Then, 10 degrees rotation and 25% brightness adjustment were made on the images for better recognition of each image. After the performed operations, the number of images of the data set was updated to 44100. The clustered datasets are divided into 70% training data, 10% validation data and 20% test data.

Modeling

The results we obtained to show the accuracy of the created data set are included in this section. In order to get better results in the studies, the Graphics Processing Unit (GPU), which can create clear graphics using the processing resources, and the Google Colaboratory technology, which provides cloud environment support that provides a virtual storage, were used. CUDA (Compute Unified Device Architecture) technology produced by NVIDIA company is established in Jupyter Notebook created in Colab environment. While creating the data set, labeling operations were carried out with the bounding box method and Roboflow technology was used for these operations. In order to use the YOLOv3 technology, which can perform object detection using Convolutional Neural Networks (CNN) with the created data set, a Jupyter Notebook was created in the Colaboratory cloud environment created by the Google company, and the necessary code blocks, parameter values, technologies and files were transferred to the cloud environment and the training process was started.

3. Experimental Results

The accuracy of the model trained with the created data set is explained in this section. The studies were carried out in the Google Colaboratory environment, which was created by the Google company, which provides GPU and cloud storage to the users. Images included in the data set to be used for model training were labeled with the bounding box method using Roboflow technology. The Training Charts obtained after applying the necessary preprocessing steps to the created data set are shown in Figure 3.

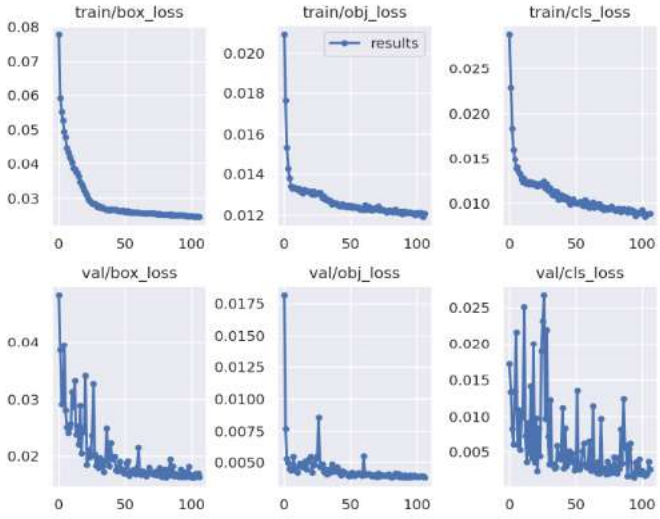

Figure 3. Training graphs loss values

The train values in the graph in Figure 3 represent the measurements of the values of the training set, while the val values represent the measurements of the values of the validation set. The box_loss value focuses on the measure of the loss rate that will occur after the application of the bounding box technique used in labeling operations. Low values in the graph indicate that the model has improved to generalize and the data set is better labeled. The cls_los value shows the measure of the loss rate resulting from the classification. The decrease in the value in the graph indicates that a better classification is done.

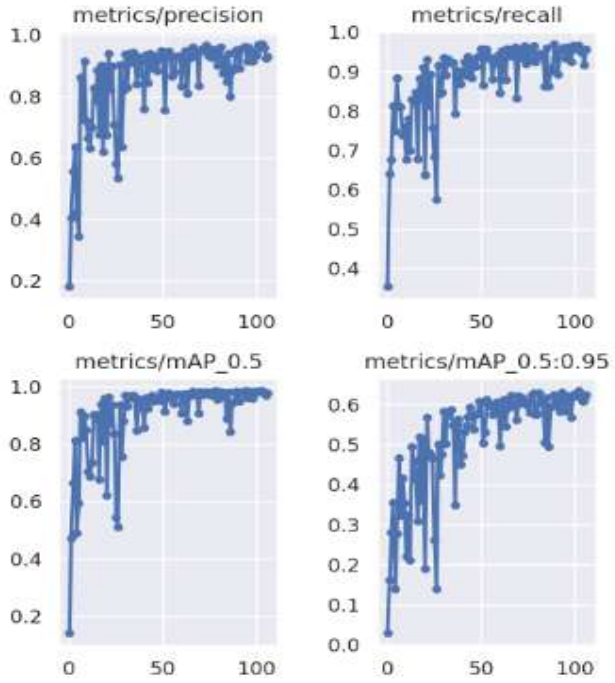

Figure 4. Training graphs metrics values

The precision value in Figure 4 shows the precision values in the given prediction of the model, while the recall value shows the current performance of the system. The value of mAP_0.5 in the other graph indicates the average sensibility value, and the value of mAP_0.5:0.95 indicates the average precision. From the results in the graph, it is seen that the modeling process was successful and a good data set was created.

Experiment study and results analysis

In order to carry out the model training process, firstly, the necessary codes were written in the code block created in Jupyter Notebook, and Darknet technology was put into use and cloned to the cloud environment was carried out. Darknet technology is used to print the detection rate of the images entered into the model to be used in the detection of deepfake images. After the Darknet technology has been cloned, the CUDA technology offered by NVIDIA, which we will use to perform the training, has been uploaded to the cloud.

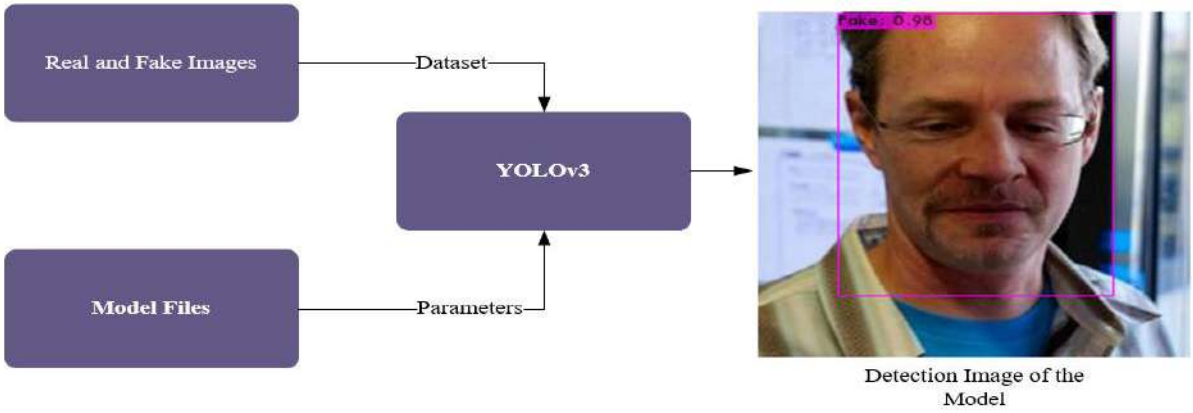

Figure 5. Model architecture

As seen in Figure 5, first of all, real and fake images were collected manually and turned into a data set. The necessary model files and the parameters in the files were prepared and the data set was entered into the YOLOv3 model for training. After the training was carried out with YOLOv3 technology, the required directory was changed and the weight values obtained as a result of the training were entered into the Backup file opened by entering the Google Drive account. According to the weight values obtained, the deep learning average loss value was obtained as 0.1552, different images were entered into the model, and as a result of evaluating the deepfake probability, results above 95% were obtained.

Figure 6. The rates of detection of whether a few of the images in the dataset are fake or real.

Figure 6 shows the accuracy percentages obtained as a result of determining the probability of the image being fake or real by entering the images in the dataset containing deepfake and real images into the model. In order to obtain these values, necessary information was given to the model from the Backup file in which the weight values obtained

as a result of using YOLOv3 technology were recorded, and these ratios were printed with Darknet 53 technology. The results show that the images in the dataset were detected with high accuracy.
Rates obtained in deep learning studies on deepfake images and videos

Many studies have been carried out in the literature using different data sets for the detection of deepfake images and videos. In this article, a table was created showing the accuracy rates obtained from studies using deep learning techniques and the accuracy rates obtained from other studies in the literature. Comparison Results With Studies In The Literature are shown below.

Table 1. Comparison results with studies in the literature

Referance	Dataset	Methods applied to the images used in the model	Accuracy Rates
[12]	OpenForensics	The images were compressed by dividing into 8x8 blocks and training was carried out.	99.20%
[14]	Kaggle Deepfake Detection Challenge	Model training was performed using low-resolution video image data.	94.93%
[14]	Face Forensics++	Model training was performed using low-resolution video image data.	93.20%
This Study	Mixed dataset created by the authors	Model training was carried out with real and fake image data by performing resizing and automatic orientation.	95.00%

In the first study in Table 1 the authors aimed to design a deepfake detector that is resistant to background and image size variability by properly detecting resized and compressed images. While performing this process, they first took the images in the OpenForensics data set as input data and divided them into 8x8 blocks. The obtained outputs were processed with the Discrete Cosine Transform. When they tested the CNN architecture they designed, they achieved 99.2% accuracy. In the second study in the table, the authors have trained a Convolutional Neural Network that detects deep fakes in low-resolution and short-duration video data found in the Kaggle Deepfake Detection Challenge (DFDC) and Face Forensics++ datasets. As a result of the training they performed, they obtained an accuracy value of 94.93% for the DFDC dataset, while an accuracy value of 93.2% for the FaceForensics++ Dataset in detecting fake videos. Finally, in this study, a data set was created by bringing together real images of people from different videos and data sets on the internet and fake images obtained from these images using deepfake technology. Using the YOLOv3 technology working with the Convolutional Neural Network (CNN) with the created data set, a model was created that can detect whether the images are fake or real. This model, which was created as a result of the studies, was found to be 95% successful.

4. Results

The ease of sharing personal images on the Internet and the increase in digitalization have greatly increased the opportunity for people to access their images. With the increase of these images, it is also used maliciously to manipulate the photos or videos of famous individuals, to create and spread fake news content, and to defame or blackmail politicians or government officials. For these reasons, deepfake images have become a growing concern today. In order to prevent these situations, the techniques developed for the detection and identification of deepfake images are also gaining importance. Although deepfake technology is an area with potential risks, it is possible to reduce these risks with the development of detection and prevention methods. In this study, a method has been developed to detect deepfake images. First, a dataset was created and images created with different deepfake techniques were added to this dataset. Then, a model is trained to detect deepfake images with YOLOV3 technology, which uses Convolutional Neural Networks (CNN), one of the deep learning methods. The model obtained as a result of the training was used to evaluate the possibility of deepfake in new images. As a result of model training and evaluation, more than 95% successful results were obtained. This shows that it is an effective method for detecting deepfake images. However, as deepfake techniques are constantly evolving, it is of great importance to maintain a continuous effort to update the model and recognize new deepfake methods. In future studies, it is aimed to enlarge the data set and to get better results by integrating new technologies into our model. In this context, different deepfake images will be collected manually and added to the dataset in order to enlarge the dataset. Then, as a result of training

the expanded data set in different versions of YOLO technology, the rates obtained in these versions will be compared. As a result of the studies, the YOLO version that gives the best result will be selected and it will be provided to help the researchers who will work in this field.

5. Acknowledgements

This study was supported by the TUBİTAK (The Scientific and Technological Research Council of Turkey) under Grant No: 122E676.

6. References

[1] Tero Karras, Samuli Laine and Timo Aila. A Style-Based Generator Architecture for Generative Adversarial Networks. IEEE/CVF Conference on Computer Vision and Pattern Recognition, 2019.

[2] Jun-Yan Zhu, Taesung Park, Phillip Isola and Alexei A. Efros. Unpaired Image-to-Image Translation Using Cycle-Consistent Adversarial Networks. IEEE/CVF International Conference on Computer Vision, 2017.

[3] Yunjey Choi, Minje Choi, Munyoung Kim, Jung-Woo Ha, Sunghun Kim and Jaegul Choo. StarGAN: Unified Generative Adversarial Networks for Multi-Domain Imageto-Image Translation. IEEE/CVF Conference on Computer Vision and Pattern Recognition, 2018.

[4] Justus Thies and Michael Zollh¨ofer and Marc Stamminger and Christian Theobalt and Matthias Nießner. Face2face: Real-Time Face Capture and Reenactment of RGB Videos. IEEE/CVF Conference on Compute Vision and Pattern Recognition, 2016.

[5] Li. Y, Zhang. C, Sun. P, Ke. L, JU. Y, Qi. H and Lyu. S "DeepFake-o-meter: An Open Platform for DeepFake Detection.", China, 2021 IEEE.

[6] C. Szegedy, W. Liu, Y. Jia, P. Sermanet, S. Reed, D. Anguelov, D. Erhan,V. Vanhoucke, and A. Rabinovich, "Going deeper with convolutions,"in CVPR, 2015.

[7] Y. Li and S. Lyu, "Exposing deepfake videos by detecting face warping artifacts," in IEEE Conference on Computer Vision and Pattern Recognition Workshops (CVPRW), 2019.

[8] H. H. Nguyen, F. Fang, J. Yamagishi, and I. Echizen, "Multi-task learning for detecting and segmenting manipulated facial images and videos," in IEEE International Conference on Biometrics: Theory, Applications and Systems (BTAS), 2019.

[9] H. H. Nguyen, J. Yamagishi, and I. Echizen, "Use of a capsule network to detect fake images and videos," arXiv preprint arXiv:1910.12467, 2019.

[10] S.-Y. Wang, O. Wang, R. Zhang, A. Owens, and A. A. Efros, "Cnngenerated images are surprisingly easy to spot... for now," in CVPR, 2020.

[11] R. Durall, M. Keuper, and J. Keuper, "Watch your up-convolution: Cnn based generative deep neural networks are failing to reproduce spectral distributions," in CVPR, 2020.

[12] S. Concas, G. Perelli, G. L. Marcialis and G. Puglist, "Tensor-Based Deepfake Detectıon In Scaled And Compressed Images," University of Cagliari, Italy, 2022 IEEE.

[13] Trung-Nghia Le, Huy H. Nguyen, Junichi Yamagishi, and Isao Echizen, "Openforensics: Large-scale challenging dataset for multi-face forgery detection and segmentation in-the-wild," in Proceedings of the IEEE/ (ICCV), October 2021,

[14] A.Rahman, N. Siddique, M. J. Moon, T. Tasnim, M. Islam, Md. Shahiduzzaman and S. Ahmed, "Short And Low Resolution Deepfake Video Detection Using CNN," 10th Region 10 Humanitarian Technology Conference (R10-HTC), 2022 IEEE.

[15] "Faceswap," https://github.com/deepfakes/faceswap.

[16] S. Jia, X. Li and S. Lyu, , "Model Attrıbutıon Of Face-Swap Deepfake Vıdeos," ICIP 2022 IEEE.

[17] S. Jia, X. Li and S. Lyu, , "Model Attrıbutıon Of Face-Swap Deepfake Vıdeos," ICIP 2022 IEEE.

[18] Y. Lecun and Y. Bengio, "Deep learning - review."

[19] N. Srivastava and R. Salakhutdinov, "Multimodal Learning with Deep Boltzmann Machines,",2012.

[20] Z A. Krizhevsky, I. Sutskever, and H. Geoffrey E., "ImageNet Classification with Deep Convolutional Neural Networks," *Adv.Neural Inf. Process. Syst. 25*, pp. 1–9, 2012.

[21] J. Deng, W. Dong, R. Socher, L.-J. Li, K. Li, and L. Fei-Fei, "Imagenet: A large-scale hierarchical image database," in 2009 IEEE Conference on Computer Vision and Pattern Recognition, 2009, pp. 248-255: IEEE.

[22] A. Belhi, H. Gasmi, A K. Al-Ali, A. Bouras, S. Foufou, X. Yu and H. Zhang, “Deep Learning and Cultural Heritage: The CEPROQHA Project Case Study,” 2019 IEE.
[23] S.V. Viraktamath, M. Yavagal and R. Byahatti, “ Object Detection and Classification using YOLOv3”, International Journal of Engineering Research & Technology, Dharwad, India, 2021.
[24] U. Kulkarni, Meena S M, P. Joshua, K. Rodrigues and S V. Gurlahosur, “Integrated Crowdsourcing Framework Using Deep Learning for Digitalization of Indian Heritage Infrastructure. ”, 2020 IEEE.

International Conference on Advances and Innovations in Engineering

Crowd Analysis by Using Image Processing and Deep Learning Methods

Volkan Yamaçlı[1], Özer Tanrıverdi[2]
[1]Computer Engineering Department, Engineering Faculty, Mersin University, Mersin, Turkey.
[2]Electrical and Automation Department, Vocational School, Toros University, Mersin, Turkey.
[1]vyamacli@mersin.edu.tr, [2]ozer.tanriverdi@toros.edu.tr

[1](ORCID: 0000-0003-0331-8818), [2](ORCID: 0000-0002-5203-4443)

Abstract
One of the main areas of study in computer vision for surveillance is crowd analysis. Numerous tasks are involved, such as crowd density estimate and person counting, crowd tracking, and crowd behavior detection. Many present methods of detection, tracking, and activity recognition, which are only relevant to sparse scenes, do not perform well in crowded settings due to the enormous number of individuals gathered there with frequent and strong occlusions. The total number of people in crowded activities or places such as concerts, celebrations, commemorations, political rallies or demonstrations, sports events, public transportation stations, shopping malls are desired to be estimated due to security and other various reasons. It can be said for a case that whether the approximate number of people in a crowded demonstration on the streets is known, it can be determined how many security guards and security vehicles should be on duty, which roads should be closed, and what kind of traffic arrangement should be made within the scope of the security measures to be taken. Within the scope of this paper, the estimated density of people in a crowded environment is desired to be obtained by means of cameras, cameras, mobile phones. For this purpose, deep learning models namely AlexNet and ResNet are the convolutional neural network architectures used in in this study for image classification and estimation. The results show that images with the features of different angle, color depth, resolution and size can be processed and classified successfully with high accuracy.

Keywords: crowd counting, crowd analysis, people density, deep learning, image processing

1. Introduction

It is crucial to estimate the total number and density of people in crowded activities such as concerts, celebrations, commemorations, political rallies or demonstrations, sports events, public transportation stations, shopping malls for various reasons. Among these reasons; video surveillance, public safety, city planning and planning for the future activities are the most countable. For example; if the approximate number of people in a crowded demonstration on the streets is known, it can be determined how many security guards and security vehicles should be on duty, which roads should be closed, and what kind of traffic arrangement should be made within the scope of the security measures to be taken. Ensuring safety and security in environments with high human density is one of the priority issues. It is important to know the approximate number of people in order to take adequate precautions and make arrangements. In addition to this, benefits will be provided to the crowd gathered at the exit of an event, such as preventing them from waiting for a long time by sending a sufficient number of transportation vehicles such as buses and taxis, and taking action by the responsible persons to create new areas in case the space reserved for the people gathered in an open area for an event is not sufficient. This study will allow the knowledge of people in such places by using deep learning aided classification methods.
The two main categories of crowd counting techniques are supervised and unsupervised. In supervised crowd counting, the input data is predetermined and labeled, and the machine's objective function (hidden model) determination is all that is done. Before the objective function is established in unsupervised crowd counting, the machine is used to categorize and label the raw data [1]. Additionally, there are four categories of supervised crowd counting: detection, density estimation, and CNN. Clustering by counting is included in the unsupervised category.

[1]Corresponding author

The recognition structure, which used a sliding window as a sensor to identify and count the number of individuals at the scene, was the subject of a lot of the early research. Sensing-based methods train object detectors to locate and count each individual in the crowd by determining where they are in relation to one another [2]. Monolithic and part-based detection-based techniques are the two categories. The classifier in the monolithic approach is trained for every body part. For specific bodily parts, a classifier is created using the part-based technique [3]. In order to count the crowd, common features are derived from crowd photos, however their recognition performance is constrained in densely populated settings. Part-based approaches are employed to count pedestrians in order to circumvent this issue by detecting particular body parts, such as the head or shoulders [4]. While fragment-based techniques are used to make object detection in scenarios with high crowd density easier, they are less effective in situations with extremely high crowd densities or noisy background images. The researchers suggested using regression-based approaches to count objects in order to get around this problem. After completing regression between picture characteristics and crowd size, the regression-based technique predicts the number of features [2]. Separating the image or video is against the rules when counting by regression. Through a general analysis of crowd behavior, it calculates the number of crowds. Regression modeling and low-level feature extraction are the two components used. Edges, textures, and gradient characteristics are examples of low-level information that is encoded using the responsibilities of the two components. Then, within the context of surveillance videos, these features are applied and carried out. In order to continue to enhance the mapping between the actual and estimated crowd sizes, the linear regression model is constructed with the realization of the features [5]. Utilizing observed data to estimate a probability density function that is not observable is known as counting by density estimation. By combining the use of spatial data with the density estimate strategy, this technique has made it possible to solve the congestion and clutter problem [1]. While earlier methods dealt with diffraction and scene grouping satisfactorily, the majority of them regressive from spherical characteristics to direct object counts, discarding any spatial information that might have been there. In contrast, later research adopted a linear mapping between local patch features and associated density maps in order to add spatial information into the learning process. As a result, the challenging work of locating and recognizing individual instances of object was avoided, and a novel method for estimating image density was developed [6]. This method's integral over every image region provides the number of objects in that region. Cluster counting is a different method of counting. According to the presumption that visual characteristics and particular ranges of motion are homogeneous, counting by clustering divides similar features into various categories [1]. Image clustering is defined by input picture clustering, also referred to as image segmentation, which transforms the image into a meaningful format and makes it simpler to analyze by segmenting the digital image into a set of pixels or a series also referred to as super-pixels [7].

Recent studies have placed a greater emphasis on deep learning approaches, particularly CNN-based algorithms because of their performance and resilience, as opposed to earlier studies that concentrated on heuristic models, such as detection, regression, and clustering-based methods. Results indicate that while CNN models are more effective in packed datasets, heuristic models perform better in sparse datasets [8]. Today, Convolutional Neural Networks (CNN), a special kind of multi-layer perceptron (MLP), are frequently utilized because they produce the best results in the field of computer vision. CNN was developed by mimicking the human visual system. They are employed in the solving of prediction issues, object recognition, categorization, tracking, and semantic parsing in natural language processing [9]. The fundamental idea is to scan the content from left to right or top to bottom in order to grasp the many properties of the examined image, and then to combine the different local features scanned to classify. The convolutional layer, the pooling layer, and the fully connected layer are the three layers that make up a CNN [8]. The convolutional layer's main function is to apply filters to identify features in the input image and produce several feature maps to aid in identifying or classifying it. A linear function ReLU activation is used to convert the negative pixel values in the feature map to zero values after each convolution process. The output feature map produced by the convolution is sent to the pooling layer. The objective is to create a specific function, such as max pooling, to reduce complexity for more layers. To produce the final classification result, every neuron in the previous layer is connected to every neuron in the following layer in the completely connected layer.
In this study, the crowd density classification is applied to crowd-oriented images by using AlexNet and ResNet-50 deep learning models. Also, by applying learning-rate optimization the training and validation loss are minimized for the current dataset.

2. Dataset Description

In this study, a randomized dataset containing 4 classes is generated by authors or using online search portals and image repositories. Some crowd images are obtained by means of Google-images are some are obtained by online datasets [10], [11]. These generated crowd dataset images have different sizes, resolutions and color depths and were used in this state without any normalization process. The classes are named as CL1, CL2, CL3 and CL4 for corresponding people density of maximum, above-medium, below-medium and minimum, respectively. This dataset contains 160 training, 40 validation and 40 test images. Some random images for each class are given in Figure 1.

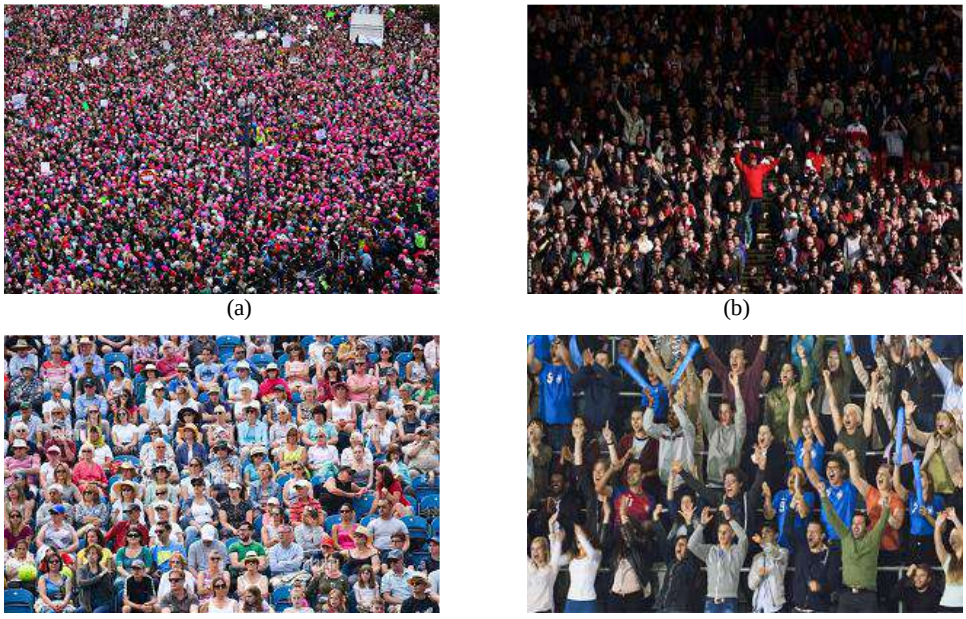

(a) (b) (c) (d)

Figure 1. Exemplary dataset images for each class. (a) CL1, (b) CL2, (c) CL3, (d) CL4

3. Deep Learning Algorithms and Methods

In this study, the CNNs are employed and used to achieve successful classification for crowd image density. A general CNN architecture is given in Figure 2.

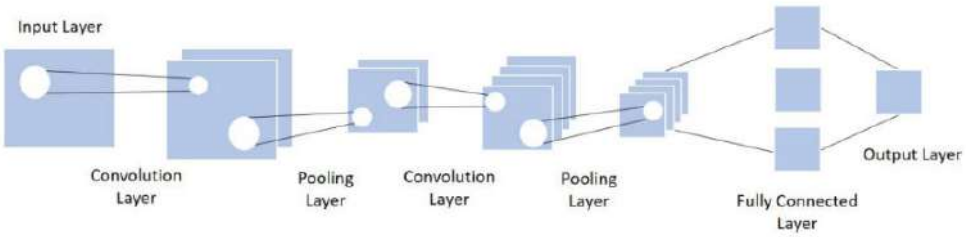

Figure 2. A general CNN architecture [6]

Deep learning-based classification techniques, AlexNet and ResNet-50 architectures are used. In this paper, it is aimed to successfully solve the categorization issue of crowded images by using these CNNs. Due to its originality at the time, it was first introduced, AlexNet is one of the most popular models and a significant milestone in visual recognition tasks of CNNs in image classification studies. Eight layers total in this model, five of which are convolutional and three of which are fully connected [12]. The most significant architectural characteristics that set AlexNet apart from other CNNs are its overlapping pooling and Rectified Linear Unit (ReLU) non-linearity. AlexNet is also a highly quick CNN to train compared to other well-known CNNs. The ReLU function, which offers an

advantage over tanh in terms of training speed, is used by AlexNet in place of the tanh function, which was the industry standard at the time. The input data of AlexNet is chosen as 227×227 pixels RGB image.
Also, another deep learning model, ResNet-50 architecture is used. Various ResNet models are proposed in 2015 [13], implementing the concept of residual learning into CNNs. The most significant and distinctive aspects of ResNet architecture are the use of skip-connections and residual learning model for CNNs to discard the vanishing gradient problem. The ResNet-50 input is used as RGB image data with 224×224 pixels for training and classification. The complexity of ResNet-50 architecture is higher than AlexNet.

4. Results and Discussion

The findings of the suggested deep learning algorithms are presented and discussed in this section. Python 3.10.1 and Tensorflow 2.10.1, Keras 2.10.0 were used for all analyses in this study, on a Windows® 11 computer with an Intel® Core (TM) i7-10700F processor running at 2.90 GHz, 32.0 GB of RAM, and GeForce RTX 3080 GPU. The deep learning parameters, batch size and maximum epoch are chosen as 16 and 400, respectively.
In this study, image data augmentation is also applied to training images by using the *ImageDataGenerator* class of Keras. The augmentation parameters are chosen as given in Table 1.

Table 2. Image data augmentation parameters

Parameter	Value	Parameter	Value
rotation_range	30	width_shift_range	0.2
horizontal_flip	True	height_shift_range	0.2
vertical_flip	True	brightness_range	[0.4, 1.5]
zoom_range	0.5	shear_range	0.2

At the end of the both CNNs, a classification layer containing *softmax* activation function is also added. The learning rate is chosen between 1×10^{-2} and 1×10^{-6}. At first, the training is performed for those minimum and maximum learning rate limits before obtaining the best value. By using the step size of 1×10^{-3}, the optimal learning rate for the current dataset is obtained. An example training and validation for ResNet-50 model for minimum and maximum learning rate values are given in Figure 3.

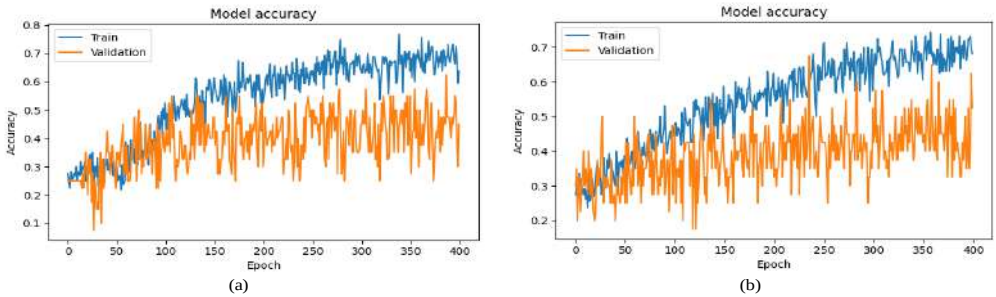

Figure 3. Training and validation accuracy for ResNet-50 model. (a) Learning rate of 1×10^{-2}, (b) Learning rate of 1×10^{-6}

By training the ResNet-50 model with the optimization of learning rate, the training and validation accuracy is obtained as seen in Figure 4 for learning rate 3×10^{-5}. The confusion matrix regarding to test accuracy is also given in Figure 5. It can be seen from the graphics that the training reaches up to 97.50% while validation and test accuracies are 60% and 62.50%.

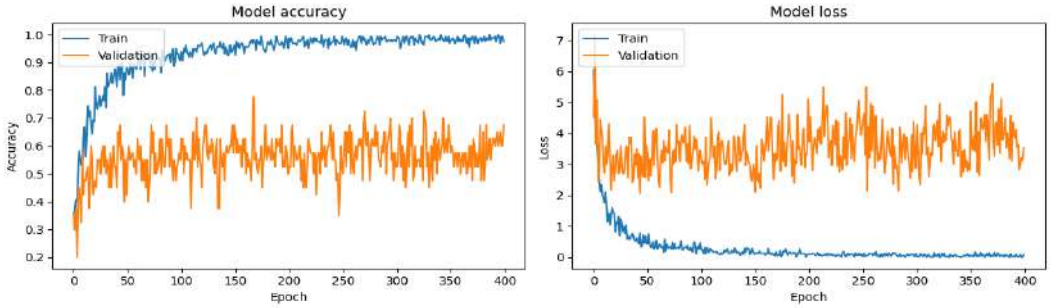

Figure 4. Training and validation accuracy for optimal learning rate of 3×10^{-5} for ResNet-50 model.

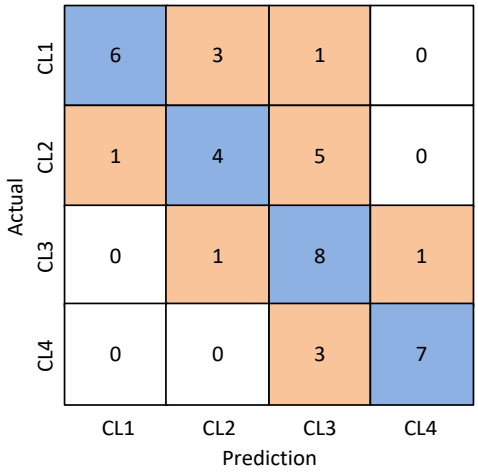

Figure 5. Confusion matrix for test dataset for ResNet-50 model.

After evaluating the performance of the ResNet-50 model, AlexNet model is taken into consideration and simulations are applied. The AlexNet training and validation process graphics are given in Figure 6 while the confusion matrix of test image classification is given in Figure 7. By the figures, it can be concluded that AlexNet model converges to 82.50% accuracy for training and 52.50% accuracy for validation. In addition, 72.50% accuracy for the test image dataset is also obtained.

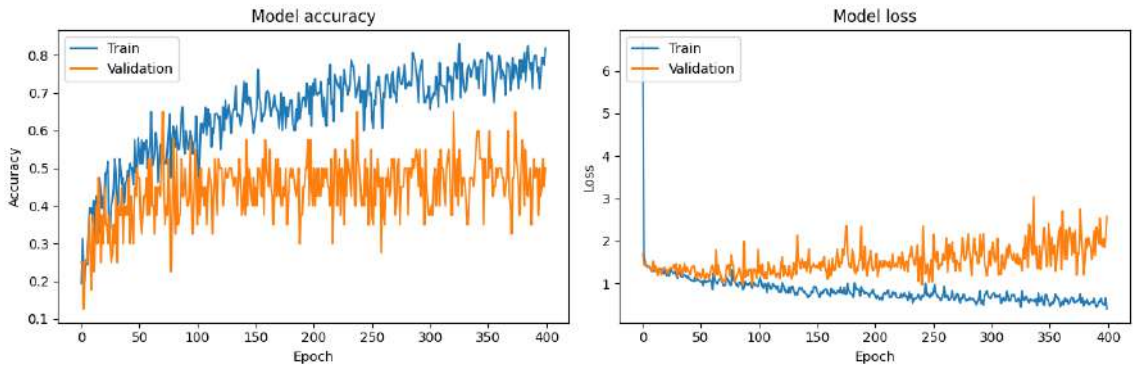

Figure 6. Training and validation accuracy for optimal learning rate of 2.1×10^{-4} for AlexNet model.

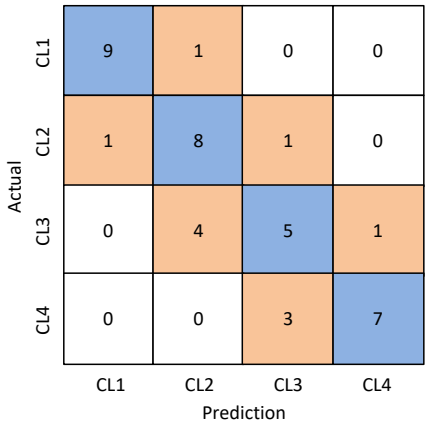

Figure 7. Confusion matrix for test dataset for AlexNet model

5. Results

In this paper, crowd images with various quality, color-depth, size, and zoom attributes are successfully identified by applying deep learning algorithms in conjunction with the best learning rate settings. In this study, feature extraction, selection, and classification are carried out using the well-known deep-learning algorithms ResNet-50 and AlexNet. The ResNet-50 and AlexNet training, test and validation accuracies very close to each other but also the validation and test performances are much lower than training performance. Validation and test performances for the models are resulted in 62.50% and 72.50% for ResNet-50 and AlexNet respectively which are acceptable but improvable. The main reason for having considerably lower performance of validation and test is having various crowd images in the dataset with no image pre-processing. In order to increase the accuracy performance of the models, hyperparameter optimization or image pre-processing may be applied in future papers and researches.

6. Acknowledgements

This study is financially supported by Mersin University, Department of Scientific Research Projects with project number BAP-2023-1-TP2-4874.

7. References

[1] Ilyas N, Shahzad A, Kim K. “Convolutional-neural network-based image crowd counting: review, categorization, analysis, and performance evaluation”. Sensors, 20(1), 43, 2020.

[2] Khan A, Kadir KA, Shah JA, Albattah W, Saeed M, Nasir H, Noor M N, Khel M H. “A deep learning approach for crowd counting in highly congested scene”. Computers, Materials & Continua, 73(3), 5825-5844, 2022.

[3] Patwal A, Diwakar M, Tripathi W, Singh P. “Crowd counting analysis using deep learning: a critical review”. Procedia Computer Science, 218, 2448-2458, 2023.

[4] Ilyas N, Ahmad Z, Lee B, Kim K. “An effective modular approach for crowd counting in an image using convolutional neural networks”. Scientific Reports, 12, 5795, 2022.

[5] Chrysler A, Gunarso R, Puteri T, Hendric S. “A literature review of crowd-counting system on convolutional neural network”. International Conference on Biospheric Harmony Advanced Research, Jakarta, Indonesia,729, 23–24 June 2020.

[6] Rafik G, Akhloufi MA, Shahbazi M. “Advances in convolution neural networks based crowd counting and density estimation”. Big Data and Cognitive Computing, 5(4), 50, 2021.

[7] Jeevitha S, Rajeswari R. “A review of crowd counting techniques”. International Journal of Research and Analytical Reviews, 5(3), 1343-1348, 2018.

[8] Hassen KBA, Machadi JJM, Tavares JMRS. “Convolutional neural networks and heuristic methods for crowd counting: a systematic review”. Sensors, 22(14), 5286, 2022.

[9] Kızrak MA, Bolat B. “Derin öğrenme ile kalabalık analizi üzerine detaylı bir araştırma”. Bilişim Teknolojileri Dergisi, 11(3), 263-286, 2018.
[10] Kaggle. “ShanghaiTech Crowd Dataset”. https://www.kaggle.com/datasets/tthien/shanghaitech (20.08.2023).
[11] University of Central Florida. “UCF-QNRF - A Large Crowd Counting Data Set”. https://www.crcv.ucf.edu/data/ucf-qnrf/ (20.08.2023).
[12] Krizhevsky A, Sutskever I, Hinton GE. “ImageNet classification with deep convolutional neural networks”. Advances in Neural Information Processing Systems Conference, Nevada, USA, 3–8 December 2012.
[13] He K, Zhang X, Ren S, Sun J. “Deep residual learning for image recognition”. IEEE Conference on Computer Vision and Pattern Recognition, Las Vegas, USA, 27–30 June 2016.

International Conference on Advances and Innovations in Engineering

Design of Optimal and Combinational Logic Circuit Using Karnaugh Method in Quantum Circuits

Tuba ŞANLI [1] , Orhan YAMAN [2], Mehmet KARAKÖSE [3]
[1,2]Department of Digital Forensics Engineering, Fırat University, Elazig, Turkey
[3]Department of Computer Engineering, Fırat University, Elazig, Turkey
[1]222144109@firat.edu.tr, [2]orhanyaman@firat.edu.tr, [3]mkarakose@firat.edu.tr

[1](ORCID: 0009-0002-8636-1386), [2](ORCID: 0000-0001-9623-2284),[3](ORCID: 0000-0002-3276-3788)

Abstract
Today, quantum computers are still in development and are an area actively studied by researchers. Although quantum computers have high potential, there are significant technical difficulties and obstacles to achieving practical applications. Many research labs and companies are working on increasing the number of qubits, solving stability problems, and improving error correction techniques, and scalability. These efforts aim at advances such as the development of more stable and reliable qubits, the discovery of more precise control and reading techniques, and the design of more advanced algorithms. This study aims to establish a connection between quantum computers and classical computers. To achieve this, research and work have employed a Karnaugh-based approach. Karnaugh maps serve as highly useful tools in the analysis of complex logic circuits. Depending on one's needs and design requirements, different logic functions can be analyzed and simplified using Karnaugh maps. In this study, the Karnaugh map-based method is utilized to obtain the Boolean function from the state table of the Quantum circuit generated from the RCViewer+ synthesis tool. Subsequently, the obtained function is transformed into a combinational logic circuit. As a result, an optimal combinational circuit corresponding to the quantum circuit can be obtained.

Keywords: Quantum Circuits, Karnaugh Method , Quantum, Combinational Logic Circuit.

1. Introduction

Quantum computers are potentially revolutionary devices that offer a different computing paradigm from traditional computers [1]. These computers, based on quantum mechanics, have the potential to perform some calculations faster and more effectively than classical computers cannot. Quantum computers are made up of basic units called quantum bits or "qubits" [2]. Qubits have the ability to be the same in both 0 and 1 states, thanks to a phenomenon called superposition, unlike ordinary bits that can only take a value of 0 or 1. The state of superposition grants quantum computers the capability to concurrently process vast amounts of information in parallel. The most remarkable aspect of quantum computers is their potential to achieve a substantial speedup in solving certain computational problems by leveraging phenomena such as quantum parallelism and quantum entanglement [3]. In particular, quantum computers can have a significant impact on solving complex mathematical problems such as factorization. This can have significant consequences for deciphering and breaking cryptographic systems. But, quantum computer development and deployment still face significant technical challenges. Stability, fault tolerance, data readability, and scalability of qubits are still areas of study and improvement. In addition, the development of algorithms, software, and hardware tools for the widespread use of quantum computers is an important step. In short, quantum computers are devices that offer different computing power and potential than traditional computers, but still need development and have significant technical challenges. Their potential has the potential to make a huge impact in areas such as cryptography, optimizing, and molecular modeling. However, further research and development is required for quantum computers to become widespread.

[1]Corresponding author

Literature Summary

In recent years, existing studies and articles in the literature related to quantum technology, in general, have also been seen in research on topics such as cost calculation, fault tolerance[4], and quantum optimization. In addition, there are many studies on reversible logic [5]. Reversible logic is a vital topic today and has applications as diverse as low-power CMOS, quantum computing, nanotechnology, cryptography, optical computing, DNA computing, digital signal processing (DSP), quantum dot cellular automata, communications, and computer graphics. There are many studies in the literature related to these application areas. Gaur et al. [6] compared the operating costs of quantum gates in their study. Thus, they contributed to future studies on the operating cost of common doors. In addition, 3*3 MCT and MCF gates are also explained and used in this study [6]. Roy et al. [7] presented an implementation of a reversible ALU (Arithmetic Logic Unit). This application demonstrates a reversible ALU that uses the MRI (Modified Reversible Gate) gate and the HNG (Hybrid Nanometric Gate) gate to generate six logical computations [7]. In Rather et al. [8], a low quantum cost 4×4 reversible gate TKG (Assembly of Reversible Gates) was presented, and then a 4-bit reversible multiplier was designed. In the proposed study, a new 4×4 reversible gate, TKG, is proposed. TKG was used in both designs. Her work has made a significant contribution to trade [8]. Anwar et al. [9], proposed a new 4*4 reversible RR (Reed-Muller) gate. The reduced latency and quantum cost of a reversible universal shift register using a gate was calculated. The proposed design was functionally tested and verified [9]. Garipelli et al. [10], introduced basic reversible logic gates that can perform more complex operations using reversible circuits designed for more complex systems [10]. Mia et al. [11], some reversible logic gates that can carry out more complex operations using data and quantum computers in the design of more complex systems with reversible circuits have been studied. The article shows data on reversible gates that help design complex circuits [11]. Thakral et al. [12], discussed the proposed new reversible logic gates and their quantum implementation using the RCViewer+ tool. The methods used were seen as Toffoli Networking Methodology, Quick Guide for RCViewer/RCViewer+ Tool, and Quantum Implementation of Reversible Logic Gates [12]. The continuation of the literature summary is presented in Table 1 in tabular form.

Table 1. Historical development and results of studies in the literature on the synthesis of quantum reversible circuits

Scientific Study	Year	Dataset	Method	Result	Synthesis Tool
Nagamani et al.[13]	2015	Vedic math techniques Toffoli, Peres and Fredkin gates	4x4 Urdhva Tiryakbhayam Multiplier design	QC: 143 CL(Ancilla): 32 GO:28 UD:34δ TRLIC: 240	RCViewer+ Decompose Circuit Tool
Misra et al.[14]	2017	QCA field in nanoelectronics	QCADesigner DC gate	QC:%25 GC:%66 GO%50	RCviewer +
Sultana et al.[15]	2017	16 units 4 variable gates	Toffoli mapping Reversible Comparison	Ort QC:24,5 Ort GC:9,25 Ort TG:23,25	RCViewer+
Misra et al.[16]	2018	CNOT, NOT, CV	R-CQCA Flipflops BCD	QC: %36,66 R-CQCA:%65.49	RCVeiwer+
Thakral et al.[17]	2018	Fredkin gate	Quantum Application of Fredkin Gate	QC: 7 GC: 7 TG: 7	RCViewer+

**T-depth: Depth of gate is a measure of how many 'layers' of t-gate are executed in parallel, t-number: total number of t-gates in the quantum circuit, Qubit cost: Qubit Cost is Total Qubits Required to Design the Quantum. DFT: Design for Several Testability Using the Method of Converting a Standard Circuit to Its Testable Form, QCA: Quantum Dot Cellular Automaton, GC: Gate Count, QC: Quantum Cost, UD: Unit Delay, LC: Logical Computing, GO: Garbage Output, CI: Fixed Input, QCA: Binary Decoder, Low-Cost Module, BEDesigner: 1D Codec with Binary Low Cost, BEDesigner: 1DQD, BG-2: Binary Gray, GB-2: Gray Binary, NG-R1: New Gate = New Gate, R = Reversible, TG: Two-Qubit Gate Number, R-CQCA: Reversible Conservative Quantum Cellular Automaton

Motivation

Generally, combinational logic circuits are used for conventional computers and electronic devices. Quantum circuits, on the other hand, play an important role as a potential technology of the future in the fields of quantum

information processing and computation. Classical circuits focus on providing deterministic and error-free results. Quantum circuits, on the other hand, enable parallel operations and potentially faster and more efficient computations using quantum properties such as superposition and aliasing. There are still significant technical challenges to the development, and deployment of quantum circuits. At the same time, there isn't much study and research on the connection between classical circuits and quantum circuits. This situation provided motivation for the proposed study.

Combinational Logic Circuits

Combinational logic circuits are electronic circuits that combine electronic components to perform a specific logical operation. Computers, cell phones, televisions, digital clocks, and many other electronic devices contain logic circuits. Logic circuits perform logical operations based on two basic logical values (true and false, often denoted as "1" and "0"). These operations can be expressed using layers of boolean algebra principles and basic expenditure operations (such as and, or, not). Combinational logic circuits are built with a combination of basic structures known as connectors. Logical elements produce results on behaviors, uses, and outputs applied to inputs "Example logical elements encompass gates (such as AND, OR, XOR), flip-flops, multiplexers, and decoders.[18] The design and analysis of combinational logic circuits constitute a vital subject in electronic engineering and computer science. Advanced combinational logic circuits are tailored to fulfill diverse requirements like high performance, low power consumption, and optimized functionality. These circuits serve as the fundamental building blocks for processors, memory units, buses, and other intricate digital systems."

2. Material

In the study, the RCViewer+ simulator and Karnaugh map were used. The Karnaugh map is preferred because it offers significant advantages in the design of smaller and simpler logic circuits. In addition, the study of the combinatorial logic circuit equivalent of the quantum circuit also provides the connection between them by using the truth table.

Rcviewer+ Synthesis Tool

RCViewer is a simple application software written in C++.TFC format [12]. An explanation of the array indexes given in Table 2 indicates what the codes and indexes in the ".tfc" file given in Figure 1 mean. It is also used in the design of reversible circuits and parameter extraction [19].

```
.v A,B,C,D
.i A,B,C,D
.o A,B,C,D
BEGIN
t3 A,C,D
t3 C,B,A
t3 A,B,D
t2 B,A
t2 C,B
t1 B
t2 B,D
END
```

Figure 1. Example TFC File

The '.tfc' format in Figure 1 is explained below.
"A, B, C, D": Shows the list of all variables in the network.
".v A, B, C, D": Shows the list of input variables in the network.
".i A, B, C, D": Shows the list of output variables in the network.
".o A, B, C, D": Input constant in the network
BEGIN: Indicates the network start of the gateway.
In the lines after BEGIN, the doors are arranged according to the prescribed format.

END: Indicates the network end of the gateway.
In electronics and computer science, "gates" are basic elements used for information processing and performing logic operations in digital logic circuits. These gates produce outputs by applying certain logical operations relative to the inputs. Conventional digital logic gates are used in classical circuits while quantum gates are used in quantum circuits. The ".tfc" format of the gates in quantum circuits is shown in Table 2.

Table 2. Display of doors in ".tfc" format [12]

GATE		TFC Format
NOT gate	TOF(Φ;a)	t1 a
Cnot gate	TOF(a;b)	t2 a,b
CCNOT gate	TOF(a,b;c)	t3 a,b,c
SWAP gate	FRE(Φ;a,c)	F2 a,b
FREDKİN gate	FRE(a;b,c)	F3 a,b,c
V Gate		V
V^+ Gate		V^+

Karnaugh Map-Based Method

Karnaugh Map is a tool used to simplify boolean algebra and design logic circuits [20]. It is named after the American mathematician Maurice Karnaugh. The K-map consists of cells arranged in a grid and representing combinations of boolean variables. The purpose of the Karnaugh Map is to express a boolean function in a simpler form. It optimizes the design of the combinatorial logic circuit. These maps visually represent the "1" and "0" values of the boolean functions. It makes it easy to find a simplified expression by grouping similar combinations. Using K-maps, boolean equations can be found in logic tables or circuit diagrams. Karnaugh maps are generally used for the analysis of functions with 2, 3 or 4 inputs. It uses a quadrilateral map for a two-input function, an octagonal map for a three-input function, and a hexadecimal map for a four-input function. Each cell is associated with neighboring cells on the map. A simpler expression is obtained by combining similar neighboring cells.
The basic usage steps of Karnaugh Map are:

I. The truth table of the boolean function is created.
II. The size of the Karnaugh Map is determined (2x2, 4x4, etc.), this size depends on the number of variables.
IV. By grouping the "1" cells in the map, their cells are combined to obtain a simplified expression.
V. The simplified expression is expressed in boolean algebra notation that represents the original boolean function.

Examples of Some Commonly Used Basic Logic Gates in the Karnaugh Map

The examples in Figure 2 show how some logic functions with different input numbers are represented by Karnaugh maps. These are just a few examples, and larger Karnaugh maps can be used for functions with more inputs.

NOT Function (1 input):

A	Exit
0	1
1	0

NOR Function (2 inputs):

A\B	0	1
0	1	0
1	0	0

AND Function (2 inputs):

A\B	0	1
0	0	0
1	0	1

3-input AND Function:

A\B\C	00	01	11	10
0	0	0	0	0
1	0	1	1	1

OR Function (2 inputs):

A\B	0	1
0	0	1
1	1	1

3-input OR Function:

A\B\C	00	01	11	10
0	0	1	1	1
1	1	1	1	1

XOR Function (2 inputs):

A\B	0	1
0	0	1
1	1	0

3-input XOR Function:

A\B\C	00	01	11	10
0	0	1	1	0
1	1	0	0	1

NAND Function (2 inputs):

A\B	0	1
0	1	1
1	1	0

4-input NAND Function:

A\B\C	00	01	11	10
0	0	1	1	0
1	1	0	0	1

Figure 2. Karnaugh map representation of logic functions

3. Proposed Method

In the study, the proposed method consists of three steps, these are quantum, Karnaugh-Map, and classical circuit steps. The block diagram of the proposed method is shown in Figure 3. Later in this section, these steps are explained in detail.

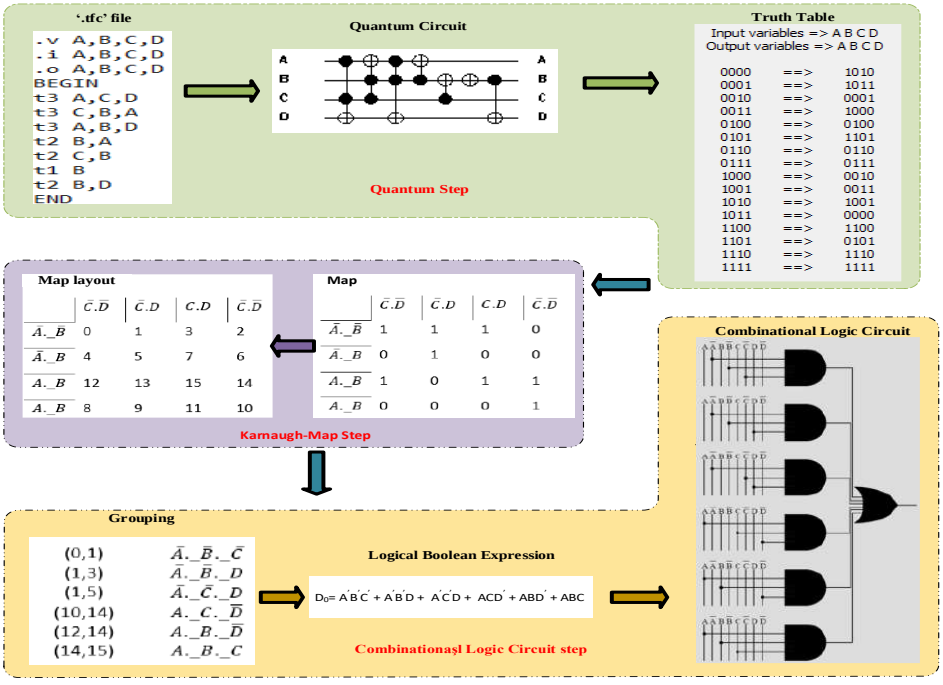

Figure 3. Block diagram of the proposed method

Quantum Step

Quantum circuit design involves arranging and controlling logic gates (quantum gates), which are used to make quantum computers work and solve certain computational problems. Quantum circuits differ from conventional computer circuits in that quantum gates represent gates with properties unique to quantum mechanics, rather than classical logic gates, and are designed using a variety of synthesis tools. In the quantum step of the study, a sample ".tfc" file is created, as can be seen in Figure 4, and the ".tfc" file is run with the RCViewer+ Tool installed on classical computers and converted into a quantum circuit. The truth table of the Quantum circuit consisting of four inputs, four outputs, and seven gates is
taken.

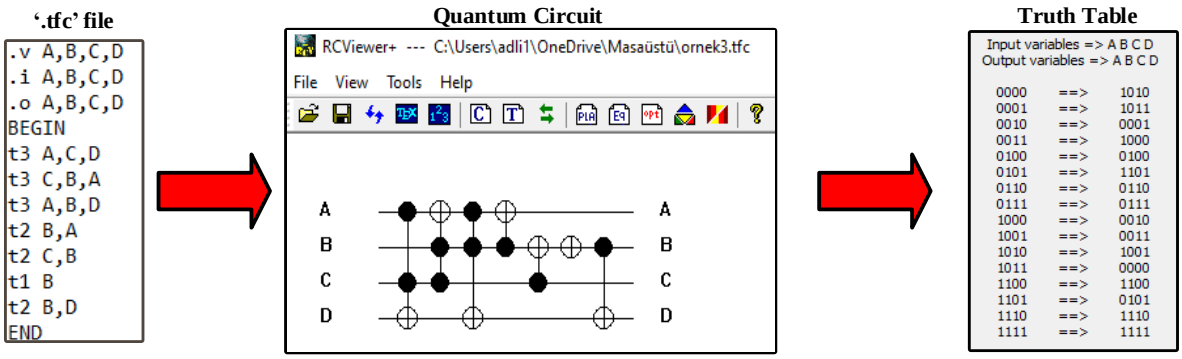

Figure 4. The result of the quantum circuit design and truth table of the sample ".tfc" file

Karnaugh-Map Step

In the Karnaugh step, as seen in Figure 5, the Karnaugh-Map-based method is applied to the truth table obtained in the quantum step. In practice, one of the 4-input A, B, C, and D variables, D output, whose value is equal to 1, is taken and written in place of D0. A hexadecimal map is then used for a four-input function. Each cell is associated with neighboring cells in the map, and a simpler expression is obtained by combining similar neighboring cells. The map layout is created by replacing the values corresponding to the bits.

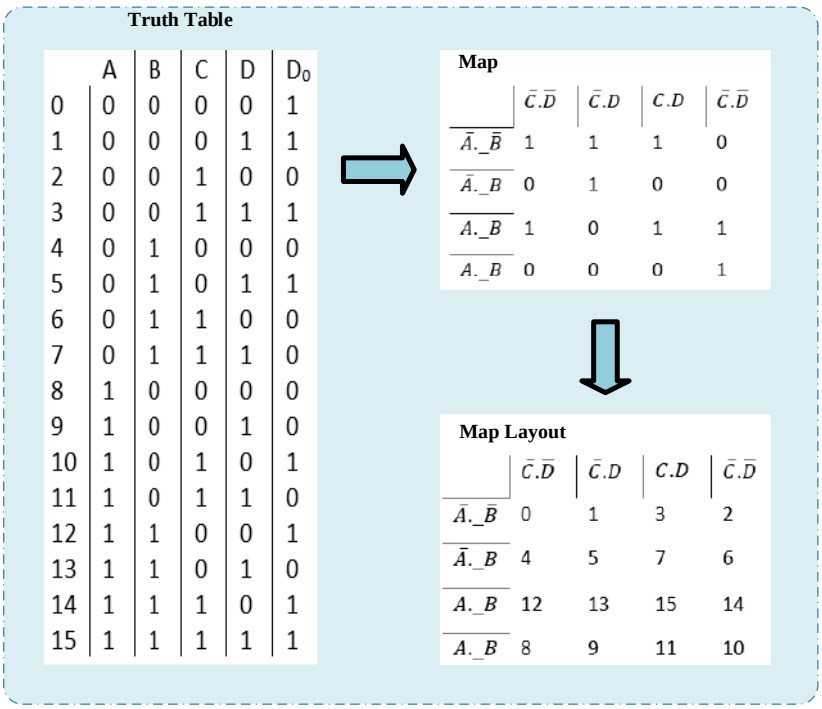

	A	B	C	D	D_0
0	0	0	0	0	1
1	0	0	0	1	1
2	0	0	1	0	0
3	0	0	1	1	1
4	0	1	0	0	0
5	0	1	0	1	1
6	0	1	1	0	0
7	0	1	1	1	0
8	1	0	0	0	0
9	1	0	0	1	0
10	1	0	1	0	1
11	1	0	1	1	0
12	1	1	0	0	1
13	1	1	0	1	0
14	1	1	1	0	1
15	1	1	1	1	1

	$\bar{C}.\bar{D}$	$\bar{C}.D$	$C.D$	$C.\bar{D}$
$\bar{A}._\bar{B}$	1	1	1	0
$\bar{A}._B$	0	1	0	0
$A._\bar{B}$	1	0	1	1
$A._B$	0	0	0	1

	$\bar{C}.\bar{D}$	$\bar{C}.D$	$C.D$	$C.\bar{D}$
$\bar{A}._\bar{B}$	0	1	3	2
$\bar{A}._B$	4	5	7	6
$A._\bar{B}$	12	13	15	14
$A._B$	8	9	11	10

Figure 5. Using karnaugh-Map from the sample state table

Combinational Logic Circuit Step

A hexadecimal map is then used for a four-input function. Each cell is associated with neighboring cells in the map, and a simpler expression is obtained by combining similar neighboring cells. The map layout is created by replacing the values corresponding to the bits.

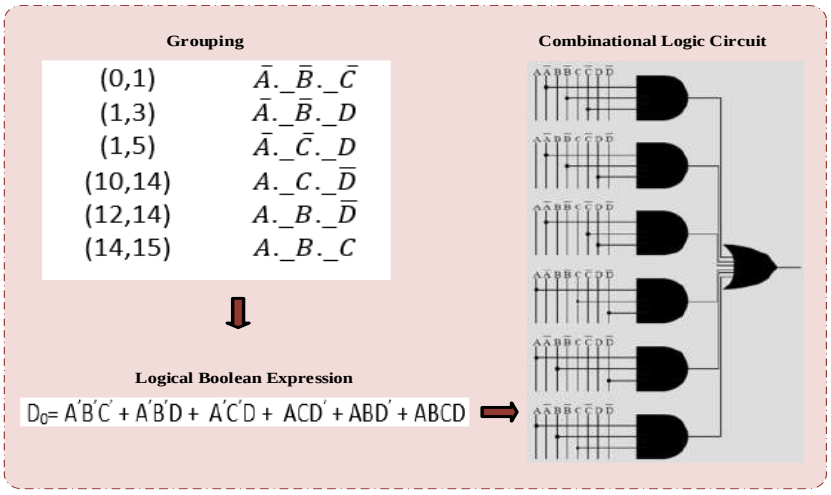

Figure 6. Classical circuit generation from the resulting logical expression

4. Conclusion

Because quantum circuits are built on a different paradigm than combinatorial logic circuits, they should not be applied directly, like the traditional Karnaugh map. The design and optimization of quantum circuits are carried out with special algorithms and techniques that take into account the properties of quantum mechanics. However, as can be understood from the explanations and studies, the Karnaugh map provides advantages such as simplifying the operation structures, reducing the delay times and facilitating the debugging process. The connection of quantum circuits with combinational logic circuits has been tested. It has also been found that it can be used to quickly analyze complex logic functions with a large number of inputs and outputs. It is foreseen that the use and development of this method in the future will contribute to the study. The Karnaugh map is a viable and effective method only for a certain number of entries (2, 3, or 4 entries). Other techniques and methods may need to be used for logical expressions with more inputs.

5. Acknowledgment

This work was supported by the TUBITAK (The Scientific and Technological Research Council of Turkey) under Grant No: 121E439.

6. References

[1] Yetis H, Karakose M. A New Framework for Quantum Image Processing and Application of Binary Template Matching. 2022 26th Int. Conf. Inf. Technol. IT, Zabljak, Montenegro: IEEE; 2022, p. 1–4. https://doi.org/10.1109/IT54280.2022.9743534.

[2] Yetiş H, Karaköse M. A New Framework Containing Convolution and Pooling Circuits for Image Processing and Deep Learning Applications with Quantum Computing Implementation. Trait Signal 2022;39:501–12. https://doi.org/10.18280/ts.390212.

[3] Yetis H, Karakose M. Quantum Circuits for Binary Convolution. 2020 Int. Conf. Data Anal. Bus. Ind. Way Sustain. Econ. ICDABI, Sakheer, Bahrain: IEEE; 2020, p. 1–5. https://doi.org/10.1109/ICDABI51230.2020.9325659.
[4] Yilmaz R, Yaman O, Karaköse M. Kuantum Devrelerinde Kapı ve Giriş Tespiti için YOLO Tabanlı Bir Yöntem. Fırat Üniversitesi Mühendis Bilim Derg 2023. https://doi.org/10.35234/fumbd.1269274.
[5] Yetis H, Karakoes M. Investigation of Noise Effects for Different Quantum Computing Architectures in IBM-Q at NISQ Level. 2021 25th Int. Conf. Inf. Technol. IT, Zabljak, Montenegro: IEEE; 2021, p. 1–4. https://doi.org/10.1109/IT51528.2021.9390130.
[6] Gaur HM, Singh AK, Ghanekar U. In-depth Comparative Analysis of Reversible Gates for Designing Logic Circuits. Procedia Comput Sci 2018;125:810–7. https://doi.org/10.1016/j.procs.2017.12.103.
[7] Roy VG, Indurkar PR, Khatri MDM. A Survey on Design Approaches towards Quantum ALU using Reversible Logic Structures 2014;5.
[8] Rather TA, Ahmed S, Kakkar V. Modelling and Simulation of a Reversible Quantum Logic based 4 × 4 Multiplier Design for Nanotechnology Applications. Int J Theor Phys 2020;59:57–67. https://doi.org/10.1007/s10773-019-04285-3.
[9] Anwar vd. JAB. A Novel Design of Reversible Universal Shift Register. Int J Comput Sci Mob Comput n.d.
[10] Garipelly, P.Madhu Kiran, A.Santhosh Kumar. A Review on Reversible Logic Gates and their I mplementation. Int J Emerg Technol Adv Eng n.d.
[11] Mia MdS, Mukib MdA, Islam MdS. An Extended Review on Reversible Logic Gates and their Implementation. Int J Latest Eng Res Appl IJLERA n.d.
[12] Thakral S, Manhas P, Verma J. Quantum Implementation of Reversible Logic Gates Using RCViewer+ Tool. In: Dutta P, Chakrabarti S, Bhattacharya A, Dutta S, Piuri V, editors. Emerg. Technol. Data Min. Inf. Secur., vol. 491, Singapore: Springer Nature Singapore; 2023, p. 409–18. https://doi.org/10.1007/978-981-19-4193-1_39.
[13] Nagamani AN, Prasad HV, Hathwar RS, Agrawal VK. Design of optimized reversible multiplier for high speed DSP application. 2015 10th Int. Conf. Inf. Commun. Signal Process. ICICS, Singapore: IEEE; 2015, p. 1–5. https://doi.org/10.1109/ICICS.2015.7459869.
[14] Misra NK, Sen B, Wairya S, Bhoi B. Testable Novel Parity-Preserving Reversible Gate and Low-Cost Quantum Decoder Design in 1D Molecular-QCA. J Circuits Syst Comput 2017;26:1750145. https://doi.org/10.1142/S0218126617501456.
[15] Sultana M, Prasad M, Roy P, Sarkar S, Das S, Chaudhuri A. Comprehensive quantum analysis of existing four variable reversible gates. 2017 Devices Integr. Circuit DevIC, Kalyani, India: IEEE; 2017, p. 116–20. https://doi.org/10.1109/DEVIC.2017.8073918.
[16] Misra NK, Wairya S, Sen B. Design of conservative, reversible sequential logic for cost efficient emerging nano circuits with enhanced testability. Ain Shams Eng J 2018;9:2027–37. https://doi.org/10.1016/j.asej.2017.02.005.
[17] Thakral S, Bansal D. A Quick Guide to Implement Reversible Logic. 2018 4th Int. Conf. Comput. Commun. Autom. ICCCA, Greater Noida, India: IEEE; 2018, p. 1–5. https://doi.org/10.1109/CCAA.2018.8777469.
[18] Yetiş H, Karaköse M. An improved and cost reduced quantum circuit generator approach for image encoding applications. Quantum Inf Process 2022;21:203. https://doi.org/10.1007/s11128-022-03546-1.
[19] Pathak N, Misra NK, Bhoi BK, Kumar S. Concept and Algorithm of Quantum Computing During Pandemic Situation of COVID-19. In: Somani AK, Mundra A, Doss R, Bhattacharya S, editors. Smart Syst. Innov. Comput., vol. 235, Singapore: Springer Singapore; 2022, p. 523–35. https://doi.org/10.1007/978-981-16-2877-1_48.
[20] Kheirandish D, Haghparast M, Reshadi M, Hosseinzadeh M. Efficient designs of reversible sequential circuits. J Supercomput 2021;77:13828–62. https://doi.org/10.1007/s11227-021-03735-2.

International Conference on Advances and Innovations in Engineering

A seq2seq based approach for generation of quantum circuits using deep learning

Musa YENİLMEZ[1] , Niyazi Furkan BAR[2], Mehmet KARAKÖSE [3]
[1,2,3]Department of Computer Engineering, Firat University, Elazig, Turkey.
[1]musayenilmez@protonmail.com, [2]nfbar@firat.edu.tr, [3]mkarakose@firat.edu.tr

[1](ORCID: 0009-0006-1722-3050), [2](ORCID: 0000-0002-3393-004X),[3](ORCID: 0000-0002-3276-3788)

Abstract
Artificial intelligence, machine learning, and deep learning all significantly affect our daily lives. These technologies are utilized in a variety of fields, including voice assistants, social media, health, and internet search engines. Computers with high computing speed are required for these technologies. The speed of today's classical computers is insufficient for these processes. Quantum computing has made it possible to reach high processing power. In this situation, converting classical computer algorithms to quantum computing algorithms is a difficult task. This study proposes an approach based on deep learning and natural language processing. The proposed approach transforms classical code into quantum coding. The proposed approach involves developing a neural network. The dataset contains C code as classical code, and TFC code as quantum code. The preprocessing of the dataset included operations like normalization, tokenization, and vectorization. The proposed approach used the preprocessed dataset to train the neural network. The proposed approach is evaluated as accuracy rate and loss value. As a result of this evaluations, the proposed approach has been verified.

Keywords: Quantum computing, Natural Language Processing, Deep Learning

1. Introduction

Information technologies play a significant role in our lives as a result of the modern world's rapid technological growth, and their use gradually becomes essential. A variety of industries, including computer vision, satellite imaging, health, the Internet of Things, text and speech analysis, have begun to adopt emerging deep learning technology[1]. With the increase in studies in these areas, more powerful equipment is needed. When studies in this field are desired to be done with classical computers, time and energy costs are high. In this context, researchers have sought alternative solutions. They turned to software solutions, but these solutions were also insufficient. On the hardware side, reaching the upper limits of Moore's Law limits developments. According to Moore's Law, a microprocessor's transistor count will double every two years. This law is no longer valid[2–4]. Solutions consisting of classical computers and methods are insufficient. The development of quantum computers and quantum computing in the laboratory environment has been a ray of hope for the field of artificial intelligence. Quantum computers have some advantages as well as some disadvantages. The most important of these disadvantages is that there is not enough quantum algorithm to run classical algorithms on a quantum computer[2,5]. However many researchers try to use the advantages of quantum computing for different problems[6–9].

In this study, quantum circuits are built from a high-level language using deep learning methods. From these algorithms, long short-term memory architecture, which is an improved version of the recurrent neural network (RNN), which provides high efficiency in the field of natural language processing, has been utilized[10,11]. Long short-term memory has the benefit of having a gate that determines whether or not its network data is important. The

[1]Corresponding author

Google Colab platform was utilized to speed up model training for the application, which was written in the Python programming language. The platform enables the use of T4 GPUs with several cores for tensor processing. Tensorflow library, which is frequently used in artificial intelligence, machine learning, and deep learning, is used. The LSTM structure and layers that we will employ in the neural network are produced with the aid of the TensorFlow library. It has been vectorized so that the computer can process and interpret commands more quickly.[12]. This increases the accuracy of the predictions by clustering the vectorially nearest values together.

The C programming language code given as a source to the application is initially preprocessed. The preprocessed dataset is then vectorized and tokenized. The neural network can take this data set as input. The vectorially generated output values from the neural network are used to create a TFC data file that represents Toffoli-Fredkin gates. This generated data is the quantum circuit equivalent of the source C language program. This method allows for the conversion of some classical computer algorithms into quantum circuits. As a result, a solution is offered for applications like artificial intelligence that need high speed.

There are studies like source code generation and word/sentence prediction. Text-based studies include automatic code completion and source code generation using deep learning techniques. In one of them[13], a method using abstract syntax tree (AST) and deep learning is proposed. LSTM and Multiple Layer Perceptron networks were used in the experiments and their comparison with other methods was discussed. Source code is produced with the method used. The method produces efficient results for compiled languages such as C++ and Java. In this study, the Multi-Layer Perceptron's accuracy is 90.1%, whereas that of the LSTM-created neural network is 90.3%. Automatic text production using the LSTM model is covered in another work in the literature[14]. The text, which is given as free from punctuation marks, is processed and a new text related to this text content is produced. The accuracy rate of the produced texts as a result of the training is 80%.

2. Background

2.1. Quantum Computing

In the early 1900s, studies were started in the field of quantum mechanics. In quantum mechanics, photons and subatomic particles can represent two different states called superpositions[15,16]. They maintain their superposition state as long as no observation is made. The best-known example of this situation is Schrödinger's Cat experiment. The cat is in a box with a bottle of poison and radioactive material. Like photons and subatomic particles, the cat inside the box is both dead and alive until observed. When we adapt this situation to the computer structure, unlike classical computers, quantum computers can store both 0 and 1 values in superposition at the same time. The storage units here are called qubits. Qubits represent the processing capacity of a quantum computer. While current classical computers have 64-bit processing power, this capacity can reach 2000 qubits levels in quantum computers. Today's studies show that quantum computers with more qubit numbers are being produced[17,18].

The biggest advantage of quantum computers is that they complete the sequential operation of classical computers in a single unit of time in parallel. This saves a great deal of time. The disadvantage is the requirement for a temperature-controlled laboratory environment. To get accurate results, the system temperature should be kept at 0 Kelvin (-273.15 °C)*[5]*. Since it is difficult to keep the system at absolute 0 temperature, incorrect measurements occur in the operations. Therefore, algorithms are run more than once in quantum computers and the average of these values is accepted as the result. Quantum computers are much more advantageous than today's general-purpose computers and supercomputers in terms of time and energy. *Although access to quantum computers is limited today, there are many simulators available to researchers.* Quantum simulators such as Qiskit, Ocean, Q#, and CIRQ are currently used for quantum programming*[19–21]*. Quantum circuit equivalents of high-level languages here can be defined with quantum scripts such as OpenQASM, cQASM, Quil, and Blackbird. Quantum computing programs are currently operated through these simulators. Access to physical quantum computers operating in the laboratory environment is provided by the cloud services of IBM and Microsoft.

2.2. Natural Language Processing with Deep Learning

Natural language processing is a method for the creation and analysis of spoken and machine languages. The first concrete studies in the field of NLP were made by ARPA in the 1960s. As a result of these studies, the Harpy system was established with a dictionary of 1000 words. The Harpy system successfully understood up to 90% of the spoken language Then, MIT created a chat program called Eliza that can respond with advice in the role of a psychotherapist. The answers given by the application were insufficient in terms of meaning. This and similar studies work on a rule-based. The computer makes predictions by making inferences with predefined rules. In cases where languages change, these rules need to be changed and this is a difficult process to manage. By the 2000s, machine learning and deep learning methods began to develop. These methods achieved high performance in text processing areas. Deep learning and machine learning methods are used in research on natural language processing. In deep learning, recurrent neural networks (RNN) and long short-term memory (LSTM) algorithms are generally used. Recurrent neural networks are often used in text processing.

LSTM has been developed for situations where RNN is insufficient. It also stores state values in its memory and uses state values in its predictions. LSTM can make high-performance predictions in multi-class classification applications. LSTM consists of input, output, forget gate, c and h states. The feature that distinguishes it from other networks is that it has a forget gate in its structure. Forget Gate is responsible for deciding whether the data in the network will be forgotten or not. An example LSTM structure is shown in Fig. 1.

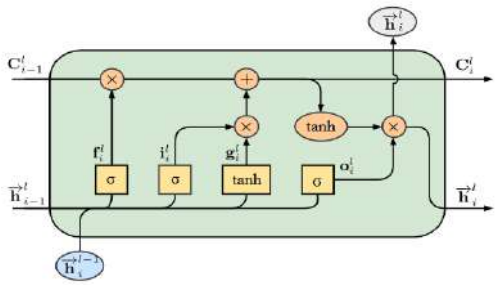

Figure 1. LSTM Architecture

3. The Proposed Approach

The proposed approach contains a system for converting classical computer code to quantum computer code. This method transforms C programming language codes into TFC codes. The proposed method first preprocesses the C code before submitting it to a neural network. The Seq2Seq model was used as the neural network. The LSTM neural network, the decoding unit, and the tokenization and vectorization of the data from the data set are all included in this model. The TFC code of the C code is created by decoding the neural network's output. The block diagram of the proposed approach is given in Fig. 2.

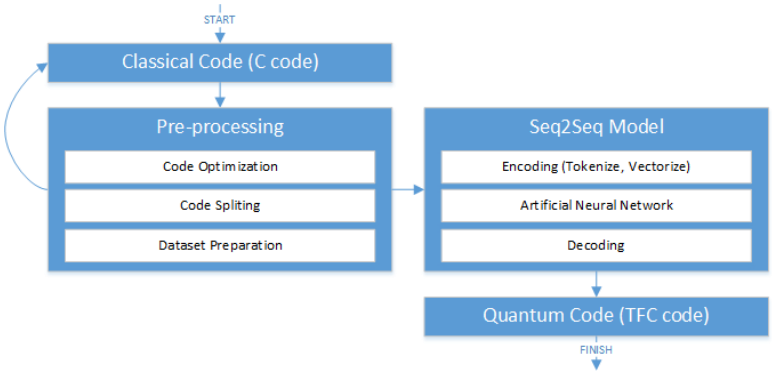

Figure 2. The block diagram of the proposed approach

There are different codes in each line of the data set file used for training this system. The number of rows here indicates the amount of data we have. For the data set to take up less memory on the computer and be processed faster, the data is preprocessed to digitize. The preprocessing steps of the data consist of the following three stages.

Standardization. <*START*> and <*STOP*> tags are added to indicate the start and end of the commands in the dataset. In command expressions, a space is used to separate the operator and operand. All data is split with spaces and each expression is processed separately.

Tokenization. It is the stage of creating a special numeric value equivalent for each of the expressions in the data set and storing it in an array. In this approach, the computer will be able to process quickly with numeric values instead of textual expressions.

Vectorization. The deep learning algorithm we will use in the application cannot directly process tokenized categorical data. This data must be converted into digitized vectors for the algorithm to process it. In this stage, the data from the tokenization stage is converted into binary vectors with the One Hot Encoding method.

The proposed approach, it is aimed to transform high-level programming language commands into quantum circuits by utilizing natural language processing and deep learning algorithms The Tensorflow library was used to build a neural network. Two inputs, two LSTMs, and a dense layer make up the neural network that has been formed. The first input layer encodes the input data and the second input layer is responsible for decoding the input data. The incoming data is compared to the data already recorded in the LSTM layer's memory before being passed on as input to the following layer. The dense layer is equipped with a softmax activation function, which provides high performance in multi-class classification operations. In this way, probabilistic values reach the output of the network and estimates are made accordingly. The architecture of the neural network is given in Fig. 3.

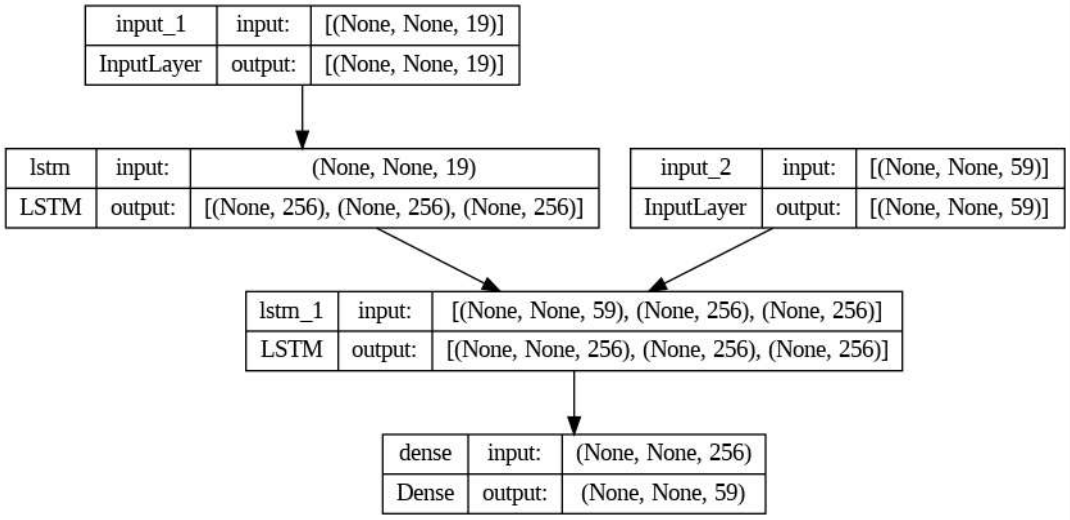

Figure 3. The architecture of the neural network

The neural network's dense layer outputs can include both probabilistically negative and positive values. It is ensured that all outputs fall between the range of 0 and 1 and that their sum is 1, by using the softmax activation function. Decoding is used together with these probability values and the LSTM state data. Starting from the <START> tag, until it encounters the <STOP> tag, all expressions in between are decoded. TFC commands are produced as output from the decoded statements.

4. Experiments and Results

The proposed approach uses deep learning to create neural networks with two inputs, two LSTM, and one dense layer. If the batch size is increased because of the experiments, the model starts to overfit and produces incorrect results. Increasing the epoch value increases the training time, but the accuracy increases linearly with the epoch

value. The epoch value is chosen as high as possible within the hardware resources. For the neural network model to produce the most efficient results, the optimum parameter values were determined by experiments. The most successful training results were obtained with the optimum parameter values in Table 2.

Table 2. Parameters

Parameter Name	Parameter Value
Optimizer	Adam
Loss Function	Categorical Cross Entropy
Activation Function	Softmax
Learning Rate	0,001
Epoch	100
Batch Size	25
Shuffle	True

Adam and RMSProp are widely used algorithms in applications for natural language processing. RMSProp and Adam algorithms were tried as optimization functions in the training process. The Adam algorithm was more successful than the RMSProp algorithm. The success rate is negatively affected by decreasing the learning rate. The Softmax function, which provides high efficiency in multi-class classification, is used in the application[22]. As a result, the output vectors have values between 0 and 1, and the total of all values is equal to 1. The Shuffle parameter is among the most crucial parameters, along with the activation function. Higher accuracy is achieved when the shuffle parameter is true. Instead of using datasets for the training, we used realistic data that we created ourselves. This dataset consists of C codes and TFC codes. A part of this dataset is given in Fig. 3.

```
a++;     t5 4,3,2,1,0;t4 3,2,1,0;t3 2,1,0;t2 1,0;t1 0;
++a;     t5 4,3,2,1,0;t4 3,2,1,0;t3 2,1,0;t2 1,0;t1 0;
a+=1;    t5 4,3,2,1,0;t4 3,2,1,0;t3 2,1,0;t2 1,0;t1 0;
a=a+1;   t5 4,3,2,1,0;t4 3,2,1,0;t3 2,1,0;t2 1,0;t1 0;
a=1+a;   t5 4,3,2,1,0;t4 3,2,1,0;t3 2,1,0;t2 1,0;t1 0;
b++;     t5 9,8,7,6,5;t4 8,7,6,5;t3 7,6,5;t2 6,5;t1 5;
++b;     t5 9,8,7,6,5;t4 8,7,6,5;t3 7,6,5;t2 6,5;t1 5;
b+=1;    t5 9,8,7,6,5;t4 8,7,6,5;t3 7,6,5;t2 6,5;t1 5;
b=b+1;   t5 9,8,7,6,5;t4 8,7,6,5;t3 7,6,5;t2 6,5;t1 5;
b=1+b;   t5 9,8,7,6,5;t4 8,7,6,5;t3 7,6,5;t2 6,5;t1 5;
```

Figure 4. A part of the dataset

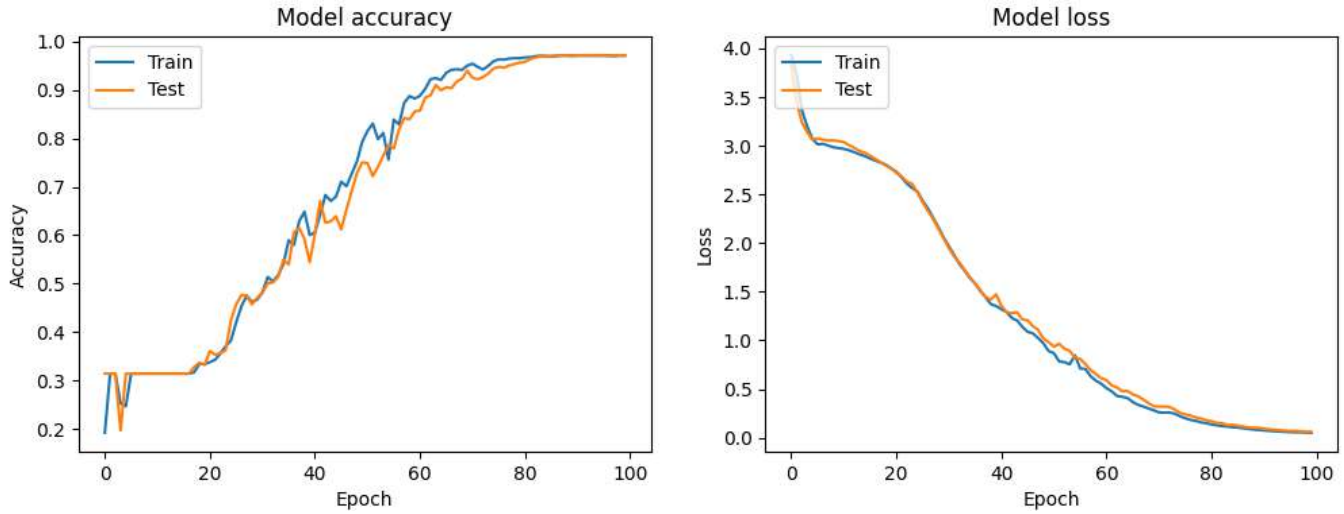

Figure 5. Accuracy rate and loss value of the proposed approach during training

The results of the experiments, 80% of the source data being training and 20% testing, are as in Fig. 5. This figure shows the change in the accuracy rate and loss value of the training made with 100 epoch values of the neural network and 25 batch sizes. While the accuracy rate does not exceed 50% in the first 30 epoch iterations, the accuracy rate exceeds 90% after reaching the 80th iteration. The batch size has not been increased to avoid overfitting the model. *The training result accuracy rate was 96.9%.*

5. Conclusions

In this study, an approach is proposed to create quantum circuits for quantum computers, which have much faster computational power than classical computers. Thanks to the proposed approach, it is predicted that it will accelerate the development of studies in the fields of artificial intelligence, machine learning, and deep learning. In order to create quantum circuits used in quantum computers, LSTM neural network architecture is used. The neural network is trained with categorical cross-entropy loss function, Adam optimization algorithm, 25 batch size, and 100 epoch iterations. Real data were produced for the training of the neural network and the trainings were made with these data. Successful results have been obtained in the training. Considering successful and unsuccessful results, the analysis of the effective factors was made. A success rate of 96.9% was achieved with optimum parameters. After these success rates, it is thought that there will be a shift from computers with high hardware costs to quantum computers. Thanks to this study, classical algorithms will be adapted to quantum computing.

6. Acknowledgments

This study was supported by the TUBITAK (The Scientific and Technological Research Council of Turkey) under Grant No: 121E439

7. References

[1] M. DIxit, A. Tiwari, H. Pathak, and R. Astya, "An overview of deep learning architectures, libraries and its applications areas," *Proceedings - IEEE 2018 International Conference on Advances in Computing, Communication Control and Networking, ICACCCN 2018*, pp. 293–297, 2018, doi: 10.1109/ICACCCN.2018.8748442.

[2] N. F. Bar and M. Karakose, "A DNN Based Approach to Automatically Generating Operator Matrix in Quantum Computing," Munich, Germany, May 2023.

[3] R. Van Meter, "Quantum Computing's Classical Problem, Classical Computing's Quantum Problem," *Found Phys*, vol. 44, no. 8, pp. 819–828, Aug. 2014, doi: 10.1007/s10701-014-9807-z.

[4] A. A. Chien and V. Karamcheti, "Cover Feature." 2013. doi: 10.1109/MC.2013.431.

[5] H. Yetiş and M. Karaköse, "Makine Öğrenmesi Yöntemlerinde Yüksek Başarım için Kuantum Bilgisayar ve Hesaplamanın Kullanımı," *Türkiye Bilişim Vakfı Bilgisayar Bilimleri ve Mühendisliği Dergisi*, vol. 14, no. 1, pp. 47–56, 2021, doi: 10.54525/tbbmd.845472.

[6] N. F. Bar, H. Yetis, and M. Karakose, "An efficient and scalable variational quantum circuits approach for deep reinforcement learning," *Quantum Inf Process*, vol. 22, no. 8, p. 300, Aug. 2023, doi: 10.1007/s11128-023-04051-9.

[7] N. F. Bar, H. Yetis, and M. Karakose, "A Quantum-Classical Hybrid Classifier Using Multi-Encoding Method for Images," in *2023 27th International Conference on Information Technology (IT)*, IEEE, Feb. 2023, pp. 1–4. doi: 10.1109/IT57431.2023.10078617.

[8] H. Yetis and M. Karakose, "A New Framework for Quantum Image Processing and Application of Binary Template Matching," in *2022 26th International Conference on Information Technology, IT 2022*, Institute of Electrical and Electronics Engineers Inc., 2022. doi: 10.1109/IT54280.2022.9743534.

[9] N. F. Bar, H. Yetis, and M. Karakose, "An Approach Based on Quantum Reinforcement Learning for Navigation Problems," in *2022 International Conference on Data Analytics for Business and Industry, ICDABI 2022*, Institute of Electrical and Electronics Engineers Inc., 2022, pp. 593–597. doi: 10.1109/ICDABI56818.2022.10041570.

[10] R. Sumathy, S. F. Sohail, S. Ashraf, S. Y. Reddy, S. Fayaz, and M. Kumar, "Next Word Prediction While Typing using LSTM," in *2023 8th International Conference on Communication and Electronics Systems (ICCES)*, IEEE, Jun. 2023, pp. 167–172. doi: 10.1109/ICCES57224.2023.10192602.

[11] P. A. Naidu, K. D. K. Yadav, B. Meena, and Y. V. N. Meesala, “Sentiment Analysis By Using Modified RNN And A Tree LSTM,” *Proceedings - 2022 International Conference on Computing, Communication and Power Technology, IC3P 2022*, pp. 6–10, 2022, doi: 10.1109/IC3P52835.2022.00012.
[12] L. Ma and Y. Zhang, “Using Word2Vec to Process Big Text Data,” in *IEEE International Conference on Big Data*, IEEE, 2015. doi: 10.1109/BigData.2015.7364114.
[13] R. Tiwang, T. Oladunni, and W. Xu, “A Deep Learning Model for Source Code Generation,” in *Conference Proceedings - IEEE SOUTHEASTCON*, 2019, pp. 1–14. doi: 10.1109/SoutheastCon42311.2019.9020360.
[14] H. V. K. S. Buddana, S. S. Kaushik, P. S. V Manogna, and S. K. P.S, “Word Level LSTM and Recurrent Neural Network for Automatic Text Generation,” *International Conference on Computer Communication and Informatics*, 2021, doi: 10.1109/ICCCI50826.2021.9402488.
[15] R. Van Meter and D. Horsman, “A blueprint for building a quantum computer,” *Commun ACM*, vol. 56, no. 10, pp. 84–93, Oct. 2013, doi: 10.1145/2494568.
[16] F. Jazaeri, A. Beckers, A. Tajalli, and J.-M. Sallese, “A Review on Quantum Computing: Qubits, Cryogenic Electronics and Cryogenic MOSFET Physics,” Aug. 2019, [Online]. Available: http://arxiv.org/abs/1908.02656
[17] D. Willsch *et al.*, “Benchmarking Advantage and D-Wave 2000Q quantum annealers with exact cover problems,” *Quantum Inf Process*, vol. 21, p. 141, 2022, doi: 10.1007/s11128-022-03476-y.
[18] N. Elsayed, A. S. Maida, and M. Bayoumi, “A Review of Quantum Computer Energy Efficiency,” in *2019 IEEE Green Technologies Conference(GreenTech)*, IEEE, Apr. 2019, pp. 1–3. doi: 10.1109/GreenTech.2019.8767125.
[19] N. F. Bar and M. Karakose, “Kuadrosim: An Optimized and Practical Quantum Circuit Simulator,” *SoftwareX*, 2023, doi: http://dx.doi.org/10.2139/ssrn.4467630.
[20] K. Bertels *et al.*, “Quantum Computer Architecture Toward Full-Stack Quantum Accelerators,” *IEEE Transactions on Quantum Engineering*, vol. 1, pp. 1–17, 2020, doi: 10.1109/TQE.2020.2981074.
[21] M. A. Serrano *et al.*, “Quantum Software Components and Platforms: Overviewand Quality Assessment,” *ACM Comput Surv*, vol. 55, no. 8, p. 164, 2022, doi: 10.1145/3548679.
[22] F. Ertam and G. Aydın, “Data classification with deep learning using tensorflow,” *2nd International Conference on Computer Science and Engineering, UBMK 2017*, pp. 755–758, 2017, doi: 10.1109/UBMK.2017.8093521.

International Conference on Advances and Innovations in Engineering

Fault Detection Method Using Truth Table in Quantum Circuits

Reyhan YILMAZ[1], Tuba ŞANLI [2], Orhan YAMAN [3], Mehmet KARAKÖSE [4]
[1,2,3]Department of Digital Forensics Engineering, Fırat University, Elazig, Turkey
[4]Department of Computer Engineering, Fırat University, Elazig, Turkey
[1]211144104@firat.edu.tr, [2]222144109@firat.edu.tr, [3]orhanyaman@firat.edu.tr, [4]mkarakose@firat.edu.tr

[1](ORCID:0000-0001-5899-0957), [2](ORCID:0009-0002-8636-1386), [3](ORCID:0000-0001-9623-2284), [4](ORCID:0000-0002-3276-3788)

Abstract
Quantum circuits are the foundation of quantum computers and quantum technologies. These circuits are created using quantum systems called quantum bits (qubits). Qubits are in a complex state that can take both a 0 and a 1 state at the same time, unlike the bits used by traditional computers. This provides features such as the ability of quantum circuits to perform parallel processing and solve some computational problems faster. There are many types of faults in quantum circuits. It is important to detect faults so that the quantum circuits to be developed can produce accurate results. In this study, a method using a truth table is proposed to detect possible faults that may occur in quantum circuits. The truth table is obtained from the '.tfc' files used in the creation of quantum circuits. The obtained truth table is compared with the output of the quantum circuit.

Keywords: Quantum Circuits, Fault Detection, Quantum Computing, Truth Table.

1. Introduction

Quantum computers are a revolutionary technology that has the potential to have computational speeds unmatched by conventional computers. The basis of this technology is the design and use of circuits called quantum circuits. Quantum circuits are created using complex quantum systems and are the basis of quantum computers and other quantum technologies. However, it is very important to ensure and test the accuracy of these circuits. The truth table of quantum circuits is a table that shows the results of all the input combinations of a quantum circuit. This table shows the correct output for each combination of inputs and is used to test the functionality of the quantum circuit and check its accuracy. To construct the truth table, first, all combinations of the input states of the quantum circuitry are listed Then the output is calculated for each combination of inputs, and the results are added to the table. The table is used to test the functionality of the quantum circuit. And it can be used to check accuracy. Creating a truth table in quantum circuits ensures the circuit works properly. This table can also detect faults within the quantum circuitry and for development purposes.

Tools Used in Quantum Applications

• Qiskit: It is a library developed by IBM Quantum that enables quantum calculations with Python. Qiskit is a common tool used to build and simulate quantum circuits and generate truth tables. With Qiskit, the functionality of quantum circuits can be tested and the results analyzed.
• Cirq: It is a quantum programming framework developed by Google and a tool for the creation and analysis of quantum circuits with Python. Cirq can be used to generate truth tables when simulating quantum circuits.
• PyQuil: It is a library developed by Rigetti Computing that enables the creation and control of quantum circuits in Python language. PyQuil can be used as a tool to create and analyze truth tables of quantum circuits.

[1] Corresponding author

• Q# Language: It is a quantum programming language developed by Microsoft. This language, which is integrated with Python, can be used for the creation and simulation of quantum circuits and the creation of truth tables.
• Quantum Inspire: It is a cloud-based quantum computing platform developed by QuTech. It comes with Python integration and can be used for the creation and simulation of quantum circuits and the creation of truth tables.
Widespread use of the Python programming language in the quantum computing community has led to the development of various tools for constructing truth tables in quantum circuits. Tools such as Qiskit, Cirq, PyQuil, Q# Language, and Quantum Inspire are common tools used for the creation and analysis of truth tables of quantum circuits. These devices have powerful capabilities for performing quantum computations and modeling quantum circuits.

Related Studies

Quantum computing is a very exciting field with the potential to exceed the limitations of traditional computers. Quantum circuits form the basic building blocks of quantum computers and are circuits where quantum gates perform various calculations by manipulating the states of qubits. Truth tables are important for analyzing the functionality and performance of quantum circuits.
Detection and isolation of faults is an extremely critical step in the physical realization of quantum circuits. The field of quantum computing, another interesting topic, is also developing rapidly. Today, there is a shortage of professionals with deep computer and physics knowledge who can meet the needs of companies developing and researching quantum technologies.
This article focuses on extensive studies of faults in quantum circuits. The studies in the literature on truth tables used to evaluate the functionality of quantum circuits are examined. The literature review includes some of the theoretical information and studies from past years to the present on quantum fault tolerance and quantum computing.
Rahaman et al.[1] focused on fault diagnosis in reversible circuits under the missing gate fault model. Under this model, they presented a new fault detection technique in a combination circuit with missing gate faults [1].
Barends et al.[2] present a quantum-related study by showing a set of universal logic gates in superconducting multiqubit processors. They stated that the average one-qubit gate accuracy reached 99.92% and the two-qubit gate accuracy reached 99.4% [2]. Lin et al.[3] By introducing a tool called physical design sensitive fault-tolerant quantum circuit synthesis (PAQCS), they offer a 30.1% reduced overhead in converting logic circuits to physical circuits compared to previous work [3]. Bera [4] showed that the behavior of faulty quantum circuits under the single fault assumption can be fully characterized by faulty gates and corresponding fault patterns [4]. Orts et al.[5] analyzed state-of-the-art reversible adders for quantum computing and classified them using metrics comparing their strengths and weaknesses [5]. Bocharov et al.[6] showed that they developed a simpler and more general method for reversibly synthesizing probabilistic quantum circuits [6]. Cai et al.[7] examined the recent development of bosonic codes and discussed the opportunities of bosonic codes in fault-tolerant quantum computation and other quantum applications [7]. Chen et al.[8] investigated the previously uncontrollable quantum circuits by proving the conditions for the two circuits to be partially equivalent, and developing algorithms based on this condition [8]. Gurl et al.[9]stated that decision diagrams are a promising data structure in quantum circuit simulation and they have found a successful application [9]. Wang et al.[10] focused on a new image encryption algorithm and showed that the truth table is based on the new chaos and spread values [10]. Mirizadeh et al.[11] used the FHAS algorithm by designing fault-tolerant reversible half and full adders/subtractors [11]. Singh et al.[12]implemented quantum circuits in Python in different test scenarios faster using Qiskit [12]. Swathi et al.[13] made applications focusing on various reversible logic Gates [13]. Yetis et al.[14] developed a new algorithm for optimal circuit generation and focused on image data [14]. Karmakar et al.[15] proposed a fault-tolerant logic gate-based RO PUF [15]. Golestan et al.[16] discussed the use of quantum computing in power systems and summarized recent developments [16]. Sharma et al.[17] continued their studies by focusing on various issues [17]. Kissinger et al. [18] proposed a method that aims to reduce the number of non-Clifford gates in fault-tolerant quantum computations [18]. Bar et al. [19] aimed to overcome the limited qubit number barrier by using a variational quantum circuit (VQC) [19].

Motivation

Quantum circuits serve as the fundamental components of quantum computers, and quantum gates and circuits are designed to achieve specific quantum operations. The truth table is a tabular representation that maps input evaluations to corresponding output states, commonly used in classical computers to depict logical operations.
In the literature concerning reversible quantum circuits, it becomes evident that understanding the count of inputs, outputs, and gates is crucial for optimizing quantum circuits. An identified gap in the literature pertains to the automatic determination of inputs, outputs, and gate quantities within quantum circuits. This existing gap within the literature constitutes the principal motivation for our study. The motivation to detect the truth table in quantum circuits is important for quantum computers to become more complex and scalable. Under this motivation, determining truth tables of quantum circuits can help evaluate factors such as fault tolerance, side effects, and efficiency of quantum gates and circuits. Thus, it can guide the development process to enable quantum computers to produce more reliable and accurate results.

2. Types of Faults in Quantum Circuits

Quantum circuits are constructed using single-qubit and multi-qubit quantum gates. Circuit failures can arise during the creation of quantum circuits. There are various reasons for circuit faults, including issues within the system, faults in system components, and disruptions from the external environment. There are types of faults that permanently or temporarily affect the capabilities of a circuit for a long or limited time. Failure models that may occur in quantum circuits have been examined in five types in the literature. These fault types are shown in Figure 1.

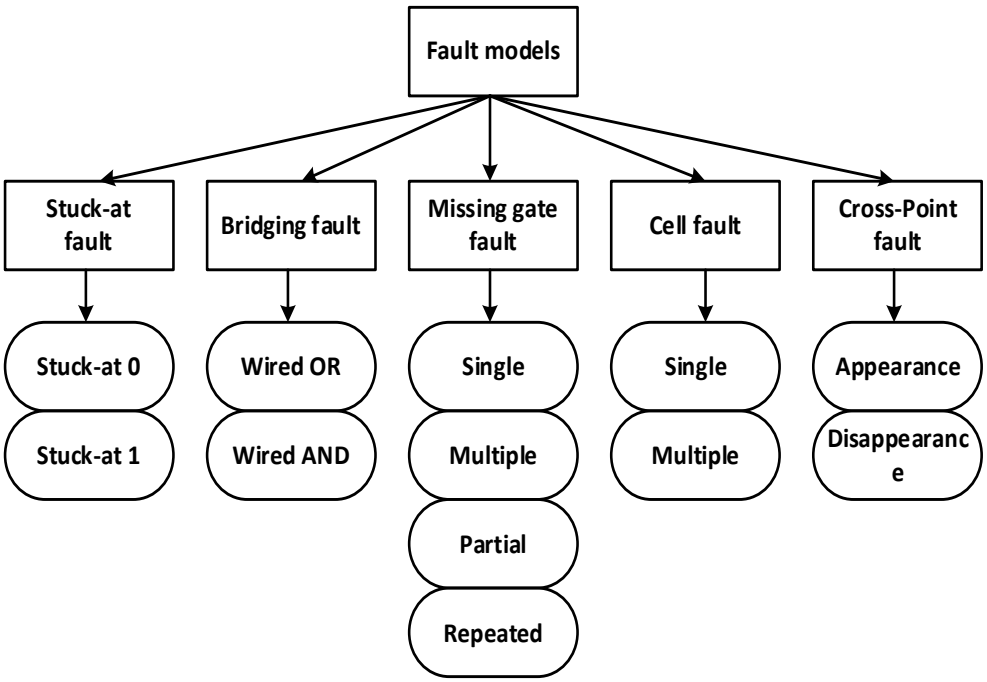

Figure 1. Failure models in quantum circuits[20]

As depicted in Figure 1, quantum circuits can experience failures such as Stuck-at, Bridging, Missing gate, Cell, and Cross-Point faults. These failures can have an impact on the results of quantum circuits. Figure 2 illustrates the instances of Stuck-at, Bridging, Missing gate, Cell, and Cross-Point failures.

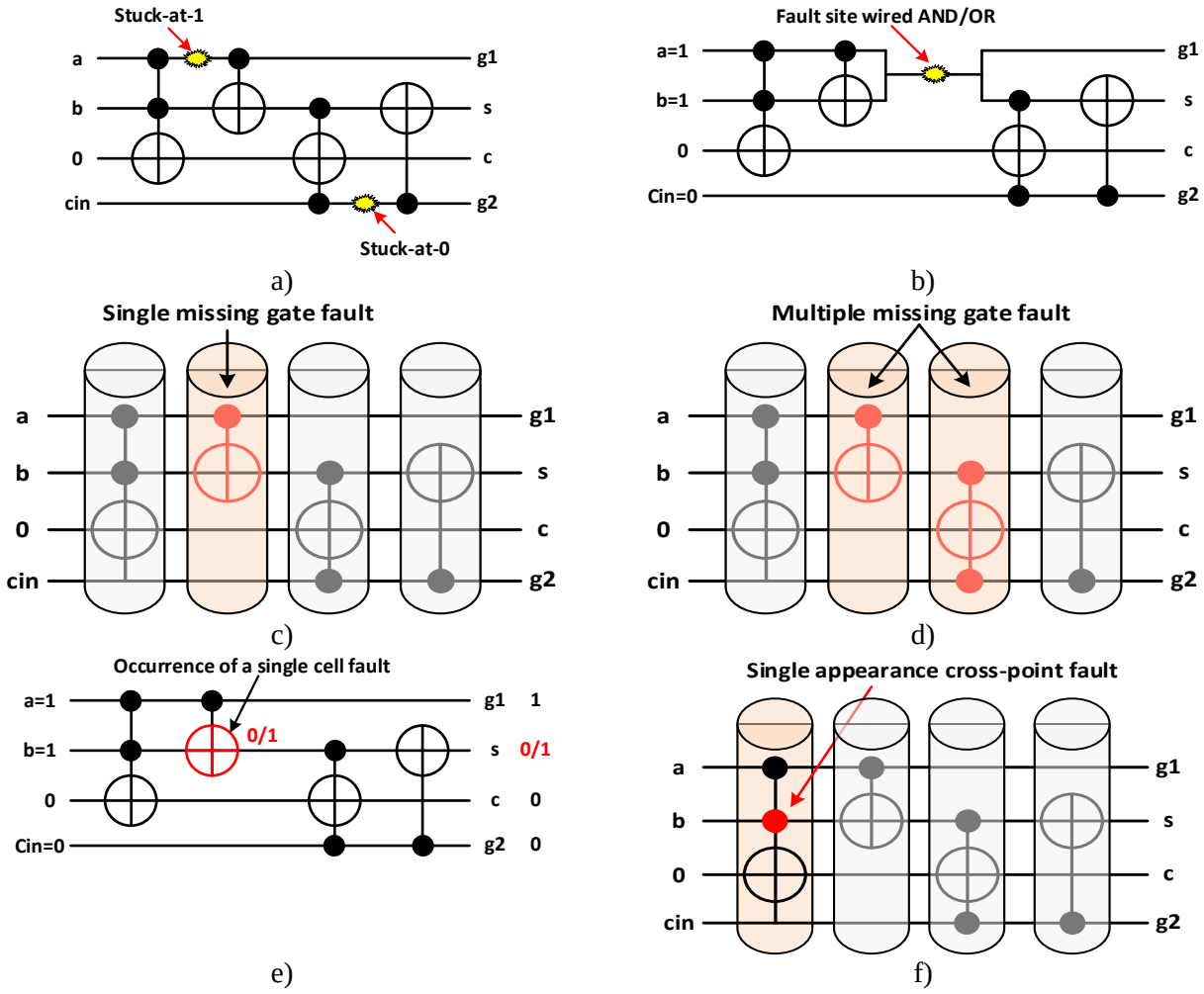

Figure 2. Fault types of quantum circuits[20] a) The stuck-at fault model b) The bridging fault model c) The single missing gate fault model d) The multiple missing gate fault model e) The single-cell fault model f) The single appearance cross-point fault model

3. Material Method

The initial phase involves the generation of sample quantum circuits. During the construction of these circuits, a MATLAB program was employed, leading to the development of a specialized software package. Within this software package, ".tfc" files are generated. Subsequently, the necessary modifications were made to these ".tfc" files, resulting in the transformation of these files into quantum circuits. This transformation was accomplished utilizing the "RCViewer+" quantum simulation tool. The purpose of creating these data sets is to extract the state table of these circuits and to compare the state table we want with the state table of the faulty circuit to determine whether there is an fault in this circuit. The truth table was obtained after the quantum circuit converted from the ".tfc" file was passed through matrix multiplication. Next, the truth table was extracted using the "RCViewer+" quantum simulator from the previously generated ".tfc" file. The acquired truth tables will be subjected to a comparative analysis. An illustrative representation of the approach introduced in this research is provided in Figure 3.

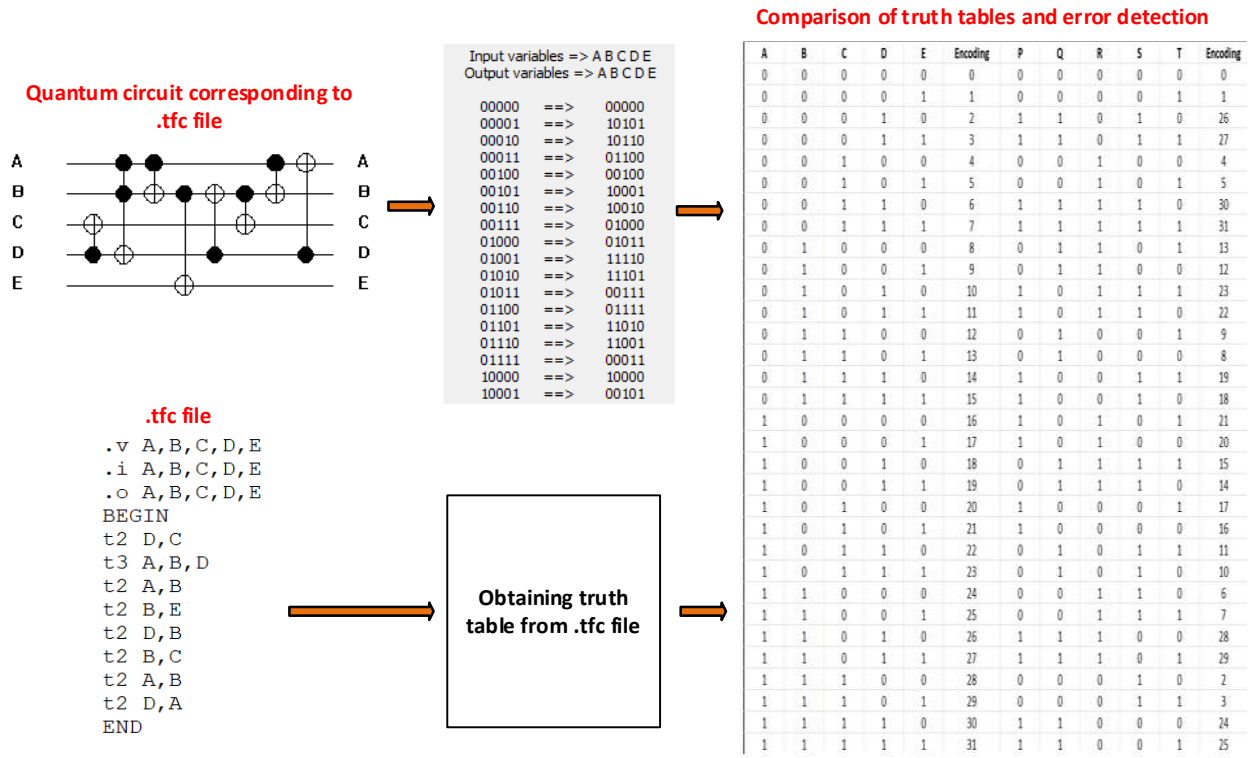

Figure 3. Graphical summary of the proposed method for the detection of the quantum circuit and input number

Data Set

In this study, the primary objective is to assemble a dataset using quantum simulators that are implemented on conventional computers. The dataset will then be subjected to image processing techniques and harnessed by deep learning models to identify various elements within the circuits, including inputs, outputs, gates, and circuit components. By acquiring the state tables of the scrutinized quantum circuits, it becomes feasible to detect any faults present within these circuits. The approach employed to determine the output of a provided input in the quantum circuit is elucidated in Figure 4.

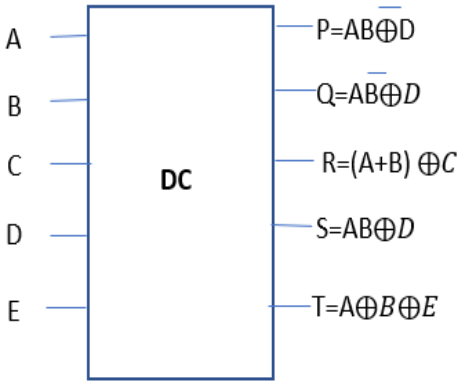

Figure 4. The equation used to construct the truth table of the quantum circuit

The process of generating the truth table then involves calculating all combinations of the inputs of the quantum circuit and determining the output for each combination. These results can then be collected in a table.
It presents the complete array of input state combinations alongside the associated circuit outputs for each state. These outputs have been pre-determined for every possible input combination. This computation is achieved by performing matrix multiplications of gates that are deployed within the qubits of the circuit, corresponding to each distinct input state. The truth table that emerges from this process is depicted in Figure 5.

A	B	C	D	E	Encoding	P	Q	R	S	T	Encoding
0	0	0	0	0	0	0	0	0	0	0	0
0	0	0	0	1	1	0	0	0	0	1	1
0	0	0	1	0	2	1	1	0	1	0	26
0	0	0	1	1	3	1	1	0	1	1	27
0	0	1	0	0	4	0	0	1	0	0	4
0	0	1	0	1	5	0	0	1	0	1	5
0	0	1	1	0	6	1	1	1	1	0	30
0	0	1	1	1	7	1	1	1	1	1	31
0	1	0	0	0	8	0	1	1	0	1	13
0	1	0	0	1	9	0	1	1	0	0	12
0	1	0	1	0	10	1	0	1	1	1	23
0	1	0	1	1	11	1	0	1	1	0	22
0	1	1	0	0	12	0	1	0	0	1	9
0	1	1	0	1	13	0	1	0	0	0	8
0	1	1	1	0	14	1	0	0	1	1	19
0	1	1	1	1	15	1	0	0	1	0	18
1	0	0	0	0	16	1	0	1	0	1	21
1	0	0	0	1	17	1	0	1	0	0	20
1	0	0	1	0	18	0	1	1	1	1	15
1	0	0	1	1	19	0	1	1	1	0	14
1	0	1	0	0	20	1	0	0	0	1	17
1	0	1	0	1	21	1	0	0	0	0	16
1	0	1	1	0	22	0	1	0	1	1	11
1	0	1	1	1	23	0	1	0	1	0	10
1	1	0	0	0	24	0	0	1	1	0	6
1	1	0	0	1	25	0	0	1	1	1	7
1	1	0	1	0	26	1	1	1	0	0	28
1	1	0	1	1	27	1	1	1	0	1	29
1	1	1	0	0	28	0	0	0	1	0	2
1	1	1	0	1	29	0	0	0	1	1	3
1	1	1	1	0	30	1	1	0	0	0	24
1	1	1	1	1	31	1	1	0	0	1	25

Figure 5. The truth table obtained as a result of matrix multiplication

4. Experimental Results

In this research, the creation of the dataset involved the generation of ".tfc" files through the MATLAB program. These generated ".tfc" files were subsequently imported into the "RCViewer+" program, and the resulting quantum circuits were saved in ".bmp" format. The truth tables of the recorded quantum circuits were created by the “RCViewer+” generation and compared with the truth tables we created with the “.tfc” code. These two states recorded the same result for life in the table. The fact that the two-state tables are the same shows that there is no fault in the circuit.

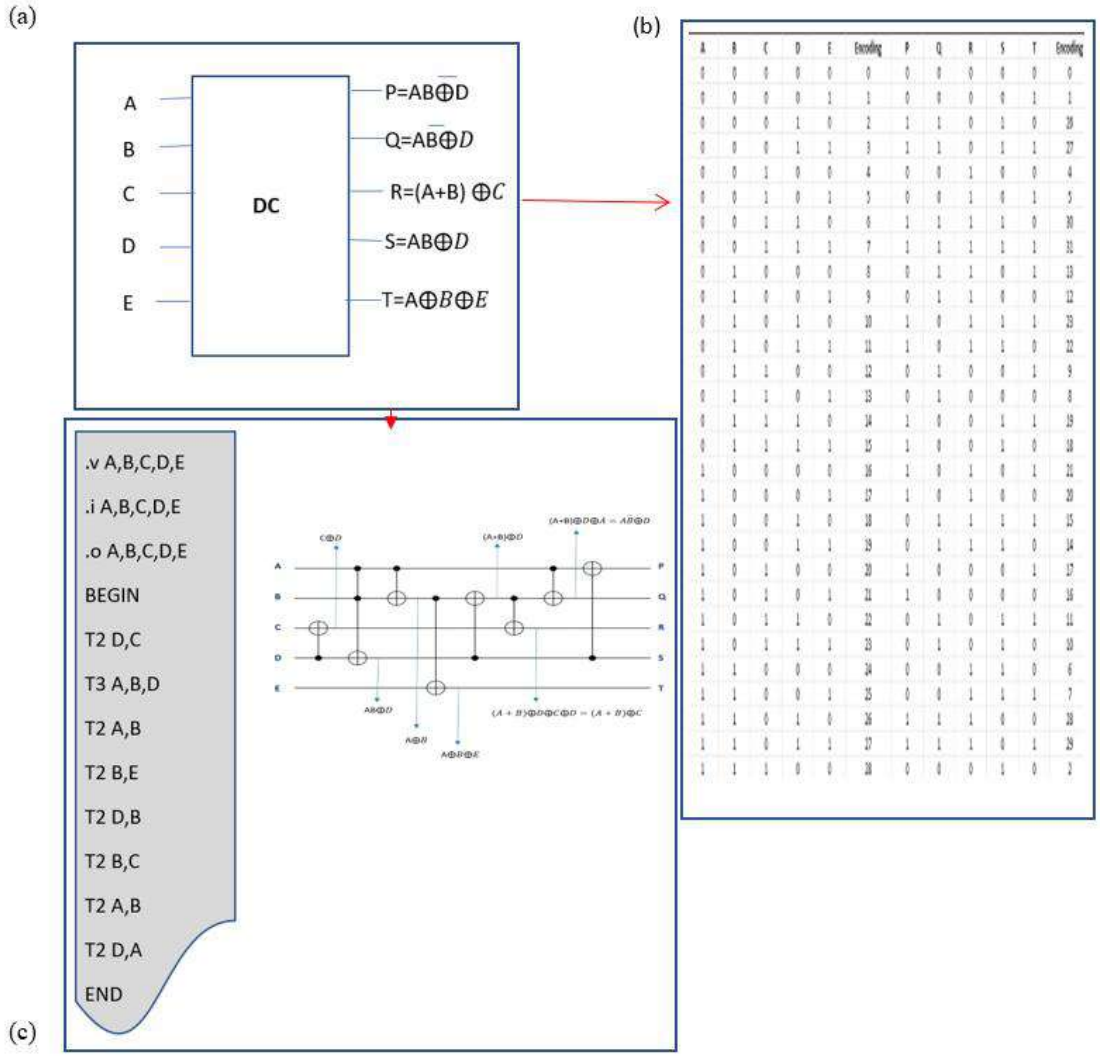

Figure 6. Comparison of truth tables created by two different methods

The accuracy of quantum circuits holds paramount importance in the success of quantum computing, as faults can rapidly accumulate and undermine the integrity of computation results. To evaluate the performance of quantum circuits, truth tables are employed. These truth tables facilitate the assessment of quantum circuits by juxtaposing their outputs against the anticipated outputs. Such tables offer insights into the precision of individual quantum gates as well as the overall accuracy of the entire circuit. Accurate truth tables play a pivotal role in the design of efficient quantum circuits, enabling researchers to pinpoint and rectify faults within the circuitry. Consequently, the generation of precise truth tables stands as a crucial and indispensable phase in the advancement of quantum computing technology.

Experimental results obtained in the process of constructing the truth table of quantum circuits are used to test the functionality of quantum circuits and check their accuracy. These results show that the output is calculated correctly for all combinations of the input states of the quantum circuit.

Experimental results are constantly studied and improved to improve the accuracy of quantum circuits and to be able to solve more complex problems. These studies will help quantum computers and quantum technologies become more widespread.

5. Conclusions

In this study, the complete array of input states for the quantum circuit is generated through the utilization of the TFC library. Subsequently, by computing the output value for each distinct combination, a comprehensive truth table is

formulated. This procedure aids in comprehensively documenting the behavior of the quantum circuit across all potential input scenarios.

Truth tables have a wide variety of potential applications in quantum computing. It can be used to optimize the design of quantum circuits, identify and correct faults in quantum hardware, and evaluate the performance of quantum algorithms. Additionally, accurate truth tables can be used to compare the performance of different quantum computers and simulators, allowing researchers to compare their results and identify areas for improvement.

Experimental results have shown that the generated truth table accurately reflects the functionality of the quantum circuit. This method could be valuable for testing quantum circuits and checking their accuracy.

This endeavor establishes an initial foundation for constructing truth tables for quantum circuits. Subsequent efforts could potentially enhance and fine-tune this methodology, or even explore alternative approaches tailored for more extensive and more intricate quantum circuits. The realm of truth table creation within quantum computing holds numerous uncharted avenues for future investigation and innovation. These opportunities extend to research and development, offering prospects for devising novel techniques to generate comprehensive truth tables.

6. Acknowledgements

This work was supported by the TUBITAK (The Scientific and Technological Research Council of Turkey) under Grant No: 121E439.

7. References

[1] Rahaman H, Kole DK, Das DK, Bhattacharya BB. Fault diagnosis in reversible circuits under missing-gate f ault model. Comput Electr Eng 2011;37:475–85. https://doi.org/10.1016/j.compeleceng.2011.05.005.

[2] Barends R, Kelly J, Megrant A, Veitia A, Sank D, Jeffrey E, et al. Superconducting quantum circuits at the surface code threshold for fault tolerance. Nature 2014;508:500–3. https://doi.org/10.1038/nature13171.

[3] Lin C-C, Sur-Kolay S, Jha NK. PAQCS: Physical Design-Aware Fault-Tolerant Quantum Circuit Synthesis. IEEE Trans Very Large Scale Integr VLSI Syst 2015;23:1221–34. https://doi.org/10.1109/TVLSI.2014.2337302.

[4] Bera D. Detection and Diagnosis of Single Faults in Quantum Circuits. IEEE Trans Comput-Aided Des Integr Circuits Syst 2018;37:587–600. https://doi.org/10.1109/TCAD.2017.2717783.

[5] Orts F, Ortega G, Combarro EF, Garzón EM. A review on reversible quantum adders. J Netw Comput Appl 2020;170:102810. https://doi.org/10.1016/j.jnca.2020.102810.

[6] Bocharov A, Roetteler M, Svore KM. Efficient synthesis of probabilistic quantum circuits with fallback. Phys Rev A 2015;91:052317. https://doi.org/10.1103/PhysRevA.91.052317.

[7] Cai W, Ma Y, Wang W, Zou C-L, Sun L. Bosonic quantum error correction codes in superconducting quantum circuits. Fundam Res 2021;1:50–67. https://doi.org/10.1016/j.fmre.2020.12.006.

[8] Chen T-F, Jiang J-HR, Hsieh M-H. Partial Equivalence Checking of Quantum Circuits 2022.

[9] Grurl T, Fus J, Wille R. Noise-Aware Quantum Circuit Simulation With Decision Diagrams. IEEE Trans Comput-Aided Des Integr Circuits Syst 2023;42:860–73. https://doi.org/10.1109/TCAD.2022.3182628.

[10] Wang X, Zhang M. An image encryption algorithm based on new chaos and diffusion values of a truth table. Inf Sci 2021;579:128–49. https://doi.org/10.1016/j.ins.2021.07.096.

[11] Mirizadeh SMA, Asghari P. Fault-tolerant quantum reversible full adder/subtractor: Design and implementation. Optik 2022;253:168543. https://doi.org/10.1016/j.ijleo.2021.168543.

[12] Singh PN, Aarthi S. Quantum Circuits – An Application in Qiskit-Python. 2021 Third Int. Conf. Intell. Commun. Technol. Virtual Mob. Netw. ICICV, Tirunelveli, India: IEEE; 2021, p. 661–7. https://doi.org/10.1109/ICICV50876.2021.9388498.

[13] Swathi M, Rudra B. Implementation of Reversible Logic Gates with Quantum Gates. 2021 IEEE 11th Annu. Comput. Commun. Workshop Conf. CCWC, NV, USA: IEEE; 2021, p. 1557–63. https://doi.org/10.1109/CCWC51732.2021.9376060.

[14] Yetiş H, Karaköse M. An improved and cost reduced quantum circuit generator approach for image encoding applications. Quantum Inf Process 2022;21:203. https://doi.org/10.1007/s11128-022-03546-1.

[15] Karmakar M, Naz SF, Shah AP. Fault-tolerant reversible logic gate-based RO-PUF design. Mem - Mater Devices Circuits Syst 2023;4:100055. https://doi.org/10.1016/j.memori.2023.100055.

[16] Golestan S, Habibi MR, Mousazadeh Mousavi SY, Guerrero JM, Vasquez JC. Quantum computation in power systems: An overview of recent advances. Energy Rep 2023;9:584–96. https://doi.org/10.1016/j.egyr.2022.11.185.
[17] Kumar Sharma D, Goyal P, Patidar M, Hiteshkumar Bhupatbhai M, Rangari M. An efficient design and demonstration of fault-effects in full-adder circuits based on quantum-dot computing circuits. Mater Today Proc 2023:S2214785323014207. https://doi.org/10.1016/j.matpr.2023.03.374.
[18] Kissinger A, Van De Wetering J. Reducing the number of non-Clifford gates in quantum circuits. Phys Rev A 2020;102:022406. https://doi.org/10.1103/PhysRevA.102.022406.
[19] Bar NF, Yetis H, Karakose M. An efficient and scalable variational quantum circuits approach for deep reinforcement learning. Quantum Inf Process 2023;22:300. https://doi.org/10.1007/s11128-023-04051-9.
[20] Kheirandish D, Haghparast M, Reshadi M, Hosseinzadeh M. Efficient techniques for fault detection and location of multiple controlled Toffoli-based reversible circuit. Quantum Inf Process 2021;20:370. https://doi.org/10.1007/s11128-021-03292-w.

International Conference on Advances and Innovations in Engineering

Quantum Neural Network Models: Literature Review and Application Analysis

Mehmet KARAKÖSE[1], Hasan YETİŞ[2], Çağatay Umut ÖĞDÜ[3], Osman Furkan KÜÇÜK[4]
[1,2,3,4]Bilgisayar Mühendisliği Bölümü, Mühendislik Fakültesi, Fırat Üniversitesi, Elazığ, Türkiye
[1]mkarakose@firat.edu.tr, [2]h.yetis@firat.edu.tr, [3]21026004@firat.edu.tr, [4]21026042@firat.edu.tr

[1](ORCID: 0000-0002-3276-3788), [2](ORCID: 0000-0001-7608-3293), [3](ORCID: 0009-0004-1697-4392), [4](ORCID: 0009-0002-5594-3009)

Abstract

Deep learning methods, capable of finding solutions to a wide range of problems and widely applicable in almost every field due to the increasing computing power, have become the popular technology of today. Global companies are increasing their investments in this direction, leading to the emergence of numerous new start-up companies. Similar developments are also evident in the field of quantum computers and quantum computing. While the birth of physical quantum computers is still relatively new, it is predicted that quantum computing will revolutionize health, finance, cybersecurity sectors, and various complex computational problems. In recent literature research, significant attention has been given to the intersection of these fields, with a focus on the development of quantum neural network models and the interest in quantum algorithms for increasing efficiency in machine learning. This study demonstrates the current state of artificial intelligence fields such as artificial neural networks, deep learning, machine learning, in conjunction with quantum computing technology, and showcases the achievements attained. The studies are presented by conducting domain-specific analyses, showcasing their position and financial magnitude in the industry. The success of quantum neural networks in recent literature studies has been mentioned.

Keywords: quantum computing, artificial neural networks, quantum neural network, artificial intelligence

1. Introduction

The concept of Artificial Neural Network (ANN) has emerged as a result of mimicking the neuron structure of the human brain. Artificial neural networks are systems composed of components resembling neurons that have the capacity to encode, store, and use information for various tasks. Over time, quantum computing has made fascinating progress, and these efforts have had a significant impact on its faster operation. Additionally, when compared to classical computation, quantum computing possesses a much stronger potential. The advancement of quantum computing offers unprecedented opportunities to overcome problems that traditional computers cannot solve. For example, Shor [1] is a quantum algorithm used to rapidly find the factors of large numbers. This algorithm can factorize numbers that would take years to compute using classical methods, in a short period of time. Moreover, the Grover algorithm [2] is a quantum search algorithm used to quickly locate a specific target in a database. It has demonstrated superior performance compared to classical computations.

Classical Artificial Neural Networks (Classical ANN) require more computational resources and time to perform certain complex tasks. On the other hand, Quantum Neural Networks (QNN) can leverage the advantages of quantum computation to solve more complex problems faster and more effectively. The concept of quantum neural network computation was first proposed by Kak [3] in 1995 and later studied in detail. In 1995, Menneer and Narayanan [4] suggested Quantum-inspired Neural Networks (QINN), and this topic was extensively addressed in Menneer's [5] doctoral thesis. Narayanan and Menneer [6] demonstrated through experimental and simulation methods that quantum ANNs are more powerful and efficient compared to traditional ANNs. In 2003, Kouda and his team [7] introduced the Qubit Neural Network model, which is based on qubits. Additionally, Figure 1 provides the number

[1] Corresponding author

of published articles and total citations containing the term 'Quantum Neural Networks' over the years, reflecting both the quantitative and qualitative dimensions of research on this term.

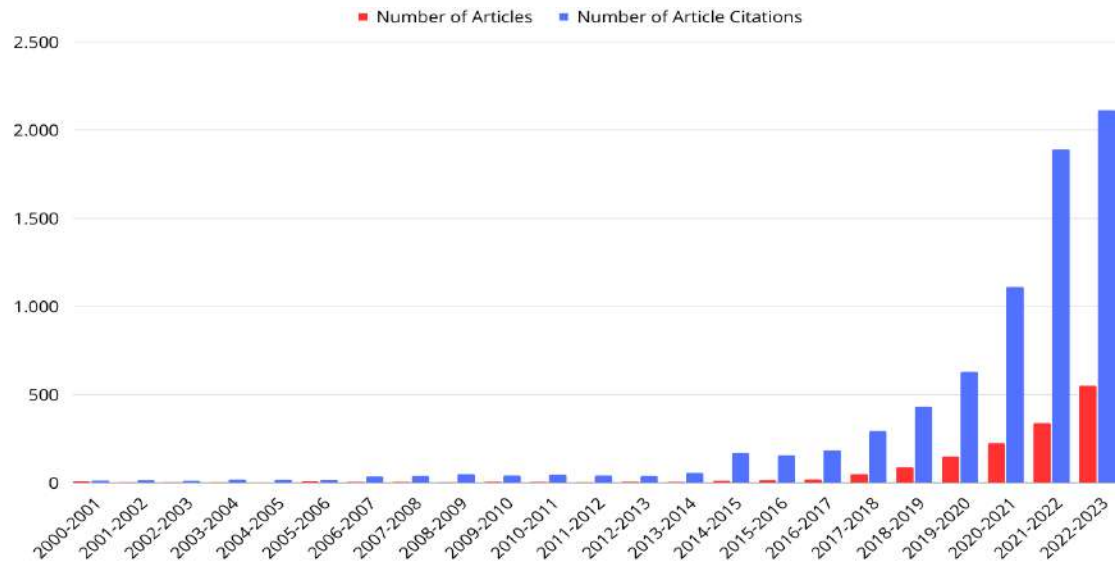

Figure 1. Published articles and total citation count containing 'Quantum Neural Networks'.

It has been suggested that both classical and quantum components could be utilized for the more effective functioning of quantum neural networks. In 2014, Schuld and his team [8] proposed a Quantum Neural Network (QNN) model that combines the unique characteristics of quantum computation with those of neural network computation. In this study, they presented a systematic approach to enhance the QNN model by examining various methods, thereby providing a more organized perspective on QNN research. Schuld and his team [8] proposed several requirements for the creation of a meaningful QNN model. These requirements are listed below:

- The initial state of the quantum system can encode any binary sequence of length N. For instance, it should be able to represent a binary sequence like 001101. This implies that QNN possesses a form of memory capability and enables the representation of input data.
- QNN can reflect one or more fundamental neural computation mechanisms. These mechanisms encompass the operating principles of neural networks (attractive dynamics, synaptic connections, integration and firing, training rules, the structure of a neural network).
- It is based on quantum effects such as evolution, superposition, entanglement, interference and is fully compatible with quantum theory.

- Below are listed some advantages of quantum neural networks compared to classical artificial neural networks:
- Evaluating multiple different possibilities simultaneously through the properties of superposition and entanglement [9].
- Better analysis of specific molecular structures and properties [10].
- Faster and more effective results in optimization problems [10].
- Achieving high performance with fewer hidden neurons [9].
- Faster learning ability compared to traditionals [11].
- High processing speed [12].
- Superposition provides an exponential storage advantage to the quantum network [13].

With the presence of these features, scientists are showing intense interest in advancing quantum neural networks. The future potential of quantum neural networks is highly expansive, making the subject exceptionally compelling.

2. Current State of Quantum Neural Networks

Quantum neural networks are a unique model created by combining the fundamental structure of traditional artificial neural networks with principles of quantum mechanics. In this section, we will take a closer look at how quantum neural networks operate and delve into the topic in more detail by examining some existing models.

2.1. Basic principles of quantum neural networks

Artificial neural networks (ANNs) emulate the biological neural system for information processing [14]. ANNs employ artificial neurons to process input data and generate outputs, adjusting inter-neuron weights through learning. They excel at recognizing intricate data patterns. In the standard three-layer configuration (input, hidden, and output layers), external data is initially processed by the input layer [15,16]. Hidden layers meticulously process inputs, aiding in extracting high-level features, and the output layer derives results from processed data, showcasing the learning potential of ANNs.

Quantum Neural Networks (QNNs) combine classical ANN traits with quantum mechanics' properties, resulting in an intriguing model [10], [17], [18]. QNNs represent artificial neurons as quantum circuits housing parameters of quantum gates. Quantum effects govern inter-neuron connections, enhancing learning and computation.

QNNs synergize the advantages of quantum computing with the processing prowess of artificial neural networks, establishing a potent computational paradigm. Notably, QNNs transcend classical ANNs' limitations, particularly in processing extensive datasets or solving complex problems [17]. This transformative potential in addressing conventional ANN constraints distinguishes QNNs as a pivotal innovation.

2.2. Quantum neural network models

2.2.1. Quantum Multi-Layer Perceptron (M-P) neural network

The Quantum M-P neural network is an extended version of the traditional M-P (Multi-Layer Perceptron) artificial neural networks, incorporating principles of quantum mechanics. Zhou and Ding [19] aimed to enhance the performance of classical neural networks by developing this model to utilize quantum computing capabilities. The Quantum M-P neural network aims to process data using the concept of quantum linear superiority and incorporates principles of quantum computation.

In traditional M-P neural networks, each processing unit calculates the output by multiplying the input and weight values and then applies an activation function. The output of a neuron depends on the weighted sum of inputs and a predetermined threshold. If the threshold is exceeded, the neuron gets activated and produces an output [20]. This activation function is often referred to as a function that provides the nonlinear structure of the neural network.

The Quantum M-P Neural Network introduces a new approach to the learning and processing capabilities of neural networks by incorporating quantum mechanics into traditional neural network computations. By leveraging the advantages of quantum computing, this model has the potential to offer better performance, especially for complex data processing and learning tasks.

2.2.2. Variational Quantum Circuit Neural Networks (VQ-DQN)

The VQ-DQN model is a noteworthy subject among recent advanced-level researches. This model has been addressed in the study by [13], and it has been demonstrated to provide an effective approach for the most advanced quantum processors in recent times. In this context, it is crucial to closely examine the fundamental structure and operating principle of the model. The mentioned VQ-DQN model incorporates the circuit model shown in Figure 2.

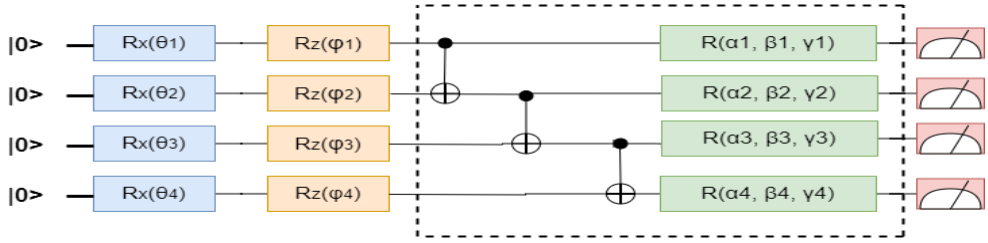

Figure 2. VQ-DQN model architecture [13].

This circuit model integrates the quantum processor and classical computer, aiming to harmonize quantum advantages with classical robustness. Figure 2's circuit model involves quantum gates and parameterized adjustments. Parameterized quantum gates, like Rz(θ) with θ, enhance model flexibility. The classical computer processes inputs, adapting them for the quantum circuit format, yielding the desired output. Parameters in the quantum circuit are updated based on the loss function outcome versus target output. This generates new input sets for improved results, iterated until desired accuracy is met. This model robustly merges quantum and classical computation strengths.

2.2.3. Hybrid Quantum Neural Network (HQNN)

A Hybrid Quantum Neural Network (HQNN) is a vital advancement in this new era, offering advantages, especially with Noisy Intermediate-Scale Quantum (NISQ) devices. This model integrates classical and quantum computing seamlessly. Despite NISQ limitations, these devices hold promise, leveraging complex quantum system traits for quantum advantage.

An artificial intelligence model, the Hybrid Quantum Neural Network (HQNN), involves the integration of classical and quantum devices. The fundamental structure of HQNNs is built upon a processing logic consisting of five steps. The first step involves preprocessing the input data and preparing its features. Subsequently, the input is transformed into quantum form through data encoding. In the third step, the quantum circuit is parameterized and undergoes unitary evolution. Quantum measurements are performed in the fourth step to obtain quantum state information. The final step involves the classical processing of the obtained quantum state [21]. The overall structure of HQNNs demonstrates the effective combination of quantum and classical computation. Particularly, unlike classical artificial neural networks, the importance of preserving nonlinear features is emphasized in HQNNs. To achieve this goal, classical neuron layers can be used in the output processing stage.

A Hybrid Quantum Neural Network (HQNN) stands as a noteworthy development in this emerging era, showcasing several benefits, especially in the context of Noisy Intermediate-Scale Quantum (NISQ) devices. This approach seamlessly merges classical and quantum computing. Despite the inherent constraints of the NISQ era, these devices retain substantial promise, making notable strides in unlocking quantum advantages through the utilization of intricate quantum system attributes.

2.2.4. Qubit Neural Network

Matsui and colleagues [22] have proposed a Qubit neuron structure that showcases quantum learning capabilities. This original Qubit neuron model demonstrates the ability to effectively overcome challenges like data compression. They put forth a suggestion for a Qubit neural network that governs the interactions between neurons according to quantum rules [6]. This Qubit neuron structure has paved the way for the emergence of a layered, new quantum feedforward neural network structure, as described by Kouda and colleagues [20].
Jeswal and his team [12] explain that a qubit neural network constitutes a multi-layered structure composed of quantum bit neurons. In his own study, Jeswal demonstrates a general model of a quantum neuron, drawing upon Kouda's previous research [7]. The qubit neuron model is given in Figure 3.

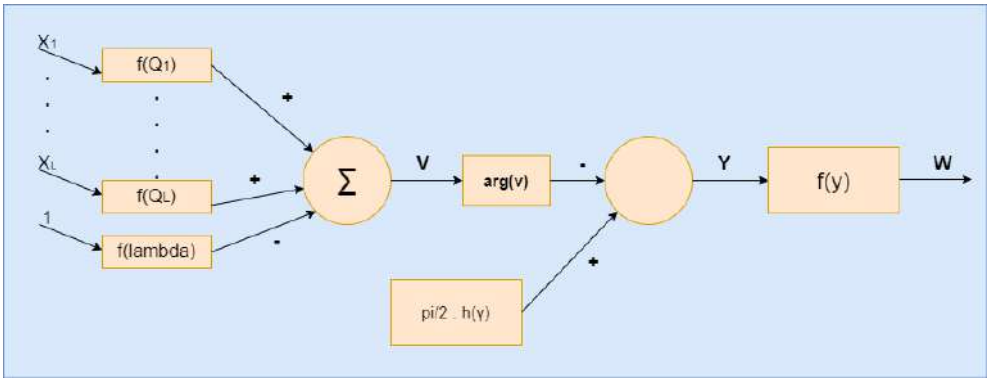

Figure 3. Qubit neuron model [7].

Kouda and his team [6], through an analysis of simulation results based on the qubit neuron structure, observed that the qubit model is significantly more effective in learning problems compared to the traditional model. Additionally, as mentioned in the study [12], the learning capability of the qubit neural network was examined using the 4-bit parity control problem. As a result, the qubit model exhibited superior performance. In this context, the multi-layered qubit neural network proposed by Matsui and colleagues [23] has been integrated into a neural network composed of qubit neurons to test pattern recognition and similar problems within the neural network.

Figure 4 summarizes the advantages and disadvantages of the described quantum neural network models. Each model has been developed using quantum mechanics properties in different ways and has various application domains. The advantages and disadvantages listed in the table reflect the factors that should be considered when choosing these models. The performance of the models will be influenced by application requirements and the proper utilization of quantum technology. Therefore, it's important to carefully examine the table when determining which model is more suitable for a given situation.

Quantum Neural Network Model	Advantages	Disadvantages
Quantum M-P Neural Network	It is a model developed based on quantum properties. It provides fast learning.	May have limited learning capacity. Effective use of quantum features is required.
Variational Quantum Circuit Neural Networks	It effectively moves nonlinear operations from classical computers to quantum processors.	The error-prone nature of quantum computations and the possibility of environmental uncertainties to affect their results.
Hybrid Quantum Neural Network	By combining the strengths of classical and quantum devices, it may be possible to solve more complex problems.	Its design and optimization is complex. The limitations of quantum devices may cause implementation difficulties for this model.
Qubit Neural Network	It has quantum learning abilities and efficient learning capacity. It can achieve effective results in areas such as data compression and control problems.	Quantum computations need to be performed stably and reliably. Calculations can be complex and require high computational power.

Figure 4. Advantages and disadvantages of quantum neural network models.

3. Literature Research and Applications

In this section of our paper, we aim to provide readers with insights into the usage areas and applicability of QNNs by discussing current literature research and applications we previously mentioned.
In the article [24], the authors proposed a hybrid application aiming to recognize handwritten characters by adding a quantum convolutional layer to a model based on convolutional neural networks (CNN). This model processes input data through the quantum convolutional layer to generate feature maps. The quantum convolutional filter operates on spatially local subregions of the images. Subsequently, these subregions are encoded into quantum states, passed

through a random quantum circuit and subjected to a decoding process. In the experiment, both the convolutional neural network model and the proposed quantum convolutional model were used. When the size of the training dataset was smaller, the proposed quantum model outperformed the classical CNN model; however, as the dataset size increased, the accuracy difference between them decreased.

In the article [25], a new model called Hybrid Quantum Convolutional Neural Network (HQCNN) is proposed and utilized for the classification of symmetry-protected topological (SPT) phase data. This paper aims to expedite the training process by combining a traditional fully connected network with a quantum filter. The quantum filter extracts features from the data using quantum convolution (QConv) and quantum pooling (QPool) layers, followed by the activation of a fully connected neural network. The HQCNN model with 4 quantum filters exhibited superior performance compared to other models with 1, 2, 3 and 5 filter, achieving a classification accuracy of 99.22% on test data. The results demonstrate that the combination of quantum filters and traditional neural networks is an effective approach in the task of SPT phase classification.
In the article [26], the Parallel Self-Organizing Neural Network (PSONN) architecture presents an approach using errors guided by fuzzy measures and incorporating quantum integrators for backpropagation. The Quantum Version of Parallel Self-Organizing Neural Network (QVPSONN) architecture performs processing in multiple stages for denoising color images and extracting pure color objects. Initially, color images are divided into segments, which are then sent to QMLSONN (Quantum Multi-Layer Self-Organizing Neural Network) for parallel processing. During this process, the QVPSONN architecture adjusts weights using the quantum backpropagation algorithm to rectify errors in the object extraction process. The experiment was conducted on both synthetic and real-world images, revealing that QVPSONN outperforms PSONN in terms of image extraction quality and processing time.

In the article [27], a QNN and Quantum Generative Adversarial Networks (QGAN) were developed for binary image classification. The proposed QNN model, designed specifically for binary classification, so dataset has been created by selecting only the digits 0 and 6 from the MNIST handwritten digit dataset. Subsequently, the QGAN model was utilized to generate new data samples based on examples from the original dataset, thereby augmenting the dataset. To adhere to the qubit limits in the model, the dimensionality reduction method Principal Component Analysis (PCA) was employed. The proposed quantum neural network (QNN) model in the article was designed using the TensorFlow Quantum library. It's mentioned that the proposed QNN model consists of four dense layers, which are organized in the following sequence:

- The data size is reduced.
- Data is transformed into quantum information using the Projected Quantum Kernel Feature (PQK) technique.
- The transformed data serves as input to each layer of the model.
- Throughout the training of the QNN model, hyperparameters are optimized, and training is conducted.

[25]
The model trained with 12,000 image data points and it was tested using 2,000 data points. Test results were compared with a Fully Connected Neural Network (FNN), and the proposed QNN model achieved higher performance than the FNN model. The QNN model attained an accuracy rate of 98.6%, precision of 98.5%, sensitivity of 98.8%, and specificity of 98.5%.

In the article [28], a Hybrid Quantum Neural Network (HQNN) is proposed for predicting the response of drugs in cancer cells, which combines graph convolutional, convolutional, and fully connected layers. The application uses the GDSC dataset, the largest database containing information on cancer cell line susceptibility to drugs and genetic relationships. When tested on a reduced dataset consisting of 5000 training and 1000 testing drug/cell line pairs provided by the dataset, the quantum model outperformed the classical model.

The article [29] explores the feasibility of using the QNN algorithm for breast cancer diagnosis. The QNN model employed the actual breast cancer dataset and achieved success in training and data recognition. When compared to classical Convolutional Neural Networks (CCNN) for mammogram image diagnosis, our study showcases the advantage of QNN in providing higher accuracy in a shorter training time. From this examination, it can be concluded that the commercial utilization of real quantum computers would be a powerful tool for detecting breast cancer rapidly and with high accuracy.

In the article [30], an experimental application of quantum neural networks for recognizing and analyzing facial patterns is presented. Using Principal Component Analysis (PCA), the most significant features of facial patterns from the LFW facial dataset were extracted. The extracted data was then used to train QNN, and the system was tested using programs developed in the Matlab language. When the system was tested using faces of 5 different individuals, it achieved a Total Classification Accuracy (TCA) of 89%.

In the article [31], a hybrid approach combining classical Convolutional Neural Networks (CNN) and QNN is used to detect amplitude shift keying cyber-attacks in a Controller Area Network (CAN) dataset. The dataset was generated by subjecting CAN data recorded from a KIA Soul vehicle to amplitude shift keying attacks. In the experimental phase, CAN data was first transformed into feature maps using a classical neural network (CNN), and these maps were further transformed into quantum data using quantum encoding. The transformed data was then used for attack detection with a QNN. This QNN is a customized quantum classification model to detect attack using quantum data. The hybrid system was compared with a standalone quantum neural network (QNN) and a Long Short-Term Memory Neural Network (LSTM NN). The models were developed using the TensorFlow Quantum library and tested on the provided Cirq simulator in the same library. The hybrid QNN, standalone QNN, and LSTM NN achieved accuracy rates of 93.9%, 62.0%, and 87.8%, respectively, with using their respective test datasets. The experimental results demonstrated that the hybrid network was more efficient in detecting complex cyber attack patterns. Finally, it was concluded that the hybrid quantum neural network could be extended to detect other types of cyber-attacks as well.

Figure 5 depicts the success probabilities of the quantum neural network method proposed in some of the described articles and the compared classical methods. Success rates obtained from [24] with 3500 training images and 1500 test images, success rates obtained from [26] for real-world images exposed to noise with the same ratios, accuracy rates achieved through standard performance metrics on 12,000 handwritten images trained and 2000 test images in [27], a performance rate difference of 15% calculated based on the mean squared error function in [28], and the success rates of the proposed hybrid quantum neural network and the LSTM neural network in [31] are sequentially displayed.

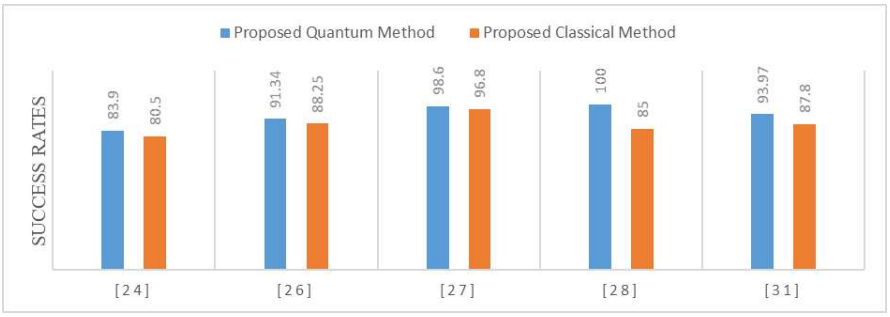

Figure 5. Comparison of proposed quantum methods and classical methods.

4. Conclusion

This research has demonstrated that quantum neural networks yield impressive results, particularly in data analytics and classification tasks, compared to classical neural networks. These networks stand out for their ability to uncover complex relationships and patterns that traditional methods might struggle to solve. Thanks to the computational power of quantum systems, they can achieve higher accuracy rates even in cases of data insufficiency or complexity. Furthermore, quantum neural networks draw attention with their enhanced data processing and modeling capacities.

The conducted studies are gaining popularity and it has been observed that the performance of quantum neural networks can be further enhanced, also their application can be extended to various types of problems. Although concrete applications on quantum computers are not currently feasible, many experimental results hold great promise for the future.

5. Acknowledgements

Fig. 1. This study was supported by the TUBİTAK (The Scientific and Technological Research Council of Turkey) under Grant No: 121E439.

6. References

[1] Shor PW (1994) Algorithms for quantum computation: discrete logarithms and factoring. In: Foundations of computer science, 1994 proceedings. 35th annual symposium on IEEE, pp 124–134

[2] Grover LK (1996) A fast quantum mechanical algorithm for database search. In: Proceedings of the twenty-eighth annual ACM symposium on theory of computing, pp 212–219

[3] Kak S (1995) On quantum neural computing. Inf Sci 83:143–163

[4] Menneer T, Narayanan A (1995) Quantum-inspired neural networks, Department of Computer Science, University of Exeter, Exeter, United Kingdom, Technical Report, p 329

[5] Menneer T (1998) Quantum artificial neural networks. PhD thesis, University of Exeter

[6] Narayanan A, Menneer T (2000) Quantum artificial neural network architectures and components. Inf Sci 128(3):231-255

[7] Kouda N, Matsui N, Nishimura H, Peper F (2003) Qubit neural network and its efficiency. In: International conference on knowledge-based and intelligent information and engineering systems, pp 304–310

[8] Schuld M, Sinayskiy I, Petruccione F (2014) The quest for a quantum neural network. Quantum Inf Process 13(11):2567

[9] Ezhov AA, Ventura D (2000) Quantum neural networks. In: Kasabov N (ed) Future directions for intelligent systems and information sciences. Physica, Heidelberg, pp 213–235

[10] Abbas, A., Sutter, D., Zoufal, C. et al. The power of quantum neural networks. Nat Comput Sci 1, 403–409 (2021). https://doi.org/10.1038/s43588-021-00084-1

[11] Z. Huang, L. Qian and D. Cai, "Analysis on the recent development of quantum computer and quantum neural network technology," 2022 IEEE International Conference on Artificial Intelligence and Computer Applications (ICAICA), Dalian, China, 2022, pp. 680-684, doi: 10.1109/ICAICA54878.2022.9844614.

[12] Jeswal, Sumit & Chakraverty, S.. (2018). Recent Developments and Applications in Quantum Neural Network: A Review. Archives of Computational Methods in Engineering. 26. 10.1007/s11831-018-9269-0.

[13] Samuel Yen-Chi Chen and Chao-Han Huck Yang and Jun Qi and Pin-Yu Chen and Xiaoli Ma and Hsi-Sheng Goan, “Variational Quantum Circuits for Deep Reinforcement Learning”, 2020, 1907.00397 arXiv.

[14] Öztemel, Ercan. "Yapay sinir ağlari." PapatyaYayincilik, Istanbul (2003).

[15] Garg, Siddhant and Goutham Ramakrishnan. “Advances in Quantum Deep Learning: An Overview.” ArXiv abs/2005.04316 (2020): n. pag.

[16] Wu, Yc., Feng, Jw. Development and Application of Artificial Neural Network. Wireless Pers Commun 102, 1645–1656 (2018). https://doi.org/10.1007/s11277-017-5224-x

[17] Kwak, Yunseok, Won Joon Yun, Soyi Jung and Joongheon Kim. “Quantum Neural Networks: Concepts, Applications, and Challenges.” 2021 Twelfth International Conference on Ubiquitous and Future Networks (ICUFN) (2021): 413-416.

[18] Beer, Kerstin: Quantum neural networks. Hannover : Gottfried Wilhelm Leibniz Universität, Diss., 2022, IX, 179 S., DOI: https://doi.org/10.15488/11896

[19] da Silva, A.J., de Oliveira, W.R. & Ludermir, T.B. Comments on “Quantum M-P Neural Network”. Int J Theor Phys 54, 1878–1881 (2015). https://doi.org/10.1007/s10773-014-2393-1 Zhou R (2010) Quantum competitive neural network. Int J Theor Phys 49:110–119

[20] Kouda N, Matsui N, Nishimura H (2004) A multilayered feedforward network based on qubit neuron model. Syst Comp Jpn 35(13):43–51

[21] M. Kashif and S. Al-Kuwari, "Demonstrating Quantum Advantage in Hybrid Quantum Neural Networks for Model Capacity," 2022 IEEE International Conference on Rebooting Computing (ICRC), San Francisco, CA, USA, 2022, pp. 36-44, doi: 10.1109/ICRC57508.2022.00011.Matsui N, Takai M, Nishimura H (2000) A network model based on qubit-like neuron corresponding to quantum circuit. Electron Commun Jpn (Part III: Fundam Electron Sci) 83(10):67–73

[22] Matsui N, Nishimura H, Isokawa T (2009) Qubit neural networks: its performance and applications. In: Nitta T (ed) Complex-valued neural networks: utilizing high-dimensional parameters, information science reference. IGI Global, Hershey, pp 325–351

[23] Matsui N, Takai M, Nishimura H (2000) A network model based on qubit-like neuron corresponding to quantum circuit. Electron Commun Jpn (Part III: Fundam Electron Sci) 83(10):67–73

[24] A. P. Patil, S. Pandey, N. Das Kasat, S. Modi, S. Raj and R. Kulkarni, "Implementation of Handwritten Character Recognition using Quanvolutional Neural Network," 2022 IEEE North Karnataka Subsection Flagship International Conference (NKCon), Vijaypur, India, 2022, pp. 1-4, doi: 10.1109/NKCon56289.2022.10126600.

[25] A. P. J, K. K, P. Sandeep, S. C. Dattatreya and S. N. S. Anil, "Symmetry-Protected Topological Phase Classification Using Hybrid Quantum Convolutional Neural Network with Three Quantum Filters," 2022 Second International Conference on Advances in Electrical, Computing, Communication and Sustainable Technologies (ICAECT), Bhilai, India, 2022, pp. 1 6, doi: 10.1109/ICAECT54875.2022.9807939.

[26] Pal, Pankaj & Bhattacharyya, Siddhartha & Mani, Ashish. (2016). Pure Color Object Extraction from a Noisy State using Quantum Version Parallel Self Organizing Neural Network. International Journal of Computers and Applications. 38. 10.1080/1206212X.2016.1237164.

[27] Pandian, Arun, et al. "Quantum Generative Adversarial Network and Quantum Neural Network for Image Classification." 2022 International Conference on Sustainable Computing and Data Communication Systems (ICSCDS). IEEE, 2022.

[28] Sagingalieva, A. B., Mohammad Kordzanganeh, Nurbolat Kenbayev, Daria Kosichkina, Tatiana Tomashuk and Alexey Melnikov. “Hybrid Quantum Neural Network for Drug Response Prediction.” Cancers 15 (2022): n. Pag

[29] Al Ali, Musaddiq & Sahib, Amjad & Al Ali, Muazaz. (2022). Investigation of Early-Stage Breast Cancer Detection Using Quantum Neural Network. 10.20944/preprints202210.0208.v1.

[30] Alrikabi, H. T., A. Aljazaery, I. ., Qateef, J. S. ., Alaidi, . A. H. M., & Al_airaji, R. M. . (2022). Face Patterns Analysis and Recognition System Based on Quantum Neural Network QNN. International Journal of Interactive Mobile Technologies (iJIM), 16(08), pp. 34–48. https://doi.org/10.3991/ijim.v16i08.30107

[31] M. Islam, M. Chowdhury, Z. Khan and S. M. Khan, "Hybrid Quantum-Classical Neural Network for Cloud-Supported In-Vehicle Cyberattack Detection," in IEEE Sensors Letters, vol. 6, no. 4, pp. 1-4, April 2022, Art no. 6001204, doi: 10.1109/LSENS.2022.31539.

International Conference on Advances and Innovations in Engineering

Unet With Layer-based Hybrid Convolution For Retinal Vessel Segmentation

Hakan ÖCAL[1]
[1]Computer Engineering, Faculty of Engineering, Architecture, and Design, Bartın University, Bartın, Türkiye.
[1]hocal@bartin.edu.tr
[1](ORCID: 0000-0002-8061-8059)

Abstract
Deformations in retinal vessels inform us about dangerous conditions such as glaucoma, macular degeneration, and ophthalmic diseases. Manual segmentation of retinal vessels from fundus images is challenging for board-certified physicians. Deep learning-based automatic segmentation methods have recently succeeded in segmenting organs and vessels. This study emphasizes a fully automatic deep learning-based retinal blood vessel segmentation method to help specialist physicians. The most crucial innovation in the proposed architecture is applying the hybrid convolution technique. The model based on the Unet architecture uses standard convolution and Depthwise separable convolution together. This way, the number of parameters has been reduced significantly. In addition, the depth-wise separable convolution enables the proposed architecture to focus on high-level features along the channel and depth. The proposed architecture achieved a 99.6% dice score in the DRIVE dataset. This obtained score showed that the proposed model is very robust.

Keywords: Unet, depthwise separable convolution, layer-based hybrid convolution, retinal vessel segmentation

1. Introduction

The Fundus camera is used to view the fundus region formed by the inner and posterior surface of the eye. Diseases such as glaucoma, macular degeneration, arteriosclerosis, and other ophthalmologic disorders can be detected in the images obtained from the fundus camera[1]. The fundus camera allows a view of the blood vessels in the eye, optic disc and pit, fovea, and other elements such as the retina [2]. Thanks to fundus images, it allows the diagnosis of ophthalmological and ocular diseases. However, manually segmenting vessels and observing differences in vessels in fundus images is time-consuming and challenging [3], [4]. In addition, diagnostic differences that vary among physicians are another problem. In addition, diagnostic differences that vary among physicians are another problem. Due to the difficulties of manual segmentation from fundus images, examinations with computer-aided technologies have become increasingly important in recent years. Deep learning (DL) architectures with convolutional neural networks (CNN) layers trained using effective data processing techniques have started to show superior performance as computer-aided diagnostic methods in recent years [5]. The emergence of the U-Net architecture in organ segmentation has revolutionized deep learning-based biomedical image analysis [6]. The contributions of this study, which was obtained by making various modifications to the U-Net architecture, to the literature are as follows:

- The computational cost is considerably reduced by using depthwise separable convolution in the convolutional layers of the U-Net architecture.
- Thanks to the depthwise separable convolution, the network gives more importance to the high-level features in the image, both channel and spatial, for more precise segmentation of vessels in retinal blood vessel images.

Figure 1 shows some image examples and basic facts from the DRIVE dataset.

[1]Corresponding author

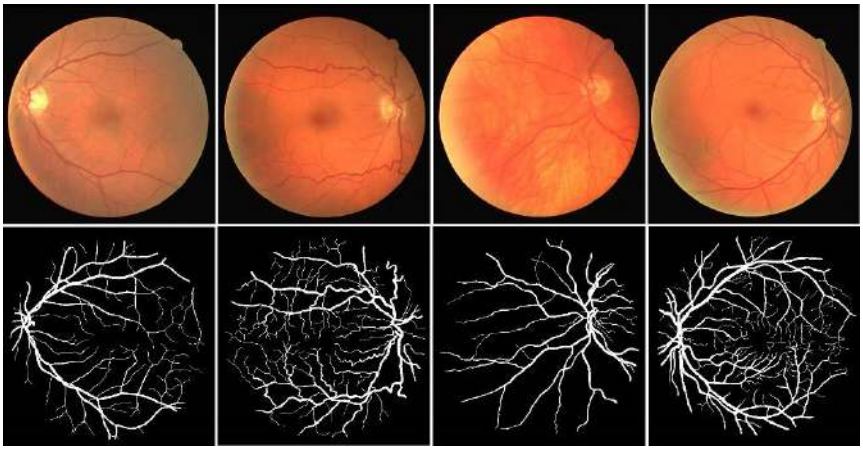

Figure 1. Examples from the DRIVE dataset

2. Related works

Many researchers have focused on U-shaped and V-shaped DL networks. Among these researchers, Gu et al. proposed a bottom-up and top-down deep-controlled CNN network in the method they named BTS-DSN [7]. Arsalan et al. proposed the PLRS-Net architecture, which reduces pooling time and preserves feature maps of blood vessels by using residual blocks without a pooling layer. In addition, thanks to the inter-spatial information, the loss is rapidly reduced, and convergence becomes faster [8]. The attention module U-Net with stepped residual blocks (CRAUNet) proposed by Dong et al. uses a DropBlock module added to the residual blocks to prevent overfitting. Thus, low and high-level features are equalized to highlight the boundaries of the segmentation region [9]. Wang et al. proposed a context-sensitive network (CA-Net) with multiple expanded convolutions at different rates to obtain contextual information at a multi-scale [10]. As detailed by Hussain et al., dilated convolutions U-Net (DilU-Net) is a CNN architecture that upsamples by combining high-level features from different decoders [11]. Lin et al. proposed the Stimulus-Guided Adaptive Transformer Network (SGAT-Net), which includes inductive bias and self-attention mechanisms for retinal blood vessel segmentation. This architecture proposes an approach that captures details in the image with a residual block encoder[12].

3. Methodology

This section gives information about the data set used for training and testing, the architectural structure of the proposed methodology, the loss function, and the performance metric used.

3.1. Preparing the dataset

DRIVE dataset consisting of fundus images was used in the training and testing stages of the proposed method [13]. The DRIVE dataset consists of 40 color fundus images, 33 of which are non-diabetic and 7 of which are diabetic. The dataset contains 20 training and 20 test images. The original images in the DRIVE dataset are in TIF format with 565 x 584 pixels dimensions. The ground truth images are 565 x 584 and in GIF format. The images in the dataset and their basic facts were first converted to PNG, a high-quality image format. The training data was increased to 810 by applying various data augmentation methods such as random crop, flip vertical, flip horizontal, flip left-right, random zoom, and random rotate($\pm 90^{o}$) to the images converted to PNG format. Some images obtained after the data augmentation techniques applied to the data set are shown in Figure 2.

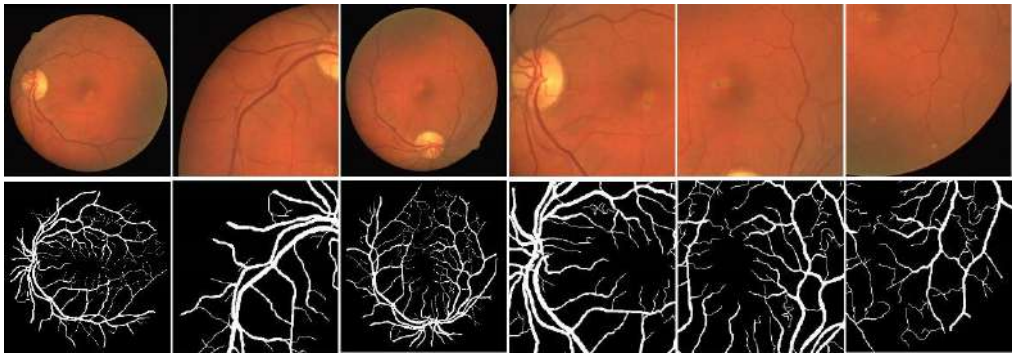

Figure 2. Sample training set images obtained from data augmentation methods

3.2. Details of the Proposed Architectures

The architectural structure of the proposed methodology is shown in Figure 3. It is obtained by replacing the second layers in the binary standard convolution blocks in the Unet architecture with the depthwise separable convolution layer. 2 x 2 filters were used in the standard convolution layers, shown in orange in both the encoder and decoder blocks. In the depthwise separable convolution layers, 3 x 3 filters for depthwise convolution and 1 x 1 filters for pointwise convolution were used. Unlike the standard convolution, thanks to the depthwise separable convolution, high-value features in the images are monitored spatially and in channel size, resulting in better network performance. In addition, the computational cost is significantly reduced, and a solution is brought to the hardware limitations. Besides, the proposed architecture uses ADAM as the optimization algorithm and ReLU as the activation function [14].

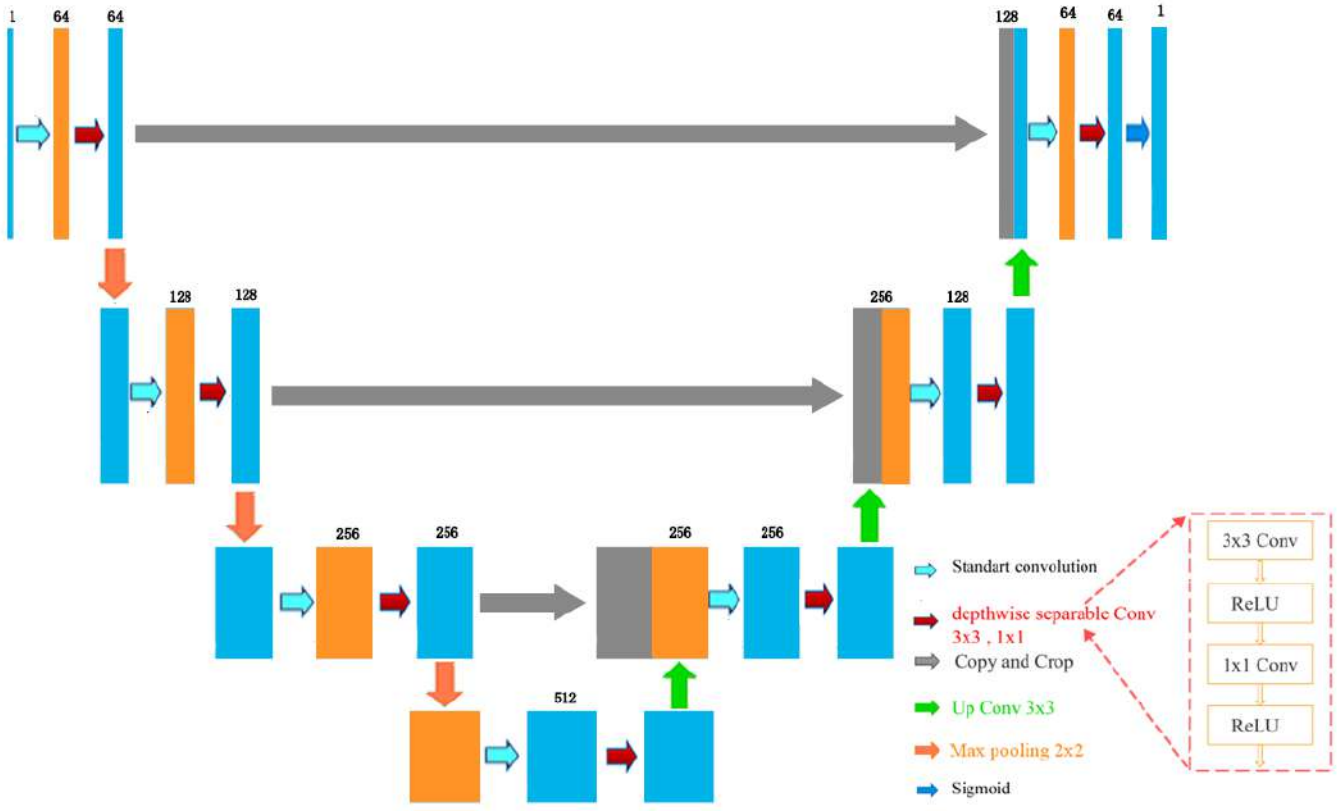

Figure 3. The proposed architectural structure

3.3. The Dice Loss Function

The cost calculated for the backpropagation of the proposed architecture is based on the Dice Loss(DL) function. Dice loss and its derivatives (hybrid loss functions) are among the most used loss functions in segmentation in the literature. Dice loss is obtained by subtracting the Dice Similarity Coefficient (DSC) from 1. In DSC, TP stands for True Positives, FP stands for False Positives, and FN stands for False Negatives. DSC and DL mathematical expressions are shown in Eq. 1 and Eq. 2.

$$DSC = (2*TP)/(2*TP+FP+FN) \quad (1)$$

$$Dice\ Loss=1-DSC \quad (2)$$

3.4. Performance metric

For the performance measurement of the proposed architecture, DSC, which is one of the most used coefficients in the proposed methodologies for segmentation in the literature, was used. The mathematical expression of DSC is shown in Eq. 1.

4. Experimental results and discussion

4.1. Model's implementation details

ADAM optimization algorithm was used to optimize the parameters of the proposed model, and the learning rate was chosen as 0.0001 after experimental studies. The proposed model has been trained and tested using the NVIDIA GTX_1080_TI graphics card and Anaconda ecosystem with Pytorch cuda library version 1.13.1. The DRIVE dataset is fed into the proposed architecture with dimensions of 565 x 584 and 3 channels. In addition, the mini batch_size was chosen as 2.

4.2. Ablation studies

The proposed model was first tested with an architecture from 16 channels to 512 channels. Then, the encoder started with 32 channels and ended with 512. However, the most ideal result was obtained with the model from 64 channels to 512 channels. Table 1 shows ablation studies for 25 epochs. In addition, since the input channels of the proposed model are 64 and the batch_size is set to two or higher, Cuda offers sharing with the help of a ram accelerator, so the training was relatively slow. That's why it set the batc_size to 1. Besides, the training result was very low when both convolutional layers in the convolutional blocks had depthwise separable convolutions.

Table 1. Ablation studies for 25 epochs

Architecture	Number of starting channels	Training DSC(%)	Validation DSC(%)	Test DSC(%)	Epoch
Unet with Layer-based hybrid convolution	16	93	93.3	94	25
Unet with Layer-based hybrid convolution	32	95	95.6	96	
Unet with Layer-based hybrid convolution	64	99.9	99.4	99	
Unet with Layer-based hybrid convolution	128	97	97.4	98	

4.3. Performance analysis on the DRIVE dataset

The training and test DSC performance values of the proposed model in comparison with the basic Unet model are shown in Table 2. As can be seen from Table 2, it is seen that the proposed model is a robust model with a test performance of 99.6% in both parameter and performance measurement results.

Table 2. Comparative performance results

Architectures	Methods	Parameters(M)	Training DSC(%)	Validation DSC(%)	Test DSC(%)	Epoch
Baseline Unet	Fundus images	7.7	99.7	99.4	99	25
Unet with Layer-based hybrid convolution	Fundus images	5.1	99.9	99.8	99.6	

In Figure 4, the prediction and ground realities of the proposed model are shown comparatively. It is seen that the estimated values in the qualitative analyses are almost the same as the ground truth images.

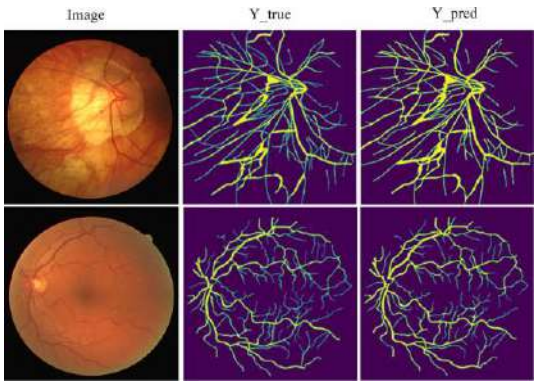

Figure 4. Qualitative analysis of images predicted by Unet with Layer-based hybrid convolution method

The proposed model is a robust model. However, when the number of parameters in the model decreases, it is seen that the model tends to fail in the training test stages. Layer-based hybrid convolution can be used to reduce computational costs in very high parameter and complex models.

5. Conclusion

To the best of our knowledge, this study performed a layer-based hybrid convolution for the first time. The proposed methodology performs standard convolution in the first layer in each convolutional block and depthwise separable convolution in the second layer. Depthwise separable convolution has enabled the number of parameters to be significantly reduced. Reducing the number of parameters in complex models is essential due to computational limitations. More importantly, it provides better feature extraction as it listens to layers both in channel depth dimension and spatially. However, the depthwise separable convolution performance in architectures with low parameters gradually decreases. A new computational approach is considered in future studies, including graph structures distinct from convolution.

6. References

[1] Azzopardi G, Strisciuglio N, Vento M, Petkov N. “Trainable COSFIRE filters for vessel delineation with application to retinal images”. Medical Image Analysis, vol. 19, no. 1, pp. 46–57, 2015, [PubMed] [CrossRef] [Google Scholar].

[2] Nguyen U T V, Bhuiyan A, Park L A F, Ramamohanarao K. “An effective retinal blood vessel segmentation meth od using multi-scale line detection”. Pattern Recognition, vol. 46, no. 3, pp. 703–715, 2013, [CrossRef] [Google Scholar].

[3] Bandara A M R R, Giragama P. W. G. R. M. P. B. “A retinal image enhancement technique for blood vessel segmentation algorithm”. in Proceedings of the 2017 IEEE international conference on industrial and information systems (ICIIS), pp. 1–5, IEEE, Peradeniya, Sri Lanka, 2017 December.

[4] Dharmawan D A, Li D, Ng B. P., Rahardja S. “A new hybrid algorithm for retinal vessels segmentation on fundus images”. IEEE Access, vol. 7, pp. 41885–41896, 2019.

[5] Ayhan M S, Kühlewein L, Aliyeva G, Inhoffen W, Ziemssen F, Berens P. “Expert-validated estimation of diagnostic uncertainty for deep neural networks in diabetic retinopathy detection”. Med. Image Anal. 64, 101724, 2020.

[6] Ronneberger O, Fischer P, Brox T.“U-net: Convolutional networks for biomedical image segmentation ”. In: International Conference on Medical Image Computing and Computer-Assisted Intervention. Springer, pp. 234–241, 2015.

[7] Guo S, Wang K, Kang H, Zhang Y, Gao Y, Li T. “BTS-DSN: Deeply supervised neural network with short connections for retinal vessel segmentation”. Int. J. Med. Inform. 126, 105–113, 2019.

[8] Arsalan M, Haider A, Lee Y W, Park K R. “Detecting retinal vasculature as a key biomarker for deep learning-based intelligent screening and analysis of diabetic and hypertensive retinopathy”. Expert Syst. Appl. 200, 117009, 2022.

[9] Dong F, Wu D, Guo C, Zhang S, Yang B, Gong X. “CRAUNet: A cascaded residual attention U-net for retinal vessel segmentation”. Comput. Biol. Med. 105651, 2022.

[10] Wang X, Li Z, Huang Y, Jiao Y. “Multimodal medical image segmentation using multi-scale context-aware network”. Neurocomputing 486, 135–146, 2022.

[11] Hussain S, Guo F, Li W, Shen Z. “DilUnet: A U-net-based architecture for blood vessels segmentation”. Comput. Methods Programs Biomed. 218, 106732, 2022.

[12] Lin J, Huang X, Zhou H, Wang Y, Zhang Q. “Stimulus-guided adaptive transformer network for retinal blood vessel segmentation in fundus images”. Medical Image Analysis,Volume 89, 2023,102929,ISSN 1361-8415,https://doi.org/10.1016/j.media.2023.102929.

[13] Staal J, Abràmoff M D, Niemeijer M, Viergever M A, Van Ginneken B. “Ridge-based vessel segmentation in color images of the retina”. IEEE Trans. Med. Imaging 23 (4), 501–509, 2004.

[14] Ba J, Kingma DP. “Adam: a method for stochastic optimization”. in: International Conference on Learning Representations (ICLR), pp.1–11, 2015.

International Conference on Advances and Innovations in Engineering

Development of the Tool that Converts Machine Readable Format to OpenQASM and Quirk for Quantum Computing: tfc2OpenQASM and tfc2Quirk

Hasan YETİŞ[1], Mehmet KARAKÖSE[2]
[1,2]Department of Computer Engineering, Engineering Faculty, Fırat University, Elazığ, Türkiye.
[1]h.yetis@firat.edu.tr, [2]mkarakose@firat.edu.tr

[1](ORCID: 0000-0001-7608-3293), [2](ORCID: 0000-0002-3276-3788)

Abstract
Quantum and reversible circuits may need to be represented in different ways depending on their intended use. Different formats are used to represent these circuits in different environments. Researchers in the field of applied quantum computing may need different forms of quantum circuits, and they perform this conversion manually. In this study, a tool is developed to automatically convert quantum circuits kept in tfc format to OpenQASM and Quirk environments to facilitate researchers working in the field of applied quantum computing. With the developed tool, it is aimed to make the process, which is performed manually in an error-prone and time-consuming manner, quick and without errors. The tool, which is coded in the Python environment, includes two main modules. These are the tfc2OpenQASM and tfc2Quirk modules. The modules take the tfc file path as input, and check the compatibility of the gates used in the tfc file with the environment to which it will be converted. If appropriate the conversion is performed by rule-based, and the output is the converted format. We hope that the developed tool will provide convenience to researchers working in the field of applied quantum computing.

Keywords: applied quantum computing, machine readable form, OpenQASM, Quirk, reversible circuits, tfc

1. Introduction

Reversible circuits are circuits that produce the same result when a series of operators repeat in reverse order [1]. The circuits used in quantum computing must be reversible circuits, so the gates used to create the circuit must be reversible gates. For example, the NCT (NOT, CNOT, and Toffoli) gate cluster consists of reversible gates [2]. When a NCT gate is applied twice, the original input is obtained as a result of the reverse of reverse. Today, quantum computers can operate gates of only 1 or 2 qubits. However, the Toffoli gate can be operated thanks to a set of gates that consists of one or two qubits [3]. In theoretical reversible logic, multi-qubit notations can be used as a practical representation, although they cannot be operated by real quantum computers. MCT notations (Multi-Controlled Toffoli) are examples of these notations. There are (n-1) control qubits and 1 target qubit in n qubit MCT notations. For MCT notations, if all control qubits satisfy the condition, NOT operation is applied to the target qubit. MCT notations basically have the ability to express NOT, CNOT, and Toffoli gates. The NOT gate can be expressed as a 1-qubit MCT, the CNOT gate as a 2-qubit MCT, and the Toffoli gate as a 3-qubit MCT. The symbol t is used to represent MCT notations in a reversible circuit expressed in machine readable format (.tfc) [4]. In this format, the NOT gate is denoted by t1, the CNOT gate t2, and the Toffoli gate t3. A general MCT gate of n qubits is denoted by tn. The expressions after the symbol tn represent qubits and the last qubit is often used as the target qubit. The NOT, CNOT, Toffoli and MCT gates/notations used in this study are given in Table 1.

[1]Corresponding author

Table 1. Essential quantum gates used in this study [5]

Gate Name	Symbol	Mission
Pauli-X (NOT)		Take the inverse of the qubit
Controlled Not (CNOT)		Take the inverse of the target qubit only if the control qubit is 1
Toffoli (CCNOT)	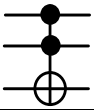	Take the inverse of the target qubit only if the control qubits are 1
Multi Controlled Toffoli (MCT)	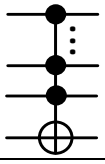	Take the inverse of the target qubit only if the control qubits are satisfied the condition. If it has only 2 control qubits, the gate is called Toffoli.

The reversible gates are not limited to NOT, CNOT, Toffoli, and MCT [6]. However, only MCT based quantum gates that can be expressed with tfc files are included in the study. Tfc files are preferred in the representation of reversible circuits because they are easy to express and understand theoretically. There are many example reversible circuits stored in tfc format on the RevLib web site [7]. However, they need to be converted to a suitable format in order to run them in a simulation environment or on physical computers. Researchers working in the field of quantum computing have to perform this conversion manually. OpenQASM is another representation used for quantum circuits [8]. Quantum circuits can be modeled with this language in services offered by service providers such as IBM [9]. Modeled quantum circuits can be run on simulation or physical quantum computers. On the other hand, the Quirk simulator developed by Algassert offers a practical use in real time and is a popular simulation environment preferred by researchers in this field [10].

In summary, quantum circuits can be expressed in different ways (formats). Tfc, real, OpenQASM, Quirk are among the different forms of representation. Reversible circuits represented in tfc format can be opened through applications such as RCViewer+, and quantum circuits can be compared and optimized [11]. In addition, files in .tfc format can be converted to .real format with RCViewer+. However, tfc files may need to be converted to OpenQASM language to run on simulator or real backends. Or these circuits may need to be converted for real-time simulation in Quirk environment. In this study, a tool has been developed to convert tfc files to OpenQASM and Quirk formats in order to save time for researchers in this conversion process.

2. Tfc, OpenQASM, and Quirk Formats

This section describes the tfc, OpenQASM and Quirk formats used to represent quantum circuits in different environments. Machine readable format (tfc, real) is used for practical storage of reversible circuits. Operations such as viewing, plotting and optimizing reversible circuits expressed in machine readable format can be performed with the application named RCViewer+ [12], [13]. This application supports conversion between tfc and real formats. On the other hand, OpenQASM is the generally used representation for quantum circuits. Apart from these, there is a URL syntax rule for displaying quantum circuits in the Quirk environment. Researchers studying in the field of quantum computing may need to make tfc files suitable for OpenQASM and Quirk [14].

Tfc files are a format created for storing reversible logic circuits. According to this format, the features that tfc files should have are given below [13]:

All variables must be specified with '.v', and ',' should be used between variables (.v a,b,c)

Variables that take input should be expressed with .i (.i a,b). These variables must be defined also in '.v' before.

Output variables should be expressed with .o (.o b,c). These variables must be defined also in '.v' before. If output is not specified, the inputs are used as output.
Quantum notations are written between the BEGIN and END tags. There must be at least one notation between the tags.
The # symbol is used for comment lines.

In tfc files, NOT, CNOT, Toffoli and MCT gates/notations can be represented respectively as "t1 a;", "t2 a,b;", "t3 a,b,c;", and "tn a,b,…n". The tfc format representation of the sample quantum circuit including NOT, CNOT and Toffoli gates is given in Fig. 1.a. Diagram of the quantum circuit after opening with RCViewer+ is given in Fig. 2.b.

```
1  # comment line
2  .v a,b,c
3  .i a,b,c
4  .o a,b,c
5  BEGIN
6  t1 a
7  t2 a,b
8  t3 a,b,c
9  t2 b,a
10 t3 a,c,b
11 END
```

(a)

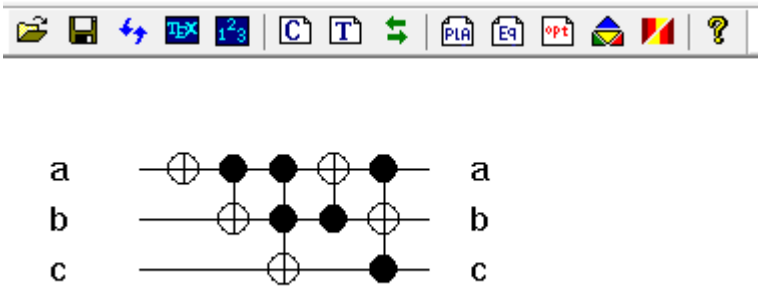

(b)

Figure 1. Example quantum circuit representation in tfc format (a) tfc file format, (b) RCViewer+ screenshot

Operations such as circuit cost calculation on reversible circuits presented in this format can be practically performed with RCViewer+. Calculating the circuit cost is important to measure the efficiency of algorithms in quantum computing. Usually, quantum circuits are stored in RevLib with this cost value [7]. The cost metrics calculated by the RCViewer+ of the quantum circuit given in Fig. 1 is given in Table 2. With this application, it is possible to perform simple optimization operations such as simplification of sequential gates.

Table 2. Cost metrics by RCViewer+ for the quantum circuit in Fig.1

Number of input/outputs	3
Gate Count	5
Quantum Cost	11
Two-qubit cost model:	
Number of two-qubit gates	12
Number of one-qubit gates	1

For the most general universal representation of quantum circuits, QASM is used. Quantum circuits expressed in the OpenQASM language can be run in environments such as IBMQ Experience [15]. In the OpenQASM language, NOT, CNOT and Toffoli gates are supported among the gates given in Table 1. It has been stated that quantum computers can operate 1 or 2 qubit gates, and the Toffoli gate is operated using an equivalent gate set of 1 and 2 qubits [3]. Although the representation of MCT notations is possible with Toffoli gates, disadvantages such as the use of extra qubits may arise [16]. In the OPENQASM language, qubit and classical bit numbers must be defined first. In OpenQASM, NOT is expressed as "x q[t];", CNOT is expressed as "cx q[c], q[t];" Toffoli is expressed as "ccx q[c1], q[c2], q[t]", where t is the target and c,c1,c2 are control qubits. The example quantum circuit given in Fig.1 and its OpenQASM version are given in the Fig. 2.

```
1  OPENQASM 2.0;
2  include "qelib1.inc";
3  qreg q[3];
4  creg c[3];
5  x q[0];
6  cx q[0], q[1];
7  ccx q[0], q[1], q[2];
8  cx q[1], q[0];
9  ccx q[0], q[2], q[1];
```

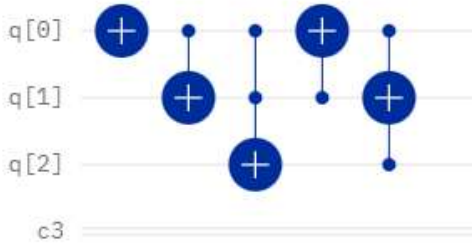

(a) (b)

Figure 2. Representation of the example circuit in Fig. 1 with OpenQASM language, a) OpenQASM language, b) IBMQ Experience screenshot

In the code written in the OpenQASM language, first definitions are made and the library is included in the project. The numbers of quantum bits (qubits) and classical bits are defined with qreq and creg words respectively. Classical bits are used for reading outcomes, and collapsed qubits are stored in classical bits. It is noted that the first qubits are the control qubits and the last qubit is the target qubit for the gate operations.

Quirk, on the other hand, is a real-time simulation environment that enables the simulation of quantum circuits. It offers practical use for circuit corrections as the effects of added and removed gates are observed instantly in the Quirk environment. Quirk is a web-based simulator and the screenshot of the quantum circuit created in this environment is given in Fig. 3. For the representation of the circuit in the figure, the following expression should be added to the Quirk url address: #circuit={"cols":[["X"],["•","X"],["•","•","X"],["X","•"],["•","X","•"]]}. In the quirk format, each substring in the cols array represents the columns in the quantum circuit, that is, the gates at the same tn runtime. The screenshot of this expression created by the Quirk simulator environment is given in Fig. 3. As it is shown in the figure there are 5 gates executed in 5 different tn runtimes. In this way, NOT statements are denoted by "X" and control statements by "•" symbol. Thus, a generalized structure is obtained for the representation of MCT notations. Thus, a generalized structure is obtained for the representation of MCT notations, including NOT, CNOT, and Toffoli gates. ["X"] in the given expression actually corresponds to ["X",1,1]. In Quirk Simulator, qubits not used are shown as 1. The absence of a control qubit means that a NOT gate must be applied to the first qubit. When looking at the last column the expression ["•","X","•"] shows. Here, it is understood that the first and third qubits are the control qubits and the second is the target qubits. Therefore, this gate refers to the Toffoli.

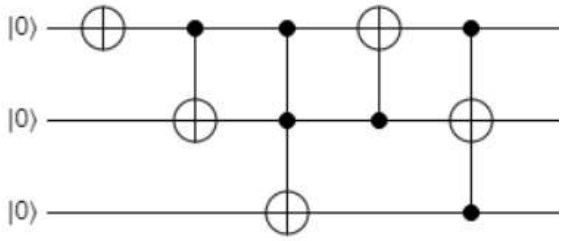

Figure 3. Quirk screenshot for the expression ["X"],["•","X"],["•","•","X"],["X","•"],["•","X","•"]

3. The Developed Tool

In this study, conversion of a reversible circuit stored in tfc format are carried out to express it in OpenQASM and Quirk. OpenQASM is a quantum circuit representation language also used by IBM Quantum Experience. Quantum circuits modeled in this language can be simulated or run on real quantum backends. On the other hand, Quirk is a web-based practical simulator, which allows to create circuits in line with the parameters coming from the url. Information about tfc, OpenQASM and Quirk formats is given in the previous section. The tfc version of the quantum circuit that sums two 2-qubit inputs and overwrites the output on the 2nd input is given in Fig. 4.a. The RCViewer+ screenshot of the circuit is given in Fig. 4.b.

```
# 2 qubit self adder circuit
# ba input1, dc input2, edc output
.v a,b,c,d,e
.i a,b,c,d,e
.o a,b,c,d,e
BEGIN
t2 b,d
t2 b,e
t3 a,c,b
t3 b,d,e
t2 b,d
t3 a,c,b
t2 a,c
t2 b,d
END
```

(a)

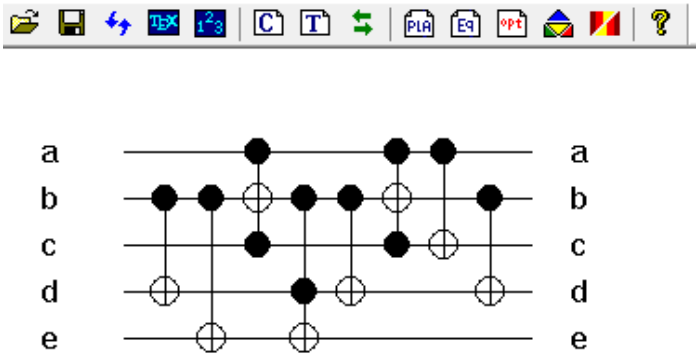

(b)

Figure 4. 2-qubit adder representation, a) tfc format, b) RCViewer+ screenshot

In order to convert tfc files to OpenQASM or Quirk environment, it is necessary to open the file and read the input-output number and qubit tags. In order to extract the necessary information from the tfc files, the line starting with .v should be read and the tags here should be stored in an array. The elements in the array represent qubits, and the qubit order will be used instead of the label in the transformed circuit. In order to provide input-output flexibility in the developed tool, the restrictions imposed on these have not been taken into account. After reading the number of qubits and tags, appropriate meta information is generated if necessary. Then the lines written between BEGIN and END are read step by step. At this stage, it is necessary to ignore the blank lines. The conversion of the gates written between BEGIN and END should be provided appropriately. This step differs depending on the OpenQASM or Quirk environment. Since MCT notations are not supported in OpenQASM, the module will fail if there are gates other than NOT, CNOT and Toffoli. The pseudo code for converting tfc files to OpenQASM is given in Table 3.

Table 3. Pseudo code for converting tfc to OpenQASM

```
1- Read the tfc file
2- qubit_labels[] = split the line which starts with ".v" to obtain qubit labels
3- Print OpenQASM metadata
4- tLine = read the lines from BEGIN to END:
    4.1 – If tLine == '' than go to step 4.
    4.2. – If the gate in the tLine has a gate different from 't' than alert and go to step 5.
    4.3. – Read the qubit labels in the tLine
        4.3.1. – If qubit number == 1: than apply x gate to corresponding qubit order in qubit_labels
        4.3.2. – Else if qubit number == 2: than apply cx gate to corresponding qubits
        4.3.3. – Else if qubit number == 3: than apply ccx gate to corresponding qubits
        4.4.4. – Else: Error and go to step 5.
5- End
```

Since the tfc and OpenQASM structures are similar to each other, as can be seen in Table 3, a practical conversion can be made as x if t1, cx if t2, and ccx if t3. The Python code of the method whose pseudo code is given in the table is given in Appendix A. After the 2-qubit adder tfc file given in Fig.4 is given as input to the module, the OpenQASM output in Fig. 5 is obtained. OpenQASM output is shown with a red rectangle in Fig 5.b. In order to change the inputs of this circuit, the NOT operation is applied to the qubits q[1] and q[3]. Since the inputs q[3]q[2] and q[1][0] are 10, the output of q[4]q[3]q[2] is 100.

```
1   OPENQASM 2.0;
2   include "qelib1.inc";
3   qreg q[5];
4   creg c[5];
5   cx q[1], q[3];
6   cx q[1], q[4];
7   ccx q[0], q[2], q[1];
8   ccx q[1], q[3], q[4];
9   cx q[1], q[3];
10  ccx q[0], q[2], q[1];
11  cx q[0], q[2];
12  cx q[1], q[3];
```

(a)

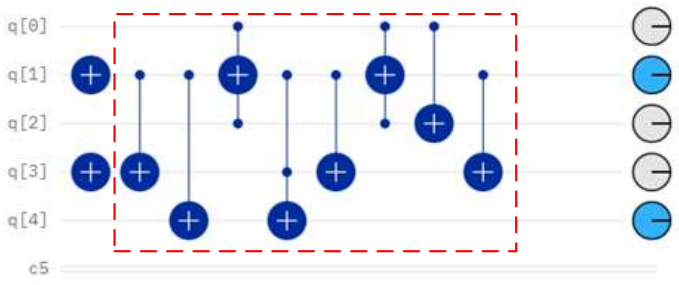

(b)

Figure 5. Converted OpenQASM format of Fig.4, a) OpenQASM format, b) IBMQ Experience screenshot

The conversion process for the Quirk simulator is a bit more complicated. As explained in the previous section, circuits in Quirk are not expressed by gates applied to rows, but by gates applied to columns at runtime tn. Therefore, in order to perform this conversion, it is necessary to write the relevant sign in the order of the qubit in which the gate is applied by using the nested for loop. There are three possibilities here. First, the gate is not connected to the qubit, which in this case is expressed as 1. Secondly, the gate connects to the qubit, but this connection is not the last connection, in this case it will be the control qubit, denoted by "•". Finally, if the gate connects with the qubit and the qubit is located in the last element of the gate, the qubit is the target and is represented by the "X" sign. The tfc to Quirk pseudo code is given in Table 4. The Python code of the pseudo code given in the table is available in Appendix B.

Table 4. Pseudo code for converting tfc to Quirk

```
1- Read the tfc file
2- qubit_labels[] = split the line which starts with ".v" to obtain qubit labels
3- tLine = read the lines from BEGIN to END:
    3.1 – If tLine == '' than go to step 3.
    3.2. – If the gate in the tLine has a gate different from 't' than alert and go to step 5.
    3.3. – For each qubit label (q1) in the tLine:
        3.3.1 – For each qubit label (q2) in the qubit_labels[]:
            3.3.1.1. If q1!=q2: than add 1 to URL
                3.3.1.1. If q1==q2 and q1 is not the last element: than add "•" to URL
                3.3.1.2. If q1==q2 and q1 is the last element: than add "X" to URL
4- End
```

The tfc file of the 2-qubit adder example in Fig. 4 is given as an input to the module. The output of the module is given below:
https://algassert.com/quirk#circuit={%22cols%22:[[1,"•",1,"X",1],[1,"•",1,1,"X"],["•","X","•",1,1],[1,"•",1,"•","X"],[1,"•",1,"X",1],["•","X","•",1,1],["•",1,"X",1,1],[1,"•",1,"X",1]]}
The Quirk simulator screenshot generated by this output is shown in the red rectangle in Fig. 6. On this output circuit, the NOT gate is applied to the 2nd and 4th qubits from the top. Therefore, as in the previous OpenQASM example, the ba and dc inputs are set to 10. In this case, the edc output is expected to be 100. The url expression specified for each column has been added to the figure. In this figure, it is seen that "X" is used for target qubits and "•" (it is shown by "*" in figure) is used for control qubits from top to bottom order.

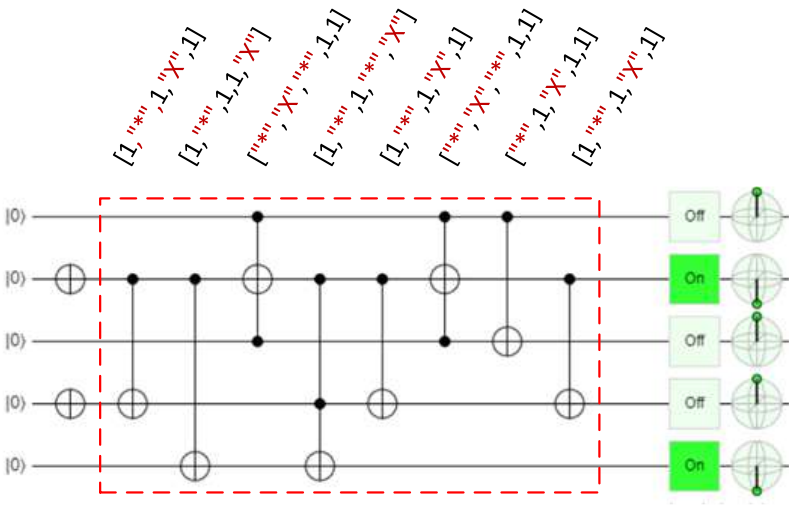

Figure 6. Quirk Simulator screenshot

4. Conclusion

In the field of applied quantum computing, researchers may need to represent quantum circuits in different environments. Since quantum circuits are stored in different formats in different environments, the conversion process is carried out manually by the researchers. Automating these time-consuming and error-prone works is important in terms of preventing time loss and minimizing errors.

In this study, it is aimed to transfer reversible circuits stored with tfc files to OpenQASM and Quirk. Quantum circuits containing NCT (Not, CNOT and Toffoli) gates can be converted to OpenQASM code from the tfc files thanks to the developed tool. Since generalized MCT gates include NCT gates, they can be expressed in Quirk simulator. As a result, the developed tool has the ability to transfer quantum circuits containing MCT gates to Quirk simulator. The developed tools are coded in the Python language and presented in the appendixes. It is hoped that the developed tool will provide practicality for researchers in this field.

5. Acknowledgements

This study was supported by the TUBİTAK (The Scientific and Technological Research Council of Turkey) under Grant No: 121E439.

6. References

[1] C. Moraga ve F. Z. Hadjam, "The Fredkin gate in reversible and quantum environments", *Facta universitatis-series: Electronics and Energetics*, c. 36, sy 2, ss. 253-266, 2023.

[2] V. Deibuk, O. Dovhaniuk, ve T. Kyryliuk, "The Extended Fredkin Gates with Reconfiguration in NCT Basis", içinde *International Conference on Computer Science, Engineering and Education Applications*, Springer, 2023, ss. 95-105.

[3] H. Yetiş ve M. Karaköse, "An improved and cost reduced quantum circuit generator approach for image encoding applications", *Quantum Information Processing*, c. 21, s. 203, Haz. 2022, doi: 10.1007/s11128-022-03546-1.

[4] N. K. Misra, B. Sen, ve S. Wairya, "Towards designing efficient reversible binary code converters and a dual-rail checker for emerging nanocircuits", *Journal of Computational Electronics*, c. 16, sy 2, ss. 442-458, 2017.

[5] H. Yetiş ve M. Karaköse, "A New Framework Containing Convolution and Pooling Circuits for Image Processing and Deep Learning Applications with Quantum Computing Implementation", *Traitement du Signal*, c. 39, sy 2, ss. 501-512, Nis. 2022, doi: 10.18280/ts.390212.

[6] H. Yetiş ve M. Karaköse, "Obtaining Quantum Gate Models from Known Input and Output Values", s. 4.

[7] jungmann@informatik uni-bremen de Lisa Jungmann, "RevLib - An Online resource for Reversible Benchmarks". https://www.revlib.org/ (erişim 25 Ağustos 2023).

[8] A. Cross *vd.*, "OpenQASM 3: A broader and deeper quantum assembly language", *ACM Transactions on Quantum Computing*, c. 3, sy 3, ss. 1-50, 2022.
[9] J. Su, X. Guo, C. Liu, S. Lu, ve L. Li, "An improved novel quantum image representation and its experimental test on IBM quantum experience", *Scientific Reports*, c. 11, sy 1, ss. 1-13, 2021.
[10] A. G. de la Barrera, I. G.-R. de Guzmán, M. Polo, ve J. A. Cruz-Lemus, "Quantum Software Testing: Current Trends and Emerging Proposals", içinde *Quantum Software Engineering*, Springer, 2022, ss. 167-191.
[11] S. Thakral, P. Manhas, ve J. Verma, "Quantum Implementation of Reversible Logic Gates Using RCViewer+ Tool", içinde *Emerging Technologies in Data Mining and Information Security*, P. Dutta, S. Chakrabarti, A. Bhattacharya, S. Dutta, ve V. Piuri, Ed., içinde Lecture Notes in Networks and Systems. Singapore: Springer Nature, 2023, ss. 409-418. doi: 10.1007/978-981-19-4193-1_39.
[12] R. YILMAZ, O. YAMAN, ve M. KARAKÖSE, "Kuantum Devrelerinde Kapı ve Giriş Tespiti için YOLO Tabanlı Bir Yöntem", *Fırat Üniversitesi Mühendislik Bilimleri Dergisi*, c. 35, sy 2, ss. 527-540, 2023.
[13] "Reversible Benchmarks". https://reversiblebenchmarks.github.io/ (erişim 25 Ağustos 2023).
[14] "Quirk: Quantum Circuit Simulator". https://algassert.com/quirk (erişim 25 Ağustos 2023).
[15] IBMQ, "IBM Quantum Platform". Erişim: 25 Ağustos 2023. Erişim adresi: https://quantum-computing.ibm.com/
[16] L. Biswal, D. Bhattacharjee, A. Chattopadhyay, ve H. Rahaman, "Techniques for fault-tolerant decomposition of a multicontrolled Toffoli gate", *Physical Review A*, c. 100, sy 6, s. 062326, 2019.

Appendix A

```
    import re
[1] def tfc2OpenQASM (filename):
  f = open(filename, "r")
  tfcfile = f.read()

  #Reading qubit layers and numbers
  variablesLine = re.search(r'\.v.*', tfcfile).group()
  variables = variablesLine.split(" ")[1].split(",")
  qubit_number = len(variables)

  strOut = "OPENQASM  2.0;\ninclude \"qelib1.inc\";\n"
  strOut += "qreg q["+str(qubit_number)+"];\n"
  strOut += "creg c["+str(qubit_number)+"];\n"

  #Reading the lines after the BEGIN tag
  tfcCodeBlock = tfcfile.split("BEGIN\n")[1]
  tfcCodeLines = tfcCodeBlock.split("\n")
  for i in range(len(tfcCodeLines)-1):
    if(tfcCodeLines[i] == "" or tfcCodeLines[i] ==  "END"):
      continue
    gateAndQubits = tfcCodeLines[i].split(" ")
    if(gateAndQubits[0][0] != "t"):
      strOut = "Unsupported Operator"
      break
    qubits = gateAndQubits[1].split(",")
    if(len(qubits)==1):
      strOut += "x q["+ str(variables.index(qubits[0])) + "];\n"
    elif(len(qubits)==2):
      strOut += "cx q["+ str(variables.index(qubits[0])) + "], q["+ str((variables.index(qubits[1]))) + "];\n"
    elif(len(qubits)==3):
      strOut += "ccx q["+ str((variables.index(qubits[0]))) + "], q["+ str((variables.index(qubits[1]))) + "], q["+
    str((variables.index(qubits[2]))) + "];\n"
    else:
      strOut = "Only Toffoli and lower gates are supported in OPENQASM "
      break
 print(strOut[:-1])
```

Appendix B

```
      import re
[1]   def tfc2Quirk(filename):
    f = open(filename, "r")
    tfcfile = f.read()

    #Reading qubit layers and numbers
    variablesLine = re.search(r'\.v.*', tfcfile).group()
    variables = variablesLine.split(" ")[1].split(",")
    qubit_number = len(variables)

    #Reading the lines after the BEGIN tag
    tfcCodeBlock = tfcfile.split("BEGIN\n")[1]
    tfcCodeLines = tfcCodeBlock.split("\n")

    strUrl="https://algassert.com/quirk#circuit={%22cols%22:[";
    for k in range(len(tfcCodeLines)-1):
        if(tfcCodeLines[k] == "" or tfcCodeLines[k] ==  "END"):
            continue
        gateAndQubits = tfcCodeLines[k].split(" ")
        if gateAndQubits[0][0] != 't':
            strUrl = "Unsupported Operator"
            break
        qubits = gateAndQubits[1].split(",")
        strUrl = strUrl + "["
        for i in range(qubit_number):
            urlChar = '1'
            for j in range(len(qubits)):
                if variables[i] == qubits[j]:
                    urlChar = "'•'"
                    if j == len(qubits)-1:
                        urlChar = "'X'"
                    break
            strUrl+= urlChar+','
        strUrl = strUrl[:-1]+ "],"
    if strUrl != "Unsupported Operator":
        strUrl = strUrl[:-1] + "]}"
    print(strUrl)
```

International Conference on Advances and Innovations in Engineering

Optimization of Supply Chain Management for Medical Drug Warehouses using Genetic Algorithms

Ayşe KAHVECİ YETİŞ[1] , Mehmet KARAKÖSE[2], İlker GÜRELLİ[3], Onur TOKEL[4], Eray HANOĞLU[5]
[1,3,4,5] Panates Information Technologies, İzmir, Turkey.
[2]Department of Computer Engineering, Fırat University, Elazig, Turkey
[1]ayse.kahveci@panates.com, [2]mkarakose@firat.edu.tr, [3]i.gurelli@panates.com, [4]o.tokel@panates.com, [5]e.hanoglu@panates.com

[1](ORCID: 0000-0002-0832-892X), [2](ORCID: 0000-0002-3276-3788),[3](ORCID: 0009-0006-8117-0475), [4](ORCID: 0000-0002-1962-0432),[5](ORCID: 0000-0001-9491-7028)

Abstract
Supply chains play a crucial role in health, as in many other sectors. Supply chains are used also to deliver medicines to patients, like all products used in the field of health. It is important that the drug is supplied from the warehouses as soon as possible so that patients can buy drugs from components such as clinics, pharmacies, hospitals, nursing homes. In this study, permutation-based genetic algorithms are used to reach drugs from warehouses to distribution channels such as clinics, pharmacies, hospitals and nursing homes in the shortest way. The solutions are arranged to be supplied drugs from the closest warehouses to distribution centers in different locations. As a result of the experiments, it is seen that approximately between 17-22% more efficient process is obtained compared to random distribution.

Keywords: Supply chain management, Genetic algorithms, Medical drug warehouses.

1. Introduction

With the increase in the human population, many basic needs such as clothing, nutrition and shelter have entered into a constantly evolving cycle. In order for this cycle flow to progress smoothly, different needs and concepts have emerged. The cycle flow basically aims to satisfy the product reaching the end user in terms of high efficiency and speed performances. At this point, the supply chain process, which goes through until the product reaches the end user, should be carried out smoothly. Supply chain management systems ensure that the product is delivered to the end user in the fastest and most efficient way. One of the sectors where supply chain management is most necessary is the health sector. Procurement and storage of medical supplies or drugs is of great importance for healthcare institutions serving patients such as hospitals, clinics, and pharmacies. The health sector is one of the sectors where innovations are frequently experienced in order to reveal different health problems depending on the human population and to meet the demand for health needs.

Supply chains are expressed as the whole of the stages that a product starts with the raw material supplier and reaches the end user [1]–[3]. The health sector supply chain is the whole of the processes from the manufacturer to the end user, including activities such as design, research and development, planning, purchasing, delivery and storage [4]. The purpose of these activities is to prevent the disruption of the process and to ensure high efficiency. In order to eliminate the problem of product supply in sectors that are in a flow, the products obtained through supply chains must be preserved and stored under appropriate conditions. In this case, the need for supply warehouses for products arises. For example, with the flow of the health sector, products such as medical electronic devices, hygiene products, medical supplies, drugs are used. These products are kept in medical warehouses under appropriate conditions in order not to waste time on procurement as needed. As in every sector, accuracy in demand forecasts is seen as the basis of efficiency in the health sector supply chain. Because demand forecast accuracy is directly effective in stages such as raw material supply for the product to be produced, production planning, inventory management, and

[1]Corresponding author

determination of financial targets. Especially companies producing pharmaceuticals need to make better demand forecasts. Any mismatch between supply and demand can adversely affect patients. Experiencing this situation in the drugs that chronic patients should use continuously can cause loss of life as well as permanent damage to the patient [5].
The supply chain is of great importance in the healthcare industry. Thanks to the supply chain, the supply of medical supplies that are consumed and needed in the health sector, which is in a loop, is provided quickly. The importance and urgency of drugs and materials needed by patients is one of the factors that explain the importance of this supply chain. Moreover, by analyzing the consumption rates, medical supplies, whose current amount is at critical levels, can be procured in excess of the need and stored in medical warehouses [6], [7].

The distribution network of the healthcare industry pharmaceutical supply chain is shown in Figure 1. In Figure 1, where the drug distribution network is visualized, the formulations developed by the research and development team are combined with the raw materials, resulting in drug manufacturing. After manufacturing, the packaged drugs are sent to global warehouses via global carriers. Medicines brought to local warehouses through local carriers are delivered to patients if they are obtained from hospitals, pharmacies, nursing homes and clinics [5], [8]–[15].

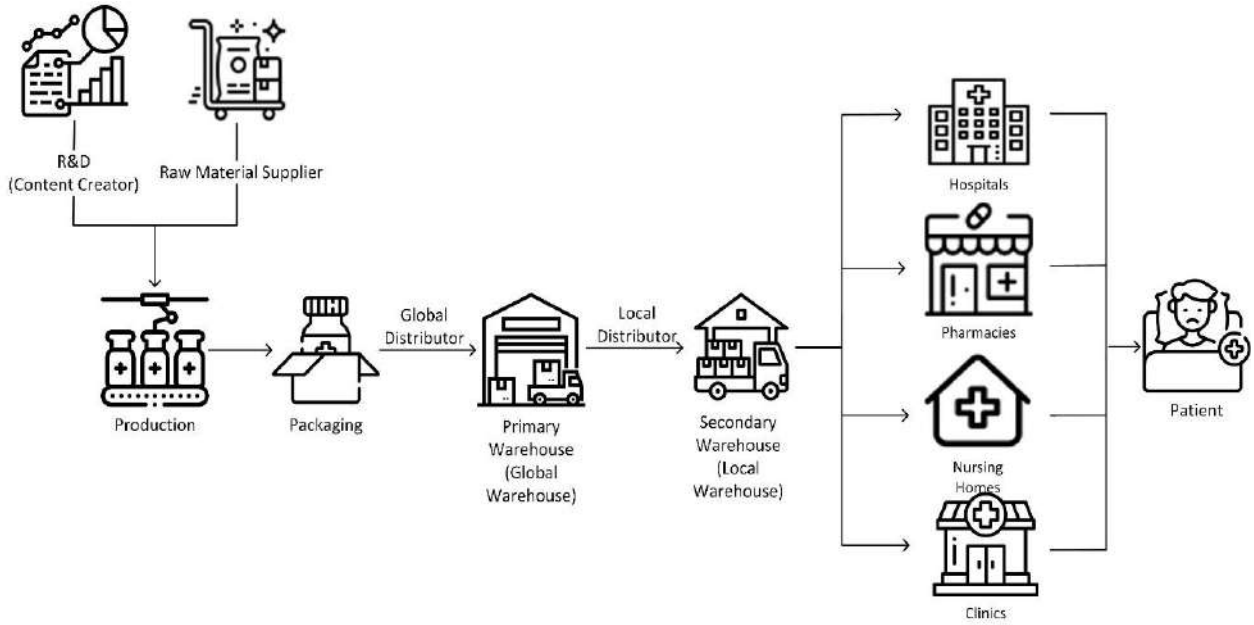

Figure 1. Drug Distribution Network [5]–[13].

2. Genetic Algorithms

Genetic algorithm is a type of heuristic algorithm inspired by natural events. It is preferred for solving optimization problems. Another reason for preference is that the genetic algorithm can be applied to more than one problem and has a multi-solution structure [16]. The main purpose of the genetic algorithm is to protect the strongest individuals in the population and to discard the weakest individuals. In the genetic algorithm, it is aimed to create new generations and increase the population in a quality way with the transfer of similar genes in the remaining strong individuals [17]. A genetic algorithm is a computational, population-based search technique that finds exact or optimal optimized solutions for the survival of the fittest and fittest [17]–[19].The genetic algorithm aims to provide the best possible solution as quickly as possible [20]. In order to do this, it allows the discovery and development of multiple potential solutions at the same time. Genetic algorithm aims to produce better children by sharing certain gene traits from two existing parents and inheriting them genetically [21].

Genetic algorithms are based on the logic of combining the genetic inheritance of two parents and certain gene traits to create new individuals who inherit the good traits of the parents. In order to change the genes in the reproduction of new individuals, a structure expressed as a genetic operation is needed. Selection, crossover and mutation are commonly used genetic operators. By using genetic operators such as selected chromosomes, crossover and mutation,

new offspring are created. With the help of the crossover operator, the good characteristics of the two parents selected from the current population are used to create an offspring.
The mutation operator motivates the gene's potential to generate new genetic information. The aim is to derive a different knowledge from the existing knowledge. Thus, the optimum solution area is expanded and the probability of finding a more suitable solution increases. The reproduction steps continue, being passed down from generation to generation, until the desired solution or maximum evaluation is reached. The termination of the genetic algorithm is usually accomplished by meeting the termination criteria.

3. The Proposed Method

In the study, the distribution is optimized according to the nearest drug warehouses and the nodes where the drugs will be distributed. Considering the problem as a ranking problem, it can be compared to the traveling salesman problem. First, the nodes to the warehouses are clustered according to their proximity. These sub nodes are then efficiently visited using permutation-based genetic algorithm. According to permutation-based coding, all nodes are arranged in a non-repeatable manner to form chromosome structures. The visual of the proposed approach is given in Figure 2.

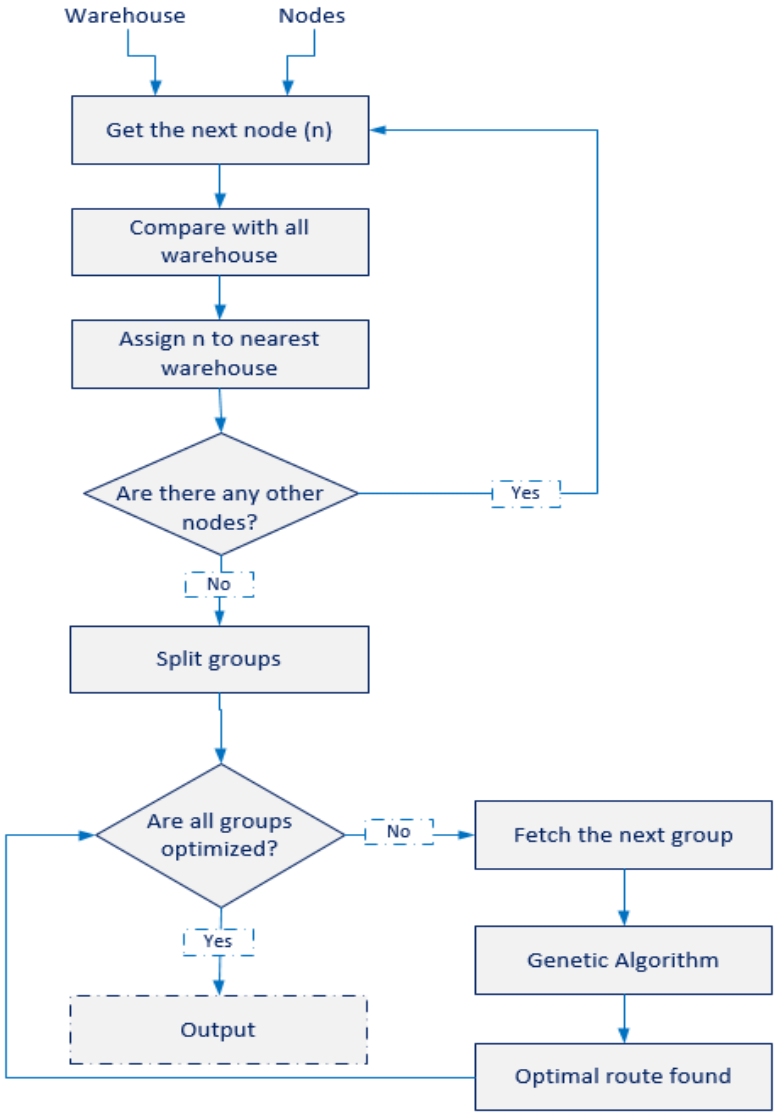

Figure 2. The proposed approach

In genetic algorithms in the Figure 2, the crossover operation can be performed as single-point, double-point and multi-point, similar to general genetic algorithms. An example of a double-point crossover is given in the Figure 3. In Figure 3.b, it is seen that unsuitable chromosomes occur as a result of crossing two individuals. Because, in Figure 3.b, nodes 1 and 5 are located twice on the first chromosome. As a solution, when we see repeated values in these chromosomes, it is necessary to replace the first unused node with the repeating node.

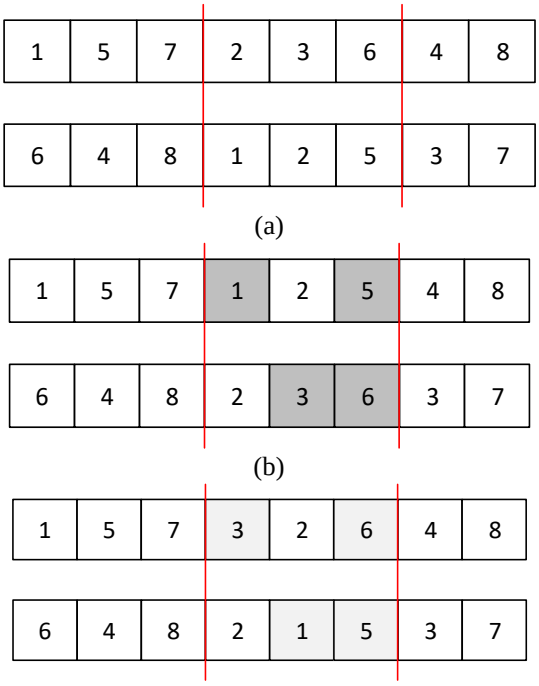

Figure 3. Double-point crossover example in permutation-based genetic algorithms
a) determination of crossover points, b) performing the crossover, c) Optimizing the chromosome

In permutation-based genetic algorithms, mutation operation is usually performed by swap operation. In swap mutation, the contents of two genes are replaced with each other. Swap mutation example is given in Figure 4.

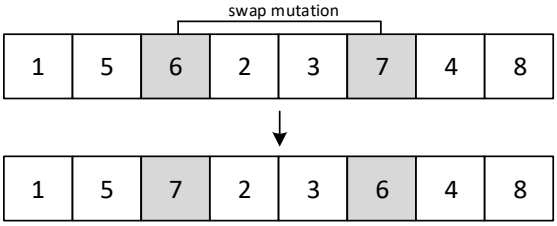

Figure 4. Example of swap mutation

4. Expreimental Results

In order to test the problem, 5 warehouses and 40 nodes that need to distribute drugs are created synthetically. The nodes created represent components such as hospitals, pharmacies, clinics and nursing homes where drugs will be delivered to the patient. In the problem, it is assumed that the drugs needed by the nodes are available in all warehouses. For more complex cases, it can be taken into account that some drugs are not available in some warehouses or they are available in insufficient numbers. The locations of the synthetically created warehouses and nodes are given in Figure 5. In the figure, red circles represent nodes, and black diamonds represent warehouses.

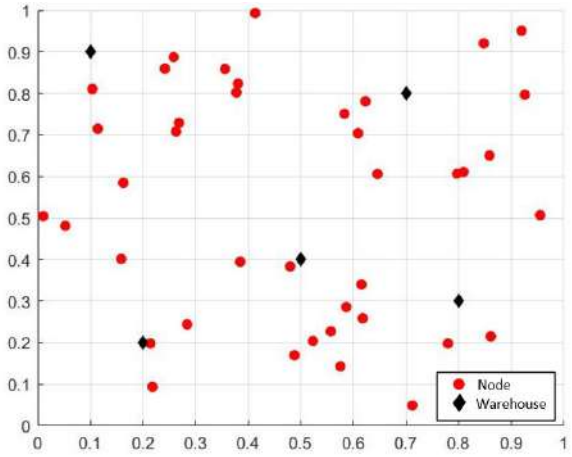

Figure 5. Locations of nodes and warehouses synthetically created

The following steps were followed to solve the problem:
1- Group nodes by nearest warehouse
2- Calculate optimum routes with the help of Genetic Algorithm within the group
The optimum routes obtained as a result of the studies are shown in Figure 6. Here, the locations of the warehouses are also randomly generated, and determining the locations of the warehouses according to the nodes may be the subject of another research.

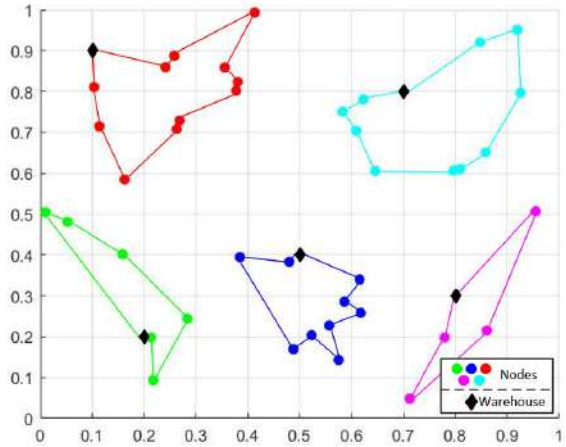

Figure 6. Experimental results

In order to show the effect of the study, the nodes grouped according to the nearest warehouse then they were randomly sorted by brute force algorithm. The results of process, which was run 100 times and 1000 times, are given in Table 1.

Table 1. Min, max and avg distances of randomly generated routes for 100 and 1000 runs

Nodes	Random 100 Execution			Random 1000 Execution			Optimized
	Min	Max	Avg	Min	Max	Avg	
Red	1.7632	2.9924	2.4281	1.7476	3.0633	2.4314	1.2222
Green	1.0250	2.0712	1.5266	1.0090	2.0712	1.5844	1.0052
Turquoise	1.8654	3.0810	2.5110	1.6436	3.2885	2.5079	1.1110
Blue	1.1283	1.9099	1.5513	0.9589	2.0378	1.5618	0.9158
Purple	1.0402	1.3194	1.1897	1.0402	1.3194	1.1824	1.0402
TOTAL	6.8221	11.3739	9.2067	6.3993	11.7802	9.2679	5.2944

As a result of running 100 times, the costs of all nodes were found to be 6.8221 in total. As a result of running 1000 times, this cost decreased to 6.3993. As a result of the optimization performed with the proposed method, the total cost is 5.2944. When these results are evaluated, it is seen that the proposed method provides approximately 22% according to the situation repeated 100 times and approximately 17% compared to the situation repeated 1000 times.

5. Conclusion

The flow steps of distribution systems are of great importance for supply chains. It is more important that the supplies in the medical fields arrive quickly and without any problems. In addition to medical supplies, it is vital that medicines reach patients as soon as possible. In this study, the process between warehouses that play an active role in the drug supply process to patients and components such as clinic, pharmacy, hospital, nursing home has been optimized. First, the closest warehouses to these components were determined. It is assumed that all required drugs are available in all warehouses. Then, the order of the components that must be visited by each warehouse is optimized with the help of genetic algorithms. As a result of the studies, it is seen that a more efficient process is obtained by 17-22%.

6. Acknowledgment

This study was supported by the Panates Information Technologies-R&D under Grant No: PAN013-TBTK4. (TUBİTAK Application Number: 3230442)

7. References

[1] E. D. Brechtelsbauer, B. Pennell, M. Durham, J. B. Hertig, and R. J. Weber, “Review of the 2015 drug supply chain security act,” Hosp. Pharm., vol. 51, no. 6, pp. 493–500, 2016.

[2] M. M. Habib and I. Hasan, “Supply Chain Management (SCM)–Is it Value Addition towards Academia?,” in IOP Conference Series: Materials Science and Engineering, IOP Publishing, 2019, p. 012090.

[3] S. Safaei, P. Ghasemi, F. Goodarzian, and M. Momenitabar, “Designing a new multi-echelon multi-period closed-loop supply chain network by forecasting demand using time series model: a genetic algorithm,” Environ. Sci. Pollut. Res., pp. 1–15, 2022.

[4] T. Hassan, “Logistique hospitalière: organisation de la chaîne logistique pharmaceutique aval et optimisation des flux de consommables et des matériels à usage unique,” PhD Thesis, INSA de Lyon, 2006.

[5] X. Zhu, A. Ninh, H. Zhao, and Z. Liu, “Demand forecasting with supply-chain information and machine learning: Evidence in the pharmaceutical industry,” Prod. Oper. Manag., vol. 30, no. 9, pp. 3231–3252, 2021.

[6] Shweta, A. K. Yadav, and D. Kumar, “Structural modelling and ranking the warehouse activities in a pharmaceutical supply chain system,” Int. J. Six Sigma Compet. Advant., vol. 14, no. 1, pp. 84–106, 2022.

[7] K. Xie, S. Zhu, P. Gui, and Y. Chen, “Coordinating an emergency medical material supply chain with CVaR under the pandemic considering corporate social responsibility,” Comput. Ind. Eng., p. 108989, 2023.

[8] G. Subramanian, A. S. Thampy, N. V. Ugwuoke, and B. Ramnani, “Crypto pharmacy–digital medicine: A mobile application integrated with hybrid blockchain to tackle the issues in pharma supply chain,” IEEE Open J. Comput. Soc., vol. 2, pp. 26–37, 2021.

[9] M. Uddin, K. Salah, R. Jayaraman, S. Pesic, and S. Ellahham, “Blockchain for drug traceability: Architectures and open challenges,” Health Informatics J., vol. 27, no. 2, p. 14604582211011228, 2021.

[10] K. Abbas, M. Afaq, T. Ahmed Khan, and W.-C. Song, “A blockchain and machine learning-based drug supply chain management and recommendation system for smart pharmaceutical industry,” Electronics,. 9(5), p. 852, 2020.

[11] G. Merkuryeva, A. Valberga, and A. Smirnov, “Demand forecasting in pharmaceutical supply chains: A case study,” Procedia Comput. Sci., vol. 149, pp. 3–10, 2019.

[12] A. Musamih et al., “A blockchain-based approach for drug traceability in healthcare supply chain,” IEEE Access, vol. 9, pp. 9728–9743, 2021.

[13] M. M. Habib, F. Chowdhury, S. Sabah, and D. Debnath, “A Study on Hospital Supply Chain Management,” Am. J. Ind. Bus. Manag., vol. 12, no. 5, pp. 806–823, 2022.

[14] A. Singh and R. Parida, “Decision-Making Models for Healthcare Supply Chain Disruptions: Review and Insights for Post-pandemic Era,” Int. J. Glob. Bus. Compet., pp. 1–12, 2022.

[15] S. Donato, J. Parry, and S. Roth, “Strong Supply Chains Transform Public Health: By ensuring the efficient and effective delivery of medicines and commodities, supply chains support healthy populations and regional health security,”, ADB Briefs, 2016.
[16] A. G. M. Güler, “P-Medyan Tesis Yeri Seçimi Problemi Genetik Algoritma Uygulamasi,” Yenilenebilir Kaynaklardan, p. 93, 2022.
[17] P. D. Thanh, H. T. T. Binh, and T. B. Trung, “An efficient strategy for using multifactorial optimization to solve the clustered shortest path tree problem,” Appl. Intell., vol. 50, no. 4, pp. 1233–1258, 2020.
[18] P. Dinh Thanh, H. T. Thanh Binh, D. Dinh Dac, N. Binh Long, and L. M. Hai Phong, “A Heuristic Based on Randomized Greedy Algorithms for the Clustered Shortest-Path Tree Problem,” ArXiv E-Prints, p. arXiv-2005, 2020.
[19] H. Yang, R. Mayne, and Y. Deng, “A Bio-inspired Network Design Method for Intelligent Transportation.,” Int. J. Unconv. Comput., vol. 14, 2019.
[20] O. Cosma, P. C. Pop, and I. Zelina, “An effective genetic algorithm for solving the clustered shortest-path tree problem,” IEEE Access, vol. 9, pp. 15570–15591, 2021.
[21] A. F. Shukur, N. S. Chin, S. Norhayati, and B. N. Taib, “Design and optimization of valveless micropumps by using genetic algorithms approach,” J. Eng. Sci. Technol., vol. 10, no. 10, pp. 1293–1309, 2015.

International Conference on Advances and Innovations in Engineering

Fine Tuning and Comparative Performance Analysis of Pre-trained Transformers for Dialogue Texts Abstractive Summarization

Turan Göktuğ ALTUNDOĞAN[1] , Mehmet KARAKÖSE [2], Senem TANBERK [3], Öykü Berfin MERCAN [4]
[1]Department of Computer Engineering, Engineering Faculty, Manisa Celal Bayar University, Manisa, Turkey.
[2]Department of Computer Engineering, Engineering Faculty, Firat University, Elazig, Turkey.
[3,4]Huawei Telecommunication Foreign Trade Co. Ltd.
[1]turan.altundogan@cbu.edu.tr, [2]mkarakose@firat.edu.tr, [3]senem.a.tanberk@gmail.com, [4]oyku.berfin.mercan@huawei.com,
[1](ORCID: 0000-0002-8677-3105), [2](ORCID: 0000-0002-3276-3788)

Abstract
After the spread by digital communication like email, message and online meeting applications, automatic summarizing of the dialogues or conversations become more important. In this study we focused on abstractive dialogue summarization by transformers. Researchers and engineers solves different nlp problems by transformers with high performance. But training a transformer with high accuracy requires large data set and hardware which have high compute capability. So, many researchers and engineers prefer to use pre-trained transformers like BART, T5, GPT etc. and fine tune these pre-trained models for a specific task. There are so many pre-trained transformers trained for summarization on the online platforms. We fine-tuned four most popular of these pre-trained transformers (BART, T5, LED, BlenderBot) for dialogue summarization task and compare their performance by different criterions. Dialogsum dataset was used for the fine tuning operations. In the training phase we obtained lowest loss value from fine tuning of the BART (0.72). BART also has obtained highest ROUGE-1, ROUGE-2 and ROUGE-L scores from the experiments. BlenderBot model has lowest ROUGE scores. T5 model has minimum trainable parameters and BlenderBot model has maximum trainable parameters. When the summaries produced by fine tuned models are examined, it is seen that all models generate meaningful, accurate and highly successful summaries from the dialogue texts.
Keywords: Abstractive Summarization, Deep Learning, Dialog Summarization, Fine Tuning, Transformers

1. Introduction

Summarization applications are a very important area for natural language processing. There are summarization applications with two different perspectives, namely Abstractive and Extractive summarization. In extractive summarization approaches, the obtained summary text consists of the sentences in the original text. Statistical or unsupervised techniques are generally used in extractive summarization applications [1]. In abstractive summarization applications, sentences that are not in the original text are usually produced by a neural architecture. In this study, Transformer neural architectures, which are frequently used in natural language processing and achieve high results, were used to summarize dialogue texts. Transformers are a kind of encoder – decoder neural architecture. With the special structures such as self-attention and positional embedding in it, Seq2Seq is much more capable than classical encoder - decoders in solving problems. However, Transformers, especially used in text applications of natural language processing, need a lot of training data and hardware with high computational ability and memory. Companies such as OpenAI, Facebook, HuggingFace have developed high-performance Transformers by processing very large data on hardware with high computing capability and memory in order to implement certain natural language processing applications and presented them to users on online platforms. Researchers and engineers who want to implement specific natural language processing applications perform fine-tuning by applying a new training process in these pre-trained Transformers. In this study, we fine-tuned some pre-trained Transformers that perform abstractive text summarization and compared each model obtained according to some criteria in the performance and training stages. Before the detailed explanation of the proposed method, it is important to give the existing dialogue summarization approaches [2-14] in the literature in this section to understand the importance of the subject and the current methods used.
One study focused on summarizing patient-doctor dialogues using the mT5 pre-trained Transformer neural architecture [2]. The main purpose of choosing the mT5 model in the study is due to the fact that the model used can

[1]Corresponding author

support different languages. Because the language of the dataset used is Chinese (Outpatient dataset). The performance of the proposed method was evaluated with R-1, R-2, R-L (ROUGE metric), BLEU and BERTS metrics. The performance of the proposed method was determined as 0.2085 with the R-1 metric. In another study, a neural approach was developed for abstractive summarization of meeting recordings [3]. In the study, an Encoder – Decoder architecture was developed in which BiLSTM layers and attention mechanisms are used. The proposed method was evaluated with the metrics R-1, R-2, R-3 and R-L. The R-1 performance of the proposed method was determined as 0.6834 and the R-L performance as 0.4993. In another study, a neural network approach with Transformer architecture was developed for the dialog summarization problem [4]. The Transformer architecture used in the developed method is BART. The proposed method was evaluated with the ROUGE metric as in previous studies and obtained 0.4786 R-1, 0.2564 R-2 and 0.4473 R-L performances. Another study focused on the dialogue summarization with a neural architecture in the Encoder – Decoder structure [5]. The model developed in the study performs sequence tagging and dialog summarization processes together. The proposed method was evaluated with ROUGE and BERT metrics, and SamSum was used as the data set. The encoder – decoder architecture used is the BART neural architecture. The proposed method yielded 0.43 R-1, 0.189 R-2 and 0.42 R-L scores. In another study, a transformer-based method was developed in which hierarchical relations were determined in the word and expression coding phase, focusing on the inadequacy of classical summarization methods in terms of distinguishing personal pronouns [6]. In the proposed method, the SamSum data set was used for training and the ROUGE metric was used to evaluate the proposed method. As a result, 0.4733 R-1, 0.2266 R-2 and 0.3967 R-L scores were obtained. In another study, an extractive summarization method was developed for customer relations dialogues [7]. In the study, some predefined questions and key points were determined in the dialogue, and the summarization problem was transformed into a machine's reading comprehension problem with a distance control mechanism. The proposed method was evaluated with the ROUGE metric. The R-1 score was calculated as 0.4827, the R-2 score as 0.2985, and the R-L score as 0.4828. In another study, he developed a BART-based transformer architecture by making use of local and global relations in the dialogue to overcome the disadvantages of classical summarization methods in personal pronoun matching [9]. In the proposed method, SamSum data set was used and evaluation was performed with the ROUGE metric (R-1:51.42, R-2:25.18, R-L:50.25). In a study, an abstractive dialog summarization method was developed by using transformers with ALBERT and BART pre-training [10]. The proposed method yielded 0.501 R-1, .0.2664 R-2 and 0.4622 R-L scores. In another study, the summaries of the news dialogues were extracted using a method based on the interests of the users by using the reader profiles [11]. In the proposed method, BERT architecture was used to obtain sentence features. The R-1 rating of the proposed method was determined as 0.863. In one study, summarizing the dialogs found on developer platforms such as GitHub was performed by fine-tuning the T5 model [13]. The proposed method was evaluated with a score of 0.5209 R-1, 0.4061 R-2 and 0.5152 R-3.

2. Proposed Approach

In this study, performance analysis was performed by performing fine tuning of pre-trained Transformer architectures to perform the dialog summarization process. Neural perspective methods are generally used for abstractive summarization. Training Seq2Seq architectures focused on natural language processing requires a lot of data, computation and memory costs. Therefore, researchers and engineers can perform fine tuning on pre-trained transformers with a smaller data set to solve specific problems. In this study, we performed a fine tune operation using the DialogSum dataset of four different Transformer architectures with abstractive summarization capability. The block diagram of the proposed method is given in Figure 1. When Figure 1 is examined, the data set is first subjected to the preprocessing step. Preprocessed training data is used for retraining pretrained Transformers from the HuggingFace hub for fine tuning. The resulting FineTuned Transformer is again saved to the HuggingFace Hub for later use. During the inference and evaluation phase, the preprocessed test texts are sent to the fine-tuned Transformer for summary. The outputs of the Transformer are evaluated with the ROUGE metric. For a better understanding of the proposed method, it is useful to explain each step in detail.

A. Data Preprocessing

In the preprocessing step;

.

- Dialogue texts that do not meet the maximum length criteria are excluded from the dataset.
- In the dialogue performed by #Person1 and #Person2 in the raw dialogue text, message tagging of each person is performed.

- All text is converted to lowercase letters.
- All punctuation marks and special symbols are deleted.
- • Abbreviated expressions such as "I'm, You've" are replaced with their original expressions,
- Padding is performed so that all dialog texts are of equal length.

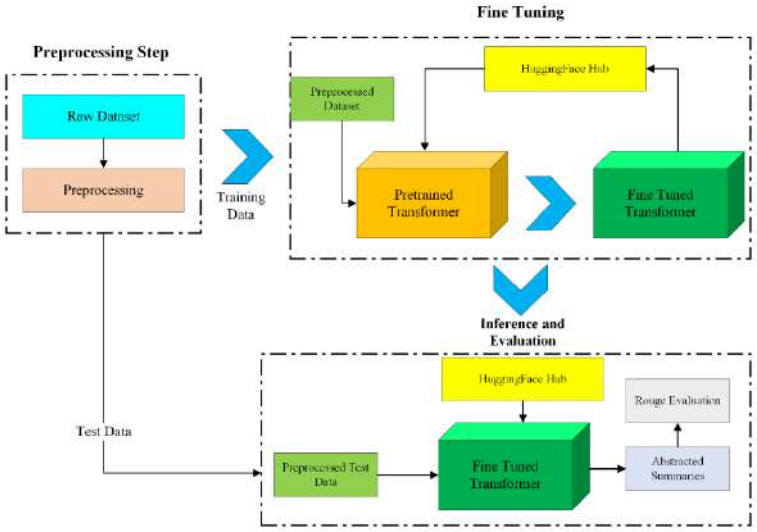

Figure 1. Block diagram of the Proposed Approach.

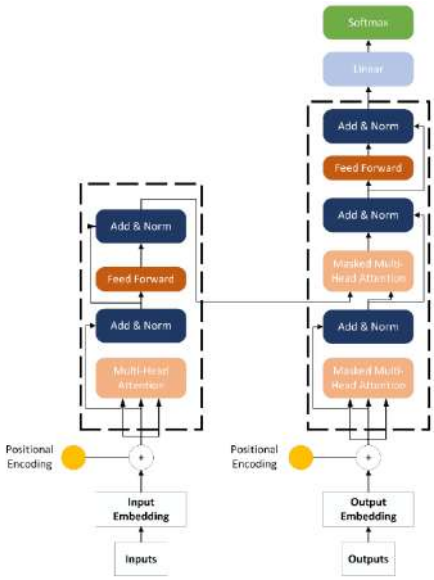

Figure 2. Block diagram of the Transformers [15].

B. Transformers and Fine Tuning

Problems such as question – answering, summarizing belonging to natural language processing are called Seq2Seq. For the solution of Seq2Seq problems, neural architectures expressed as encoder – decoder are used. The aim here is to obtain sequential results by encoding the features obtained from the input data on the Encoder side of the neural architecture and sending these coded features to the Decoder side. In Seq2Seq problems whose input and output are text, firstly the text is tokenized on a word-by-word basis. Each of these tokens obtained is expressed with an index value and fed to the neural network in a one-hot encoded sequence format of this vocabulary size. Following the one-hot expression of the words, the process of making the text understandable by the neural network is completed by using the Embedding weights obtained at the time of or before the training. Seq2Seq problems with long sequence size cause a big disadvantage, especially in Encoder – Decoder architectures where RNN layers are used. Mechanisms called Attention have been developed to solve this problem. There are Attention and Positional Encoding mechanisms in the Encoder and Decoder layers separately in Transformers [15]. In addition, any recurrent or convolutional network structure is not included in the Transformers. It performs its operations with fully Attention mechanism learning. In the Attention mechanisms used here, the handled element in the text is expressed with Query, the other elements in the text are Key, and the relationship between Query and Key is expressed with value. If a single key, query and value triplet is used in the Attention operation, that is, a single relation calculation operation is performed, this structure in the Transformer is called self attention. In the Attention mechanism, if the value is calculated from more than one key and query, that is, if the Attention operation is performed with more than one head, this is called Multi-head attention. Since there are no repetitive and convolutional layers in transformers, the words belonging to the sequence do not have a concept of order. With Postional Encoding, this problem has been solved by adding additional spatial information to word embeddings. A block diagram expressing the structure of the Transformer is given in Figure 2 [15].

The performance of the Transformer structure in Seq2Seq problems and the more parallelizability of the training process have caused many different problems to be handled with Transformers. In addition, many pretrained transformers in different architectures can be accessed. Transfer learning is a frequently used approach in solution

proposals using deep learning, even before the use of Transformers. Especially for solving problems where training data is scarce, transfer learning is a very effective method to maximize training performance. In Object Detection models (LeNet, VGG, etc.) developed by companies such as Google for computer vision problems, pre-trained CNN layers that extract features from the image are used in networks trained to detect different objects, while structures such as pre-trained embedding layer can be used in Natural Language Processing applications. In Transformers, on the other hand, the Transformer architectures developed by different companies and research institutions are obtained, and fine-tuning operations are performed with a low number of training data and small training iteration numbers (epoch) of the problem addressed. In this study, four different trained Transformer structures (BART, T5, LED, BlenderBot) that were previously trained for text summarization were used for the dialog summarization process. Detailed information about these architectures used is given in the Experimental Results section.

C. Inference and Evaluation

The models obtained after the fine-tuning of the pre-trained Transformers were recorded on the HuggingFace Hub. Fine-tuned models are recovered through the HuggingFace Hub to extract summaries from the original dialogue texts. Then, the output summaries obtained using the section of the data set reserved for testing are subjected to ROUGE evaluation. The ROUGE metric, the result text and the target summary text in the data set, have features such as the total number of common words (ROUGE-1), the number of n sequential common word groups (ROUGE-N), and the sequential maximum number of common word groups (ROUGE-L). uses a relative comparison method. Since the ROUGE metric is widely used in Seq2Seq-oriented studies in the literature, the evaluation of the results was performed with ROUGE.

3. Experimental Results

In this study, four different Pretrained Transformers (BART, LED, BlenderBot, T5) DialogSum [16] were fine-tuned to perform abstractive dialog summarization. All Pre-Trained models used were obtained from the HuggingFace platform. Training and inference processes were carried out by using the Python library called Transformer, developed by HuggingFace, and the Tensorflow library. All training and inference processes were carried out on Google's GPU-supported Colab platform. The detailed representation of the experimental results was carried out under different sub-headings. In the first stage, four different models were trained with low training iteration numbers and they were compared according to different criteria. Then, these models were evaluated with the test data, and the model that obtained the highest ROUGE score was trained in the higher training iteration and re-evaluated.

A. Dataset and Preprocess Results

DialogSum, which presents abstractive summaries of dialogue texts in daily life, was used as a data set [16]. The train, validation and test data numbers of the data set are given in Table 1 [16]. In the preprocessing step, firstly, data with input size larger than 300 and output size larger than 50 were removed from the data set. Table 1 also includes the amount of data used in each split after the preprocess step. In Table 2, three sample dialogue texts taken from the data set and their abstractive summaries are given.

Table 1. Data splits and amounts belong to DialogSum [16].

Data Split	Amount	Pre-processed Data Amount
Training	12460	12457
Validation	500	497
Test	1500	1497
Total	14460	14451

Table 2. Example dialogue texts and summaries taken from dataset [16].

Dialogue Text	Abstractive Summary
#Person2#: I've tried hundreds of times, but I just can't seem to kick the habit. #Person1#: Well, we have classes and some medications that might help. I'll give you more information before you leave. #Person2#: Ok, thanks doctor.	Mr. Smith's getting a check-up, and Doctor Hawkins advises him to have one every year. Hawkins'll give some information about their classes and medications to help Mr. Smith quit smoking.
#Person1#: Happy birthday, Aims! #Person2#: Thank you, Lisa. #Person1#: Here is a present for you. I hope you like it. #Person2#: Oh, great! I love it! You know I've been expecting this for a long time. #Person1#: I'm very glad to hear that. #Person2#: Come here ; let me introduce some friends to you.	Lisa gives Aims a birthday present and Aims loves it.

B. Transformer Fine Tuning

As mentioned before, four different pretrained neural architectures were used for Transformer training;BART [17]

- BlenderBot [18]
- LED [19]
- T5 [20]

Each of the models used here has pre-training for text summarization. The purpose of fine tuning is to give the model the ability to summarize dialogue. In Table 3, the number of trainable parameters for each model, the number of epochs, the amount of GPU memory consumed by the pre-trained models, the space occupied by the models on the hard disk, the average time spent for each epoch and the training – validation loss values at the end of the training are given. In Figure 3, the training and validation loss graphs of each model are given.

Table 3. Model features, training parameters and results.

Model	Trainable Params	Epoch	GPU Memory	Disk	Time Per Epoch	Training – validation loss
BART-base	139420416	3	33 GB	558 MB	250 sec	0.8034 – 0.7758
BlenderBot	364802560	3	33 GB	1.46 GB	315 sec	0.7608 – 0.9011
LED	161844480	3	33 GB	648 MB	624 sec	0.6565 – 0.7310
T5-Small	60506624	3	17.0 GB	374 MB	172 sec	1.1630 – 1.0659

Table 4. ROUGE evaluations of fine tuned models.

Model	ROUGE-1	ROUGE-2	ROUGE-L
BART	0.4751	0.2080	0.3964
BlenderBot	0.4009	0.1833	0.3240
LED	0.4223	0.2000	0.3778
T5-Small	0.4256	0.1625	0.3429

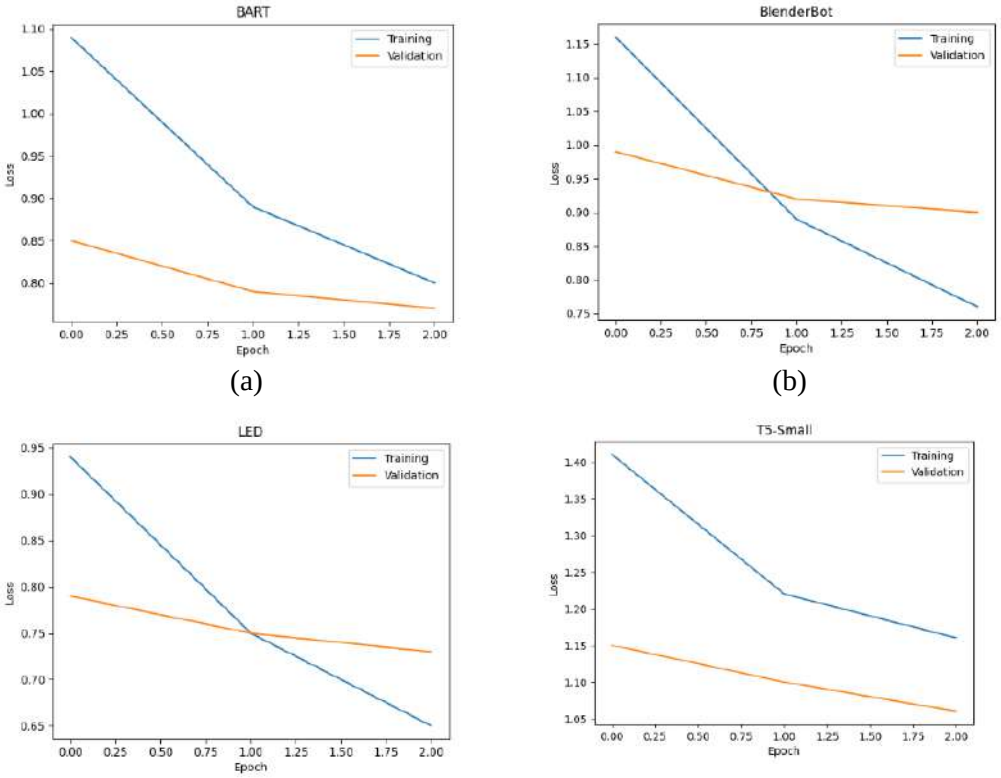

Figure 3. Loss graph of Transformer trainings (a: BART, b: BlenderBot, c: LED, d: T5-Small).

C. Inference and Evaluation

After the completion of the training processes, the recorded models were evaluated with the test data. Table 4 shows the ROUGE scores of each model for 50 sample dialogue texts taken from the test data. In Table 5, a sample dialogue text from the test data, the target summary expected to be extracted from the dialogue text and the summaries obtained from each model are given. When Table 4 was examined, it was seen that the best ROUGE evaluation was obtained with the fine-tuned BART model. When the graphics in Figure 3 are examined, it is clearly seen that the most stable education process is carried out with this model. When the training and evaluation results of other models were examined, it was observed that the fine-tuning process again achieved successful results. When Table 5 is examined, it is seen that all models produce summaries in accordance with the sample dialogue text given. However, it has also been observed that the LED model creates a less comprehensive abstraction than other models. It was decided to retrain and evaluate the BART model with a higher training iteration due to both the stability of the training and the high ROUGE scores it obtained.

Table 5. Example dialogue text taken from dataset and summaries generated by models from that.

Input Dialogue Text	
#Person1#: Honey, I think you should quit smoking.	
#Person2#: Why? You said I was hot when smoking.	
#Person1#: But I want you to be fit.	
#Person2#: Smoking is killing. I know.	
#Person1#: Check out this article. It says smoking can lead to lung cancer.	
#Person2#: I don't believe it.	
#Person1#: But you know that smoking does harm to health, right?	
#Person2#: Of course I know it, but you know it's hard to quit smoking. . .	
#Person1#: Stop beating around the bush. Will you quit or not?	
#Person2#: Yes, ma'am. Whatever you say.	
Original Summary:	#Person1# asks #Person2# to quit smoking for health. #Person2# thinks it's hard but agrees.
Model	Predicted Summary
BART	#person1# advises #person2# to quit smoking because smoking is killing and smoking can lead to lung cancer #person2# doesnt believe it but agrees to listen to #person
BlenderBot	#person2# tells #person1# smoking can lead to lung cancer #person2# thinks smoking is hard to quit
LED	#person1# tells #person2# smoking is killing and suggests quit
T5-Small	#person1# tells #person2# that smoking can lead to lung cancer maam says smoking does harm to health right and says smoking can cause lung cancer

D. Re-Tuning and Evaluation of BART

After evaluating the training process and inference results of different models for 3 epochs, it was decided to retrain the BART model for another 10 epochs. The results of this trained model are given in Table 6. In Figure 4, the loss graph of the model is given. The ROUGE evaluations obtained are given in Table 7. In Table 8, abstractive summaries produced by the model from different test data are given. When Table 6 is examined, it is seen that the loss values of the model decrease with increasing the number of epochs. When Figure 4 is examined, the validation loss of the model is slightly behind compared to the Training loss, which shows that the number of epochs should not be increased too much in fine tuning processes. When Table 7 is examined, it is seen that the ROUGE results obtained by the model are parallel to those in the literature. When the data in Table 8 were examined, it was observed that the text summaries obtained were inclusive of the dialogue text and did not have any semantic contradictions with the dialogue text.

Table 6. Example dialogue text taken from dataset and summaries generated by models from that.

Model	Trainable Params	Epoch	GPU Memory	Disk	Time Per Epoch	Training – validation loss
BART-base	139420416	10	33 GB	558 MB	250 sec	0.4850– 0.7496

Table 7. ROUGE evaluations of re-tuned BART.

Model	ROUGE-1	ROUGE-2	ROUGE-L
BART	0.4835	0.2467	0.4065

Table 8. Example dialogue text taken from dataset and summaries generated by re-tuned BART model from that.

Input Dialogue Text	
"#Person1#: Excuse me, can you tell me how to get to the Rainbow Restaurant from here?	
#Person2#: Drive two blocks and turn left. Continue on until you reach Heath Street and turn right.	
Then turn left at the second stop light. You can't miss it."	
Original Summary:	#Person1# asks #Person2# the way to the Rainbow Restaurant.
Model	Predicted Summary
BART	#person2# tells #person1# how to get to the rainbow restaurant from #person1# tells here the way to it is simple and easy

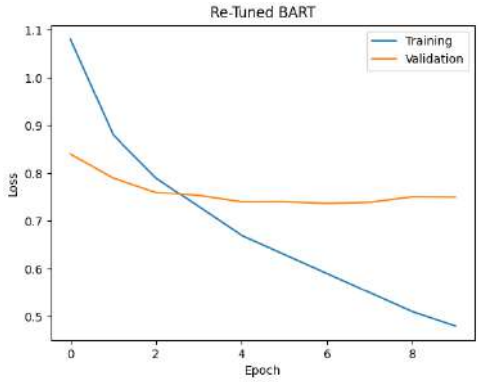

Figure 4. Loss graph of BART 10 epoch training.

4. Conclusions

In this study, some pre-trained Transformer networks were fine-tuned to summarize the dialogue texts. In this context, BART, BlenderBot, LED and T5 models were retrained with the DialogSum dataset and compared based on many different criteria. The main motivation for realizing such a perspective of the proposed method is based on providing problem solving with a small data set and low hardware costs. When the training results and model structures are examined, it is seen that the number of training parameters increases the training time and hardware costs. On the other hand, it was seen that the number of trainable parameters of the BART model, for which we obtained the best results, was lower than many models taken in comparison. Obtaining the minimum performance in the model with the highest number of trainable parameters was associated with the smallness of the data set used. After the scenario in which the four models were compared, the BART model, in which the best performance was obtained, was retrained with a higher number of training iterations. As a result of this training, it was observed that the validation loss value decreased less than the training loss value. This led to the conclusion that working with very high epoch values in fine tuning processes may decrease the model performance. The ROUGE performance of the final model obtained is higher than the model developed with low training iteration. When the abstractive summaries obtained from all models were examined, it was observed that the results contrary to the original text were not obtained and the summarization process was carried out more comprehensively than the results in the data set. When the ROUGE evaluations of the models were examined, it was seen that they had performances parallel to the results in the literature.

5. Acknowledgements

This study was supported by the TUBİTAK (The Scientific and Technological Research Council of Turkey) under Grant No: 5220154.

6. References

[1] T. G. Altundogan and M. Karakose, "LSTM Encoder Decoder Based Text Highlight Abstraction Method Using Summaries Extracted by PageRank," 2023 27th International Conference on Information Technology (IT), Zabljak, Montenegro, 2023, pp. 1-4, doi: 10.1109/IT57431.2023.10078652.

[2] H. -Y. Tsai, H. -H. Huang, C. -J. Chang, J. -S. Tsai and H. -H. Chen, "Patient History Summarization on Outpatient Conversation," 2022 IEEE/WIC/ACM International Joint Conference on Web Intelligence and Intelligent Agent Technology (WI-IAT), Niagara Falls, ON, Canada, 2022, pp. 364-370, doi: 10.1109/WI-IAT55865.2022.00060.

D. -W. Goo and Y. -N. Chen, "Abstractive Dialogue Summarization with Sentence-Gated Modeling Optimized by Dialogue Acts," 2018 IEEE Spoken Language Technology Workshop (SLT), Athens, Greece, 2018, pp. 735-742, doi: 10.1109/SLT.2018.8639531.

[3] L. Jiang, Y. Hao and J. Lin, "Dialogue Text Summarization Method Combined Self-supervised Learning and Neural Architecture Search," 2022 2nd International Conference on Big Data, Artificial Intelligence and Risk Management (ICBAR), Xi'an, China, 2022, pp. 65-69, doi: 10.1109/ICBAR58199.2022.00020.

[4] S. Lee, K. Yang, C. Park, J. Sedoc and H. Lim, "Who Speaks Like a Style of Vitamin: Towards Syntax-Aware Dialogue Summarization Using Multi-Task Learning," in IEEE Access, vol. 9, pp. 168889-168898, 2021, doi: 10.1109/ACCESS.2021.3124556.
[5] Y. Lei, Y. Yan, Z. Zeng, K. He, X. Zhang and W. Xu⋆, "Hierarchical Speaker-Aware Sequence-to-Sequence Model for Dialogue Summarization," ICASSP 2021 - 2021 IEEE International Conference on Acoustics, Speech and Signal Processing (ICASSP), Toronto, ON, Canada, 2021, pp. 7823-7827, doi: 10.1109/ICASSP39728.2021.9414547.
[6] B. Ma, H. Sun, J. Wang, Q. Qi and J. Liao, "Extractive Dialogue Summarization Without Annotation Based on Distantly Supervised Machine Reading Comprehension in Customer Service," in IEEE/ACM Transactions on Audio, Speech, and Language Processing, vol. 30, pp. 87-97, 2022, doi: 10.1109/TASLP.2021.3133206.
[7] H. Lin et al., "Topic-Oriented Dialogue Summarization," in IEEE/ACM Transactions on Audio, Speech, and Language Processing, vol. 31, pp. 1797-1810, 2023, doi: 10.1109/TASLP.2023.3271118.
[8] P. Yi and R. Liu, "A Relation Enhanced Model For Abstractive Dialogue Summarization," 2022 International Conference on Cyber-Enabled Distributed Computing and Knowledge Discovery (CyberC), Suzhou, China, 2022, pp. 240-246, doi: 10.1109/CyberC55534.2022.00047.
[9] S. D. Halder, M. K. Paul and B. Islam, "Abstractive Dialog Summarization using Two Stage Framework with Contrastive Learning," 2022 25th International Conference on Computer and Information Technology (ICCIT), Cox's Bazar, Bangladesh, 2022, pp. 540-544, doi: 10.1109/ICCIT57492.2022.10055286.
[10] H. Takatsu, M. Okuda, Y. Matsuyama, H. Honda, S. Fujie and T. Kobayashi, "Personalized Extractive Summarization for a News Dialogue System," 2021 IEEE Spoken Language Technology Workshop (SLT), Shenzhen, China, 2021, pp. 1044-1051, doi: 10.1109/SLT48900.2021.9383568.
[11] Singhal, K. Khatter, T. A and J. R, "Abstractive Summarization of Meeting Conversations," 2020 IEEE International Conference for Innovation in Technology (INOCON), Bangluru, India, 2020, pp. 1-4, doi: 10.1109/INOCON50539.2020.9298305.
[12] Fan, G., Chen, S., Wu, H., Gao, C., Xiao, J., Xue, X., & Feng, Z. (2023). Dialog summarization for software collaborative platform via tuning pre-trained models. Journal of Systems and Software, 111763.
[13] Zhao, L., Xu, W., Zhang, C., & Guo, J. (2022). Leveraging speaker-aware structure and factual knowledge for faithful dialogue summarization. Knowledge-Based Systems, 245, 108550.
[14] Vaswani, A., Shazeer, N., Parmar, N., Uszkoreit, J., Jones, L., Gomez, A. N., ... & Polosukhin, I. (2017). Attention is all you need. Advances in neural information processing systems, 30.
[15] Chen, Y., Liu, Y., Chen, L., & Zhang, Y. (2021). DialogSum: A real-life scenario dialogue summarization dataset. arXiv preprint arXiv:2105.06762.
[16] Lewis, M., Liu, Y., Goyal, N., Ghazvininejad, M., Mohamed, A., Levy, O., ... & Zettlemoyer, L. (2019). Bart: Denoising sequence-to-sequence pre-training for natural language generation, translation, and comprehension. arXiv preprint arXiv:1910.13461.
[17] Roller, S., Dinan, E., Goyal, N., Ju, D., Williamson, M., Liu, Y., ... & Weston, J. (2020). Recipes for building an open-domain chatbot. arXiv preprint arXiv:2004.13637.
[18] Beltagy, I., Peters, M. E., & Cohan, A. (2020). Longformer: The long-document transformer. arXiv preprint arXiv:2004.05150.
[19] Raffel, C., Shazeer, N., Roberts, A., Lee, K., Narang, S., Matena, M., ... & Liu, P. J. (2020). Exploring the limits of transfer learning with a unified text-to-text transformer. The Journal of Machine Learning Research, 21(1), 5485-5551.

International Conference on Advances and Innovations in Engineering

Mask R-CNN Based Video Segmentation ın Smart Campus Areas

Merve YİLMAZER[1] , Mehmet KARAKOSE [2], Senem TANBERK [3], Samed ARSLAN[4]
[1]Department of Computer Engineering, Engineering Faculty, Munzur University, Tunceli, Türkiye.
[2]Department of Computer Engineering, Engineering Faculty, Firat University, Elazig, Türkiye.
[3,4]Huawei Telecommunication Foreign Trade Limited Company, Istanbul, Türkiye
[1]merveyilmazer@munzur.edu.tr, [2]mkarakose@firat.edu.tr, [3]senem.a.tanberk@gmail.com, [4]samed.arslan@huawei.com

[1](ORCID: 0000-0001-7055-6299), [2](ORCID: 0000-0002-3276-3788), [3](ORCID: 0000-0003-1668-0365)

Abstract
Nowadays, security and monitoring systems in cities and campus areas are made with video recordings. Applications such as detection of foreign objects and condition monitoring in video recordings, which are very large in size, require a lot of time and labor. For this reason, artificial intelligence-based intelligent analysis methods have been developed for video analysis in the literature. In this study, Mask R-CNN was trained with a deep neural network to perform video segmentation of 6 different classes such as bus, car, hike, dog, motorbike and tennis, which are found in the DAVIS dataset and are frequently encountered in campus areas. The training was repeated at different batch_size and learning rate values and its accuracy was tested. The accuracy of the training, which was done with 0.01 learning rate and 4 batch_size values, was measured as 91.7%. In the next studies, it is aimed to increase the adaptability of the video instance segmentation method with the videos obtained in real time in the campus areas.

Keywords: video segmentation, mask r-cnn, davis dataset, smart campus

1. Introduction

With the widespread use of security and monitoring systems in many areas today, video data has grown rapidly. The increasing success rates of intelligent systems and models such as machine learning and deep learning on visual data have allowed image analysis and video analysis to be done with automated systems. like this, video and image analyzes that require a long time and labor can be done in a shorter time and with higher accuracy. Many successful studies have been carried out in the fields of image processing, image semantic segmentation and instance segmentation, especially with the models proposed in the field of deep learning. Video data is more complex than image data. Such that in image semantic segmentation, a category tag is assigned for each pixel in a particular image. In video semantic segmentation, on the other hand, each pixel in each frame of a given video must be assigned a category tag [1]. Video instance segmentation, unlike semantic segmentation, separates the instances of the same class in the sample segmentation image, as well as the selection of each pixel in an image [2].

Rapid developments in technology have led to an increase in interaction between objects and people. Accordingly, the integration of remotely controlled processes into social life has led to the spread of smart systems and fields. Campus areas where smart systems are integrated are being developed so that both students, faculty members and administrators can use campus areas more efficiently. The basis of smart campus applications is the creation of campus technological infrastructure. Among the main technologies supporting smart campus applications are cloud computing, internet of things (IoT), augmented reality (AR) and artificial intelligence (AI) [3].

In this study, video segmentation method is proposed in order to automate the examination of video recordings recorded for security and monitoring purposes in smart campus areas. Video segmentation is used in a wide variety of applications such as autonomous vehicle [4], video summarization [5], scene comprehension [6], action recognition [7], object tracking [8], and video annotation [9]. For this reason, there are many studies proposed in the field of video segmentation in the literature. Some of these studies are as follows:

[1]Corresponding author

Liu et al. [10] proposed a CPU-based face detection method as an alternative to CNN systems that require high-speed GPU use using RAI dataset. They showed that their proposed method could detect face from 93.2% F1 Score. Le et al. [11] performed the DAVIS Test-Challenge dataset using the Contextual Guided Segmentation (CGS) method to perform video segmentation. In the method they proposed, they showed that they could determine the categories of human/non-human, hard/deformable from the video with a Global Score of 75.4%. Qi et al. [12] showed that by training the OVIS dataset in 25 categories with CMaskTrack R-CNN, they could detect an object with an AP value of 15.4%. Brissman et al. [13] obtained an AP success value of 16.0% by training the OVIS dataset consisting of 25 categories with Graph neural network (GNN) for video segmentation. Huang et al. [14] proposed a video segmentation method based on Scribble-Supervised, whose block diagram is given in Figure 1, using Youtube and DAVIS datasets.

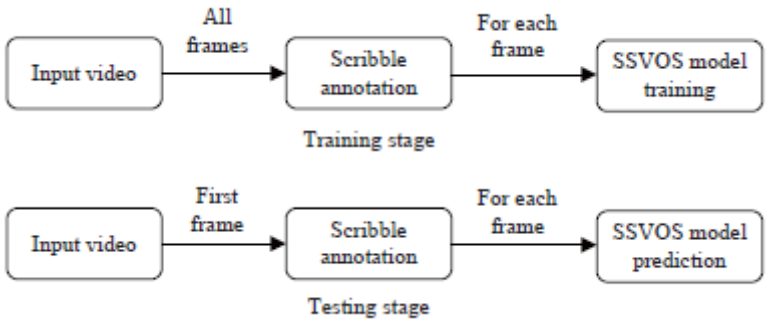

Figure 1. Scribble-Supervised video segmentation model [14]

Sistu et al. [15] proposed two architectures based on recurrent FCN (RFCN) and Multi-Stream FCN (MSFCN) networks to perform video semantic segmentation. The researchers who tested the proposed architectures for SYNTHIACVPR'16, SegTrack V2, DAVIS, KITTI and SYNTHIA datasets showed an improvement in the accuracy of the datasets. Lin et al [16] proposed a video segmentation method based on the Propose-Reduce Paradigm. With their proposed method, they obtained 47.6% AP in the YouTube-VIS validation set and 70.4% J&F in the DAVISUVOS validation set.

In this study, a method on segmentation of video data, which is one of the important steps to develop smart campus areas, is proposed. In the proposed method, DAVIS dataset, which includes objects frequently encountered in campus areas such as cars, buses, dogs, walking people, tennis players, and motorcycles, was used. The number of original data has been increased with techniques such as cropping, flipping and rotation used for data augmentation. Performance comparisons were made against different hyperparameters by training the rich content DAVIS dataset used in many state of the art architectures at different learning rates and different banch_size values using Mask R-CNN deep neural network. Contributions of this study can be listed as follows, according to other methods suggested in the field of video segmentation in the literature.

- The images in the bus, car, hike, dog, motorbike and tennis classes, which are frequently seen in campus areas and found in the DAVIS dataset, were augmented using data augmentation techniques and trained with the mask r cnn video instance segmentation model.
- The adaptability of the method was measured by repeating the model training at different banch_size and learning rate rates.

2. Materials And Method

2.1. Mask R-Cnn Framework

Mask R-CNN, the fourth member of the R-CNN family and proposed by Facebook AI Research (FAIR), is based on estimating the mask of the object in addition to the bounding box used in the Faster R-CNN algorithm. Using Mask R-CNN COCO dataset, 80k train images were trained with 35k val images. It allows training using different backbones. In each RoI sampled during training, the multi-task loss is defined as L = Lcls + Lbox + Lmask [17, 18].

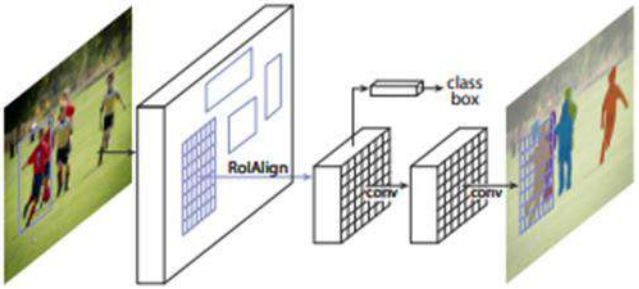

Figure 2. Mask R-CNN framework [17]

2.2. Proposed Approach

The automatic realization of security and monitoring systems in smart campus areas has been developed using self-learning machine learning and deep learning methods. In the growing video data, applications such as object detection, segmentation, and keyframe detection have increased the success of watching, examining, summarizing and inferring video records. In this study, bus, dog, hike, car, motorbike and tennis datasets containing images that are frequently encountered in campus areas of the DAVIS dataset were used. The original images in the dataset were augmented using various data augmentation techniques. The names of the classes used in the DAVIS datset, the number of original data and the number of augmented data are given in Table 1. A dataset consisting of a total of 560 images with 408 originals and 152 augmented images with 854x480 dimensions was obtained. 70% of this dataset is trained at different learnin rate and batch_size values for video instance segmentation using Mask R-CNN deep neural network ResNet Backbone. Model evaluation was carried out with the remaining data.

Table 1. Dataset Classes and Counts

Dataset Classes	Number of Original data	Augmented Data	Total Number of Data
Bus	80	20	100
Car_roundabout	75	20	95
Dog	60	30	90
Hike	80	20	100
Motorbike	43	42	85
Tennis	70	20	90

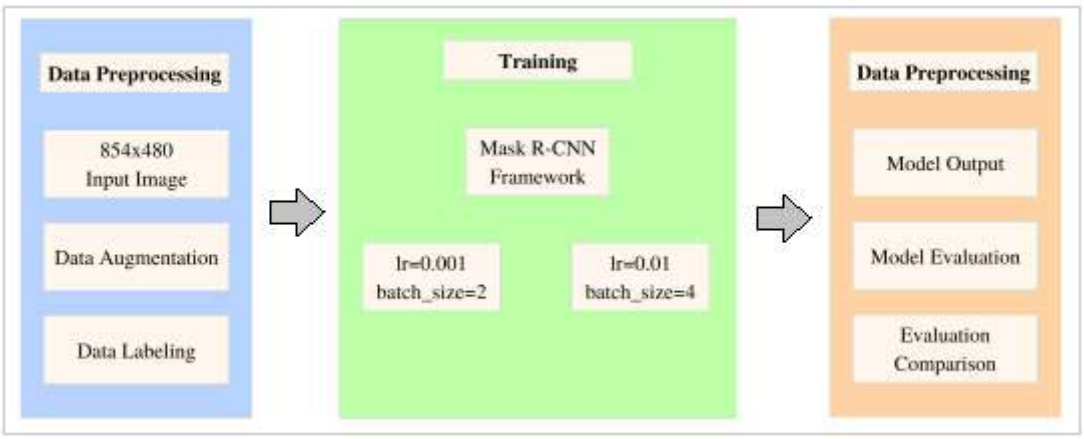

Figure 3. Proposed Approach Block Diagram

The implementation steps of the method, whose block diagram is given in Figure 3, are given below.

- The images of the bus, dog, hike, car, motorbike and tennis classes determined in the Davis dataset were augmented with data augmentation methods such as cropping, flipping, and rotation.
- Data was tagged in JSON format using the Labelme data labeling tool.
- A train dataset was created with 70% of the tagged data. The test dataset was created with the remaining 30%.
- Mask R-CNN deep neural network was trained for different batch_size and learning rate values using the Detectron2 library developed by Facebook AI to perform Object detection, segmentation, key point detection processes.
- The iterative method for different hyperparameters was tested with test images. Performance was measured using model evaluation metrics.
- Model outputs and evaluation results are given in the experimental results section.

3. Experimental Results

As an alternative to manual analysis of videos recorded in campus areas, deep learning-based video segmentation has been studied. Mask R-CNN deep neural network was trained using 854x480 images found in bus, car, dog, hike, motorbike, tennis classes. The training was repeated for 0.001 lr, 2 batch_size and 0.01 lr, 4 batch_size values. During model training, the change of loss_cls, loss_box_reg and loss_mask values corresponding to epoch values is 0.001 lr, Table 2 for 2 batch_size and 0.01 lr for 4 batch_size, Table 3 and Figure 5 for 4 batch_size.

Table 2. Loss values for Lr = 0.001, Batch_size = 2

Epoch	Batch_size	loss_cls	loss_box_reg	loss_mask
19	2	1.635	0.2189	0.6898
59	2	0.2044	0.2246	0.6175
99	2	0.1621	0.2208	0.4611
139	2	0.1308	0.2168	0.2808
179	2	0.09947	0.2072	0.1941
219	2	0.06678	0.1974	0.1187
259	2	0.04001	0.1766	0.1068
299	2	0.02778	0.129	0.09447
339	2	0.02781	0.104	0.0884
379	2	0.02087	0.08411	0.09325
399	2	0.02452	0.08236	0.09004

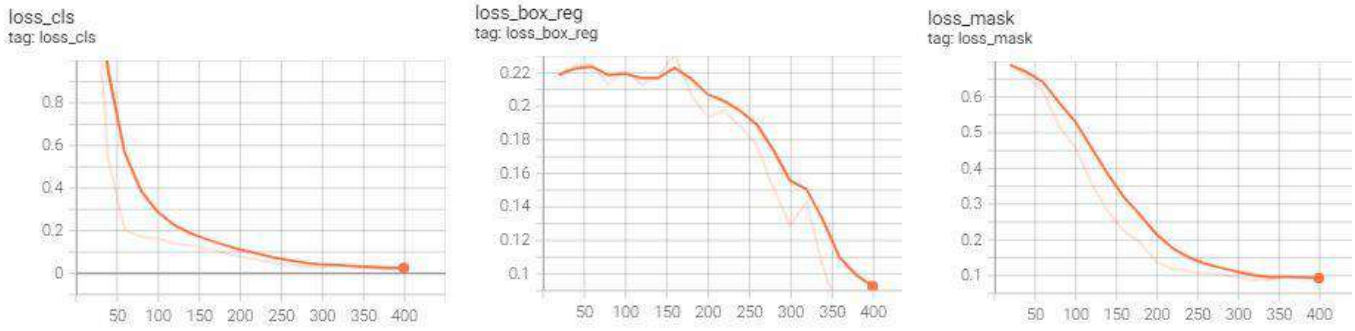

Figure 4. Loss graphs for Lr = 0.001, Batch_size = 2

Table 3. Loss values for Lr = 0.01, Batch_size = 4

Epoch	Batch_size	loss_cls	loss_box_reg	loss_mask
19	4	0.9144	0.2166	0.677
59	4	0.1382	0.2195	0.2149
99	4	0.06339	0.1866	0.1066
139	4	0.02532	0.1168	0.08415
179	4	0.02421	0.09425	0.1
219	4	0.02043	0.05848	0.08774
259	4	0.01838	0.0682	0.08392
299	4	0.01913	0.08032	0.0817
339	4	0.01591	0.05157	0.07931
379	4	0.01869	0.05122	0.08925
399	4	0.01498	0.05293	0.07681

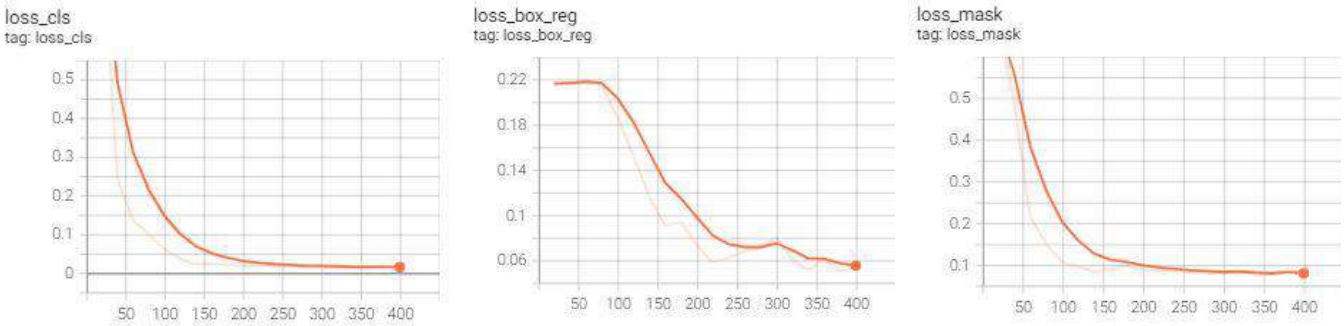

Figure 5. Loss graphs for Lr = 0.01, Batch_size = 4

For Lr = 0.001, Batch_size = 2 : As a result of the training, the total_loss value is 0.2479 and the train accuracy value is 0.9611.
For Lr = 0.01, Batch_size = 4 : As a result of the training, the total_loss value is 0.1879 and the train accuracy value is 0.9673. Total_loss and train accuracy graphs obtained at the end of the training are given in Figure 6.

Lr = 0.001, Batch_size = 2

Lr = 0.01, Batch_size = 4

Figure 6. Total_loss and train accuracy

The output images of the model trained for 6 different classes are given in Figure 7.

Figure 7. Model output images

Performance evaluation was made using the formulas given in Mask R-CNN framework equation (1), (2), (3) and (4), which were trained for different lr and batch_size values. Calculated accuracy, precision, recall and f1-score values are given in Table 4.

$$accuracy = \frac{\sum_{i=1}^{N} TP(C_i)}{\sum_{i=1}^{N}\sum_{j=1}^{N} C_{i,j}} \quad (1)$$

$$precision\ (for\ C_i\ class) = \frac{TP(C_i)}{TP(C_i)+FP(C_i)} \quad (2)$$

$$recall\ (for\ C_i\ class) = \frac{TP(C_i)}{TP(C_i)+FN(C_i)} \quad (3)$$

$$F1-score\ (for\ C_i\ class) = 2 * \frac{precision\ (for\ C_i\ class) * recall\ (for\ C_i\ class)}{precision\ (for\ C_i\ class)+recall\ (for\ C_i\ class)} \quad (4)$$

Table 4. Model Performance Evaluation

	0.001 learning rate, 2 batch_size				0.01 learning rate, 4 batch_size			
	accuracy	precision	recall	f1-score	accuracy	precision	recall	f1-score
Bus		87.9%	96.6%	92.0%		93.5%	96.7%	95.1%
Car_roundabout		87.1%	90.0%	88.5%		90.3%	96.5%	93.3%
Dog	89.0%	84.6%	81.5%	83.0%	91.7%	92.0%	88.5%	90.2%
Hike		87.1%	90.0%	88.5%		90.3%	93.3%	91.8%
Motorbike		88.5%	85.2%	86.8%		92.3%	88.9%	90.6%
Tennis		91.3%	80.7%	85.7%		91.7%	84.6%	88.0%

Video segmentation is carried out for various purposes by using different datasets in different areas. Within the scope of this study, certain classes were used in the DAVIS dataset in order to increase the video segmentation adaptability in smart campus applications. The comparison of dataset method and model performance of this study with other video segmentation studies in the literature is given in Table 5.

Table 5. Literature Comparison

References	Dataset	Method	Evaluation
[10]	RAI dataset	CPU-based face detection methods	F1 Score : 93,2%
[12]	OVIS dataset	CMaskTrack R-CNN	AP : 15.4%
[13]	OVIS dataset	Graph neural network (GNN)	AP : 16.0%
Proposed Method	Davis Dataset (6 classes)	Mask R-CNN	Accuracy : 91.7%

4. Conclusions

Smart campuses are areas that contain many applications and whose infrastructure has been developed with various technologies. It ensures that students, faculty and administrative staff benefit from campus facilities at the highest level and remotely when necessary. One component of smart campuses equipped with various technologies is security systems. Manual examination of the increased video data in campus areas controlled by video cameras takes a lot of time and there may be situations that may create an overlooked security problem. The development of intelligent systems such as deep learning, which has achieved successful results on image data, has made it possible to implement applications such as video segmentation, video summarization, scene detection and suspicious situation detection.

In this study, video segmentation method based on Mask R-CNN Framework is proposed. For the training of the model, bus, car_roundabout, dog, hike, motorbike and tennis classes in the DAVIS dataset were preferred because they are frequently encountered objects in campus areas. In addition, the dataset was enriched by using various data augmentation techniques. The performance of the model trained at different learning rate and batch size values was

measured by calculating accuracy, precision, recall f1-score parameters. As a result of the model trained with 0.001 lr and 2 batch size hyperparameters, 89.0% segmentation accuracy was obtained. With the model trained with 0.01 lr and 4 batch size hyperparameters, it was observed that 91.7% segmentation accuracy was achieved and produced more successful results. In future studies, it is planned to increase the scope, accuracy and adaptability of the method with real-time images to be obtained from campus areas.

5. Acknowledgements

This study was supported by the TUBİTAK (The Scientific and Technological Research Council of Turkey) under Grant No: 5220154.

6. References

[1] Wang H, Wang W, Liu J. "Temporal memory attention for video semantic segmentation". In 2021 IEEE International Conference on Image Processing (ICIP), pp. 2254-2258, IEEE, September, 2021.
[2] Le T N, Nguyen T V, Tran M T. "Contextual Guided Segmentation Framework for Semi-supervised Video Instance Segmentation". Machine Vision and Applications, 33(2), 24, 2022.
[3] Altun G, Zencirkiran M. "Akıllı Kampüs Teknolojileri Ve Uygulamaları Üzerine Bir Araştırma". Mimarlık Ve Yaşam, 6(2), 319-336, 2021.
[4] Brabandere B D, Neven D, Gool L V. "Semantic instance segmentation for autonomous driving". In: CVPR Workshops, 2017.
[5] Lee Y J, Grauman K. "Predicting important objects for egocentric video summarization". IJCV 114(1), 1073, 2015.
[6] Xiong Y, Liao R, Zhao H, Hu R, Bai M, Yumer E, Urtasun R. "Upsnet: A unified panoptic segmentation network". In: CVPR, 2019.
[7] Ji J, Buch S, Soto A, Niebles J C. "End-to-end joint semantic segmentation of actors and actions in video". In: ECCV, 2018.
[8] Wang Q, Zhang L, Bertinetto L, Hu W, Torr P H. "Fast online object tracking and segmentation: a unifying approach". In: CVPR, 2019.
[9] Le T N, Nguyen T V, Tran Q C, Nguyen L, Hoang T H, Le M Q, Tran M T. "Interactive video object mask annotation". In: AAAI, 2021.
[10] Liu H, Fan Z, Chen Q, Zhang X. "Enhancing face detection in video sequences by video segmentation preprocessing". Applied Intelligence, 53(3), 2897-2907, 2023.
[11] Le T N, Nguyen T V, Tran M T. "Contextual Guided Segmentation Framework for Semi-supervised Video Instance Segmentation". Machine Vision and Applications, 33(2), 24, 2022.
[12] Qi J, Gao Y, Hu Y, Wang X, Liu X, Bai X, Bai S. "Occluded video instance segmentation: A benchmark". International Journal of Computer Vision, 130(8), 2022-2039, 2022.
[13] Brissman E, Johnander J, Danelljan M, Felsberg M. "Recurrent Graph Neural Networks for Video Instance Segmentation". International Journal of Computer Vision, 131(2), 471-495, 2023.
[14] Huang P, Han J, Liu N, Ren J, Zhang D. "Scribble-supervised video object segmentation". IEEE/CAA Journal of Automatica Sinica, 9(2), 339-353, 2021.
[15] Sistu G, Chennupati S, Yogamani S. "Multi-stream cnn based video semantic segmentation for automated driving". arXiv preprint arXiv:1901.02511, 2019.
[16] Lin H, Wu R, Liu S, Lu J, Jia J. "Video instance segmentation with a propose-reduce paradigm". In Proceedings of the IEEE/CVF International Conference on Computer Vision, pp. 1739-1748, 2021.
[17] He K, Gkioxari G, Dollár P, Girshick R. "Mask r-cnn". In Proceedings of the IEEE international conference on computer vision, pp. 2961-2969, 2017.
[18] Yilmazer M, Karakose M. "Mask R-CNN architecture based railway fastener fault detection approach". In 2022 International Conference on Decision Aid Sciences and Applications (DASA), pp. 1363-1366, IEEE, March, 2022.

International Conference on Advances and Innovations in Engineering

A New Approach to Reduce False Detections in Deepfake Detection

Serhat ATAS[1] , Mehmet KARAKOSE[2]
[1,2]Computer Engineering Department, Engineering Faculty, University of Fırat (FU), Elazig, Turkey.
[1]serhatats99@gmail.com, [2]mkarakose@gmail.com

Abstract
Today, the great development of artificial intelligence and technology, together with the use of malicious people, has started to cause great concern by causing fake content images, namely deepfakes. In fact, this situation has become increasingly serious and a large technology company in China has started to sell deepfakes. It has become quite difficult to detect such fake content. In this article, a new approach is presented by analyzing the shortcomings and needs of the studies for the detection of deepfake images. The proposed method is to analyze and comprehensively analyze the symptoms in deepfake images together with different neural networks, reducing the inaccuracy of the detections rather than making the detection, Because in this serious situation, if a wrong detection is made on a sample image, it can lead to big problems. In summary, after making a determination on an image with the CNN and RNN neural networks used in the proposed method, the model built on the RNN and the EfficientNetB4 model, the model results used from both neural networks are compared and the image is interpreted according to whether the answers are equal or not.

Keywords: Deepfake Detection, Deep Learning, CNN, RNN

1. Introduction

Although the great development of artificial intelligence affects our lives positively, it poses a big problem when it is used by malicious people. With the use of artificial intelligence by malicious people, deepfake images have become a big problem in our age, and this problem has grown day by day and started to cause concern for the society. However, besides this situation, good software for deepfake detection has also been developed, but this event has become a chase with the development of deepfake and the continuous improvement of detection processes. As we can understand from all this development, a wrong determination on important images and images that will adversely affect the society can lead to major problems. Generally, various improvements have been made to increase the accuracy rate in applications. In this article, the detection methods available today are analyzed in detail and focused on one of the biggest problems, false detection. In this article, the proposed method and this method are conveyed with its innovative aspects and tried to be demonstrated with experimental results.

In the proposed method, using two different neural networks, CNN and RNN, fraud detection is performed separately with the newly created model over EfficientNetB4 and RNN, which is the ready model and trained over CNN, and if the result is the same from both models, the detection result is obtained, but different. When the results are received, the image is marked as unrecognized to avoid major problems. For this purpose, both models keep each other in balance, preventing false detections. The special data set was used as the data set, the images taken from Kaggle were placed in the data set and the private data set was tried to be supported. In the improvement we have made before, we have tried to use different models according to the areas where they are good [1].

Yang et al. Specifically, they tried to detect forgery by utilizing a spatio-temporal attention module to learn the features of multiple face regions [2]. Cozzolino et al. They used a comparative learning paradigm to detect forgery in videos consisting of audio, video and audio-video combinations with the method they developed [3]. Dixit et al. In forgery on voice, they found the literature review scarce and made a literature review and turned it into an article in terms of benefit [4]. Stanciu et al. They aimed to increase deep fake detection datasets by using deep learning

[1]Corresponding author

architectures such as Autoencoders or U-Net [5]. By using Thing et al. CNN and Transformers, fraud detection on Google DFD, Celeb-DF, Deeper Forensics and DFDC datasets, revealed their weaknesses and strengths [6]. Ahmed et al. They outlined how to make detection methods better and more robust by raising a critical discussion about the problems, opportunities and prospects of deepfake technology [7]. Rana et al. By examining 112 related articles presenting various methodologies from 2018 to 2020, they divided them into 4 different groups and produced a systematic literature review, as a result of which they tried to prove by comparison that deep learning-based methods are better [8]. Gu et al. developed a paradigm that performs spatio-temporal inconsistency learning to detect on deep fake videos [9]. Tariq et al. He developed an LSTM-based network and tried to contribute to deep fraud detection using the FaceForensics++ dataset [10]. Kharbat et al. using support vector machines (SVM)They tried to extract the picture features and detect forgery [11]. Khan et al. tried to detect forgery by applying 3D reconstructions on over a hundred [12]. Deng et al. They compared it with the EfficientNet-V2 network by detecting forgery [13].

2. Proposed Approach

The proposed approach is made using CNN (Convolutional Neural Network) and RNN (Recursive Neural Network). In the approach, the Blazeface model was used in the face removal process. EfficientNetB4, one of the models used for fraud detection, is trained over ImageNet, while the RNN-based model is trained using a special data set. In the approach, after face subtraction with Blazeface, the extracted face frame enters the EfficientNetB4 and RNN model, at this stage, two different models are predicted, the results from the two models are compared in order to reduce the false detection rate of the models, and if there are the same results, the prediction is given as output. is marked as unrecognized image to avoid false detection if different results are obtained.

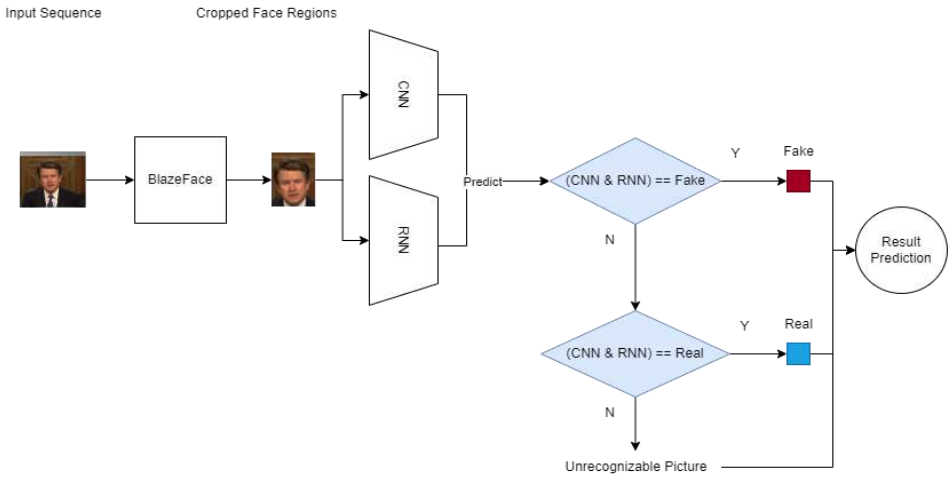

Figure 1. Suggested Approach Block Diagram (The model separation made in the proposed approach and the joint decision taken as a result are given step by step.)

Utilizing two different neural networks and models in the proposed approach provided a safer prediction inference in fraud detection. This approach has emerged to eliminate inferences that are based on a single architecture and a single model, which can cause major problems when incorrectly detected. In addition to these, great improvements have been made in fraud detection by using the special data set and the RNN-based model created within this approach. There are 10000 images in total, 5000 fake and 5000 real, in the special data set, 80% of these images are used as training data and 20% are used as test data (8000 training, 2000 tests).

A. Model Training

For the created RNN-based model training, training was provided with 8000 images by using the train file in the special data set.

B. Face Removal Process

By using the BlazeFace model while performing the face extraction process, the cropped face frame extraction was provided from the image entered as an example. BlazeFace is a very fast and effective model produced by Google. Kolosov et al. used the blazeface model to extract relevant areas from the video and showed that it is a good approach in this area [14].

C. Fraud Detection with CNN and RNN

In the proposed approach, the extracted face frame enters the CNN's previously trained EfficientNetB4 model and outputs a prediction. The basic network structure of the EfficientNet family is given in Figure 2 below [15].

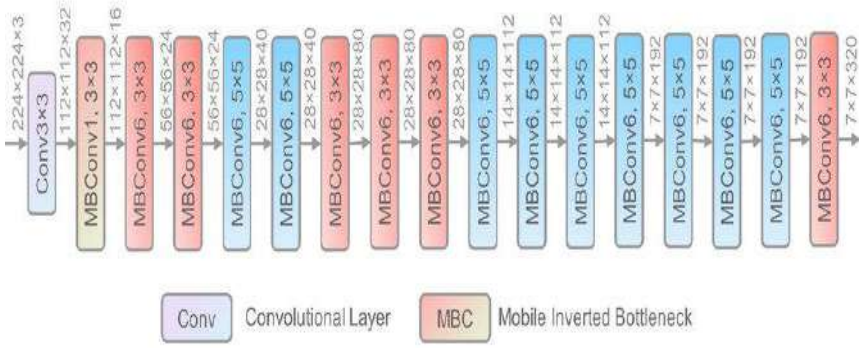

Figure 2. EffficientNet Basic Network Structure

The same face frame is entered into the RNN-based and trained model from the special data set, and a prediction output is obtained from here. The model structure is given in Figure 3 below.

```
Layer (type)                 Output Shape              Param #
=================================================================
time_distributed_57 (TimeDi  (None, 1, 62, 62, 32)     896
stributed)

time_distributed_58 (TimeDi  (None, 1, 31, 31, 32)     0
stributed)

time_distributed_59 (TimeDi  (None, 1, 30752)          0
stributed)

lstm_19 (LSTM)               (None, 64)                7889152

dense_38 (Dense)             (None, 64)                4160

dropout_19 (Dropout)         (None, 64)                0

dense_39 (Dense)             (None, 1)                 65

=================================================================
Total params: 7,894,273
Trainable params: 7,894,273
Non-trainable params: 0
_________________________________________________________________
```

Figure 3. RNN model structure

Then, the estimation results from both models are compared. If the two prediction results are the same, for example, if both of them made a false prediction, the image is faked, and if they both make a true prediction, the image is output as real, but if one of the models is false, the image is marked as an unrecognized picture in order to reduce the false rate and avoid false detection. The improvement is made exactly here, reducing the rate of false detection.

3. Experimental Results

The experimental results obtained were obtained by working on Google Colaboratory. The special data set used in the study, including images taken from Kaggle, consists of 10000 images. Of these images, 5000 are reserved, and 5000 are real. The images in the data set are 5KB-25KB in size and 256*256 in size. 80% of the total data set, ie

8000, was used as training data and 20%, ie 2000, was used as test data. The details of the data set are given in Table 1 and Table 2 below.

Table 1. Train data set

Train Data Set	Number of Image
fake	2500
Real	2500
Total Images	**5000**

Table 2. Test data set

Test Data Set	Number of Image
fake	2500
Real	2500
Total Images	**5000**

The model is trained with the train data set given in the table above. The graph of loss and accuracy rates obtained as a result of model training is given in Figure 4 below.

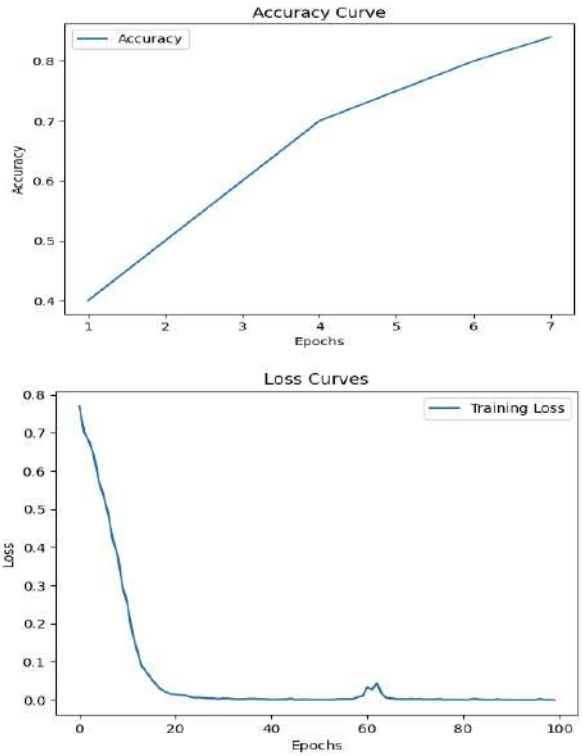

Figure 4. Loss and accuracy values for Training [1]

After training the RNN model, the test data set mentioned is given as input to the proposed method, allowing the images to enter both the EfficientNetB4 model and the RNN model. As a result, the model performances are given in Table 3 below, both separately and according to the false detection rate that is tried to be reduced, by converting them to numerical values.

Table 3. Model performance

Test Data Set	**Model Performance in Test Images**	**False Detection Rate**
EffectiveNetB4	92.4%	7.6%
RNN Model	84.1%	15.9%
Total Performance	**88.25%**	**5.8%**

In the experimental results obtained in the study, the false detection rates are given in Figure 5 below in clusters.

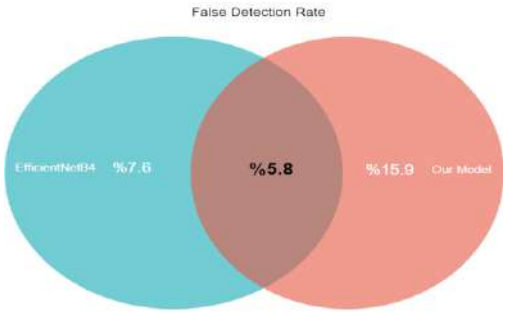

Figure 5. False Detection Rate Intersection Set of Models

In the results of working the results of the estimations obtained according to the data sets are given in Tables 4 and 5 below.

Table 4. Model performance in real images

Test Data Set	Model Performance in Real Images
EffectiveNetB4	89.8%
RNN Model	83.0%
Total Performance	**86.40%**

Table 5. Model performance in fake images

Test Data Set	Model Performance in Fake Images
EffectiveNetB4	95.0%
RNN Model	85.2%
Total Performance	**90.1%**

In addition to all these, the comparison of the proposed method with the studies in the literature is given in Table 6 When we look at the table, both the false detection rate being lower than other studies and the improvement achieved with the method introduced in deep fraud detection come to the fore.

Table 6. Comparison studies

Reference	Technique	Data Set	False Detection Rate
Khalil et al. [16]	LBP-CNN	Private	8.3%
Matern et al. [17]	MLP	CelebA+ProGAN +Glow	16%
Amerini et al. [18]	CNN	Face2Face	VGG16=18.39% ResNet50=24.54%
Nguyen et al. [19]	Capsule Network	FaceForensics++-Face2Face	6.89%
Montserrat et al. [20]	CNN+RNN	DFDC	8.2%
Proposed Method	**CNN+RNN**	**private**	**5.8%**

4. Conclusion

In this article, it has been contributed to the detection of deep fraud by trying to explain how much of a concern deep fraud is today, how false detection rates cause major problems, and how important fraud detection is.

In the method, deep fraud detection using a CNN-based deep learning algorithm is made with EfficientNetB4 model and an RNN-based model, contributing to deep fraud detection from a different perspective. As can be understood from the improvement, if only the EfficientNetB4 model was used, it would cause a 7.6% false detection, on the contrary, if only the RNN model was used, it would have a 15.9% false output. With the improvement provided by the proposed method, the total accuracy rate of the two models was 88.25%, but if we add unrecognized images to

this accuracy rate, the total accuracy rate is 94.2%. The reason for adding to this accuracy rate in unrecognized pictures is that only 5.8% of the images given as input gave an incorrect output, 5%. Since it marked 95 of them as unrecognized pictures, the false detection rate was only 5.8%. In summary, this study achieved its main purpose, not to increase the accuracy rate, but to reduce the false detection rate.

5. Acknowledgements

This study was supported by the TUBITAK (The Scientific and Technological Research Council of Turkey) under Grant No: 122E676.

6. References

[1] ATAS, Serhat; ILHAN, Ismail; KARAKOSE, Mehmet. An Efficient Deepfake Video Detection Approach with Combination of EfficientNet and Xception Models Using Deep Learning. In: 2022 26th International Conference on Information Technology (IT). IEEE, 2022. p. 1-4.

[2] YANG, Ziming, et al. Masked relation learning for deepfake detection. IEEE Transactions on Information Forensics and Security, 2023, 18: 1696-1708.

[3] COZZOLINO, Davide, et al. Audio-visual person-of-interest deepfake detection. In: Proceedings of the IEEE/CVF Conference on Computer Vision and Pattern Recognition. 2023. p. 943-952.

[4] DIXIT, Abhishek; KAUR, Nirmal; KINGRA, Staffy. Review of audio deepfake detection techniques: Issues and prospects. Expert Systems, 2023, e13322.

[5] STANCIU, Dan-Cristian; IONESCU, Bogdan. Autoencoder-based Data Augmentation for Deepfake Detection. In: Proceedings of the 2nd ACM International Workshop on Multimedia AI against Disinformation. 2023. p. 19-27.

[6] THING, Vrizlynn LL. Deepfake Detection with Deep Learning: Convolutional Neural Networks versus Transformers. arXiv preprint arXiv:2304.03698, 2023.

[7] AHMED, Saadaldeen Rashid, et al. Analysis survey on deepfake detection and recognition with convolutional neural networks. In: 2022 International Congress on Human-Computer Interaction, Optimization and Robotic Applications (HORA). IEEE, 2022. p. 1-7.

[8] RANA, Md Shohel, et al. Deepfake detection: A systematic literature review. IEEE Access, 2022.

[9] GU, Zhihao, et al. Spatiotemporal inconsistency learning for deepfake video detection. In: Proceedings of the 29th ACM International Conference on Multimedia. 2021.p. 3473-3481.

[10] TARIQ, Shahroz; LEE, Sangyup; WOO, Simon S. A convolutional lstm based residual network for deepfake video detection. arXiv preprint arXiv:2009.07480, 2020.

[11] KHARBAT, Faten F., et al. Image feature detectors for deepfake video detection. In: 2019 IEEE/ACS 16th International Conference on Computer Systems and Applications (AICCSA). IEEE, 2019. p. 1-4.

[12] KHAN, Sohail Ahmed; DAI, Hang. Video transformer for deepfake detection with incremental learning. In: Proceedings of the 29th ACM International Conference on Multimedia. 2021.p. 1821-1828.

[13] DENG, Liwei; SUO, Hongfei; LI, Dongjie. Deepfake video detection based on EfficientNet-V2 network. Computational Intelligence and Neuroscience, 2022, 2022.

[14] KOLOSOV, Dimitrios, et al. Contactless Camera-Based Heart Rate and Respiratory Rate Monitoring Using AI on Hardware. Sensors, 2023, 23.9: 4550.

[15] XU, Renjie, et al. A forest fire detection system based on ensemble learning. Forests, 2021, 12.2: 217.

[16] KHALIL, Samar Samir; YOUSSEF, Sherin M.; SALEH, Sherine Nagy. iCaps-Dfake: An integrated capsule-based model for deepfake image and video detection. Future Internet, 2021, 13.4: 93.

[17] MATERN, Falko; RIESS, Christian; STAMMINGER, Marc. Exploiting visual artifacts to expose deepfakes and face manipulations. In: 2019 IEEE Winter Applications of Computer Vision Workshops (WACVW). IEEE, 2019. p. 83-92.

[18] AMERINI, Irene, et al. Deepfake video detection through optical flow based cnn. In: Proceedings of the IEEE/CVF international conference on computer vision workshops. 2019.p. 0-0.

[19] Nguyen HH, Yamagishi J, Echizen I. Capsule-forensics: Using capsule networks to detect forged images and videos. InICASSP 2019-2019 IEEE International Conference on Acoustics, Speech and Signal Processing (ICASSP) 2019 May 12 (pp. 2307-2311). IEEE.

[20] Montserrat DM, Hao H, Yarlagadda SK, Baireddy S, Shao R, Horváth J, Bartusiak E, Yang J, Guera D, Zhu F, Delp EJ. Deepfakes detection with automatic face weighting. InProceedings of the IEEE/CVF conference on computer vision and pattern recognition workshops 2020 (pp. 668-669).

International Conference on Advances and Innovations in Engineering

Current Technologies for Bioethanol Production

Aysun Şener GEDÜK[1]
Department of Food Engineering, Adana Alparslan Turkes Science and Technology University, Adana, TURKEY
asener@atu.edu.tr

(ORCID: 0000-0001-5306-6722)

Abstract
A large part of nature and energy is obtained from fossil fuels such as oil, coal and natural gas. However, the amount of fossil fuels is gradually decreasing due to the increasing energy consumption in parallel with world consumption and benefits. Fossil fuels are a major contributor to climate change, and as the demand for energy production increases, alternative sources (e.g., renewables) are becoming more attractive. Biofuels such as bioethanol reduce reliance on fossil fuels and can be compatible with the existing fleet of internal combustion engines. Production of biofuels from renewable feedstocks has captured considerable scientific attention since they could be used to supply energy and alternative fuels. Bioethanol is one of the most interesting biofuels due to its positive impact on the environment. Currently, it is mostly produced from sugar and starch containing raw materials. However, various available types of lignocellulosic biomass such as agricultural and forestry residues, and herbaceous energy crops could serve as feedstocks for the production of bioethanol, energy, heat and value-added chemicals. Lignocellulosic biomass is inexpensive, renewable and abundant source for bioethanol production. Bioethanol production includes pretreatment, hydrolysis and fermentation processes.

Keywords: Bioethanol, lignocellulose, pretreatment, hydrolysis, fermentation

1. Introduction

The increasing need for energy has led all the countries of the world to seek a clean, renewable and sustainable energy source. There are many reasons for using biomass resources as an energy source. These are that biomass is renewable and it is an environmentally friendly raw material compared to petroleum products when it comes to the emissions it creates. Biomass is the most important carbon-containing raw material obtained from sources such as plants, animals and microorganisms [1]. Biomass is obtained from forest wastes, agricultural wastes (corn, rice, etc.), energy crops (branched millet, etc.), cellulosic wastes (household solid waste, kitchen waste, etc.). Various fuels that can be obtained using biomass energy are bioethanol, biodiesel, biogas and biohydrogen [2]. Biofuels, especially biodiesel and bioethanol, are renewable primary energy sources. Biofuel use and production are important for the solution of the global energy crisis. In its decision taken in 2008, the EU commission brought the requirement that the fuel used in transportation in the member countries should be supported by 10% biofuel until 2020 [3]. Making the use of biodiesel and bioethanol mandatory in the EU, as well as in our country due to the EU harmonization process, will increase the demand for biofuels. A new communiqué dated 27 September 2011 and numbered 28067 was published by amending the "Technical Regulation on Gasoline Types" published in the Official Gazette dated 7/8/2009 and numbered 27312. According to this communiqué, bioethanol produced from domestic agricultural products must be added at least 2% as of January 1, 2013, and 3% as of January 1, 2014 [4].

1.1. Bioethanol

Bioethanol is a clear, colorless liquid with a characteristic odor and can be used in internal combustion engines by blending it in 10% without the need for any modification. The two most common uses of bioethanol are E-10 (10% Bioethanol + 90% Gasoline) and E-85 (85% Bioethanol + 15% Gasoline) (EIE 2017a). For this reason, it is important to carry out studies to increase bioethanol production in our country. It is very important to find cheap and abundant raw materials in biofuel production. Bioethanol, from simple sugars (sugar beet, cane sugar) molasses, etc.), and starchy foods (corn, potato, etc.) and cellulose by fermentation [5]. In the world, approximately 50% of ethanol

[1]Corresponding author

production is produced using sugar beet and sugar cane, while the remaining 50% is produced using cereals (corn, wheat). Corn is the most used plant for ethanol production in the United States, but sugar cane and sugar beet are mostly used in other ethanol producing countries. There are three companies in our country that produce anhydrous bioethanol that can be used as fuel in vehicles. These are Agricultural Chemistry Technologies (TARKİM) and Tezkim Tarımsal Kimya (TEZKİM) produce bioethanol from wheat and corn, and Konya Şeker-Çumra Factory produces bioethanol from sugar beet. These three companies produce an average of 162 million liters of bioethanol per year. 76 million liters of this is fuel bioethanol. 92% of the produced fuel bioethanol is blended with gasoline domestically and the remaining 8% is exported. In large-scale bioethanol production, ethanol production from sugar and starch-containing substances is undesirable because these substances are nutrients [6]. Lignocellulosic biomass basically consists of cellulose, hemicellulose and lignin linked together in a complex structure. Cellulose has an important place in biomass in terms of carbon content. Cellulose contains D-glucose subunits linked by β-1,4 glycosidic bonds. This special and complicated structure causes celluloses to be resistant to biological and chemical treatment. Unlike cellulose, hemicellulose is a heteropolymer structure consisting of 5-carbon sugars such as xylose and arabinose and 6-carbon sugars such as galactose and mannose. Lignin is composed of three different phenolic acids (p-coumaryl). alcohol, coniferyl alcohol and synapyl alcohol) has a complex structure. It is connected by a three-dimensional structure that is hardly biodegradable. Lignin can be degraded both chemically and enzymatically [7].

Most of the lignocellulosic biomass is discarded or incinerated. But lignocellulosic biomass is not a waste and can be converted into valuable products. These are biodiesel, bioethanol, biogas, pyrolytic gas, hydrogen (EIE 2017b). Due to the lignin in the structure of lignocellulosic biomass, sufficient efficiency cannot be obtained in the production of bioethanol. In order to increase the yield, the biomass must be subjected to some preliminary treatment. The pretreatment processes used in the degradation of lignocellulosic wastes change the micro and macro structure and chemical composition of lignocellulose. This process breaks the lignin and hemicellulose structure. Removes lignin. It degrades hemicellulose. It changes the crystal structure of cellulose. Cellulose remains free. Enzyme and substrate accelerate sugar hydrolysis. In addition, the applied pretreatment processes should not cause reducing sugar loss, should not create by-products harmful to microorganisms and enzymes during the fermentation process, and should be a cheap and applicable method [8]

2. Pretreatment Procedures

Pretreatment processes increase the surface area that the wastes can react with and disrupt the crystalline structure of cellulose. The main purpose of these processes is to increase the conversion efficiency of agricultural waste into products such as bioethanol or biogas. These transactions are; includes physical, chemical, physicochemical and biological methods [9].

2.1. Physical Preparation Procedures

2.1.1. Mechanical grinding

By splitting the biomass into smaller pieces, the surface area is increased. Thus, it is ensured that the next methods are used more easily and effectively. It includes dry grinding, wet grinding, vibratory ball mill and compaction methods. Lignin and hemicellulose cannot be removed by this process. In a study, enzymatic hydrolysis of rice straw was investigated after grinding with ball and wet disc. The conversion efficiencies of glucose and xylose were 78.5% and 41.5%, respectively, after ball mill-enzymatic hydrolysis, wet disc mill-enzymatic hydrolysis, respectively. After that, they stated that it was 89.4% and 54.3%, respectively [10].

2.1.2. Microwave preparation procedures

Microwaves are non-ionizing electromagnetic waves with a wavelength of 1 mm-1 m and a frequency range of 300 MHz to 300 GHz, covering a certain part of the electromagnetic spectrum. In conventional thermal processes, energy is transferred to the material by convection, conduction and radiation. In contrast, microwave energy transfers energy directly to the material through molecular interaction with electromagnetic waves. Therefore, the heating rate is high

and the processing time is short . It increases the enzyme activity by increasing the surface area of the lignocellulosic material [11].

2.1.3 Ultrasonic pretreatment

Ultrasound is described as sound waves propagating at high frequencies that cannot be perceived by the human ear . When ultrasonic pretreatment is applied, bubble formation occurs in the liquid. After the bubbles formed reach a certain size, they deflate and heat generation takes place. Thus, solid objects and bacteria are broken down. At the same time, oxidation in the biomass structure, deterioration of composition, and molecular chains are fragmented [12].

2.1.4 Pretreatment with high-energy electron radiation

It is the transfer of an energy greater than the ionization energy of the atom or molecule to the atom or molecule. For this purpose, the most commonly used radiation sources as high energy sources are 60 °C, 137 Cs, electron beams, and X-rays. The photon emanating from the radiation source first interacts with the solvent in the environment and releases millions of dissolved electrons. These dissolved electrons that are released change the chemical and physicochemical properties of the substance as a result of their interaction with the substance. Depending on the intensity of irradiation, large molecules are broken down and converted to molecules, ions or radicals with smaller molecular weights [13].

2. 2. Chemical Preparation Processes

2.2.1. Pretreatment with acid

Acidic pretreatment processes are carried out using inorganic acids (sulfuric, nitric, hydrochloric and phosphoric acids) and organic acids (formic, acetic and propionic acids). Acidic pretreatment processes can be divided into dilute and concentrated acid methods. The concentrated acid method is to use an acid concentration above 30%. It is used with low temperature. Since concentrated acids are toxic and corrosive, the equipment to be used must be resistant to corrosion. In addition, acids must be recovered. In dilute acid treatment, the acid concentration is below 10%. It is applied with high temperature. Acid recovery is not required. It is a suitable process for continuous production. The use of inorganic acids such as H2SO4 and HCl is more common [14].

2.2.2. Pretreatment with alkali

NaOH, KOH, Ca(OH)2 and NH4OH are generally used in the preliminary treatment of lignocellulosic wastes using alkali. Thanks to the preliminary preparation processes, the lignin structure is deteriorated and the porosity of the raw material increases. Thus, the surface area that enzymes can reach is expanded. The raw material becomes more suitable for the next step, enzyme hydrolysis. In alkaline pretreatment processes using NaOH, it has been reported that the saccharification efficiency increases at low temperature and long residence time [15].

2.2.3 Pretreatment with oxidant

Combined advanced oxidation processes such as O3, O3/H2O2, VUV, H2O2/UV, O3/UV, O3/H2O2/UV, Fenton, photo-Fenton, sonochemical oxidation (Ultrasound/H2O2, Ultrasound/O3 etc.), photocatalysis process It is stated that there are processes that produce radicals with high capacity. It is based on the principle of generating hydroxyl radicals (OH) for the oxidative breakdown of organics [16].

2.2.4.Pre-treatment with organic solvent

It is a process for the degradation of lignin and hemicellulose structure, in which organic solvents (methanol, ethanol, acetone, ethylene glycol, ethylene glycol) are used under inorganic acid catalysis (H2SO4 or HCl). With the applied pretreatments, lignin and hemicellulose bonds are broken and pure and high quality lignin is obtained. The α-aryl ether and arylglycerol-β-aryl ether (β –O-4) bonds in the lignin macromolecule are broken, thus reducing the lignin

content in the cell wall. The disadvantages of the system are that the organic solutions are expensive and the reaction time is long [17].

2.3. Physicochemical Preparation Processes

2.3.1. Steam explosion

It is one of the most widely used pretreatment processes. The biomass is blasted with high pressure steam. By suddenly reducing the pressure, the lignocellulosic structure is broken down and hydrolysis of the hemicellulose structure is facilitated. The purpose of this process is to release hemicellulose and monomeric sugars present in cellulose. Steam blasting method as a preliminary treatment of lignocellulosic biomass, enzymatic hydrolysis without the use of chemicals. It is an environmentally friendly method because it increases its effectiveness [18].

2.3.2. Ammonia application (AFEX)

It is the process of treating the raw material with an aqueous ammonia solution at high pressure and temperature. Ammonia is one of the effective reagents because it preserves plant carbohydrates and increases enzymatic degradation. In order to ensure the economy of the method, ammonia must be recovered. It is a simple method and the processing time is short. With this process, cellulose and lignin can be removed. No production of fermentation-inhibiting substances. The AFEX method was used to obtain fermentable sugar from corn straw and the efficiency of the process was investigated. The AFEX process was performed both alone and using hydrogen peroxide (H-AFEX) and the results were evaluated. It has been stated that AFEX and H-AFEX processes improve enzymatic hydrolysis efficiency by breaking down the complex structure [19].

2.3.3. CO2 application

It is the process of treating with carbon dioxide at high pressure. Under high pressure (critical pressure 73 atm), carbon dioxide is kept in its supercritical state. When the carbon dioxide pressure is rapidly removed, the biomass explodes and the surface area of the biomass increases. Thus, the accessibility of cellulose in biomass becomes easier. No inhibition compounds are produced, which affect the subsequent hydrolysis and fermentation steps. Increases enzyme activity by expanding the surface areas of substrates [20].

3. Hydrolysis

The next step after the pre-treatment process is hydrolysis. Hydrolysis means the breakdown of a molecule by adding water and can be expressed by the following formulas; $(C6H10O5)n + nH2O \rightarrow n\ C6H12O6$ and $C6H12O6 \rightarrow 2CH3CH2OH + 2CO2$. Before fermentation, carbohydrate polymers in lignocellulosic material must be converted into simple sugars by a process called hydrolysis. There are several possible processes for the hydrolysis of lignocellulose. We can divide these hydrolysis methods into chemical hydrolysis and biological hydrolysis. At the end of the reaction, lignin remains as a by-product, while cellulose and hemicellulose can be converted into bioethanol by hydrolysis and fermentation processes. In addition to the above two hydrolysis methods, there are other hydrolysis methods such as gamma or electron irradiation and microwave irradiation. However, these processes have no commercial application. Complete hydrolysis of cellulose results in glucose, while hydrolysis of hemicellulose yields pentose and hexose sugars obtained. Hemicelluloses in softwood materials mainly contain mannose, while in hardwoods the predominant component is xylose [21].

3.1. Chemical hydrolysis

The degradation of cellulose by acids usually takes place in two stages, depending on the concentration. In the first stage, acids break down and remove the amorphous regions that they can easily reach. The cellulose whose amorphous region is removed is called hydrocellulose. Therefore, the degree of crystallinity of the cellulose remaining intact increases. As a result of using concentrated acids and prolonging the reaction time, cellulose can be converted to glucose, which is its monomeric building block. The acid hydrolysis method is divided into two: hydrolysis with concentrated acid and hydrolysis with dilute acid. Generally, for the hydrolysis process, the

hydrolysis method with dilute acid is used. This method is usually carried out either as a step to support fermentation or directly to obtain sugars from lignocellulosic material. Hydrolysis with acids is a batch process. A two-step method is generally preferred to avoid the formation of undesirable by-products. Accordingly, while mild conditions are applied in the first step, severe conditions are applied in the second step. In the first step, maximum product is obtained from hemicellulose at low temperature, while in the second step, more cellulose is hydrolyzed.

The parameters affecting the acid hydrolysis of lignocellulosic material are the properties of the substrate used, the acidity of the system and the rate of decomposition of the products during hydrolysis. The properties of the substrate used; neutralization capacity, easy hydrolysis of cellulose and hemicellulose, proportion of difficult-to-hydrolyzable materials, length of macromolecules, degree of polymerization of cellulose, configuration of cellulose chains and other protective polymeric structures of cellulose in the plant cell wall such as lignin, pectin, hemicellulose, proteins, minerals, elements determines the relationship. The acidity of the system is the concentration of acid used, the amount of acid solution, the amount of acid released from the biomass during hydrolysis, the neutralization capacity of lignocellulose, the liquid-solid ratio, and the solubility of the solution during heating depends on the movement. The rate of degradation of the products during hydrolysis depends on temperature, acidity, reaction time and sugar concentration [22].

3.2. Enzymatic hydrolysis

Lignocellulose is degraded in nature by bacteria and fungi. Cellulase, xylanase, peroxidase and laccases mainly play a role in the degradation of lignocellulose, while accessory enzymes such as β-xylosidase, α-L-arabinofuranosidase, α-Dglucuronosidase, acetyl xylan esterase and hydroxycinnamyl acid esterase play a role. Enzymes are commercially available from companies such as Novazyme, Zytex India Private Limited, although they are used to isolate from microorganisms or as enzyme cocktails [23].

4. Fermentation

Technologies for fermentation of monomeric sugar units into ethanol include separate hydrolysis and fermentation, simultaneous saccharification and fermentation (SSF), simultaneous saccharification and co-fermentation (SSCF). It is also used in non-isothermal simultaneous saccharification and fermentation, simultaneous saccharification, filtration and fermentation, consolidated bioprocessing. Other types of fermentation include batch, batch feed, continuous and solid state fermentation, while some of these fermentation methods are as follows:

4.1. Continuous fermentation process

This process involves adding substrates, culture medium, nutrients to a fermenter containing active microorganisms and continuous withdrawal of products. The resulting products are usually ethanol, cells and residual sugar. The advantages of the continuous fermentation process are high productivity, small fermenter volumes, low investment and operating cost. Disadvantages include potential reduction in yeast capacity to support ethanol production due to the possibility of crop contamination and long cultivation time [24].

4.2. Fed-batch fermentation process

This is a combination of batch and continuous fermentation processes that involve loading the substrate into the fermenter without removing the medium. Compared with other fermentation processes, the batch feed process has higher productivity, more dissolved oxygen in the medium, shorter fermentation time and lower toxic effect of the medium. The disadvantage is that ethanol productivity is limited by cell mass concentration and feed rate [25].

4.3.Separate hydrolysis and fermentation (SHF)

Enzymatic hydrolysis differs from fermentation by allowing the enzymes to operate at high temperature and the fermenting microorganisms to operate at medium temperature for optimum performance. Since hydrolytic enzymes and fermentation organisms work under optimum conditions, ethanol yield is expected to be high. The disadvantages

of SHF are the high capital cost, high reaction time requirement, especially since two reactors are required, and the possibility of limiting cellulase activities by the sugars released during the hydrolysis step [26].

4.4.Simultaneous saccharification and fermentation (SSF)

Here, saccharification of cellulose and fermentation of monomeric sugars are carried out simultaneously in the same reactor. Since the hydrolyzate is used for simultaneous fermentation, the usual inhibition of cellulase activities can be avoided. The disadvantage of SSF is the change in optimum temperature required for efficient performance of cellulase and microorganisms during hydrolysis and fermentation, respectively. The high temperature required by cellulase for hydrolysis can reduce microorganisms such as yeast used for fermentation [27].

4.5.Simultaneous condensation and co-fermentation (SSCF)

This involves hydrolysis and saccharification being carried out in the same unit with the co-fermentation of pentose sugars. Generally, genetically modified *Saccharomyces cerevisiae* strains capable of fermenting xylose have been used since normal. *Saccharomyces cerevisiae* cannot ferment pentose sugar. Like SSF, SSCF has the advantages of lower cost, higher ethanol yield, and shorter processing time. In addition, SSCF helps to minimize the inhibition caused by sugars during the enzymatic hydrolytic process and increases the glucose concentration ratio of xylose as most of the microorganisms consume xylose [28].

4.6.Consolidated biological processing (CBP)

For this, enzyme production, hydrolysis and fermentation must take place in a single unit. The most commonly used microorganism in this process, *Clostridium thermosellum*, is capable of synthesizing cellulase, which reduces lignocellulose to monomeric sugars and produces ethanol. Although CBP is still in its infancy, advantages such as less energy intensive, cheaper enzyme cost, lower investment cost and less contamination possibility have been identified [29].

5. Conclusion

Due to reasons such as increasing oil demand and prices, research on sustainable life, decrease in oil reserves, foreign dependency, governments in many countries are turning to renewable energy sources instead of using fossil fuels. The geographical and economic conditions of a country generally affect which renewable resources such as hydropower, geothermal energy, wind energy and biomass energy are preferred. Considering the geographical conditions, forest lands, cultivated lands and lignocellulosic waste potential of our country, biomass-based bioethanol can be considered as an alternative to petroleum. Therefore, the right choice of the raw material source and accordingly the appropriate pretreatment, hydrolysis and fermentation processes can reduce the cost of bioethanol production and increase product productivity.

Considering all these, the use of biomass-based bioethanol in our country as an alternative to oil or by mixing it with oil at a higher rate will reduce our country's dependence on foreign sources, make better use of organic wastes and agricultural lands, reduce people's access to energy, and provide employment with a different job field of agricultural origin will be provided.

6. References

[1] Parisutham V, Kim TH, Lee SK. " Feasibilities of consolidated bioprocessing microbes: from pretreatment to biofuel production" Bioresource Technology, 161, 431–440, 2014.

[2] Demirbaş A. "Progress and recent trends in biofuels" Progress in Energy and Combustion Science", 33, 1-18, 2007.

[3] Pieragostini C, Aguirre P, Mussati MC. "Life cycle assessment of corn-based ethanol production in Argentina", Science of the Total Environment, 472, 212–225, 2014.

[4] European Commission. “Proposal for a Directive of the European Parliament and of the Council on the promotion of the use of energy from renewable sources”, Procedure, 2008/0016/COD, COM 19 final, 2008
[5] Onsoy T, Thanonkeo P, Thanonkeo S, Yamada M. “Ethanol production from Jerusalem artichoke by Zymomonas Mobilis in batch fermentation”, KMITL Science Technology Journal, 7-S1, 55-60, 2007.
[6] Huber GW., Iborra S, Corma A. “Synthesis of transportation fuels from biomass: chemistry, catalysts, and engineering”, Chemical Reviews, 106, 4044-4098, 2006.
[7] Hansdah D, Murugan S. “Bioethanol fumigation in a DI diesel engine”, Fuel, 130, 324-333, 2014.
[8] Eggleston G, Tew T, Panella L, Klasson T. “Ethanol from sugar crops”, In: Industrial Crops and Uses, CABI, Chippenham, UK, 60–83, 2010.
[9] Nakagame S, Chandra RP, Sadller JN. “The influence of lignin on the enzymatic hydrolysis of pretreated biomass substrate”, Sustainable Production of Fuels, Chemicals, and Fibers from Forest Biomass, ACS Symposium Series, 1067, 145–167, 2011.
[10] Thangavelu AK, Ahmed AS, Ani FN. “Bioethanol production from sago pith waste using microwave hydrothermal hydrolysis accelerated by carbon dioxide”, Applied Energy, 128, 277–283, 2014.
[11] Mori T, Tsuboi Y, Ishida N, Nishikubo N, Demura T, Kikuchi J. “Multidimensional high-resolutionmagic angle spinning and solution-state NMR characterization of 13C-labeled plant metabolites and lignocellulose”, Scientific Reports, 5, 1–12, 2015.
[12] Chiesa S, Gnansounou E. “Use of empty fruit bunches from the oil palm for bioethanol production: A thorough comparison between dilute acid and dilute alkali pretreatment”, Bioresource Technology, 159, 355-364, 2014.
[13] Kristiani A, Abimanyu H, Setiawan AHA, Sudiyarmanto FA. “Effect of pretreatment process by using diluted acid to characteristic of oil palm’s frond”, Energy Procedia, 32, 183 – 189, 2013.
[14] Michalska K, Miazek K, Krzystek L, Ledakowicz S. “Influence of pretreatment with Fenton's reagent on biogas production and methane yield from lignocellulosic biomass”, Bioresource Technology, 119, 72–78, 2012.
[15] Alvira P, Tomás-Pejó E, Ballesteros M, Negro M. “Pretreatment technologies for an efficient bioethanol production process based on enzymatic hydrolysis: a review”, Bioresource Technology, 101, 4851–4861, 2010.
[16] Keller FA, Hamilton JE, Nguyen QA. “Microbial pretreatment of biomass: potential for reducing severity of thermochemical biomass pretreatment”, Applied Biochemistry Biotechnology, 27-41, 105-108, 2003.
[17] Mood SH, Golfeshan AH, Tabatabaei M, Jouzani GS, Najafi GH, Gholami M, Ardjmand M. “Lignocellulosic biomass to bioethanol, a comprehensive review with a focus on pretreatment”, Renewable and Sustainable Energy Reviews, 27, 77-93, 2013.
[18] Moretti MM, Bocchini-Martins DA, Nunes C, Villena MA, Perrone OM, Silva R, Boscolo M. Gomes E. “Pretreatment of sugarcane bagasse with microwaves irradiation and its effects on the structure and on enzymatic hydrolysis”, Applied Energy, 122, 189–195, 2014.
[19] Sun Y, Cheng J. “Hydrolysis of lignocellulosic materials for ethanol production: a review, Bioresource Technology”, 83, 1–11, 2002.
[20] Aita GA, Salvi DA, Walker MS. “Enzyme hydrolysis and ethanol fermentation of dilute ammonia pretreated energy cane”, Bioresource Technology, 102(6), 4444-4448, 2011.
[21] Karimia K, Kheradmandiniaa S, Taherzadeh MJ. “Conversion of rice straw to sugars by dilute-acid hydrolysis”, Biomass Bioenerg., 30, 247-253, 2006.
[22] Taherzadeh MJ, Eklund R, Gustafsson L, Niklasson C, Liden G. “Characterization and fermentation of dilute acid hydrolyzates from wood”, Ind. Eng. Chem. Res., 36(11), 4659-4665,
1997.
[23] Dashtban M, Maki M, Leung KT. “Cellulase Activities in Biomass Conversion: Measurement Methods and Comparison”, Crit. Rev. Biotechnol., 1-8, 2010.
[24] Balat M, Balat H, Öz, C. “Progress in Bioethanol Processing”, Prog. Energ. Combust., 34: 551-573, 2008.
[25] Horn GM. “Biofuels. Energy Todays”, Chelsea Club House, 48s. New York, 2010.
[26] Menegol D, Fontana RC, Dillo AJP, Camassola M. “Second generation ethanol production from elephant grass at high total solids”, Bioresource Technology, 211, 280–290, 2016.
[27] Chen H, Liu J, Chang X, Chen D, Xue Y, Liu P, Lin H, Han S. “A review on the pretreatment of lignocellulose for high-value chemicals”, Fuel Processing Technology, 160, 196–206, 2017.

[28] Banik S, Bandyopadhyay S, Ganguly S. “Bioeffects of microwave-a brief review”, Bioresource Technology, 87, 155-159, 2003.
[29] Hongzhang C, Liying L, “Unpolluted fractionation of wheat straw by steamexplosion and ethanol extraction”, Bioresource Technology, 98, 666–676, 2007.
[30] Kuhar S, Nair LM, Kuhad RC. “Pretreatment of lignocellulosic material with fungi capable of higher lignin degradation and lower carbohydrate degradation improves substrate acid hydrolysis and the eventual conversion to ethanol”, Canadian Journal of Microbiology, 54(4), 305–313, 2008.

International Conference on Advances and Innovations in Engineering

The Main Pivot For Resilient City Versus Disaster: Geographic Knowledge

Emine AKMAN[1], İlhan Oğuz AKDEMİR[2]

[1,2] Department of Geography, Faculty of humanities and social sciences, Fırat University, Elazığ, Türkiye
[1] e.akman47@outlook.com [2] ioakdemir@firat.edu.tr

[1](ORCID: 0000-0001-8040-5769) [2](ORCID: 0000-0002-3767-3984)

Abstract
In urbanization and urban planning; Failure to approach the concept of "land use and planning in harmony with the ground" throughout the last 100 years is unfortunately the main reason for many technical, administrative, financial and even socio-cultural problems and painful disasters that have been and are being experienced in settlements. Resilient cities, which are described as a sustainable backbone formed by physical systems and social structure, are of great importance for the common benefit of the city and society. Cities dealing with dynamic population changes, decrease in energy resources, disasters and crises carry the heavy burden of change on their shoulders.
The task of reducing all these problems and minimizing their effects places the responsibility on urban resilience. Urban resilience is not only about measures to increase the durability of the building stock in the city, but also about how to design urban spaces and the organization of functions in space. For this reason, the necessity of "geographic information" that will help urban resilience in order to prevent possible risks and to recognize problems in advance and take precautions becomes prominent once again. Cities with high fragility emerge as a result of the "risky urban texture" built on natural problems of geological, topographic, morphological, hydrographic and meteorological origin in the urban fabric. Therefore, one of the most realistic and basic ways to understand the typology and morphology of the city is to have geographical knowledge. Today's sociology and architectural knowledge understand the effect of spatial coordinates on human identity and interpret social movements through this understanding. In urban planning, creating land use that is risk-free and provides maximum benefit is only possible by analyzing the geographical space and geographical criteria and forming a decisive basis in the decision process. Today, it is understood that geographical information is necessary in effective decision-making and planning in many different fields and institutions. Making cities resilient with pre-disaster risk reduction measures and emphasizing the necessity of geographical information to ensure the safety of the city and society are among the main objectives of this study.

Key Words: Geography, Geographic Information, Disasters, City, Urban Resilience

1. Introductıon

Today, most of the world's population lives in cities. Cities are the center of both economic growth and social life. However, this dense urban lifestyle leads them to face various crises such as natural disasters, climate change, economic crises and other emergencies. At this point, the concept of urban resilience gains great importance. Urban resilience refers to the ability of cities to withstand such crises. However, urban resilience is not limited to the physical resilience of buildings and infrastructure. Urban resilience also involves the design, organization and management of urban spaces. This is where geographic information comes into play. By adopting a lifestyle that is in harmony with the natural environment in which they live, people try to change and transform the physical environment in which they live to a large extent for their own benefit. Today, however, due to the dominance of human dominance, we are in a fragile structure where the physical environment is exposed to negative impacts and urban systems are subjected to unexpected destructive changes, triggering complexity and uncertainties. Today, due to inadequacies in urban planning processes and practices, cities have to struggle with many different problems such as social justice, spatial segregation due to the socio-economic structure of the population, inequitable distribution of resources and services, unemployment, urban sprawl, environmental pollution and resource depletion. "Settlement areas" or "human

[1] Corresponding author

settlements" are the places where "human beings and society and the living environment are shaped and sustained" in the concept of "environment", which is defined as all the physical, social and cultural conditions that affect the existence and development of a whole organism and the environments in which they are sheltered. These places are a three-elemented whole consisting of an "artificial environment" in which all technical initiatives are shaped to meet all kinds of needs of human and society, that is, the human environment, which constitutes the target element, and a piece of nature surrounding it, that is, the "natural environment" [17]. It is important that these three elements, the natural environment, the artificial environment and the human environment, are compatible within themselves and can be adapted to changing conditions over time. However, human beings try to create an artificial environment independent of the natural environment without planning, projecting and geographical information.

Today, all cities and their inhabitants face a series of natural and/or man-made shocks and stresses such as earthquakes, floods, famine, drought, rapid migration, cyber-attacks, epidemics, due to rapid urbanization, changing climate and political instability. In almost every region of the world, man-made and shaped cities have become systems that are directly affected by disasters, while triggering disaster risks that we have faced throughout history and which have taken a more dangerous dimension today. In this rapidly changing and more complex world order, where future predictions become more difficult, individuals, institutions, societies and cities are expected to be able to cope with, adapt to and even direct the changes and transformations as well as natural and unnatural disasters. In this context, it is vital for all cities to analyze physical, social, economic and institutional systems well and to maintain "continuous development and adaptation in the face of changing conditions". In other words, in a rapidly changing and increasingly complex world, individuals, institutions and societies need to be able to cope with, adapt to and shape change. This approach overlaps with the concept of "resilience", which seeks to explain how to cope with the changes and challenges of an uncertain world.

It can be said that the technical application of the concept of resilience to the urban area started with ecological approaches. In the urban area, resilience is mainly evaluated in the context of urban planning approach in the context of climate change and disaster risks in connection with sustainability. It is aimed to create urban resilience by planning cities before and after they encounter environmental disasters. When the concept of resilience is associated with urban goals such as sustainability, economic development and governance, the importance of creating a resilient city in urban planning will be more clearly understood in terms of the ability of the urban system to transfer information and resources [8]. In this study, the necessity of "geographical information" in creating urban resilience and the necessity of geography for the city and urban resilience with the science of geography becoming an applied science will be emphasized. Applied geography is important in terms of showing the ways of utilizing the natural and social structure of the space in an appropriate and efficient way. Therefore, the necessity of geography in creating resilient cities and increasing urban resilience will be the main axis of this study.

2. Urban Resilience and Geographic Information: A Powerful Alliance Shaping the Future of Cities

Urban areas are continuously growing centers that house a large proportion of the world's population. While this growth increases economic opportunities and the intensity of social life, it also forces cities to cope with natural disasters, climate change, economic crises and other unexpected events. It is in this context that the concept of "urban resilience" gains importance. While cities have the potential to improve people's quality of life, economic development and social welfare, they also pose a range of environmental, economic and social challenges. This paper explores the critical role of geographic information in building resilient cities. Dense urban lifestyles expose us to a variety of crises such as natural disasters, climate change, economic crises and other emergencies. Urban resilience refers to the ability of cities to withstand such crises. But it is not limited to the physical resilience of buildings and infrastructure. The design, organization and management of urban spaces are also central to this concept. This is where geographic information comes into play.

Geographic information is a key component of urban resilience. Collecting, analyzing and using geographic data is critical for cities to become resilient to disasters and cope with crises. Geographic information systems (GIS) fulfill important tasks such as identifying potential hazards, conducting risk analyses and coordinating emergency management.

Human beings, who have developed close ties with the natural environment and its surroundings, have changed their environment with the transition to settled life and have been affected by the conditions of the natural environment. Cities, which constitute the important stage of this interaction, have revealed the most magnificent results of the interaction of human and nature. Change, which is one of the most important features of cities that have been shaped over time in the historical process, continues at a dizzying pace today.

One of the most important factors that cause this change is the increase in the need for housing with the increasing population and the need for work and living spaces cause the growth and development tendencies of cities. As a result of this tendency, horizontal and vertical urban growth is realized by ignoring physical and human geography conditions. As a result, human mind, intelligence, experience and preferences come to the forefront as the main determining factors in urban structuring rather than the natural environment.

As a living space, cities are human ecosystems where many natural and cultural factors coexist and interact with each other. In this system, on the one hand, natural environmental conditions such as air, soil, water and plants, and on the other hand, socio-economic activities such as transportation, trade, industry and tourism, which must be continuously developed for economic development, are in the same area and intertwined. Cities are places where people with different ethnic, social and cultural habits, lifestyles and social profiles, with varying environmental perceptions, have to live together. Such a large size, dense construction and urban mobility create a serious pressure on the urban environment, and cities often turn into "risk spaces" that become the focus of environmental degradation and pollution [12]. In particular, overpopulation due to migration and the accompanying misuse of land have a negative impact on the resilience of cities. At the same time, heavy traffic, excessive industrial production, irregular settlement areas and illegal structures have led to increased discussion of livability, sustainability and urban ecology in the city.

The piece of nature on which the city is settled is subject to a certain order of functioning created primarily by the components of the natural environment. Natural environmental components such as geological structure and geomorphological features, climatic conditions, hydrography, water resources, soil and vegetation determine the future of the settlement by shaping the lifestyles and economic activities of the people living in the city (Koçman, 1991:102, Karadağ and Koçman, 2007: 5). Therefore, the emergence, development and urban identity of a city depends on natural environmental components such as site-situation conditions and topography (geological and geomorphological), climate, soil, vegetation and water resources. The natural and cultural environmental components that make up the "Geographical Environment" overlap with urban areas. In urban settlements, it is imperative to create a settlement layout/space organization in accordance with the natural environmental components functioning in the selected geographical or ecological environment.

The concept of resilience is related to the capacity of socio-ecological systems to cope with change, adapt and direct change, as well as the capacity to adapt and direct change, and to get used to living with unexpected changes [4]. Servillo and Reimer (20132) define resilience as "return to normalcy in the face of changes and threats caused by changes". In addition to the different definitions that try to explain the concept of resilience, the main points that are focused on are "the ability to adapt and transform to change". Integrating resilience into the urban planning process, using the evolutionary explanation of the concept, is of strategic importance for successfully managing change and increasing the rapid recovery capacity of cities.

The concept of "urban resilience" or "urban resilience", which is one of the fundamental principles of sustainable urban development in global development frameworks and goals, is the concept of "urban resilience", which refers to the ability of individuals, communities, institutions, businesses and systems in a city to survive whatever chronic stresses and acute shocks they experience, The future of societies and cities is directly proportional to how resilient they can be in the face of such situations and necessitates urban policies and practices that include multi-layered, multi-dimensional, holistic approaches.

The concept of resilience was first introduced in ecology by Holling in 1973 as "the ability to absorb disturbance and change without losing the interrelationship between its constituent elements prior to disturbance" [10]. However, this definition of resilience by Holling has been criticized for focusing on the structure and identity of the system. Because it is stated that ecological resilience is related to the state of the functions of the system rather than the state of the elements of the system [5]. The fact that resilience is addressed by ecological and other disciplines has led to

multidimensional and different definitions of the subject. But ultimately, resilience has emerged in response to environmental hazards emerging in the social and institutional perspective in relation to cities and planning [19]. Therefore, it is addressed within the context of disaster threats related to sustainability in cities and urban areas, climate change and rapid population growth.

3. Geographic Information: The Main Axis of Urban Resilience

Geographic information helps cities become more prepared and resilient to natural disasters, climate change and other crises, while contributing to building more sustainable and livable cities. This powerful alliance is an important tool to improve people's quality of life and safety while shaping the future of cities. As a key axis of urban resilience, geographic information will continue to play a critical role in making the cities of the future safer, more resilient and more sustainable.

The human and artificial environment created by human modification of the natural environment brings various dangers as well as facilitating life. However, human greed and the ability to disrupt the natural balance brings risks with it. However, seismicity, geological risks and natural resources are ignored when making settlements or urban planning. Urban settlements where population and building stock accumulate over time face the devastating consequences of disasters. In order to minimize the consequences of being caught unprepared for natural disasters that cause loss of life, property and urban fabric in a short time and unexpectedly, the geographical information axis, which is essential for urban resilience, is of great importance. Öztaş (1994) states that "the problems experienced in today's cities, in addition to inevitable natural causes, are mostly caused by urban planning mistakes that do not comply with local principles and decisions, unconscious and unmethodical settlement area choices, and uncontrolled and inadequate technical initiatives in implementation.

As a result of the "risky urban fabric" built on natural problems of geological, topographic, morphological, hydrographic, meteorological origin in the urban fabric, cities with high vulnerability emerge. Therefore, one of the most realistic and fundamental ways to understand the typology and morphology of the city is to have geographical knowledge. Topographical knowledge is a process that controls urban life, and the topographical factors on which cities are located are important elements that people living in cities are not aware of but affect their lives. These factors such as geomorphology, slope, elevation and aspect have a great impact on urban texture. When these topographical elements are ignored during the planning phase of cities, the result is cities that are not resilient. Therefore, the relief drawn by topographical processes has strategic value in urban planning. Especially in the planning, establishment and development processes of the city, topographical characters should be analyzed well. Knowing the characteristics such as geological structure, faults, seismicity at the planning stage of the city will ensure that the city planning process and the following stages are carried out in a healthy way. Therefore, geomorphology, one of the important axes of topography, is a stakeholder in the functioning of spatial planning.

Factors affecting urban morphology and urban form in general;

- Natural factors (Features of the place of establishment such as mountains, plains, valleys)
- Population structure
- Economic structure of the city
- Political preferences
- Level of technological development
- Transportation systems

Such features have an impact on urban structure and urban resilience. The planning of urban space by taking geographical elements into consideration, evaluates the ways in which geographical elements and settlements come together, with their spatial dimensions, and addresses change over time.

Kentlerin kuruluşu, gelişimi, büyümesi ve sosyo-ekonomik büyümesi lokasyonlarına ve doğal ortam özelliklerine bağlı olarak değişmektedir. Yükselti, iklim, yer şekilleri, bakı, toprak ve hidrografya gibi doğal ortam özelliklerinin birinin veya birkaçının yerleşme yeri seçiminde ön plana çıktığı görülür [13]. The majority of settlements in Turkey have developed without taking into account the natural environment characteristics of the place where they were

established. Especially in cities with a deep-rooted history in terms of settlement history, cities grow towards the peripheries without taking structural features into consideration. However, cities that grow uncontrolled with rapid urbanization transform the natural environment with transportation, settlement texture and industrialization. In order to minimize the damages that may arise from this transformation, urban development must be controlled. "For this purpose, geological and geotechnical conditions as well as social, cultural and economic conditions of the region should be evaluated very well" [14]. However, in our country, urban plans are generally carried out on the basis of ready-made plans and thus the relations between the natural environment and urbanization remain in the second plan. Therefore, geological structure is one of the most important natural environmental features that should not be neglected in urban development, especially in site selection.

Population criterion is an important factor to be taken into consideration in resilient urban structuring. "Population growth" refers to the density of the population in Turkey and the world as a result of the different design, distribution and dispersion of the population on the globe, continent, country, region and smaller geographical units, even on a neighborhood or street basis. Asylum seekers and refugees are the second global problem that is a derivative of population, and migration, as a movement of displacement, precedes geographical logic. According to the first census in 1927, Turkey had a population of 13,648,270, with 75.8% of the population living in towns and villages and 24.2% in provincial and district centers. According to the results of the Address Based Population Registration System 2021 announced by TurkStat, 93.2% of the population lives in provincial and district centers (World Bank, 2021) (Chart 1). With nearly half of the world's population now living in urban areas (projected to increase to two-thirds by 2050), urban areas are overpopulated beyond their carrying capacity, leading to urban problems. Overpopulation negatively affects urban resilience. In an overpopulated city, dealing with unexpected events such as natural disasters or epidemics can become more difficult. Therefore, it is important for local governments to consider overpopulation in urban planning and take necessary measures.

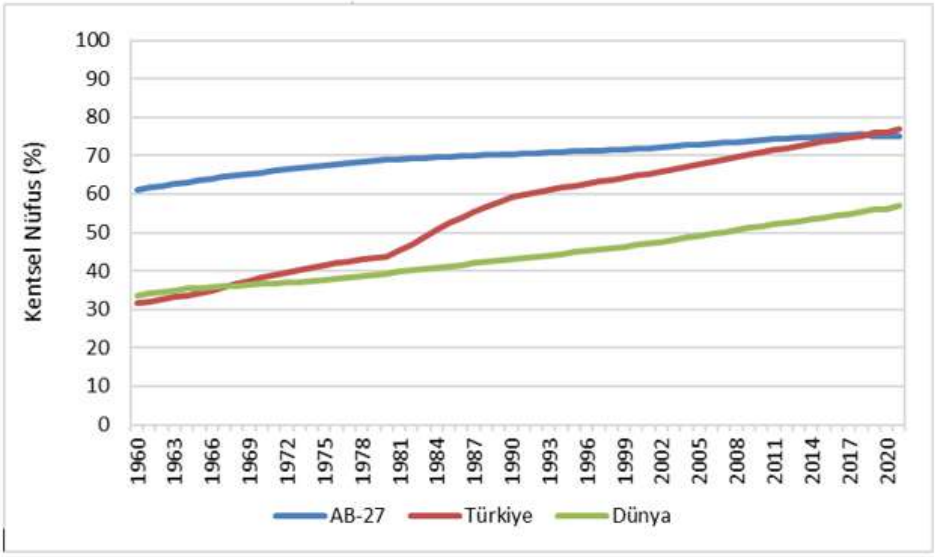

Figure 1. Urban Population Rates in Turkey and the World by Years (%) Source: https://data.worldbank.org/indicator

Climate characteristics; the distribution of large cities on the world map proves the fact that climates suitable for human life are effective in the birth and development of cities. The dominant wind direction plays an important role in the placement of industrial-residential areas of cities. Settlements established in the fully dominant direction cause dust, smoke, soot and pollution [11]. Risks and threats such as extreme weather events, climate change, floods, floods, sea level rise, severe storms, drought, forest fires threaten urban areas. Environmental and socio-economic risks arising from climate characteristics differ according to the level of development of countries and the resilience levels of cities. Therefore, for urban resilience, it is important to know the resilience power of each city's physical, environmental, socio-economic and morphological characteristics against climate change in order to reveal the "resilient city" phenomenon. As Denton et al. (2014) [7]. state, in order to build resilient cities against climate change and climate-related uncertainties, it is necessary to both mitigate the risks, threats and impacts of climate change and ensure adaptation.

As a result, climate is one of the most important factors determining the general appearance and potential of a region. Since the climate is effective in various issues such as planning of the area, industrial site selection, agricultural potential, heating needs of dwellings, capacity of air conditioning facilities, road construction and even the construction of insurances related to natural disasters, applied climatology studies should be taken into consideration while planning. Applied climatology provides information on where, when and how to perform the work in the best and most rational way, as well as offering solutions to the problems to be encountered [2].

Thanks to urban planning, detailed information on the landforms, general geological structure, climatology, soil structure and vegetation distribution of the area contributes to the healthy execution of the planning phase and a detailed analysis of the area is made. As Öztan (1994:131) emphasizes, "in addition to the inevitable natural causes of the problems experienced, urban planning mistakes that do not comply with local principles and decisions, unconscious and unmethodical settlement area choices and uncontrolled, inadequate or incorrect technical initiatives in practice are much more important.

As stated by Akdemir et al. (2015), "it is emphasized that the first preparation in the preparation phase of regional and city plans should be done primarily by geographers. However, by emphasizing that the plan will not be entirely the work of geography science, attention has been drawn to geographical knowledge in planning. In order to ensure resilience in planning, it is essential to determine the geographical potential of the area. The landforms, general geological structure, climatological characteristics, hydrography, water resources, soil structure and vegetation cover of the area where the city will be established should be determined through detailed research.

The Role of Geographical Information in Urban Planning; Geographical information contains important information about the natural environment in which the city is built. Having this information offers various advantages in urban planning. Some important aspects of the role of geographic information in urban planning:

- Geology-Geomorphology Information: Understanding the geological and geomorphological conditions under which a city is built is important for the safety of settlements. Knowledge of geology and geomorphology forms the basis of urban resilience. Proper use of this knowledge helps cities become more resilient to natural disasters, environmental threats and other risks and supports urban sustainability.
- Climate and Hydrography Knowledge: Climate conditions and the management of water resources are critical to urban sustainability. Geographic information is crucial for protecting water resources, reducing flood risks and optimizing energy consumption.
- Vegetation and Pedology Knowledge: Knowledge of vegetation and soil properties is important for the protection of green areas, the development of agriculture and the preservation of environmental balance.
- Population and Settlement Information: Identifying population distribution and settlement areas helps in planning infrastructure and services. As the population of cities increases, this information is needed to provide better services in areas such as transportation, education and health.
- Knowledge of Urban Geography and Economic Activities: knowledge of urban geography and economic activities plays a critical role in strategic planning and management to enhance urban resilience. Based on this knowledge, factors such as job opportunities, infrastructure, environmental protection and social solidarity can strengthen urban resilience and enable cities to be better prepared for crises.

Geographic Information Systems (GIS): A Key Tool for Urban Resilience

Geographic Information Systems (GIS) and urban resilience are two important concepts that play a critical role in preparing for and coping with the various crises facing modern cities. With geographic information systems (GIS), applying geographic information to the city has become a functional situation. Practical benefits are provided with the help of three-dimensional visuals such as queries, comparisons and possible scenarios. Geographic Information Systems (GIS) is an information system created for collecting, entering, storing, querying, spatial analysis, displaying and outputting spatially based information (graphics and attributes) in computer environment. GIS uses both spatial data and non-spatial attribute data to solve spatial problems and answer some questions. This feature is the most

important feature that distinguishes GIS and GIS software from other software and systems (CAD mapping software, etc.). GIS constitutes the meeting point of technological fields and traditional disciplines.

Coğrafi Bilgi Sistemleri (CBS), kentsel dirençliliğin fiziksel bileşenlerinin analizinde kullanılan bir araçtır. Günümüzde, mekânsal ve mekânsal olmayan verilerden yararlanılarak, afetler karşısında olası risklerin öngörülmesi, gerekli analiz süreçlerinin yürütülmesi, hazırlıklı olma ve zarar azaltma aşamaları için gerekli eylem planları, politikalar ve uygulamaların hayata geçirilmesi gibi tüm aşamalarda bilgi teknolojilerinin avantajlarından yararlanılmaktadır. Kentsel sistemler gibi karmaşık yapıdaki problemlerin çözülmesi ve afet riskinin minimum düzeye indirilebilmesi için teknoloji tabanlı uygulamalar başvurulması gereken temel kaynaklar haline gelmiştir [6]; [20];[22].

In interdisciplinary studies such as disaster management, GIS provides fast and effective solutions for purposes such as storing, analyzing, querying, mapping, managing spatial and non-spatial data that can be obtained from different institutions (relevant ministries, AFAD, local governments, universities, non-governmental organizations, etc.) in different formats (vector data, raster data, etc.), analyzing, querying, mapping, managing and directing the planning process by using them in decision support systems [3]. Through these web-based platforms, which are created using Geographic Information Systems (GIS) technologies and frequently updated, risk scenarios and policies can be developed at local and central scales in order to be more prepared and resilient in the face of disasters, and gains that will change the course of the pandemic in favor of humanity can be achieved [9]; [15]. GIS opens the door to new ways of thinking, planning and problem solving using spatial information. This technology is already in use in many public and private sectors, enabling decision-makers to present "information-oriented and complex data in a meaningful and visual way". GIS makes it possible to process and analyze more information in a short time.

Geographic Information Systems (GIS), which stand out as an important tool for urban resilience, help cities to be more prepared for crises and manage them effectively. Here are some key points on the importance and role of GIS in urban resilience:

- **Risk Analysis and Mapping**: GIS is a critical tool for identifying potential hazards and creating risk maps. Identifying factors such as earthquake hazard, flood risk, fire risk and mapping this information is a fundamental step in urban planning and crisis management. By showing these risks geographically, GIS helps identify which areas are more vulnerable.
- **Emergency Management**: GIS increases the capacity for a quick and effective response in a crisis. By using geographic information data, emergency management teams can quickly reach the scene and effectively coordinate needs and resources. GIS also plays an important role in emergency planning processes such as determining evacuation routes and locating emergency shelters.
- **Infrastructure and Resource Management:** For the sustainability and resilience of urban infrastructure, GIS provides the necessary data to maintain and improve infrastructure. The use of geographic information is critical for the management and emergency repair of basic services such as electricity, water, gas, communication. GIS is used to determine how this infrastructure can be improved according to settlements.
- **Urban Planning and Management:** GIS improves and guides urban planning and management processes. Regulation of construction in risky areas, protection of green areas and planning of emergency evacuation routes become more effective with the use of geographic information. During urban planning, GIS makes it possible to design safer and more sustainable urban developments.

GIS is therefore a fundamental tool to increase urban resilience and help cities become more prepared and resilient to crises. The geographical information provided by GIS can be used in many areas such as risk identification, crisis management, infrastructure improvement and urban planning to make the future of cities safer and more sustainable. Therefore, the role and importance of GIS in urban resilience is increasing.

4. Conclusıon And Assessment

Today, urbanization is increasing rapidly, posing new challenges to the sustainability and resilience of cities. However, one of the main reasons why cities are facing various problems is that in the past, and even today,

insufficient attention has been paid to land use and planning in harmony with the ground. This leads to the emergence of technical, administrative, financial and socio-cultural problems and bitter disasters.

Urban resilience aims to help cities become resilient to such problems and cope with crises. Geographic information is a very important tool for achieving this resilience. Geographic information provides a better understanding of the relationship between cities and their natural environment. Analyzing natural factors such as geology, topography, hydrography, climate and many more helps to identify risks in advance. With the help of geographical information, it makes a great contribution to improving urban infrastructure, improving transportation, carrying out urban transformation works effectively and creating a healthier city and urban society. The use of geographic information to make cities safer and more sustainable plays a critical role in reducing environmental threats and minimizing the effects of disasters.

Geography is a synthesis science that reveals the characteristics of spaces formed by the mixing of natural and human elements in different proportions according to place and time, and a cultural discipline that explains the reasons for the different appearances of spaces. Knowing the character of the place and evaluating it in line with the original place character, taking the dynamic harmony with the function area and its environment, that is, sustainability as a basis, is the main factor in making the planning safe, functional and economically feasible. As a result of the "risky urban fabric" built on natural problems of geological, topographic, morphological, hydrographic, meteorological origin in the urban fabric, cities with high vulnerability emerge. Therefore, one of the most realistic and fundamental ways to understand the typology and morphology of the city is to have geographical knowledge. The fact that the urban structure is not only composed of physical structures but also a social, political, economic, ideological, cultural structure imposes many different perspectives and different meanings. The city is not only a physical, ecological, but also a social, economic and political structure where resistance must be developed against deterioration and disturbances.

The issue of which climate change-based disaster threats and their negative impacts the city will face and what is the vulnerability level of the city against them can be evaluated in the context of various factors such as geographical characteristics of the city, climate structure, population size, population density, vulnerable population size, income status and welfare level, socio-economic structure, size and distribution of urban green areas, access to health and infrastructure services, institutional structure. Thus, depending on the size of the area and population that will be exposed to the negative impacts of climate change, the size of permeable surfaces, socio-economic development level, access to infrastructure services, and the existence and effectiveness of disaster management, the capacity of a city to cope with disasters, to show resilience against disasters and to compensate / recover from possible damages as soon as possible is revealed. As a result, thanks to "geographic information" to create resilient cities:

- To create resilient cities that do not threaten the environment and are not threatened by disasters,
- To have knowledge of geology-geomorphology, climate, hydrography, vegetation, pedology related to the natural environment in which cities are established, as well as knowledge about population, settlement, housing, urban geography and economic activities related to the human environment,
- That the continuous and uncontrolled growth of cities is contrary to the natural processes on which human well-being depends,
- We should not forget that as long as we do not give due importance to the natural environment, social values, social needs and living together, we will face the risk of facing disasters.

In conclusion, geographic information is a key element that shapes the future of cities. Geographic information should be recognized as a guiding principle in identifying and solving the fundamental problems facing the world. Integrating geographic information and logic is inevitable for cities to become resilient, protect the environment and ensure the safety of society. Therefore, the use of geographic information in urban planning and management is important for shaping the future of cities and creating a more livable world.

5. References

[1] Akdemir, İ. O. (2013). Şehirsel Fonksiyonlar-Doğal Ortam İlişkileri: Elazığ Eğitim Fonksiyonu Örneği . Fırat Üniversitesi Sosyal Bilimler Dergisi , 23 (1) ,

[2] Akdemir, İ. O. , Çağlıyan, A. & D.dağlı, -. (2015). Kentsel Planlamada Coğrafi Bilgi: Elazığ Uygulaması . Fırat Üniversitesi Harput Araştırmaları Dergisi , 2 (1) , 53-76 .
[3] Alkayis, M. H., Karslioglu A., Onur M. İ. (2022). "Muğla İli Menteşe Yöresi Orman Yangını Risk Potansiyeli Haritasının Coğrafi Bilgi Sistemleri İle Belirlenmesi". Geomatik Dergisi, 7 (1), 10- 16.
[4] Brand, F.S and Reimer, M., (2013). Focusing the meaning(s) of resilience as a descriptive concept and a boundary object, Ecolojy and society, cilt: 12, s.1.
[5] Chelleri, Lorenzo (2012) "From the 'Resilient City' to Urban Resilience A Review Essay on Understanding and İntegrating The Resilience Perspective for Urban Systems", Documents d'Anàlisi Geogràfica, 58(2): 287-306.
[6] Çağlayan, N., Satoğlu, Ş. I., Kapukaya, E. N. (2018). "Afet Yönetiminde Büyük Veri Ve Veri Analitiği Uygulamaları: Literatür Araştırması", 7. Ulusal Lojistik ve Tedarik Zinciri Kongresi, ULTZK 2018 Bildiriler Kitabı, 3-5 Mayıs 2018, Bursa.
[7] Denton, F., Wilbanks, T. J., Abeysinghe, A. C., Burton, I., Gao, M. C., Lemos, T., Masui, K.L., Brien, O., Warner, K. (2014), Climate-Resilient Pathways: Adaptation, Mitigation, AndSustainable Development In Climate Change: Impacts, Adaptation, And Vulnerability. Part A:Global And Sectoral Aspects. Contribution Of Working Group II To The Fifth AssessmentReport Of The Intergovernmental Panel On Climate Change. Cambridge University Press, Cambridge, United Kingdom and New York, USA, 1101-1131.
[8] Desouza, Kevin C. ve Trevor H. Flanery (2013), "Designing, Planning and Managing Resilient Cities: A Conceptual Framework", Cities, 35 : 89-99.
[9] Henderson, J. C., Venkatraman, H. (1999). "Strategic alignment: Leveraging information technology for transforming organizations". IBM Systems Journal, Vol. 38, 2.3, pp. 472-484.
[10] Holling, c.s. (1973), "Resilience and Stability of Ecological Systems", Annual Review of Ecology and Systematics, 4: 1-23.
[11] Karadağ A. 2000, Kentleşme Süreci, Çevresel Etkileri Ve Sorunları İle İzmir, Egekoop, İzmir.
[12] Karadağ, A. (2009). Kentsel Ekoloji : Kentsel Çevre Analizlerinde Coğrafi Yaklaşim . Ege Coğrafya Dergisi , 18 (1-2) , 31-47 .
[13] Karadoğan, S. (2019). Kuruluş Yeri Açısından Diyarbakır Kentinin Sitüasyonu ve Jeoloji-Jeomorfoloji İlişkileri. Uluslararası Katılımlı 72. Türkiye Jeoloji Kurultayı (s. 890-895). Jeoloji Mühendisleri Odası, Ankara.
[14] Kasapoğlu, E. (2007). TMMOB Jeoloji Mühendisleri Odası. Haber Bülteni, s. 3.
[15] Memiş, L., Babaoğlu, C. (2020). "Acil Durum ve Afet Yönetiminde Süreç Yaklaşımı Ve Teknoloji". Ömer Halisdemir Üniversitesi İktisadi ve İdari Bilimler Fakültesi Dergisi, 13 (4), 776- 791.1.
[16] Öztaş T., 1994; "Jeoloji de Yeni Odak Noktası : Kent ve Çevre Jeolojisi," 47. Türkiye Jeoloji Kurultayı Bildiri Özleri, Ankara.
[17] Öztaş, T., 2012, "Planlama Disiplininde Zorunlu Yeni Odak: Kentsel Jeoloji," TMMOB Jeoloji Mühendisleri Odası, Haber Bülteni, No:22, Ankara.
[18] Servillo, L. and Reimer, M., (2013). "Strategic Spatial Planning and Institutional Resilience: Theoretical Thoughts and some Empirical Devices", **AESOP-ACSP 5**th **Ortak Konferansı Bildiri Kitapçığı**, 15-19 Temmuz 2013, Dublin.
[19] Spaans, M., Bas Warterhout (2017), "Building up Reilience in Cities Worldwide-Rotterdam as Participant in the 100 Resilient Cities Programme, Cities, 61: 109-116.
[20] Sun, W., Bocchini, P., Davison, B. D. (2020). "Applications of artificial intelligence for disaster management", Natural Hazards (2020) 103:2631–2689, https://doi.org/10.1007/s11069-020- 04124-3.
[21] Yaman Galantini, Z. D., 2019, "Belirsizliklere Karşı Kurumsal Dayanıklılık ve Beş Bileşenli Kent Planlama Süreci", Dünya Şehircilik Günü 43. Kolokyumu: "Planlama, Kavramlar ve Arayışlar" Bildiri Sunumu, 7-9 Kasım 2019, TED Üniversitesi, Ankara.
[22] Yiğitcanlar, T., Desouza, K. C., Butler, L, Roozkhosh, F. (2020). "Contributions and Risks of Artificial Intelligence (AI) in Building Smarter Cities: Insights from a Systematic Review of the Literature", Energies 2020, 13, 1473; doi:10.3390/en13061473.

International Conference on Advances and Innovations in Engineering

The Effects of Pesticides on Aquatic Ecosystems

Gokhan Onder ERGUVEN[1], Numan YILDIRIM[2], Nuran Cıkcıkoglu YILDIRIM[3]

[1] Munzur Unıversity, Faculty of Economics and Administrative Sciences, Department of Urbanization and Environmental Issues, Tunceli, Turkey
[2] Munzur University, Tunceli Vocational School, Department of Plant and Animal Production, Organic Agriculture Programme, Tunceli, Turkey
[3]Munzur University, Pertek Sakine Genç Vocational School, Department of Veterinary Medicine, Laboratorian and Veterinarian Health Programme, Tunceli, Turkey

[1] gokhanondererguven@gmail.com, [2] numanyildirim44@gmail.com, [3] nurancyildirim@gmail.com

[1](ORCID: 0000-0003-1573-080X),[3](ORCID: 0000-0003-1109-8106), [4](ORCID: 0000-0003-3975-6705)

Abstract

Pesticides are essential tools in modern agriculture, aiding in the protection of crops against various pests and diseases. However, their pervasive use has raised significant concerns regarding their impact on aquatic ecosystems. This review provides a succinct overview of the effects of pesticides on these delicate environments, synthesizing key research findings and highlighting the urgency of addressing this issue. Pesticides can have direct toxic effects on aquatic organisms, including fish, amphibians, invertebrates, and even microorganisms. These toxic impacts can lead to reduced populations and potential disruptions to the ecosystem's structure and function. Pesticides can set off a chain reaction of ecological consequences. By targeting specific pest species, they can inadvertently disrupt natural predator-prey dynamics, potentially leading to cascading effects throughout the food web. Pesticides can degrade water quality by altering nutrient levels, reducing dissolved oxygen, and affecting pH levels. These changes can disrupt the overall health of aquatic systems, making them less habitable for native species. Certain pesticides have the ability to bioaccumulate in aquatic organisms. This bioaccumulation can lead to elevated pesticide concentrations in species higher up the food chain, ultimately affecting not only wildlife but also human health when contaminated organisms are consumed.

The aim of this review is to shed light on the critical issue of pesticide pollution in aquatic ecosystems, emphasizing the far-reaching consequences it holds for both the environment and human society. In this text, we endeavor to provide a comprehensive understanding of how pesticides, despite their agricultural benefits, can disrupt the delicate balance of aquatic ecosystems.

Keywords: ecosystem, biomagnification, pesticides, toxic effect

[1]Corresponding author

1. Introduction

Pesticides, while designed to protect crops and manage pest populations, have become a significant environmental concern due to their potential as pollutants. When pesticides are used in agricultural and non-agricultural activities, they can enter ecosystems and water bodies, leading to a range of environmental problems [1].

2. Pesticides

Pesticides are a vital component of modern agriculture, serving as a crucial tool to protect crops from pests, diseases, and weeds. They have played a significant role in increasing food production, ensuring food security, and reducing crop losses due to various threats. However, the use of pesticides also raises important environmental and health concerns, necessitating a careful balance between their agricultural necessity and environmental responsibility. Pesticides are classified into different categories based on their mode of action, chemical composition, and intended use. Here is an overview of the main types of pesticide classification [2]

2.1. Based on target pest

Insecticides: These pesticides are designed to control insects, including pests like aphids, mosquitoes, and caterpillars. Insecticides can be further classified based on their target insects, such as herbivorous, sap-sucking, or chewing insects [3].

Herbicides: Herbicides are used to control unwanted vegetation or weeds that compete with crops for nutrients, water, and sunlight. They are designed to selectively target plants while minimizing harm to other organisms [4].

Fungicides: Fungicides are used to prevent or treat fungal infections in plants, such as powdery mildew, rust, or blight. They help protect crops from diseases caused by fungi [5].

Rodenticides: These pesticides are formulated to control rodent pests, including rats and mice. They are used in agricultural and urban settings to prevent damage and disease transmission. In developed countries, rodenticides are primarily used to control commensal rodents such as brown rat (*Rattus norvegicus*), roof rat (*R. rattus*), and house mice (Mus spp.) for hygienic and public health reasons, in agricultural animal husbandry, in the food industry, and to a lesser extent for storage and material protection. Rodents pose a hazard to human health because they carry and transmit a vast array of diseases to humans and their domesticated animals [6].

2.2. Based on chemical composition

Organophosphates: This class of pesticides includes compounds like malathion and diazinon. They affect the nervous system of pests and are used to control a wide range of insects and some mites [7].

Pyrethroids: Pyrethroids, such as permethrin and cypermethrin, are synthetic chemicals modeled after pyrethrins, natural insecticides derived from chrysanthemum flowers. They target a variety of insects. Six natural pyrethrins are insecticidally active chemicals in pyrethrum and are formed by cyclopropylcarboxylic acid and cyclopentenone (or alcohol) through esterification. Pyrethroids are biomimetically synthesized by chemical methods of simulating the structure of pyrethrins [8].

Neonicotinoids: Neonicotinoid pesticides, like imidacloprid and clothianidin, affect the central nervous system of insects and are commonly used in agriculture. Neonicotinoids (NEOs), a class of relatively highly selective insecticides, have quickly swept one-fourth of the global market since the launch of imidacloprid (IMI) in 1991 [9].

Glyphosate: Glyphosate is a widely used non-selective herbicide that inhibits the growth of plants by interfering with their ability to produce essential proteins. These compounds are usually classified by their herbicidal mode of action and their molecular targets . Atrazine, a member of triazines family, is a photosynthesis inhibitor. It interacts with the D1 protein of plant cells' photosystem II (PSII), impairing the electron transport chain [10].

2.2. Based on mode of action

Contact Pesticides: These pesticides work upon direct contact with the target pest. They are often used for fast-acting control but may require thorough coverage.
Systemic Pesticides: Systemic pesticides are absorbed by plants and then ingested by pests that feed on them. They offer longer-lasting protection.

Residual Pesticides: Residual pesticides remain effective for an extended period after application. They are often used to create a barrier against pests.

Fumigants: Fumigant pesticides are volatile compounds that form toxic gases when applied. They are used to control pests in enclosed spaces like grain storage facilities [11].

3. Pesticides as a pollutant

3.1. Distruption of food webs

Aquatic ecosystems rely on intricate food webs where various species are interconnected. When pesticides are introduced into these systems, they can have a cascading effect. The elimination of certain species due to pesticide exposure can disrupt the balance of these food webs. For example, the loss of aquatic insects can harm fish populations that depend on them for food. Any insecticide can disrupt a food web when susceptible species directly encounter toxic residues at the time of application or come into contact with contaminated media. This environmental exposure, at lethal or sublethal levels, can weaken links in food webs and, depending on the trophic level affected, can reduce prey availability, alter competition, and release prey from top-down control [12].

3.2. Habitat alteration

Pesticides that find their way into aquatic systems can lead to habitat alterations. Herbicides, for instance, may kill aquatic plants, leading to reduced oxygen levels and changes in water chemistry. This can have a detrimental impact on the entire ecosystem, affecting both aquatic flora and fauna [13].

3.3. Bioaccumulation

Some pesticides are persistent and can accumulate in the tissues of aquatic organisms. This process, known as bioaccumulation, can result in high concentrations of pesticides in top predators. When humans consume fish or other aquatic species exposed to pesticides, they may unknowingly ingest these harmful chemicals, posing risks to human health. Most of the pesticides used are a threat to living organisms, both terrestrial and aquatic, due to their high toxicity and ability to bioaccumulate [14].

3.4. Algal Blooms

Certain pesticides, such as those used in agriculture, can promote the growth of algae in water bodies. Algal blooms can deplete oxygen levels in water, leading to "dead zones" where aquatic life cannot thrive. These dead zones can have devastating effects on aquatic ecosystems and the organisms that depend on them. The

lethal effect of four insecticides (chlorpyrifos, diazinon, endosulfan and malathion) applied at 10 or 40 μg/L on waterfleas and copepods induced trophic cascades that facilitated algal blooms and abiotic changes [15].

3.5. Contamination of Drinking Water

Pesticides can leach into groundwater and contaminate drinking water supplies, affecting human health. Vulnerable communities that rely on these water sources may be at risk of exposure to pesticide residues The traditional pesticide before the 1940s was derived from the toxic heavy metal of arsenic, copper, lead and mercury. These chemicals are partially soluble in water; therefore, their residues present in foods are of far greater concern than in drinking water [16].

3.6. Pesticide Toxicity in Aquatic Ecosystems

Pesticides are designed to be toxic to target pests, but they can also harm non-target organisms in aquatic environments. Fish, amphibians, aquatic invertebrates, and even aquatic plants can be highly sensitive to pesticide exposure. Pesticides may disrupt the nervous systems of aquatic organisms, impair their reproduction, or cause acute and chronic health issues [17].

Pesticides, designed to combat pests and boost agricultural productivity, are a double-edged sword when it comes to aquatic ecosystems. While they are effective in controlling crop-damaging pests on land, these chemical warriors can become aquatic assailants when they find their way into water bodies. The toxicity of pesticides in aquatic ecosystems is a complex and concerning issue that warrants careful examination. Among all the toxic substances that run off into the aquatic ecosystem, pesticides are of major concern as they are known to cause serious threats to the biological organisms, including human beings. Through several different routes such as spillage, industrial effluent, surface runoff, or through pesticide-treated soils, these toxic substances enter into the water sources [17-18].

3.6.1. Routes of Entry into Aquatic Ecosystems

Pesticides can infiltrate aquatic ecosystems through various pathways:

Surface Runoff: Rainwater or irrigation can carry pesticide residues from treated fields into nearby rivers, lakes, and streams.

Leaching: Pesticides can percolate through soil and into groundwater, eventually reaching surface water bodies or contaminating drinking water supplies.

Drift: During pesticide application, wind can carry pesticide particles away from their intended target areas, depositing them into adjacent water bodies or sensitive habitats. Through several different routes such as spillage, industrial effluent, surface runoff, or through pesticide-treated soils, these toxic substances enter into the water sources [19-20].

3.6.2. Toxic Effects on Aquatic Life

Pesticides, once introduced into aquatic ecosystems, can have a range of toxic effects:

Direct Mortality: Many pesticides are toxic to aquatic organisms upon direct contact or ingestion. Fish, amphibians, aquatic invertebrates, and even aquatic plants can suffer from acute poisoning, which can lead to death.

Sublethal Effects: Even non-lethal pesticide exposures can have detrimental effects. Sublethal doses can disrupt behavior, reproduction, and growth, ultimately affecting the population dynamics of aquatic species.

Bioaccumulation: Some pesticides are persistent and can accumulate in the tissues of aquatic organisms over time. This bioaccumulation can lead to high concentrations of pesticides in top predators, increasing their vulnerability to toxic effects.

Altered Ecosystem Dynamics: Pesticides can disrupt the delicate balance of aquatic ecosystems by affecting the abundance and distribution of species. For example, the elimination of aquatic insects can harm fish populations that rely on them as a food source [21-23].

3.6.3. Environmental Persistence

Certain pesticides are designed to persist in the environment, which can exacerbate their toxicity in aquatic ecosystems. Persistent pesticides can accumulate in sediments, where they may remain for extended periods, continuing to impact aquatic life long after their initial application [24].

3.6.4. Human Health Concerns

Pesticides that contaminate water bodies can pose risks to human health when used for drinking water supplies or recreational activities. Additionally, pesticide residues on fish and other aquatic organisms can pose health concerns when consumed by humans. It has been shown that exposure to pesticide residues may cause reproductive toxicity to both men and women, disruption in the endocrine system, enhancement of human breast cancer and prostate cancer, Parkinson's disease, and cardiovascular toxicity [25-29].

Pesticide toxicity in aquatic ecosystems is a critical environmental concern that demands careful consideration and responsible management. Balancing the need for pest control in agriculture with the protection of aquatic habitats is crucial for preserving biodiversity, safeguarding human health, and maintaining the health of our water bodies. Achieving this balance requires a collaborative effort among farmers, regulators, scientists, and the public to mitigate the detrimental effects of pesticides on aquatic ecosystems [27-28].

4. Conclusion

In conclusion, the effects of pesticides on aquatic ecosystems are undeniably significant and multifaceted. While pesticides serve a crucial role in modern agriculture by safeguarding crops against pests, they also pose a considerable threat to the delicate balance of aquatic environments. The unintended consequences of pesticide use in these ecosystems are far-reaching and encompass a range of ecological, biological, and environmental impacts.

Pesticides, when they enter aquatic systems through runoff, drift, or direct application, can exhibit toxic effects on various aquatic organisms, from fish and amphibians to invertebrates and plants. These toxic effects can disrupt the normal functioning of these ecosystems, leading to imbalances in food chains, biodiversity loss, and habitat alterations.

Moreover, pesticides have the potential to persist in water bodies, posing long-term threats to aquatic life, as well as human health when contaminated water sources are used for consumption. The phenomenon of bioaccumulation further exacerbates these concerns, as higher trophic level organisms may accumulate pesticide residues to dangerous levels.

Efforts to address the detrimental effects of pesticides on aquatic ecosystems require a multi-pronged approach. This includes the promotion of responsible pesticide use practices, the development and adoption of integrated pest management strategies, and the continual improvement of pesticide formulations that are less harmful to non-target species and the environment. Robust regulatory frameworks, strict monitoring, and public education also play pivotal roles in safeguarding these vital ecosystems.

In this ever-evolving relationship between agriculture and the environment, striking a balance is paramount. The challenge lies in ensuring food security and sustainable agricultural practices while minimizing the ecological and health risks posed by pesticide pollution in our aquatic ecosystems. A harmonious coexistence between agriculture and the environment is not only possible but essential for the well-being of both ecosystems and humanity in the long term.

5. References

[1] al-Saleh IA. "Pesticides: a review article". The Journal of Environmental Pathology, Toxicology, and Oncology,13(3), 151-161, 1994

[2] Mahmood I, Imadi SR, Shazadi K, Gul A, Hakeem KR. "Effects of Pesticides on Environment1. In: Hakeem, K., Akhtar, M., Abdullah, S. (eds) Plant, Soil and Microbes. Springer, Cham, 2016.

[3] Ramesh C Gupta "Biomarkers in Toxicology (Second Edition)" Academic Press, 2019,

[4] Belz RG, Duke SO. "Herbicides and plant hormesis". Pest Management Science, 70, 698–707, 2014.

[5] Artz DR, Pitts-Singer TL. "Effects of fungicide and adjuvant sprays on nesting behavior in two managed solitary bees, Osmia lignaria and Megachile rotundata". PLoS ONE, 10(8), 0135688, 2015.

[6] Regnery J, Friesen A, Geduhn A. et al. "Rating the risks of anticoagulant rodenticides in the aquatic environment: a review". Environmental Chemistry Letters, 17, 215–240, 2019.

[7] Kishi R, Covaci A. "Biomonitoring of organophosphate flame retardants and plasticizers in c hildren: Associations with house dust and housing characteristics in Japan" Environmental Research, 172, 543-551, 2019.

[8] Spurlock F, Lee M. "Synthetic pyrethroid use patterns, properties, and environmental effects" ACS (Am. Chem. Soc.) Symposium Series, 991, 3-25, 2008.

[9] Bass C, I. Denholm MS, Williamson RN. "The global status of insect resistance to neonicotinoid insecticides". Pesticide Biochemistry and Physiology, 121, 78 – 87, 2015.

[10] Martins-Gomes C, Silva TL, Andreani T, Silva AM. "Glyphosate vs. Glyphosate-Based Herbicides Exposure: A Review on Their Toxicity". Journal of Xenobiotics, 12, 21-40, 2022.

[11] Sparks TC, Storer N, Porter A, Slater R, Nauen R. "Insecticide resistance management and industry: the origins and evolution of the Insecticide Resistance Action Committee (IRAC) and the mode of action classification scheme". Pest Manag Sci, 77, 2609-2619, 2021.

[12] John FT, Kirsten AP. "Newer characters, same story: neonicotinoid insecticides disrupt food webs through direct and indirect effects". Current Opinion in Insect Science, 46, 50-56, 2021.

[13] Iwata T, Nakano SI, Inoue M. "Impacts of past riparian deforestation on stream communities in a tropical rain forest in Borneo Ecological Applications". 13, 461–73, 2003.

[14] Nicolopoulou-Stamati P, Maipas S, Kotampasi C, Stamatis P, Hens L. "Chemical pesticides and human health: The urgent need for a new concept in agriculture". Frontiers in public health, 4, 148, 2016.

[15] Hua J, Relyea R. "Chemical cocktails in aquatic systems: Pesticide effects on the response and recovery of > 20 animal taxa". Environmental Pollution, 189, 18–26, 2014.

[16] Syafrudin M, Kristanti RA, Yuniarto A, Hadibarata T, Rhee J, Al-onazi WA, Algarni TS, Almarri AH, Al-Mohaimeed AM. "Pesticides in Drinking Water—A Review". International Journal of Environmental Research and Public Health, 18, 468, 2021.

[17] Ansara-Ross TM, Wepener V, van den Brink PJ, Ross MJ. "Pesticides in South African fresh waters". African Journal of Aquatic Science, 37, 1-16, 2012.

[18] Uddin MA, Saha M, Chowdhuryl MAZ, Rahman MA. "Pesticide residues in some selected pond water samples of Meherpur region of Bangladesh". Journal of the Asiatic Society of Bangladesh, Science, 39,77-82, 2013.

[19] Jabali Y, Millet M, El-Hoz M. “Spatio-temporal distribution and ecological risk assessment of pesticides in the water resources of Abou Ali River, Northern Lebanon”. Environmental Science and Pollution Research, 1-16, 2020.
[20] Patnaik L, Patra AK. “Haemoatopoietic alterations induced by carbaryl in Clarias batrachus (LINN). Journal of Applied Sciences and Environmental Management, 10, 5-7, 2006.
[21] López-Pacheco IY, Silva-Núñez A, Salinas-Salazar C, Arévalo-Gallegos A, Lizarazo-Holguin LA, Barceló D, Iqbal HMN, Parra-Saldívar R. “Anthropogenic contaminants of high concern: Existence in water resources and their adverse effects”. Science of The Total Environment, 690, 1068-1088, 2019.
[22] Acosta-Sánchez A, Soto-Garita C, Masís-Mora M, Cambronero-Heinrichs JC, Rodríguez-Rodríguez CE. “Impaired pesticide removal and detoxification by biomixtures during the simulated pesticide application cycle of a tropical agricultural system”. Ecotoxicology and Environmental Safety, 195, 2020.
[23] Mensah PK, Palmer CG, Muller WJ. “Lethal and sublethal effects of pesti-cides on aquatic organisms: the case of a freshwater shrimp exposure to Roundup®”. Pesticides: Toxic Aspects, InTech Publica-tions, Rijeka, Croatia, 163-185, 2014
[24] Muhammad B, Hafiz MNI, Damiá B. “Persistence of pesticides-based contaminants in the environment and their effective degradation using laccase-assisted biocatalytic systems”. Science of The Total Environment, 695, 2019.
[25] El-Nahhal Y. “Pesticide residues in honey and their potential reproductive toxicity”. Science of The Total Environment, 741, 139953, 2020.
[26] Miranda-Contreras L, Gómez-Pérez R, Rojas G, Cruz I, Berrueta L, Salmen S. et al. “Occupational exposure to organophosphate and carbamate pesticides affects sperm chromatin integrity and reproductive hormone levels among Venezuelan farm workers”. Journal of Occupational Health, 55, 195-203, 2013.
[27] Yang KJ, Lee J, Park HL. “Organophosphate pesticide exposure and breast cancer risk: a rapid review of human, animal, and cell-based studies”. International Journal of Environmental Research and Public Health, 17(14), 5030, 2020..
[28] Pardo LA, Beane Freeman LE, Lerro CC, Andreotti G, Hofmann JN, Parks CG, Sandler DP, Lubin JH, Blair A, Koutros S. “Pesticide exposure and risk of aggressive prostate cancer among private pesticide applicators” Environmental Health: a global access science source, 19(1), 30, 2020.
[29] Pouchieu C, Piel C, Carles C, Gruber A, Helmer C, Tual S, Marcotullio E, Lebailly P, Baldi I. “Pesticide use in agriculture and Parkinson's disease in the AGRICAN cohort study” International Journal of Epidemiology, 47(1), 299-310, 2018.

International Conference on Advances and Innovations in Engineering

Heavy Metal Pollution and Risks in Aquatic Environments

Barbaros DURMUŞ[1], Gokhan Onder ERGUVEN[2], Numan YILDIRIM[3], Nuran Cikcikoglu YILDIRIM[4]

[1]Firat University, Department of Environmental Engineering, Elazığ, Faculty of Engineering, Elazig, Turkey
[2] Munzur Unıversity, Faculty of Economics and Administrative Sciences, Department of Urbanization and Environmental Issues, Tunceli, Turkey
[3] Munzur University, Tunceli Vocational School, Department of Plant and Animal Production, Organic Agriculture Programme, Tunceli, Turkey
[4]Munzur University, Pertek Sakine Genç Vocational School, Department of Veterinary Medicine, Laboratorian and Veterinarian Health Programme, Tunceli, Turkey
[1]barbarosdurmus@gmail.com, [2] gokhanondererguven@gmail.com, [3] numanyildirim44@gmail.com, [4]nurancyildirim@gmail.com

[1](ORCID: 0000-0002-4991-2436), [2](ORCID: 0000-0003-1573-080X),[3](ORCID: 0000-0003-1109-8106), [4](ORCID: 0000-0003-3975-6705)

Abstract

Heavy metal pollution in aquatic environments poses a growing global concern due to its detrimental impact on ecosystem health, biodiversity, and human well-being. This review provides a comprehensive examination of the sources, distribution, and ecological risks associated with heavy metal contamination in aquatic ecosystems. It synthesizes recent research findings and emphasizes the urgent need for effective mitigation and management strategies. The review elucidates various sources of heavy metal contamination, including industrial discharges, agricultural runoff, urbanization, and atmospheric deposition. It underscores the role of anthropogenic activities in exacerbating metal concentrations in aquatic systems. Through a thorough analysis, the review maps the pathways of heavy metals in aquatic ecosystems, from entry points to their transport, transformation, and accumulation in sediments and biota. It highlights the complexity of metal dynamics and their persistence in aquatic environments. The article investigates the adverse ecological consequences of heavy metal contamination, including toxicity to aquatic organisms, disruptions in food webs, and long-term ecosystem degradation.
This comprehensive review underscores the critical need to address heavy metal pollution in aquatic environments as a pressing global environmental challenge. The synthesis of recent research findings and the emphasis on mitigation and management strategies underscore the urgency of taking concerted action to safeguard the health and sustainability of our aquatic ecosystems.

Keywords: Heavy metals, Aquatic Environments, Toxic effect

1. Introduction

Accumulation of heavy metals (HMs) in receiving aquatic environments constitutes a problem on a universal scale as it causes bioaccumulation in aquatic organisms. All previous studies have shown that HM accumulation causes dangerously toxic effects on aquatic organisms. Common toxicities caused by HMs also include growth inhibition of living things, decreased survival ability, oxidative stress formation, tissue damage, respiratory tract obstruction, and intestinal microbial dysbiosis.

The most important problems caused by HM accumulation are exposure to various toxic effects (oxidative stress, inflammation, histological damage and genetic mutations) and microbial changes that occur in the intestines. [1]. Since heavy metals also contain toxic properties, when they penetrate the body through permeable membranes (such as gills), the natural metal ions of metabolic enzymes are changed and protein structures are disrupted, DNA cross-links are formed that can disrupt the cell cycle, and pose a problem when they interfere with different reactions [2].

[1]Corresponding author

When aquatic environments are exposed to heavy metal pollution, it is inevitable that another component of aquatic environments is heavy metal toxicity. The majority of these heavy metal sources consist of industrial wastewater containing numerous types of heavy metals, wastewater from mining activities and finally urban sewage water [3]. Although the degradation of heavy metals is quite laborious and difficult, they pose serious dangers in terms of environmental safety, living food and health, thanks to the bond chains they have, as their bioaccumulation becomes easier in living organisms. As a result, it is important to evaluate and detect the impact of heavy metals on ecological societies [5].

It is obvious that living creatures in the aquatic environment and people who benefit from these environments can be negatively affected by pollution caused by industry, transportation, agriculture, mining, energy production, nuclear energy, weapons production, and other activities. Some pollutants, especially heavy metals, that penetrate aquatic environments cause bioaccumulation in biota in water systems, with to their properties of being both persistent and toxic. The pollution load caused by heavy metals from industrial and agricultural activities negatively affects fish and wildlife. Acidic conditions accumulated in streams, rivers and lakes exposed to pollution from metal mining operations are factors that increase toxicity [6]. The sources of heavy metals naturally found in coastal ecosystems are anthropogenic practices such as mining, urban development, wastewater treatment, agriculture, burning of fossil fuels, marine disposal of municipal solid waste and anti-fouling paints [6].

The ways that living things in the marine ecosystem are exposed to heavy metals consist of ingestion through digestion, passage into the intestines, and entry into the gills through respiration [7]. When heavy metal intake exceeds the threshold value for detoxification and excretion, these toxic substances will bioaccumulate in various tissues, including the gills, intestine, liver, muscle and kidneys, and therefore these substances reaching high concentrations can cause death due to poisoning in fish, reduced growth, reproductive disorders, respiratory and It may cause toxic effects such as damage to osmoregulation and so on.

Oxidative stress may occur in sharks and many other aquatic creatures damaged by heavy metals [10]. Accumulation of heavy metals in the tissues of aquatic organisms can also penetrate biological molecules, resulting in the formation of reactive oxygen species (ROS), which cause protein denaturation, lipid peroxidation, and DNA mutations. Specifically, transition metals react with hydrogen peroxide and also induce oxidative stress, primarily through the Fenton reaction. As a result, hydroxyl radical formation occurs [12]. Enzymes such as superoxide dismutase (SOD), catalase (CAT) and glutathione peroxidase (GPx) are involved in the conversion of ROS into harmless forms [13]. SOD catalyzes the conversion of superoxide anion radical to hydrogen peroxide, and through the enzymatic action of CAT or GPx, hydrogen peroxide is also converted to water [12].

Scientists believe that many living organisms, including fish, need trace amounts of heavy metals to continue their vital activities. Of course, excessive amounts of some heavy metals can also harm organisms, while mercury, lead and cadmium do not have much effect on organisms, and long-term exposure in the body can cause fatal or permanent diseases. Heavy metals are also elements that have a density of at least 5 times the density of water. Toxicity caused by heavy metals, as well as other metals or elements that may cause toxic effects, depends on the route of exposure, the nutritional status of exposed individuals, the chemical species or the age, genetics, and sex of the organism [15]. Organisms, including fish species, absorb toxic substances from water (directly) and food chains (indirectly). Some toxic effects of heavy metals on fish and aquatic invertebrates lead to reduced developmental activities, increased developmental abnormalities, or reduced survival of fish (especially at the beginning of exogenous feeding), and the extinction of entire populations in contaminated reservoirs. [16]. Heavy metals generally penetrate aquatic animals through their primary food sources. In fish, they can enter through mechanical capture of suspended hydroxide particles in the gills as well as through chemical adsorption of ions on the mucous membrane [17].
The presence of metals in the aquatic environment may vary. If we list these differences, they can be in dissolved, particulate, or chelated/combined forms in sediments or aquatic organisms [18]. It has been determined that heavy metals such as Pb, Fe, Mn, Ni, Zn and Cr, which are found in dissolved or particulate forms in the Pacific and Atlantic Oceans, cause pollution [19]. It has also been determined that freshwater bodies (such as rivers and lakes) contain high concentrations of heavy metals (such as Cr, Cd, Cu, Zn and Pb) [20]. It is known that atmospheric accumulations created by such heavy metals can enter the receiving aquatic environments due to erosion, surface runoff and precipitation and cause pollution [20]. The stable state of water in its environment, higher retention time and depth of the water column cause heavy metals to remain in sediments for a long time and accumulate directly, and because

of this situation, aquatic ecosystems also serve as a storage unit or tank. Heavy metals are then incorporated into streams or tributaries of streams and are transported from there to the oceans [21]. Aquatic living organisms such as molluscs, crustaceans, fish [22], squids [23] and sharks [24] indicate high accumulation of different heavy metals (such as Cu, Hg, Zn, Pb, Cd, Cr, Ni). Heavy metal accumulation causes various toxic effects that can be lethal in organisms.

2. Material and Method

In this review study, references from some studies on pollution caused by heavy metal loads penetrating the aquatic receiving environment ecosystems and enzyme activities activated due to such pollution are mentioned.

In a study conducted by Dudley et al. (2000), they stated that the enzymes of some shark species carry out simultaneous purification activities [25]. It has been stated that the differences in heavy metal concentrations taken up by tissues between species are greatly affected by trophic levels and related nutrition, as well as by ecology [26].

The thesis defended by Gilbert et al. (2015) is that it has been reported that heavy metal concentrations of Cd, Cu and Zn are found in the muscle tissues of dusky, sandy (*Carcharhinus plumbeus*) and white sharks in southeastern Australian waters [27]. Where this study differs from other studies is that the observed metal values were also found in other shark species, including blue sharks, milk sharks (*Rhizoprionodon acutus*), star hounds (*Mustelus asterias*), shortfin makos, and Atlantic sharpnose sharks (*R. terraenovae*). It was among the values observed and reported in the literature. (Wosnick et al., 2021) [28].

Carlson et al. (2008) defined a different ecological niche in another study on the effects of heavy metals on sharpnose sharks in the Atlantic. [29]. Vélez-Alavez et al. (2013) similarly determined that SOD activity was detected in higher CAT and GPx only in short-finned makos. [30]. López-Cruz et al. (2010), when they compared white and tiger sharks, they found that silky shark (*Carcharhinus falciformis*), short-finned mako and smooth hammerhead (*Sphyra zygaena*) sharks had similar CAT activity and lower GPx activity [31]. It is apparent that differences in shark activity level can also lead to differences in antioxidant enzyme concentration among various species. ROS, on the other hand, causes an increase in oxygen flow to the mitochondria in muscle cells and therefore causes inefficiency in electron transport to be produced during exercise [32]. Considering all these reasons, it is believed that sharks that are more active may cause higher baseline values of antioxidant enzymes to protect against oxygen damage during vital activities [30]. This protects them against accidental metal exposure. Other factors such as the organism's metabolic activities, environmental conditions, age, gender, physiological state, individual behavior, and nutritional habits can also affect ROS production and antioxidant capacity.

Antioxidant enzyme activity increases with low metal exposure levels and may decrease with higher metal exposure levels. [32]. In their study, Barrera-García et al. (2012) described the correlations between oxidative stress indicators and trace elements (Zn, Cd, and arsenic [As]) in the livers and kidneys of blue sharks [33].

Yazdi et al. (2012), in their study on carnivorous and herbivorous fish, stated that these metals remained at the same level in two different trophic levels because they contained equal amounts of Cu and Zn [34]. Hosseini et al. (2015) showed that the heavy metal content (Cd, Co, Cu, Ni, Pb, Fe and Hg) in fish off the Khuzestan coast (northwest of the Persian Gulf) changed strongly due to habitat and food preference habits [35].

In a study conducted by Mazej et al. (2010) on the tissues of fish in Lake Velenjsko (Slovenia), they found that Zn and Hg values in muscle, liver and gills differed between tissues and species [36]. Klavins et al. (2009) found the highest metal concentration (including Cu and Zn) in two organs of sea bass (liver and gills) and the lowest metal concentration in the muscles of this species (inland waters of Latvia) [37]. Järv et al. (2013) determined more Hg in sea bass muscles than in the liver and higher Zn and Cu content in the liver than in the muscles of this species [38]. Svecevičius et al. (2014) also reported that Zn accumulated mostly in the gills and Hg accumulated in the muscles of the fish examined [39]. According to Jovičić et al. (2014), it was concluded that the data obtained because of direct exposure of gills to pollutants in water could be an important indicator of water quality [40].

According to Jezierska and Witeska (2001), when the liver/muscle ratio is below 1, the mercury content in the muscles is higher than in the liver [41]. These researchers have proven that high metal concentrations in the liver are closely related to the excretion and detoxification processes occurring in these organs.

Previous studies have shown that zinc levels in the muscle tissues of sea bass in Lake Plusz are negatively related to sea bass size [42]. It was concluded that the correlations discussed in this study were not statistically significant, but these results were compatible with the data of previous studies. Miloskovic and Simic (2015) also argued that the accumulation of heavy metals As, Sn, Ni, Co, Al, Se, and Fe is related to fish body mass index and weight [43]. In another study, Szarek-Gwiazda and Amirowicz (2006) observed a relationship between fish length or body weight and Cu concentration in the studied tissues (liver, kidney, muscles, and gills) of sea bass and roach [44]. No statistically significant correlation could be detected between the accumulation of zinc and copper in the muscle tissues of sea bass and the weight or length of these fish ($P > 0.05$) [45]. heavy metal levels of Hg, Zn, Pb, Cd and Cr increased with size increase in the species in the Dije river basin (Dvorak et al., 2014) [46]. A significant positive relationship between body weight and Hg levels in cockroaches from the Odra River (Poland) was also reported by Kalisinska et al. (2017) observed. [47]. Svecevičius et al. (2014) also found a statistically significant positive correlation between the Cu content in the liver and the hepatosomatic index ($r = 0.92$) of predatory fish (2014) [48].

Alkan et al. (2016) determined different correlations between GSI or FCF of fish species (*Trachurus mediterraneus, Engraulis encrasicolus ponticus* and *Sprattus sprattus*) in their investigation with metals including Cu and Zn [49]. Noël et al. (2013) also determined the mercury content in the muscles of eight freshwater fish from different fishing areas of France (2013) [50].

3. Conclusion

Even though the heavy metal pollution index has low values, the diversity and quality of fish species can be good indicators of water quality. Similarly, when the danger index values that can be created by the targeted hazardous elements are high level, it is believed that this situation is important for other people who use the receiving environments for recreational purposes. Therefore, we recommend that more research is needed in this area to better understand the effects of heavy metals on the biotic factors of organisms in the receiving environment and whether they pose a health hazard to other fish species in this ecosystem.

Heavy metals can bioaccumulate in all organisms in the aquatic food chain (including algae, zooplankton, molluscs, crustaceans, benthic animals, as well as sharks and mammals), mostly in the gills, and these substances are highly toxic. The accumulation of these substances can increase out of the body with increasing trophic levels, and top predators can accumulate them at the maximum level with the help of the food chain. There are many studies examining the toxic effects of major heavy metals (such as Cd, Cu, As and Hg) on aquatic organisms (especially fish and crustaceans). However, toxicological studies are mostly limited to physiological, biochemical and histological changes. The scarcity of research on the intestinal microbiota should direct researchers to work in this field.

4. References

[1] Qian D. et al. “Toxic effect of chronic waterborne copper exposure on growth, immunity, anti-oxidative capacity and gut microbiota of Pacific white shrimp Litopenaeus vannamei”. Fish Shellfish Immunology, 100, 445-455, 2020

[2] Garai P. et al. “Effect of heavy metals on fishes: toxicity and bioaccumulation”. Journal of Clinical Toxicology, 11 (10), 2021.

[3] Goher ME, Mangood AH, Mousa IE, Salem SG, Hussein MM. “Ecological risk assessment of heavy metal pollution in sediments of Nile River, Egypt” Environmental Monitoring and Assessment, 193(11), 1-16, 2021.

[4] Zhang P, Pan X, Wang Q, Ge G, Huang Y. “Toxic effects of heavy metals on the freshwater benthic organisms in sediments and research on quality guidelines in Poyang Lake, China”. Journal of Soils and Sediments, 20(10), 3779-3792, 2020.

[5] Huang B, Zhou R, Han X, Lu S, Li, N. “China's industrial gray water footprint assessment and implications for investment in industrial wastewater treatment”. Environmental Science and Pollution Research, 27, 7188-7198, 2020.
[6] Echols KR, Meadows JC, Orazio CE. “Pollution of Aquatic Ecosystems II: Hydrocarbons, Synthetic Organics, Radionuclides, Heavy Metals, Acids, and Thermal Pollution”. Encyclopedia of Inland Waters, 120-128, 2009.
[7] Mathews T, Fisher NS. “Dominance of dietary intake of metals in marine elasmobranch and teleost fish”. Science of The Total Environment, 407(18), 5156-5161, 2009.
[8] Eyckmans M, Lardon I, Wood CM, De Boeck G. “Physiological effects of waterborne lead exposure in spiny dogfish (Squalus acanthias)”. Aquatic Toxicology, 126, 373-381, 2013.
[9] De Boeck G, Hattink J, Franklin NM, Bucking CP, Wood S, Walsh PJ, Wood CM. “Copper toxicity in the spiny dogfish (*Squalus acanthias*): urea loss contributes to the osmoregulatory disturbance”. Aquatic Toxicology, 84, 133-141, 2007.
[10] Somerville RS, Fisher M, Persson L, Ehnert-Russo S, Gelsleichter J, Bielmyer-Fraser GK.” Analysis of heavy metal concentrations and anti-oxidant enzyme activity in muscle tissue of *Rhizoprionodon terraenovae*”. Archives of Environmental Contamination and Toxicology, 79, 371-390, 2020.
[11] Ray PD, Huang BW, Tsuji Y. “Reactive oxygen species (ROS) homeostasis and redox regulation in cellular signaling”. Cell Signal, 24(5), 981-990, 2012.
[12] Close DC, Hagerman AE, Alessio HM, Hagerman AE. “What are reactive oxygen species? Oxidative Stress, Exercise, and Aging”. Imperial College Press, London, 1-8, 2006.
[13] Birben E, Sahiner UM, Sackesen C, Erzurum S, Kalayci O. “Oxidative stress and antioxidant defense”. World Allergy Organization Journal, 5, 9-19, 2012.
[14] Azaman F, Juahir H, Yunus K, Azid A, Kamarudin MKAK, Toriman ME, Mustafa AD, Amran MA, Hasnam CNC, Saudi ASM. “Heavy metal in fish: analysis and human health-a review”. Journal of Technology, 77(1), 61-69, 2015.
[15] Tchounwou PB, Yedjou CG, Patlolla AK, Sutton DJ. “Heavy metals toxicity and the environment”. NIH Public Access. Author Manuscript. 101, 133–164, 2012.
[16] Khayatzadeh J, Abbasi E. “The effects of heavy metals on aquatic animals”. The 1st International Applied Geological Congress Department of Geology Islamic Azad University-Mashad Branch, Iran, 688–694, 26-28 April 2010.
[17] Shesterin IS. “Water pollution and its impact on fish and aquatic invertebrates”. Lysenko G, Squires V, Verheye WH. (Eds.) Interactions: Food, Agriculture and Environment, Encyclopedia of Life Support Systems (EOLSS). EOLSS, UK, 437 pp, 2010.
[18] Amankwaa G et al. “Heavy metals concentration profile of an aquatic environment and health implications of human exposure to fish and prawn species from an urban river (Densu)” Iran Journal of Fisheries Sciences. 20 pp. 529-546, 2021.
[19] Sujitha SB. et al. “Occurrences and ecotoxicological risks of trace metals in the san benito archipelago, eastern pacific ocean, Mexico Ocean Coast” Management 184, Article 105003, 2020.
[20] Yang HT. et al. “Pathogen invasion changes the intestinal microbiota composition and induces innate immune responses in the zebrafish intestine” Fish & Shellfish Immunology, 71, 35-42, 2017.
[21] Kakade A., Sharma M, Salama ES, Zhang P, Zhang L, Xing X, Yue J, Song Z, Nan L, Yujun S, Li X. “Heavy metals (HMs) pollution in the aquatic environment: Role of probiotics and gut microbiota in HMs remediation” Environmental Research, 223, 115186, 2023.
[22] Bonsignore M. et al. “Bioaccumulation of heavy metals in fish, crustaceans, molluscs and echinoderms from the Tuscany coast” Ecotoxicology and Environmental Safety, 162, 554-562, 2018.
[23] Xie J. et al. “Mercury and selenium in squids from the Pacific Ocean and Indian Ocean: the distribution and human health implications”. Marine Pollution Bulletin, 173, Article 112926, 2021.
[24] Wang MH. et al. “Assessment of trace metal concentrations in Indian Ocean silky sharks Carcharhinus falciformis and their toxicological concerns” Marine Pollution Bulletin, 178, Article 113571, 2022.
[25] Dudley SF, Anderson-Reade MD, Thompson GS, McMullen PB “Concurrent scavenging off a whale carcass by great white sharks, *Carcharodon carcharias*, and tiger sharks, *Galeocerdo cuvier*”. Fishery Bulletin, 98, 646-649, 2000.
[26] Turoczy NJ, Laurenson LJB, Allinson G, Nishikawa M, Lambert DF, Smith C, Cottier JPE, Irvine SB, Stagnitti F. “Observations on metal concentrations in three species of shark (*Deania calcea, Centroscymnus*

crepidater and *Centroscymnus owstoni*) from southeastern Australian waters". Journal of Agricultural and Food Chemistry, 48, 4357-4364, 2000.

[27] Gilbert JM, Reichelt-Bruschett AJ, Butcher PA, McGrath SP, Peddemors VM, Bowling AC, C hristidis L. "Metal and metalloid concentrations in the tissues of dusky *Carcharhinus obscurus*, sandbar *C. plumbeus* and white *Carcharodon carcharias* sharks from south-eastern Australian waters, and the implications for human consumption". Marine Pollution Bulletin, 92, 186-194, 2015.

[28] Wosnick N, Niella Y, Hammerschlag N, Chaves AP, Hauser-Davis A, Ch´avez da Rocha RC, Jorge MB, Santos de Oliveira RW, Nunes JLS. "Negative metal bioaccumulation impacts on systemic shark health and homeostatic balance". Marine Pollution Bulletin, 168, 1-11, 2021.

[29] Carlson JK, Heupel MR, Bethea DM, Hollensead LD. "Coastal habitat use and residency of juvenile Atlantic sharpnose sharks (*Rhizoprionodon terraenovae*)". Estuaries and Coasts, 31, 931-940, 2008.

[30] Vélez-Alavez M, Labrada-Martagón V, Méndez-Rodriguez LC, Galván-Magaña F, Zenteno-Savín T. "Oxidative stress indicators and trace element concentrations in tissues of mako shark (*Isurus oxyrinchus*)". Comparative Biochemistry and Physiology A, 165, 508-514, 2013.

[31] López-Cruz RI, Zenteno-Savín T, Galván-Magaña F. "Superoxide production, oxidative damage, and enzymatic antioxidant defenses in shark skeletal muscle". Comparative Biochemistry and Physiology Part A, 156, 50-56, 2010.

[32] Cooper CE, Vollaard NBJ, Choueiri T, Wilson MT. "Exercise, free radicals and oxidative stress". Biochemical Society Transactions, 30, 280-285, 2002.

[32] Duckworth CG, Picariello CR, Thomason RK, Patel KS, Bielmyer-Fraser GK. "Responses of the sea anemone, *Exaiptasia pallida*, to ocean acidification conditions and zinc or nickel exposure". Aquatic Toxicology, 182, 120-128, 2017.

[33] Barrera-García A, O'Hara T, Galván-Magaña F, Méndez-Rodríguez LC, Castellini JM, Zenteno-Savín T. "Oxidative stress indicators and trace elements in the blue shark (*Prionace glauca*) off the east coast of the Mexican Pacific Ocean" Comparative Biochemistry and Physiology Part C: Pharmacology, Toxicology and Endocrinology, 156, 59-66, 2012.

[34] Yazdi RB, Ebrahinpour M, Mansouri B, Rezaei MR, Babaei H. "Contamination of metals in tissues of Ctenopharyngodon idella and Perca fluviatilis, from Anzali wetland Iran". Bulletin of Environmental Contamination and Toxicology, 89 (4), 831-835, 2012.

[35] Hosseini M, Nabavi SMB, Nabavi SNN, Pour NA. "Heavy metals (Cd, Co, Cu, Ni, Pb, Fe, and Hg) content in four fish commonly consumed in Iran: risk assessment for the consumers". Environmental Monitoring and Assessment, 187, 230-237, 2015.

[36] Mazej Z, Al Sayegh-Petkovšek S, Pokorny B. "Heavy metal concentrations in food chain of Lake Velenjsko jezero, Slovenia: an artificial lake from mining". Archives of Environmental Contamination and Toxicology, 58, 998-1007, 2010.

[37] Klavins M, Potapovics O, Rodinov V. "Heavy metals in fish from lakes in Latvia: concentrations and trends of changes" Bulletin of Environmental Contamination and Toxicology, 82, 96-100, 2009.

[38] Järv L, Kotta J, Simm M. "Relationship between biological characteristics of fish and their contamination with trace metals: a case study of perch *Perca fluviatilis* L. in the Baltic Sea". Proceedings of the Estonian Academy of Sciences, 62(3), 193-201, 2013.

[39] Svecevičius G, Kazlauskienć N, Kesminas V, Staponkus R, Taujanskis E, Sauliutć G. "Heavy metal accumulation in fishes of different ecological groups from Kairiai landfill regional aquatic ecosystem". The 9th International Conference Environmental Engineering selected papers, Vilnius, Lithuania, 22-23 May 2014,.

[40] Jovičić K, Lenhardt M, Višnjić-Jeftić Ž, Đikanović V, Skorić S, Smederevac-Lalić M, Jaćimović M, Gačić Z, Jarić I, Hegediš A. "Assessment of fish stocks and elemental pollution in the Danube, Sava and Kolubara rivers on the territory of the city of Belgrade, Serbia". Acta Zoologica Bulgarica, 7, 179-184, 2014.

[41] Jezierska B, Witeska M. "The metal uptake and accumulation in fish living in polluted waters" Soil Water Pollution Monitoring. Prot. Remed, 23, 107-114, 2006.

[42] Łuczyńska J, Brucka-Jastrzębska E. "Determination of the heavy metals in the muscles of some fish species from lakes of the north-eastern Poland". Polish Journal of Food and Nutrition Sciences, 15/56(2), 141-146, 2006.

[43] Miloskovic A, Simic V. “Arsenic and other trace elements in five edible fish species in relation to fish size and weight and potential health risks for human consumption”. Polish Journal of Environmental Studies, 24(1), 199-206, 2015.
[44] Szarek-Gwiazda E, Amirowicz A. “Bioaccumulation of trace elements in roach, silver bream, rudd, and perch living in an inundated opencast sulphur mine”. Aquatic Ecology, 40, 221-236, 2006.
[45] Klavins M, Potapovics O, Rodinov V. “Heavy metals in fish from lakes in Latvia: concentrations and trends of changes”. Bulletin of Environmental Contamination and Toxicology, 82, 96-100, 2009.
[46] Dvorak P, Andreji J. Dvorakova-Liskova Z, Vejsada P. “Assessment of selected heavy metals pollution in water, sediments and fish in the basin Dyje, Czech Republic”. Neuroendocrinology Letters, 35(2), 26-34, 2014.
[47] Kalisinska E, Lanocha-Arendarczyk N, Kosik-Bogacka D, Budis H, Pilarczyk B, Tomza-Marciniak A, Podlasińska J, Cieslik L, Popiolek M, Pirog A, Jedrzejewska E. “Muscle mercury and selenium in fishes and semiaquatic mammals from a selenium-deficient area”. Ecotoxicology and Environmental Safety, 136, 24-30, 2017.
[48] Svecevičius G, Kazlauskienć N, Kesminas V, Staponkus R, Taujanskis E, Sauliutć G. “Heavy metal accumulation in fishes of different ecological groups from Kairiai landfill regional aquatic ecosystem” The 9th International Conference Environmental Engineering selected papers, Vilnius, Lithuania, 22-23 May 2014.
[49] Alkan N, Aalkan, Gedik K, Fisher A. “Assessment of metal concentrations in commercially important fish species in Black Sea”. Toxicology and Industrial Health, 32(3), 447-456, 2016.
[50] Noël L, Chekri R, Millour S, Merlo M, Leblanc J.-Ch, Guérin T. “Distribution and relationship of As, Cd, Pb and Hg in freshwater fish from five French fishing areas”. Chemosphere, 90, 1900-1910, 2013.

International Conference on Advances and Innovations in Engineering

Green Buildings and Environmental Problems

Fatih YILMAZ[1] , Gokhan Onder ERGUVEN [2], Numan YILDIRIM [3]
[1] Tunceli Provincial Directorate of Environment, Urbanization and Climate Change
[2] Munzur Unıversity, Faculty of Economics and Administrative Sciences, Department of Urbanization and Environmental Issues, Tunceli, Turkey
[3] Munzur University, Tunceli Vocational School, Department of Plant and Animal Production, Organic Agriculture Programme, Tunceli, Turkey

[1]fatihyilmaz@hotmail.com, [2]gokhanondererguven@mail.com, [3]numanyildirim44@gmail.com

[1](ORCID: 0009-0002-9279-6378), [2](ORCID: 0000-0003-1573-080X),[3](ORCID: 0000-0003-1109-8106)

Abstract

Since green buildings are designed and built in accordance with certain standards, design and construction practices that cause less harm to residents than standard buildings. In this study, it is aimed to evaluate the land in the most appropriate way, to use recyclable and recyclable materials, to turn to renewable energy sources, to consume fossil fuels as little as possible, to make maximum use of daylight, to control indoor air quality, to save on heating, cooling and lighting costs, to use gray water, The negative aspects of buildings that give importance to rainwater collection and treatment, encourage solid waste management and maximize roof, wall and window insulation are also explained. The construction technology in the traditional construction sector and the techniques used, as well as environmentalist preperations, are brought along. However, despite all these negativities, the development of environmental problems in the sector will gain momentum with the spread of greenhouses.

Keywords: Green buildings, Recyclable materials, Renewable energy sources

1. Introduction

The need for energy, one of today's priority needs, has led people to renewable energy sources and the construction of sustainable/green buildings. Green buildings are structures that cause less harm to the environment than buildings constructed using traditional methods. These buildings not only minimize the current energy need but also bring a horizon-opening vision to the construction industry in terms of art and design.

2. Green buildings

Green building is a design and construction practice that causes less harm to residents and the environment than standard buildings because it is designed and built in accordance with certain standards. Green Buildings are also known as sustainable buildings [1].
Article 4 of the Green Certificate Regulation for Buildings and Settlements, which came into force after being published in the Official Gazette dated 12.06.2022 and numbered 31864, states that “Green building: Site selection, design, construction, operation, maintenance, renovation, demolition, disposal of waste and wastewater.” It refers to a building that is sustainable throughout its life cycle, energy efficient, compatible with nature, has low emissions and has minimized negative effects on the environment.” provision is included [2].
Green buildings utilize land in the most appropriate way, use recyclable and recyclable materials, turn to renewable energy sources, consume fossil fuels as little as possible, make maximum use of daylight, control indoor air quality, save on heating, cooling and lighting costs, use gray water, These are buildings that give importance to rainwater collection and treatment, encourage solid waste management and maximize roof, wall and window insulation [1].

[1]Corresponding author

Figure 1. Sample of a Green building [3]

2.1. Purposes in the construction of green buildings

Urbanization increased rapidly with the industrial revolution in the 19th century. Along with modernization, industrialization and urbanization practices, the negative effects of human activities on the environment have also increased. Especially in recent years, social awareness about climate change caused by global warming has begun to increase. Terms such as carbon footprint have become part of our everyday language. Not only civil society, local governments and states, but also the private sector are taking action on how to build a more sustainable future. For this reason, the purposes of constructing green buildings are as follows:

- Minimizing consumptions,
- Minimizing emissions,
- Minimizing waste,
- Minimizing the impacts on the field,
- Maximizing indoor environment quality [3]

2.3. Factors to consider in the construction of green buildings

Green building refers to the structure and implementation of environmentally responsible and resource-efficient processes throughout the life cycle of a building: from planning to design, construction, operation, maintenance, renovation and demolition, the environmental impact is taken into account [4].

2.4. Materials used in green building construction

•Materials made from soil
•Wood
•Bamboo
•Straw bale
•Natural stones
•Composites
•Natural fiber
•Glass fiber
•Cellulose
•Natural clay
•Natural fiber flooring
•Fiber cement
•Recycled plastic
•Ash
•Cork board [5].

2.5. What is being done in Green Building Projects?

•Using LED bulbs in lamps
•Collecting rainwater falling on hard surfaces and using it in landscape irrigation
•Creating more green areas on the ground and preventing heat islands by building parking areas in basements
•Using efficient batteries and reservoirs that consume less water, thus saving water
•Designing and positioning building facades to benefit from daylight to the maximum extent
•Grey water cycle
•Solar panels producing electrical energy on roofs
•Use of thermal insulation materials
•Using plants that consume less water
•To obtain energy from renewable energy (wind, solar, etc.) instead of obtaining energy from fossil fuels.
•Low flow sink faucets
•Natural ventilation
•Double flush toilet cisterns
•Low emission paints and floor coverings

3. Environmental Problems

3.1. Situation in the traditional construction sector

In traditional construction and usage processes, it consumes approximately 16% of the world's fresh water resources, 25% of wood resources, 30% of material resources and 40% of energy resources. 35% of the CO2 that causes global warming comes from construction. 40% of land waste occurs as a result of the construction process and the subsequent storage of waste. 50% of the chemicals that deplete the ozone layer in the stratosphere are produced by the traditional building sector.

3.2. Advantages of green buildings

Research on green buildings has shown that if buildings are designed and operated in this way, they will reduce energy use by 24% to 50%, carbon emissions by 33% to 39%, water consumption by 30% to 50%, and water consumption by 30% to 50% compared to the average building designed and operated using conventional methods. It shows that a 70% reduction in the amount of waste and a 13% reduction in maintenance costs can be achieved [6].

4. Certificates

4.1. Certificates of green buildings

Green Buildings aim to save energy, focus on renewable resources and cause minimal damage to nature. The certificate certifying that buildings have been built or renovated for these purposes is called a green building certificate. The most accepted certificates in the world are:

Figure 2. Certificate samples for Green buildigs [5]

• LEED (America)
• BREEAM (United Kingdom) First 1990
• DGBN (Germany)
• Green Star (Australia)
• ITACA (Italy)
• CASBEE (Japan)
• HQE (Haute Qualité Environnementale) (France)
• LBC (Living Building Challenge) (Canada)
The most common of these certificates is the LEED Certificate [7].

4.2. Leadership in Energy and Environmental Design (LEED)

The LEED Green Building concept was born in 1998. LEED Certificate is the most valid green building certificate in the world, taking its name from the initials of the words Leadership in Energy and Environmental Design.

LEED Certification is one of the green building rating systems developed by the American Green Building Council USGBC. LEED, the most widely used rating system in the world, reveals sustainable design, construction and operation criteria from buildings to the city scale. LEED Certified Buildings are more environmentally friendly, healthy and economical buildings than traditional buildings.

LEED is a valid and comprehensive green building rating system developed as a global system for all building types such as hospitals, data centers, historical buildings, schools and business centers.

4.3. LEED Certification Levels

With the LEED certificate, how energy efficient, water efficient and healthy buildings are is determined by the points they collect. In order for a building to receive certification, it must first meet the minimum requirements and mandatory prerequisites. By meeting these conditions and scoring at least 40 points, you are entitled to receive a simple Certificate. As points are obtained from the credits determined by LEED, the points earned increase and the certificate level increases. The maximum score is 110. A certificate is obtained after 40 points, silver after 50 points, gold after 60 points, and platinum certificate if more than 80 points are obtained [8].

Figure 3. LEED certificates

4.4. Main headings of leed green building certificate

•Sustainable Land

•Water efficiency

•Energy and Atmosphere

•Materials and Resources

•Interior Space and Quality of Life

•Innovation

Scoring is done according to these headings and a certificate is given to the building according to the score received. According to current statistics in Turkey, a total of 49 buildings were eligible to receive LEED certification in 2021 and 40 buildings in 2022. The first LEED certified public building in Turkey was the Turkish Grand National Assembly Presidential Residence. In addition, the first building in our country to receive the LEED Gold certificate was Gama Holding's Head Office Building in Ankara [9]. Turkey's first green university building was Boğaziçi University Hamlin Hall building [10]. Turkey's first LEED Platinum Certified building was Eser Holding Head Office [11].

Figure 4. Gama Holding Center Office (9)

Figure 5. Boğaziçi University Hamlin Hall Building [10].

Figure 6. Head Office of Eser Holding (11)

5. Results and Discussion

Considering the environmental damage of traditional buildings and the environmental, economic and social benefits of green buildings, they need to be increased. Providing incentives and grants by the relevant Ministry for the construction of green buildings will increase the number of certified green buildings.

6. Conclusion

Developments in the green building sector have not been easy. Even though the conditions are difficult, many changes have been made in city structures, the construction sector, and factories in industrialized cities all over the world. There are many new technological developments that are more environmentally friendly and maintain and improve ecological balance. New ones are added every day. The most popular change, especially in the construction industry and in today's homes and buildings, is renewable energy. Today, heating and electricity needs in the house can be met with solar energy and even wind energy. In addition, the concept of "green building" is dynamic and rapidly developing today. “Green Buildings” are buildings that treat the natural ecology and obtain all their energy needs from recyclable natural resources.

7. References

[1] Doğru M. “Yeşil Binalar Hakkında Her Şey: 1- Yeşil Bina Nedir? Yeşil Bina Standartları ve Yönetmelikleri”. https://www.ecobuild.com.tr/post/2019/10/15/ye-c5-9fil-binalar-hakk-c4-b1nda-her-c5-9eey-1-ye-c5-9fil-bina-nedir-ye-c5-9fil-bina-st. 2019.

[2] T.C. Resmî Gazete, Binalar ile Yerleşmeler için Yeşil Sertifika Yönetmeliği, 12.06.2022, 4.

[3] Yeşil Bina Nedir? Yeşil Binalar Hakkında Her Şey! https://www.sentrum.com.tr/blog/yesil-bina-nedir-yesil-binalar-hakkinda-her-sey. 2022

[4] Çevre Dostu Yeşil Binalar. https://www.massatelier.com.tr/category/mimari/yesilbina/. 16.03.2023

[5] Yeşil Bina Nedir ve Nasıl Yapılır? Faydaları Nelerdir ve Sertifikası Nedir? http://www.cevrebilinci.com/yesil-bina-nedir/ 2019
[6] Çalapkulu S "Yeşil Binalar". 09.12.2022. https://www.medyasiirt.com/yesil-binalar-green-buildings-makale,227.html
[7] Yeşil Bina Sertifikaları, https://winergytechnologies.com/yesil-bina-sertifikalari/
[8] Aşan D. "LEED Sertifikası". https://www.dilekasan.com/leed-sertifikasi/
[9] Türkiye'nin ilk LEED EB sertifikası GAMA'ya verildi. https://yesilekonomi.com/turkiyenin-ilk-leed-eb-sertifikasi-gamaya-verildi/
[10] Türkiye'nin ilk "yeşil" üniversite binası Boğaziçi Üniversitesi'nde. https://haberler.boun.edu.tr/tr/haber/turkiyenin-ilk-yesil-universite-binasi-bogazici-universitesinde#:~:text=Leed%20%E2%80%9CGOLD%E2%80%9D%20Sertifikas%C4%B1'na,a%C3%A7%C4%B1s%C4%B1ndan%20att%C4%B1%C4%9F%C4%B1%20ad%C4%B1mlardan%20yaln%C4%B1zca%20biri%E2%80%A6. 20.01.2015
[11] Türkiye'nin İlk LEED Platin Alan Binası https://www.altensis.com/proje/eser-holding-merkez-ofisi-ilk-leed-platin-sertifikali-bina/

International Conference on Advances and Innovations in Engineering

A Peroxyelectrocoagulation Method Application to Remove Chemical Oxygen Demand from Tannery Wastewater

Zilan ŞİRP[1], Ayşe ÖZGÜVEN[2], Dilara ÖZTÜRK[3]

[1,2,3] Van Yüzüncü Yıl University, Faculty of Engineering, Department of Environmental Engineering, Van, Turkey
[1*] zilansirp@yyu.edu.tr, [2]ayseozguven@yyu.edu.tr, [3]dozturk@yyu.edu.tr

[1](ORCID: 0000-0002-8124-4714), [2](ORCID: 0000-0003-1071-2813)[3](ORCID: 0000-0003-2689-560X)

Abstract

Tannery wastewater contains high levels of organic pollutants such as fats, dyes, tanning agents and inorganic pollutants such as nitrogen, salts, and chromium. Effective treatment of such wastewater before discharge is essential to minimize the ecotoxicological risk. In this study, chemical oxygen demand (COD) removal from tannery wastewater was investigated by the peroxyelectrocoagulation method in a batch system. The wastewater was supplied from a tannery industry which was operated in Malatya in Turkey. The peroxyelectrocoagulation method can be thought of as a modified electro-Fenton process, with the difference that Fe^{2+} is supplied from the anode iron electrode without adding iron from the outside. In addition, H_2O_2 was not added from the outside in the process, and it was produced with an air supply under the in-situ cathode electrode (graphite). In the study, the initial pH value of wastewater (3.5, 6.5, 7.5, 8.5), applied current intensity (5 A, 7.5 A, 10 A, 15 A), and supporting electrolyte concentration (0.05 M, 0.1 M, 0.2 M, 0.3 M NaCl) parameters were investigated to remove COD from tannery wastewater. The reaction temperature, reaction time, and aeration rate were fixed at 20 ℃, 60 min, and 2 L/min, respectively. According to the data obtained, the optimum parameters were determined as; pH value of 6.5, applied current of 10 A, and supporting electrolyte concentration of 0.2 M NaCl. Under these conditions, the COD removal efficiency was found to be 95%.

Keywords: Chemical oxygen demand, organic pollutants, peroxyelectrocoagulation, tannery wastewater

1. Introduction

Increasing industrial activities, population growth, supply and competition bring increased production/consumption and as a result, industrial wastes have also increased. Industrial processes use large volumes of clean water during operations and also generate large volumes of wastewater and discharge into receiving water environments. The tannery is a sector where dyes are used extensively, as well as complex chemicals. Tannery wastewater contains high chemical oxygen demand (COD) and biological oxygen demand (BOD), different types of salts, Chromium, dyes, suspended solids, turbidity, color, sulfide, chlorides and other organic and inorganic pollutants [1].

Since tannery wastewater is toxic and contains many non-biodegradable components, it must be treated before being released into receiving environments [2]. The pollution risk of these wastewaters in the environment also leads to different health problems. The majority of these health problems are related to hexavalent chromium-containing compounds found in tannery wastewater [3]. High chromium (VI) concentrations cause disruption of ecosystems and also have a negative impact on human health as it causes cancer and DNA damage, chronic bronchitis, liver and kidney damage, [4-5]; These negative effects have led to stricter regulations by governments and the promotion of effective treatment methods to reduce the risk of pollution [6]. Some studies demonstrating the toxicity and environmental risks of tannery wastes have been carried out and it has been stated that these wastewaters should be treated before being released into the environment in order to reduce their negative effects on humans, animals and the environment [1,7-9]. De-Nicola et al. [10] performed several bioassays to determine the toxicity of tannery wastewater against marine microalgae *and Daphnia magna*. As a result of biological tests, it has been determined that these wastewaters have toxic effects on living things.

[1]Corresponding author

Since these wastewaters have a very complex structure, effective and economical treatment is very important. The performance of treatment technologies is closely related to the characteristics of wastewater and operational conditions. Due to the complex pollutants and toxicity of tannery wastewater, it can be difficult to treat them biologically. Treatment methods such as nanofiltration [11], chemical coagulation [12], adsorption [13], advanced oxidation processes [14] are mostly applied for this type of wastewater.
Electrochemical processes such as electrocoagulation, electrooxidation, electro fenton etc. are frequently preferred advanced oxidation processes. Electrochemical technologies have both advantages and disadvantages in wastewater treatment. Although the use of electrical energy and the financial burden it brings, the expensiveness of the electrodes used and the necessity of renewing the electrodes for some processes are among the disadvantages, the important advantages are short treatment, not being affected by toxicity, tolerance to high organic-inorganic load and the absence of secondary waste generation for some processes (eg: electrooxidation) [15].

Peroxyelectrocoagulation is not actually a single process, but a combined process involving H_2O_2 oxidation and electrocoagulation. In this study, wastewater from a tannery industry operating in Malatya province in Turkey was treated based on COD removal with in-situ H_2O_2 production, unlike the classical peroxyelectrocoagulation process. In-situ H_2O_2 production was provided by air supply under the graphite cathode, while iron electrode was used as anode for electrocoagulation. The operational parameters that investigated in this study were initial wastewater pH value, applied current and supporting electrolyte concentration.

2. Material and Method

The wastewater used in this study was obtained from a tannery industry operating in Malatya, Turkey, and the wastewater was not subjected to any treatment/pre-treatment. COD, pH and EC of wastewater were 3250 mg/L, 4.3 and 5.32 mS/cm, respectively. The characterization of the wastewater used was presented in detail in the previous work of one of the authors [16]. The electric current was supplied by using a direct current power supply (TTI/QPX1200S), an Iron plate electrode (4 cm x 22 cm) was used as the anode material and a graphite plate electrode (4 cm x 22 cm) was used as the cathode. A heat-jacketed reactor with an internal diameter of 7 cm and a depth of 22 cm was used for batch trials.

2.1. Experimental procedure and calculations

The heat-jacketed reactor was filled with tannery wastewater and the internal temperature was adjusted to room temperature. Then, NaCl, which was used as the supporting electrolyte, was added to the reactor at the desired concentrations and dissolved. Then, with the help of a compressor (Kuletaş, Turkey), air was supplied to the reactor at a flow rate of 2 L/min for about 10 minutes. Afterwards, the pH value of the wastewater was adjusted and the air flow was supplied to the system at the desired value, and the experiment was started. 5 mL samples were taken at certain time intervals and COD values were analyzed according to the closed reflux colorimetric method [17] using UV-vis spectrophotometer (WTW 6100 vis). The process of supplying air into the reactor under the cathode continued throughout the reaction. The concentration of in-situ H_2O_2 produced was determined by the iodide method [18-19]. Equation (1) is used for COD calculation to eliminate H_2O_2 interference [20].

$$COD_{(mg/L)} = COD_{(analyzed)} - a \times b \quad (1)$$

Where *a* is the remaining H_2O_2 concentration (mg/L) in the sample and *b* value is the correction factor which is 0.25. In the experiments, the effect of the initial pH value of wastewater (3.5, 6.5, 7.5, and 8.5), applied current (5 A, 7.5 A, 10 A and 15 A), and supporting electrolyte concentration (0.05 M, 0.1 M, 0.2 M and 0.3 M) on COD removal was investigated.

3. Results

3.2. Effect of initial pH

The effect of wastewater initial pH value was investigated for 3.5, 6.5, 7.5, and 8.5. Fixed operational parameters are; applied current: 10 A, air flow rate: 2 L/min, NaCl: 0.2 M, and reaction time: 60 min. COD removal yields are shown in Table 1.

Table 1. COD removal yields at different initial pH values

pH: 3.5	pH: 6.5	pH: 7.5	pH: 8.5
COD removal: 74%	COD removal: 95%	COD removal: 62%	COD removal: 77%

The pH value is a very important parameter in the peroxyelectrocoagulation process as it is in the classical electrocoagulation process. As can be seen in the table, the efficiency is highest when the pH value is 6.5, and the COD removal efficiency is low at acidic and basic pH values. Hydroxide ions produced at acidic pH values precipitate, causing insufficient iron hydroxide formation [21]. This situation causes low removal efficiency in the coagulation process. On the other hand, unsuitable soluble iron hydroxide ($Fe(OH)_4^-$) formation occurs in coagulation at basic pH values [21]. In addition, less iron dissolution occurs (less flock formation) due to the layer formed on the iron plate, and the removal efficiency is also low in this case. At pH 6.5, $Fe(OH)_3$ is formed, which is the most effective form of iron for coagulation [22]. For this reason, it was assumed that the most active pH value was 6.5, and this value was kept constant in subsequent trials. The concentration of H_2O_2 produced is affected by the pH value. The concentration of produced H_2O_2 at low pH values has been reported as advantageous in the literature [16] Alkaline and neutral pH values are disadvantageous as a result of the decomposition of H_2O_2 to HO_2 (Equations 2 and 3). In this study, the inability to obtain high efficiency in acidic conditions may be explained by the electrocoagulation process being dominant over the peroxidation process in the peroxyelectrocoagulation process.

$$O_2 + H_2O + 2e^- \rightarrow HO_2^- + OH^- \quad (2)$$

$$2H_2O_2 \rightarrow 2H_2O + O_2 \quad (3)$$

3.3. Effect of applied current

The effect of wastewater applied current was investigated for 5 A, 7.5 A, 10 A, 15 A. Fixed operational parameters are; initial pH: 6.5, air flow rate 2 L/min, NaCl: 0.2 M, and reaction time: 60 min. COD removal yields are shown in Table 2.

Table 2. COD removal yields at different applied currents

5 A	7.5 A	10 A	15 A
COD removal: 53%	COD removal: 73%	COD removal: 95%	COD removal: 94%

While the applied current increased from 5 A to 10 A, a clear increase was observed in the COD removal efficiency. However, when the applied current increases from 10 A to 15 A, there is stability in the removal efficiency. As the applied current increases, more iron is dissolved from the anode and more $Fe(OH)_3$ is formed, and more H_2O_2 production is also supported [16]. The stable COD value observed at 15 A may indicates that there is sufficient iron hydroxide formation at 10 A. For this reason, the optimum applied current was determined as 10 A .

3.4. Effect of supporting electrolyte concentration

The effect of supporting electrolyte concentration was investigated for 0.05 M, 0.1 M, 0.2 M, 0.3 M NaCl. Fixed operational parameters are; initial pH: 6.5, applied current: 10 A, air flow rate: 2 L/min, and reaction time: 60 min. COD removal yields are shown in Table 3.

Table 3. COD removal yields at different supporting electrolyte concentrations

0.05 M	0.1 M	0.2 M	0.3 M
COD removal: 80%	COD removal: 82%	COD removal: 95%	COD removal: 83%

As can be seen from Table 3, COD removal efficiency increased as NaCl concentration increased, but COD removal efficiency decreased at concentration above 0.2 M NaCl concentration. Increasing dose of NaCl causes the formation of OCl^- (at alkaline pH) and $HOCl^-$ (at acidic pH) which only results in more organic matter oxidation [23]. However, higher concentrations of NaCl caused the accumulation of ferric hydroxide film on the electrode surface, which caused resistance, resulting in low COD removal [21]. For this reason, the optimum NaCl concentration was chosen as 0.2 M.

4. Conclusion

In this study, wastewater from a tannery operating in Malatya province was investigated on COD removal by peroxyelectrocoagulation method in a batch system. Low COD removal was observed in acidic and alkaline values of wastewater initial pH value, while increased applied current had a positive contribution to COD removal. In addition, a decrease was observed in the support electrolyte concentration at dosing above the optimum dose may be due to the accumulation of ferric hydroxide film on the electrode surface in COD removal. The optimum operational parameters were determined as initial pH value of 6.5, applied current of 10 A, and NaCl concentration of 0.2 M. Under these conditions, the COD removal yield was calculated as 95%. It can be said that the peroxyelectrocoagulation method is suitable for COD removal from tannery wastewater.

5. Acknowledgements

The authors would like to thank the Van Yuzuncu Yil University Department of Environmental Engineering for laboratory facilities.

6. References

[1] Mustapha S, Tijani JO, Ndamitso MM, Abdulkareem SA, Shuaib DT, Mohammed AK, Sumaila AJSR. "The role of kaolin and kaolin/ZnO nanoadsorbents in adsorption studies for tannery wastewater treatment". Scientific Reports, 10(1), 13068, 2020.

[2] Masindi V, Tekere M, Foteinis S. "Treatment of real tannery wastewater using facile synthesized magnesium oxide nanoparticles: Experimental results and geochemical modeling". Water Resources and Industry, 29, 100205, 2023.

[3] Elabbas S, Ouazzani N, Mandi L, Berrekhis F., Perdicakis M, Pontvianne S, Pons MN, Lapicque F, Leclerc JP. "Treatment of highly concentrated tannery wastewater using electrocoagulation: Influence of the quality of aluminium used for the electrode". Journal of Hazardous Materials, 319, 69-77, 2016.

[4] Chhikara, S, Hooda A, Rana L, Dhankhar, R. "Chromium (VI) biosorption by immobilized Aspergillus niger in continuous flow system with special reference to FTIR analysis". Journal of Environmental Biology, 31(5), 561-566, 2010.

[5] Daneshvar E, Zarrinmehr MJ, Koush M, Hashtjin AM, Saratale GD, Maiti A, Vithanage M, Bhatnagar A. "Hexavalent Chromium Removal from Water by Microalgal-Based Materials: Adsorption, Desorption and Recovery Studies". Bioresource Technology, 293, 122064, 2019.

[6] Urbina-Suarez NA, Machuca-Martinez F, Barajas-Solano AF. "Advanced oxidation processes and biotechnological alternatives for the treatment of tannery wastewater". Molecules, 26(11), 3222, 2021.

[7] Montalvao MF, De Souza JM, Guimaraes ATB, De Menezes IPP, Da Silva Castro AL, De Lima Rodrigues AS, Malafaia G. "The genotoxicity and cytotoxicity of tannery effluent in bullfrog (Lithobates catesbeianus)". Chemosphere, 183, 491-502, 2017.

[8] Tigini V, Giansanti, P, Mangiavillano, A, Pannocchia, A, Varese, GC. "Evaluation of toxicity, genotoxicity and environmental risk of simulated textile and tannery wastewaters with a battery of biotests". Ecotoxicology and Environmental Safety, 74(4), 866-873, 2011.

[9] Zhao J, Wu Q, Tang Y, Zhou J, Guo H. "Tannery wastewater treatment: conventional and promising processes, an updated 20-year review". Journal of Leather Science and Engineering, 4(1), 10, 2022.

[10] De Nicola E, Meriç S, Della Rocca C, Gallo M, Iaccarino M, Manini P, Petruzzelli D, Belgiorno V, Cheggour M, Di Gennaro A, Moukrim A, Tünay O, Pagano G. "Wastewater toxicity of tannin- versus chromium-based leather tanneries in Marrakesh, Morocco". Archives Environmental Contamination Toxicology, 53(3), 321–328, 2007.

[11] Fernandez-Medrano V, Cuartas-Uribe B, Bes-Pia MA, Mendoza-Roca JA. "Application of nanofiltration and reverse osmosis membranes for tannery wastewater reuse". Water, 14(13), 2035, 2022.

[12] Appiah-Brempong M, Michelle Korkor Essandoh H, Yaw Asiedu N, Kwame Dadzie S, Yao Momade F. "Performance Optimization of Chemical and Green Coagulants in Tannery Wastewater Treatment: A Response Surface Methodology

Approach". Journal of Optimization, 2023.
[13] Merzouki M, Kachkoul R, Belhassan H, Miyah Y, Amakdouf H, Elmountassir R, Lahrichi A. "Fixed-bed adsorption of tannery wastewater pollutants using bottom ash: An optimized process". Surfaces and Interfaces, 22, 100868, 2021.
[14] Villasenor-Basulto DL, Picos-Benitez A, Pacheco-Alvarez M, Perez T, Bandala E. R, Peralta-Hernandez JM. "Tannery wastewater treatment using combined electrocoagulation and electro-Fenton processes. Journal of Environmental Chemical Engineering, 10(2), 107290, 2022.
[15] Suman H, Sangal VK, Vashishtha M. "Treatment of tannery industry effluent by electrochemical methods: A review". Materials Today: Proceedings, 47, 1438-1444, 2021.
[16] Ozturk D. "Fe_3O_4/Mn_3O_4/ZnO-rGO hybrid quaternary nano-catalyst for effective treatment of tannery wastewater with the heterogeneous electro-Fenton process: Process optimization". Science of The Total Environment, 828, 154473, 2022.
[17] Eaton AD, Clesceri LS, Rice E, Greenbaerg AE, Franson MAH. "Standard Methods for Examination of Water and Wastewater". Centennial Edition, American Public Health Association (APHA), Washington, DC, USA. 2005.
[18] Wang A, Qu J, Ru J, Liu H, Ge J. "Mineralization of an azo dye Acid Red 14 by electro-Fentons reagent using an activated carbon fiber cathode". Dyes Pigments 65(3), 227-233, 2005.
[19] Fayazi M, Ghanei-Motlagh M. "Electrochemical mineralization of methylene blue dye using electro-Fenton oxidation catalyzed by a novel sepiolite/pyrite nanocomposite". International Journal of Environmental Science Technology, 17, 4541–4548, 2020.
[20] Torun FE, Cengiz İ, Kul S. "Zeytin karasuyunun ileri oksidasyon prosesleri ile arıtımının incelenmesi". Journal of the Institute of Science and Technology, 10(3), 1597-1606, 2020
[21] Eryuruk K, Un UT, Ogutveren UB. "Electrochemical treatment of wastewaters from poultry slaughtering and processing by using iron electrodes". Journal of Cleaner Production, 172, 1089-1095, 2018.
[22] Mariah GK, Pak KS. "Removal of brilliant green dye from aqueous solution by electrocoagulation using response surface methodology". Materials Today: Proceedings, 20, 488-492, 2020.
[23] Costa CR, Montilla F, Morallon, E. Olivi P. "Electrochemical oxidation of acid black 210 dye on the boron-doped diamond electrode in the presence of phosphate ions: Effect of current density, pH, and chloride ions". Electrochimica Acta, 54(27), 7048-7055, 2009.

International Conference on Advances and Innovations in Engineering

Effect of Titanium on High Temperature Properties of NiAl-34Cr Eutectic Alloy Produced by Electric Current Assisted Sintering

Nuri ERGİN[20], Cihan ÇEPER[2], Ahmet ŞİMŞEK[3], Necati KOÇAK[4], Özkan ÖZDEMİR[5]

[1,2,3,4,5]Sakarya University of Applied Sciences, Sakarya, Türkiye.
[1]nergin@subu.edu.tr, [3]ahmetsimsek@subu.edu.tr, [4]necatikocak@subu.edu.tr, [5]oozdemir@subu.edu.tr,

Abstract
NiAl-34Cr-xTi (x = at.% 1, 3 and 5) eutectic alloys were produced by electric current assisted sintering (ECAS) method in the current range of 3500-4200 A with a waiting time of 47 minutes. Microstructure and phase investigations of the obtained samples were carried out with the help of scanning electron microscope (SEM-EDS) and x-ray diffraction analysis (XRD). In order to determine the effect of Ti element added to NiAl-34Cr eutectic alloy at high temperatures, oxidation and corrosion tests were carried out at 800, 900 and 1000°C for 165 hours (11 hours-15 cycles) in open atmosphere environment and 25% K_2SO_4 and 75% Na_2SO_4 salt environment. After hot corrosion and oxidation experiments, microstructural analyses of the samples were performed by SEM-EDS studies, phase structures were examined by XRD analyses and activation energy values were calculated by performing weight changes and kinetic analyses. It was determined that the activation energy values of the alloys in the oxidation environment decreased from 169 kJ/mol to 152 kJ/mol and the activation energy values in the corrosion environment decreased from 155kJ/mol to 141 kJ/mol depending on the increase in Ti content. It was observed that the activation energy decreased with the increase in the amount of Ti in the alloy.
Keywords: NiAl-34Cr eutectic alloy, High Temperature Proporties, Electric Current Activated Sintering

1. Introduction

NiAl, which belongs to the group of intermetallic materials obtained by two or more different pure metals forming crystalline compounds or solid solutions, has a good potential for materials used at high temperatures such as jet engines and gas turbines with its low density (5.95 g/cm^3), high melting point (1638°C), excellent oxidation resistance at high temperatures (up to 1400°C) and high elastic modulus properties [1,2]. However, NiAl's insufficient strength at high temperatures, low ductility and fracture toughness at room temperature limit its use and necessitate the need to improve its mechanical properties. It is known that various researches have been carried out to improve these weak properties of NiAl. One of the studies is to obtain eutectic alloys with other phases that have a more ductile structure than NiAl and to improve the ductility by forming composite structures by controlled cooling. Another recent study is the development of directional solidification eutectics to improve the properties of NiAl at high temperatures. For this purpose, the possible eutectic transformations of refractory metals such as Cr, Mo, W, Ta and Nb with NiAl were investigated and it was revealed that the addition of these refractory metals to the NiAl structure increases both the strength of NiAl at high temperatures and its toughness at room temperature. For example, compared to the polycrystalline NiAl alloy obtained by casting method, it is seen that the room temperature fracture strengths of directionally solidified NiAl-34Cr or NiAl-28Cr-6Mo alloys increase 3-4 times [3-7].

Different production methods such as melting and casting, self-propagating high-temperature synthesis, hot extrusion reaction synthesis, powder metallurgy and electric current assisted sintering have been tried for the production of intermetallic compounds [8]. Electric current assisted sintering (ECAS), which has developed rapidly in recent years, is a production method with remarkable features compared to traditional production methods. ECAS method, where the starting materials can be powder or materials with a certain bulk density, is a production method that enables the sintering of materials with the help of mechanical pressure and electric current [9,10].

[20]Corresponding author

In this study, NiAl-34Cr-xTi eutectic alloys were produced by electric current assisted sintering method by adding Ti to NiAl-34Cr alloy at the rates of atomically 1%, 3% and 5%, respectively. The effect of Ti addition on the eutectic alloy was investigated. Phase analyses and morphologies of the produced samples were determined by scanning electron microscopy (SEM-EDS) and X-ray diffraction analysis (XRD) methods. In addition, hot oxidation and corrosion tests were carried out to determine the behaviour of the manufactured products at high temperatures.

2. Experimental

In the first stage of the experimental studies, a mixture was prepared from the powders whose properties are given in Table 1 at the stoichiometric ratios given in Table 2. In order to obtain a homogeneous mixture, the mixture was mixed in a ball mill for 12 hours by using a zirconia ball and with a ball/powder ratio of 2/1. The prepared powder mixtures were placed in a die with an inner diameter of 20 mm and a height of 50 mm and shaped by pre-pressing under 50 MPa pressure. Then, these samples were sintered in the mold in open atmosphere under 50 MPa single axis pressure and using an electric current of 3500-4200 A with an electric current assisted sintering device for 47 minutes. As a result of the sintering process, samples with a diameter of 20 mm and a height of 5 mm were obtained.

Table 1. Properties of the powders used in the experiments.

Material	Purity (%)	Powder Size (μm)	Manufacturer	Product Code
Aluminum	99,5	7-15	Alfa Aesar	CAS: 7429-90-5
Nickel	99,8	3-7	Goodfellow	NI006021
Chromium	99,8	1-5	Alfa Aesar	CAS: 7440-47-3
Titanium	99,5	≤40	Alfa Aesar	CAS: 7440-32-6

Table 2. Compositions of the produced samples.

Alloy Elements (at.%)				
Composition	Ni	Al	Cr	Ti
1. Alloy	32,5	32,5	34	1
2. Alloy	31,5	31,5	34	3
3. Alloy	30,5	30,5	34	5

The sintered samples were grinded with SiC sandpaper up to 1200 meshes for metallographic examinations and then polished with 0,3 μm alumina solution. The morphology of the polished samples were examined using a JOEL JSM-6060LV scanning electron microscope (SEM) and elemental analysis was performed by point EDS analysis of the different phase regions observed. In addition, XRD analysis was performed using Cu Kα (λ=1.5418 °A) beams in RIGAKU D MAX 2200 PC brand x-ray diffractometer for the analysis of the obtained phases.

The oxidation and corrosion behaviours of the prepared samples were investigated at high temperature. Before both processes, the surface areas of the samples were measured using SolidWorks software and the initial weights were measured with an electronic balance capable of measuring 10-5 g precision. In order to determine the high temperature oxidation behaviour, the samples were heated in an open atmosphere furnace at 800, 900 and 1000°C for a total of 165 hours (15 cycles). Oxidation experiments were carried out in cycles, each cycle being 11 hours. After each cycle, the weight change of the samples was determined and the next cycle was started. In addition, in order to determine the high temperature corrosion behaviour, the specimens embedded in molten salt were kept for 165 hours (11 hours-15 cycles) at temperatures of 800, 900 and 1000°C and in corrosion environment with a composition of wt.75% Na_2SO_4 + wt.25% K_2SO_4. After each cycle, the samples were boiled in water for 5 minutes to be desalinated and after drying, the weight change was determined and the next cycle was started. SEM-EDS and XRD analyses were performed to examine in detail the layers formed on the surfaces of the samples as a result of oxidation and corrosion experiments.

The weight changes (mg/mm^2) of the samples exposed to hot oxidation and corrosion tests were determined for all 3 temperatures. The parabolic rate constant (kp) values of the samples were calculated using the formula given in Equation 2.1. Activation energy values were calculated using the formula given in Equation 2.2.

$$\left(\frac{\Delta m}{A}\right)^2 = kp.t \qquad (2.1)$$

In the Equation 1, Δm is weight change (mg), A is surface area (mm^2) and kp is parabolic rate constant (gr^2/cm^4.sec).

$$\ln kp = ko.e^{-\frac{Q}{R.T}} \qquad (2.2)$$

In the Equation 2, T is absolute temperature (K), Q is activation energy (kJ/mol), ko is Arrherius Equation constant and R is the gas constant with a value of 8.314 J/mol.K [11].

3. RESULTS AND DISCUSSION

3.1. Material Characterization

SEM images of the alloys produced by sintering the powder mixtures prepared by adding Ti powder to NiAl-34Cr eutectic alloy at ratios of at.1%, 3% and 5% by ECAS method and EDS analysis results are given in Figure 1-3. The SEM images are examined and it is observed that the samples consist of light and dark coloured structures. The EDS analyses of these structures were examined and it was determined that the samples consisted of Ni-Al-rich phase, which is observed as a matrix structure and has a flat surface appearance, Cr-rich phase, which appears protruding around the grain boundaries, and Ni-Al-Ti phases that appear lighter in colour. It was observed that the Ni-Al-Ti phase in the structure is compatible with the eutectic alloy phases NiAl (A2) and Cr (B2). According to the analysis results, the average composition of the Ni-Al-Ti phase is atomically 30% Al, 23% Ti and 40% Ni. In the Al-Ti phase diagram, the maximum 1.2% wt. Ti and Ni-Ti phase diagram, the maximum 10.6% wt. Ti is dissolved. In the Ti-Cr phase diagram, Cr solubility is 100%wt. at high temperatures and only 0.2%wt. in αTi at low temperatures [12].

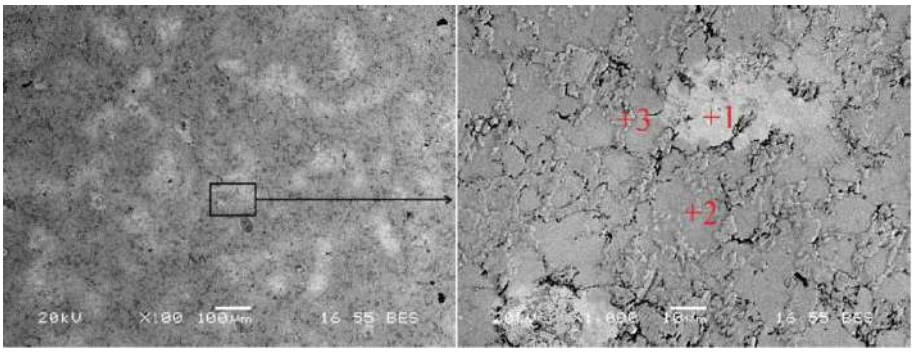

Element	1	2	3
Al	31,5	50,0	10,0
Ti	22,6	0,3	0,1
Cr	3,2	12,3	81,9
Ni	42,7	37,4	8,0

Figure 1. SEM image and EDS analysis values of NiAl-34Cr-1Ti alloy (at. %).

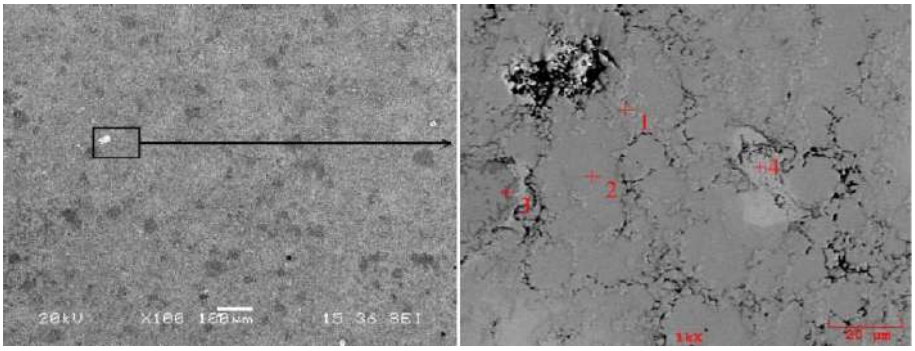

Element	1	2	3
Al	3,7	57,2	36,9
Ti	0,1	0,3	46,3
Cr	91,7	2,1	4,4
Ni	4,5	40,5	12,5

Figure 2. SEM image and EDS analysis values of NiAl-34Cr-3Ti alloy (at. %).

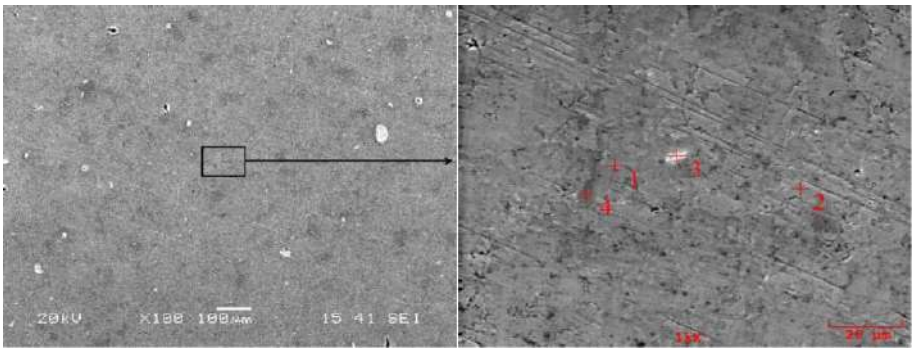

Element	1	2	3
Al	41	17	60,2
Ti	0,9	0,1	0,3
Cr	31,5	79	2,3
Ni	26,6	3,9	37,3

Figure 3. SEM image and EDS analysis values of NiAl-34Cr-5Ti alloy (at. %).

XRD patterns obtained using x-ray diffraction method for the determination of the phases formed in NiAl-34Cr-xTi eutectic alloys after sintering are given in Figure 4. Hagihara et al. [13] reported that Heusler phase (L2 -Ni_{12} AlTi) was detected in the Ti added eutectic alloy with an atomic composition of 47% Ni + 30.8% Al + 3.2% Cr + 0.09% Mo + 18.9% Ti. Although the composition of the structure observed as the light coloured phase in the NiAl-34Cr-1Ti eutectic alloy produced in this study (at. 42.7%Ni + 31.5Al + 3.2Cr + 22.6Ti) is very close, the Heusler phase could not be detected in XRD analysis. Li et al. [14] reported that Ti added to the eutectic alloy causes the formation of Ni_2AlTi Heusler phase and β-TiM (M=Cr,Ni) solid solution and these phases increase the normal temperature strength and ductility. In this study, in the XRD analysis of the eutectic alloy to which Ti was added (Figure 4), TiNi phase was detected as a minor phase with eutectic phases (NiAl-A2 (cI2) and Cr-B2 (cP2)) and it was observed that the TiNi peak intensity increased with the increase in the amount of Ti element added.

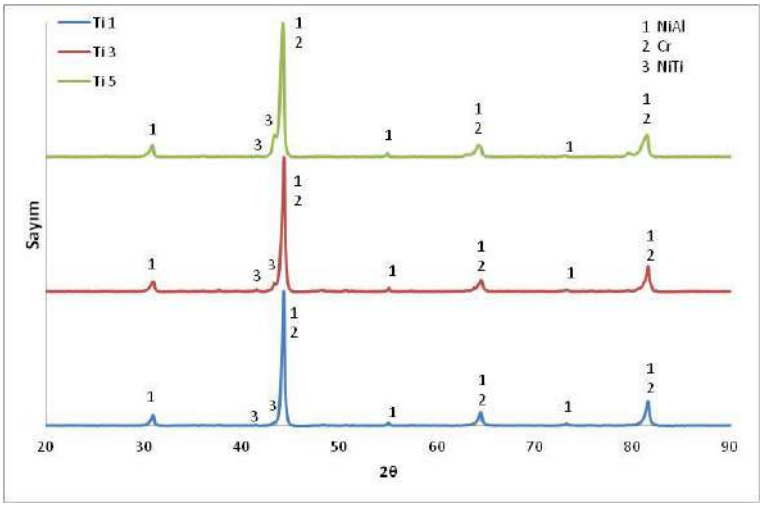

Figure 4. XRD analysis of NiAl-34Cr eutectic alloy with 1, 3 and 5 % atomic addition of Ti alloying elements.

3.2. Oxidation Behaviors

Many metal-based materials are not stable under open atmosphere conditions and tend to oxidise by forming lower free energy compounds by giving electrons to oxygen in the air [11]. As a result of this reaction of metals with oxygen, oxide layers are formed on their surfaces [15]. A formed oxide layer grows by diffusion of metal and oxygen ions into each other. Formed oxide layers are divided into two as protective and non-protective oxide layers. Metals that have a tendency to react with oxygen must have a protective layer on their surfaces in order to be resistant to oxidation at high temperatures. The type of oxide layer formed depends on the volume of oxide formed on the metal surface relative to the base metal. If the ratio of oxide volume to metal volume is less than 1, it indicates that a non-protective thin oxide layer is formed on the metal surface. If the oxide volume is more than 2 times the metal volume, high stresses occur in the structure, causing the oxide layer to crack and spall. If the ratio of oxide volume to metal volume is between 1 and 2, the layer formed is protective and in this case oxidation can continue only by solid state diffusion [16,17]. This widely accepted approach to explain the oxidation behaviour of metals is called the Pilling-Bedworth ratio [11].

In order to investigate the oxidation behaviour of NiAl-34Cr eutectic alloy doped with 1, 3 and 5 at.%Ti added NiAl-34Cr eutectic alloys produced by electric current assisted sintering method were exposed to oxidation at 800, 900 and 1000°C in an open atmospheric furnace for a total of 165 hours (11 hours-15 cycles) to investigate their oxidation behaviour under high temperature conditions.

SEM-EDS microstructure images and analysis results of the surface obtained after cyclic oxidation of NiAl-34Cr-1Ti alloy at the specified temperatures are given in Figure 5 and Table 3. On the surface of the sample exposed to oxidation at 1000°C, a third phase formation was observed together with Cr-B2 and NiAl-A2 phases, and according to the EDS analysis result taken from point 1, it was determined that it was a phase consisting of Ti-Ni-O.

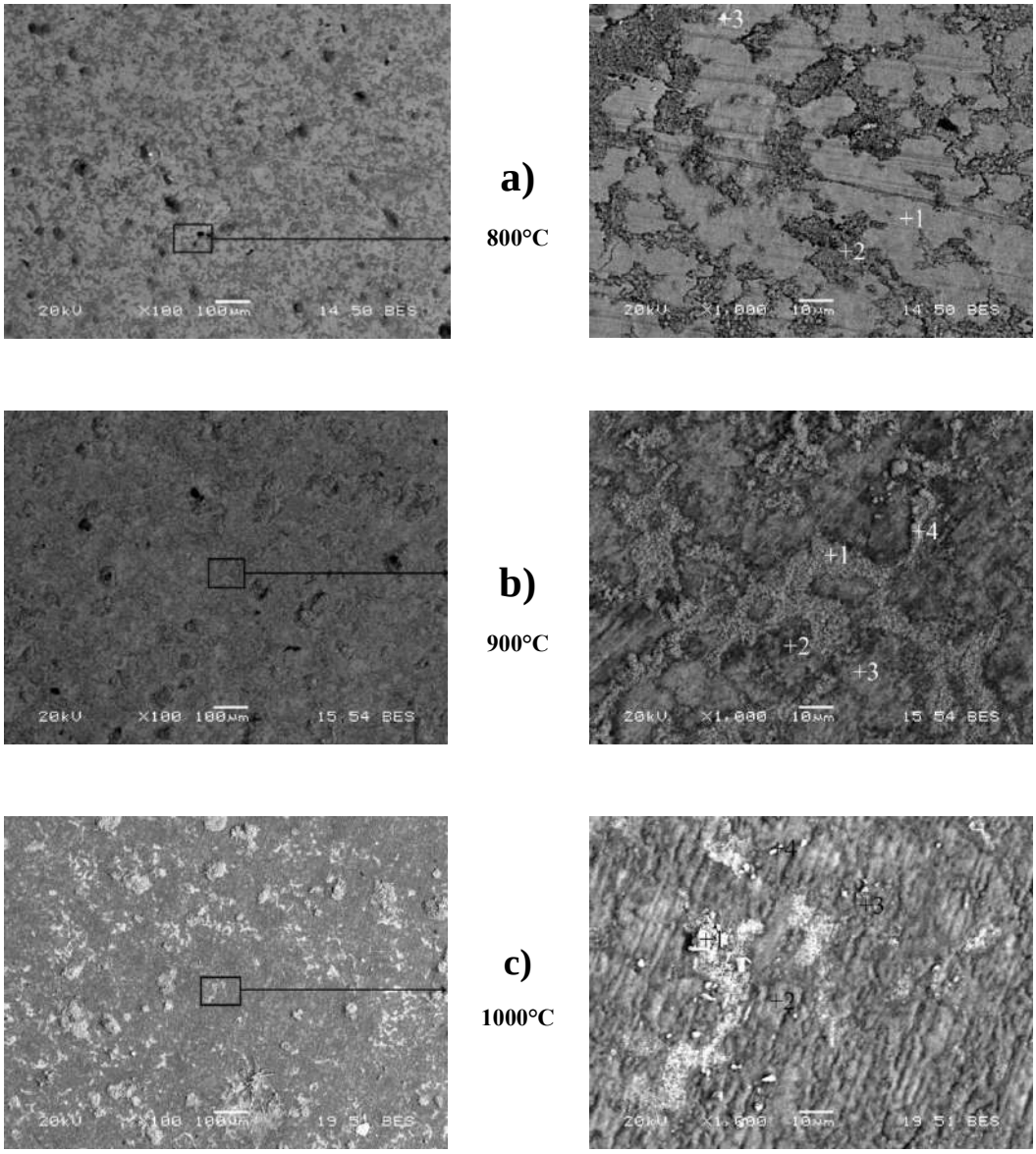

Figure 5.SEM images of NiAl-34Cr-1Ti alloy exposed to oxidation. a) 800°C, b) 900°C, c)1000°C

Table 3. EDS analysis values of exposed to oxidation NiAl-34Cr-1Ti alloy (at. %).

	800°C			900°C				1000°C			
Element	1	2	3	1	2	3	4	1	2	3	4
O	44,2	46,7	28,2	57,7	46,6	44,1	73,8	57,6	47,8	42,8	60,8
Al	30,4	22,1	41,0	7,9	45,0	34,8	6,1	4,6	42,7	39,4	24,9
Ti	0,1	0,1	0,1	0,2	0,1	0,1	0,6	18,1	0,1	0,1	9,6
Cr	6,7	17,0	3,2	33,8	4,3	6,5	18,4	3,6	3,7	7,1	2,4
Ni	18,6	14,1	27,5	0,4	4,0	14,5	1,1	16,1	5,7	10,6	2,3

SEM surface images of NiAl-34Cr-3Ti alloy are given in Figure 6. Surface morphology is similar to the alloy containing 1% Ti was observed, but needle-shaped structures were observed at 1000 °C. According to the point EDS analysis results taken from these regions and given as 1000 °C and 3rd point in Table 4, Ti rich oxide phase was observed.

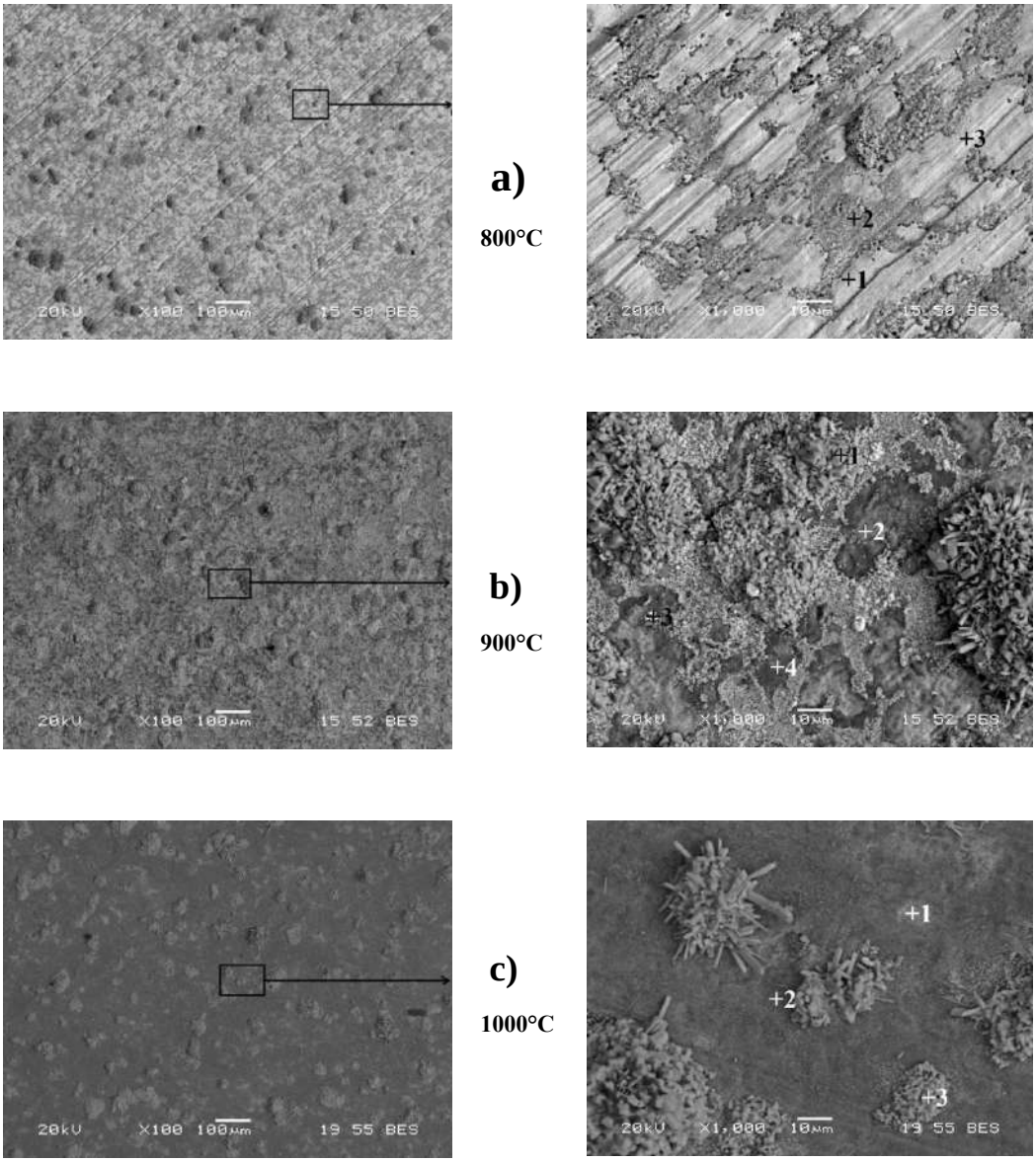

Figure 6. SEM images of NiAl-34Cr-3Ti alloy exposed to oxidation. a) 800°C, b) 900°C, c)1000°C

Table 4. EDS analysis values of exposed to oxidation NiAl-34Cr-3Ti alloy (at. %).

	800°C			900°C				1000°C		
Element	1	2	3	1	2	3	4	1	2	3
O	34,0	38,0	35,7	71,2	60,0	66,0	51,7	56,6	53,3	62,0
Al	35,7	16,8	29,0	0,4	32,2	13,8	45,0	21,2	33,1	7,0
Ti	0,2	0,2	0,3	26,5	0,2	0,3	0,3	0,4	2,7	25,0
Cr	5,1	43,0	17,6	1,7	7,1	19,1	2,4	21,5	10,6	5,2
Ni	25,0	2,0	17,4	0,2	0,5	0,8	0,6	0,3	0,3	0,8

The surface structures of the NiAl-34Cr-5Ti sample are given in Figure 7 and EDS analyses are given in Table 5 and it was found that the oxidation surface morphologies were similar to the alloy with 3% Ti addition. It was found that oxidation increased with increasing temperature in all three samples.

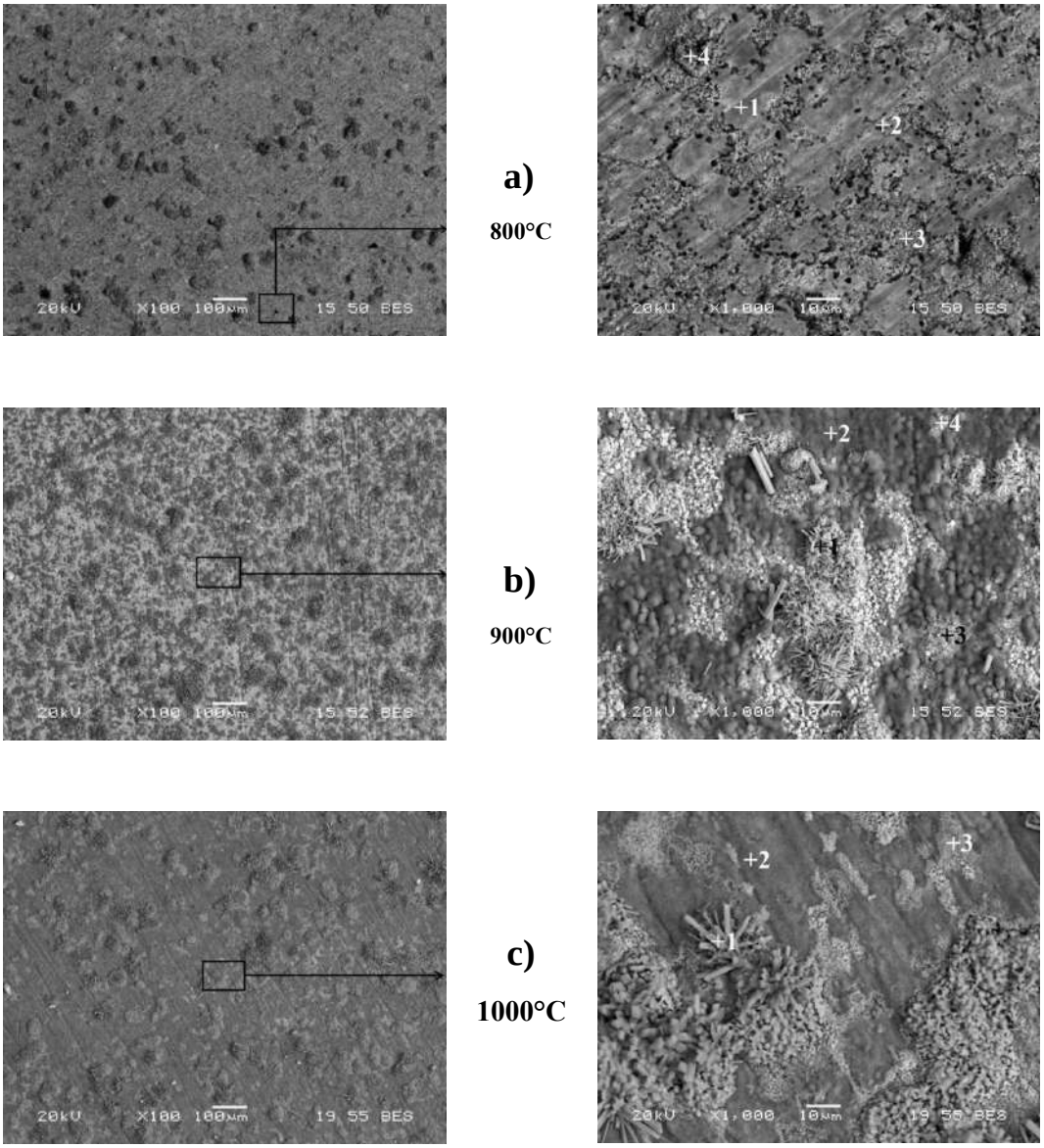

Figure 7. SEM images of NiAl-34Cr-5Ti alloy exposed to oxidation. a) 800°C, b) 900°C, c)1000°C

Table 5. EDS analysis values of exposed to oxidation NiAl-34Cr-5Ti alloy (at. %).

	800°C				900°C				1000°C		
Element	1	2	3	4	1	2	3	4	1	2	3
O	39,8	43,4	56,3	58,9	69,8	50,1	67,6	34,8	69,5	47,9	61,9
Al	41,5	28,9	10,5	6,6	9,2	46,8	11,9	24,0	5,5	36,9	18,5
Ti	0,1	0,1	0,2	20,6	10,0	0,2	5,2	0,3	21,8	0,2	0,3
Cr	3,7	22,0	30,9	13,0	10,3	2,0	14,4	37,5	2,8	11,4	18,1
Ni	14,9	5,6	2,1	0,9	0,7	0,9	0,9	3,4	0,4	3,6	1,2

In the XRD patterns taken from the oxidation surface of NiAl-34Cr-1Ti alloy given in Figure 8a, Cr_2O_3, Al_2O_3, NiO ve $(Al_{0,9}Cr_{0,1})_2O_3$ phases were detected at 800°C. At 900°C and 1000°C, unlike 800°C, TiO_2 phase was also observed. The XRD patterns of NiAl-34Cr-3Ti alloy shown in Figure 8b show that the alloy contains similar phases, but $Al_{0,9}Ni_{1,1}$ peaks were detected in addition to these phases at 900°C. In the NiAl-34Cr-5Ti alloy shown in Figure 8c, in addition to the phases identified in other alloys, Ni_3Al peaks were detected at 900°C and it was observed that these peaks were strengthened at 1000°C. Also, NiO peak is observed as the strongest at 1000°C.

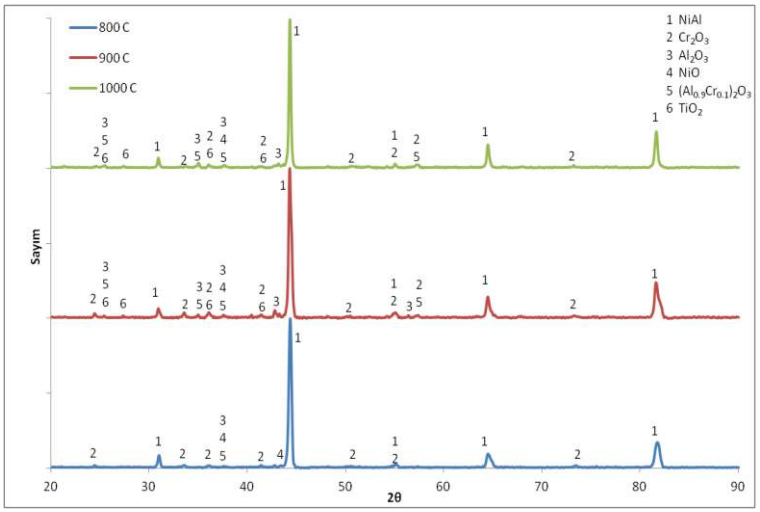

(a)

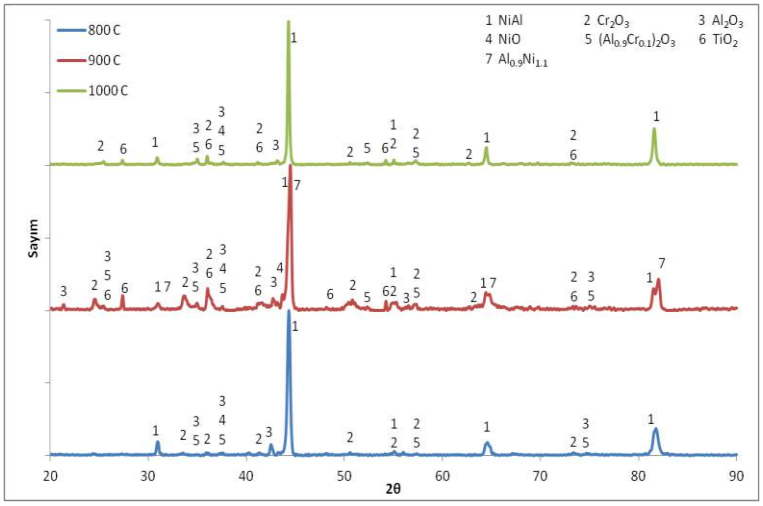

(b)

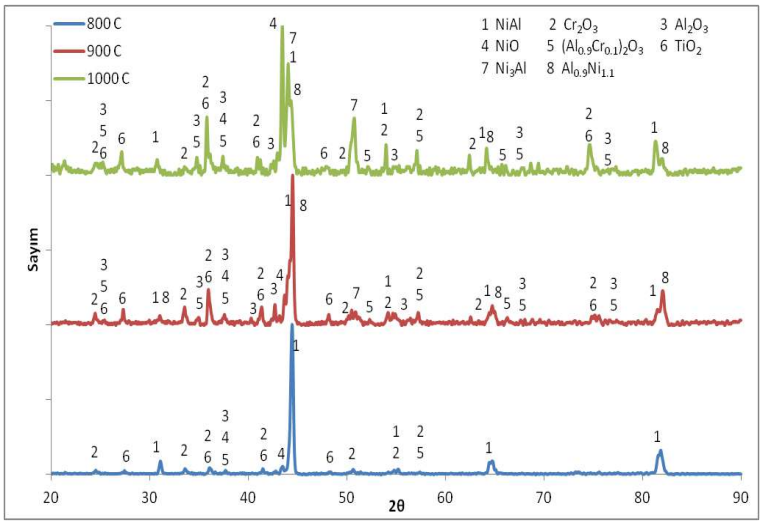

(c)

Figure 8. XRD analysis of NiAl-34Cr-xTi (at.%) alloy exposed to oxidation a)1Ti, b)3Ti, c)5Ti.

The weight changes per unit area of NiAl-34Cr eutectic alloys containing at.% 1, 3 and 5 Ti, which were exposed to oxidation for 165 hours, are given in Figure 9. It is seen that the slope of these graphs increases with increasing temperature, that is, increasing temperature promotes oxidation. The slope values of the obtained weight change graphs and the calculated parabolic rate constants are given in Table 6. It is also seen that increasing temperature and Ti content increase the parabolic rate constants.

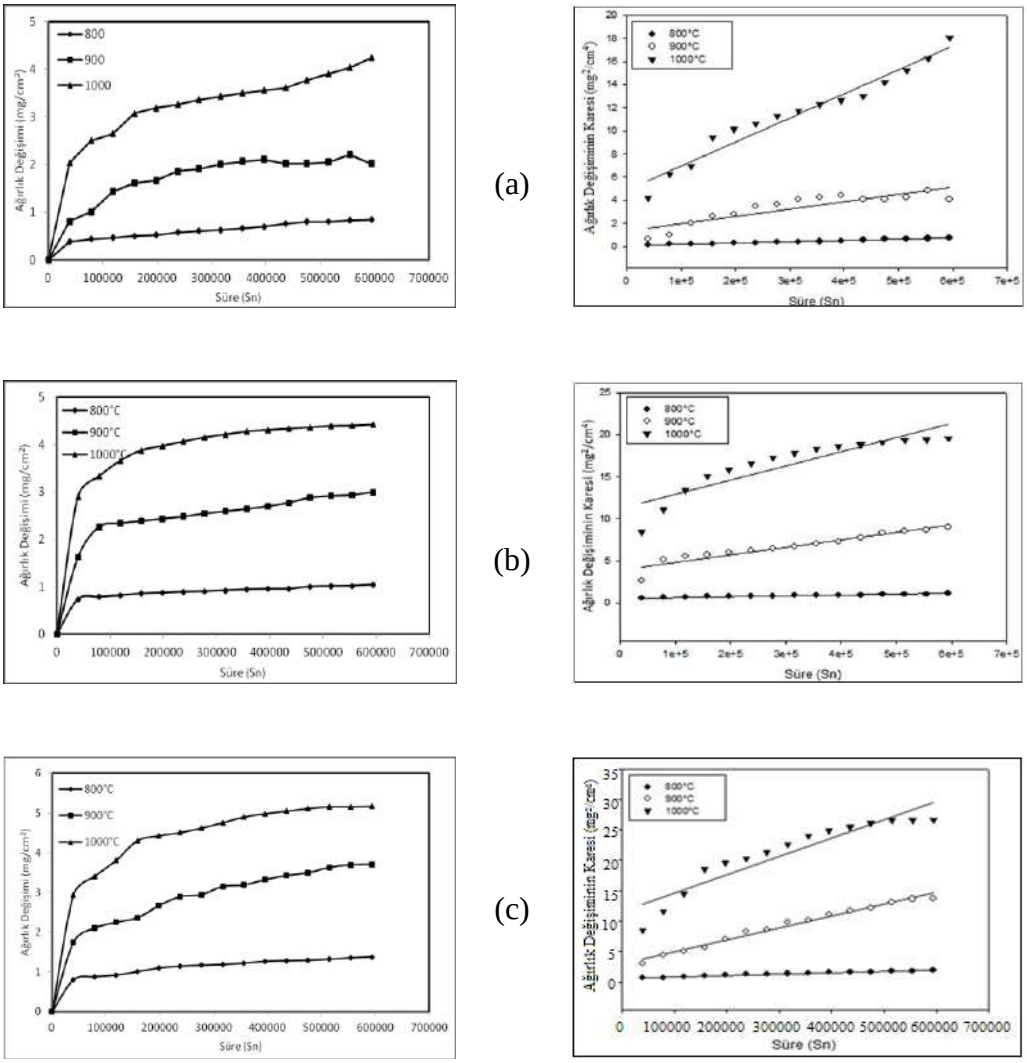

Figure 9. Time and temperature dependent weight plots of NiAl-34Cr-xTi (at.%) alloy exposed to oxidation a)1Ti, b)3Ti, c)5Ti.

Table 6. Temperature varying parabolic rate constants of NiAl-34Cr-xTi alloy exposed to oxidation.

Malzeme	Parabolic Rate Constants, kp (gr2/cm4.sec)		
	Temperature (°C)		
	800	900	1000
NiAl-34Cr-1Ti	1,1x10-12	6,3x10-12	21x10-12
NiAl-34Cr-3Ti	0,9x10-12	5,5x10-12	15x10-12
NiAl-34Cr-5Ti	2,2x10-12	20x10-12	31x10-12

The graphs of the change of the rate constant with time drawn according to the Arrhenius equation are listed in Figure 10, and the -Q/R and activation energy values calculated from the slope of these graphs are listed in Table 7. When the calculated activation energy values of NiAl-34Cr-xTi (at. x: 1, 3 and 5 %) alloys exposed to 165 h cyclic oxidation

are compared, it is seen that the increase in the amount of Ti in the alloy has a slight effect on the activation energy. This shows that titanium added to the alloy promotes oxide formation.

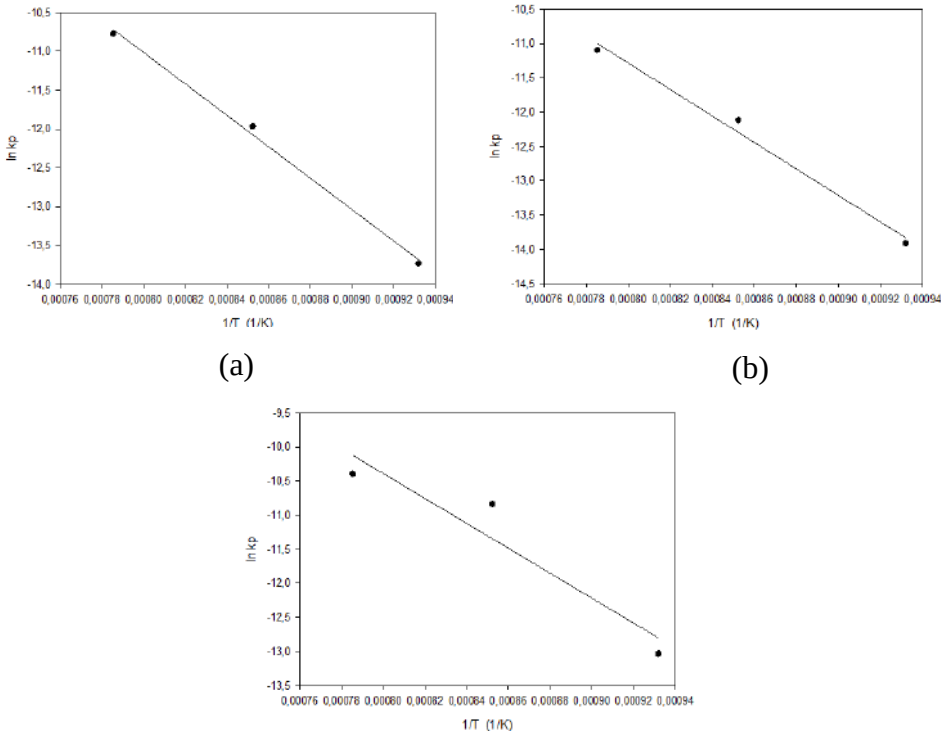

Figure 10. Arrhenius curves of NiAl-34Cr-xTi (at.%) alloy exposed to oxidation plotted depending on Ln kp and 1/T for a)1Ti, b)3Ti and c)5Ti.

Table 7. -Q/R and activation energy values of NiAl-34Cr-xTi (at.%) alloy exposed to oxidation.

Material	-Q/R	Activation energy (Q) kJ/mol
NiAl-34Cr-1Ti	20272,6	168,6
NiAl-34Cr-3Ti	19338,2	160,8
NiAl-34Cr-5Ti	18296,5	152,1

3.3. Hot Corrosion Behaviors

Hot corrosion tests of the produced samples were carried out cyclically in a salt mixture with 75% Na_2SO_4 and 25% K_2SO_4 by weight, at temperatures of 800, 900 and 1000°C for a total of 165 hours. SEM microstructure images taken from the surfaces of NiAl-34Cr-1Ti alloy as a result of corrosion tests are given in Figure 11 and EDS analysis results are given in Table 8.

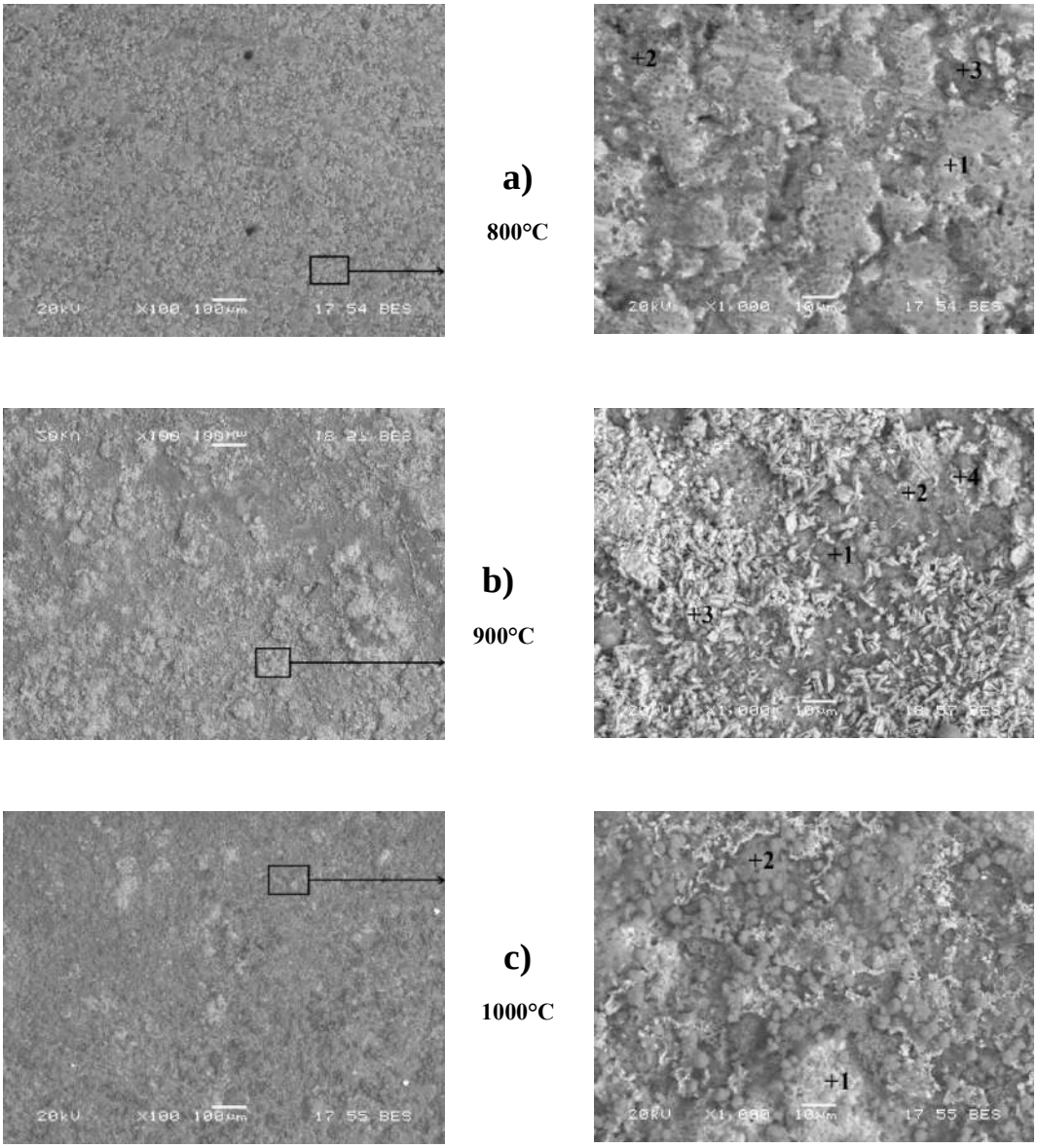

Figure 11. SEM images of NiAl-34Cr-1Ti alloy exposed to hot corrosion. a) 800°C, b) 900°C, c)1000°C

Table 8. EDS analysis values of exposed to hot corrosion NiAl-34Cr-1Ti alloy (at. %)

	800°C			900°C				1000°C	
Element	1	2	3	1	2	3	4	1	2
O	34,5	60,2	42,1	49,2	61,4	65,1	60,5	67,8	63,3
Al	39,6	29,2	28,8	42,4	25,3	3,7	19,4	1,7	13,9
Ti	0,1	0,1	0,1	0,2	0,1	0,3	0,1	2,5	0,7
Cr	1,6	9,2	25,4	8,0	13,0	30,5	19,1	27,8	21,8
Ni	24,2	1,3	3,6	0,2	0,2	0,4	0,9	0,2	0,3

SEM microstructure images taken from the surfaces of NiAl-34Cr-3Ti alloy as a result of corrosion tests are given in Figure 12 and EDS analysis results are given in Table 9.

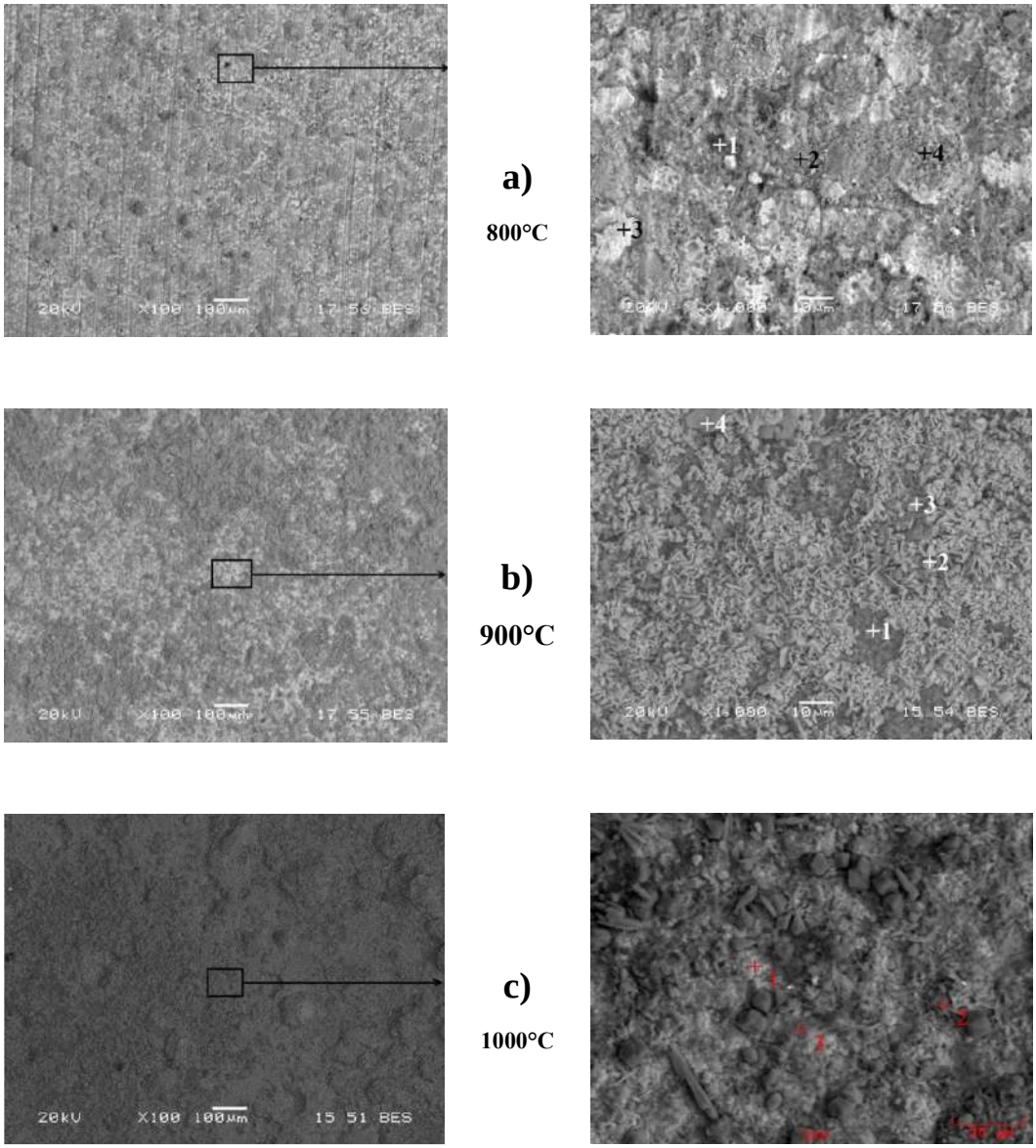

Figure 12. SEM images of NiAl-34Cr-3Ti alloy exposed to hot corrosion. a) 800°C, b) 900°C, c)1000°C

Table 9. EDS analysis values of exposed to hot corrosion NiAl-34Cr-3Ti alloy (at. %)

	800°C				900°C				1000°C		
Element	1	2	3	4	1	2	3	4	1	2	3
O	38,7	43,4	33,1	56,5	48,4	66,7	30,6	63,3	53,9	65,4	46,5
Al	24,1	25,1	41,5	14,6	42,5	10,7	7,1	6,3	9,1	13,8	43,5
Ti	0,4	12,5	0,3	25,0	0,4	1,1	2,5	1,4	1,0	1,7	1,0
Cr	16,4	2,9	1,7	2,6	7,8	20,9	58,6	28,2	35,4	18,1	8,4
Ni	20,4	16,1	23,4	1,3	0,9	0,6	1,2	0,8	0,6	1,0	0,6

SEM microstructure images taken from the surfaces of NiAl-34Cr-5Ti alloy as a result of corrosion tests at different temperatures are given in Figure 13 and EDS analysis results are given in Table 10. When the results are examined, small cavities in the form of spalling were observed on the surface at 800°C. At 900°C, it was determined that the amount of these cavities increased. At 1000°C, it was observed that the layer in the form of thin oxide film started to spall from the surface.

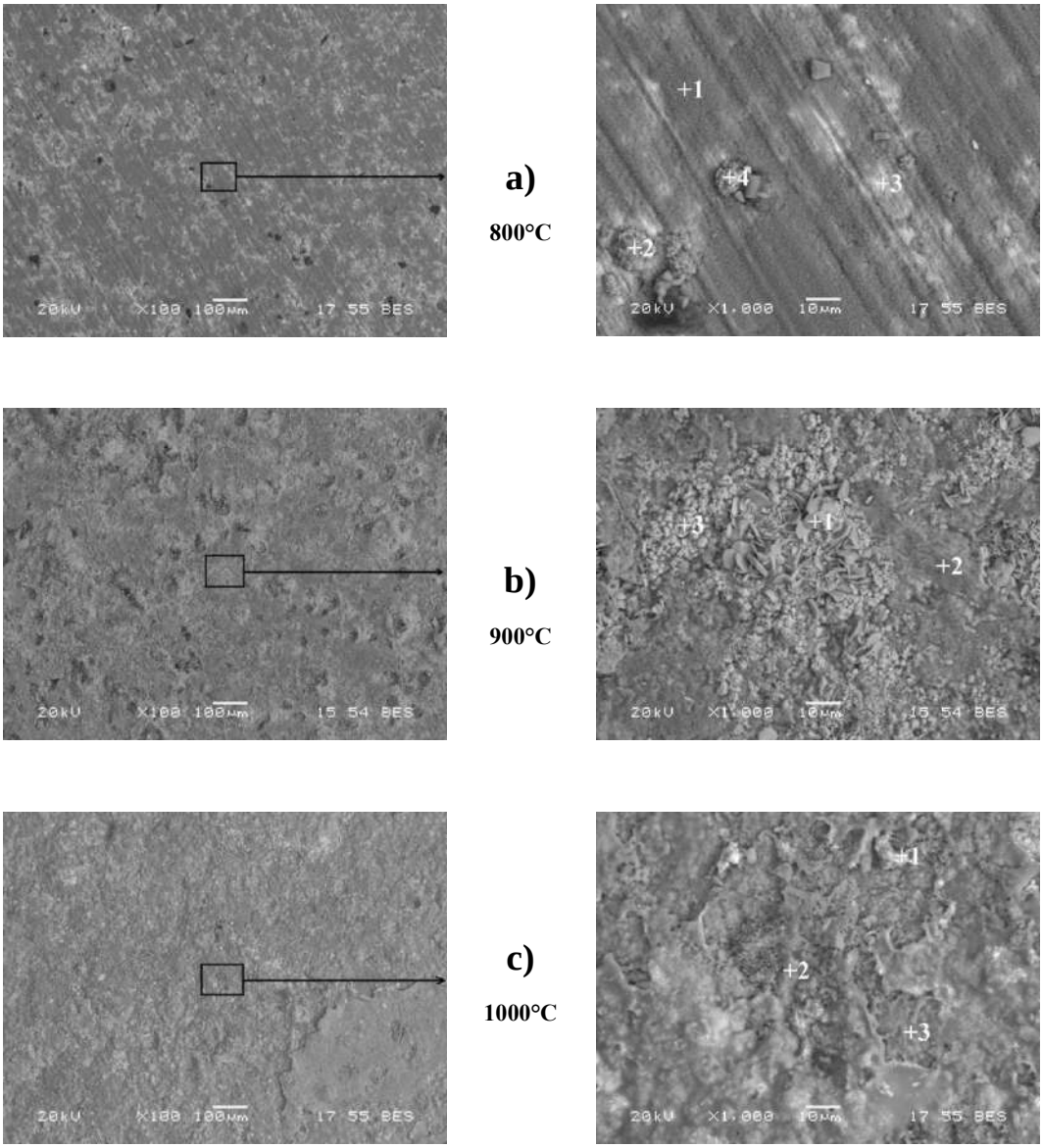

Figure 13. SEM images of NiAl-34Cr-5Ti alloy exposed to hot corrosion. a) 800°C, b) 900°C, c)1000°C

Table 10. EDS analysis values of exposed to hot corrosion NiAl-34Cr-5Ti alloy (at. %)

	800°C				900°C			1000°C		
Element	1	2	3	4	1	2	3	1	2	3
O	49,3	54,2	38,2	55,1	45,6	52,8	67,9	72,1	53,0	50,8
Al	46,6	26,6	36,4	18,2	14,0	34,8	4,2	11,7	36,9	42,7
Ti	0,1	18,0	1,3	25,7	2,4	0,6	0,9	0,1	0,1	0,1
Cr	1,0	0,6	23,3	0,3	36,9	11,6	26,7	14,5	3,2	6,1
Ni	3,0	0,6	0,8	0,7	1,1	0,2	0,3	1,6	6,8	0,3

XRD patterns taken to determine the phases formed on the surface as a result of corrosion of Ti added NiAl-34Cr eutectic samples are given in Figure 14 (a-c). In the XRD pattern taken from the sample surface exposed to corrosion at 800°C, NiAl, Cr_2O_3, Al_2O_3, NiO and $(Al_{0,9}Cr_{0,1})_2O_3$ phases were detected. At 900°C and 1000°C temperatures, unlike 800°C, $Ni_3(Al,Ti)$, Ni_3Al and $Al_{0.42}Ni_{0.58}$ phases were also detected. This shows that at 900°C and 1000°C, aluminium is intensively oxidised and consumed in the matrix and deviations from stoichiometry occur. Therefore, it is thought that nickel-rich phases are formed in the matrix.

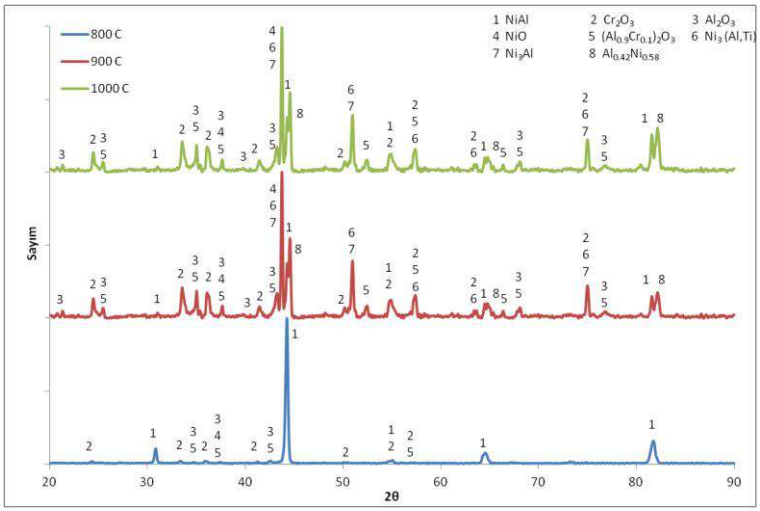

(a)

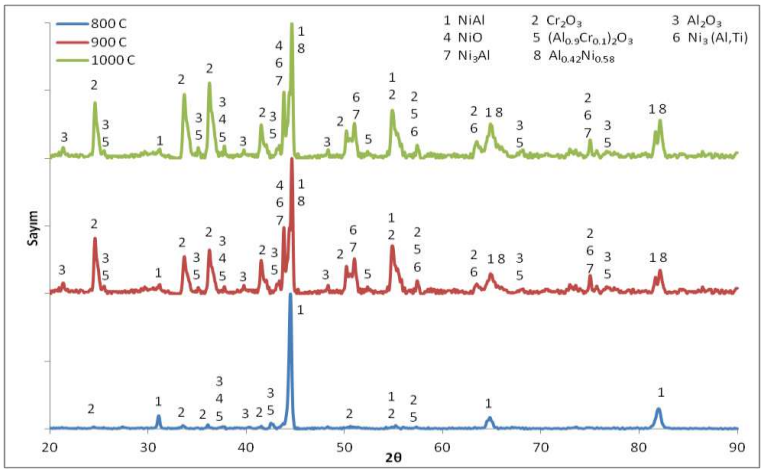

(b)

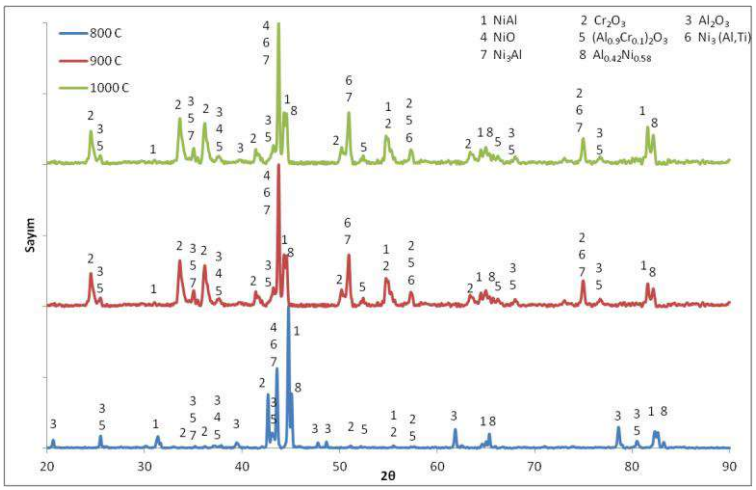

(c)

Figure 14. XRD analysis of NiAl-34Cr-xTi (at.%) alloy exposed to hot corrosion a)1Ti, b)3Ti, c)5Ti.

Weight change graphs per unit area of hot corroded NiAl-34Cr-xTi alloys depending on time and temperature are given in Figure 15(a-c), and parabolic rate constants calculated from the slope of these graphs are given in Table 11.

The graphs of variation with time of the rate constant drawn on the basis of the Arrhenius equation are listed in Figure 16(a-c) and the -Q/R and activation energy values calculated from the slope of the graphs are listed in Table 12.

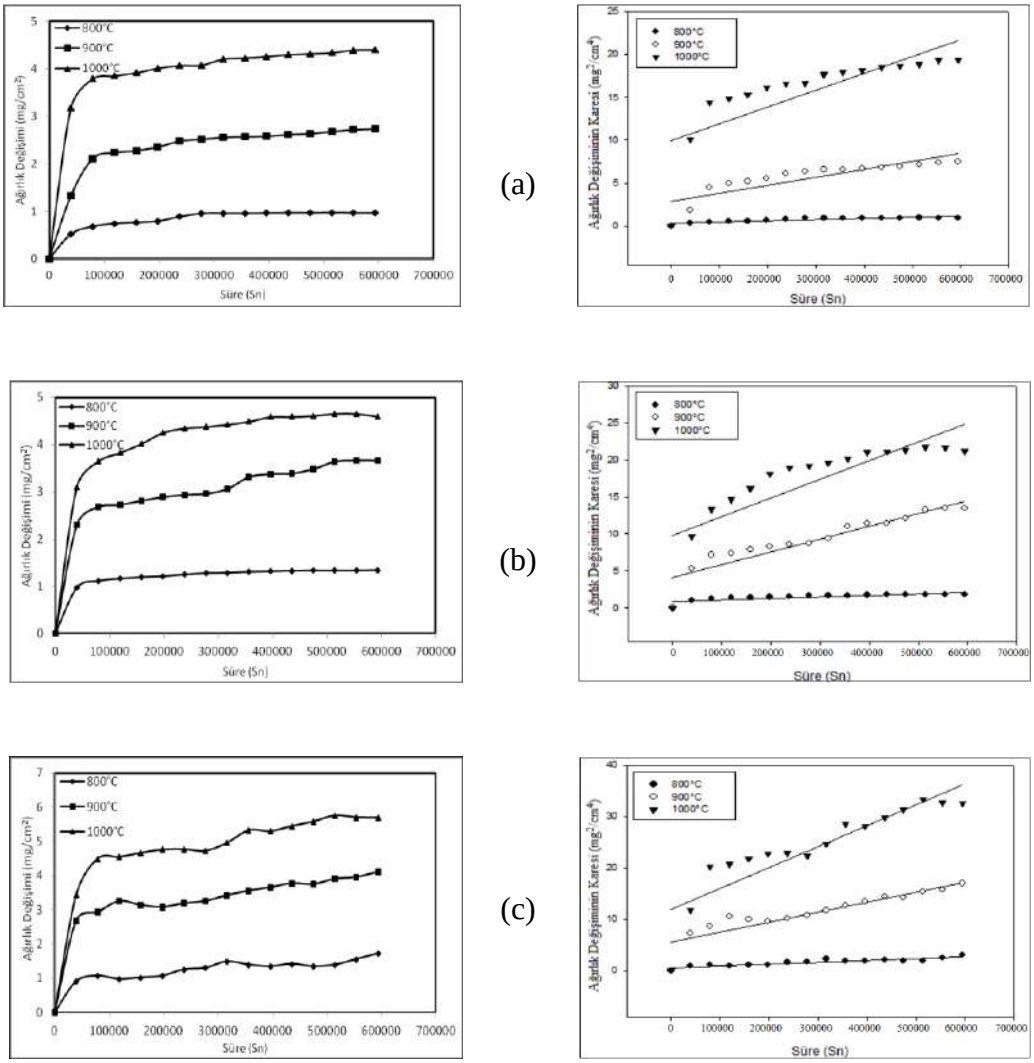

Figure 15. Time and temperature dependent weight change graphs of NiAl-34Cr-xTi (at.%) alloy exposed to hot corrosion a)1Ti, b)3Ti and c)5Ti.

Table 11. Temperature varying parabolic rate constants of NiAl-34Cr-xTi alloy exposed to hot corrosion.

Materials	Parabolic Rate Constant, kp (gr2/cm4.sec) Temperature (°C)		
	800	900	1000
NiAl-34Cr-1Ti	1,3x10-12	9,3x10-12	20x10-12
NiAl-34Cr-3Ti	1,9x10-12	17x10-12	25x10-12
NiAl-34Cr-5Ti	3,5x10-12	20x10-12	41x10-12

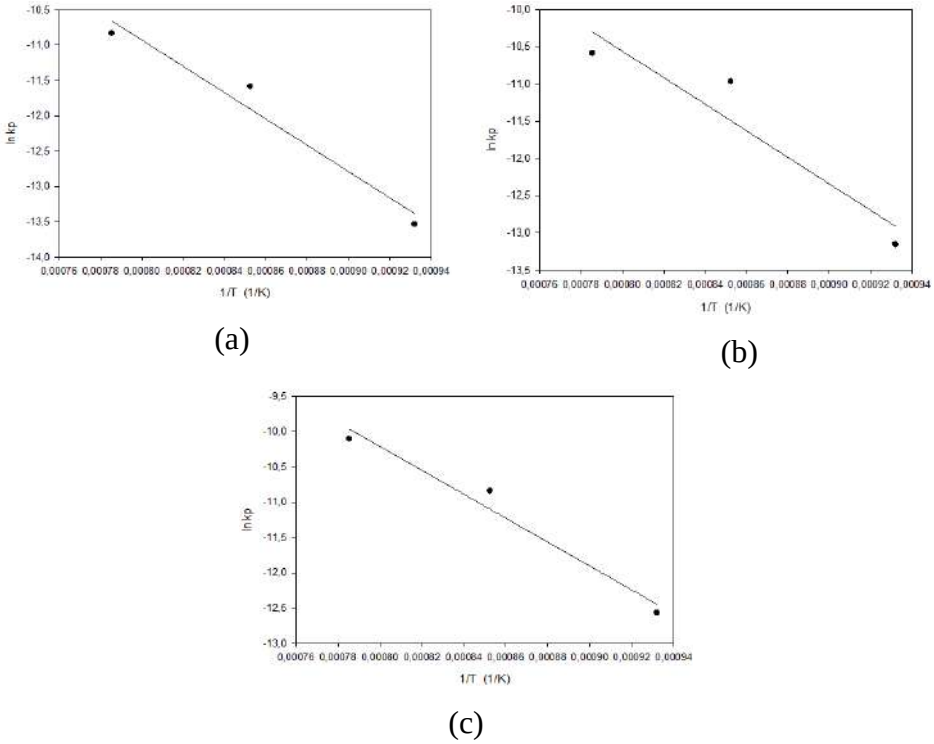

Figure 16. Arrhenius curves of NiAl-34Cr-xTi (at.%) alloy exposed to hot corrosion plotted depending on Ln kp and 1/T a)1Ti, b)3Ti, c)5Ti.

Table 12. -Q/R and activation energy values of NiAl-34Cr-xTi (at.%) alloy exposed to hot corrosion.

Material	-Q/R	Activation Energy (Q) kJ/mol
NiAl-34Cr-1Ti	18641,6	155,0
NiAl-34Cr-3Ti	17851,8	148,4
NiAl-34Cr-5Ti	16963,9	141,1

It was observed that the addition of titanium to the NiAl-34Cr eutectic alloy has an effect to reduce the activation energy.

4. Conclusions

In this study, the effect of titanium added to NiAl-34Cr eutectic alloy by electrically assisted current sintering (ECAS) method at atomic ratios of 1, 3, 5 % on the properties of the alloy was investigated.

- As a result of SEM-EDS analyses, it was determined that 2-phase samples were produced in accordance with the eutectic reaction with complete phase transformation. It was observed that the added Ti was dissolved in the eutectic structure. As a result of XRD analyses of the samples, it was determined that the produced materials contain NiAl (B2) and αCr (A2), which are NiAl-34Cr eutectic alloy phases, and trace amounts of NiTi phases.
- The oxidation behavior of the produced NiAl-34Cr-xTi eutectic alloy samples (at 800, 900 and 1000°C - 165 hours (11 hours-15 cycles)) was investigated. Compared to the parabolic rate constant (kp) of the alloy with at.1% Ti added at 1000°C ($21x10^{-12}$ $gr^2/cm^4.sec$), the kp value of the alloy with at.3% Ti added ($15x10^{-12}$ $gr^2/cm^4.sec$) decreased, it was determined that it increased in the alloy with 5% Ti added ($31x10^{-12}$ $gr^2/cm^4.sec$).

- Activation energy values of 168.6, 160.8 and 152.1 kJ/mol were measured for alloys oxidised at 800, 900 and 1000°C, respectively. These values mean that increasing titanium content slightly decreases the oxidation resistance of the alloy.
- Corrosion experiments were carried out in 75 wt. % Na2 SO4 and 25 wt.% K2 SO4 environment at 800, 900 and 1000°C for 165 h cycles (11 hours-15 cycles). The lowest kp value was obtained at 1000°C in the alloy with 1% Ti addition ($20x10^{-12}$ gr^2/cm^4.sec). 3% Ti added alloy, the kp value was $25x10^{-12}$ gr^2/cm^4.sec, while at. 5% Ti addition, the kp value was calculated as $25x10^{-12}$ gr^2/cm^4.sec.
- The activation energy values measured for the alloys exposed to corrosion tests at 800, 900 and 1000°C are 155, 148.4 and 141.1 kJ/mol, respectively. In this study, it was determined that Ti, which was selected as the alloying element, decreased the corrosion resistance in the temperature range of 800-1000°C under cyclic conditions in salt environment.

5. References

[1] Bochenek, K., & Basista, M. (2015). Advances in processing of NiAl intermetallic alloys and composites for high temperature aerospace applications. *Progress in Aerospace Sciences*, *79*, 136-146.

[2] Stoloff, N. S., Liu, C. T., & Deevi, S. C. (2000). Emerging applications of intermetallics. *Intermetallics*, *8*(9-11), 1313-1320.

[3] Bochenek, K., & Basista, M. (2015). Advances in processing of NiAl intermetallic alloys and composites for high temperature aerospace applications. *Progress in Aerospace Sciences*, *79*, 136-146.

[4] Sheng, L. Y., Nan, L., Zhang, W., Guo, J. T., & Ye, H. Q. (2010). Microstructure and mechanical properties determined in compressive tests of quasi-rapidly solidified NiAl-Cr (Mo)-Hf eutectic alloy after hot isostatic pressure and high temperature treatments. *Journal of Materials Engineering and Performance*, *19*, 732-736.

[5] Sheng, L. Y., Fang, Y. A. N. G., Xi, T. F., Zheng, Y. F., &Guo, J. T. (2013). Microstructure and room temperature mechanical properties of NiAl–Cr (Mo)–(Hf, Dy) hypoeutectic alloy prepared by injection casting. *Transactions of Nonferrous Metals Society of China*, *23*(4), 983-990.

[6] Song, C., Lu, W., Xie, K., Zhang, Y., Xia, W., Han, K., &Zhai, Q. (2014). Microstructure and mechanical properties of sub-rapidly solidified Fe–18 wt% Mn–C alloystrip. *Materials Science and Engineering: A*, *610*, 145-153.

[7] Yu, D., An, K., Chen, X., &Bei, H. (2015). Temperature-dependent phase-specific deformation mechanisms in a directionally solidified NiAl-Cr (Mo) lamellar composite. *Journal of Alloys and Compounds*, *656*.

[8] Nakae, H.,Fujii, H., Nakajima, K., &Goto, A. (1997). Infiltration and combustion synthesis of an intermetallic compound Ni3Al. *Materials Science and Engineering: A*, *223*(1-2), 21-28.

[9] Grasso, S., Sakka, Y., & Maizza, G. (2009). Electric current activated/assisted sintering (ECAS): a review of patents 1906–2008. *Science and Technology of Advanced Materials*, *10*(5), 053001.

[10] Orru, R., Licheri, R., Locci, A. M., Cincotti, A., & Cao, G. (2009). Consolidation/synthesis of materials by electric current activated/assisted sintering. *Materials Science and Engineering: R: Reports*, *63*(4-6), 127-287.

[11] Çeper, C. (2019). *Nial-34cr-X(Fe, Nb, Ti) Alaşımının Elektrik Akım Destekli Sinterleme (Ecas) Yöntemiyle Üretimi Ve Karakterizasyonu*, (Yüksek Lisans Tezi). https://tez.yok.gov.tr/UlusalTezMerkezi/

[12] Okamoto, H., Schlesinger, M.E., Mueller, E.M. (2016). ASM Handbook Volume 3: Alloy Phase Diagrams.

[13] Hagihara, K., Sugino, Y., & Umakoshi, Y. (2006). The effect of Ti-addition on plastic deformation and fracture behavior of directionally solidified NiAl/Cr (Mo) eutectic alloys. *Intermetallics*, *14*(10-11), 1326-1331..

[14] Li, H. T., Guo, J. T., Ye, H. Q., Wang, Q., & He, J. C. (2008). Simultaneous improvement of strength and ductility in NiAl–Cr (Mo)–Hf near eutectic alloy by small amount of Ti alloying addition. *Materials Letters*, *62*(1), 61-64.

[15] Moricca, M. D., & Varma, S. K. (2008). The high-temperature oxidation characteristics of alloys from the Nb-W-Cr system with C additions. *JOM*, *60*, 66-69.

[16] Xu, C., & Gao, W. (2000). Pilling-Bedworth ratio for oxidation of alloys. *Material Research Innovations*, *3*, 231-235.

[17] Jiang, Q., Lu, D., Liu, C., Liu, N., & Hou, B. (2021). The Pilling-Bedworth ratio of oxides formed from the precipitated phases in magnesium alloys. *Frontiers in Materials*, *8*, 761052.

International Conference on Advances and Innovations in Engineering

Health Classification for Plants by Using Computer-Aided Deep Learning Methods

Volkan YAMAÇLI[1], Muhammet Kürşat YILDIRIM[2]

[1]Computer Engineering Department, Engineering Faculty, Mersin University, Mersin, Turkey.
[2]M.Sc. Student, Graduate School of Natural and Applied Sciences, Mersin University, Mersin, Turkey.
[1]vyamacli@mersin.edu.tr, [2] m.kursatyildirim33@gmail.com

[1](ORCID: 0000-0003-0331-8818), [2](ORCID: 0000-0001-7346-8868)

Abstract
Due to climate change and increasing food demand, the importance of sustainable agriculture is constantly increasing. Our country has both large and fertile soils and a favorable climate for agricultural activities. The active implementation of agricultural activities in each of the seven geographical regions in our country requires separate evaluation of agricultural plants, air temperature, soil structure, irrigation and maintenance needs, detection and monitoring of pests and pests, specific to these regions. In order for the plant to grow healthy, it is necessary to consider the pests that affect the plant health, as well as the water, humidity and temperature conditions. It is not possible to save the plant and the crop after the effects of harmful insects living as parasites on the plants are visible. For this reason, by using deep learning methods, the available data are processed and the health status of plants are classified according to the appropriate categories and it will be determined which category the new data belong to. In this paper, deep learning techniques, which are one of the types of machine learning, and image processing method are be used through the Python programming language. In this study, deep learning models namely convolutional neural networks as AlexNet, ResNet and Xception are used to show the efficiency and quick classification time of the proposed system. Also, by improving and embedding the system in various distributed servers, it may be possible to advance the system into a prototype for commercial and personal purposes with no problems.

Keywords: deep learning, image processing, image enhancement, agriculture, sustainable agriculture

1. Introduction

In recent years, modern agriculture faced a critical mission of feeding the rapidly expanding global population and ensuring food security. However, the challenges brought about by swift population growth and climate change imperil plant health, a cornerstone of agricultural productivity [1]. Plant ailments, pests, droughts, and other environmental stressors have the potential to hinder plant growth, lead to yield deficits, and jeopardize food security. Overcoming these challenges and advancing sustainable agricultural practices necessitates innovative approaches that transcend traditional methodologies.

Monitoring and managing plant health constitute essential pillars of agriculture, and early diagnosis coupled with precise prediction of plant diseases are pivotal pathways for augmenting productivity. Traditionally, plant diseases have been visually diagnosed and monitored. Yet, these methods often rely on individuals to visually detect disease symptoms, and they can be time-intensive [2]. This is where the domain of deep learning comes into play.

Deep-learning was first described in a 2006 work by Hinton et al. [3] that published in Science Journal. Using neural networks for learning characteristics and data evaluation lies at the heart of deep learning. Through a variety of hidden layers, each of which serves as a perceptron, data characteristics are recovered. Utilizing a perceptron, low-level features are generated, which are then merged to provide abstract features at a high level. This can greatly mitigate the challenge of local minima. Deep-learning based models can overcome the limitation of traditional algorithms, which heavily rely on artificially designed features. As a result, it has garnered increasing attention from researchers and has successfully found applications in scientific areas such as computer vision, pattern and speed detection, natural language processing and computer-aided decision systems [4]. In recent years, deep-learning based models

[1]Corresponding author

have wrought a revolution in the agricultural sector. These techniques have been effectively employed in realms such as plant health monitoring, disease diagnosis, and comprehensive plant performance assessment [5]. Leveraging their capability to rapidly analyze extensive datasets and discern intricate patterns, deep learning algorithms offer valuable insights into plant health, encompassing everything from leaf imagery to soil moisture levels [6], [7]. The potential of deep learning in identifying plant health issues is genuinely promising. While traditional methods for monitoring plant health and diagnosing diseases frequently consume substantial time, deep learning techniques have the potential to automate, expedite, and amplify these processes [8]. For instance, by scrutinizing images of plant leaves, it becomes feasible to detect early indications of diseases, facilitating more effective interventions [9].

The integration of deep learning techniques in the agricultural sector holds immense promise, not only for monitoring plant health but also for boosting agricultural efficiency and sustainability. In particular, these techniques can aid in crafting more efficient and targeted farming practices [10]. Furthermore, rapid disease detection can curtail the propagation of outbreaks, thereby mitigating adverse impacts on agricultural yields [11]. Numerous studies [12], [13] focused on image-based plant disease identification adopt a foundational approach that involves preprocessing steps such as background removal and segmentation of lesion tissues in diseased plants. Subsequently, discriminative features are extracted to conduct in-depth analysis of plant diseases, culminating in the creation of models for disease classification. In the work of Al-Hiary et al. [12] used certain threshold settings to identify and then mask green-colored pixels. The obtained accuracy varied from 83% to 94%. For example, in the study by Mokhtar et al. [13], the research team discussed the recognition of two diseases, namely Tomato yellow leaf curl virus (TYLCV) and Tomato yellow leaf curl disease (TYLCD), in tomato crops using their leaves. Other researchers have focused on particular plants to identify diseases. They employed the N-fold cross-validation technique as their model and achieved an average accuracy of 90%. Earlier endeavors in the field of plant disease classification have relied on traditional machine learning approaches. In the work of Arivazhagan et al. [14], the authors explored the detection of unhealthy regions on plant leaves, utilizing texture features alongside the minimum distance criterion and SVM classifier for plant leaf disease classification.

The purpose of this article is to delve into the potential applications of deep learning for plant health monitoring. The incorporation of deep learning techniques within the realm of agriculture could signify a significant stride towards achieving sustainable agricultural objectives, transcending conventional plant health approaches and potentially heralding a new era in agriculture.

2. Plant Disease Dataset

In this study, a plant disease dataset obtained from online image repository [15] is used. This dataset contains more than 80.000 images in 38 classes. The image number is not equal, some classes have much more images while some classes have lower but in general there are considerable and enough images to conduct research and study on classification and identification with no problems. The images presented in this dataset are used for 7 classes 200 image each total 1400 images. These classes are*; apple-black-rot, apple-scab, apple-heathy, cherry-powdery-mildew, cherry-healthy, corn-rust* and *corn-healthy*. Some random images the dataset consists are given in Figure 1. These images generally have boundaries and different backgrounds so the images used in our study is divided in 2 cases. In the first case, the original images are cropped from the center point for obtaining 50×50-pixel resolution. Also, for another case, the images have been cropped from the center point by 100×100-pixel resolution. So, not only low-resolution images are processed, but also it is aimed to show that even for small part of the image the classification can be achieved successfully.

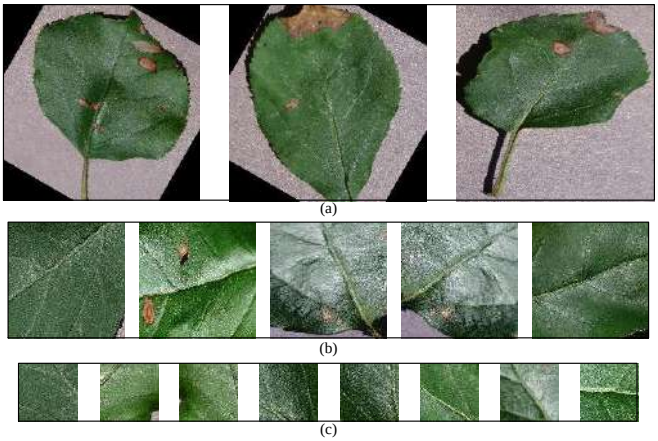

Figure 1. Random dataset images of original and cropped data. (a) Original, (b) 100-pixels, (c) 50-pixels

3. Deep Learning Algorithms and Methods

In this study, AlexNet, ResNet-50 and Xception CNNs are used. AlexNet and ResNet-50 architectures are one of the most popular CNNs in the area of computer vision and detection. AlexNet [16] is one of the first models consisting of Rectified Linear Unit (ReLU) which enables a better non-linearity performance. Also, ResNet [17] uses residual learning for stacking the characteristics of the previous calculations. Xception is a newly proposed CNN which is a modified version of Inception-v3. In Xception, there are depth-wise separable convolutions which help model to train better and with higher performance. The Xception model has 36 convolutional layers forming the feature extraction base of the network [18]. The depth-wise separable convolutions schematic diagram is given in Figure 2 [19]. The input data of AlexNet, ResNet-50 and Xception are 227×227 pixels, 224×224 pixels and 299×299 pixels, respectively.

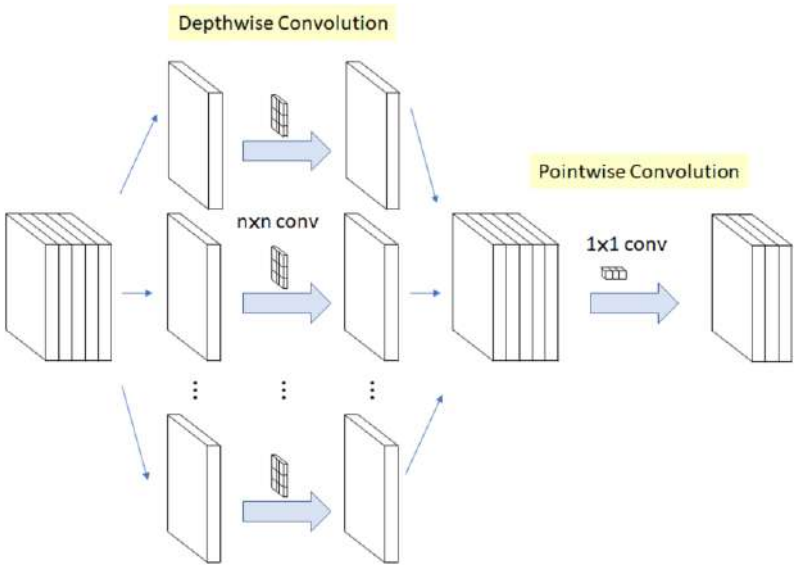

Figure 2. Depth-wise convolution of Xception [19]

4. Results and Discussion

In this study different random images of the plant disease dataset are used. These images are pre-processed and cropped as 50- and 100-pixels to emphasize the efficiency of the algorithms and also training convergence speed. In this study, Tensorflow 2.10.1, Keras 2.10.0 were used on Python 3.10.1 on Windows® 11 computer with an Intel® Core (TM) i7-10700F processor running at 2.90 GHz, 32.0 GB of RAM, and GeForce RTX 3080 GPU.

Deep learning training batch-size, epoch and initial learning rate are chosen as 16, 50 and 1×10^{-4}, respectively. Also, for the image data, augmentation is used by given parameters in Table 1.

Table 3. Image augmentation parameters

Parameter	Value	Parameter	Value
horizontal_flip	True	height_shift_range	0.2
vertical_flip	True	width_shift_range	0.2
zoom_range	0.3	shear_range	0.2

Some exemplary images for data augmentation are given for 100-pixels images in Figure 3. These images are may or may not be related to each other since randomized without taking the image number or name into consideration. These images have 224×224-pixels resolution instead of 100×100-pixel resolution because the augmented images are obtained during the training process of ResNet-50 model by the help of *ImageDataGenerator* class.

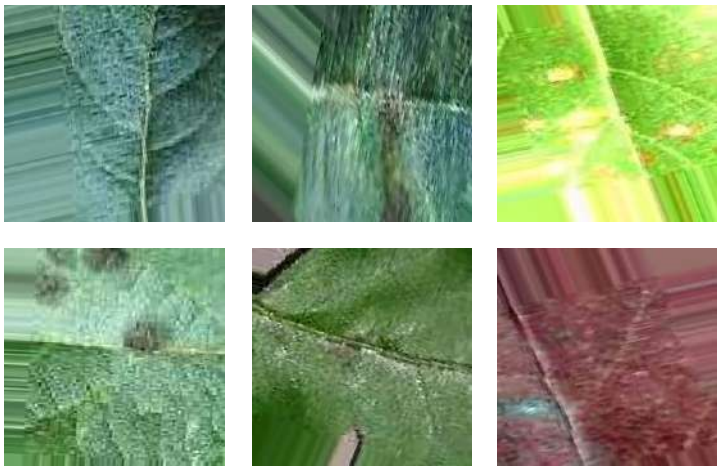

Figure 3. Exemplary augmented images of random augmentation.

4.1. Case 1 – Classification for 50-Pixel Images

In this Section, 50×50-pixels images are used as input for training and validation of AlexNet, ResNet-50 and Xception models. By training the CNNs with the parameters given in Section 4, the training graphics for the models are obtained as given in Figure 4.

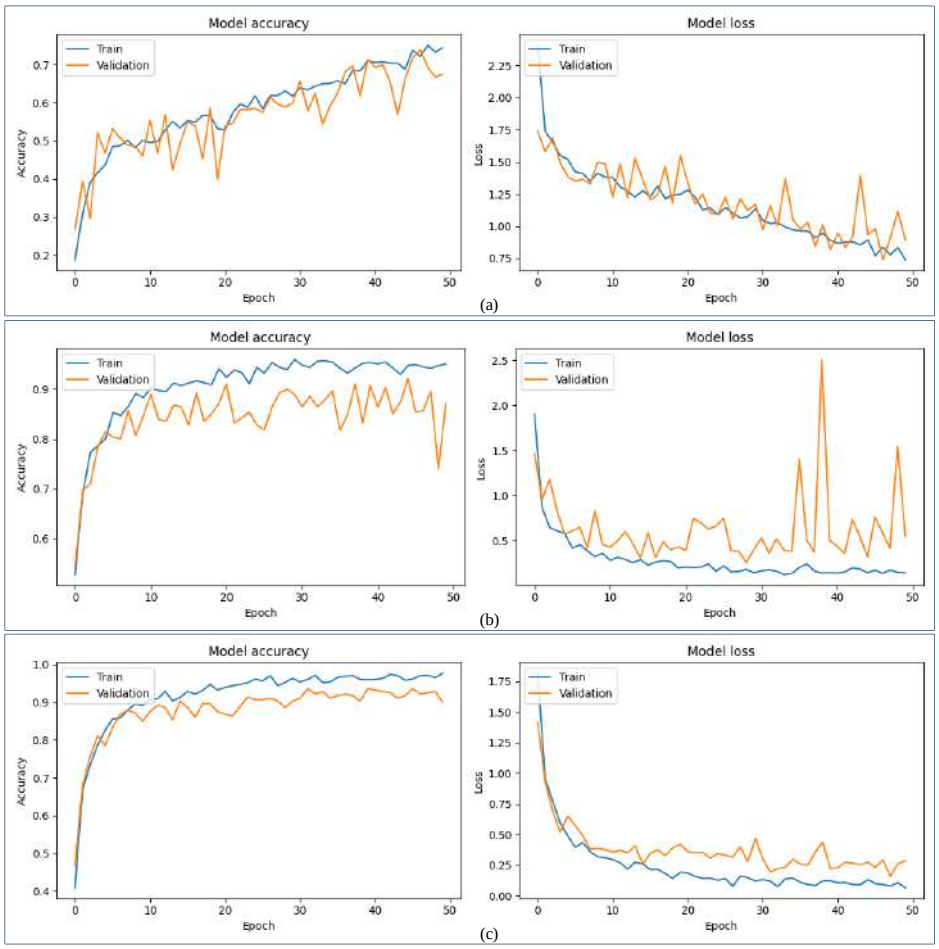

Figure 4. Training and validation accuracy for 50-pixels. (a) AlexNet, (b) ResNet-50, (c) Xception

As seen from the graphics, AlexNet reaches up to 74.46% for training and 67.50% for validation accuracy. ResNet-50 reaches up to 95.09% and 87.14% for training and validation accuracy, respectively. Also, Xception can successfully train with 97.68% accuracy and 90.00% with validation accuracy. Each batch processing by using the models vary due to complexity of the CNNs. For each batch, AlexNet needs approximately 11ms while ResNet-50 and Xception consume 12 and 21ms, respectively. Xception model's training time is almost twice of AlexNet and ResNet-50 models.

4.2. Case 2 – Classification for 100-Pixel Images

In this Section, 100×100-pixels images are used as input for training and validation of AlexNet, ResNet-50 and Xception models. By training the CNNs with the same parameters, the training performances and validation accuracies are obtained and presented in Figure 5.

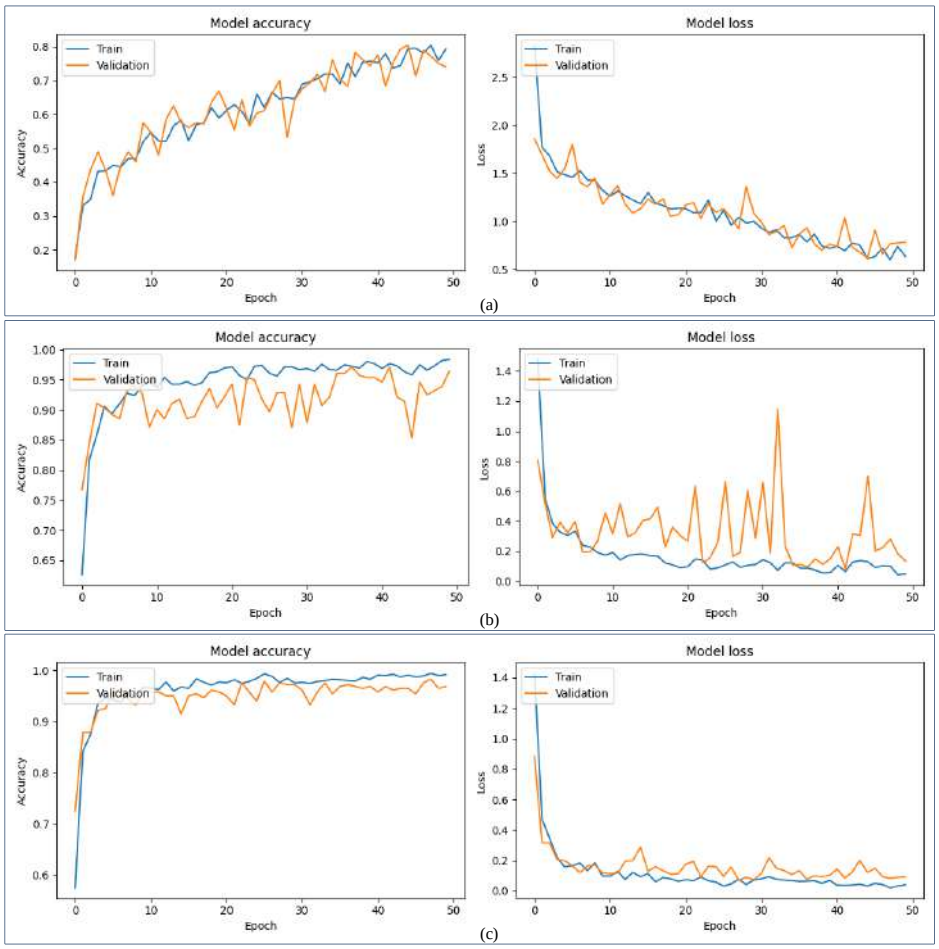

Figure 5. Training and validation accuracy for 100-pixels. (a) AlexNet, (b) ResNet-50, (c) Xception

In this Case, AlexNet reaches up to 79.29% for training and 73.93% for validation accuracy. ResNet-50 also increases performance with 98.39% training and 96.43% for validation accuracy. In addition to this, Xception can successfully train with 99.11% accuracy and with 96.79% validation accuracy. In this case, AlexNet and ResNet-50 take 12ms for each batch for training while Xception consumes 21ms.

5. Results

In this paper, the leave images of plants are used in order to detect and classify the healthy or non-healthy status by using deep learning models. Deep learning models, AlexNet, ResNet-50 and Xception are used to detect and classify the status of the plants with a high success. It can be seen from the results that Xception and ResNet-50 achieves a great classification performance while AlexNet cannot due to low complexity and low epoch number. The conclusions can be drawn as follows:

1. One of the proposed deep-learning based models, Xception, is able to detect and classify the health status of the plants with success of 96.79%.
2. By using other deep-learning based models such as AlexNet and ResNet-50, it is concluded that Xception and ResNet-50 achieves the better results compared to AlexNet.

6. References

[1] Smith M, Jones L. "Challenges and opportunities in modern agriculture". Journal of Agricultural Science, 158(5-6), 301-312, 2020.
[2] Johnson AC, Smith DL. "Plant disease management: historical perspectives and current challenges". Journal of Agricultural Research, 45(3), 567-578, 2018.

[3] Hinton GE, Salakhutdinov R. “Reducing the dimensionality of data with neural networks”. Science, 313(5786), 504-507, 2006.
[4] Liu W, Wang Z, Liu X. “A survey of deep neural network architectures and their applications”. Neurocomputing, 234, 11-26, 2017.
[5] Wang S, Li L. “Applications of deep learning in agricultural automation”. Computers and Electronics in Agriculture, 157, 426-437, 2019.
[6] Zhang C, Zhang D. “Plant disease detection using deep learning: a review”. Neurocomputing, 267, 378-384, 2017.
[7] Brown TB, Chan AB. “WaterNet: a deep learning model for remote sensing image classification and semantic labeling of water bodies”. Remote Sensing of Environment, 213, 1-17, 2018.
[8] LeCun Y, Bengio Y, Hinton G. “Deep Learning”. Nature, 521(7553), 436-444, 2015.
[9] Picon A, Becker S. “Plant disease detection and classification through deep learning techniques”. Computers in Industry, 120, 103265, 2020.
[10] Kamilaris A, Prenafeta-Bold FX. “Deep learning in agriculture: a survey”. Computers and Electronics in Agriculture, 147, 70-90, 2018.
[11] Minervini M, Abdelsamea MM, Tsaftaris SA. “Image-based plant phenotyping with machine learning methods: a review”. IEEE Transactions on Pattern Analysis and Machine Intelligence, 38(8), 1696-1710, 2015.
[12] Al Hiary S, Bani A, Reyalat M, Braik M, ALRahamneh Z. “Fast and accurate detection and classification of plant diseases”, Inter. J. Com. Appl., 17(1), 31-38, 2011.
[13] Mokhtar U, Ali MA, Hassanien AE, Hefny H. “Identifying two of tomatoes leaf viruses using support vector machine”. Information Systems Design and Intelligent Applications, 771-782, 2015.
[14] Arivazhagan S, Shebiah RN, Ananthi S, Varthini SV. “Detection of unhealthy region of plant leaves and classification of plant leaf diseases using texture features” Agricultural Engineering International, 15(1), 211-217, 2013.
[15] Kaggle. “New Plant Disease Dataset”. https://www.kaggle.com/ datasets/vipoooool/new-plant-diseases-dataset (20.08.2023).
[16] Krizhevsky A, Sutskever I, Hinton GE. “ImageNet classification with deep convolutional neural networks”. Advances in Neural Information Processing Systems Conference, Nevada, USA, 3–8 December 2012.
[17] He K, Zhang X, Ren S, Sun J. “Deep residual learning for image recognition”. IEEE Conference on Computer Vision and Pattern Recognition, Las Vegas, USA, 27–30 June 2016.
[18] Chollet F. “Xception: deep learning with depthwise separable convolutions”. Computer Vision and Pattern Recognition, arXiv:1610.02357.
[19] Junejo IN, Ahmed N. “Depthwise separable convolutional neural networks for pedestrian attribute recognition”. SN Computer Science, 2, 100, 2021.

International Conference on Advances and Innovations in Engineering

Harmonics generated during the electric vehicle charging process

Arkadiusz Dobrzycki[1] , Muhammed Sefa ÇETİN[2], Muhsin Tunay GENÇOĞLU[3]

[1] Institute of Electrical Engineering and Electronics, Faculty of Control, Robotics and Electrical Engineering, Poznan University of Technology, Poznan, Poland.
[2,3]Department of Electrical and Electronics Engineering, Faculty of Engineering, Fırat University, Elazığ, Türkiye.
[1]arkadiusz.dobrzycki@put.poznan.pl, [2]mscetin@firat.edu.tr, [3]mtgencoglu@firat.edu.tr

[1](ORCID: 0000-0001-5640-685X), [2](ORCID: 0000-0001-5587-0001),[3](ORCID: 0000-0002-1774-1986)

Abstract
Paper deals with electromobility, specially with battery charging process. Several tests of charging process were conducted for different vehicles. Analyzed parameter was connected with potential influence of charging into user's (owner's) home electrical installation. During test THD (Total Harmonic Distortion) and separate harmonics were analyzed. Performed test provided that charging process can influence on the electricity parameters and cause potential problems to the user even if energy parameters suits legal regulations requirements. Problems can be connected with voltage asymmetry and nonsinusoidal residual currents. Because of that conclusions for designers and users about house charging stations and needed installations equipment were formulated.

Keywords: electromobility, harmonics, electrical vehicles charging

1. Introduction

In the era of decarbonization one of the main area of interests is transportation. Research are concentrated on low emission during production of electrical energy and ecological energy sources are improved.

Currently it can be observed number of important research topics. One of them is analyzing of carbon footprint connected with life cycle of electrical vehicles or batteries [1,2]; how charging strategies can be optimized to decrease emissions [3]. Authors made analysis of cumulative CO_2 emissions during life cycle for electrical and combustion cars [4] and made analysis for particular car markets, ie. in China [5]. Other area of interest is connected with reduction of energy consumption and increasing of using green technologies in production of electricity. Researches prove that electrical vehicles can be opportunity to reduce emissions [6], even in public transportation [7]. Authors also noticed combined influence on decreasing emissions and fuel consumption [8]. One of most interesting topics to consider is influence of electrical vehicles on the power network, and some particular topics are discussed. One of them is necessity of taking into account possibility of increasing of power demand for houses and prepare energy management strategies which can handle with that [9,10]. This topic is connected with minimization of transmission power losses [11] and methods of extend range of electrical vehicles what is connected with density of charging stations in particular areas [12]. Other idea is combined power system with nuclear power plant, renewable energy sources and electrical vehicles as method of reducing emissions in transportation and production of energy [13]. Last but not least popular topic is durability of batteries in case of production, effective utilization, forecasting of lifetime and ecological utilization [14-16].

Our research are connected with analyzing of power and energy parameters. This parameters can vary, especially when we connect to home electrical installation one 'big load' (charger). Such charger is nonlinear load and our test proved that during designing installation and utilization it with of EV charger we must consider possible problems. Conducted tests confirmed that during charging process user may expect changes in parameters of electrical energy (e.g. harmonics) which can influence on other equipment.

[1]Corresponding author

2. Materials and Methods

Combination with zero emission means of transport can be treated like the most ecological idea of using it. Many people are using ‘clean’ personal means of transport like bicycles, scooters, bikes which contains electrical batteries as energy source. Other segment in transportation are electrical cars and buses.

The main difference between this groups is battery capacity and motor power. Energy which must be stored in batteries is connected with charging process. Most of vehicles have individual on-board (e.g. cars) or separate chargers (e.g. scooters, bikes, kick scooters). Main goal of provided analysis is analyzing impact of the charging process on the quality parameters of electricity, specially generated harmonics. The test were provided with the use of different cars (EV and PHEV) and electric scooters.

For the purpose of carrying out the tests, a measuring stand equipped with a 22 kW AC charger was developed. The station has been equipped with the necessary number of single and three-phase sockets, which allows it to be powered from any point (mains socket) of the LV network using a single cable. The station is also equipped with analyzers of electric energy parameters consumed by the vehicle during charging. The analyzers used were able to continuous recording of selected parameters of electricity. View of test stand is presented on figure 1.

Figure 1. View of test stand. Wallbox in the center, below power and energy analyzers with probes; tested car on the left.

During the test, the conditions similar to the typical way of using the vehicle were maintained. The following were considered as: starting charging the vehicle when batteries SOC (State of Charge) level was at the level of 20%, charging started immediately after the end of the journey. The only exception was charging the battery to 100% instead of the recommended by vehicle producers 80%. It was assumed that this would be charging while traveling and therefore the maximum power of the car's on-board charger (or supplied with the scooter) was used. The tests (registration of parameters) were completed when the on-board charger cut off the power supply.

3. Results

The following electric cars were used to carry out the tests: VW ID.3, Fiat 500e, Kia eNIRO. In addition, the Alfa Romeo Tonale PHEV plug-in hybrid, electric scooters and a kick scooter were used.

When charging electric vehicles, it was observed that all of them had three-phase chargers with a power of 11 kW, and during the charging process, charging was carried out at maximum power, the current consumed in each phase reached 16 A and it was a symmetrical load, with slight fluctuations towards the end, i.e. when the degree of charge was greater than 95%. In turn, charging the plug-in hybrid was carried out with a power of 7.4 kW, except that it was single-phase. The consequence of this was a current consumption of 32 A. A significant difference was observed during this process, with significant fluctuations in current consumption when the batteries reached a charge level greater than 80%. During the last 20%, the current consumed varied from 1 to 32 A. In addition, it was the only time when the cooling fans of the charging system and batteries turned on after charging. In the case of scooters, charging was as follows: for BMW C evolution, charging was linear with full power, except that in the last stage (the last few percent of capacity) there was an exponential decrease in power consumption from the network. In the case of the second scooter, an older one of an unknown brand, the power consumption, and thus the current, oscillated around the maximum value of the charger current throughout the charging process, and at the end it dropped to the minimum value in a short time. The scooter, on the other hand, drew very little current throughout the charging process.

Despite these differences, it was observed that in none of the analyzed cases were the normative quality parameters of electricity exceeded. At the same time, the analysis of the harmonic distribution showed that the chargers generate current and voltage harmonics in the range from the DC component to the 50th harmonic, which distribution depends of the vehcle.

Figures 2 to 4 presents content of harmonics registered during charging process respectively for VW ID.3, Fiat 500e, Kia eNIRO. Only first 25 harmonic are presented on the figures, highest than 25 are negligibly low.

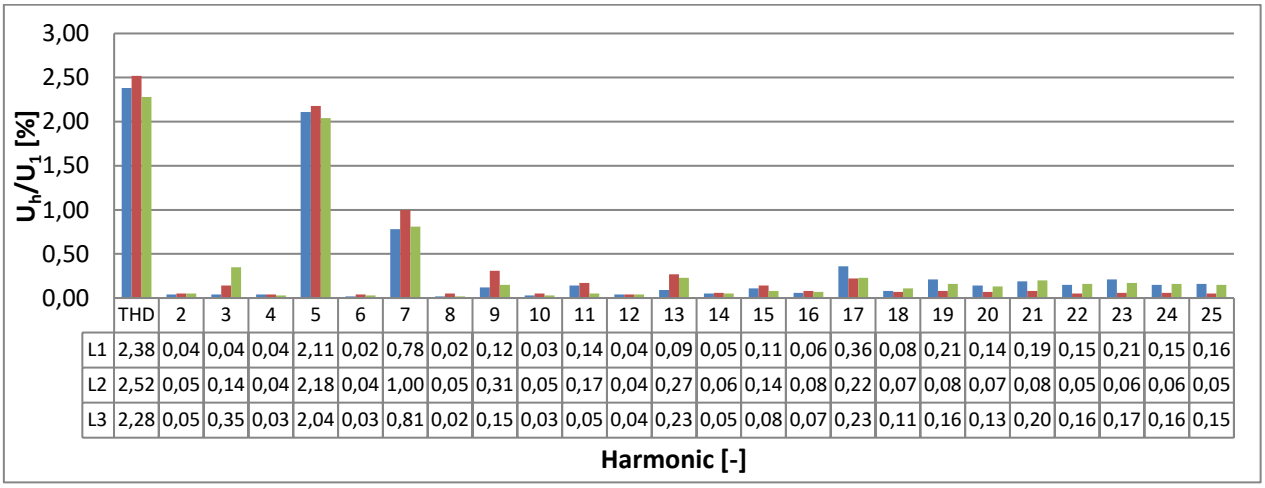

	THD	2	3	4	5	6	7	8	9	10	11	12	13	14	15	16	17	18	19	20	21	22	23	24	25
L1	2,38	0,04	0,04	0,04	2,11	0,02	0,78	0,02	0,12	0,03	0,14	0,04	0,09	0,05	0,11	0,06	0,36	0,08	0,21	0,14	0,19	0,15	0,21	0,15	0,16
L2	2,52	0,05	0,14	0,04	2,18	0,04	1,00	0,05	0,31	0,05	0,17	0,04	0,27	0,06	0,14	0,08	0,22	0,07	0,08	0,07	0,08	0,05	0,06	0,06	0,05
L3	2,28	0,05	0,35	0,03	2,04	0,03	0,81	0,02	0,15	0,03	0,05	0,04	0,23	0,05	0,08	0,07	0,23	0,11	0,16	0,13	0,20	0,16	0,17	0,16	0,15

Figure 2. THD and individual harmonic content for VW ID.3

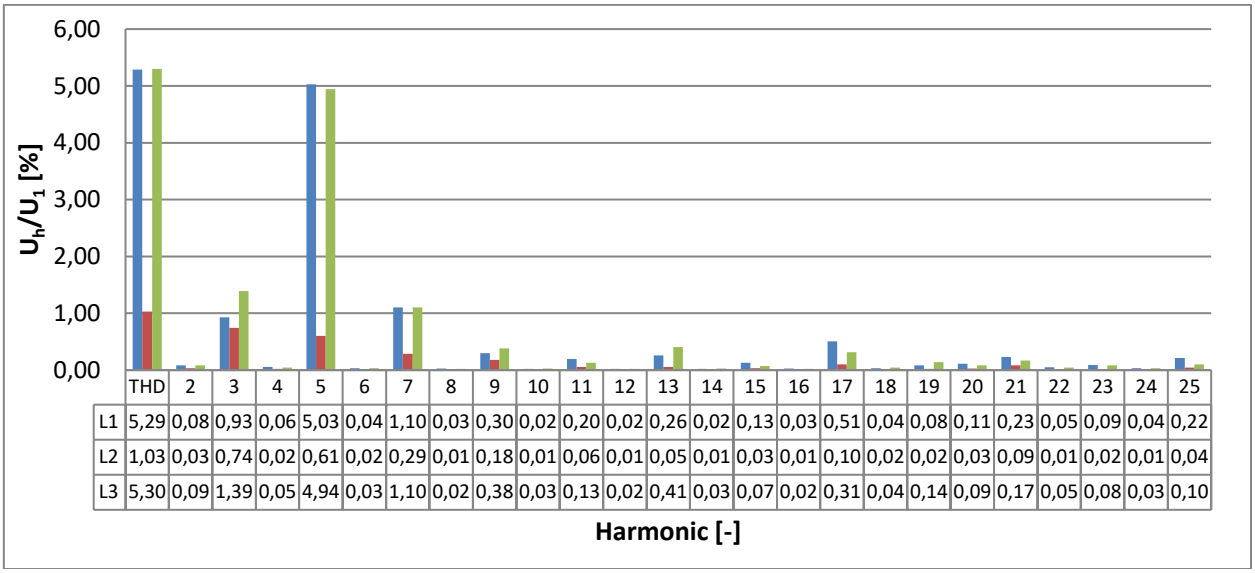

	THD	2	3	4	5	6	7	8	9	10	11	12	13	14	15	16	17	18	19	20	21	22	23	24	25
L1	5,29	0,08	0,93	0,06	5,03	0,04	1,10	0,03	0,30	0,02	0,20	0,02	0,26	0,02	0,13	0,03	0,51	0,04	0,08	0,11	0,23	0,05	0,09	0,04	0,22
L2	1,03	0,03	0,74	0,02	0,61	0,02	0,29	0,01	0,18	0,01	0,06	0,01	0,05	0,01	0,03	0,01	0,10	0,02	0,02	0,03	0,09	0,01	0,02	0,01	0,04
L3	5,30	0,09	1,39	0,05	4,94	0,03	1,10	0,02	0,38	0,03	0,13	0,02	0,41	0,03	0,07	0,02	0,31	0,04	0,14	0,09	0,17	0,05	0,08	0,03	0,10

Figure 3. THD and individual harmonic content for Fiat 500e

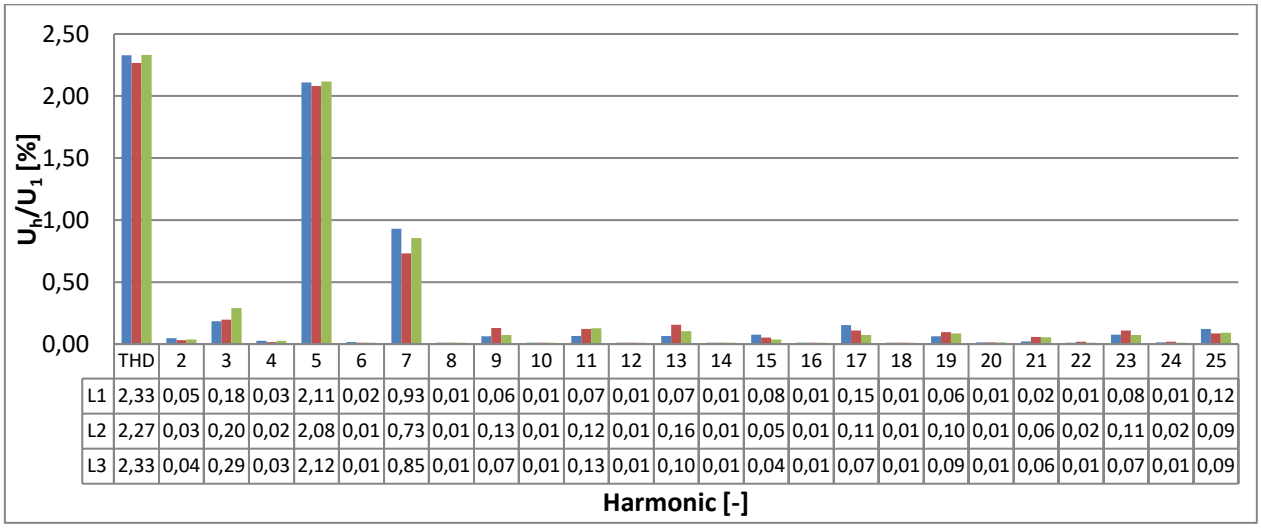

	THD	2	3	4	5	6	7	8	9	10	11	12	13	14	15	16	17	18	19	20	21	22	23	24	25
L1	2,33	0,05	0,18	0,03	2,11	0,02	0,93	0,01	0,06	0,01	0,07	0,01	0,07	0,01	0,08	0,01	0,15	0,01	0,06	0,01	0,02	0,01	0,08	0,01	0,12
L2	2,27	0,03	0,20	0,02	2,08	0,01	0,73	0,01	0,13	0,01	0,12	0,01	0,16	0,01	0,05	0,01	0,11	0,01	0,10	0,01	0,06	0,02	0,11	0,02	0,09
L3	2,33	0,04	0,29	0,03	2,12	0,01	0,85	0,01	0,07	0,01	0,13	0,01	0,10	0,01	0,04	0,01	0,07	0,01	0,09	0,01	0,06	0,01	0,07	0,01	0,09

Figure 4. THD and individual harmonic content for Kia eNIRO

Presented above measurement results were obtained in similar weather conditions, sunny spring day with temperature about 20ºC. On-board chargers parameters were also similar: 3x400 V AC, 11 kW. All test provide that such nonlinear load influence on voltage in the installation and generates higher harmonics. In all cases highest values are for 5^{th} , 7^{th} and 3^{rd} harmonic. What is important we can see all odd harmonics, and levels of particular harmonic are different for all phases. It can be noticed that the highest THD were registered for Fiat.

Figures from 5 to 7 presents content of harmonics registered during charging process respectively for Alfa Romeo Tonale PHEV, BMW C evolution and E-Scooter ESA 800. These batteries are charged from 1 phase socket 230 V AC, powers and currents are different for every charger.

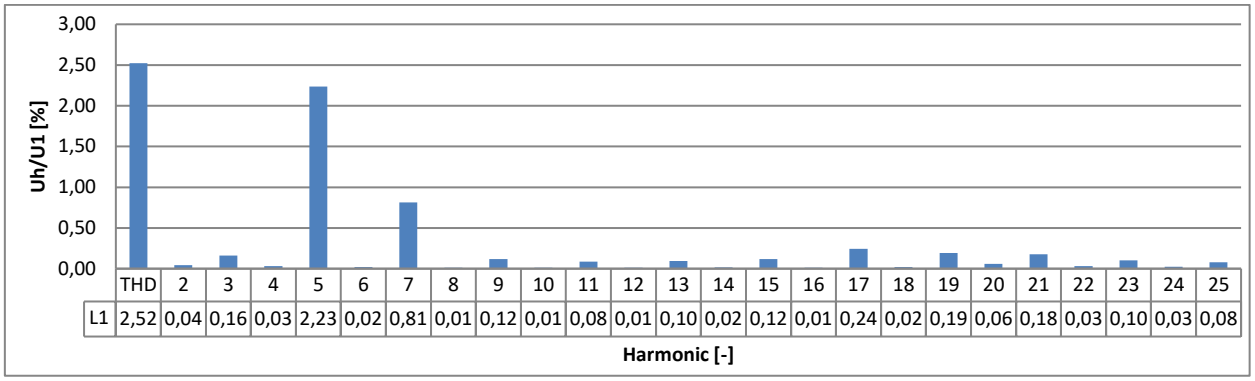

Figure 5. THD and individual harmonic content for Alfa Romeo Tonale PHEV

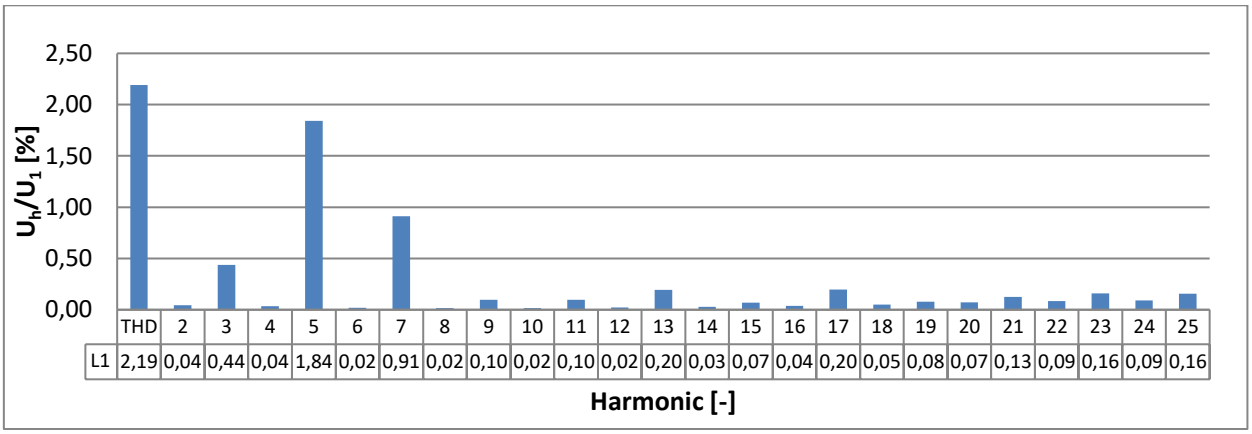

Figure 6. THD and individual harmonic content for BMW C evolution

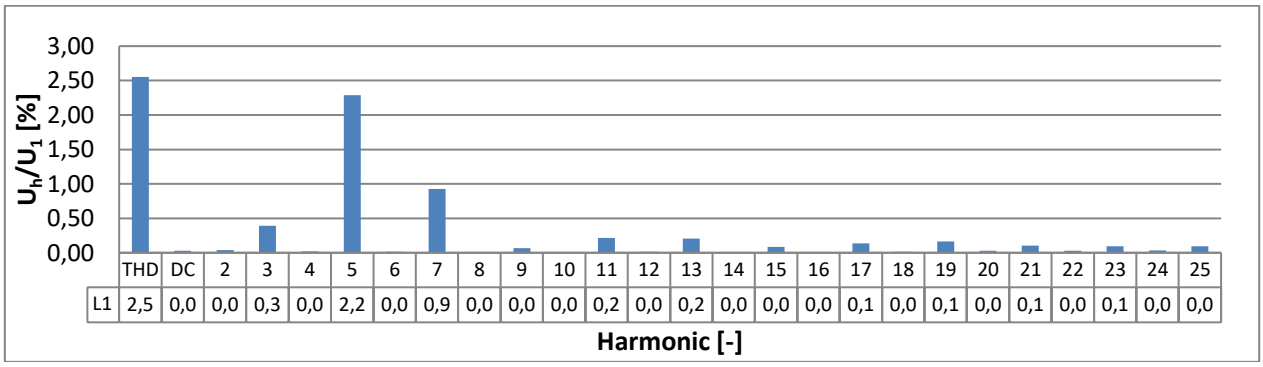

Figure 7. THD and individual harmonic content for kick scooter E-Scooter ESA 800

Results are similar to these obtained for three phase chargers. It should be noticed that supply current were equal 32 A for Alfa Romeo, 10 A for BMW and 2 A for E-Scooter. This difference didn't influence on harmonics, but it influences on voltage symmetry, highest current in one phase means lower voltage in that phase. In case of Alfa Romeo that difference was equal to 3V while cross-section of lines was equal to 6 mm^2. Lower cross-sections will cause higher voltage drops and voltage asymmetry.

4. Conclusions

Based on the conducted research, the following conclusions can be formulated, which are both guidelines for the users and designers of chargers installed in electric vehicles.

1. All tested on-board battery chargers for electric vehicles meet the requirements for the quality of electricity.
2. Charging the battery over 80% of its capacity is characterized by the possibility of dynamic changes in current consumption from the network, which, especially in the case of single-phase chargers, can lead to voltage asymmetry in the installation.

3. The occurring harmonics may result, depending on the power supply system, in the occurrence of zero, positive or negative sequence components, which may affect the operation of other devices in the installation; efforts should be made to reduce the share of higher harmonics.
4. Users must compare power of the charger, specially line current, with maximum line current and overcurrent protection of their installation. In Alfa Tonale PHEV we could use charging current equal to 32 A, while e.g. in Poland typical line and socket at homes are designed for currents equal to 16 A. We got information, that some producers limited maximum AC current in case of meet local typical requirements. In in Kia You can have 22 kW or 11 kW charger depend of country.
5. High current one phase chargers can be sources of voltage asymmetry in electrical installations.
6. It is strongly recommend use RCD's type B as equipment against electrical shock protection in circuits with chargers, because we have many harmonics and sometimes DC components.

5. Acknowledgements

Muhammed Sefa ÇETİN was supported by The Scientific and Technological Research Council of Türkiye (TÜBİTAK) within the scope of Directorate of Science Fellowships and Grant Programmes (BİDEB) 2211-A National PhD Scholarship Program.

6. References

[1] Li P., Xia X., Guo J. "A review of the life cycle carbon footprint of electric vehicle batteries. Separation and Purification Technology", 121389. (2022).
[2] Fattler S., Regett A. "Environmental Impact of Electric Vehicles: Influence of Intelligent Charging Strategies. In Electrified Mobility 2019: including Grid Integration of Electric Mobility", 167-176, Wiesbaden: Springer Fachmedien Wiesbaden, 2022
[3] Zimakowska-Laskowska, M., & Laskowski, P. " Emission from internal combustion engines and battery electric vehicles: Case study for Poland.", Atmosphere, 13(3), 401, 2022
[4] Neugebauer M., Żebrowski A., Esmer, O., "Cumulative Emissions of CO_2 for Electric and Combustion Cars: A Case Study on Specific Models", Energies, 15(7), 2703, 2022
[5] Sheldon T. L., Dua R., Alharbi O. A., "How Cost-effective are Electric Vehicle Subsidies in Reducing Tailpipe-CO_2 Emissions? An Analysis of Major Electric Vehicle Markets.", The Energy Journal, 44(3), 2023
[6] Elkelawy M., Alm ElDin Mohamad H., Samadony M., Elbanna A. M., Safwat A. M., "A Comparative Study on Developing the Hybrid-Electric Vehicle Systems and its Future Expectation over the Conventional Engines Cars." Journal of Engineering Research, 6(5), 21-34., 2022
[7] Morfeldt J., Shoman W., Johansson D. J., Yeh S., Karlsson, S., "If Electric Cars Are Good for Reducing Emissions, They Could Be Even Better with Electric Roads.", Environmental Science & Technology, 56(13), 9593-9603, 2022
[8] Alimujiang A., Jiang P., "Synergy and co-benefits of reducing CO2 and air pollutant emissions by promoting electric vehicles—A case of Shanghai.", Energy for Sustainable Development, 55, 181-189, 2020
[9] Manzolli J. A., Trovão J. P., Antunes C. H., A review of electric bus vehicles research topics–Methods and trends." Renewable and Sustainable Energy Reviews, 159, 112211, 2022
[10] De Cauwer C. et al., "Electric vehicle use and Energy consumption based on real-world electric vehicle fleet trip and charge data and its impact on existing EV research models", World Eletcric Vehicle Journal Vol7., 2015.
[11] Electric power transmission and distribution losses, The World Bank, https://data.worldbank.org/indicator/EG.ELC.LOSS.ZS?locations=1W-EU (13.07.2023)
[12] Charging time summary for EVs, The Mobility House, https://www.mobilityhouse.com/int_en/knowledge-center/charging-time-summary (13.07.2023)
[13] Evtimov I. et al., Life cycle assessment of electric and conventional cars Energy consumption and CO2 emissions, MATEC Web of Conferences 234, 02007 (2018).
[14] Majeau-Bettez G., Hawkins T. R., Strömman A. H., Life Cycle Environmental Assessment of Lithium-Ion and Nickel Metal Hydride Batteries for Plug-In Hybrid and Battery Electric Vehicles, Norwegian University of Science and Technology (NTNU).
[15] Dunn J. B. et al., The significance of Li-ion batteries in electric vehicle life-cycle Energy and emissions and recycling's role in its reduction, Energy & Environmental Science, 2015, 8, 158.
[16] Dunn J. et al., Life Cycle Analysis Summary for Automotive Lithium-Ion Battery Production and Recycling,

Argonne National Laboratory, 2016.

Fatih TATBUL[1] , Meral ÖZARSLAN YATAK[2]

[1]Department of Electrical-Electronic Engineering, Institute of Science, Gazi University, Ankara, Türkiye.
[2]Department of Electrical-Electronic Engineering, Faculty of Technology, Gazi University, Ankara, Türkiye.
[1]fatih.tatbul@gazi.edu.tr, [2]ozarslanm@gazi.edu.tr

[1](ORCID: 0000-0003-2298-3004), [2](ORCID: 0000-0002-1091-1647)

Abstract
Liquid level regulation is a crucial procedure for the vast majority of industrial applications. RT 512 liquid level trainer system manufactured by GUNT Hamburg contains a microcontroller with PID controller algorithm on it. In this study, sliding mode control algorithm has been developed as an alternative to the traditional control algorithm of the RT 512 liquid level control device. The signals that are obtained from voltage-current and current-voltage converter units on the system are sent to sliding mode control algorithm running on Arduino. It has been observed that sliding mode control algorithm can be successfully applied on the liquid level trainer system by critically reducing the chattering problem.

Keywords: chattering, GUNT RT 512, liquid level trainer, sliding mode control

1. Introduction

Control and monitoring of liquid level are frequently used in industrial applications as a result of continuous advancements in automation technology. PID controllers are frequently used due to their reliability, simple structure, and easy parameter adjustment for liquid level systems. However, these types of controllers with fixed parameters are often inadequate in eliminating errors that occur in the system and are generally not suitable for controlling nonlinear systems since they cannot adapt to changing conditions. Therefore, various control methods such as fuzzy control, adaptive control, and sliding mode control are used to cope with the nonlinear structure and parameter uncertainties in processes like temperature, pressure, level, humidity, velocity, and flow.

Sliding mode control method is widely used due to its ease of design, robust control technique, high accuracy performance, and stable control against system uncertainties and external disturbances. This method is one of the most common control method that has been used not only for the industry but also for process control like liquid level. Mathematical modeling of coupled-tank system and designing of sliding mode control for liquid level control were studied by Abbas et. al. [1]. Also, Chen et. al designed a sliding mode controller for a water tank liquid level control system to realize level position regular and tracking control [2]. There are also many studies about the fuzzy sliding mode control. Pam and Nguyen proposed an adaptive PI sliding mode controller for two tank system [3]. They found with simulation study that PI sliding mode control ensured that the actual liquid level reached the desired level in a finite time and reduced chattering around the sliding surface. Alli and Yakut used fuzzy logic sliding mode control algorithm in their study on the isolation of seismic earthquake sensitive structures. Against parameter uncertainties and model deficiencies, it was aimed to eliminate the chattering effect without loss of robustness [4]. Another fuzzy sliding mode control algorithm application was carried out on pattern level control by Bedi et al. [5]. The die level control system includes a number of non-linear features such as hold-release friction in the sliding door, time delay, friction force variability between the reached steel and the inner wall of the die, and nozzle filling/clogging. Ayten and Dumlu proposed Fractional Order Proportional Integral Derivative type sliding mode control (FO-PIDSMC) technique and controlled effectively the uncertain non-linear liquid level coupled tank system in undesired circumstances experimentally [6].

[2] Corresponding author

The existing UDC5000 controller on GUNT RT 512 liquid level controller is designed as execution of only PID control [7]. The contribution of this study is to run alternative control algorithms, e.g. sliding mode controller, and adapt them to the same type of systems with minor modifications on the designed circuits, and foresee a more robust system control with reduced costs.

In this study, a nonlinear control method, sliding mode control, was used to regulate the liquid level control system's output with uncertainties, disruptions, and modeling defects. The primary goal of sliding mode control is to establish a sliding manifold, or hyperplane in the system's state space, which directs the system's trajectory in the direction of a desired state. The state trajectory of the system slides along the sliding manifold towards the desired state rather than converge to it asymptotically as in previous control strategies because the sliding manifold is made to have a switching property. Designing a controller that can simultaneously monitor the liquid level and manage the pump is a difficult task. Sliding mode control, which was implemented on the GUNT RT512 liquid level trainer, was tested and its effectiveness was assessed.

The organization of this paper is as follows: Section 2 includes technical properties and mathematical model of controlled system. Section 3 is on sliding mode control and its application for the system. The necessary mathematical parameters are given in this section. Section 4 includes experimental results for some level data. The last section 5 is on the results and future works.

2. GUNT RT 512 Liquid Level Trainer

The major goal of liquid level control process shown in Fig. 1 is to maintain the liquid level at the process tank at a desired level [8]. The controller gets periodic updates from the pressure sensor on the liquid level at the process tank. In order to achieve the reference level, the controller will compare the liquid level with a desired set point and either increase or reduce the pump's flow rate.

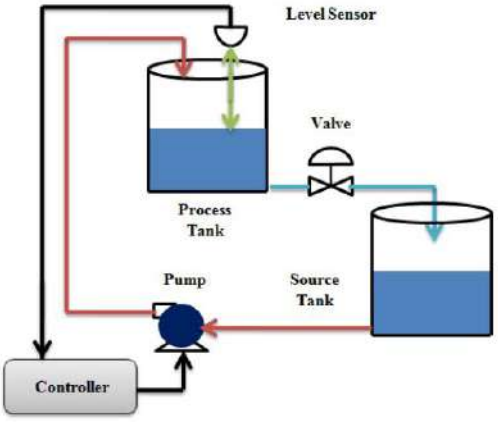

Figure 1. Liquid level control process

GUNT RT 512, liquid level trainer, is outfitted with industrial-grade control systems. The trainer offers thorough experimental level control applications. To maintain the water level in the tube at a specified reference level and follow a predetermined reference trajectory is the goal of the water level management method. Fig. 2 and Fig. 3 show the plant's principal components and its block diagram, respectively.

The liquid in the liquid storage tank is sent to the transparent liquid level tube by means of the pump. The liquid pressure in the liquid level tube is measured by the pressure sensor located under the tube and the current equivalent of the liquid is sent to the controller by means of a pressure current converter operating in the 4-20 mA range. The controller, in turn, opens the electro-pneumatic control valve at the required range and ensures that the desired liquid level is met. With the ball valve at the output, noise can be generated within a certain scale. Electrical connections between components are made inside the switch cabinet.

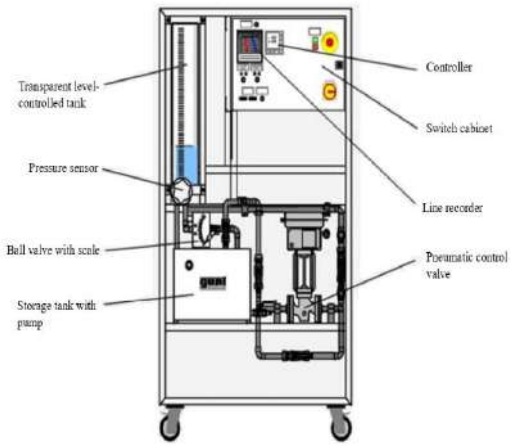

Figure 2. Components of the GUNT RT 512

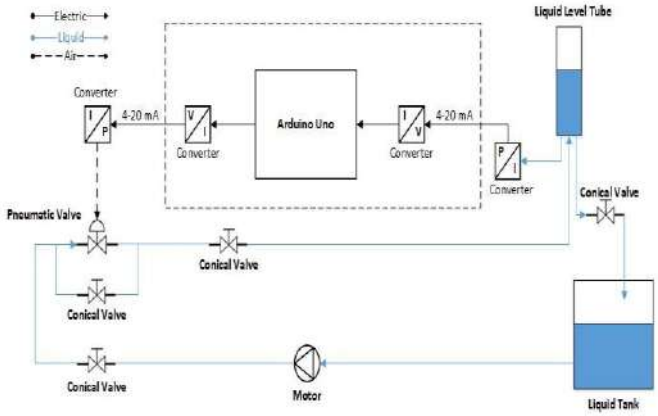

Figure 3. Process for controlling water level in a block diagram

A. System model

First order Transfer Function is used to simulate many engineering systems and it is given in (1),

$$\frac{\textbf{Output signal}}{\textbf{Input signal}} = \frac{H(s)}{I(s)} = \frac{K_p}{\tau s+1} \tag{1}$$

The liquid capacity of the liquid level tube is 7 liters. Its height is 60 cm and its diameter is 113 mm. Since there is a pipe valve at the outlet of the GUNT RT 512 liquid level system, resistance occurs in the system. This resistance is denoted by R. In the case where the change in the liquid height in the system is expressed as H and the liquid flow out of the liquid level tank is expressed as q_0. The resistance of the system is denoted by (2),

$$R = \frac{\textbf{Change in liquid height } (mm)}{\textbf{Flow of the liquid } (mm^3/sec)} = \frac{H}{q_0} \tag{2}$$

In the case, where the ratio of the change in liquid volume V to the change in liquid height is expressed as C, the liquid flow into the liquid level tank is expressed as qi, the capacitance of the system is represented by (3),

$$C = \frac{\textbf{Change in liquid volume } (mm^3)}{\textbf{Change in liquid height } (mm)} = \frac{dV}{dH} \tag{3}$$

In this case, assuming that the liquid level tank is linear, the capacitance equation is written as in (4).

$$C\frac{dH}{dt} = q_i - q_0 \tag{4}$$

Eq. 5 is obtained by substituting (4) into (2),

$$RC\frac{dH}{dt} + H = Rq_i \tag{5}$$

By taking Laplace Transform of (5), Eq. 6 is obtained,

$$G_t(s) = \frac{H(s)}{Q_i(s)} = \frac{R}{RCs+1} \tag{6}$$

In order to obtain the mathematical model of the system, it is necessary to calculate the liquid resistance R and capacitance C values. Ergüzel calculated these values as R=0.012 and C=10032 in his study [9]. In this case, the transfer function of the system is expressed as in (7):

$$G_p(s) = \frac{168}{120.38*s+1} \quad (7)$$

B. Test setup

The inputs are provided to the pneumatic valve and liquid is sent to the liquid level tube through the Arduino Uno. The Arduino Uno records the information produced by the pressure sensor located under the liquid level tube after the necessary signal conversions. The implemented test setup is shown in Figure 4.

The UDC 5000 controller, which performs PID control in the system, was disabled along this study. The signal sent from the pressure/current transducer on the system, under the transparent liquid level tube, is the current signal. Liquid level was read as voltage on Arduino Uno by means of current voltage converter. A voltage signal was sent from Arduino Uno for opening signal of the pneumatic valve. For opening of the pneumatic valve, the voltage signal was converted into current and the control of the valve is thus provided. Current/voltage and voltage/current converters were used to perform these operations. Test setup photo taken from the laboratory can be seen from Figure 5.

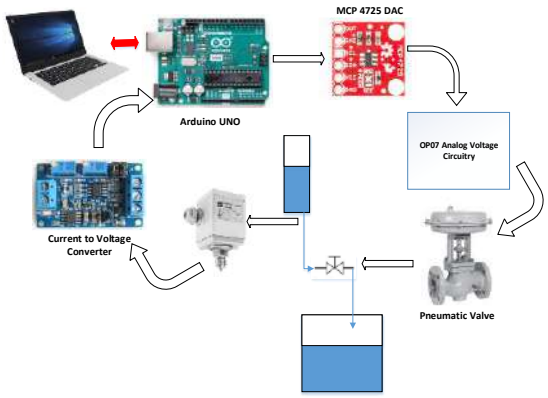

Figure 4. Test setup

Figure 5. Test setup in control laboratory

3. Sliding Mode Controller Design

Early in the 1950s, Emelyanov proposed and developed the variable structure control (VSC) with sliding mode control (SMC) in collaboration with a number of co-researchers from the Soviet Union, including Utkins and Itkis. VSC and SMC have attracted a lot of interest in the control research community during the past few decades. Sliding mode control can be used to regulate and track a system's output even when there are uncertainties, disruptions, and modeling flaws. The primary goal of sliding mode control is to establish a sliding manifold, or hyperplane in the system's state space, which directs the system's trajectory in the direction of a desired state. The state trajectory of

the system will slide along the sliding manifold towards the desired state rather than converge to it asymptotically as in previous control strategies because the sliding manifold is made to have a switching property.

One of the most intriguing features of sliding mode is the discontinuous nature of the control action, in which each feedback channel's primary function is to switch between two clearly distinct system structures, resulting in the existence of a new kind of system motion known as sliding mode in a manifold. This uncommon system property is said to produce excellent system performance, including total rejection of disturbances and insensitivity to parameter fluctuations [10]. However, discontinuous control inputs, commonly known as chattering, cause high-frequency oscillations of the system's state about the sliding manifold in most circumstances of practical interest [11]. There are two potential mechanisms that could result in chattering. First, when parasitic dynamics are present in series with the plant and there are no switching nonidealities, such as delays, the switching device switches ideally at an infinite frequency, leading to the appearance of a small amplitude high-frequency oscillation near the sliding manifold. Second, such high-frequency oscillations can be produced by the switching nonidealities alone. [10]

A sliding mode controller has the ability to control system trajectory. After the initial reaching phase, the system asserts that it "slides" along the line s=0. The particular s=0 surface is selected because, when limited to it, it exhibits good reduced-order dynamics.

The sliding mode function used in this study is given by (8),

$$s(t) = ce(t) + \dot{e}(t) \tag{8}$$

c must satisfy the Hurtwitz condition c>0. Error and its derivative are as defined (9),

$$e(t) = x(t) + x_d(t) \tag{9}$$
$$\dot{e}(t) = \dot{x}(t) + \dot{x_d}(t) \tag{10}$$

where x(t) is the practical liquid height signal and xd(t) is the ideal liquid height signal. Then (11) is obtained,

$$\dot{s}(t) = c\dot{e}(t) + \ddot{e}(t) = c\dot{e}(t) + \ddot{x}(t) + \ddot{x_d}(t) \tag{11}$$

A popular finite-time reaching condition is given in (12)

$$s\dot{s} < 0 \text{ whenever } s \neq 0 \tag{12}$$

Since we need to satisfy (12) above, we designed the sliding mode controller as in (13).

$$u(t) = -\big(\dot{e}(t) - K * sat(s(t))\big);$$
$$if\ abs(s(t)) \leq psi, then\ \ sat(s(t)) = \frac{s}{psi} \tag{13}$$
$$\boldsymbol{if\ abs(s(t)) > psi, then\ sat(s(t)) = sign(s(t))}$$

Where u(t) is the control input, k is the control gain, psi is the boundary layer thickness and s(t) is the sliding surface, which represents the difference between the desired system state and actual system state. The sign function, or sign(), gives positive values a return value of +1 and negative ones a return value of -1. The system slides along the required trajectory as a result of the control input being forced to switch based on the sign of the sliding surface.

Compared to PID, this control law has a number of benefits. Its simplicity (no differentiation, no integration), as well as its complete insensitivity to disturbances, are examples of this.

It is impossible to implement the signum (sign) function (much like a relay without a deadzone). It causes chattering, an indefinitely quick switching action over s = 0. In its substitute, a continuous approximation can be used or boundary layer thickness can be amplified. In our study, since the system response is very slow, we used a large boundary layer thickness so that small chattering occurs.

4. Simulation and Experimental Results

In order to verify the efficiency of sliding mode control, various experiments were conducted. The system was tested with different liquid levels. Simulation results can be seen from Figure 6, 7 and 8.

Figure 6 shows both the reference and actual liquid levels on the same graph. It can be seen from the figure that high precise tracking performance occurs on the simulation of sliding mode control of GUNT RT512 liquid level trainer.

Accurate modeling of the system dynamics and perfect controller design result with minimizing the tracking error and responding quickly to changes in the reference signal. Figure 7 shows the switching characteristics of the control input so that chattering phenomena can be interpreted and Figure 8 point out the error vs time graph. 50 cm reference liquid level can be satisfied at almost 50 seconds. Switching action is very small. Large boundary layer thickness, large sampling time, slow tracking performance results in small switching action. Therefore, there is not a chattering phenomenon occurs in the simulation of sliding mode control of GUNT RT512 liquid level trainer. Similar to the switching action, error vs time graph also shows good tracking performance and small chattering phenomena on the Figure 8.

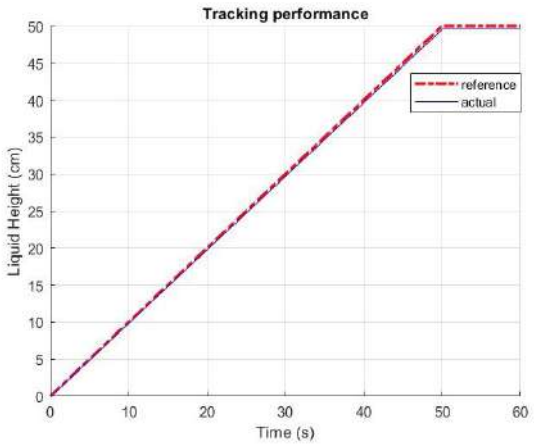

Figure 6. Simulation tracking performance

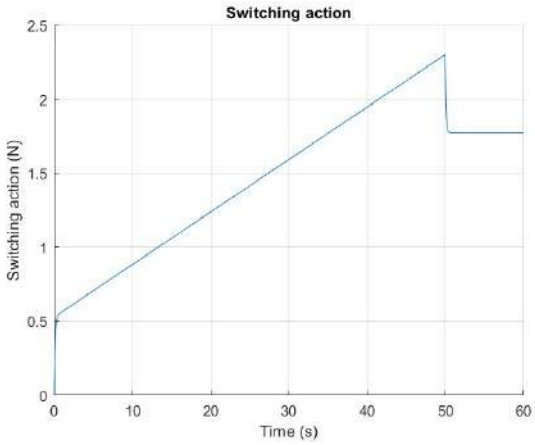

Figure 7. Switching characteristic

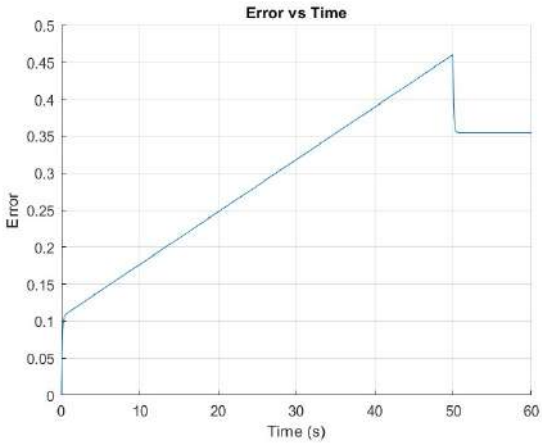

Figure 8. Error vs Time

Real experiment results can be seen from Figure 9, 10 and 11. Figure 9 shows both the reference and actual liquid levels on the same graph. Figure 10 shows the switching characteristics of the control input for MCP4725 DAC and

Figure 11 shows out the error vs time graph. 50 cm reference liquid level can be satisfied by the actual liquid level at almost 30 seconds, After the reference level is satisfied, tracking performance is also satisfactory although there is a lot of disturbance coming from nonlinearities of V/I and V/I converters. Discretization of Simulink Arduino Uno library also effects badly the tracking performance. In spite of low sampling time, large boundary layer thickness there is almost no chattering in our experiment. The control input axes corresponds to the input of MCP-4725 Digital to Analog converter, which works between 0-4095 integer values on Figure 9. Constant control input at specific time intervals means no chattering.

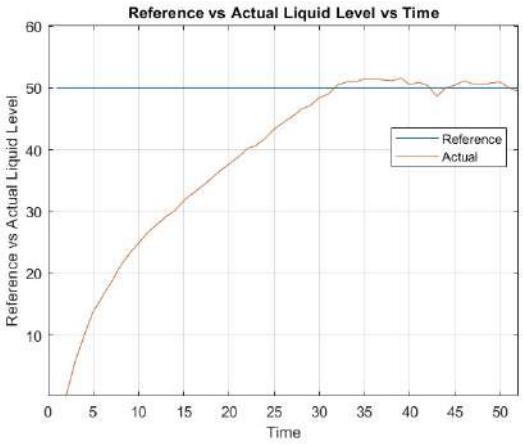

Figure 9. GUNT RT 512 reference vs actual liquid level

Similarly, error vs time graph from Figure 11 also shows good tracking performance and low chattering because of the same reasons explained above.

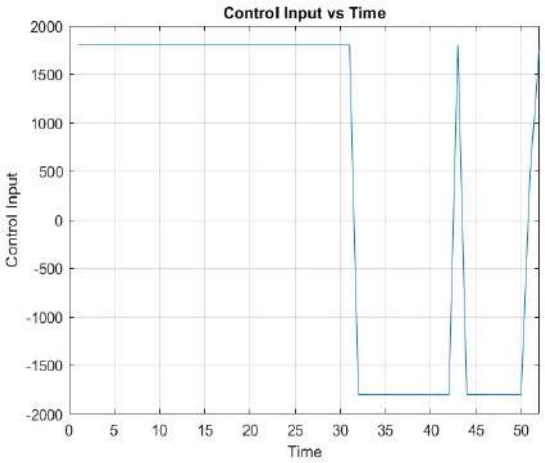

Figure 10. GUNT RT512 control input for MCP 4725 DAC

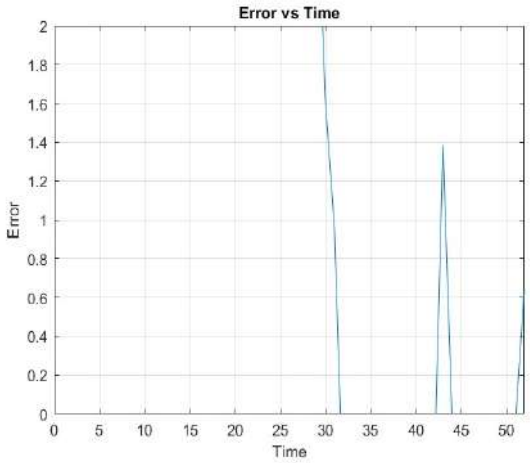

Figure 11. GUNT RT 512 Error vs Time

5. Conclusion

The process of liquid level and control is essential in a variety of sectors, including those that make paper, treat water, process pharmaceuticals, and refine oil. There are numerous ways to regulate the liquid level. In this paper, sliding mode controller was implemented on GUNT RT 512 Liquid Level Trainer. Sliding mode control can be easily implemented on most of the nonlinear systems. It can be concluded from this study that sliding mode controller design works well with simulation and real time experiments. It can be get better by modeling system dynamics more efficiently and using converters that are more precise on the system environment. Fuzzy sliding mode is also advantageous control algorithm in terms of chattering reduction and in the future studies fuzzy sliding mode control will be implemented on GUNT RT 512 liquid level trainer system.

6. Acknowledgments

The article is not supported by any institution, project, person, etc.

7. References

[1] Abbas H, Asghar S, Qamar S. “Sliding mode control for coupled-tank liquid level control system”. 10th International Conference on Frontiers of Information Technology, Islamabad, Pakistan, 325-330, 17-19 December 2012. doi: 10.1109/FIT.2012.65.

[2] Chen HM.,. Chen ZY, Su JP. “Design of a sliding mode controller for a water tank liquid level control system”. 2nd International Conference on Innovative Computing, Informatio and Control, Kumamoto, Japan, 335-335, 05-07 September 2007.

[3] Pham TT, Nguyen CN. “Adaptive fuzzy proportional integral sliding mode control for two-tank interacting system”, J. Eng. Technol. Sci., 54(3), 580-592, 2022.

[4] Alli, H, Yakut O. “Fuzzy sliding-mode control of structures,” Engineering Structures, 2, 277-284, 2005.

[5] Bedi JS, Kueon Y, Kim Y,d Lim CG. “Fuzzy sliding mode mould level control in continuous casting process," FUZZ-IEEE'99. 1999 IEEE International Fuzzy Systems. Conference Proceedings Seoul, Korea (South), 1376-1381,1999.

[6] Ayten K.K, Dumlu A., “Implementation of a PID type sliding-mode controller design based on fractional order calculus for industrial process system”, Elektronika Ir Elektrotechnika 27(6), 4-10, 2021.

[7] Özarslan M., Bay ÖF. “ GUNT RT 512 sıvı seviye denetim cihazının bulanık denetimi”. Otomatik Kontrol Ulusal Toplantısı (TOK’06), Türkiye, 6-8 Kasım 2006.

[8] Alotaibi M, Balabid M, Albeladi W, Alharbi F. “Implementation of liquid level control system”. 2019 IEEE International Conference on Automatic Control and Intelligent Systems (I2CACIS), Selangor, Malaysia, 311-314, 29 June 2019. doi: 10.1109/I2CACIS.2019.8825058.

[9] Erguzel TT. “A hybrid PSO-PID approach for trajectory tracking application of a liquid level control process”, Int. J. Optim. Control, Theor. Appl., 5(2), 63–73, Jun. 2015.

[10] Young KD, Utkin VI, Ozguner U. “A control engineer's guide to sliding mode control”. IEEE Transactions on Control Systems Technology, 7(3), 328-342, May 1999, doi: 10.1109/87.761053.

[11] Mohammadi K, L’Afflitto A., “Continuous First-Order Sliding Mode Control Law,”. ASME 2017, Virginia, USA. October 11–13, 2017. V001T09A002. ASME. https://doi.org/10.1115/DSCC2017-5082.

International Conference on Advances and Innovations in Engineering

G-GLOVE: A VR/AR Glove That Sensates at Your Fingertips

Hatice Meltem Nergiz Şirin[1] , Enes Arslan [2], Muhammed Furkan Ölçal [3]

[1]Department of Software Engineering, Faculty of Engineering, Hasan Kalyoncu University, Gaziantep, Turkey.
[2]Department of Computer Engineering, Faculty of Engineering, Hasan Kalyoncu University, Gaziantep, Turkey.
[3]Department of Electrical-Electronics Engineering, Faculty of Engineering, Hasan Kalyoncu University, Gaziantep, Turkey.
[1]hatice.sirin@hku.edu.tr, [2]enes.arslan@std.hku.edu.tr, [3]mfurkan.olcal@std.hku.edu.tr

[1](ORCID: 0000-0002-7354-1364)

Abstract
Recent advances in telecommunications and the tactile internet have opened doors to explore the human senses through wearable technology. Wearable technology enables tactile sensations and control over the network using virtual reality (VR). Within the scope of this project, we are developing a unique tactile glove with a unique mechanical design, offering a more realistic and economical option than existing solutions. The tactile glove allows users to have an interactive experience by feeling virtual objects in virtual reality environments. This project aims to support Turkey's AR / VR equipment production and contribute to the national technology move. The glove's innovative design plays an important role in achieving this goal by offering a choice of high-quality and cost-effective equipment. The importance and potential of the AR/VR sector is combined with wearable technologies, emphasizing the main purpose of our project. Glove design plays an important role in enhancing the impact and engagement of AR/VR experiences by experiencing tactile sensations and control in virtual environments. Tactile glove technologies are wearable devices that allow users to detect objects in VR and AR environments. These technologies provide users with tactile sensations and control, making VR and AR experiences more realistic and interactive. In this context, using the glove produced by the G-GLOVE project, users can feel and interact with virtual objects as if they were real objects.

Keywords: Information and Communication Technology, Wearable Technologies, AR/VR, IoT

1. Introduction

The significance and potential of the AR/VR sector, combined with wearable technologies, are central to our project's objective of enhancing the sense of realism in virtual experiences. Therefore, the foundational aspect of our project is the design of a glove, which is a crucial step in elevating the sense of realism. This glove enables users to gain tactile sensations and control in virtual environments, contributing to more immersive and interactive AR/VR experiences.

Tactile glove technologies are wearable devices that allow individuals to feel objects in virtual reality (VR) and augmented reality (AR) environments. These technologies provide users with tactile sensations and control, making VR and AR experiences more lifelike and interactive. In this context, users can use the glove produced by the G-GLOVE project to feel and interact with virtual objects as if they were real.

The tactile feedback feature at the core of our project is adaptable for use in various fields, enabling the production of both high-quality and cost-effective products. Our future goal is to adapt and advance this project for different sectors such as education and healthcare. By designing various variations of our product, we aim to contribute to the realization of quality projects that allow users to feel and interact with operations in virtual environments.

2. Overview of Wearable Technology

Wearable technology can be described as a series of smart devices worn on the body that enrich and simplify people's lives. These devices offer users the opportunity to track daily activities, monitor their health, manage personal data,

[1]Corresponding author

communicate, and enhance entertainment experiences. Wearable technology provides users with a continuously connected and interactive experience, helping them lead more efficient, enjoyable, and healthy lives.

Wearable technology products must meet certain criteria for user comfort, including comfortable and ergonomic design, sensory feedback, a pleasant sensation on the skin, freedom of movement without restriction, ease of cleaning and hygiene, personalization and adjustability, durability, and energy efficiency. The acceptance of these criteria by users makes it easier for wearable technology to become a part of daily life. [1]

The growth potential of Turkey's wearable technology market is driven by the development of technology infrastructure in the country and the young population's interest in technology. Additionally, as Turkish consumers' interest in technology increases, it is expected that sales and market share of wearable technology products will rise. While Turkey's market has significant growth potential for wearable technology, success in this field can be attributed to offering user-centric and innovative products. It is believed that companies can successfully capitalize on Turkey's wearable technology market by understanding customer needs and developing products accordingly.

Our project is based on a solid foundation, established through literature review and the examination of existing systems. This demonstrates that a product has been developed that will contribute to Turkey's scientific and technological strength in this field. In conclusion, this tactile glove project offers a competitive and innovative product that contributes to Turkey's national and indigenous technology initiative for AR/VR equipment production. This vision allows Turkey to take forward-looking steps in the field of wearable technology and attain a strong position in the international market.

3. Methodology

Wearable technologies are considered one of the most significant technological elements of the 21st century, as acknowledged by [9]. They represent a category of electronic devices that can be worn as accessories, adhere to the user's body, or be embedded in clothing. These devices are practical tools that are supported by microprocessors, capable of receiving and transmitting data over the internet, and can be used hands-free. They facilitate information transmission through smart sensors and are associated with various technology domains in the literature, such as sensors, virtual reality (VR), and the Internet of Things (IoT).

During the initial ideation phase of our wearable technology project, we conducted research and data collection, and it was observed that wearable gloves produced by companies like Tesla, Oculus, and Haptx existed in the market. However, these gloves were not easily accessible due to their high cost. [2], [3], [4], [5]. In the thematic literature of wearable technologies developed in Turkey, it was found that there were devices capable of sensing the environment and transmitting these sensations through touch [6]. Additionally, there were projects related to professional training simulations using data gloves [7], as well as sign language recognition gloves [8]. However, no similar project to the one we are proposing has been encountered.

We have provided the sensitivity results obtained during the testing phases of our project in the attached documents. To evaluate the product's supply and demand dynamics, we conducted a survey among students majoring in software, electrical-electronics, and computer engineering. According to the survey results, 64% of the respondents expressed their interest in using virtual gloves while playing VR games.

Figure 1 illustrates the hardware structure of the glove to be produced in our project. The necessary work packages for hardware and software integration in our project are listed below.

Hardware and Software Integration Work Packages

Design and Planning: This phase involves the initial design of the wearable glove, including the selection of materials and components. Prototypes will be developed to test the feasibility of the design. To design the hardware components necessary for a wearable digital glove, the first step is to create part designs using SolidWorks, as illustrated in Figure 2. During the planning phase, careful consideration is given to selecting a flexible glove (made of fabric) that is compatible with our product and choosing the appropriate programming board.

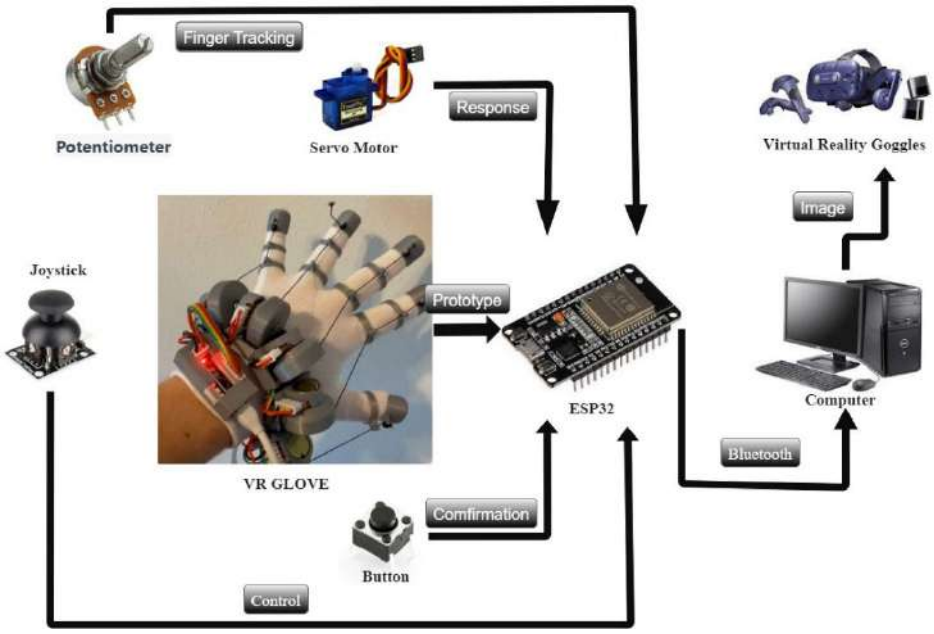

Figure 1. Hardware structure of the Glove.

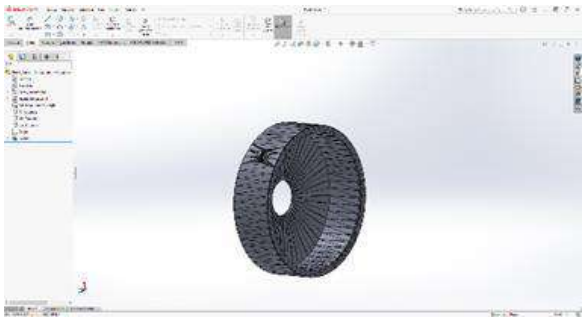

Figure 2. Solidwork Part Designs.

Prototyping: The prototype depicted in Figure 3 showcases the spools that have been 3D printed as part of our wearable device. Assembly of the printed parts, spools, and electronic hardware is carried out during the prototyping stage. Subsequently, the circuit created is connected to the programming board, and the prototype software is developed.

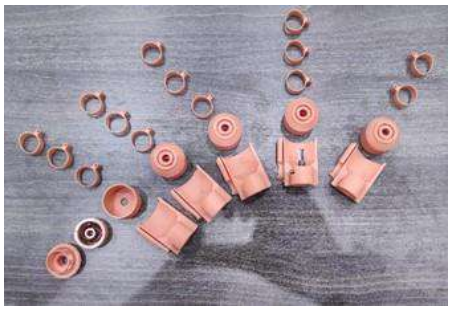

Figure 3. 3D-Printed Parts

Analysis and Test: Our hardware product, depicted in Figure 4, was initially subjected to testing, which included open bench tests, tests conducted on a breadboard, and assessments of mechanical efficiency and usability.

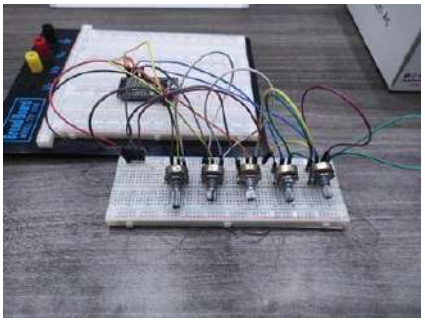

Figure 4. Testing Phase

Software Development: The software required to interface with the glove, interpret sensor data, and provide user feedback will be developed. This may include developing applications for VR/AR environments. Extensive user testing will be conducted to evaluate the effectiveness and comfort of the glove, making necessary adjustments based on feedback. Following the manufacturing process, the digital glove is tested in both a simulation environment and the Unity platform, as depicted in Figure 5. Furthermore, the glove has been evaluated in a VR environment and a VR game, and these tests are showcased in the project presentation video.

Figure 5. Simulation.

In summary, our methodology for developing this wearable technology project involves a comprehensive approach, encompassing design, hardware integration, software development, testing, and optimization. The project aims to address the accessibility and cost issues associated with existing wearable gloves and introduce a unique solution to the field of sensory feedback and interaction in VR/AR environments.

4. Results

The digital glove, as depicted in Figure 6, not only showcases its design but also underscores its extensive range of potential applications, including simulation-based training, medical rehabilitation, sports and entertainment, and VR gaming. The digitization of finger movements also makes it an ideal tool for therapists to remotely monitor and evaluate rehabilitation progress. Through tactile feedback, our product, which we plan to produce affordably and with high quality, has the potential for modification to serve various fields. In the upcoming phases of our project, we aspire to develop a product that can deliver a similar sensory experience, particularly in the education sector and for individuals with physical disabilities. By offering the capability for live training and introducing alternative variations, this product will empower a trained workforce to engage in virtual operations while experiencing them firsthand.

Figure 6. G-Glove.

5. Acknowledgements

This work was financially supported by Hasan Kalyoncu University Scientific Project Research Coordination under grant Student-Centered Project.

6. References

[1] Gribel, L., 2021. Drivers Of Wearable Computing Adoption: An Empirical Study Of Success Factors Including IT Security And Consumer Behaviour-Related Aspects. [online] Pearl.plymouth.ac.uk.
[2] HI5 VR GLOVE BUSINESS EDITION, https://hi5vrglove.com/store/hi5glove, (29.11.2022)
[3] MANUS xsens metagloves, https://www.manus-meta.com,(29.11.2022)
[4] HaptX Gloves G1, https://haptx.com, (29.11.2022)
[5] Plexus Developer Kit, http://plexus.im/, (29.11.2022)
[6] Salman Alihan, Algebra Veri Eldiveni ve Arttırılmış Gerçeklik ile Mesleki Eğitim, http://ibrahimturkoglu.com/?p=481, (29.11.2022)
[7] Aksoy Yusuf Can, İşaret Dilini Algılayan Eldiven, https://tubitak.gov.tr/sites/default/files/2750/2242_final_kitapcik_2020.pdf, (29.11.2022)
[8] Özgönüz, Mustafa Ali, Virtual Eyes, https://tubitak.gov.tr/sites/default/files/2750/2242_final_kitapcik_2020.pdf, (29.11.2022)
[9] Sönmez Çakır, Fatma & Aytekin, Alper & Akgün, Fatma. (2018). Nesnelerin İnterneti ve Giyilebilir Teknolojiler. 4. 84-95.

International Conference on Advances and Innovations in Engineering

FPGA Implementation of Fractional Order Volta's Chaotic System
Kesir Dereceli Volta Kaotik Sisteminin FPGA'da Gerçeklenmesi

Muhammet Ali ARSERİM[1]

Electrical and Electronics Engineering Department, Engineering Faculty, Dicle University, Diyarbakır, Turkey.
marserim@dicle.edu.tr

(ORCID: 0000-0002-9913-5946)

Abstract

In this study, FPGA hardware-in-loop implementation of the Volta chaotic system was carried out. Fractional Order integrator was designed as FIR filter by using Power Series Expansion. FIR filter order was chosen as 5, sampling rate was 1e-6. It was seen that chaotic behavior was achieved with commensurate order, q= 0.98. Simulation and hardware-in loop implementation were created in MATLAB/Simulink software by using System Generator toolbox for Xilinx-AMD FPGAs. Results of Simulation and hardware-in-loop were same which means that the model can be run in the related hardware successfully. After all, the proposed model can be used in high speed chaotic system applications as chaotic control and cryptology.

Keywords: Fractional Order, Volta chaotic system, FPGA, hardware-in-loop

1. Introduction

Chaos phenomena was first introduced by Lorenz by his study names as Deterministic Non-Periodic Flow in 1963[1]. Since then, famous chaotic systems such as Liu, Chen, Lü, Rössler, and Arnedo were presented [2]. A deterministic system can be chaotic if its behavior sensitively depends on initial conditions [3]. Besides, nonlinear dynamics of a system may form a chaotic behavior [4]. Chaotic systems can be applied in many applications such as communications systems, encryption, pseudo-random generators and in many fields of science such as chemistry, physics, biology, control, and others [5].

Fractional calculus had an history about 300 years and famous mathematicians as Euler, Lagrange, Laplace, Fourier, Rieman, Liouville, Grünwald and so many others contributed it [2]. It can be said that fractional calculus is the generalized form of classical calculus. Fractional Order(FO) calculus can describe the system better than the integer order in several real world systems such as long electrical lines, electrochemical processes, dielectric polarization, colored noise, viscoelastic materials, chaos, and control theory [6].

FPGA design of the systems provides low power consumption, high speed processes due to high parallelism and real time computation [7]. In addition, several studies about FPGA implementation of fractional order chaotic systems were carried out. Some examples of fractional order FPGA implementation of chaotic systems are Chua's chaotic system, Liu chaotic system and controllable V multishape system, Lorentz and multi-scroll, Dadras, Aizawa, Thomas and 4 Wings attractors [8].

The aim of this study is to implement FPGA hardware-in loop design of FO Volta chaotic system by a low cost FPGA trainer card, name as Basys3. Therefore, System generator toolbox in MATLAB/Simulink software is used for model design.

Rest of the paper is organized as follows. Section 2 gives brief information about Volta chaotic system, fractional order calculus and Basys3 FPGA card. Section 3 includes the implementation of FO Volta chaotic system and the findings. Also, results are discussed in Section 4.

[1]Corresponding author

2. Material and Methods

In this section first of all, Integer Order Volta system will be described and then FO FIR filter approach by using Power Series Expansion will be given. Finally, Basys3 FPGA trainer card will be explained.

2.1. Volta chaotic system

Volta chaotic system was found by Volta during his doctorate thesis in 1984 [9]. The state space equations were given as,

$$\frac{dx(t)}{dt} = -x(t) - 5y(t) - z(t)y(t) \quad (1)$$

$$\frac{dy(t)}{dt} = -y(t) - 85y(t) - x(t)z(t) \quad (2)$$

$$\frac{dz(t)}{dt} = 0.5z(t) + x(t)y(t) + 1 \quad (3)$$

and initial conditions were (8,2,1). Regarding initial conditions, Lyapunov exponentials(LE) of the system were 0.064979, -1.0708, and -1.4936 [9]. One positive LE can be commented as the chaotic behavior of the system. Simulink model of the Volta system can be given as Figure 1

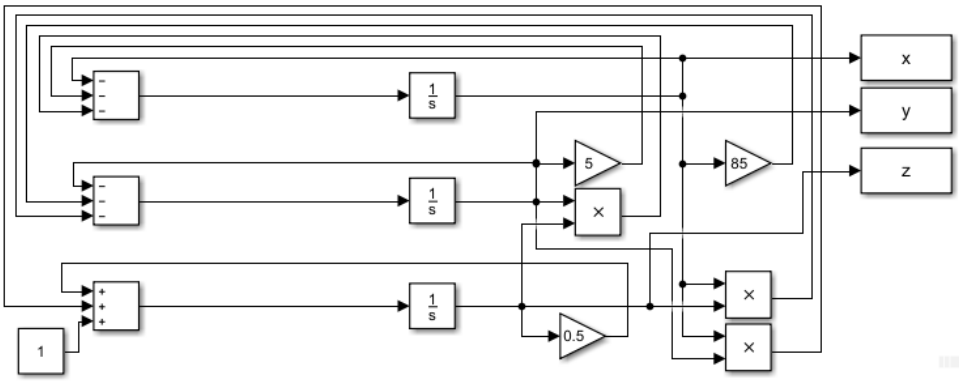

Figure 1. Simulink model of Volta system

Three dimensional plot of x, y, and z space state variables is given in Figure 2. It can be seen from the figure that the orbits of the system are non-periodic.

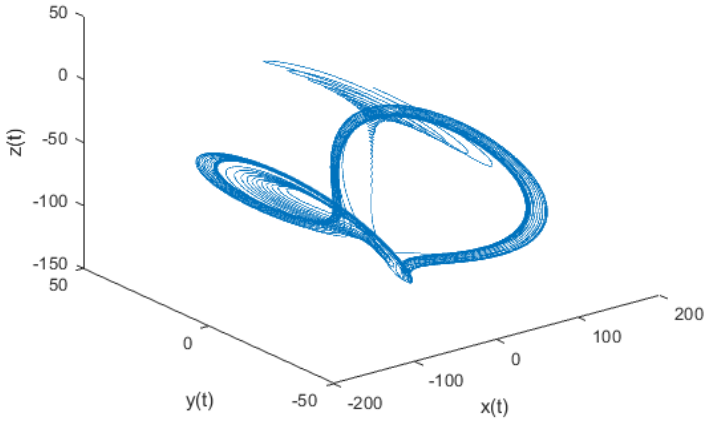

Figure 2. Three dimensional view of Volta system

2.2. Fractional calculus

Fractional calculus can be described as generalization of the integer order differentiation and integration by using ${}_aD_t^r$ operator [2]. Here, r denotes the order, a and t denote the limits of the integration. The definition of continuous integro-differential operator is given in (4),

$$ {}_aD_t^q = \begin{cases} \frac{d^q}{dt^q} & q > 0 \\ 1 & q = 0 \\ \int_a^t (d\tau)^{(-q)} & q < 0 \end{cases} \quad (4) $$

There are three well-known fractional integro-differential definitions as Grünwald-Letnikov(GL), Rieman-Liouville(RL) and Caputo [2]. In this study GL definition will be used. GL definition is given as (5),

$$ \frac{d^q f(t)}{dt^q} = \lim_{h \to 0} \frac{1}{h^q} \sum_{j=0}^{q} (-1)^j \binom{q}{j} f(t - jh), \quad (5) $$

where q denotes the order and $\binom{q}{j}$ is binomial coefficient. Discretization of the systems are important for real time applications due to implement system in a hardware [2]. The discretization methods generally makes s→z transformation [10]. There are several discretization method and Power Series Expansion(PSE) is the one of them. The FO integral or derivative is given in (6),

$$ \boldsymbol{G(s) = s^{\pm q}, q \in [0\ 1] \subseteq R^+} \quad (6) $$

where s is Laplace operator and q is the order. If the backward Euler is used, then FO integral and derivative can be defined as,

$$ \boldsymbol{\nabla_T^{\pm q} f(nT) = T^{\pm q} \sum_{k=0}^{\infty} (-1)^k \binom{\mp q}{k} f\big((n-k)T\big).} \quad (7) $$

Power series expansion of a function forms a polynomial function so it can be designed as a FIR filter [10].

2.3. Bayss3 FPGA card

Basys3 is low cost but efficient FPGA trainer card produced by Digilent firm. It has an artix-7 FPGA and its clock rate is 100 MHz. It has sufficient switches, LEDs and other I/O devices to carry out designs without the need for any additional hardware. Basys3 trainer card is suitable for programming it by using MATLAB/Simulink via System Generator [11].

3. Experimental Study

In the experimental study, FO Volta chaotic system was modeled in Matlab/Simulink software. In the model, FO integrator was designed as FIR filter by using dfod2() function, formed by Ivo Petras [12]. In addition, commensurate fractional order q=0.98 was chosen, filter order was 5 and samping frequency was chosen as 1 MHz. The transfer function of designed filter is given as below,

$$ \boldsymbol{TF = \frac{1 - 0.02z^{-1} - 0.0098z^{-2} - 0.006468z^{-3} - 0.004819z^{-4} - 0.003836z^{-5}}{0.7586} \frac{10^{-6}}{1 - z^{-1}}} \quad (8) $$

Therefore, Simulink model of FO Volta system, constructed with FPGA blocks, was simulated and after successful simulation results, hardware-in-loop bit file, and related Simulink block was generated by using System generator block. The simulation model and its hardware- in- loop model is shown in Figure 3.

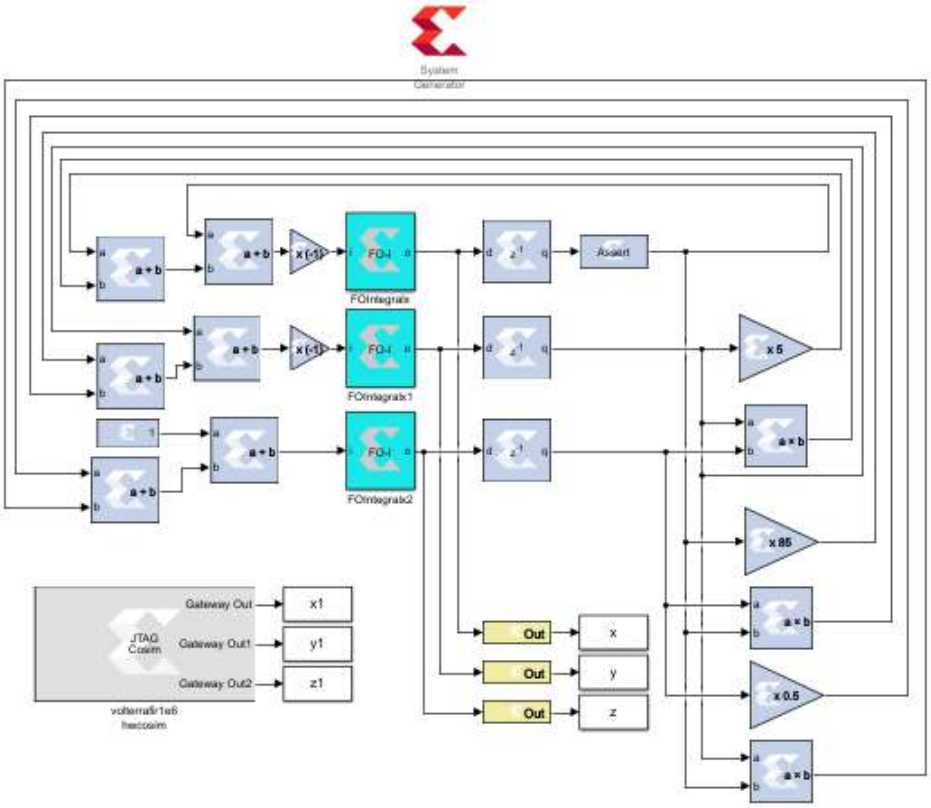

Figure 3. Simulation and hardware-in-loop model of Volta system

In addition, 5th order FIR filter design of FO integral is shown in Figure 4. For each state space equation one FO Integral block is added.

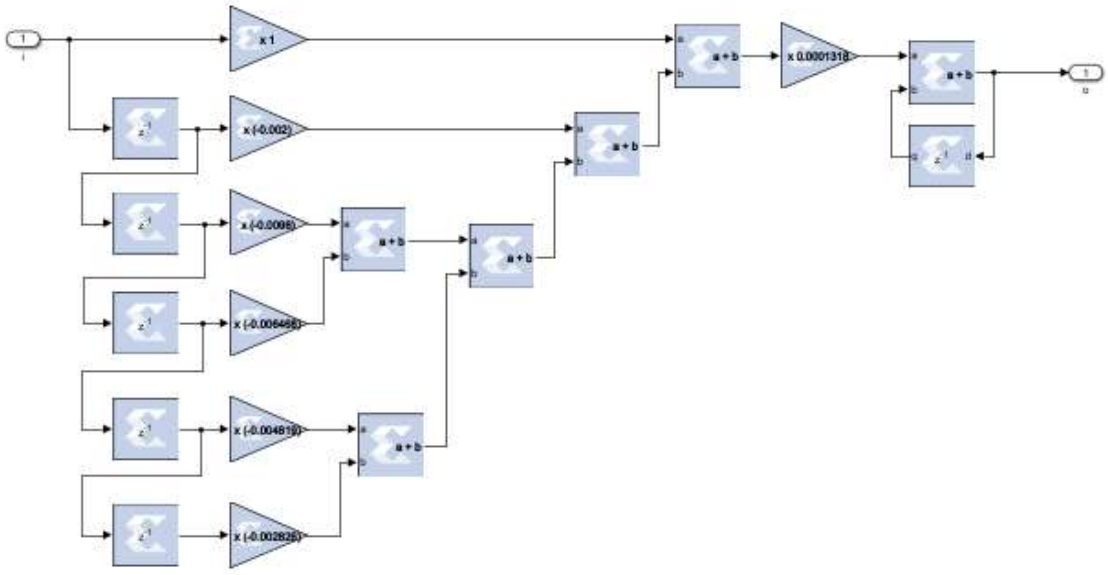

Figure 4. Simulation and hardware-in-loop model of Volta system

Simulation and hardware-in-loop simulation results were 3-D superimposed in Figure 5. Therefore, from the Figure 5 it can be seen that both results are coincided.

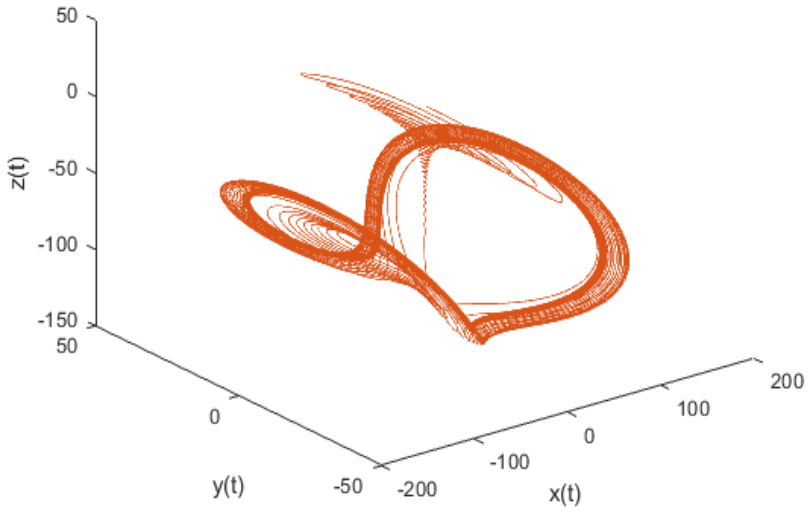

Figure 5. 3D plot of simulation and hardware-in-loop simulation results

4. Results

Designed FO Volta chaotic system in FPGA had a high operating speed as 1 Mhz. The high sampling rate may provide using the design in cryptology and control areas. The FIR filter order was truncated as 5 and this will yield an approximation error, but it can be seen from Figure 5 that FO Volta system behavior is obtained. On the other hand, low filter order increases the operating speed. As a result, FO Volta chaotic system is successfully operated in a low cost FPGA. Further studies, it will be planned to apply the designed system in real time applications.

5. Acknowledgements

The author thanks to AMD- Xilinx firm for donation of Basys3 hardware and Vivado software license

6. References

[1] Lorenz, E. N. “Deterministic nonperiodic flow". Journal of Atmospheric Sciences 20(2), 130-141, 1963.
[2] Petráš, Ivo. Fractional-order nonlinear systems: modeling, analysis and simulation. 1st ed. Heidelberg, Germany, Springer Science & Business Media, 2011.
[3] Boccaletti, S., Grebogi, C., Lai, Y. C., Mancini, H., & Maza, D. “The control of chaos: theory and applications”. Physics Reports, 329(3), 103-197, 2000.
[4] Shah, D. K., et al. "FPGA implementation of fractional-order chaotic systems". AEU-International Journal of Electronics and Communications 78, 245-257, 2017.
[5] Sayed, W. S., et al. "Chaotic dynamics and FPGA implementation of a fractional-order chaotic system with time delay". IEEE Open Journal of Circuits and Systems 1, 255-262, 2020.
[6] Dorcák E., Valsa J., Terpák J. and Gonzalez E., "Comparison of the methods for the calculation of fractional-order differential equations". 12th International Carpathian Control Conference (ICCC), Velke Karlovice, Czech Republic, 80-84, 25-28 May, 2011,
[7] Abd El-Maksoud, A. J., et al. "FPGA implementation of fractional-order Chua's chaotic system". 7th International conference on modern circuits and systems technologies (MOCAST). Thessaloniki, Greece, 1-4, 9-10 May 2018.

[8] Pano-Azucena, A. D. et al. "FPGA-based implementation of different families of fractional-order chaotic oscillators applying Grünwald–Letnikov method". Communications in Nonlinear Science and Numerical Simulation 72, 516-527, 2019.
[9] Petráš, I. "Chaos in the fractional-order Volta's system: modeling and simulation". Nonlinear Dynamics, 57, 157-170, 2009.
[10] Das, S. and Indranil P. "Fractional order signal processing: introductory concepts and applications." 1st ed. Heidelberg, Germany, Springer Science & Business Media, 2011.
[11] Digilent reference https://digilent.com/reference/programmable-logic/basys-3/start (14.8.2023)
[12] Petras I. "Digital Fractional Order Differentiator/integrator - FIR type". https://www.mathworks.com/matlabcentral/fileexchange/3673-digital-fractional-order-differentiator-integrator-fir-type (14.8. 2023)

International Conference on Advances and Innovations in Engineering

Forecasting Wind Speed Measured From Nacelle Anemometer: Integrating Empirical Mode Decomposition, Convolutional Neural Network and Gated Recurrent Unit

Ceyhun YILDIZ[1]

Department of Electricity and Energy, Elbistan Vocational School, K.Maraş İstiklal University, K.Maraş, Turkey.
ceyhun.yildiz@istiklal.edu.tr

(ORCID: 0000-0002-5498-4127)

Abstract
There is a cubic order relationship between wind speed and wind power. Therefore, accurate wind speed forecasts are necessary for wind power forecasting. However, forecasting wind speed is a challenging process due to the uncertain and variable characteristics of the wind speed signal. In this study, a three stage deep learning model was proposed to forecast wind speed. The efficient signal decomposition method called empirical mode decomposition (EMD) was used in the first stage to extract features from the original wind speed signal. In the second stage, a convolutional neural network (CNN) was employed to capture spatial patterns from the extracted features. The gated recurrent unit (GRU) network was used in the third stage to capture temporal patterns from CNN outputs. The performance tests of the proposed model were realized using the wind speed data set measured from the nacelle anemometer of a grid-tied wind turbine. To confirm the effectiveness of the proposed model, the obtained results were compared with the forecasting models based on multi-layer perceptron (MLP), EMD-MLP, and EMD-GRU. The results of this study indicated that the proposed forecasting model has promising performance and can be used effectively for wind speed forecasting.

Keywords: convolutional neural network, empirical mode decomposition, gated recurrent unit, wind speed forecasting

1. Introduction

The installed capacity of wind power plants has rapidly increased all around the world [1]. However, the uncertain and variable nature of wind power resulted in technical and economic problems for electrical grid systems. To overcome these problems, forecasting wind power is critical for the secure and economic operation of wind power plants.

The majority of approaches proposed in the literature employed wind-to-power and wind-to-wind forecasting methods for wind power forecasting [2]. The uncertain and variable nature of wind speed complicates the process of wind speed forecasting. Furthermore, the third-order relationship between wind speed and wind power increases the complexity of wind power forecasting. Therefore, achieving precise wind speed forecasting can help alleviate this complexity.

Extensive literature has emerged around the topic of wind speed forecasting, encompassing various approaches. Researchers proposed physical, statistical, machine learning (ML), and deep learning (DL)-based models for long, medium, and short-term wind speed forecasting [3]. Physical approaches often employ Numerical Weather Prediction (NWP) models. However, these models need numerous input parameters, including topographic maps and a multitude of initial condition values specific to the studied regions. Moreover, due to the high computational cost associated with NWP models, physical approaches necessitate a significant amount of time to generate wind speed forecasts. [4]. Therefore, data-driven approaches based on statistical, ML, and DL are more suitable for real-time forecasting of short-term wind speed. The statistical models based on autoregressive moving average (ARMA) and

[1]Corresponding author

autoregressive integrated moving average (ARIMA) were proposed in [5] and [6]. These traditional statistical models are computationally efficient and can easily be implemented for real time wind speed forecasting. However, these traditional statistical approaches, such as ARMA and ARIMA, were initially designed for modeling linear relationships between input and output parameters. On the contrary, it is well known that wind speed data has nonlinear and uncertain characteristics. It is well known that ML-based approaches are successful in nonlinear data modeling processes. [7] proposed a support vector machine (SVM)-based model for short term wind speed forecasting. [8] compared the wind speed forecasting capabilities of three different artificial neural network (ANN) structures. Another ML algorithm called extreme learning machine (ELM) was proposed in [9] for the wind speed forecasting problem. These ML-based models achieved successful results. Yet, over the past twenty years, the adoption of robust hardware architectures like graphical processing units has unleashed the potential of deep learning (DL) models in diverse fields. Accordingly, researchers developed different DL models for the wind speed forecasting problem. [10] proposed bidirectional long-short-term memory (LSTM) based-DL architecture to forecast short-term wind speed. [11] introduced a convolutional neural network (CNN)-based wind speed forecasting model. The authors stated that they achieved promising results. Indeed, the literature on DL-based wind speed forecasting exhibits several notable gaps. One area that requires further investigation is the exploration of various DL model architectures and their performances across different datasets. By delving into these aspects, significant contributions can be made to enhance the understanding and effectiveness of wind speed prediction using DL techniques.

In this study, a three-stage DL-based model was introduced for short-term wind speed forecasting. The first stage employed the Empirical Mode Decomposition (EMD) algorithm for feature extraction. In the second stage, a CNN network was utilized to capture spatial patterns form the extracted features. Subsequently, in the third stage, a Gated Recurrent Unit (GRU) network was employed to capture temporal information from the outputs of the CNN network. The primary focus of the model was to predict wind speed values from a nacelle anemometer installed on a grid-tied wind turbine.

The contributions of this study can be outlined as follows:
1-Introduction of a robust forecasting model that integrates EMD, CNN, and GRU techniques for wind speed prediction using data from a wind turbine's nacelle anemometer.
2-Execution of performance comparison analyses utilizing real-site data collected from the grid-tied wind turbine's nacelle anemometer.

The rest of this paper is organized as follows: Section 2 establishes the theoretical framework underpinning the methods employed in this study. In Section 3, a comprehensive exploration of the proposed wind speed forecasting model is presented. Implementation specifics and the outcomes of the experimental investigations are summarized in Section 4. Finally, Section 5 concludes the study.

2. Theoretical Background

In this study, a three stage forecasting model was developed for wind speed measured from a nacelle anemometer. The model input data (historical wind speed signal) was decomposed in the first stage to extract meaningful features. The EMD algorithm was used in this stage to effectively decompose historical records of the input parameters. The next subsection presents the theoretical foundation of the EMD algorithm.

2.1. Empirical Mode Decomposition

The EMD algorithm was introduced in [12] for the decomposition of nonlinear and non-stationary signals. It has taken the great attention of researchers from many fields [13]. The main component of the EMD is sifting any function $s(t)$ to obtain a new function $y(t)$ through the following steps:

1- Determine the local minima and maxima values of $s(t)$.
2- Obtain lower and upper envelopes of $s(t)$ from local minima and maxima values, respectively.
3- Subtract the mean of the lower and upper envelopes from $s(t)$ and obtain a new function $y(t)$.

The flow diagram of the iterative sifting process of the EMD algorithm is given in Figure 1. The algorithm starts by assigning the original signal as a residue. The total number of extrema and energy ratio values for residue are checked in the second stage. The following equation gives the energy ratio of the residue signal r_i,

$$\text{Energy Ratio} \triangleq 10\log_{10}\left(\frac{\|e\|_2}{\|r_i\|_2}\right) \tag{1}$$

Where e is the mean envelope of r_i. In addition, the number of $Imfs$ is compared with a predefined threshold value in this step. The residue value is stored as $Temp.Residue$ for iterative sifting operations. In the next step, $Temp.Residue$ is sifted until the relative tolerance and sift iteration number are reached. While these two conditions are satisfied the sifted $Temp.Residue$ ($New\ Residue$) is assigned as Imf_i and algorithm loops to second step.

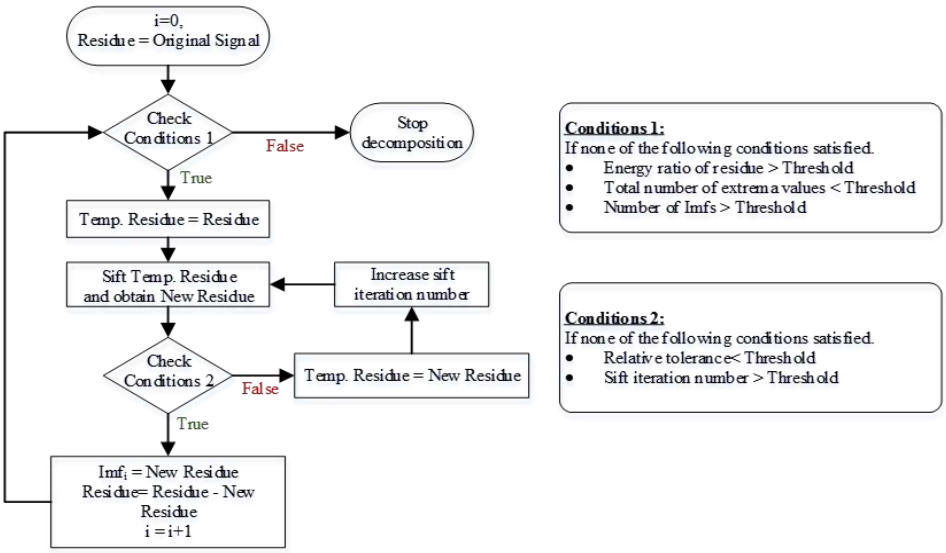

Figure 1. The flow diagram of the EMD algorithm

In this study, the Python toolbox [14] was used to perform the EMD algorithm. The default threshold values of the toolbox for energy ratio, relative tolerance, and sift iteration number were used in the implementation. The threshold value for the number of $Imfs$ was set to 6. The obtained Imf and residue signals are given in Figure 2.

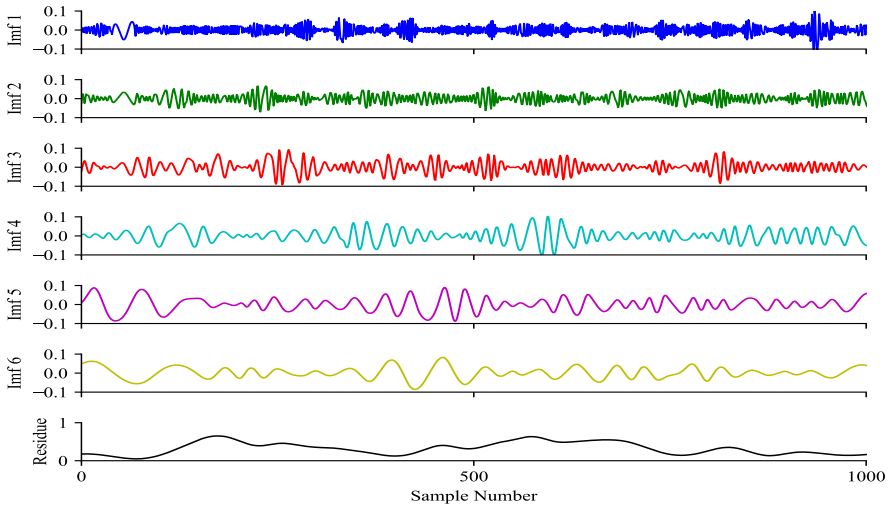

Figure 2. Imf and residue signals obtained from original wind speed signal

2.2. Convolutional Neural Network

The CNN, a remarkable feed-forward neural network type, stands out due to its effective decrease in the necessary trainable parameters. The CNN has the inherent ability to receive multiple arrays as input and then subject this input to convolutional operations across local regions, mimicking the perceptual approach used by the human visual system to process images, in contrast to conventional neural network architectures like the multilayer perceptron (MLP) [15]. To put it another way, CNN tries to understand the complex relationship between input and output, storing its knowledge in its filter weights. The simple CNN structure is given in Figure 3.

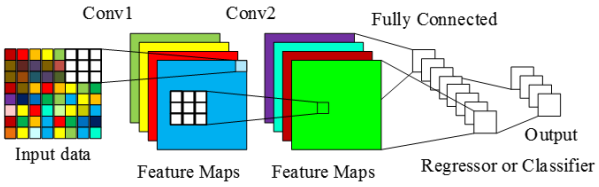

Figure 3. CNN network

The given CNN structure has two convolution layers for feature extraction and one fully connected layer for regression or classification. This network structure can be formulated with following equations,

$$\mathbf{Y_1} = f(\mathbf{X} \otimes \mathbf{W_1} + b_1) \quad (2)$$

$$\mathbf{Y_2} = f(\mathbf{Y_1} \otimes \mathbf{W_2} + b_2) \quad (3)$$

$$\mathbf{Y} = f(\mathbf{Y_2} \times \mathbf{W_3} + b_3) \quad (4)$$

Where $\mathbf{X}$ and $\mathbf{Y}$ denote network input and output, respectively. $\mathbf{W}$ and b are weight matrix and bias. $f(.)$ is activation function and $\otimes$ is convolution operation.

In this study, a CNN structure was employed to capture spatial patterns from the features extracted from the original wind speed signal. The conventional fully connected layer was replaced with GRU layers to enhance the time series forecasting capability. The following subsection describes the foundational principles of GRU.

2.3. Gated Recurrent Unit

It is widely recognized that recurrent neural networks (RNN) are suitable for time series forecasting tasks. However, deep RNN structures have some drawbacks. The high computational cost, the gradual forgetting of first inputs while training them on long sequences, and the unstable gradient problem are the major drawbacks of classical RNN structures. The improved RNN structure called the long-short-term memory network (LSTM) was proposed in [16] to overcome these problems. The authors proposed adding cell units and control gates to improve the classical RNN structure. The success of LSTM in time series forecasting tasks has been proven in many applications [17]. Another improved RNN structure called gated recurrent unit GRU was introduced in [18]. The input and forgetting gates of LSTM were combined in GRU. This simplification improved the convergence speed during the training process. The structure of GRU is given in Figure 4.

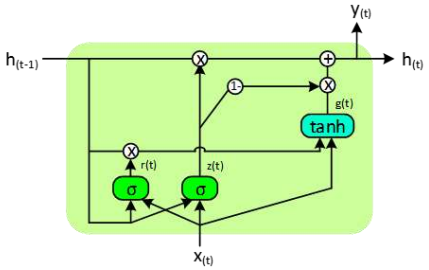

Figure 4. GRU structure

The GRU network structure can be formulated with following equations,

$$\mathbf{z}_t = \sigma(\mathbf{W}_z^T \mathbf{x}_t + \mathbf{U}_z^T \mathbf{h}_{t-1} + \mathbf{b}_z) \quad (5)$$

$$\mathbf{r}_t = \sigma(\mathbf{W}_r^T \mathbf{x}_t + \mathbf{U}_r^T \mathbf{h}_{t-1} + \mathbf{b}_r) \quad (6)$$

$$\mathbf{g}_t = \tanh(\mathbf{W}_g^T \mathbf{x}_t + \mathbf{U}_g^T (\mathbf{r}_t \odot \mathbf{h}_{t-1}) + \mathbf{b}_g) \quad (7)$$

$$\mathbf{h}_t = \mathbf{z}_t \odot \mathbf{h}_{t-1} + (1 - \mathbf{z}_t) \odot \mathbf{g}_t \quad (8)$$

$$\mathbf{y}_t = \mathbf{h}_t \quad (9)$$

Where, $\mathbf{h}$ is the state vector, $\mathbf{x}$ and $\mathbf{y}$ are input and output of the network. b is bias, $\mathbf{W}$ and $\mathbf{U}$ are weight matrixes. $\sigma(.)$ is sigmoid function and $\odot$ denotes element-wise multiplication. $\mathbf{z}$ and $\mathbf{r}$ are update and reset gate vectors. In this study, the GRU network was employed to capture temporal information from sequential feature data. The overall proposed forecasting model is described in the following subsection.

3. The Proposed Model Architecture

In this subsection, the architecture of the proposed wind speed forecasting model is explained. The general diagram of the model is given in Figure 5. As can be seen from the figure, the proposed architecture incorporates three stages to effectively forecast short-term wind speed.

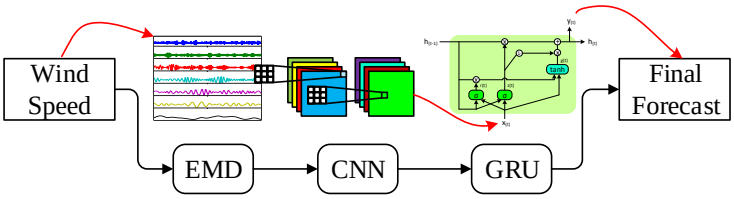

Figure 5. The proposed wind speed forecasting model

The signal decomposition algorithm EMD was used in the first stage to extract features from the historical wind speed signal. The CNN network was employed to capture spatial patterns from extracted features in the second stage. Then GRU was used to capture temporal information from sequential CNN outputs. The implementation details of the proposed forecasting model are given in the next subsection.

4. Experimental Study and Results

The experimental study was conducted on the wind speed dataset obtained from the nacelle anemometer of a grid-tied wind turbine. An overview of the wind turbine is provided in Figure 6. The dataset comprises 56,791 samples, representing the industry-standard 10-minute mean wind speed values. For model development, 80% of the dataset was allocated for training and validation, while the remaining 20% was reserved for testing the model.

Figure 6. General view of the wind turbine

The proposed deep forecasting model was developed using the TensorFlow framework and the Python programming language, utilizing Google Colab as the development environment. The Python-based EMD toolbox was employed to decompose the original wind speed signal into six $Imfs$ and a residue signal. The last 20 samples of these seven signals were used to construct the 20x7 dimensional CNN layer inputs. The sequential outputs generated from the

CNN layer were used as the GRU layer inputs. Further details regarding the architecture and configuration of the proposed deep network are given in Table 1.

Table 4. The structure and parameters of the proposed CNN-GRU network

Layers	Parameters
Convolution	Input shape: 20x7
	Number of kernels:20
	Size of kernels:1x2
GRU1	Number of units: 20
	Return sequences: True
GRU2	Number of units: 20
	Return sequences: False
Dense	Number of nodes: 1

The well-known adaptive moment estimation based optimizer called Adam was utilized to train the network. The initial learning rate was set to 0.01 and exponential learning rate decay method was used to improve the stability of the training process. To confirm the effectiveness of the proposed deep network, obtained results were compared with similar deep networks. These networks were multi-layer perceptron (MLP) with three layers and [20, 20, 1] nodes, and GRU network utilized in the proposed network architecture. The obtained results are summarized in Table 2. It can be inferred from the figure and table that EMD significantly improved the performance and the proposed network achieved the best metric values.

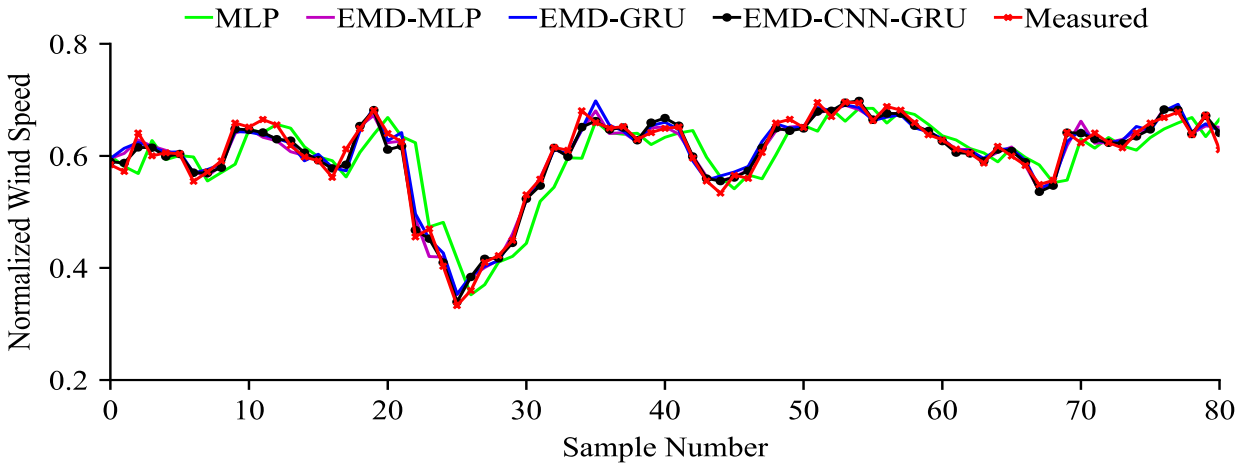

Figure 7. Forecasting results for the proposed comparison models

Table 2. The performance metric values for the proposed and benchmark models

Metric	MAE	RMSE	R	MAE	RMSE	R
Horizon	1 step ahead			3 steps ahead		
EMD-CNN-GRU	**1.430**	**2.191**	**98.971**	**2.339**	**3.292**	**97.657**
EMD-GRU	1.534	2.363	98.800	2.372	3.313	97.635
EMD-MLP	1.710	2.501	98.657	2.452	3.418	97.470
MLP	3.269	4.614	95.364	4.972	6.905	89.307

5. Conclusion

In this study, a comprehensive three-stage model was proposed for the short-term prediction of wind speed values, measured from the nacelle anemometer of a grid-tied wind turbine. Initially, The EMD algorithm was utilized to

extract features from historical wind speed signals. CNN and GRU networks were used to capture spatial and temporal patterns from the extracted features. The efficacy of the proposed model was examined through performance comparison tests conducted on a dataset derived from actual site measurements. The proposed model results were compared with alternative deep networks, namely EMD-GRU, EMD-MLP, and MLP. The conclusions drawn from the study's findings are as follows:

1-The utilization of EMD-based feature extraction yields a substantial enhancement in forecasting performance.
2-The incorporation of CNN and GRU networks to capture spatio-temporal information from the extracted features contributes to an improvement in forecasting accuracy.

The outcomes of this study revealed the promising performance of the proposed wind speed forecasting model, suggesting its potential applicability for wind power forecasting. For future research, using improved CNN and GRU network architectures and utilizing wind turbine power curves to convert wind speed forecasts into wind power forecasts will be interesting.

5. References

[1] Summerfield-Ryan O, Park S. “The power of wind: The global wind energy industry’s successes and failures”. Ecological Economics, 210, 107841, 2023.
[2] Santhosh M, Venkaiah C, Vinod Kumar DM. “Current advances and approaches in wind speed and wind power forecasting for improved renewable energy integration: A review”. Engineering Reports, 2(6), 1–20, 2020.
[3] Wang J, Song Y, Liu F, Hou R. “Analysis and application of forecasting models in wind power integration: A review of multi-step-ahead wind speed forecasting models”. Renewable and Sustainable Energy Reviews, 60, 960–981, 2016.
[4] Chen Y, Wang Y, Dong Z, Su J, Han Z, Zhou D, Zhao Y, Bao Y. “2-D regional short-term wind speed forecast based on CNN-LSTM deep learning model”. Energy Conversion and Management, 244, 14451, 2021.
[5] Erdem E, Shi J. “ARMA based approaches for forecasting the tuple of wind speed and direction”. Applied Energy, 88(4), 1405–1414, 2011.
[6] Aasim S, Singh SN, Mohapatra A. “Repeated wavelet transform based ARIMA model for very short-term wind speed forecasting”. Renewable Energy, 136, 758–768, 2019.
[7] Liu D, Niu D, Wang H, Fan L. “Short-term wind speed forecasting using wavelet transform and support vector machines optimized by genetic algorithm”. Renewable Energy, 62, 592–597, 2014.
[8] Li G, Shi J. “On comparing three artificial neural networks for wind speed forecasting”. Applied Energy, 87(7), 2313–2320, 2010.
[9] Liu H, Tian H. Q, Li YF. “Four wind speed multi-step forecasting models using extreme learning machines and signal decomposing algorithms”. Energy Conversion and Management, 100, 16–22, 2015.
[10] Joseph LP, Deo RC, Prasad R, Salcedo-Sanz S, Raj N, Soar J. “Near real-time wind speed forecast model with bidirectional LSTM networks”. Renewable Energy, 204, 39–58, 2023.
[11] Wang HK, Song K, Cheng Y. “A Hybrid Forecasting Model Based on CNN and Informer for Short-Term Wind Power”. Frontiers in Energy Research, 9, 1–11, 2022.
[12] Huang, NE, Zheng S, Steven RL, Manli CW, Hsing HS, Quanan Z, Nai-Chyuan Y, Chi CT, Henry HL. “The Empirical Mode Decomposition and the Hilbert Spectrum for Nonlinear and Non-Stationary Time Series Analysis”. Proceedings of the Royal Society of London. Series A: Mathematical, Physical and Engineering Sciences, London, 903–95, 8 March 1998.
[13] Harshal C, Sanjay LN, Rashmee S. “A review on intrensic mode function of EMD”. 2016 International Conference on Electrical, Electronics, and Optimization Techniques, Chennai, India, 2349–2352, 24 November 2016.
[14] Laszuk D. “Python implementation of empirical mode decomposition algorithm”. GitHub Repository, 2017.
[15] Zhang Q, Zhang M, Chen T, Sun Z, Ma Y, Yu B. “Recent advances in convolutional neural network acceleration”. Neurocomputing, 323, 37–51, 2019.
[16] Hochreiter S, Schmidhuber J. “Long short-term memory”. Neural Computation, 9(8), 1735–1780, 1997.
[17] Yu Y, Si X, Hu C, Zhang J. “A review of recurrent neural networks: LSTM cells and network architectures”. Neural Computation, 31(7), 1235–1270, 2019.
[18] Kyunghyun C, Bart VM, Caglar G, Dzmitry B, Fethi B, Holger S, Yoshua B. “Learning phrase representations using RNN encoder-decoder for statistical machine translation”. Arxiv Preprint, arXiv1406.1078, 2014.

International Conference on Advances and Innovations in Engineering

Fractional-Order High-Pass Filter Using Operational Transresistance Amplifier

Sadullah KUTLUSOY[1], Selçuk KILINÇ [2]

[1,2]Department of Electrical and Electronics Engineering, Dokuz Eylül University, İzmir, Türkiye.
[1]sadullah.kutlusoy@deu.edu.tr, [2]selcuk.kilinc@deu.edu.tr

[1](ORCID: 0000- 0002-7989-8831), [2](ORCID: 0000- 0001-7866-709X)

Abstract

This study focuses on the use of fractional-order capacitors with a voltage-mode high-pass filter. Three different fractional order values of capacitor and a single operational transresistance amplifier (OTRA) are used in the circuit. The fractional-order values of capacitor are chosen as 0.2, 0.5 and 0.8. It is also used the conventional capacitor to compare with the fractional-order effects on the circuits. The simulation of high-pass fractional-order filter are performed using SPICE. A CMOS implementation of the OTRA element is used in the simulations. The transistor model has 0.35 μm CMOS process parameters. The OTRA is also simulated using its ideal model to compare the effect of CMOS on the filters. The frequency responses of the filter are individually examined in the frequency range of 1 Hz - 100 MHz.

Keywords: analog filters, fractional-order capacitors, operational transresistance amplifier, SPICE simulation

1. Introduction

Fractional-order capacitors, also known as Constant Phase Elements (CPE), are fundamental components used to implement fractional-order signal processing systems [1]. A CPE is defined by two parameters, $\{C_\alpha, \alpha\}$, where C_α is referred to simulated capacitance expressed in Farad/$s^{1-\alpha}$, and α represents the fractional degree [2]. The impedance of a CPE is defined in the s-domain using Equation (1) [3].

$$Z(s) = \frac{1}{C_\alpha s^\alpha} = \frac{1}{C_\alpha \omega^\alpha \left(\cos\left(\frac{\alpha\pi}{2}\right) + j\sin\left(\frac{\alpha\pi}{2}\right)\right)} \tag{1}$$

The relationship between simulated capacitance and traditional capacitance (in Farads) can be expressed as in Equation (2) [3].

$$C = \frac{C_\alpha}{\omega^{1-\alpha}} \tag{2}$$

Since fractional-order capacitors are not commercially available [4-6], these capacitors can be derived through the following methods: (a) by employing integer-order capacitors, known as integer-order filters, with well-known RC pairs such as Foster or Cauer, in place of traditional (i.e., integer-order) capacitors, and (b) by utilizing the Laplace fractional-order operator in an appropriate expression [7-10], thereby implementing rational integer-order transfer functions obtained by substitution (as presented by approaches like Oustaloup [7], Continuous Fractional Expansion [8,11], Matsuda [9], El-Khazali [10], etc.).

The term s^α in Equation (1) is transformed into the form shown in Equation (3) using the method of continuous fractional expansion [12].

[1]Corresponding author

$$s^a \cong \omega_o^\alpha \cdot \frac{a_n s^n + a_{n-1}\omega_o s^{n-1} + \cdots + a_1 \omega_o^{n-1} s + a_o \omega_o^n}{b_n s^n + b_{n-1}\omega_o s^{n-1} + \cdots + b_1 \omega_o^{n-1} s + b_o \omega_o^n} \tag{3}$$

where *n* represents the degree of the approximation, and ω_0 represents the center frequency.

Using Equations (1)-(3), the obtained Equation (4) allows us to determine the resistance and capacitance values of the RC circuit that provides the desired fractional-order capacitor [12].

$$Y(s) = C\omega_o \cdot \frac{a_n s^n + a_{n-1}\omega_o s^{n-1} + \cdots + a_1 \omega_o^{n-1} s + a_o \omega_o^n}{b_n s^n + b_{n-1}\omega_o s^{n-1} + \cdots + b_1 \omega_o^{n-1} s + b_o \omega_o^n} \tag{4}$$

In this study, the fractional-order capacitor is employed in a high-pass filter. The filter originally includes an operational transresistance amplifier (OTRA), three resistors and two traditional capacitors. One of these capacitors is replaced with a fractional-order capacitor. Therefore, we obtain an OTRA-based fractional-order high-pass filter. The circuit has been simulated using SPICE program with different fractional-orders of the capacitor.

2. Modeling of the Fractional-Order Capacitor

A 1nF capacitor is modeled using the Foster-II circuit model [12] shown in Figure 1 for fractional orders α of 0.8, 0.5, and 0.2. The resistance and capacitor values of the corresponding structure are determined using the fifth-order continuous fractional expansion approach through the MATLAB command in [12]. The values of passive elements are provided in Table 1.

The values obtained in Table 1 are used in the circuit model shown in Figure 1 to obtain capacitor models of fractional orders of 0.2, 0.5, and 0.8. These capacitors are used in place of traditional capacitors in the design of RC filters.

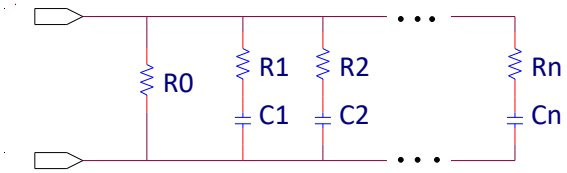

Figure 1. Foster-II RC circuit

Table 1. Resistance and capacitance values obtained for the 1nF capacitor with different α values [12]

	$\alpha = 0.2$	$\alpha = 0.5$	$\alpha = 0.8$
R_0	399.28 kΩ	1.75 MΩ	11.96 MΩ
R_1	145.38 kΩ	17.73 kΩ	2.17 kΩ
R_2	463.72 kΩ	151.06 kΩ	118.44 kΩ
R_3	729.15 kΩ	375.39 kΩ	496.82 kΩ
R_4	807.89 kΩ	619.49 kΩ	1.22 MΩ
R_5	619.43 kΩ	805.87 kΩ	2.53 MΩ
C_1	40.33 pF	185.58 pF	536.29 pF
C_2	89.64 pF	219.74 pF	217.23 pF
C_3	194.77 pF	318.33 pF	201.41 pF
C_4	575.66 pF	622.04 pF	263.35 pF
C_5	4.08 nF	2.29 nF	556.27 pF

3. OTRA-Based Fractional-Order High-Pass Filter

OTRA element is an analog building block that offers several advantages compared to the traditional active elements. These advantages include higher operating speed, lower power consumption, greater linearity, operation at lower

voltages, larger gain-bandwidth product, high CMRR (Common-Mode Rejection Ratio), high slew rate, and a wider dynamic range [13, 14].

OTRA has a structure with two input terminals and one output terminal. The fact that the input terminals are at ground potential largely eliminates the effects of parasitic capacitances and resistances, making the circuit insensitive to leakage capacitances [14].

The circuit symbol of the employed OTRA is provided in Figure 2. The terminal relationships are as given in Equation (5).

$$\begin{aligned} \boldsymbol{V_p} &= \boldsymbol{0} \\ \boldsymbol{V_n} &= \boldsymbol{0} \\ \boldsymbol{V_z} &= \boldsymbol{R_m}(\boldsymbol{I_p} - \boldsymbol{I_n}) \end{aligned} \tag{5}$$

R_m represents the transresistance of the OTRA. In an ideal OTRA, its value is infinitely large. When resistors and capacitors are connected to the OTRA element shown in Figure 2, high-pass filter circuit is formed as depicted in Figure 3. The provided circuit is initially simulated using the ideal model of the OTRA, which is shown in Figure 4.

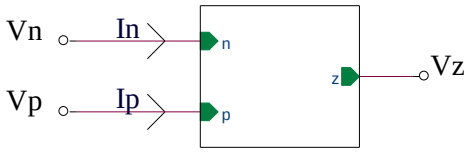

Figure 2. OTRA circuit symbol

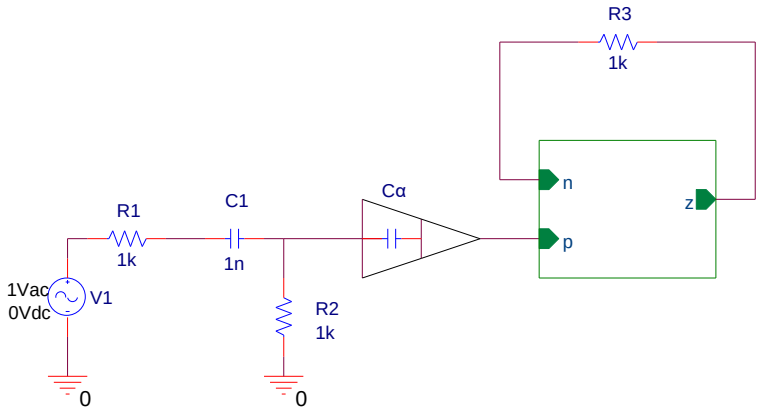

Figure 3. OTRA-based high-pass filter designed with fractional-order capacitor

After substituting the values into Figure 3, the C_α capacitors are replaced with the fractional-order capacitors provided in Figure 1, and the changes in frequency responses compared to the traditional capacitor are examined. The frequency responses for four different capacitor orders (α=0.2, α=0.5, α=0.8, α=1) of the fractional-order high-pass filter based on the ideal OTRA model are presented in Figure 5.

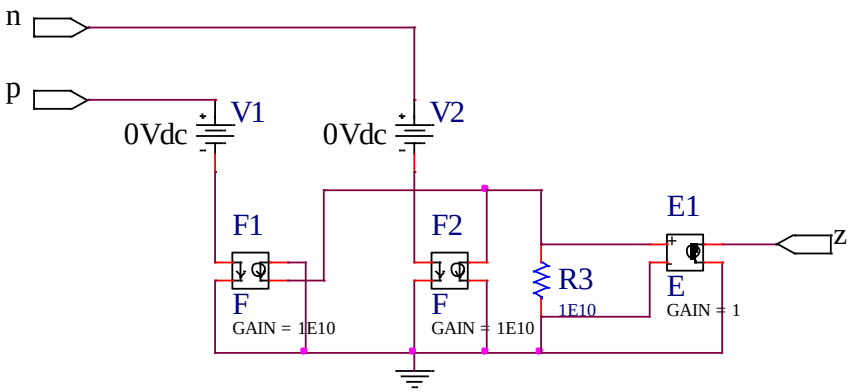

Figure 4. SPICE circuit model for ideal OTRA

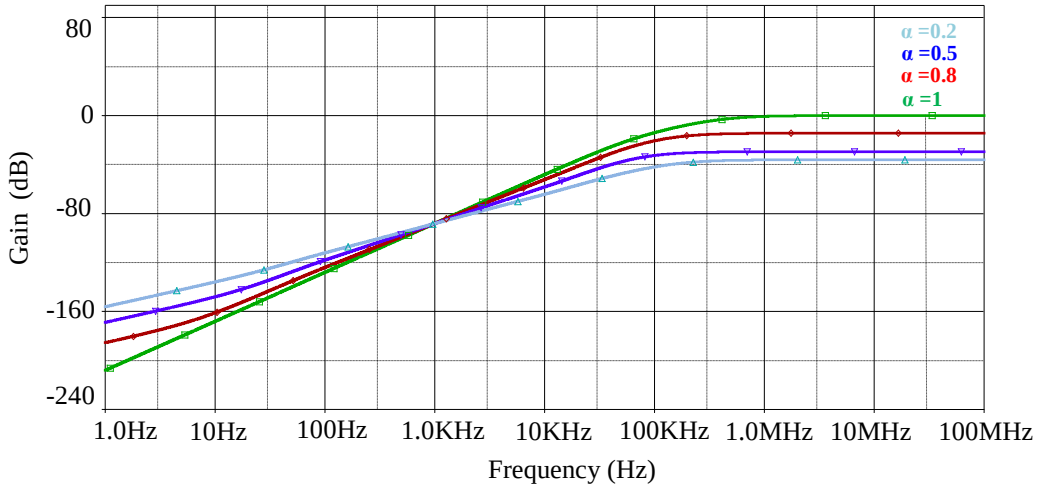

Figure 5. Frequency responses of high-pass filter for three different fractional-orders and a traditional capacitor (α=0.2, α=0.5, α=0.8, α=1) using the ideal OTRA model

The simulation performed with the ideal OTRA has been repeated using the CMOS implementation shown in Figure 6 [15]. Here, transistor dimensions are chosen as specified in Table 2 [16]. The supply voltages are ±1.5 V, bias voltages are VB1= -0.5 V and VB2=0.1 V, and the bias current is IB=100 µA. Figure 7 shows the frequency responses of the high-pass filter for three different fractional-orders and a traditional capacitor (α=0.2, α=0.5, α=0.8, α=1) using the CMOS OTRA.

Table 2. Transistor dimensions (Width/Length)

Transistör	*W(µm)/L(µm)*
M1- M3	100/2.5
M4 - M7	50/2.5
M8 - M11	50/2.5
M12,M13	30/2.5
M14,M15	50/2.5
M16	10/2.5
M17	50/0.5

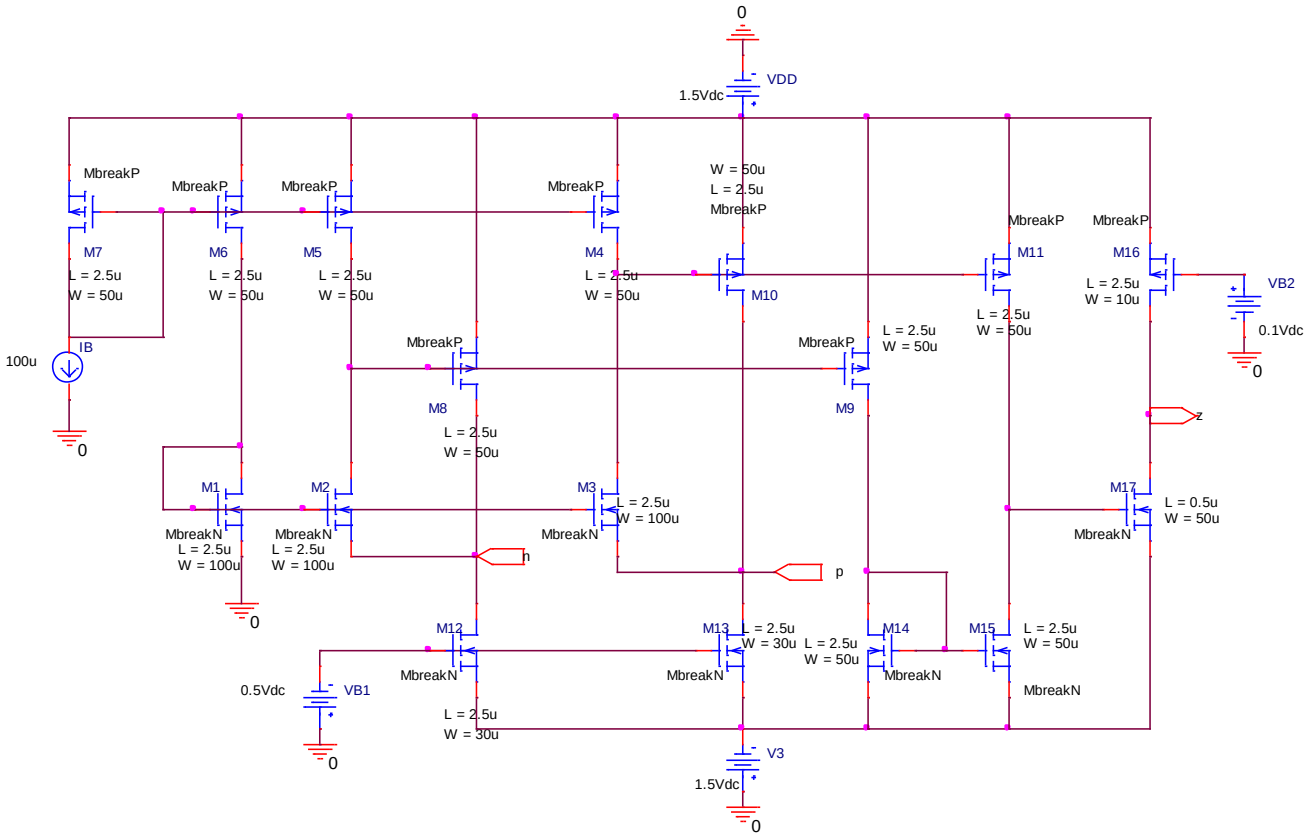

Figure 6. A CMOS implementation of OTRA [15]

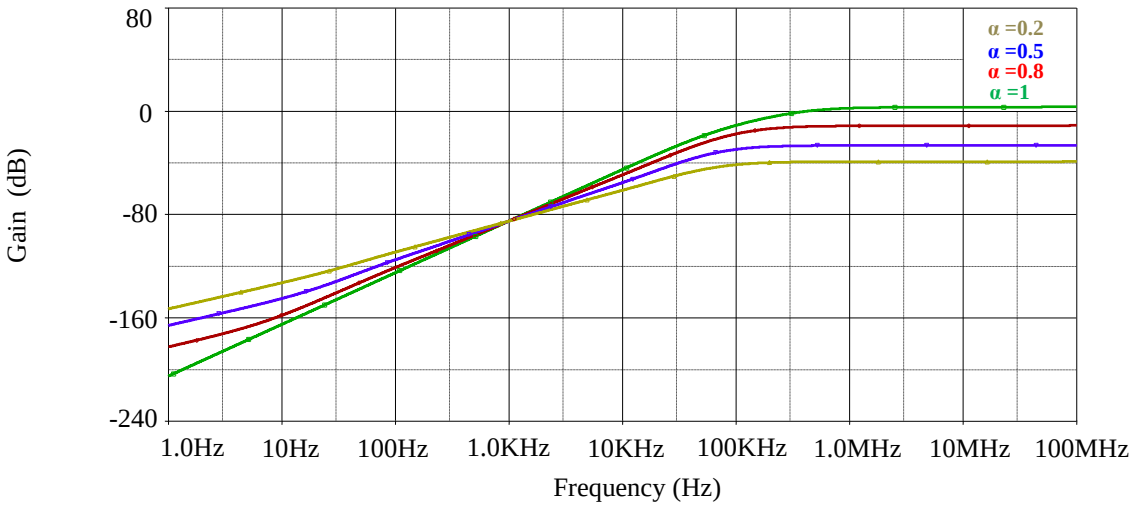

Figure 7. Frequency responses of high-pass filter for three different fractional-orders and a traditional capacitor (α=0.2, α=0.5, α=0.8, α=1) using the CMOS OTRA

4. Conclusion

In this study, SPICE simulation results of a fractional-order high-pass filter based on OTRA are presented. Ideal OTRA model and CMOS OTRA have been separately employed in the simulations. For high-pass filters, a decrease in the fractional order led to a reduction in amplitudes. The deterioration of the frequency response is a desired outcome in achieving intermediate steps for filters. The frequency responses obtained with CMOS OTRA have been close to those obtained with the ideal OTRA.

5. References

[1] Elwakil A.S. "Fractional-order circuits and systems: an emerging interdisciplinary research area". IEEE Circuits Syst. Mag. 10 (4), 40–50, 2010.

[2] Westerlund S, Ekstam L. "Capacitor theory". *IEEE Trans. Dielectr. Electr. Insul*. 1 (5), 826–839, 1994.

[3] Kapoulea S, Psychalinos C, Elwakil A.S. "Realizations of simple fractional-order capacitor emulators with electronically-tunable capacitance". *Integration*, 69, 225-233, 2019.

[4] Agambayev A, Farhat M, Patole S.P., Hassan A.H., Bagci H, Salama K.N. "An ultra-broadband single-component fractional-order capacitor using MoS2-ferroelectric polymer composite". *Appl. Phys. Lett.* 113, 093505, 2018.

[5] Biswas K, Caponetto R, Di Pasquale G, Graziani S, Pollicino A, Murgano E. "Realization and characterization of carbon black based fractional order element". *Microelectron. J.* 82, 22–28, 2018.

[6] Caponetto R, Di Pasquale G, Graziani S, Murgano E, Pollicino A. "Realization of Green Fractional Order Devices by using Bacterial Cellulose". *AEU Int. J. Electron. Commun*. 112, 152927, 2019.

[7] Oustaloup A, Levron F, Mathieu B, Nanot F.M. "Frequency-band complex noninteger differentiator: Characterization and synthesis". *IEEE Trans. Circuits Syst. I Fundam. Theory Appl.* 47, 25–39, 2000.

[8] Krishna B. "Studies on fractional order differentiators and integrators: A survey. Signal Process. 91, 386–426, 2011.

[9] Matsuda K, Fujii H. "H(infinity) optimized wave-absorbing control-Analytical and experimental results." *J. Guid. Control Dyn.* 16, 1146–1153, 1993.

[10] El-Khazali R. "On the biquadratic approximation of fractional-order Laplacian operators." *Analog. Integr. Circuits Signal Process.* 82, 503–517, 2015.

[11] Tsirimokou G, Kartci A, Koton J, Herencsar N, Psychalinos C. "Comparative study of discrete component realizations of fractional-order capacitor and inductor active emulators". *J. Circuits Syst. Comput*. 27, 1850170, 2018.

[12] Tsirimokou G. "A systematic procedure for deriving RC networks of fractional-order elements emulators using MATLAB". *AEU-International Journal of Electronics and Communications*, 78, 7-14, 2017.

[13] Tewari P, Garia. "Technological Advancements in Current Conveyors & their Applications". *1st National Conference on Recent Advances in Sciences & Technology*, 1, 320-326, 2015.

[14] Tewari P, Rachana A. "Design and Realization of Fractional Low-Pass Filter of 1.5 Order Using a Single Operational Transresistance Amplifier". *International Journal of Signal Processing, Image Processing and Pattern Recognition* 9, 69-76. 2016.

[15] Salama K.N., Soliman A.M. "CMOS operational transresitance amplifier for analog signal processing applications". *Microelectronics Journal*, 30, 235-245, 1999.

[16] Soliman A.M., Mostafa H. "A Modified CMOS Realization of the Operational Transresistance Amplifier (OTRA)". *Frequenz*, Berlin, 60, 3-4, 2006.

International Conference on Advances and Innovations in Engineering

Intelligent Advert Insertion into Videos Using YOLOv4 Object Detection Method and Centroid Tracking Algorithm

Kerim ERGÜN[1] , Selçuk KILINÇ [2], Ayça Kumluca TOPALLI [3]

[1]The Graduate School of Natural and Applied Science, Dokuz Eylül University, İzmir, Turkey.
[2]Department of Electrical and Electronics Engineering, Dokuz Eylül University, İzmir, Turkey.
[3]Department of Electrical and Electronics Engineering, İzmir University of Economics, İzmir, Turkey.
[1]kerim.ergun@ogr.deu.edu.tr, [2]selcuk.kilinc@deu.edu.tr, [3]ayca.topalli@ieu.edu.tr

[1](ORCID: 0009-0008-1489-729X), [2](ORCID: 0000-0001-7866-709X),[3](ORCID: 0000-0001-7712-5790)

Abstract
In this paper, a study is presented that determines timestamp in a video clip for advert insertion purposes by evaluating the number of car objects and the time spent in the video broadcast using artificial intelligence methods. Artificial intelligence driven YOLOv4 object detection algorithm and centroid object tracking algorithm have been used by creating metadata to detect objects in videos. Designed system finds the time instant for advertising in video by evaluating contextual in the video scenes according to car objects' duration spent in the video and the number of cars.

Keywords: object detection, object tracking, advert insertion

1. Introduction

Online videos and video broadcasts are becoming very popular with the rapid development of nearly ubiquitous Internet access in recent years. This situation makes possible to be added powerful features into video broadcasts. One of these features is the method developed for video advertising. The primary goal of video advertising is to deliver a relevant advert that engages target consumers at an appropriate time of the video. Thus, a lot of video content analysis can be done in order to present the adverts [1,2]. Logo, actor, scene analyses can be done in advertising methods according to video content. In addition to objects and faces, spatial analysis such as kitchen and living room can be made and related advertisements can be inserted in scene analysis. As an example, there are a dining table, chairs and bottles in a restaurant according to the paper in [1]. The system decides to present an orange juice advertisement in which a person orders juice at a restaurant based on this information. The advert focuses on the juice bottle.

In another example, Mirriad company [3] performs video content analysis to find contextually relevant moments and emotional context using artificial intelligence, computer vision and object detection technology. It offers an advertising experience within the video by evaluating the contextually relevant to the objects and their relations with other objects emotionally in the video scene.

It is possible to be benefited from object detection technologies to make content analysis in videos. These can be different types of object detection algorithms including the one based on the Convolutional Neural Network (CNN) especially [1,4,5]. You Only Look Once (YOLO) is one of the object detection methods incorporating CNN. There are different versions of YOLO.

In the present study, YOLOv4 object detection algorithm and centroid tracking algorithm have been used to determine advert insertion timestamp in video. The car objects in the video have been detected with the YOLOv4 object detection method and counted according to their types. At the same time, centroid tracking algorithm has been used as the tracking algorithm to determine the time spent in the video for each car object. Then, system decides

[1]Corresponding author

when to insert an advert in the video broadcast by capturing contextually relevant moments based the time spent in the video.

This paper is organized as follows. YOLOv4 object detection algorithm has been briefly described in Section 2. Section 3 presents the basics of the centroid tracking algorithm. CNN has been trained and the results have been obtained as given in Section 4. Finally, conclusions are drawn in Section 5.

2. YOLOv4

YOLOv4 is the fourth version of the YOLO object detection algorithm introduced in 2020 [6] as an improvement over YOLOv3. YOLOv4 algorithm adopts the best optimization strategy in the CNN field so that YOLOv4 is a high-precision single-stage object detection model, which transforms object detection task into a regression problem by generating bounding box coordinates and assigning probabilities to each class [7].

The YOLOv4 algorithm includes three parts: Backbone (the backbone feature extraction network), Neck (the feature pyramid) and YOLO Head. The head part consists of YOLOv3 and the detection process is executed here. Backbone uses CSPDarkNet53 to extract the model features (Figure 1). The CSPDarknet53 network is an improvement on the Darknet53 network. There are convolutional layers in the Darknet53 network. Neck part includes SPP (Spatial Pyramid Pooling) structure and PANet (Path Aggregation Network) structure. SPP is the max pooling of the result in the feature layer after convolutions. SPP layer pools the image features and generates outputs that aim to give input to fully connected layers or other classifiers. PANet enhances the whole feature level by using the bottom-up path and accurate positioning signals, thus shortening the information path between the bottom and top features. Role of YOLO Head is to use the features extracted from the previous part to obtain the final prediction results, including the class of the target, the Bbox (Bounding box) and the Confidence [6,7].

The loss function of YOLOv4 is CIoU (complete intersection over union). The CIoU loss is expressed by the following equation [7]:

$$L_{\mathrm{CIoU}} = 1 - \mathrm{IoU} + \frac{p^2(b,b^{gt})}{c^2} + \alpha \mathrm{v} \tag{1}$$

where b and b^{gt} denote the central points of B and B^{gt}. In other words, they represent the center points of the estimated bounding box and the actual bounding box, respectively. $p(\cdot)$ is the Euclidean distance, c is the diagonal length of the smallest enclosing box covering the two boxes, α is the weight function, v is used to compare the consistency of the width to height ratio of the two anchor box. IoU is the overlapping space. In short, IoU is a function that measures how accurately the predicted bounding box is positioned on the actual bounding box.

3. Centroid Tracking Algorithm

The centroid tracking algorithm is a combination of multiple step processes. It uses a simple calculation to track the point using Euclidean distance. Euclidean distance or Euclidean metric is the straight-line distance between two points in Euclidean space. It finds the distance between the current frame and the referenced frame using Euclidean distance for each object [8] as in the following equation.

$$d_{(p,q)} = \sqrt{\sum_{i=1}^{n}(q_1 - p_1)^2} \tag{2}$$

It computes the centroid using the coordinates of the bounding box and assigns an ID to every bounding box it detects. For example, assume that the same object will be moved the minimum distance compared to other centroids, which means the two pairs of centroids having minimum distance in subsequent frames are considered to be the same object. Then, it is assigned the IDs to the moved centroid that will indicate the same object.

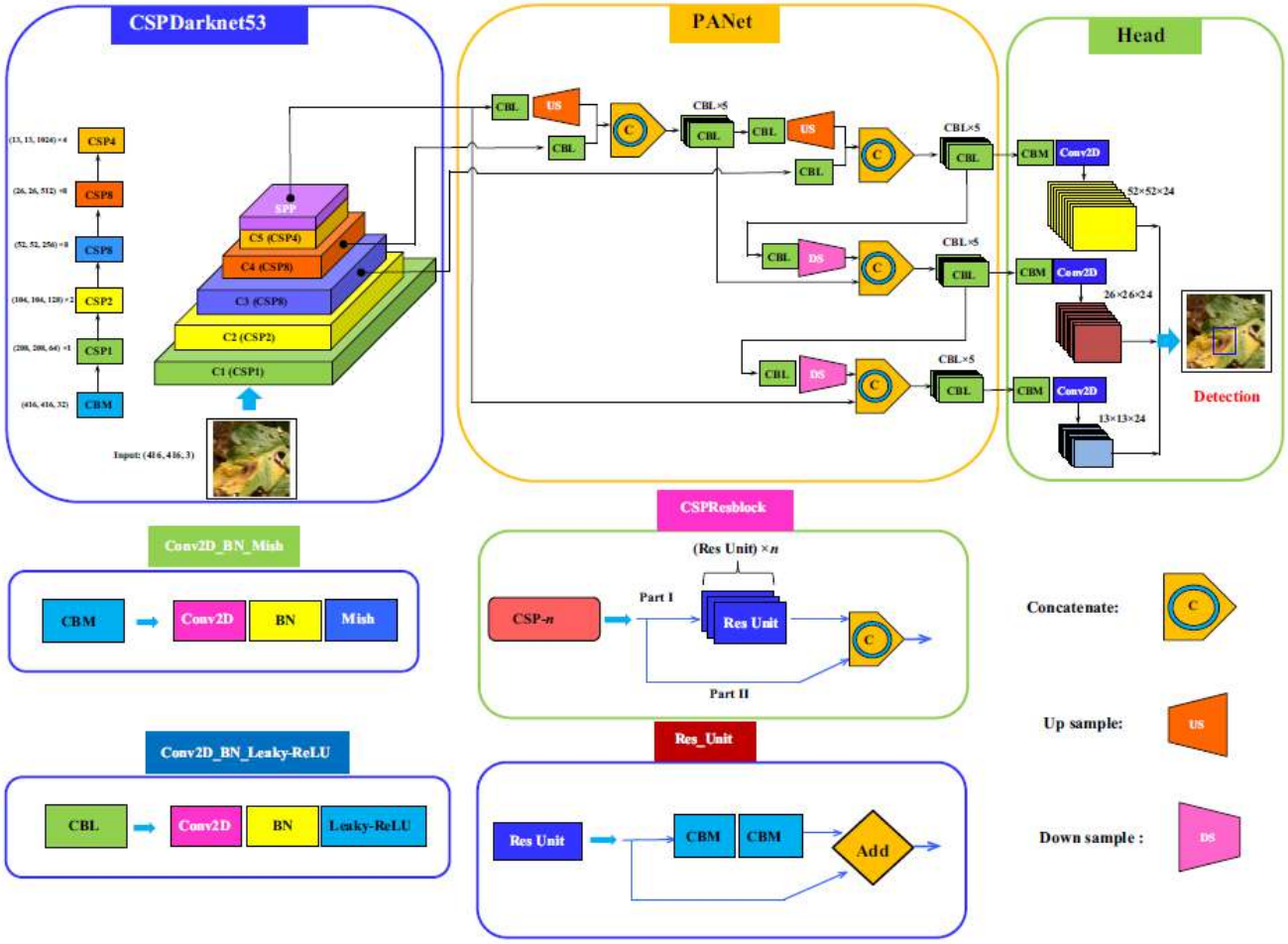

Figure 1. Schematic of the YOLOv4 network architecture consisting of CSPDarknet53 [7]

Figure 2 shows that three objects have been detected. Two pairs that are close together are two existing objects. Next, Euclidean distances are calculated between each pair of original centroids (yellow) and new centroids (purple). Figure 3 shows the process of using minimum Euclidean distances according to object centroids.

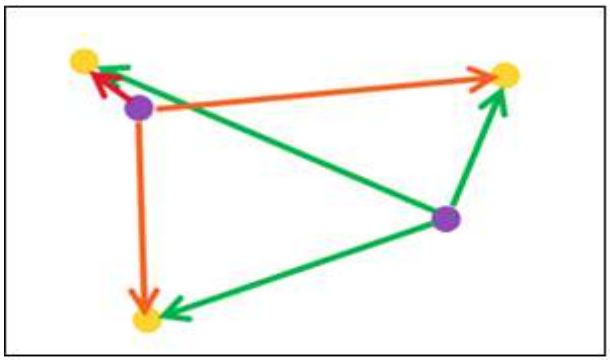

Figure 2. Euclidean distances between existing objects

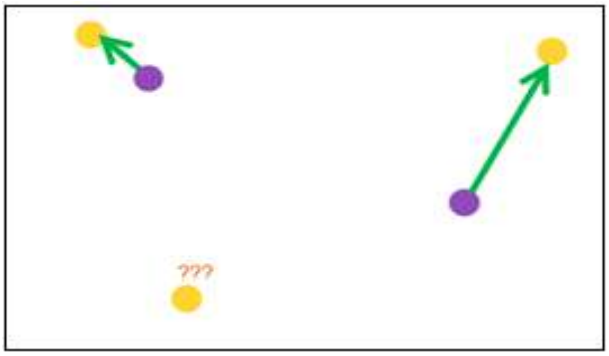

Figure 3. Minimum distances between center points of objects

4. Training and Results

Training has been conducted in Google COLAB with custom dataset using the YOLOv4 transfer learning feature in this study. The obtained new weights in the training results were pulled from Google COLAB and transferred to the

Pycharm platform. The project was implemented by using these weights on the Pycharm platform and developing the object detection and object tracking algorithm with Opencv-python.

4.1. Training with custom data

Dataset containing car photos has been downloaded from the Kaggle website [9] and used for training. 670 car images are reserved for training and 67 car images are reserved for testing. Before starting the training, all pictures have been labeled in "MAKESENSE" [10] as in Figure 4. After labeling, the files have been saved for the YOLO format. A text file has been created for each image as follows. (The first value from the left, "0", is the label number. The other numbers are the coordinates of the object.)

0 0.514749 0.518498 0.949853 0.856195

After labeling the car pictures, the training process has been carried out using the learning transfer feature of YOLOv4 in Google COLAB. Wandb [11] has been used for training visual results. The number of epochs has been selected as 50 for training in Google COLAB. Learning rate has been chosen as 0.01 and Stochastic Gradient Descent (SGD) has been used as the optimization method. SGD has been chosen since it gives better results compared to the other optimization methods even if it is slower. Training results are given in Figures 5 and 6.

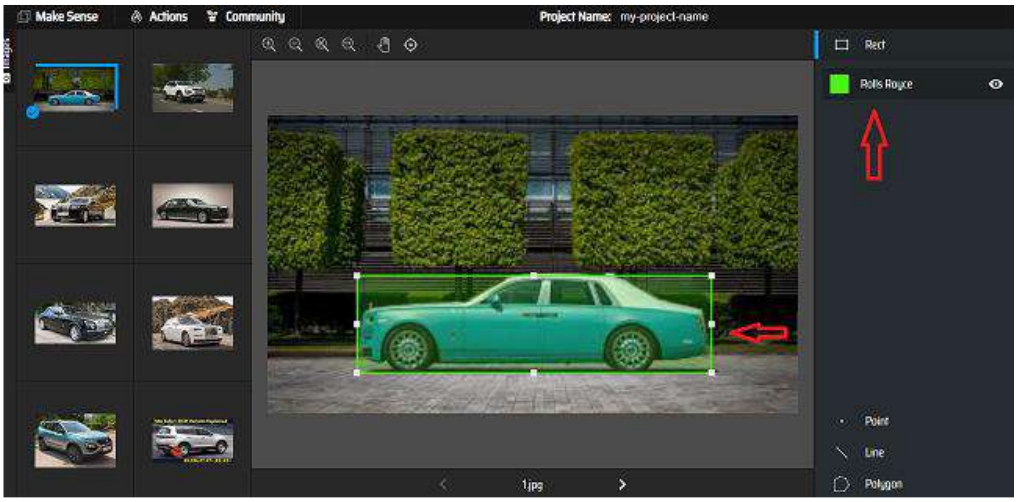

Figure 4. Labeling process for YOLO in "MAKESENSE"

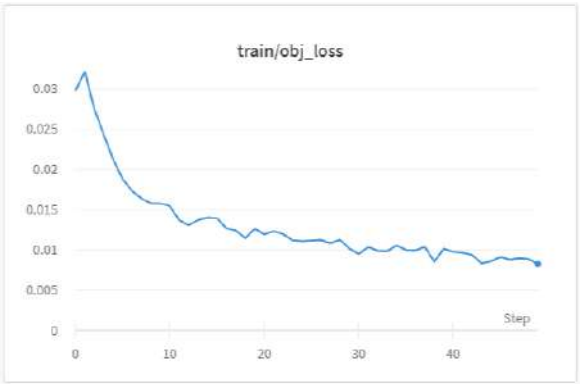

Figure 5. Training loss curve

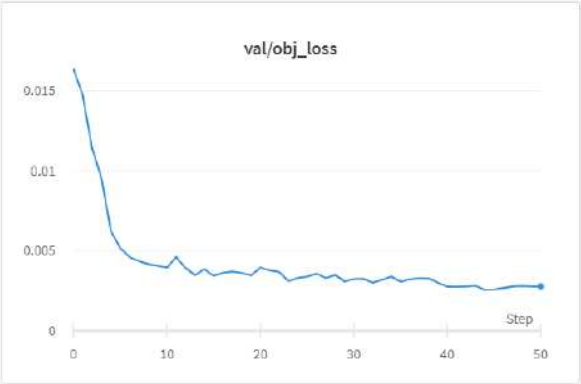

Figure 6. Validation loss curve

Figure 5 shows the training loss curve whereas Figure 6 depicts the validation loss curve. At the end of the 50th training cycle, as can be seen from the graphs, the loss values are converged to zero and moving towards the favorable values. When the datasets have been increased and the training parameters have been changed, different results can be obtained [6,7].

4.2. Object detection and object tracking algorithm for advert insertion into videos

Videos consist of frames. One second of the video consists of 24 frames according to traditional standard [12] (fps: frames per second, which usually runs at 24 frame per second). Therefore, videos actually consist of images/photos. For this reason, object detection can be executed in the video with the weights as a result of the training study using car pictures.

Process steps for object detection are as follows: Firstly, YOLOv4 weights have been defined with Python on the Pycharm platform for the videos. The car objects have been detected in random video frame using Python capabilities. The coordinates of the objects (bounding box) have been extracted and the car objects have been counted. Then, object tracking has been started using these object coordinates. Centroid tracking algorithm determines the time spent in the video for each car object as shown in Figure 7.

In the previous works, (besides the cars) the number of common objects that can be related, such as the highway, forest road, botanical garden can be taken into account [1]. On the other hand, the time spent by the car objects in the video has been also evaluated in this study. In addition to that, advert insertion clock time within the video/broadcast can be determined according to the evaluation of the car objects and their interactions in video scenes.

5. Conclusion

In this study, after car objects have been analyzed with object detection and object tracking algorithms for broadcast videos/online videos, the artificial intelligence-driven work that determines the advert insertion time in the video is determined. Using the bounding box coordinates of the cars in the frame where each car object has been detected, the object tracking algorithm is started at the same time. To use in object detection and object tracking algorithms the number of cars and their duration as a result of the spent time in the video of objects has been determined. By evaluating the conceptual contexts created in the video, in order to be able to advertise according to these, a method of determining the time to insert advertisements within the video has been presented.

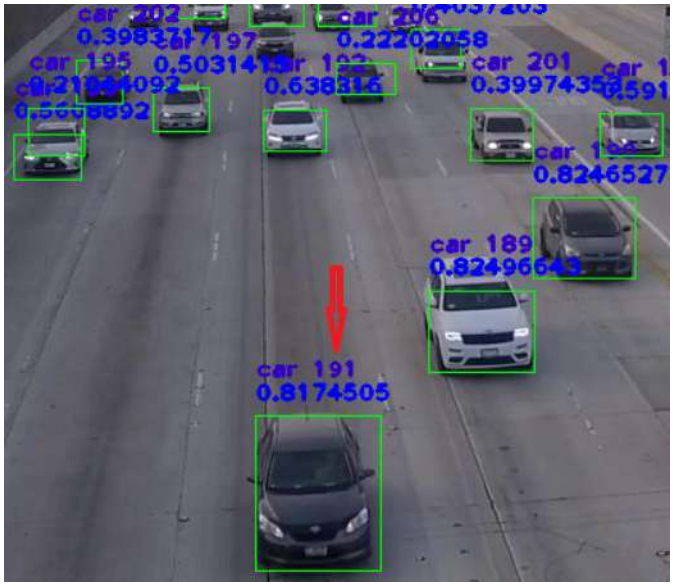

Figure 7. Video object detection and object tracking process

6. References

[1] Tapu R, Mocanu B, Zaharıa T A. “DEEP-AD: A Multimodal Temporal Video Segmentation Framework for Online Video Advertising”. IEEE Access (Volume: 8) 99582-99597, 2020.

[2] Mei T, Hua S X. “Contextual Internet Multimedia Advertising”. Proceedings of the IEEE (Volume: 98, Issue: 8, August), 1416 – 1433, 2010.
[3] https://mirriad.com/
[4] Bulkan U, Dagiuklas T, Iqbal M. “Smart Advertisement Insertion for Online Video Streaming”. London South Bank University School of Engineering, London, UK, 2022.
[5] Yu J T, Lee P C, Lim M K, Razak A F S. “AI-Based Targeted Advertising System”. Indonesian Journal of Electrical Engineering and Computer Science, Vol. 13, No. 2, pp. 787~793, 2019.
[6] Bochkovskiy A, Wang Y C, Liao M Y H. “YOLOv4: Optimal Speed and Accuracy of Object Detection”. arXiv:2004.10934v1, 2020.
[7] Roy M A, Bose R, Bhaduri J. “A fast accurate fine-grain object detection model based on YOLOv4 deep neural network”, 2021.
[8] Bakliwal A, Puranik A, Modi A, Jain A, Jaiswal A, Godani D, Bhanodia P, Jangde P. “Crowd Counter: An Application of Centroid Tracking Algorithm”. International Research Journal of Modernization in Engineering Technology and Science, e-ISSN: 2582-5208, 2020.
[9] https://www.kaggle.com/datasets?tags=12402- Automobiles + and + Vehicles
[10] https://www.makesense.ai/
[11] https://wandb.ai/site
[12] Dehkordi B A, Pourazad T M, Nasiopoulos P. “The Effect of Frame Rate on 3D Video Quality and Bitrate”. arXiv:1803.04826, 2018.

International Conference on Advances and Innovations in Engineering

Speed Control of Single Phase Induction Motor Using Asymmetric PWM with PI Controller

Ece YILMAZ[1] , Sencer ÜNAL [2], Mehmet ÖZDEMİR [3]

[1,2,3]Electrical and Electronics Engineering, Faculty of Engineering, Fırat University, Elazığ, Turkey.
[1]211113112@firat.edu.tr, [2]sencerunal@firat.edu.tr, [3]mozdemir@firat.edu.tr

[1](ORCID: 0000-0002-4960-3836), [2](ORCID: 0000-0001-5990-933X),[3](ORCID: 0000-0002-1178-060X)

Abstract
In this study, a system that produces asymmetric PWM with a hysteresis loop was created for the speed control of a single-phase asynchronous motor, which is closed loop with a PI controller. In the design in question, asymmetric PWM signals created by the hysteresis band were created. High-speed power electronic switches are used in the AC chopper circuit controlled by these signals. PI controller was used to completely control the speed of the single-phase asynchronous motor, which is controlled by the chopper circuit. MATLAB/ Simulink package program was used to create and analyze the model. The positive results obtained from the experimental results of the designed model are presented in this study with the necessary graphics.

Keywords: induction motor, pwm, speed control.

1. Introduction

3-phase asynchronous motors are the most used motors in the industry. However, single-phase asynchronous motors are widely used in low-power drive systems. They are used in various fields such as fans, compressors, pumps, conveyors, food processors, electric train drives and household appliances. The speed of asynchronous motors varies little with load. While the speed of direct current motors can be varied within large limits, the speed of the induction motor can be increased or decreased to a limited extent in conventional control methods. Considering all aspects of asynchronous motors, they are cheaper, require less periodic maintenance, and no electric arc occurs during their operation. Due to these features, 3- and single-phase asynchronous motors have become the most used motors in the industry. However, in many applications, efficiency, speed control and engine speed must be able to respond to various applications and loads. [1-3]. While classical control methods are generally preferred in the control of industrial systems, they yield results in the control of simple structured systems, but are inadequate in complex structures.[4] Despite these advantages, single-phase asynchronous motors are a nonlinear, fifth-order system that is complex to model. Although traditional speed control methods are sufficient for linear applications, they are not sufficient for single-phase asynchronous motors, which have a non-linear structure [5]. Since single-phase asynchronous motors provide a wider speed range at load torques that vary with the square of the speed, an alternating current (AC) chopper is considered a suitable solution [6].

Modulated (PWM) AC chopper circuits with the developments in the field of power electronics, Nabil A. A., Kenji A. and Masaaki included this period in their works. This method, in addition to some technical simplicity, also has the advantage of being able to control large amounts of power economically [7]. Widjonarko, Andi S. and Ardhiansyah used the AC chopper circuit in their designs to provide speed control of the unstable speed motor under loaded and unloaded conditions [8]. Again, in the system designed by Yıldırım and Bilgiç, it was aimed to control the speed of the motor with a PWM-controlled AC chopper, and the features of this control circuit, such as reducing input harmonics and simplicity, were revealed [9]. In their study, Duranay and Güldemir studied the speed control of a single-phase asynchronous motor using a PI controller as well as a PWM-controlled AC chopper circuit and obtained positive results [10]. In this study, better results were obtained by making a closed loop with a PI controller for a single-phase asynchronous motor whose speed is controlled with asymmetric PWM. In chapters 2, 3 and 4, the methods used in the design are explained, and the data obtained from experimental studies are presented in the conclusion.

[1]Corresponding author

2. PWM Controlled AC Chopper

AC voltage choppers are widely used in the speed control of 3-phase and single-phase asynchronous motors, especially in load moments that vary with the square of the speed. The control methods used in these choppers cause non-uniform waveforms in supply voltages and load currents. The AC chopper with pulse width modulation control for single phase proposed by Kwon has increased power factor, low harmonics input current and high efficiency. In this system used in motor speed control, power switches are used to cut the source voltage. This method will cause the pulse width of the AC voltage waveform to change. Therefore, this AC voltage control method is called symmetric pulse width modulation. The circuit diagram of the system is given in Figure 1 [11].

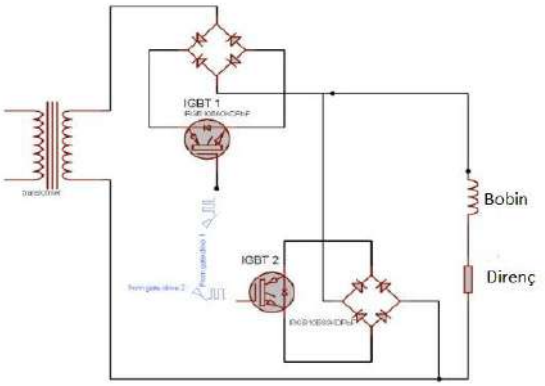

Figure 1. Symmetrical PWM AA chopper circuit scheme

3. Asymmetric PWM

As shown in Figure 2, the reference sinusoidal wave is sampled regularly during half of each switching period. With this sampling, the logic 1 time T_1 in the first half of each switching period and the logic 0 time T_2 in the second half can be calculated with equations (1) and (2). By calculating these times, the PWM signal can now be realized digitally. If the intersection points of the asymmetrically regularly sampled reference sinusoidal wave and the triangular wave are found in Figure 2, the T_1 and T_2 times are found as follows [12].

$$T_1 = t_2 - t_1 = \frac{T_S}{4}(1 + msin\omega t_1) \quad (1)$$

$$T_2 = t_4 - t_3 = \frac{T_S}{4}(1 - msin\omega t_3) \quad (2)$$

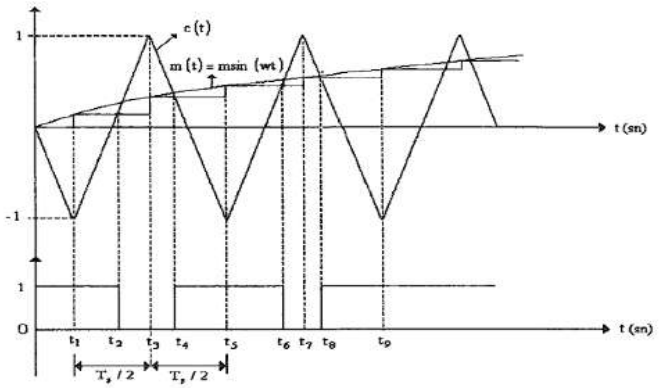

Figure 2. PWM with asymmetric regular sampling

4. PI Audit

PID (Proportional-Integral-Derivative) control is one of the well-known classical control methods, which is frequently used in the industry due to its simple structure. In order for the system output to follow the desired reference value in PID control, the KP, KD, KI coefficients must be determined appropriately. In this method, u(t) controller output is obtained by multiplying and summing the e(t) error signal with the proportional term KP, the integral of the error signal with the integral term KI , and the derivative of the error signal with the KD derivative term[13].

The PI type control organ or controller, which is obtained by adding the integral effect to the proportional effect, eliminates permanent state errors that cannot be eliminated in case of proportional effect alone. On the other hand, adding a proportional effect to the integral effect (I effect) also accelerates the response time in the case of only the integral effect and allows the integral effect time to be kept shorter. PI type controller structure is relatively simple and it is known that PI control is used in 90% of industrial applications. The integral effect creates a control output proportional to the accumulated error, allowing the error to be reset over time [14].

5. Materiel and Method

5.1. System design

System Model MATLAB/Simulink package program with has been carried out. Designed in the model hysteresis tape with created asymmetric PWM signals with control AC chopper only phased asynchronous your engine speed control provided. Only phased asynchronous to the engine belonging ticket information it is given in Figure 3.

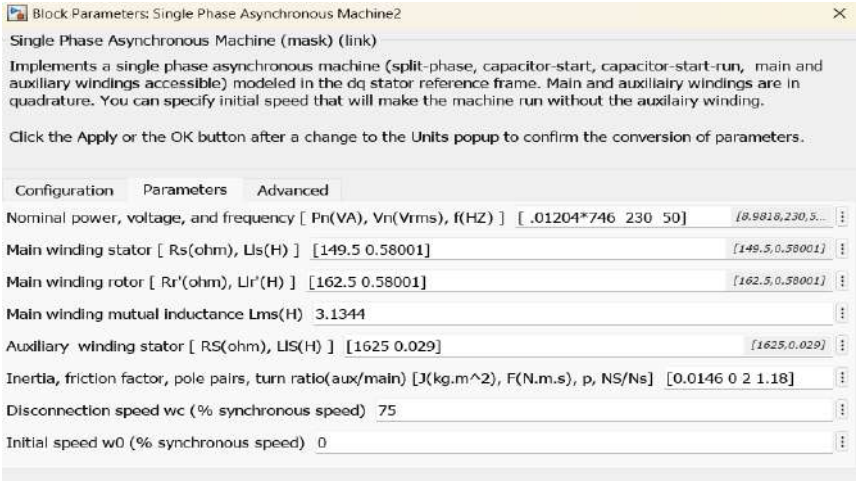

Figure 3. Label information for single-phase asynchronous motor

5.2. Research Findings

Speed control provided only phased asynchronous your engine loading after that speed in the graph occur incoming your fall before to go past for blurry logic controller with closed cycle created. (0.05-0.055-0.06-0.065-0.07-0.075-0.08) Nm to the engine 7 different load value gradual as from the 25th second 10 seconds from at intervals is connected. The designed model is shown and given in Figure 4.

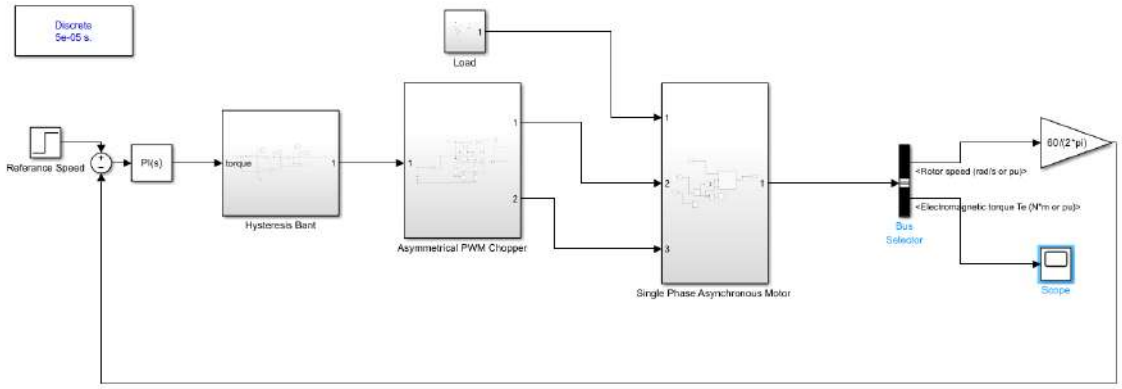

Figure 4. Model of speed control of single phase asynchronous motor using asymmetric PWM with PI controller

Model PI controller using designed. PI controller for chosen to constants similar studies by examining trial and error by decision given. Different reference speed values model tested for And different reference speed values for same PI constants has been used.
PI controller without being used with asymmetric PWM speed control realized only phased asynchronous to the engine belonging speed graph loaded and unloaded situations for Figure 5 and It is given in Figure 6.

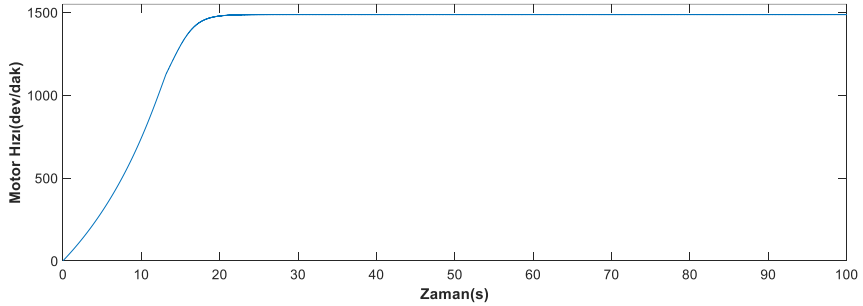

Figure 5. Velocity graph for no-load condition

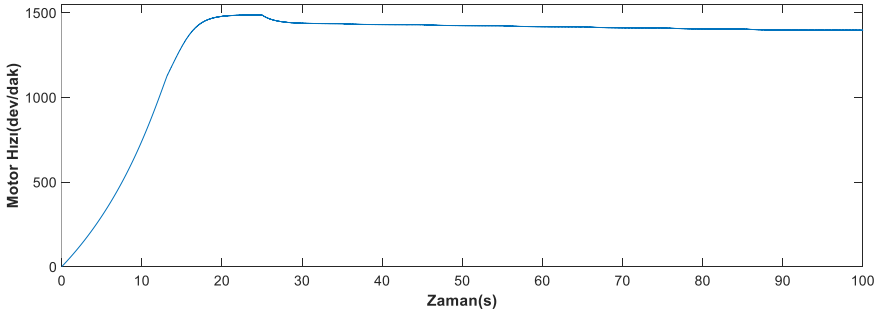

Figure 6. For installed case speed chart

Speed, voltage, current and torque graphs produced by the motor for 1200 rpm reference speed value and (0.05-0.055-0.06-0.065-0.07-0.075 and 0.08) Nm load values Figure 7, Figure 8, Figure 9 and Figure 10 is also given.

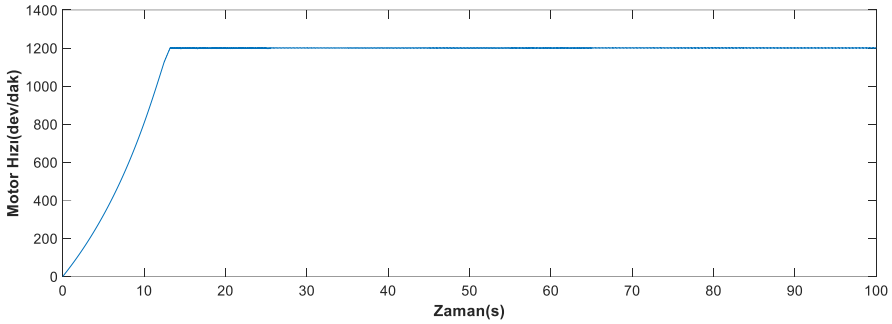

Figure 7. 1200 rpm reference speed value for to the engine belonging speed chart

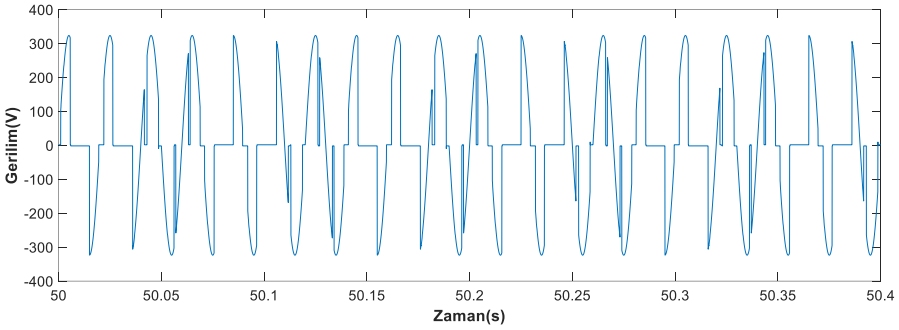

Figure 8. 1200 rpm reference speed value for income chart

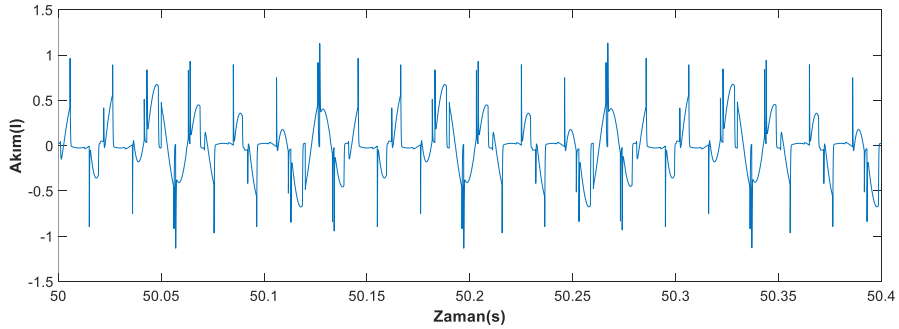

Figure 9. 1200 rpm reference speed value for flow chart

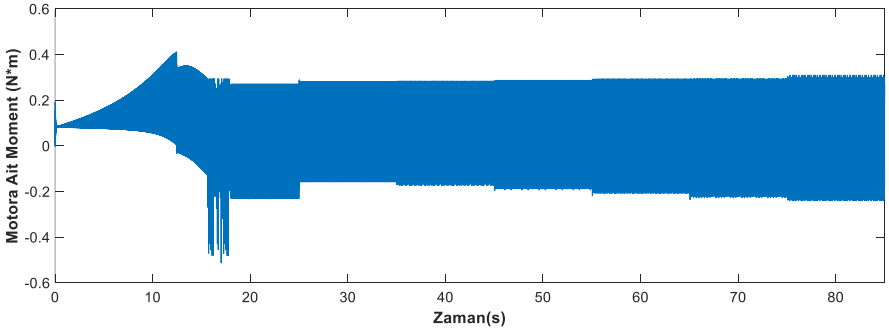

Figure 10. 1200 rpm reference speed value for of the engine moment graph produced

The speed, voltage, current and torque graphs produced by the motor for the 1400 rpm reference speed value and (0.05-0.055-0.06-0.065-0.07-0.075 and 0.08) Nm load values are shown in Figure 11, Figure 12, Figure 13 and Figure 14 is also given.

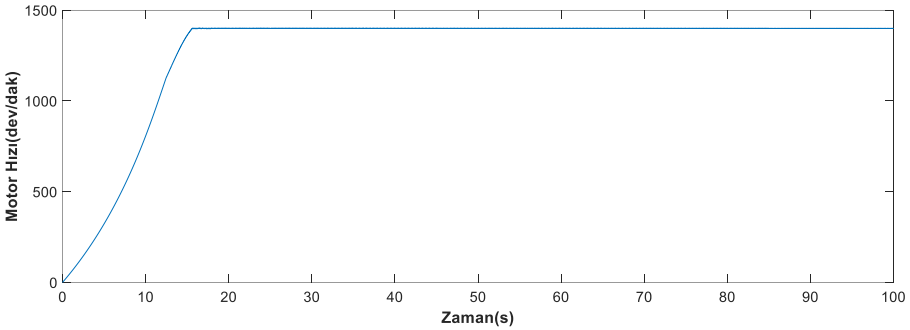

Figure 11. 1400 rpm reference speed value for to the engine belonging speed chart

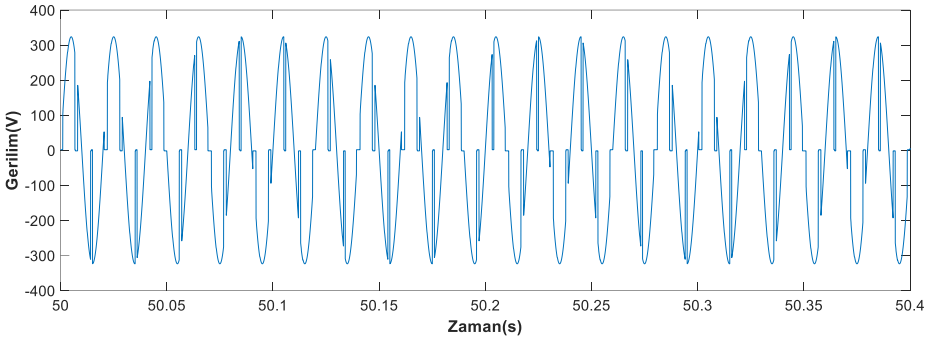

Figure 12. 1400 rpm reference speed value for income chart

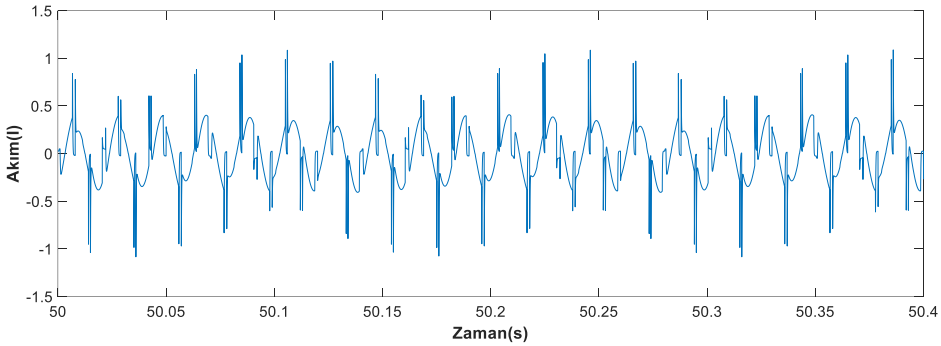

Figure 13. 1400 rpm reference speed value for flow chart

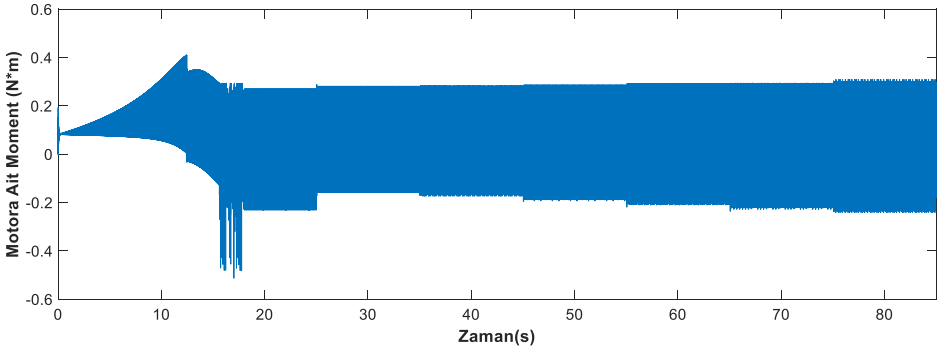

Figure 14. 1400 rpm reference speed value for of the engine moment graph produced

6. Conclusions

In this model designed for single-phase asynchronous motor, asymmetric PWM signals were first created with hysteresis band. Speed control of the single-phase asynchronous motor was achieved by controlling the AA chopper with the generated asymmetric PWM signals. The switches used in the chopper allow the current to reach the single-phase asynchronous motor in the first period, while disconnecting the source and the motor in the second period. In the second period, the single-phase asynchronous motor, which acts as a source, provides current to the power electronic components until its energy is completely exhausted. For the AA chopper circuit used, high-speed switching features of power electronic elements were utilized. However, the decrease in the speed graph for the loading condition could not be prevented. After the load connected to the motor by creating a closed loop with the PI controller, the speed graph was kept constant for all reference speed values. The same constants are used at each reference speed value for the PI controller block. Positive results were obtained from the model tested under different reference speed conditions. System design and experiments were carried out with the MATLAB / Simulink package program and the results given in the study were obtained from this program.

7. References

[1] Saçkan A. H. , Asynchronous Motors , Birsen Publishing House, 1994

[2] Zigirkas G, Kalomiros J. “Voltage control of single-phase induction motors using asymmetrical PWM and fuzzy logic”. 5th International Conference on Modern Circuits and Systems Technologies, 2016.

[3] Wang D, Shi Y. " Sensorless fuzzy speed control for single phase induction motors". Sixth International Conference on Fuzzy Systems and Knowledge Discovery, 2009

[4] Alışkan İ, Ünsal S. " Different inference to your methods owner blurry logic controllers using permanent magnetic synchronicity your engine speed control ". Pamukkale University engineering sciences Magazine, 24(2), 185 -191, 2018.

[5] Holtz, J., speed Estimation oath Sensorless Control of Drives, Proc. IEEE Int. Conf. Ten Ind. Elec. Cont. oath Intr (IECON'93), November 1993, Maui, Proceedings: 649 -654

[6] Jain N. , Funde NH, Meshram NP, Shrikant S. “ Speed Control of Single phase Induction Motor using AC Chopper by Asymetrical PWM Technique ”. *GRD Journal for Engineering*, 2016, vol. 1, No. 4, pp. 1-6

[7] Ahmed NA, Amei K, Sakui M. A New Configuration of Single-Phase Symmetrical PWM AC Chopper Voltage Controller, Vol.46, No.5, October, 1999.

[8] Widjonarko, Setiawan A, Ilhami AF. “AC Chopper Design as Universal Motor Driver Based On Fuzzy Logic Controller”. REKAYASAMESIN, 2477-6041 article 6, pp. 47-55, 2022.

[9] Yildirim D, Bilgic M. “PWM AC Chopper of Single-Phase Inductor Motor _ Variable-Speed Fan Application”. IEEE, 978-1-4244-1766-7, 2008.

[10] Duranay ZB, Güldemir H. “AA Chopper Feed Single Phase Asynchronous Motor Speed Control”. Fırat University Journal of Engineering Sciences, 30(2), 111-119, 2018.

[11] Bashi SM., Mailah NF, Cheng WB, “Development of a Single Phase AC Controller”, Pertanika J. Sci&Technol.,2008 Vol 16, No.2, pp.119-127

[12] Hakan Ç., Space “Speed Control of Three Phase Asynchronous Motor with Vector Pulse Width Modulation”. Master's Thesis Fırat University Institute of Science and Technology, Elazığ 2004

[13] Taşçı G., Küçükyıldız G., Ertunç HM, Ocak H. (2012). “DSPIC Based Position Control of DC Motor in Real Time with PID and Fuzzy Logic”, Automatic Control National Meeting, 11-13 October, Niğde, TOK-2012

[14] Yüksel İ., “Automatic Control System Dynamics and Control Systems”. Dora Press Release, 2016

International Conference on Advances and Innovations in Engineering

Determination of conventional binder properties of bitumen modified with activated carbon from olive pomace and vinasse

Merve POLAT[1] , Erkut YALÇIN[2]

[1,2]Fırat University, Faculty of Engineering, Department Civil Engineering, Elazığ, Turkey
1mervepolat151@hotmail.com, [2]erkutyalcin@firat.edu.tr

Abstract

In recent years, many studies have been carried out on obtaining activated carbon from various organic wastes and these materials are used in the production/improvement of various engineering materials. In this study, modified bitumens were obtained by using activated carbon obtained from olive pomace and vinasse through various chemical processes as additives. Penetration and softening point tests were performed on the modified binders obtained by using activated carbon at 5%, 10% and 15% by weight of the bituminous binder and compared with the pure binder. The results showed that the consistency of the bitumen increased significantly with the use of additives, the degree of penetration increased and the softening point values increased compared to the pure binder. It was also observed that the penetration index values increased, indicating that the use of additives reduces the thermal sensitivity of the bitumen.

Keywords: Bitumen, Modified bitumen, Activated carbon, Conventional binder tests

1. Introduction

Bitumen, which is used as a binding material in highway construction, is obtained from the refining process of petroleum, while aggregates, which act as skeletons, are obtained from the crushing and crumbling of rocks [1, 2]. Both materials are considered as non-renewable resources and therefore it is important to reduce their use. At the same time, it is also very important to improve their properties [3, 4]. The use of waste materials both as binder additives and as aggregates/filler is also an environmentally important development.

For this purpose, various waste materials have been used as modifiers [5–7]. While crumb rubber obtained by grinding waste vehicle tires is commonly used, recently waste plastics, organic wastes, oils, polymers are also preferred. Yan et al. inspected the rheological properties of asphalt using waste tire rubber and ethylene vinyl acetate, one of the most widely used waste modifiers, and concluded that its high temperature performance was improved [8]. Mashaan et al. added waste PET (Polyethylene Terephthalate) as an additive to bituminous binder and investigated its performance characteristics. The results showed that PET addition improved rutting resistance, elastic properties, resistance to aging and fatigue life of bituminous binders [9]. According to Ahmadinia, it is necessary to use cheaper and *recycled materials when obtaining polymer modified bituminous hot mixes. For this purpose, he investigated the engineering properties of stone mastic asphalt by adding waste plastic in his study. He investigated the volumetric and mechanical properties of stone mastic asphalt samples containing various percentages of waste plastic and obtained a suitable additive rate of 6%. He also stated that the addition of waste plastic has positive effects on the engineering properties of stone mastic asphalt [3].

Organic materials and bio-based materials can also be used in asphalt modification [10–12]. Especially organic wastes that are subjected to pyrolysis process are a strong carbon source. Carbon-based materials obtained from waste materials can be used as asphalt additives and interesting results are obtained [13–15].

In this study, activated carbon derived from olive pomace and shredded olive pomace was evaluated as bitumen additive. For this purpose, activated carbon was added to the bituminous binder at 5%, 10% and 15% by weight. Conventional binder experiments were carried out on pure and modified bitumen.

[1]Corresponding author

2. Materials and Method

In the study, 70/100 penetration grade bitumen obtained from TÜPRAŞ Batman refinery was used. The pre-supplied olive pomace waste and vinasse samples were mixed at a mixing speed of 22000 rpm. The mixing process continued until homogeneity was completely achieved. The mixture was passed through N_2 gas and carbonization process was completed and grinding process was applied. After various physical processes, the final additive material was obtained by drying. The SEM image of additive was given in Figure 1. When Figure 1 is examined, it is clearly seen that the activated carbon obtained has a microporous structure.

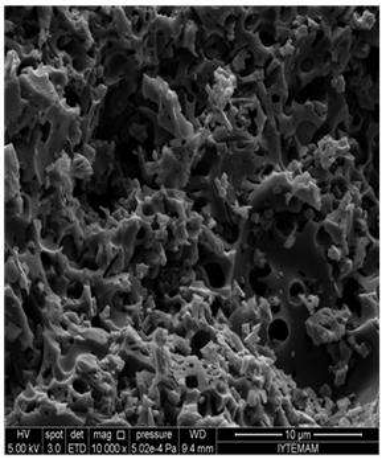

Figure 1. SEM image of activated carbon

The obtained activated carbon and 70/100 penetration grade pure bitumen were mixed at 1500 rpm at 180°C for 1 hour. The modification procedure was the same for all binder types. Conventional binder tests were performed on pure and modified bitumen.

2.1. Penetration Test

This test, which is carried out to determine the hardness and consistency of bitumen, is carried out in accordance with EN 1426 standard. Within the scope of the test, a standard needle weighing 100 grams is inserted into a bituminous binder sample conditioned at 25°C for 5 seconds. The vertical distance it travels in the bitumen gives the penetration value. An increase in penetration value means a decrease in consistency. The penetration test apparatus is shown in Figure 2.

Figure 2. Penetration test device

2.2. Softening Point Test

The softening point value, which is associated with the high temperature resistance of bitumen, is determined by this test and the test is carried out in accordance with TS EN 1427 standard. Within the scope of this standard, there is a standard ball dropped on the bituminous binder filled in the ring. In this system, which is heated at a certain speed, the temperature at which the softened binder falls to the ground gives the softening point value. The softening point test device and experimental setup are given in Figure 3. In the experiment carried out in pure water at 5°C, the ball is placed in the center of the ring.

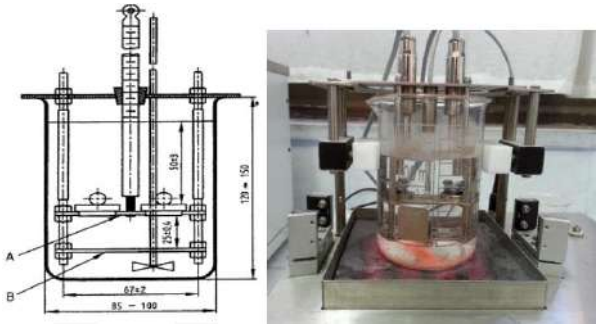

Figure 3. Softening Point Test Setup

2.3. Penetration Index (PI)

In this study, PI was used to determine the thermal sensitivity of bitumen. Although the penetration and softening point test results provide a conclusion about the modification effect, in some cases they may not be clear about the thermal sensitivity properties. With the PI value, it is possible to obtain a clearer information about the thermal sensitivity. The PI value is determined by Formula 1:

$$PI = \frac{1952 - 500 \cdot \log(\text{Pen}) - 20 \cdot \text{SP}}{50 \cdot \log(\text{Pen}) - \text{SP} - 120} \quad (1)$$

In Eq. (1), '(SP)' represents the softening point of the binders, while '(Pen)' represents the penetration value of the binders at 25°C.

3. Results

Within the scope of the study, conventional binder tests were performed on pure and 5%, 10%, 15% activated carbon modified bitumen. Penetration test results for all binder samples are given in Figure 4.

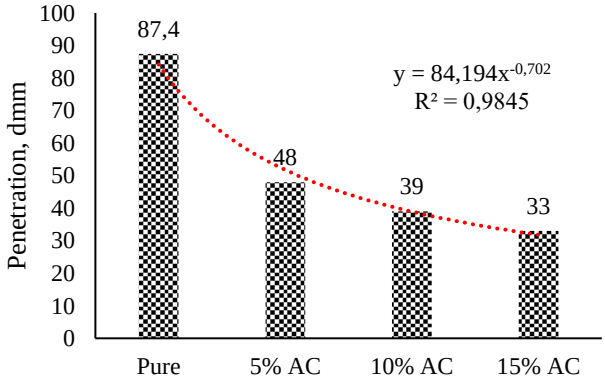

Figure 4. Penetration values of pure and modified binders

Figure 4 shows that activated carbon added to pure binder with 70/100 penetration class decreased the penetration values of pure bitumen. The additive had the effect of increasing the consistency of the bitumen. Increasing the

consistency of the bitumen, in other words hardening, means increasing its resistance to permanent deformations. Furthermore, when the test results were fit to the curve shown in the figure, it was observed that the accuracy ratio (R^2) was higher than 0.98. The softening point test results are given in Figure 5.

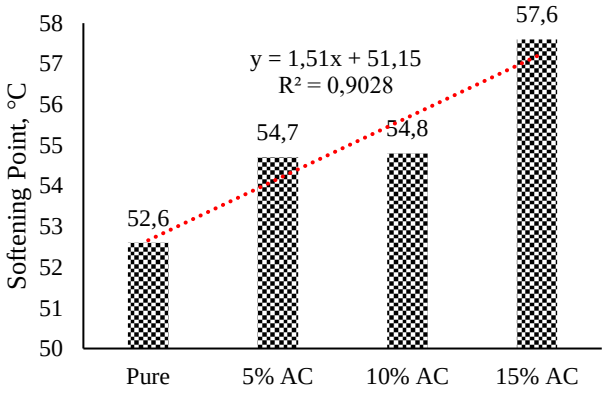

Figure 5. Softening point values of pure and modified binders

The softening point value refers to the temperature at which bitumen starts to lose its properties. According to Figure 5, it is seen that higher softening point values are obtained at each additive ratio compared to pure binder. This indicates an increase in high temperature resistance. The use of 5%, 10% and 15% additives increased the softening point values by 3.9%, 4.18% and 9.5% respectively compared to pure binder. PI values, a measure of the temperature sensitivity of the binders, are presented in Figure 6.

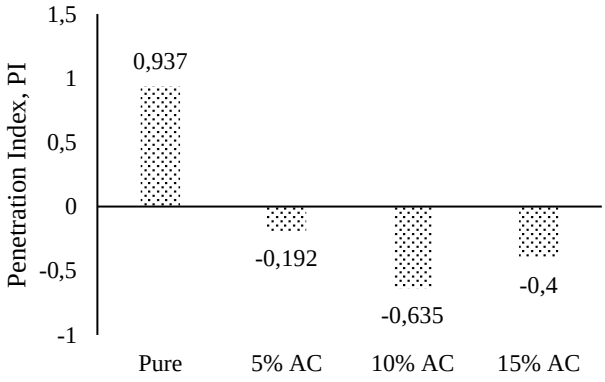

Figure 6. Penetration Index (PI) results

Şekil 6'ya göre aktif karbonun saf bitümlü bağlayıcıya ilavesi PI değerlerinde

4. Discussions

In this study, activated carbon was obtained by passing olive pomace and olive slurry through various chemical processes and modified bitumens were obtained by using 5%, 10% and 15% by weight of bitumen. Conventional binder tests were performed on pure and modified bitumen and various analyses were carried out. According to the results of the standard penetration test, the penetration values decreased at each additive ratio compared to the pure binder. This indicates that this bitumen can be used especially in harsher climates by increasing the resistance against permanent deformations with the use of additives. When the softening point tests were analyzed, it was observed that the use of additives increased the softening point values of 70/100 bitumen. This confirms the results of the penetration test. According to the test results, the highest softening point value was observed in bitumen with 15% activated carbon. There is an increase of 9.5% at this addition rate compared to pure bitumen. The PI results, which

is a measure of sensitivity to temperature, showed that the additive increased the temperature sensitivity of the bitumen.

5. Acknowledgements
This paper was produced from my thesis titled "Investigation of the physical, chemical and rheological properties of bituminous binders prepared with activated carbon obtained from different organic wastes and slurry".

6. References

[1] Kim YR. Modeling of Asphalt Concrete. Ed: Kim YR McGraw-Hill Education, 2009.
[2] Hunter R, Self A, Read J. The Shell Bitumen Handbook, 6th edition. 2015.
[3] Ahmadinia E, Zargar M, Karim MR, Abdelaziz M, Shafigh P. "Using waste plastic bottles as additive for stone mastic asphalt". Materials & Design, 32(10): 4844–4849, 2011.
[4] Yalcin E, Munir Ozdemir A, Vural Kok B, Yilmaz M, Yilmaz B. "Influence of pandemic waste face mask on rheological, physical and chemical properties of bitumen". Construction and Building Materials, 337: 127576, 2022.
[5] Ho S, Church R, Klassen K, Law B, MacLeod D, Zanzotto L. "Study of recycled polyethylene materials as asphalt modifiers". Canadian Journal of Civil Engineering, 33(8): 968–981, 2006.
[6] Suganya S. "A Study on Mechanical Properties of fly ash Brick with Waste Plastic Strips". International Journal of Applied Engineering Research, 10 2015.
[7] Huang Y, Bird RN, Heidrich O. "A review of the use of recycled solid waste materials in asphalt pavements". Resources, Conservation and Recycling, 52(1): 58–73, 2007.
[8] Yan K, Chen J, You L, Tian S. "Characteristics of compound asphalt modified by waste tire rubber (WTR) and ethylene vinyl acetate (EVA): Conventional, rheological, and microstructural properties". Journal of Cleaner Production, 258: 120732, 2020.
[9] Mashaan NS, Chegenizadeh A, Nikraz H, Rezagholilou A. "Investigating the engineering properties of asphalt binder modified with waste plastic polymer". Ain Shams Engineering Journal, 12(2): 1569–1574, 2021.
[10] Hemida A, Abdelrahman M. "Component analysis of bio-asphalt binder using crumb rubber modifier and guayule resin as an innovative asphalt replacer". Resources, Conservation and Recycling, 169: 105486, 2021.
[11] Yilmaz B, Ozdemir AM, Gürbüz HE. "Assessment of Thermal Properties of Nanoclay-Modified Bitumen". Arabian Journal for Science and Engineering, 2022.
[12] Ozdemir AM, Yalcin E, Yilmaz M. "Prediction of Rheological Parameters of Asphalt Binders with Artificial Neural Networks". In The Eurasia Proceedings of Science Technology Engineering and Mathematics pp. 7–16 (2021).
[13] Zhang R, Dai Q, You Z, Wang H, Peng C. "Rheological Performance of Bio-Char Modified Asphalt with Different Particle Sizes". Applied Sciences, 8(9): 1665, 2018.
[14] Cong P, Xu P, Chen S. "Effects of carbon black on the anti aging, rheological and conductive properties of SBS/asphalt/carbon black composites". Construction and Building Materials, 52: 306–313, 2014.
[15] Kumar A, Choudhary R, Narzari R, Kataki R, Shukla SK. "Evaluation of bio-asphalt binders modified with biochar: a pyrolysis by-product of Mesua ferrea seed cover waste". Cogent Engineering, 5(1): 1548534, 2018.

International Conference on Advances and Innovations in Engineering

2ICAIE

Seismic Site Effects of Elazığ-Sürsürü District

Nurullah AKBULUT[1] , Rüveyda Emanet YILMAZ[2]

[1,2]Department of Civil Engineering, Faculty of Engineering, Hasan Kalyoncu University, Gaziantep, Türkiye.
[1]nurullah.akbulut@hku.edu.tr, [2]ruveydaemanet@gmail.com

[1](ORCID: 0000-0002-4280-1581), [2](ORCID: 0000-0001-8759-0338)

Abstract

Earthquakes are a natural phenomenon with the potential to affect millions of people worldwide each year. Turkey lies in one of the most seismic regions globally, and it has witnessed several destructive earthquakes with short return intervals during recent decades. Elazig is a Turkish province located in an area with high seismic activity. On January 24, 2020, Elazig-Sivrice district was hit by a severe earthquake measuring Mw=6.8 at 20:55 (17:55 GMT) local time. Unfortunately, it resulted in significant devastation, including structural damage and loss of life. The aim of this study is to present the findings and results concerning the seismic impact of the earthquake. The intent is to minimize the impact of future earthquakes and provide recommendations based on seismic parameters. Important structural damage occurred in the Elazig-Sürsürü district, mainly this area is consisting of young sediments classified as brown gravelly sandy clay, with the groundwater table located below a depth of 15 meters. Prior to conducting the study, geotechnical and geophysical data about Sürsürü district were collected via 91 boreholes to create an idealized soil profile. The investigation was performed in using ArcGIS software. The study provides a soil amplification and site dominant vibration period maps of Elazig-Sürsürü district. It is essential to note that inaccuracies in the geotechnical borehole data used may affect the study's outcome since the data gathered were assumed as valid and representative throughout the analysis.

Keywords: Earthquake, Elazığ-Sürsürü, site effect, seismic zonation maps.

1. Introduction

Increasing population forces cities to expand and causes the opening of new development areas for this reason. Alluvial soils are preferred as new settlement areas in cities both in Türkiye and in the world due to the ease of excavation-filling operations during the construction period, the rapid progress of the basic stage of building manufacturing, and the ease of transportation works. In countries such as Türkiye, which is located on a tectonic belt with intensely active earthquake zones, it has been painfully experienced again and again at the end of each major earthquake that these alluvial areas are the areas most affected by earthquakes.

Türkiye is in the Alpine orogenic mountain belt, with its active tectonics, is one of the countries with high earthquake frequency and damage risk. It is on the borders of the Eurasian, African and Arabian plates. There are two main fault zones, particularly the East Anatolian and North Anatolian faults, and many local faults in Türkiye, which periodically produce large earthquakes. The fault lines within the borders of Türkiye have produced 47 earthquakes of 6.5 Mw and above in the last century. Considering that 42% of Türkiye is located in 1st degree, 24% in 2nd degree and 18% in 3rd degree earthquake zones and 71% of our population lives in 1st and 2nd degree earthquake zones, it becomes clear that earthquake in Türkiye is not only a natural disaster causing loss of life and property, but also a national security problem [1-2]. For cities located in active earthquake zones, the possibility of being exposed to the destructive effects of earthquakes has made it obligatory to predict structural and spatial damages and to take precautions [3]. Elâzığ province is located on the Eastern Anatolia Fault Zone in the Eastern Anatolia Region of Türkiye. The Eastern Anatolia Fault Zone is a left lateral, strike-slip, active fault zone cutting in the NE-SW direction [4]. This fault line, which starts from Karlıova and continues towards the southwest with the Palu-Hazar Lake segment in the eastern part, determines the seismicity of the region. On January 24, 2020, Elazığ-Sivrice district was

[1]Corresponding author

hit by a severe earthquake measuring Mw=6.8 at 20:55 (17:55 GMT) local time. Unfortunately, it resulted in significant devastation, including structural damage and loss of life.

It is known that earthquake waves increase significantly when passing through soft soils compared to hard soils and this increase has a great share in the damage caused by the earthquake. Seismic waves travel from the bedrock to the surface and pass-through different ground layers along the way. Along this path, the differences between the layers make a significant difference in the wave frequency and amplitude felt. The magnified motion transmitted to the foundation of the structure increases the deformation levels on the structural elements and results in possible local collapse or structural collapse. For this reason, in geotechnical engineering, when designing a structure anywhere, it is necessary to know all local soil properties and seismic loads of that soil in order to design earthquake resistant structures. While the analysis of the source mechanism and the effect of geological formation on the propagation path of the earthquake wave are within the scope of seismology, the investigation of the effect of local ground conditions on strong ground motion is one of the interests of geotechnical engineering [5-6].

The aim of this study is to present the findings and results concerning the seismic impact of the earthquake. The intent is to minimize the impact of future earthquakes and provide recommendations based on seismic parameters. The investigation was performed using ArcGIS software to create the soil amplification and site dominant vibration period maps by geographic information system (GIS).

2. Materials and Method

2.1. General Information about the Study Area

Elazığ province is located in the southwest of the Eastern Anatolia Region, in the Upper Euphrates Region. The province, which has a total area of 9151 km^2 and constitutes 1.2% of Turkey's territory with this area, lies between 40º 21 and 38º 30 east longitudes and 38º 17 and 39º 11 north latitudes. Within this framework, Elazığ province, which roughly resembles a rectangle in shape, has a length of approximately 150 km in the E-W direction and a width of approximately 65 km in the N-S direction. The province is surrounded by Bingöl from the east, Tunceli from the north via Keban Dam Lake, Malatya from the west and southwest via Karakaya Dam Lake, and Diyarbakır from the south. Elazığ is surrounded by the western extensions of the Southeastern Taurus Mountains to the east, west and south. The Southeastern Taurus Mountains extend eastward within the borders of Malatya and pass through Elazığ. They continue in curves towards the south of Lake Van and leave the borders of our country. The highest point of these mountains is Hasan Mountains (2118 m) in the west of the province [7].

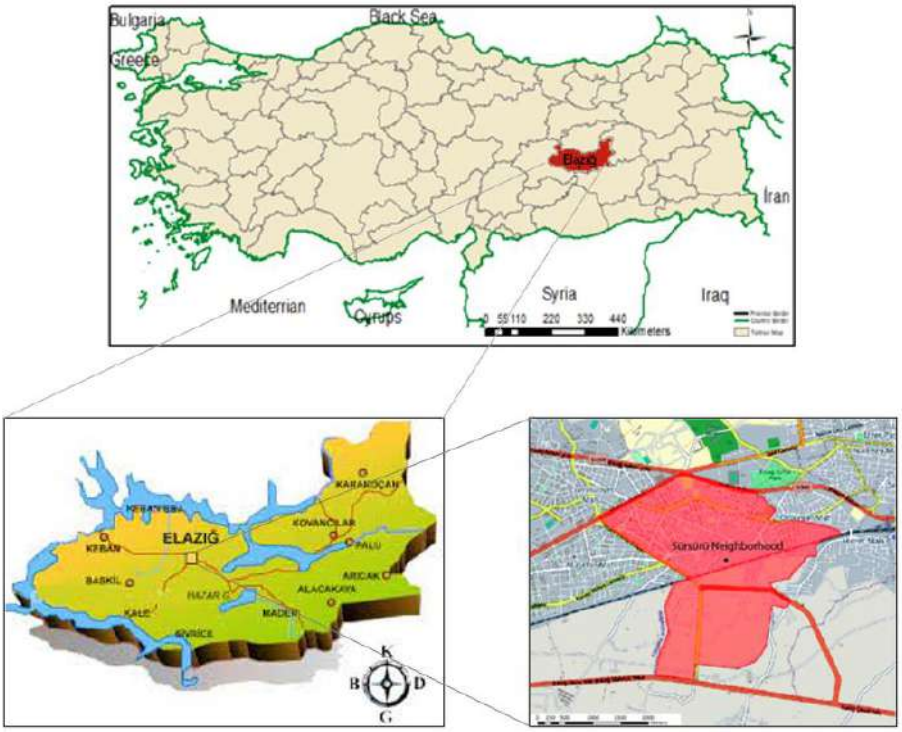

Figure 2.1. Location map of the study area

2.2. Geology of the Study Area

Figure 2.2 displays the geological formations observed in and around Elazığ province. Additionally, Figure 2.3 presents the sequence of these formations, arranged in order from oldest to youngest. Keban Metamorphites, these are crystallized limestones that originated during the Permo-Triassic period. Elazığ Magmatites, Senonian-aged rocks, such as granite, granodiorite, basalt, basaltic pillow lava, andesite, dacite dykes, and volcano sedimentary rocks, belong to this formation. Harami Formation, it consists of massive limestones formed during the Upper Maestrichtian epoch. Kırkgeçit Formation, this formation spans the Middle Eocene to Upper Oligocene period and comprises pebbles, sandstones, marls, and limestones. Maden Complex, both sedimentary rocks (mudstone, sandstone, claystone) and igneous rocks (basalt, andesite, diabase) can be found in this complex. Karabakır Formation, this formation, which dates back to the Upper Miocene-Lower Pliocene era, includes tuff, agglomerates, basaltic lava, and laterally transitioning lacustrine limestones. These descriptions provide an overview of the different geological units in the area and their respective ages [8].

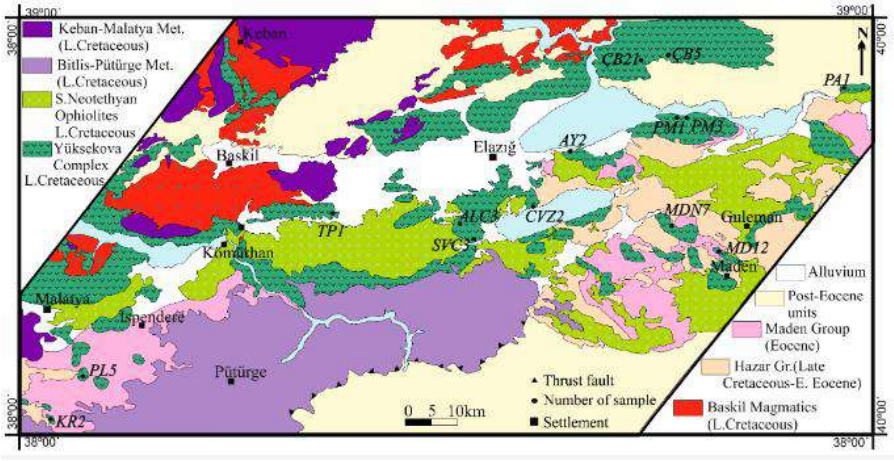

Figure 2.2. Geological map of Elazığ region and the study area [9]

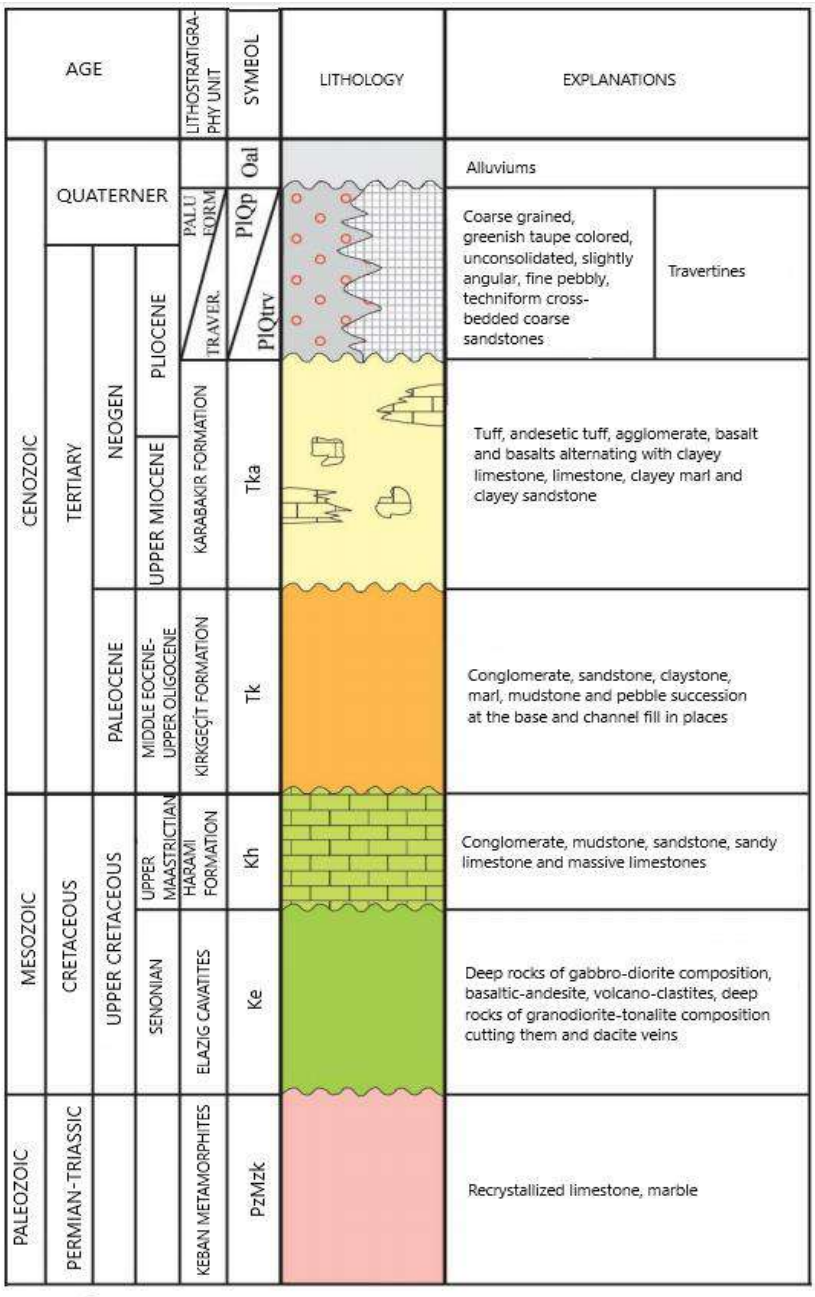

Figure 2.3. Stratigraphy of Elazığ region [8]

2.3. Seismicity of the Region

Elazig city is situated in an area characterized by high seismic activity, between the North Anatolian Fault Zone to the north and the Eastern Anatolian Fault Zone to the south. The eastern part of the Eastern Anatolian Fault Zone, starting from Karlıova, extends southwestward along the Palu-Hazar Lake segment. This particular segment greatly influences the seismicity of the region. Additionally, the Karakoçan Fault Zone, located northeast of Elazig province and aligned in the NW-SE direction, is also a significant source of earthquakes. The Eastern Anatolian Fault Zone has experienced numerous devastating earthquakes throughout history, some of which have been recorded both historically and instrumentally (as depicted in Figure 2.4) [10]. Notable historical earthquakes in the region include the 1789 Palu earthquake, 1866 Elazığ earthquake, 1874 Elazığ earthquake, 1875 Bingöl-Elazığ earthquake, and 1893 Malatya earthquake [11- 19].

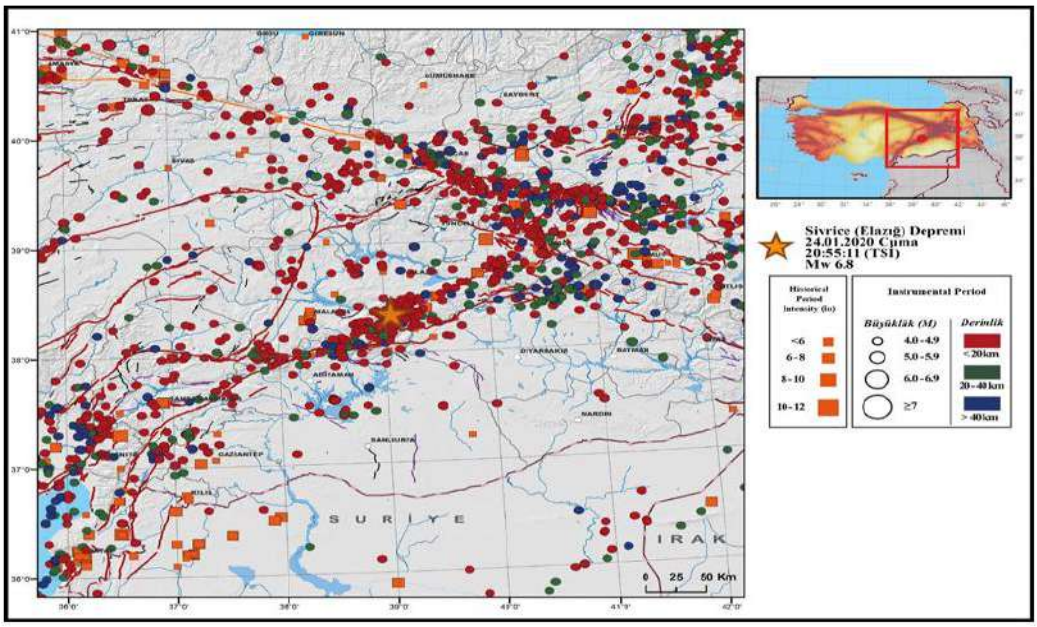

Figure 2.4. Earthquake activity in the historical and instrumental period along the EAF zone [10]

3. Results and Discussions

Measurements were conducted to assess seismic activity in the project area, determining soil amplification values and the dominant vibration period values at the site (T_0). It is well-known that during earthquakes, if the ground beneath a structure vibrates or shakes, the structure itself also oscillates. When the period of an engineering structure and the period of the ground on which it is located are similar, resonance can occur, resulting in greater damage than expected. The amount of energy transferred from the ground to the structure depends on the magnitude of the earthquake at that specific location and the proximity of the natural period of the structure to the site dominant vibration period of the ground. Consequently, the compatibility between the natural periods of the structure and the site dominant vibration period of the ground, referred to as "structure-ground compatibility", plays a crucial role in achieving a balance between safety and cost-effectiveness, which is a key goal in engineering [20].

Table 3.1 (a) Criterias according a) to site dominant vibration periods and (b) according to spectral amplifications [21]

Site dominant vibration period (sec)	Criterion Definition	Spectral amplification	Level of danger
0.10 – 0.30	A	0.0 – 2.5	A (Low)
0.30 – 0.50	B	2.5 – 4.0	B (Medium)
0.50 – 0.70	C	4.0 – 6.5	C (High)
0.70 – 1.00	D		

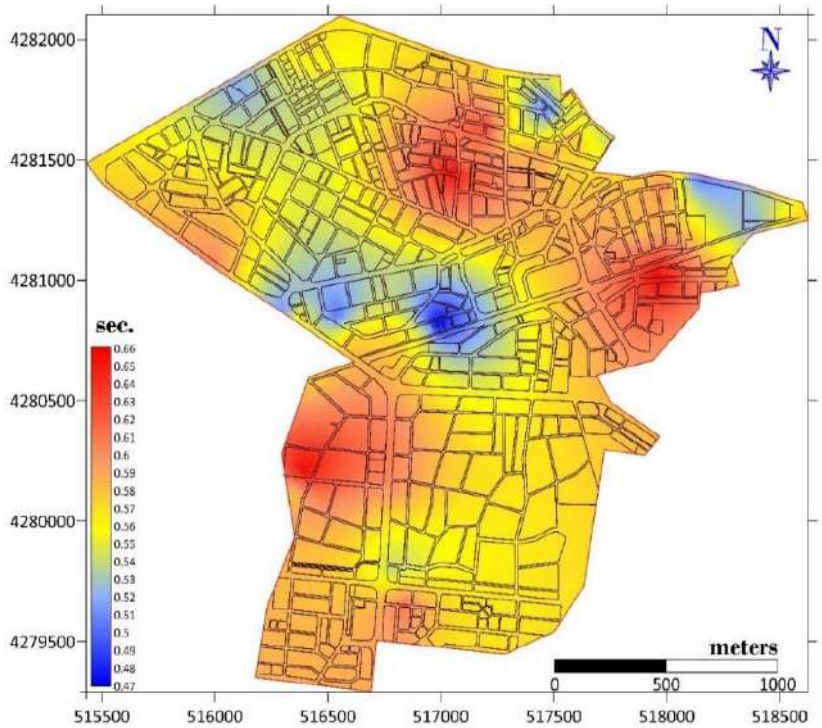

Figure 3.1. Map of site dominant vibration period (To) of the study area.

Based on the criteria defined by Ansal et al., (2004) in the Table 3.1, the map reveals that the blue-colored sections, representing hard and residual soils with a value of 0.47-0.50, are classified as "B, medium hazard level" in terms of the dominant vibration period at the site. On the other hand, the light blue, yellow, orange, and red-colored areas on the map, where loose soils are present with a value between 0.51-0.66, are classified as "C, high hazard level."

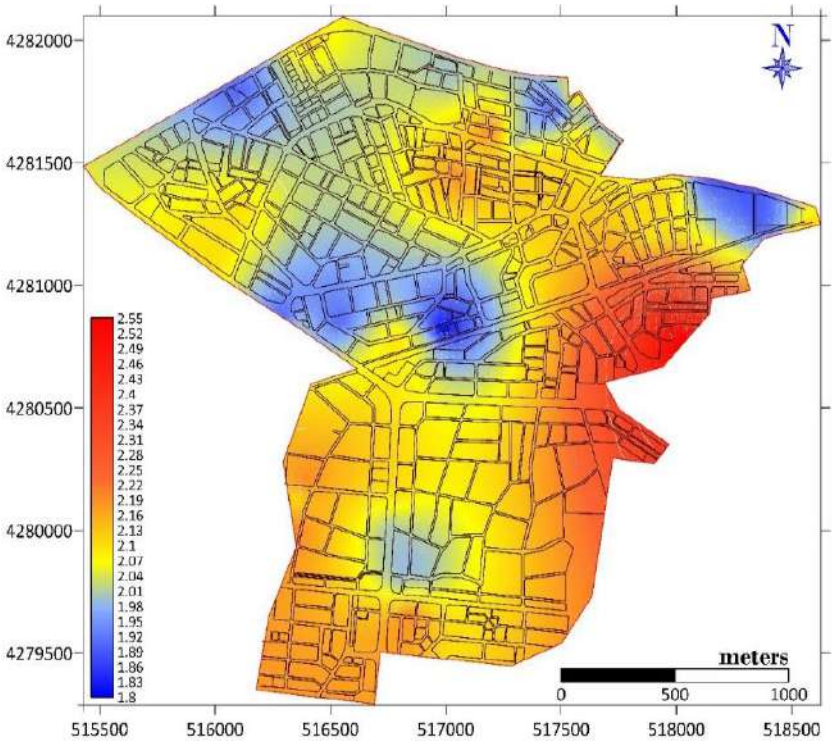

Figure 3.2. Map of seismic amplification distribution of the study area.

The relative soil amplification factors for the soil units in the study area range from 1.8 < A < 2.55. By analyzing the distribution map of soil amplification in Figure 3.2 and considering the classification provided by Ansal et al. (2004) in Table 3.1, it is evident that the blue, yellow, and orange-colored areas in the study area are classified as "A, low hazard level", while the red-colored areas are classified as "B, medium hazard level".

4. Conclusions

The findings of this study indicate varying levels of seismic hazard classification. According to the soil amplification values across the study area, "A" and "B" hazard levels found in areas with different soil conditions while "B" and "C" hazard levels examined according to the site dominant vibration periods. Based on Ansal et al.(2004) criterias:

- Site dominant vibration period ranged between 0.47-0.50 for residual soils and 0.51- 0.66 for loose soils.
- "B" and "C" hazard levels examined according to the site dominant vibration periods
- Soil amplification factors were between 1.8 to 2.55 in the study area.
- The soil amplification hazard level of the study area as "A, low hazard level" and "B, medium hazard level."

5. References

[1] Türkoğlu, N. (2001). Türkiye'nin yüzölçümü ve nüfusunun deprem bölgelerine dağılışı. Ankara Üniversitesi Türkiye Coğrafyası Araştırma ve Uygulama Merkezi Dergisi, 8, 133-148.

[2] Sönmez, M.E. (2011). Coğrafi Bilgi Sistemleri (CBS) tabanlı deprem hasar riski analizi: Zeytinburnu (İstanbul) örneği. Türk Coğrafya Dergisi, 56, 11-22.

[3] Taş, N. (2003). "Yerleşim alanlarında olası deprem zararlarının azaltılması". Uludağ Üniversitesi Mühendislik-Mimarlık Fakültesi Dergisi, 8(1), 225-231.

[4] Özdemir, M.A. ve İnceöz,M., (2003). "Doğu Anadolu Fay Zonunda (Karlıova-Türkoğlu Arasında) Akarsu Ötelenmelerinin Tektonik Verilerle Karşılaştırılması"; Afyon Kocatepe Üniv. Sosyal Bilimler Dergisi, Cilt 5, Sayı l,s.89-114, 2003

[5] Kramer S.L., (1996). Geotechnical earthquake engineering, Prentice-Hall, New Jersey, USA,708ss.

[6] Sonmezer, Y. B., Celiker M., Bas, S., (2019). "An Investigation on the Evaluatio of Dynamic Soil Characteristics of the Elazig City through the 1-D Equivalent Linear Site-Response Analysis, Bulletin of Engineering Geology and Environment.

[7] https://www.elazig.bel.tr/kent-rehberi/cografi-yapi/217/

[8] Palutoğlu, M., (2014) Elazığ Kent Merkezinin Tektoniği, Depremselliği ve Mikrobölgelemesi. [Doktora tezi, Fırat Üniversitesi]. Yüksek Öğretim Kurulu Ulusal Tez Merkezi. (Tez No: 355727)

[9] MTA, (2011). 1/100000 Scaled Geological Maps of Turkey. In General Directorate of Mineral Research and Exploration; Department of Geological Research of General Directorate of MTA: Ankara, Turkey.

[10] The Ministry of Interior, Disaster and Emergency Management Administration (DEMA), January 24, 2020 Sivrice (Elazığ) Earthquake Report, Turkey Republic, 2020.

[11] K. Ergin, U. Güçlü, Z. Uz, (1967). "A catalog of earthquake for Turkey and surrounding area (11 A.D. to 1964 A.D.)," Istanbul Technical University, Faculty of Mining Engineering, Istanbul, Turkey.

[12] K. Ergin, U. Güçlü, G. Aksay, (1971). "A Catalog of Earthquakes of Turkey and Surrounding Area (1965–1970)," Istanbul Technical University, Faculty of Mining Engineering, Institute of Physics of the Earth, Technical Report 28.

[13] H. Eyidogan, U. Güçlü, Z. Utku, E. Değirmenci, (1991). "Macro-Seismic Directory of Major Earthquakes in Turkey (1900–1988)," ITU Mining Faculty, Department of Geophysical Engineering, Istanbul.

[14] N.N. Ambraseys, (1989). "Temporary seismic quiescence: SE Turkey," Geophysical Journal, vol. 96, pp. 311-331.

[15] N. N. Ambraseys, C. Finkel, (1995). "Seismicity of Turkey and neighbouring regions 15001800," Geophysical Journal of International, vol. 133, pp. 390-406.

[16] N. N. Ambraseys, J.A. Jackson, (1998). "Faulting associated with historical and recent earthquakes in the Eastern Mediterranean region," Geophysical Journal International, vol. 133, pp. 390−406.

[17] O. Tan, M.C. Tapırdamaz, A. Yörük, (2008). "The Earthquakes Catalogues for Turkey," Turkish Journal of Earth Science, vol. 17, pp. 405418.

[18] D. Kalafat, Y. Güneş, K. Kekovalı, M. Yılmazer, (2011)."A revised and extended earthquake catalogue for Turkey since 1900 (M ≥ 4.0) (in Turkish)," Boğaziçi University, Kandilli Observatory and Earthquake Research Institute, Istanbul, pp 640-1049.

[19] Ö. Emre, T.Y. Smoke, S. Özalp, H. Elmacı, Ş. Olgun, F. Şaroğlu, (2013). "1/1.250.000 Scaled Active Fault Map of Turkey," General Directorate of Mineral Research and Exploration Special Publications Series, Ankara, Turkey,

[20] Aytun A., (2001), Olası Deprem Hasarını En Aza İndirmek Amacıyla Yapıların Doğal Salınım Periyotlarının Yerin

Baskın Periyodundan Uzak Kılınması: Uşak İli ve Dolayı (Frigya) Depremleri Jeofizik Toplantısı, (73-82)., 2001
[21] Ansal, A. (2004). Recent Advances in Earthquake Geotechnical Engineering and Microzonation, Kluwer Academic Publishers

International Conference on Advances and Innovations in Engineering

Drought evaluation of Elazığ in Turkey using SPI and SPEI

Veysi KARTAL[1]

[1,2]Department, Faculty, University, Province, Country.
[1]Civil Engineering, Engineering Faculty, Siirt University, Siirt, Turkey.
[1]veysikartal@siirt.edu.tr

[1](ORCID: 0000-0003-4671-1281)

Abstract

Water is necessary for all human living creatures. It is therefore essential to supply water and use it efficiently. One of the factors affecting the availability of water is drought. To evaluate the drought of Elazığ province in Turkey, a total of 42 years of time series were evaluated. In this study, meteorological drought analysis was carried out in Elazığ province, located in the Eastern Anatolia region, monthly and annual periods using the Standardised Precipitation Index (SPI) method and SPEI. Meteorological data (temperature, evaporation, and precipitation) from Ağın, Baskil, Keban ve Elazığ-Central observation stations between 1980-2022 were used. As a result, Run Test was used for the precipitation data of 8 meteorological stations. The results showed that the monthly and annual values of SPI and SPEI showed almost similar results at the selected stations. Although there were periods of severe drought, normal drought levels were observed in the overall average. The wet and dry periods were identified, and the results were presented graphically. As a result, the trend results for precipitation and temperature in this area will contribute to the water resources planning management in the region.

Keywords: Water, Drought, SPI, SPEI, Elazığ

1. Introduction

The water is essential for the survival of living things and is required for their life demands. The water requirement for living things is provided from surface and groundwater resources. The allocation of water resources involves the determination of the efficiency of water resources. The historical changes in meteorological data are crucial for water management and water resources planning. The drought phenomenon is considered to be one of the biggest challenges regarding water availability under climate change. Therefore, to assess drought, hydro-meteorological measurements are very significant in the region's development and planning. The changes in the hydro-meteorological variables (precipitation, temperature, streamflow, evaporation, etc.) have an impact on the climate change of the region. Although drought is considered a major hazard that mankind has encountered since ancient times, it affects more people than any other hazard and has the most complicated structure of all potential natural disasters. [1,2]. Drought, unlike hurricanes, tornadoes, hurricanes and floods, happens slowly and steadily, and its onset and end are not simple to identify [3]. Droughts can last for weeks, months, years, decades and even centuries, as their impact is gradual. The frequency of drought events has a significant impact on the continued warming of the global climate, the living conditions of people and the sustainable development of society. [4]. Wilhite and Glantz, (1985) noted that drought is usually characterized by a lack of rainfall in a region over a long period of time, causing water scarcity. It has been shown in many different ways that spatially or spatio-temporally dependent droughts are defined by characteristics such as frequency, magnitude and intensity of their causes and impacts on the environment (Degefu and Bewket, 2014)). Drought studies have become widespread in recent years [8–13]. Furthermore, there have been many studies to compare various methods and indices for assessment of drought. A variety of drought-related indexes have been recommended to date to accurately identify and quantify drought phenomena (magnitude,

[1]Corresponding author

severity, duration, etc.). For example, the standard precipitation index (SPI) is widely used to characterize and make comparisons of drought in various climatic areas. [14,15]. Nevertheless, there is consensus from a large number of studies that a rising global temperature has resulted in an increasing need for water because of evapotranspiration [16]. For this reason, the SPEI was developed to take into account precipitation and potential evapotranspiration (PET) [17,18]. The drought assessment of Elazığ was conducted based on the monthly temperature, precipitation and evapotranspiration data. The SPI and SPEI indices were computed for the range of 1980- 2022.

This study aimed: (1) to obtain SPI and SPEI drought indices for 1- and 12-month scale, (2) to compare the performances of SPI and SPEI for Elazığ.

2. Study Area

The city of Elazığ is located in the Upper Euphrates Region in the southwest of the Eastern Anatolia Region. It covers an area of 9153 km^2 and constitutes 0.12% of Turkey's territory. The region, which lies between 40 0 21' and 380 30' east longitudes and 38 0 17' and 39 0 11' north latitudes, is bordered by Bingöl in the east, Tunceli in the north (via Keban Dam Lake), the cities of Malatya in the west and southwest (via Karakaya Dam Lake) and Diyarbakır in the south. The climate of Elazığ is very distinctive and characteristic of the rest of the region, located in the southwest of the Eastern Anatolia Region. The geographical location and morphological features of the city are the most effective factors in the favorable climate. The climate in the province is continental, with cold and rainy winters and hot and dry summers. However, the dam lakes formed around the province cause deviations in the climate. The study area is shown in Fig. 1

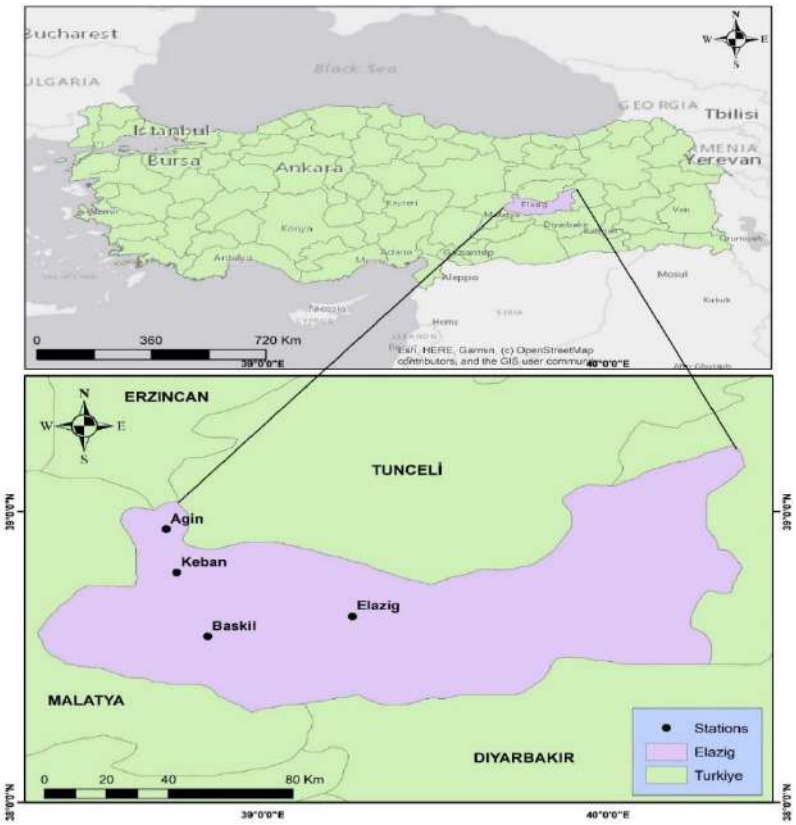

Figure 1. Study area

3. Method and Materials

3.1. Data analysis

Meteorological data were supply from the General Directorate of Meteorology (MGM). Station name, altitude (m), latitude (°) and longitude (°) were given in Table 1. The data in the study vary between 1980 and 2022.

Table 1. Locations

Station names	Latitude	Longitude	Altitude (m)
Elazig	38.6443	39.2561	989
Agin	38.9413	38.7182	900
Keban	38.7933	38.7492	823
Baskil	38.5725	38.8352	1300

3.2. Drought indices

3.2.1. SPI

SPI can be computed for one month, but it can also be applied to SPI values for 3, 6, 9, 12, etc. months. SPI are calculated as below [3]:

$$(x) = \frac{p^{\alpha-1} e^{\frac{-p}{\beta}}}{\beta^{\alpha} T(\alpha)} \quad (1)$$

$$\propto = \frac{1}{4A}\left(1 + \sqrt{\frac{4A}{3}}\right) \quad (2)$$

$$\beta = \frac{\bar{x}}{\alpha} \quad (3)$$

$$A = \ln(\bar{x}) - \frac{\ln(\bar{x})}{n} \quad (4)$$

in which P: precipitation amount, β:scale parameter, α:shape parameter n: the number of observations, T: Gamma-function by integration,

3.2.2. SPEI

The SPEI is a meteorological drought-related drought index that considers temperature and variability of rainfall to evaluate drought in a region. To calculate the SPEI, the first step is to derive the monthly potential evapotranspiration (PET). Usually, when more data are available, a more complete estimation of drought variability is feasible by computing PET with a more sophisticated method. The water balance equation is then performed to calculate the monthly deficit (D_i) as follows.

$$D_i = P_i - \mathrm{PET}_i \quad (5)$$

where P_i refers to total rainfall at i^{th} month.

Finally, the fitted open values are normalized and fitted to a log-logistic distribution function. The SPEI values for the first month are the normalized values of the probability (p) of exceeding a given Di value and are derived by Eq. (6) [20], while Table 2 shows the classification of the drought for SPEI.

$$\mathrm{SPEI}_i = W_i - \frac{2.515517 + 0.802853 W_i + 0.010328 W_i^2}{1 + 1.432788 W_i + 0.189269 W_i^2 + 0.001308 W_i^3} \quad (6)$$

$$W_i=\begin{cases} p<0.5, & \sqrt{-2lnp} \\ p>0.5, & \sqrt{-2\ln(1-p)} \end{cases}$$

In which p refers to exceeding probability of for computed values of D_i

Table 2. Drought classification of CZI, SPI ve SPEI indices Barua et al. (2011)

Condition	SPI and SPEI
Extremely wet	$value \geq 2.00$
Very wet	$1.50 \leq value < 2.00$
Moderately wet	$1.00 \leq value < 1.50$
Near normal	$-1.00 \leq value < 1.00$
Moderately dry	$-1.50 \leq value < -1.00$
Severely dry	$-2.00 \leq value < -1.50$
Extremely dry	$value \leq -2.00$

4. Results and Discussions

4.1 Analysis of Climate Data for Elazig

The monthly temperature (max, min, mean), rainfall, and evaporation data for Elazig were analyzed for 1980-2022 in the study and descriptive statistics of rainfall data were shown in Table 3. As seen in Table 3, the precipitation data for all stations were not randomly distributed.

Table 3. Descriptive Statistics of data

Station name	Maximum	Mean	Std. deviation	R	r Expected value	p-value (Two-tailed)
Agin	174.300	39.382	37.732	181	253.326	**<0,0001**
Baskil	208.100	33.983	31.747	187	255.773	**<0,0001**
Elazig	160.500	33.440	31.591	193	252.130	**<0,0001**
Keban	174.400	28.927	27.861	203	252.130	**<0,0001**

Test interpretation:
H_0: Data are randomly distributed.
H_a: Data are not randomly distributed
As the computed p-value is lower than the significance level alpha=0,05, one should reject the null hypothesis H_0, and accept the alternative hypothesis, Ha.

4.1. SPI and SPEI drought indices

By applying the SPI and SPEI drought indices for Elazığ, analyses were conducted for SPI-1 and SPI-12. These time series are shown in Fig. 2. If the drought values of the month are below zero, they represent the dry period, while the drought values are above zero, they represent the humid period. While SPI is calculated using only monthly precipitation data, SPEI is computed using rainfall evapotranspiration. SPI values were calculated for each month and evaluated by considering the precipitation of each month. To reach a general conclusion for a one-month period (SPI-1), drought values were plotted for SPI-1 and SPI-12 values in Fig. 4. Finally, dry and wet periods were observed at Elazığ between 1980 and 2022 both SPI-1 and SPI-12. SPEI and SPI values for monthly and yearly are compatible with each other.

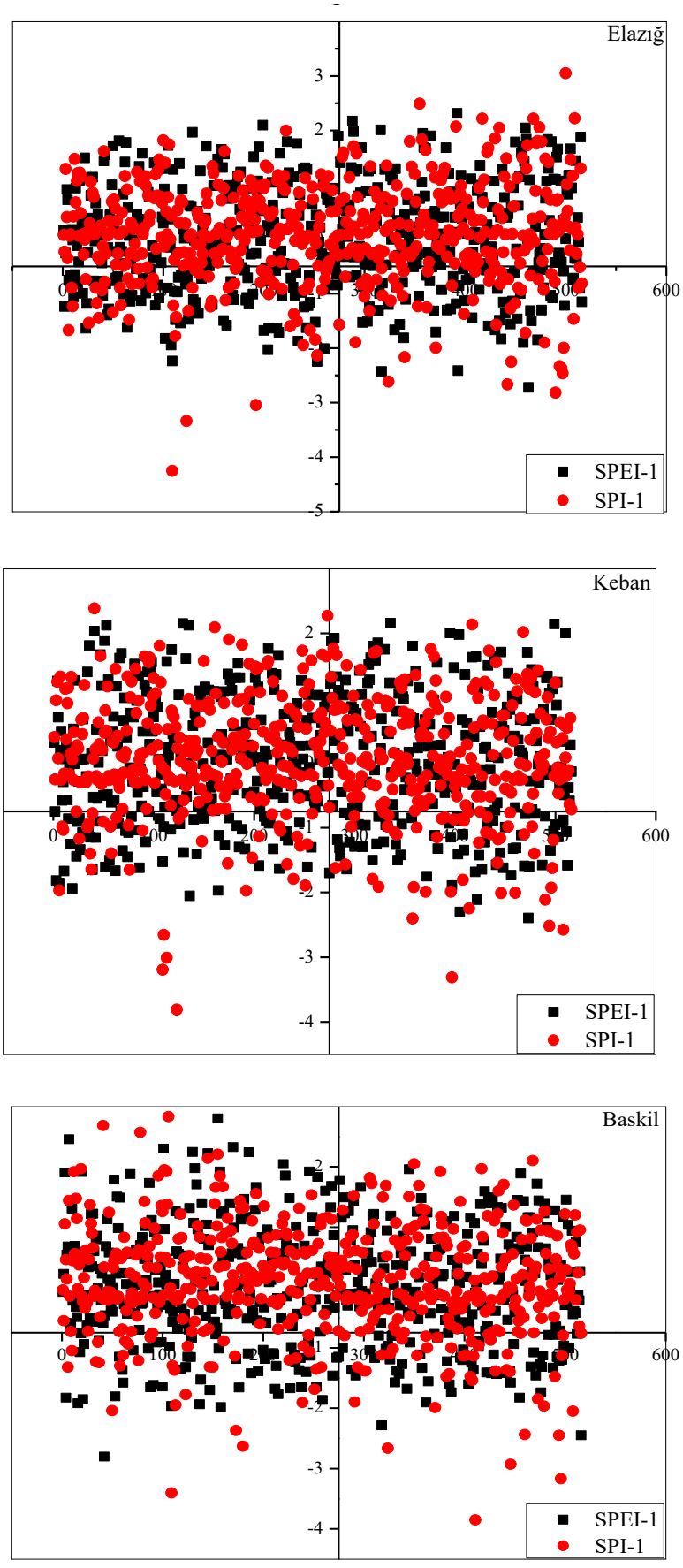

Figure 2. The SPI and SPEI indices for Elazığ

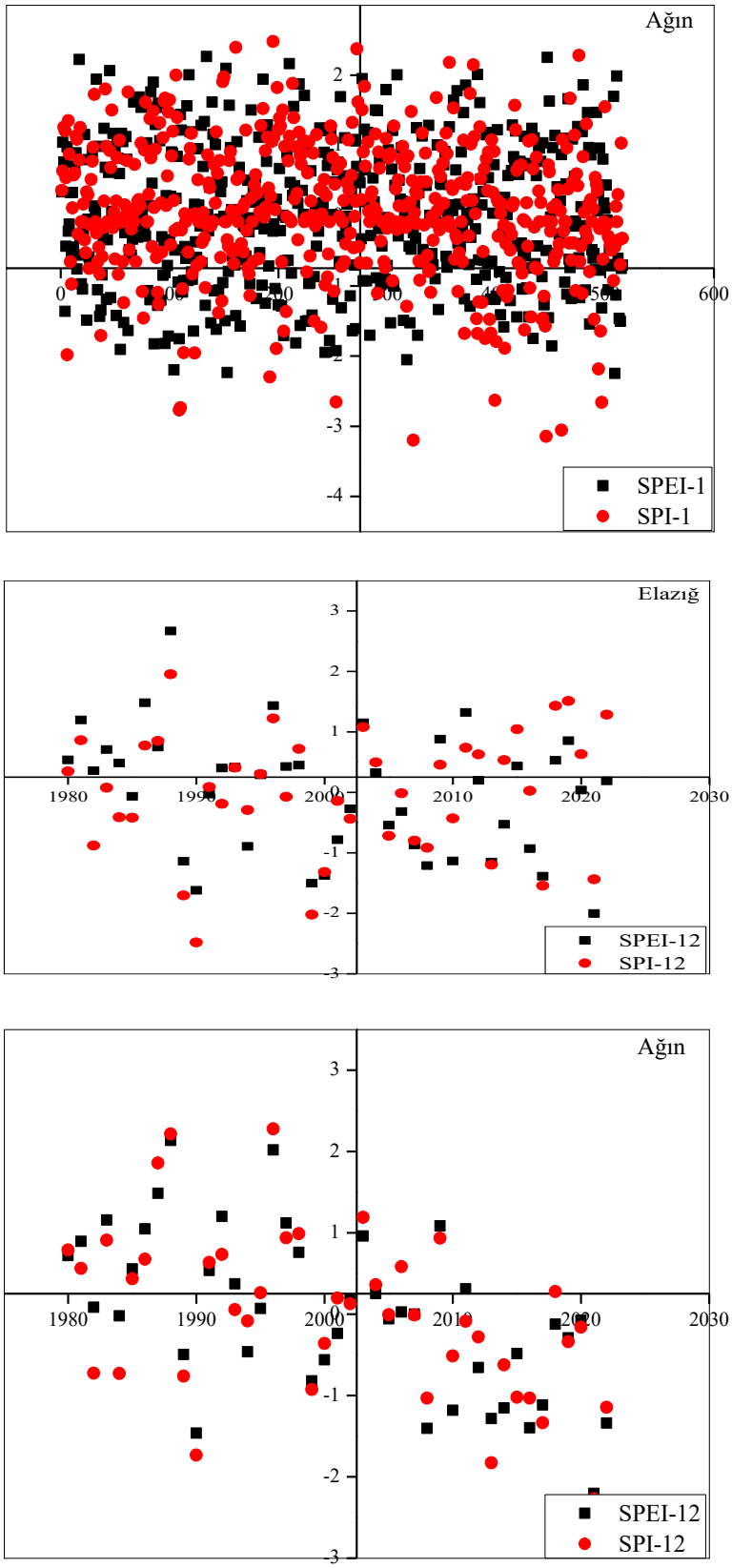

Figure 2. The SPI and SPEI indices for Elazığ (More)

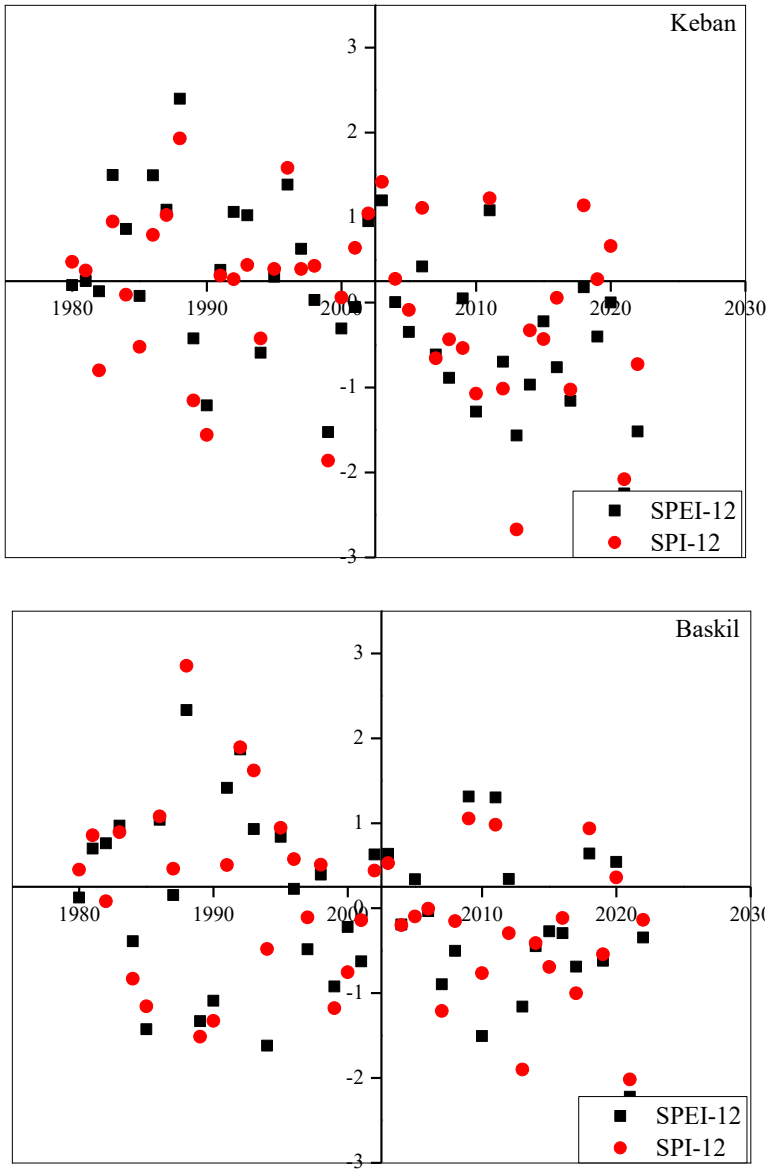

Figure 2. The SPI and SPEI indices for Elazığ (More)

4.2. The comparison of SPEI and SPI

By applying SPI and SPEI drought indices, the drought of Elazığ was analyzed for 1- and 12-month time series. These time series are shown in Fig. 3. The months below 0 represent the dry period, while the months above 0 represent the humid months. While SPI is calculated using only monthly precipitation data, SPEI considers both precipitation and temperature data. Both drought indices show a similar relationship between 1980 and 2022. To compare the results obtained with SPI and SPEI drought indices for monthly and yearly, they are plotted in Fig. 3 for Elazığ. As shown in Fig. 3, SPI and SPEI drought indices are generally consistent with each other for annual time series. However, the relationship with SPI and SPEI has not consistent for monthly time scales due to different calculation of these indices.

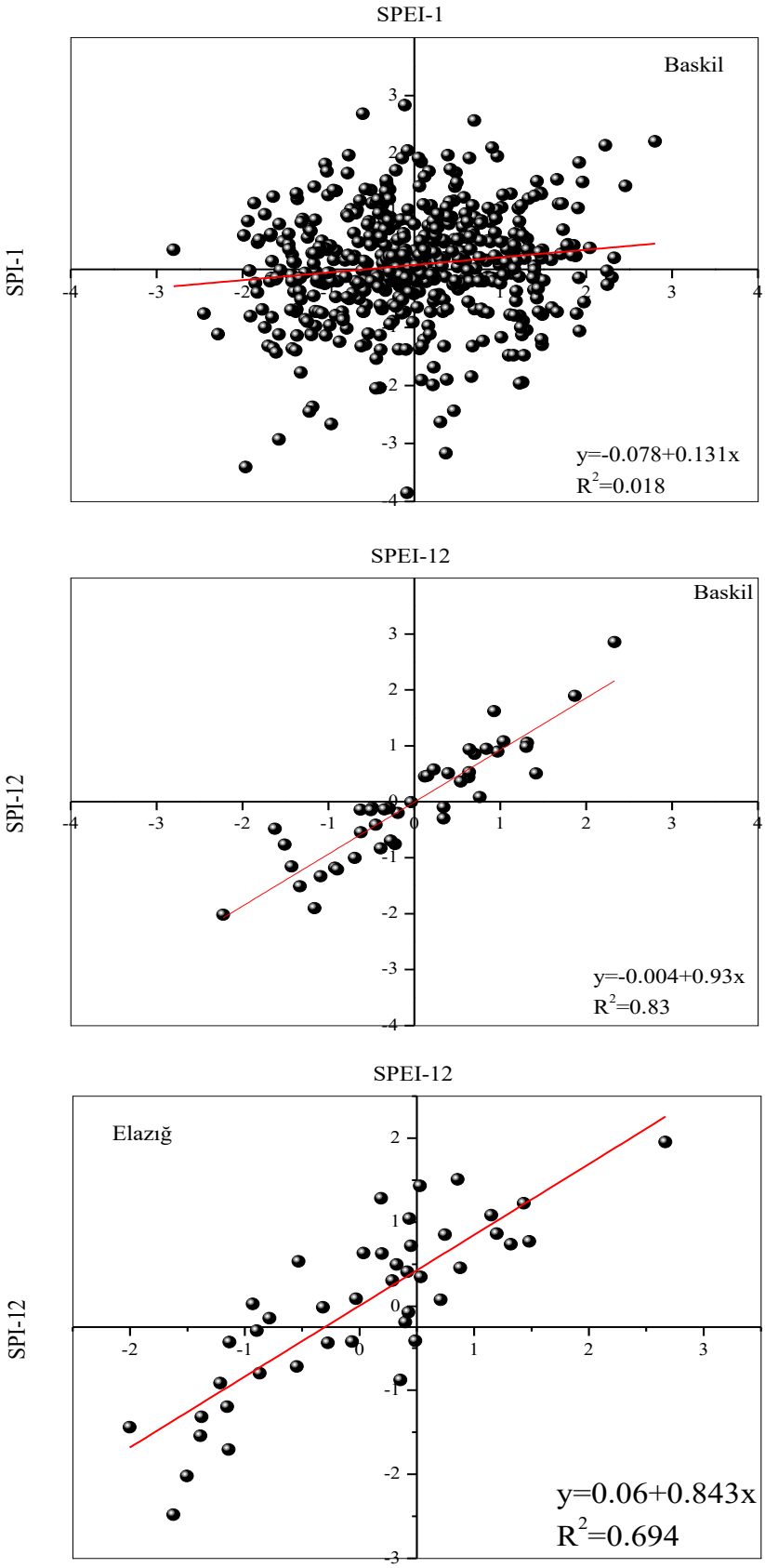

Figure 3. The comparisons of SPI and SPEI indices for Elazığ

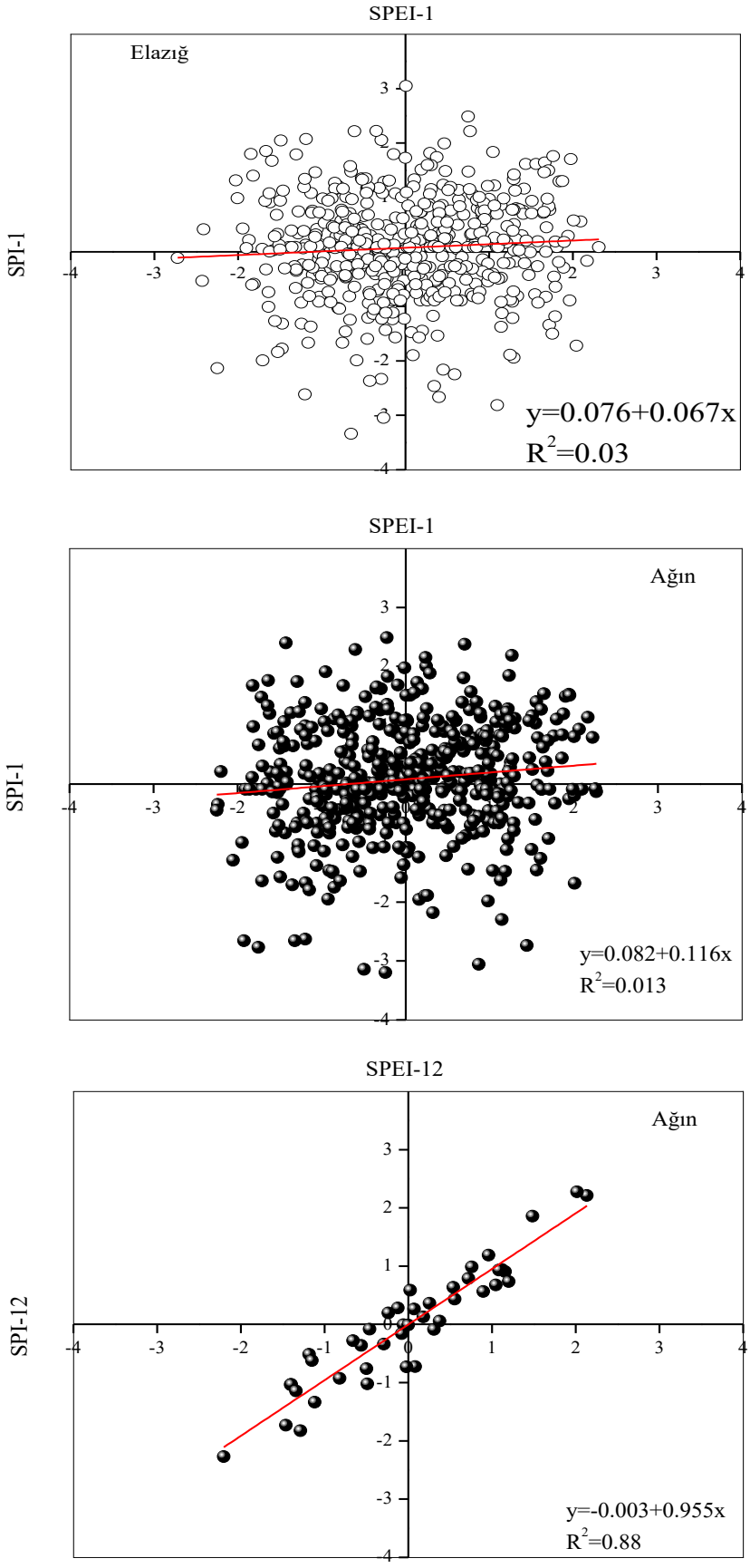

Figure 3. The comparisons of SPI and SPEI indices for Elazığ (More)

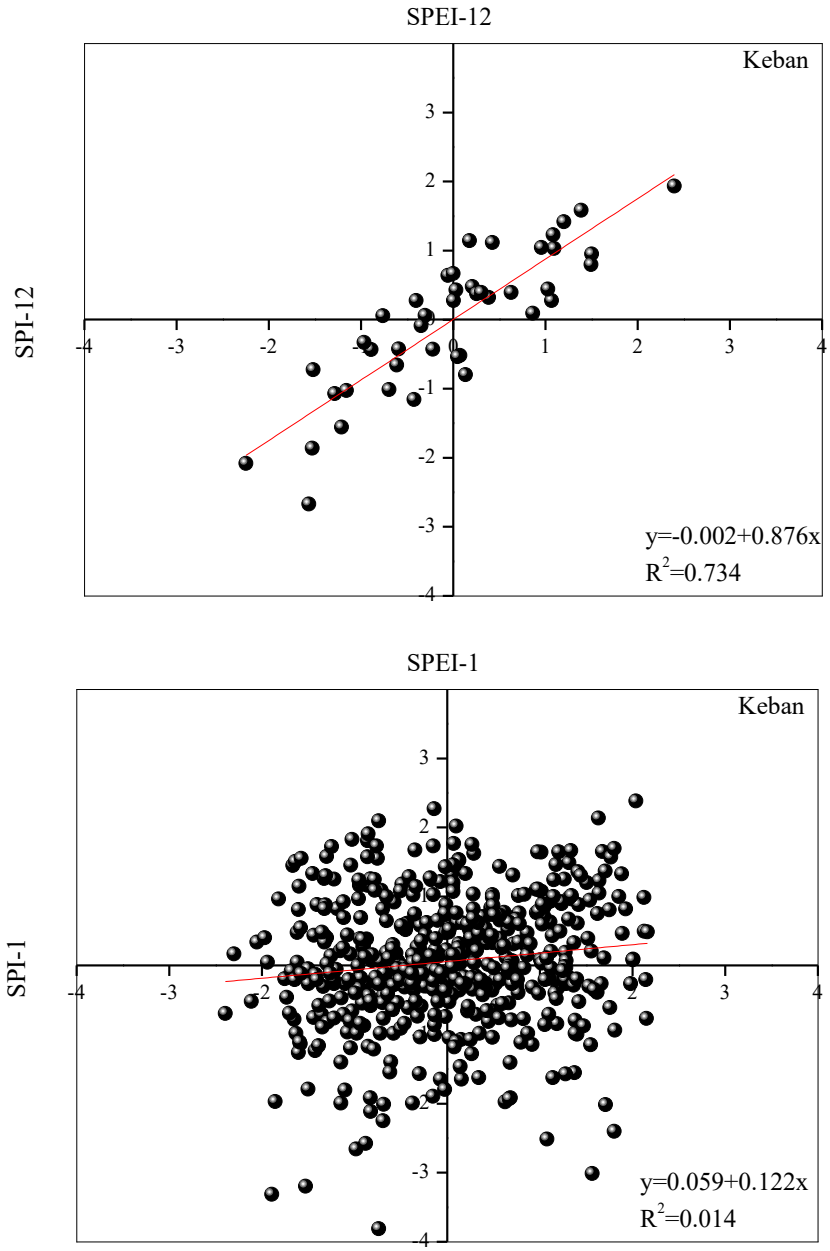

Figure 3. The comparisons of SPI and SPEI indices for Elazığ (More)

5. Conclusion

The general objective of this study is to make a detailed drought analysis for Elazig in monthly and annual time scales by SPI and SPEI. For this reason, drought analysis was performed by considering the period between 1980-2022 with SPEI and SPI indices. The effects of climate change on temperature (max, min, average), precipitation, and evapotranspiration parameters were examined in detail. An increase trend was detected in temperature and evaporation data based on 95% confidence, while a decreasing trend was detected in rainfall data. Although normal drought has the highest share among drought categories, very severe drought has the lowest share. it is determined that SPEI gives more sensitive results in the very severe drought category than SPI index. It is expected to shed light on the drought analyses to be made in the field for Elazığ

6. Acknowledgements

Special thanks to the General Directorate of Meteorology (MGM) for providing the database used in this study.

Declarations

Funding: There is no funding.

Conflicts of interest: The authors declare no conflicts of interest.

Data availability: The datasets used and/or analyzed in the present study are available from the corresponding author on reasonable request.

Code availability: None.

Ethics approval: Not applicable.

Consent to participate: Not applicable.

7. References

[1] D.A. Wilhite, Drought: A Global Assessment, in: Chapter 1:Drought: A Global Assessment, Drought Mitigation Center Faculty Publications, London, 2021: pp. 3–18. https://doi.org/10.4324/9781315830896-24.

[2] M.S. Ashraf, I. Ahmad, N.M. Khan, F. Zhang, A. Bilal, J. Guo, Streamflow Variations in Monthly, Seasonal, Annual and Extreme Values Using Mann-Kendall, Spearmen's Rho and Innovative Trend Analysis, Water Resources Management. 35 (2021) 243–261. https://doi.org/10.1007/s11269-020-02723-0.

[3] WMO, Guidelines on the Defintion and Characterization of Extreme Weather and Climate Events, 2023.

[4] J. Thomas, V. Prasannakumar, Temporal analysis of rainfall (1871-2012) and drought characteristics over a tropical monsoon-dominated State (Kerala) of India, Journal of Hydrology. 534 (2016) 266–280. https://doi.org/10.1016/j.jhydrol.2016.01.013.

[5] D.A. Wilhite, M.H. Glantz, Understanding: the Drought Phenomenon: The Role of Definitions, Water International. 10 (1985) 111–120. https://doi.org/10.1080/02508068508686328.

[6] J. Sheffield, E.F. Wood, Projected changes in drought occurrence under future global warming from multi-model, multi-scenario, IPCC AR4 simulations, Climate Dynamics. 31 (2008) 79–105. https://doi.org/10.1007/s00382-007-0340-z.

[7] M.A. Degefu, W. Bewket, Variability and trends in rainfall amount and extreme event indices in the Omo-Ghibe River Basin, Ethiopia, Regional Environmental Change. 14 (2014) 799–810. https://doi.org/10.1007/s10113-013-0538-z.

[8] M.M. Moghimi, A.R. Zarei, Evaluating Performance and Applicability of Several Drought Indices in Arid Regions, Asia-Pacific Journal of Atmospheric Sciences. 57 (2021) 645–661. https://doi.org/10.1007/s13143-019-00122-z.

[9] S. Dogan, A. Berktay, V.P. Singh, Comparison of multi-monthly rainfall-based drought severity indices, with application to semi-arid Konya closed basin, Turkey, Journal of Hydrology. 470–471 (2012) 255–268. https://doi.org/10.1016/j.jhydrol.2012.09.003.

[10] S.T. Chen, C.C. Kuo, P.S. Yu, Historical trends and variability of meteorological droughts in Taiwan, Hydrological Sciences Journal. 54 (2009) 430–441. https://doi.org/10.1623/hysj.54.3.430.

[11] G. Tayfur, Discrepancy precipitation index for monitoring meteorological drought, Journal of Hydrology. 597 (2021) 126174. https://doi.org/10.1016/j.jhydrol.2021.126174.

[12] A. Malik, A. Kumar, O. Kisi, N. Khan, S.Q. Salih, Z.M. Yaseen, Analysis of dry and wet climate characteristics at Uttarakhand (India) using effective drought index, Natural Hazards. 105 (2021) 1643–1662. https://doi.org/10.1007/s11069-020-04370-5.

[13] M.I. Yuce, M. Esit, Drought monitoring in Ceyhan Basin, Turkey, Journal of Applied Water Engineering and Research. 9 (2021) 293–314. https://doi.org/10.1080/23249676.2021.1932616.

[14] N.J.D. and J.K. Thomas B. McKee, The relationship of drought frequency and duration to time scales, in: Eighth Conference on Applied Climatology, California, 1993. https://doi.org/10.1002/jso.23002.

[15] D. Mersin, A. Gulmez, M.J.S. Safari, B. Vaheddoost, G. Tayfur, Drought Assessment in the Aegean Region of Turkey, Pure and Applied Geophysics. 179 (2022) 3035–3053. https://doi.org/10.1007/s00024-022-03089-7.

[16] R.R. Heim, A comparison of the early twenty-first century drought in the United States to the 1930s and 1950s drought episodes, Bulletin of the American Meteorological Society. 98 (2017) 2579–2592. https://doi.org/10.1175/BAMS-D-16-0080.1.

[17] C. Liu, C. Yang, Q. Yang, J. Wang, Spatiotemporal drought analysis by the standardized precipitation index (SPI) and standardized precipitation evapotranspiration index (SPEI) in Sichuan Province, China, Scientific Reports. 11 (2021) 1–14. https://doi.org/10.1038/s41598-020-80527-3.

[18] S.M. Vicente-Serrano, S. Beguería, J.I. López-Moreno, A multiscalar drought index sensitive to global warming: The standardized precipitation evapotranspiration index, Journal of Climate. 23 (2010) 1696–1718. https://doi.org/10.1175/2009JCLI2909.1.

[19] E. Yacoub, G. Tayfur, Evaluation and Assessment of Meteorological Drought by Different Methods in Trarza Region, Mauritania, Water Resources Management. 31 (2017) 825–845. https://doi.org/10.1007/s11269-016-1510-8.

[20] A. Danandeh Mehr, B. Vaheddoost, Identification of the trends associated with the SPI and SPEI indices across Ankara, Turkey, Theoretical and Applied Climatology. 139 (2020) 1531–1542. https://doi.org/10.1007/s00704-019-03071-9.

[21] S. Morid, V. Smakhtin, M. Moghaddasi, Comparison of seven meteorological indices for drought monitoring in Iran, International Journal of Climatology. 26 (2006) 971–985. https://doi.org/10.1002/joc.1264.

[22] S. Barua, A.W.M. Ng, B.J.C. Perera, Comparative Evaluation of Drought Indexes: Case Study on the Yarra River Catchment in Australia, Journal of Water Resources Planning and Management. 137 (2011) 215–226. https://doi.org/10.1061/(asce)wr.1943-5452.0000105.

International Conference on Advances and Innovations in Engineering

Assessment of the Mechanical Properties of a Masonry Church in Malatya by Non-Destructive Testing

Alper ÖZMEN[1] , Erkut SAYIN [2]

[1]Civil Engineering, Engineering Faculty, Inonu University, Malatya, Turkey.
[2] Civil Engineering, Engineering Faculty, Fırat University, Elazig, Turkey.
[1]alper.ozmen@inonu.edu.tr, [2]esayin@firat.edu.tr

[1](ORCID: 0000-0003-1335-3780), [2](ORCID: 0000-0003-0266-759X)

Abstract

Historical masonry structures are an important part of the cultural heritage. Historic buildings can be damaged by various external factors such as wind, floods, fires, and earthquakes. To prevent damage to historic structures from these factors, it is important to obtain accurate information on their material properties for reliable computational modelling and strengthening intervention programs. There are several methods to determine the material properties of masonry structures. These are destructive, semi-destructive and non-destructive techniques. Destructive and semi-destructive techniques can damage a structure. Non-destructive techniques are generally used to determine the material properties of historical masonry structures. In this study, the material properties of the historical masonry Taşhoran Church located in Malatya, Turkey, were determined using non-destructive techniques. Schmidt Hammer, Ultrasonic Pulse Velocity (UPV) and Infrared Thermography methods were used to determine the material properties of Taşhoran Church. The compressive strength, Poisson ratio, young modulus and density of stones were determined. The stone types were also assessed by visual observation and mechanical properties. There are several studies in the literature that have used non-destructive techniques to determine the material properties of masonry structures. However, different types of stones are used for the construction of buildings in different regions. Therefore, it is important to examine different structures in different regions. This will help to determine the material properties of the stones in these regions.

Keywords: Non-destructive techniques (NDT), historical masonry structures, material properties, Schmidt hammer, infrared thermography

1. Introduction

Many civilizations have lived in the Anatolian geography in the past. It has one of the richest cultural heritages in the world. The lifestyle of past civilizations can be shown through historical masonry structures. Therefore, it is very important to protect these structures. Masonry structures are affected by various internal and external factors (earthquakes, floods fire, wars etc.). Understanding the structural behavior of these structures is essential for protection and strengthening. In order to understand the structural behavior of historical masonry structures, the material characteristics of these structures should be well known. For the mechanical assessment of masonry heritage structures, destructive testing (DT) and non-destructive testing (NDT) techniques can be used [1]. Masonry structures are valuable to damage during the use of the DT techniques. Therefore, for the determination of the material properties of masonry structures, NDT techniques may be preferable. There have been several studies in the literature on the use of NDT for the determination of the material properties of masonry structures. Aksoy and Karaton [2] used a Schmidt hammer and an ultrasound device to obtain the mechanical properties of Diyarbakır Ulu Mosque's stone. Also, they applied an acid loss test to khorasan mortar that was taken from non-load-bearing walls. Grinzato et al. [3] used the IR thermography method to observe the deformation and changes of walls and obtain the moisture content. Fort et al. [4] noticed various types of granite in two different historical heritage monuments. They used nondestructive, portable techniques (Schmidt hammer rebound and ultrasound velocity) for assessing these granites. Pirchio et al. [5] used two different NDT and two expert judgment-based investigation techniques (i.e., the masonry

[1]Corresponding author

quality index and mechanical properties ranges based on the Commentary to the Italian Building Code) for assessing the quality of the masonry walls of the Italian medieval churches.

In this study, the material properties of a historical masonry church were determined through NDT techniques. Malatya Taşhoran Church was chosen as a case study. Ultrasonic Pulse Velocity (UPV), Schmidt hammer and infrared thermography (IR), which are among the NDT techniques, were used. Compressive strength, young modulus, Poisson ratio and unit weight of masonry units are determined. In 2021, the Malatya Metropolitan Municipality undertook the restoration of the case study. On-site observations, it was seen that the restoration stones were different from the original stones. As a result, this study focused on a comparative analysis between the original stones and restoration stones.

2. Description of the Case Study

The Historical Taşhoran (Surp Yerrortutyun) Church was built using cut stones and has a single dome. Its construction was started in 1878 and finished in 1893. In 1893, an earthquake was occured and the dome of the Taşhoran Church collapsed. In 1905, 12 years later, the dome was repaired. However, during the late 1960s, a fire led to the collapse of the dome once again, resulting in significant harm to the epitaph. In 2021, the Malatya Metropolitan Municipality undertook the restoration and strengthening of the church. The previously fallen stone dome was reinforced using a steel structural system. Restoration stones were used for the door of the baptismal room, according to the restoration project and visual observations [6]. Some views of Taşhoran Church are given in Fig 1. Views of before and after restoration process can be seen in Fig. 1.

(a)

(b)

Figure 1. Views of Malatya Taşhoran Church (a) Before restoration, (b) After restoration

3. Non-destructive Testing (NDT)

Various non-destructive testing (NDT) methods have been discussed in the existing literature. In the present study, the most common NDT techniques, namely the Schmidt hammer, ultrasonic wave velocity and thermography methods, have been used.

3.1. Schmidt hammer test

The Schmidt hammer test stands out as one of the most frequently employed non-destructive testing methods. This test operates on the principle that the absorbed elastic energy in a material corresponds to its strength. In the context of this study, the test was executed on unplastered components following the guidelines of [7] and [8]. A Schmidt hammer with an L-shaped design and a lens-shaped striking tip was utilized for the testing (Fig. 2).

3.2. Ultrasonic pulse velocity (UPV) test

The pulse velocity test is an NDT method utilized to ascertain the speed at which ultrasonic waves travel through masonry walls. The ultrasonic wave velocity test is used to assess the consistency of masonry, gauge the depth of cracks, and identify internal voids [9,10]. The ultrasonic wave velocity test was conducted following the international standards ASTM C597 [11] and EN 12504-4 [12]. The testing apparatus for measuring ultrasonic wave velocity is depicted in Fig. 3. Cylindrical probes attached to transducers were employed. These transducers were designed to operate at a nominal frequency of 54 kHz. Various testing configurations (direct, indirect, and semi-direct) are outlined in ASTM C597 (Fig. 4). The indirect method was used in the present study. For each location, a minimum of three measurements were gathered, and the pulse velocity of the masonry unit was determined as the average of these values.

Figure 2. L Type Schmidt hammer

Figure 3. UPV device that was used in the study

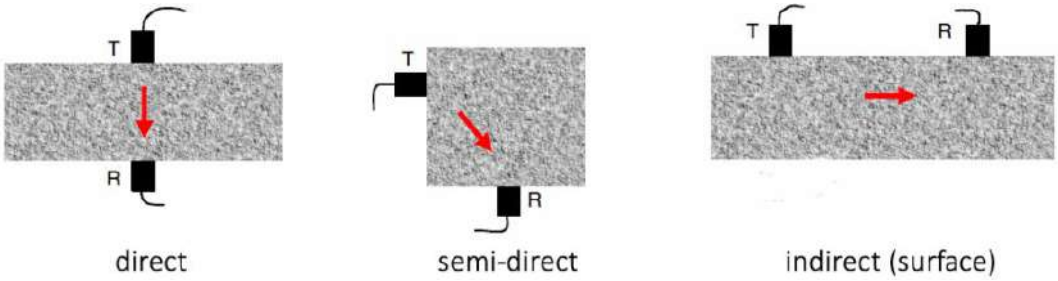

Figure 4. Configurations of UPV test

3.3. Infrared thermography (IRT) test

Infrared Thermography (IRT) is a widely adopted non-destructive and assessment technology with a broad array of applications, ranging from enhancing nocturnal visibility to identifying flaws on structural surfaces.
IRT is a valuable NDT for investigating masonry heritage structures, their building materials and their state of conservation, because it allows investigation without requiring samples and the ability to investigate large areas [13].

In the field of heritage conservation, two approaches are used for IRT investigations [14,15]. These two approaches are called passive and active thermography. When the features of interest are naturally at a different temperature than the background, passive thermography is used. The passive approach is often employed for architectural surface examination, where the materials under investigation are typically inspected qualitatively (identification of discontinuities/interfaces, defects, voids, etc.). When the characteristics of interest are in thermal equilibrium with the surroundings and hence difficult to separate, active thermography is used, in which an energy source is used to provide a thermal contrast (heating or cooling) between the feature of interest and the backdrop [16].

4. Result and Discussion

On the walls of the masonry Taşhoran Church, Schmidt Hammer, UPV and infrared thermography testing methods were applied. This section presents the results obtained from the tests.

4.1. Schmidt hammer

The Schmidt hammer is an economical and user-friendly tool that is employed for on-site assessment of cultural heritage structures [17,18]. In this research, an L-type Schmidt hammer was employed to obtain the surface hardness of the walls of the historical Malatya Taşhoran Church. A view of the application is given in Fig. 5a. The Schmidt Hammer test was performed at six different façades on the historical Malatya Taşhoran Church (Fig. 6). To compute the compressive strength of the construction stones, the method outlined in [19] was adopted. The average Schmidt rebound values for these six different locations are presented in Table 1.

From the in-situ Schmidt rebound results it can be concluded that location 1, 2, 3, 5 and 6 consist of the same type of stone. The mean Schmidt rebound values were calculated to be 42 for original stones (OS) and 28 for restoration stones (RS). According to the relations between Schmidt rebound and UCS suggested by Buyuksagis and Goktan [19], the UCS values of OS and RS were determined. The relationship between the Schmidt rebound and UCS can be seen in Fig. 7a. The UCS values of OS and RS were calculated as 57.83 MPa and 23.13 MPa, respectively. Also, the dry densities of OS and RS were calculated using the relation suggested by [20]. The relationship can be seen in Fig. 7b. According to the relation suggested by Chawre [20], the dry densities of OS and RS calculated as 2.72 g/cm^3 and 2.6 g/cm^3.

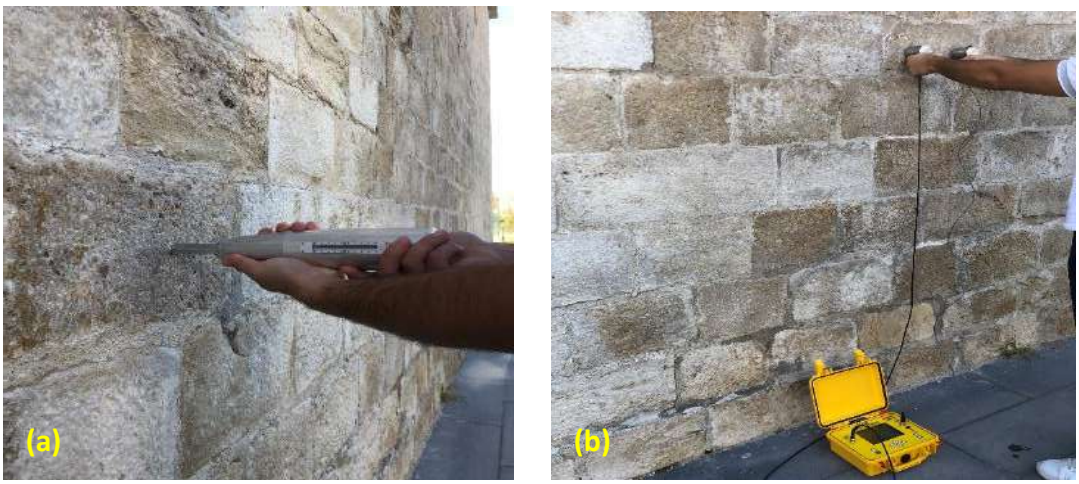

Figure 5. Application of schmidt hammer test (a) and UPV test (b)

Table 1. Mean ultrasonic velocities and rebound values of the walls

Location (Loc.)	Loc.1	Loc.2	Loc.3	Loc.4	Loc.5	Loc.6	Mortar
Mean R	39	43	43	28	42	41	11
Mean Vp (m/s)	3390	3100	3350	2300	3210	3660	-
Mean Vs (m/s)	1885	1722	1861	1483	1783	2033	-

*R: Schmidt rebound value, Vp: P wave velocity , Vs: Shear wave velocity

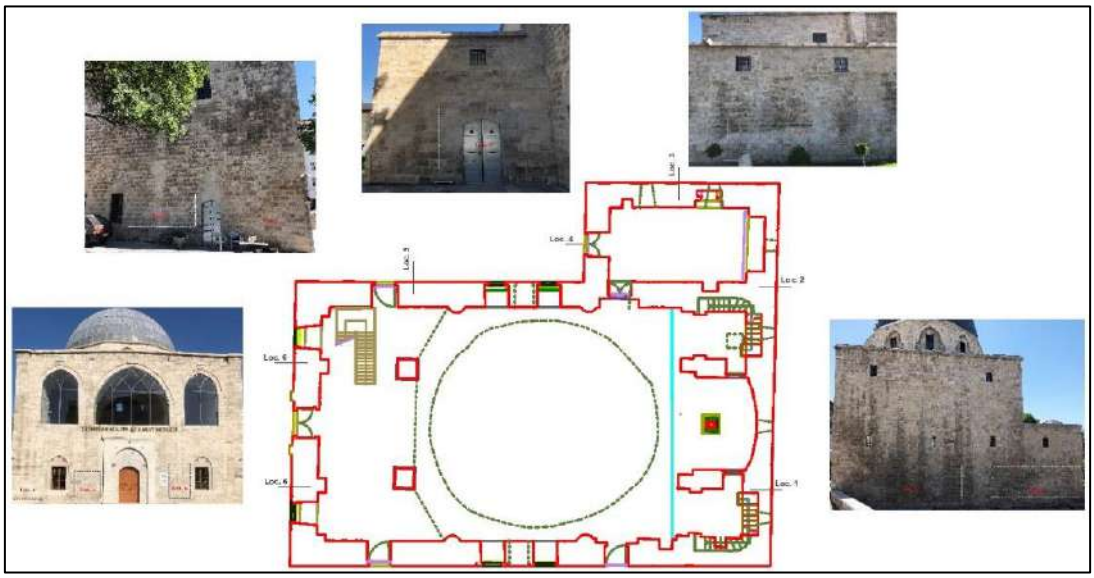

Figure 6. In-situ test locations of historical Malatya Taşhoran church

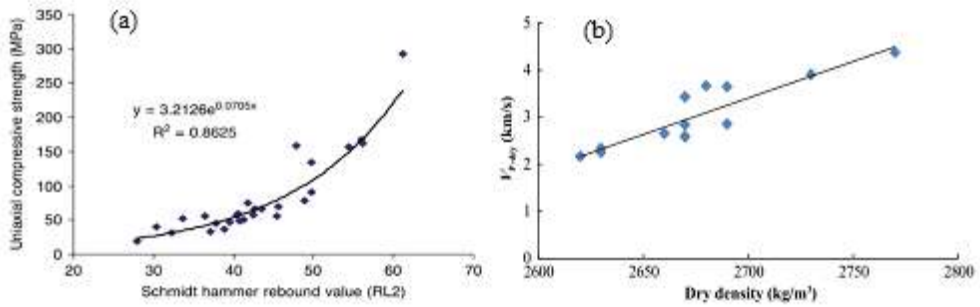

Figure 7. Suggested relations for determination of UCS and dry density, (a) Relation between UCS and Schmidt rebound [19], (b) Relation between Vp and dry density [20]

4.2. UPV test results

In this section, the elastic material properties of the historical Malatya Taşhoran Church were obtained using the UPV test. In the test, a James Instruments V-Meter MK IV™ Ultrasonic Pulse Velocity device was used (Fig. 5b). In the on-site UPV test, the indirect method was employed. The average velocities for s-waves and p-waves that were measured are provided in Table 1. Furthermore, the measurement locations are given in Fig. 6. According to the visual inspection, restoration stones (RS) were seen at location 4, while original stones (OS) were observed at the other locations. Hence, s and p velocities for the location 4 was lower than s and p velocities of the other locations.

Based on the in-situ ultrasonic pulse velocity findings, it can be inferred that locations 1, 2, 3, 5, and 6 are composed of a same stone type. The average p-wave velocity (v_p) for these locations is 3342 m/s, while the mean p-wave velocity for location 4 was recorded at 2340 m/s. Additionally, the average s-wave velocity (v_s) for locations 1, 2, 3, 5, and 6 is 1856 m/s, whereas the mean s-wave velocity for location 4 was found to be 1483 m/s. For the calculation of the E_{dyn} (dynamic elasticity modulus) and μ_{dyn} (Poisson ratio), the suggestion of ASTM D2845-08 was considered. According to ASTM D2845-08 μ_{dyn} and E_{dyn} can be determined with Eq. 1 and Eq. 2, respectively.

$$\mu_{dyn} = \left(v_p^2 - 2v_s^2\right) \Big/ \left[2\left(v_p^2 - v_s^2\right)\right] \tag{1}$$

where, $\boldsymbol{v_s}$: s velocity (m/s), $\boldsymbol{v_p}$: p velocity (m/s) and $\boldsymbol{\mu}$: dynamic Poisson ratio. The dynamic Poisson ratio of OS and RS were calculated as 0.27 and 0.14, respectively.

$$E_{dyn} = \frac{\left[\rho v_s^2\left(3v_p^2 - 4v_s^2\right)\right]}{\left(v_p^2 - v_s^2\right)} \tag{2}$$

where, E = Young's modulus of elasticity (Pa) and ρ = density (kg/m^3).

The dynamic elasticity modulus of original stones (OS) and restoration stones (RS) was computed as 23930 MPa and 9059 MPa, respectively. Also, Poisson ratios of original stones and restoration stones were calculated as 0.27 and 0.14, respectively. The summaries of the results of all the NDT tests are shown in Table 2.

Table 2. Summery of NDT test results

	NDT		Difference (%)
	OS	***RS***	
Vp (m/s)	3342	2340	30.0
Vs (m/s)	1856	1483	20.1
R	42	28	33.3
UCS (MPa)	57.83	23.13	60.0
v	0.27	0.14	48.1
E (MPa)	23930	9059	62.1
Dry density (g/cm^3)	2.72	2.6	4.4

4.3. Infrared Thermography test

Infrared thermography test (IRT) is a widely recognized non-destructive assessment method capable of detecting flaws on structural surfaces [13]. The buildup of heat signifies detachment in the areas of the cracks at this specific location. For this study, a TESTO 868 thermal camera was preferred for evaluation purposes. The thermographic images have dimensions of 320 pixels horizontally and 240 pixels vertically. The noise equivalent temperature difference of this camera is less than 80 mK, and the utilized optical lens possesses a focal length of 50 mm. Figure 8a and 8b were captured from a distance of 2 meters away from the wall, while Figure 8c was captured at a distance of 0.7 meters from the wall. The measurement distance remained consistent between different locations, and the angle between the camera and the wall was always maintained at 90 degrees.

Some deformations were noticed on the surfaces of the walls of the historical Malatya Taşhoran Church. The thermal images of these walls captured through IRT are depicted in Fig. 8. When comparing the visual observations with the

IRT images, Fig. 8a and 8b reveal both deformed stones and stones in proper condition. Additionally, Fig. 8c shows thin and sizable cracks in various colors.

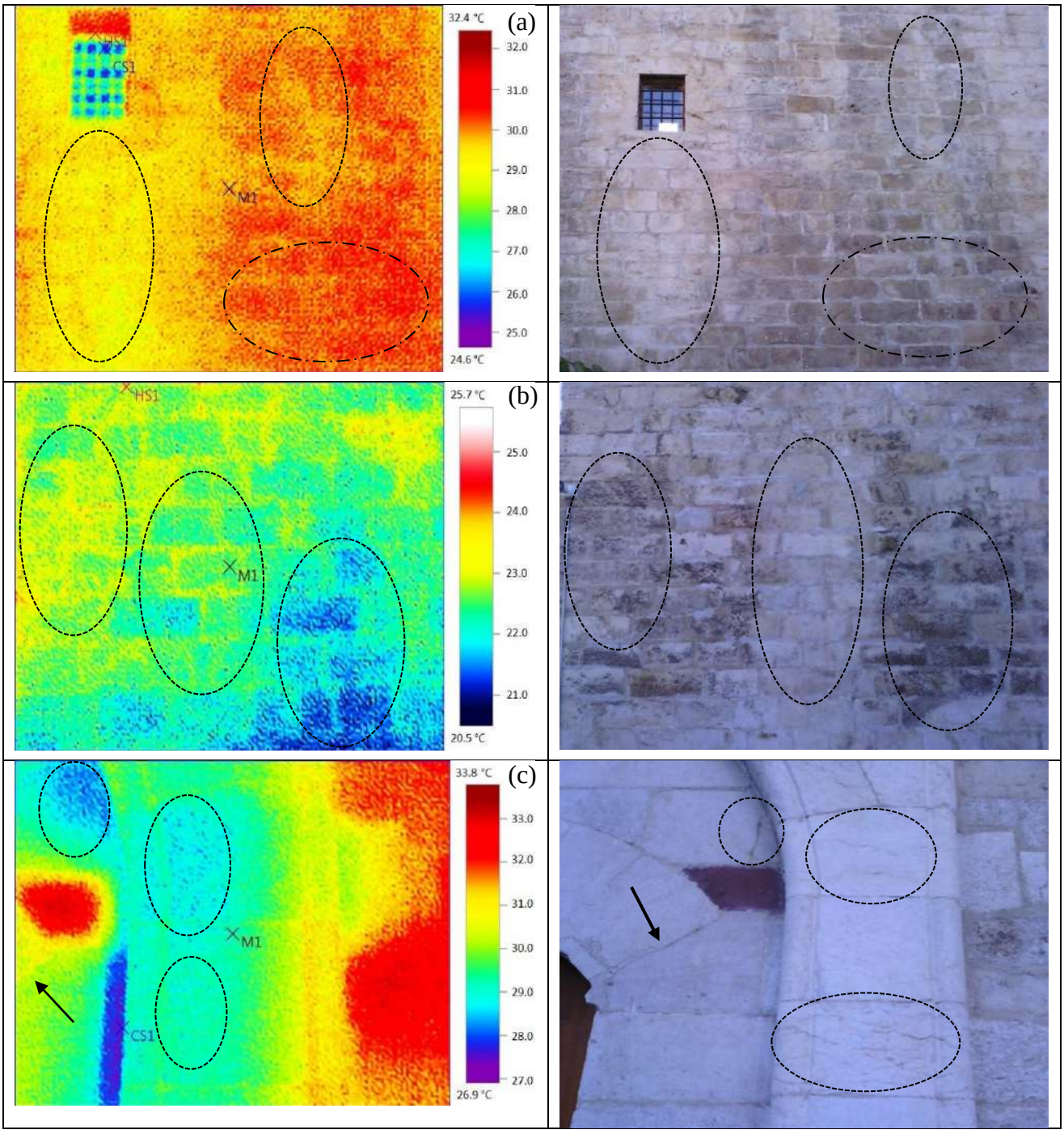

Figure 8. IRT output of the Malatya Taşhoran Church

5. Conclusion

Historical masonry reflects how past civilizations used to live. For this reason, it is important that these structures survive and that they are passed on to future generations. In order to understand the structural behavior of masonry structures, the material characteristics of historical structures should be well known. In the present paper, the elastic material properties (Compressive strength, Poisson ratio, young modulus and density) of the historical Malatya Taşhoran Church were investigated with Non-Destructive techniques (NDT).

Schmidt hammer results and UPV results indicate that RS stones was used only one location of the historical Malatya Taşhoran Church. Compressive strength, dynamic elasticity modulus, Poisson ratio and dry density values of OS and RS were calculated using with Schmidt hammer and UPV results. All elastic material properties of the OS were higher than those of the RS. The difference between the compressive strength of OS and RS was calculated as 60%.

Additionally, difference between the young modulus of OS and RS was calculated as 62.1%. According to the obtained results, the original and the restoration stones have different material properties. In the restoration and conservation works, it is very important to using similar materials. Otherwise, the behavior of the structure will be affected.

6. References

[1] Lombillo I, Villegas L, Elices, J. "Minor destructive techniques applied to the mechanical characterization of historical rubble stone masonry structures". Structural Survey, 28, 53-70, 2010.

[2] Aksoy H.S, Karaton M. "Tarihi Yığma Yapıların Malzeme Karakteristiklerinin Hasarsız Yöntemlerle Belirlenmesi: Diyarbakır Ulu Camii Örneği". Bitlis Eren Üniversitesi Fen Bilimleri Dergisi, 2019.

[3] Grinzato E, Bison P. G, Marinetti S. "Monitoring of ancient buildings by the thermal method". Journal of Cultural Heritage, 3, 21-29, 2002.

[4] Fort R, de Buergo M A, Perez-Monserrat E. M. "Non-destructive testing for the assessment of granite decay in heritage structures compared to quarry stone". International Journal of Rock Mechanics and Mining Sciences, 61, 296-305, 2013.

[5] Pirchio D, Walsh K. Q, Kerr E, Giongo I, Giaretton M, Weldon B. D, Sorrentino L. "An aggregated non-destructive testing (NDT) framework for the assessment of mechanical properties of unreinforced masonry Italian medieval churches". Construction and Building Materials, 342, 128041, 2022.

[6] Malatya Metropolitan Municipality. Malatya Culture Inventory, 2021.

[7] ASTM C805/C805M-13a. Standard test method for rebound number of hardened concrete, 2013.

[8] EN 12504-2:2012. Testing Concrete In Structures—Part 2: Non-destructive Testing—Determination of Rebound Number, 2012.

[9] McCann D. M, Forde M. C. "Review of NDT methods in the assessment of concrete and masonry structures". NDT & E International, 34, 71-84, 2001.

[10] Martini R, Carvalho J, Barraca N, Arêde A, Varum H. "Advances on the use of non-destructive techniques for mechanical characterization of stone masonry: GPR and sonic tests". Procedia Structural Integrity, 5, 1108-1115, 2017.

[11] A C597-97. Standard Test Method for Pulse Velocity Through Concrete, 1997.

[12] EN 12504-4. Concrete Tests—Part 4: Determination of Ultrasonic Pulsed Wave Velocity, 2012.

[13] Moropoulou A, Labropoulos K. C, Delegou E. T, Karoglou M, Bakolas A. "Non-destructive techniques as a tool for the protection of built cultural heritage". Construction and Building Materials, 48, 1222-1239, 2013.

[14] Maldague X. Theory and practice of infrared technology for nondestructive testing, 2001.

[15] Avdelidis N. P, Moropoulou, A. "Applications of infrared thermography for the investigation of historic structures". Journal of Cultural Heritage, 5, 119-127, 2004.

[16] Bisegna F, Ambrosini D, Paoletti D, Sfarra S, Gugliermetti F. "A qualitative method for combining thermal imprints to emerging weak points of ancient wall structures by passive infrared thermography–A case study". Journal of Cultural Heritage, 15, 199-202, 2014.

[17] Karaton M, Aksoy H. S, Sayın E, Calayır Y. "Nonlinear seismic performance of a 12th century historical masonry bridge under different earthquake levels". Engineering Failure Analysis, 79, 408-421, 2017.

[18] Brencich A, Sabia D. "Experimental identification of a multi-span masonry bridge: The Tanaro Bridge". Construction and Building Materials, 22, 2087-2099, 2008.

[19] Buyuksagis I. S, Goktan R. M. "The effect of Schmidt hammer type on uniaxial compressive strength prediction of rock". International Journal of Rock Mechanics and Mining Sciences, 44, 299-307, 2007.

[20] Chawre B. "Correlations between ultrasonic pulse wave velocities and rock properties of quartz-mica schist". Journal of Rock Mechanics and Geotechnical Engineering, 10, 594-602, 2018.

International Conference on Advances and Innovations in Engineering

Mitigating the out-of-plane seismic vulnerability of unreinforced masonry façades with viscoelastic devices

Elesban NOCHEBUENA-MORA[1] , Nuno MENDES [2]

[1,2] University of Minho, ISISE, ARISE, Department of Civil Engineering, Guimarães, Portugal.
[1]enochemora@gmail.com [2]nunomendes@civil.uminho.pt

[1](ORCID: 0000-0002-6661-0122), [2](0000-0002-1796-686X)

Abstract

Surveys conducted after earthquakes have revealed that the most common and hazardous collapse mechanism observed in unreinforced masonry façades is the out-of-plane overturning. Traditional techniques such as tie rods, ring beams, and rigid slab-to-wall connections have been employed to enhance the seismic performance of unreinforced masonry (URM) buildings. However, there are alternative strengthening systems that may improve the performance compared to these conventional techniques. While passive energy dissipation (PED) devices are utilized in framed structures to mitigate dynamic response, their application to URM buildings remains limited. In this study, the effectiveness of three different strengthening techniques, namely rigid slab-to-wall connections, steel tie rods, and viscoelastic devices was investigated. A FEM model of a partial façade with a transversal wall was created to simulate the out-of-plane behaviour. Nonlinear dynamic analyses were conducted using recorded earthquakes as input. The performance of each technique was evaluated by comparing various parameters, namely displacements, base shear forces, plastic energy, and damage distribution. The results revealed that viscoelastic devices exhibited better performance in reducing displacements and mitigating the vulnerability of façade overturning.

Keywords: energy dissipation, viscoelastic device, unreinforced masonry, out-of-plane collapse

1. Introduction

Masonry has been a prevalent construction material used for centuries in various types of structures. Unreinforced masonry (URM) buildings, including historical structures, are vulnerable to seismic loads due to the limited shear and tensile strength of the material. The damage of masonry walls during earthquakes can be classified into two types: in-plane (IP) failure and out-of-plane (OOP) failure. Among these, OOP failure is a frequent damage that involves flexural cracks that may eventually lead to partial or total wall collapse [1]. This failure mode has a brittle nature and requires less energy for its initiation, thereby OOP mechanisms can be triggered even by small or moderate ground motions [2], [3]. Thus, the OOP overturning of façades or segments thereof represent a substantial risk for human life during an earthquake. The occurrence of this failure is more likely in buildings where the connection between perpendicular walls or floor-to-walls, or other construction techniques capable of inducing the box-type behaviour are inadequate or absent.

Different strengthening techniques have been developed to improve the dynamic behaviour of URM buildings. Some of these techniques have local effects such as injections of grouts in the walls or application of external layers of mortar or concrete reinforced with steel meshes or fibre materials (FRP and TRM). Other techniques act on a global level to enhance the box-type behaviour, for example, the construction of ring beams on top of the walls, stiffening floors and roofs, implementing a rigid connection between floors/roofs and walls, or introducing steel tie rods [4]. However, these strengthening techniques are not always capable of achieving the safety requirements prescribed in the current codes. In some cases, the retrofitting operation demands a large and expensive intervention to satisfy these requirements. Therefore, in the last decades, engineers and scholars have been studying alternatives aiming at reducing the seismic demand and energy dissipation. Base isolation was the first of these techniques being applied to the City Hall of Salt Lake City (USA) in the decade of 1980 [5]. Thereafter, base isolation has been implemented

[1]Corresponding author

in other buildings, particularly in USA and Italy, to reduce the seismic demand [6–9]. Although effective, such technique is only applied to important monuments because of its high cost.

While the reduction of seismic demand is attained by base isolating the building, dampers are capable of passively suppressing vibrations by dissipating energy. The dissipation is given by the yielding of metals, friction, deformation of shape memory alloys (SMA), resistance of a solid body moving in viscous fluids (VF), or shear deformation of viscoelastic (VE) materials. Dampers or passive energy dissipation (PED) devices are mainly used in frame structures. However, researchers have tested and applied some devices especially developed for URM buildings, mainly to control the OOP motion of walls and parapets. Some remarkable examples are the use of SMA in churches [10], the friction and yielding devices tested by [11], and the LICORD device, which is a combination of springs and VF devices [12]. For more details about the implementation of PED and base isolation on existing URM buildings, the reader is referred to [13]. Extensive literature exists concerning the characterizing VE devices and their application in framed structures. Nevertheless, there is currently a lack of research focused on implementing these devices in existing URM buildings. The present work focuses on the application of VE devices to reduce the OOP displacements of façades. For this purpose, FEM models were created in Abaqus/Explicit [14] and several nonlinear dynamic analyses were conducted. The VE device was implemented, and the results were compared with other strengthening techniques, namely steel tie rods and floor-to-wall rigid connections.

2. Case Study

A large stoke of historical URM constructions in Mexico is vulnerable to earthquakes due to their location in seismic-prone areas. The remaining Mexican viceregal dwellings were built in the 17th and 18th centuries during the Spanish colony. Figure 1 shows a characteristic viceregal dwelling. For this work, a section of a viceregal dwelling was selected for conducting nonlinear dynamic analyses. The architectural layout of these buildings typically features rooms surrounding one or two courtyards. The structure is normally composed of two floors with interstory heights varying between 4.95 and 5.10 m. The façade thickness is approximately 0.90 m, while the inner walls measure 0.80 m on the ground level and 0.60 m on the upper floor. The windows and doors on the upper floor are often aligned with those on the ground level, contributing to a uniform distribution across the façades [15], [16].

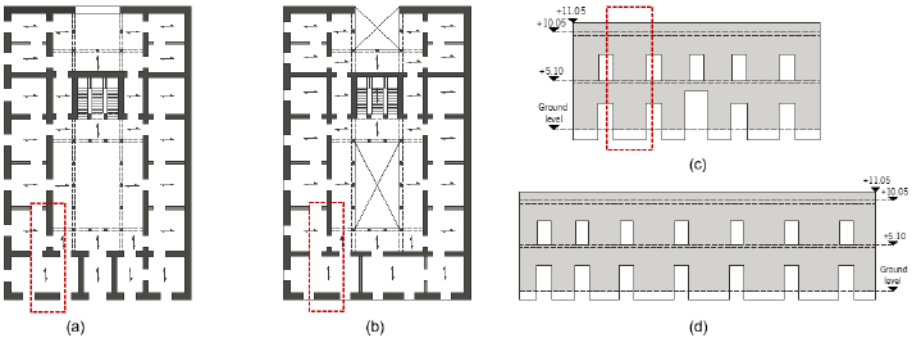

Figure 1. Typical viceregal building in Mexico: (a) ground floor (b) upper floor, (c) main façade, and (d) lateral façade.

Foundations and walls are frequently built with irregular stone units using lime mortar for joints. Columns, archers, and opening frames are made of dressed stones. The floor and roof slabs are flexible diaphragms consisting of a large set of beams (cross-section of 0.15 x 0.20 m) placed perpendicular to the façade and spacing 0.30 m. The beams are simply supported in pockets or recesses in the walls, relying only on friction to avoid sliding. Finally, a layer of bricks, compacted earth, and pavement is placed on top of the beams [17].

3. Numerical Model

3.1. Mesh

The numerical model, shown in Figure 2, was developed based on the highlighted section depicted in Figure 1. To represent the walls, 3D-solid hexahedral elements with reduced integration were chosen. This element type effectively addresses the shear locking effect characteristic in fully integrated linear elements for bending problems.

Additionally, reduced integration elements contribute to decreasing the computational demands. For enhanced accuracy in capturing the flexural behaviour, the façade thickness was divided into five elements [18]. The stiffness control (scaling factor of 0.03) implemented in Abaqus is applied to mitigate the onset and propagation of the hourglass effect, which is inherent in linear elements with reduced integration. The beams were modelled using linear beam elements, with additional mass incorporated to account for the dead and live loads of the floors. Wall-to-beam connections were simulated using translator-type connectors with nonlinear properties. The connection properties were set to have a high stiffness under compression and low stiffness for tension to represent the sliding of the beams from the pockets. Truss and shell elements were used for the steel tie rods and plates, respectively. VE devices were simulated by axial-type connectors featuring linear stiffness and linear damping coefficient.

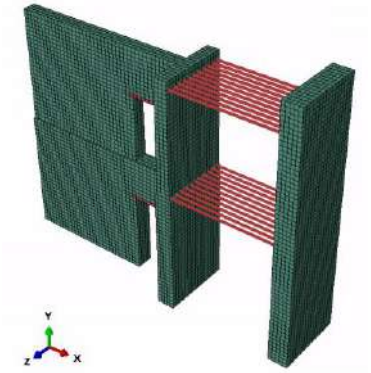

Figure 2. Numerical model of a section of the viceregal building

3.2. Mechanical properties and constitutive law

The values for Young's modulus, density, and compression strength for masonry were taken from a set of experimental tests conducted by Chávez et al. [19]. The tensile strength was estimated as 10% of compressive strength. These data were used to calculate the stress-strain curves for compression and tension. Steel and timber were assumed to be linear elastic throughout the analysis. The mechanical properties of the materials are in Table 1.

Table 5. Mechanical properties of the materials

Material	Density (kg/m^3)	Young's modulus (N/m^2)	Poisson's ratio	Compressive strength (N/m^2)	Tensile strength (N/m^2)	Tensile fracture energy (N/m)
Masonry	1794	1.43e+09	0.2	1.90e+06	1.90e+05	50
Timber	610	8.80e+09	0.3			
Steel	8000	2.10e+11	0.3			

The concrete damage plasticity (CDP) model can capture the nonlinear behaviour of quasi-brittle materials such as concrete and masonry [18], [20]. This model has been extensively employed by researchers for conducting nonlinear dynamic analyses of historical buildings [21–23]. The material behaviour in this model is governed by four parameters: damage evolution, hardening/softening law, yield criterion, and flow rule.

Tensile cracking and compressive crushing are described by the damage evolution parameter $\boldsymbol{d}$, estimated using the approximation $\boldsymbol{d = 1 - \sigma/\sigma_{max}}$, where $\boldsymbol{\sigma}$ is the compressive or tensile stress in the softening branch of the stress-strain curves. The parameter $\boldsymbol{d}$ accounts for the stiffness degradation after passing the post peak during the loading-unloading cycle. This degradation can be expressed in a simplified manner as $\boldsymbol{\sigma = (1 - d)E_0(\varepsilon - \varepsilon^{pl})}$, where $\boldsymbol{E_0}$ is the initial Young's modulus, $\boldsymbol{\varepsilon}$ is the total strain, and $\boldsymbol{\varepsilon^{pl}}$ is the plastic strain. The hardening/softening law is determined by the uniaxial compressive and tensile stress-strain curves [18].

The yield criterion requires two values provided by the ratio between the initial biaxial and initial uniaxial compressive stresses $\boldsymbol{\sigma_{b0}/\sigma_{c0}}$, and the parameter $\boldsymbol{K}$, which defines the yield surface's cross-section [24], [25]. The

flow rule is governed by the dilation angle $\boldsymbol{\psi}$ and the eccentricity $\boldsymbol{e}$. The values for these parameters presented in Table 2 have demonstrated a satisfactory performance for masonry [26], [27].

Table 2. Values for the yield surface and flow rule

Dilation angle ψ	Eccentricity e	σ_{b0}/σ_{c0}	K
10°	0.1	1.16	2/3

4. Mechanical properties of VE materials

VE materials feature an elastic component, characterized by the shear storage modulus $\boldsymbol{G'}$, and a viscous component, described by the shear loss modulus $\boldsymbol{G''}$. The elastic energy, which is the capacity of the material to recover its original shape after loading removal, is described by $\boldsymbol{G'}$, while $\boldsymbol{G''}$ is related to the energy dissipation. Both moduli are related through the loss factor $\boldsymbol{\eta}$, calculated as $\boldsymbol{\eta = G''/G'}$. These mechanical properties are sensitive to strain, load frequency, and temperature variations [28]. Some VE materials exhibit a linear behaviour for shear strain up to 150% [29].

VE dampers typically consist of multiple layers of a VE material bonded to steel plates. The energy dissipation occurs when the layers undergo cyclic shear deformations imposed by the relative displacement between plates. VE dampers can be designed to present linear behaviour by setting the thickness of the layers and defining a maximum admissible relative displacement, known as an operating strain. In the linear regime, the relationship between equivalent stiffness $\boldsymbol{k}$ and equivalent damping $\boldsymbol{c}$ and their corresponding moduli $\boldsymbol{G'}$and $\boldsymbol{G''}$ is expressed by:

$$\boldsymbol{k = \frac{nG'A}{t}}, \quad \boldsymbol{c = \frac{nG''A}{\omega t}} \tag{1}$$

where $\boldsymbol{t}$ is the thickness of the layer, $\boldsymbol{n}$ is the number of layers, $\boldsymbol{A}$ is the shearing area of one layer, and $\boldsymbol{\omega}$ is the loading frequency in rad/s. Aiken and Kelly [29] proposed a straightforward procedure to quantify the volume of VE material to attain a desired damping level. The thickness is then defined based on the operating strain. Subsequently, the area of the layers is determined according to the number of layers and devices. For numerical analysis, $\boldsymbol{k}$ and $\boldsymbol{c}$ are calculated using Eq. 1. This calculation involves using values for $\boldsymbol{G'}$and $\boldsymbol{G''}$ from manufactures or databases at an expected operating frequency and temperature. For this work, EAR-C-2003 material was selected for dampers, considering an ambient temperature of 20° C. Operating frequencies were determined through eigenvalue analyses of the model, using the frequency of the first OOP mode of the façade.

5. Seismic actions

For the nonlinear dynamic analysis, three records were employed to take into account seismic actions with different characteristics [30]. The seismic events included the Emilia Romagna (25th May 2012 in Italy), characterized by an impulsive action; Mexico "Chiapas" earthquake (8th September 2017), which shows a regular shaking pattern; and Northridge earthquake (17th January 1994, USA), classified as a vibratory motion. It's worth noting that explicit solvers tend to perform better when dynamic loads are applied as velocities. As displayed in Figure 3, the seismic loads for the three chosen earthquakes are illustrated in terms of velocities. For all analyses, excitations were exclusively applied in the X direction to trigger the OOP mechanism of the façade.

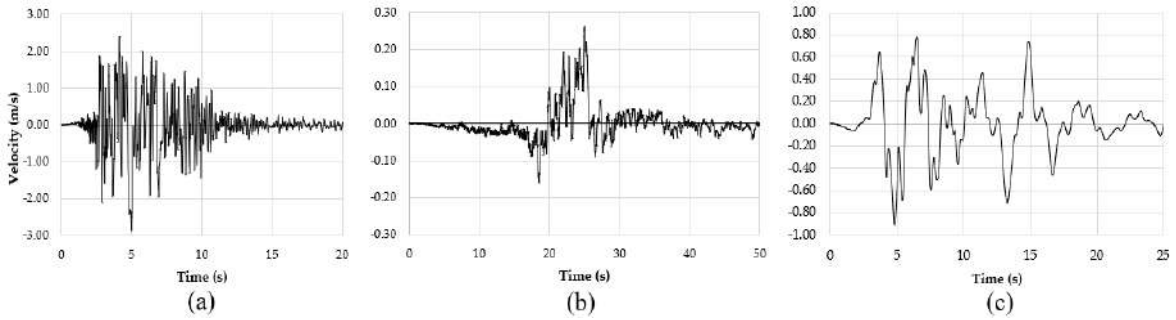

Figure 3. Earthquake record in terms of velocity of (a) Emilia Romagna (b) Mexico "Chiapas", and (c) Northridge.

6. Results

It is important to note that when employing hourglass suppression techniques, close attention should be paid to the artificial energy (AE) increment to ensure the validity of the results. In this study, a maximum increment of 10% was chosen as the threshold. Any results obtained beyond this limit are considered unreliable. A control point at the top of the façade was used to track the relative displacement and evaluate the OOP behaviour.

6.1. Unreinforced model

In the first set of analyses, the unreinforced model was subjected to the three earthquakes applying 100% amplitude. The results, shown in Figure 4 in terms of displacements and damage pattern, correspond to the specific time when the AE reached the 10% threshold. Severe damage appeared when the OOP displacement of the façade approximated to 0.10 m. Particularly, the façade exhibited a brittle failure during the Northridge earthquake. In general, the damage pattern in the three cases is similar. Longitudinal cracks developed along the base and at floor levels of the façade, while a diagonal-like crack running through the corners of the doors also appeared, splitting the perpendicular wall into two bodies.

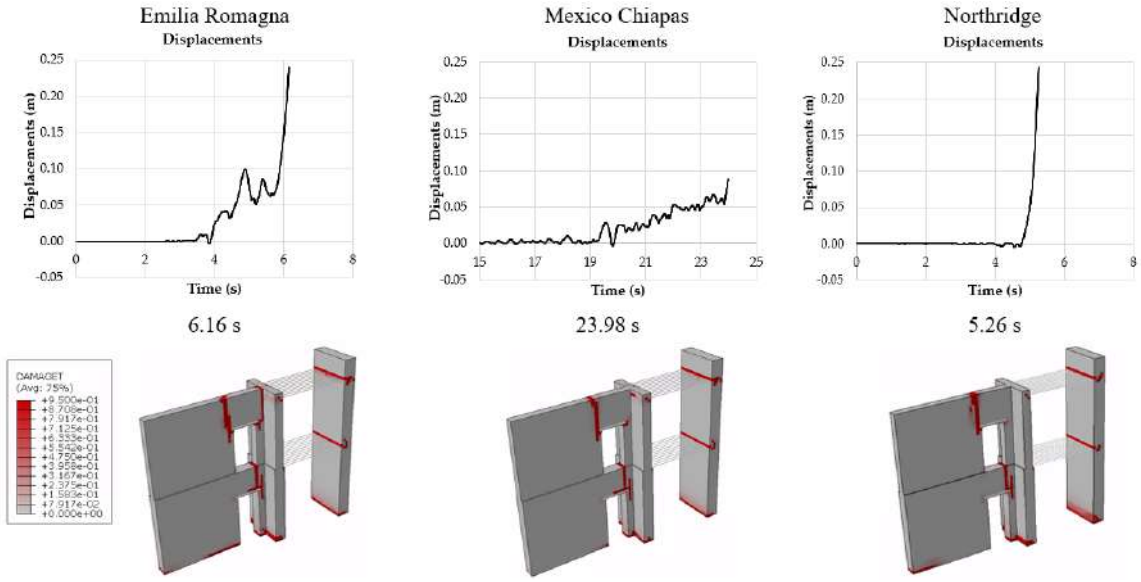

Figure 4. Results in terms of displacements and crack pattern of the unreinforced model

6.2. Reinforced models

Three reinforcement techniques were implemented in the model, mainly, rigid connections between the beams and the walls, steel tie rods, and the incorporation of VE dampers to the tie rods, as shown in Figure 5. Regarding the properties of the dampers, the equivalent stiffness ***k*** was set to 6.88e+06 N/m and the equivalent damping coefficient ***c*** was calculated as 3.10e+05 Ns/m. The models were subjected to the three seismic actions, each with an amplitude of 100%. The results are presented in terms of energy dissipated due to hysteresis (plastic and damage energies), time-history of displacements, base shear forces, and damage pattern.

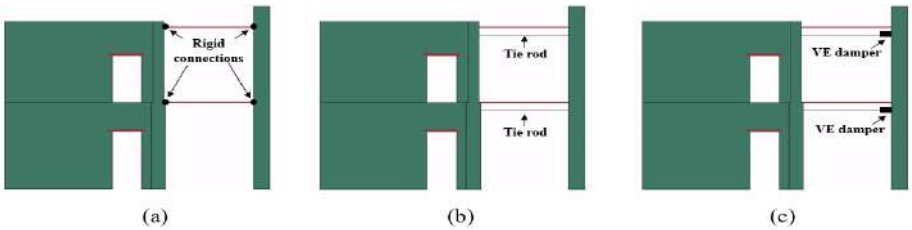

Figure 5. Reinforcement techniques: (a) rigid connections, (b) steel tie rods, and (c)VE dampers

Figure 6 depicts the results from the Emilia Romagna earthquake comparing two instants of the analyses. These times correspond to the point where the AE reached the 10% limit for both the model with rigid connections (at 4.74 s) and the model with tie rods (at 5.44 s). In the case of rigid connections, their efficacy in preventing the out-of-plane (OOP) collapse of the façade was limited, resulting in a failure mode similar to the unreinforced model. Although the tie rods prevent the OOP motion of the façade, they transmit significant inertial forces that led to severe damage in the perpendicular wall. The application of VE dampers seemed to yield a more favourable response. This technique controlled the displacements, induced lesser damage to the perpendicular wall, and reduced the base shear forces, particularly during the early stages of the earthquake.

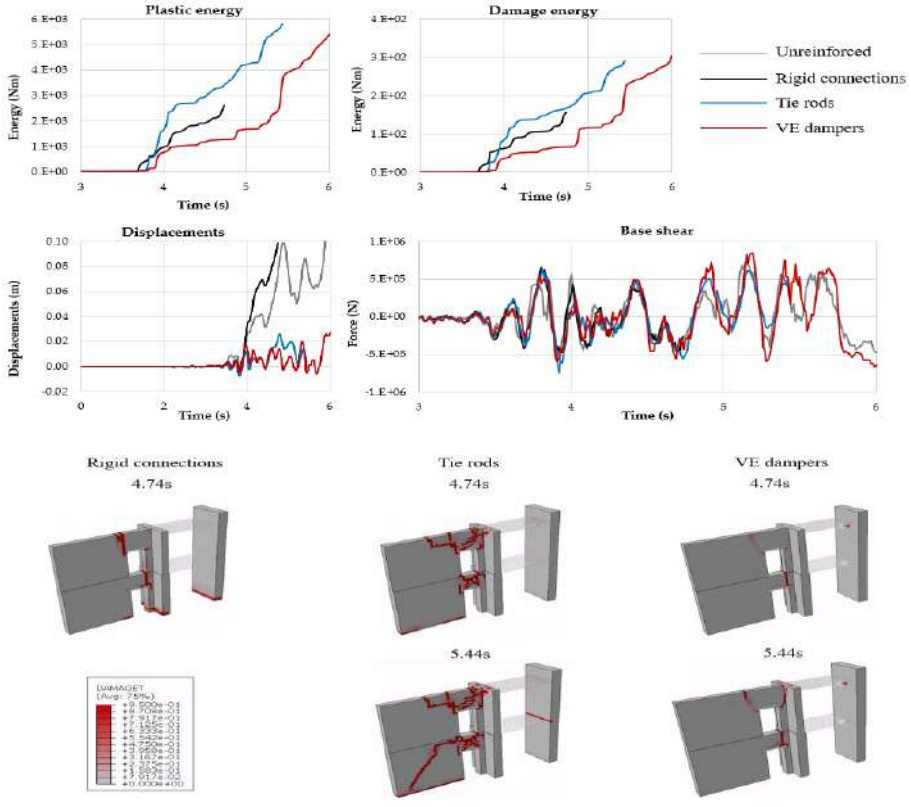

Figure 6. Results from the Emilia Romagna earthquake for the three reinforcement techniques (More)

The results from the Mexico "Chiapas" earthquake are depicted in Figure 7. The behaviour exhibited by the three reinforcement techniques is similar to the previous results. Rigid connections proved to be ineffective in preventing the OOP motion of the façade. In this scenario, a vertical craked developed along the height of the transition zone between walls. Conversely, the tie rods effectively constrained the displacements, but yielding to severe damage to the transversal wall. On the other hand, VE dampers were capable of controlling the OOP motion of the façade, demonstrating a substancial drop of 50% in comparison to the tie rods. The application of VE dampers led to a decrement in the energy dissipated by material hysteresis (plastic and damage energy). Additionally, the base shear forces were reduced, particularly at the beginning of the earthquake.

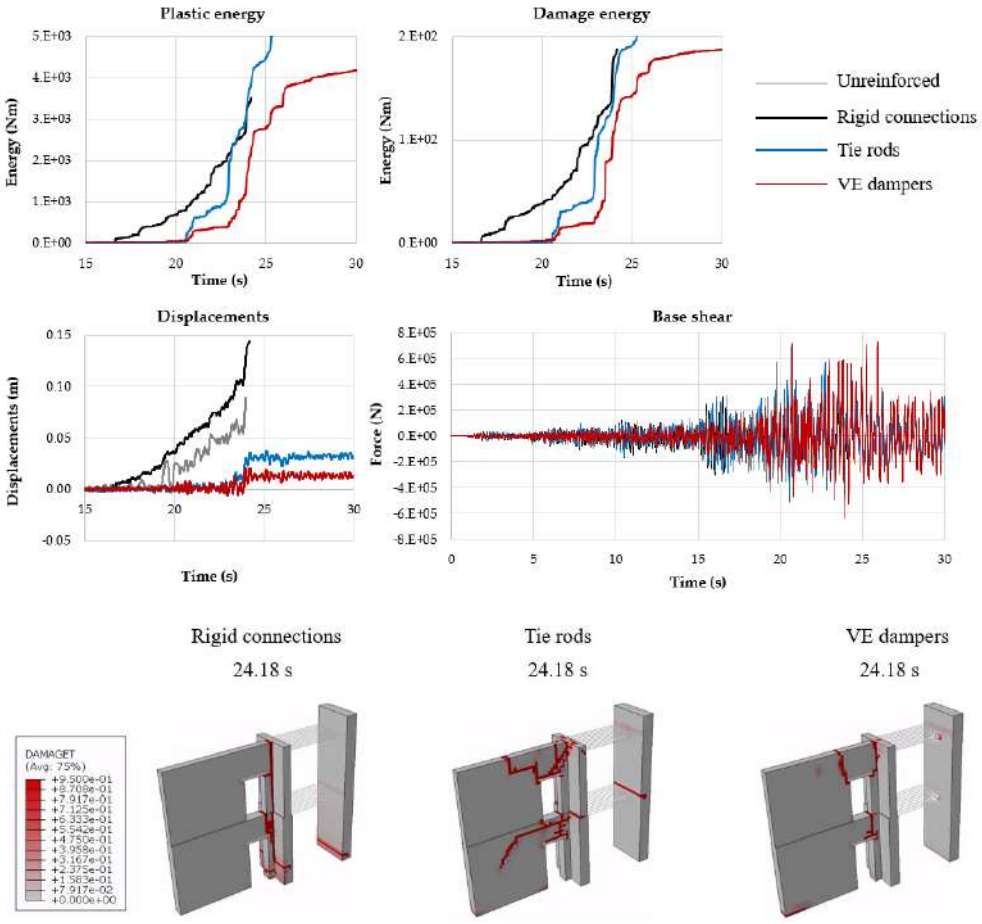

Figure 7. Results from the Mexico "Chiapas" earthquake for the three reinforcement techniques

Figure 8 shows the outcomes from the Northridge earthquake in the first seconds of the ground motion. The images correspond to the instant when the AE reached the threshold of 10% in the model with rigid connections (at 4.90 s) and the model with tie rods (at 5.83 s). As observed in the two previous sets of analyses, rigidly connecting the beams to the wall is insufficient to prevent the collapse of the façade. This resulted in no improvement in the global behaviour of the structure, with severe local damage developing in the connection areas, which produced early numerical problems. Both tie rods and VE dampers were incapable of preventing the failure of the façade during the Northridge earthquake. However, VE dampers delayed the collapse of the building, which can be a key factor for the life safety of the occupants. It is worth noting that for the three seismic actions, local damage appeared in the zone surrounding the dampers.

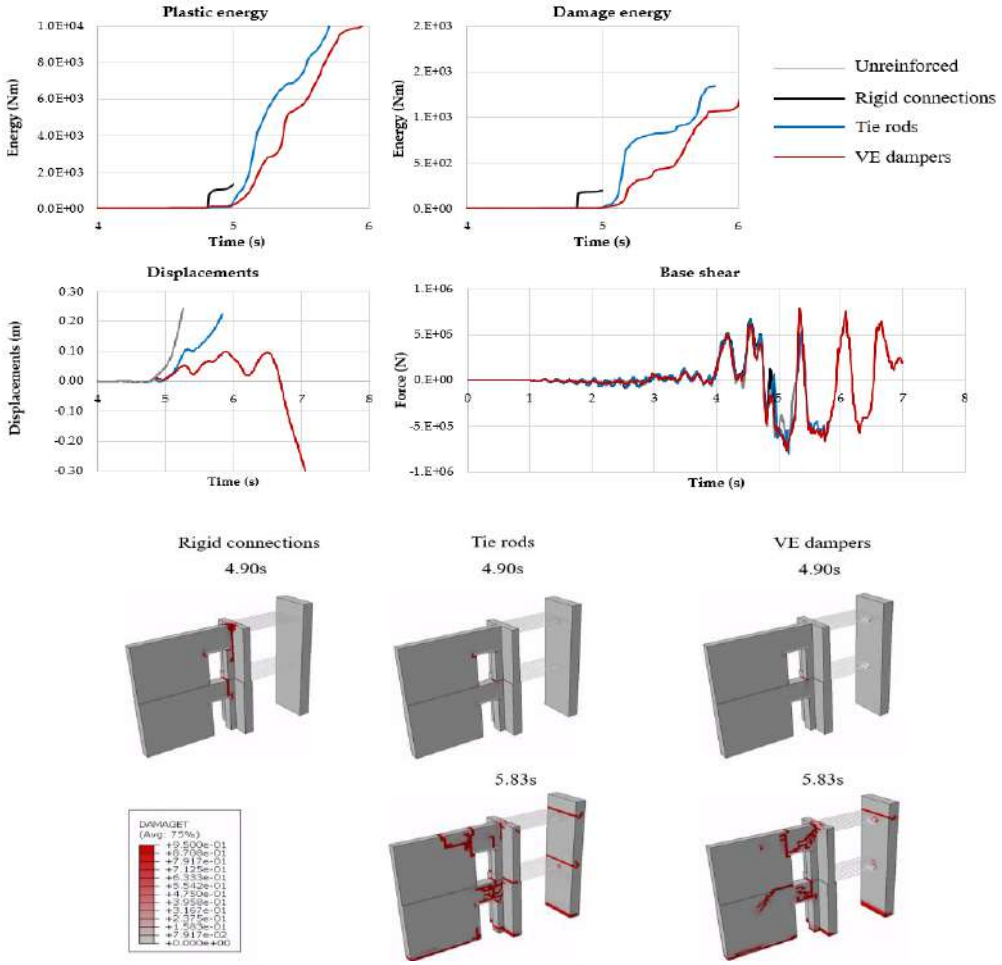

Figure 8. Results from the Northridge earthquake for the three reinforcement techniques.

7. Conclusions

The application of passive energy dissipation (PED) devices, also known as dampers, to existing unreinforced masonry (URM) buildings remains ongoing research. The high nonlinearity of masonry and its low ductility represent a challenge to the implementation of dampers. While a few PED devices specifically designed for URM constructions have been developed in recent years, there is a lack of detailed literature available regarding their performance. Common types of passive devices used in seismic applications include viscous fluid dampers, friction dampers, and metallic dampers. However, further research and evaluation are needed to fully understand the effectiveness and limitations of these devices in strengthening URM buildings. This study aimed to evaluate the impact of VE dampers on the global response of a simplified model through nonlinear dynamic analyses. The effectiveness of VE dampers was compared to two other reinforcement techniques: beam-to-wall rigid connections and the implementation of steel tie rods. The numerical results indicate that VE dampers are a promising reinforcement technique for controlling the out-of-plane motion of façades and enhancing the overall response of structures. The devices can dissipate kinetic energy without causing extensive damage to the supporting elements, such as transversal walls. In certain cases, the implementation of VE dampers can even delay the collapse of the structure, providing additional time for the safe evacuation of the building. Local damage reduction is a critical issue that needs to be addressed when implementing PED devices. This can be achieved by decreasing the forces transmitted between the structural elements or by applying local reinforcement. An optimization process is required to further mitigate the seismic vulnerability of structures. The optimization process should consider different properties, ambient temperature, and the location and number of VE devices. Future parametric analyses must be conducted on larger models to better understand the performance of VE devices in reducing overall damage and damage to individual stories and structural elements.

8. Acknowledgements

This work was funded by FCT – Foundation for Science and Technology within the scope of project EXPL/ECI-EGC/0940/2021. The first author is grateful for the funding from the Mexican National Council for Science and Technology (Consejo Nacional de Ciencia y Tecnología CONACYT), grant number 2018-000013-01EXTF-00137.

9. References

[1] De Felice, G., De Santis, S., Lourenço, P. B., and Mendes, N. "Methods and Challenges for the Seismic Assessment of Historic Masonry Structures." *International Journal of Architectural Heritage*, 2016, pp. 1–18. https://doi.org/10.1080/15583058.2016.1238976.

[2] Ferreira, T. M., Costa, A. A., Vicente, R., and Varum, H. "A Simplified Four-Branch Model for the Analytical Study of the out-of-Plane Performance of Regular Stone URM Walls." *Engineering Structures*, Vol. 83, 2015, pp. 140–153. https://doi.org/10.1016/j.engstruct.2014.10.048.

[3] Griffith, M. C., Magenes, G., Melis, G., and Picchi, L. "Evaluation of Out-of-Plane Stability of Unreinforced Masonry Walls Subjected to Seismic Excitation." *Journal of Earthquake Engineering*, Vol. 7, No. sup001, 2003, pp. 141–169. https://doi.org/10.1080/13632460309350476.

[4] Gkournelos, P. D., Triantafillou, T. C., and Bournas, D. A. "Seismic Upgrading of Existing Masonry Structures: A State-of-the-Art Review." *Soil Dynamics and Earthquake Engineering*, Vol. 161, 2022, p. 107428. https://doi.org/10.1016/j.soildyn.2022.107428.

[5] Bailey, J., and Allen, E. "Seismic Isolation Retrofitting of the Salt Lake City and County Building." *Nuclear Engineering and Design*, Vol. 127, No. 3, 1991, pp. 367–374. https://doi.org/10.1016/0029-5493(91)90060-U.

[6] Poole, R. A., and Clendon, J. E. "N. Z. Parliament Buildings Seismic Protection by Base Isolation." *Bulletin of the New Zealand Society for Earthquake Engineering*, Vol. 25, No. 3, 1992, pp. 147–160. https://doi.org/10.5459/bnzsee.25.3.147-160.

[7] Mokha, A. S., Amin, N., Constantinou, M. C., and Zayas, V. "Seismic Isolation Retrofit of Large Historic Building." *Journal of Structural Engineering*, Vol. 122, No. 3, 1996, pp. 298–308. https://doi.org/10.1061/(ASCE)0733-9445(1996)122:3(298).

[8] Vetturini, R., Cecchini, W., and Mariani, R. "Intervento di isolamento sismico alla base di un edificio in muratura di pregio storico-artistico in L'Aquila - Seismic base-isolation of a historical masonry building in L'Aquila." *Progettazione Sismica*, No. 1, 2013, pp. 95–118. https://doi.org/10.7414/PS.4.1.95-118.

[9] Clemente, P., and Martelli, A. "Seismically Isolated Buildings in Italy: State-of-the-Art Review and Applications." *Soil Dynamics and Earthquake Engineering*, Vol. 119, 2019, pp. 471–487. https://doi.org/10.1016/j.soildyn.2017.12.029.

[10] Indirli, M., and Castellano, M. G. "Shape Memory Alloy Devices for the Structural Improvement of Masonry Heritage Structures." *International Journal of Architectural Heritage*, Vol. 2, No. 2, 2008, pp. 93–119. https://doi.org/10.1080/15583050701636258.

[11] D'Ayala, D. F., and Paganoni, S. "Testing and Design Protocol of Dissipative Devices for Out-of-Plane Damage." *Proceedings of the Institution of Civil Engineers - Structures and Buildings*, Vol. 167, No. 1, 2014, pp. 26–40. https://doi.org/10.1680/stbu.12.00087.

[12] Giresini, L., Solarino, F., Taddei, F., and Mueller, G. "Experimental Estimation of Energy Dissipation in Rocking Masonry Walls Restrained by an Innovative Seismic Dissipator (LICORD)." *Bulletin of Earthquake Engineering*, Vol. 19, No. 5, 2021, pp. 2265–2289. https://doi.org/10.1007/s10518-021-01056-6.

[13] Nochebuena-Mora, E., Mendes, N., Lourenço, P. B., and Covas, J. A. "Vibration Control Systems: A Review of Their Application to Historical Unreinforced Masonry Buildings." *Journal of Building Engineering*, Vol. 44, 2021, p. 103333. https://doi.org/10.1016/j.jobe.2021.103333.

[14] Dassault Systèmes. Abaqus CAE. Dassault Systèmes, Providence, , 2019.

[15] Bühler, D. *Puebla, patrimonio de arquitectura civil del Virreinato*. Deutsches Museum ICOMOS, München, 2001.

[16] Barrera Barrera, M. *Los inmuebles habitacionales en Valladolid de Michoacán, siglo XVIII, sistemas constructivos y proporcionamiento del espacio.pdf*. Master thesis. Universidad Michoacana de San Nicolás de Hidalgo, Morelia, 2012.

[17] González Avellaneda, A., Hueytletl Torres, A., Pérez Méndez, B., Ramos Molina, L., and Salazar Muñoz, V. *Manual técnico de procedimientos para la rehabilitación de monumentos históricos en el Distrito Federal*. Instituto Nacional de Antropología e Historia, Ciudad de México, 1988.
[18] Dassault Systèmes Simulia Corp. Abaqus Analysis User's Guide Version 6.14. , 2014.
[19] Chávez, M. M., Durán, D., Peña, F., and García, N. Mechanical Characterization of Masonry Samples Extracted of Mexican Convent Churches from Sixteenth Century. Presented at the Construction Pathology, Rehabilitation Technology and Heritage Management REHABEND 2020, Granada, Spain, 2020.
[20] Lourenço, P. B., and Gaetani, A. *Finite Element Analysis for Building Assessment: Advanced Use and Practical Recommendations*. Routledge, New York, 2022.
[21] Castellazzi, G., D'Altri, A. M., De Miranda, S., Chiozzi, A., and Tralli, A. "Numerical Insights on the Seismic Behavior of a Non-Isolated Historical Masonry Tower." *Bulletin of Earthquake Engineering*, Vol. 16, No. 2, 2018, pp. 933–961. https://doi.org/10.1007/s10518-017-0231-6.
[22] Tarque, N., Camata, G., Spacone, E., Varum, H., and Blondet, M. "Nonlinear Dynamic Analysis of a Full-Scale Unreinforced Adobe Model." *Earthquake Spectra*, Vol. 30, No. 4, 2014, pp. 1643–1661. https://doi.org/10.1193/022512EQS053M.
[23] Acito, M., Bocciarelli, M., Chesi, C., and Milani, G. "Collapse of the Clock Tower in Finale Emilia after the May 2012 Emilia Romagna Earthquake Sequence: Numerical Insight." *Engineering Structures*, Vol. 72, 2014, pp. 70–91. https://doi.org/10.1016/j.engstruct.2014.04.026.
[24] Lubliner, J., Oliver, J., Oller, S., and Oñate, E. "A Plastic-Damage Model for Concrete." *International Journal of Solids and Structures*, Vol. 25, No. 3, 1989, pp. 299–326. https://doi.org/10.1016/0020-7683(89)90050-4.
[25] Lee, J., and Fenves, G. L. "Plastic-Damage Model for Cyclic Loading of Concrete Structures." *Journal of Engineering Mechanics*, Vol. 124, No. 8, 1998, pp. 892–900. https://doi.org/10.1061/(ASCE)0733-9399(1998)124:8(892).
[26] D'Altri, A. M., Cannizzaro, F., Petracca, M., and Talledo, D. A. "Nonlinear Modelling of the Seismic Response of Masonry Structures: Calibration Strategies." *Bulletin of Earthquake Engineering*, Vol. 20, No. 4, 2022, pp. 1999–2043. https://doi.org/10.1007/s10518-021-01104-1.
[27] AlGohi, B. H., Baluch, M. H., Rahman, M. K., Al-Gadhib, A. H., and Demir, C. "Plastic-Damage Modeling of Unreinforced Masonry Walls (URM) Subject to Lateral Loading." *Arabian Journal for Science and Engineering*, Vol. 42, No. 9, 2017, pp. 4201–4220. https://doi.org/10.1007/s13369-017-2626-8.
[28] Shu, Z., You, R., and Zhou, Y. "Viscoelastic Materials for Structural Dampers: A Review." *Construction and Building Materials*, Vol. 342, 2022, p. 127955. https://doi.org/10.1016/j.conbuildmat.2022.127955.
[29] Aiken, I. D., and Kelly, J. M. *Earthquake Simulator Testing and Analytical Studies of Two Energy-Absorbing Systems for Multistory Structures*. Publication NSF/IENG-90003. University of California, Berkeley, 1990.
[30] Bianchini, N., Mendes, N., Calderini, C., and Lourenço, P. B. "Modelling of the Dynamic Response of a Reduced Scale Dry Joints Groin Vault." *Journal of Building Engineering*, Vol. 66, 2023, p. 105826. https://doi.org/10.1016/j.jobe.2023.105826.

International Conference on Advances and Innovations in Engineering

A study on lost time coefficient in determining optimum cycle time at signalized intersections

Ziya CAKICI[1] , Mehmet Sinan YILDIRIM [2]

[1]Civil Engineering Department, Engineering Faculty, Izmir Demokrasi University, Izmir, Turkey.
[2]Civil Engineering Department, Engineering Faculty, Manisa Celal Bayar University, Manisa, Turkey.
[1]ziya.cakici@idu.edu.tr, [2]msyildirim35@gmail.com

[1](ORCID: 0000-0001-7003-815X), [2](ORCID: 0000-0001-5347-2456)

Abstract

Webster's optimum cycle time model is one of the earliest mathematical models developed to determine optimum cycle time and signal timings at signalized intersections. Although this model was developed about 65 years ago, it is still frequently used by many researchers and traffic engineers today. In the model, total lost time, lost time coefficient (usually assumed to be 1.5 in generally) and total traffic flow rate parameters are used to determine the optimum cycle time. In this study, it is aimed to determine the actual value of the lost time coefficient (ϕ) in Webster's optimum cycle time model. For this purpose, firstly, an optimization model based on delay minimization is created for a four approaches signalized intersection operated with four phases. Then, 48 different traffic scenarios were analyzed separately, considering this optimization model. As a result of the analyzes, it has been seen that the ϕ coefficient, which is accepted as 1.5 for signalized intersections operated with three or more phases, can take a different value for each traffic scenario. In addition, it is determined that this coefficient generally varies between 1.2 and 1.4, especially in cases where the total traffic volume at the intersection is equally distributed to the all intersection approaches or to the all lanes. Consequently, it can be said that it would be a more accurate and realistic approach to use the Webster's delay model instead of Webster's optimum cycle time model in minimizing the average vehicle delay at the intersection.

Keywords: optimum cycle time, delay model, lost time coefficient, signalized intersection, optimization

1. Introduction

Signalized intersections are the areas where traffic problems on road networks are most common. Therefore, waste of time, noise pollution, fuel consumption, and exhaust emissions are at a very high level in these areas [1]. Traffic engineers and transportation planners have been working on measures against the negative effects of these problems for many years. Various performance measures such as control delay, travel time, and capacity utilization ratio are taken into account and accordingly, decisions are taken by decision-makers for new regulations [2].

The control delay is used to determine the performance and level of service of signalized intersections. Therefore, the calculation and measurement of this parameter is a very important issue in terms of traffic engineering [3]. The control delay consists of three components: deceleration delay, stop delay, and acceleration delay. During the initial phase of the deceleration period, drivers begin to reduce their speed due to the signalization systems. Once the deceleration phase concludes, the vehicles come to a complete stop and remain stationary throughout the stop delay. At the beginning of the acceleration delay, drivers increase their speed again, and at the end of the acceleration delay they reach their regular cruising speed [4]. The trajectory diagram of a vehicle at a signalized intersection approach is shown in Figure 1 [5].

[1]Corresponding author

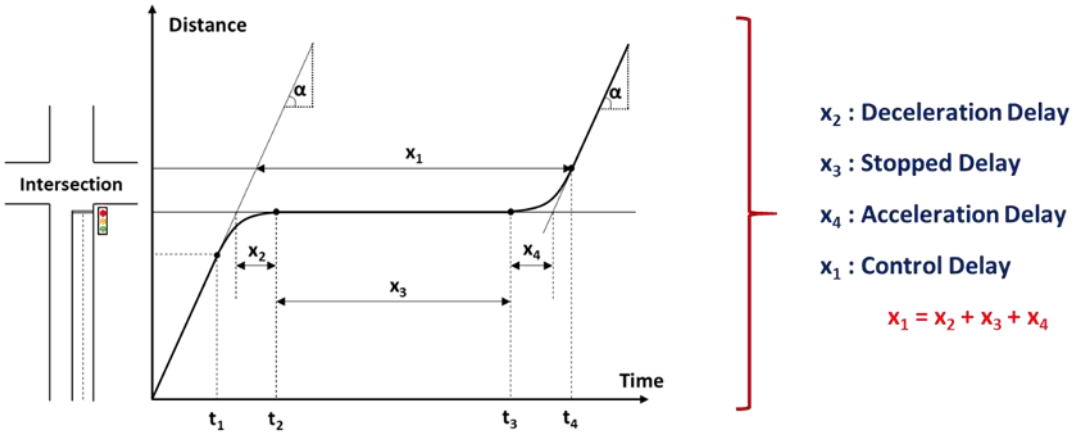

Figure 1. Trajectory diagram of a vehicle at a signalized intersection approach

Many traffic engineers and researchers have been working on control delay modeling for nearly 60 years. Webster, Highway Capacity Manual (HCM) and Australian (Akcelik) delay models are most used and well-known delay models. In these models, control delay is expressed mathematically using various data such as green time, cycle time, traffic volume, traffic flow rate, etc [6]. Although these models are created based on mathematical foundations, some of them may be insufficient in reflecting reality in some cases. As a sample, when the degree of saturation (volume/capacity) value is equal to or greater than 1.0, the Webster delay model gives unrealistic results. Besides, especially in oversaturated cases, similar results cannot be obtained by HCM and Australian model [7].

In general, control delays at at-grade signalized intersection approaches can be minimized by assigning optimum signal timings [8]. Webster, HCM, and Australian delay models can be used to determine optimum signal timings. In addition to this, optimum cycle time and green time equations are also presented in Webster and Australian models. When Webster, HCM and Australian delay models are examined carefully, it is seen that Webster and HCM models suggest phase-based signal design, while Australian model proposes movement-based signal design [9]. In this study, Webster's control delay and optimum cycle time model are considered. Within the scope of the study, it is aimed to determine the actual value of the lost time coefficient (ϕ) in Webster's optimum cycle time model.

This paper is organized as follows: In the next section, Webster's control delay and optimum cycle time model are explained in detail. In the third section, created delay minimization-based optimization model is presented. The analysis made within the scope of the study are included in the fourth section. In the last section, obtained results are evaluated and interpreted.

2. Webster's Control Delay and Optimum Cycle Time Model

Webster's Control Delay and Optimum Cycle Time models were introduced by Webster in 1958 [10]. The model is presented in Equation (1):

$$d = \frac{C \times (1-\lambda)^2}{2 \times (1-\lambda x)} + \frac{x^2}{2q \times (1-x)} - 0.65 \times \left(\frac{C}{q^2}\right)^{\frac{1}{3}} \times x^{(2+5\lambda)} \quad (1)$$

In Equation (1);
d : Average vehicle delay for each vehicle at each intersection approach (sec/veh)
C : Cycle time (sec)
λ : Ratio of effective green time to cycle time
x : Degree of saturation
q : The number of vehicles per unit time (veh/sec)

Webster proposes an optimum cycle time model to minimize the average vehicle delay at signalized intersections. This model is given in Equation (2):

$$C_{opt} = \frac{\phi L + 5}{1 - Y} \tag{2}$$

In Equation (2);

C_{opt} : Optimum cycle time (sec)

L : Lost time (sec)

ϕ : Lost time coefficient (coefficient between 1.25 and 1.98). This coefficient should be taken as 1.5 when the signalized intersection is managed with three or more phases.

Y : Total flow ratio $\left(Y = \sum_{i=1}^{n} y_i \right)$

y_i denotes flow ratio for traffic flow i. It can be calculated by using Equation (3):

$$y_i = \frac{Q_i}{S_i} \tag{3}$$

In Equation (3);

Q_i : Hourly traffic volume for traffic flow i (veh/h)

S_i : Saturation flow for traffic flow i (veh/h/lane)

Degree of saturation is defined as the ratio of volume to capacity. It can be calculated by using Equation (4):

$$x_i = \frac{q_i}{\lambda \times S_i} \tag{4}$$

In Equation (4);

q_i : The number of vehicles per unit time for traffic flow i (veh/sec)

λ : Ratio of effective green time to cycle time

S_i : Saturation flow for traffic flow i (veh/h/lane)

Webster calculates the green times as shown in Equation (5):

$$g_i = \frac{y_i}{Y} \times (C - L) \tag{5}$$

In Equation (5);

g_i : Effective green time (sec)

y_i : Flow ratio for traffic flow i

Y : Total flow ratio

C : Cycle time (sec)

L : Lost time (sec)

3. Optimization Model

In this study, a signalized intersection with four intersection approaches is considered for the analyzes. It is assumed that each intersection approach has a right of way in one phase. Therefore, it can be said that this signalized intersection model is managed with four phases. In the first phase, the right of way belongs to East intersection approach. In the second phase, the South intersection approach has right of way. In the third and fourth phases, the right of way belongs to West and North intersection approaches, respectively. Within the scope of this study, considered signalized intersection plan is shown in Figure 2.

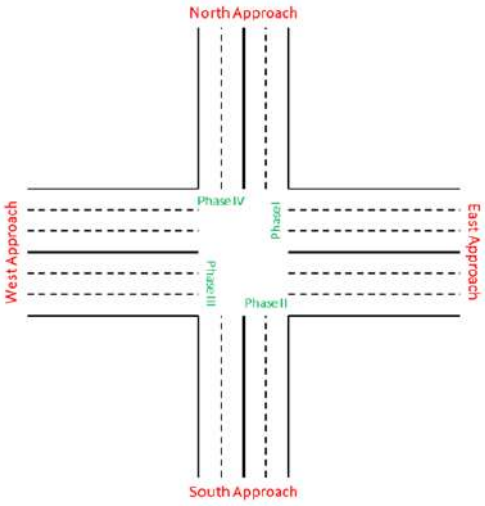

Figure 2. Signalized intersection plan

As seen in Figure 2, the East and West approaches of the intersection have three enter and exit lanes. Also, other approaches include two entrance and two exit lanes. Saturation flow value for each lane is selected as 1800 veh/h/lane. This saturation flow value is accordance with the results given in the Highway Capacity Manual [11]. Information and data (phase plan and cycle diagram) related to this intersection are presented in Figure 3.

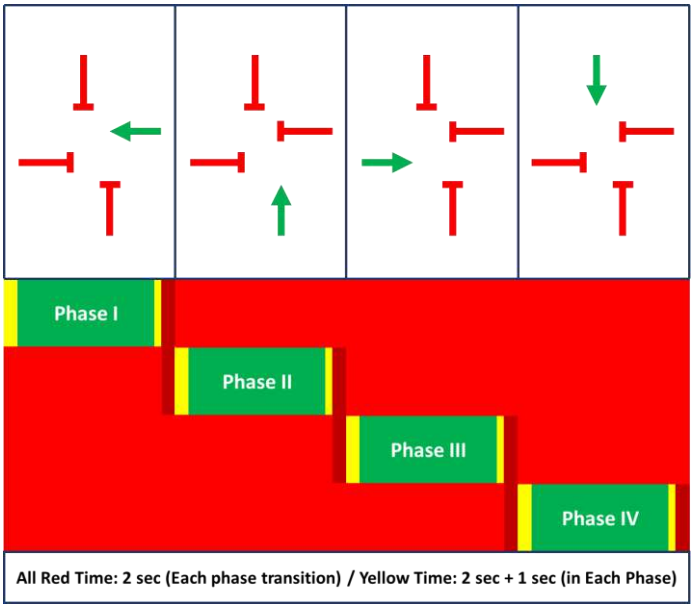

Figure 3. Phase plan and cycle diagram for considered signalized intersection

As seen in Figure 3, the total lost time for this signalization system is a total of 20 sec. After the phase plan is determined, signal timing optimization model is created. This model consists of one objective function (minimization of the average vehicle delay), four decision variables (green times) and nine different constraints (one of them is

cycle time constraints, four of them is green time constraints and the others are degree of saturation constraints). The objective function, decision variables and the set of constraints for the created optimization model are given in Table 1 in details.

Table 1. The objective function, decision variables and the set of constraints for created optimization model

Objective Function		$f = \min\left(d = \frac{\sum_{i=1}^{n=4} Q_i \times d_i}{\sum_{i=1}^{n=4} Q_i} \right)$
Decision Variables		x_1 : Green time for Phase I x_2 : Green time for Phase II x_3 : Green time for Phase III x_4 : Green time for Phase IV
The Set of Constraints	**Cycle Time Constraints**	$40 \le C_{opt} \le 180$
	Green Time Constraints	$7 \le x_1 \le 45$ $7 \le x_2 \le 45$ $7 \le x_3 \le 45$ $7 \le x_4 \le 45$
	Degree of Saturation Constraints	$0 \le \frac{q_1 \times C}{x_1 \times S_1} \le 0.95$ $0 \le \frac{q_2 \times C}{x_2 \times S_2} \le 0.95$ $0 \le \frac{q_3 \times C}{x_3 \times S_3} \le 0.95$ $0 \le \frac{q_4 \times C}{x_4 \times S_4} \le 0.95$

After the signal timing optimization model was created, an optimization script was written in MATLAB environment, taking this model into consideration. Differential Evolution Algorithm, one of the powerful-simple and easy meta-heuristic optimization algorithms, is preferred by many researchers in solving many engineering problems such as retaining wall, dam and foundation design [12-14]. Therefore, in the scope of this study, Differential Evolution algorithm was used to optimize the signal timings. For this algorithm, considering the previous studies in the literature, population size, the number of iteration, Crossover Rate (CR) and mutation factor (F) were selected as 1000, 50, 0.8 and 0.8, respectively [15].

4. Analyzes and Results

Within the scope of the study, firstly, 16 different traffic scenarios were created. Intersection approach-based traffic volumes were given in Table 2 for each scenario.

Table 2. Intersection approach-based traffic volumes for 16 different traffic scenarios

Scenario No	Traffic Volumes (veh/h)				Total Volume (veh/h)
	East	South	West	North	
1	371	54	344	105	874
2	511	56	428	112	1107
3	651	58	512	119	1340
4	784	87	718	158	1747
5	777	91	782	173	1823
6	895	97	750	195	1937
7	977	86	768	178	2009
8	914	107	920	204	2145
9	1045	116	957	211	2329
10	1051	123	1058	235	2467
11	1302	115	1024	237	2678
12	1278	139	1071	279	2767
13	1306	145	1196	264	2911
14	1470	181	1232	363	3246
15	1661	222	1392	446	3721
16	1700	262	1417	526	3905

Then, optimum cycle times and optimum green signal timings were obtained by using optimization script. In the third stage, lost time coefficient (ϕ) for each scenario was calculated by using obtained optimum cycle times. Webster's optimum cycle time model was used in the calculation process. The lost time coefficient (ϕ_{cal}) was calculated by using Equation (6):

$$\phi_{cal} = \frac{\left(\left(C_{opt} \times (1 - Y)\right) - 5\right)}{L} \tag{6}$$

The optimum green signal timings, optimum cycle times, average vehicle delays for the base 16 different traffic scenarios were shown in Table 3.

Table 3. Analysis results for the base 16 different traffic scenarios

Scenario No	Optimum Signal Timings (sec)					Average Vehicle Delay (sec/veh)
	Phase I	Phase II	Phase III	Phase IV	Cycle Time	
1	7	7	7	7	48	19.66
2	9	7	8	7	51	20.59
3	12	7	9	7	55	21.55
4	13	7	12	7	59	23.38
5	13	7	13	7	60	23.74
6	15	7	13	7	62	24.25
7	17	7	13	7	64	24.72
8	16	7	16	7	66	25.52
9	18	7	17	7	69	26.71
10	18	7	18	7	70	27.76
11	24	7	19	7	77	29.53
12	23	7	20	8	78	30.92
13	25	7	23	8	83	32.36
14	31	7	26	12	96	38.65
15	42	9	35	17	123	54.60
16	45	11	38	21	135	70.82

Lost time coefficients calculated for the base 16 different traffic scenarios were also presented graphically in Figure 4.

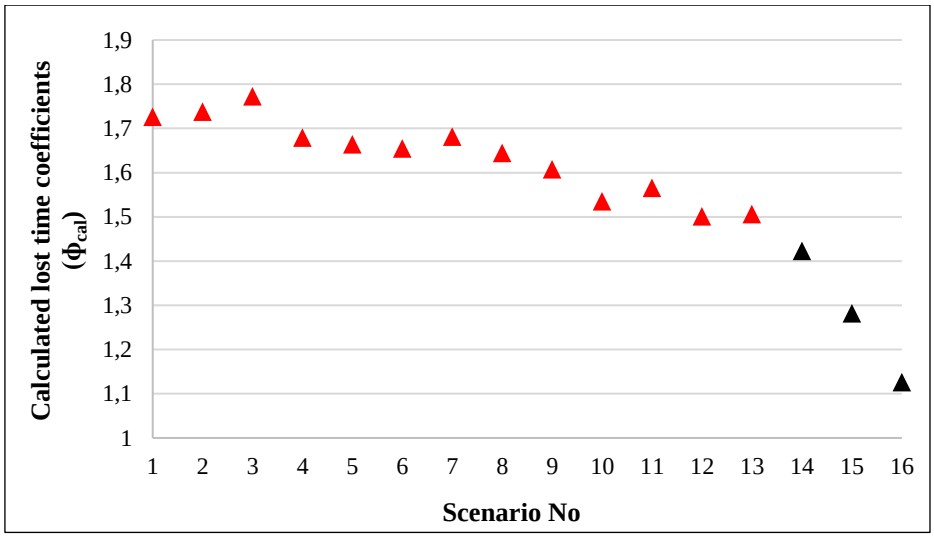

Figure 4. Calculated lost time coefficients (ϕ_{cal}) for base 16 different traffic scenarios

As seen on Figure 4, most of the lost time coefficients (ϕ_{cal}) for base 16 different traffic scenarios were above 1.5. Obtained results prove that the lost time coefficient of 1.5 is not a precise value for minimizing the average vehicle delay at the intersection [16, 17].

In the next stage, 16 new different traffic scenarios were created to determine lost time coefficient in different conditions. In this stage, for all scenarios, total traffic volumes presented in Table 2 were equally distributed to the intersection approaches. All new scenarios were then analyzed. In the case of equal distribution of total traffic volumes to all intersection approaches, the analysis results were presented in Table 4.

Table 4. Analysis results in case of equal distribution of total traffic volumes to all approaches

Scenario No	Optimum Signal Timings (sec)					Average Vehicle Delay (sec/veh)
	Phase I	Phase II	Phase III	Phase IV	Cycle Time	
17	7	7	7	7	48	19.32
18	7	7	7	7	48	19.92
19	7	7	7	7	48	20.86
20	7	9	7	9	52	23.44
21	7	9	7	9	52	24.10
22	7	10	7	10	54	25.36
23	7	10	7	10	54	26.24
24	8	11	8	11	58	28.02
25	9	13	9	13	64	31.02
26	10	14	10	14	68	33.55
27	12	17	12	17	78	38.32
28	13	18	13	18	82	40.88
29	15	21	15	21	92	45.42
30	21	30	21	30	122	61.01
31	-	-	-	-	-	-
32	-	-	-	-	-	-

As seen in Table 4, since degree of saturation value is more than 1.0 for North and South approaches in the thirty first and thirty second scenarios, no results could be obtained in case of equal distribution of total traffic volumes to all intersection approaches. In addition, lost time coefficients for remaining 14 (from scenario 17 to scenario 30)

scenarios were calculated by using Equation (6). Calculated lost time coefficients (ϕ_{cal}) for the created scenarios were given in Figure 5.

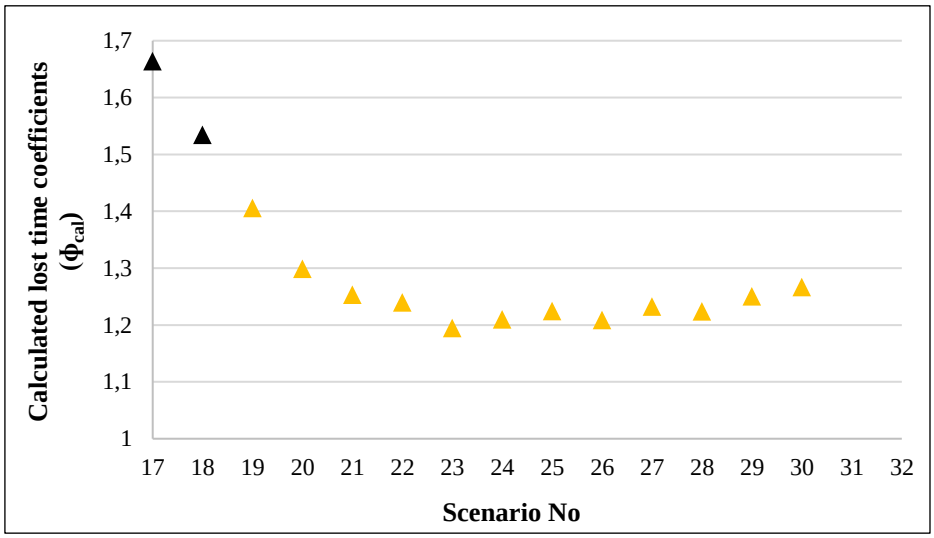

Figure 5. Calculated lost time coefficients (ϕ_{cal}) in case of equal distribution of total traffic volumes to all approaches

In Figure 5, it can be seen that the calculated lost time coefficients disperse between 1.2 and 1.4, in generally. Only in seventeenth and eighteenth scenarios, lost time coefficients were calculated as 1.664 and 1.535, in respectively.

In the last stage, 16 new different traffic scenarios were created in order to determine lost time coefficient in case the total traffic volume at the intersection is distributed equally to all lanes. In this stage, for all scenarios, total traffic volumes presented in Table 2 were equally distributed to the all lanes at the intersection. Then, the new scenarios were analyzed in the MATLAB environment. In case of equal distribution of total traffic volumes to all lanes at the intersection, the analysis results were presented in Table 5.

Table 5. Analysis results in case of equal distribution of total traffic volumes to all lanes at the intersection

Scenario No	Optimum Signal Timings (sec)					Average Vehicle Delay (sec/veh)
	Phase I	Phase II	Phase III	Phase IV	Cycle Time	
33	7	7	7	7	48	19.23
34	7	7	7	7	48	19.72
35	7	7	7	7	48	20.36
36	7	7	7	7	48	22.53
37	7	7	7	7	48	23.26
38	8	8	8	8	52	24.44
39	8	8	8	8	52	26.24
40	9	9	9	9	56	26.88
41	11	10	11	10	62	29.46
42	12	11	12	11	66	31.72
43	14	13	14	13	74	35.79
44	15	14	15	14	78	37.85
45	17	16	17	16	86	41.65
46	23	22	23	22	110	53.92
47	40	39	40	39	178	90.14
48	-	-	-	-	-	-

As seen in Table 5, optimum green signal timings and cycle time could not be obtained for the forty eighth scenario because degree of saturation value for all intersection approaches exceeded 1.0 for this scenario. Thus, the lost time coefficient could not be calculated for this scenario also. Lost time coefficient for remaining 15 (from scenario 33 to

scenario 47) scenarios were calculated by using Equation (6). Calculated lost time coefficients (ϕ_{cal}) for these new scenarios were depicted in Figure 6.

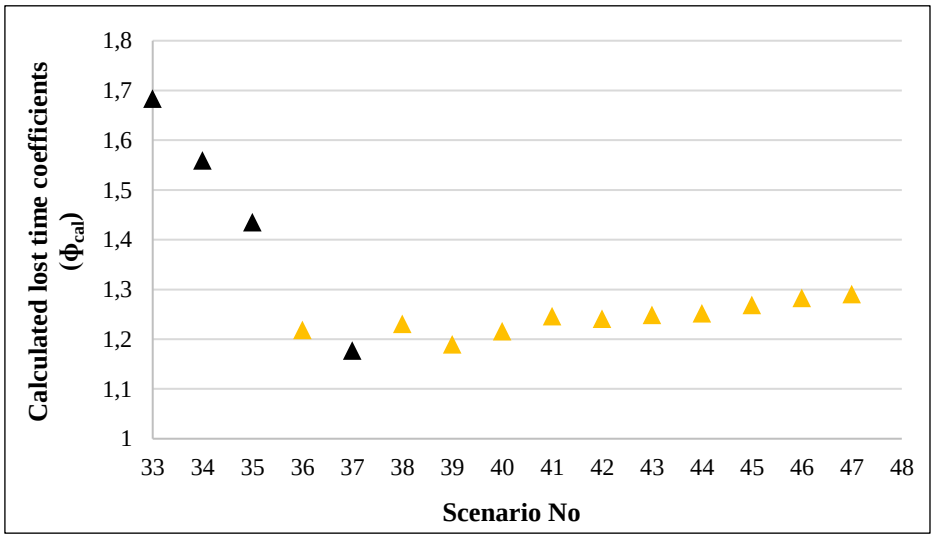

Figure 6. Calculated lost time coefficients (ϕ_{cal}) in case of equal distribution of total traffic volumes to all lanes at the intersection

When Figure 6 is examined carefully, it is seen that the calculated lost time coefficients are between 1.2 and 1.3, in generally. Although the lost time coefficients for thirty third, thirty fourth and thirty fifth scenarios were over 1.4, the lost time coefficient for thirty seventh scenario was below 1.2. However, the calculated lost time coefficient (1.178) was close to 1.2 for the thirty seventh scenario.

5. Conclusions

In this study, it is aimed to determine the actual value of the lost time coefficient (ϕ) in Webster's optimum cycle time model. For this purpose, firstly, an optimization model based on delay minimization is created for a four approaches signalized intersection operated with four phases. Then, 48 different traffic scenarios were analyzed separately, considering this optimization model. As a result of the analyzes, it has been seen that the lost time coefficient, which is accepted as 1.5 for signalized intersections operated with three or more phases, can take a different value for each traffic scenario. In addition, for considered traffic scenarios, it is determined that this coefficient generally varies between 1.2 and 1.4, especially in cases where the total traffic volume at the intersection is equally distributed to the all intersection approaches or to the all lanes. In the light of these results, it can be said that it would be a more accurate and realistic approach to use the Webster's delay model instead of Webster's optimum cycle time model in minimizing the average vehicle delay at the intersection.

It should be noted that the lost time coefficient may differ in different traffic conditions. The number of approaches at the intersection, the number of phase, traffic volumes, lost time value, limit values related to signal timings, saturation flow value for each lane and etc. are the some key parameters for lost time coefficient. Therefore, different traffic conditions should be taken into account and the number of analyzes should be increased in the future studies. It is thought that this may allow to obtain more realistic and reliable lost time coefficient for Webster's optimum cycle time model.

6. References

[1] Dion F, Rakha H, Kang Y S. "Comparison of delay estimates at under-saturated and over-saturated pre-timed signalized intersections". Transportation Research Part B: Methodological, 38(2), 99-122, 2004.

[2] Samadi S, Rad A P, Kazemi F M, Jafarian H. "Performance evaluation of intelligent adaptive traffic control systems: A case study". Journal of Transportation Technologies, 2(3), 248-259, 2012.

[3] Akgungor A P. “A new delay parameter dependent on variable analysis periods at signalized intersections, part 1: model development”. Transport, 23(1), 31-36, 2008.
[4] Çakıcı Z. Sinyalize Kavşaklar için Optimizasyon Tabanlı Trafik Yönetim Modeli. Doktora Tezi, Pamukkale Üniversitesi, Denizli, Türkiye, 2020.
[5] Darma Y, Karim M R, Mohamad J, Abdullah S. “Control delay variability at signalized intersection based on HCM method” Eastern Asia Society for Transportation Studies Conference, Bangkok, Thailand, 945-958, 2005.
[6] Sekhar C R, Raj P, Parida P, Gangopadhyay S. “Estimation of delay and fuel loss during idling of vehicles at signalized intersection in Ahmedabad”. Procedia-Social and Behavioral Sciences, 104, 1178-1187, 2013.
[7] Korkmaz E, Akgungor A P. “Comparison of artificial bee colony and flower pollination algorithms in vehicle delay models at signalized intersections”. Neural Computing and Applications, 32(8), 3581-3597, 2020.
[8] Hadi M A, Wallace C E. “Optimization of signal phasing and timing using cauchy simulated annealing”. Transportation Research Record, 1456, 64-71, 1994.
[9] Cakici Z, Murat Y S. “A differential evolution algorithm-based traffic control model for signalized intersections”. Advances in Civil Engineering, Article ID: 7360939, 1-16, 2019.
[10] Webster F V. “Traffic Signal Settings Report”, Michigan University: H. M. Stationery Office, 1958.
[11] Highway Capacity Manual 2010, National Research Council, Washington D.C., 2010.
[12] Deepika R, Suribabu C R. “Optimal design of gravity dam using differential evolution algorithm”. International Journal of Optimization in Civil Engineering, 5(3), 255-266, 2015.
[13] Kamal M, Inel M. “Optimum design of reinforced concrete continuous foundation using differential evolution algorithm”. Arabian Journal for Science and Engineering, 44, 8401-8415, 2019.
[14] Vu V T. “Optimisation of gravity retaining walls under bounded uncertainties”. Geomechanics and Geoengineering, 18(5), 418-425, 2023.
[15] Başkan Ö, Ceylan H. “Ulaşım ağ tasarımı problemlerinin çözümünde diferansiyel gelişim algoritması tabanlı çözüm yaklaşımları”. Pamukkale Üniversitesi Mühendislik Bilimleri Dergisi, 20(9), 324-331, 2014.
[16] Akcelik R. “Traffic signals: capacity and timing analysis”. Australian Road Research Board, Research Report ARR No: 123, 1998.
[17] Zakariya A Y, Rabia S I. “Estimating the minimum delay optimal cycle length based on a time-dependent delay formula” Alexandria Engineering Journal, 55(3), 2509-2514, 2016.

International Conference on Advances and Innovations in Engineering

A random forest model optimized with genetic algorithm for cantilever retaining walls

Utku KÖKTAN[1] , Gökhan DEMİR [2]

[1,2]Department of Civil Engineering, Faculty of Engineering, Ondokuz Mayıs University, Samsun, Türkiye..
[1]utku.koktan@omu.edu.tr, [2]gokhan.demir@omu.edu.tr

[1](ORCID: 0000-0002-8287-9586), [2](ORCID: 0000-0002-3734-1496)

Abstract
Retaining walls are structures that are widely used in civil engineering applications. Determination of the safety factor is critical in the design of these structures. For this purpose, a machine learning model that can predict the safety factor of cantilever retaining walls has been introduced. Firstly, analyses were carried out in Plaxis 2D software with different inputs: cohesion, internal friction angle, unit weight, Poisson's ratio, elasticity modulus of the soil and width, height, elasticity modulus of the wall and groundwater level, and horizontal seismic acceleration coefficient. As a result of these analyses, the safety factor was obtained as an output. Secondly, a random forest model optimized with genetic algorithm that can predict the safety factor was created using this data. The performance of the obtained model was evaluated with root mean square error and coefficient of determination. The results of the study showed that the proposed model can predict the safety factor of cantilever retaining walls with high accuracy.

Keywords: cantilever retaining wall, genetic algorithm, random forest

1. Introduction

Retaining walls are structures built for the ground to be kept at two different elevations. These special engineering structures are frequently used in many areas where civil engineering applications are carried out. This widespread use often brings with it the necessity of constructing retaining structures in areas with high earthquake risk. Considering all these, it is of vital importance that retaining walls be constructed in an earthquake-resistant manner. For this reason, it is essential to determine the safety factor correctly at the design stage.

Many studies have been carried out, and various methods have been developed to determine the dynamic behavior of retaining walls. It is possible to collect these methods in three categories: 1) traditional approaches where the relative motion of the wall and backfill material is large enough to cause a limit or failure state in the soil, 2) approaches based on the assumption that the backfill soil behaves linearly elastic, 3) approaches that describe the soil behavior as a nonlinear [18]. In addition to these, in recent years, the use of artificial intelligence methods in engineering problems has become increasingly common, depending on the development of computer technologies. In parallel with this, studies on using artificial intelligence to determine the behavior of retaining walls are available in the literature. In particular, machine learning is one of the most used in artificial intelligence-based studies. Many researchers have used machine learning to solve stabilization, deformation, dimensioning, etc., problems in retaining walls.[1, 3, 4, 6, 7, 9, 12, 15-17, 19, 20]. In these studies, a data pool was created based on the analysis of retaining walls, and various machine learning methods were developed with these data. The performance of these machine learning models is often improved with various optimization algorithms.

In this study, parametric analyses were made on cantilever retaining walls using Plaxis 2D software. These analyses used cohesion, internal friction angle, unit weight, Poisson's ratio, elasticity modulus of the soil and width, height, elasticity modulus of the wall and groundwater level, and horizontal seismic acceleration coefficient as input parameters. In response to these input parameters, the factor of safety of the wall is obtained as an output. In this

[1]Corresponding author

way, a data pool was created by performing one thousand analyses. A random forest (RF) model optimized with the genetic algorithm was created using this data pool. The model's performance was evaluated with the root mean square error (RMSE) and the coefficient of determination (R^2). According to the result of the RF model, RMSE was obtained as 0,01423 and R^2 as 0,95278. These results showed that the RF model could successfully predict the factor of safety of the wall. Obtained results are presented in tables and graphs.

2. Methodology

2.1. Finite element analyses

Firstly, dynamic analyses were performed in Plaxis 2D software. The input and output parameters used in the analyses are presented below (Table 1.).

Table 1. Input and output parameters

	Inputs and Output	Category	Unit	Values
Soil	Cohesion (c)	Input	kN/m^2	0, 5, 10, 15, 20, 25, 30
	Internal Friction Angle (Φ)	Input	Degree	0, 5, 10, 15, 20, 25, 30
	Dry unit weight (γ)	Input	kN/m^3	15, 17, 19, 21, 23
	Submerged unit weights (γ')	Input	kN/m^3	18, 20, 22, 24, 26
	Elasticity Modulus (E)	Input	kN/m^2	10000,40000,70000,100000,130000
	Poisson Ratio (ν)	Input	-	0.2, 0.3, 0.4
Wall	Wall Height (H)	Input	meter	3, 5, 7, 9
	Wall Width (t)	Input	meter	0.2, 0.4, 0.6, 0.8
	Elasticity Modulus (E)	Input	kN/m^2	$28x10^6$, $30x10^6$, $32x10^6$
	Underground Water Level	Input	meter	0, 1, 3, 5, 7, 9, 11
	Peak Ground Acceleration	Input	g	0.1, 0.2, 0.3, 0.4, 0.5
	Factor of Safety (FS)	Output	-	-

The model geometry used in finite element analyses was 80x30 meters (Figure 1.). Plane strain elements with 15 nodes were used in the analyses. The material behavior of the soil is represented by the Mohr-Coulomb constitutive model. The wall is modeled with plate elements, and its behavior is assumed to be linear elastic. Boundary conditions were created to be totally fixed at the bottom of the model and normally fixed at the right and left sides. Earthquake behavior was implemented by the pseudo-static method, and earthquake acceleration was effected in the horizontal direction.

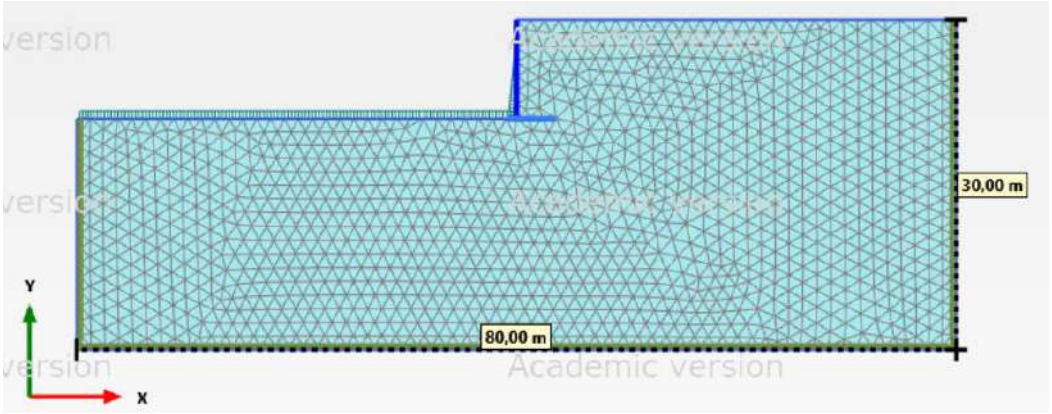

Figure 1. Model geometry

The foundation dimensions of the cantilever retaining wall were determined depending on the wall height (Figure 2.). After that, one thousand dynamic analyses were carried out, and a RF model optimized with the genetic algorithm was developed with the obtained data pool.

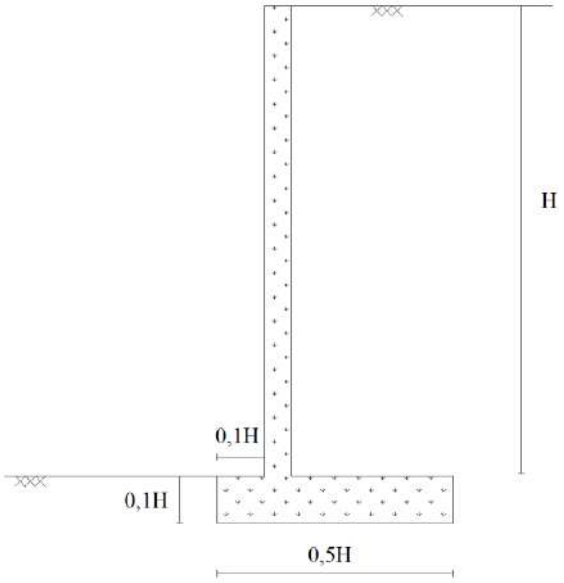

Figure 2. Wall geometry

2.2. Random forest

Decision tree is one of the algorithms used in the non-parametric classification process in recent years. Due to processing speed, decision tree algorithms offer fast solutions in classifying extensive data and complex areas. Modeling a decision tree consists of two steps: (1) tree building and (2) tree pruning. Tree building divides the training set area into non-overlapping regions based on the Gini Index. The tree obtained during the building phase may have many branches, and tree pruning is performed next to prevent overfitting. [2, 13].

RF algorithm combines the predictions of a set of single decision trees to create a strong prediction. Single decision trees are trained on randomly selected subsets of the entire training set using bagging and random feature selection methods. The average value of the individual tree predictions determines the overall model prediction [3, 5].

2.3. Genetic algorithm

The genetic algorithm was developed by John Holland in 1992 [8]. These algorithms are widely used to generate high-quality solutions to optimization and search problems based on bio-inspired operators such as mutation, crossover, and selection. It is an algorithm based on the principle of survival of the fittest [11, 14]. Genetic algorithm is a type of directed random search algorithm. It simulates the genetic development of living things through selection. The algorithm uses an initial population formed by some of the solutions in the research space. Initial populations are developed in succession in each generation using natural selection and reproduction. The fittest individual of the latest generation is the optimal solution to the problem [4, 10].

3. Results and Discussion

A RF model optimized with a genetic algorithm was created using the data obtained from dynamic analyses. The model's performance was measured by Root Mean Square Error (RMSE) and coefficient of determination (R^2). One thousand finite element analyses were carried out, and 70% of the data obtained from these analyses were used for training and 30% for testing. The RMSE value of the model is 0,01423 and R^2 is 0,95278. Graphics showing the performance of the model are presented below. Figure 3 presents the scatter plot of the predicted and observed values of factor of safety. Figure 4 presents a graph of one hundred predicted and observed factor of safety data randomly selected during the test phase.

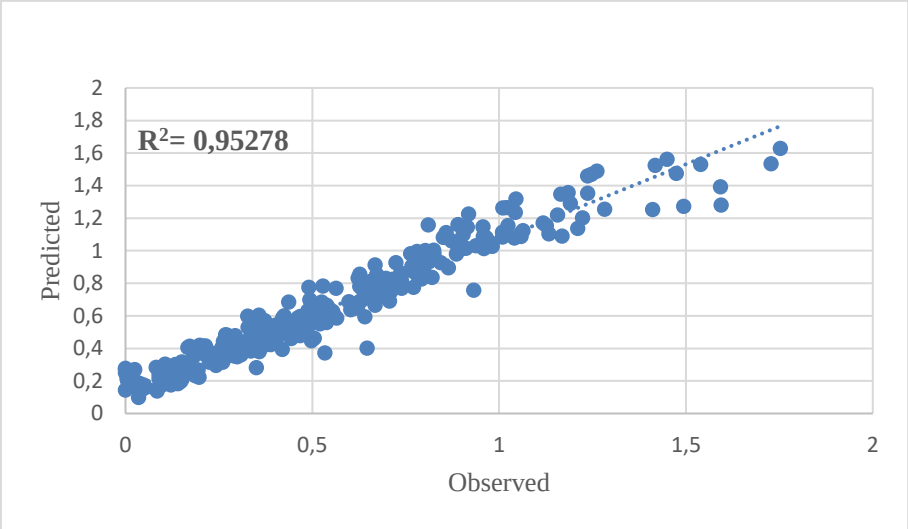

Figure 3. Observed and predicted values of factor of safety

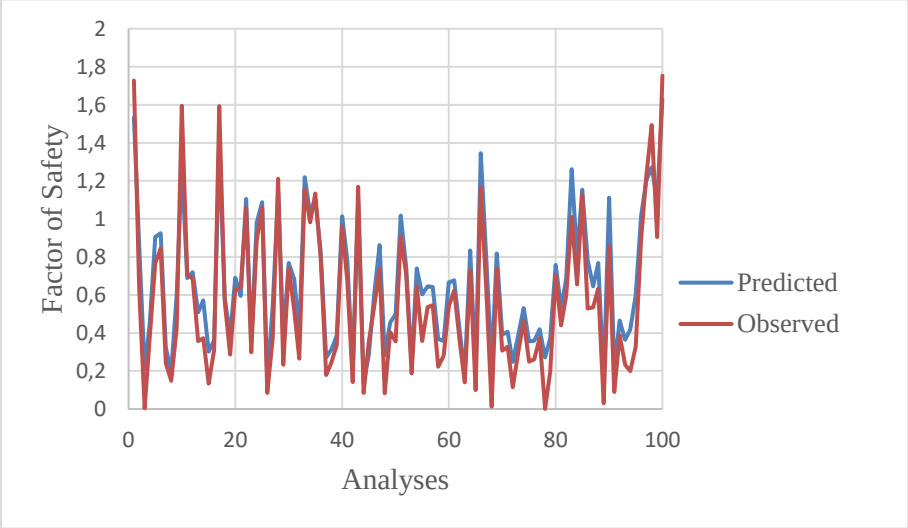

Figure 4. Comparison of observed and predicted 100 numbers of data, which was selected randomly in the test phase

4. Conclusion

In this study, one thousand dynamic analyses were performed on retaining walls with Plaxis 2D software. In the analysis, cohesion, internal friction angle, unit weight, elasticity modulus, Poisson's ratio of the soil, and height, width, elasticity modulus of the wall, and horizontal seismic acceleration coefficient and groundwater level were used as input parameters. In response to these input parameters, the factor of safety was obtained as an output. Then, with the obtained data, an optimized RF model was created with a genetic algorithm. The performance of the RF model was measured with RMSE and R^2. Considering the results, the R^2 was obtained as 0.95278 and RMSE 0.01423.

When the results obtained were examined, it was seen that the model created showed high performance. It is thought that the created model can help determine the dynamic behavior of cantilever retaining walls. In future studies, it aims to create new models by using different machine learning methods and optimization techniques and to compare these models.

5. Acknowledgements

This study was supported by the Scientific Research Projects Coordination Agency of Ondokuz Mayıs University with the project number PYO.MUH.1904.21.012.

6. References

[1] Bekdaş G, Cakiroglu C, Kim SGeem ZW, Optimal dimensioning of retaining walls using explainable ensemble learning algorithms. Materials, 15(14): p. 4993. 2022.

[2] Breiman L, Classification and regression trees. Vol.: Routledge. 2017.

[3] Cakiroglu C, Islam K, Bekdaş GNehdi ML. Data-driven ensemble learning approach for optimal design of cantilever soldier pile retaining walls. in Structures. Elsevier. 2023.

[4] Chen H, Asteris PG, Jahed Armaghani D, Gordan BPham BT, Assessing dynamic conditions of the retaining wall: developing two hybrid intelligent models. Applied Sciences, 9(6): p. 1042. 2019.

[5] Feng D-C, Wang W-J, Mangalathu S, Hu GWu T, Implementing ensemble learning methods to predict the shear strength of RC deep beams with/without web reinforcements. Engineering Structures, 235: p. 111979. 2021.

[6] Ghaleini EN, Koopialipoor M, Momenzadeh M, Sarafraz ME, Mohamad ETGordan B, A combination of artificial bee colony and neural network for approximating the safety factor of retaining walls. Engineering with Computers, 35(2): p. 647-658. 2019.

[7] Gordan B, Koopialipoor M, Clementking A, Tootoonchi HTonnizam Mohamad E, Estimating and optimizing safety factors of retaining wall through neural network and bee colony techniques. Engineering with Computers, 35(3): p. 945-954. 2019.

[8] Holland JH, Genetic algorithms. Scientific american, 267(1): p. 66-73. 1992.

[9] Kalemci EN, İkizler SB, Dede TAngın Z. Design of reinforced concrete cantilever retaining wall using Grey wolf optimization algorithm. in Structures. Elsevier. 2020.

[10] Karaboğa D, Yapay Zeka Optimizasyon Algoritmaları. Vol. Ankara: Nobel Akademik Yayıncılık. 2018.

[11] Katoch S, Chauhan SSKumar V, A review on genetic algorithm: past, present, and future. Multimedia tools and applications, 80: p. 8091-8126. 2021.

[12] Koopialipoor M, Murlidhar BR, Hedayat A, Armaghani DJ, Gordan BMohamad ET, The use of new intelligent techniques in designing retaining walls. Engineering with Computers, 36(1): p. 283-294. 2020.

[13] Mangalathu S, Jang H, Hwang S-HJeon J-S, Data-driven machine-learning-based seismic failure mode identification of reinforced concrete shear walls. Engineering Structures, 208: p. 110331. 2020.

[14] Michalewicz Z, Genetic Algorithms+ Data Structures= Evolution Programs. Springer-Verlag, 1999. Google Scholar Google Scholar Digital Library Digital Library. 1999.

[15] Mishra P, Samui PMahmoudi E, Probabilistic design of retaining wall using machine learning methods. Applied Sciences, 11(12): p. 5411. 2021.

[16] Mustafa R, Samui P, Kumari S, Mohamad ETBhatawdekar RM, Probabilistic analysis of gravity retaining wall against bearing failure. Asian Journal of Civil Engineering: p. 1-21. 2023.

[17] Ozturk T, Artificial neural networks approach for earthquake deformation determination of geosynthetic reinforced retaining walls. International Journal of Intelligent Systems and Applications in Engineering, 2(1): p. 1-9. 2014.

[18] Veletsos AYounan A, Dynamic soil pressures on rigid vertical walls. Earthquake engineering & structural dynamics, 23(3): p. 275-301. 1994.

[19] Xu C, Gordan B, Koopialipoor M, Armaghani DJ, Tahir MZhang X, Improving performance of retaining walls under dynamic conditions developing an optimized ANN based on ant colony optimization technique. IEEE Access, 7: p. 94692-94700. 2019.

[20] Yang H, Koopialipoor M, Armaghani DJ, Gordan B, Khorami MTahir M, Intelligent design of retaining wall structures under dynamic conditions. Steel and Composite Structures, An International Journal, 31(6): p. 629-640. 2019.

International Conference on Advances and Innovations in Engineering

Comparison of Flow Trends of The Eastern Mediterranean Basin with Mann Kendall and Innovative Trend Analysis Methods

Erdinç İKİNCİOĞULLARI[1] , Enes GÜL[2], Ahmet TOPRAK[3]

[1]Department of Civil Engineering, Faculty of Engineering , Bingol University, Bingol, Türkiye.
[2]Department of Civil Engineering, Faculty of Engineering , Inonu University, Malatya, Türkiye.
[3]Department of Geography, Faculty of Humanities and Social Sciences, Firat University, Elazig, Türkiye.

[1]erdincikinciogullari@gmail.com, [2]enes.gul@inonu.edu.tr, [3]atoprak@firat.edu.tr

[1](ORCID: 0000-0003-2518-980X), [2](0000-0001-9364-9738),[3](ORCID: 0000-0001-6790-1856)

Abstract

Climate change affects the water cycle, along with factors such as rising temperatures, heavy rainfall, drought, and melting glaciers. These changes can affect the amount of flow, seasonal distribution, and even the flow regime of streams. Therefore, climate change affects the future status of water resources by changing flow trends. Streamflow trend analysis is crucial for understanding water resource dynamics and guiding sustainable water management. Parametric and non-parametric tests are commonly used for this purpose. Mann-Kendall (MK) test is widely employed to detect monotonic trends in streamflow data. Furthermore, Şen Innovative Trend Analysis (Şen-ITA) method, which does not rely on distributional assumptions, has recently gained attention for its versatility in trend analysis. In this study, streamflow data from the Eastern Mediterranean Basin were analyzed using the MK and Şen-ITA methods, and the results were explained using graphs and tables. According to the results, both methods observed a decreasing trend in all station data.

Keywords: Eastern Mediterranean Basin, Flow observation data, Mann-Kendall (MK) Method, Şen Innovative Trend Analysis (Şen-ITA)

1. Introduction

Water is an indispensable blessing for every living organism. This blessing is necessary to preserve and sustain ecosystems in various areas, ranging from drinking and domestic use to agriculture, industrial activities, and energy production. While approximately 97.5% of the water that covers two-thirds of our planet consists of salt water, the freshwater quantity is only about 2.5%. However, a significant portion of this small fraction is occupied by polar ice caps. Consequently, the accessible freshwater source accounts for only 0.10% of the total water quantity (Fig. 1) [1].

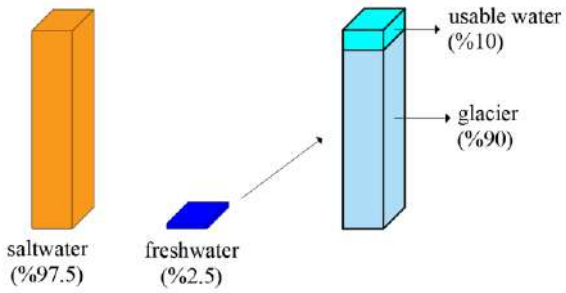

Figure 1. Distribution of water on earth

Streams are our most easily accessible source of fresh water. In addition to reaching this source, which has periodic differences in the amount of flow, it may also be necessary to store the water source. For this reason, dams are the most effective water structures to meet the water needs of societies due to the increasing population. For the proper

[1]Corresponding author

design of a water structure and the effective use and management of these resources, it is necessary to determine the flow changes [2].

A trend is when the value of a random variable increases or decreases over time. Examining trends in streamflow data plays a crucial role in understanding the dynamic nature of water resources for a basin. Researchers can extract meaningful information about the trends and variations in streamflow by employing statistical methods. These findings provide a basis for effective water management strategies, enabling decision-makers to address the challenges of changing hydrological patterns in the region. Two types of tests, parametric and non-parametric, are used to examine the trend. The biggest advantage of parametric methods is their simplicity. In order to use parametric methods correctly, data variables must be normally distributed. The advantage of non-parametric methods is that they have the same effect as parametric methods [3, 4], although they do not assume any distribution state for the data. Non-parametric tests are preferred for analysis. This situation is because it eliminates problems such as short duration, randomness, and irregularity of observations. These tests are independent of the distribution of the random variable of the data and the data parameters. The most widely used non-parametric test is the Mann-Kendall (MK) test [6]. Numerous studies in the literature have successfully applied the MK method [6-11].

Many different methods have been proposed in the literature to perform trend analysis. Innovative trend analysis (Şen-ITA) method was introduced by Şen (2012) [12] recently. The most important feature of this applied test is that it does not contain assumptions. Compared to other methods, the most important advantage of the Şen-ITA method is that the independent or dependent time series does not change the trend and can be safely applied to all series. For these reasons, the Şen-ITA method has been used in recent studies to examine climate and hydrological data [13-17].

The results obtained from the trend analysis provide valuable insights into the behavior of a basin's flow patterns over the studied period. By comparing the outcomes derived from the MK and Şen-ITA methods, researchers can gain a comprehensive understanding of the detected trends and assess the robustness of the findings. This comparative approach contributes to a more accurate and reliable evaluation of the flow characteristics, allowing for informed decision-making and sustainable water resource management in the region. Within the scope of this study, flow data of the Eastern Mediterranean Basin published by DSİ were analyzed using MK and Şen_ITA methods. Obtained results are interpreted comparatively.

2. Study Area, data, and methods

The Eastern Mediterranean Basin is located in the Mediterranean Region south of Turkey. It is surrounded by the Seyhan Basin in the east, the Antalya Basin in the west, the Konya Closed Basin in the north, and the Mediterranean Sea in the south. Although the biggest streams of the basin are Göksu River and Tarsus (Berdan) Stream, the streams are short, and their bed slopes are high. The most important mainstream is the Göksu River and its tributaries. Apart from this, Tarsus (Berdan) Stream, Anamur Stream, Limonlu Stream, Efrenk Stream, Alata Stream, Çubuk Stream, Kirmir Stream, Ova Stream, and Seydi Stream are other streams in the basin. Eastern Mediterranean Basin constitutes 2.8% of our country, with an area of 2,180,704 hectares and a precipitation area of 21,807 km^2. While the annual average precipitation is 745 mm, the average flow is 11.07 km^3/year [18]. This basin, with a total length of 129 km, consists of 10 sub-basins as Tarsus (Berdan) Stream Sub-Basin, Lamas (Lemon) Stream Sub-Basin, Göksu River Sub-Basin, and Dragon (Anamur) Stream Sub-Basin (Fig. 2).

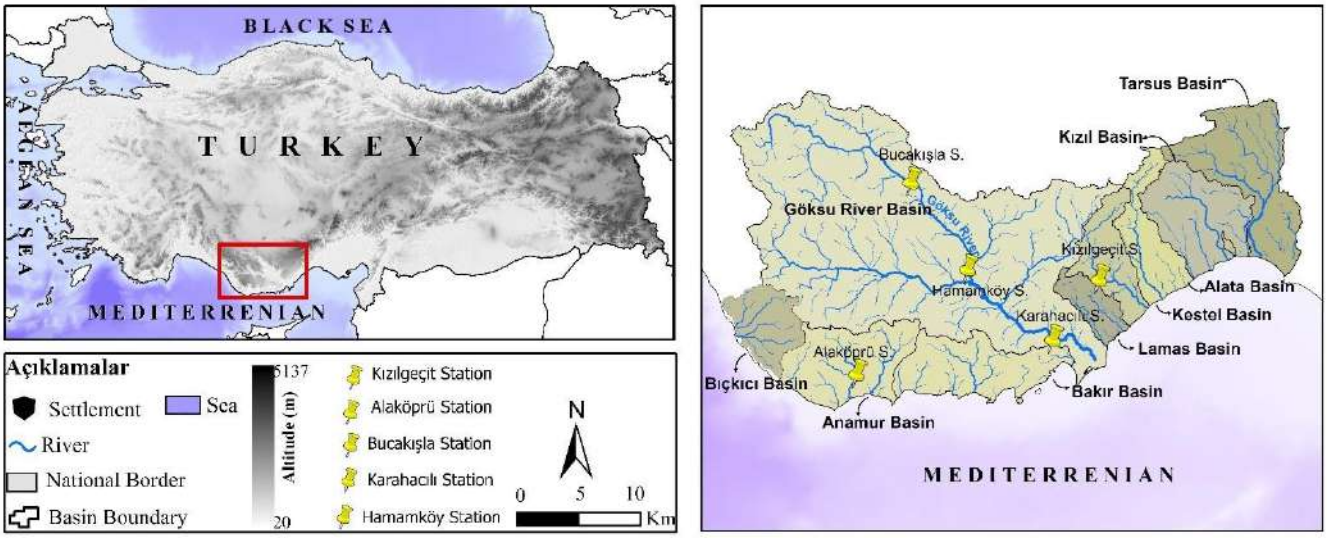

Figure 2. Eastern Mediterranean Basin and sub-basins map.

Within the scope of the study, the flow observation station data of Bucakışla, Karahacılı, and Hamamköy (on the Göksu River), Kızılgeçit (on Lamas Stream), and Alaköprü (on Anamur Stream) published by DSI were used. The station information is summarized in Table 1. The obtained data were arranged and analyzed according to Mann Kendall and innovative trend analysis method.

Table 1. Identification of stations used in the study

	Station No	Station Name	Stream	Time series
Station 1	E17A012	Bucakışla	Göksu	1962-2011
Station 2	E17A014	Karahacılı	Göksu	1961-2011
Station 3	E17A017	Kızılgeçit	Lamas	1967-2011
Station 4	E17A020	Hamamköy	Göksu	1966-2011
Station 5	1721	Alaköprü	Anamur	1968-2011

Şen Innovation Trend Analysis (Şen-ITA) Method

If the data stays above (below) this line, an ascending (descending) trend is assumed. In addition, a more detailed interpretation of the trend can be made by drawing ±5% and ±10% lines parallel to the no trend line axis [19]. If the data distribution is between the no trend line and ±5%, it is interpreted as there is a 'trend.' If it is between ±5% and ±10%, it means there is a 'strong trend,' if it is above the ±10% line, it means 'there is a very strong trend' [19] (Fig. 3). In the ITA method, besides the presence of a trend, it can also be determined on which data the trend is effective [12, 14, 19].

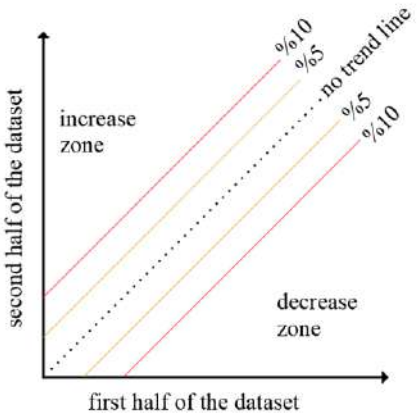

Figure 3. Display of the trends [12]

Mann-Kendall (MK) Method

The Mann-Kendall test is a non-parametric test widely used to identify statistically significant patterns in hydro-meteorological data [20, 21]. The biggest advantage of this test over parametric tests is that the statistical distribution of data variables does not affect the trend result. For this reason, in the method in question, rather than the size of the variables, the most important thing is ordering the data sizes. This test uses the 'H_0:no trend' function to determine whether a time series has a trend [22]. This approach uses the S test statistic and sign function, as shown in Eqs. 1 and 2, respectively. Then, using Eqs. 3 and 4, the variance of the S and Z test statistics is calculated.

$$\boldsymbol{S} = \sum_{\boldsymbol{i=1}}^{\boldsymbol{n-1}} \sum_{\boldsymbol{j=i+1}}^{\boldsymbol{n}} \boldsymbol{sign}(\boldsymbol{x_j} - \boldsymbol{x_i}) \tag{1}$$

$$\boldsymbol{sign}(\boldsymbol{x_j} - \boldsymbol{x_i}) = \begin{cases} \boldsymbol{-1}, & \boldsymbol{x_j < x_i} \\ \boldsymbol{0}, & \boldsymbol{x_j = x_i} \\ \boldsymbol{+1}, & \boldsymbol{x_j > x_i} \end{cases} \tag{2}$$

$$\boldsymbol{var(S)} = [\boldsymbol{n(n-1)(2n+5)} - \sum_{\boldsymbol{i=1}}^{\boldsymbol{m}} \boldsymbol{t_i i(i-1)(2i+5)}]/\boldsymbol{18} \tag{3}$$

$$\boldsymbol{Z} = \begin{cases} \frac{\boldsymbol{S-1}}{\sqrt{\boldsymbol{var(s)}}}, & \boldsymbol{S > 0} \\ \boldsymbol{0}, & \boldsymbol{S = 0} \\ \frac{\boldsymbol{S+1}}{\sqrt{\boldsymbol{var(s)}}}, & \boldsymbol{S < 0} \end{cases} \tag{4}$$

Where, n is the total number of observations, x denotes the observations at periods i and j, m denotes the total number of repeated observations in the data set, and the value of t_i denotes the repetition of observations across a length i series.

H_0 hypothesis, at the α significance level $|Z|$ accepted if $\leq Z_a/2$. The positive value of S indicates an increasing trend, and the negative value indicates a decreasing trend.

The flow ranges of the 5 stations examined within the scope of the study are shown in Fig. 4. In this graph, known as the plot box, the same time series (1968-2011) was used for all stations to establish a clear relationship between all stations. According to this graph, it is possible to see the flow changes in all stations according to the months. The lower line shows the minimum flow value, and the upper line shows the maximum flow value. While the colored part in between shows the range of accumulation in the flow values, the line in the middle shows the average value. Accordingly, Station 2 (Karahacılı) has the widest flow range, while Station 3 (Kızılgeçit) has the narrowest flow range. In April, when the widest flow range is in, the flow range of Station 2 is approximately 50-450 m3/s, while

the flow range of Station 3 is approximately 10-25 m3/s. For September, when the narrowest flow range is, the flow range of Station 4 is about 20-50 m3/s, while it is quite small for Station 3.

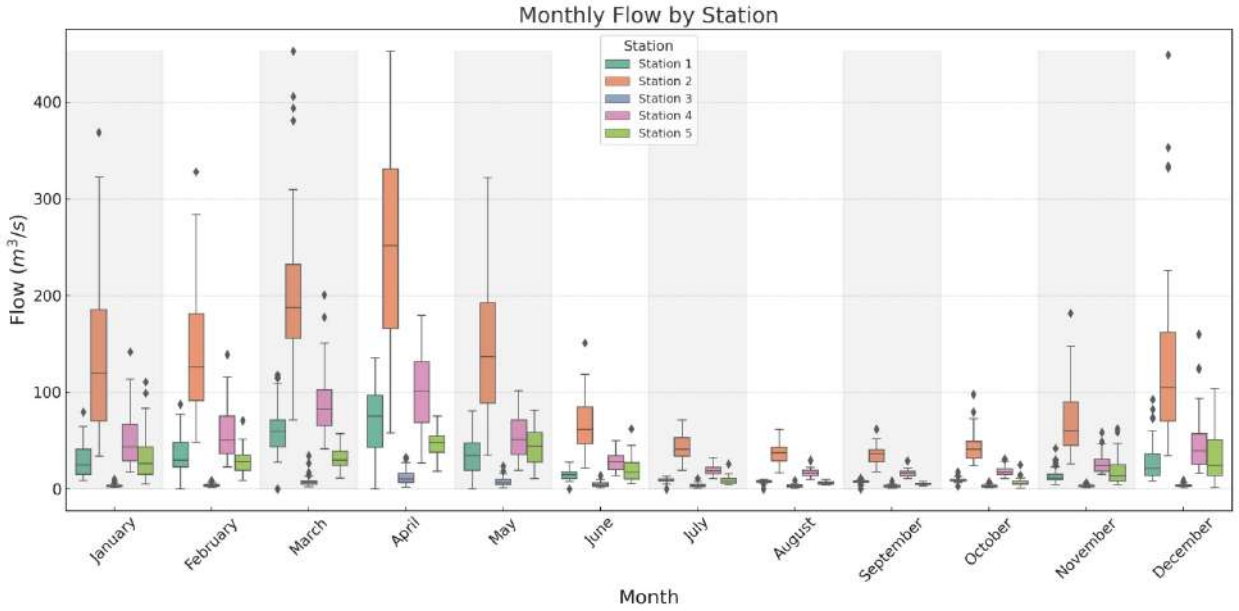

Figure 4. Box-plot for the stations

3. Results and Discussion

Within the scope of the study, trend analysis was performed using the Şen-ITA method for the flow data of 5 stations in the Eastern Mediterranean basin between 1962 and 2011. According to the results, a decreasing trend dominates in all stations (Fig. 5). When the graphs are examined in more detail, it is seen that there is a 'strong decreasing trend' for Bucakışla and Alaköprü stations because the data are distributed between (-5%) and -10% (Fig. 5a-e). It has been observed that the distribution of the data obtained from Karahacılı and Hamamköy stations is generally in the range of -5% to -10%, but for a short period, it falls below -10%, therefore it is in the range of a 'very strong decreasing trend' (Fig. 5b-d). When the flow data obtained from Kızılgeçit Station are examined, the distribution is much lower than the -10% line, so a 'very strong decreasing trend' is recorded at this station (Fig. 5c). At the stations where approximately 50 years of flow data are examined, the amount of flow observed in the second time zone is less than in the first time zone. These values were calculated as -7.36 m^3/s for Bucakışla Station, -37.55 m^3/s for Karahacılı Station, -2.79 m^3/s for Kızılgeçit Station, -14.31 m^3/s for Hamamköy Station, and -5.30 m^3/s for Alaköprü Station.

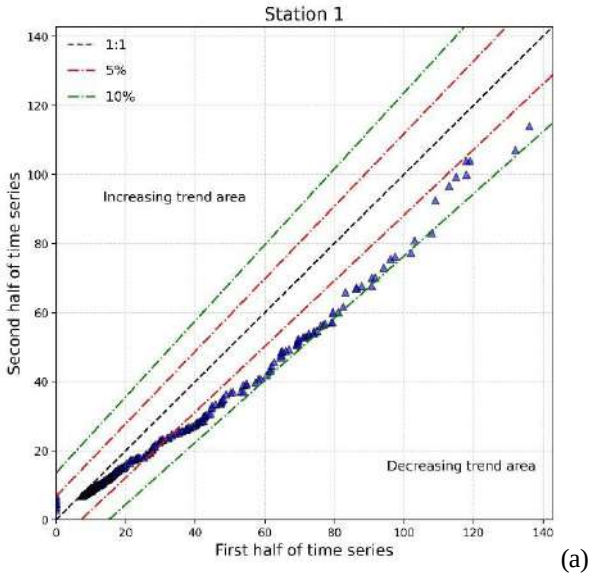

(a)

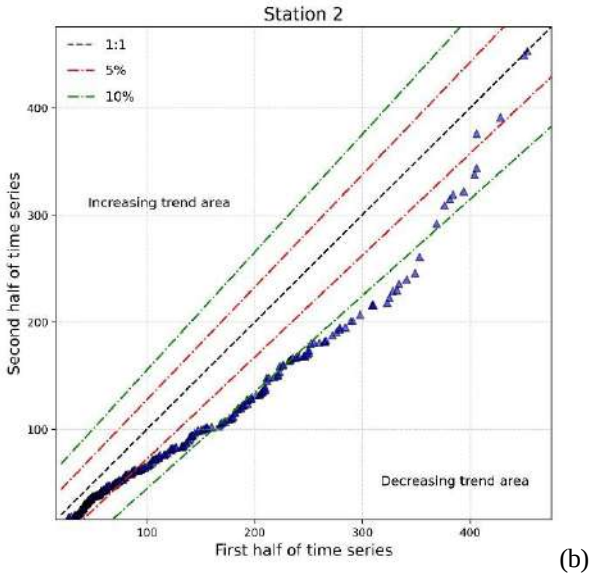

(b)

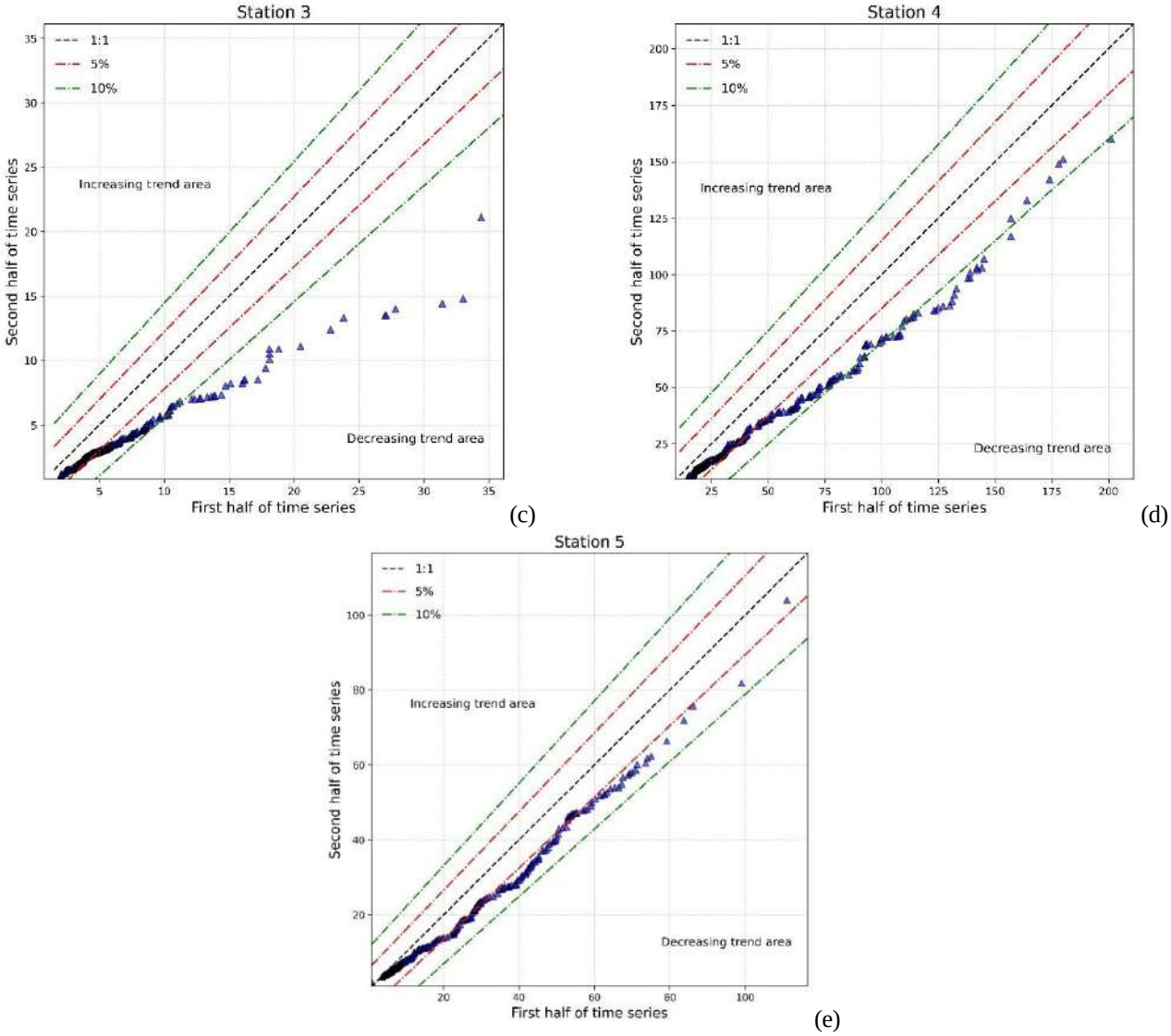

Figure 5. Şen-ITA trend graphs for: a) Bucakışla Station, b) Karahacılı Station, c) Kızılgeçit Station, d) Hamamköy Station, and e)Alaköprü Station

The results obtained for the 5 stations where MK trend analysis was applied are shown in Table 2. According to the table, it is observed that there is a decrease in the flow values at all stations, and this decrease is over the accepted value of 1.96. Therefore, there is a decreasing trend in the flow. The decreasing trend among the stations examined within the scope of the study was the 5th Station (Alaköprü), the station closest to the acceptable degree (-2.53). In contrast, the furthest decrease trend from the critical value was observed at Station 3 (Kızılgeçit) (-12.37). Therefore, when the approximately 50-year flow trends of 5 stations are compared according to Şen-ITA and MK methods, it is seen that there is a decrease in flow trends in all stations in both methods. According to both trend methods, the largest decreasing trend was observed at Station 3, while the lowest was recorded at Station 5.

Table 2. Mann-Kendall Method Trend Analysis Results

Station	Critical Z value	s	var_s	Calculated Z value	H_0	Trend
1	±1.96	-20796	24059459	-4.24	True	decreasing
2	±1.96	-31254	25530938	-6.19	True	decreasing
3	±1.96	-51802	17544195	-12.37	True	decreasing
4	±1.96	-28912	18738735	-6.68	True	decreasing
5	±1.96	-10256	16401499	-2.53	True	decreasing

Figure 6 shows the correlation matrix between stations. Each cell in this table, drawn between 1968 and 2011, shows the Pearson correlation coefficient between the flow data of the two stations concerned, so equal data for all stations are drawn. The correlation coefficient is a statistical measure that ranges from -1 to 1. A correlation coefficient close to 1 indicates a strong positive relationship between the two variables. On the other hand, a correlation coefficient close to -1 indicates a strong negative relationship. When the correlation coefficient is close to 0, it suggests a weak or negligible relationship between the two variables. According to this, it is seen that the closest relationship is between Station 1 and Station 4, with a value of 0.97. When the relationship between Station 4 and Station 2 is examined, it is seen that there is a high correlation of 0.96. This situation is thought to be because the mentioned stations are on the same river.

Figure 6. Correlation matrix between stations.

4. Conclusion

It is known that global warming caused by climate change also has effects on flow data. Especially the known flow change is important for more efficient use and management of water resources. This study examined flow trends using data from 5 flow observation stations in the eastern Mediterranean basin. Şen-ITA and MK methods have been used to analyze the data. According to the results obtained, a decreasing trend was observed in the flow data of all stations according to both methods. According to the correlation matrix created using the same time series, it was observed that there was a close relationship between stations on the same river.

5. Acknowledgements

The authors thank the General Directorate of State Hydraulic Works (DSI) for the “flow observation station” data used in the study.

6. References

[1] T.C. Çevre, Şehircilik ve İklim Değişikliği Bakanlığı, Meteoroloji Genel Müdürlüğü, ‘Hidrometeoroloji’ https://www.mgm.gov.tr/genel/hidrometeoroloji.aspx?s=3#:~:text=D%C3%BCnyam%C4%B1z%C4%B1n%202%2F3%20%C3%BC%20su,tabakalarda%20yeralt%C4%B1%20suyu%20olarak%20bulunur. (26.06.2023)

[2] Dey P. and Mishra A. “Separating the impacts of climate change and human activities on streamCow: A review of methodologies and critical assumptions” J. Hydrol. 548 278–290, 2017.

[3] Yükseler U. Küresel iklim değişikliğinin akarsuların akış potansiyellerine etkisi; Bingöl Göynük Çayı örneği. Yüksek Lisans Tezi, Fırat Üniversitesi, Denizli, Türkiye, 2019.

[4] Zhang, Q., Xu, C. Y., Zhang, Z., Chen, Y. D. “Changes of temperature extremes for 1960–2004 in Far-West China”. Stochastic Environmental Research and Risk Assessment, 23(6), 721-735, 2009.

[5] Zhang, X., Harvey, K. D., Hogg, W. D., Yuzuk, T. R. “Trends in Canadian streamflow”. Water Resources Research, 37(4), 987-998, 2001.
[6] Partal, T., Kahya, E. “Trend analysis in Turkish precipitation data”. Hydrological Processes: An International Journal, 20(9), 2011-2026, 2006.
[7] Ahn, K. H., Merwade, V. “Quantifying the relative impact of climate and human activities on streamflow”. Journal of Hydrology, 515, 257-266, 2014.
[8] Cannarozzo, M., Noto, L. V., Viola, F. “Spatial distribution of rainfall trends in Sicily (1921–2000)”. Physics and Chemistry of the Earth, Parts A/B/C, 31(18), 1201-1211, 2006.
[9] Tayanç, M., İm, U., Doğruel, M., Karaca, M. “Climate change in Turkey for the last half century”. Climatic Change, 94(3-4), 483-502, 2009.
[10] Dabanlı, İ., Şen, Z., Yeleğen, M. Ö., Şişman, E., Selek, B., & Güçlü, Y. S. “Trend assessment by the innovative-Şen method”. Water resources management, 30(14), 5193-5203, 2016.
[11] Alashan, S. “Combination of modified Mann-Kendall method and Şen innovative trend analysis”. Engineering Reports, 2(3), e12131, 2020.
[12] Şen Z.“Innovative Trend Analysis Methodology”. Journal of Hydrologic Engineering, 17, 1042-1046, 2012.
[13] Yükseler, U., Dursun, Ö. F., & Alashan, S. “Yağışların Mevsimsel Değişimlerinin Eğilim Analiz Yöntemleri İle Araştırılması: Bingöl İli Örneği”. El-Cezeri, 8(1), 45-59, 2021.
[14] Gümüş, V., Dinsever, L. D., & Şimşek, O. “Diyarbakır istasyonunda 1929–2016 boyunca tarihsel kuraklığın yenilikçi şen yöntemi ile trend analizi”. 2021.
[15] Gümüş, V., & Yenigün, K. “Aşağı Fırat Havzası akımlarının trend analizi ile değerlendirilmesi”. Yedinci Uluslararası İnşaat Mühendisliğinde Gelişmeler Kongresi, 11, 13, 2006.
[16] Alashan, S. “Innovative trend analysis methodology in logarithmic axis”. Konya Journal of Engineering Sciences, 8(3), 573-585, 2020.
[17] Alashan, S. “Comparison of sub-series with different lengths using şen-innovative trend analysis”. Acta Geophysica, 71(1), 373-383, 2023.
[18] T.C. Orman ve Su İşleri Bakanlığı, Su Yönetimi Genel Müdürlüğü, Taşkın ve Kuraklık Yönetimi Dairesi Başkanlığı ‘Doğu Akdeniz Havzası Kuraklık Yönetim Planı’ Ankara, 2018. https://www.tarimorman.gov.tr/SYGM/Belgeler/Kurakl%C4%B1k%20Y%C3%B6netim%20Planlar%C4%B1/Do%C4%9Fu%20Akdeniz%20Havzas%C4%B1%20Kurakl%C4%B1k%20Y%C3%B6netim%20Plan%C4%B1%20Y%C3%B6netici%20%C3%96zeti.pdf (26.06.2023)
[19] Tosunoglu F., Kisi O., “Trend Analysis of Maximum Hydrologic Drought Variables Using Mann-Kendall and Şen's InnovativeTrend Method”. River Research and Applications, 33, 597-610, 2017.
[20] Mann H B. “Nonparametric tests against trend”. Econometrica 13 245–259, 1945.
[21] Kendall M G. “Rank correlation methods” GriDn, London, 202p, 1948.
[22] Yenigun K., Gumus V. and Bulut H. “Trends in streamCow of the Euphrates basin, Turkey”. Water Manag. 161(4) 189–198, 2008.

International Conference on Advances and Innovations in Engineering

Optimizing Post-Conflict Building Reconstruction in Iraq: A Multi- Criteria Decision-Making Approach in Public Projects

Aya SULAIMAN [1] , Salah HAJISMAIL [2], Bahadir CALISKAN [3]

[1] Civil Engineering, Yildirm Beyazit University, Ankara, Turkey.
[2,3] Architecture, Yildirm Beyazit University, Ankara, Turkey.
1aya.falahi@gmail.com, 2salah.hajismail@aybu.edu.tr, 3ebcaliskan@aybu.edu.tr

[1](ORCID: 0009-0004-5594-8787), [2](ORCID: 0000-0001-6682-6663),[3](ORCID: 0000-0002-5258-2976)

Abstract

Multi-Criteria Decision-Making (MCDM) offers a systematic approach for navigating intricate scenarios involving conflicting objectives. This research investigates MCDM's applicability in post-conflict Iraq's public building reconstruction. Examining potential benefits and challenges, the study aims to establish its suitability. Drawing from selected sources, it showcases how MCDM facilitates informed evaluation, identifying optimal intervention strategies aligned with Iraq's context. The study identifies six key factors shaping Iraq's reconstruction projects, including building condition, finances, time, functionality, resources, and cost. The research encompasses various intervention methods like jacketing, Carbon Fiber Reinforced Polymer use, and steel incorporation, often involving partial or full structural renewal. Additionally, the study addresses obstacles hindering effective MCDM integration in reconstruction, encompassing coordination, financial constraints, security issues, personnel scarcity, time constraints, and data accessibility. Practical recommendations are offered to mitigate these challenges, aiming to enhance reconstruction outcomes.

Keywords: Intervention Strategies, Post-Conflict Reconstruction, Criteria Evaluation, MCDM, Reconstruction Management, Decision-Support

1. Introduction

In the aftermath of conflict and destruction, the reconstruction of public buildings in war-torn regions like Iraq presents an immense challenge. The decisions made during this critical phase can significantly influence the path of recovery, determining the resilience and sustainability of the rebuilt infrastructure. The complexity of reconstruction projects necessitates a comprehensive evaluation process that considers a multitude of factors, ranging from economic feasibility and social impact to environmental sustainability and cultural relevance. Traditional decision-making approaches often fall short in addressing these multifaceted considerations, underscoring the need for innovative and adaptive methodologies. This conference paper delves into the promising potential of Multi-Criteria Decision-Making (MCDM) techniques as a means to address the complexities of reconstruction projects in Iraq. MCDM is a systematic and structured approach that enables decision-makers to assess different decisions using multiple criteria simultaneously, allowing for a more comprehensive and informed evaluation of intervention methods [1]. By integrating diverse perspectives, interests, and expertise, MCDM can facilitate the identification of optimal reconstruction strategies that strike a balance between various dimensions of development.

The primary objective of this research is to explore the possibilities and obstacles associated with implementing MCDM techniques in the context of reconstruction projects in Iraq. Through an in-depth analysis of current intervention methods and stakeholder perspectives, this study seeks to shed light on the potential benefits of MCDM in fostering sustainable, inclusive, and culturally sensitive reconstruction practices. The importance of this research lies in its potential to enhance the reconstruction practices in Iraq. By applying Multi-Criteria Decision-Making (MCDM) techniques to reconstruction projects, we can move beyond the limitations of conventional decision-making and embrace a more holistic, informed, and inclusive approach.

[1]Corresponding author

2. Research Objective and Methodology

This research aims to analyse the application of Multi-Criteria Decision-Making (MCDM) techniques in reconstruction projects in Iraq. The objective is to explore the possibilities and benefits of using MCDM in this context and identify the obstacles and challenges that may arise. By critically reviewing existing literature and case studies, the paper intends to provide valuable insights to enhance decision-making processes for post-conflict reconstruction in Iraq.

The research follows the following systematic approach:

- Conduct a thorough review of existing literature and research papers related to MCDM applications in the reconstruction practices.
- Investigate the Post-Conflict Reconstruction Challenges in Iraq: particularly concerning public buildings. Aiming to identify the key challenges and considerations specific to reconstruction projects in the country.
- Analyse Reconstruction Projects of Public Buildings in Terms of MCDM Phases: This section is divided into three sub-sections, each examining different phases of MCDM in the reconstruction projects of public buildings. The criteria considered, intervention techniques, and decision-making processes utilizing MCDM techniques are explored in-depth.
- Application on a case study for further understanding and checking the ability of MCDM in obtimizing the public buildings reconstruction in Iraq.
- Present Results and discuss the findings from the literature review, case studies, and analysis of reconstruction projects in Iraq using MCDM techniques. Highlight the possibilities and address the obstacles of using MCDM in reconstruction, providing insights for successful integration in the reconstruction context.

3. Literature Review

Multi-criteria decision-making (MCDM) is a decision-making approach specifically designed to handle situations where multiple objectives need to be considered, even when these objectives may conflict with one another. By employing MCDM techniques, decision-makers can navigate the complexities of decision-making in building renovation, effectively balancing and prioritizing different objectives to achieve desired outcomes [2].

MCDM (Multi-Criteria Decision Making) involves several main steps to guide the decision-making process. Firstly, relevant criteria are identified to evaluate the alternatives. Then, weights are assigned to the criteria to indicate their importance. Alternatives are established and evaluated against the criteria to determine their performance values. Next, the criteria and weights are aggregated to obtain composite scores for each alternative. By ranking the alternatives based on their scores, the most favourable option can be identified. Figure 1 illustrates the main MCMD pashes.

Figure 6 - MCDM Application phases flowchart (Researcher)

4. Post-Conflict Reconstruction Challenges in Iraq

The decision-making process in these projects often relies on knowledge-based or single criteria decision-making techniques, with a predominant focus on the technical aspect, particularly through structural assessments. In some cases, initial cost assessments are also employed as part of the decision-making process [3]. However, it is important to note that this approach, which predominantly emphasizes the technical dimension and initial cost considerations, presents limitations in fully addressing the complexities and multidimensional nature of reconstruction projects. By solely focusing on structural assessments and initial cost estimates, other crucial aspects such as environmental, social, and long-term economic factors may be overlooked. In the context of reconstruction projects in Iraq, the managerial aspect continues to encounter significant obstacles that hinder its overall performance.

Post-conflict reconstruction in Iraq presents several challenges that need to be addressed to ensure effective and efficient rebuilding of public buildings. One of the key challenges is the coordination between various competent authorities involved in the reconstruction process. Limited financial support is another significant constraint, often leading to rationing of resources and necessitating minimal intervention [4]. The prevailing difficult security conditions further impede the movement of personnel and transportation of essential materials, hampering the reconstruction efforts. Additionally, there is a shortage of experienced staff, which can hinder the successful implementation of reconstruction projects. The limited time frame for reconstruction does not allow for a comprehensive review and audit of the original building design. Moreover, accessing technical documents related to the building's construction and maintenance history can be problematic, hindering the decision-making process during reconstruction [5].

According to [6], contractor-related problems were the top-ranking issues. The following sub-issues were identified as the dominant ones within this broad category: 1) lack of leadership capabilities and skills, 2) lack of standards for human resources management, 3) lack of education in what drives performance, 4) lack of skills in dealing with time limitations, 5) lack of building of harmonic work teams, 6) lack of vision of how to deal with the owner, external parties, and the work teams, and 7) lack of strategic planning of the work performed by subcontracting companies.

5. Reconstruction Projects of Public Buildings in Terms of MCDM Phases

During interventions for damaged public buildings, it is important to consider not only the functional aspects but also the symbolic, social, and environmental significance of the building. However, it has been observed that in many cases, the demolition option is often preferred without giving sufficient attention to these aspects. The symbolic value of a building holds cultural, historical, and architectural importance that contributes to the identity and heritage of a community. Preservation and restoration of these symbolic structures can foster a sense of pride, continuity, and cultural identity among the people[4]. Public buildings often serve as gathering spaces and community hubs, playing a vital role in the social fabric of a neighbourhood or city. The loss of such buildings can disrupt social connections and community cohesion. Demolition and reconstruction can have significant environmental implications, including the generation of construction waste, increased energy consumption, and the loss of embodied energy in the existing structure. Adopting sustainable practices such as adaptive reuse, retrofitting, or incorporating environmentally friendly materials can minimize the environmental footprint and promote sustainable development [7].

5.1. The Criteria Considered

Having well-defined criteria considered in MCDM phases is crucial for making informed decisions, allocating resources optimally, ensuring safety, preserving cultural heritage, engaging the community, and promoting sustainability and long-term viability. It also helps in managing time efficiently and mitigating potential risks, leading to successful and meaningful reconstruction outcomes.

[3] highlight six key factors: building condition, funding availability, time needed, meeting the intended function, resource availability, and total cost. Assessing the building's structural integrity and safety, along with available financial resources, influences the chosen approach—whether reconstruction or repair. Minimizing downtime and

efficiently serving the building's intended purpose are vital considerations. Evaluating the availability of skilled labour, materials, and technology enables effective planning. Additionally, managing costs and adhering to budget constraints is crucial for a sustainable reconstruction process. Overall, a thorough evaluation of these criteria empowers decision-makers to make informed choices that lead to successful reconstruction projects, benefitting communities in Iraq.

Additional criteria were proposed following a thorough review of the existing literature, aimed at enhancing the consideration of economic, social, and environmental dimensions. These newly introduced criteria encompass availability of knowledge and technology, meeting the funding conditions, maximization of functionality, user contentment, energy efficiency, and emissions. The Criteria are listed in Table 1.

Table 1. Criteria Suggested

Code	Criteria	Category
C1	Building condition	Technical
C2	Resources availability	
C3	Time needed	
C4	Meeting the required function	
C5	Maintainability	
C6	Availability of Knowledge and Technology	
C7	Total cost	Economic
C8	Meeting the funding Conditions	
C9	Maximization of functionality	Social
C10	User Satisfaction	
C11	Energy efficiency	Environmental
C12	Emissions	

5.2 Intervention Methods

Various intervention methods have been employed to repair, strengthen, and restore these damaged structures. The selection of intervention methods depends on several factors, including the extent of damage, structural conditions, available resources, and the specific requirements of each building [4]. Commonly, repair methods involve repairing damaged components of the building, to restore their functionality and structural integrity. Strengthening techniques are applied when the structural stability of the building has been compromised. These methods aim to enhance the building's resistance to future damage by adding additional supports or reinforcing existing elements. In severe cases where the damage is extensive or poses significant safety risks, reconstruction may be necessary. This involves demolishing the damaged structure and rebuilding it using new materials and construction techniques, ensuring compliance with safety standards and regulations [8].

The most common intervention methods for damaged public buildings are full or partial demolition and reconstruction, and repair. The choice between these methods is often influenced by the availability of financial resources. If sufficient resources are available, reconstruction is typically chosen as the preferred option. On the other hand, if financial resources are limited, the repair option is usually pursued. Repair involves selectively addressing the specific areas or components of the building that have been damaged, without undertaking a complete reconstruction [3].

5.3 Technique for Order of Preference by Similarity to Ideal Solution (TOPSIS)

TOPSIS, a multicriteria decision-making method developed by Hwang and Yoon in 1981, aims to find the best alternative based on the closest distance to the ideal solution and furthest from the anti-ideal solution. This approach employs the Euclidean distance to evaluate the relative proximity of an alternative to the optimal solution [9].

The decision to utilize the TOPSIS technique in this case was based on several factors that contribute to its suitability and effectiveness in the context of reconstruction projects in Iraq.

- Firstly, TOPSIS has already gained widespread acceptance and application in the engineering community in the construction projects, making it a familiar and accessible method for decision-makers in the field. This familiarity reduces the need for extensive explanations and enhances the ease of implementation.
- Additionally, previous research by [10] indicated that TOPSIS is the most commonly used technique, reinforcing its relevance and applicability in this specific domain. By leveraging a well-established and frequently employed method, decision-makers can benefit from existing knowledge and experiences, leading to more informed and reliable decision-making.
- Moreover, the distance-based nature of the TOPSIS technique contributes to its efficiency as a decision support tool. By measuring the distances of alternatives from the ideal and negative ideal solutions, TOPSIS allows for a clear differentiation between alternatives, facilitating the identification of the best possible option. This efficiency is particularly valuable in reconstruction projects, where time constraints and resource limitations often demand a streamlined decision-making process.
- Furthermore, the simplicity and ease of implementation of TOPSIS have contributed to its widespread use, and its steps remain the same regardless of the number of attributes. Moreover, the method can be easily programmed and implemented using different software applications such as Microsoft Excel, Decerns MCDA, Scikit-Criteria, R, Online Output, and MATLAB makers [11].

TOPSIS is a multicriteria decision-making method that considers both the distance to the positive ideal solution (Si+) and the negative ideal solution (Si-) to determine the proximity of each alternative to the ideal solution. Based on this comparison, an alternative priority arrangement (Ai) can be achieved. The positive ideal solution (A+) is defined as the sum of the best attainable values for each attribute, while the negative ideal solution (A-) is the sum of the worst values [12] As presented in Figure 7, after constructing the initial decision matrix with alternatives, criteria and their corresponding performance values.

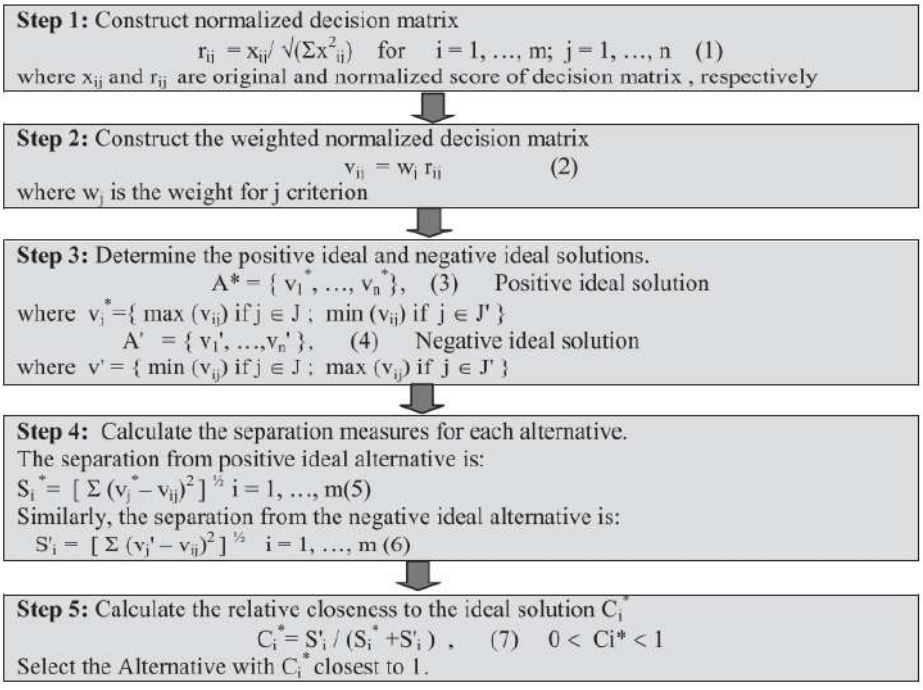

Figure 7. Main steps of TOPSIS methodology, Source:[13]

6. Case Study Application

To demonstrate the practical application of the MCDM application, a detailed case study of a public building reconstruction project in Iraq will be presented. The case study will showcase the tool's efficacy in addressing real-world challenges, weighing diverse criteria, and guiding stakeholders towards sustainable and socially responsible

reconstruction decisions. The case study project involves the reconstruction of a hospital situated in the city of Hit within the al-Anbar province of Iraq. The hospital's reconstruction aims to enhance medical services, cater to the community's healthcare needs, and contribute to the overall rehabilitation of the region.

Work began at the hospital in 2012. Military operations started in the city of Hit in 2015, causing a halt in its operations. Hit Hospital was subjected to bombardment several times during the years 2015 and 2016. The hospital consists of a reinforced concrete structure with the partitions built using concrete blocks. The building is composed of 6 main sections, along with two sections for the doctor's residence and a section for the service building (See Figure 3).

Figure 8. The building top view and plan layout

6.1. Decision Making Process

In the case of the hospital reconstruction project in Hit, the tool covers a diverse set of criteria representing technical, economic, environmental, and social aspects as explained in the previous section. These criteria include but are not limited to structural integrity, construction cost, energy efficiency, environmental impact, community impact, and functionality.

The decision to incorporate these alternatives was based on expert input, ensuring a comprehensive exploration of possible strategies. Each criterion is assigned a weight that reflects its relative importance in achieving the project's overall objectives. The process of assigning weights involves engaging stakeholders and experts to provide their insights and preferences. The process of decision making is illustrated in Table 2 and Table 3.

Table 2. Decision Making Matrix

weightage	***0.15***	***0.1***	***0.08***	***0.08***	***0.06***	***0.1***	***0.08***	***0.12***	***0.06***	***0.05***	***0.07***	***0.05***
	Benf.	***Benf.***	***Non Benf.***	***Benf.***	***Benf.***	***Benf.***	***Non Benf.***	***Benf.***	***Benf.***	***Benf.***	***Benf.***	***Benf.***
	C1	**C2**	**C3**	**C4**	**C5**	**C6**	**C7**	**C8**	**C9**	**C10**	**C11**	**C12**
Change of use	1	8	12	1	4	4	750	1	3	2	5	8
Retrofit	6	7	18	9	6	7	1500	8	6	9	7	7
Partially Demolition	6	8	20	9	7	8	2500	7	7	7	6	3
Full Demolition	3	7	24	9	9	8	10000	5	8	6	5	1
Retrofit + Partially Demolition	9	7	18	9	7	7	2000	8	7	8	7	6
Reduce Capacity	9	8	8	6	2	5	1000	9	3	5	7	7

Table 3. Performance score for each alternative

Alternatives	Si+	Si-	Pi
Change of use	0.144	0.077	0.348
Retrofit	0.081	0.108	0.570
Partially Demolition	0.095	0.099	0.511
Full Demolition	0.138	0.062	0.310
Retrofit + Partially Demolition	0.079	0.121	0.606
Reduce Capacity	0.019	0.165	0.897

6.2. Results Discussion

The final decision emerges from a rigorous analysis of diverse stakeholder experts' inputs and assessment results. It is a product of merging subjective opinions, technical analysis, and quantitative evaluations. The chosen intervention method is the one that emerges as the most promising and aligned with the project's goals, considering factors like cost-effectiveness, functionality enhancement, and implementation feasibility.

The most suitable intervention strategy for this case is to prioritize capacity reduction, provided it is a feasible option. In situations where capacity reduction is not feasible, the alternative intervention approach of retrofitting combined with partial demolition emerges as the preferred solution. The prioritization of capacity reduction reflects a proactive approach to address the hospital's immediate needs while also factoring in potential future demands, optimizing resource allocation, and ensuring a sustainable and resilient healthcare facility. The chosen intervention strategy, whether it is the prioritization of capacity reduction, or the retrofitting combined with partial demolition approach, is fundamentally aligned with the overarching goals and objectives of the reconstruction project.

The insights garnered from expert opinions provide valuable perspectives on both the contributions of the newly devised reconstruction decision-making framework. Experts unanimously acknowledge that the Multi-Criteria Decision-Making (MCDM) significantly contributes to the field of reconstruction by providing a structured and comprehensive approach that surpasses the conventional methods. This holistic perspective equips decision-makers to navigate the intricate web of reconstruction dynamics and ensures a more sustainable and resilient outcome. Experts appreciate the systematic integration of stakeholder preferences, thereby enhancing the transparency, inclusivity, and consensus-building aspects of the decision-making process.

Uncertainties can arise from factors such as changing economic conditions, unforeseen challenges during implementation, and variations in stakeholder preferences. These uncertainties can impact the accuracy of criteria weights and alternative evaluations, potentially leading to different outcomes under altered conditions. Additionally, assumptions made during the decision-making process, like the availability of resources or the long-term effectiveness of chosen interventions, should be carefully examined for potential biases. Despite these challenges, experts concur that the MCDM tool remains a remarkable step forward in advancing the reconstruction decision-making domain.

7. Conclusion

The review reveals that Multi-Criteria Decision-Making (MCDM) techniques have been applied to construction projects of public buildings in Iraq, showcasing their potential to enhance decision-making processes. Meanwhile, the application of MCDM particularly in reconstruction projects, has been significantly overlooked in Iraq, as evidenced by the scarcity of previous studies. The limited focus on environmental and social aspects, coupled with an exclusive emphasis on initial costs within the economic aspect, has led to erroneous decision-making practices. Furthermore, the pervasive issues of corruption and inadequate technological resources have further complicated matters, increasing the likelihood of resource wastage.

In Iraq, the conventional approach to decision-making in construction projects has been primarily focused on single-criteria analysis, with a primary emphasis on cost reduction to maximize profits. In recent years, there has been an increasing recognition of the need to adopt a holistic approach that goes beyond purely technical considerations when making decisions regarding reconstruction projects in Iraq. This recognition stems from an understanding that reconstruction efforts not only involve technical aspects, but also have broader implications for the environment, society, and the economy. However, this approach has led to a lack of comprehensive criteria in decision analysis. Previous studies have also tended to focus on specific aspects of the project, further limiting the range of criteria considered.

The application of Multi-Criteria Decision-Making (MCDM) techniques in the reconstruction projects of public buildings as seen in the case study, offers several significant benefits, including comprehensive evaluation of criteria, transparency, stakeholder engagement, flexibility, risk management, and improved project outcomes. Embracing MCDM techniques enables more informed and accountable decision-making, fostering resilient and inclusive reconstruction in post-conflict regions like Iraq.

The findings indicate several possibilities and benefits associated with employing MCDM techniques in reconstruction projects. Firstly, MCDM allows for a systematic and structured approach to decision-making, promoting transparency and objectivity. Secondly, by incorporating social, economic, environmental, and cultural criteria, MCDM fosters more sustainable and inclusive development. Thirdly, the integration of stakeholder perspectives empowers local communities and promotes ownership, resulting in more contextually appropriate and culturally sensitive interventions. Despite the potential benefits, the review identifies certain obstacles and challenges in the successful implementation of MCDM techniques in Iraq's reconstruction projects. Limited availability of reliable data, especially in post-conflict environments, may hinder the accurate assessment of criteria. Additionally, the complexity of some MCDM methods may pose challenges for decision-makers with limited technical expertise. Ensuring effective stakeholder engagement and consensus-building may also be challenging, as diverse interests and perspectives may need to be reconciled.

8. Acknowledgements

The authors would like to extend their heartfelt gratitude to Mr.Abdalla Alhamdany, Mr.Muaffeq Othman, Mr.Abdulfattah Jawhar and Mr.Ayman Hameed for their valuable contributions and expertise that greatly enriched this research.

9. References

[1] T. Comes, M. Hiete, N. Wijngaards, and F. Schultmann, “Decision maps: A framework for multi-criteria decision support under severe uncertainty,” *Decis. Support Syst.*, vol. 52, no. 1, pp. 108–118, 2011, doi: 10.1016/j.dss.2011.05.008.

[2] A. N. Nielsen, R. L. Jensen, T. S. Larsen, and S. B. Nissen, “Early stage decision support for sustainable building renovation - A review,” *Build. Environ.*, vol. 103, pp. 165–181, 2016, doi: 10.1016/j.buildenv.2016.04.009.

[3] M. Othman, “Personal Communication,” 2023, p. June.

[4] A. Hameed, “Personal Communication,” 2023.

[5] A. Jawhar, “Personal Communication,” 2023, p. June.

[6] R. A. Waheeb and B. S. Andersen, “Causes of Problems in Post-Disaster Emergency Re-Construction Projects—Iraq as a Case Study,” *Public Work. Manag. Policy*, vol. 27, no. 1, pp. 61–97, 2022, doi: 10.1177/1087724X21990034.

[7] S. Raoof, “A Study about the Demolition of Traditional Houses in Mosul (Social and Economical Study),” *Tanmiyat Al-Rafidain*, vol. 32, no. 97, pp. 264–279, 2010, doi: 10.33899/tanra.2010.161916.

[8] R. M. Alhamawe, “The Role of united Nations Development program in the Reconstruction of Afflicted cities,” *Coll. Law Polit. Sci.*, vol. 25–7, no. 16, p. 45, 2022.

[9] A. Afshari, M. Mojahed, and R. Yusuff, “Simple additive weighting approach to personnel selection problem,” *Int. J. Innov. Manag. Technol.*, vol. 1, no. 5, pp. 511–515, 2010, doi: 10.7763/IJIMT.2010.V1.89.

[10] M. M. Alam and A. Hammad, “A Hybrid Multi-Criteria Decision Support System for Selecting the Most

Sustainable Structural Material for a Multistory Building Construction," *Sustain.*, vol. 15, no. 4, 2023, doi: 10.3390/su15043128.

[11] N. A. Azhar, N. A. M. Radzi, and W. S. H. M. Wan Ahmad, "Multi-criteria Decision Making: A Systematic Review," *(Recent Adv. Electr. Electron. Eng. (Formerly Recent Patents Electr. Electron. Eng.*, vol. 14, no. 8, pp. 779–801, 2021, doi: 10.2174/2352096514666211029112443.

[12] M. M. D. Widianta, T. Rizaldi, D. P. S. Setyohadi, and H. Y. Riskiawan, "Comparison of Multi-Criteria Decision Support Methods (AHP, TOPSIS, SAW & PROMENTHEE) for Employee Placement," *J. Phys. Conf. Ser.*, vol. 953, no. 1, 2018, doi: 10.1088/1742-6596/953/1/012116.

[13] M. Behzadian, S. Khanmohammadi Otaghsara, M. Yazdani, and J. Ignatius, "A state-of the-art survey of TOPSIS applications," *Expert Syst. Appl.*, vol. 39, no. 17, pp. 13051–13069, 2012, doi: 10.1016/j.eswa.2012.05.056.

International Conference on Advances and Innovations in Engineering

An overview of the global land water storage data set release 2 (GLWS2.0)

Emel Zeray ÖZTÜRK[1]

[1]Department of Geomatics Engineering, Faculty of Engineering and Natural Sciences, Konya Technical University, Konya, Türkiye.
[1]ezozturk@ktun.edu.tr

[1](ORCID: 0000-0002-7498-5258)

Abstract

This research focuses on the evaluation of the new global land water storage dataset, GLWS2.0. This dataset is generated by assimilating monthly GRACE/GRACE-FO mass change maps into the WaterGAP global hydrology model via a set of Kalman filters. GLWS2.0 encompasses anomalies in total water storage (TWSA) across global land regions (excluding Greenland and Antarctica). With a spatial resolution of 0.5°, it spans from 2003 to 2019 continuously. The applicability of GLWS2.0 was examined in three distinct regions with varying characteristics, utilizing different datasets. It is illustrated that, in some regions, GLWS2.0 fits better than GRACE/GRACE-FO mascons to GLDAS CLSM observations of total water storage anomalies.

Keywords: GLWS, GRACE, GRACE-FO, GLDAS CLSM, Total water storage anomalies

1. Introduction

In geodesy and geodynamics, model-based mass redistribution maps are being superseded by The Gravity Recovery and Climate Experiment (GRACE) and GRACE-FollowOn (GRACE-FO) data, increasingly. Additionally, GRACE/GRACE-FO TWSA monthly anomalies are widely used in climate and hydrology applications. These include quantifying glacier mass balance trends [1], evaluating groundwater variations [2], assessing droughts [3–6] examining vegetation response to moisture [7,8], enhancing land surface and atmospheric models [9], and refining soil process representation in models [10]. However, considering the 11-month data gap between the GRACE and GRACE-FO missions as well as the spatial resolution of GRACE/GRACE-FO of about 300 km, working with GRACE-based TWSA time series might be challenging.

Recent studies have attempted to predict forecast TWSA by modeling the gaps between GRACE/GRACE-FO missions or the pre-GRACE period through machine learning [11,12]. There are also studies assimilating TWS anomalies that can be reduced to canopy water, soil moisture and groundwater variations by integrating in situ and remote sensing data [13,14]. Nevertheless, many of these applications focusing on hydrological applications are regionally limited. In addition, some assimilations use GRACE/GRACE-FO level-3 data grids, which means that some adjustable procedures in the standard solutions are ignored. Taking into account all of these, an alternative to the Catchment Land Surface Model (CLSM), which is one of the few global products, and at the same time a model with known uncertainty quantification was needed.

The new global land water storage version 2.0 data (GLWS2.0), which will be examined in this study, has been produced and made available to meet the needs mentioned above. The model combines data from the GRACE/GRACE-FO and WATERGAP model and offers a TWSA dataset that includes surface mass changes eligible for geodetic and geodynamic investigations. In this study, the usability of TWS anomalies obtained from the GLWS 2.0 model was investigated by comparing them with Global land data assimilation system (GLDAS) catchment land surface models (CLSM) and GRACE level-3 (mascon) TWS anomalies at 3 different points. This contribution starts with a description of GLWS2.0 Model. Then, the GLDAS CLSM and GRACE/GRACE-FO

[1]Corresponding author

mascons used for comparison and evaluation are introduced. Next, GLWS2.0 is compared to GRACE/GRACE-FO mascons and GLDAS CLSM TWSA in the selected points and the results are discussed.

2. Validation Data and GLWS2.0 Model

Land surface models (LSMs) simulate the interactions between the Earth's surface and the atmosphere. They are effective instruments for analyzing the terrestrial water balance and forecasting changes in the land surface [15,16,17]. The Global Land Data Assimilation System (GLDAS), enabled by NASA, offers consistent and frequent data on water and energy components. [18]. It combines data from remote sensing and ground-based observations to provide measurements (such as evapotranspiration, runoff, and snow water equivalent) that are not directly observable through satellite data [18] or achievable through basic models. In this contribution, GLDAS Version 2.1 is employed for the evaluation of GLWS2.0. Version 2.1 provides data from 2000 to present, which is forced with a combination of observation and model data from the NOAA/GDAS (Global Data Assimilation System, [19]), GPCP (Global Precipitation Climatology Project [20,21] and the AGRMET (Air Force Weather Agency's AGRicultural METeorological modeling system). GLDAS-2.1 is publicly available and does not include data assimilation.

GRACE satellite mission, conducted jointly by the German Aerospace Center (DLR) and NASA's Jet Propulsion Laboratory (NASA/JPL). It utilized a K-band instrument to carry out range-rate measurements between two co-orbiting platforms tracked by GNSS (Global Navigation Satellite System). Launched in 2002, GRACE was originally planned for a five-year mission but operated for nearly 15 years until its conclusion in 2017 [22]. Its successor, GRACE-FO, was launched in 2018 and remains in orbit. In this study, GRACE/GRACE-FO GSFC (Goddard Space Flight Center) 1-arc-degree mascons are used between 2002-2020, which was determined as the study period in order to validate GLWS2.0. These set of mascons are publicly available.

GLWS2.0 with a spatial resolution of 0.5º was developed by assimilation based on the Kalman filter approach [23]. The model, synthesizing the GRACE/GRACE-FO and WaterGAP projects, provides a TWSA dataset containing reference surface mass changes for geodetic and geodynamic studies [24]. For obtaining GLWS2.0, level-2 spherical harmonic geopotential coefficients derived from GRACE/GRACE-FO instrument data collected at TU Graz were employed. The choice of the ITSG 2018 data product was based on its inclusion of complete error information which is considered essential to represent the predominant uncertainty patterns associated with GRACE during assimilation. The level-2 data were subsequently transformed into Total Water Storage Anomaly (TWSA) maps using standard processing steps, including replacing specific lower degree coefficients, applying a de-striping technique (DDK) as outlined by [25], eliminating the temporal mean from 2003 to 2016 (a timeframe determined before the GRACE/GRACE-FO gap). In order to remove gravity changes connected to glacial isostatic adjustment, the model proposed by [26] was used. Another dataset used to acquire GLWS2.0, the WaterGAP hydrology model simulates water flows and reservoirs on a 0.5º grid by resolving equations for vertical and horizontal water balances. What sets WaterGAP apart from various other land surface models is its incorporation of human-driven water consumption, which includes irrigation, livestock husbandry, manufacturing, domestic usage, and cooling of thermal power plants.

The gridded GLWS 2.0 TWSA which is publicly available is decomposed into different layers that include storage changes such as groundwater, soil, snow and surface water. The previous version (GLWS1.0) has been improved by updating with a new WaterGAP model version and a few bug fixes.

3. Results

The points selected for the test are given in Figure 1. These points S1, S2 and S3 are chosen from the centers of the mascon numbers of #9013, #8990 and #9079, respectively. Hereafter mascons #9013, #8990 and #9079 are referred to as mascon1, mascon2 and mascon3. The trends of each mascon are given in Figure 2.

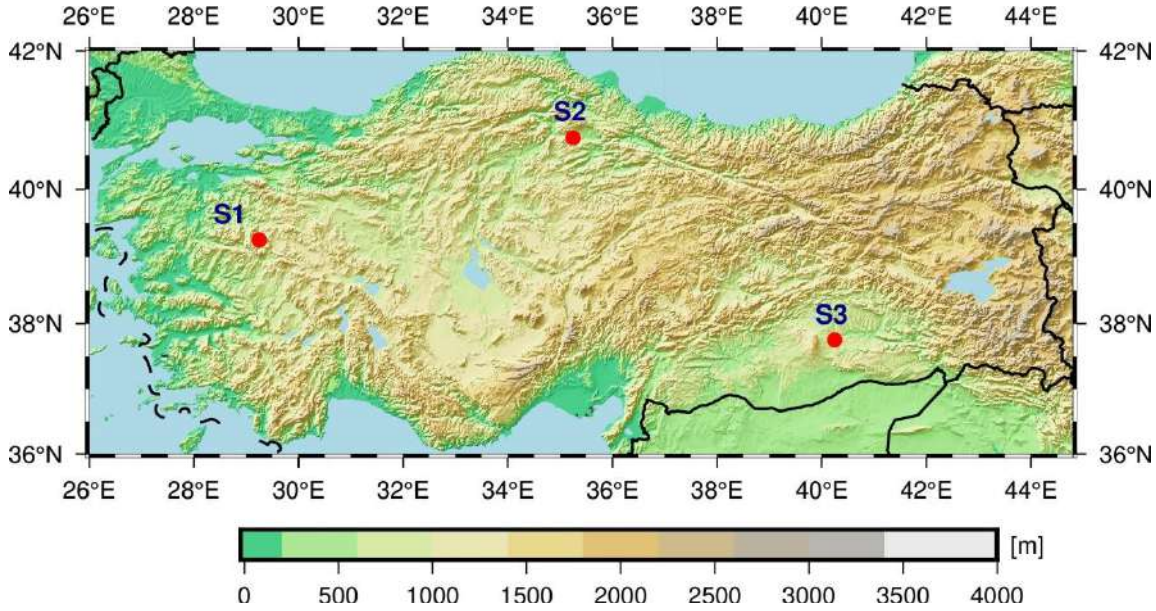

Figure 1. Test points S1, S2, S3

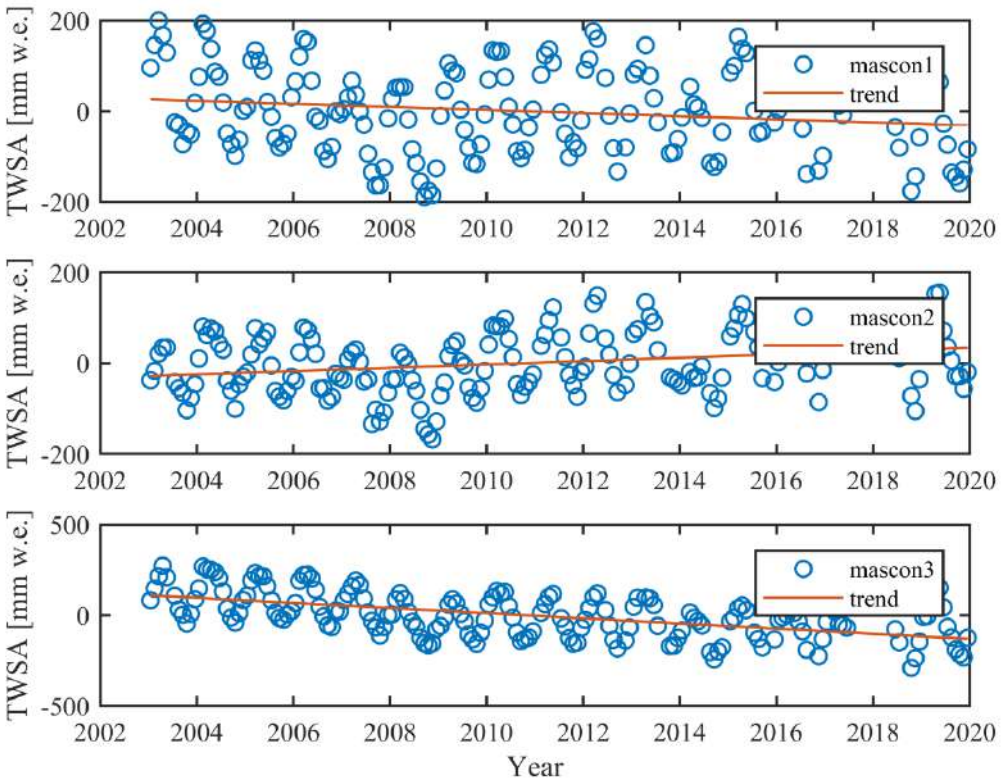

Figure 2. Time series of three mascons and their trends

According to Figure 2, selected 3 points have different features and trend rates. In the time series given in Figure 2 for the years 2002-2020, mascon2 shows a positive trend of 3.66 mm/year, while mascon3 shows a negative trend of 14.13 mm/year. Mascon1 also shows a negative trend with a rate of 3.40 mm/year. However, it has a smaller trend rate and is close to stationary compared to mascon3.

GLWS2.0 was evaluated with 2 different data sets (GLDAS and mascons) at 3 test points and the differences between them were analyzed. The time series of the 3 data sets at the 3 test points are illustrated in Figure 3.

Statistics of the GLWS-GLDAS and GLWS-mascons differences at S1, S2, S3 test points are given in Table 1. From the results, it can be stated that at S1, the GLWS and mascon datasets best overlapped. In addition to this, the difference between the GLWS and mascon datasets at point S3 has the highest standard deviation value. Moreover, both data sets have the lowest correlation at point S2. The differences between mascon and GLWS seen at points S2 and S3 can be attributed to the flexibility in the processing of GRACE/GRACE-FO based spherical harmonics used to obtain the GLWS. The correlations between the GLWS and the corresponding GLDAS and mascon data range from 10.0 to 81.7%. They induced high correlation at points S1 and S3. In Table 1, it can be seen that the standard deviations of GLWS and GLDAS differences vary from 4.4 to 8.4 cm.

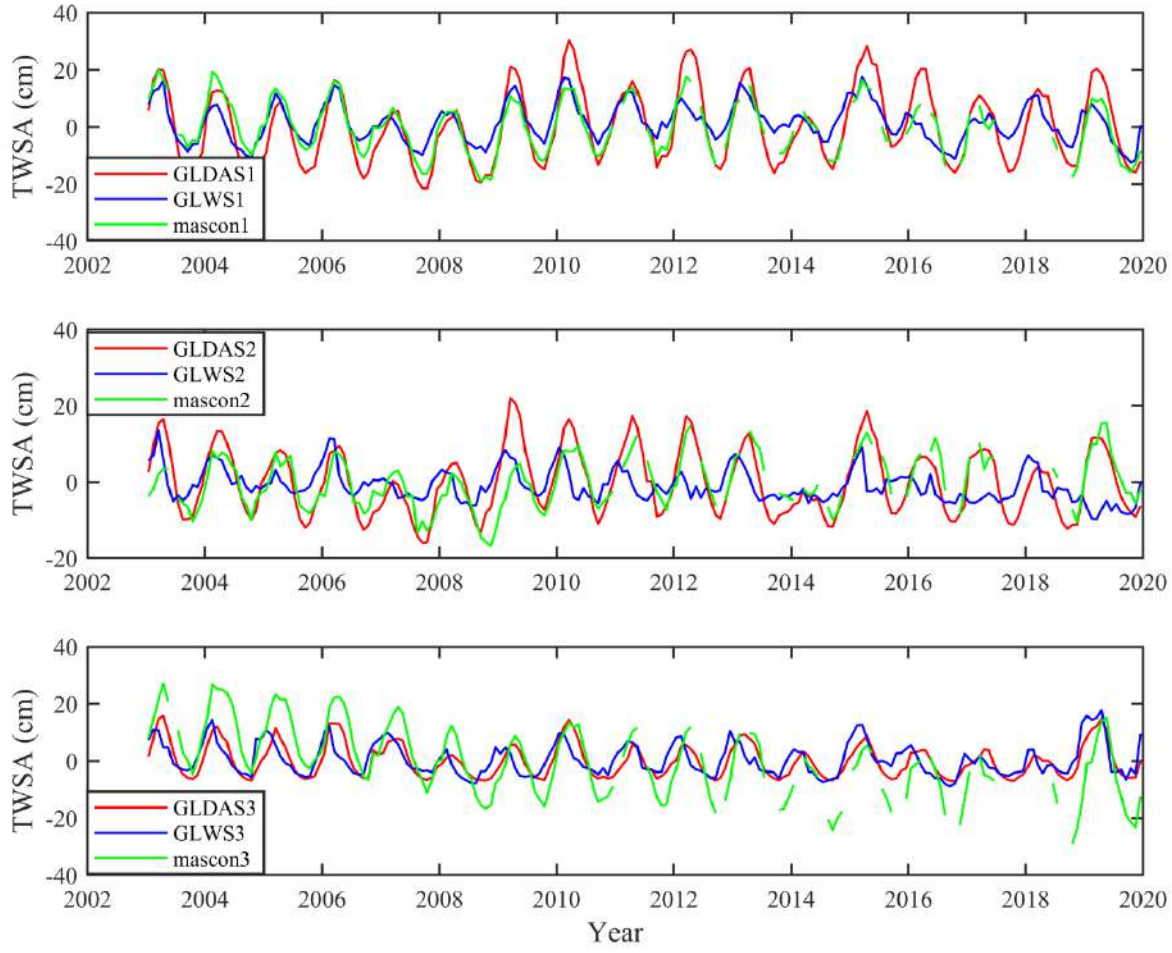

Figure 3. Time series of total water storage anomalies for S1, S2, S3 test points

Table 6. Statistics of the GLWS-GLDAS and GLWS-mascons differences at S1, S2, S3 test points [cm]

1. Column	Min	Max	Mean	Std	Corr. coef
GLWS1 - GLDAS1	-23.9	15.6	1.3	8.4	0.8
GLWS1 - mascon1	-13.1	13.9	1.4	5.4	0.8
GLWS2 – GLDAS2	-21.5	12.6	-0.9	7.9	0.4
GLWS2 – mascon2	-22.5	16.3	-0.9	7.6	0.1
GLWS3 – GLDAS3	-11.6	11.3	0.5	4.4	0.7
GLWS3 – mascon3	-22.5	28.5	1.0	11.0	0.4

The results show that the agreement between GLWS, GLDAS and mascon datasets might vary according to the characteristics of the study area. Generally, GLDAS and GLWS have higher correlations at all three test points. In future studies, it is recommended that the independent data sets GLWS2.0 and GLDAS-2.1 be evaluated together in regions where interannual variations of TWSA values are high.

4. Acknowledgements

The author would like to thank NASA and GSFC for publicly available data.

5. References

[1] Wouters B, Gardner AS, Moholdt G. “Global glacier mass loss during the GRACE satellite mission (2002-2016)”. Frontiers in earth science, 7, 96, 2019.
[2] Richey AS, Thomas BF, Lo M-H, Reager JT, Famiglietti JS, Voss K, Swenson S, Rodell M. “Quantifying renewable groundwater stress with GRACE”. Water Resour Res., 51(7):5217–5238, 2015.
[3] Zhao M, Geruo A,Velicogna I, Kimball JS. “A global gridded dataset of grace drought severity index for 2002–14: comparison with PDSI and SPEI and a case study of the Australia millennium drought”. J Hydrometeorol., 18(8):2117–2129, 2017.
[4] Gerdener H, Engels O, Kusche J. “A framework for deriving drought indicators from the Gravity Recovery and Climate Experiment (GRACE)”. Hydrol Earth Syst Sci, 24(1):227–248, 2020.
[5] Reager JT, Thomas BF, Famiglietti JS. “River basin flood potential inferred using GRACE gravity observations at severalmonths lead time”, Nat Geosci., 7(8):588–592, 2014.
[6] Han S-C, Ghobadi-Far K, Yeo I-Y, McCullough CM, Lee E, Sauber J. “GRACE Follow-On revealed Bangladesh was flooded early in the 2020 monsoon season due to premature soil saturation”. Proc Natl Acad Sci, 118(47):e2109086118, 2021.
[7] Geruo A, Velicogna I, Kimball JS, Du J, Kim Y, Colliander A, Njoku E. “Satellite-observed changes in vegetation sensitivities to surface soil moisture and total water storage variations since the 2011 Texas drought”. Environ Res Lett, 12(5):054006, 2017.
[8] Gerdener H, Kusche J, Schulze K, Ghazaryan G, Dubovyk O. “Revising precipitation–water storages–vegetation signatures with grace-based data assimilation”. J Hydrol, 612(A):128096, 2022.
[9] Springer A, Kusche J, Hartung K, Ohlwein C, Longuevergne L. “New estimates of variations in water flux and storage over Europe based on regional (re)analyses and multisensor observations”. J Hydrometeorol, 15(6):2397–2417, 2014.
[10] Swenson SC, Lawrence DM. “Assessing a dry surface layer-based soil resistance parameterization for the Community Land Model using GRACE and FLUXNET-MTE data”. J Geophys Res: Atmos, 119(17):10299–10312, 2014.
[11] Li F, Kusche J, Chao N, Wang Z, Löcher A. “Long-term (1979-Present) total water storage anomalies over the global land derived by reconstructing GRACE data”. Geophys Res Lett, 48(8):e2021GL093492, 2021.
[12] Humphrey V, Gudmundsson L. “GRACE-REC: a reconstruction of climate-drivenwater storage changes over the last century”. Earth Syst Sci Data, 11(3):1153–1170, 2019.

[13] Tangdamrongsub N, Steele-Dunne SC, Gunter BC, Ditmar PG,Weerts AH. “Data assimilation of GRACE terrestrial water storage estimates into a regional hydrological model of the Rhine River basin”. Hydrol Earth Syst Sci, 19(4):2079–2100, 2015.
[14] Springer A, Karegar MA, Kusche J, Keune J, KurtzW, Kollet S. “Evidence of daily hydrological loading in GPS time series over Europe”. J Geodesy, 93(10):2145–2153, 2019.
[15] Gao H, Tang Q, Ferguson CR, Wood EF, Lettenmaier DP. “Estimating the water budget of major US river basins via remote sensing”. International Journal of Remote Sensing, 31(14), 3955–3978, 2010.
[16] Bai P, Liu X, Yang T, Liang K, Liu C. “Evaluation of streamflow simulation results of land surface models in GLDAS on the Tibetan plateau”. Journal of Geophysical Research: Atmospheres, 121(20), 12180–12197, 2016.
[17] Fisher RA, Koven C. “Perspectives on the future of land surface models and the challenges of representing complex terrestrial systems”. Journal of Advances in Modeling Earth Systems, 12(4), e2018MS001453, 2020.
[18] Rui H, Beaudoing H, Loeser C. “README document for NASA GLDAS version 2 data products”. In: goddart earth sciences data and information services center (GES DISC): Greenbelt. MD, 2020.
[19] Derber JC, Parrish DF, Lord SJ. “The new global operational analysis system at the national meteorological center”. Weather and Forecasting, 6(4), 538–547, 1991.
[20] Huffman GJ, Bolvin DT, Braithwaite D, Hsu K, Joyce R, Xie P, Yoo, S-H. “NASA global precipitation measurement (GPM) integrated multi-satellite retrievals for GPM (IMERG)”. Algorithm Theoretical Basis Document (ATBD) Version, 4, 2019.
[21] Adler RF, Huffman GJ, Chang A, Ferraro R, Xie P-P, Janowiak J, Rudolf B, Schneider U, Curtis S, Bolvin D, Gruber A, Susskind J, Arkin P, Nelkin E. “The version-2 global precipitation climatology Project (GPCP) monthly precipitation analysis (1979–Present)”. Journal of Hydrometeorology, 4(6), 1147–1167, 2003.
[22] Tapley BD, Watkins MM, Flechtner F, Reigber C, Bettadpur S, Rodell M, Sasgen I, Famiglietti JS, Landerer FW, Chambers DP, Reager JT,GardnerAS, Save H, Ivins ER, Swenson SC, Boening C,Dahle C,Wiese DN, Dobslaw H, TamisieaME, Velicogna I. “Contributions of GRACE to understanding climate change”. Nat Clim Chang, 9(5):358–369, 2019.
[23] Evensen G. “The ensemble Kalman filter: theoretical formulation and practical implementation”. Ocean Dyn, 53(4):343–367, 2003.
[24] Gerdener H, Kusche J, Schulze K, Döll P, Klos A. “The global land water storage data set release 2 (GLWS2. 0) derived via assimilating GRACE and GRACE-FO data into a global hydrological model”. Journal of Geodesy, 97(7), 73, 2023.
[25] Kusche J. “Approximate decorrelation and non-isotropic smoothing of time-variable GRACE-type gravity field models”. Journal of Geodesy, 81(11):733–749, 2007.
[26] Geruo A,Wahr J, Zhong S. “Computations of the viscoelastic response of a 3-D compressible Earth to surface loading: an application to Glacial Isostatic Adjustment in Antarctica and Canada”. Geophys J Int, 192(2):557–572, 2013.
[27] Luthcke, SB, TJ Sabaka, BD Loomis et al. “Antarctica, Greenland and Gulf of Alaska land ice evolution from an iterated GRACE global mascon solution”, J. Glac., 59(216), 613-631, 2013.

International Conference on Advances and Innovations in Engineering

2ICAIE

Evaluation of Library Buildings in Terms of Lighting: İsmail Hakki Tonguc Library Sample

Aslıhan MERAL[1], Şule YILMAZ ERTEN[2]

[1]Post Graduate Architectural Student, Institute of Sciences, Trakya University, Edirne, Turkey.
[2]Architectural Department, Architecture Faculty, Trakya University, Edirne, Turkey.
[1]aslihanmeral97@gmail.com, [2]suleyilmaz@trakya.edu.tr

[1](ORCID: 0009-0008-9748-6196), [2](ORCID: 0000-0003-2183-05321)

Abstract

Lighting plays an active role in the construction of the building characteristics in library buildings that have functions such as reading and protecting valuable works. The lighting levels in the library buildings and especially the controlled use of daylight are among the parameters to be considered. Providing visual comfort in libraries where reading and working is one of the most important steps. This is related to the lighting intensity, the surface properties of the materials in the interior (light reflection, absorption effect, etc.) and the light multiplier values of the colors used. When there is a problem of lack of natural light in libraries where the effect of daylight is extremely important, the most suitable artificial lighting solution should be created for the interior of the library. The most suitable type of artificial lighting should be found for human health and visual comfort psychologically and physiologically, and the ideal lighting level should be achieved with the necessary calculations. In this study, the current lighting of İsmail Hakkı Tonguç Library, which is insufficient for daylight, has been evaluated, the necessary lighting values have been determined to make this place the most comfortable, and the lighting system required by the Dialux program has been tested and reported on the library modeling. The steps to be followed while measuring the lighting performances were determined, and the existing parameters and improved parameters were compared.

Keywords: visual comfort, library lighting, dialux simulation program

1. Introduction

Lighting is the application of light on certain objects and surfaces in the most appropriate way for visual perception. The purpose of lighting is to make the environment and objects visible. Light indirectly affects an individual's norms, actions, reactions and behaviors. Therefore, the importance of lighting in our daily lives is quite high. Lighting is one of the important topics to be considered during building design. It is understood that the lighting element should be seriously examined in order for a building to be useful, aesthetic and attractive. Especially in libraries where activities such as studying and reading are performed, it is extremely important to provide visual comfort. Natural light should be utilized sufficiently, and where it is insufficient, artificial lighting elements that are closest to natural light and most suitable for the space should be activated.
In this study, it is aimed to measure the adequacy of the current lighting of Istanbul İsmail Hakkı Tonguç Library, which is thought to be insufficient in terms of natural lighting, with the help of Dialux, a visual lighting simulation program, and to propose suitable artificial lighting elements to provide lighting suitable for the function in case it is not sufficient.

2. Visual comfort in libraries

Natural lighting is a form of illumination that is caused by direct natural sources of light into the space. The most effective main source of natural lighting is the sun. Windows and rooflights are important natural lighting elements [1],[2]. Light shelves and light pipes are other important natural lighting elements that are widely used today. In

[1]Corresponding author

lighting design, which plays an important role in energy consumption, it is important to reduce the use of artificial lighting by effectively utilizing natural lighting.

Library lighting levels are very important for users to adapt to the space. However, the performance of readers is also significantly related to satisfaction in the reading environment. There are two types of lighting in library spaces: natural and artificial. Natural lighting is usually done by windows in the walls or skylights. The variables affecting natural lighting are illuminance level, daylight multiplier, luminance distributions, glare prevention, shading, light direction and light color [3]. Mostly natural lighting environment should be provided in the library space. Daylight controls the biological time of the body. It affects the eye and brain organs and controls hormone secretion. However, in cases where natural lighting is insufficient or absent, artificial lighting should be used. The places where the best lighting should be provided are reading rooms. In these sections, light that does not tire the eyes should be used and both general and local lighting should be used when necessary. In addition, books in libraries should be protected from intense light. The main cause of damage is the U.V. rays emitted by white light sources. However, in any case, the greatest danger is determined as direct sunlight. Therefore, U.V. absorbing filters are recommended as the most effective solution to prevent U.V. damage where natural light coming through windows is used. In addition, uncontrolled daylight can cause unwanted glare. Window and roof skylights should be oriented or covered with window covers to protect bookshelves and other sensitive materials from direct sunlight [4].

In reading and working areas, light that does not tire the eyes should be used and both general and local lighting should be used [5]. Another factor that directly affects lighting is the colors used in the space. In order for the lighting to be efficient, the ceiling, walls and floor should be created with light colored materials [6]. Light colors give a higher percentage of light reflection compared to dark colors [7]. Thus, a brighter space can be obtained with less energy.

Artificial ligting in libraries

In artificial lighting used indoors, the illuminance level distribution is divided into groups in order to understand how the light comes to the surface (Table 1). Direct lighting is provided indoors by directing 90% to 100% of the light directly to the surface to be illuminated. Indirect lighting occurs when luminaires direct 0 to 10% of the light downwards and the rest towards the upper parts of the walls and ceiling [8]. Indirect lighting is preferred in spaces with high reflection factor. Ceiling and wall colors have an important effect [9].

Table 1. Lighting types and their characteristics

LIGHTING TYPE	FEATURES	ENERGY EFFICIENCY
DIRECT LIGHTING	✓ Direct light from luminaires to the ceiling ✓ It is important to suppress glare at straight angles ✓ Dark ceiling (cave effect) ✓ No shadows.	High
INDIRECT LIGHTING	✓ A lighting effect can occur where there are no shadows. ✓ Glare-free lighting	Low

In a study, it was emphasized that the minimum illumination level should be 400 lux in areas where library users are present [10]. In addition to this, the Lighting engineering community has a proposal for the ideal illuminance level for library buildings (Table 2) [11].

Table 2. Recommended illuminance levels for library buildings by the Illuminating Engineering Society-IES (2013)

LIBRARY PARTS	IDEALLY LIGTING LEVELS (LUX)
Reading Rooms	200
Tables	400
Desks	600
Closed Book Storages	100
Bookbinding	600
Catalog, sorting, storage	400

In another study, it was stated that library buildings should provide an average illuminance level of 500 lux for working areas. The reflection coefficient of interior surfaces is also important. The appropriate amount should be 70 to 90 percent for ceilings, 30 to 50 percent for floors, and 40 to 60 percent for walls [12].
During the design of the library's lighting plan, it should be aimed to provide the illumination levels necessary for the reader to make the best use of the spaces in the library and to provide library services comfortably. When appropriate lighting design is made, users stay in the library longer and use the library more frequently. Library staff also work more comfortably in their workplaces. Otherwise, there will be negative effects such as library staff being less efficient and users visiting the library less [13]. In order to provide these lighting levels, the types of lighting used are of great importance.

3. Materials and methods

The DiaLux program was used to determine the suitability of this library building, which is generally insufficient from natural lighting, according to the ideal illuminance value with the luminaires used. To mention the Dialux program; Dialux is a program for indoor and outdoor lighting design, where illuminance levels can be calculated according to the characteristics and number of luminaires and the reflection multipliers of the space. With the Dialux evo version, it has become a design and simulation program frequently used by lighting designers and architects by providing three-dimensional visualization. In the study, firstly, the amount of illumination provided by daylight independent of artificial lighting was measured, then the illuminance level was determined within the existing artificial lighting, and finally, the type and number of luminaires were simulated using Dialux to achieve the required illuminance level.

3.1. Field study: İstanbul İsmail Hakki Tonguc Library

The building is located in the Sultaniye neighborhood of Esenyurt district of Istanbul (Figure 1). The library section is located on the 2nd basement floor of the 7-storey business center (Figure 2). The entrance façade and window openings are located on the south-west façade as it is the only façade facing the exterior. The height of the space is 380 cm and it has a gross area of 1114.30 m².

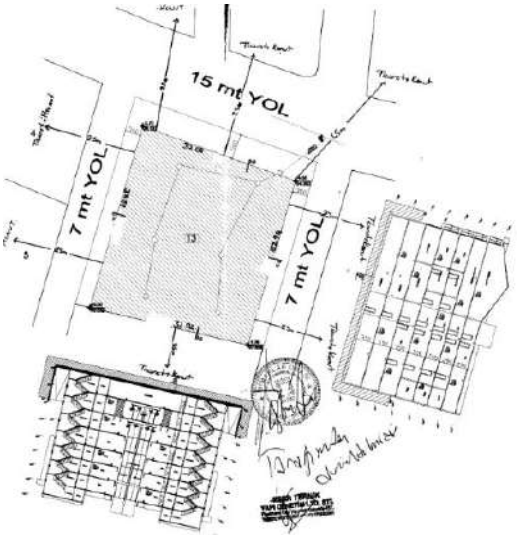

Figure 1. Site Plan

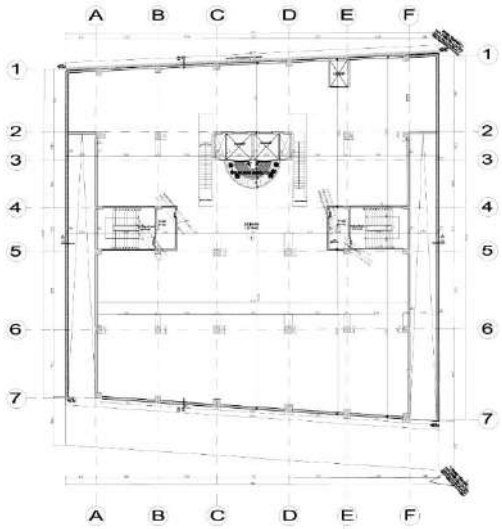

Figure 2. Library Floor Plan

The library part of the building receives natural light from the horizontal band windows on the façade. Therefore, there is a limited light flow into the interior as natural lighting. There are 169 spotlights to provide diffused lighting in the space with artificial lighting and 51 pendant lighting elements to directly illuminate the seating and working areas (Figure 3-4).

Figure 3. Horizontal band windows

Figure 4. Library Entrance Area

If we look at the interior arrangement, it has an organization in dark tones. Wood materials and parquets in oak tones and dark colors are used on the ceiling. The surface of the parquets used is glossy and reflects light. Daylight utilization is at minimum level. Apart from the entrance hall, there are 12 skylights. They are also prevented from letting in direct light and their surfaces are covered. No lighting elements were used on the shelves. The materials used are generally in dark tones.

Figure 5. Entrance to the Library

Figure 6. Study Desks

The walls are predominantly white in color (Figure 5-6). However, it is seen that daylight is insufficient in the photographs taken in the morning hours. In the next section, the building was simulated with the Dialux program and the illuminance level was determined.

3.2. Current Situation

DiaLux program was used to determine the suitability of this library building, which is generally considered to be insufficient in terms of natural lighting, according to the ideal illuminance value with the luminaires used. With Dialux program, performance analysis of artificial lighting is performed[14]. With the DIALux evo version, it has become a design and simulation program frequently used by lighting designers, electrical-electronics engineers, architects and project managers with a great improvement in three-dimensional visualization. In the study, firstly, the amount of illumination provided by daylight independent of artificial lighting was measured, then the illuminance level was determined within the artificial lighting as it is, and finally, the type and number of luminaires were simulated by the program to achieve the required illuminance level. The stages of the study are given in Table 3.

Tablo 3. Methodology of the study

[1]

Phases	Doğal Aydınlatma Performansı	Yapay Aydınlatma Performansı
Preparation Phase	✓ Determination of existing window-door openings ✓ Hourly observation and photography	✓ Determination of color and technical properties of materials ✓ Identification of existing lighting fixtures
Measurement Phase	✓ Determining the location of the building ✓ Measurement of window sizes. ✓ Exporting measurements to data files	✓ Transferring color and texture properties of materials to data files ✓ Identification of luminaires close to the technical specifications of existing luminaires
Evaluation Phase	✓ Organization of measurement results through graphs and tables. ✓ Evaluation of the results with the relevant criteria according to the literature research	✓ Obtaining the illuminance level at the working plane or account points under natural and artificial lighting ✓ Organizing the data obtained through graphs and tables ✓ Evaluation of data according to relevant standards

After the current state of the building was created in the Dialux program, window openings and luminaire placements were completed. In the first stage, it was attempted to obtain only daylight data without luminaires activated. However, the Dialux program warned that "a daylight calculation is not possible without daylighting openings" and could not calculate the data due to insufficient daylight. In this case, the current artificial lighting situation was analyzed. Accordingly, 151 spotlights and 69 pendant lighting elements were placed in the space, and as a result of the simulation, the average illumination value in the reading - working parts of the library was given as 357 lux (Table 4-a). The list of luminaires used for the current study is as follows (Table 4-b,c,d). The false colors representation is also given in the table (Table 4-e,f).

Table 4. Illuminance values and skylights used in the baseline simulation

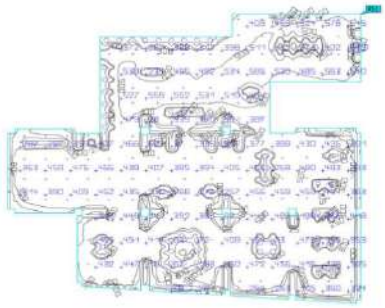

Özellikler	Ē	E_{min}	E_{maks}	g_1	g_2	İndeks
Alan sonuç objesi 1 Dikey aydınlatma gücü (adaptif) Yükseklik: 0.000 m	357 lx	1.93 lx	731 lx	0.005	0.003	RST

(a)

Işıklık listesi

Φ_{lamba}	P_{lamba}	Işık verimi
519974 lm	4267.2 W	121.9 lm/W

Adt.	Üretici	Ürün No.	Ürün adı	P	Φ	Işık verimi
51	FAGERHULT	53405-402	Globia LED D450 white 4K PMMA	28.0 W	2912 lm	104.0 lm/W
169	Philips		DN460B LED20S/840 C DIA-VLC-E WH	16.8 W	2198 lm	130.8 lm/W

(b)

FAGERHULT

Ürün No.	53405-402
P	28.0 W
Φ_{lamba}	2912 lm
Işık verimi	104.0 lm/W
CCT	3000 K
CRI	100

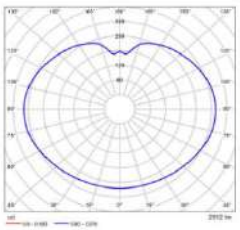

Polar LDC

(c)

PHILIPS

P	16.8 W
Φ_{lamba}	2200 lm
Φ_{lamba}	2198 lm
η	99.91 %
Işık verimi	130.8 lm/W
CCT	3000 K
CRI	100

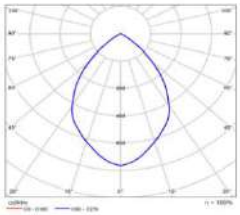

Polar LDC

(d)

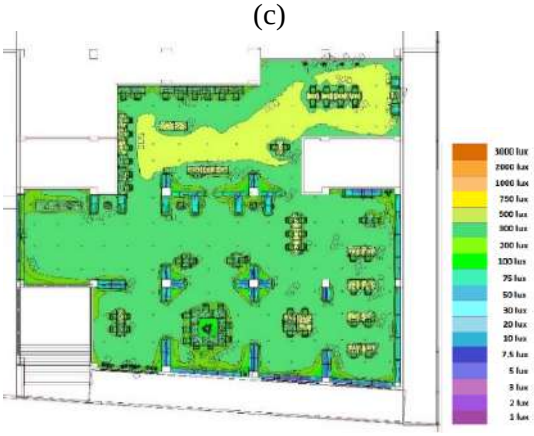

(e)

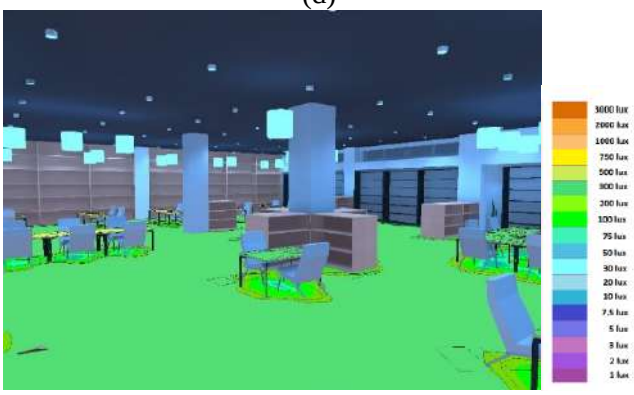

(f)

The distance of the direct lighting elements used for the tables is 240 cm from the table. These luminaires do not provide sufficient illumination and also prevent the efficient use of energy.

Table 5. Illuminance values and luminaires used in the simulation of the proposed case

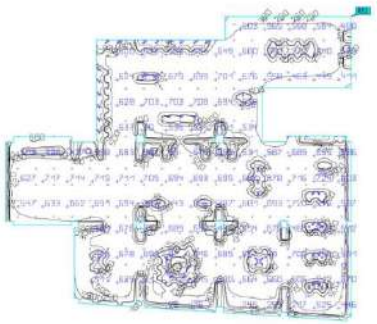

Özellikler	Ē	E_{min}	E_{maks}	g_1	g_2	İndeks
Alan sonuç objesi 1 Dikey aydınlatma gücü (adaptif) Yükseklik: 0.000 m	507 lx	2.65 lx	734 lx	0.005	0.004	RS1

(a)

Işıklık listesi

Adt.	Üretici	Ürün No.	Ürün adı	P	Φ	Işık verimi
21	Ares s.r.l.	507131	delta led	9.0 W	424 lm	47.1 lm/W
8	Ares s.r.l.	981700	clara	24.0 W	473 lm	19.7 lm/W
50	Trimless	11602	Large Adjustable Desk Lamp With Wood	4.0 W	142 lm	35.5 lm/W
9	FAGERHULT	53405-402	Q3000 LED D450 white 4K PWMA	28.0 W	2912 lm	104.0 lm/W
269	Philips		DN480B LED30S/840 C DA-VLC4 WH	16.8 W	2198 lm	130.8 lm/W

(b)

FAGERHULT

Ürün No.	53405-402
P	28.0 W
Φ_{lamba}	2912 lm
Işık verimi	104.0 lm/W
CCT	3000 K
CRI	100

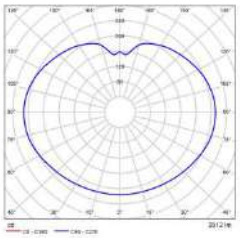

Polar LDC

Ares s.r.l. - clara

ares THE OUTDOOR BY FLOS

Ürün No.	981700
P	24.0 W
Φ_{lamba}	1800 lm
$\Phi_{ışık}$	473 lm
η	26.30 %
Işık verimi	19.7 lm/W
CCT	3000 K
CRI	84

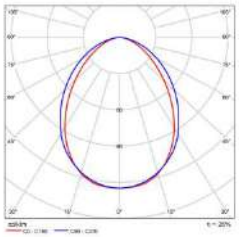

Polar LDC

(c)

PHILIPS

P	16.8 W
Φ_{lamba}	2200 lm
$\Phi_{ışık}$	2198 lm
η	99.91 %
Işık verimi	130.8 lm/W
CCT	3000 K
CRI	100

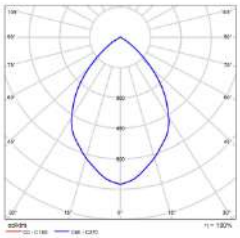

Polar LDC

Ares s.r.l. - delta led

ares THE OUTDOOR BY FLOS

Ürün No.	507131
P	9.0 W
Φ_{lamba}	430 lm
$\Phi_{ışık}$	424 lm
η	98.64 %
Işık verimi	47.1 lm/W
CCT	6000 K
CRI	70

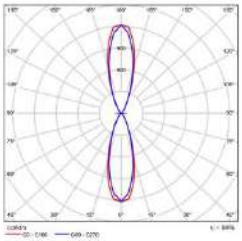

Polar LDC

(d)

(e)

(f)

In the proposed model, additional table lamps are used for localized lighting on the tables, thus providing a more effective working environment and efficient use of energy in general lighting (Table 5- a,b). Since there is currently no additional lighting on the bookshelves, the proposed model uses zonal lighting elements that directly illuminate the shelves from above on the wall-mounted shelves. Pendant lights were used only in the information desk and rest areas. While there are 220 artificial lighting elements in the existing design, a total of 353 artificial lighting elements were used in the proposed model to provide sufficient and necessary lighting (Table 5-c,d). The false color representation of the proposed model is given in Table 5-e,f). While this situation increases the initial investment cost, it is thought that it can amortize the investment costs in a short time as it will ensure efficient use of energy in general lighting. With the proposed scenario, visual comfort is provided for library activities, direct and regional efficient and correct use of energy is aimed, and lighting support is provided to each area with the luminaires it needs.

According to the lighting proposal scenario, the illuminance value inside the library reached 507 lux. In the library, where activities such as reading and studying are carried out, "the lighting size should be at least 400 lux" (Faulkner-Brown, 1999). With this arrangement, the minium illuminance value required for efficient work meets the standards in the literature.

3. Results

With the scenario proposed in the study, the illuminance value inside the library reached 507 lux. The minium illuminance value required for efficient work in the library where activities such as reading and studying are carried out is thus provided. Table lamps were proposed for direct lighting on the tables, thus providing a more effective working environment and efficient use of lighting. In addition, since there is no lighting on the bookshelves in the current situation, direct lighting elements that illuminate the shelves from above on the shelves mounted on the wall were proposed in the proposal study.

İsmail Hakkı Tonguç Library is located in the basement of the building, so when simulated with the dialux program, daylight illumination is insufficient for its function. For this reason, in line with the results obtained in the study, suggestions were developed for lighting suitable for the sections of the library. With the proposed scenario, visual comfort is provided for the library actions, direct and correct use of energy is ensured, and the required lighting level for each function is provided in terms of standards with the proposed scenario.

5. References

[1] Tregenza, P., Loe, D., “The design of lighting”. E&FN, Spand, London, 1998.

[2] Aydın Yağmur, Ş., Şerefhanoğlu Sözen, M., "Visual Comfort in Classrooms and the Effect of Interior Surfaces". Megaron, Volume 11, Issue 1, 2016.

[3] Erlalelitepe İ., Aral D., Kazanasmaz T., Investigation of Educational Buildings in terms of Natural Lighting Performance, Megaron, Volume 6, Issue 1, 2011.

[4] Köymen, E., A Parametric Solution to the Problem of High Level Natural Lighting in Wide Interior Openings: IZU Library Interior Shading Installation, European Journal of Science and Technology, Issue 19, pp 904 – 915, 2020.

[5] Kuru, R. Türkyılmaz, Ç., Ergonomic Evaluation of the Spatial Organization of Library Buildings: The Case of Bahçeşehir University Library Building, Erconomics, Volume 2, Issue 3, 2019.

[6] Zahoar, R.L., Library Lighting, Guidelines for Library Planners. Keith Doms & Howard Rovelstad. ALA, Chicago, 1960.

[7] Kamaruddin, M. Athir. Arief, Y. Ahmad, M. Hafizi, Energy Analysis Of Efficient Lighting System Design For Lecturing Room Using Dialux Evo 3, Applied Mechanics and Materials, Volume 818, pp 174-178, 2016.

[8] Şahin, M., Oğuz, Y., Büyüktümtürk, F., Technical Comparison of Semi-Direct and Mixed Lighting Types, CBU Journal of Science and Technology,2015.

[9] Dursun, B., "Analysis of Lighting Calculation Techniques in Indoor Environments and an Application Example" Marmara University Institute of Science and Technology, Master's Thesis, Istanbul, 2005.

[10] Faulkner-Brown, H., Some Thoughts on The Design of Major Library Buildings. Bisbourck, M.F. and Chauvenic, M. (Ed.). Intelligent Library Buildings, München,1999.

[11] Bozkurt, A., Lighting Design and Technological Developments in Twenty-First Century Public Libraries Evaluation in Terms of Reflections, Master Thesis, Mimar Sinan Fine Arts University, 2013.

[12] Kime, B.Ali , Comparative Analysis of Day lighting and Artificial Lighting in Library Building; Analyzing the Energy Usage of the Library, International Journal of Advanced Research in Science, Engineering and Technology, Volume 5, Issue 12, 2018.
[13] Hashempour, L., Effect and Importance of Lighting Systems in School Libraries, IASL Conference Proceedings, 2018.
[14] Omar, O. Fernandez, B. Balbuena, A. Molini, D., Optimization of daylight utilization in energysaving application on the library in faculty ofarchitecture, design and built environment, BeirutArab University, Alexandria Engineering Journal, Volume 57, Issue 4, 2018.

International Conference on Advances and Innovations in Engineering

The Production of Durable Precast Concrete Using Reactive Powder Concrete at Various Mixing Ratios in High-Rise Structures

Sedat SAVAŞ[1], Dursun BAKIR[2 *]

[1,2] Fırat University, Faculty of Engineering, Department of Civil Engineering, 23100, Elazığ
[1]ssavas@firat.edu.tr, [2]dbakir@firat.edu.tr

Abstract
Recent earthquakes in Elazığ, İzmir, and Maraş have raised concerns about the safety and cost of reinforced concrete structures in our country. Basalt, silica fume, marble, and rock wool waste material from Alacakaya district were used to breach safety and economic restrictions in the Elazığ region, where the stock is high. Steel, carbon, and glass fibers were added to the mixture. This study manufactured high-strength prefabricated concrete using these components, compacted in 4x4x16 cm sample molds, and tested for compressive and flexural strength after 7 days. The concrete was manufactured from local materials and delivered at an affordable price with strong compressive and flexural strength. Reactive powdered concrete (RPC) employing crystallized limestone powder, steel fiber produced economic and strong prefabricated concrete by enhancing compressive and tensile strength.
Keywords: Reactive Powdered Concrete, limestone powder, high strength concrete, steel fiber

1. Introduction

Reactive Powdered Concrete (RPC) is a type of ultra high performance concrete (UHPC)[1]. The application of recent discoveries in nanomaterials science has been employed to enhance the compressive strength of concrete, while concurrently decreasing the size and weight of its constituent elements. This has resulted in cost savings and enhanced visual appeal of the structures. Ultra-high performance concretes (UHPCs) are characterized as cementitious composites possessing exceptional material qualities, enabling them to endure compressive pressures of up to 150 MPa and tensile loads of up to 8 MPa. Furthermore, UHPCs demonstrate strain hardening tendency when subjected to uniaxial tension[2–4]. The RPC method was chosen due to its mechanical and durability characteristics, as well as its resistance to climatic and chemical influences[5]. RPC, also known as Reactive Powder Concrete, exhibits distinct variations from conventional concrete in terms of its production processes and techniques, utilization of a higher proportion of binder, incorporation of siliceous materials, implementation of advanced water lowering chemicals, and reduction of the water-to-binder ratio[6]. It is also important to note that approximately 82% of the 28-day compressive strength of RPC can be obtained with 2 days of hot air curing[7]. The utilization of concretes possessing a compressive strength ranging from 15-25 MPa was initiated during the 1960s, afterwards being superseded by concretes exhibiting a compressive strength of 40-50 MPa throughout the 1970s. The observed enhancement in compressive strength has correspondingly resulted in variations in the water-to-cement (w/c) ratio. During the 1950s, the water-to-cement (w/c) ratio, originally ranging from 0.60 to 0.70, underwent a decrease in the 1970s to approximately 0.40-0.55 due to the introduction of plasticizers into concrete. Subsequently, in 1980, the w/c ratio in concrete was further reduced to 0.25. Silica fume, a supplementary cementitious material, was then included, leading to a reduction in the water-to-cement ratio to a value below 0.20. Nevertheless, it was observed that the compressive strength of concrete exhibited a notable increase beyond the threshold of 150 MPa following a curing period of 28 days. The implementation of recycling practices has yielded a significant advancement in promoting sustainability, a paramount concern in contemporary times. The utilization of silica fume in reactive powder concrete (RPC) leads to an enhancement in its strength[8,9]. RPC is actually an ultra-high strength composite construction material with its mechanical and physical properties due to its low void ratio. Removing large aggregates from the concrete mix, reducing the s/w ratio in the mix, reducing the amount of CaO-SiO_2 with silica and mixing steel fibers into the mix make RPC a high performance material. Steel fiber increases the flexural strength of RPC[10]. Fiber

*Corresponding author

reduces the compressive strength of concrete cubes and cylinders. At the same time it greatly increases the compressive and flexural tensile strength of RPC[11,12]. The individual engaged in an investigation pertaining to reactive powdered concrete. The present study aimed to examine the mechanical properties of normal strength concrete (NWC), high strength concrete (HWC), and reactive powder concrete (RPC). Flexural strengths within the range of 50-140 MPa were achieved with the use of steel fiber. The flexural strengths and fracture energies exhibited a direct correlation with the quantity of steel fibers incorporated. Furthermore, in terms of durability, the presence of a void-free and tightly structured RPC demonstrated excellent resistance against chemical and environmental influences. Reactive Powder Concrete (RPC) exhibits enhanced mechanical and durability characteristics in comparison to alternative forms of concrete. Nevertheless, similar to high-strength concrete, RPC (Reactive Powder Concrete) is prone to brittle fracture. The majority of research endeavors have focused on the examination of robust concrete specimens that were fabricated inside controlled laboratory settings. Typically, the mixtures employed consist of coarse pebbles and steel fibers. The utilization of heavy aggregate types as coarse or fine powder was limited. Furthermore, it was observed that exclusively steel fibers were present in the fibrous combinations.
This study aims to investigate the production of high strength concrete through the utilization of the Reactive Powder Concrete (RPC) technology. The experiment will involve varying curing conditions in conjunction with the selected ingredients. The objective is to provide cost-effective and long-lasting concrete by enhancing the properties of conventional concrete, while the reduced curing time will significantly contribute to time efficiency. Efforts were made to continuously enhance the strength of concrete.

2. Method

The molds depicted in Figure 1 were cast using the mixture ratios specified in Table 1, with dimensions of 16x16x4 cm. The aforementioned blend was meticulously constructed utilizing concrete mixers in a manner tailored specifically to the composition of the combination. The produced mixes were carefully positioned within the molds, as seen in Figure 2, and subsequently subjected to compaction. In order to investigate the significant contributions of the temperature curing application of the RPC method, specimens were made at various temperatures. The specimens were enveloped in a damp covering and maintained in a hydrated state for a duration of 24 hours. Subsequently, three samples of each mixture were subjected to thermal treatment at temperatures of 200, 250, 300, and 350 °C, respectively, within an oven for a duration of 24 hours. Following this, the samples were maintained at a constant temperature of 90 °C for a period of 7 days. Therefore, a total of 60 samples were prepared for testing, with each mixture consisting of an equal number of samples.

Figure 1. Shape-dimensions of mold and sample

Figure 2. Preparation of Samples

Table1. Mixture Ratios

Ingredients	*W(gr)*				
	1. Mixture	*2. Mixture*	*3.Mixture*	*4.Mixture*	*5. Mixture*
Cement (CEM I 52.5)	1500	1500	1500	1500	1500
Silica Fume	325	350	375	400	425
Basalt (0-100)	935	1335	1335	1335	1335
Plasticizer	30	30	30	30	30
Water	300	300	300	300	300
Crystallized Limestone	1000	1000	1000	1000	1000
Steel Fiber	250	250	250	250	250
Rock wool	435	1500	1500	1500	1500

Following the completion of the curing process, the specimens underwent three-point bending tests at a rate of 0.2 kN/s and compression testing at a rate of 2.4 kN/s (Fig3).

Figure 3. Three-point bending test and pressure test

3. Conclusions

Upon evaluating the average results of the three-point bending tests conducted at temperatures of 200, 250, 300, and 350°C, it was noticed that blend 2 exhibited the most favorable bending behavior. However, the remaining blends also shown satisfactory performance in terms of bending (Table2-3-4-5-6).

Mixture 3 has the highest level of optimization in compression testing. Upon doing the evaluation of temperatures, it was seen that a temperature of 300 °C yielded favorable results in both compressive and flexural testing. The quantity of rock wool in the initial combination was augmented and thereafter maintained at a constant level, resulting in enhanced flexural and compressive strengths relative to the initial mixture. An increase in oven temperature resulted in an observed increase in the strengths of the samples. Based on these findings, the material under investigation exhibits potential applications in various domains. It can be utilized in protective structures deployed at security checkpoints, incorporated into the construction of crenellations, employed in the fabrication of energy-dissipating water structures, serving as a viable substitute for steel in scenarios necessitating high strength, and

contributing to the development of lightweight and portable building components by reducing the volume of concrete required.

Table 2. Results of concrete mix design-1

İ.N.	Temperature °C	Flexural strength (kN/mm²)	Compressive strength (kN/mm²)
1	R.T.	3.31	22. 23
	200	7.2	28.77
	250	6.36	36.69
	300	5.289	36.84
	350	7.22	28
2	R.T.	2.64	24.4
	200	4.831	48.33
	250	5.72	17
	300	3.03	28.74
	350	5.689	30
3	R.T.	5.5	25.1
	200	6.64	30
	250	5	42
	300	8.2	52
	350	6	42

Table 3. Results of concrete mix design-2

İ.N.	Temperature °C	Flexural strength (kN/mm²)	Compressive strength (kN/mm²)
1	R.T.	5.48	22.72
	200	5.54	50.63
	250	2.136	58.34
	300	7.227	49.58
	350	5.24	42
2	R.T.	5.5	21.4
	200	11.5	65.63
	250	9.23	90.674
	300	10.44	77.66
	350	11.166	41.34
3	R.T.	5.48	23.36
	200	7.25	65.76
	250	7.9	79.76
	300	9.4	41
	350	10.11	43

Table 4. Results of concrete mix design-3

İ.N.	Temperature °C	Flexural strength (kN/mm²)	Compressive strength (kN/mm²)
1	R.T.	3.925	23.218
	200	4.794	82.588
	250	5.491	93.807
	300	6.467	88.035
	350	8.428	79.672
2	R.T.	5.517	21.815
	200	6.868	88.124
	250	5.509	92.386
	300	7.857	100.36
	350	5.277	104.65
3	R.T.	7.722	26.1
	200	5.931	94.06
	250	5.567	108.81
	300	6.238	86.618
	350	6.007	103.1

Table 5. Results of concrete mix design-4

İ.N.	Temperature °C	Flexural strength (kN/mm²)	Compressive strength (kN/mm²)
1	R.T.	5.31	21.423
	200	4.416	56.072
	250	4.516	77.786
	300	5.962	63.728
	350	5.123	77.232
2	R.T.	6.48	23.97
	200	5.09	110.38
	250	5.129	112.4
	300	4.79	108.03
	350	5.34	117.33
3	R.T.	2.96	26.46
	200	5.8	105.16
	250	5.79	102.3
	300	4.25	101.82
	350	3.48	114.91

Table 6. Results of concrete mix design-5

İ.N.	Temperature °C	Flexural strength (kN/mm²)	Compressive strength (kN/mm²)
1	R.T.	4.36	22
	200	5.432	65
	250	5.201	72.45
	300	6.427	100.12
	350	5.0	86.54
2	R.T.	7.77	22.04
	200	6.45	114.02
	250	4.78	102.9
	300	5.87	118.5
	350	5.55	110.78
3	R.T.	3.33	22.44
	200	4.8	95.9
	250	6.54	92.3
	300	5.10	111.85
	350	4.25	117.56

4. References

[1] O.A. Mayhoub, E.-S.A.R. Nasr, Y.A. Ali, M. Kohail, The influence of ingredients on the properties of reactive powder concrete: A review, Ain Shams Eng. J. 12 (2021) 145–158. https://doi.org/10.1016/j.asej.2020.07.016.

[2] N.-H. Yi, J.-H.J. Kim, T.-S. Han, Y.-G. Cho, J.H. Lee, Blast-resistant characteristics of ultra-high strength concrete and reactive powder concrete, Constr. Build. Mater. 28 (2012) 694–707. https://doi.org/10.1016/j.conbuildmat.2011.09.014.

[3] H. Almansour, Z. Lounis, Innovative design approach of precast–prestressed girder bridges using ultra high performance concrete, Can. J. Civ. Eng. 37 (2010) 511–521. https://doi.org/10.1139/L09-169.

[4] F. Sayed Ahmad, G. Foret, R. Le Roy, Bond between carbon fibre-reinforced polymer (CFRP) bars and ultra high performance fibre reinforced concrete (UHPFRC): Experimental study, Constr. Build. Mater. 25 (2011) 479–485. https://doi.org/10.1016/j.conbuildmat.2010.02.006.

[5] A.H.M. Algburi, M.N. Sheikh, M.N.S. Hadi, Analytical investigation on the behavior of circular and square RC columns strengthened with RPC and wrapped with FRP under uniaxial compression, J. Build. Eng. 25 (2019) 100833. https://doi.org/10.1016/j.jobe.2019.100833.

[6] I.S.A. Issa, Effect of mineral additives on reactive powder concrete properties, Kastamonu university, 2020.

[7] P. Hiremath, S.C. Yaragal, Investigation on Mechanical Properties of Reactive Powder Concrete under Different Curing Regimes, Mater. Today Proc. 4 (2017) 9758–9762. https://doi.org/10.1016/j.matpr.2017.06.262.
[8] E. Dallaire, M. Pierre-Claude Aitcin; Lachemi, High-performance powder, Am. Soc. Civ. Eng. 68 (1998) 48–51.
[9] O. Bonneau, M. Lachemi, E. Dallaire, J. Dugat, P.-C. Aitcin, Mechanical Properties and Durability of Two Industrial Reactive Powder Concretes, ACI Mater. J. 94 (1997). https://doi.org/10.14359/310.
[10] M.Y. Taşdemir, M. A., F. Bayramov, Yeni Kuşak Süperakışkanlaştırıcıların Yüksek Performanslı Çimento Esaslı Kompozitlerdeki İşlevleri, in: Kimyasal Katkılar Sempozyumu Bildir., 2005: pp. 201–222.
[11] R. Selvaraj, R. Priyanka, Reactive Powder Concrete with and without Fibers, in: Int. J. Eng. Res. Technol., 2015: pp. 884–890.
[12] H. Yazıcı, E. Deniz, B. Baradan, The effect of autoclave pressure, temperature and duration time on mechanical properties of reactive powder concrete, Constr. Build. Mater. 42 (2013) 53–63. https://doi.org/10.1016/j.conbuildmat.2013.01.003.

International Conference on Advances and Innovations in Engineering

Determination of Flood Risk Areas by AHP and Frequency Ratio Method; A Case Study for Fatsa (Ordu)

Ufuk YÜKSELER[1], Ömerul Faruk DURSUN[2]

[1]Phd.Student. İnönü University, Engineering Faculty, Civil Engineering Department. Malatya/TÜRKİYE.
[2]Prof. Dr. İnönü University, Engineering Faculty, Civil Engineering Department Malatya/TÜRKİYE
[1]ufukyukseler12@gmail.com, [2]ofdursun@gmail.com

[1](ORCID: 0000-0002-7233-0821), [2](ORCID: 0000-0003-3923-5205)

Abstract

Floods are frequently experienced in the Eastern Black Sea region due to climatic and topographic features. In the last hundred years, around 650 flood events have occurred in this region and 42 of them have caused significant loss of life and property. For this reason, it is important to determine the causes of flooding for this basin, to carry out studies on first aid scenarios in case of flood and the flood situation of the basin in the coming years.
In this study, it is aimed to determine the flood risk areas of Cevizdere and Elekçi streams located in and around Fatsa district of Ordu province. To this aim; Flood hazard maps of the basin were created using Analytical Hierarchy Process (AHP) and Frequency Ratio method (FR). In addition, the effective parameters (Elevation, Slope, etc.) in the flood were determined in the study. It has been studied with 220 flooded and 220 non-flooded data obtained from 440 different point flood datum. The accuracy of the methods was evaluated with the Receiver Operating Characteristics Curve (ROCC).
As a result of the analyses, it was observed that the Frequency Ratio (FR) model gave relatively better results in the flood hazard analysis. In addition, it was determined that the most effective parameters in flood formation, Altitude and Precipitation, were common in both methods. While both methods had close ROCC values, the AHP method determined the risk map in a wider area than the FR method.

Keywords: Flood, AHP, Frequency ratio method, Geographic ınformation systems, Multi-criteria decision making methods

1. Introduction

Most of the studies on the determination of flood risk areas have been made using multi-criteria decision-making methods (Ahp, Topsis, Electra etc.) or methods based on learning from current experiences such as Frequency Ratio. Tokgözlü et al. (2018); they used the AHP method to evaluate the flood risk of Aksu Stream. The order of importance of the parameters used in the study was determined as precipitation (47%), slope (26.1%), land use (13.7%), soil (5.9%), distance to stream (3.6%) and lithology (3.6%). According to the study, 40% of historical floods occur in "Low risk (2)", 30% "Medium risk (3)" and 30% "Risky (4)" areas, and it has been determined that no flooding has occurred in the areas evaluated as risk-free. Saral et al. (2010) studied flood risk analysis with Information Diffusion and Multi-Criteria decision making methods. The Ayamama Stream in Istanbul has been determined as the study area. Precipitation (53%), Soil use (19.4), Geology (18.2%), and Topographic Wetness (9.4%) data were studied. In the study, it was observed that the two methods gave different results. When the necessary interpretations were made in the created risk map, it was determined that the areas with "Very High" flood risk remained on the settlement area and these areas were determined as the places with the highest probability of being damaged in a possible flood. It is stated that the reason for the great differences between the two methods in terms of their domains is that the real data required for the second method cannot be obtained from the relevant authorities and the use of representative data as input to the program [6]

Taş et al. (2022), the Behzat (Tokat) stream was determined as the study area. Precipitation (50.3%), geology (6.8%), slope (13.4%), aspect (1.2%), land use (26%), distance to stream (1.1%), soil (0.2%) parameters were studied. According to the study, it has been revealed that 38.9% of the study area has areas that can be exposed to moderate flooding, and 5.4% of the study area has areas that can be exposed to high-level flood hazards.

[1]Corresponding author

Goztepe et al. (2022) determined that the flood effective parameters for Hatip Stream (Ankara) as; distance to the stream (7.79%), altitude (12.98%), aspect (14.71%), slope (19.98%), lithology (32.47%), land use (12.99%), precipitation (6.06%). According to the findings obtained as a result of the study, it was determined that 63% of the basin has high and very high flood sensitivity. Approximately 85% of the settlements in the basin are located in areas with high and very high flood susceptibility. In addition, it has been determined that one of the most important problems in the basin is incorrect land use. Çamcı et al. (2022) gave Aydın province flood parameters as; precipitation (42%), distance to the stream (23%), slope (12%), elevation (10%), soil (6%), land use (4%), aspect (3%). As a result of the study, it was determined that 499.14 km^2 of the study area consists of low risk, 551.69 km^2 low risk, 305.45 km^2 medium risk, 263.64 km^2 high risk and 9.83 km^2 very risky areas in terms of flood hazard. Şengün et al. (2019) selected Tavşanlı stream (Sivas) as the study area. Flood effective parameters; Aspect (4.8%), slope (18.5%), vegetation (15.1%), land use (12.6%), soil (13.6%), altitude (20.6%), geology (14.8%). As a result of the study, it was reported that the most sensitive area of the basin to the flood area is the plain areas in the north [7, 8].

Ertan et al. (2021) calculated basin flood parameters of Karamenderes (Çanakkale) as; distance to the stream (7.7%), slope (7.4%), aspect (3%), elevation (33.2%), geology (7.6%), land use (15.5%) and precipitation (25.6%). As a result of the study, while forest areas have low sensitivity in terms of flood risk, agricultural areas and urbanization areas were found to be risky. It is seen that the rivers have changed direction and the points where the river branches meet have high flood and flood sensitivity in the past floods examined. Precipitation was determined as the most effective parameter for flooding [11].

Sütünç et al. (2022) found that the flood effective parameters for Kezer region of Siirt as; flow (30%), precipitation (10%), geology (5%), land use (5%), slope (15), elevation (25), drainage density (10%). The study area is located in a moderate flood risk area. Considering the distribution of land cover/use, it is seen that the riskiest areas are in the regions where the city structure is dense and represented by 14.02%. The most risk-free areas are forest areas and it is 0.1% in percentage distribution. The percentage of the areas with the highest and the highest flood risk in the research area is 21.62%[9].

In the study of Duman et al. (2022), Flood effective parameters for Çankırı province are; distance to the stream (33.7%), slope (25.6%), precipitation (18%), land use (11%), soil (6%), aspect (3.5%), geology (2.2%). According to the findings, 1.8% (25.9 km^2) of Çankırı central district is very high; 16.6% (239.3 km^2) is high; 32.7% (471.8 km^2) is medium; It is stated that 38% (547.2 km^2) has low flood sensitivity, 10.8% (151.8 km^2) has very low flood susceptibility [10].

Yilmaz et al. (2017), in his study for Çorum province, the flood parameters; precipitation (28.37%), distance from streams (24%), slope (13.84%), elevation (10.6%), land use/cover (7.94%), geology (6%), aspect (4%), size of sub-basins (2.9%), the shape of the sub-basins (2.2%). The risk map created in the study and the existing measures were compared and it was observed that the places determined as first and second degree risky in the risk map overlap with the areas that are already in the existing precautionary plans [12].
In this study, it is aimed to determine the risk areas by AHP and Frequency Ratio methods based on the flood events in the Cevizdere and Elekçi streams in and around Fatsa district of Ordu province. In addition, it is aimed to determine the effective parameters in hazards for study area.

In this study, it is aimed to determine the risk areas by AHP and Frequency Ratio methods based on the flood events in the Cevizdere and Elekçi streams in and around Fatsa district of Ordu province. In addition, it is aimed to determine the effective parameters in hazards.

2. Study Area

The elevation of the basin determined as the study area varies from sea level to 2000 meters. The flooded streams flow into the Black Sea, but take their sources from the mountains at an altitude of 2000 meters. Some parts of the passage route of the stream are in the form of narrow-deep valleys with "V" shape. The precipitation value, which varies between 720 mm and 1100 mm throughout the basin, can turn into a triggering parameter especially for flooding. Precipitation values differ from north to south. The main reason for this can be explained as the humid winds of the Black Sea, while abundant precipitation is seen on the summits of the mountains and in the high parts,

it is gradually decreasing in the coastal areas. In addition to the alluvial soils formed at the point where the river meets the Black Sea, gray brown podzolic and reddish yellow podzolic soil types are dominant in most of the basin. The growth of districts in the river basin and therefore the increase in impermeable areas also cause an increase in surface flow and floods (see Fig. 1).

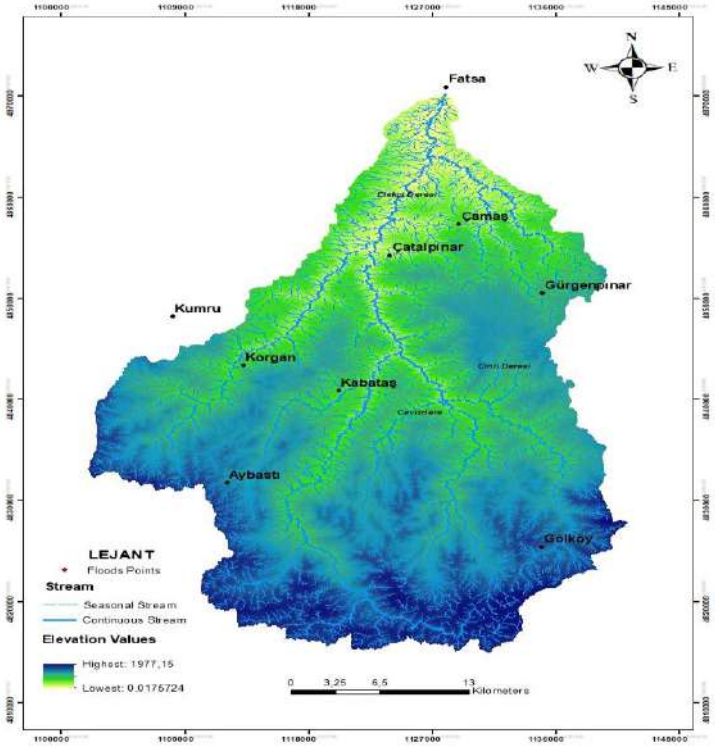

Figure 1. Study Area

On August 9, 2018, with an average of 80 kilograms of precipitation per square meter in Ordu, 9 large bridges collapsed as a result of the overflow of streams in 7 districts, especially in Ünye, Fatsa and Perşembe districts. As a result of the flood, serious damage occurred in nearly 100 streets, 2 people lost their lives and 8 people were injured. According to the reports of the Governorship of Ordu, 9 houses were flooded, 123 electrical transformers and 60 vehicles were damaged, 161 roads were closed to transportation, 98 culverts were damaged, and 9 bridges were completely destroyed. 165 workers were trapped in the factory and were rescued by AFAD teams (see Figure 2.)

a) b) c)

Figure 1. Flood Images from Study Area

In order to create flood disaster risk maps, 9 flood parameters were used within the scope of the study. The method of obtaining the necessary inventories to establish these parameters is given in Table 1. 9 parameters affecting the flood in the study area were created with the help of ArcGIS software (see Figure 3).

Tabel 1. Characteristics of Flood Triggering Data in Ordu-Fatsa District and Its Surroundings

Place/Institution where the parameter was obtained	Flood Trigger Factor	Data Type	Pixel Size
BCA, AFAD, MGM. Damage Assessment Records	Flood Locations	Nokta-Poligon	-
Digital Elevation Model (DEM) obtained from aerial photographs of the General Directorate of Mapping	Slope	Raster	5*5
	Aspect	Raster	5*5
	Topographic Humidity Index	Raster	5*5
	Stream Power Index	Raster	5*5
	Drainage Density	Raster	5*5
https://www.worldclim.org. precipitation map	Precipitation	Raster	5*5
https://earthexplorer.usgs.gov/ Landsat 8 OLI	NDVI	Raster	30*30
1/100.000 scaled geology maps belonging to the Mining Technical Exploration Directorate	Lithology	Raster	100*100
1/100,000 scaled Directorate of Survey and Project Department of the General Directorate of Rural Services under the Ministry of Agriculture, Forestry and Rural Affairs	Soil Type map	Vektör	100*100

a.

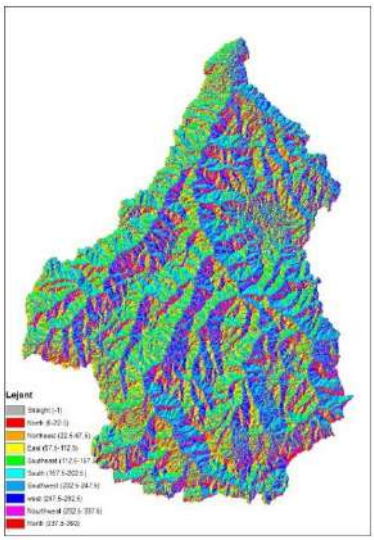

b.

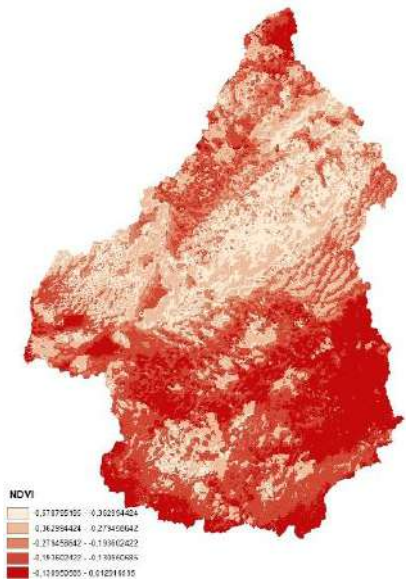

c.

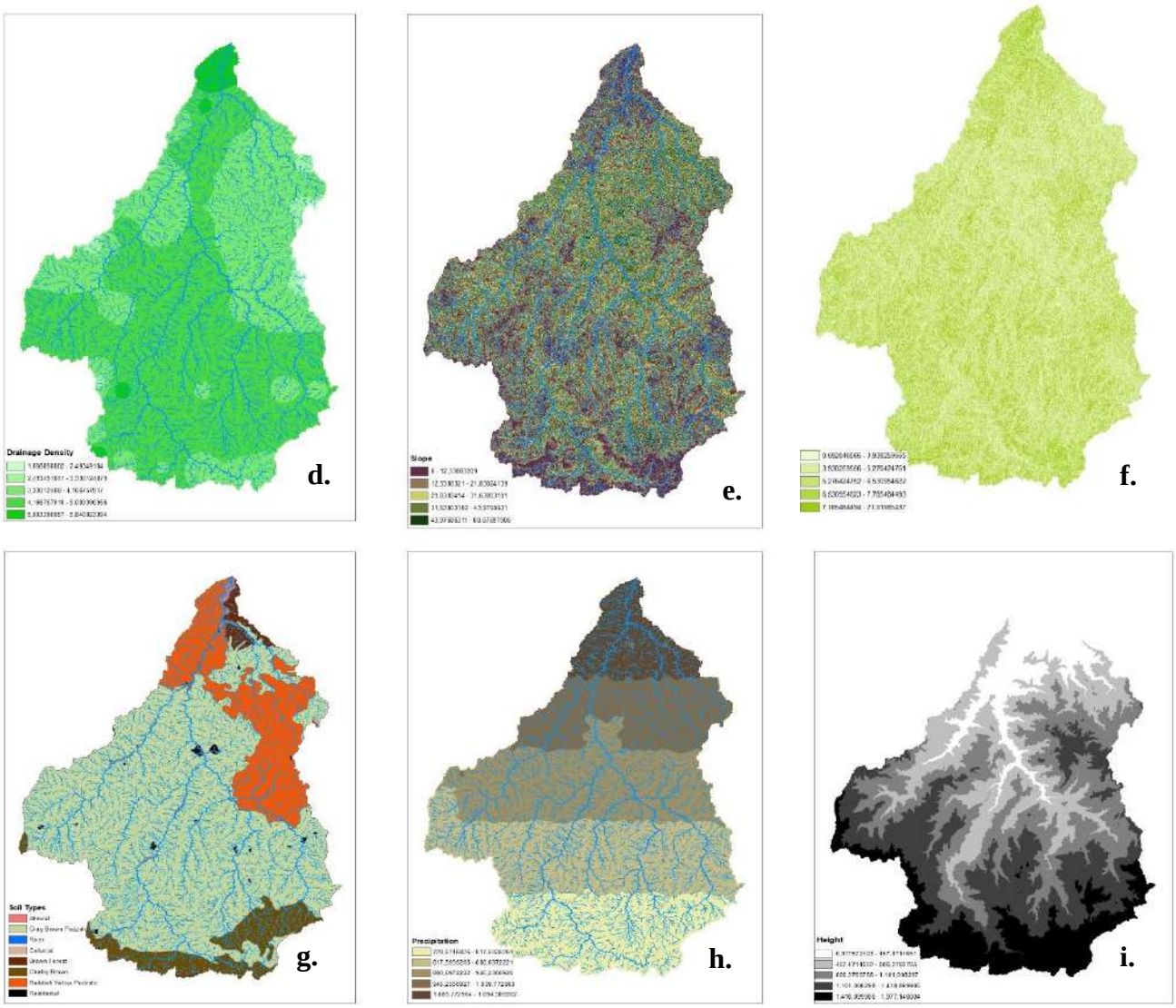

Figure 3. Maps of Parameters Affecting Flood (a: SPI(Stream power index), b: Aspect, c: NDVI, d: Drainage Density, e: Slope, f: Topographic Wetness Index, g: Soil Type, h: Precipitation, i: Elevation)

4. Methodology

The study area has a surface area of 440 km². For this area, a total of 440 flooded and non-flooded point data were assigned. These 440 point data, 220 flooded and 220 non-flooded data were used. The working algorithm of the models is shown in Figure 4.

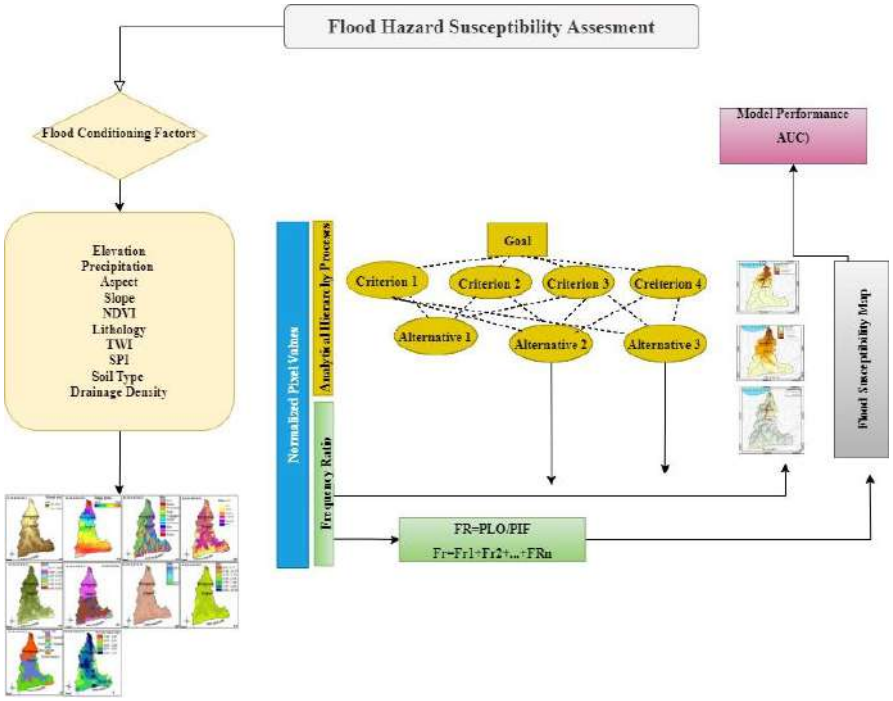

Figure 4. Flow Chart of Methodologies

4.1. Analytical Hierarchy Process (AHP)

Analytical hierarchy process, which is one of the multi-criteria decision making methods, has been used as a well-known and useful method to get the priorities of each alternative in multi-criteria decision making problems [5]. AHP is pairwise comparison theory and relies on expert opinions to find priority scales (Saaty, 2008). The modeling of the AHP decision problem consists of basic steps such as evaluation of weights and sensitivity analysis [4].

Tabel 2. AHP Hierarchy Table (Saaty, 1977)

Importance Values	Value Definitions
1	Equal importance of both factors
3	The situation where the 1st factor is more important than the 2nd factor
5	The situation where the 1st factor is more important than the 2nd factor
7	The situation where the 1st factor has a very strong importance compared to the 2nd factor
9	The situation where the 1st factor has an absolute superior importance compared to the 2nd factor
2, 4, 6, 8	Intermediate values

Comparisons are considered to be consistent if the consistency ratio is equal to or below 10%. If the rate is higher than this rate, the comparison should be reviewed. In this study, the superiority of the flood values over each other was made by the average of the values in the literature studies, and the consistency ratio was found at the desired rates.

4.2. Frequency Ratio Method

Factors causing hazards in the past shed light on future hazards [1]. (Considering this approach, it is thought that the connection between flooded areas and the factors in these areas is related to the link between the places where there was no disaster in the past and the factors of those regions [3]. Frequency Ratio Method can be defined as the ratio of the probability of occurrence of an event to the probability of not happening (Erener et al. 2010). The Frequency Ratio method is used to investigate the correlation of each flood-causing factor, taking into account the locations of

past floods. For this reason, each factor causing flooding was categorized and the frequency ratio of each factor in each category was calculated using GIS functions. Equation 7 is used for Frequency Ratio calculations.

$$FR = PLO/PIF \quad (7)$$

PLO= Percentage of flood presence in its subcategories of a parameter affecting flooding
PIF= Percentage of each category of a parameter affecting flooding

If the calculated Frequency ratio values are greater than 1, the result is that the parameter affecting the flood and the flood relationship are high and low, and the relationship is low. In this method, past disaster records are of great importance.

5. Discussion

When the Frequency Ratio Method is compared, the flooding points are determined as Very High Risk in the method. Elevation, Precipitation and Drainage Density (Dy) were found to be the 3 most effective parameters in this method. In the flood hazard analysis according to the Analytical Hierarchy process, values between 1 and 9 were used for the classification of factors and subclasses. While the value of 1 was determined as the least effective value, the value of 9 was determined as the most effective value in the flood. As a result of the literature readings, the ranking among the parameters used in the Analytical Hierarchy process was evaluated and carried out like an expert. In the AHP method, the most effective parameters were determined as elevation, precipitation and slope. In the Analytical Hierarchy Process, unlike the Frequency Ratio method, the entire basin is taken into account. Consistency values were tested and found below 5%. The literature was used to determine the interval value of each factor (Seejata et al., 2018; Goumrasa et al., 2021). Analytical Hierarchy Process has created a map with a larger risk area compared to the Frequency Ratio method (see Figure 5.)

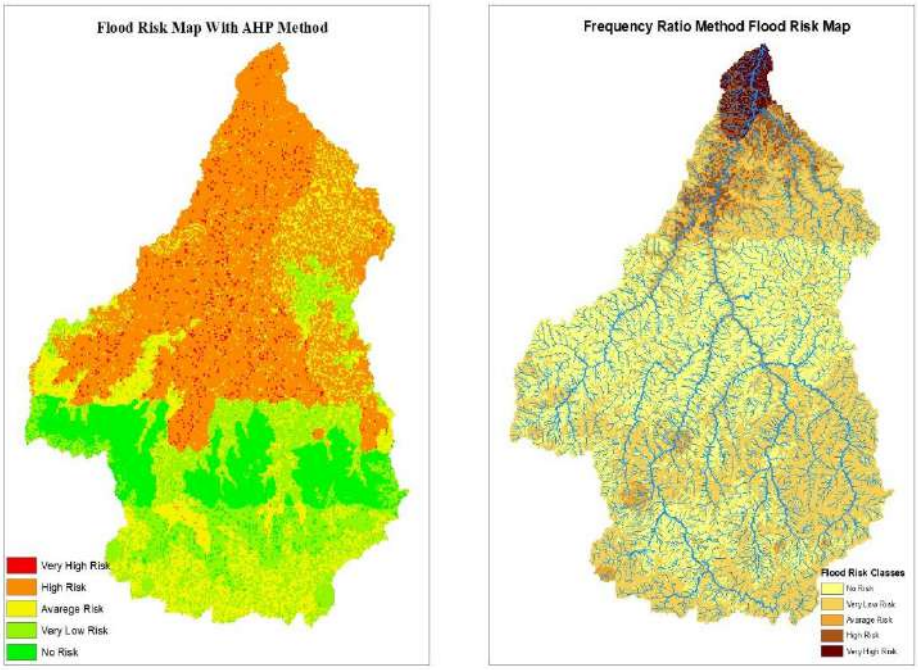

Figure 5. In the study area; a) Analytical Hierarchy Process, b) Flood Hazard Prediction Maps by Frequency Ratio.

When the risk maps formed in the frequency ratio and AHP methods are compared with the real maps, the AUC value of the frequency ratio method was found to be 0.828, while the AUC value of the AHP method was found to be 0.774.

6. Results

The basins of Cevizdere and Elekçi streams, which are within the borders of Fatsa district of Ordu Province, which are the study area, are areas with a high risk of flooding. For this reason, in this study, places with high flood risk in these basins will be determined by different methods.

In this study, Analytical Hierarchy Process (AHP) and Frequency Ratio Method (FR) methods, which are frequently used in the literature, were used to identify flood risk areas. The main purpose of using these methods in the study is to determine the flood risk areas of the basin and to create bases for flood protection plans for these areas. According to the results, the Frequency Ratio method (FR) gives successful results in determining the risk areas of flooding according to the Analytical Hierarchy (AHP) method. This success was found by comparing the AUC validation values and the actual flood maps with the method maps. While the Frequency Ratio method determined the risk in a narrower area than the AHP method, the AHP method was more reliable and determined the wider area as risky.

Flood is a disaster that directly affects the loss of life and property of people. The determination of flood risk maps constitutes a serious base especially for the basin planning to be made in the coming years and the construction of disaster prevention structures. The results of this study will be beneficial in the work of municipalities and relevant organizations while constructing flood protection structures in determining the areas to be settled in the coming years.

Funding

This research was supported by the Research Fund of the Inonu University Scientific Research Projects Unit (project IDs FDK-2022-2796).

7. References

[1] Chung C.F And Fabbri A.G,(1999), Probabilistic Prediction Models For Landslide Hazard Mapping, Photogrammetric Eng. And Remote Sen., 65 (12), 1388-1399.

[2] De Moel, H., Jongman, B., Kreibich, H., Merz, B., Penning-Rowsell, E., & Ward, P. J. (2015). Flood Risk Assessments At Different Spatial Scales. *Mitigation And Adaptation Strategies For Global Change*, *20*(6), 865-890.

[3] Lee S., Choi J., Min K., (2004), Landslide Hazard Mapping Using Gıs And Remote Sensing Data At Boun, Korea. Int J Remote Sensing 25, 2037-2052.

[4] Ossadnik, W., Schinke, S., Kaspar, R. H. (2016). Group Aggregation Techniques For Analytic Hierarchy Process And Analytic Network Process: A Comparative Analysis. Group Decision And Negotiation, 25(2), 421-457.

[5] Rashidpour, K. (2013). Using Improved Ahp Method In Maintenance Approach Selection. Yüksek Lisans Tezi, Mälardalen Üniversitesi/ Yenilik, Tasarım Ve Mühendislik Fakültesi

[6] Saral, A. (2010). Çok Kriterli Karar Verme Ve Bilgi Difüzyonu Yöntemleri Yardımıyla, Taşkın Risk Analizi Yetkisinin Gerçekleştirilmesi (Doktora Tezi, Bilişim Ensititüsü).

[7] Çamci, Kg, Ahmet, Ü. Nal, & Tonyaloğlu, Ee Çok Kriterli Karar Analizi İle Doğal Afetlerde Haritalama: Aydın İli Sel-Taşkın Riski Örneği. Ulisa: Uluslararası Çalışmalar Dergisi , 6 (2), 136-150.

[8] Şengün, Mt, Karadeniz, E., & Şaman, B. (2019). Tavşanlı Deresinde (Sivas-Hafik) Taşkın Risk Analizi, 1. İstanbul Uluslararası Coğrafya Kongresi Bildiri Kitabı , 20 (22), 653-668.

[9] Sütünç, H. S., & Yavuz, V. S. Taşkın Risk Alanlarının Analitik Hiyerarşi Süreci Kullanılarak Mikro-Havza Ölçeğinde Değerlendirilmesi. İdealkent, 13(37).
[10] Duman, N., & İrcan, M. R. Coğrafi Bilgi Sistemleri Tabanlı Çankırı Merkez İlçesinin Taşkın Duyarlılık Analizi. Jeomorfolojik Araştırmalar Dergisi, (9), 50-66.
[11] Ertan, A., Özelkan, E. Ve Karaman, M. (2021). Analitik Hiyerarşi Süreci Kullanılarak Coğrafi Bilgi Sistemleri Ortamında Sel Ve Taşkın Alanlarının Belirlenmesi: Çanakkale Karamenderes Havzası Örneği. Atmosfer Biliminde Araştırma Dergisi , 3 (2).
[12] Yılmaz, İ., Öztürk, D., & Kırbaş, U. (2017). Çorum Ili Taşkın Tehlikesinin Analitik Hiyerarşi Yöntemi Kullanılarak Incelenmesi. Tmmob Harita Ve Kadastro Mühendisleri Odası, 16, 3-6.

International Conference on Advances and Innovations in Engineering

Location and Seasonal Evaluation of Major Flood Hazards in Rize Province

Ufuk YÜKSELER[1] , Ömerul Faruk DURSUN [2]

[1]Phd.Student. İnönü University, Engineering Faculty, Civil Engineering Department. Malatya/TÜRKİYE.
[2]Prof. Dr. İnönü University, Engineering Faculty, Civil Engineering Department Malatya/TÜRKİYE
[1]ufukyukseler12@gmail.com, [2]ofdursun@gmail.com

[1](ORCID: 0000-0002-7233-0821), [2](ORCID: 0000-0003-3923-5205)

Abstract

Flood hazards that occur dozens of times every year in our country cause serious loss of life and property. Establishing a flood inventory of the past years and investigating the causes of floods are important for the prevention of possible hazards in the coming years.

In this study, 12 major floods occurred within the borders of Rize province from 1923 to the present were examined. To this aim; the available data about the floods were obtained from AFAD, DSI and the Presidency Hazard Coordination Center and mapped with the ArcGIS program supported by Geographic Information Systems. The elevation map of the basins was created with digital elevation models with a resolution of 5 meters. As a result of the analyzes; although the rainiest season in Rize is autumn, it is seen that the majority of the floods occurred in the summer months, and the short-term heavy rains in the summer turned into hazards in the region. In addition, the floods generally occurred in the region close to the place where the rivers spill into the Black Sea, and less floods were seen in the main or side branches of streams. It has been observed that some areas of the basin have close to sea level are flood hazard susceptibility areas. It is important that areas with flood hazard susceptibility should be carefully examined in the construction of urbanization and river regulation structures.

Keywords: Flood, Geographic Information Systems, ArcGIS, Flood hazard susceptibility regions, Rize province

1. Introduction

Flood is defined as a hazard that causes loss of life and property as a result of the extreme flow of the stream. It occurs in the first place among meteorological hazards in our country, and second hazards after earthquakes. In Turkey, most flood hazards are occur in the Black Sea region due to its topographic and meteorological characteristics. Rize is one of the provinces where flood hazards are occurring most frequently in our country.

Although it is very difficult to predict the flood hazard, estimations are made by creating risk maps with certain methods. Mehebub Sahana (2018) reported that the lower Kosi River Basin in India experienced many floods in the past and tried to reveal the factor that was effective in the formation of these floods. Flood sensitivity analysis was performed using frequency ratio and fuzzy logic models. As a result of this study, he stated that the closest results to the real flood situation occur in the fuzzy logic method and that the most effective factor causing flooding in these regions is sudden heavy precipitation. Webster et al. (2012) performed flood modeling with MIKE 11 and MIKE 21 software in their study on the Phillip river in Oxford. They used terrestrial elevation data and interpolated data, as well as topographic and bathymetric data. They showed that the results they obtained with MIKE 21 showed a general similarity with the observed tides. In MIKE 11, they compared the results of the flood models they obtained with real observations and conducted a detailed research. Rungo and Olesen (2003) mentioned that two-dimensional modeling has been widely used in flood areas in recent years in order to perform flood modeling correctly. They mentioned that MIKE flood modeling consists of a combination of one-dimensional and two-dimensional models. They mentioned that the domains of MIKE 11 and MIKE 21 are calculated in detail at each step. In recent years, MIKE21 has been developed in order to make more two-dimensional flood modeling, and thanks to these developments in the model; They mentioned that it is possible to make realistic simulations of flood propagation. Selvanathan and Dynmond (2010) discussed the application of programs and modules in the analysis of flood and flood analysis using ArcGIS, FloodwayGIS and Hec-RAS from Geographic Information Systems technologies. With FloodwayGIS, they

[1]Corresponding author

have developed an algorithm that will eliminate the need to switch between HecRas and GIS during the flood modeling process and save time in analysis. Mohammad Ahmadlou (2020) has worked on flood susceptibility mapping and evaluation using a new deep learning model that combines multi-layer perceptron and auto-encoder neural networks. In this study, Iran's Golistan region and India's heavily flooded regions were examined. They obtained significant results with values of 91%, 90.74 and 93% in artificial intelligence models. As a result of these findings, it was stated that artificial intelligence models showed serious success in detecting flood points. Patel and Srivastava (2013) performed the integration of satellite and GIS datasets for the mapping of flood zones of Surat district, Gujarat, India. The obtained high resolution remote sensing images were combined with hydraulic analysis and digital elevation model (DEM) to determine the flood-prone area of various regions divided into North, South, East, and West. They emphasize the importance of using GIS models to reduce the degree of hazard due to future flood events to reduce flood hazards. As a result of the study, it was determined that while the western and south-western regions showed a flood tendency, the eastern region was the least.
In this study, the areas of 12 largest floods in different basins in Rize province were determined and the reasons for the occurrence of these floods in terms of periods, locations and characteristics of the basins were tried to be interpreted.

2. Study Area

The province of Rize, which is selected as the study area, is a place where “V” profile valleys with steep slopes are frequently encountered. “V” profile valleys with an altitude of up to 2000 meters are followed by “U” profile lands up to 3200 meters. This province, which has a lot of rough terrain, has a coastal part of 80 km in length and 50-150 meters in width on the Black Sea coast. The region is mostly covered with broad-leaved dense forests due to the high humidity and rainfall. Approximately 25% of Turkey's forests are located in this region. The fact that the annual average precipitation is over 2300 mm/m^2 is another trigger for flood events. While the least precipitation is occur in the spring season, the most precipitation is occur in the autumn season and the humidity is over 75%. There were 12 major hazards in the study area (see Table 1.) Within the scope of this study, the study areas were visualized with the reports received from different institutions (see Figure 1.)

Table 1. Major flood hazards within the borders of Rize province since 1923 (Prime Ministry Republic Archive (BCA), Disaster and Emergency Management Presidency (AFAD))

Date	Balance sheet
14.07.1973	Floods occurred in Güneysu sub-district of Rize province and Kalkandere districts. 11 people died, including 7 people in Pazar village, along with other villages (see Figure 1.a)
30.07.1977	Floods occurred in Pazar and Hemşin districts of Rize. In addition to serious economic losses, 33 lives were lost. (see Figure 1.b)
19.07.1983	As a result of the overflow of Abuçağlayan, Sümer, Hemşin and Bodasarı streams in Rize province, flood hazards occurred in Fındıklı and Pazar districts. In the hazard in which 22 people lost their lives, serious property losses occurred. (see Figure 1.c)
21.08.1988	Hemşin, Bodasarı, Ardeşen, Fırtına, Konak, Işıklı streams caused floods covering Pazar, Ardeşen and Fındıklı districts. The flow discharge values obtained are the highest value measured by the station to date. While 13 people died in the hazard, serious property losses occurred. (see Figure 1.d)
31.08.1995	Floods occurred in and around Rize province, especially in Ardeşen, Pazar, Çayeli and Güneysu districts. The basins where the floods are effective are the small river basins between Güneysu and Işıklı Stream, 2-5 km from the coast. According to the researches, it was the biggest flood in the last 70 years in this region. As a result of the flood, 9 people lost their lives. (see Figure 1.e)
11.11.2001	Due to the overflowing of the Fırtına, Şairler, Aşıklar, Hemşin, Bodasarı, Dolana, Işıklı and Arılı streams in Çayeli district of Rize province, 10 people died, many agricultural lands were damaged and it caused serious property losses. (see Figure 1.f)
23.07.2002	Due to the overflow of Güneysu and Çayeli Streams, the centers of the two districts were flooded. As a result of the landslide in the Yeni Mosque area of Selamet Village of Güneysu District, 4 houses remained under the ground. In the villages of Limanköy and Yenihisar in Çayeli, 5 people lost their lives. Because the rains **Major flood hazards within the borders of Rize province since 1923 (Prime Ministry Republic Archive (BCA), Disaster and Emergency Management Presidency (AFAD)) (More)** continued, the villages of Selamet, Islahiye, Limanköy, Yenihisar and the houses of Muradiye were completely evacuated. As a result of the hazard, 34 people lost their lives. (see Fig. 1.g)

Table 1. Major flood hazards within the borders of Rize province since 1923 (Prime Ministry Republic Archive (BCA), Disaster and Emergency Management Presidency (AFAD))

11.07.2005	It resulted in the death of 12 citizens due to the overflow of the side streams near Veliköy Village in Rize province. (see Figure 1.h)
26.08.2010	As a result of the landslide and flood, 14 peoples lost their lives and over a hundred buildings were severely damaged and rendered unusable. A total of 27 people died in the floods. (see Figure 1.i)
01.09.2016	5 people died as a result of the overflow of Çağlayan, Kalkandere and Arılı streams in Fındıklı and Kalkandere districts of Rize province. In the mentioned basin, there were 290 kg/m^2 of precipitation within 24 hours and a flood was occured. According to the report published by DSI as a result of the hazard, it was decided that the closed section of the culvert located in the city center of Rize, which was determined to be insufficient in capacity as a result of the Kale Stream hydrodynamic modeling studies and could cause flooding, should be demolished and rebuilt in appropriate sections and the interventions to the stream bed should be removed (see Figure 1. j).
10.02.2017	Due to the overflow of Sabuncular and Büyükdere in the Çayeli district of Rize, 2 people died in the villages of Kesikpınar, Gürpınar and Beydere, and serious property losses occurred. The highway is flooded. There were problems with transportation. As a result of the flooding of the tributary streams, blockages occurred at the road crossings and caused the main stream to overflow. One of the 2 people who fell under the landslide in the Çayeli Kaptanpaşa Village Gürpınar Neighborhood died, and the other was injured. Çayeli Kaptanpaşa Village road closed to road transportation (see Figure 1.k).
22.08.2020	250 kilograms of precipitation per square meter in the last 24 hours in Rize caused a hazard. In the city affected by floods and landslides, 2 people lost their lives, 10 people were injured and rescued. In the city, where access to 12 villages could not be achieved, 2 houses, roads and bridges collapsed, infrastructure and superstructure were damaged, dozens of vehicles were flooded, and the remaining 36 people were evacuated. According to the report prepared by DSI, it was stated that due to the hydraulic inadequacy of the Historical Kemer Bridge, a dam was formed in front of the water and the hazard enlarged. The water that rises to the road level due to excessive rainfall hinders the access (see Figure 1.1).

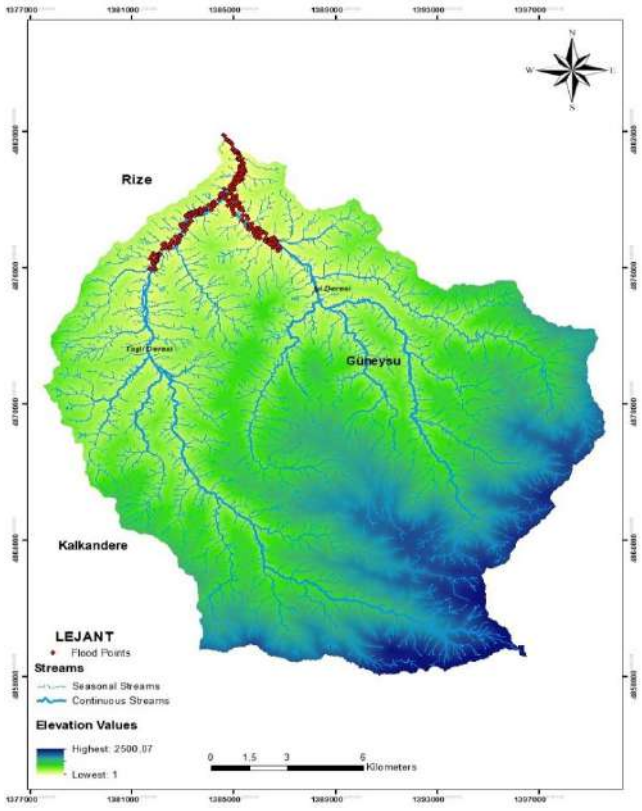

Figure 1. Flooded areas and flood dates **a.**

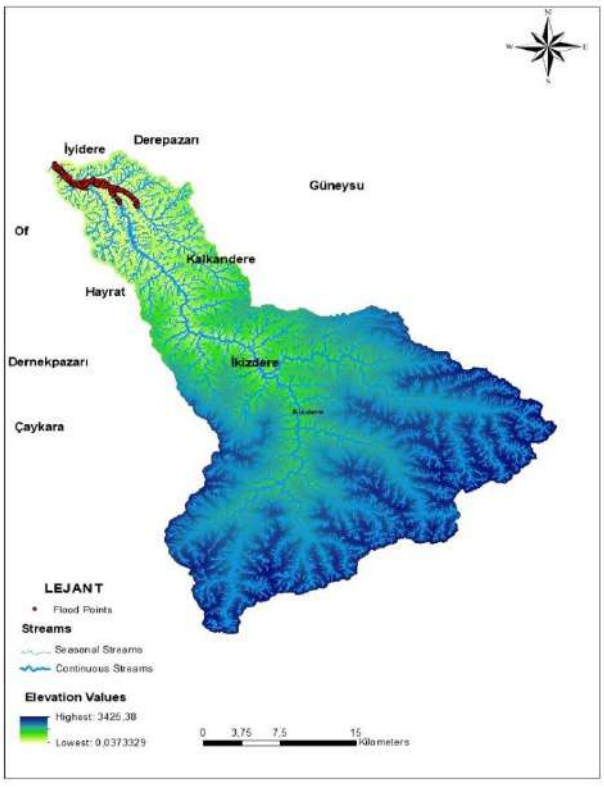

Figure 1. Flooded areas and flood date **b.**

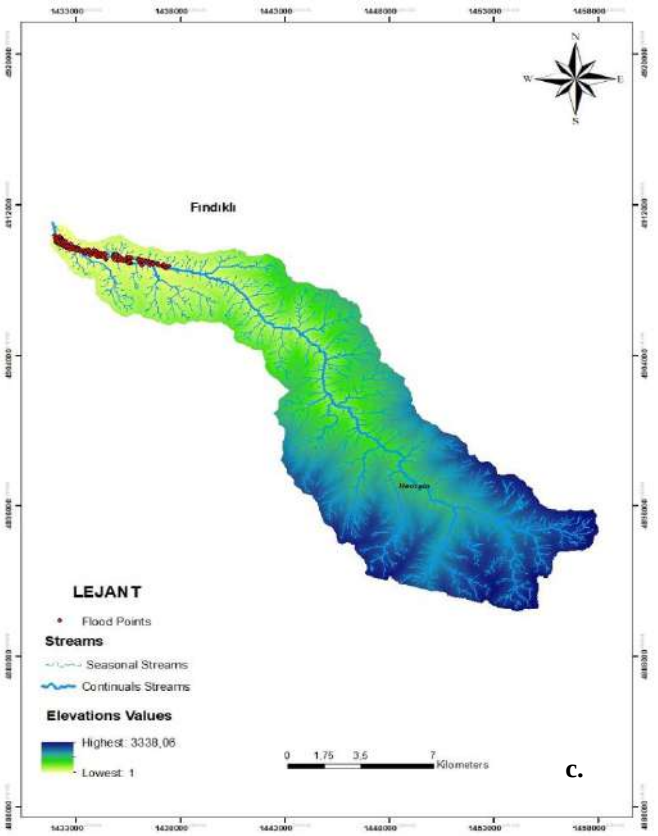

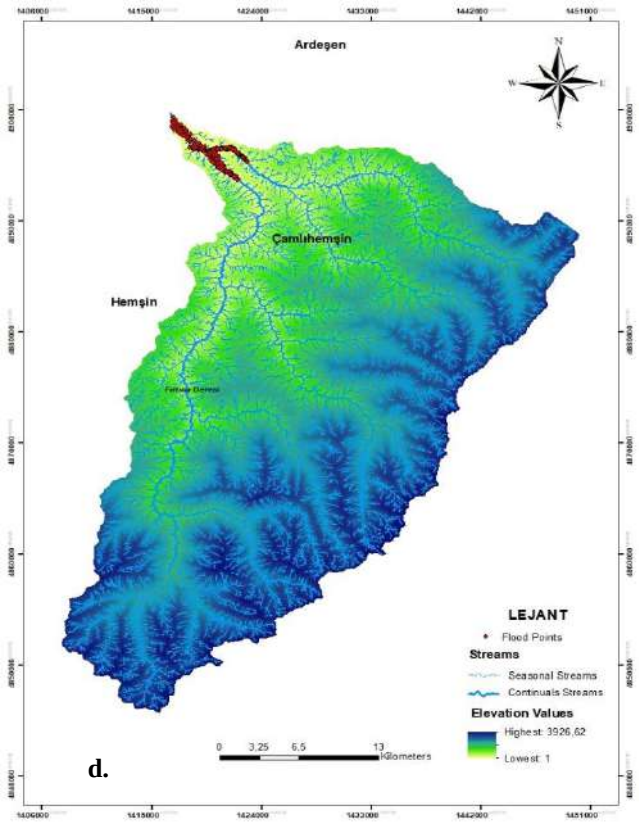

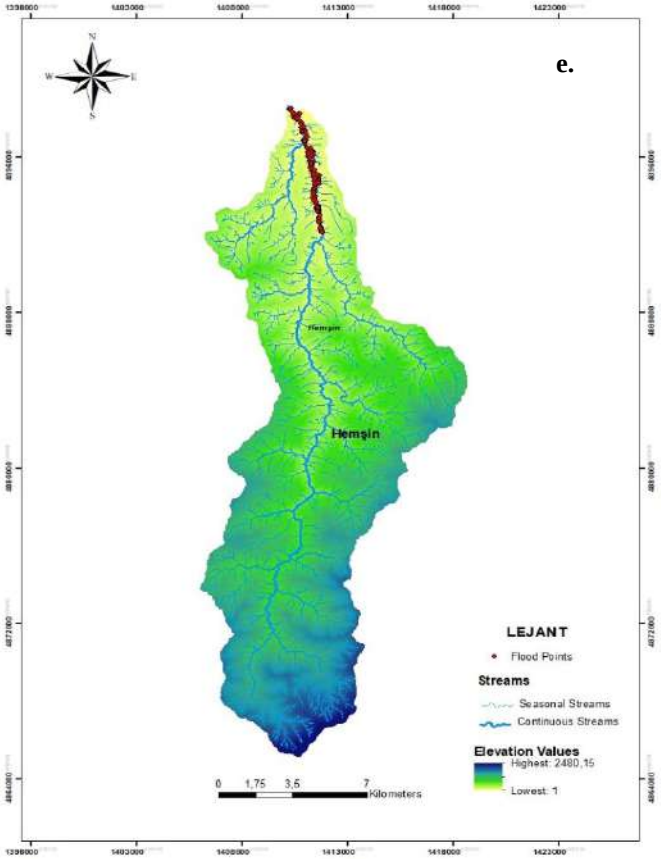

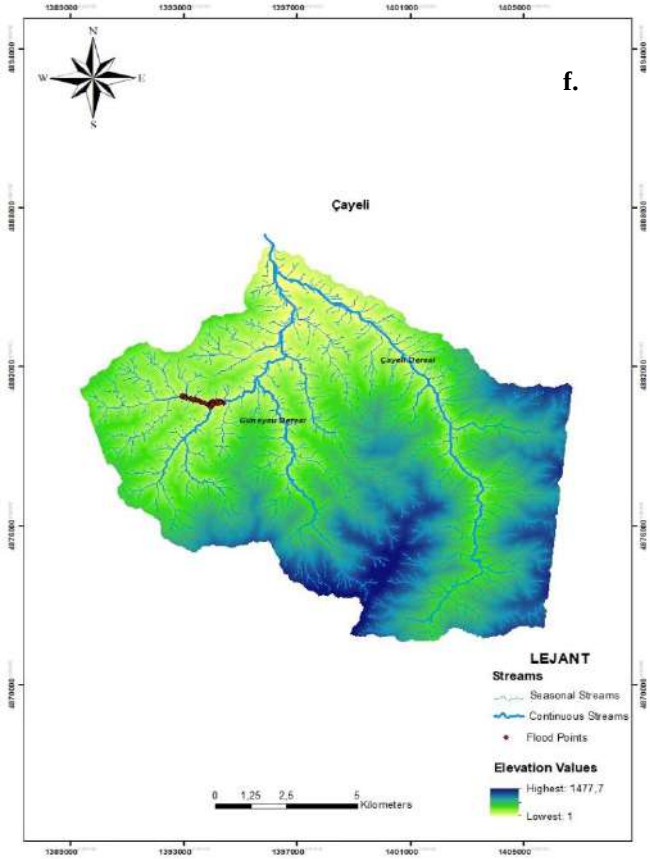

Figure 1. Flooded areas and flood dates

Figure 1. Flooded areas and flood dates

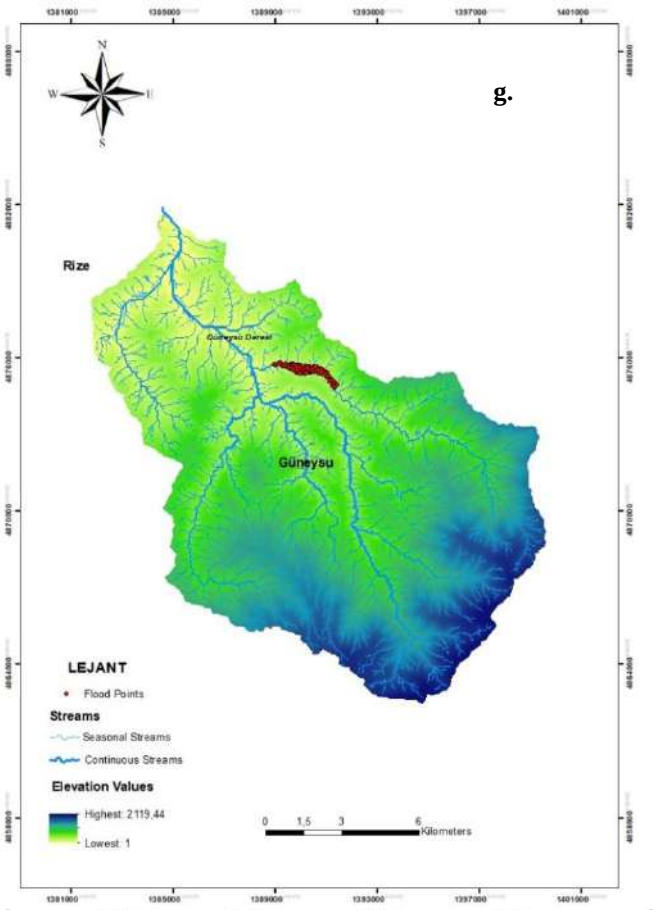

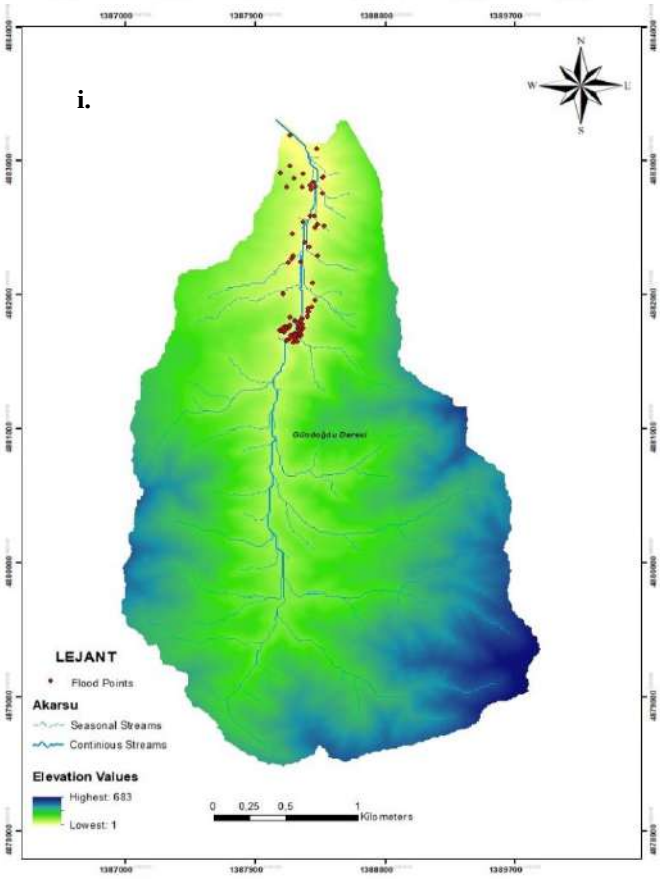

Figure 1. Flooded areas and flood dates

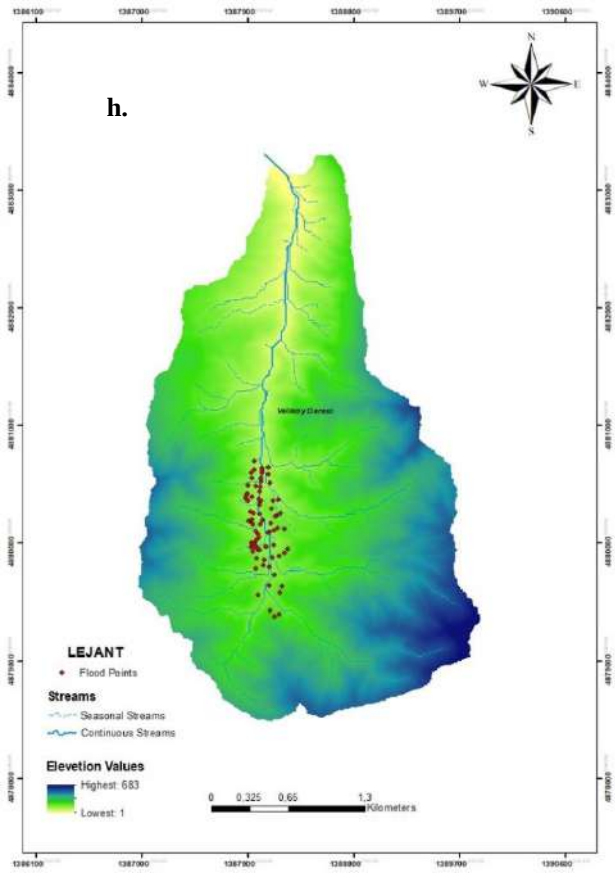

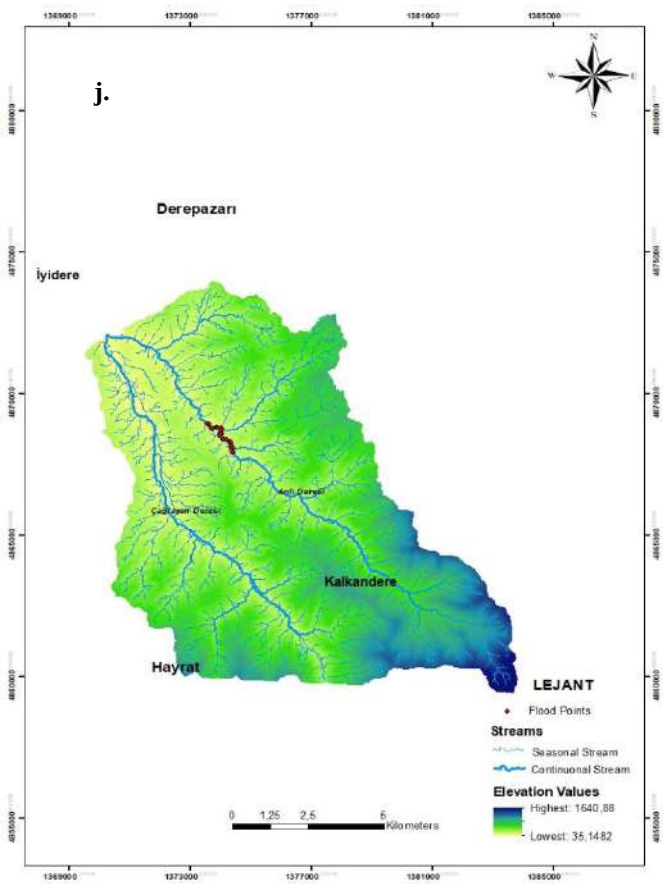

Figure 1. Flooded areas and flood dates

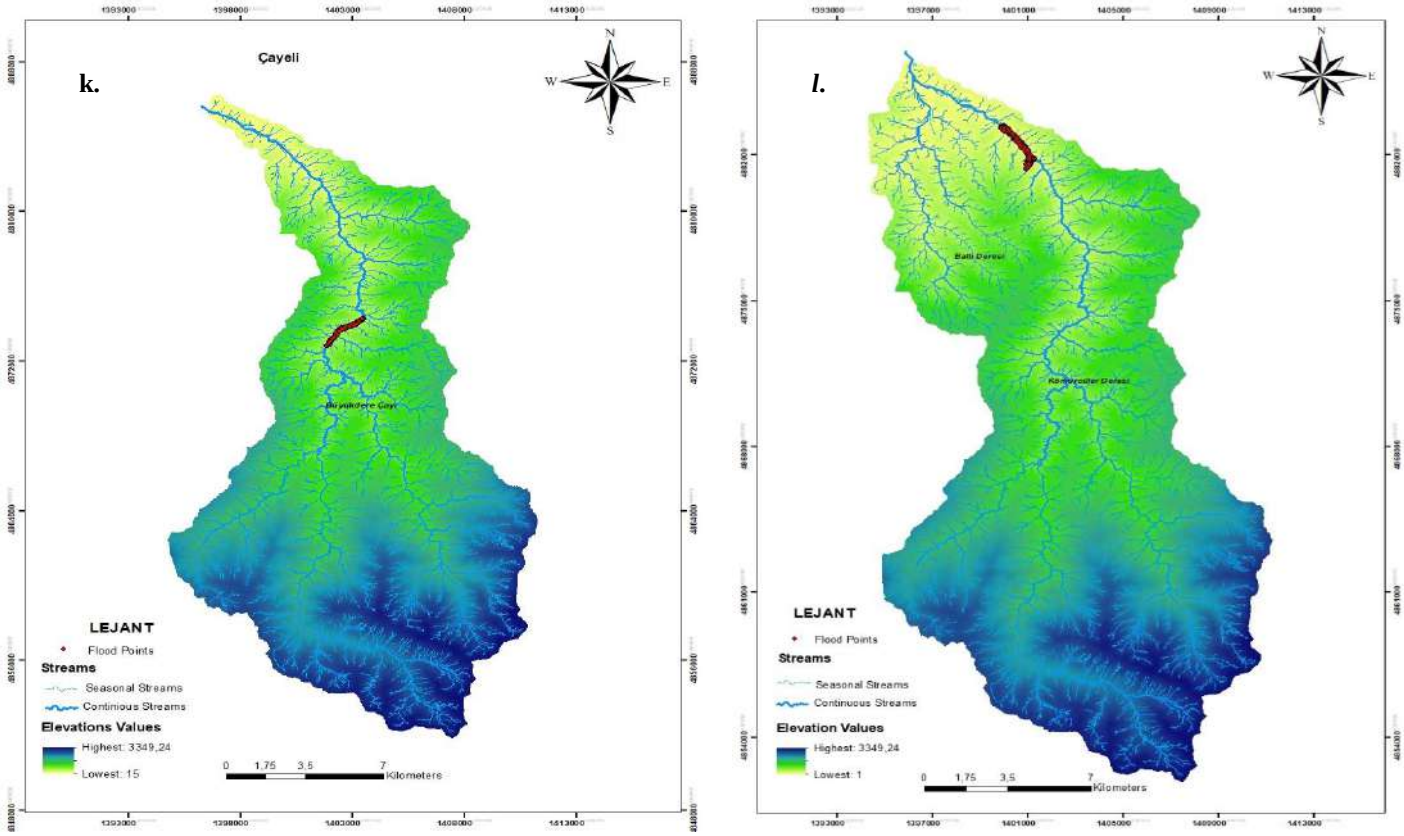

Figure 1. Flooded areas and flood dates
(a; 1973, b;1977, c;1983, d;1988, e;1995, f;2001, g;2002, h;2005, i;2010, j;2016, k;2017, *l*; 2020)

3. Discussion

Rize province is one of the provinces of our country that receives the most rainfall and is exposed to flood hazards. When the hazards are evaluated seasonally, it is seen that 5 hazards (1973, 1977, 1983, 2002, 2005) occurred in July, 4 hazards (1988, 1995, 2010, 2020) occurred in August, and the other three hazards occurred in November, September and February. When the climatic situation of the region is examined, it is seen that although the most rainfall occurs in the autumn season, 75% of the hazards that cause great loss of life and property occur in the summer months. According to these results, it can be said that sudden and heavy summer rains in Rize province caused a hazard. This situation; It can also be interpreted that the leakage capacity of soil surfaces is higher in the spring and autumn seasons.

When the altitude values of the hazard areas are examined, it is seen that 8 hazards (1973, 1977, 1983, 1988, 1995, 2005, 2010, 2020) are occured at values up to 0-300 meters. In addition, 4 hazards (2001, 2002, 2016, 2017) were happened at altitudes of 300-600 meters. While 6 hazards (1973, 1977, 1983, 1988, 1995, 2005) were experienced in the downstream part of the river flowing into the Black Sea, 2 hazards (2001, 2002) occurred in the side branches of the river and 4 hazards (2005, 2016, 2017, 2020) occurred in the main branch. While the flood hazards occurred in1973, 2001 and 2002 in the basins of the same river, the 1973 flood occurred in the downstream, and the 2001 and 2002 floods occurred in the side branches. While there was a flood in the main branch of the black water in 2005, the flood in 2010 occurred in the downstream (Table 2).

Table 2. Flood months, elevation and location information

Months	Elevation Range (m)	Location in the Stream
July	0-300	Downstream
July	0-300	Downstream
July	0-300	Downstream
August	0-300	Downstream
August	0-300	Downstream
November	300-600	Tributary stream
July	300-600	Tributary stream
July	150-250	Main Stream
August	0-100	Downstream
September	300-500	Main Stream
February	300-500	Main Stream
August	0-300	Main Stream

4. Results

In this study, the locations, periods and elevation values of hazards that occurred in Rize in the past were examined and evaluated.

According to the findings of the study; Flood hazards in Rize province mostly occurred in the summer months (July and August). According to the meteorological records of Rize province, although the most rainfall occurs in the autumn months, the fact that floods occur in the summer months has shown that sudden and heavy rains cause floods. In addition, floods mostly occur at elevations between 0-300 meters, that is; It has been seen in the parts of the rivers flowing into the Black Sea. In some basins, floods at altitudes of 300-600 meters were experienced in the main and side branches. The fact that floods occur more than once in some streams shows that these parts are flood sensitive areas. It is necessary to be more careful in terms of the measures to be taken and flood protection structures to be built in these streams.

Flood is a hazard that causes serious loss of life and property. The fact that a flood hazard is affected by multiple parameters challenges the predictability of the hazard. It is very important to determine flood risk areas and make preliminary assessments about flood periods in determining the settlement areas of municipalities and in the construction of river regulatory structures. This study also aimed to eliminate the lack of verbal expression but not mapping of the flood areas previously experienced in the region. In addition, the relationships between the elevation of floods and the location of the flood location on the stream were tried to be revealed.

Funding

This research was supported by the Research Fund of the Inonu University Scientific Research Projects Unit (project IDs FDK-2022-2796).

5. References

Sahana, M., & Patel, P. P. (2019). A comparison of frequency ratio and fuzzy logic models for flood susceptibility assessment of the lower Kosi River Basin in India. *Environmental Earth Sciences*, *78*(10), 1-27.

Webster, T., Crowell, N., McGuigan, K. and Collins, K., 2012. Integrated River and Coastal Hydrodinamic Flood Risk Mapping, Applied Geomatics Research Group Centre of Geographic Sciences Nova Scotia Community College, Middleton .Atlantic Climate Adaptation Solutions Association.

Rungo, M. and Olesen, K. W., Combined 1- and 2- Dimensional Flood Modelling, Erişim Tarihi:02.09.2013 http://www.afshinsalari.ir/files/articles/mike.pdf, (2003).

Selvanathan, S., & Dymond, R. L. (2010). FloodwayGIS: An ArcGIS visualization environment to remodel a floodway. *Transactions in GIS*, *14*(5), 671-688.
Ahmadlou, M., Al-Fugara, A. K., Al-Shabeeb, A. R., Arora, A., Al-Adamat, R., Pham, Q. B., & Sajedi, H. (2021). Flood susceptibility mapping and assessment using a novel deep learning model combining multilayer perceptron and autoencoder neural networks. *Journal of Flood Risk Management*, *14*(1), e12683.

Patel, D. P., Srivastava, P. K. (2013). Flood hazards mitigation analysis using remote sensing and GIS: correspondence with town planning scheme. Water resources management, 27(7), 2353-2368.

Prime Minister Rebuplic Archive (BCA), Fund Code: 030,10/117,818,30.

Prime Minister Rebuplic Archive (BCA), Fund Code: 490,01/948,677,1

Disaster and Emergency Management Presidency (AFAD), Flood Balance Sheet Report (2021). (unpublished)
DSI Archive, Flood Reports of Rize Province. (unpublished)

International Conference on Advances and Innovations in Engineering

Evaluation of Ceramic Cake Waste in Asphalt Concrete

Murat KARACASU[1], Zahir WAFAIE[2], Kadir Berkhan AKALIN[3]

[1,2,3] Civil Engineering Department, Engineering and Architectural Faculty, Eskisehir Osmangazi University, Eskisehir, TURKEY

[1]muratk@ogu.edu.tr, [2]e-zahirwafaye2018@gmail.com, [3]kbakalin@ogu.edu.tr

[1](ORCID: 0000-0001-9721-0984), [2](ORCID: 0000-0003-3572-073X), [3](ORCID: 0000-0001-6720-5498)

Abstract

Global population growth has led to an increase in the use of vehicles and industrial products, resulting in heightened production levels. This intensified production inevitably generates waste, which, when not managed effectively, contributes to environmental pollution and poses challenges for waste storage. In response to this issue, scientific research has focused on repurposing waste materials across various sectors. One such application involves utilizing ceramic waste in road construction. In this particular study, we explored the utilization of ceramic cake waste as an alternative aggregate material in asphalt concrete. Marshall Samples were prepared by incorporating ground ceramic waste at varying rates: 10%, 20%, 30%, and 40% by weight of the aggregate. Our test results suggest that incorporating up to 20% of ceramic cake waste in asphalt concrete production is feasible. This approach has the potential to mitigate environmental and visual pollution, making it a promising avenue for further in-depth investigation.

Keywords: Asphalt concrete, ceramic cake, waste recycling, environmental studies, sustainable materials.

1. Introduction

Asphalt concrete pavements stand as the preferred pavement type in road networks due to their performance and ease of maintenance. Typically, asphalt concrete comprises two primary components: aggregates and bitumen. It's worth noting that bitumen carries a higher material cost compared to aggregates. Although bitumen makes up approximately 5% of asphalt concrete by proportion, it accounts for a significant 80% to 90% of the total cost. In contrast, aggregates, despite constituting only 10-20% of the total cost, comprise around 95% of the composition of asphalt concrete. While the bitumen content in Hot Mixture Asphalt (HMA) may be relatively low, it plays a crucial role in determining the overall coating performance [1-3]. On the other hand, due to industrial production, the amount of waste is increasing day by day. The inadequacy of natural resources and storage areas causes environmental problems. For this reason, studies on the reuse and recycling of wastes in various production sectors have increased and gained importance all over the world. One of these production sectors is the road construction sector [4].

Environmental wastes are used in the production of asphalt concrete both within the scope of evaluating environmental wastes in road construction and improving the performance properties of asphalt concrete. These studies can be in the form of modified asphalt concrete mix [5, 6] or modified bitumen [7, 8]. The amount of material used in the mixture modification is higher than the bitumen modification. For this reason, environmental wastes can be evaluated at higher rates in the mixture modification of asphalt concrete. The amount of modifier used in bitumen modification is less. These additives can be used in the form of industrial production or as environmental waste [9, 10]. Industrial production materials increase the production cost of asphalt concrete [11]. Evaluation of environmental wastes in asphalt concrete generally reduces the cost [12].

[1]Corresponding author

Kara and Karacasu examined the effects of completely mixed ceramic waste on the mechanical behavior of HMA. In this study, it has been proven that the optimum bitumen content (OBC), voids in mineral aggregate (VMA) and void ratio (V) values increase with the increase in the waste rate. However, as the waste content increases, Marshall Stability (MS), voids filled with asphalt or bitumen (VFA), and specific gravity (SG) values decrease [13].

This study investigates the feasibility of using waste cake ceramics from ceramic factories in the Inönü region of Eskişehir, Turkey, in the production of asphalt concrete (Figure 1). The study constitutes a certain part of the waste generated in ceramic factories. In ceramic factories, waste is generated in the form of floors, walls, and ceramic cakes. Three separate master's studies are ongoing and projects are being carried out for the three mentioned wastes. Only some of the ceramic cake waste studies will be given here. The paper will form a basis for international literature. In the study, 10%, 20%, 30%, and 40% of the aggregate weight of ceramic cake waste (CCW) was used in the asphalt concrete mixture, replacing it according to the corresponding grain size, and the results were obtained.

Figure 1. Ceramic waste materials

2. Material and Method

The properties of the bitumen and limestone aggregates used within the scope of the study are given in Table 1 and Table 2, respectively.

Table 1. Properties of the bitumen used in the study

Properties	Value	Standard
Penetration (25°C, 100 g)	64	ASTM D5
Softening point (°C)	48	ASTM D36/D36M-09
Ductility (25°C, 5 cm/min)	>100 cm	ASTM D113-07
Loss of Heating (%)	0.430	ASTM D6-95
Flash Point (°C)	314	ASTM D92-05a
Specific Gravity (g/cm^3)	1.026	ASTM D70-09e1
Viscosity (at 135°C, cP)	437.5	ASTM D4402-06
Viscosity (at 165°C, cP)	137.5	ASTM D4402-06

Table 2. Properties of the aggregates used in the study

Properties	Value	Standard
Apparent specific gravity (g/cm^3) of coarse aggregate (CA)	2.709	ASTM C127, C128
Specific gravity (g/cm^3) of coarse aggregate (CA)	2.695	ASTM C127, C128
Saturated surface dry gravity (g/cm^3) of coarse aggregate (CA)	2.691	ASTM C127, C128
Apparent specific gravity (g/cm^3) of fine aggregate (FA)	2.858	ASTM C127, C128
Specific gravity (g/cm^3) of fine aggregate (FA)	2.727	ASTM C127, C128
Saturated surface dry gravity (g/cm^3) of fine aggregate (FA)	2.688	ASTM C127, C128
Specific gravity (g/cm^3) of filler (MF)	2.783	ASTM C127, C128
Water Absorption (%)	0.380	ASTM C127, C128
Compacted Bulk Density (g/cm^3)	1.572	ASTM C 29
Loose Bulk Density (g/cm^3)	1.301	ASTM C 29
Los Angeles Abrasion Test (%)	16.200	ASTM C 131
Flatness Index (%)	16	ASTM D 4791
Freeze-Thaw Resistance (%)	4	ASTM C 88

The aggregate material was designed to meet the limits for Marshall Mix Design (MMD) for wearing course type 2 in the Turkish General Directorate of Highways Technical Specification (HTS) and Superpave Mix Design (SMD) [14, 15]. The design and sieve analysis of aggregate is given in Table 3.

Table 3. The design and sieve analysis of aggregate

					MMD		**SMD**	
Aggregate Type	**Sieve No (in)**	**Sieve Size (mm)**	**$X^{0.45}$**	**Passing (%)**	**Lower Limit**	**Upper Limit**	**Lower Limit**	**Upper Limit**
CA	3/4"	19.000	3.76	**100**	*100*	*100*	*100*	*100*
CA	1/2"	12.500	3.12	**94**	*100*	*100*	*90*	*100*
CA	3/8"	9.500	2.75	**80**	*80*	*100*	-	-
CA	# 4	4.750	2.02	**49**	*55*	*72*	-	-
FA	# 8	2.360	1.47	**34**	-	-	*47.2*	*47.2*
FA	# 10	2.000	1.37	**31**	*36*	*53*	*36.8*	*42.4*
FA	# 16	1.180	1.08	**24**	-	-	*31.6*	*37.6*
FA	# 30	0.600	0.79	**18**	-	-	*23.5*	*27.5*
FA	# 40	0.425	0.68	**16**	*16*	*28*	*21.1*	*23.8*
FA	# 50	0.300	0.58	**14**	-	-	*18.7*	*18.7*
FA	# 80	0.180	0.46	**11**	*8*	*16*	-	-
FA	# 100	0.150	0.43	**10**	-	-	-	-
MF	# 200	0.075	0.31	**5.5**	*4*	*8*	-	-

CCW is a byproduct obtained through the filtration of production sludge. Prior to filtration, the sludge settles, and the residual water is recycled in the production process. After filtration, the moisture content of the waste cake sludge ranges from approximately 28% to 32%. We sieved the CCW waste material using a 1.18 mm sieve, ensuring it aligns with the grain size requirements for asphalt concrete aggregate. The images of the samples are given in Figure 2, and characteristics of CCW waste and XRF analysis results are given in the Table 4 and Table 5, respectively.

Figure 2. CCW samples

Table 4. Properties of the CCW used in the study

Properties	Value
Dry Strength (kg/cm3)	5.4
Cooked Size (mm)	89.95*179.85
Total Firing Shrinkage (%)	10.06
Baked Strength (kg/cm3)	464.5
Compacted Bulk Density (g/cm^3)	1.471
Loose Bulk Density (g/cm^3)	1.298
Water Absorption (%)	31.64
Black Core	NA
Color – L	54.45
Color – A	2.76
Color – B	10.09

Table 5. XRF analysis of CCW used in the study

Report Name	Result	Report Name	Result
L.O.I (%)	5.795	Na_2O	0.378
SrO (%)	0.021	SiO_2	63.510
ZrO_2 (%)	0.738	P_2O_5	0.132
NiO (%)	0.030	CuO	1.896
ZnO(%)	0.675	Al_2O_3	18.304
BaO (%)	0.171	SO_3	0.079
PbO (%)	0.014	TiO_2	0.661
Fe_2O_3 (%)	1.699	Cr_2O_3	0.024
CeO_2 (%)	0.155	K_2O	1.835
HfO_2 (%)	0.133	CaO	3.748

In our study, we employed the globally recognized MMD method for asphalt concrete [16, 17, 18]. We prepared samples with bitumen content ranging from 3.5% to 6.5%, in 0.5% increments, resulting in a total of 21 samples, with three samples for each ratio. This approach yielded 105 samples, including both control and CCW-containing specimens, each comprising 1150 g of aggregate mixed thoroughly with bitumen at 160°C. Subsequently, each sample underwent 75 impacts on both surfaces, and their heights were measured and analyzed using a Marshall Stability tester. Key parameters such as MS, flow (F), practical specific gravity (PSG), and void properties (V, VMA, and VFA) were measured for each sample. These values played a critical role in determining the OBC. All samples met the specified control criteria outlined in the HTS which is shown in Table 6.

Table 6. MMD criteria outlined in the HTS

Experiment Name	**Bitumen Content (BC) (%)**	
Layer Type	*Binder*	*Wearing*
Unit Weight (g/cm^3)	Max.	Max.
MS (kg)	Min. 750	Min. 900
V (%)	4-6	3-5
VFA (%)	60-75	65-75
VMA (%)	Min. 13	Min. 14
F (mm)	2-4	2-4

3. Test Results and Evaluation

OBC graphs for control and CCW-containing samples were determined separately and the results are shown in Figure 3. OBC increases with increasing addition of CCW compared to standard asphalt concrete samples. In this case, it is necessary to comparatively evaluate the waste material usage cost and bitumen usage cost and conduct a feasibility study.

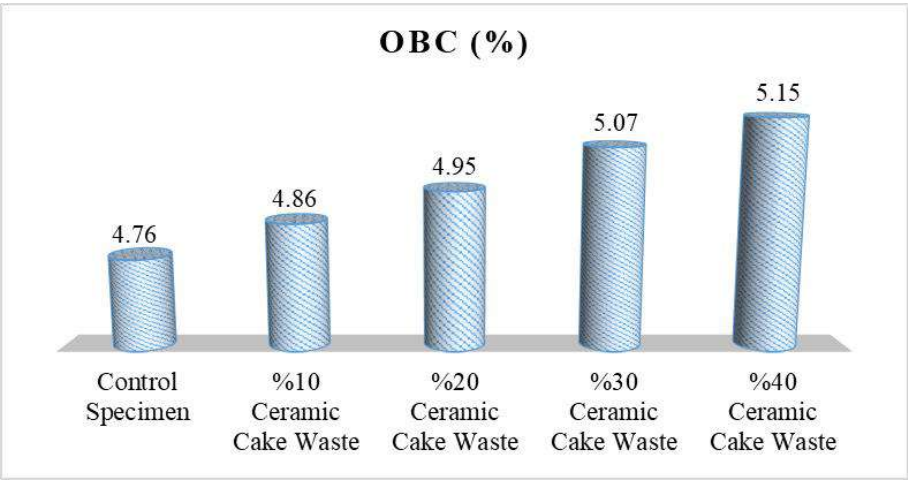

Figure 3. OBC values for each specimen type

PSG values of CCW-containing samples are lower than that of control samples. The void ratio in asphalt concrete increases as the CCW material increases. For this reason, as the CCW additive rate increases, PSG values naturally decrease (Figure 4). As the CCW ratio increases, the void ratio also increases due to the porous structure of CCW (Figure 5).

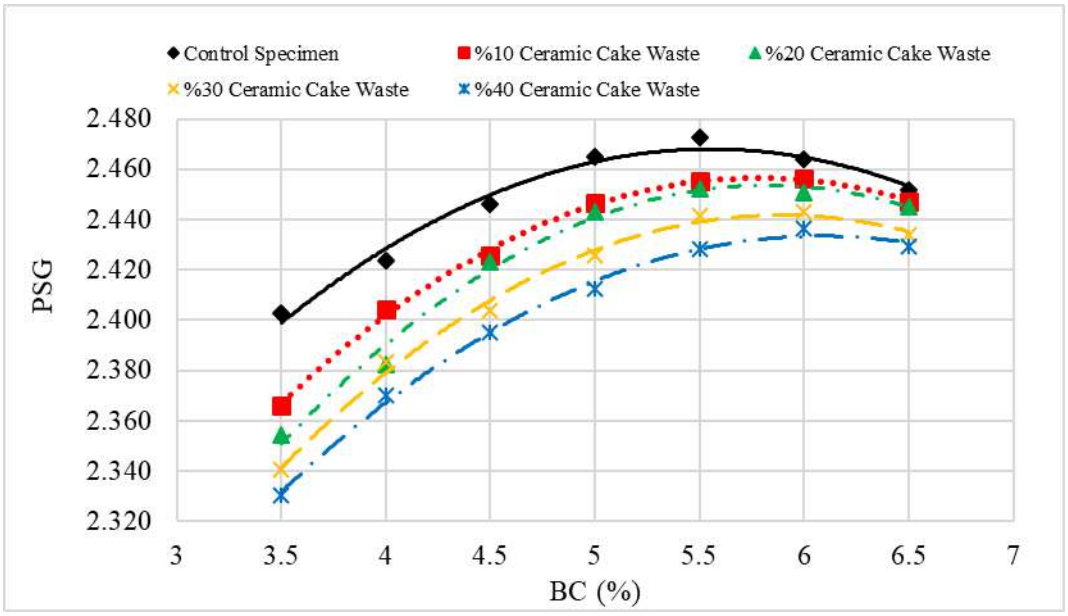

Figure 4. PSG and BC curves graph for each specimen type

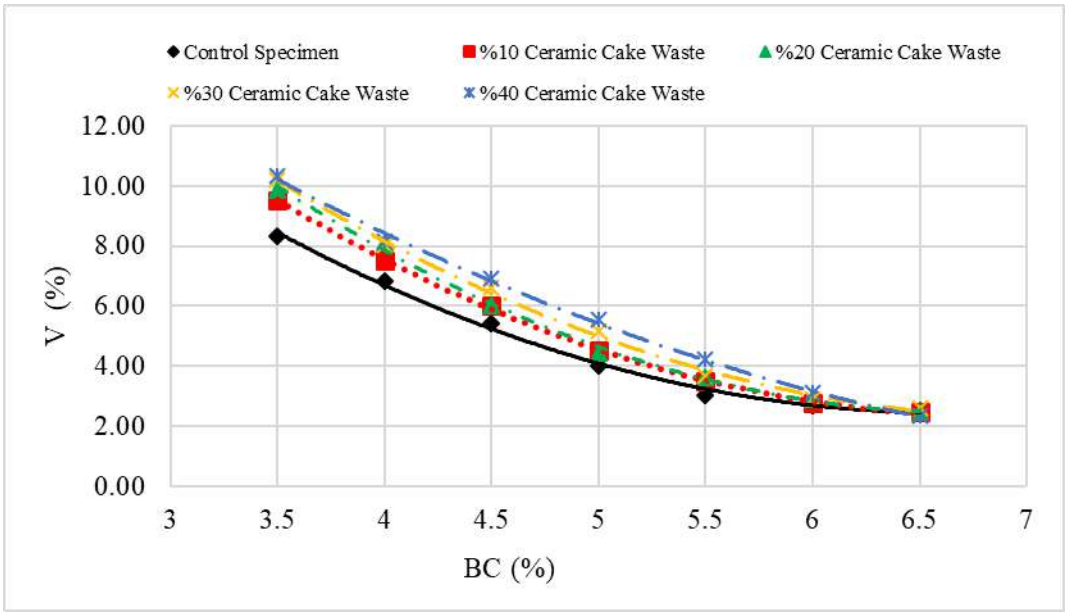

Figure 5. V and BC curves graph for each specimen type

As the BC increased, the VFA increased. According to the experimental results, VFA values decrease as the CCW ratio increases (Figure 6). MS was lower in CCW-containing samples than in control samples. As can be understood from here, stability decreased with the increase in void ratio due to the CCW materials (Figure 7).

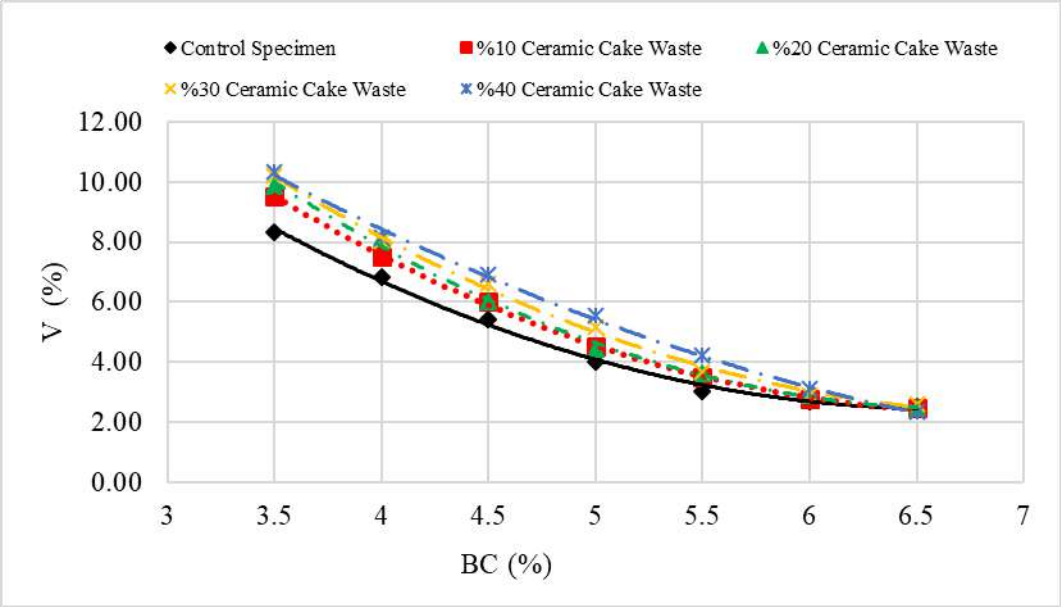

Figure 6. V and BC curves graph for each specimen type

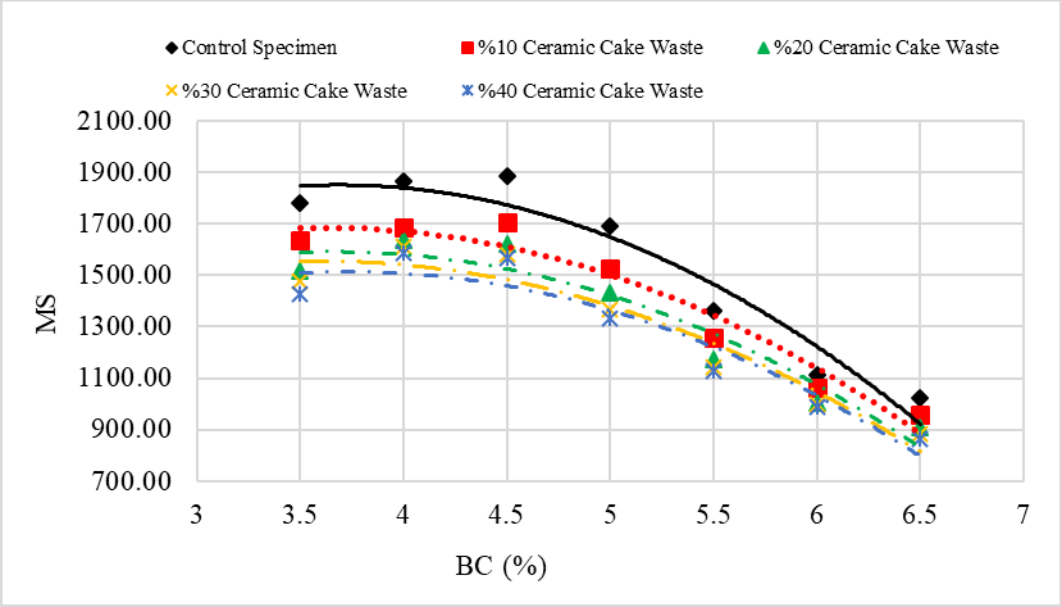

Figure 7. MS and BC curves graph for each specimen type

Flow (F) values may vary depending on the manufacturing of the sample and grain distribution. F values in samples containing waste have similar values compared to control samples. All yield values remain within the specification limits (Figure 8). Marshall Quotient (MQ) is expressed as the ratio of MS to F (MS/F) and is a measure of the stiffness of the samples. This value is desired to be as high as possible. MQ ratios were lower in CCW-containing samples than in control samples (Figure 9). The results of MS also exhibited a consistent correlation with the MQ results. When VMA ratios varying with BC were examined, it was seen that the lower limits of the specification (≥14%) were met for all samples (Figure 10).

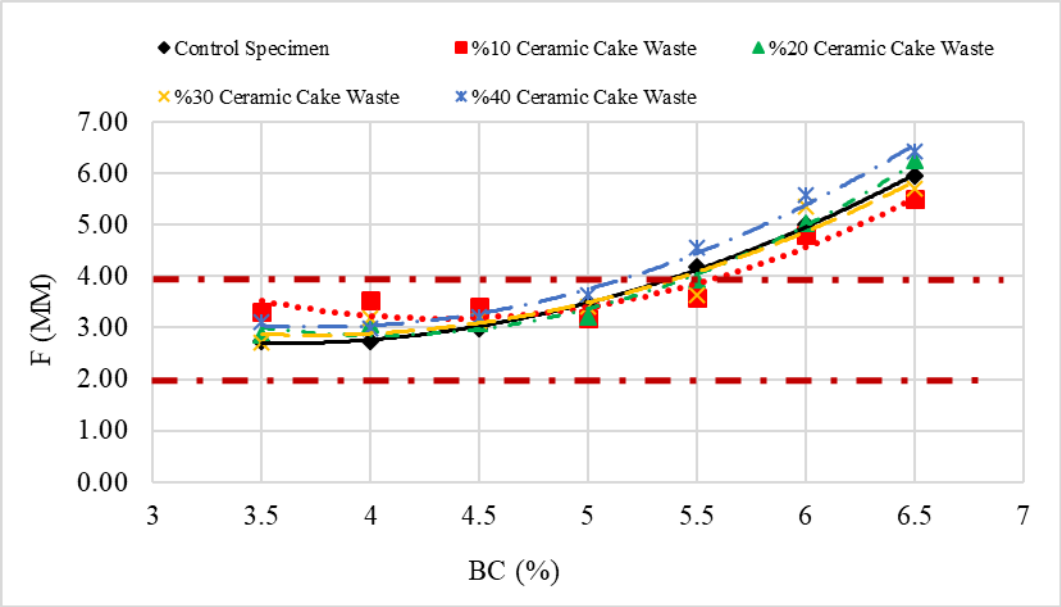

Figure 8. F and BC curves graph for each specimen type

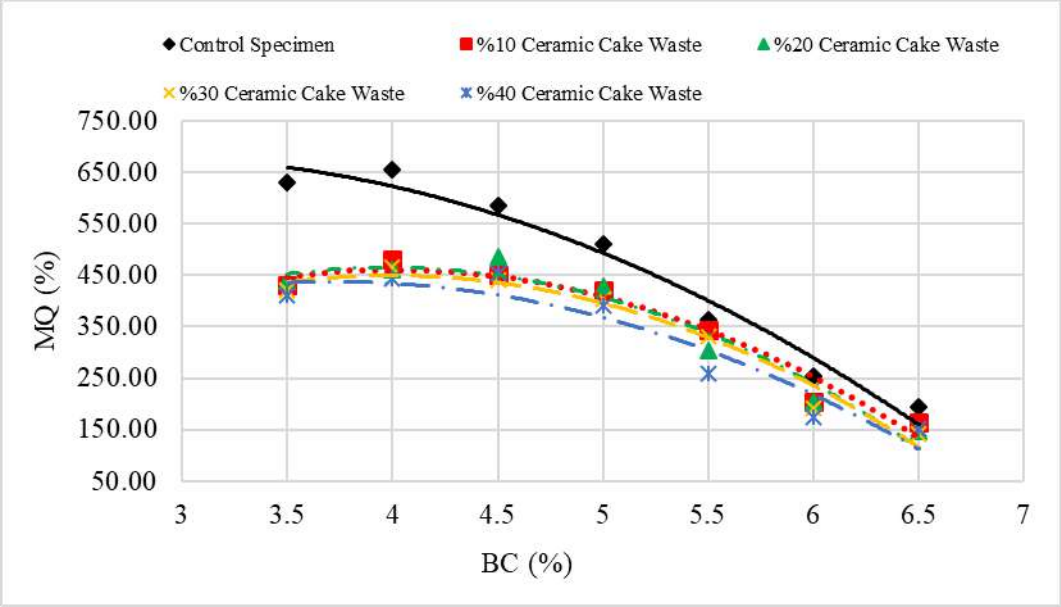

Figure 9. MQ and BC curves graph for each specimen type

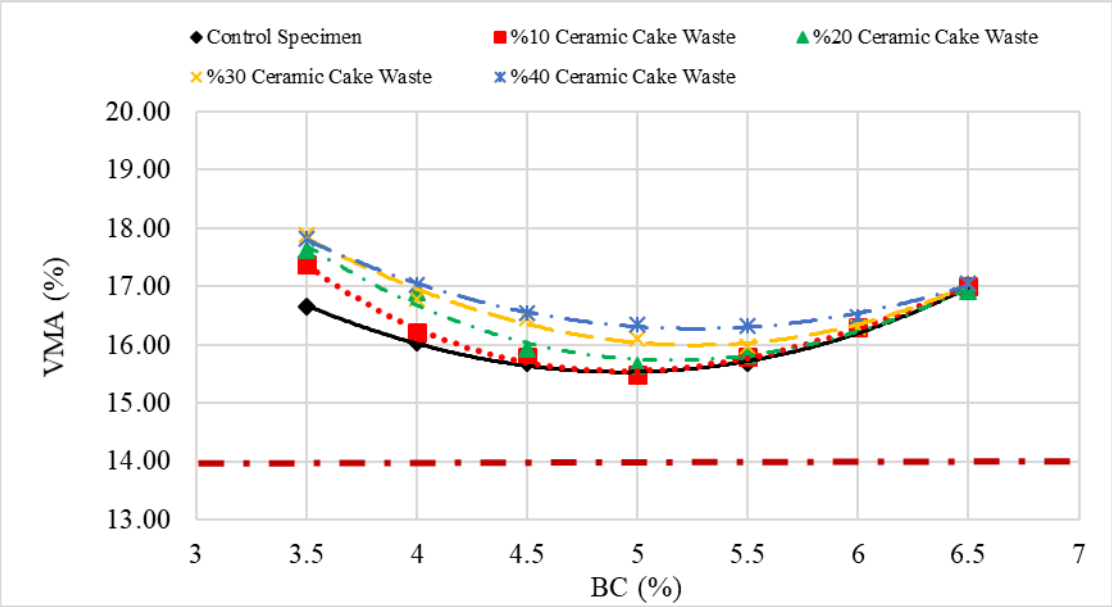

Figure 10. VMA and BC curves graph for each specimen type

4. Conclusion

This study investigated the feasibility of incorporating ceramic cake waste (CCW) materials into the production of asphalt concrete. A total of 105 asphalt concrete samples were prepared and subjected to various tests. The results of the Marshall Mix Design (MMD) tests revealed several trends: as the CCW content increased, values for void ratio (V), voids in mineral aggregate (VMA), flow (F), and optimum bitumen content (OBC) in the samples increased. Conversely, values for Marshall Stability (MS), practical specific gravity (PSG), voids filled with asphalt or bitumen (VFA), and Marshall Quotient (MQ) decreased. Ultimately, the study concluded that utilizing 20% CCW in asphalt concrete aligns with Turkish General Directorate of Highways Technical Specification. This research contributes to the promotion of ceramic cake waste reuse in road construction, effectively reducing environmental and visual pollution while optimizing waste storage and resource utilization. Such sustainable practices contribute to a healthier environment and quality of life.

5. References

[1] T. Abdulrasool and e. al., "The Effect of Cow Dung Ash as A Filler on The Mechanical Characteristics of Hot Mix Asphalt," IOP Conference Series: Earth and Environmental Science, vol. 961, no. 1, p. 012041, 2022.
[2] L. Sang and e. al, "Evaluation of The Performance of Waste Marble Dust as a Mineral Filler In Hot-Mix Asphalt Concrete," Journal of Civil Engineering, Science and Technology, vol. 12, no. 1, pp. 1-14, 2021.
[3] M. Keskin and M. Karacasu, "Effect of boron containing additives on asphalt performance and sustainability perspective," Construction and Building Materials , vol. 218, pp. 434-447, 2018.
[4] W. Jiang and e. al, "Analysis of rheological properties and aging mechanism of bitumen after short-term and long-term aging," Construction and Building Materials , vol. 273, p. 121777, 2021.
[5] A. M. Ali and T. Al-Mansoori, "Investigation of asphalt binder performance modified with ceramic waste powder," In IOP Conference Series: Materials Science and Engineering, vol. 1090, no. 1, p. 012055, 2021.
[6] E. Fatima and e. al, "Use of ceramic waste as filler in semi-dense bituminous concrete," American Journal of Civil Engineering and Architecture, vol. 2, no. 3, pp. 102-106, 2014.
[7] Ö. Gülşah and M. Saltan, "Pirinanın Bitüm Modifikasyonunda Kullanımının Araştırılması," Uluslararası Teknolojik Bilimler Dergisi, vol. 12, no. 1, pp. 1-9, 2020.
[8] W. Cao, "Study on properties of recycled tire rubber modified asphalt mixtures using dry process," Construction and building materials, vol. 21, no. 5, pp. 1011-1015, 2007.
[9] G. Kaçaroğlu and M. Saltan, "Cocamide Diethanolamide Kimyasalinin Bitüm Modifikasyonunda Kullanımı," Pamukkale Üniversitesi Mühendislik Bilimleri Dergisi, vol. 26, no. 6, pp. 1042-1047, 2020.
[10] C. Sanchez and H. Edgar , "Influence of recycled concrete aggregates from different sources in hot mix asphalt design," Construction and Building Materials , vol. 259, p. 120427, 2020.

[11] B. V. Kök, M. Yilmaz and N. Kuloğlu, "Asfaltit ve SBS Modifiyeli Bitümlü Sıcak Karışımların Mekanik Özelliklerinin Değerlendirilmesi," Politeknik Dergisi, vol. 14, no. 3, pp. 193-197, 2011.
[12] S. Wu and L. Montalvo, "Repurposing waste plastics into cleaner asphalt pavement materials: A critical literature review," Journal of Cleaner Production, vol. 280, p. 124355, 2020.
[13] C. Kara and K. Murat, "Use of ceramic wastes in road pavement design," Proceedings of the world congress on new technologies, p. 226, 2015.
[14] Karayolları Genel Müdürlüğü, Karayolu Teknik Şartnamesi, ankara: Karayolları Genel Müdürlüğü, 2013.
[15] Superpave Series No 2, Superpave Mix Design, 56. s., 1996.
[16] M. Khodadadi and e. al, "Reuse of drill cuttings in hot mix asphalt mixture: A study on the environmental and structure performance," Construction and Building Materials , vol. 256, p. 119453, 2020.
[17] S. Tapkın, A. Çevik and Ü. Uşar, "Prediction of Marshall test results for polypropylene modified dense bituminous mixtures using neural networks," Expert Systems with Applications, vol. 37, no. 6, pp. 4660-4670, 2010.
[18] M. Karacasu, Yol üstyapı deneyleri, Ankara: Sözkesen Matbaacılık Ltd. Şti, 2016.

International Conference on Advances and Innovations in Engineering

2023 Kahramanmaraş and Hatay earthquakes: Structural seismic performance, lessons learnt, measures for resilient cities

Alper ILKI [1], Caglar GOKSU [2, 3], Bilal SARI [4], Cem DEMIR[5], Hasan Huseyin AYDOGDU[6]

[1, 2, 4, 5, 6] Faculty of Civil Engineering, Istanbul Technical University, Istanbul, Türkiye.
[3] Tashkent University of Architecture and Civil Engineering, Tashkent, Uzbekistan.
[1]ailki@itu.edu.tr, [2, 3]goksuc@itu.edu.tr, [4]sarib19@itu.edu.tr, [5]demirce@itu.edu.tr, [6]aydogduha@itu.edu.tr

[1](ORCID: 0000-0002-4853-7910), [2,3](ORCID: 0000-0002-0596-6918), [4](ORCID: 0000-0002-6295-1210), [5](ORCID: 0000-0001-8274-5361), [6](0000-0002-4590-0067)

Abstract
In February 2023, a series of earthquakes struck Türkiye, affecting 11 provinces with a total population exceeding 16 million. These seismic events were followed by numerous aftershocks, resulting in significant devastation. More than 90,000 reinforced concrete buildings suffered heavy damage, leading to the loss of more than 50,000 lives. This research aims to provide an overview of on-site assessments conducted on the impacted reinforced concrete structures with the objective of identifying typical causes of structural failures. The study further examines the rapid seismic safety assessment for existing buildings and explores the feasibility of retrofitting techniques to enhance seismic resilience in Istanbul, as a case study.

Keywords: reconnaissance, reinforced concrete, retrofitting, seismic

1. Introduction

Türkiye is susceptible to seismic activities due to its location between the Eurasian and Arabian tectonic plates. The Anatolian Block, which constitutes the mainland, is situated between two significant fault systems: the North Anatolian Fault (NAF) to the north and the East Anatolian Fault (EAF) to the southeast. In February 2023, Türkiye experienced a series of three significant seismic events along the EAF. These earthquakes measured M_w of 7.7, 7.6, and 6.4, respectively, as reported by the Disaster and Emergency Management Authority (AFAD) [1]. The first earthquake originated in Kahramanmaraş-Pazarcık, followed by successive earthquakes with epicenters in Kahramanmaraş-Elbistan and Hatay-Yayladağı (Figure 1). Eleven provinces were affected, namely, Kahramanmaraş, Adıyaman, Hatay, Osmaniye, Gaziantep, Kilis, Şanlıurfa, Diyarbakır, Malatya, Adana, and Elazığ, with 16 million people. These events resulted in extensive structural damage, leading to the collapse of over 10,000 reinforced concrete (RC) buildings, as documented by the Ministry of Environment, Urbanization, and Climate Change (MoEUCC) [2]. The loss of life was reported to be more than 50,000 and in excess of 100,000 people injured [3]. The economic loss upwards of $100 billion, as estimated by the Strategy and Budget Office of the Presidency of Türkiye [4].

This research is primarily centered on the outcomes derived from on-site structural evaluations conducted in the aftermath of the February 2023 earthquakes in Türkiye. The aim of the paper is the identification of vulnerabilities and root causes contributing to structural failures. The need for seismic risk mitigation and the implementation of proactive strategies is highlighted by lessons learnt from the recent seismic events. As a result, this study provides a brief explanation of a rapid seismic assessment methodology and examine the comparative effectiveness of retrofitting versus reconstruction, drawing insights from an investigation by Demir et al. [5]. Within this framework, the manuscript defined the potential of fiber-reinforced polymers (FRPs) for increasing building resilience, summarizing prior experimental investigations and real-world applications. It's important to emphasize that the damages and failure causes observed during on-site investigations following earthquakes are not limited only to the scope covered in this paper. Additional examples of various types of damages, such as the influence of high axial stress, the vulnerability of short columns, the corrosion of steel reinforcing bars contributing to structural damage, and the effect of construction year on structural failures can be found elsewhere [6-8].

[1]Corresponding author

2. Characteristics of Earthquakes

Figure 1 provides a visual representation, highlighting the key characteristics of the primary seismic events that occurred in Türkiye during February 2023. The figure depicts the geographical locations, focal mechanisms, and magnitudes of three major earthquakes, as well as their subsequent aftershocks. Specifically, these seismic events were centered around Kahramanmaraş-Pazarcık and Kahramanmaraş-Elbistan on February 6, 2023, resulting in surface ruptures spanning approximately 300 km and 130 km, respectively. These ruptures were accompanied by significant displacements exceeding 6.5 meters [3].

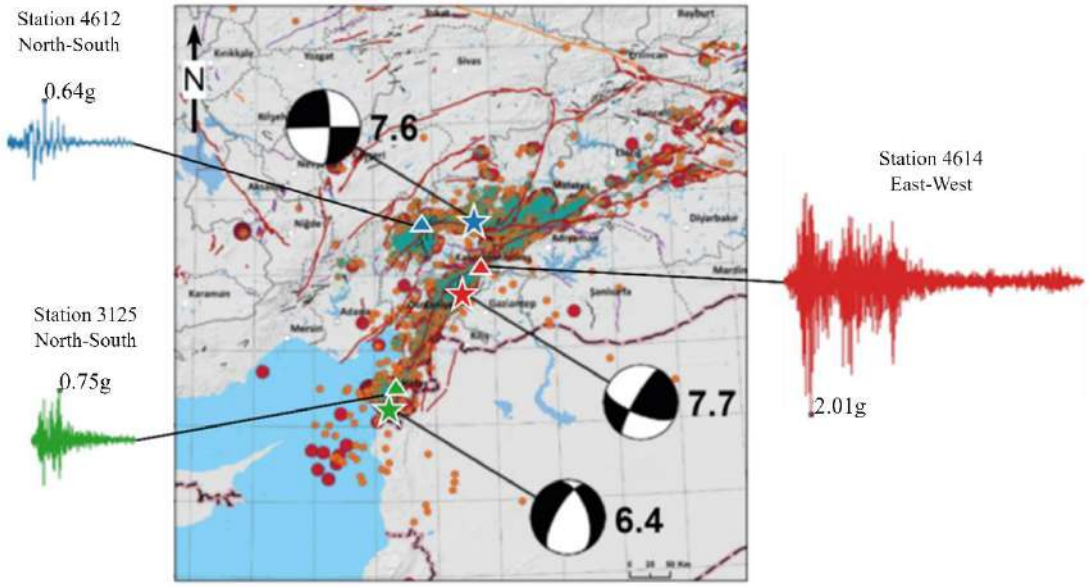

Figure 1. Characteristics of three major earthquakes and the highest acceleration records [modified from 3, 9].

When considering the acceleration data gathered from strong ground motion stations within the earthquake-affected area, it becomes evident that peak ground acceleration (PGA) values reached significantly high levels, with values of up to 2g being documented at a station in close proximity to the epicenter of the initial earthquake in Kahramanmaraş-Pazarcik. The acceleration-time relationships, derived from the data collected at the stations recording the highest PGA values during the three primary earthquakes, are illustrated in Figure 1.

3. Distribution of Structural Damages and Causes of Failures

In February 2023, the seismic events primarily impacted 11 provinces, spanning approximately 110,000 km^2, encompassing a variety of building types. Post-earthquake assessments revealed substantial structural deficiencies in many buildings within the affected region (Figure 2). Based on the assessment conducted by MoEUCC [2], around 1.2 million RC structures were surveyed. Among these, 1.0% suffered collapse, 0.9% required immediate demolition, 6.4% heavily damaged, 2.8% moderately damaged, 25.7% had minor damage, while the rest 63.2% remained undamaged.

In Türkiye, the year of construction can be deemed as an indicator of both construction quality and seismic vulnerability. The profound impact of the 1999 Marmara Earthquakes prompted significant advancements in construction methods and inspection procedures. The introduction of the Building Inspection Law in 2001 [10], initially implemented in 19 pilot provinces (including Gaziantep and Hatay, which are affected from earthquakes), and its subsequent nationwide adoption in 2011, marked a crucial step towards standardized inspection practices. Technological progress in manufacturing, the availability of modern technical guidelines, and the widespread use of deformed steel reinforcement bars and ready-mixed concrete have contributed to the continuous improvement of construction quality over time.

Figure 2. A mid-rise RC building to be urgently demolished.

For the buildings constructed before the year 2000, the utilization of ready-mix concrete was not prevalent, resulting in generally lower concrete compressive strength. This, in turn, led to higher axial load ratios in RC columns and shear walls, consequently reducing their moment capacity and ductility. Inadequate seismic-resistant detailing revealed several significant deficiencies regarding transverse reinforcement. The incorrect use of 90° stirrup hooks instead of the recommended 135° seismic hooks, the absence of cross-ties, and excessive spacing of stirrups exceeding the maximum limits stipulated in seismic codes can be given as examples for the buildings constructed before 2000 (Figure 3a). These deficiencies compromised the necessary confining effect on concrete essential for ductile behavior. It should be noted that the accelerations generated by these earthquakes created a significant ductility demand at certain regions, and led to collapse for the buildings lacking sufficient ductility. It should be highlighted that similar patterns of damage were observed in previous seismic events [11-13].

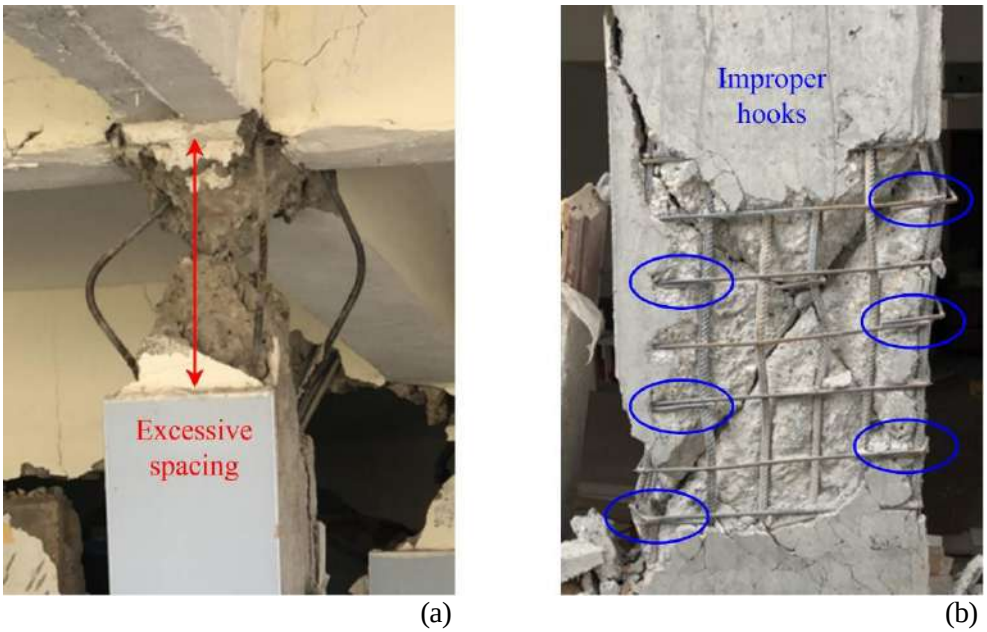

(a) (b)

Figure 3. Deficiencies regarding the transverse reinforcement for the buildings.(a) Constructed before the year 2000, (b) Constructed after the year 2000

Field observations have identified structural irregularities such as torsion, slab and frame discontinuities, overhangs, soft and weak stories as primary contributors to damages and failures regardless of the construction year of the buildings. Additionally, despite the use of closely-spaced stirrups, there remain issues concerning insufficient

detailing of transverse reinforcement, including the widespread absence of crossties and the use of ties with 90° hooks for the buildings constructed after the year 2000 (Figure 3b). Nevertheless, there have been improvements in the quality of building materials, such as the more common use of ready-mix concrete and deformed steel reinforcing bars.

4. Seismic Risk Assessment for the Building Stock: Istanbul Case

A 2019 study conducted in Istanbul shed light on a critical issue in the city. Out of the 1.17 million buildings within its boundaries, 84% were constructed using RC. Among this significant RC portion, approximately 65% (equivalent to 631,000 buildings) were built prior to the year 2000 [14]. Many of these buildings do not conform to modern seismic codes as well as the seismic codes of their construction periods. This highlights a concern regarding the potential risks to life and property posed by these buildings. The urgency of identifying these vulnerable buildings and implementing mitigation measures is crucial. However, the conventional method of individually assessing seismic performance according to seismic codes for such a large number of structures is impractical due to the immense time and financial resources required. Moreover, current regulations in Türkiye classify buildings as either satisfying or not satisfying a specific performance criterion, such as life safety performance. This classification categorizes a significant number of buildings in Istanbul as high-risk when evaluated using these existing regulations, creating a serious problem.

To address this complex issue, an innovative approach known as PERA2019 was introduced [15-17]. This methodology aims to provide a simplified, cost-effective, yet robust assessment of seismic vulnerability in buildings. Its primary goal is to categorize buildings based on their risk levels and prioritize them for necessary seismic risk mitigation measures. Notably, PERA2019 was applied to assess over 25,000 RC residential buildings, which were constructed before 2000 [5, 16-17]. The collected data from this inventory underwent a comprehensive analysis using PERA2019 for a simulated earthquake scenario (M_w 7.5). As a result, it was found that one in four structures falls into the very high-risk category, indicating a significant level of vulnerability.

Additionally, a thorough cost-benefit analysis was conducted [5], comparing the financial implications of pre-earthquake interventions aimed at enhancing seismic resilience, including retrofitting or reconstruction for various risk levels of buildings. The analysis revealed that in the majority of cases, retrofitting emerged as the more economically viable option compared to reconstruction. This presents a practical and cost-effective solution for addressing the seismic vulnerability of these buildings. It should be noted that this section of the keynote paper builds upon prior research findings presented in previous publications [5, 15-17].

5. Retrofitting Strategies for Existing Structures

Prioritizing seismically resilient buildings calls for the implementation of retrofitting measures prior to earthquakes. This is because resilience refers to a structure's ability to withstand and recover from adverse conditions, such as seismic events while maintaining its fundamental functions and structural integrity. Implementing retrofitting measures not only reduces structural damage but also minimizes casualties and injuries during seismic events. Additionally, these measures facilitate post-event recovery, potentially reducing the need for temporary and permanent housing construction following the earthquakes. Taking proactive steps towards retrofitting significantly enhances a building's ability to withstand seismic forces and protect its occupants. This involves improving the seismic performance of key structural components such as columns, beams, and shear walls, a process known as member retrofitting. Alternatively, if member-level retrofitting is insufficient in terms of strength, rigidity, deformation capacity, or economic viability, system retrofitting can be considered.

Türkiye Building Earthquake Code [18] provides several options for member retrofitting, including RC jacketing, steel jacketing, or the use of fiber-reinforced polymers (FRPs). These approaches may aim to enhance ductility, load capacity (bending moment, axial load or shear force capacities) and stiffness characteristics as well as addressing deficiencies in lap splices of RC structural elements. Figure 4a presents the application of FRP wrapping to improve the ductility of an RC column. Additionally, partition walls within an RC frame, exhibiting continuous behavior from the foundation to the top, can also be reinforced using FRP sheets or steel mesh-reinforced concrete layers.

On the other hand, within the framework of TBEC [18], system retrofitting methods involve the use of in-situ cast RC shear walls to strengthen RC structural systems with insufficient lateral stiffness and strength, as shown in Figure 4b. Another effective technique is the introduction of steel braces into the RC structural framework. Additionally, strategies may include reducing earthquake loads through actions such as removing the excessive mass. More detailed information on widely adopted element and system retrofitting methods can be found in Section 15 of TBEC [18]. Comprehensive details of the authors' experimental investigations into the use of FRPs for strengthening RC structural components are available elsewhere [19-23].

(a) (b)

Figure 4. Examples for retrofitting of an RC building. (a) Member retrofitting, (b) System retrofitting

6. Conclusions

In this study, it is aimed to convey the insights gathered from on-site inspections carried out on the affected RC structures following February 2023 Türkiye earthquakes. The primary goal was to shed light on deficiencies and common causes for structural failures. Moreover, this research presents an evaluation of seismic safety for existing buildings, with Istanbul serving as a prominent case study. The study also included an assessment of the viability of seismic retrofitting strategies aimed at improving both seismic resilience and performance.

The on-site inspections revealed that there is a recurrence pattern on prevalent construction deficiencies within the examined structures. These deficiencies were primarily related to sub-standard construction practices, notably evident in reinforcement detailing and the quality of building materials. The field observations also identified that structural system irregularities, particularly in the case of soft story and weak story configurations, were the primary causes for damages and structural failures.

In Istanbul, many buildings constructed before 2000 do not conform to current seismic regulations, highlighting vulnerabilities exposed by the February 2023 Türkiye earthquakes. It is essential to recognize and address these buildings to avoid the loss of both lives and property. The PERA2019 methodology, applied as a case study in Istanbul, acted as a rapid seismic safety assessment tool. The findings indicated that 25% of the examined buildings were classified as 'very high risk.' Additionally, a cost-benefit analysis was carried out, comparing pre-earthquake actions like retrofitting and reconstruction across different risk levels. The results showed that retrofitting proved to be a more cost-effective option than reconstruction.

To conclude, the assessment of specific buildings in Istanbul revealed that a significant portion of these structures were vulnerable to earthquakes, emphasizing the need to strengthen these buildings. Retrofitting appears as a practical and cost-effective approach with respect to the complete demolition and reconstruction, ultimately leading the improved seismic resilience.

Acknowledgement

The authors would like to express their gratitude to Istanbul Technical University (ITU), Türkiye Earthquake Foundation (TDV), Turkish Natural Catastrophe Insurance Pool (DASK), Ministry of Interior Affairs Disaster and Emergency Management Authority (AFAD), Turkish Ministry of Environment, Urbanization and Climate Change (MoEUCC), Istanbul Metropolitan Municipality (IMM), and Kordsa, Hilti, Arup companies for their support.

7. References

[1] Disaster and Emergency Management Presidency of Ministry of Interior Affairs of Türkiye (AFAD). https://www.afad.gov.tr (13.04.2023).

[2] Ministry of Environment, Urbanization and Climate Change (MoEUCC) of Türkiye. https://www.csb.gov.tr (10.05.2023).

[3] Disaster and Emergency Management Presidency of Ministry of Interior Affairs of Türkiye (AFAD). "06 February 2023 Pazarcık-Elbistan (Kahramanmaraş) Mw: 7.7 – Mw: 7.6 Earthquakes Report". 2023. [in Turkish]

[4] Strategy and Budget Office of Presidency of Türkiye (SBO). "2023 Kahramanmaraş and Hatay Earthquakes Report". 2023.

[5] Demir C, Comert M, Aydogdu HH, Ilki A. Seismic Risk Assessment and Preliminary Intervention Cost-Benefit Analysis for the Building Stock of Istanbul. Editors: Vacareanu R, Ionescu C. Progress in European Earthquake Engineering and Seismology (ECEES 2022), 212-224, Cham, Springer, 2022.

[6] Goksu C, Sari B, Gullu MF, Orakcal K, Ilki A. "Outline of the Performances of Reinforced Concrete Buildings During February 2023 Türkiye Earthquakes and Potential Use of FRPs Towards More Resilient Buildings". 11th International Conference on Fiber-Reinforced Polymer (FRP) Composites in Civil Engineering (CICE 2023), Rio de Janeiro, Brazil, 24-26 July 2023.

[7] Ilki A, Goksu C, Demir C, Sari B. "2023 Field Observations from February 2023 Türkiye Earthquakes, Seismic Safety Evaluation and Strengthening of Existing Buildings". International Steel Rolling Symposium (ISRS 2023), Hatay, Türkiye, 14-15 September 2023.

[8] Ilki A, Goksu C, Sari B, Aydogdu HH, Demir C. "2023 Kahramanmaras Earthquakes and Lessons Learnt Towards Building Resilient Cities with a Focus on Istanbul". 20th International Symposium of Macedonian Association of Structural Engineers (MASE), Skopje, North Macedonia, 28-29 September 2023.

[9] Disaster and Emergency Management Presidency of Ministry of Interior Affairs of Türkiye (AFAD). https://tadas.afad.gov.tr (13.04.2023).

[10] Official Gazette of Republic of Türkiye. "Law on Building Inspection". No: 4708. 29.06.2001. [in Turkish]

[11] Gurbuz T, Cengiz A, Kolemenoglu S, Demir C, Ilki A. "Damages and failures of structures in Izmir (Turkey) during the October 30, 2020 Aegean Sea earthquake". Journal of Earthquake Engineering, 27(6), 1565-1606, 2023.

[12] Tapan M, Comert M, Demir C, Sayan Y, Orakcal K, Ilki A. "Failures of structures during the October 23, 2011 Tabanlı (Van) and November 9, 2011 Edremit (Van) earthquakes in Turkey". Engineering Failure Analysis, 34, 606-628, 2013.

[13] Celep Z, Erken A, Taskin B, Ilki A. "Failures of masonry and concrete buildings during the March 8, 2010 Kovancılar and Palu (Elazığ) earthquakes in Turkey". Engineering Failure Analysis, 18(3), 868-889, 2011.

[14] Kandilli Observatory and Earthquake Research Institute (KOERI). "Project for Updating Probable Earthquake Loss Predictions in Istanbul Province". 2019. [in Turkish]

[15] Ilki A, Comert M, Demir C, Orakcal K, Ulugtekin D, Tapan M, Kumbasar N. "Performance based rapid seismic assessment method (PERA) for reinforced concrete frame buildings". Advances in Structural Engineering, 17(3), 439–459, 2014.

[16] Aydogdu HH, Demir C, Kahraman T, Ilki A. "Evaluation of rapid seismic safety assessment methods on a substandard reinforced concrete building stock in Istanbul". Structures, 56, 104962, 2023.

[17] Aydogdu HH, Demir C, Comert M, Kahraman T, Ilki A. "Structural characteristics of the earthquake-prone building stock in Istanbul and prioritization of existing buildings in terms of seismic risk-A pilot study conducted in Istanbul". Journal of Earthquake Engineering, 2023.

[18] Official Gazette of Republic of Türkiye. "Türkiye Building Earthquake Code (TBEC)". No: 30364. 18.03.2018. [in Turkish]

[19] Ilki A, Tore E, Demir C, Comert M. Seismic Performance of a Full-Scale FRP Retrofitted Sub-standard RC Building. Editor: Pitilakis K. Recent Advances in Earthquake Engineering in Europe (ECEE 2018), 519-544, Cham, Springer, 2018.
[20] Ghatte HF, Comert M, Demir C, Akbaba M, Ilki A. "Seismic retrofit of full-scale substandard extended rectangular RC columns through CFRP jacketing: Test results and design recommendations". Journal of Composites for Construction, 23(1), 04018071, 2019.
[21] Kaya E, Kütan C, Sheikh S, Ilki A. "Flexural retrofit of support regions of reinforced concrete beams with anchored FRP ropes using NSM and ETS methods under reversed cyclic loading". Journal of Composites for Construction, 21(1), 04016072, 2017.
[22] Ilki A, Bedirhanoglu I, Kumbasar N. "Behavior of FRP-retrofitted joints built with plain bars and low-strength concrete". Journal of Composites for Construction, 15(3), 312-326, 2011.
[23] Goksu C, Polat A, Ilki A. "Attempt for seismic retrofit of existing substandard RC members under reversed cyclic flexural effects". Journal of Composites for Construction, 16(3), 286-299, 2012.

International Conference on Advances and Innovations in Engineering

Investigation of doleritic rocks around Konakalmaz (Elazig) by Confocal Raman Spectroscopy

Cedide KAYMAK[1] , Melek URAL [2]

[1,2]Department of Geology, Engineering Faculty, Firat University, Elazığ, Turkey.
[1]cdkaymak@gmail.com, [2]melekural@gmail.com

[1](ORCID: 0000-0002-8209-8296), [2](ORCID: 0000-0002-4174-6058)

Abstract

The study area includes mafic magmatic dykes belonging to Yüksekova arc complex, one of the accretionary prism products around Konakalmaz (Elazığ, Eastern Turkey) located on the Bitlis suture zone. Mineralogy and alteration mineralogy can be obtained by examining the doleritic outcrops around Konakalmaz of the unit, which has been dealt with for various purposes such as geology and geochemistry, for the first time, by means of Confocal Raman spectroscopy. Accordingly, the raman data (spectrum, peak values and appearances) of this studies are compatible with the general mineralogical indicators (augite, diopsitic) in the region. Homogeneous mineralogy in these rocks strengthens the possibility that the magma chamber source from which it feeds is monogenic.

Keywords: Konakalmaz, Raman spectroscopy, dolerite.

1. Introduction

The study area is located around the east of Elazig (Eastern Turkey) located on the Bitlis suture zone (Figure 1). In this area, products of the Yüksekova arc complex are represented by mafic dyke stocks (Ural, 2012, Ural vd., 2019). It is unconformably overlain by Gehroz limestones belonging to the Hazar group, which is accepted as Late Maastrichtian-Middle Eocene aged, in the north, without being visible on the basement rocks (Çelik, 2013). When the findings obtained from the observations in this area and the studies compiled from the region are combined (Ural et al., 2019), the relationship of the unit with the ceiling rock, which can not be observed in some areas, can be observed more clearly, while a tectonic relationship where it is found on the serpentinized cumulates belonging to the Guleman ophiolites on the slopes of the Mastar Mountain in some places at the base.

The outcrops of the unit, which was examined for various purposes, around Konakalmaz were examined for the first time by means of confocal Raman spectroscopy. In Raman spectroscopic studies conducted on the basis of mineralogy in our country, the minerals in such igneous rocks are determined, so that data about the main magma source can be revealed by comparing the spectra.

2. Material and Method

In this study, Confocal Raman measurements on pyroxene and plagioclase minerals were analyzed by obtaining spectra using Horiba Jobin Yvon Labram HR model Thermo DXR Raman Confocal Spectrometer instrument and CCD detector in Ankara University Yebim laboratory.

3. Petrography

The bodies cropping out as doleritic dyke stocks around Konakalmaz mainly consist of plagioclase (40-60%), pyroxene (25-45%), olivine (5-20%) and opaque (5-15%) minerals (Figure 4.35). Thin and elongated prismatic semi-hedral plagioclases are in rodlike, bundle-like, radial-looking forms, and small pyroxene crystals fill in between the

[1]Corresponding author

prismatic plagioclases. There are also occasional chlorite accumulations between medium-sized plagioclases or these pyroxenes are uralitized. In this way, they stand out as rocks with both intergranular and intersertal texture and sometimes reflecting typical doleritic texture (Figure 4.36). Intersertal and more microlitic textured basaltic lavas are also observed to be more degraded. In general, nomenclature of these rocks can be defined as dolerite in this area.

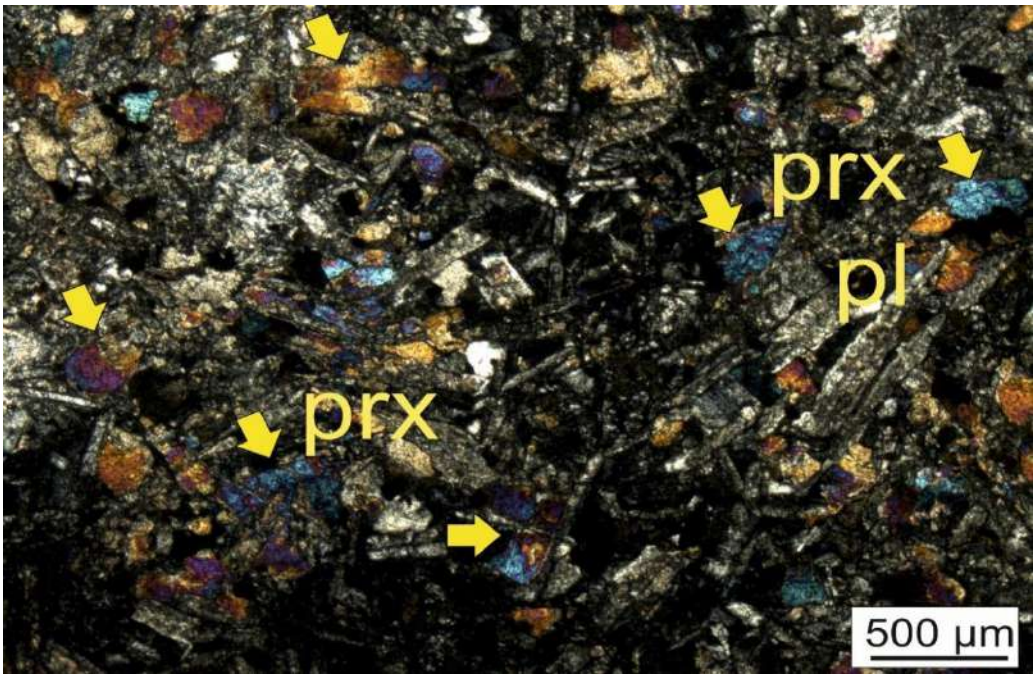

Figure 1. Microphoto shows the doleritic, intergranular relationship around Konakalmaz. Prx: pyroxene, pl: plagioclase.

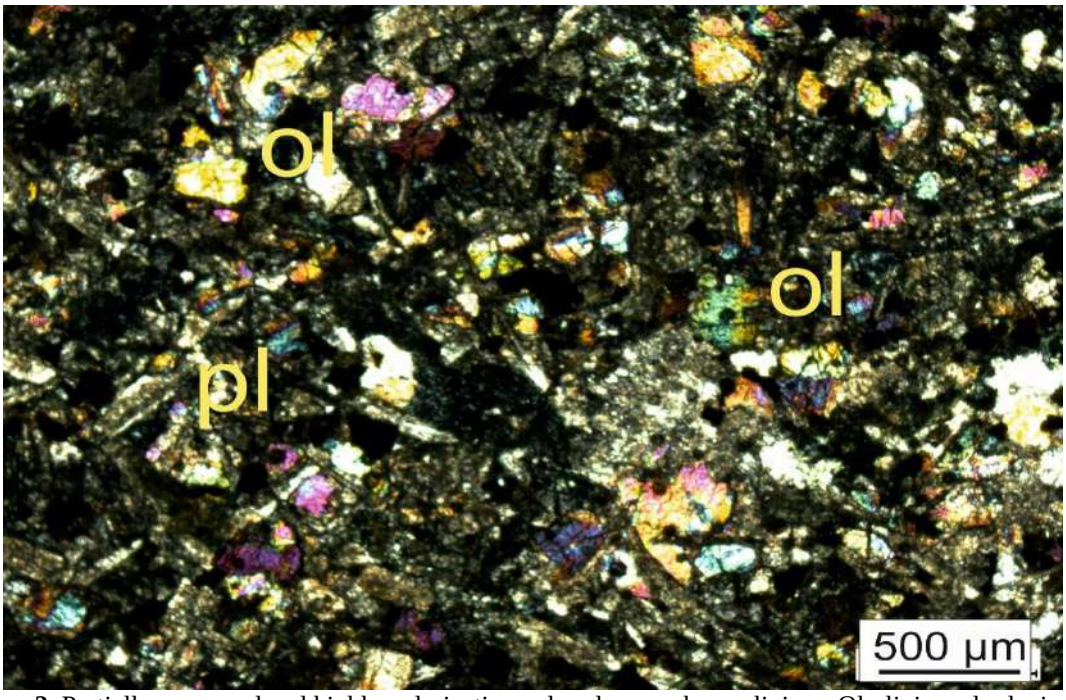

Figure 2. Partially preserved and highly polarization colored, amorphous olivines. Ol:olivine, pl: plagioclase

4. Confocal Raman Studies

In this area, the measured Raman peaks (Figure 3), Raman spectrum (Figure 4) and the peak values from small to large appear as 190.70, 229.09, 325.05, 357.87, 393.16, 557.22, 666.19, 1009.19 (Figure 5). 'Augite', an inosilicate group mineral with $(Ca,Na)(Mg,Fe,Al,Ti)(SiAl)_2O_6$ composition, is the composition obtained. Analysis view of the

plagioclase mineral in the same sample, measured Raman peaks (Figure 6), Raman spectrum (Figure 7) and peak values measured from small to large 195.65, 263.14, 409.87, 479.21, 506.46, 562.80, 702.10, 785.06 (Figure 7), and it is a labradorite with (Ca,Na) (SiAl)2O8 composition.

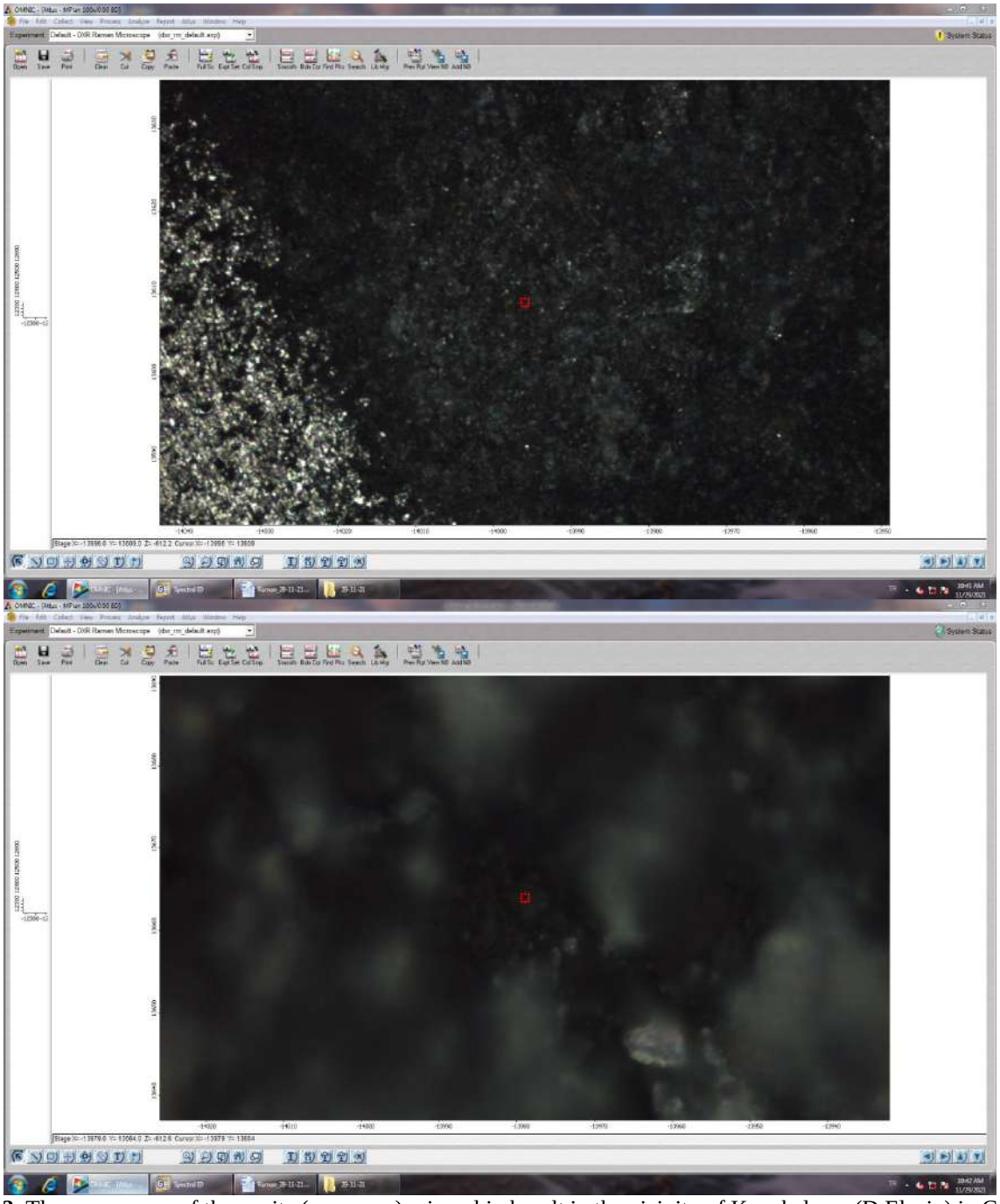

Figure 3. The appearance of the augite (pyroxene) mineral in basalt in the vicinity of Konakalmaz (D Elazig) in Confocal Raman Spectrometer and the analyzed point views.

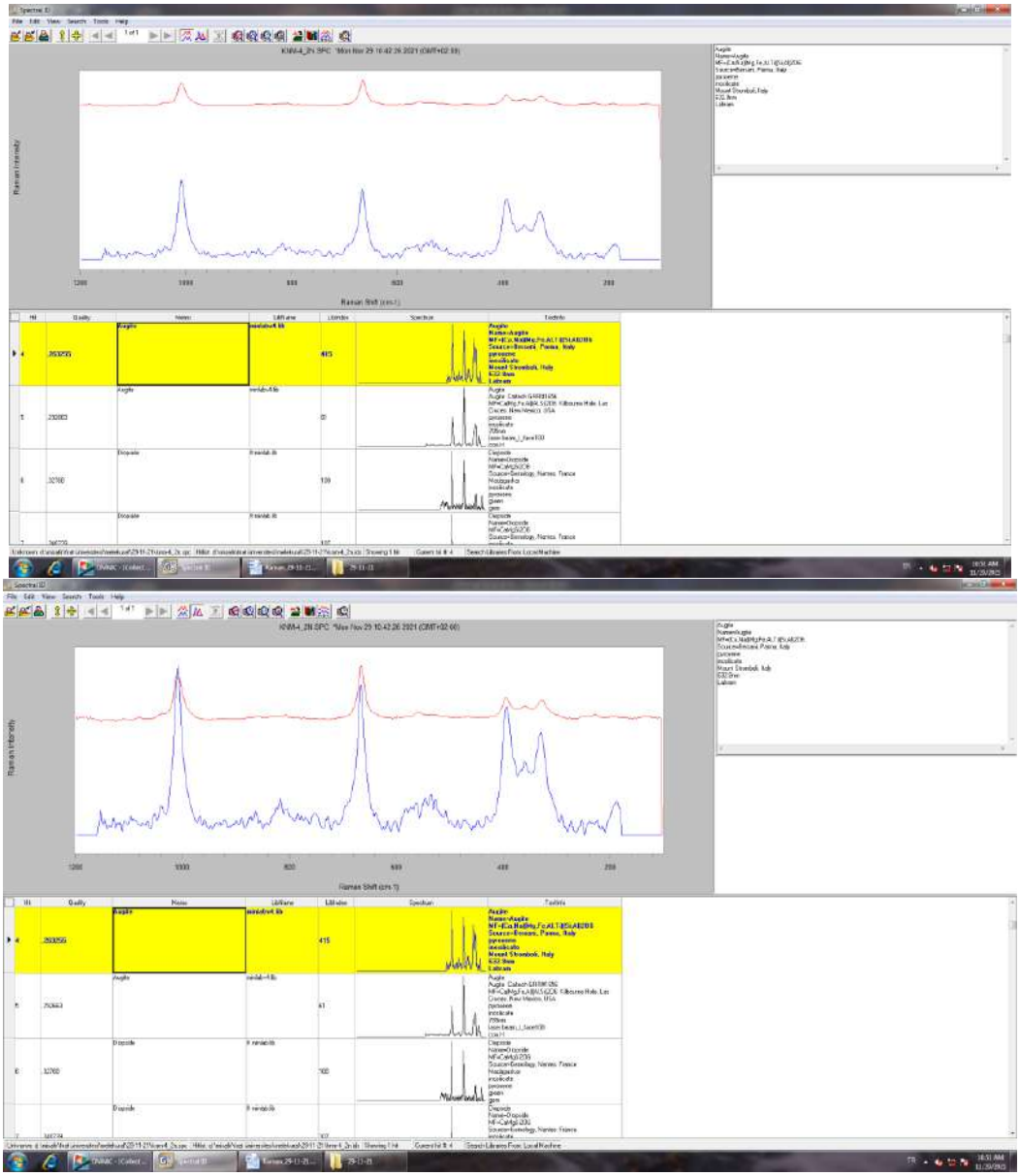

Figure 4. Measured peak graphs of augite (pyroxene) mineral in basalt in the vicinity of Konakalmaz (D Elazig). The blue line is the reference peak, the red line is the measured peak. Sample no: KM-4.

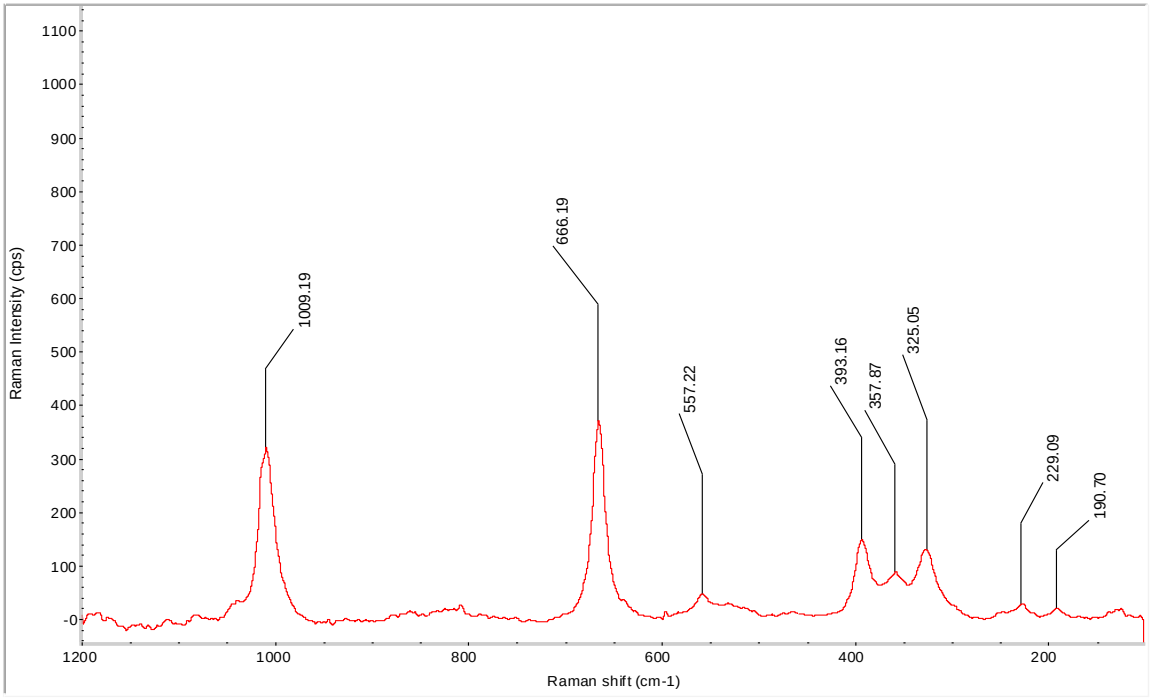

Figure 5. Raman peak spectrum of augite (pyroxene) mineral in basalt near Konakalmaz (D Elazig). Sample KM-4.

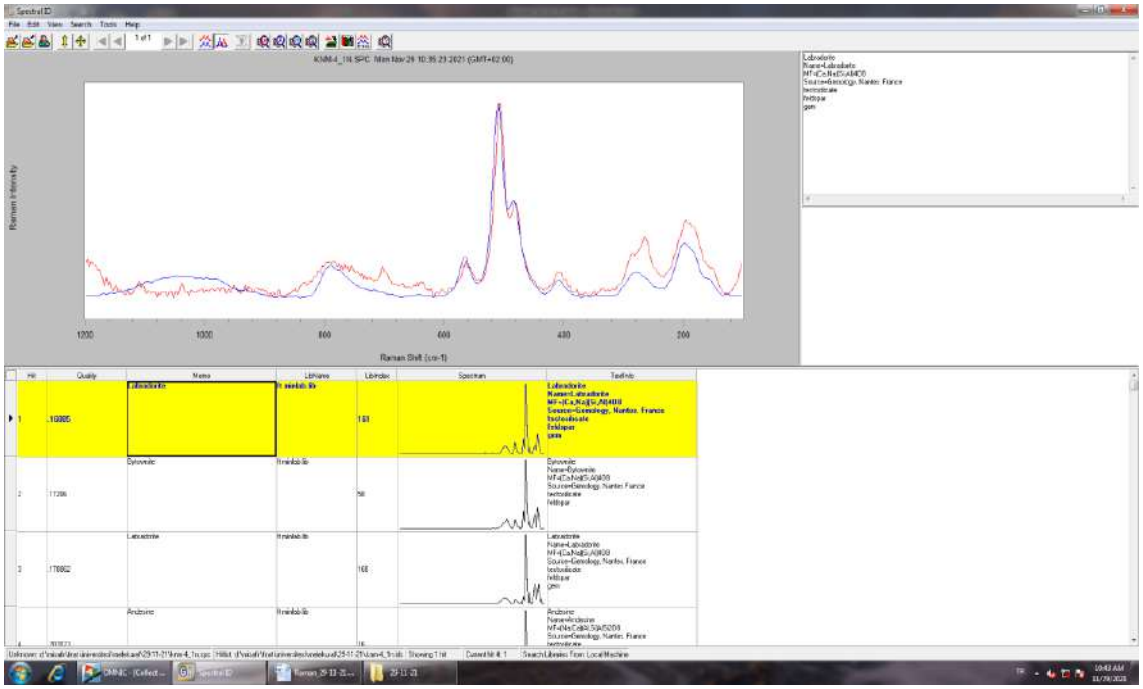

Figure 6. Measured peak graphs of plagioclase (labradorite) mineral in basalt around Konakalmaz (D Elazig). The blue line is the reference peak, the red line is the measured peak. Sample No: KM-4.

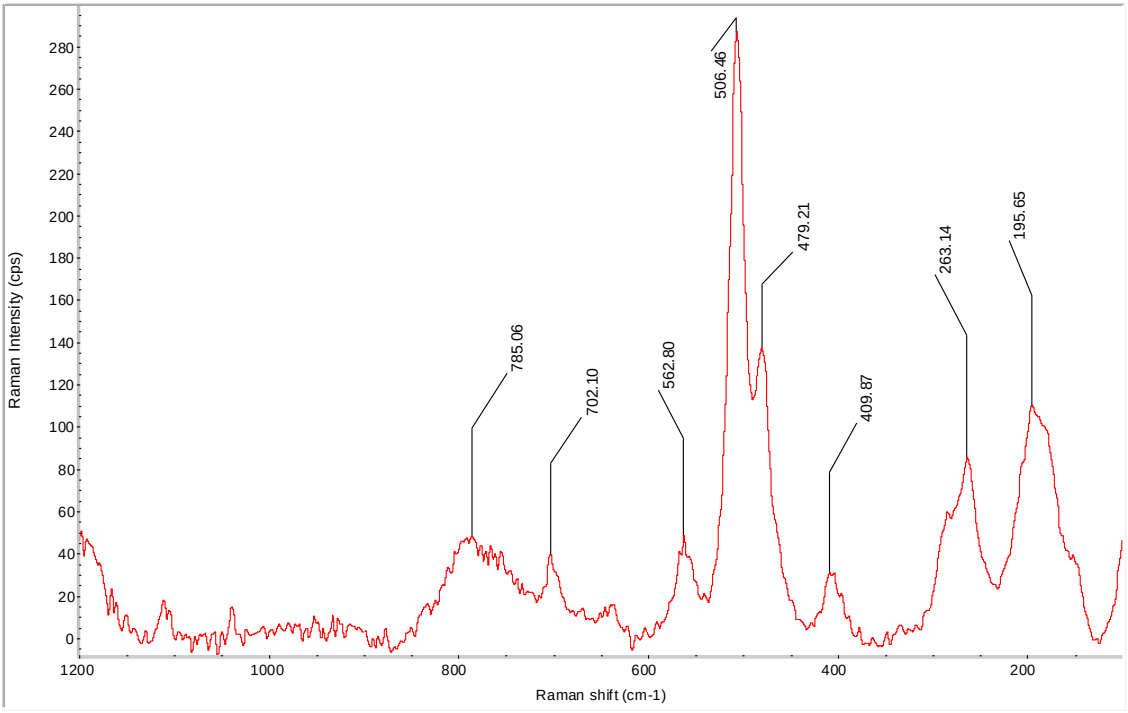

Figure 7. Raman peak spectrum of the plagioclase (labradorite) mineral in basalt around Konakalmaz (D Elazig). Sample No: KM-4.

5. Discussion and Results

The mafic volcanics around Konakalmaz are predominantly doleritic in composition and mainly consist of plagioclase, pyroxene and lesser olivine and opaque minerals. Rocks have intergranular, intersertal and doleritic textures. They are mainly categorized in class of doleritic rock. The 'augite' composition was obtained with the peak values of 190.70, 229.09, 325.05, 357.87, 393.16, 557.22, 666.19, 1009.19 of the analyzed sample belonging to the pyroxene mineral in basaltic pillow lavas around Konakalmaz. Raman peak values of the plagioclase mineral obtained from the same area yielded 'labradorite' as 195.65, 263.14, 409.87, 479.21, 506.46, 562.80, 702.10, 785.06. Homogeneous mineralogical formation and distribution weakens the possibility that the source of the magma chamber it is fed from is diverse and points to a monogenic source.

6. References

[1], Ural, M. “Elazığ ve Malatya çevresindeki Yüksekova Karmaşığı bazik volkanitlerinin petrokimyası, petrolojisi ve yaşı”. Fırat Üniversitesi, Fen Bilimleri Enstitüsü, Doktora Tezi, Elazığ, 174s.

[2], Ural, M., Deniz, K., Sayit, K. Mafic Volcanic and Subvolcanic Rocks from the Yüksekova Complex in the İçme-Kesikköprü Province (East of Elaziğ, Eastern Turkey): Whole-Rock Geochemistry and Confocal Raman Spectroscopy Characterization. In IOP Conference Series: Earth and Environmental Science (Vol. 362, No. 1, p. 012122). IOP Publishing, 2019.

[3], Çelik, H. “The effects of linear coarse-grained slope channel bodies on the orientations of fold developments: a case study from the Middle Eocene-Lower Oligocene Kırkgeçit Formation, Elazığ, eastern Turkey”. Turkish Journal of Earth Sciences, 22(2), 320-338, 2013.

International Conference on Advances and Innovations in Engineering

Changes in the unconfined compressive strength of high plasticity clay with basalt fiber reinforcement

Yasemin Aslan TOPÇUOĞLU[1] , Zülfü GÜROCAK [2]

[1,2]Fırat University, Faculty of Engineering, Department of Geological Engineering, Elazig, Türkiye.
[1]yaslan@firat.edu.tr, [2]zgurocak@firat.edu.tr

[1](ORCID: 0000-0002-3135-5926), [2](ORCID: 0000-0002-1049-8346)

Abstract

Although there are many methods to improve the engineering properties of clay soils, chemical stabilization using additives the such as silica fume, fly ash, volcanic tuff, volcanic ash, lime has been used for many years. However, in recent years, the use of fiber has gained importance and its use in soil reinforcement has become an alternative to old methods. Especially basalt fibers, whose raw material is basalt rock, attract attention because basalt rock is natural and widespread in nature. The interest in basalt fibers is increasing day by day due to their high strength and chemical resistance, resistance to micro-organisms and high temperatures, and the fact that no additives are used during their production. In soil reinforcements with basalt fibers, it is seen that the fiber length and ratio used are important. In this study, the changes in the unconfined compressive strength of high plasticity bentonite clay reinforcemented with basalt fiber were determined. For this purpose, 12 mm long basalt fiber in different proportions (1, 2, 3, 4 and 5%) was used as reinforcement in bentonite clay and the optimum fiber ratio that provided the maximum increase in strength was determined. According to the results of the experimental in the study, it was determined that the maximum strength was achieved with 12 mm long basalt fiber reinforcement in bentonite clay at 4% basalt fiber ratio, and the strength value decreased at basalt fiber ratios higher than this ratio.

Key Words: Basalt fiber, Bentonite clay, Reinforcement, Unconfined compressive strength

1. Introduction

The use of fiber (glass, polypropylene, basalt, etc.) as an alternative to traditional methods in soil improvement has shown a remarkable development in recent years. Ekincioğlu [1] defines fibers as materials that can be found naturally or produced by humans, one dimension of which is much larger than the other dimension, and having a higher strength and elasticity modulus than the larger shape of the same material. Of the two types of fibers, natural and artificial, the artificial one is used more. Artificial fibers are preferred because they have high strength, are light, flexible and highly resistant to environmental effects [2]. One of these fibers is basalt fibers (BF) which has attracted attention in recent years, produced from basalt rock, The raw material of BF is basalt rock, which is a volcanic rock and is widely distributed in nature and easy to access. BFs have superior properties such as high chemical resistance and resistance to temperature and microorganism effects. The fact that no additives are used during production is also an advantage for BFs. When soil reinforcement studies with BF reinforcement are examined, it is seen that BF length and rate are important for successful reinforcement.

As a matter of fact, Gao et al. [3] used BF reinforcement in a clayey soil and stated that the fiber ratio in which the maximum strength was determined was 0.25% and the fiber length was 12 mm. Gisymol & Ramya [4] found that the maximum increase in the strength of the organic soil with 10 mm length and 0.05% BF reinforcement occurred after 28 days of curing, while Kenan & Özocak [5] found that the optimum fiber ratio was 1.5% in their study on a silty soil. Pandit et al. [6] showed that according to the results of experimental studies using BF reinforcement in the soil, the maximum dry unit weight value of the soil increased and the optimum water content value decreased with the ratio of 4% BF. Moreover, Ocakbaşı [7] reported that the maximum strength value in the soil was increased by

[1]Corresponding author

2% BF and she stated that the fiber length was determined as 24 mm. Sungur et al. [8], determined that the shear strength increases up to a fiber length of 15 mm in BF reinforced clay soil, and the shear strength values decrease at a fiber length greater than that. Gürocak and Aslan Topçuoğlu [9] conducted experimental studies on the samples prepared by using 20, 25, 30 and 35% water content in kaolin clay by using BF (0, 1, 2, 3 %). According to the test results, they stated that the maximum strength value was obtained with 1% BF reinforcement and 25% water content. The aim of this study is to determine the changes in the unconfined compressive strength of the bentonite and the optimum fiber ratio that provides the maximum increase in strength when 12 mm long BF at different rates is used for reinforcement. The results obtained from the study will contribute to future studies on the use of BF in soil reinforcement.

2. Materials and Methods

In this study, bentonite was used as the clayey soil and BF, whose use has increased in recent years and the database still needs to be strengthened with new studies, was used as the reinforcement material.

2.1. Bentonite clay and basalt fiber

Bentonite clay, which is a clay mineral belonging to the montmorillonite family and formed as a result of the chemical decomposition or degradation of volcanic ash, lava and tuff rich in aluminum and magnesium content Önem [10], Akbulut [11], consists of chemically hydrated aluminum and magnesium silicates. In the experimental studies, pure bentonite clay produced in the Tokat-Reşadiye (Turkey) clay quarry was used (Figure 1), and according to the results of the XRF analysis performed on the clay, it was determined to be Na-Bentonite type clay [12].

Figure 1. Bentonite clay used in the study

BF produced from basalt, which is a hard, fine-grained, dark-coloured volcanic rock widely found in the world, is used for reinforcement soils due to its economical, natural and high strength properties. Basalt has the property of melting when heated, like thermo-plastic materials [13]. BF with a length of 12 mm was used in the study (Figure 2) and was purchased from the company that sold the fiber.

Figure 2. Unseparated (a) and separated (b) basalt fiber used in the study

2.2. Laboratory studies

Firstly, liquid limit, plastic limit and standard proctor tests were carried out on bentonite in the laboratory studies. In the second stage, unconfined compressive strength tests were carried out after the mixtures in which different amounts of BF were used as reinforcement in B were compressed at optimum water content. Laboratory studies were carried out at Fırat University, Department of Geological Engineering, Rock-Soil Mechanics Laboratory.

2.2.1. Liquid and plastic limit tests

At this stage of laboratory studies, LL and PL values of unreinforced B were determined according to the ASTM D4318-17e1 [14] standard. For this purpose, a total of 15 tests were carried out. According to the test results, the average LL and PL values of unreinforced B was found as 507% and 41%, and the PI value was calculated as 466%. It was determined that the clay used in this study was the high plasticity (CH) clay according to the Unified Soil Classification (USCS) (Table 1).

Table 1. Results of consistency limits and Standard proctor tests

Feature	Value
LL (%)	507
PL (%)	41
PI (%)	466
Soil class (USCS)	CH
w_{opt} (%)	38.50
γ_{kmax} (kN/m^3)	12.36

2.2.2. Sample preparation and standard proctor experiments

The optimum water content (w_{opt}) value of B was determined by standard proctor tests performed in accordance with the ASTM D698-12e2 [15] standard. The test was carried out by letting a 2.5 kg load fall freely from a height of 30.5 cm on the soil and compressing the soil in three layers in the formwork, and the test results are given in Table 1. Firstly, BF separated by compressor was added to the clay, which was dried in an oven at 105^{o}C for 24 hours and mixed with the help of a mixer (Figure 3). B samples reinforced BF were mixed again with a mixer by spraying distilled water at optimum water content, and a separate manual mixing process was applied in order to ensure homogeneous distribution of the fibers in B and to prevent fiber aggregation/agglomeration. In this study, the mixing time was determined as 10 minutes and 5 separate mixtures were prepared. BF ratios used in the mixtures are shown in Table 2.

Figure 3. Preparation of B and BF mixtures

Table 2. BF rates used in experimental studies

BF Length (mm)	BF Rate (%)	Sample Name
12	0	B
	1	B+1%BF
	2	B+2%BF
	3	B+3%BF
	4	B+4%BF
	5	B+5%BF

2.2.3. Unconfined compressive strength tests

According to ASTM D2166M-16 [16] standard, unconfined compression tests were carried out on cylindrical soil samples whose length is twice the diameter length to determine the compressive strength (q_u) of the soil. Experiments were carried out on 35 cylindrical specimens compressed to optimum water content and reinforced with 12 mm long BF (Figure 4).

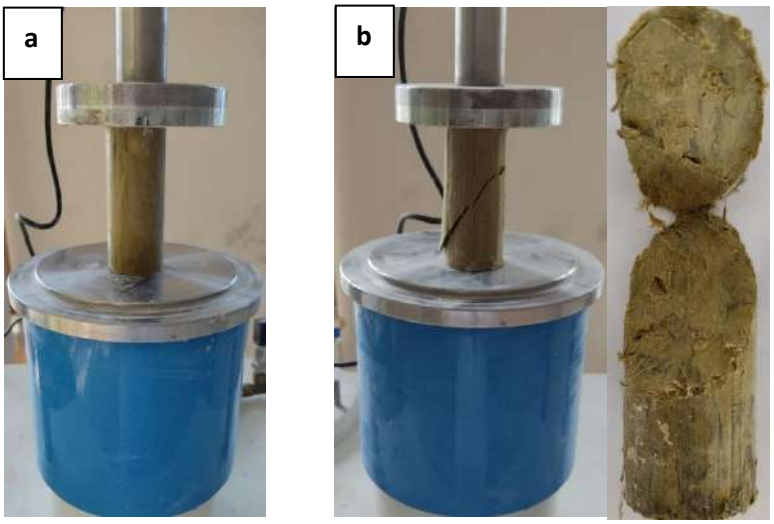

Figure 4. Unconfined compressive strength (a) before sample and (b) after sample

According to the results of the unconfined compression tests, the q_u value of the unreinforced B was determined as 206.93 kPa. The q_u values of the BF reinforced samples were found to be in the range of 197.09-267.66 kPa (Table 3).

Table 3. q_u values of unreinforced and BF reinforced samples

BF Length (mm)	Sample Name	q_u (kPa)
12	B	206.93
	B+1%BF	223.64
	B+2%BF	229.00
	B+3%BF	247.42
	B+4%BF	267.66
	B+5%BF	202.74

3. Results and Discussion

With the experimental studies, it was tried to determine the changes in the unconfined compressive strength values of the unreinforced and BF reinforced B samples. In addition, the optimum fiber ratio, which provides the best improvement in strength, was determined. The q_u value of unreinforced B is 206.93 kPa. The sample in which the

maximum strength was determined with BF reinforcement is B+4%BF and its q_u value is 267.66 kPa. The lowest q_u value was determined as 197.09 kPa in the B+5%BF sample. The q_u values increased with increasing BF ratios but decreased after a certain BF ratio. (Table 3, Figure 5). This BF ratio was determined as 4%.

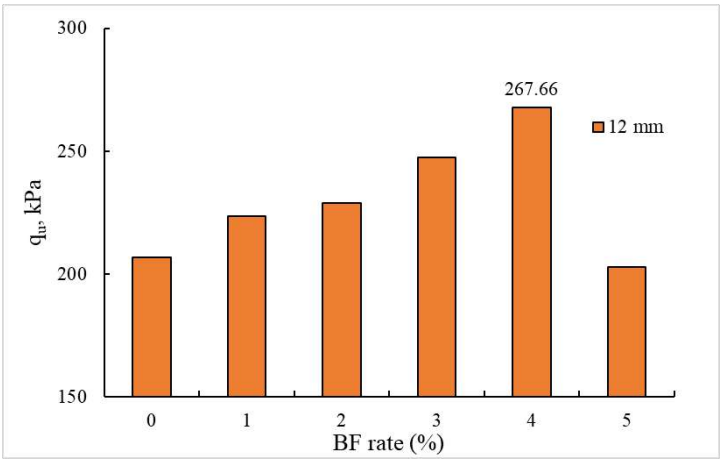

Figure 5. Relationship between q_u - BF ratio in unreinforced and BF reinforced clay samples

The increases in the qu values of the reinforced samples with 1, 2, 3 and 4% BF compared to unreinforced B were found as 8.08, 10.67, 19.57, 29.35%, respectively. However, there is a decrease of 2.02% in the 5%BF reinforced sample (Table 4, Figure 6).

Table 4. Percentage changes in q_u values of unreinforced and reinforced clay samples

BF Length (mm)	Sample Name	q_u (% Change)
12	B	-
	B+1%BF	8.08
	B+2%BF	10.67
	B+3%BF	19.57
	B+4%BF	29.35
	B+5%BF	-2.02

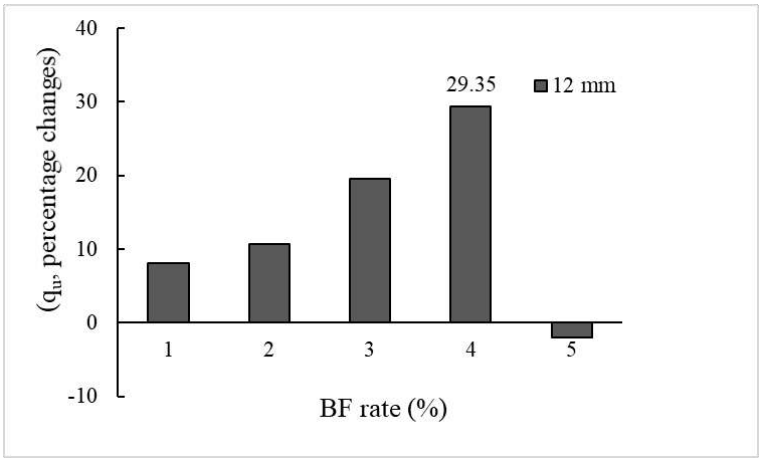

Figure 6. The relationship between percentage changes of q_u - BF ratio of unreinforced and reinforced clay samples

The q_u value of the clay increased up to 4% BF reinforcement, but after 4% BF, the q_u value decreased. The reason for this is the difficulty in aggregating, aggregating and dispersing the fibers in the soil as the fiber ratio increases.

When the fiber ratio is high in the soil, electrostatic interaction occurs between the fibers. For this reason, the fibers that are not homogeneously dispersed in the soil are collected in clusters and thus the strength decreases [3].

4. Results

The results of this experimental study, which was conducted to determine the optimum BF ratio for reinforcement high plasticity clay soils, are briefly summarized below

1. In unconfined pressure tests, the strength value of unreinforced B was determined as 206.93 kPa. The q_u values of BF reinforced mixtures vary between 197.09-267.66 kPa.

2. In BF reinforced samples, q_u values increased up to 4% BF, but higher BF reinforcement caused a decrease in q_u values. It can be said that the reason for this is the formation of fiber agglomerations due to increased fiber ratio.

3. The data obtained from this study will contribute to the studies and literature on the use of environmentally friendly BF, which is abundant and naturally found in nature, in soil reinforcement applications.

5. References

[1] Ekincioğlu Ö. Mechanical behavior of cement based composites reinforced with hybrid fibres-an optimum design. Master's thesis, Istanbul Technical University, Istanbul, Türkiye, 2003.

[2] Aral M. Mechanical behavior of cement based composites with hybrid fibres-an optimum design, Master Thesis, Istanbul Technical University, Istanbul, Türkiye, 2006.

[3] Gao L, Hu G, Xu, N, Fu J, Xiang C, Yang C. "Experimental study on unconfined compressive strength of basalt fiber reinforced clay soil". *Advances in Materials Science and Engineering*, 2015, 1-8, 2015.

[4] Gisymol PG, Ramya K. "A study on the effect of basalt fiber in organic soil". *IOSR Journal of Mechanical and Civil Engineering (IOSR-JMCE)*, 14*(*4), 13-17, 2017.

[5] Kenan A, Özocak A. "Effect of basalt fiber addition on shear strength of silty soils". *International Symposium on Natural Hazards and Disaster Management*, 918-924, 2018.

[6] Pandit VM, Rohit C, Tushar K, Ayushi C. Bhushan G, Deepali C. "Study of basalt fiber on compaction characteristics of black cotton soil". *6th International Conference on Recent Trends in Engineering & Technology (ICRTET)*, 850-853, 2018.

[7] Ocakbaşı P. The effect of basalt fiber addition on undrained shear strength of clayey soils. Master's Thesis, Sakarya University, Sakarya, Türkiye, 2019.

[8] Sungur A, Yazıcı MF, Keskin SN. "Experimental research on the engineering properties of basalt fiber reinforced clayey soil". *European Journal of Science and Technology Special Issue*, 28, 895-899, 2021.

[9] Gürocak Z, Aslan Topçuoğlu Y. "The effect of basalt fiber use on the unconfined compressive strength of low plasticity clay". *Gümüşhane University Journal of Science and Technology*, 13(3), 688-701, 2023.

[10] Önem Y. "Sanayi Madenleri". Kozan Ofset, Ankara, 2000.

[11] Akbulut A. "Bentonit". MTA Eğitim Serisi-32, Ankara, 1996.

[12] Aslan Topçuoğlu Y. The effect of different additive materials on the engineering properties of soils. PhD Thesis, Fırat University, Elazığ, Türkiye, 2020.

[13] Jamshaid H, Mishra R. "A green material from rock: basalt fiber-a review". *The Journal of the Textile Institute*, 107(7), 923-937, 2015.

[14] Standard Test Methods for Liquid Limit, Plastic Limit and Plasticity Index of Soils. American Society for Testing and Materials, ASTM D4318-17e1, 2017.

[15] Standard Test Methods for Laboratory Compaction Characteristics of Soil Using Standard Effort, American Society for Testing and Materials ASTM D698- 12e2, 2012.

[16] Standard Test Method for Unconfined Compressive Strength of Cohesive Soil, American Society for Testing and Materials ASTM D2166M-16, 2016.

International Conference on Advances and Innovations in Engineering

Risk Analysis and Risk Assessment in Limestone Quarry: L Matrix Method

Vedat KARAHAN[1], Ercan AYDOĞMUŞ[2], Erdal CANPOLAT[3]

[1,2]Department of Chemical Engineering, Faculty of Engineering, Fırat University, 23119, Elazığ, Türkiye.
[3]Department of Science Education, Faculty of Education, Fırat University, 23119, Elazığ, Türkiye.
[1]vdtkrhn@gmail.com, [2]ercanaydogmus@firat.edu.tr, [3]ecanpolat@firat.edu.tr

[1](ORCID: 0000-0002-0913-7826), [2](ORCID: 0000-0002-1643-2487),[3](ORCID: 0000-0002-1167-0881)

Abstract

In this research, within the scope of occupational health and safety, risk analysis and risk assessment have been carried out using L matrix method in limestone quarries. In the risk analysis, a total of 70 risks are identified. Of the identified risks, 17 (24.28 %) are at high risk, 44 (62.85 %) are at medium risk, and 9 (12.85 %) are at low risk. It should be ensured that multiple risks are kept under control in limestone quarries and that employees are affected by these risks at the minimum level. To prevent occupational accidents, it is necessary to take the necessary occupational health and safety measures against the determined risks at the highest level. During the operation of limestone quarries, it can have negative effects not only on the employees but also on the environment. For these reasons, the points to be considered in the operation of limestone quarries are stated below. It should be under constant supervision in terms of technology and safety in blasting activities. Necessary environmental precautions should be taken to minimize environmental impacts during blasting. The deficiencies of the work machines working in the quarry in terms of occupational health and safety should be eliminated. Periodic inspections of these places should be made and they should be operated by occupational health and safety rules. Emergency teams should be formed for emergencies that may occur in limestone quarries and such training should be provided for employees. Occupational health and safety rules must be followed in the quarry operation, taking into account the environmental effects.

Keywords: L matrix method, limestone quarry, occupational health and safety, risk analysis and assessment.

1. Introduction

Occupational health and safety is a discipline that is constantly developing and innovating as a result of the importance given to the employee in contemporary societies. All activities within the scope of occupational health and safety have two main purposes. These are to protect employees against work accidents and occupational diseases and to ensure that employees work in a healthier environment. Because there are many technological developments for the production of high-quality and low-cost products and the technology is quite widespread, it also increases its competitiveness. Due to the intense competition, work accidents and occupational diseases are mentioned a lot in the industry. Even though manpower has been replaced by machinery and advanced technological equipment due to the technology that has developed and becomes widespread from the production lines, the importance of the employees is increasing day by day. All plans and investments made for occupational health and safety aim to prevent direct and indirect costs that may arise after an occupational accident [1].

The basic approach in occupational health and safety is to protect the health and safety of employees. In this way, the health status of the employees is constantly observed and the sources of risk in the working environment are reduced. It is aimed to eliminate the dangers and to prevent diseases and injuries [2]. All activities for occupational health and safety are one of the most important elements of working life beyond the concern of all employees. Data on occupational health and safety provide important indicators of working life and the development level of the country. In occupational health and safety studies, ten basic problems should be taken into account in the solution of all kinds of occupational safety problems. Reducing occupational risks, conducting research, protecting the health of employees, and preventing dangerous movements and situations are among the basic principles. Besides, increasing

[1]Corresponding author

the efficiency of the process (machinery and used equipment) in occupational health and safety is also included in these principles. The basic principles of occupational health and safety are stated below [3].

- Dangerous movements and situations should be avoided.
- 88 % of work accidents are caused by dangerous movements, 10 % by dangerous situations, and 2 % by unavoidable events.
- The effect and size of the damage that may occur as a result of the accident cannot be predicted, it depends entirely on coincidence.
- There are 29 losses of limbs and 300 non-injury events based on every event resulting in serious injury or death.
- The causes of dangerous actions are listed as personal defects (carelessness, indifference, etc.) arising from the constitution and natural structure of the worker, unsuitable mechanical conditions, environmental problems, and lack of knowledge and skills.
- To prevent accidents, methods such as engineering and revision, persuasion and encouragement, utilizing ergonomics, and disciplinary rules are applied.
- The methods of prevention from accidents and production, cost, and quality control methods show similarities and parallelism.
- Top managers should participate in the rules and measures to be taken in the work related to occupational safety and share the responsibility.
- Foremen, foremen, and similar first-level managers are the most prominent personnel in preventing accidents.
- Two factors play a driving role in the provision of occupational safety, as well as the human feelings that guide work safety studies. One of them is the reduction of production costs in the enterprise. The other is that the payments to be made when the accident occurs are about five times the expenditures to be made for the prevention of the accidents.

The basic principle of World Health Organization and International Labor Organization in occupational health and safety is to maximize the physical, mental, and social well-being of workers in all occupations, to maintain them at this level, and to prevent the deterioration of workers' health due to working conditions. Also, it is aimed to protect the workers from the dangers caused by unhealthy factors during their employment and to place the physiological and psychological conditions of the workers in the most appropriate occupational environments. The main goal is to maintain these situations and, in summary, to ensure that the work fits the people and each person's job [4,5].

World Health Organization defines an occupational accident as an event that causes most unplanned personal injuries, damage to machinery and equipment, and production stoppage for a certain period. International Labor Organization defines an occupational accident as an unplanned, unknown, and uncontrolled event that can harm the environment. When accidents are examined, it is understood that they occur as a result of the succession of 5 basic factors such as human weakness in the face of mechanical forces, personal defects, dangerous behavior and dangerous situation, accident event, injury, or damage. Unless one of these five basic factors is called the accident chain, the next one does not occur, and unless the chain is completed, there is no accident or injury. For an occupational accident to be in the definition of an accident, the stage of injury (damage) must be present [5-9].

The aim of risk management in occupational health and safety is to deal with the causes of work accidents and occupational diseases and the factors affecting them with the most valid and correct approach. It is also to collect the necessary information, taking into account all the circumstances, and to establish an effective safety net to prevent the emergence of unseen dangers. A good risk analysis with a large team is of great importance in terms of protection from work accidents that may occur. In this context, it is ensured that invisible dangers are revealed and effective security measures are taken [10-13].

2. Materials and Methods

In this study, the limestone quarry, which is the main source of many structural productions, has been evaluated in terms of occupational health and safety. Problems occurring during production in limestone quarries and risks existing in limestone production are determined; risk analysis and evaluation are carried out.
While performing risk analysis and evaluation, it is basically to identify the risk focus, eliminate the risks, or minimize the degree of impact. The analysis is carried out by grading the risks in order of importance according to their risk scores. Risk scores are taken into consideration while the risks are analyzed within themselves and necessary precautions and improvements are made accordingly. Risk analysis and assessment ensure that not only occupational accidents that may occur in the enterprise but also the loss of equipment that may occur in the enterprise are prevented. In this study, risk analysis and assessment are carried out using 5x5 L Matrix method (decision matrix), which is developed to meet the system security program requirements, also known as US military standard MIL-STD-882-D.
Risk has two basic components:

- The probability of not achieving a certain outcome or the probability of an undesirable event occurring (probability),
- The effect on the outcome if the risk occurs.

The probability of occurrence of the event for each identified hazard is given in the probability scale in Table 1, and the severity of the hazards when they occur is given in the severity scale in Table 2. According to Eq. 1 and Eq. 2, the risk score (score) is calculated.

Risk = f (Probability, Severity) (1)
Risk score (Score) = (Probability)·(Severity) (2)

Table 1. Risk probability scale

Score	Likelihood	Likelihood of occurrence
1	Unlikely	So unlikely
2	Remote	Unlikely, but possible to occur
3	Occasional	Likely to occur sometime in the life of an item
4	Moderate	Will occur several times in the life of an item
5	Frequent	Likely to occur frequently

Table 2. Occupational health and safety risk score

Score	Likelihood	Potential Consequence
1	Negligible	İnjuries and diseases that do not require medical treatment
2	Minor	Minor injuries that require first-aid only
3	Serious	Severe injuries that require hospitalization or multiple medical treatments
4	Very Serious	Life-threatening injuries or multiple injuries that require hospitalization
5	Critical	Death or multiple injuries that pose a threat to life

5x5 L type risk decision matrix is given in Table 3, and occupational health risk assessment charts are expressed in Table 4.

Table 3. 5x5 L type risk decision matrix

		SEVERITY				
		Critical (5)	**Very Serious (4)**	**Serious (3)**	**Minor (2)**	**Negligible (1)**
LIKELIHOOD	**Frequent (5)**	Not tolerated (25)	High (20)	High (15)	Moderate (10)	Low (5)
	Moderate (4)	High (20)	High (16)	Moderate (12)	Moderate (8)	Low (4)
	Occasional (3)	High (15)	Moderate (12)	Moderate (9)	Low (6)	Low (3)
	Remote (2)	Moderate (10)	Moderate (8)	Low (6)	Low (4)	Low (2)
	Unlikely (1)	Low (5)	Low (4)	Low (3)	Low (2)	Insignificant (1)

Table 4. The risk assessment table for occupational health

Risk Score	**Risk Degree**	**Actions should be taken to prevent the risk**
25	Not tolerated	The process must not be operated until the risk is reduced to an acceptable level. it is necessary to stop single-being-studied actions. The activities must be canceled if the risk cannot be prevented.
15, 16, 20	Critical	The situation is an emergency or required actions must be taken in the nearest time. The action can be continued under supervision and control if the risk has no dangerous potential
8, 9, 10, 12	Moderate	The required protective actions must be taken to reduce risk levels.
2, 3, 4, 5, 6	Minor (maybe tolerated)	The emergency measure is not needed but the ruling measures must continue.
1	Negligible	Taking precautions is not a priority

3. Results and Discussions

In this risk analysis study, 70 risks are identified. Risks are rated according to high, medium, and low risk. As seen in Table 5, 17 of them are found to be at high risk, 44 at medium risk, and 9 at low risk.

Table 5. Frequency of risk grades

Risk Degree	Number of risks	% frequency
High Risk	17	24,29
Medium Risk	44	62,86
Low Risk	9	12,86
Total	70	100,00

The distribution of the obtained risk scores according to the number of risks is shown in Figure 1. Considering the risk scores, there is a maximum number of hazards with a risk score of 12. The risk score and the number of risks identified as a result of the risk assessment performed are also given in Table 6.

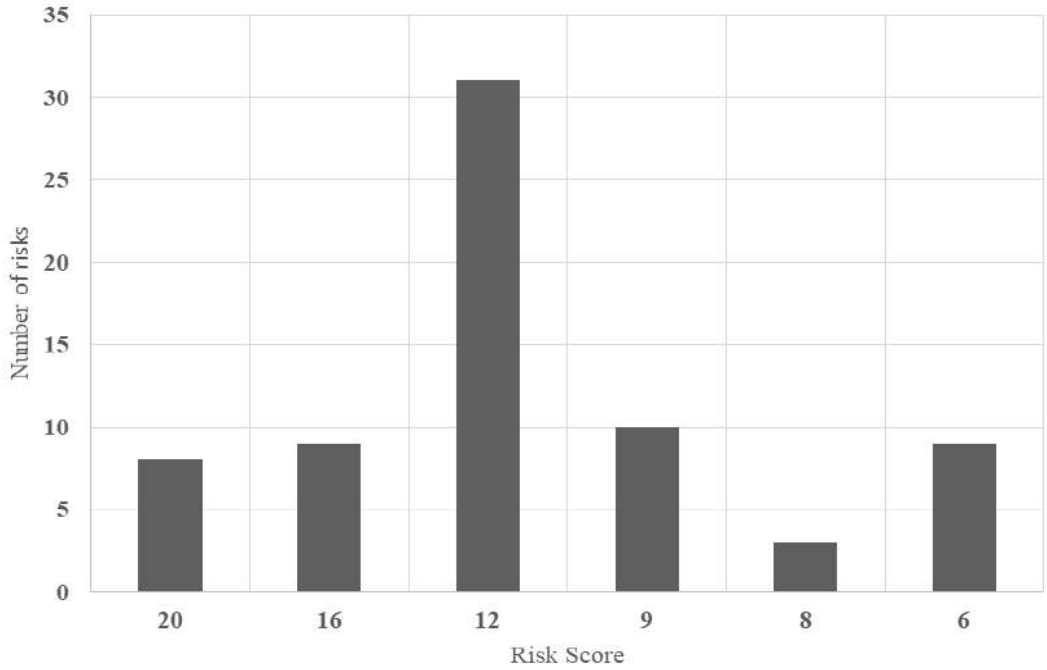

Figure 1. Risk score distribution

Table 6. Number of risks and risk score (score)

Risk Score	Number of Risks
20	8
16	9
12	31
9	10
8	3
6	9

4. Conclusions

In the risk analysis and evaluation study, the hazards and the risks that may arise from these hazards are revealed by using L Type Matrix method in the limestone quarry. Necessary measures should be taken by the legal legislation to reduce the risks from a high-risk level to an acceptable risk level. As a result, risks with high and medium risk levels should be reduced to low-risk levels and should be within the acceptable risk score range. In this research, various suggestions are presented to eliminate the deficiencies and to provide a healthier and safer working environment.

- Emergency teams should be established for emergencies that may occur in the quarry area, necessary training should be given to these emergency teams, and all working personnel should be informed about what to do in possible emergencies.
- Fire extinguishing equipment should be available against fires that may occur in the furnace area, and fire extinguishing training should be given to the fire extinguishing team and all employees. Fire extinguishing equipment should be located so that everyone can see it, and annual maintenance should be done.

- Annual emergency drills should be conducted against all emergencies such as fire, earthquake, and work accidents that may occur in the quarry. Occupational health and safety training should be given to all working personnel and the participation of employees at all levels should be ensured.
- All safety and environmental precautions to be taken before the blasting operation to be carried out in the quarry must be complied with. After all, precautions are controlled, blasting should be done.
- The personnel should be provided with the necessary personal protective equipment against risk factors such as dust and noise that may arise in the blasting process and they should be provided to use them.
- All necessary occupational health and safety precautions should be taken during the storage of the explosive material provided for use in the blasting process (it should be stored appropriately) and until use.
- All warning sounds and markings of the work machines working in the quarry should be made.
- The quarry roads required for the transport and loading of the ore in the quarry should be determined, and care should be taken not to use these roads other than the necessary work machines.
- All periodic checks of the mobile tankers that will refuel the construction equipment should be made and their use should be prevented except by authorized personnel.
- The personal protective equipment of all working personnel should be checked and renewed at regular intervals.
- In case of malfunctions that may occur in the work machines, the malfunction should be eliminated by authorized persons and periodic maintenance should be done regularly.
- Ergonomic equipment suitable for the use of personnel who will work with screened tools should be provided and adequate workspace allocation should be made.
- Necessary occupational safety markings must be made in the furnace and occupational safety precautions must be fulfilled completely.

5. References

[1] Karahan V, Aydoğmuş E. "Risk analysis and risk assessment of laboratory work by Fine Kinney method". International Journal of Advanced Natural Sciences and Engineering Researches, 7(4), 442-446, 2023.

[2] Karahan V, Aydoğmuş E. "Risk analysis and risk assessment in laboratory studies". European Journal of Science and Technology, (49), 55-60, 2023.

[3] Semerci, O. "İş sağlığı ve güvenliğinde risk değerlendirmesi: Metal sektöründe bir uygulama". Ege Üniversitesi, Sosyal Bilimler Enstitüsü, Yüksek Lisans Tezi, 2012.

[4] Bayraktar B, Uyguçgil H, Konuk A. "Türkiye madencilik sektöründe iş kazalarının istatistiksel analizi". Madencilik, 85-90, 2018.

[5] Kurt, M. "İş Kazalarının Ergonomik Analizi". Gazi Üniversitesi, Fen Bilimleri Enstitüsü, Doktora Tezi, Ankara, 1993.

[6] T.C. İş Sağlığı ve Güvenliği Risk Değerlendirmesi Yönetmeliği, Resmi Gazete, 28512, 29.12.2012

[7] Koltan A, Orhon HY, Yılmaz S, Altay M, Yılmaz S, Çay İ. "Risk değerlendirmede kullanılan L tipi karar matrisi yönteminin işçi sağlığına uygunluğunun değerlendirilmesi". Türk Tabipleri Birliği Mesleki Sağlık ve Güvenlik Dergisi, 10, 38-43, 2010.

[8] Altın ZG, Dağ M, Aydoğmuş E. "Risk analysis by Fine Kinney method in a laboratory". Journal of Physical Chemistry and Functional Materials, 1(1), 54-58, 2018.

[9] Altın ZG, Dağ M, Öz A, Aydogmus E. "Risk Analysis by FMEA method in hotel". Journal of Physical Chemistry and Functional Materials, 1(1), 59-65, 2018.

[10] Zehra Gülten Yalçın, Mustafa Dağ, Ercan Aydoğmuş. "Gübre fabrikasında 5x5 L tipi matris metoduyla risk analizi". 2nd International Eurasian Conference on Science, Engineering and Technology (EurasianSciEnTech 2020), Gaziantep, 2020.

[11] Yalçın ZG, Dağ M, Şahin S, Aydoğmuş E. "Macaroni production plant is HACCP (hazard analysis of critical control points) risk study". International Conference on Physical Chemistry and Functional Materials (PCFM'18), Elazığ, 2018.

[12] Yalçın ZG, Dağ M, Şahin S, Aydoğmuş E. "Fine Kinney risk analysis study in fuel laboratory with expert system implementation". 2nd International Eurasian Conference on Science, Engineering and Technology (EurasianSciEnTech 2020), Gaziantep, 2020.

[13] Yalçın ZG, Dağ M, Şahin S, Aydoğmuş E. "Kimya mühendisliği bölüm ofislerinde FMEA risk değerlendirmesi". 5. Uluslararası Mühendislik Teknoloji Yöntemi Kongresi, İstanbul, 2021.

International Conference on Advances and Innovations in Engineering

Degradation of Amoxicillin in the Presence of Metal-free Composite Photocatalysts

Burcu PALAS[1] , Öykü AKDAĞ[2], Tümay ÇETİNBAŞ[3], Gülin ERSÖZ[4]

[1,2,3,4]Chemical Engineering Department, Faculty of Engineering, Ege University, İzmir, Turkey.
[1]burcu.palas@ege.edu.tr, [2]oykuakdagg@gmail.com, [3]cetinbastumay@gmail.com, [4]gulin.ersoz@ege.edu.tr

[1](ORCID: 0000-0002-2815-0057), [4](ORCID: 0000-0002-5875-5946)

Abstract

The development of metal–free green photocatalysts for wastewater treatment is of significant scientific interest. Organic photocatalysts have many advantages including tunable structures and strong light absorption property. The utilization of organic semiconductors is a promising method to accomplish the expected photocatalytic performance by avoiding the high prices of metal catalysts and metal contamination. In recent years, perylene diimide has been reported as one of the most effective n-type organic photocatalysts due to its photostability and thermal stability. In order to enhance the surface area, electron transzfer and photocatalytic activity, perylene diimide has been coupled with non-metal substances such as graphene, carbon nanotubes, graphitic carbon nitride, and carbon quantum dots. Graphene based composite catalysts have gained attention for their high adsorption capacity and promoted electron transfer. In this study, graphene oxide/self-assembled perylene diimide catalyst (GO/PDI) was prepared, characterized and its photocatalytic activity was tested for the removal of amoxicillin from aqueous solutions. Response surface methodology and Box-Behnken design were used to investigate the interactive effects of photocatalytic oxidation parameters and determine the optimum reaction conditions. The influences of the catalyst loading, pH, and the initial amoxicillin concentration on amoxicillin degradation efficiency were examined. The optimum reaction conditions were determined as 0.51 g/L catalyst loading, pH 6, and 12.4 mg/L amoxicillin concentration in the presence of GO/PDI composite catalyst. Under the optimized reaction conditions, 47.7% amoxicillin degradation was achieved.

Keywords: Amoxicillin removal, Graphene oxide, Metal-free photocatalyst, Perylene diimide

1. Introduction

Water is one of the most essential substances on earth ensuring the existence of life. The excessive increase in water consumption and release of industrial pollutants into aquatic medium reduce the availability of clean water. The presence of organic pollutants including antibiotics, herbicides, pesticides and fertilizers cause intensive water contamination. Pharmaceuticals as the emerging water pollutants have gained increasing concern all over the world due to their potential hazards to environmental and human health [1].

Amoxicillin, one of the broad-spectrum β-lactam class antibiotics, is widely used for the prevention of diseases in humans and animals. It is reported that amoxicillin is one of the most frequently used antimicrobial drug active substances in 71 countries [2]. Amoxicillin, which has a higher usage rate than other antibiotics with a prescription rate of 750-2250 mg per day [3], is used in the effluent of wastewater treatment plants, sewage water, surface water and detected in hospital wastewater.

Although the antibiotic concentrations detected in wastewater treatment factory effluents, surface and ground waters are generally at the nanogram/liter-microgram/liter level [4], much higher concentrations of antibiotics are detected in pharmaceutical factory wastewater. While the COD value in amoxicillin wastewater reaches several thousand mg/L, the amoxicillin concentration can reach several hundred mg/L [5], Various studies have reported that pharmaceutical industry wastewater contains 218.29 mg/L [6], 210 mg/L [7], 50 mg/L [8] amoxicillin. Improperly

[1]Corresponding author

treated wastewaters contaminated with antibiotics poses a serious problem for surface and drinking water. Therefore use of effective wastewater treatment methods for the removal of pharmaceuticals compounds is of great importance. Advanced oxidation methods are one of the most effective technologies for the removal of recalcitrant organic pollutant in water. Among advanced oxidation processes, photocatalysis is of great interest because it is one of the most cost efficient and environmentally friendly methods compared to many conventional wastewater treatment processes. The basic steps of heterogeneous photocatalysis include the transfer of the reactants in the liquid phase to the catalyst surface, the adsorption of the reactant on the catalyst surface, the reaction in the adsorbed phase, the desorption of the reaction products and the removal of the final products in the liquid phase. When the photocatalyst absorbs light, electrons are promoted from the valence band to the conduction band and electron-hole pairs (h_{vb}^+ and e_{cb}^-) are generated. Holes react with surface bound H_2O to produce hydroxyl radicals, while electrons react with O_2 to produce superoxide radical anion. These radicals react with organic compounds and provide mineralization of pollutants [9].

The high cost, poor structural controllability, low efficiency and toxicity of conventional semiconductor (especially inorganic semiconductor materials) photocatalysts limit their use. Therefore, the development of innovative photocatalysts is important. Supramolecular organic semiconductors have been shown to be one of the most promising materials for photocatalytic processes. Supramolecular organic semiconductors are formed by the self-assembly of small molecules with conjugate planes through intermolecular supramolecular forces (π-π interactions, hydrogen bond interactions, etc.). Perylene-3,4,9,10-tetracarboxylic diimide (PDI) and its derivatives have been effectively used for the degradation of water contaminants in photocatalytic processes [10,11]. Studies have shown that these materials are suitable for the removal of many antibiotics from water, which contain functional groups that can react with phenol and oxidizing active species, due to strong oxidizing active species ($^{\bullet}O_2^-$, h^+, etc.) released in the presence of PDI catalysts (Dai et al., 2020).

The photocatalytic activity and mechanical strength of the catalysts can be improved by using carbon based support materials in composite catalyst structures. Graphene is an excellent catalyst support to be used in heterogeneous photocatalysis due to its large surface area, unique optical, mechanical and physicochemical properties. Graphene is a sp^2 hybridized carbon-based material with a hexagonal (benzene ring) monolayer network. In comparison with other carbon allotropes, graphene offers the greatest intrinsic carrier mobility at room temperature, with perfect atomic lattice, promising mechanical strength, chemical and thermal stability [12].

In literature there are several studies on use of graphene derivatives and perylene diimide containing composite materials for the photocatalytic degradation of various organic compounds such as dyes [13,14] and phenol [15]. However, no study was found investigating the amoxicillin removal performance of Graphene Oxide/Perylene Diimide composite catalysts. Therefore, in the present study, GO/PDI (GO: Graphene Oxide, PDI: Perylene Diimide) composite materials have been synthesized and used for the photocatalytic degradation of amoxicillin. The interactive effects of the catalyst loading, pH, and the initial amoxicillin concentration were investigated and the reaction conditions were optimized by using response surface methodology and Box-Behnken design.

2. Materials and Methods

2.1. Chemicals

Graphite powder (Sigma-Aldrich), sulfuric acid (Merck, 95-97%), and potassium permanganate (Merck, 99.0-100.5%), were used to prepare graphene oxide. Perylene-3,4,9,10 tetracarboxylic dianhydride (Sigma-Aldrich, 97%), imidazole (Thermo Scientific, %99), β-alanine (Sigma-Aldrich, 99.3%), ethanol (Merck), hydrochloric acid (Tekkim Kimya, 30-32%), triethylamine (Sigma-Aldrich) and nitric acid (Merck) were used to synthesize graphene oxide/perylene diimide composite catalyst. The model antibiotic, amoxicillin trihydrate (AFG Bioscience) was used in photocatalytic oxidation.

2.2. Preparation of graphene oxide/perylene diimide supramolecular catalyst

Composite GO/PDI supramolecular catalysts were prepared according to the procedures given in literature [16–19]. In order to synthesize of perylene diimide, 1.376 g perylene 3,4,9,10-tetracarboxylic dianhydride, 18 g imidazole,

and 2.5 g 3-aminopropionic acid were mixed at 100°C for 3 hours. 2 M 300 mL HCl and 100 mL ethanol were added and mixed for 2 h at room temperature. PDI particles were filtered by using a 0.45 μm membrane and washed with pure water until neutral pH was reached. Then PDI particles were dried at 60°C. For the synthesis of self-assembled perylene diimide, 200 mL of 5 mM PDI solution was prepared by adding 834 μL of trimethylamine. Graphene oxide was prepared from graphite powder by the modified Hummers method [20]. PDI stock solution was prepared by using 0.534 g PDI and 834 microliters of trimethylamine in 200 mL water. Equal amount of graphene oxide is added and the mixture was ultrasonicated for 30 minutes. 27.3 mL 4.0 M HNO_3 was added and the mixture was stirred for 1 hour at 60°C. After cooling to room temperature, GO/PDI particles were filtered and washed with pure water. Lastly, the catalyst was dried in oven.

2.3. Characterization of graphene oxide/perylene diimide supramolecular catalyst

The surface texture and elemental distribution of the supramolecular catalyst was realized in Ege University Materials Research Center Research Test and Analysis Laboratories via a Thermo Scientific Apreo S scanning electron microscope. The surface area measurements and N_2 adsorption-desorption analysis were performed in İzmir Institute of Technology Materials Research Center via a Micromeritics Gemini V. The samples were degassed at 150°C for 180 min. The X-ray powder diffraction analysis was carried out in Middle East Technical University Central Laboratory by using a Rigaku Ultima-IV X-Ray diffraction device. XRD pattern of the supramolecular photocatalyst is recorded in an angle range of 2θ=5-80°. FT-IR spectrum of GO/PDI was recorded between 4000 – 400 cm^{-1} via a Bruker IFS 66/S in Middle East Technical University Central Laboratory.

2.4. Experimental system

In the photocatalytic oxidation experiments, two 6 Watt UV-C lamps radiating at 254 nm were used as the light source. A magnetic stirrer was used for homogeneous mixing of the reaction liquid and a water bath was used to control the temperature in the experiments carried out in batch processes. Spectrophotometric analysis was performed by taking samples from the drug solutions treated in the experiments at certain intervals.

2.5. Experimental plan

The interactive effects of catalyst loading, pH, and the initial amoxicillin concentration were investigated and the photocatalytic oxidation conditions were optimized by using Box–Behnken design as a response surface method. The experimental conditions are given in Table 1.

Table 1. Independent variables used in the experimental design and their ranges

Factor	Low	Medium	High
	-1	0	+1
pH	3	5	7
Catalyst Loading (g/L)	0.1	0.55	1
Initial amoxicillin concentration (mg/L)	5	10	15

2.6. Analysis

The photocatalytic activity and amoxicillin removal performances of the supramolecular catalyst were evaluated by monitoring the absorbance values of the samples via a Thermo Genesys 10S UV-visible spectrophotometer. The degradation of amoxicillin was determined by measuring the absorbance values at 230 nm [21].

The antibiotic degradation efficiencies were calculated according to Equation 1:

$$\text{Degradation (\%)} = \frac{A_o|_{@230\ nm} - A_t|_{@230\ nm}}{A_o|_{@230\ nm}} \times 100 \quad (1)$$

where A_o is the initial absorbance and A_t is the absorbance at time t.

3. Results and Discussion

3.1. Characterization of composite supramolecular catalyst

The scanning electron microscopy images, EDX spectrum, and elemental mapping analysis results of GO/PDI supramolecular catalyst are presented in Figure 1. The surface morphology of GO/PDI shows the characteristic rod-like structure of perylene diimide. GO/PDI catalyst micrographs showed that the graphene doping did not affect the ordered self-assembly of perylene diimide and improved the perylene diimide dispersion. The length and width of microrods of different sizes are generally below 5 and 1 μm, respectively. Mapping and EDX analyzes of supramolecular composite catalyst show that GO/PDI surface is homogeneous and consists of C, N, and O elements.

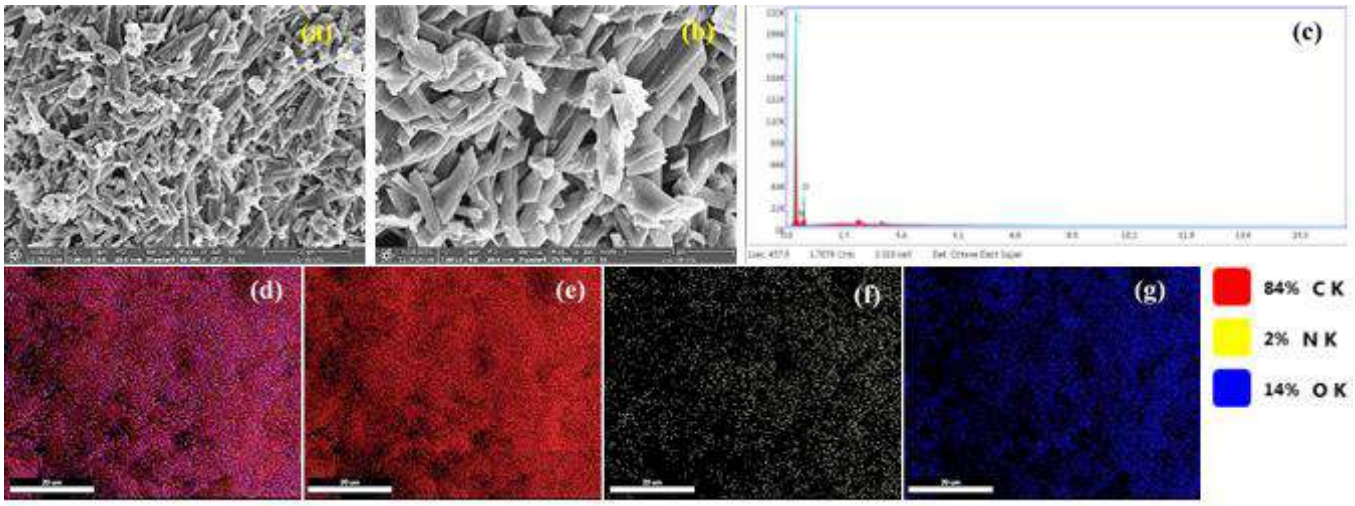

Figure 1. SEM micrographs at 10000 and 25000 magnifications (a-b), EDX spectrum (c), SEM mapping images (d-g) of graphene oxide/perylene diimide composite catalyst

The X-Ray diffraction pattern of the GO/PDI is shown in Figure 2. High peak intensities in the XRD pattern of the composite catalyst indicated that GO/PDI has a crystal structure. The peaks appeared in the range of 5–30° and 24–28° are associated to the characteristic π-π stacking property of PDI [22]. The peak observed around $2\theta = 26°$ associated to the 3.3-3.6 Å lattice spacing of PDI based materials.

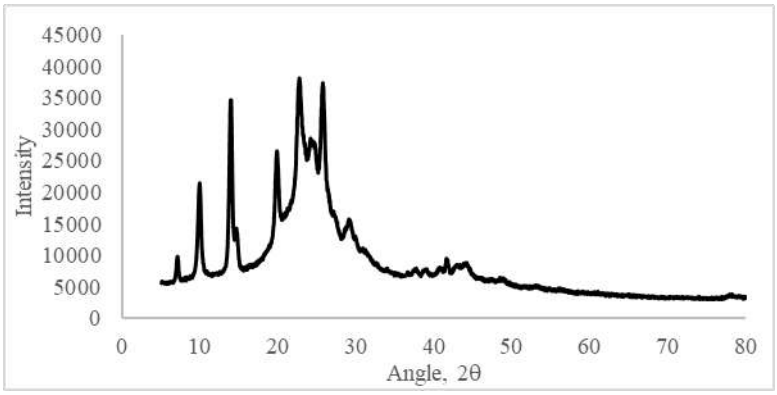

Figure 2. XRD pattern of GO/PDI

According to the FT-IR spectrum of GO/PDI catalyst presented in Figure 3, stretching vibrational bands of C=O and C=C bonds in the benzene ring of the PDI are observed at 1680 and 1650 cm^{-1}, respectively. The peaks observed at 1590 and 1340 cm^{-1} shows stretching of the perylene ring. The band appeared at 1590 cm^{-1} correspond to C=C bonds in aromatic structure. The peak around 1400 cm^{-1} associated to the amide groups in the supramolecular catalyst structure. The peaks between 1030–1240 cm^{-1} correspond to the -N-CH_2 groups [23–25].

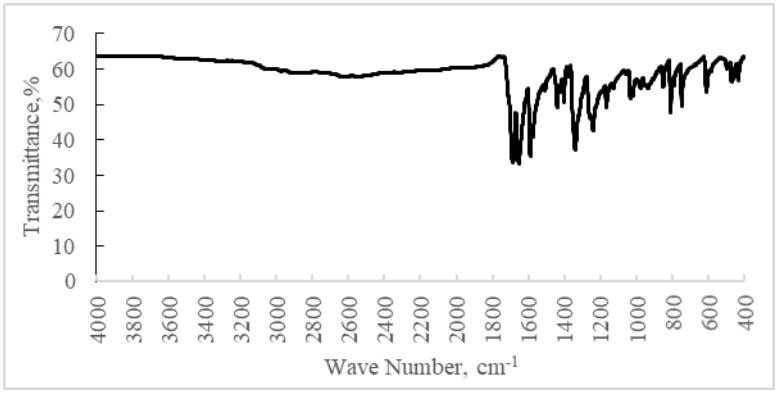

Figure 3. FT-IR spectrum of GO/PDI

Surface area measurements of GO/PDI show that BET surface area, pore volume and pore sizes of GO/PDI are 21.7 m^2/g 0.041 cm^3/g and 76.2 Å, respectively, and N_2 adsorption isotherm of GO/PDI is shown in Figure 4. The surface area of the composite supramolecular catalyst is an acceptable range based on the surface areas of the supramolecular catalysts reported in literature [11,15] According to IUPAC classification, N_2 adsorption isotherm of the composite photocatalyst correspond to Type III isotherm representing multilayer structures and weak interactions between adsorbent and adsorbate.

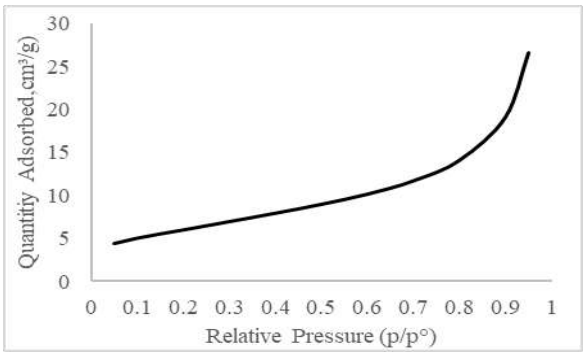

Figure 4. N_2 adsorption isotherm of GO/PDI

3.2. Interactive effects of the reaction parameters and optimization of operational conditions

The effects of the pH (3-7), catalyst loading (0,1-1 g/L) and initial concentration of amoxicillin (5-15 mg/L) were investigated in the presence of GO/PDI catalyst. The three dimensional surface plots and analyzing the interactive influences of the reaction parameters are presented in Figure 5. As can be seen in Figure 5, the antibiotic removal efficiency increased with increasing pH and catalyst loading. However, after the pH value reached to an optimum value, the removal percentage started to decrease. Similar behavior was observed for catalyst loading. The reason for the decrease in the removal efficiency above the optimum catalyst loading is that the surface area of the catalyst is reduced by agglomeration at high catalyst amounts. In addition, excess amount of catalyst can reduce the light penetrating the reaction liquid, causing a decrease in the photocatalytic oxidation efficiency. Therefore, it is concluded that the removal of amoxicillin increases when the catalyst loading is increased up to around 0.5 g/L, and decreases above this value.

When the effect of pH value and initial concentration of amoxicillin on antibiotic removal was examined, it was determined that the pH factor was less effective than the initial amoxicillin concentration. For example, when amoxicillin concentration (10 mg/L) and catalyst loading (0.1 g/L) were kept constant and the pH was increased from 3 to 7, it was observed that the removal increased from 13.1% to 24.7%. Similarly, when the catalyst loading (0.1 g/L) and pH (5) were kept constant and the amoxicillin concentration was increased from 5 mg/L to 10 mg/L, the removal was found to increase from 5.6% to 40%. This is also seen when the p-values are compared.

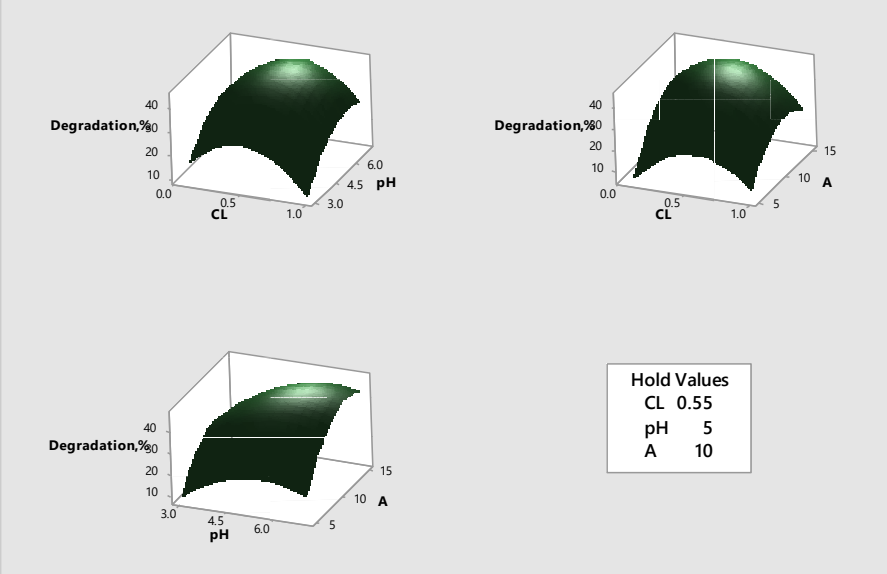

Figure 5. Interactive effects of catalyst loading, pH, and the initial amoxicillin concentration on antibiotic removal in the presence of GO/PDI catalyst

Although the increase in the pH value of the reaction liquid increases the amoxicillin removal up to a certain value, the amoxicillin removal efficiencies tend to decrease above the optimum pH value. In the literature studies, it has been stated that the highest pollutant removal is achieved around pH 5-6 for the removal of pharmaceutical compounds from aqueous solutions [26,27].

The relationships with the independent variables for amoxicillin degradation in the presence of GO/PDI were represented by the quadratic polynomial equation. The model equation resulting from Box-Behnken design studies is given below:

Degradation, % = -104.6 + 78.6 CL + 21.9 pH + 10.82 A - 69.3 CL*CL - 2.181 pH*pH - 0.473 A*A + 1.75 CL*pH - 1.47 CL*A + 0.269 pH*A

Where CL is catalyst loading and A is the initial amoxicillin concentration.

The regression coefficient, R^2 and the adjusted regression coefficient, R^2_{adj} values for the amoxicillin degradation model were found to be 90.88% and 74.47%, respectively. High regression coefficient values indicate good agreement between the obtained and calculated results.

By maximizing the amoxicillin degradation efficiency, optimum reaction conditions were determined as 0.51 g/L catalyst loading, pH 6 and 12.4 mg/L amoxicillin initial concentration. The optimum values of the reaction parameters are shown in Figure 6. As a result of the experiments performed to compare the estimated and experimental percent removal efficiencies under optimum reaction conditions, it was observed that there was a difference of less than 4% between the experimental results obtained from the model equation and the experimental results.

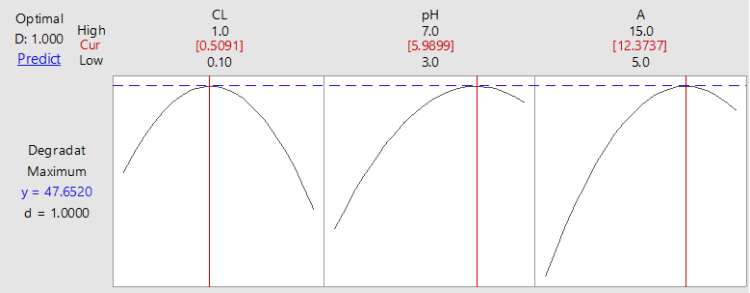

Figure 6. Optimization of the photocatalytic oxidation conditions in the presence of GO/PDI catalyst

The results of analysis of variance (ANNOVA) of the quadratic model, whose statistical significance was checked with the F-test (significance level 95% confidence), is given in Table 2.

Table 2. Analysis of variance results for the quadratic model derived for amoxicillin degradation

Source	DF	Adj SS	Adj MS	F-Value	P-Value
Model	9	2599.21	288.801	5.54	0.037
Linear	3	1184.18	394.725	7.57	0.026
CL	1	20.79	20.792	0.4	0.555
pH	1	437.55	437.547	8.39	0.034
A	1	725.84	725.838	13.92	0.014
Square	3	1332.77	444.258	8.52	0.021
CL*CL	1	728.03	728.027	13.96	0.013
pH*pH	1	280.94	280.938	5.39	0.068
A*A	1	515.68	515.677	9.89	0.026
2-Way Interaction	3	82.26	27.42	0.53	0.684
CL*pH	1	9.91	9.913	0.19	0.681
CL*A	1	43.49	43.492	0.83	0.403
pH*A	1	28.85	28.854	0.55	0.49
Error	5	260.75	52.15		
Lack-of-Fit	3	249.14	83.048	14.31	0.066
Pure Error	2	11.61	5.803		
Total	14	2859.96			

According to Table 2, the interactive interactions of the selected parameters are not as effective as the single parameters, based on the p-values obtained when the interactions between the model terms and parameters are taken into account. It is seen that all of the individual parameters are less than 0.05, except for the catalyst loading factor. In other words, it can be said that pH and amoxicillin concentration affect the total removal efficiency. It is also seen that catalyst loading and initial concentration squares of amoxicillin are effective.

4. Conclusions

The photocatalytic activity of graphene oxide/perylene diimide composite supramolecular catalyst was tested for the removal of the target antibiotic, amoxicillin from water. According to the characterization results, supramolecular catalyst structure is compatible with the SEM, XRD, FT-IR, and BET analysis results given in the literature. Supramolecular catalysts have perylene diimide rod-like characteristic structure and graphene oxide contribution has been achieved successfully. The photocatalytic oxidation conditions were optimized at 0.51 g/L catalyst loading, pH=6 and 12.4 mg/L amoxicillin initial concentration. Under these optimum conditions, 47.7% amoxicillin removal was obtained in 2 hours. The promising pharmaceutical removal efficiency obtained in the present study encourage the use of composite supramolecular catalysts in practical applications at high scales.

5. Acknowledgements

This study has been supported by the Scientific and Technological Research Council of Turkey (Project Number: 122M167).

6. References

[1] Muhmood T, Uddin A. "Fabrication of spherical-graphitic carbon nitride via hydrothermal method for enhanced photo-degradation ability towards antibiotic". Chem Phys Lett, 753, 137604, 2020.
[2] Nguyen TT, Nam SN, Son J, Oh J. "Tungsten Trioxide (WO_3)-assisted Photocatalytic Degradation of Amoxicillin by Simulated Solar Irradiation". Sci Rep, 9, 1–18, 2019.
[3] Sodhi KK, Kumar M, Singh DK. "Insight into the amoxicillin resistance, ecotoxicity, and remediation strategies". J Water Process Eng, 39, 101858, 2021.
[4] Moarefian A, Golestani HA, Bahmanpour H. "Removal of amoxicillin from wastewater by self-made Polyethersulfone membrane using". J Environ Heal Sci Eng, 12, 1–10, 2014.
[5] Meng L, Li X, Wang X, Ma K, Liu G, Zhang J. "Amoxicillin effects on functional microbial community and spread of antibiotic resistance genes in amoxicillin manufacture wastewater treatment system". J Environ Sci (China), 61, 110–7, 2017
[6] Carvalho JF d., Moraes JEF d. "Treatment of simulated industrial pharmaceutical wastewater containing amoxicillin antibiotic via advanced oxidation processes". Environ Technol, 42(26), 4145-4157, 2021.
[7] Verma M, Haritash AK. "Photocatalytic degradation of Amoxicillin in pharmaceutical wastewater: A potential tool to manage residual antibiotics". Environ Technol Innov, 20, 101072, 2020.
[8] Marcelino RBP, Leão MMD, Lago RM, Amorim CC. "Multistage ozone and biological treatment system for real wastewater containing antibiotics". J Environ Manage, 195, 110–6, 2017.
[9] Park H, Park Y, Kim W, Choi W. "Surface modification of TiO_2 photocatalyst for environmental applications". J Photochem Photobiol C Photochem Rev, 15, 1–20, 2013.
[10] Wang J, Shi W, Liu D, Zhang ZJ, Zhu Y, Wang D. "Supramolecular organic nanofibers with highly efficient and stable visible light photooxidation performance". Appl Catal B Environ, 202, 289–97, 2017.
[11] Zhang Q, Jiang L, Wang J, Zhu Y, Pu Y, Dai W. "Photocatalytic degradation of tetracycline antibiotics using three-dimensional network structure perylene diimide supramolecular organic photocatalyst under visible-light irradiation". Appl Catal B Environ, 277, 119122, 2020.
[12] Julkapli NM, Bagheri S. "Graphene supported heterogeneous catalysts: An overview". Int J Hydrogen Energy, 40, 948–79, 2015.
[13] Sheng Y, Miao H, Jing J, Yao W, Zhu Y. "Perylene diimide anchored graphene 3D structure via π-π interaction for enhanced photoelectrochemical degradation performances". Appl Catal B Environ, 272, 118897, 2020.
[14] Maridiroosi A, Abolhosseini Shahrnoy A, Mahjoub AR, Afsar P. "Functionalization of graphene oxide by using perylenediimide: An efficient visible-light driven sensitizer for photocatalytic reaction". Diam Relat Mater, 116, 108404, 2021.
[15] Yang J, Miao H, Wei Y, Li W, Zhu Y. "Π–Π Interaction between self-assembled perylene diimide and 3D graphene for excellent visible-light photocatalytic activity". Appl Catal B Environ, 240, 225–33, 2019.
[16] Ji Q, Xu Z, Xiang W, Wu Y, Cheng X, Xu C, Qi C, He H, Hu J, Yang S, Li S, Zhang L. "Enhancing the performance of pollution degradation through secondary self-assembled composite supramolecular heterojunction photocatalyst BiOCl/PDI under visible light irradiation". Chemosphere, 253, 126751, 2020.
[17] Yang J, Miao H, Li W, Li H, Zhu Y. "Designed synthesis of a p-Ag_2S/n-PDI self-assembled supramolecular heterojunction for enhanced full-spectrum photocatalytic activity". J Mater Chem A, 7, 6482–90, 2019.
[18] Zhang K, Wang J, Jiang W, Yao W, Yang H, Zhu Y. "Self-assembled perylene diimide based supramolecular heterojunction with Bi_2WO_6 for efficient visible-light-driven photocatalysis". Appl Catal B Environ, 232, 175–81, 2018.
[19] Zhong Z, Li R, Lin W, Xu X, Tian X, Li X, Chen X, Kang L. "One-dimensional nanocrystals of cobalt perylene diimide polymer with in-situ generated FeOOH for efficient photocatalytic water oxidation". Appl Catal B Environ, 260, 118135, 2020.
[20] Hu J, Ma J, Wang L, Huang H, Ma L. "Preparation, characterization and photocatalytic activity of Co-doped $LaMnO_3$/graphene composites". Powder Technol 254, 556–62, 2014.
[21] Bergamonti L, Bergonzi C, Graiff C, Lottici PP, Bettini R, Elviri L. "3D printed chitosan scaffolds: A new TiO_2 support for the photocatalytic degradation of amoxicillin in water". Water Res, 163, 114841, 2019.
[22] Shi K, Wang F, Li X, Huang W, Lu K-Q, Yu C, Yang K. "MIL-53(Fe)@perylene Diimide All-Organic Heterojunctions for the Enhanced Photocatalytic Removal of Pollutants and Selective Oxidation of Benzyl Alcohol". Catalysts, 13, 471, 2023.
[23] Zhang S, Zhang X, Wang Z, Yao L, Shi L." Preparation of 1D/1D perylene diimide nano-rod modified Bi_4O_7 rod with highly active photocatalytic performance". Opt Mater (Amst), 138, 113734, 2023.

[24] Cai T, Zeng W, Liu Y, Wang L, Dong W, Chen H, Xia X. "A promising inorganic-organic Z-scheme photocatalyst Ag_3PO_4/PDI supermolecule with enhanced photoactivity and photostability for environmental remediation". Appl Catal B Environ, 263, 118327, 2020.
[25] Xu Y, Zhu X, Yan H, Wang P, Song M, Ma C, Chen Z, Chu J, Liu X, Lu Z. "Hydrochloric acid-mediated synthesis of $ZnFe_2O_4$ small particle decorated one-dimensional Perylene Diimide S-scheme heterojunction with excellent photocatalytic ability". Chinese J Catal, 43, 1111–22, 2022.
[26] Zhang Y, Zhang Q, Dong Z, Wu L, Hong J. "Degradation of acetaminophen with ferrous/copperoxide activate persulfate: Synergism of iron and copper". Water Res, 146, 232–43, 2018.
[27] Tak S-Y, Kim M-K, Lee J-E, Lee Y-M, Zoh K-D. "Degradation mechanism of anatoxin-a in UV-C/H_2O_2 reaction". Chem Eng J, 334, 1016–22, 2018.

International Conference on Advances and Innovations in Engineering

Selection of ore for boric acid production: Why must use the colemanite ore

Fatih KAYA[1], Şeyda TAŞAR[2]

[1,2]Department of Chemical Engineering, Faculty of Engineering, Fırat University, Elazığ, TURKEY.

[1]fatihkaya@firat.edu.tr, [2]sydtasar@firat.edu.tr

[1](ORCID: 0000-0002-4063-8362), [2](ORCID: 0000-0003-3184-1542)

Abstract

In this study, an evaluation and analysis was made for boron ores used in boric acid production. Within the scope of this evaluation, the commercial value of the ores, their usage areas and the by-products that may be formed from these ores during producing boric acid were taken into consideration. Moreover, it was interpreted which ore would be appropriate for the boric acid production process. Thus, it is concluded that the use of colemanite ore as a raw material in boric acid production may be more appropriate. However, the advantage of colemanite ore is relative. Because this advantage is revealed with the use of reactants such as sulfuric acid.

Keywords: Colemanite, Borax, Ulexite, Boric acid production

1. Introduction

Boron compounds are very important materials in terms of variant application in industry. Boron only exists as ore in nature, and the most frequent ones are colemanite, ulexite, kernite and tincal ores. The formulas and names of some boron minerals are given in Table 1 [1]. At this point, the difference in terminology between ore and mineral must be interpreted. The minerals term represents pure structure, and its chemical formula is clear. However, ore term does not represent pure structure and its structure is complex. The ore can consist of many different minerals, and is called with the name of the most abundant mineral in its structure. For example, colemanite ore can contain side minerals such as clay, calcite and strontium borate minerals except for colemanite mineral [2]. While the relative abundance ratio of this side mineral in the colemanite ore was found to be 16%, the colemanite mineral's relative abundance ratio in the colemanite ore was found to be 84% in a previous study [3]. Namely, the relative abundance ratio of colemanite mineral is the highest in colemanite ore. For this reason, it is called colemanite ore.

Table **1.** Some boron minerals and chemical formula

Ore's name	Chemical formula	Structural or oxide formula
Kernite	$Na_2B_40_7.4H_2O$	$Na_2O.2B_2O_3.4H_2O$
Tincal or borax	$Na_2B_40_7.10H_2O$	$Na_2O.2B_2O_3.10H_2O$
Ulexite	$NaCaB_50_9.8H_2O$	$2CaO.Na_2O.5B_2O_3.16H_2O$
Colemanite	$Ca_2B_6O_{11}.5H_2O$	$2CaO.3B_2O_3.5H_2O$

A variety of boron compounds have been produced with processed of boron ores. Boric acid (H_3BO_3) among these compounds is one of the most important because it is widely used in the industry both as an additive chemical and as a raw material [4]. Boric acid has been used in areas such as glass, glass fiber, nuclear and organic synthesis. Another usage area is Thin Film Transistor-Liquid Crystal Display (TFT-LCD) glass production. Boric acid with a low alkali concentration is particularly important in this area [5]. Boric acid is also utilized as a raw material in the production of a variety of boron compounds like zinc borate [6].

[1]Corresponding author

2. Reactions for the Boric Acid Production

Boric acid can be produced from the reactions of boron ores such as colemanite, ulexite and borax with sulfuric acid solution. In this context, the following reactions can be taken into consideration. Reactions 1,2 and 3 numbers represent boric acid production from colemanite, borax and ulexite ores, respectively.

$$2CaO.3B_2O_3.5H_2O + 2H_2SO_4 + 6H_2O \rightarrow 6H_3BO_3 + 2(CaSO_4.2H_2O) \quad (1)$$

$$Na_2O.2B_2O_3.10H_2O + H_2SO_4 \rightarrow 4H_3BO_3 + Na_2SO_4 + 5H_2O \quad (2)$$

$$2CaO.Na_2O.5B_2O_3.16H_2O + 3H_2SO_4 \rightarrow 10H_3BO_3 + Na_2SO_4 + 2(CaSO_4.2H_2O) \quad (3)$$

Which must be chosen for industrial production? What are the advantages and disadvantages? Which type of ore is found in the country matters in this aspect. Some countries can naturally prefer to produce with the type of ore they possess. However, in countries with ore diversity, the selection criteria will also vary. We can evaluate these criteria as follows.

3. Usage Area and Commercial Value of the Ore

Borax can only be used as ground or dehydrated form for a variety of industrial applications without being converted into any chemical form. That is, can be evaluated directly. However, colemanite ore directly or alone may be useless any industrial purpose. For this reason, in countries that have both borax and colemanite ores, colemanite may be preferred for boric acid production. Otherwise, it may not be possible to evaluate the Country's colemanite reserves.

4. The Importance of By-product

The aforementioned reactions demonstrate that two different by-products can be produced during the manufacture of boric acid. These are sodium sulfate and calcium sulfate dehydrate (gypsum). Sodium sulfate is formed when borax is used, and gypsum is formed when colemanite is used. Both of the by-products are formed when ulexite is used. As can be understood from the reaction stoichiometry, a high amount of by-product is occurred in the reaction medium. But there is an important difference. The solubility value of sodium sulfate in aqueous media is very high. However, gypsum is low-solubility sulfate salt. Gypsum is consequently precipitated in the reaction medium and easily filtrated from it. This situation offers process relief for the production of boric acid. Additionally, it may also be advantageous for the production of pure boric acid. Whereas, it is not easy to separate sodium sulfate from the reaction medium.

Gypsum which is a by-product may be considered as a building material. However, It may contain many contaminants in its composition, which some may even be toxic metals like arsenic. To be utilized as a building material, it might need to be refined.

5. Reactant Selection

Strong acids, such as hydrochloric acid and nitric acid, can be employed as reactants in the manufacture of boric acid instead of sulfuric acid [7,8]. Moreover, organic acids such as acetic acid and propionic acid can be utilized for boric acid production [2,9]. The reactions of colemanite ore with hydrochloric acid and nitric acid are shown in reactions 4 and 5, respectively. As a result of these reactions, calcium nitrate and calcium chloride are formed as by-products. These by-products are highly soluble salts like sodium sulfate. Namely, it is difficult to separate them from the reaction medium. Consequently, it may be challenging to purify the final product, boric acid.

$$2CaO.3B_2O_3.5H_2O + 4HCl + 2H_2O \rightarrow 6H_3BO_3 + 2CaCl_2 \quad (4)$$

$$2CaO.3B_2O_3.5H_2O + 4HNO_3 + 2H_2O \rightarrow 6H_3BO_3 + 2Ca(NO_3)_2 \quad (5)$$

Boron ores can be considered as hydrated oxides of alkali metals such as especially sodium and calcium [10]. The aforementioned all reactions demonstrate that a salt is absolutely formed as by-product from the reaction of these ores with strong acids. It's crucial to note the salt's limited solubility, which arises from the interaction of the acid's anion root and metal root in the ore. Because low-solubility salts or by-products precipitate in the reaction medium and thus the process is relieved in terms of impurities. One of the best examples of this convenience is the reaction that occurs when colemanite ore with sulfuric acid are combined.

6. Conclusions

The reaction between colemanite ore with sulfuric acid is considered a more reasonable process for boric acid production. This process has been also used on an industrial scale in Turkey.

The use of sulfuric acid as a reactant is advantageous for several reasons, including its low cost, high reactivity, and accessibility. Its tendency to produce calcium sulfate is another significant advantage. When (1) number reaction is used nitric acid or hydrochloric acid instead of sulfuric acid, calcium nitrate and calcium chloride occurs as by-product, respectively. Calcium nitrate and calcium chloride are high soluble salts like sodium sulfate obtained from borax or ulexite processes. That is, the advantage of this method is lost if another strong acid other than sulfuric acid is used to processed colemanite ore. As a result, the formation of low-solubility by-products with references to the boron ore and acid used is important for process relieving. The best example of this is the reaction between colemanite ore with sulfuric acid.

7. References

[1] **https://www.etimine.com/boron-minerals/**, 08.28.2023

[2] Bulutcu A.N., Ertekin C.O., Kuskay Celikoyan M.B. “Impurity control in the production of boric acid from colemanite in the presence of propionic acid”. Chemical Engineering and Processing: Process Intensification, 47; 2270–2274, 2008.

[3] Kaya F. Borik Asit Üretim Prosesinde Safsızlık Kontrolü ve Ürün Veriminin Artırılması. Doktora Tezi, Fırat Üniversitesi, Elazığ, Türkiye, 2021.

[4] Kaya F and Özer A. “Selective sulfate sorption from boric acid factory process liquor: Chitosan-bentonite biocomposite film synthesis as sorbent”. Minerals Engineering, 187, 107777, 2022.

[5] Schubert D.M., Steffee E. “A Borate Supplier ’s View of the Glass Industry, in: Proc. Borate Glas. Crystals, Melts”. 7th Int. Conf., Nova Scotia-CANADA, 2011: pp. 1–8, 2011.

[6] Ata O.N., Şayan E. and Engin B. “Optimization and modeling of zinc borate ($2ZnO.3B_2O_3.3,5H_2O$) production with the reaction of boric acid and zinc oxide”. Journal of Industrial and Engineering Chemistry, 17, 493-497, 2011.

[7] Sis H., Bentli İ., Demirkıran N. and Ekmekyapar A. “Dissolution kinetics of colemanite in HCl solutions by measuring particle size distributions”. Separation Science and Technology, 53(1), 198-205, 2018.

[8] Yeşilyurt M. “Determination of the optimum conditions for the boric acid extraction from colemanite ore in HNO_3 solutions”. Chemical Engineering and Processing 43, 1189-1194, 2004.

[9] Özmetin C., Kocakerim M., Yapıcı S. and Yartaşı A. “A Semiempirical Kinetic Model for Dissolution of Colemanite in Aqueous CH_3COOH Solutions”. Industrial Engineering Chemistry Research, 35, 2355-2359, 1996.

[10] Powoe, S.P.B., Kromah V., Jafari M. and Chelgani S.C. “A Review on the Beneficiation Methods of Borate Minerals”. Minerals, 11, 318, 2021.

International Conference on Advances and Innovations in Engineering

Numerical Simulation of Ballistic Impact on Layered Kevlar Armor

İsmail Furkan SARUHAN[1] , Recep GÜNEŞ [2]

[1] CES Advanced Composite and Defense Technologies, R&D Department, Ankara, Turkey.
[2]Mechanical Engineering, Engineering Faculty, Erciyes University, Kayseri, Turkey.
[1]furkan.saruhan@ces.com.tr, [2]recepg@erciyes.edu.tr

[1](ORCID: 0000-0002-2297-3204), [2](ORCID: 0000-0001-8902-0339)

Abstract

In this study, a ballistic performance study was carried out on composite armor, which is one of the current armor technologies. Kevlar armor, which are still widely used today, have high strength and low weight. The ballistic performance of Kevlar laminae modelled in ANSYS/ACP is investigated according to STANAG V_{50}. Composite damage models and contact relationships were defined in ANSYS/LS Dyna and ANSYS/LS Dyna was used as solver. A new and much more convergent numerical model has been developed based on experimental studies taken from the literature. Kevlar ballistic limit was determined on the developed model and converged with the experimental results.

Keywords: Numerical Simulation, FE method, Ballistic Limit, Kevlar Laminates, Composite Armors, ANSYS/LS Dyna

1. Introduction

In today's technologies, the use of composite materials is increasing in different engineering fields. These areas can be listed as defense, space and aviation, automobile, construction sectors etc. Especially polymer composites will find a place in future technologies with their light, strong, rigid behavior, and high energy absorption. Ballistic limit studies used as delamination and perforation resistance as ballistic mechanisms are generally discussed. It is possible to divide the fabrics used in the field of ballistics into two as knitted and woven fabrics. Although knitted fabrics show superior properties compared to woven fabrics, woven fabrics are generally preferred in military fields due to their complex production methods and costs. The most commonly used weaving types are plain weave and basket weave. Basket weave provides 10% more energy absorption than plain weave due to its weaving characteristics. The most important factors in the replacement of materials such as metal and ceramics by composites used in the field of ballistics are their light weight, higher performance compared to their weight and not limiting the mobility of the users. The most preferred fabric types are aramid and para-aramid fabrics, high molecular weight polyethylene (HMWPE), PBO and PPID fabrics [1,2].

"Aramid", derived from "aromatic polyamide", is chemically defined as "poly para phenylene terepitelamide". It is therefore also called "para-aramid". Depending on the production process, meta-aramid fabrics are also available. The most commonly used aramid types are Nomex (Dupont), Conex (Teijin) and Conex HT (Teijin). The types of aramid fabrics used in ballistic applications are para-aramid fibers. Especially Kevlar is used extensively in the production of advanced composites in the production of personal clothing and boots in the field of ballistics and is known for its high mechanical properties [3].

Ballistic limit studies are usually performed to determine ballistic performance and energy absorption. There are different approaches in the literature for the ballistic limit concept and it is necessary to define these approaches. Ballistic limit velocity V_{BL} is defined as the velocity at which the projectile cannot completely penetrate the target and velocities below this velocity. The main difference between these approaches is the different criteria for defining the perforation event. The actual assessment of the ballistic limit velocity is based on statistical tests. The ballistic

[1]Corresponding author

limit velocity is denoted by V_{50}, and this velocity is the velocity at which the projectile has the capacity to perforate 50 per cent of the target when it hits the target in a perpendicular position. As mentioned, statistical approaches are used to determine the V_{50} velocity. Basically, the ballistic limit velocity is determined by averaging the three lowest velocities that cause full penetration and the three highest velocities that cause partial penetration. The smaller the difference between the lowest velocity that penetrates the target and the highest velocity that does not penetrate the target, the higher the accuracy of the ballistic limit estimate. In this study, .22 cal Fragment Simulating Projectile (FSP) was used as a threat according to STANAG V_{50} protocol [4,5].

2. Material and Methodology

NATO STANAG 2920 AEP Ed.3 standard focuses on the VProof (Ballistic Limit) and V_{50} Ballistic tests and the national authorities can define the minimum Vproof according to the technical specifications of armor or ballistic protection materials. The main factor of defining the VProof and V50 velocity is the risk analysis of national authority. 2920 AEP Ed.3 standard gives an opportunity to have a protection against different projectiles and different Vproof and V50 threat levels based on the risk analysis of the national authority on the armor.

In this study, the threat and the plate were modelled in Solidworks. Then the composite modelling was done in ANSYS/ACP and LS-DYNA solver was used. Delivery from FSP (.22 cal) 4340 steel for STANAG V50 standard. MAT_RIGID material model is defined as a material model. The FSP modelled as a solid body is designed with a weight of 1.1 g. MAT_RIGID; A rigid domain, or a rigid body, is an idealization of a body in which the deformation is neglected. In other words, the distance between any two given points of a rigid body remains constant in time regardless of any external forces acting on it. The rigid FSP model used in the study is as shown in Figure 1.

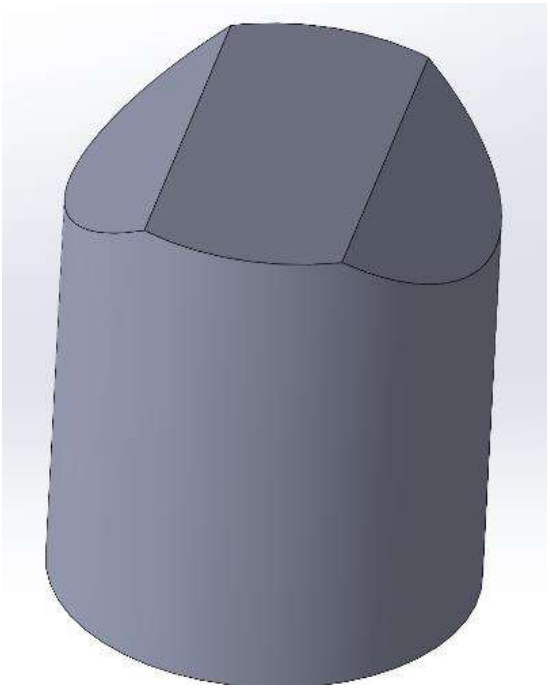

Figure 1: FSP solid model (CAD)

When modelling a part with the Finite Element method, the model is divided into basic elements consisting of small parts. This is called the mesh process. Each element has nodes at the corners. Calculations are performed on these nodes. Therefore, the physical environment is first divided into elements and the corner points of the elements become the point space representing the physical environment. The results obtained are the values on these points.

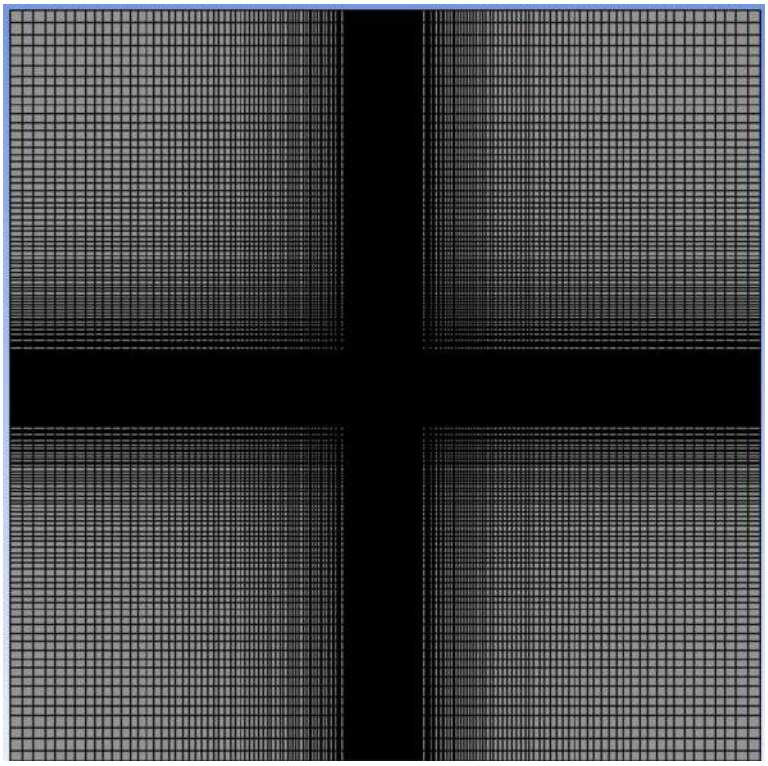

Figure 2. Mesh optimization of plates

The ballistic plate modelled as a shell in ANSYS/ACP was designed to have 20 laminates and a total thickness of 9.1 mm. The analyses continued over the shell data. The material model was selected as MAT_ENHANCED_COMPOSITE_DAMAGE and the contact relationship between the threat and Kevlar armor was defined as ERODING_SURFACE_TO_SURFACE. In ballistics tests, Hourglass type 5, i.e., "Flagan-Belytschko stiffness from with exact volume" was selected. MAT_ENHANCED COMPOSİTE DAMAGE is enhanced version of the composite model material type 22. This can use for arbitrary orthotropic materials (e.g., unidirectional layers in composite shell structures can be defined). The solution of the mesh-optimized plates was made according to the mesh in Figure 2 [6].

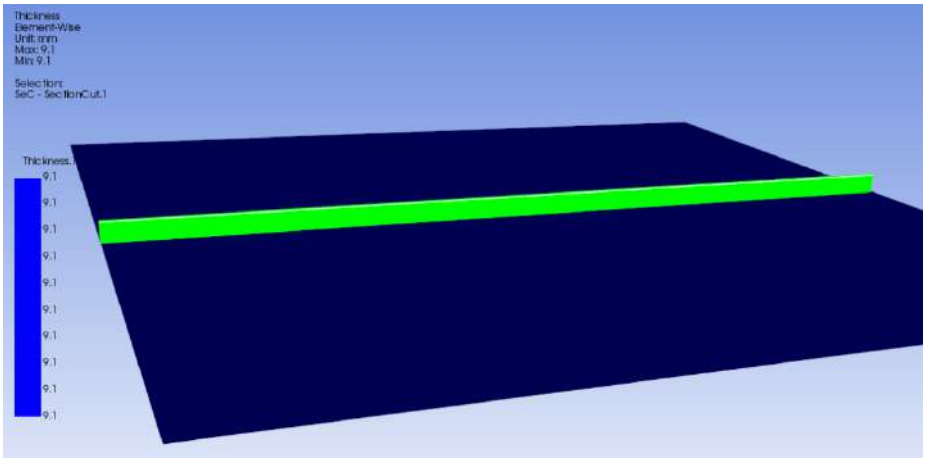

Figure 3. Composite modelling of plates

Table 1: Kevlar mechanical properties [6]

Density	1230 kg/m^3
E_1	18.5 GPa
E_2	18.5 GPa
E_3	6 GPa
G_{12}	0.77 GPa
G_{23}	2.5 GPa
G_{13}	2.5 GPa
v_{12}	0.25
v_{23}	0.33
v_{13}	0.33

Kevlar mechanical properties are as given in Table 1. The composite lay-up of Kevlar, whose mechanical properties are defined, was made as shown in Figure 3. After Kevlar lay-up, composite damage models were defined, and boundary conditions were defined. Experimental data were followed for ballistic limit calculation.
For the ballistic limit study, many ballistic impacts were performed at different speeds. A statistical study was performed, and the ballistic limit range was determined.

3. Results

.22 calibre FSPs were fired at a 400x400x9.1 mm Kevlar plate modelled in ANSYS/ACP. ANSYS/LS Dyna was used as the solver and the experimental ballistic performance of Kevlar laminates was converged with the statistical study.

Table 2. Experimental ballistic limit [7]

Ballistic Impact	Velocity (m/s)	CP	PP
1	**696.3 m/s**	**x**	
2	**691.5 m/s**	**x**	
3	**658.5 m/s**		**x**
4	**665.6 m/s**		**x**
5	**692.2 m/s**		**x**
6	**703.7 m/s**	**x**	
7	**670.2 m/s**		**x**
Experimental V50 in the literature	**686.6 m/s**		

Here, CP stands for Full Penetration and PP stands for Partial Penetration. The limit where the armour completely absorbs the energy of the threat, and the remaining velocity is very low is called the ballistic limit. Table 2 shows the experimental ballistic limit study. The ballistic impact was performed at different velocities. Full penetration (CP)

and partial penetration (PP) cases were observed. An average velocity value was taken from the experimental study and as a result, the ballistic limit was estimated. This estimate is 686.6 m/s [7].

Table 3. Current work, ballistic limit simulations

Ballistic Impact	Velocity (m/s)	CP	PP
1	**680 m/s**		**x**
2	**690 m/s**		**x**
3	**700 m/s**		**x**
4	**710 m/s**		**x**
5	**720 m/s**	**x**	
6	**730 m/s**	**x**	
7	**740 m/s**	**x**	
Result	**~720 m/s**	**During Work Ballistic Limit (± 10 m/s)**	

Many shots were fired at the model prepared for numerical simulations. Velocities were increased at 10 m/s intervals. Ballistic limit calculation was performed and highly converged with experimental ballistic limit studies. In the numerical study, the ballistic limit was found to be ~720 ± 10 m/s.
In the ballistic impact at 720 m/s, the residual velocity was read very low. In the ballistic impact performed 10 m/s below this speed, the armour could not be penetrated and in the ballistic impact performed above 10 m/s, the armor was completely penetrated. The numerical study converged 95.361% to the experimental study. The error rate was found to be 4.638%.

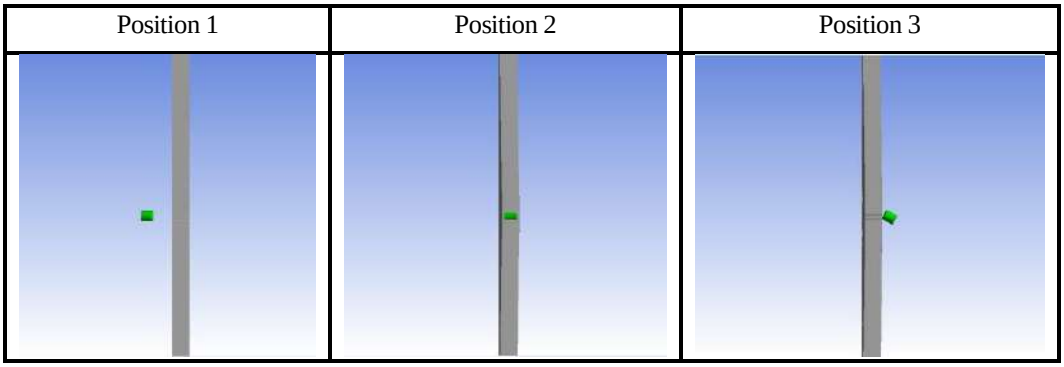

Figure 4. Ballistic limit steps

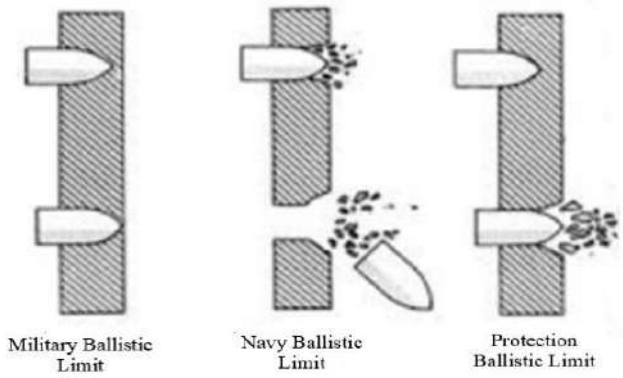

Figure 5. Ballistic limit steps according to the literature [5]

Ballistic limit modes are shown in Figure 5. The behavior of FSP and Kevlar laminates for the impact at the ballistic limit (720 m/s) speed found after the numerical simulations are given in Figure 4. Position 1 shows the initial movement of the FSP, Position 2 shows its progression in the armor and Position 3 shows the fall of the FSP because of penetration.

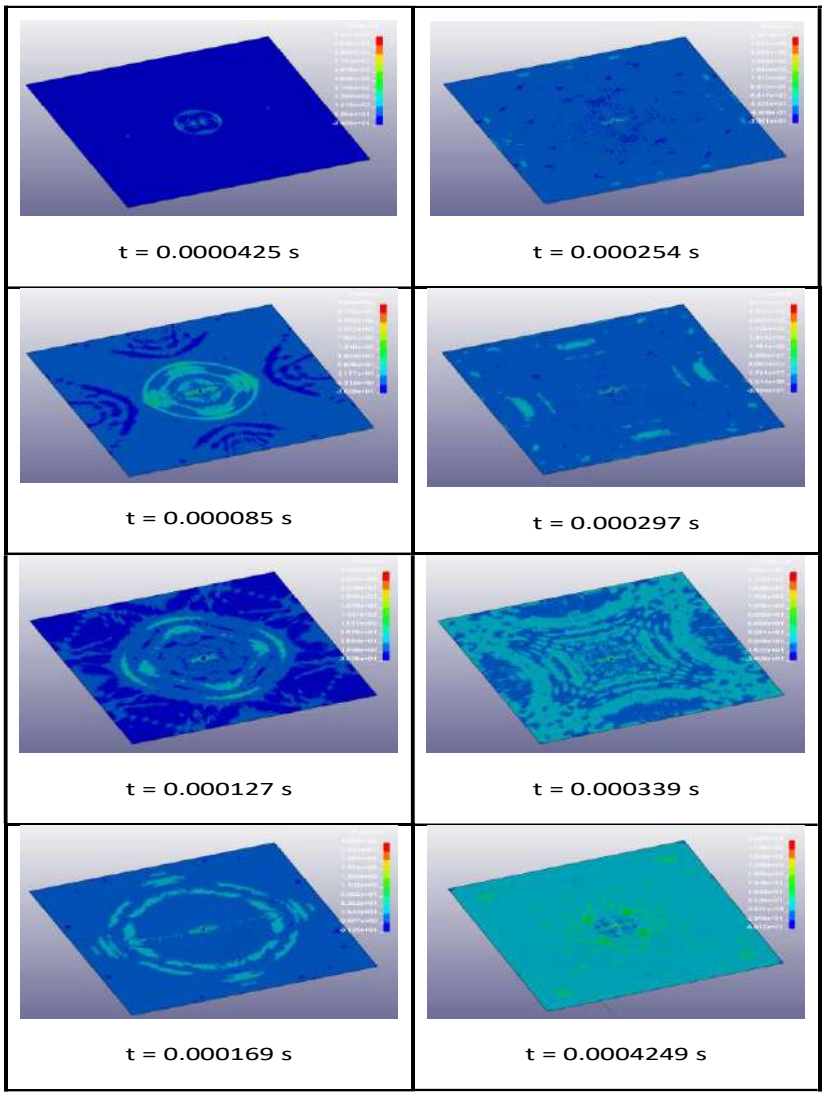

Figure 6. Pressure distribution caused by time-dependent ballistic impact

The ballistic impact creates pressure on the plates. Figure 6 shows the pressure distributions on Kevlar laminates in time steps.

4. Conclusion

With the developments in the defense industry, the need for armor on land, air and sea platforms has changed and increased. Composite materials are becoming increasingly widespread in the defense industry due to their high strength and low weight. They are used structurally on platforms and as personal ballistic protection. Kevlar composite armor provide high protection against shrapnel, explosions and shock effects, small arms, projectiles. Kevlar armor restrict the mobility of the vehicle or personnel less than their equivalents and provide high protection effect. This study analyses the ballistic performance of Kevlar by creating a working numerical model of Kevlar armor and presents a working model. The study aims to provide guidance for designers by creating a Kevlar armor model.

In the study, experimental ballistic limit studies in the literature are taken as reference. A numerical model was created for ballistic studies performed on 400x400x9.1 mm thick Kevlar plates. MAT_ENHANCED_COMPOSITE_DAMAGE damage model was used as the material model for composite plates. The 1.1 g FSP material model taken from STANAG standards was selected as MAT_RIGID.

Ballistic limit work was determined statistically with sequentially increasing velocities. It has a high degree of convergence to experimental studies. The converged speed is 720 m/s. The error rate between the model developed within the scope of this study and the experimental studies remained at a small rate of 4 %. The behavior of the composite armor under impact has been demonstrated and the progression of the FSP within the armor has been observed. Pressure values and distributions occurring in composite plates are also presented within the scope of this study. A solved and working Kevlar armor model has been brought to the literature. It is expected that the resolved composite armor behavior will guide future designs.

5. Acknowledgment

This study was supported by the Scientific Research Projects Unit of Erciyes University (ERU/BAP) under the research
Grant No. FBAÜ-2023-12517

5. References

[1] Li, Y. Fan, H. Gao, X. 2022. ‘‘Ballistic Helmets: Recent Advances in Materials, Protection Mechanisms, Performance, and Head Injury Mitigation’’, Composites Part B, DOI: https://doi.org/10.1016/j.compositesb.2022.109890

[2] A. Kumar Bandaru, ‘Ballistic İmpact Behaviour of Thermoplastic Kevlar Composites: Parametric Studies’ Journal of ScienceDirect, İndia, 2016

[3] Sözen E. ‘‘Balistik Panel ve Koruyucu Zırh Üretiminde Kullanılan Lif ve Kompozit Malzemeler’’ Bartın Üniversitesi, Orman Fakültesi, Orman Endüstri Mühendisliği Bölümü, Bartın

[4] STANAG V50 STANDART, ‘‘http://www.englands1.com/site/wp-content/uploads/8_stanag_2920.pdf’’, Temmuz 23

[5] Hakan, M. 2017. ‘‘Fonksiyonel Kademelendirilmiş Plakaların Farklı Mermi Çarpma Açılarında Balistik Limitlerinin Araştırılması’’, Erciyes Üniversitesi Fen Bilimleri Enstitüsü Makine Mühendisliği Anabilim Dalı, Yüksek Lisans Tezi

[6] Palta, E. Hongbing, F. Weggel, D.C. 2018. ‘‘Finite element analysis of the Advanced Combat Helmet under various ballistic impacts’’ İnternational Journal of Impact Engineering, 112, 125-143.

[7] M.R. Millan, ‘Development of Numerical Model for Ballistic Resistance Evaluation of Combat Helmet and Experimental Validation’, Materials and Design, 2016

International Conference on Advances and Innovations in Engineering

Investigation of Convective Heat Transfer Coefficient in Air Solar Collector Assisted Greenhouse Dryer by Experimental and Artificial Intelligence Methods

Fatma PAPATYA[1] , Fatih HOŞOĞLU [2], Muhammet Fatih İMİŞ [3], Ebru AKPINAR [4]

[1234]Mechanical Engineering Department, Engineering Faculty, Fırat University, Elazig, Türkiye.

[1]papatyafatma588@gmail.com, [2]hosoglufatih123@gmail.com, [3]m.fatih.imis@gmail.com, [4]ebru.akpinar@firat.edu.tr

[1](ORCID: 0009-0005-2277-6170), [2](ORCID: 0009-0008-4807-2210),[3](ORCID: 0009-0007-8686-8466) [4](ORCID: 0000-0003-0666-9189)

Abstract

Drying is the removal of water and other liquids from gases, liquids and solids. Solar drying of agricultural products is known as one of the oldest food preservation methods. In solar drying, food quality decreases significantly due to environmental factors. For this reason, drying with temporary artificial dryers shortens the drying time and provides a better quality and cleaner shelf-stable product. In this project, a type of greenhouse dryer supported by solar air collector (SAC) was designed to improve the quality and performance of food drying. In the designed greenhouse dryer, 15mm thick apple slices were dried. Heat and mass transfer parameters were analyzed during the drying process. For the experimentally calculated convective heat transfer coefficient value, modeling was performed with machine learning algorithms. Support vector machine (SVM) and decision tree (DT) algorithms were used as machine learning algorithms. The model with the least error value was determined as SVM with 0.0003 RMSE. Thanks to the study, the contributions of SAC to greenhouse dryer performance were revealed and the heat transfer coefficient values during the drying process were modeled with artificial intelligence methods. In the continuation of this study, more data can be obtained by drying different types and volumes of food products, and with these data sets, artificial intelligence models with lower error values can be obtained.

Keywords: Convective heat transfer coefficient, decision tree, greenhouse dryer, machine learning, solar energy

1. Introduction

In order for the food to be stored and consumed for a long time, it must be divided into pieces and then consumed in accordance with the appropriate storage conditions. At the beginning of the change in long-term storage conditions of foods is the drying process. Drying is a high-energy process, and drying units need efficient and alternative energy sources. Today, many methods are used for the drying process. One of these fragments is the drying method with solar energy. The most important feature of solar energy is that it is an energy source.

Solar energy is a clean energy source that does not run out of reserves and does not pollute the environment, and is widely used for drying without being distributed around the world due to its ability to be easily converted into heat energy. Solar dryers can be evaluated in two types as greenhouse type and collector. A greenhouse dryer is also available as a solar collector. In addition to growing the product in greenhouses where the product is grown, the product can also be dried by the drying process. Glass and nylon are generally used in greenhouse type dryers and these replacements are hemispherical, domed, tunnel, etc. may vary in construction. In addition to finding solutions to energy consumption, the designed production leads to a more hygienic drying formation without covering from perishable areas to be dried, without being exposed to negative effects from the healthy, environmental environment. The low initial investment cost of solar energy systems, the very efficient solar radiation in the provinces throughout Turkey, and the fact that solar energy is an environmentally friendly and free energy source is the unity of this system.

[1]Corresponding author

1.1. Purpose and Scope

In this design, it is aimed to design a laboratory scale prototype drying system for drying foods such as fruits and vegetables by means of solar energy and to improve their strength and storage conditions, and to manufacture them in the next process. It was tested whether the system is suitable for the intended purpose with the experiments carried out after the manufacturing phase. The aim of this project is to manufacture an air solar collector supported greenhouse dryer with the most suitable design that can be used for drying agricultural products with the help of various methods. For this purpose, the most suitable air solar collector greenhouse dryer designs for the selected product were carried out with computational fluid dynamics (CFD) analyses. Useful drying models were obtained by using artificial intelligence methods with the data obtained after the experiments in the greenhouse dryer manufactured after the design.

2. General Information

2.1. Solar Energy

Solar energy is a clean energy source that does not run out of reserves and does not pollute the environment, and it is widely used in drying agricultural products around the world due to its ability to be easily converted into heat energy. Solar energy is gaining more and more importance today, when fossil fuels such as oil and natural are on the verge of depletion. On the other hand, the damage caused to the environment during the transportation and processing of these fuels causes serious debates in the world public opinion and is thought to be the main cause of global warming.

2.2. Solar Dryers

This system performs the drying process only with the heat and light energy it receives from the sun and does not need any other energy, it produces the necessary electricity and heat energy itself through solar collectors. It dries a wide variety of Fruits and Vegetables, plant foods, cereal products in a shorter time and more hygienically.
Drying devices can be classified in various ways. A classification scheme based on the heat transfer of drying devices is shown in Figure 2.1 [1, 2, 3,]. This scheme divides dryers into subclasses operated directly or indirectly, with continuous or intermittent loading. Solar dryers can be generally classified as direct, indirect and hybrid (direct and indirect) solar dryers.

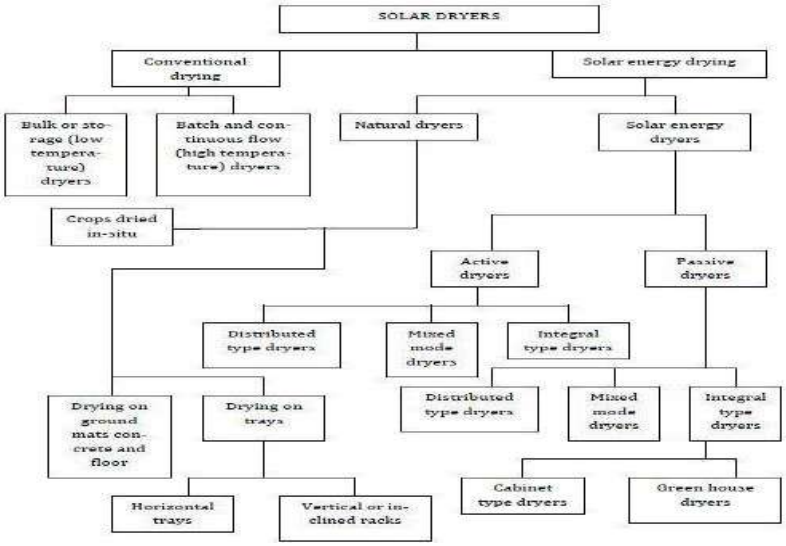

Figure 2.1. Classification of Dryers and Drying Modes

2.3. Greenhouse Type Dryer

A greenhouse dryer can also be thought of as a solar collector. In addition to growing the product in greenhouses where the product is grown, the product can also be dried by the drying process. Glass and nylon are generally used in greenhouse type dryers and these dryers are hemispherical, domed, tunnel, etc. may be in the form of structures. The heat energy required for drying is met by solar radiation. A part of the energy that comes with radiation in the system is stored in the absorber plate exposed to the sun inside the greenhouse and spreads into the greenhouse by radiation and convection. In other words, the greenhouse is used as an air solar collector.

2.4. Solar Collectors

Solar heat collectors are a special type of heat exchanger that converts solar radiation energy into internal energy. Solar collectors absorb incoming solar radiation, convert it into heat and transfer this heat to the fluid (usually air, water or oil).

There are basically 2 types of solar collectors: non-focusable or fixed and focusable solar collectors. Unfocusable solar collectors have flat surfaces and do not focus the sunlight. Focusable solar collectors usually have a concave surface and the center of solar heat is exposed to heat radiation in a very small area due to increased radiation exchange. They only benefit from direct radiation, they can provide high temperature. They have to see the sun in order to work, so focused collectors are used more efficiently in sun-rich regions [4].

2.5. Solar Air Collectors

In this type of heaters, the fluid to which the absorbed solar energy is transferred is air. In areas where hot air is required, instead of transferring the heat first to a fluid and then to the air, they are the mechanisms that transfer the heat directly to the air. It is mostly used for air conditioning of buildings, absorption cooling method, drying of agricultural and industrial products and heating of greenhouses. Plane collectors are commonly used to heat the air with solar energy. Plane collectors; They have advantages such as being easy to make, long-lasting, light in weight, and economical since they do not have a sun tracking mechanism.

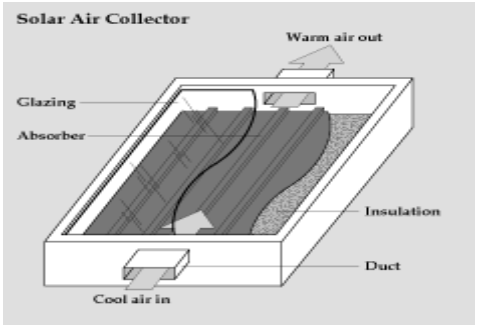

Figure 2.2. Solar Air Collectors

In recent years, many different applications have been made to increase the air temperature and efficiency achieved in plane collectors. The most commonly used among them are; These include placing filling material in the air flow channel, adding fins under the absorber plate, increasing the number of air passages, giving different shapes to the absorber, changing the dimensions of the air flow channel and using a selective surface absorber [5].

2.6. Computational Intelligence Methods

Machine learning is the most used computational intelligence method. Machine learning is the general name for computer algorithms that can learn structurally and make meaningful predictions on data. These algorithms basically work by creating models from sample data. Nowadays, it is not possible to manually process and analyze large

amounts of data. For this reason, it is aimed to reach a solution by training the data obtained from the environment of the problem with machine learning algorithms to solve a given problem [6].
Machine Learning algorithms:
1- Supervised Learning
2- Unsupervised Learning
are divided into 2 groups.

2.6.1 What are Artificial Neural Networks?

An artificial neuron can be defined as an algorithm or physical tool that generates a mathematical model inspired by the basic behavior of a biological neuron.

Based on the definition of a biological nerve cell, it can be said that an artificial nerve cell collects the signals it receives from other nerve cells and when the total signal accumulation exceeds a certain threshold, this artificial nerve cell transmits its own signal to another nerve cell. Just as biological neural networks have nerve cells, artificial neural networks also have artificial nerve cells. Artificial nerve cells are also called process elements in engineering science. As shown in Figure 2.3, each process element has 5 basic elements. These; inputs, weights, addition function, activation function and outputs.

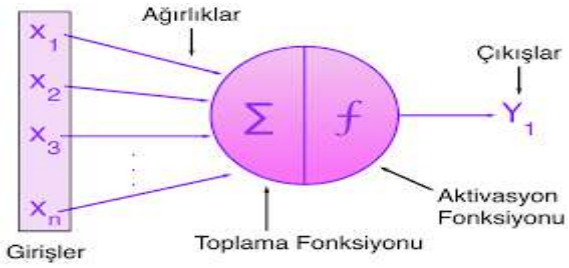

Figure 2.3. Structure of Artificial Nerve Cell

Artificial neural networks are data-based systems created by connecting artificial nerve cells in layers and aim to use the abilities of the human brain such as learning and making rapid decisions under different conditions in solving complex problems with the help of simplified models.

2.6.2. Support Vector Machine

Support Vector Machine (SVM) is an excellent Kernel-based tool for classification and regression. This learning strategy was developed by Vapnik and is a very powerful method based on the principles of machine learning algorithms [7]. A comprehensive study on the use of support vector machines in solving regression problems was done by Smola and Schölkopf.

2.6.3. Regression Analysis and Decision Tree

Linear regression analysis is to create a model that predicts the variable to be determined, based on variable(s) that can be detected more easily or earlier than the variable to be determined [8]. If a known normally distributed numerical variable is applied to predict another unknown, normally distributed numerical variable that has a relationship between them, simple linear regression is used, and when modeling is done to predict a variable by using more than one variable, it is called "multiple linear regression" is defined as.

3. Greenhouse Design and Analysis

Before starting the analyses, several models were determined for geometry selection. These models were a type of greenhouse with a roof model of 400 mm high, 1500 mm long and 1000 mm wide, as indicated in Figure 3.1. In addition, the roof length was determined as 200 mm.

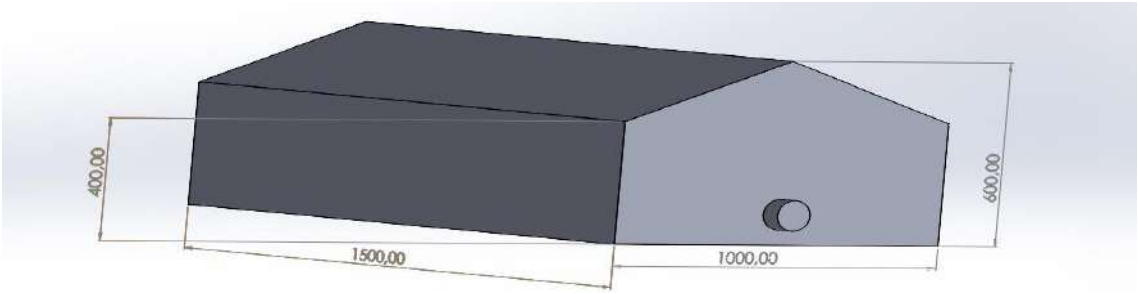

Figure 3.1 Roof Model Greenhouse in 1500x1000x400mm Dimensions

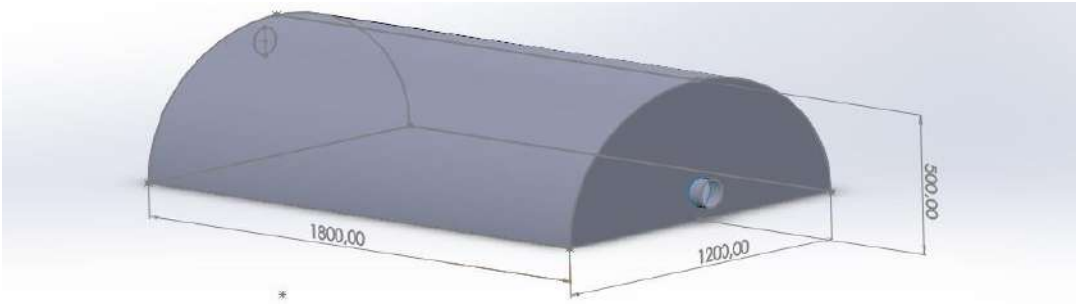

Figure 3.2 Quonset Model Greenhouse Dimension 1800mm x 1200mm x 500mm

As a result of the researches, we preferred the quonset model greenhouse among these two models because the temperature distribution is more uniform and continuous in this model.

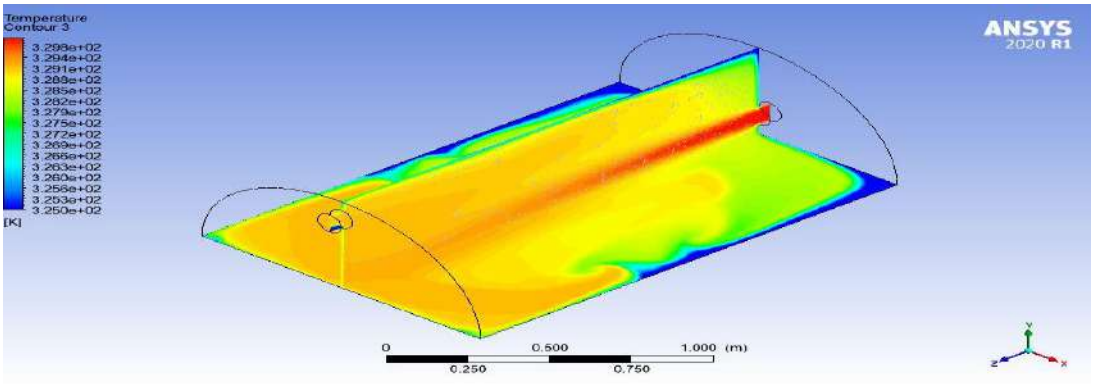

Figure 3.3 Greenhouse Temperature Analysis with Quonset Model in 1800mm×1200mm×500mm Dimensions.

4. Experiment Result Charts

In the experimental setup we designed; Sliced apple samples, which we prepared by transmitting the hot air coming from our panel to our greenhouse, were dried during the day on May 4, 2023. In our greenhouse, the wet weight is 200 gr. Drying experiments were carried out by placing sliced apple samples on the tray. During the experiment, data were taken in 15-minute periods by using our measuring devices and meteorology data.

4.1. Dry Basis Moisture Content

The final weight of the product is 58 gr according to literature data. and the equilibrium humidity was taken as 11%. According to Figure 4.1, the amount of dry base decreased over time. While a rapid decrease is observed at the beginning, we see that the change in the amount of dry base slows down as time progresses. The variation of the dry base moisture content (MCk) of the dried apple in the experimental setup with time is given in Figure 4.1.

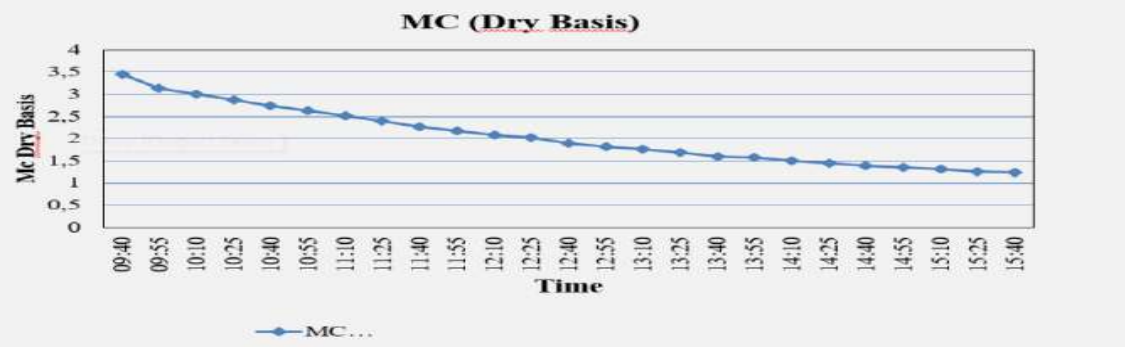

Figure 4.1. Dry Basis Chart

4.2. Wet Basis Moisture Content

According to Figure 4.2, the age base amount decreased over time. While a rapid decrease is observed at the beginning, we see that the change in the age base amount slows down as time progresses. The variation of the wet base moisture content (MCy) of the dried apple in the experimental setup with time is given in Figure 4.2.

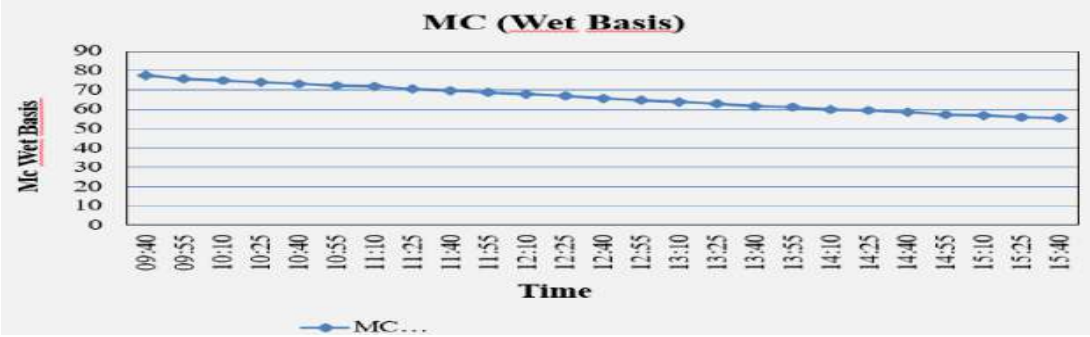

Figure 4.2. Wet Basis Chart

4.3. Moisture Rate (MR)

According to Figure 4.3, dimensionless moisture content decreased over time. While a rapid decrease is observed at the beginning, we see that the change in dimensionless humidity rate slows down as time progresses. The variation of dimensionless moisture content (MR) of the dried apple in the experimental setup with time is given in Figure 4.3.

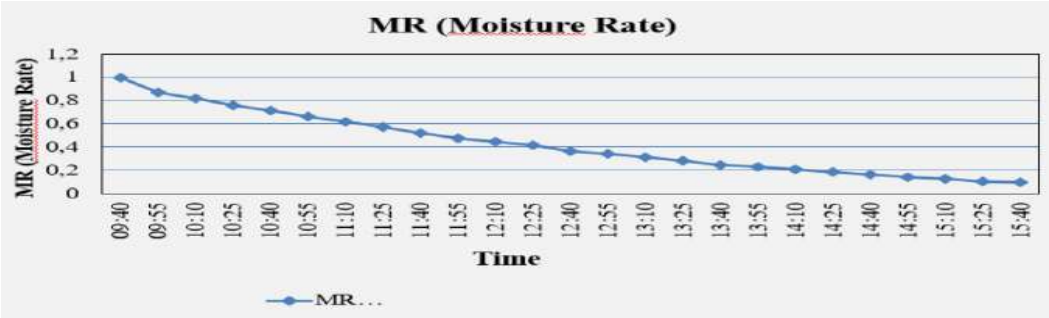

Figure 4.3. Moisture Rate Chart

4.4. Energy Efficiencies

Collector and greenhouse efficiencies are compared in Figure 4.4. Collector efficiency was over 30%. Greenhouse efficiency was between 10% and 20%. It is observed that both efficiency values increase after 10:00. As seen in Figure 5.4, our collector efficiency was higher than the greenhouse efficiency. The change in the energy efficiency of the experimental setup over time is given in Figure 4.4.

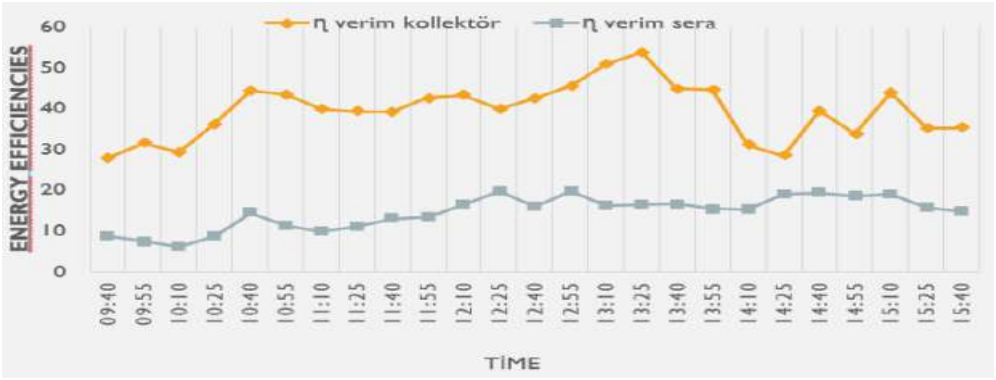

Figure 4.4. Energy Efficiencies Chart

4.5. Heat Transfer Coefficient

Since the convective heat transfer coefficient varies with the temperature difference between the air and the product, it is an important parameter in determining the drying rate and dryer design. Other factors affecting the heat transfer coefficient apart from the temperature difference factor; moisture content, radiation values, different weather conditions. Figure 4.5 shows the change in convective heat transfer coefficient values of apples dried over time, calculated with the data obtained at 15-minute intervals, over time. As can be seen from Figure 4.5, the heat transfer coefficient fluctuated between 10.29$\boldsymbol{W/m^2}$°C - 10.302$\boldsymbol{W/m^2}$°C . These changes may be due to different environmental conditions.

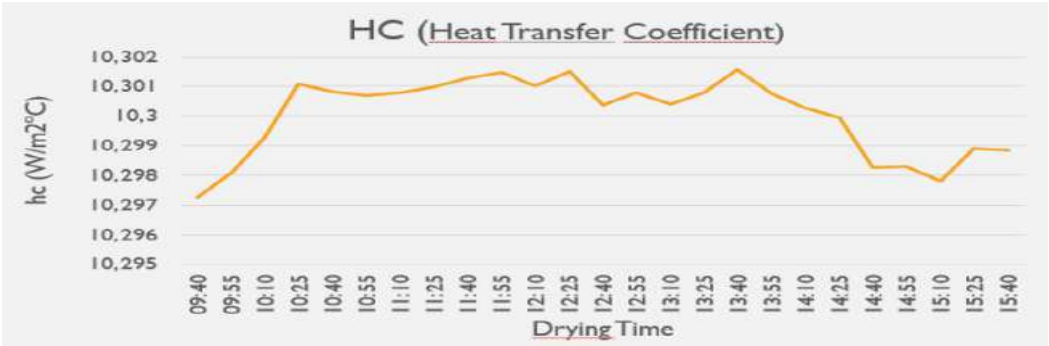

Figure 4.5. Heat Transfer Coefficient Chart

4.6. Artificial Intelligents Methods (Machine Learning)

For the analysis of the experimental HC data, the Regulation learner in the Machine Learning App on the MATLAB platform was used. This app is a comprehensive tool that contains different Machine Learning algorithms.

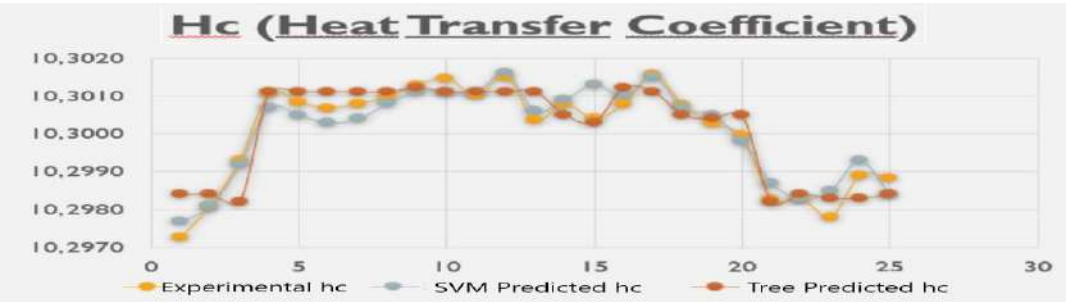

Figure 4.6. Heat Transfer Coefficient Chart

4.7. Tree and SVM Ratios in Artificial Intelligence

At the end of the hc modeling, SVM and Tree modeling were the ones that produced the most accurate results and graphics with the least errors. For this reason, these two types of supervised modeling systems were preferred in modelling.

Tree		SVM	
RMSE (Validation)	0,00047101	RMSE (Validation)	0,00034447
R-Squared (Validation)	0,86	R-Squared (Validation)	0,93

Figure 4.7. Tree and SVM Ratios in Artificial Intelligence

5. Acknowledgements

This study was supported by 2209 Tübitak project number 1919B012107893.

6. Resources

[1] O.V. Ekechukwu O.V., Norton B.Review of solar-energy drying systems II: an overview of solar drying technology, Energy Conversion & Management 40 (1999) 615-655.

[2] Ching Lik Hii, Sachin Vinayak Jangam, Sze Pheng Ong and Arun Sadashiv Mujumdar Editors in:Solar Drying: Fundamentals, Applications and Innovations,2012.

[3] Sharma, A., Chen, C.R., Lan, N. V., 2009, Solar-energy drying systems: A review, Renewable And Sustainable Energy Reviews, 13, pp.1185-1210.

[4] Özgen F., 2007. Yutucu plakası silindirik teneke kutulardan yapılmış bir havalı güneş kolektörünün ısıl performansının deneysel olarak araştırılması. Yüksek Lisans Tezi, Fırat Üniversitesi, Fen Bilimleri Enstitüsü, Elâzığ.

[5] Koçyiğit F., 2008. Yutucu plaka üzerinde farklı türde kanatçıkların yerleştirildiği bir havalı kollektörün enerji ve ekserji analizi. Yüksek Lisans Tezi, Fırat Üniversitesi, Fen Bilimleri Enstitüsü, Elâzığ.

[6] Das, M., Akpinar, E.K., 2018. Investigation of pear drying performance by different methods and regression of convective heat transfer coefficient with support vector machine. Appl. Sci. 8. https://doi.org/10.3390/app8020215

[7] Akay, O.E., Das, M., 2021. Modeling the total heat transfer coefficient of a nuclear research reactor cooling system by different methods. Case Stud. Therm. Eng. 25, 100914. https://doi.org/10.1016/j.csite.2021.100914

[8] Çerçi, K.N., Daş, M., 2019. Modeling of heat transfer coefficient in solar greenhouse type drying systems. Sustain. 11. https://doi.org/10.3390/su11185127

International Conference on Advances and Innovations in Engineering

SEM and EDS Analysis Reviews of Wear Behaviors of Carbon Nanotube Reinforced AZ91 and AZ80 Alloys

Muhammet Gökhan ALBAYRAK[1], Cevher Kürşat MACİT[2]

[1]Metallurgy and Materials Engineering Department, Engineering Faculty, Firat University, Elazığ, TÜRKİYE.
[2]Mechanical Engineering Department, Engineering Faculty, Firat University, Elazığ, TÜRKİYE.
[1]mgalbayrak@firat.edu.tr, [2]macitkursatcevher@gmail.com

[1](ORCID: 0000-0002-7107-3042), [2](ORCID: 0000-0003-0466-7788)

Abstract

The importance of lightweight materials in engineering is increasing day by day. Research on low-density materials such as magnesium is of great interest. This study was carried out to add strength to the low density of AZ series magnesium alloys by adding Carbon Nanotube in different proportions (by weight). The wear behavior of the new composites obtained was examined and the obtained findings were also examined.

Keywords: AZ91, AZ80, Carbon Nanotube.

1. Introduction

Lightness in engineering materials is an area of increasing interest day by day. The lightness of magnesium, which is softer than steel, has increased the desire of academics to study on this subject. Instead of using pure magnesium, it is desired to increase its low hardness, wear and corrosion resistance [1] by alloying it [2], [3]. Magnesium alloys are widely used today in the automotive industry, the electrical and electronics industry, the aerospace industry, the space and transportation industries, and the biomaterials industry. These materials have low inertia due to their low density values and are used for fast moving parts. It is also frequently used in industries requiring solid technology such as automobiles and aerospace. In these industries, the weight of the part is very important. Magnesium has a significant weight-reducing effect thanks to its low density. Aluminum is the most added element to magnesium. Addition of aluminum in magnesium alloys increases strength, hardness, castability and corrosion resistance at room temperature. Additionally, the addition of aluminum increases the solidification time of the alloy and reduces microporosity in casting alloys. The magnesium alloy known as the AZ series, generally contains Aluminum, Zinc and Magnesium in different amount. It has been reported that Al generally increases the hardness and strength of Mg while decreasing its continuity. In order to break this effect, Zn is added into the alloy. The amount of Zn in the alloy can be increased up to a maximum of 2% [4]. Magnesium cannot be alloyed with more than 10% Al + Zn because the ductility of the alloy will be reduced by the formation of brittle intermetallic compounds. Otherwise, it decomposes into $Mg_{17}Al_{12}$ phase and increases ductility again [5].

It is seen that the mechanical properties of nanotubes are much higher compared to steel. Even the mechanical properties of Kevlar fibers, which will be widely used in the production of bulletproof materials, are much lower than carbon nanotubes [6]. The tensile strength of single-walled carbon nanotubes was determined as 45,000 MPa in the experiments. From this value; It appears to have a much higher tensile strength than the strongest steel alloy of 2 MPa [7]. The strength of carbon nanotubes is as high as diamond. Its elastic modulus is between 1.0-1.4 TPa. The reason why the elastic modulus of carbon nanotubes is higher than carbon (C); This is explained by the increase in C-C bond strength and the corresponding increase in elastic modulus with bending and twisting of carbon nanotubes. The tensile strength used to break a bundle of tubes about 1-2 nm in diameter is about 36 GPa, which is almost 100

[1]Corresponding author

times higher than the tensile strength of steel. In addition to having higher tensile strength than steel, its density is 1/6 of steel. Carbon nanotubes have very high fracture toughness, so they can be bent and shaped without deformation. Due to its superior properties (strength, elastic modulus and flexibility), the use of Carbon Nanotube in AZ series Mg alloys is being tested by scientists [8]. The usability of composites formed by adding light metals in many fields such as automotive and aerospace industry is being examined [9]–[11].

In this study, a new composite was produced by adding different amounts of Carbon Nanotubes to AZ80 and AZ91 magnesium alloys. The effects of reinforced Carbon Nanotubes on wear were investigated by minimally affecting the density of the magnesium alloy.

2. Materials and Methods

Al (Sigma-Aldrich, CAS Number:7429-90-5), Zn (Sigma-Aldrich, CAS Number:7440-66-6), Mg (Sigma-Aldrich, CAS Number: 7439-95-4) metal powders and CNT (Nanography, SKU: NG01MW030) additive to be used in the study were commercially obtained. The names and chemical compositions of the CNT-doped AZ80 and AZ91 magnesium alloy matrix samples produced are given in Table 1. Firstly, the powders were weighed in the stoichiometric ratio and put in the milling vessel. Secondly, the CNTs were weighed in ratios 0.2, and 0.5 %wt and, homogenized for 15 min in ethanol as ultrasonically (Bandelin HD 3200). Finally, the matrix powders and the mixture of ethanol-CNTs were subjected to wet milling process for 90 min at 200 rpm in a planetary mill (Retsch PM200). The steel balls (Ø 8 mm) were used during the milling and the steel ball/powder ratios were 10/1.

Table 1: Chemical composition of samples.

Samples Names	Al (%wt)	Zn (%wt)	CNT (%wt)	Mg (%wt)
AZ80-2	8	0.5	0.2	bal.
AZ80-5	8	0.5	0.5	“
AZ91-2	6.5	0.8	0.2	“
AZ91-5	6.5	0.8	0.5	“

The wet mixture was dried at 70 °C for 12 h and the dried powder mixtures were gridded again for 15 min to make a homogeneous mixing of the powders. The powders were cold-pressed in a 12 mm diameter die under 500 MPa pressure and the preparing compacts were sintered for 2 h at 500 °C. All samples were sintered under Ar (99,005%, purity) atmosphere.

The wear tests of the samples were carried out using the pin-on-disc method under 10 and 20N load. After wear, it was imaged using Zeiss brand EVO MA10 model SEM device.

2.1. Analyses of Wear Zones

EDS analysis of AZ80-2 named sample is shown in Figure 1. In Fig.1., the chemical compositions of selected areas have C, O, Al and Mg elements. The Al and Mg elements contained in AZ series Mg alloys and the C elements contained in CNT are clearly seen in the EDS analysis. During sample preparation and sintering processes, oxygen in the environment was avoided as much as possible. For this, pressing and sintering were performed in Ar environment. However, EDS analysis shows the presence of oxygen on the surface. This can be explained by the fact that the wear test was carried out in a dry environment. EDS Mapping analysis of AZ80-5 named sample is also shown in Figure 2. In Fig.2., mapping of the elements show that all elements are almost distribute homogenously. In terms of oxygen, a similar situation with AZ80-2 is also valid for this sample.

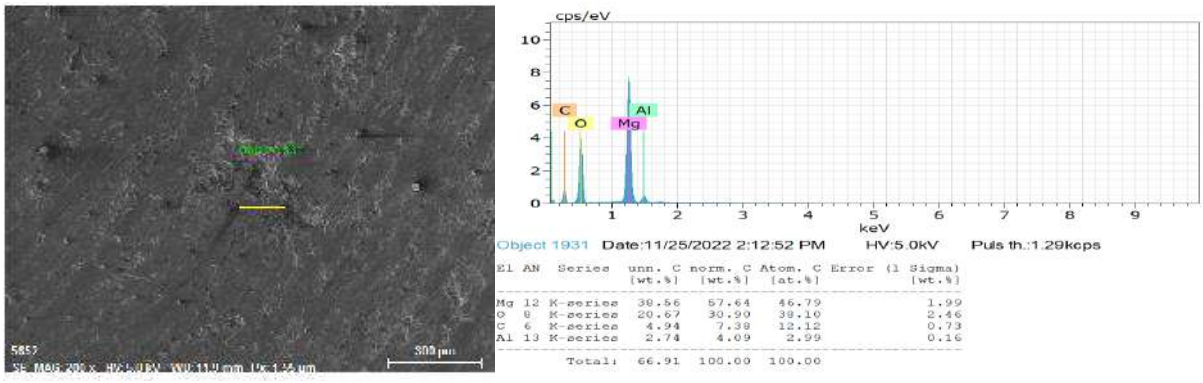

Figure 1. EDS analysis of AZ80-2 sample

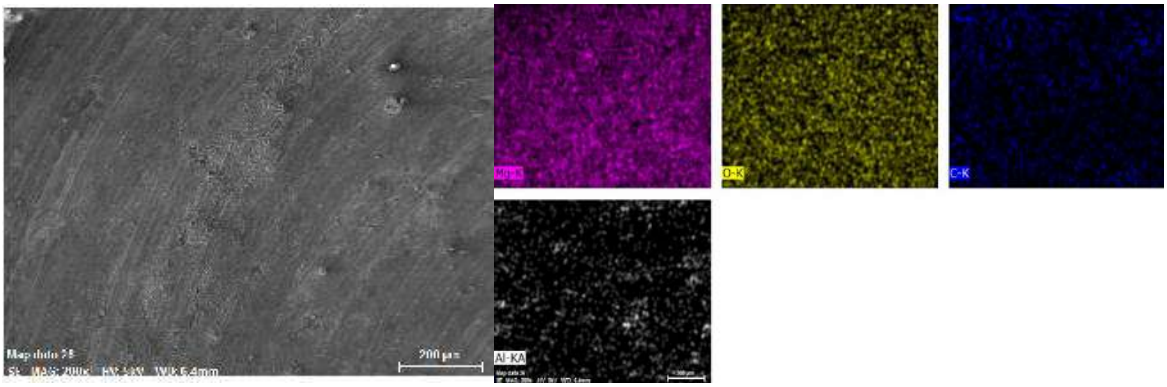

Figure 2. EDS analysis and mapping of AZ80-5 sample

EDS analysis of AZ91-2 named sample is shown in Figure 3. In Fig.3., the chemical compositions of selected areas have C, O, Al and Mg elements, just like Fig.1. The Al and Mg elements contained in AZ series Mg alloys and the C elements contained in CNT are clearly seen in the EDS analyses. EDS Mapping analysis of AZ91-5 named sample is also shown in Figure 4. In Fig.4., mapping of the elements show that all elements are almost distribute homogenously, except C element. Compared to AZ80-5 (Fig.2.), it can be seen that the distribution of CNTs in the AZ91-5 sample is not homogeneous. It is estimated that this situation is caused by the sample preparation process.

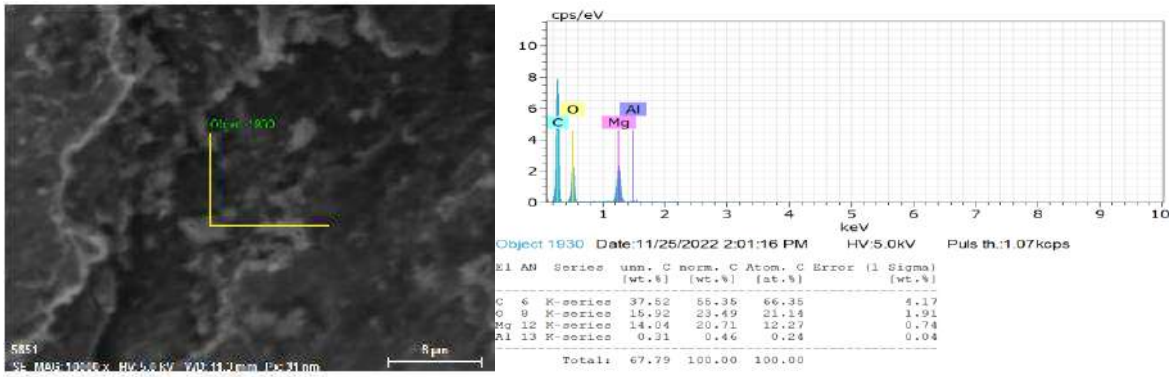

Figure 3. EDS analysis of AZ91-2 sample

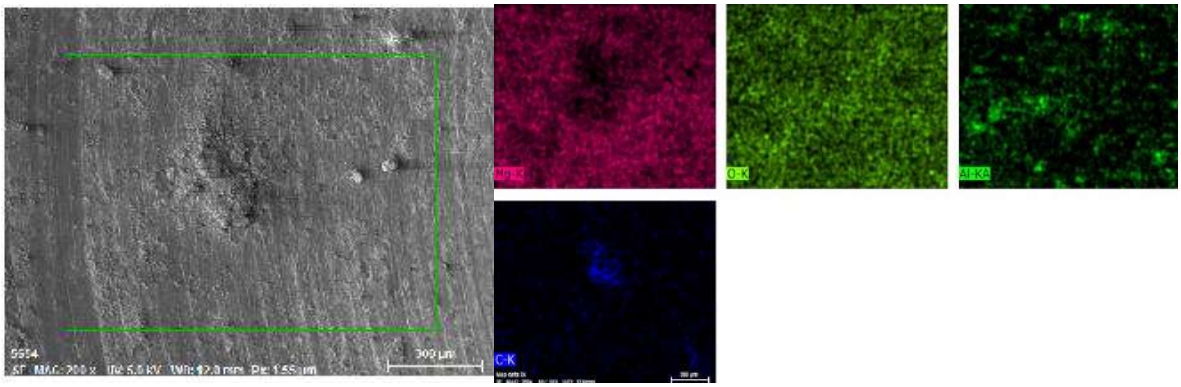

Figure 4. EDS analysis and mapping of AZ91-5 sample

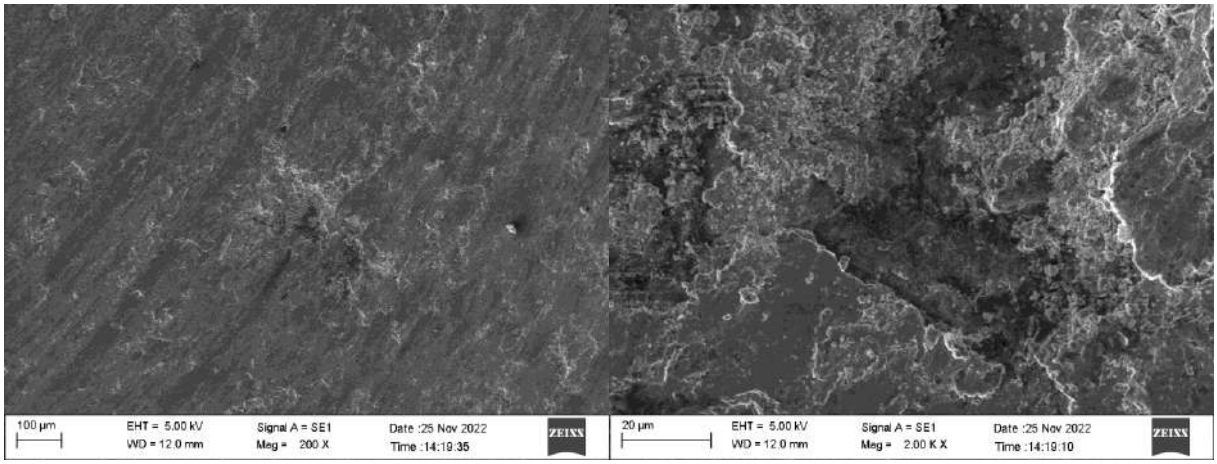

Figure 5. SEM images of AZ80-2 sample

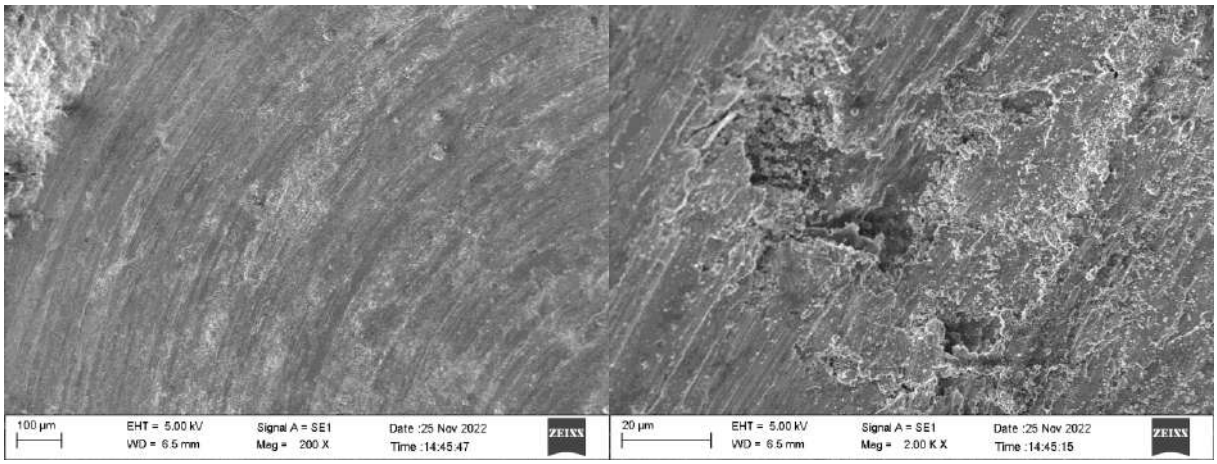

Figure 6. SEM images of AZ80-5 sample

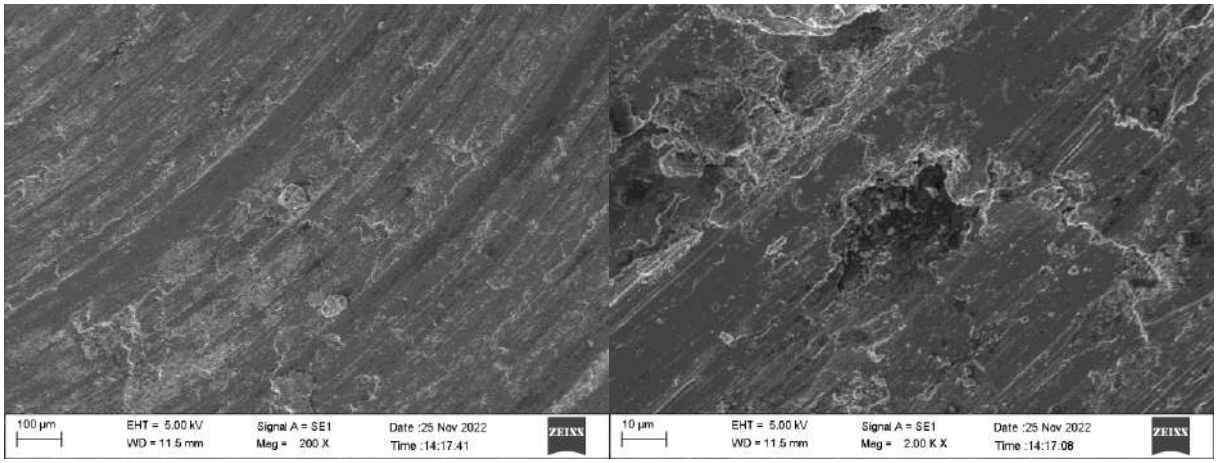

Figure 7. SEM images of AZ91-2 sample

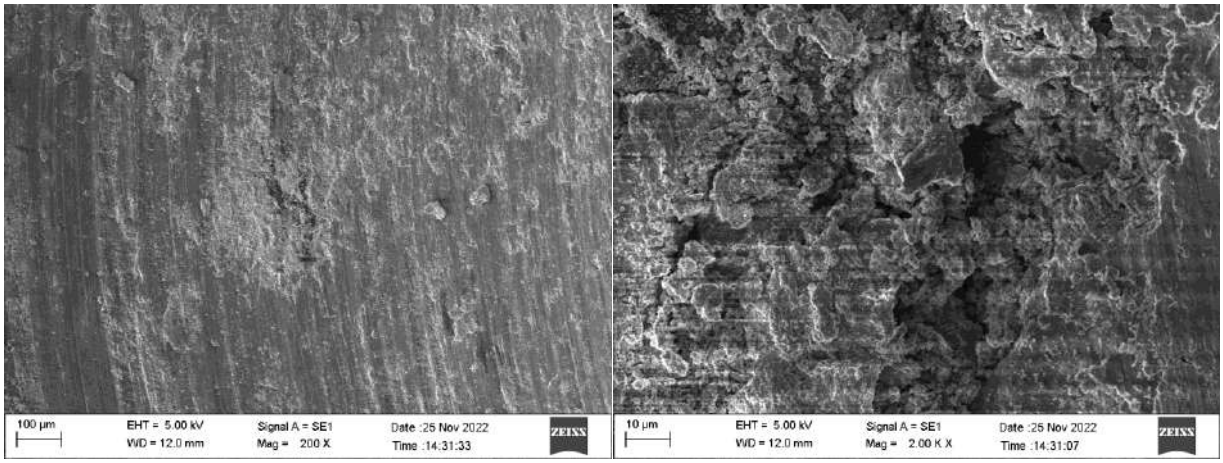

Figure 8. SEM images of AZ91-5 sample

SEM images of all samples are given Figure 5 to 8. Wear marks in the wear area are clearly visible. The sample exhibited a wear behavior suitable for abrasive wear. Marks of plastic deformation are observed on the sample surface by the abrasive which is harder than itself. Weight losses of the samples were determined under 2 different loads (10 and 20 N). Samples were weighed at every 250 m wear distance. Shimadzu AUW220D device was used during weighing. Weight loss-distance graphs of the samples are given in Figure 9.

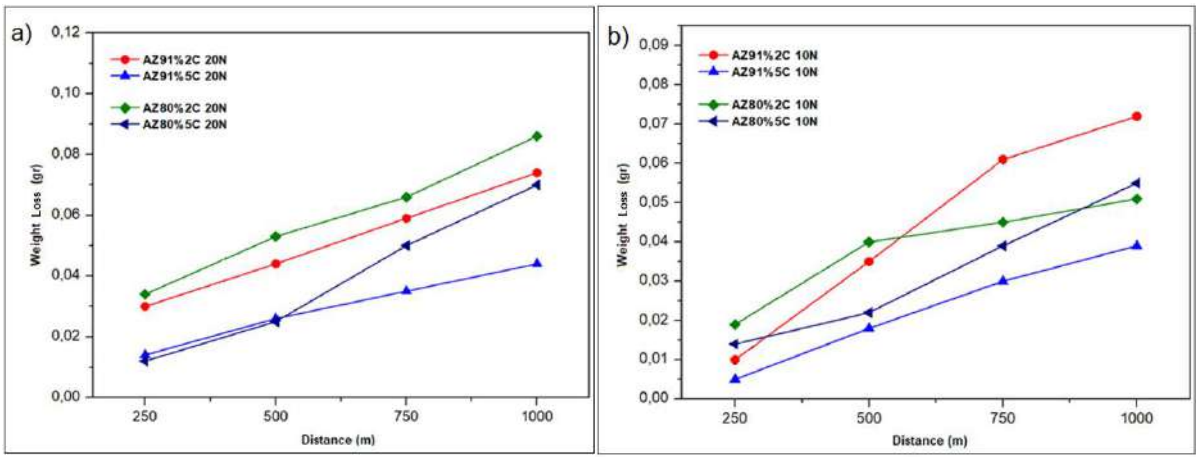

Figure 9. a) Graph of Weight Loss – Distance for under 20N, **b)** Graph of Weight Loss – Distance for under 10N.

A decrease in weight loss is observed with increasing CNT reinforcement in both AZ91 and AZ80 series Mg alloys. It is seen that under increasing load, AZ80 loses more weight than AZ91. Minimum weight loss was achieved by reinforcing AZ91 with 0.5% CNT.

3. Results

All samples were produced successfully. Oxidation formation was detected during the dry wear test on the surface. It was concluded that increased carbon nanotube reinforcement reduced weight loss during wear. The wear mechanism was determined as an abrasive wear.

4. References

[1] Y. Say, O. Guler, and B. Dikici, "Carbon nanotube (CNT) reinforced magnesium matrix composites: The effect of CNT ratio on their mechanical properties and corrosion resistance," *Mater. Sci. Eng. A*, vol. 798, no. March, p. 139636, 2020, doi: 10.1016/j.msea.2020.139636.

[2] Y. Zhang, Q. Wang, R. Ye, and C. S. Ramachandran, "Plasma electrolytic oxidation of cold spray kinetically metallized CNT-Al coating on AZ91-Mg alloy: Evaluation of mechanical and surficial characteristics," *J. Alloys Compd.*, vol. 892, p. 162094, 2022, doi: 10.1016/j.jallcom.2021.162094.

[3] S. Wang, X. Liu, X. Yin, and N. Du, "Influence of electrolyte components on the microstructure and growth mechanism of plasma electrolytic oxidation coatings on 1060 aluminum alloy," *Surf. Coatings Technol.*, vol. 381, no. November 2019, p. 125214, 2020, doi: 10.1016/j.surfcoat.2019.125214.

[4] B. L. Mordike and T. Ebert, "Magnesium Properties - applications - potential," *Mater. Sci. Eng. A*, vol. 302, no. 1, pp. 37–45, 2001, doi: 10.1016/S0921-5093(00)01351-4.

[5] F. Czerwinski, "Magnesium and Its Alloys BT - Magnesium Injection Molding," F. Czerwinski, Ed. Boston, MA: Springer US, 2008, pp. 1–79.

[6] İ. Mutluay, "Sürekli Karbon Nanotüp Üretimi," Ankara University, 2007.

[7] A. Tepe, "NANOTEKNOLOJİDE NANO ÖLÇEKTEKİ YAPILARIN YEREL OLMAYAN ELASTİSİTE ÇERÇEVESİNDE İNCELENMESİ," İstanbul Teknik Üniversitesi, 2007.

[8] Y. Zhang, Q. Wang, G. Chen, and C. S. Ramachandran, "Mechanical, tribological and corrosion physiognomies of CNT-Al metal matrix composite (MMC) coatings deposited by cold gas dynamic spray (CGDS) process," *Surf. Coatings Technol.*, vol. 403, no. September, p. 126380, 2020, doi: 10.1016/j.surfcoat.2020.126380.

[9] B. Chen *et al.*, "Solid-state interfacial reaction and load transfer efficiency in carbon nanotubes (CNTs)-reinforced aluminum matrix composites," *Carbon N. Y.*, vol. 114, pp. 198–208, 2017, doi: 10.1016/j.carbon.2016.12.013.

[10] A. Aborkin, D. Babin, A. Zalesnov, E. Prusov, A. Ob'edkov, and M. Alymov, "Effect of ceramic coating on carbon nanotubes interaction with matrix material and mechanical properties of aluminum matrix nanocomposite," *Ceram. Int.*, vol. 46, no. 11, pp. 19256–19263, 2020, doi: 10.1016/j.ceramint.2020.04.264.

[11] T. Noguchi, A. Magario, S. Fukazawa, S. Shimizu, J. Beppu, and M. Seki, "Carbon Nanotube/Aluminium Composites with Uniform Dispersion," *Mater. Trans.*, vol. 45, no. 2, pp. 602–604, 2004, doi: 10.2320/matertrans.45.602.

International Conference on Advances and Innovations in Engineering

Thermohydraulic performance analysis of a crossflow finned tube heat exchanger

Orhan KALKAN[1]

[1]Department of Mechanical Engineering, Faculty of Engineering and Architecture, Erzincan Binali Yıldırım University, Erzincan, Turkey
[1]orhan.kalkan@erzincan.edu.tr

[1](ORCID: 0000-0002-9664-1819)

Abstract

Finned-tube heat exchangers are used as condensers and/or evaporators in many refrigeration cycles. they are also preferred in many other heat transfer applications. Design parameters are significant for thermohydraulic performance of the heat exchangers. In the present study, a water-to-air finned tube heat exchanger is considered for numerical analysis using the Ansys-Fluent computational fluid dynamics package program. The effects of design parameters on the thermohydraulic performance of the modeled heat exchanger are investigated. In the numerical analysis, the outer surface of the pipe was assumed as a constant temperature of 40 °C, and the outside air was chosen at an ambient temperature of 22 °C. The numerical solutions of the modeled heat exchanger are validated with the data in the open literature. It is examined how the air outlet temperature and pressure loss in the heat exchanger are affected under different fin thickness and fin pitch dimensions. When the fin thickness decreases from 0.4 mm to 0.1 mm, the air outlet temperature and pressure drop decrease by 6.6% and 28.4%, respectively. When fin pitch increases from 2 mm to 6 mm, the air outlet temperature and pressure drop decrease by 18.1% and 69.6%, respectively. However, with this increase in the fin pitch, the compactness of the heat exchanger (m^2/m^3) also decreases by 66.7%.

Keywords: compactness, heat exchanger, pressure drop, thermohydraulic.

1. Introduction

Energy is a conservable quantity, and it can be beneficial by changing its form and using it in different fields. Many sectors such as thermal power plants, heating, cooling, and air conditioning facilities use energy intensively. In places where energy is used intensively, efficiency is of great importance. Thanks to the heat exchanger used in this industry, it achieves great savings in energy. Heat exchangers are indispensable tools in engineering applications. Because, thanks to heat exchangers, energy is transferred from one fluid to another with minimum loss. Efficiency is increased by designing various configurations in order to minimize energy losses. Heat exchangers have the most important place in the industrial field and are used in different ways such as condenser and evaporator. Heat exchangers are a field of application in science branches such as thermodynamics, fluid mechanics and material structure. Certain parameters affect the design and optimization. Many parameters such as thermal efficiency, pressure drops, temperature and flow play a major role in the design. There are many different types of heat exchangers used in the industrial field. The most widely used among these are finned tube heat exchangers, which provide heat transfer without mixing of fluids. These heat exchangers, which have different fin types according to the intended use [1].
There have been many numerical studies on finned tube heat exchangers in the literature, and some of the current studies are summarized belowRaushan et al. [2] performed a CFD analysis of a finned tube heat exchanger with six different fin designs which have a non-Newtonian working fluid. The best thermal performance was obtained with the design resembling the tree-shaped fin structure and a maximum temperature difference of 31.8 °C was determined.
Kim et al. [3] conducted the effect of air vibration on heat transfer about finned tube heat exchangers. As a result of the study, it was observed that the heat transfer improved with the increase in vibration frequency, amplitude and fin pitch. Besides, a correlation was developed for heat transfer improvement using vibration parameters.

[1]Corresponding author

Wang et al. [4] studied the heat transfer performance of elliptical finned tube heat exchangers. In the numerical study, different geometric parameters and Reynolds numbers were performed. As a result, it has been seen that elliptical fins have more successful heat transfer than circular fins.

Guo et al. [5] proposed a passive cooling method for finned tube heat exchangers under natural convection conditions. The effects of the geometric parameters of the fins on natural convection were calculated numerically. The results show that the single row coil outperforms the two-row coil for the designed system.

In this study, in order to examine the effects of fin thickness and fin pitch geometric parameters on thermohydraulic performance, a water-to-air finned tube heat exchanger is considered for numerical analysis. The finned tube heat exchanger modeled by the CFD method has been verified under certain conditions. Then, the performance analysis was performed by considering the air outlet temperature, pressure drop, and the compactness of heat exchanger.

2. Methodology

A water-to-air finned tube heat exchanger with 780×730×90 mm dimension is considered for the numerical analysis. Geometric model and dimensional parameters of the heat exchanger is shown in Figure 1. Geometrical parameters are also given in Table 1. In such heat exchangers, hot liquid fluid passes through the copper tube and air passes between the fins as a cross flow. In this study, the air flow and conjugated heat transfer mechanism are numerically modeled and examined by assuming the pipe surfaces as a constant temperature of 40 °C. In order to reduce the computational costs, the computational domain shown in Figure 2 is chosen. Solid and fluid subdomains, boundary conditions are also represented in the figure. The air domain is generated longer from the fin inlet and outlet to achieve developed flow. ANSYS-Fluent commercial program is used to model, solve, and simulate the problem numerically. The SIMPLE algorithm for velocity and pressure coupling is preferred due to robustness. Convergence criteria is selected as 10^{-6} for energy, momentum, continuity, and turbulence model equations.

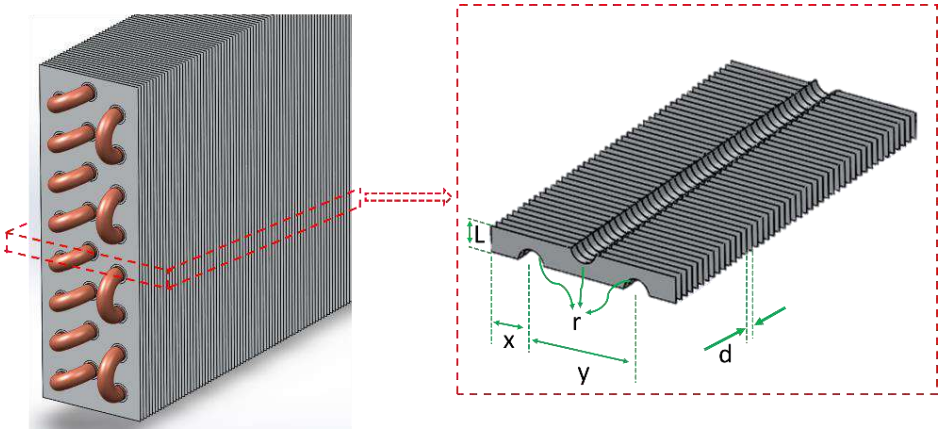

Figure 1. Geometric model and dimensional parameters of the heat exchanger

Table 1. Dimensional parameters

Parameter	Value (mm)
x	15
y	60
r (radius)	7.6
d	2.81
L	30

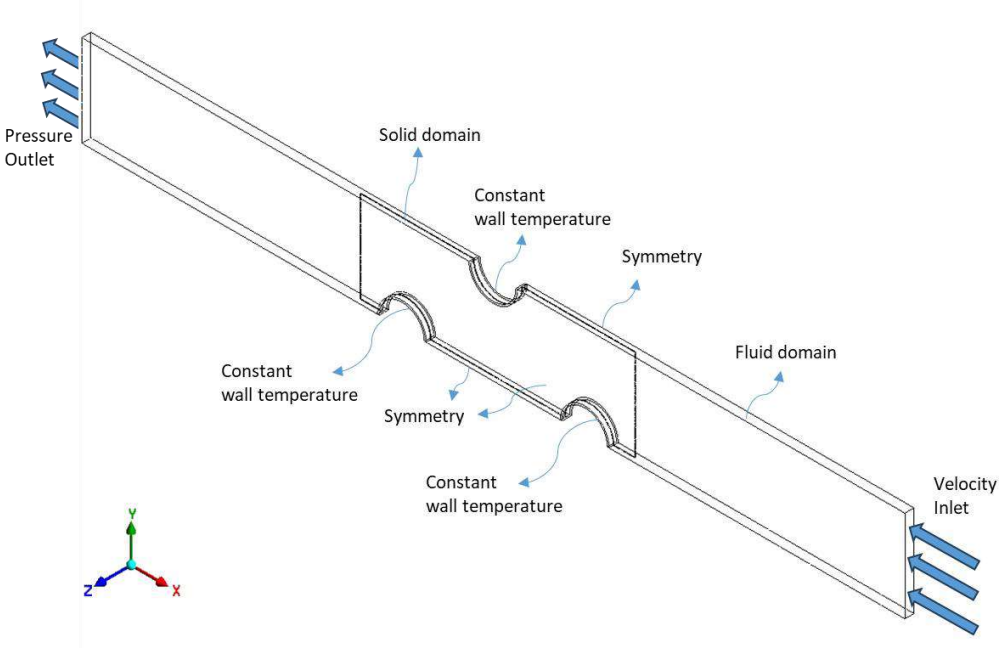

Figure 2. Computational domains and boundary conditions

2.1. Governing equations

3D simulation of the air-cooled finned tube heat exchanger numerical model is performed using the following the RANS (Reynolds Average Navier-Stokes) equations [6-7] with the conjugate heat transfer problem approach.

The mass conversation:

$$\boldsymbol{\partial \rho_{air}/\partial t + \nabla.(\rho_{air}\vec{v}) = 0} \quad (1)$$

The momentum conversation:

$$\boldsymbol{\partial(\rho_{air}\vec{v})/\partial t + \nabla.(\rho_{air}\vec{v}\,\vec{v}) = -\nabla P} \quad (2)$$

The energy conservation:

$$\boldsymbol{\partial\left(\rho_{air}c_{p,air}T_{air}\right)/\partial t + \nabla.\left(\rho_{air}c_{p,air}\vec{v}\,T_{air}\right) = -\nabla.(k_{air}\nabla\,T_{air})} \quad (3)$$

where $\boldsymbol{\rho_{air}}$ is air density, $\boldsymbol{c_{p,air}}$ is air specific heat, $\boldsymbol{\vec{v}}$ is air velocity vector, $\boldsymbol{k_{air}}$ is the thermal conductivity of air, and $\boldsymbol{T_{air}}$ is air temperature.

2.2. Mesh generation and independency test

The polyhedral mesh structure shown in the Figure 3 is created using ANSYS meshing tool to perform numerical solutions with finite volume method. Denser meshes are used in the liquid-solid domain interface to give more realistic results for the velocity and temperature boundary layer solution. In order to minimize the computational cost, truncation and rounding errors, it is necessary to create the mesh with the optimum number of elements [8-10]. Therefore, the mesh independency test is performed under the conditions of air velocity (V_i) is 1.03 m/s, air inlet temperature (T_i) is 22 °C and fin thickness is 0.2 mm and fin pitch (d) is 2.81 mm. In Table 2, pressure drops (ΔP) and air outlet temperature (T_o) values are given according to mesh numbers. Mesh structure with 388779 element number is preferred considering the maximum deviation rates.

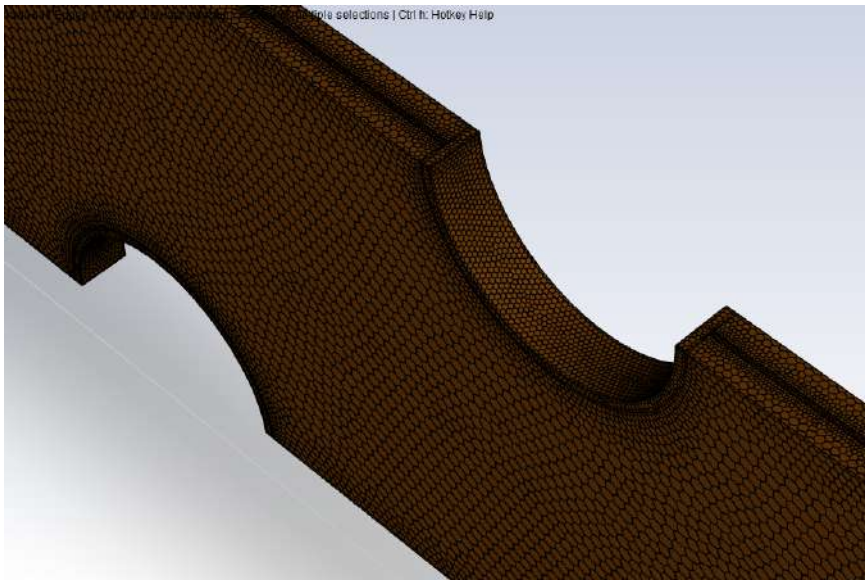

Figure 3. Representation of the mesh structure

Table 2. Mesh independency test

Mesh element number	ΔP (Pa)	T_o (°C)	Maximum deviation (%)
50142	5.59	37.41	-
232214	5.74	35.04	11.3%
388779	6.07	34.82	5.4%
612458	6.12	34.76	0.8%

3. Results and Discussion

3.1. Validation of the present study

In order to show the accuracy of numerical solutions, the numerical results of the study conducted by Batista et al. [11] in the open literature are compared with the results of this study. The pressure drop and air outlet temperatures comparison for the default geometry case (fin thickness is 0.2 mm, fin pitch is 2.81 mm) is given in Table 3. Besides, Batista et al. [11] validated their numerical results in an experimental study. When the results are compared, it is clear that there is an acceptable agreement.

On the other hand, Figure 4 shows a comparison of the temperature contours of the present study and the study by Batista et al. [11]. When the temperature distributions on the air surface are examined, the temperature values in the main flow line and dead zones are compatible with each other.

Table 3. Validation of the numerical results

V_i (m/s)	T_o (°C) by ref. [11]	ΔP (Pa) by ref. [11]	T_o (°C) of the present study	ΔP (Pa) of the present study
0.25	39.73	1.04	39.75	1.07
0.45	38.57	2.16	38.74	2.18
0.65	37.22	3.39	37.21	3.27
0.85	35.76	4.76	36.06	4.77
1.03	34.80	6.04	34.82	6.07

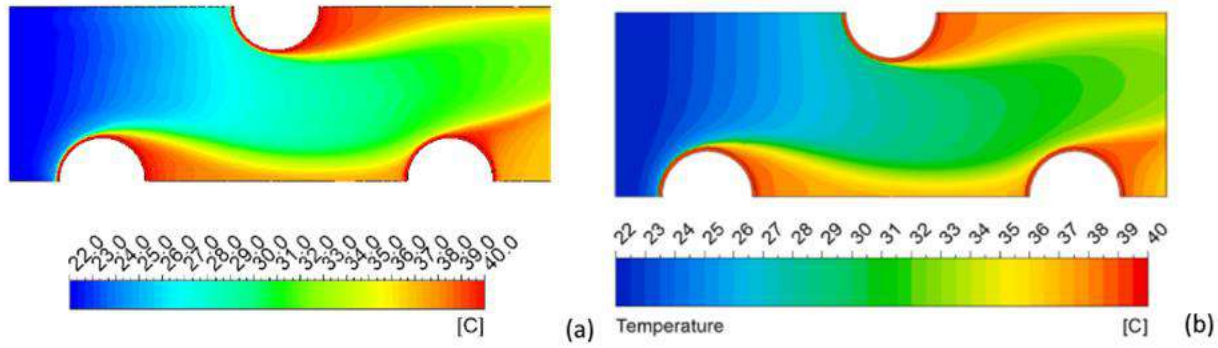

Figure 4. Comparison of the temperature contours of (a) the present study and (b) the study by Batista et al. [11]

3.2. Fin thickness effect

Numerical solutions are performed for values ranging from 0.1 mm to 0.4 mm in fin thickness. As the fin thickness decreases, it is understood that the air outlet temperature and pressure drop also decrease. As the fin thickness increases, the flow area will narrow, and the output temperature increases with the decrease in convection. In the same way, the narrowing cross-sectional area of the air domain causes the pressure drop to increase. Although it is understood that the thermo-hydraulic performance increases due to the decrease in the fin thickness, the material strength should not be ignored. It should be emphasized that in this study, only the geometric structure was examined in terms of thermal performance.

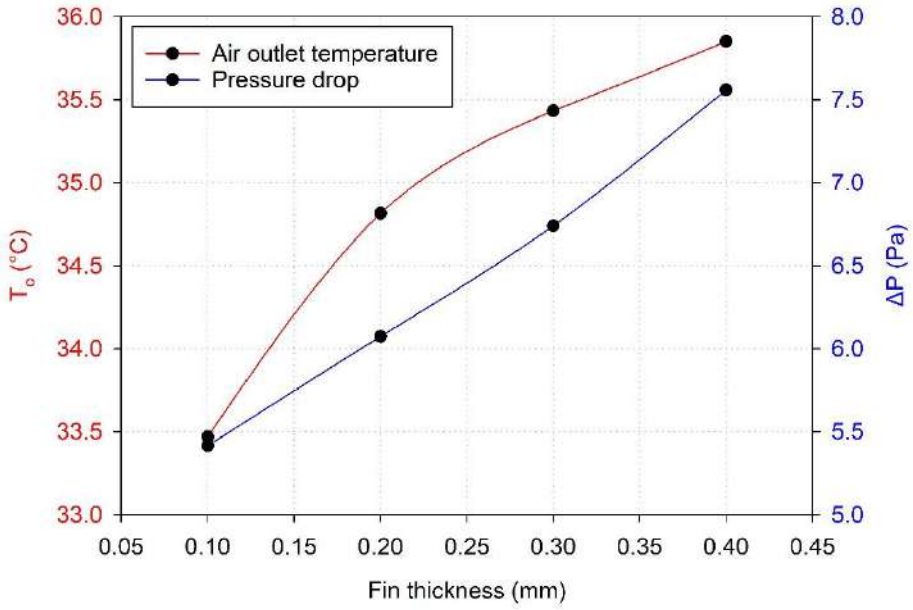

Figure 5. Comparison of the temperature

3.3. Fin pitch effect

It is examined how the fin pitch in the range of 2 mm to 6 mm affects the thermo-hydraulic performance and compactness of the heat exchanger. It is seen that the air outlet temperature and pressure loss decrease significantly with the increase of the fin pitch from 2 mm to 4 mm. However, it is understood that there is no appreciable increase in thermohydraulic performance with the increase after the 4 mm fin pitch. Although the increase in fin pitch increases the thermo-hydraulic performance, it is seen that it reduces the compactness of the heat exchanger. Compactness can be briefly defined as the ratio of the heat transfer surface area to the heat exchanger volume. In the literature, heat exchangers with a compactness number greater than 700 are considered compact [12]. Considering this situation, the fin step should be determined in the design.

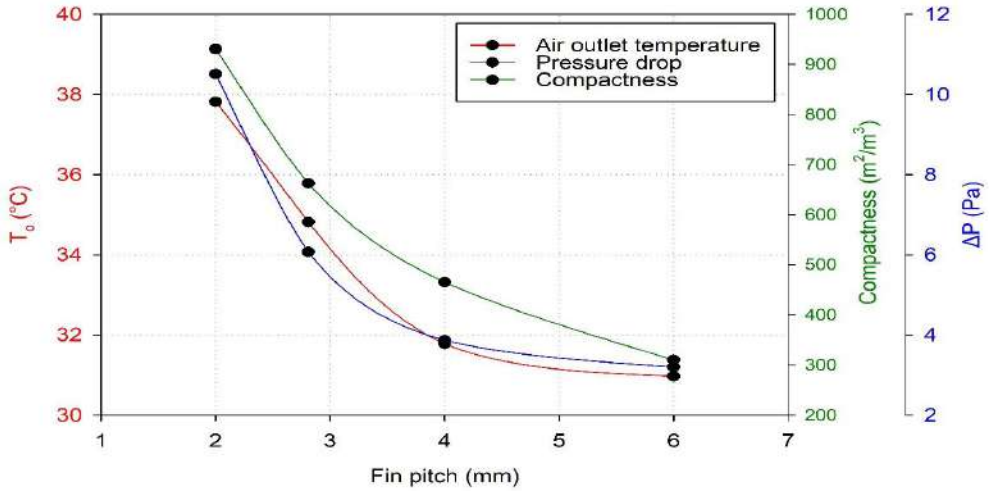

Figure 6. Comparison of the temperature

4. Conclusions

In this study, numerical analysis of a water-to-air heat exchanger is carried out to investigate how the fin thickness and fin pitch affect thermo-hydraulic performance. In the numerical analysis, the outer surface of the pipe was assumed as a constant temperature of 40 °C, and the outside air was chosen at an ambient temperature of 22 °C. The numerical solutions of the modeled heat exchanger are validated with the data in the open literature. When the fin thickness decreases from 0.4 mm to 0.1 mm, the air outlet temperature and pressure drop decrease by 6.6% and 28.4%, respectively. Although it is understood that the thermo-hydraulic performance increases due to the decrease in the fin thickness, the material strength should not be ignored. When fin pitch increases from 2 mm to 6 mm, the air outlet temperature and pressure drop decrease by 18.1% and 69.6%, respectively. However, with this increase in the fin pitch, the compactness of the heat exchanger (m^2/m^3) also decreases by 66.7%. Besides, the air outlet temperature and pressure loss decrease significantly with the increase of the fin pitch from 2 mm to 4 mm.

References

[1] Göreli M. Helisel Kanatlı Boru Demetlerinde Isı Transferi ve Basınç Düşümünün Hesaplamalı Akışkanlar Dinamiği ile Analizi. MSc Thesis, İnönü University, Malatya, Turkey, 2022.

[2] Raushan AK, Yadav R, Mohan R, Goga G. CFD analysis of different finned tube heat exchanger designs using a non newtonian fluid. Materials Today: Proceedings. In press. 2023.

[3] Kim M, Han C, Baek C, Kim Y. "Air-side heat transfer enhancement in fin-tube heat exchangers using forced vibrations under various conditions". International Communications in Heat and Mass Transfer, 144, 106798, 2023.

[4] Wang H, Fu T, Wang J, Zhang F, Zhang K, Deng X. "Study on heat transfer performance of fin-and-tube heat exchanger with elliptical fins". Journal of Energy Storage, 56, 105956, 2022.

[5] Guo S, Cheng KX, Lee PS. "Numerical study of the cold finned-tube bundle heat exchanger under natural convection for a novel passive displacement cooling system". Building and Environment, 233, 110083, 2023.

[6] Welty JR, Wicks CE, Wilson RE. Fundamentals of Momentum, Heat, and Mass Transfer, 3rd ed., John Wiley & Sons, New York, 1984.

[7] Ligett JA. Fluid Mechanics, McGraw-Hill, New York, 1994.

[8] Ryu J, Hahn I. "Numerical Modeling for Induced Eddy Current Calculation on a Non-uniform Mesh". IEEE 20th Biennial Conference on Electromagnetic Field Computation (CEFC), (pp. 1-2). IEEE, 2022.

[9] Kalkan O, Celen A, Bakirci K. "Multi-objective optimization of a mini channeled cold plate for using thermal management of a Li-Ion battery". Energy, 251, 123949, 2022.

[10] Batista J, Trp A, Lenic K. "Experimentally validated numerical modeling of heat transfer in crossflow air-to-water fin-and-tube heat exchanger". Applied Thermal Engineering, 212, 118528, 2022.

[11] Genceli OF. Isı değiştiricileri, Birsen Yayınevi, İstanbul, 2017.

International Conference on Advances and Innovations in Engineering

Numerical ınvestigation of flow and heat transfer in hybrid corrugated channels with different winglet forms

Doğukan UYSAL[1], Selma AKÇAY[2]

[1]Cankiri Karatekin University, Graduate School of Natural and Applied Sciences, Cankiri, Turkey.
[2]Cankiri Karatekin University, Engineering Faculty, Mechanical Engineering Department, Cankiri, Turkey.
[1]dogu.uysl18@gmail.com, [2]selmaakcay@karatekin.edu.tr

[1](ORCID ID: 0009-0007-1747-0024), [2](ORCID ID: 0000-0003-2654-0702)

Abstract

In this study, the effects of two different winglet designs on flow and heat transfer in hybrid corrugated channels were investigated numerically. The numerical analysis was performed using the Computational Fluid Dynamics-based ANSYS-Fluent software. The hybrid configuration of channels composed of rectangular and triangular-shaped grooves was employed as the channel geometry. Two different winglet geometries were designed in the hybrid corrugated channel, and the thermo-hydraulic performance of these winglets was investigated for Reynolds numbers in the range of $4000 \leq Re \leq 10000$. V and Y-type winglets were placed within each grooved section in the downstream. Additionally, the study compared the hybrid corrugated channel without winglets. The bottom and top grooved surfaces of the channel were kept constant at a temperature of 380 K. For each channel structure, Nusselt number (Nu), pressure drop, and thermo-hydraulic performance factor (THPF) were calculated and presented as graphs as functions of dimensionless numbers. Moreover, velocity and temperature contours were obtained at different parameters to observe the effects of the winglets and Reynolds number on flow and thermal fields. The numerical results indicated that the heat transfer obtained in the hybrid corrugated channel was higher compared to the flat channel. The winglets were caused to greatly enhance the flow and heat transfer. However the winglets slightly increased the pressure drop. Increasing Reynolds number increased the Nusselt number and pressure drop for all channel configurations. The highest heat transfer and pressure drop were obtained for the V-type winglets at high Reynolds numbers.

Keywords: hybrid corrugated channel, winglets, thermo-hydraulic performance, turbulent flow

1. Introduction

Thermal devices are widely used in many engineering fields such as heating/cooling processes, heat exchangers, cooling of nuclear reactor, food and chemical processes. Increasing the thermal efficiency of these devices plays an important role both for energy efficiency and energy saving. Therefore, passive and active heat transfer methods have been investigated for a long time to increase the heat transfer efficiency of these devices. The main purpose of these studies is to achieve the highest heat transfer performance with the least pressure drop. Passive heat transfer improvement methods are safer and more economical than other methods because they do not require any additional energy and do not have mechanical parts. For this reason, corrugated and wavy channels, which are one of the passive heat transfer methods, are widely used in many thermal devices. The main purpose of these channels is to increase the heat transfer rate by increasing the surface area that the flow contacts [1-3]. Corrugated and wavy channels also cause self-flow oscillations. These oscillations provide the flow mix to improve. A homogeneous flow increases heat transfer by preventing temperature differences within the duct. Flow and heat transfer of corrugated and wavy surfaces with different geometries have been investigated by many experimental and numerical studies [4-6]. In these studies, it was reported that high heat transfer performance was achieved with a slight increase in pressure drop in corrugated and wavy ducts [7-8]. In a numerical study, Naphon et al. [9] investigated the improvement of flow and heat transfer in a V-shaped wavy channel. Deylami et al. [10] numerically investigated the flow and heat transfer in a wavy channel for different geometric parameters. They reported that thermal and hydraulic performance were

[1]Corresponding author

highly influenced by the channel geometry. Özbolat and Şahin [11] numerically investigated the flow and heat transfer in sinusoidal wavy channels in 2500≤Re≤7500 for different geometric parameters. The channel geometry and flow conditions were analyzed to find the optimum thermohydraulic performance value.

Another passive heat transfer method is the addition of baffles or winglets into the channel. These added baffles and winglets change the flow structure by directing the flow to certain regions. The addition of winglets in different configurations into the channel significantly improves the flow and heat transfer depending on the parameters used [12-14]. In addition, the winglets cause an increase in pressure loss in the duct as they create a barrier in the flow direction [15-16]. Therefore, the effect of winglets on heat transfer should be considered together with the pressure drop. Research aims to find channel and winglets designs that provide the best heat transfer with the minimum pressure drop. Li and Gao [17] numerically investigated the effects of delta-shaped baffles on thermal performance for different apex angles in a triangular corrugated bottom wall. They calculated Nu and pressure drop for 1000≤Re≤6000 and showed that if the appropriate parameters were selected, the Nu would increase by 2.1 and 4.3 times. Sun et al. [18] experimentally and numerically examined the heat transfer of multiple rectangular wings in a circular heat exchanger under turbulent flow. They changed geometric parameters such as the number of rectangular wings (N=4, 6, 8), height ratio (HR=0.05, 0.1, 0.2) and aspect rate (PR=1.57, 3.14, 4.71). They reported the highest thermal performance factor of 1.27. Promvonge et al. [19] experimentally and numerically studied the flow and thermal performance of split V-type wings under turbulent flow. They placed the wings in the channel in two different ways and investigated the effects of different geometric parameters in 4200≤Re≤25800. They reported that the wings can increase the heat transfer up to 3.8 times if appropriate parameters are used. Akcay and Akdag [20] numerically examined heat transfer in a laminar flow conditions in a circular channel with different baffle angles (θ=30º, 90º, 180º). They declared that the baffle angles greatly affected the heat transfer and pressure drop, and they found that the highest thermal enhancement and pressure drop were obtained at the 90º baffle angle. Akcay [21] numerically analyzed the hydraulic and thermal performance of V-type winglets placed in the center of a zigzag wavy channel and obtained Nu and pressure drop in the laminar flow of the Al_2O_3-water nanofluid. It was reported that the winglets added to the channel increased the heat transfer and the best thermohydraulic performance was obtained to be 2.12 at Re=400 and φ=0.05 particle volume ratio.

As can be understood from the above studies, the effects of wavy channels with the same wave profile and winglets added in these channels on flow and heat transfer performance were investigated. In this study, hybrid wave profile was used and the thermo-hydraulic performance of two different winglet structures added to this hybrid corrugated channel was investigated numerically.

2. Material and Methods

Description of the numerical model

The hybrid corrugated channel geometry and two different winglet structures used in the study are shown in Fig.1. The corrugated channel is formed with a hybrid configuration of rectangular and triangular profiles. The height of the channel is H=18 mm. The height of the waves is a=10mm. The width of the waves and the distance between both waves are 2a and 4a, respectively. There are unheated straight sections of L_1=360mm and L_3=500mm at the entrance and exit of the channel, respectively. The heated channel section containing the hybrid corrugations is L_2=500 mm. The corrugated length of the channel (L_2) includes a total of 9 wave, 5 rectangular and 4 triangular wave profiles. Two different geometries of winglets are placed in the channel. These winglets are named V-type (Fig. 1b) and Y-type (Fig. 1c). The geometrical parameters of the winglets are shown in Table 1.

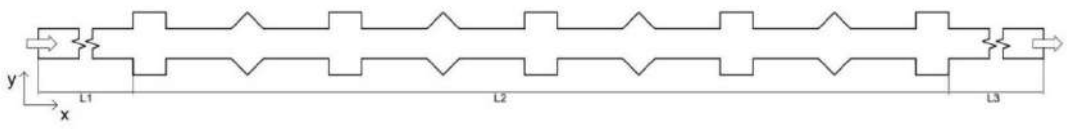

(a)

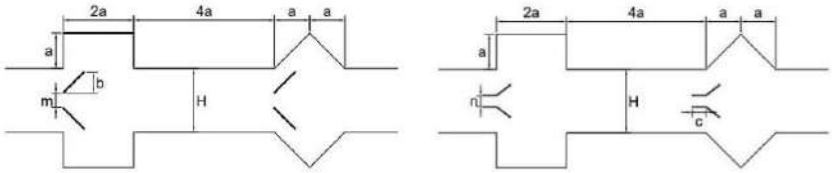

(b) **(c)**

Figure 1. (a) Hybrid corrugated channel geometry, (b) V-type winglet structure, (c) Y-type wing structure

Table 1. Geometrical parameters of winglets

Description	Symbol	Value
Distance between V-type winglet pair	m	4 mm
Height of V-type winglet	b	6 mm
Height of Y-type winglet and distance between Y-type winglet pair	n	3 mm
Horizontal lenght of Y-type winglets	c	4 mm
The thickness of the winglets	t	0.3 mm

Conservation equations

In the numerical study, the fluid is considered single-phase, incompressible and Newtonian properties. The flow field is 2d. The fluid flows in steady flow conditions and turbulence regime. Viscous terms are omitted. Fluid properties are assumed to be constant. The effect of gravity and heat transfer by radiation are not taken into account. According to the these assumptions, conservation equations for the standard k-ε turbulence model are given below:

$$\frac{\partial}{\partial x_i}(\rho \bar{u}_i) = 0 \tag{1}$$

$$\frac{\partial}{\partial t}(\rho \bar{u}_i) + \frac{\partial}{\partial x_j}(\rho \bar{u}_i \bar{u}_j) = -\frac{\partial \bar{p}}{\partial x_i} + \frac{\partial}{\partial x_j}\left[(\mu + \mu_t)\left(\frac{\partial \bar{u}_i}{\partial x_j} + \frac{\partial \bar{u}_j}{\partial x_i}\right)\right] - \rho\overline{u_i' u_j'} \tag{2}$$

$$\frac{\partial}{\partial t}(\rho c\overline{T}) + \frac{\partial}{\partial x_j}(\rho \bar{u}_i \overline{T}) = \frac{\partial}{\partial x_j}\left[(\Gamma + \Gamma_t)\left(\frac{\partial \overline{T}}{\partial x_j}\right)\right] \tag{3}$$

$$-\rho\overline{u_i' u_j'} = (\mu_t)\left(\frac{\partial u_i}{\partial x_j} + \frac{\partial u_j}{\partial x_i}\right) \tag{4}$$

$$\frac{\partial}{\partial t}(\rho k) + \frac{\partial}{\partial x_i}(\rho k \bar{u}_i) = \frac{\partial}{\partial x_j}\left[\left(\mu + \frac{\mu_t}{\sigma_k}\right)\frac{\partial k}{\partial x_j}\right] + G_k - \rho\varepsilon \tag{5}$$

$$\frac{\partial}{\partial t}(\rho \varepsilon) + \frac{\partial}{\partial x_i}(\rho \varepsilon \bar{u}_i) = \frac{\partial}{\partial x_j}\left[\left(\mu + \frac{\mu_t}{\sigma_\varepsilon}\right)\frac{\partial \varepsilon}{\partial x_j}\right] + C_{1\varepsilon}\frac{\varepsilon}{k}G_k - C_{2\varepsilon}\rho\frac{\varepsilon^2}{k} \tag{6}$$

The default values of the Fluent program are based on the constants C_1 and C_2 given in Equation 6.

Numerical method and boundary conditions

The creation of the two-dimensional numerical model and the division into cells were carried out with the Gambit program. Triangular elements were preferred for the mesh process. The number of cells where the solutions are independent of the element numbers was determined. For this reason, Nusselt numbers were calculated for different element numbers. As a result of this calculations, it was decided that 125624, 128450 and 127678 element numbers are sufficient for the hybrid channel without winglets, the hybrid channel with V-type winglets and the hybrid channel with Y-type winglets, respectively.

The numerical study was carried out using the Computational Fuid Dynamics (CFD) based ANSYS Fluent program [22]. The standard k-ε turbulence model was used as the viscous flow model. Conservation equations were discretized with the finite volume approach and the velocity-pressure relationship was handled with the SIMPLE algorithm. The

second order upwind scheme was used to discretize the equations. A value of 10^{-7} was set for all equations as the convergence criterion.

Water was used as the working fluid. The fluid enters the channel an uniformly at U velocity and T_o=300 K. The velocity of the fluid was calculated by Re. In the study, Re varies in the range of 4000≤Re≤10000. The corrugated channel surfaces (L_2) were kept constant at T_w=380 K and the non-slip wall feature was defined for the corrugated surfaces. Straight sections at the entrance and exit of the channel had adiabatic and non-slip conditions. The winglets were assumed to be adiabatic and non-slip.

Data reduction

The Reynolds number (Re) is calculated by Equation (7):

$$\mathrm{Re} = \frac{\rho U D_h}{\mu} \tag{7}$$

where, D_h is the hydraulic diameter, ρ is the density, μ is the dynamic viscosity, and U is the velocity.

Nusselt number (Nu) was used in heat transfer calculations. The average Nu is obtained by Equation (8):

$$\mathrm{Nu} = \frac{h D_h}{k_f} \tag{8}$$

where, k_f and h are thermal conductivity coefficient and convective heat transfer coefficient, respectively. The average convective heat transfer coefficient is found by Equation (9):

$$h = \frac{q''}{A_s \Delta T_{log}} \tag{9}$$

where, q" represents heat flux, ΔT_{log} shows logarithmic temperature difference, A_s is heat transfer area.

To determine the effect of the winglets on the heat transfer, the heat transfer performance (η) is described with Equation (10).

$$\eta = \frac{Nu_w}{Nu_s} \tag{10}$$

where, Nu_w and Nu_o represent the average Nusselt numbers obtained in the hybrid channel with winglets and the hybrid channel without winglets, respectively.

The friction factor (f) calculated depending on the pressure drop in the duct is given by Equation (11):

$$f = \frac{2\Delta P D_h}{\rho U^2 L} \tag{11}$$

Relative friction factor (f_w/f_o) was obtained by Equation (12):

$$f_{rel} = \frac{f_w}{f_o} \tag{12}$$

where, f_w and f_o are the average friction factors obtained in the hybrid channel with winglets and the hybrid channel without winglets, respectively.

The ratio of the heat transfer performance obtained in the channel to the relative friction factor is defined as the thermohydraulic performance factor (THPF) and is shown by Equation (13):

$$\mathrm{THPF} = \frac{\mathrm{Nu_w/Nu_o}}{(\frac{\mathrm{f_w}}{\mathrm{f_o}})^{1/3}} \quad (13)$$

The thermohydraulic performance factor (THPF) determines the improvement in heat transfer together frictions within the duct. For this, the hybrid channel without winglet is considered as a reference. The THPF of two different winglet geometries (V-type and Y-type) was compared according to the hybrid channel without winglet.

3. Results and Discussions

To validate the numerical solutions, this study was compared with previous studies (Zontul et al. [23]). Zontul et al. [23] numerically and experimentally investigated the flow and heat transfer properties in a rectangular corrugated channel and a smooth channel with the same hydraulic diameter (D_h=18mm). The results of this study and Ref. [23] were presented in Figure 2.

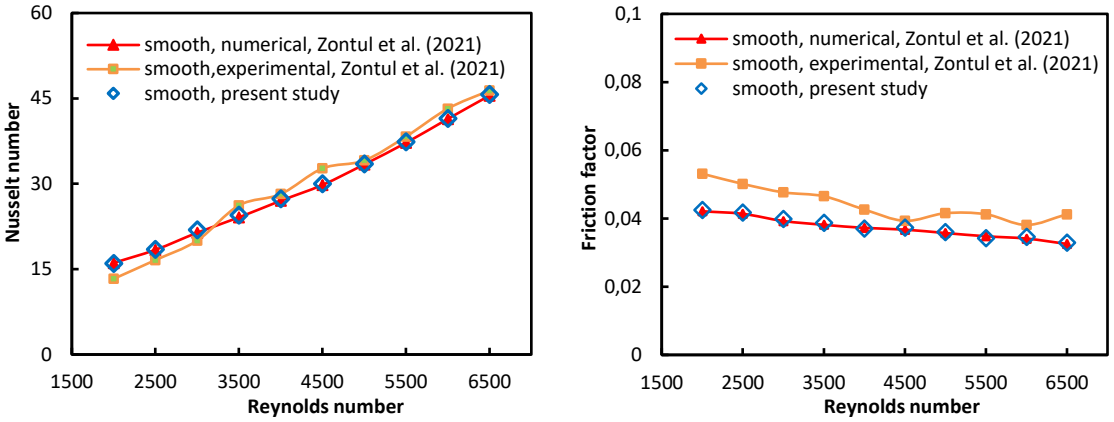

a **b**

Figure 2. Validation of the numerical study with previous studies [23], (a) Nu with Re, (b) Friction factor with Re

In this section, the effects of two different winglet designs (V-type and Y-type) in a hybrid channel were investigated for different Re (4000≤Re≤10000). At the same time, flow and temperature fields were obtained at different Re for two different winglet designs in the hybrid channel. The results were compared with the hybrid channel without winglet.

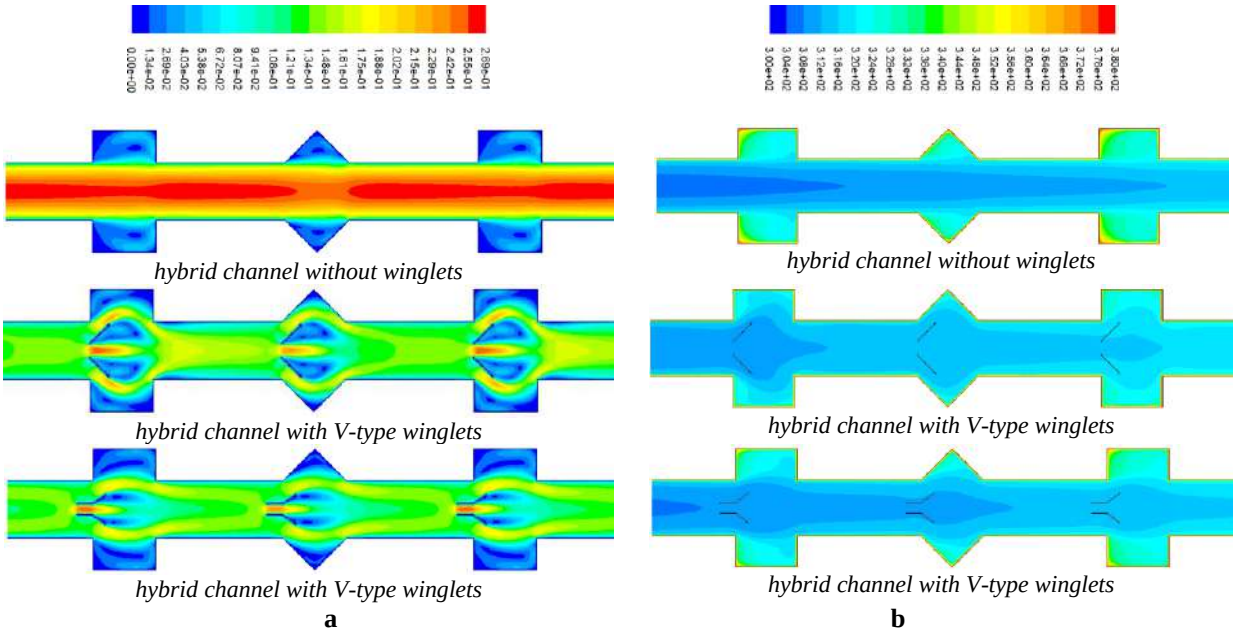

a **b**

Figure 3. Velocity contours (a), and temperature contours (b) for all channel flows at Re=4000

Velocity contours (Fig.3a) and temperature contours (Fig.3b) of the hybrid channels with/without winglets are given in Fig. 3 at Re=4000. In the hybrid channel without winglet, the main flow moves parallel to the duct axis, creating flow loops in corrugated cavities. These flow loops play an important role in lowering the surface temperature by carrying the colder fluid from the channel center to the hot channel surfaces. In the hybrid channel with V-type winglets, the main flow is divided into three branches. The winglet pairs guide the cold fluid layer at the center of the channel into the corrugated cavities. The flow separated by the winglets then merges with the flow passing between the winglet pairs. In the hybrid channel with Y-type winglets, the main flow is again divided into 3 branches and it is observed that this flow converges at a longer distance. It is seen that the fluid penetrates the corrugated cavities better in the V-type winglets. The presence of reverse flow loops in corrugated cavities is observed in both winglet designs. Fig. 4b shows the temperature fields for all channel flows at Re=4000. It is seen that the highest surface temperatures in the channel are in the hybrid channel without winglets. A significant decrease in surface temperatures was observed with the addition of winglets. Especially in the hybrid channel with V-type winglets, the wall temperatures are lower than in other cases. Fig.3 shows that the winglets added into the channel highly affect the flow and temperature fields.

Velocity contours (Fig.4a) and temperature fields (Fig.4b) of the hybrid channels with/without winglets at Re=10000 were presented in Fig. 4. Flow phenomena occurring in Fig. 3a were also seen in Fig. 4a. Inertia forces and mass transfer in the channel increased with increasing flow velocity. It was observed that the flow loops occurring within the corrugated cavities are enlarged (Fig. 4a). These flow cycles caused the displacement of the colder fluid coming from the channel center with the hot fluid near the wavy surfaces, thus reducing the temperature of the corrugated channel surfaces. The lowest wall temperature was observed in the case of V-type winglets. Fig. 4 shows that flow and temperature fields were highly affected by the Re in the hybrid corrugated channels.

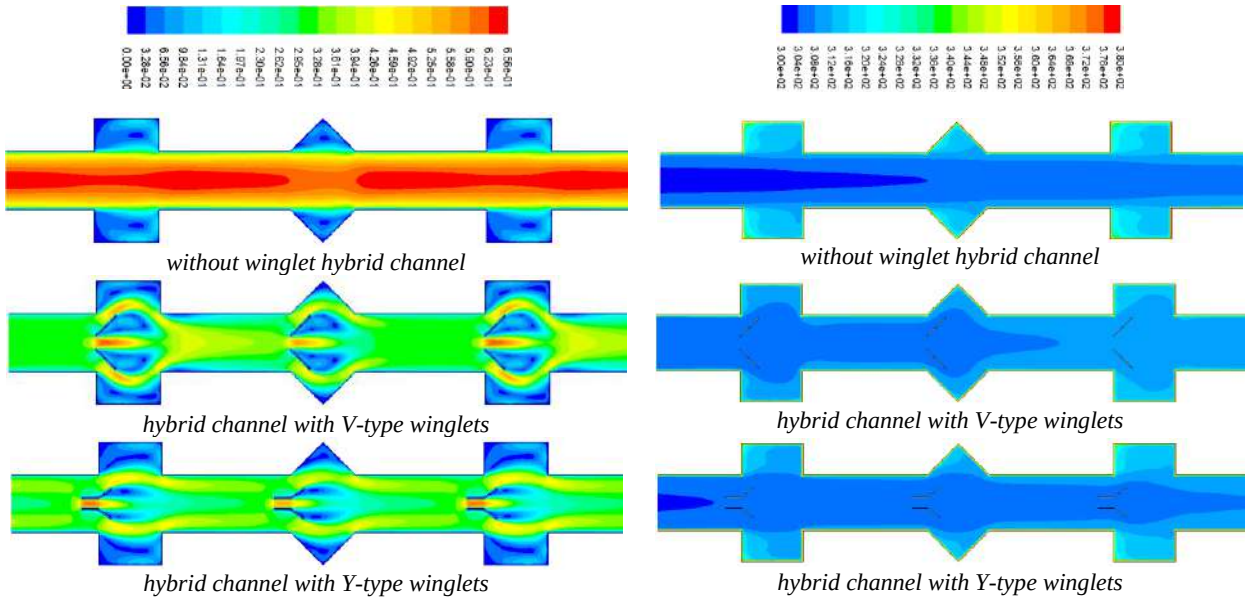

Figure 4. Velocity contours (a), and temperature contours (b) for all channel flows at Re=10000

Figure 5 shows the variation of Nusselt number (a), heat transfer performance, (b), friction factor (c), and THPF (d) with Re for all channel flows. In Fig.5a, the Nu increase with Re in all channel flows. The Nu was found the higher in the channels with Y-type and V-type winglets than in the without winglet case. The highest Nu was obtained as Nu=93.21 at Re=10000 in the V-type winglets. The heat transfer performance in the V-type winglets was higher than in the Y-type winglets (Fig.5b). Compared to the hybrid channel without winglets, the highest heat transfer performance was obtained in the V-type winglet case as η=1.50 at Re=10000. In Fig. 5c, the friction factor decreases with Re for all channel cases. The highest friction factor was obtained in the case of V-type winglets. Y-type winglets provided lower friction factor than V-type winglets. The pressure drop is higher because the V-type winglets block

the flow area. In Fig. 5d, THPF values increased with Re in all channel cases. Although the highest heat transfer performance was obtained with V-type winglets, THPF was obtained lower than Y-type winglets due to the increased friction factor. The higher THPF were obtained due to less pressure drop in Y-type winglets. The highest THPF was calculated as THPF=1.07 at Re=10000 in the Y-type winglets.

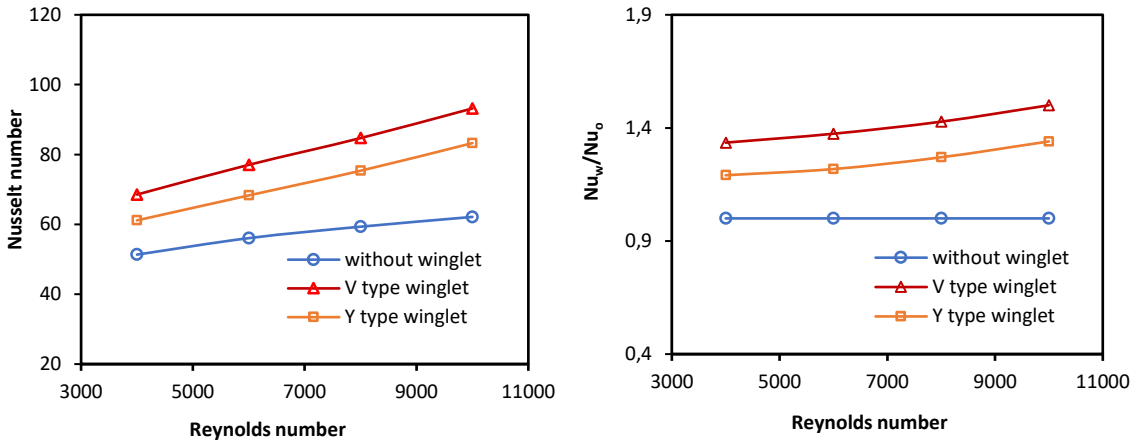

a **b**

Figure 5. (a) Nusselt number, (b) Heat transfer performance, (c) Friction factor, (d) THPF with Re

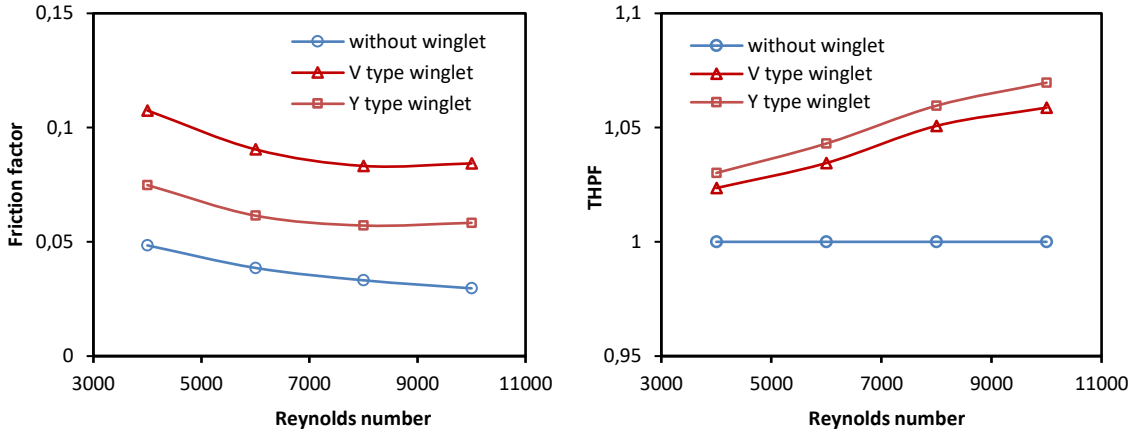

c **d**

Figure 5. (a) Nusselt number, (b) Heat transfer performance, (c) Friction factor, (d) THPF with Re (Continue)

4. Conclusion

In the numerical study, the effects of two different winglets designs on the thermo-hydraulic performance in hybrid corrugated channels were investigated numerically. Velocity and temperature contours were obtained at different Re for all studied channel flows. According to the findings, channel geometry, winglets design and Re significantly affected the flow and heat transfer. The winglets added to the corrugated channel significantly increased the heat transfer with an increase in the pressure drop. The highest Nu was obtained as Nu=93.21 at Re=10000 in the channel with V-type winglets. Heat transfer performance was higher in the V-type winglet case than in the Y-type winglet case. Compared to the hybrid channel without winglets, the highest heat transfer performance was obtained as 1.50 at Re=10000 in the V-type winglet case. The highest friction factor was obtained in the case of V-type winglet case. The highest THPF was calculated as THPF=1.07 at Re=10000 in the Y-type winglet case.

5. References

[1] Zhang F, Bian Y, Liu Y, Pan J, Yang Y, Arima H. “Experimental and numerical analysis of heat transfer enhancement and flow characteristics in grooved channel for pulsatile flow”. International Journal of Heat and Mass Transfer, 141, 1168-1180, 2019.

[2] Tokgoz N, Ozbolat V, Sahin B. “Investigation of heat transfer enhancement by using Al_2O_3/water nanofluid in rectangular corrugated channel”. KSU Journal of Engineering Sciences, 19(2), 2016.

[3] Alnak Y. “Üçgen biçimli kanatçık yüzeylerde ısı geçişinin nümerik olarak incelenmesi”. Muş Alparslan Üniversitesi Mühendislik-Mimarlık Fakültesi Dergisi, 3(1): 37-49, 2022.

[4] Akçay S. “Investigation of thermo-hydraulic performance of nanofluids in a zigzag channel with baffles”. Adıyaman Üniversitesi Mühendislik Bilimleri Dergisi, 15, 525-534, 2021.

[5] Mohammed HA, Al-Shamani AN, Sheriff JM. “Thermal and hydraulic characteristics of turbulent nanofluids flow in a rib–groove channel”. International Communications in Heat and Mass Transfer, 39, 1584-1594, 2012.

[6] Ahmed MA, Yusoff MZ, Shuaib NH. “Effects of geometrical parameters on the flow and heat transfer characteristics in trapezoidal-corrugated channel using nanofluid”. International Communications in Heat and Mass Transfer, 42, 69-74, 2013.

[7] Behzadnia H, Jin H, Najafian M, Hatami M. “Investigation of super-critical water-based nanofluid with different nanoparticles (shapes and types) used in the rectangular corrugated tube of reactors”. Alexandria Engineering Journal, 61, 2330-2347, 2022.

[8] Hassani SM, Khoshvaght-Aliabadi M, Feizabadi A, Rehman S, Alimoradi A. “Experimental and numerical analysis of curved turbulators in different arrangements through a rectangular channel”. Experimental Heat Transfer, 35(1): 22-44, 2020.

[9] Naphon, Paisarn, Kirati Kornkumjayrit. "Numerical analysis on the fluid flow and heat transfer in the channel with V-shaped wavy lower plate". International Communications in Heat and Mass Transfer, 35(7), 839-843, 2008.

[10] Deylami HM, Amanifard N, Sanaei M, Kouhikamali R. "Numerical investigation of heat transfer and pressure drop in a corrugated channel". International Journal of Engineering, 26(7), 771-780, 2013.

[11] Özbolat V, Şahin B. "Flow characteristics and heat transfer enhancement of sinusoidal corrugated channels with different configurations". Çukurova Üniversitesi Mühendislik Fakültesi Dergisi, 37(1), 93-107, 2022.

[12] Sabaghan A, Edalatpour M, Moghadam MC, Roohi E, Niazmand H. "Nanofluid flow and heat transfer in a microchannel with longitudinal vortex generators: two-phase numerical simulation". Applied Thermal Engineering, 100, 179-189, 2016.

[13] Nezaket P, Çelik H, "Kanatçık geometrisinin ısı geçişine etkisinin parametrik incelenmesi". International Journal of Multidisciplinary Studies and Innovative Technologies, 2(2), 25-29, 2018.

[14] Modi, Ashish J., and Manish K. Rathod. "Comparative study of heat transfer enhancement and pressure drop for fin-and-circular tube compact heat exchangers with sinusoidal wavy and elliptical curved rectangular winglet vortex generator". International Journal of Heat and Mass Transfer, 141, 310-326, 2019.

[15] Qureshi MZA, Ali K, Iqbal MF, Ashraf M, Ahmad S. "Intensification of heat transfer of a wavy channel with a series of detachable vortex generators; Numerical analysis with RANS model modification". The European Physical Journal Plus, 137(6), 718, 2022.

[16] Akcay S, "Numerical analysis of heat transfer improvement for pulsating flow in a periodic corrugated channel with discrete V-type winglets". International Communications in Heat and Mass Transfer, 134, 105991, 2022.

[17] Li Z, Gao Y. "Numerical study of turbulent flow and heat transfer in cross-corrugated triangular ducts with delta-shaped baffles". International Journal of Heat and Mass Transfer, 108, 658-670, 2022.

[18] Sun Z, Zhang K, Li W, Chen Q, Zheng N. “Investigations of the turbulent thermal-hydraulic performance in circular heat exchanger tubes with multiple rectangular winglet vortex generators”. Applied Thermal Engineering, 168, 114838, 2020.

[19] Promvonge P, Promthaisong P, Skullong S. “Experimental and numerical heat transfer study of turbulent tube flow through discrete V-winglets”. International Journal of Heat and Mass Transfer, 151, 119351, 2020.

[20] Akcay S, Akdag U, “Effect of baffle angles on flow and heat transfer in a circular duct with nanofluids”. International Advanced Researches and Engineering Journal, 6(3), 176-185, 2022.
[21] Akçay S. “Numerical analysis of hydraulic and thermal performance of Al_2O_3-water nanofluid in a zigzag channel with central winglets”. Gazi University Journal of Science, 36 (1), 383-397, 2023.
[22] ANSYS Inc., ANSYS Fluent User Guide & Theory Guide- Release 15.0, USA, 2015.
[23] Zontul H, Hamzah H, Kurtulmuş N, Şahin B. “Investigation of convective heat transfer and flow hydrodynamics in rectangular grooved channels”. International Communications in Heat and Mass Transfer, 126, 105366, 2021.

International Conference on Advances and Innovations in Engineering

Meso-Mechanic Analysis of Laminated Composites Reinforced with Aluminum Mesh

Kubranur Isgor Alev[1], Mete Onur Kaman[2], Cenk Yanen [3], Mustafa Albayrak [4]

[1]Public Procurement Institution, Ankara, Turkey
[2,3]Department of Mechanical Engineering, Faculty of Engineering, Firat University, Elazig, Turkey
[4]Department, Faculty, University, Province, Country. Department of Machine and Metal Technologies, Malatya Organized Industrial Zone Vocational School, Inonu University, Malatya, Turkey
[1]isgorkubranur@gmail.com, [2]mkaman@firat.edu.tr, [3]cyanen@firat.edu.tr, [4]mustafaalbayrak@inonu.edu.tr

[1](ORCID: 0000-0002-7775-1684), [2](ORCID: 0000-0003-0178-6079), [3](ORCID: 0000-0002-5092-8734),[4](ORCID: 0000-0002-2913-6652)

Abstract

In this study, meso-mechanic analysis is achieved for laminated composites reinforced with aluminum wire mesh. Woven glass fiber and epoxy matrix are used as laminated composite. Models of the composites are obtained in the Solidworks program. Then, these models are sent to Ansys Workbench finite element program. Periodic boundary condition and displacement are applied to the cutting surfaces of the model. At the end of the analysis, reaction forces calculated. To verified the analysis, experimental results from literature are compared with numerical analysis. There is a 90.6% consistency between the experimental and numerical results in terms of reaction forces.

Keywords: Meso-mechanics, wire mesh, aluminum, laminated composite

1. Introduction

Recently, the use of laminated composites has increased significantly in airframe manufacturing, automobile parts, renewable energy and aerospace applications. Properties such as ease of manufacture, high strength, and relatively low cost make laminated composites prominent [1–3]. Epoxy resins are the most preferred matrix material in composite production due to their high strength, excellent adhesion, effective electrical insulation and low cost. Glass fibers are widely used as fiber materials due to their low cost, high strength and impact resistance. Hybrid composites are produced by combining metal materials into composite layers to increase the durability of composite materials.

Woven wire mesh is a metallic fabric with significant advantages over conventional metal sheets, such as light weight, unique mechanical and thermal properties, and multifunctional application potential. Woven wire meshes are increasingly used in many engineering applications, including impact resistant structures [4], hybrid composite [5, 6], concrete reinforcements [7]. Metal wire mesh reinforced laminated composites consist of composite and metal layers that are bonded together using a suitable bonding process. They combine the benefits of composites and metal alloys while avoiding the disadvantages of each alone. Stainless steel and aluminum, which the most commonly used materials as wire mesh reinforcement, are widely used due to their good mechanical properties such as high tensile strength, exceptional fatigue and impact resistance [8–11].

Liu et al. investigated the double-point low-velocity impact and compression-after-double-impact behavior of stainless steel wire meshes reinforced with glass fiber reinforced polymer laminates [12]. Prakash and Julyes investigated the mechanical properties of hybrid composite materials reinforced with silane-treated E-glass fiber, Aluminum and stainless steel wire meshes [13]. Wang et al. investigated the dynamic mechanical response of steel wire mesh subjected to low velocity impact loading both experimentally and numerically using a finite element model

[1]Corresponding author

[14]. Sadoun et al. tried to improve the strength of E-glass fiber/epoxy composite using aluminum wire mesh [1]. Megahed et al. fabricated glass fiber epoxy composites with aluminum wire mesh using hand lay-up technique [8]. Alev investigated the effect of wire mesh reinforced laminated composites on the strength of the composite under in-plane and out-of-plane loads. For this purpose, glass and aluminum wire mesh layers were placed between woven glass fiber fabrics and their mechanical properties were determined [15].

Finite element modeling is a critical tool to investigate the response of wire mesh under impact loading. It is difficult to visualize the propagation of stress waves along the wires and to observe the complex interactions of the wires. Once the validity of the finite element model is verified, it can replace mechanical testing to some extent, which can save a lot of time and expense. However, the complex architecture of the wire mesh and the various deformation mechanisms of the wires make modeling the wire mesh a challenging task.

This study aims to investigate the reaction forces of laminated composite reinforced with aluminum wire mesh material using numerical methods. For this purpose, the finite element method wire mesh model was developed using ANSYS workbench and the simulation results were compared with the experimental data in the literature.

2. Materials and Method

In this study, laminated composite materials reinforced with aluminum wire mesh were modeled in Solidworks program. In order to be able to compare with the literature, Aluminum wire meshes were modeled in three dimensions, as shown in Figure 1, with 35 spaces per cm^2 in their actual dimensions. The diameter of the wires of the metal mesh is 0.5 mm.

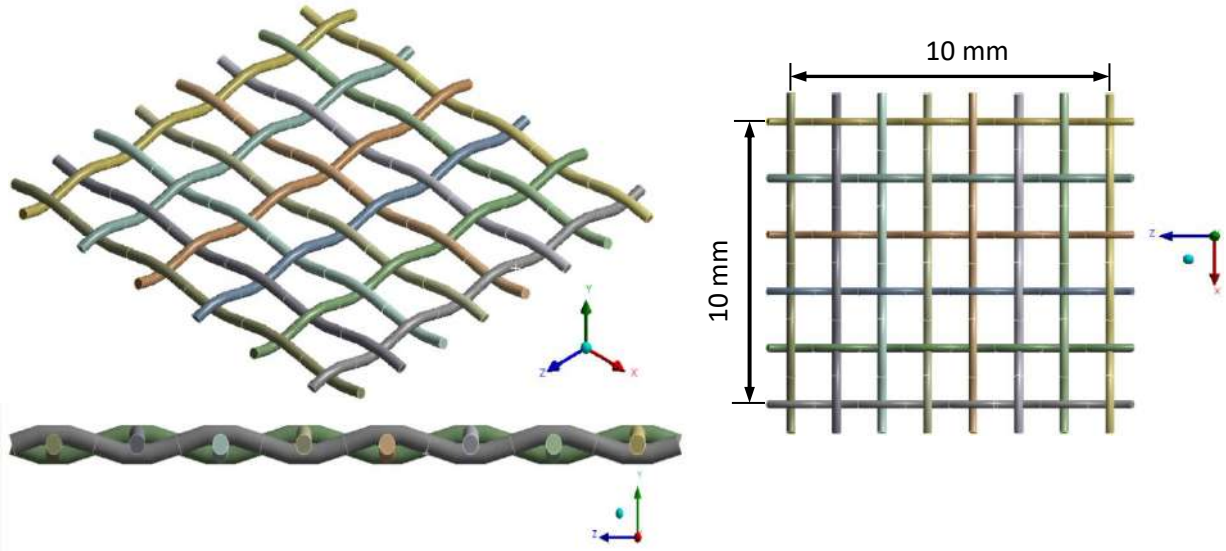

Figure 1. Aluminum wire mesh model

In this study, the material selection process was carried out according to the requirements of meso-mechanical analysis using the finite element method. Commonly used laminated composite and aluminum wire mesh were selected. Glass fiber and epoxy matrix were used as laminated composite. These materials have been preferred because they are widely used in various industries such as aerospace, aerospace technologies and automotive, where composite materials are widely used. Among the selected materials, Aluminum was used from the Ansys library, and the mechanical properties of the glass fiber epoxy composite are given in Table 1.

Table 7. Mechanical properties of glass fiber/epoxy composite [16]

Parameter	Property	Values
E_1 and E_2 (MPa)	Elastic modulus for 1 and 2 directions	20817
E_3 (MPa)	Elastic modulus for 3 directions	6000
G_{12} (MPa)	Shear modulus for $1-2$ plane	5001
G_{13} and G_{23} (MPa)	Shear modulus for $1-3$ and $2-3$ plane	3653
ν_{12}, ν_{23} and ν_{31}	Poisson's ratios for $1-2$, $2-3$ and $3-1$ plane	0.16

Finite element method (FEM) was preferred to perform the meso-mechanic analysis. ANSYS software package program was used for generate and solve finite element models. FEM analysis used a 3D approach to realistically capture the reaction forces in meso-mechanic analysis. The prepared model consists of two plates with a length and width of 12.1 mm and a thickness of 1.55 mm, bonded to each other the condition of bonded contact. The same materials were used for the upper and lower plates in the analysis. Aluminum wire mesh is bonded into glass fiber epoxy composite plates using bonded contact condition. The schematic view of the model is given in Figure 2.

In order to obtain reliable and accurate results in finite element analysis, an accurate mesh is extremely important. In this study, the mesh generation process was carefully performed to ensure the best representation of glass fiber and aluminum wire meshes. Hex20 elements were used as element type in the model and a total of 269260 nodes and 58496 elements were obtained. The mesh element quality was excellent at 99.4% on average for all elements (Figure 3).

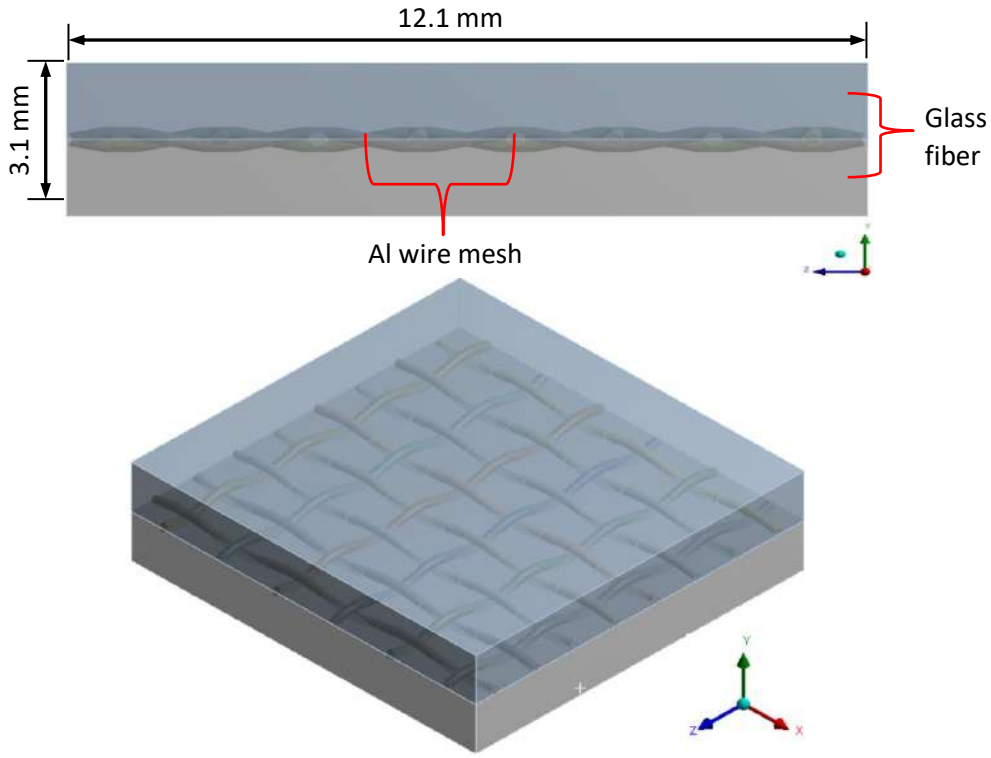

Figure 2. Schematic view of the model

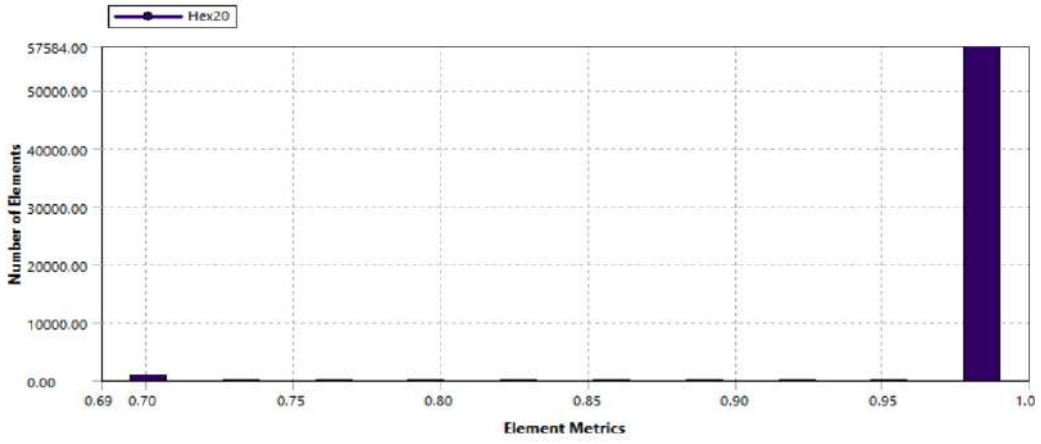

Figure 3. Element quality graph of mesh structure

As an initial condition, 2 Remote Points were defined on the opposite edges of the plate and 0.03025 mm displacement obtained from the literature was applied from the surfaces where Remote Point 2 is located. The schematic view of the model with the boundary conditions applied is given in Figure 4. In addition, the Constraint Equation given in Equation 1 is defined for the model.

$$\mathbf{0} = \mathbf{1}(\mathbf{1}/\boldsymbol{mm}) * \boldsymbol{Remote\ point}\ (\boldsymbol{Z\ Displacement}) + \mathbf{1}(\mathbf{1}/\boldsymbol{mm})\ \boldsymbol{Remote\ point}\ \mathbf{2}\ (\boldsymbol{Z\ Displacement}) \quad (1)$$

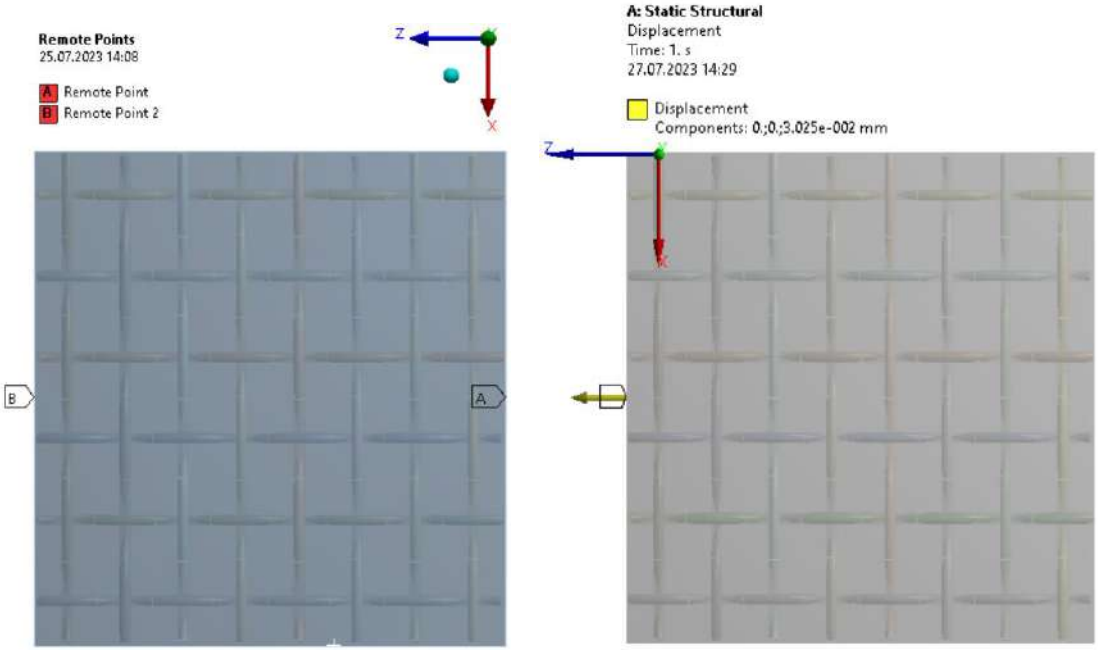

Figure 4. Initial and boundary conditions of the model

3. Results

In this chapter, the results and implications of meso-mechanic analysis of glass fiber epoxy laminated composites reinforced with aluminum wire mesh will be discussed. It will focus on the reaction forces obtained based on the displacement quantities obtained from an experimental study in the literature.

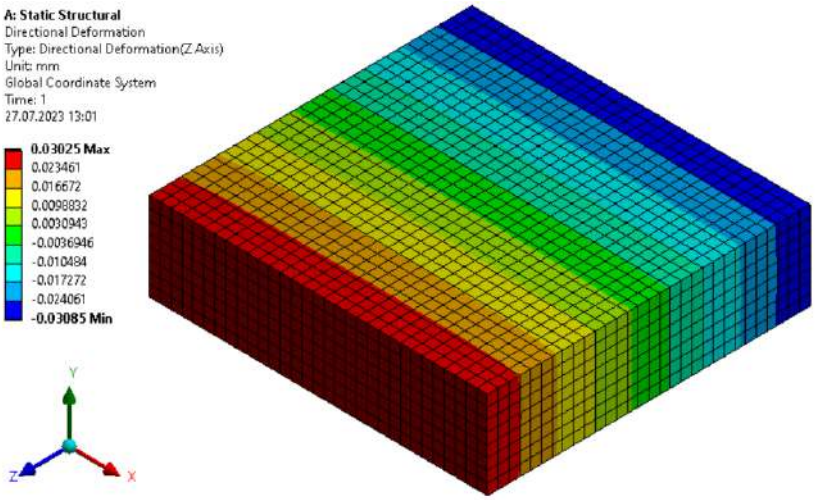

Figure 5. Directional deformation of specimen

After solving the finite element models, a comprehensive post-processing and consequence analysis was performed to gain insight into the reaction force. The results obtained were thoroughly analyzed in terms of directional deformation and reaction force values. Visualization tools and graphical representations were used to facilitate a comprehensive understanding of the analysis results. Figure 5 and Figure 6 show the directional deformation and reaction force of the specimen after analysis, respectively.

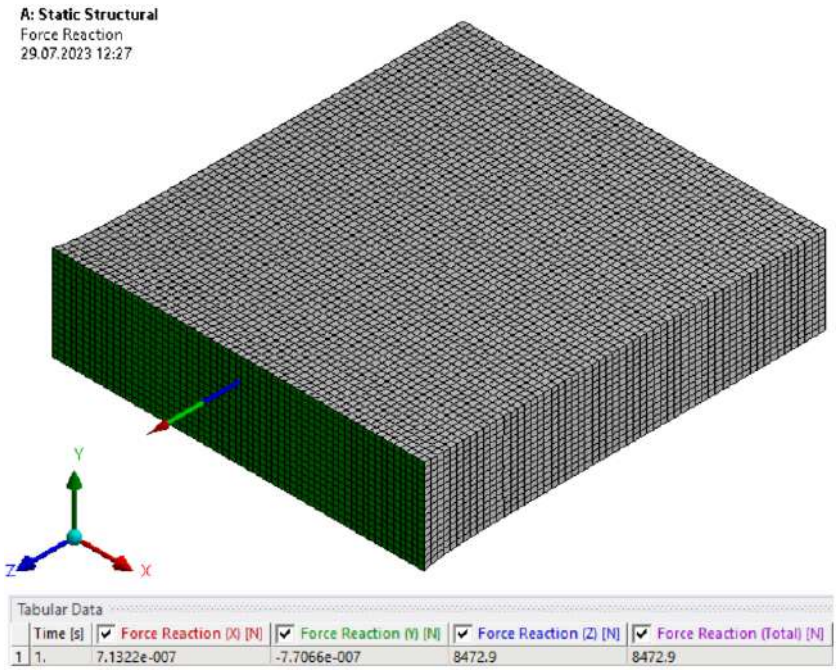

Figure 6. Reaction force of specimen

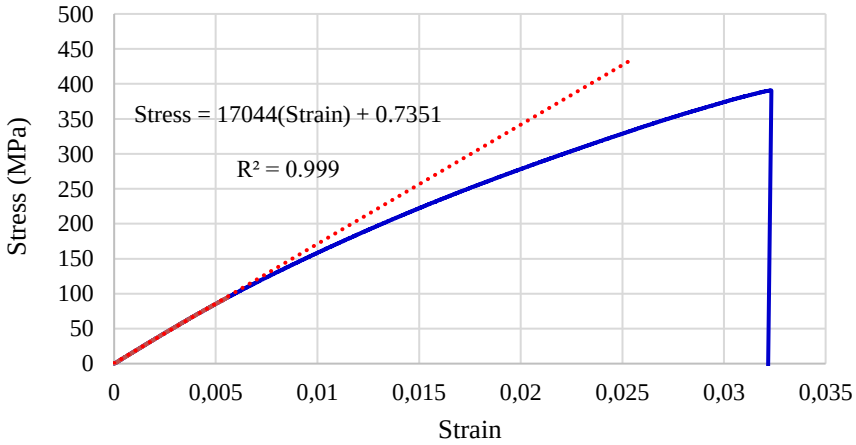

Figure 7. Experimental stress-strain graph of glass fiber composite reinforced with aluminum mesh

The stress-strain graph of the aluminum reinforced glass fiber laminated composite is given in Figure 7. Vacuum infusion method was used in the production of the composite. Details of composite fabrication can be taken from the Alev [15] study. Accordingly, the modulus of elasticity of the material is 17044 MPa. Since linear material properties are used in the numerical analysis, the strain value ε=0.0055798 at the end point of linearity is used in the graph. As a result, a displacement of 0.03025 mm in the $-z$ and $+z$ axis is entered as a load for the 12.1 mm long model (Figure 5). On the other hand, the reaction force obtained is 8472.9 N in total, which is half of this value for each section in

the $-z$ and $+z$ axis (Figure 6). Therefore, the total stress obtained numerically was obtained as 109.9 MPa. The approximation rate to the experimental results is 9.4%. One of the parameters affecting the result here is the use of ideal dimensions in the numerical model of the mesh structure. However, there may be partial shears in the geometry of the mesh structure in the production made by vacuum infusion method. In addition, the interface properties of aluminum wire and composite can also affect the result. Because the matrix ideally spreads at the interface, it is assumed that the aluminum wire and the composite bonded perfectly. However, there may be areas where the wires are not partially bonded during the production phase.

As a result, meso-mechanical analysis may be a preferable method in modeling the mechanical behavior of composites with complex internal structures. It is possible to perform multiple analyzes and get more realistic results by switching to macro-mechanical analysis, especially according to the results to be obtained in this step.

4. References

[1] Sadoun AM, El-Wadoud FA, Fathy A, et al. "Effect of through-the-thickness position of aluminum wire mesh on the mechanical properties of GFRP/Al hybrid composites." J Mater Res Technol 15:500–510, 2021.

[2] Karunagaran N, Rajadurai A. "Effect of surface treatment on mechanical properties of glass fiber/stainless steel wire mesh reinforced epoxy hybrid composites." J Mech Sci Technol 30:2475–2482, 2016.

[3] Megahed M, Fathy A, Morsy D, Shehata F. "Mechanical Performance of glass/epoxy composites enhanced by micro- and nanosized aluminum particles." J Ind Text 51:68–92, 2021.

[4] Wang C, Shankar K, Fien A. "Finite element simulation of impact response of wire mesh screens." EPJ Web Conf 94:1–6, 2015.

[5] Wan Y, Diao C, Yang B, et al. "GF/epoxy laminates embedded with wire nets: A way to improve the low-velocity impact resistance and energy absorption ability." Compos Struct 202:818–835, 2018.

[6] Truong GT, Tran H Van, Choi KK. "Tensile behavior of on- and off-axis carbon fiber reinforced polymer composites incorporating steel wire mesh." Mech Mater 137:103131, 2019.

[7] Liu J, Wu C, Li J, et al. "Numerical investigation of reactive powder concrete reinforced with steel wire mesh against high-velocity projectile penetration." Constr Build Mater 166:855–872, 2018.

[8] Megahed AA, Abd El-Wadoud F, Wagih A, Kabeel AM. "Effect of incorporating aluminum wire mesh on the notched and un-notched strengths of glass fiber/epoxy composites." Compos Struct 263:113695, 2021.

[9] Ahmed TJ, Bersee HEN, Beukers A. "Low velocity impact on woven glass compoistes reinforced with metal mesh layers." ICCM Int Conf Compos Mater 1–6, 2007.

[10] Thirumurugan A, Bhaskar GB, Poyyathappan K, et al. "Investigations on aluminium wire mesh, banana fiber and glass fiber reinforced hybrid composites." Indian J Sci Technol 9, 2016.

[11] Karunagaran N, Bharathiraja G, Muniappan A, Nanthakumar P. "Interlaminar shear strength behaviour of surface treated steel wire mesh/glass fibre reinforced hybrid composite laminate." Mater Today Proc 46:3993–3996, 2020.

[12] Liu Y, Wan Y, Zhou S, et al. "Experimental investigation on the compression-after-double-impact behaviors of GF/epoxy laminates embedded with/without metal wire nets." Case Stud Constr Mater 18:e01783, 2023.

[13] Prakash VRA, Jaisingh SJ. "Mechanical Strength Behaviour of Silane Treated E-glass Fibre/Al 6061 & SS-304 Wire Mesh Reinforced Epoxy Resin Hybrid Composite." Silicon 10:2279–2286, 2018.

[14] Wang C, Wang H, Shankar K, Hazell PJ. "Dynamic failure behavior of steel wire mesh subjected to medium velocity impact: Experiments and simulations." Int J Mech Sci 216:106991, 2022.

[15] Isgoralev K. Investigation of interfacial mechanical properties for layered composites reinforced with mesh wire. MSc Thesis Firat University, Elazıg, Turkey, 2023.

[16] Albayrak M. Investigation of impact behavior rubber reinforced composites with curved surfaces. PhD Thesis. Firat University, Elazıg, Turkey, 2022.

International Conference on Advances and Innovations in Engineering

A Review on Heat Shields

Muhammed Fatih Köseoğlu [1], Anıl Özkan [2], Nurullah Arslanoglu1,Fatih Karpat [4]

[1,2] Hünel Kalıp Sanayi ve Ticaret Ltd. Şti, Bursa, Turkey.

[3,4]Mechanical Engineering, Engineering Faculty, Bursa Uludag University, Bursa, Turkey.
[1]Fatih.Koseoglu@hunergroup.com.tr, [2] anil.ozkan@hunergroup.com.tr, [3]narslanoglu@uludag.edu.tr
[4] karpat@uludag.edu.tr

Abstract

One of the biggest problems in vehicle components is the overheating of the components and the negative effects of this situation. In order to eliminate this negative situation, elements called heat shields are used. Heat shields are elements used to prevent the heat generated by vehicle components from damaging other parts of the vehicle. It was thought that the Turkish literature on heat shield should be developed and academic studies should be done. For this reason, recent studies on heat shields have been examined. As a result, it is thought that this study will contribute to the Turkish literature and will provide a perspective to designers, researchers, manufacturers and companies working in the field of heat shields.

Keywords: Heat shield, review, vehicle components

1. Introduction

In this study, the recent studies on the application areas of heat shields in engineering and the determination of their mechanical and thermal properties are summarized. In particular, studies examining the use of heat shields in engine parts and their effects on engine performance, fuel consumption and emissions have been compiled. In addition, studies on the material properties of heat shields and their use in spacecraft and thermal systems are presented.

2.Application Areas of Heat Shields

Yaşar [1] investigated the effect of thermal barrier coatings on the performance of a diesel engine with turbocharger and intercooler. The surfaces of the combustion chamber of the experimental engine were insulated with zirconia-based ceramic materials using the plasma coating method, and the effect of thermal barrier coating on engine performance was investigated by operating the engine under different load and speed conditions. As a result, an improvement of 1% to 6% was observed in the specific fuel consumption of the engine as a result of the thermal barrier coating.

Bengi [2] examined the thermal conductivity of heat shields in his study. In the study, the effects of spray distance, powder size and plasma arc power on the thermal conductivity of the coating were investigated with the three-level Box-Behnken experimental design method.

Durmaz [3] calculated the effect of thermal insulation on surface temperatures in a turbojet engine used in aviation, verified with tests and produced a simple calculation tool and presented results.

Alchehabi [4] examined the effect of the heat shield on the performance of the motorcycle engine in his study. As a result of the experiments, the maximum engine torque of the engine covered with heat shield increased by 6,024% compared to the engine without heat shield. The average exhaust gas temperature difference of the engine with heat

[1] Corresponding author

shield coating increased by 34,875 ºC and 29,334% at 6000 rpm compared to the engine without heat shield coating. In addition, the engine's effective efficiency increased by a maximum of 5.89%, and the specific fuel consumption was decreased by a maximum of 5.82%.

The radiation heat transfer calculations [5] were conducted to compute the surface temperature of the turbocharger heat shield and the estimations were compared with the measurements.

Pereira et al. [6] developed a one-dimensional heat transfer model to predict the temperature distribution of a coated thermal barrier. The model takes into account the radiant heat flux from the flame front and convective heat fluxes from the heated combustion gases on one side, and convective heat transfer on the opposite side. To convert the analytical solution from the Laplace to the Fourier domain, a mathematical model utilizing a Padé Approximant was employed. The accuracy of the model was validated through numerical finite differences and an appropriate laboratory experimental setup. The results obtained from both validation schemes demonstrated good agreement. In the laboratory experiments, the heat transfer model accurately captured the thermal behavior of the barrier, with maximum absolute deviations of 14% on the heat source side and 8.7% on the opposite side.

Vo et al. [7] examined how the thickness of the thermal barrier coating and the presence of coolant affect the mainstream hot gas pressure ratio and temperature ratio in blade film cooling. The investigation involves simulating the conjugate heat transfer in the cooling blade of a W501F engine's first stage. A comprehensive blade design is employed to achieve an authentic heat transfer profile. The findings reveal comparable areas of high thermal stress in both the simulation and industrial models

Zhang et al [8] presented a comparative analysis and experimental evaluation of the performance of direct-flow coaxial evacuated-tube solar collectors with and without heat shields in terms of heat extraction. The study includes the development of a test system specifically designed to assess the thermal performance of medium-temperature solar collectors. The experimental findings demonstrate that the evacuated-tube solar collector exhibits superior performance when equipped with a heat shield, particularly at higher working temperatures. The solar collector with a heat shield achieved a collection efficiency of 54.70% at the highest inlet temperature of 123.9°C during the test period, which represents a 31.49% increase compared to the collector without a heat shield. Moreover, the heat-loss coefficient calculated for the evacuated-tube solar collector with a heat shield was 1.86 W/(m^2 K), indicating a significant improvement of 50.80% compared to the collector without a heat shield.

Veerasamy et al [9] investigated the tribological performance of thermal barrier coatings applied to engine liners, as well as the quality of the thermally treated coating. A multi-layer structure consisting of a top coat and bond coat is deposited on steel substrates of the same type. Heat treatments are employed to enhance the mechanical properties and hardness of both the substrate and the coating through the recrystallization of microstructures. Furthermore, heat treatments induce residual stresses resulting from varying thermal contractions and lattice misfits caused by microstructural changes. These stress factors may potentially lead to either premature failure or stress relaxation through the formation of new cracks.

Vadivel and Periyasamy [10] conducted a study on the influence of heat shields on engine performance and emission characteristics. The results demonstrated that heat shield led to a 10% improvement in thermal efficiency and a 9.8% reduction in fuel consumption compared to the engine without a heat shield. Additionally, the engine with a heat shield exhibited reduced emissions compared to the engine without one. Specifically, there was a decrease in smoke, carbon monoxide (CO), and hydrocarbon (HC) emissions in the heat shield-equipped engine compared to the baseline engine. However, it was noted that carbon dioxide (CO_2) and nitrogen oxide (NOx) emissions showed a partial increase in the heat shield-equipped engine.

Karlsson et. al [11] performed a computational fluid dynamics (CFD) study on the vehicle's underbody, effectively forecasting the thermal conditions in close correlation with experimental data. Additionally, they monitored the temperature of crucial components that were exposed to high convective and radiative heat flux. Among these critical components, the fuel tank was included. Conventional and composite heat shields were both employed beneath the fuel tank, and both installations successfully met the fuel tank's design specifications.

Ashmawey et al. [12] implemented an underbody cover with the intention of reducing environmental noise. Nonetheless, empirical evidence indicates that the underbody cover resulted in a reduction of approximately 6% in the airflow through the radiator.

Lam et al. [13] conducted computational fluid dynamics (CFD) simulations to assess the effectiveness of heat shields in minimizing the maximum temperature for engine components in the underhood region of a passenger vehicle. Their findings indicated that heat shields effectively lower the peak temperatures of the engine components.

Radiation part of heat transfer plays an crucial role in the underhood area of vehicles. Wendland [14] obtained that radiation heat transfer part is 30% of the total heat transfer in the engine manifold. Mao et al. [15] employed the net radiation enclosure model to compute the surface-to-surface radiation heat transfer.

The experimental investigation examined the impact of thermal barrier coated (TBC) surfaces on both the piston top and combustion chamber of a turbocharged diesel engine [16]. Satisfactory results were achieved using two types of coatings: TBC1, which coated the cylinder head and valves, and TBC2, which coated the cylinder head, piston top, and valves. In comparison to a standard diesel engine, the TBC-coated engines experienced a 2% increase in engine power, a 1.5-2.5% increase in engine torque, and a 4.5-9% decrease in brake specific fuel consumption (b.s.f.c.). However, it should be noted that the NOx emissions were found to be 10% higher in diesel engines with TBC coatings when compared to a standard diesel engine. Nonetheless, the application of TBC demonstrated a reduction in smoke emissions of up to 18%, as confirmed by the experimental studies.

The study aims to explore the impact of applying yttria- and alumina-stabilized zirconia coating on the piston head and cylinder lining of a single-cylinder diesel engine, along with its performance and emissions [17]. The study also investigates the utilization of varying amounts of nanoparticles of aluminum oxide as additives to diesel fuel, both in engines with and without the aforementioned coating. Remarkably, numerous metrics of the engines with the coating showed significant improvements as a result of this research. The brake thermal efficiency increased by 2.1 percent compared to a conventional uncoated diesel engine, while brake-specific consumption decreased by 3%, leading to a reduction in the emission of hazardous chemicals.

The latest advancements in Thermal Barrier Coating (TBC) pertain to engine performance, manufacturing, and associated challenges [18]. The implementation of TBC on the piston crown and valves, along with the use of diesel and Mahua Methyl Ester (MME) as a petroleum fuel, presents a promising avenue for sustainable development. In order to achieve this objective, a conventional Direct Injection (DI) diesel engine was upgraded to a Low Heat Rejection (LHR) engine by applying a 0.5 mm layer of $3Al_2O_3$-$2SiO_2$ (as TBC) on the piston crown and valves. The LHR engine utilizes MME as fuel, with a fuel injector pressure set at 200 bar for testing purposes. Comparative analysis with a standard DI diesel engine reveals that the utilization of TBC enhances brake thermal efficiency to 13.65% at 25% load. At full load, the LHR engine exhibits significant improvements in Specific Fuel Consumption (SFC) and Brake Thermal Efficiency (BTE) when using MME fuel. The combination of MME and diesel fuels with TBC results in lower exhaust gas temperatures. Notably, both MME with and without TBC demonstrate a substantial reduction in smoke density. Additionally, employing MME fuel with TBC exhibits a slight decrease in carbon monoxide emissions across all loads. Furthermore, it is evident that MME with TBC significantly reduces environmental hydrocarbon emissions under all load conditions.

2.2. Studies on Heat Shield Material Properties

Yuce and Ozel [19] investigated the thermal effects on the exhaust manifold through thermal analysis, focusing on the implementation of a 500µ ZrO_2-Y_2O_3 ceramic material coating. The investigation utilized ANSYS Fluent, a commercially available Computational Fluid Dynamics (CFD) software. The insulating capabilities of the low thermal conductivity coating were compared to an uncoated manifold. The findings demonstrated that the application of ZrO_2-Y_2O_3 substantially reduced the thermal loads on the manifold, leading to lower temperature values on the outer surface compared to the uncoated manifold.

.

Reznik et al.[20] devised techniques for forecasting the thermophysical and thermomechanical properties of carbon-ceramic composite materials utilized in aerospace craft structures' heat shields. These methods consider the material's anisotropy and internal microstructure by modeling the temperature and stressed-strained condition of representative elements within the material's volume.

Reghu et. [21] al are primarily concerned with the advancement of thermal barrier coatings (TBC) for aluminum-silicon (Al-Si) alloy castings, which are extensively utilized as automotive components such as cylinder blocks and pistons. The purpose of TBCs is to enhance combustion efficiency within diesel engine chambers, leading to improved performance and longevity of components. However, achieving a uniform coating thickness on intricate contours of automotive pistons is a globally recognized challenge, resulting in inconsistent thermal barrier properties across the non-uniform coating thickness. Coatings that lack uniformity in thickness are more likely to cause uneven thermal barrier effects throughout the TBC thicknesses, which directly impact engine performance and the lubrication system.

The temperature measurement of the piston at the point of maximum torque was conducted using the temperature plug method [22]. To address the issue of high temperatures and prevent failures, this study employed Ansys, a finite element analysis software, to examine the impact of varying ceramic coating thicknesses on the maximum temperature of the diesel engine's piston substrate. The ceramic coating comprised a 0.1 mm thick NiCoCrAlY bonding layer and an insulating layer of $La_2Zr_2O_7$ with thicknesses ranging from 0.2 mm to 0.9 mm. By increasing the ceramic coating thickness from 0.3 mm to 1.0 mm, the maximum temperature of the piston base decreased from 347.9 °C to 267.46 °C. These findings demonstrate that the application of a thermal-barrier coating effectively lowers the maximum piston temperature, significantly enhancing engine safety.

The primary objective of the study is to analyze the impact of clay coating on a cylinder in order to enhance thermal efficiency and reduce engine emissions [23]. In this study, a diesel engine's outer cylinder surface is coated with Zirconia material to a depth of 100 μm using the plasma-spray technique. The temperature distribution is then analyzed using the Limited Component Analysis method implemented through ANSYS. An experimental study is conducted to observe the changes in engine performance due to the influence of the tested coating material. The experimental setup is designed, and results are obtained for thermal efficiency, engine performance, and emissions. The obtained results are compared between an uncoated cylinder and one coated with Zirconia. Consistency between the experimental and analytical reports is confirmed, demonstrating the potential benefits of implementing this project in practical scenarios. Additionally, the project aims to transform a conventional engine into a low heat rejection (LHR) motor.

2.Conclusions

As a result, many studies have been done on heat shields and still continue to be done. Studies on the heat shield are concentrated in different areas. Studies have been carried out on the determination or development of material properties, the change of performance, fuel consumption and emissions of vehicles whose parts are covered with heat shields, as well as their use in space vehicles and thermal systems. The aim of this study is to create a guide for researchers who want to work on these issues in academia and industry.

5. References

[1] Yaşar H. Termal Bariyer Kaplamanın Türbo Doldurmalı Bir Dizel Motorunun Performansına Etkileri. Doktora Tezi, ITU, İstanbul, Türkiye, 1997.

[2] Bengi T. Termal Bariyer Kaplamalarının ısıl özelliklerinin incelenmesi ve düşük termal iletkenlik için parametre optmizasyonu. Yüksek lisans Tezi, ITU, İstanbul, Türkiye, 2009.

[3] Durmaz N. Yüksek Sıcaklık Bölgesindeki Havacılık Komponentlerinde Termal Bariyer Uygulaması. Yüksek lisans Tezi, ESOGÜ, Eskişehir, Türkiye, 2019.

[4] Alchehabi FH. Motorsiklet motorlarında termal bariyer kaplamanın motor performansı ve egzoz atık ısı geri kazanımına etkilerinin deneysel olarak incelenmesi. Yüksek lisans Tezi, DPÜ,Kütahya, Türkiye, 2023.

[5] Ayhan ÇE. Thermal Underhood Analysis of a Heavy Commercial Vehicle Using Open Source CFD Package OpenFOAM. Msc Thesis, Özyeğin University, Istanbul, Turkey, 2021.
[6] Pereira DJ, Viegas C, Panão MR. "Heat transfer model of fire protection fiberglass thermal barrier coated with thin aluminium layer". International Journal of Heat and Mass Transfer, 184,1-10, 2022.
[7] Vo DT, Mai TD, Kim B, Ryu J. "Numerical study on the influence of coolant temperature, pressure, and thermal barrier coating thickness on heat transfer in high-pressure blades". International Journal of Heat and Mass Transfer, 189, 1-22, 2022.
[8] Zhang X, You S, Ge H, Gao Y, Xu W, Wang M, He T, Zheng X. " Thermal performance of direct-flow coaxial evacuated-tube solar collectors with and without a heat shield". Energy conversion and management, 84, 80-87, 2014.
[9] Veerasamy SS, Manoharan C, Krishnaraj H, Lazar M. "Thermal barrier coating using yttria stabilized zirconia by plasma spray technique". Thermal Science, *26*, 871-882, 2022.
[10] Vadivel A, Periyasamy S. "Experimental investigation of thermal barrier (8YSZ-MGO-TIO2) coated piston used in diesel engine". Journal of Applied Fluid Mechanics, 13(4), 1157-1165, 2020.
[11] Karlsson R, Van Benthem P, Islam M. "Vehicle underbody thermal simulation using computational fluid Dynamics". SAE Technical Paper, 1999.
[12] Ashmawey M, Berneburg H, Hartung W, Werner, F. "A numerical evaluation of the thermal effects of the new V6 engine on the underhood environment of the 1993 Opel Vectra". SAE Transactions, 398-419, 1993.
[13] Lam SY, Shuaib NH, Hasini H, Shuaib NA. "Computational Fluid Dynamics investigation on the use of heat shields for thermal management in a car underhood". International Journal of Automotive and Mechanical Engineering, *6*, 785-796, 2012.
[14] Wendland DW. "Automobile exhaust-system steady-state heat transfer ". SAE technical paper, 1993.
[15] Mao S, Feng Z, Michaelides EE. "Off-highway heavy-duty truck under-hood thermal analysis". Applied Thermal Engineering, *30*(13), 1726-1733, 2010.
[16] Ciniviz M, Hasimoglu C, Şahin F, Salman MS. "Impact of thermal barrier coating application on the performance and emissions of a turbocharged diesel engine". Proceedings of the Institution of Mechanical Engineers, Part D: Journal of Automobile Engineering, 222(12), 2447-2455, 2008.
[17] Shaisundaram VS, Saravanakumar S, Balambica V, Sendil Kumar, D., Chandrasekaran, M., Muraliraja R, Muniappan A, Asres Y. "Effects of thermal barrier coating using various dosing levels of aluminium oxide nanoadditive fuel on diesel in compressed ignition engine". Journal of Nanomaterials, 2022.
[18] Vijay Kumar M, Srinivas Reddy T, Rami Reddy C, Rami Reddy SV, Alsharef M, Alharbi Y, Alamri B. (2022). "Impact of a Thermal Barrier Coating in Low Heat Rejection Environment Area of a Diesel Engine". Sustainability, 14(23), 1-15,2022.
[19] Yuce BE, Ozel S."Thermal Analysis of Ceramic Coated Exhaust Manifold". International Energy Days Conference, Sivas, Turkey,47-50, 4 October 2022
[20] Reznik SV, Prosuntsov PV, Mikhailovskii KV. "Prediction of thermophysical and thermomechanical characteristics of porous carbon–ceramic composite materials of the heat shield of aerospace craft. Journal of Engineering Physics and Thermophysics". 88, 594-601, 2015.
[21] Reghu VR, Mathew N, Tilleti P, Shankar V, Ramaswamy P. " Thermal barrier coating development on automobile piston material (Al-Si alloy), numerical analysis and validation". Materials Today: Proceedings, 22, 1274-1284, 2020.
[22] Fei C, Lei T, Qian Z, Shu, Z. "Piston thermal analysis of heavy commercial vehicle diesel engine using lanthanum zirconate thermal-barrier coating". Energies, *15*(12), 4225,2022.
[23] Moorthi SS, Kumar MV, Prakash M., Kumar RS, Muthuchari P, Haribabu K. "Effect of thermal barrier coating of piston on the performance of diesel engine". Materials Today: Proceedings. 2023.

International Conference on Advances and Innovations in Engineering

Comparison crushing performance of various types of 2-D auxetic structures by using topology optimization

Kerem GÜNAY[1] , Ülkü Asena TOSUN[2], Fatih USTA[3]

[1,2]Department of Mechanical Engineering, Gebze Technical University, Kocaeli, Turkey.
[3]Department of Aeronautical Engineering, Gebze Technical University, Kocaeli, Turkey.
[1]kerem.gunay2017@gtu.edu.tr, [2]uatosun@gtu.edu.tr, [3]fusta@gtu.edu.tr

[3](ORCID: 0000-0003-2433-7604)

Abstract

Auxetic materials with unique mechanical properties characterized by negative Poisson's ratio are important because of their potential applications in many engineering fields. This study proposes to compare the mechanical properties of auxetic and non-auxetic structures as a result of topology optimization and to improve their crushing performance. The length along the vertical and horizontal axis is selected 100x100 mm^2. The designs of auxetic structures (i.e., double arrowhead, re-entrant, and tetra-chiral) and non-auxetic structure(i.e., the hexagonal honeycomb), were created with thicknesses of 1, 2, and 3 mm. They consist of four-unit cells in the lateral direction and four unit cells in the vertical direction. As a result of the topology optimizations conducted within this scope, ideal designs have been determined for three different auxetic structures. Subsequently, experimental samples were produced using a 3D printer and compared with conventional models. These comparisons revealed that the tetra-chiral lattice model exhibited higher strength compared to the other designs. According to the experimental results, the optimal re-entrant model showed a 32.5% increase in the specific compressive strength parameter compared to the conventional model, and the optimal tetra-chiral model demonstrated a 27.8% increase in specific compressive strength and a 10.7% increase in the Specific Energy Absorption (SEA) value.

Keywords: Metamaterials, auxetic materials, topology optimization, compressive strength.

1. Introduction

Auxetic structures with their unique mechanical properties characterized by a negative Poisson's ratio, have attracted significant attention in recent years [1-9]. These structures distinguish them from conventional materials by exhibiting an unusual behavior in which they collapse laterally inward when subjected to a longitudinal compression load and expand laterally when subjected to a longitudinal tensile load. The remarkable mechanical response of auxetic structures has led to their exploration in diverse applications such as impact absorption, protective gear, and energy absorption systems.

The aerospace industry can benefit from the development of auxetic materials-based composites and related technologies [10-11]. These materials offer improved performance in areas such as impact resistance, failure resistance, energy absorption, structural health monitoring, and adaptive and deployable structures [12-16]. The combination of auxetic polymeric materials with other materials is advantageous for personal protective clothing or equipment, including items such as crash helmets, bulletproof vests, shin pads, knee pads, and gloves, owing to their exceptional energy absorption properties [17-18]. Biomedical applications include surgical implants, suture anchors, muscle/ligament anchors, and dental floss. Auxetic dental floss offers the ability to expand and adapt to varying gaps between human teeth while incorporating drug-release capabilities. Furthermore, auxetic polymeric materials show promise in hydrophones, electrodes in piezoelectric sensors, and other sensor applications due to their low bulk modulus, making them more sensitive to pressure. The versatility and potential of auxetic polymeric materials

[1]Corresponding author

continue to be explored across various sectors, presenting exciting opportunities for advancements and innovations in materials science and engineering.

2D auxetic structure designs have emerged as particularly promising for harnessing their mechanical advantages. The planar nature of 2-D auxetic structures makes them convenient to fabricate and integrate into existing systems, thereby enhancing their practicality for engineering applications. Furthermore, their two-dimensional geometry enables comprehensive investigation and evaluation of their mechanical response, making them ideal candidates for comparative analysis. In this study, we focus on comparing the crushing performance of three important 2D auxetic structure types and one non-auxetic structure type: hexagonal honeycomb, re-entrant, tetra-chiral and double arrowhead honeycomb structures. Through the application of topology optimization techniques, we aim to uncover the most efficient configuration among these structures in terms of compressive strength, energy absorption, load distribution, and deformation characteristics.

Topology optimization serves as a powerful computational methodology for the effective design and optimization of auxetic structures. By systematically searching for an optimal material distribution within a given design domain, topology optimization enables the discovery of efficient and novel configurations [19, 20]. Leveraging the power of computational algorithms, this methodology enables the exploration of a vast design space, leading to the identification of highly performant auxetic structures. The research methodology employed in this study involves the utilization of finite element analysis in conjunction with a topology optimization framework. By imposing appropriate constraints and objectives, we seek to identify the structural configurations that maximize energy absorption and compressive strength by reducing density, while ensuring structural integrity and manufacturability. Furthermore, we consider the influence of various material properties and loading conditions to comprehensively evaluate the performance of the selected auxetic structures.

The outcomes of this study will provide valuable insights into the behavior and performance of 2D auxetic structures under crushing scenarios. Through a comparative analysis, we aim to elucidate the advantages and limitations of each structure type and contribute to the broader understanding of auxetic materials for impact and energy absorption applications. Moreover, the optimal designs obtained from this study may serve as a foundation for the development of novel and efficient auxetic structures with enhanced crushing performance. In conclusion, this study, aims to contribute to the field of auxetic materials by utilizing topology optimization as a powerful tool for exploring and comparing the crushing performance of different 2-D auxetic structures by using numerical and experimental methods.

2. Materials and Methods

To understand and measure a physical phenomenon, mathematical operation must be performed, these operations can be explained with the help of partial differential equations (PDE). Various mathematical techniques have been developed to solve these PDEs by the computer. One of which is the finite element method (FEM). To provide a comprehensive analysis, it is crucial to compare the performance of auxetic structures with non-auxetic structures. The hexagonal honeycomb structure, known for its regular geometry and uniform cell arrangement, serves as an appropriate reference [21]. We selected three auxetic and one non-auxetic structures for comparison;

- Hexagonal honeycomb
- Re-entrant
- Double Arrowhead
- Tetra-Chiral

Considering the design, analysis and production processes of these structures, constraints were determined according to our computer capacity. As constraint values, the number of cells along the horizontal and vertical axis is 4x4, the length along the vertical and horizontal axis is 100x100 mm, the thickness is 2 mm, the extrude is 20 mm. In addition, FE analysis of different thicknesses of the structures was performed, as crushing resistance can be improved by changing other design parameters such as the thickness of the cell and the interior angle of the cell wall [12]. Not all structures have vertical and horizontal axis of symmetry. Since some of them do not have these axes of symmetry, is

not possible for the horizontal and vertical cell lengths to be equal to each other. Other dimensions are determined in a way that does not spoil the character of the structure. Fusion 360 was used to draw the structures shown in Figure 1.

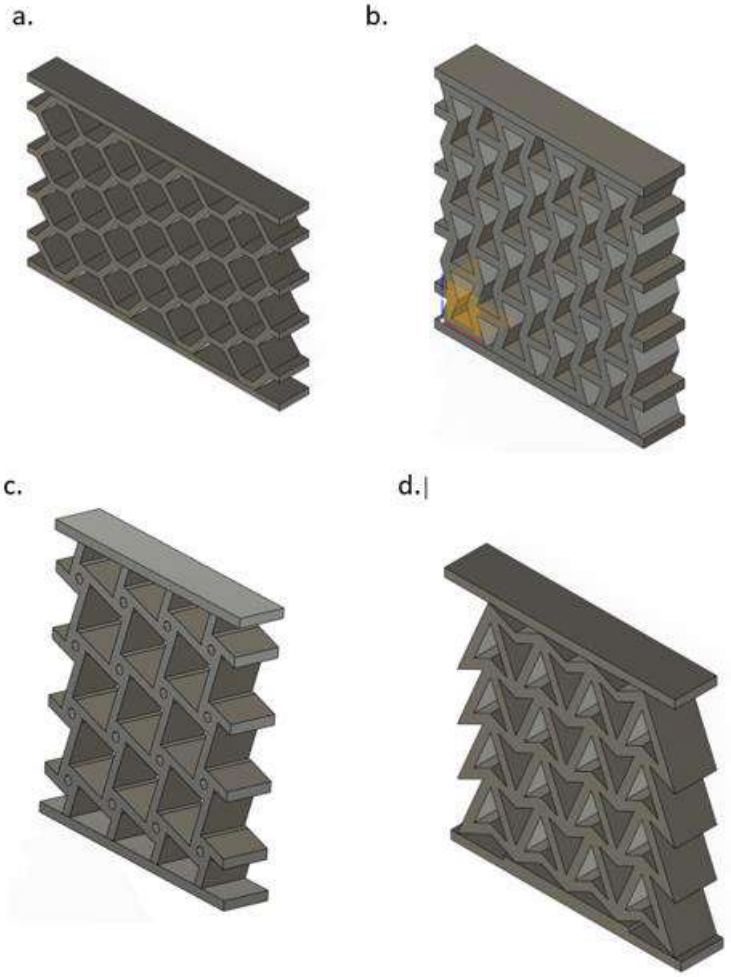

Figure 1. 3D designs of structures: a) hexagonal b) re-entrant, c) tetra-chiral and d) arrowhead honeycombs

The CAD files were transferred to the ANSYS environment to be analyzed under static loads, and their meshes were created there. During the analysis, the model was prepared by fixing the plates from the lower and upper edges of the structures in order to distribute the load on the lower and upper parts of the structures. Loads originating from direct force and weight are the subject of research. As a result of the topology optimization to be made in the light of the analysis data, it is aimed to maximize the compressive strength of each of the structures in proportion to their weight.

The relative density of a cellular structure directly affects its mechanical properties. The relative density increases with the thickness of the cell walls. Figure 2 shows unit cells of structure. The relative densities of the structures are derived as follows; $\boldsymbol{\rho}^*$ is density of the unit cell, $\boldsymbol{\rho_s}$ is density of bulk material, l is length of the inclined wall, t is thickness of cell wall, $\boldsymbol{\theta}$ is angle between the inclined wall and vertical wall, h is height of unit cell, r is radius of circle.

Hexagonal [1,2]:

$$\frac{\rho^*}{\rho_s} = \frac{t/l(h/l + 2)}{2cos\theta(h/l - sin\theta)} \quad (1)$$

Re-entrant [1,2]:

$$\frac{\rho^*}{\rho_s} = \frac{t/l(h/l + 2)}{2cos\theta(h/l - sin\theta)} \quad (2)$$

Tetra chiral [22]:

$$\frac{\rho^*}{\rho_s} = 2\left(\frac{t}{L}\right)\left[\frac{1 + \pi\left(\frac{r}{L}\right)}{1 + 4\left(\frac{r}{L^2}\right)}\right] \quad (3)$$

Arrowhead [23]:

$$\frac{\rho^*}{\rho_s} = \frac{t(sin\theta_1 + sin\theta_2)}{lsin(\theta_1 - \theta_2)} \quad (4)$$

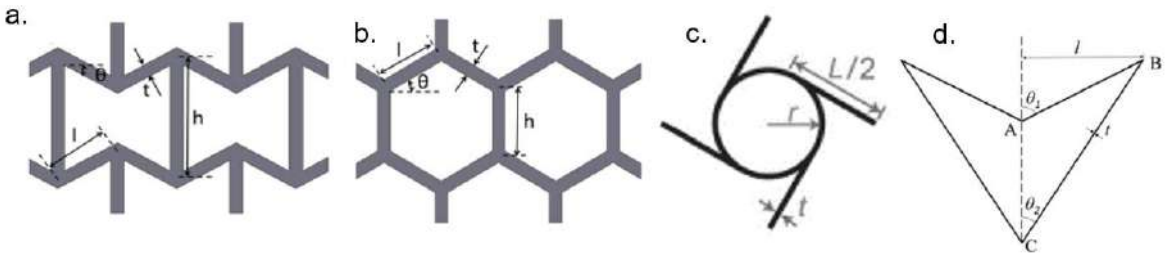

Figure 2. Unit cells of a) re-entrant b) hexagonal, c) tetra-chiral and d) arrowhead honeycombs

3. Topology Optimization

3.1. Finite Element Modeling and Optimization Steps

First of all, the Static Structural analysis system and the Structural Optimization analysis system were connected to each other to continue the process by taking the data from the solutions section of this analysis system on the Ansys Workbench and the project chart was created. Geometry and Model are also directly linked to each other. Since the result values obtained from the Static Structural section are used in the Structural Optimization section, it depends on the Setup section of the analysis system. Then, the material properties Polylactic Acid (PLA) listed in Table 1 were assigned in the Engineering Data section.

Table 1. Material properties of Polylactic Acid (PLA)

Material	Young's modulus E_s	Yield stress σ_{ys}	Poisson's ratio	Density ρ_s
PLA	1.80 GPa	27.4 MPa	0.35	1.14 g/cm^3

Then, the contact regions were created under the Connections section between different parts in order to prevent the intertwining between the main structure and the upper and lower bodies during the transfer of forces between the bodies at the top and bottom of the structure. The mesh size was determined depending on the thickness of the unit cell of the geometry. While determining the size, the mesh plan was created so that at least 6 elements fit into the thickness of the unit cell where *t* is equal to 3 mm and the element size is equal to 0.5 mm.

The purpose here is to create separate elements inside each wall of the cells while the cells are removed from the geometry during the topology optimization. Thus, the elements adjacent to the side surfaces remain separate from each other. The reason is elements on the outer surface of the structure should be excluded from the cells to be

removed in order to preserve the outline of the geometry during optimization. As shown in Figure 3, there are 4 more elements between the elements adjacent to the side surfaces in the geometry of t = 3 mm thickness.

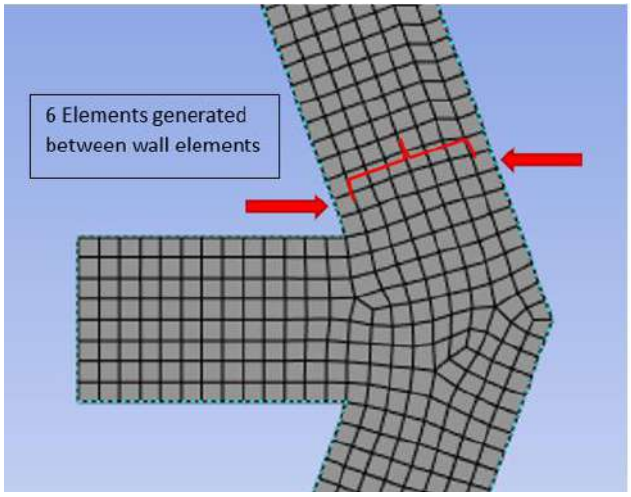

Figure 3. Internal structure consisting of 4 elements

In the Analysis Settings section under the Static Structural section, a certain displacement has been implemented to the geometry from the top to the bottom, and the geometry has been fixed using fixed support from the bottom. The same amount of displacement is implemented in all geometries and all unit cell thicknesses, compressing the geometry downwards. The exclusion region was chosen in order to preserve the original shape. The elements connected to the side surfaces are prevented from being removed from the structure during optimization. The reason why these elements are not wanted to be removed is that when they are removed from the geometry, some cells may disappear or lose its auxetic behavior. The Response Constraint value of the optimization was kept the same as 50% in all geometries. After the topology optimization was completed, the data were obtained from the Topology Density section under the "Solution(B6)" section.

3.2. Numerical Results and Discussion

Since the ribs in the direction to which the load is transmitted are the ribs that provide the strength of the main structure and topology optimization has prioritized reducing the weight at these points due to encountering lower stresses and forces in the horizontal ribs as shown in Figure 4.

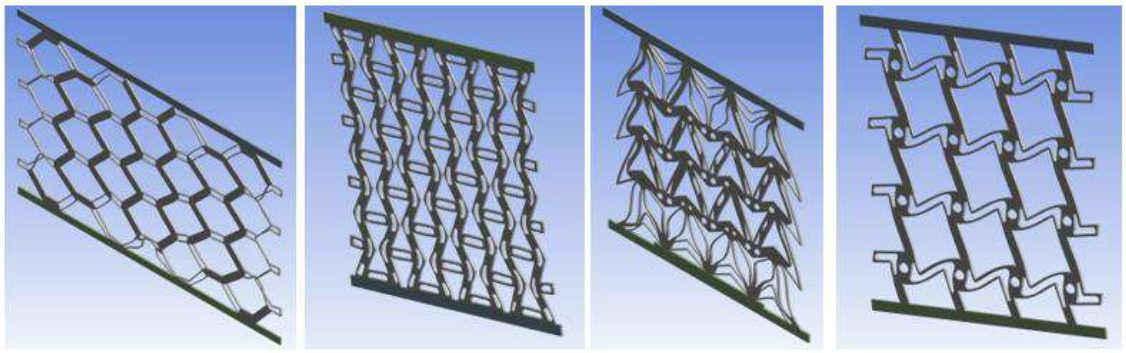

Figure 4. Results of the optimization for a) honeycomb, b) re-entrant, c) double arrowhead d) tetra-chiral

According to the results of the optimization in Figure 4, the regions where stresses are high are the connections between the vertical ribs and the cylinders. Since these areas contribute to the strength to structure, their densities have not been reduced. The results show that stresses in the horizontal ribs and the connection regions of the horizontal beams with the cylinder are significantly lower compared to other areas. Therefore, a portion of the mass has been eliminated in these regions by topology optimization, resulting in a lighter structure. Each cell is exposed

to stresses due to its auxetic structure. The re-entrant structure shows deformation from the right and left to the center. The structure makes rotational movement and this movement takes place mostly in the ribs at the edges, the effect decreases from the edge to the center of ribs, so we encounter more stress in the edge ribs, deformation is also seen in the ribs in the middle part due to the inward closing feature of the re-entrant structure.

In addition, the middle beams do not show a right or left rotational movement, but the stresses are high because the pressure is intense from the right and left. Since the upper and lower horizontal ribs in the center line are in contact with the plate fixed with boundary conditions, they are not free and have high strength. The cells on the edge are contact with the plate but since the inward closing is from the edges to the inside, those regions are subject to more deformation. When we increase the topology optimization percentage of the reentrant structure, it removes all the hollowed-out horizontal ribs from structure. But we prevented this because when the geometry of the auxetic structure should be kept, otherwise it will not give a negative Poisson's ratio. There are more stresses in the vertical beams than the horizontal beams due to the rotational movement, and since the vertical beams in the direction of load transmission provide the strength of the structure. The horizontal beams are emptied first in the topology optimization. The density of the central vertical beams in contact with the plate is also reduced because they have a tight connection with the plate, and the stresses are low as there is no free movement.

Considering the topology optimization results and stress values of the double arrowhead geometry, the geometry under the crushing force of the displacement applied from above directly transmitted the force downwards from the vertical ribs standing at an angle. As a result, the vertical ribs that transmit the force closed inward under the influence of the reaction force from below, and the angle of the vertical ribs in the geometry decreased and contracted. This result indicates that this geometry has an auxetic structure. Because the width of the geometry on the horizontal axis decreased as it was crushed under the force. Poisson's ratio was negative. Topology optimization results show that junction points of four ribs were not removed from the structure. There is no tension at the lower points of the ribs on the outer parts of the cells on the outer edges. For this reason, the interior was completely removed from the structure. Then Finite element analysis and optimization were made for each structure in four different thicknesses.

When the data obtained from the Figure 5 are examined, the performance of the optimal geometry increases as the cell thicknesses increase in the optimal versions in all geometries. In other words, the higher the cell thickness of the geometry, the more effective the optimization could be conducted. As the cell thickness increases in conventional geometries, F/Relative Density increases at a constant rate, while F/Relative Density values tend to increase parabolic in optimal geometries.

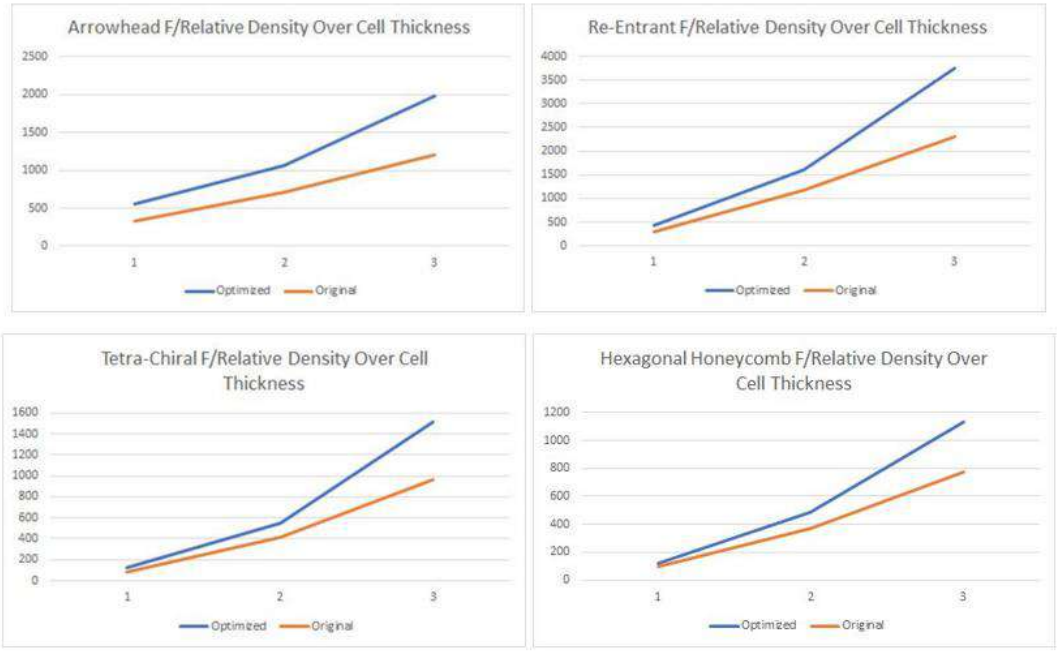

Figure 5. Re-entrant force/relative density over cell thickness

As seen in Figure 6, Re-Entrant geometry showed the best increase in F/Relative Density value as a result of topological optimization. This means that Re-Entrant is the most successful geometry in topology optimization in geometries made of PLA plastic, which has been increased from 1 mm to 3 mm cell thickness.

The success rankings along with other geometries are as follows: Re-Entrant > Tetra-Chiral > Arrowhead > Hexagonal Honeycomb, which is the oldest and most traditional of the designs (hexagonal honeycomb), gave the weakest results when optimal under crushing resistance from above. In addition, when we look carefully at the rankings, geometries with an auxetic structure (with a negative Poisson's ratio) are in the top three ranks, while the geometry with a non-auxetic structure (with a positive Poisson's ratio) is at the bottom. This proves that auxetic structures are superior to traditional structures when they are under pressure.

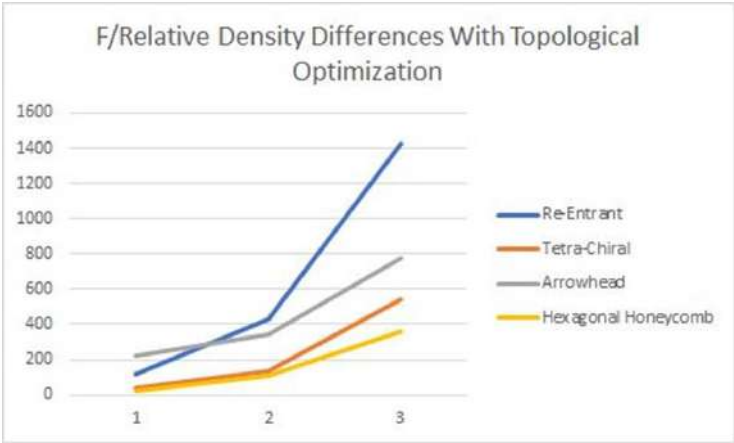

Figure 6. Force/relative density differences with topology optimization

4. Experimental Studies

In experimental studies, conventional and optimal models of re-entrant and tetra-chiral structures, determined by topology optimization, were produced and tested. The samples were manufactured using a 3D printer by using PLA material, and static compression tests were conducted using an Instron 5569 testing machine with a 50kN load cell capacity.

4.1. 3D printing conventional and optimal models

The ideal designs determined through topology optimization for experimental studies were produced using a 3D printer. The 3D printer used for production is the Ender S3 model, which operates based on FDM technology. For production, the bed temperature was set at 60°C, and the printing temperature for PLA material was defined as 230°C. In the experimental study, six samples were produced to compare the models obtained through optimization with classical auxetic models of the same thickness. The conventional and optimal 3D printed test samples are shown in Figure 7. Figure 7b and 7d displays the experimental samples of the optimal re-entrant and tetra-chiral auxetic structures obtained through topology optimization, along with the corresponding bulk models.

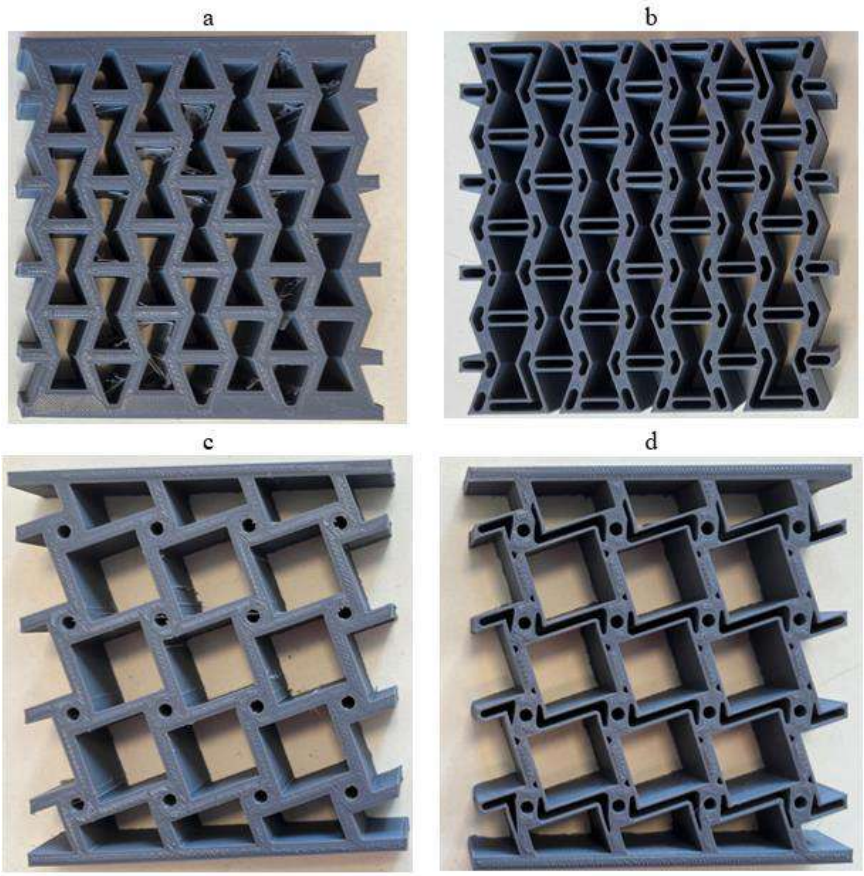

Figure 7. Conventional a) re-entrant, b) tetra-chiral, c) double arrowhead models and, Modified d) re-entrant, e) tetra-chiral and f) double arrowhead models

4.2. Compression tests

The test samples that were subjected to deformation after compression tests can be seen in Figure 8. The tests were conducted at a speed of 3 mm/min. When examining the in-plane deformation shape of the conventional re-entrant model in Figure 8a, it is observed that it folds inward in its transverse section and exhibits auxetic properties. The cells located in the middle section dominate the occurrence of damage. In the optimal re-entrant model, on the other hand, the structure exhibits a more resistant behavior in the remaining body section, while the distal ends are subjected to damage (Figure 8b). In the case of the conventional tetra-chiral structure, permanent damage occurred due to the fracture of the ligaments at the connecting points of a group of cells in the horizontal row near the top end (Figure 8c). Conversely, it is understood that the occurrence of damage affects the whole body and the optimal tetra-chiral structure exhibits a more durable behavior (Figure 8d).

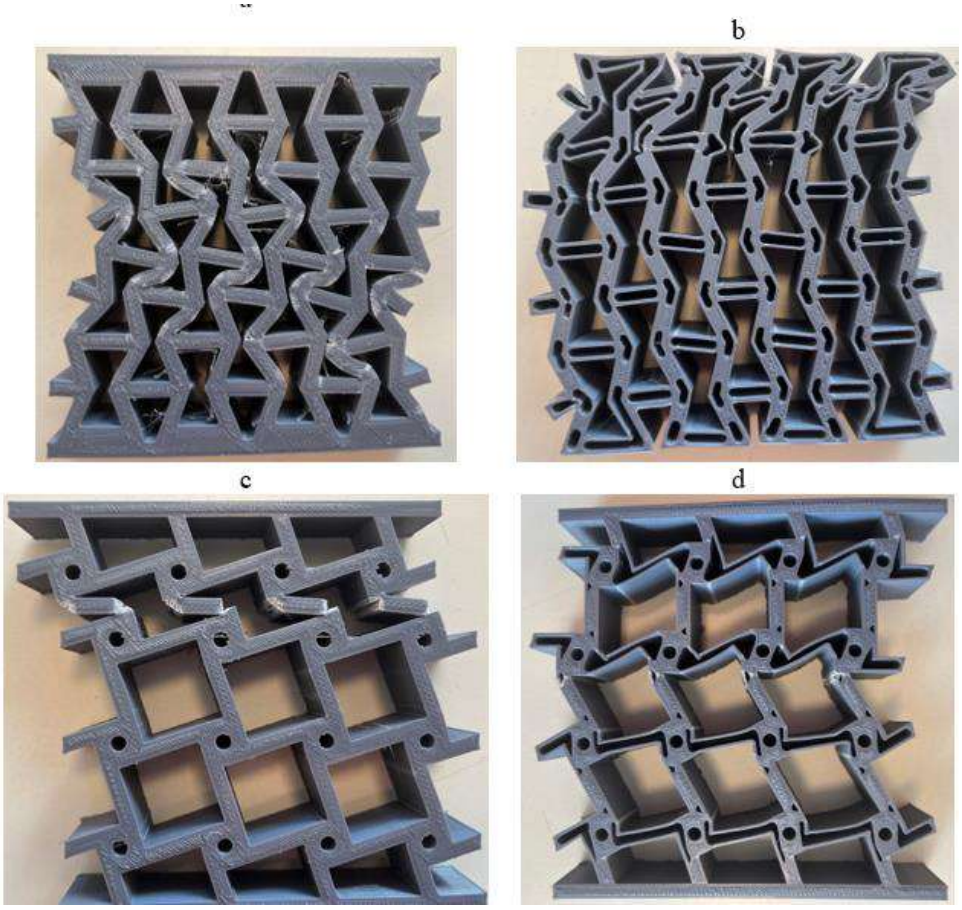

Figure 8. Conventional a) re-entrant, b) tetra chiral, c) double arrowhead models and, Modified d) re-entrant, e) tetra-chiral and f) double arrowhead models

4.3. Experimental Results and Discussion

The obtained test results were compared using the parameters specific compressive stress and specific energy absorption (SEA). The value of specific compressive stress is calculated by dividing the maximum force exhibited by each test specimen against the compressive load by the mass of the specimen. Similarly, the energy absorption capacities of the specimens are calculated by normalizing them to the mass, resulting in SEA values. Both parameters are used to compare the strength and energy absorption capacities of the structures. Figure 9 shows the specific compressive stress vs. strain curves, and Table 2 presents the numerical data.

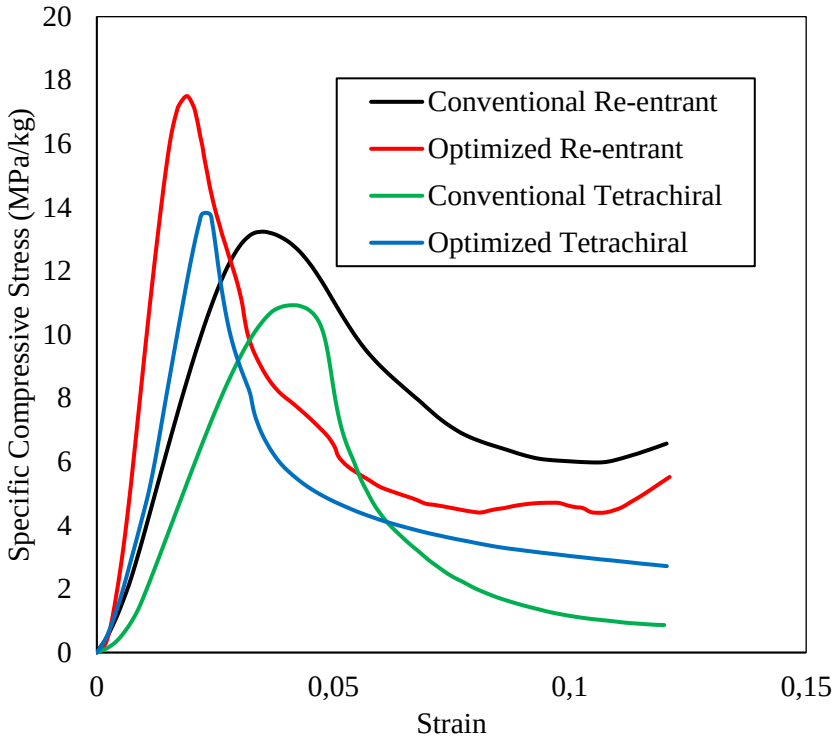

Figure 9. Specific compressive strength vs. strain curves of the conventional re-entrant, optimal re-entrant, conventional tetrachiral and optimal tetrachiral

According to Table 2, the optimal re-entrant model exhibits a 32.5% increase in specific compressive strength parameter compared to the conventional model, while experiencing a slight decrease of around 3% in SEA (specific energy absorption). The optimal re-entrant model shows a significant increase in strength, but its disadvantage is a partial decrease in energy absorption capacity. On the other hand, the optimal tetra-chiral demonstrates a 27.8% increase in specific compressive strength and increases the SEA value by 10.7%. The optimal tetra-chiral model outperforms the conventional models in both parameters. When compared among themselves, the re-entrant models show both higher strength and higher energy absorption capacity than the tetra-chiral models.

Table 2. Specific compressive strength and SEA results of tested samples

Cell type	Specific compressive strength (MPA/kg)	SEA (J/kg)
Conventional re-entrant	13.2	4025
Optimal re-entrant	17.5	3914
Conventional tetra-chiral	10.8	2943
Optimal tetra-chiral	13.8	3260

5. Conclusion

As a result, the mechanical strength and energy absorption capacities of three different commonly used auxetic lattice geometries in the literature have been experimentally and numerically investigated in this research. Re-entrant, tetra-chiral, and double arrowhead auxetic lattice structures were designed with the same cell count and external volume through topology optimization under static load. To compare the auxetic structures with non-auxetic lattice structures, a hexagonal honeycomb structure was also designed with the same cell count and volume, using topology optimization. By comparing the compression strength of auxetic and non-auxetic lattice structures, ideal designs were

obtained through topology optimization. In this comparison, it was observed that the auxetic structures exhibited higher strength compared to the non-auxetic model.

Subsequently, for the experimental investigations, the re-entrant and tetra-chiral lattice structures with high mechanical performance were selected based on the topology-optimized model and designed as experimental samples using a 3D printer. Conventional re-entrant and tetra-chiral structures were also produced for comparison. According to the experimental results, the optimal re-entrant model showed a 32.5% increase in the specific compressive strength parameter compared to the conventional model, and the optimal tetra-chiral model demonstrated a 27.8% increase in specific compressive strength and a 10.7% increase in the SEA (Specific Energy Absorption) value.

6. Acknowledgements

Support for this study was provided by the Scientific and Technological Research Council of Turkey (TUBITAK) under project number 122M925.

7. References

[1] Gibson LJ, Ashby MF. *Cellular solids: structure and properties*. Cambridge, UK, Press Syndicate of the University of Cambridge, 1997.

[2] Masters IG, Evans KE. "Models for the elastic deformation of honeycombs". *Composite Structures*, 35(4), 403-422, 1996.

[3] Spadoni A, Ruzzene M, Scarpa F. "Global and local linear buckling behavior of a chiral cellular structure". *Physica Status Solidi (b)*, 242(3), 695-709, 2005.

[4] Evans KE, Kenneth E,Alderson A. "Auxetic materials: functional materials and structures from lateral thinking!". *Advanced Materials*, 12.9, 617-628, 2000.

[5] Scarpa F, Panayiotou P, Tomlinson G. "Numerical and experimental uniaxial loading on in-plane auxetic honeycombs". *The Journal of Strain Analysis Engineering Design*, 35(5), 383-388, 2000.

[6] Du Plessis A, Broeckhoven C, Yadroitsava I, Yadroitsev I, Hands CH, Kunju R, Bhate D. "Beautiful and functional: a review of biomimetic design in additive manufacturing". *Additive Manufacturing*, 27, 408-427, 2019.

[7] Jiang H, Ziegler H, Zhang Z, Atre S, Chen Y. "Bending behavior of 3D printed mechanically robust tubular lattice metamaterials". *Additive Manufacturing*, 50, 102565, 2022.

[8] Usta F, Scarpa F, Türkmen HS. "Edgewise compression of novel hexagonal hierarchical and asymmetric unit cells honeycomb metamaterials". *Materials Today Communications*, 24, 101102, 2020.

[9] Usta F, Zhang Z, Jiang H, Chen Y. "Harnessing structural hierarchy and multi-material approaches to improve crushing performance of re-entrant honeycombs". *Journal of Manufacturing Processes*, 92, 75-88, 2023.

[10] Pal A, Bertoldi K, Pham MQ, Schaenzer M, Gross AJ. "Optimal turbine blade design enabled by auxetic honeycomb". *Smart Materials and Structures*, 29(12), 125004, 2020.

[11] Sun Y, Pugno NM. "In plane stiffness of multifunctional hierarchical honeycombs with negative Poisson's ratio sub-structures". *Composite Structures*, 106, 681-689, 2013.

[12] Usta Fatih, Türkmen HS, Scarpa F. "Low-velocity impact resistance of composite sandwich panels with various types of auxetic and non-auxetic core structures". *Thin-Walled Structures*, 163, 107738, 2021.

[13] Islam MK, Hazell PJ, Escobedo JP, Wang H. "Biomimetic armour design strategies for additive manufacturing: A review". *Materials and Design*, 205, 109730, 2021.

[14] Mirzaali MJ, Hedayati R, Vena P, Vergani LAURA, Strano M, Zadpoor AA. "Rational design of soft mechanical metamaterials: Independent tailoring of elastic properties with randomness". *Applied Physics Letters*, 111(5), 2017.

[15] Yang W, Liu Q, Gao Z, Yue Z, Xu B. "Theoretical search for heterogeneously architected 2D structures". *Proceedings of the National Academy of Sciences*, 115(31), E7245-E7254, 2018.

[16] Chen D, Zheng X.. "Multi-material additive manufacturing of metamaterials with giant, tailorable negative Poisson's ratios". *Scientific Reports*, 8(1), 9139, 2018.

[17] Usta F, Türkmen HS, Scarpa F. "High-velocity impact resistance of doubly curved sandwich panels with re-entrant honeycomb and foam core". *International Journal of Impact Engineering*, 165, 104230, 2022.

[18] Channa S, Sun D, Stylios GK. “Impact resistance of 3D cellular structures for protective clothing”. *Advanced Engineering Materials,* 25(6), 2201336, 2023.
[19] Xiao Z, Yang Y, Xiao R, Bai Y, Song C, Wang D. “Evaluation of topology-optimized lattice structures manufactured via selective laser melting”. *Materials and Design,* 143, 27-37, 2018.
[20] Usta F, Zhang Z, Kurtaran H, Scarpa F, Türkmen HS, Mecitoğlu Z. “Design optimization of modified re-entrant auxetic metamaterials reinforced with asymmetric edge cells for crushing behavior using the Taguchi method”. *Journal of the Brazilian Society of Mechanical Sciences and Engineering,* 44(9), 395, 2022.
[21] Gao, Qiang, et al. “Crashworthiness analysis of double-arrowed auxetic structure under axial impact loading”. *Materials and Design,* 161, 22-34, 2019.
[22] Mohsenizadeh M, Gasbarri F, Munther M, Beheshti A, Davami K. “Additively-manufactured lightweight metamaterials for energy absorption”. *Materials and Design,* 139, 521–530, 2018.
[23] Qiao J, Chen CQ. “Analyses on the in-plane impact resistance of auxetic double arrowhead honeycombs”. *Journal of Applied Mechanics,* 82(5), 051007, 2015.

International Conference on Advances and Innovations in Engineering

Transport by Land and Air Vehicles, Advantages, Literature Review and Classification of Flying Cars

Huseyin ŞAHIN[1]

[1]Aircraft Technology, Vocational School of Technical Science, Ankara Yildirim Beyazit University, Ankara, Turkey.
[1]hsahin@aybu.edu.tr,

[1](ORCID: 0000-0003-0464-2644)

Abstract

Recently, with the increase in the human population living in cities, the number of metropolitan cities has increased. The increase in the human population has also meant an increase in vehicle traffic. In addition to the road widening studies against vehicle traffic, developed societies have started flying car studies. Studies on flying cars have been carried out in various times and places around the world for many years against congested traffic problems. However, transport systems are developing more and more every day. The idea of a vehicle that can fly and be used in land traffic is one of the vehicle concepts that are being developed in various parts of the world. This study contributes to the development of flying cars. Vehicles used at low altitudes and used in air and ground traffic do not affect the air traffic of aircraft used at high altitudes for economic reasons. In addition, if the idea of flying and land vehicles is realised, the use of transport infrastructure will be reduced and it will be an innovative solution method that can be taken against negative conditions such as traffic congestion on highways, infrastructure and poor maintenance of roads. In this study, an investigation of flying car studies, which relieves the burden of heavy land traffic and is a fast means of transport, has been carried out. This study sheds light on the development of flying cars. Flying cars made in different configurations are examined and separated according to the methods used.

Keywords: Flying Car, Near-Ground Flight, VTOL, STOL

1. Introduction

In recent years, the populations of cities in developing and developed countries in most parts of the world have been expanding rapidly. In addition to the increasing population density, it has been observed that the vehicles used in transportation increase the traffic density. According to the literature review, existing transportation methods can be grouped under 5 main headings. These can be evaluated as underground, above ground, over water, low altitude air transportation and high altitude air transportation[1].

Underground transportation systems are generally used for short-distance transportation purposes in dense cities. This type of transportation has been selected as a potential approach to solve urbanization problems such as traffic congestion, land shortage, noise and air pollution [2]. Since the use of engines using petroleum fuel in enclosed spaces is not suitable for human health, the movement in such vehicles is carried out with the help of electric motors. The cost of building the roads of these means of transportation is usually high, while the cost of operation is low. Train systems and hyperloop systems are examples of these transportation systems. Underground transportation systems are generally used for human transportation [3], [4].

Surface transportation systems are the oldest transportation systems of humanity. These transportation systems can be used for short and long-distance transportation purposes. Special roads are built for these systems, which have been used since the invention of the wheel. They are suitable for both human and passenger transportation. Vehicles used in rail systems, such as conventional wheeled or underground transportation systems, are suitable for the use of both electric motors and engines using petroleum fuel. In recent years, fully electric or hybrid engine systems are preferred for reasons such as economy and low carbon emissions.

[1]Corresponding author

The biggest advantage of flying cars is the possibility of uncongested transportation using underutilized low-altitude airways. Flying cars provide faster transportation as they have fewer physical infrastructure obstacles than roads. With the widespread use of flying cars, the roads that will be freed up on land will become more comfortable for pedestrian traffic. Since asphalt roads are not needed for the use of flying cars, new roads and tunnels will not need to be built. Considering all these advantages, the use of flying cars will reduce traffic in cities and allow people to get around faster.

To alleviate the pressure on traffic loads, engineers have turned to vehicles that use low-altitude airspace close to land, which is less frequently used. So far, low-altitude airspace relatively close to land has been used by helicopters and small unmanned aerial vehicles (UAVs). However, the use of flying cars is attracting more and more attention and there is an increasing number of studies on the use of more aircraft in cities [5].

Some scientific studies have been carried out to introduce and discuss flying car systems [6], [7]. In addition, the historical development of flying cars and the characteristics of current flying car designs are presented. As described above, flying cars can be used to carry roads and goods while operating at low altitudes. As a result, when we start using flying cars in our daily lives, some infrastructure works such as roads and tunnels will not be necessary. Furthermore, electrically powered rotors can be designed and equipped in such a way as to significantly reduce noise and emissions in the aircraft, thus making the travel experience more comfortable for passengers.

Flying car designs date back to the early 1900s. With the spread of aviation, the idea of a vehicle that could travel both on land and in the air had begun. The first flying car produced for the first time was realized by Curtiss Aeroplane in 1917. Afterwards, many designs were realized to combine a fixed-wing aircraft with a car [1], [8].

Fixed wing flying cars could not be used on existing roads due to the large size of their wings. However, there have been innovations in flying car designs over the years. Rotary wing flying car designs started to increase. Thus, flying cars will not need a runway to take off and can take off and land vertically from where they are [9], [10].

2. METHOD

According to a 2015 study, 4 patents were granted for flying cars until 2000[11]. Studies on flying cars have gained momentum in the last 20 years. Especially in recent years, it is observed that the number of studies on flying cars is increasing day by day. Since the early 20th century, studies on these vehicles, which have been studied since the beginning of the 20th century, date back to 1901[12]. Many unsuccessful trials have been realized with this vehicle. The first patent on flying cars was realized in 1941[13].

There are many scientific articles and patents on flying cars. The studies conducted in these scientific articles and patents were analyzed. These studies are listed chronologically and according to flight types. These can be autonomous or semi-autonomous, in helicopter (VTOL) or glider (STOL) form, metamorphic or static, renewable energy, hybrid or fossil fueled. The vertical take-off and landing capability of these vehicles (VTOL) eliminates the need for a runway. It also allows the vehicle to land on any solid ground. In addition, VTOL vehicles are preferred in flying vehicles due to their ability to hover. Thus, altitude control can be easily achieved and it helps to maintain its position in possible adverse situations. Thanks to the altitude control capability, the driver does not need to think in 2 dimensions and the vertical (z) axis as in conventional land vehicles.

2.1. Some flying cars built or designed

Since the early years of aviation, there has been considerable interest in flying car designs. Although some of these designs were quite futuristic in those years, some of them were able to be produced as prototypes in real size. The reasons why these models could not be put into mass production were their high cost and the aviation rules of the period were not favorable. The first flying car model Since 1941, many flying car models have been designed. Some of these models are briefly described below.

1) AeroMobil

It made its first flight in 1990[14]. The company, which is still in operation, has produced 4 different prototypes in the intervening period. It is propelled by an internal combustion ROTAX engine[15]. In all versions, it can switch

between flight and ground mode with its fixed wings that can be opened and closed. It is the most well-known air and land vehicle among flying cars thanks to its high range and suitability for use in the city.

2) Volante Tri-Athodyne

Designed in 1957 by the famous automotive company Ford and prototyped on a small scale, the vehicle has never been on the roads or in the air[16], [17]. It is thought to stay in the air thanks to the fan engines on it.

3) Airbus Vahana

The VTOL vehicle, which made its first flight in 2018, also stays in the air thanks to the electric motors on it. With the combination of 8 motor propellers on it, it is capable of vertical take-off and landing as well as level flight[18]-[20]

4) Cartivator

Japanese electronics company NEC, the Nippon Electric Company, tested a prototype quadcopter-style flying car in August 2019. Powered by a battery, the 330-pound, 13-foot-long car was able to hover about 10 feet above the ground for one minute[21].

5) EHang

The vehicle, patented by the Chinese company GUANGZHOU EHANG Smart Technology company in 2016, has 2 different studies on flying cars. Vehicles driven by electric motors are vehicles with the appearance of drones [22], [23].

6) Joby S4

The aircraft, capable of vertical take-off and landing, was developed by the American company Joby Aviation. The vehicle with 6 electric motors also has a metamorphosis system that changes the direction of the motors. Thus, it moves like a fixed-wing aircraft and is suitable for high speed. It uses electricity as the main energy source. Joby S4, an aircraft in the VTOL category, behaves like a fixed-wing aircraft during level flight. It has a range of 150 miles on a single charge and can fly at 200 mph.[24], [25]

7) Kitty Hawk (Cora and Flyer)

The fixed wing VTOL aircraft can fulfill its flight mission with 6 electric motors on the wings and 2 electric motors in the nose. With the change of engine directions, it has high vertical take-off as well as straight flight performance.[26]

8) Opener Blackfly

The vehicle, which is energized by a total of 8 electric motors placed on two wings on the body, is a single-seater vehicle. With its efficient and silent transportation [27]

9) Lilium

The Germany-based aircraft company can perform vertical take-off and landing thanks to its engines, which can change their direction on fixed wings, and at the same time, by changing the direction of the engine, it can move at high speed like fixed-wing aircraft. [28]

10) PAL-V gyrocopter/car

Designed in 2003, the aircraft is actually a gyrocopter. While it fulfills the flight task with its large blades on it, it provides its movement on the ground thanks to the wheels on the landing gear.[29]

11) Terrafugia

Founded in 2006, the company's TF-X model is designed for both vertical take-off and overland use. It flies using 2 engines placed on fixed wings. While the aircraft is in ground mode, the wings are folded and in air mode, it has both VTOL and fixed wing aircraft characteristics by changing the engine directions.[30]

12) Volocopter

An 18-rotor drone, the volocopter is similar in design to a helicopter. Designed for air taxi missions, it is an e-VTOL aircraft propelled by electric motors.[31], [32]

13) Hoversurf

It looks like a bicycle flying with 4 motors like a quadrotor in a single-seater aircraft. It is propelled by electric motors. Since 2016, more than 20 patents have been obtained for the aircraft, which has been in the air for more than 200 hours.[33]

14) Bell Helicopter Nexus

In 2019, the world-famous bell helicopter company introduced the concept design of the Nexus 4EX model, which can fly as VTOL and can change the engine direction for level flight missions. With a 4-passenger capacity, the aircraft is also a 4-engine e-VTOL aircraft.[34], [35]

15) Cezeri

The aircraft designed by Baykar Teknoloji in 2018 is an e-VTOL aircraft with octoquad configuration.[36], [37]

16) Fulton Airphibian
Built in the 1930s, it transforms a conventional automobile into a fixed-wing aircraft with the help of a kit consisting of a tail and wings. It has an airplane design that leaves the rear tail and wings for land use. [38]
17) Aerocar
It was designed in 1949 based on the Fulton Airphibian and 5 were built. [39], [40]
18) Aerauto PL.5C
In 1948, the Aerauto, a folding fixed-wing aircraft, could easily switch to land vehicle mode. It was able to perform flight missions with a piston engine behind the fuselage.
19) AVE Mizar
Designed and prototyped in the 1970s, it is a road-going aircraft like an aerocar. The vehicle part was realized by combining the Ford Pinto tail and wing parts with the Cessna Skymaster aircraft.[41]
20) Parajet Skycar
It is an easy-to-use air vehicle that can be used both on land and in the air by installing a paramotor mechanism on the ATV, which is a small off-road vehicle built on a light chassis.[42]
21) Milner AirCar
Thanks to its folding wing design, the vehicle is suitable for use on land and air routes and is propelled by 2 engines.[43]
22) Moller Skycar
The aircraft, of which many variants have been designed, has been in the works for a long time. The aircraft, which has 2 and 4 engine models, has not progressed beyond the prototype. The aircraft, which receives its propulsion from wankel engines, has been made more efficient with the help of fans placed around the propellers.[44]
23) X-Hawk
It is a VTOL aircraft manufactured by Urban Aviation with two fan engines. Designed as a bicopter, it was certified by the FAA according to an article published in 2002.[45]
24) SAMSON MOTORWORKS
Designed as a 3-wheeled flying motorcycle, the vehicle has 3 models. The current price of the starting model of the vehicle sold as a kit is 170.000 USD. The gasoline-engine vehicle can fly thanks to its fixed wings, while in ground mode, its wings can be folded and used on the roads.[46], [47]
25) Aero-X Hoverbike
Aero-X is a VTOL aircraft that can fly up to 10 feet above the ground and reach speeds of 45 miles per hour, carrying 2 personnel.[48]
26) Aircar
The E-VTOL vehicle, an 8-rotor octoquad with 2 passenger capacity, is expected to have a range of 50-80 km. It does not have wheels for road use and has fixed landing gear.[49]
27) GF7
It is a jet engine propelled 4-wheeled fixed wing aircraft. When it switches to land mode, the wings are collected and the aircraft turns into a small automobile, and the wheels, which are also used as landing gear in air mode, are collected inside the body, allowing low friction force and high speed.[50]
28) Breeze
Designed in 2021 as an 8-rotor octoquad, the aircraft has a single passenger capacity and a range of 48 km. The main energy source of the aircraft with fixed landing gear is electricity.[51]
29) Airbus
Airbus, one of the most aircraft producing companies in the world, has many studies on flying cars. In these studies, the city Airbus nextgen model is an octocopter with 8 electric motors. The Vahana model is an OctoH model with 8 electric motors that can rotate directions connected to the wings.[52] While both models are not suitable for use on land roads, the Pop Up model is a model suitable for use both on land and in the air. The Pop Up model is a concept consisting of two vehicles. The quadcopter connected to the land vehicle allows the land vehicle to fly.[53]

2.2. Flight principles of flying cars

When flying cars are examined, it is observed that 3 different methods are used as flight principle. These are; fixed wing, rotary wing and one of them is paramotor. Some of the flying car air vehicles examined have fixed landing gear without wheels. However, these aircraft are defined as flying cars due to their small size and short range of 50 km, making them suitable for daily use.

When we examine the flying cars chronologically, we see that while the studies conducted in the early years were generally designed as a mixture of fixed-wing land vehicles and automobiles, today most of these vehicles are designed with rotary wings. The biggest reasons for this change are that rotary wing aircraft are VTOL and it is no longer possible to take off and land in cities with heavy traffic.

Only one of the vehicles examined is both suitable for use on highways and can be used as a paramotor. This vehicle was used both as a paramotor and as a land vehicle due to its light weight together with the use of composite materials in its construction.

2.3. Energy source of flying cars

When we examine the basic energy sources of flying cars, we see that while piston engines were used as the energy source of most aircraft built until the 1970s, especially with the development of drone technology and easy access to materials, the basic energy sources of flying cars started to be electricity with the resemblance of flying cars to manned drones. In addition, electric air vehicles have also increased due to the fact that electric motorized air vehicles are both low emission and can be used at high power and speed per unit weight.

3. Discussion

3.1 Results

When flying cars are analyzed, flying cars designed in the early days were designed with fixed wings using engines using petroleum products. While these aircraft were first designed with detachable wings, new generation flying cars were designed with foldable wings. Especially in flying cars designed after the 2000s, VTOL aircraft designs were preferred. In the vast majority of these aircraft, the landing gear is not suitable for use on conventional highways due to the fact that the landing gear is wheelless or the wheels are not propelled.

The vast majority of the aircraft analyzed remained at the prototype stage. Except for a few flying cars that are still saleable, most of them could not be made suitable for sale due to reasons such as economic and technological inadequacy. In order for an optimum flying car to be suitable for use in daily life, it must be a roadable VTOL flying car. In an optimum flying car, the flight task should be multi-rotor VTOL with folding rotor arms.

4. Discussion

The term flying car refers to an aircraft designed for short-distance passenger or cargo transportation for personal or shared use. The term roadable flying car is preferred for air vehicles suitable for use on the road. Flying cars designed as VTOL are suitable for use in the city by performing vertical landing and take-off in small areas in cities.

5. References

[1] G. Pan and M. S. Alouini, “Flying Car Transportation System: Advances, Techniques, and Challenges,” *IEEE Access*, vol. 9, pp. 24586–24603, 2021, doi: 10.1109/ACCESS.2021.3056798.

[2] J. Cui and J. D. Nelson, “Underground transport: An overview,” *Tunnelling and Underground Space Technology*, vol. 87, 2019, doi: 10.1016/j.tust.2019.01.003.

[3] J. G. S. N. Visser, “The development of underground freight transport: An overview,” *Tunnelling and Underground Space Technology*, vol. 80, 2018, doi: 10.1016/j.tust.2018.06.006.

[4] J. Cui, “Building three-dimensional pedestrian networks in cities,” *Underground Space (China)*, vol. 6, no. 2, 2021, doi: 10.1016/j.undsp.2020.02.008.

[5] D. P. Thipphavong *et al.*, “Urban air mobility airspace integration concepts and considerations,” in *2018 Aviation Technology, Integration, and Operations Conference*, 2018. doi: 10.2514/6.2018-3676.

[6] M. N. Postorino and G. M. L. Sarné, “Reinventing mobility paradigms: Flying car scenarios and challenges for urban mobility,” *Sustainability (Switzerland)*, vol. 12, no. 9, 2020, doi: 10.3390/SU12093581.

[7] S. S. Ahmed *et al.*, "The Flying Car—Challenges and Strategies Toward Future Adoption," *Front Built Environ*, vol. 6, Jul. 2020, doi: 10.3389/fbuil.2020.00106.
[8] A. Draghici, L. Ivascu, A. Mocan, and D. Robescu, "The Flying Car—A Solution for Green Transportation," 2021. doi: 10.1007/978-981-16-1209-1_14.
[9] M. UZUN and S. ÇOBAN, "Electrically Driven VTOL Flying Car Designing and Aerodynamic Analysis," *European Journal of Science and Technology*, 2021, doi: 10.31590/ejosat.910516.
[10] W. Ott, "HELIos, a VTOL flying car," in *AIAA and SAE World Aviation Conference, 1998*, 1998. doi: 10.2514/6.1998-5535.
[11] N. Agrawal, "On various design configurations of flying car," vol. 3, no. 1, pp. 92–96, 2015.
[12] Daniel C. Schlenoff, "Scientific American Debunks Claim Gustave Whitehead Was 'First in Flight,'" *Scientific American*, 2014. https://www.scientificamerican.com/article/scientific-american-debunks-claim-gustave-whitehead-was-first-in-flight/
[13] Bruce L. Beals, "FLYING AUTOMOBILE," 1941
[14] Aeromobil, "Aeromobil About," 2014.
[15] E. Becker, "The future of flying is near," *Tribology & Lubrication Technology;*, vol. 73–8, 2017.
[16] "1958 Ford Volante - Концепты." https://www.carstyling.ru/ru/car/1958_ford_volante/ (accessed Mar. 07, 2023).
[17] G. pan and M.-S. Alouini, "Flying Car Transportation System: Advances, Techniques, and Challenges," Apr. 2020, doi: 10.36227/TECHRXIV.12178878.V1.
[18] "Vahana - Airbus." https://www.airbus.com/en/urbanairmobility/cityairbus-nextgen/vahana (accessed Mar. 07, 2023).
[19] D. Montagnani, M. Tugnoli, A. Zanotti, M. Syal, and G. Droandi, "Analysis of the Interactional Aerodynamics of the Vahana eVTOL Using a Medium Fidelity Open Source Tool," pp. 436–451, 2020, Accessed: Mar. 07, 2023. [Online]. Available: https://re.public.polimi.it/handle/11311/1133177
[20] P. Pradeep and P. Wei, "Energy Optimal Speed Profile for Arrival of Tandem Tilt-Wing eVTOL Aircraft with RTA Constraint," *2018 IEEE CSAA Guidance, Navigation and Control Conference, CGNCC 2018*, Aug. 2018, doi: 10.1109/GNCC42960.2018.9018748.
[21] B. Dossabhoy, "Japan's Flying Car," *The E&S Magazine*, vol. 64, no. 1, p. 13, 2020.
[22] "EHang - | UAM - Passanger Autonomous Aerial Vehicle (AAV)." https://www.ehang.com/ehangaav/ (accessed Mar. 07, 2023).
[23] R. Roy, "THE FUTURE OF PERFORMANCE IMPROVEMENT: DRONES IN THE EMERGENCY MEDICAL SPACE," 2017, doi: 10.1002/pfi.21746.
[24] "Joby Aviation S4 2.0 (prototip)." https://evtol.news/joby-s4/ (accessed Apr. 05, 2023).
[25] A. Jain Bharati Vidyapeeth, M. Gupta, A. Jain Kunal Bavikar, and R. B. Gupta, "Baseline procedure for conceptual designing of an eVTOL for Urban Air Mobility Conceptual design of eVTOL for urban air mobility View project Baseline procedure for conceptual designing of an eVTOL for Urban Air Mobility", doi: 10.1109/ICECA49313.2020.9297649.
[26] "Kittyhawk." https://www.kittyhawk.aero/ (accessed Apr. 05, 2023).
[27] "Opener." https://opener.aero/ (accessed Apr. 05, 2023).
[28] H. D. Kim, A. T. Perry, and P. J. Ansell, "A Review of Distributed Electric Propulsion Concepts for Air Vehicle Technology," in *2018 AIAA/IEEE Electric Aircraft Technologies Symposium, EATS 2018*, 2018. doi: 10.2514/6.2018-4998.
[29] Y. F. Wang and T. X. Su, "Autobody modelling analysis of the flying cars," in *Applied Mechanics and Materials*, 2014. doi: 10.4028/www.scientific.net/AMM.577.1310.
[30] M. Gyula, "Smart mobility solutions in smart cities," *Interdisciplinary Description of Complex Systems*, vol. 20, no. 1, 2022, doi: 10.7906/indecs.20.1.5.
[31] D. Lenton, "The Measure of: Volocopter flying taxi," *Engineering & Technology*, vol. 13, no. 7, 2018, doi: 10.1049/et.2018.0712.
[32] S. Ong, "Electric air taxi flies over Singapore - [News]," *IEEE Spectr*, vol. 56, no. 12, pp. 7–8, Nov. 2019, doi: 10.1109/MSPEC.2019.8913820.
[33] L. Williams, "In the skies and on the ground," *Engineering and Technology*, vol. 15, no. 7, pp. 52–55, Aug. 2020, doi: 10.1049/ET.2020.0707.
[34] "Bell Nexus Evtol Moves Towards Certification," *Aerospace Testing International*, vol. 2019, no. 4, 2019, doi: 10.12968/s1478-2774(22)50413-5.

[35] H. Kinjo, “Development Trends and Prospects for eVTOL: A new Mode of Air Mobility,” *Mitsui & Co. Global Strategic Studies Institute Monthly Report*, no. June, 2018.
[36] V. YAVAŞ and A. ÖZHAN DEDEOĞLU, “Hava Taşımacılığında Değişen İş Modelleri,” *Akıllı Ulaşım Sistemleri ve Uygulamaları Dergisi*, vol. 4, no. 2, 2021, doi: 10.51513/jitsa.957540.
[37] “Cezeri YZR – Cezeri Yapay Zeka Robotik Teknolojileri.” https://www.cezerirobot.com/tr/ (accessed Aug. 29, 2023).
[38] W. F. Chana, “Flying automobiles-are they for real?,” in *SAE Technical Papers*, 1996. doi: 10.4271/965621.
[39] E. C. Sweeney, “AEROCAR 2000,” in *SAE Technical Papers*, 1998. doi: 10.4271/985515.
[40] M. B. Taylor, “The Aerocar ‘flying automobile,’” *SAE Technical Papers*, 1974, doi: 10.4271/740393.
[41] “Popular Mechanics - Google Kitaplar.” https://books.google.com.tr/books?id=LdQDAAAAMBAJ&pg=PA113&redir_esc=y#v=onepage&q&f=false (accessed Aug. 29, 2023).
[42] “Parajet Paramotorları | Motorlu Paramotor / Motorlu Yamaç Paraşütü (PPG) Birleşik Krallık.” https://parajet.com/ (accessed Aug. 30, 2023).
[43] “Milner AirCar | DAR şirketi.” https://www.darcorp.com/projects/milner-aircar/ (accessed Aug. 31, 2023).
[44] “moller skycar.”
[45] R. Yoeli, “Ducted fan utility vehicles and other flying cars,” in *2002 Biennial International Powered Lift Conference and Exhibit*, 2002. doi: 10.2514/6.2002-5995.
[46] J. Nash, “Easy Flier,” *Sci Am*, vol. 302, no. 3, 2010, doi: 10.1038/scientificamerican0310-24.
[47] “https://www.samsonsky.com/.”
[48] A. M. Intwala, “Design & analysis of vertical takeoff and landing vehicle (VTOL),” *International Journal of Applied Engineering Research*, vol. 10, no. 11, 2015.
[49] “https://www.aircar.aero/tr.”
[50] “https://newatlas.com/flying-jet-car/32287/.”
[51] “Turkish Technic Esinti.” https://evtol.news/turkish-technic-esinti (accessed Sep. 01, 2023).
[52] “Airbus | Pioneering sustainable aerospace.” https://www.airbus.com/en (accessed Sep. 01, 2023).
[53] “Popular Mechanics - Product Reviews, How-To, Space, Military, Math, Science, and New Technology.” https://www.popularmechanics.com/ (accessed Sep. 01, 2023).

International Conference on Advances and Innovations in Engineering

NOx emission reduction in a biodiesel-powered diesel engine with adiabatic humidification technique

Abdülvahap ÇAKMAK[1] , Emre DEMİRSAN [2]

[1]Mechanical Engineering Department, Faculty of Engineering, Samsun University, Samsun, Turkey.
[2]Kavak Vocational School, Samsun University, Samsun, Turkey.
[1]abdulvahap.cakmak@samsun.edu.tr, [2] emredemirsan325@gmail.com

[1](ORCID: 0000-0003-1434-6697), [2](ORCID: 0009-0007-1381-9022)

Abstract

As a pre-combustion treatment method, adiabatic humidification of engine intake air is more straightforward and cheaper than other techniques. By adiabatically humidifying the engine intake air, this study aims to reduce the high NO_X emission, a significant downside of biodiesel. The effects of a 40%, 60%, and 80% relative humidification rate on mainly NO_X and soot emissions, engine performance, and combustion characteristics of a B25-fueled diesel engine at various engine loads are investigated. Adiabatic humidification of the engine intake air successfully reduces NO emission. The highest average reduction of 19.14% in NO emission is detected with a humidification rate of 80%. However, due to reduced combustion temperature, the oxidation of CO and soot particles get slow, showing an increasing trend with an increase in humidity ratio. B25 fuel, whose engine performance is lower than diesel fuel at a standard humidity ratio (40%), its performance characteristics at partial engine loads are worsened due to adiabatic humidification. The combustion characteristics are not affected to a great extent by adiabatic humidification. Hence, an 8°C reduction in mean gas temperature is achieved by the humidity ratio of 80% at full engine load, providing lower NO formation by 22.51% than the standard case. Consequently, the adiabatic humidification technique can potentially reduce NO_X emission emitted by biodiesel-powered diesel engine; however, its effectiveness should be compared with other NO_X emission control methods.

Keywords: adiabatic humidification, biodiesel, diesel engine, NO_X emission, pre-combustion treatment method

1. Introduction

Gradually replacing petroleum fuels with biofuels is one of the primary steps to reduce the environmental impact of internal combustion engines. Various renewable alternative fuels, such as biodiesel, renewable diesel, ethanol, ammonia, methanol, and hydrogen, can be used in internal combustion engines. Biodiesel is one of the best alternatives to power diesel engines due to its closer thermochemical fuel properties to diesel fuel. Besides, biodiesel offers significant benefits like being renewable, clean, and domestic fuel. Biodiesel can increase fuel diversity, and thus, countries can enhance their energy security. It is biodegradable and non-toxic. It is compatible with fuel distribution systems and diesel engine technology. It is fully miscible in diesel fuel and can be blended with it in any portion [1]. However, some drawbacks are associated with biodiesel use in diesel engines, such as poor cold flow properties, high viscosity, and high nitrogen oxide (NO_X) emission.

Many researchers have reported that biodiesel yields lower hydrocarbon, carbon monoxide, and particulate matter emissions but higher nitrogen oxide (NOx) emissions than diesel fuel [2]. It is also termed the biodiesel-NO_X effect. Several factors associated with fuel properties, engine technology, and fuel injection parameters are essential for NOx formation [3]. The high NOx emissions of biodiesel are attributed to biodiesel's lower compressibility, reduced radiative heat loss due to less PM, higher adiabatic flame temperature, length of the ignition delay and combustion duration, and fuel effects (cetane number, oxygen content, calorific value, unsaturation degree, kinematic viscosity, surface tension, and boiling point) [4–6]. On the other hand, some researchers have also reported lower NOx

[1]Corresponding author

emissions for biodiesel-fueled diesel engines, which they ascribe to poor fuel atomization and poor combustion [7,8]. Several other studies have shown no difference or slight difference in NOx emissions between diesel and biodiesel [9].

Diesel engines operate at a high temperature and pressure that favor the production of NOx gases [10]. NOx emission, mainly composed of NO and NO_2, is a toxic gas with many adverse effects on the environment and human health. NO_X is linked to respiratory diseases, ozone layer depletion, acid rain formation, and global warming [11]. Because of this, emission regulations have been enacted to reduce NOx emissions from internal combustion engines.

NO_X is the most critical pollutant, and it alone accounts for more than half the pollutant emissions in diesel tailpipes [12]. Exhaust gas recirculation (EGR), lean NO_X-trap, and selective catalytic reduction (SCR) are the commonly used techniques in modern diesel engines for reducing NOx emission. NO_X control methods applied pre-combustion or during combustion cause a rise in other pollutants and deteriorate fuel economy. For instance, EGR can remarkably reduce NOx emissions but increase PM emissions and fuel consumption [13]. This phenomenon is termed the NO_X-PM trade-off and NO_X-BSFC trade-off, respectively. Low exhaust gas temperatures and poisoning are the problems for sophisticated and expensive post-combustion NO_X control devices like SCR and Lean NO_X-trap [14]. Therefore, current investigations focus on reducing NOx and PM emissions simultaneously while maintaining or exceeding high thermal efficiency. The low-temperature combustion (LTC) modes, such as homogeneous charge compression ignition (HCCI), reactivity controlled compression ignition (RCCI), and premixed charge compression ignition (PCCI) mode, offer promising results in that direction [15]. Nevertheless, they are expensive and complicated technologies and suffer from narrow operating ranges, unstable control at the start of combustion, high cycle-to-cycle variations, high CO and HC emissions, low exhaust gas temperature, and thus lower conversion efficiency of after-treatment systems [16]. Other NO_X control methods include using water-fuel emulsions and fuel additives. Pre-combustion NO_X emissions reduction strategies are retardation of injection timing, water injection in the engine intake manifold or direct water injection in the cylinder, water steam injection, and humidifying the engine intake air.

Compared to other methods, the adiabatic humidification method to reduce NO_X emissions from diesel engines powered by biodiesel has been less researched. In order to lower the combustion temperatures and, consequently, the NO_X emission of a diesel engine fuelled by biodiesel, this research concentrates on the adiabatic humidification of the engine intake air.

2. Materials and methods

Figure 1 shows the experimental setup schematically. The adiabatic humidification unit is connected to the engine test setup. It comprises a 450 L insulated humidification tank, relative humidity and temperature sensor, display screen, water pump, injection nozzle, and control unit. At the top surface of the tank, a hole with a diameter of 50.8 mm allows for flowing ambient air in the humidification tank. The water drain hole at the bottom surface evacuates the condensing water from the tank. The large volume of the humidification tank minimizes air flow fluctuations in the engine intake system and allows for maintaining the atmospheric pressure in the tank.

In this study, the engine intake air is adiabatically humidified to decrease the intake temperature and, thus, combustion temperature. During adiabatic humidification, the ambient air passes through an insulated cylindrical tank wherein a nozzle sprays water into the air. It follows the evaporation of the water droplets by taking the heat from the surrounding air and, therefore, drops the intake air's dry temperature and increases its relative humidity. The relative humidity and temperature of the intake air are measured by humidity and temperature sensors and monitored on the display screen. In this current study, the relative humidity of the engine inlet air is increased from 40% to 80% by a 20% increment to reduce the NO_X emission. Increasing the water injection rate by setting the control unit in the adiabatic humidification unit makes it simple to accomplish.

Experiments are performed on an unmodified single-cylinder, four-stroke, water-cooled diesel engine run at a constant speed of 1500 rpm and loads of 25, 50, 75, and 100%. Eddy current-type dynamometer absorbs engine power and measures engine brake torque. The fuel flow rate is determined via a differential pressure transmitter. The piezo pressure transducer and a crank angle encoder capture cylinder pressure-crank angle data. A K-type

thermocouple measures the exhaust gas temperature. All sensor data is collected by NI DAQ hardware and then processed by LabView-based software. Utilizing the BOSCH BEA 060 gas analyzer, CO, CO_2, HC, and NO emissions are measured. BOSCH BEA 070 smoke opacity is used to detect the smoke opacity of the exhaust gas. The details of the engine test setup apparatuses are tabulated in Table 1.

The canola oil biodiesel-diesel blend (B25) is used to investigate the effect of the adiabatic humidification method on NO_X emissions of the diesel engine. Diesel fuel is also used to compare the findings. Experiments are carried out in stabilized test conditions where engine coolant-water temperature is kept at 60-65 ℃. Four readings for performance parameters and eight for emissions are recorded to minimize errors. For combustion analysis, pressure-crank angle data throughout 100 cycles is recorded, and the mean value is processed to determine the heat release rate, pressure rise rate, and mean gas temperature. Holman's method [17] is used to calculate the uncertainty of the engine performance parameters. The maximum relative uncertainty at full engine load for fuel consumption, brake power, brake-specific fuel consumption, and effective brake efficiency is 0.7285%, 0.4661%, 0.8645%, and 0.8729%, respectively. The accuracy for emission measurement is given in Table 1. The combustion analysis results are highly accurate since the combustion parameters are derived from the cylinder pressure-crank angle data of 100 consecutive cycles.

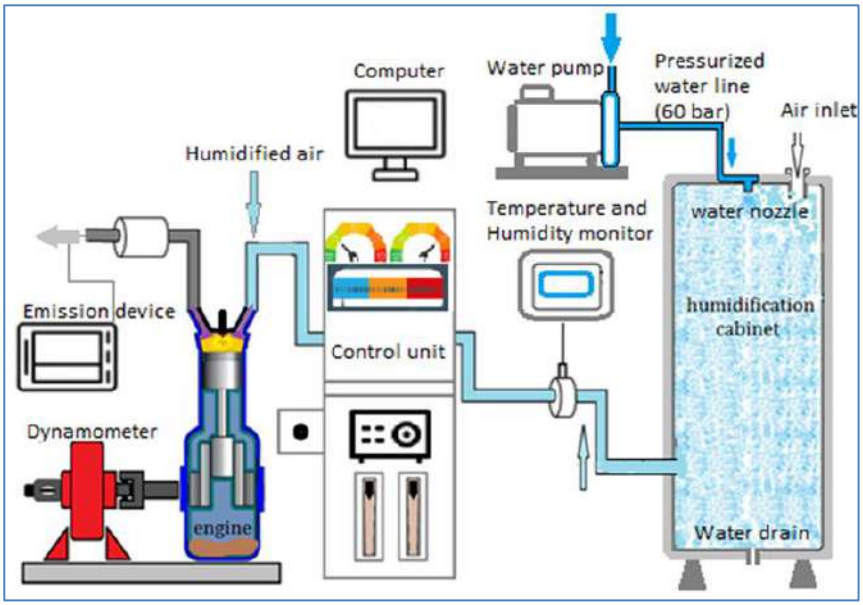

Figure 1. A diagram of the test setup

Table 8. Technical details of the test configuration

Device/Unit	Specification
Engine	Kirloskar TV1 model. Direct injection, single cylinder, water-cooled, four-stroke, stationary. Maximum power & torque: 3.5 kW & 21.8 Nm @1500 rpm
Dynamometer	Eddy-current type AG10 series, Maximum absorption capacity & rotation speed: 10 kW &10000 rpm.
Cylinder pressure sensor	Resolution: 0.07 bar, Maximum pressure: 345 bar, Accuracy: 0.1 bar
Crank angle encoder	Resolution: 1°, Measuring range:0-360°, Accuracy: ±1°
Load cell	Resolution: 0.1 kg, Measuring range:0-50 kg, Accuracy: ±0.1 kg
Fuel flow meter	Differential pressure transmitter, Measuring range: 0–500 mmH_2O
BOSCH BEA 060	NO emission. Resolution: 1 ppm, Measuring range:0-5000 ppm, Accuracy: ±1 ppm CO emission: Resolution: 0.001%, Measuring range:0-10%, Accuracy: ±0.005% HC emission. Resolution: 1 ppm, Measuring range:0-9999 ppm, Accuracy: ±10 ppm
BOSCH BEA 070	Smoke opacity. Resolution: 0.1%, Measuring range:0-100%, Accuracy: ±1%

3. Results and discussion

3.1.The effect of adiabatic humidification on exhaust emissions

Figure 2 shows the effect of adiabatic humidification of the intake air on NO emission and soot opacity. Regardless of fuel type and relative humidity rate, NO emission and smoke opacity rise as the engine load increases. Due to the high combustion temperature and pressure that promotes NO generation, NO emission rises as load increases and is caused by an increase in fuel injection rate. Meanwhile, the air-to-fuel ratio decreases, resulting in high soot. While the NO emission values of diesel fuel and B25 fuel at partial loads are very close, at full load, diesel fuel creates more NO emission by 10.11% than B25 fuel due to its low viscosity and high calorific value. However, the average NO value for B25 is lower by 3.29% than that of D in the standard case. Additionally, as the adiabatic humidification rate increases, the NO emission from B25 fuel gradually decreases; the largest reduction in NO is shown at 80% relative humidity. Raising the relative humidity rate from 40 % to 60 % and then 80% reduces NO emission at an average of 8.55 % and 19.14 % for B25. The main cause of the low NO generation during the humidification process is the decreased intake air temperature, which lowers combustion temperature [18]. Additionally, water vapor in the intake air has a higher specific heat capacity than air, resulting in a greater fall in combustion temperature [19,20]. This study's mean gas temperature curves (see Figure 5b) confirm the reduction in cylinder gas temperature when the intake air is adiabatically humidified. Due to biodiesel's high viscosity, density, high boiling point temperature, and unsaturated methyl ester content, B25 fuel emits 19.94% more soot than diesel fuel on average at the reference relative humidity rate. However, with the relative humidity increase, soot emissions increase more due to lower in-cylinder gas temperature. Compared to the standard case, the soot emission increases by an average of 1.74% and 8.95% when the relative humidity changes from 60% to 80%, respectively. This finding demonstrates that the NO-smoke opacity trade-off also applies to the adiabatic humidification technique. However, it is remarkable that the decrease rate of NO emission in the adiabatic humidification process is higher than the rise of soot emission. It can be attributed to the oxidation of more soot emissions by -OH radicals formed by the dissociation of water molecules. This result is consistent with that of Zhao and Cai [21], who claimed that engine intake air humidification can reduce NOx and soot emissions concurrently.

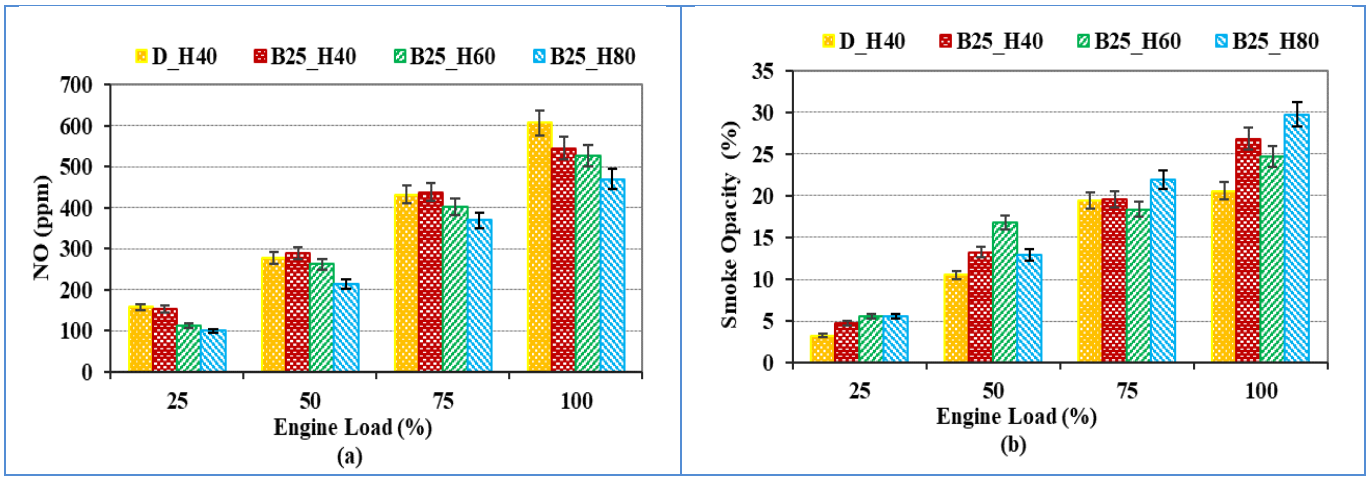

Figure 2. Variation in NO emission (a) and smoke opacity (b) with engine load and humidification rate

Figure 3 displays the CO and HC emissions change with engine load and humidification rate. CO emissions continuously decrease while HC emissions rise as engine load increases. Low cylinder temperature and the heterogeneous fuel-air mixture are the primary factors responsible for CO and HC emission formation. The higher temperature boosts the oxidation of CO to CO_2 with increasing engine load; meanwhile, HC emission increases due to a decreasing excess air coefficient. B25 fuel emits more CO than diesel fuel at all engine loads and humidity levels. Because biodiesel has lower fuel quality than diesel, it may result in worsened fuel atomization and poor combustion. Along with that, HC emission increases as the mixture becomes richer. The adiabatic humidification method, however, has the opposite impact on the CO and HC emissions of B25 fuel. Compared to the standard humidification rate of 40%, CO emission increases by 3.23% and 9.99% for the humidification rates of 60% and 80%, respectively,

while HC emission drops by 20.13% and 37.51%. The oxidation rate of CO is more sensitive to cylinder temperature than HC [22]; therefore, CO formation is more affected by temperature reduction caused by adiabatic humidification. The graph clearly shows that this circumstance supports the idea that CO emissions increase as relative humidity rises. The HC emission of B25 fuel generally reduces as the humidification rate rises and further declines at high humidification rates. It might be ascribed to the thermal decomposition of the water, which yields O, O_2, and -OH radicals which are favorable oxidizers for HCs.

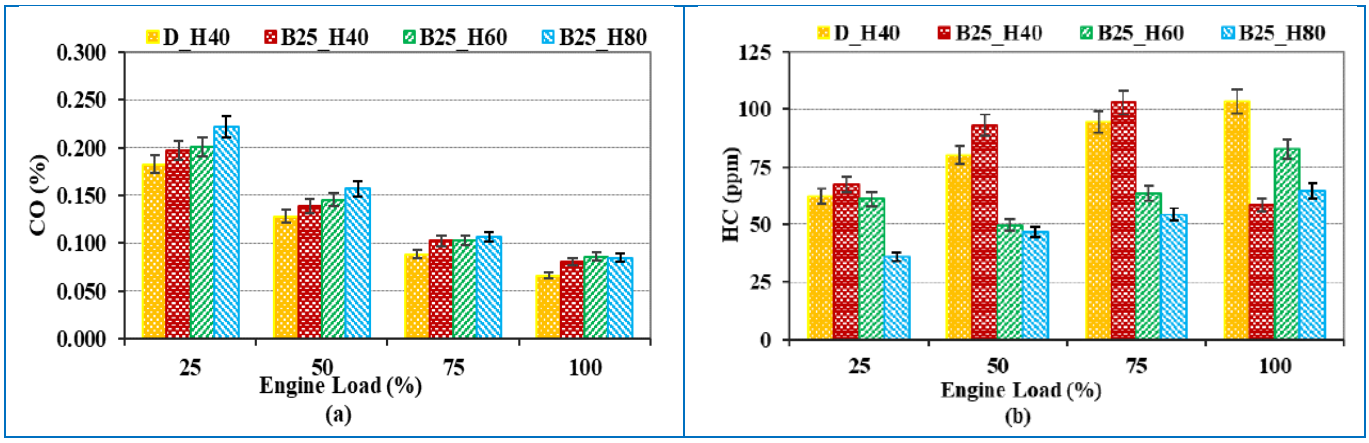

Figure 3. Variation in CO emission (a) and HC emission (b) with engine load and humidification rate

3.2. The effect of adiabatic humidification on combustion characteristics

Figure 4a-4b depicts the effect of the adiabatic humidification method on net heat release rate and cylinder pressure at full engine load. Both figures show that diesel fuel has higher combustion quality than B25 fuel at the standard humidity ratio. The heat release rate indicates the combustion speed and shapes the cylinder pressure. Diesel fuel presents the highest net heat release rate and cylinder pressure by 46.11 J/°CA at 353 °CA and 55.53 bar at 366 °CA. Unlike biodiesel, diesel fuel has lower kinematic viscosity, density, boiling point, and surface tension [24]. These features allow enhanced fuel atomization, evaporation, and mixing with air [25]. Consequently, the fuel-air mixture burns faster, increasing the combustion speed and, thus, the net heat release rate. It should be mentioned that another factor contributing to the higher net heat release rate is the high calorific value of diesel fuel. The adiabatic humidification process does not considerably influence the net heat release rate and cylinder pressure. The maximum net heat release rate for B25 fuel at a humidity ratio of 40% is 41.14 J/°CA at 354 °CA. It slightly decreases to 40.70 J/°CA at a 60% humidity rate but increases to 42.57 J/°CA at an 80% humidity rate. The maximum cylinder pressure is 54.42 bar, 54.58 bar, and 54.46 bar, in the same order.

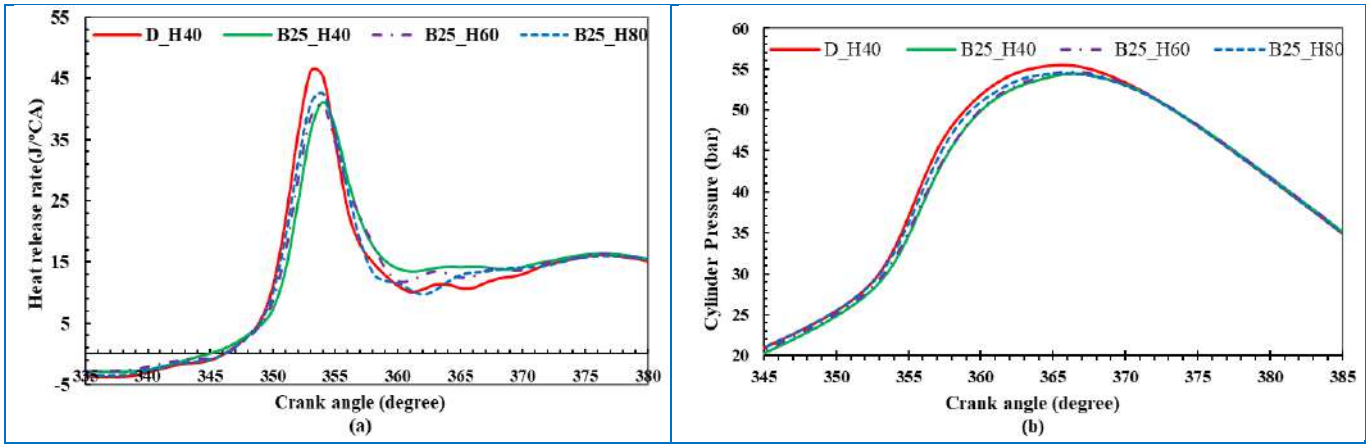

Figure 4. The effect of adiabatic humidification on net heat release rate (a) and cylinder pressure (b) at full engine load

Diesel fuel gives the highest pressure rise rate, as seen in Figure 5a, with a 4.28 bar/°CA at 353 °CA. The effect of adiabatic humidification on the pressure rise rate for B25 fuel is the same tendency observed in the net heat release rate graph. When the humidification ratio is increased from 40% to 60%, and then 80%, the peak pressure rise rate follows the order of 3.99 bar/°CA, 3.86 bar/°CA, and 4.02 bar/°CA at the 354 °CA. The in-cylinder mean gas temperature-crank angle curve for diesel fuel, and B25 fuel with adiabatic humidification ratios are shown in Figure 5b for the engine running at full load. Mean gas temperature curves for all cases follow the same trend, matching between 350°CA and 380 °CA well. The peak mean in-cylinder gas temperature belongs to B25 fuel at the humidification rate of 40%, with a value of 1125 ℃ at 385 °CA. Its value decreases to 1124 ℃ and 1117 ℃ when the humidity rate is raised to 60% and 80%, respectively. This is the targeted and expected result of the adiabatic humidification technique. Increasing the humidification rate from 40% to 80% allows an 8 ℃ reduction in cylinder mean gas temperature, which offers a maximum reduction in NO emission by 22.51% at full engine load.

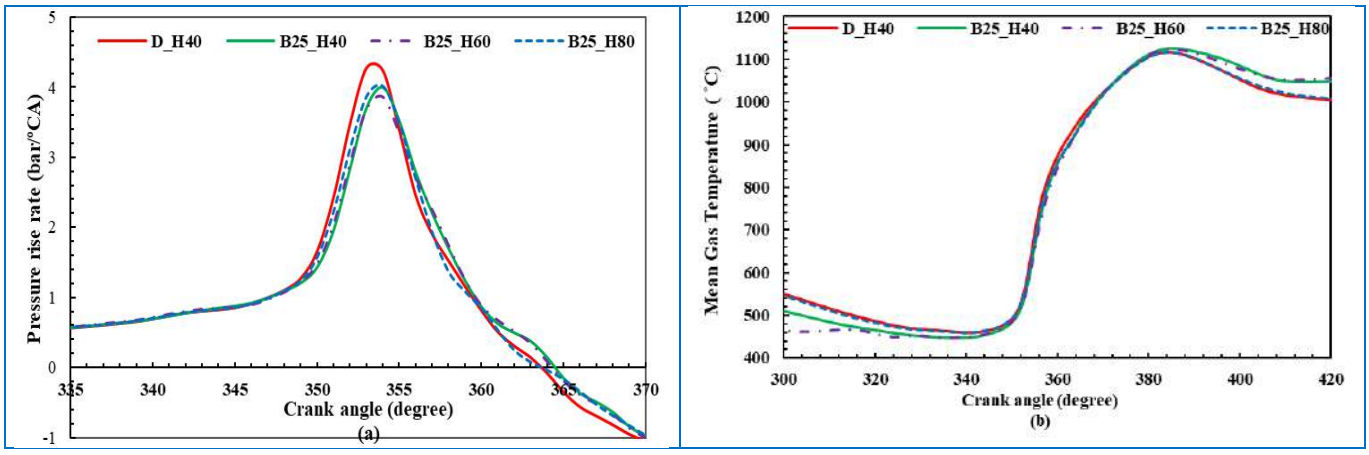

Figure 5. The effect of adiabatic humidification on pressure rise rate (a) and mean gas temperature (b) at full engine load

3.3. The effect of adiabatic humidification on engine performance characteristics

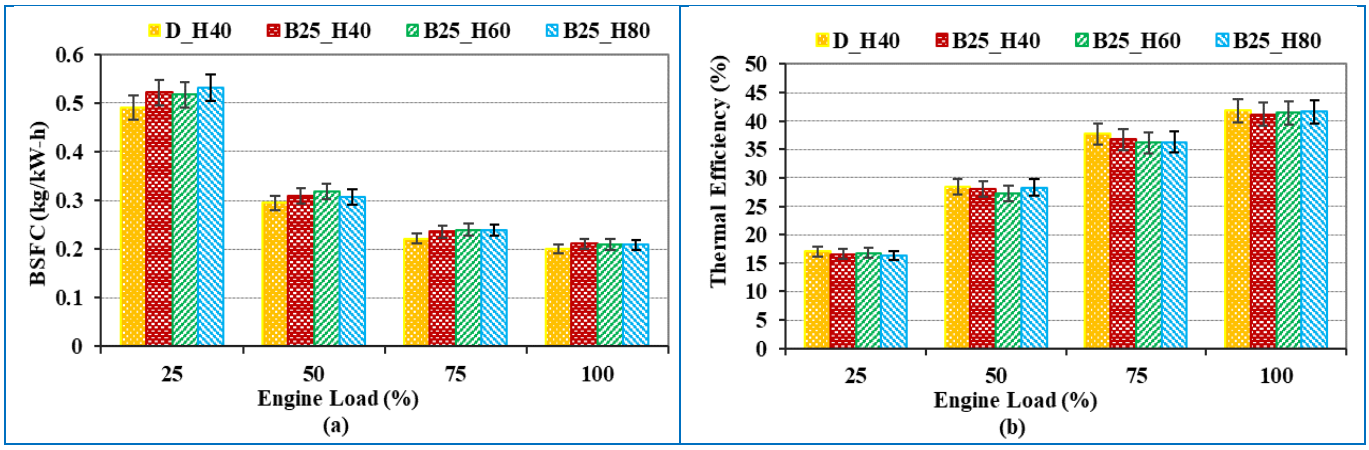

Figure 6. The effect of adiabatic humidification and engine load on brake-specific fuel consumption (a) and thermal efficiency (b)

Figure 6a and 6b shows the variation of brake-specific fuel consumption and brake thermal efficiency against the engine load and humidity rate for diesel fuel and B25, respectively. Changes in these two performance indicators with engine load exhibit an inverse tendency. The increasing engine load at a fixed engine speed allows enhanced engine power and efficiency due to reduced relative heat loss, followed by low brake-specific fuel consumption and high thermal efficiency. Compared to diesel fuel, B25 fuel has a lower average thermal efficiency of 1.90% and a higher average brake-specific fuel consumption of 1.53%. Moreover, B25's engine performance is further degrading with the humidification of the engine intake air. Compared to the standard humidification rate of 40%, the mean

brake-specific fuel consumption rises by 6.33% and 6.49% for the humidification rates of 60% and 80%, while the average brake thermal efficiency falls by 2.70% and 1.91%, respectively. Notably, the thermal efficiency loss is slightly lower at 80% relative humidity than at 60%. This could be explained by lower gas temperatures inside the cylinder, lower heat loss through the cylinder wall, and increasing thermal efficiency [20]. The thermal efficiency at 60% and 80% relative humidity is slightly higher (0.53%-1.04%) than that of the standard humidity ratio when the change in thermal efficiency at full engine load is specifically analyzed. The possible reason for this result could be the water-gas shift reaction in a high-temperature environment, reacting carbon monoxide and water vapor to produce hydrogen and carbon dioxide [26]. The formed hydrogen is a good product for combustion and is involved in combustion, enhancing engine performance. The lower CO concentration at full engine load with adiabatic humidification can support this explanation.

4. Conclusions

Massive efforts are being made to reduce exhaust emissions as emission norms are getting stringent. One method to reduce NOx emissions from internal combustion engines is to lower the combustion temperature inside the cylinder by using diverse strategies. This report presents experimental research on the adiabatic humidification method used to control NO pollution from a conventional diesel engine running on B25 fuel. The engine's intake air is adiabatically humidified at a relative humidity rate of 60% and 80%. The relative humidity rate of 40% is selected for the reference case. Diesel and B25 fuel are used in engine tests performed under various loads at a constant speed of 1500 rpm. The main conclusions are listed below.

- It is observed that adiabatically humidifying the engine's air intake effectively reduces NO emissions from B25 fuel. However, in the meantime, CO emission and smoke opacity both increase.
- As anticipated, the maximum reduction of 22.51% in NO emission is accomplished at 80% relative humidity. In this case, it is determined that the mean in-cylinder gas temperature drops by 8 °C at full engine load.
- The decreased rate of NO emission is higher than the increased rate of smoke opacity. So, it can be concluded that the adiabatic humidification method alleviates the NOx-soot trade-off.
- B25 fuel is determined to have poorer combustion properties than diesel fuel. They are not, however, significantly impacted by adiabatic humidification of the intake air.
- Compared to diesel fuel, the poorer engine performance characteristics of B25 fuel deteriorated due to adiabatic humidification, particularly at low engine loads. However, it is found that at 80% relative humidity and full engine load, there is a 1.04% gain in thermal efficiency. The reason for this is ascribed to hydrogen combustion, which is formed due to the water-gas shift reaction.

Overall, the adiabatic humidification technique reduces the NO emission of a B25-fuelled diesel engine with an expense of high smoke opacity, CO emission, and low engine performance. These negative consequences might also be present in other NOx emission control techniques. Therefore, in future studies, the effectiveness of the adiabatic humidification method should be compared to other NO_X reduction methods such as water/steam injection, water-fuel emulsion, fuel additive use, and EGR.

5. Acknowledgements

TÜBİTAK financially supports this study within the 2209-A University Students Research Projects Support Program scope.

6. References

[1] Al-Samaraae RR, Atabani AE, Uguz G, Kumar G, Arpa O, Ayanoglu A, et al. Perspective of safflower (Carthamus tinctorius) as a potential biodiesel feedstock in Turkey: characterization, engine performance and emissions analyses of butanol–biodiesel–diesel blends. Biofuels 2020;11:715–31. doi:10.1080/17597269.2017.1398956.

[2] Abed KA, Gad MS, El Morsi AK, Sayed MM, Elyazeed SA. Effect of biodiesel fuels on diesel engine emissions. Egypt J Pet 2019;28:183–8. doi:https://doi.org/10.1016/j.ejpe.2019.03.001.

[3] Rajkumar S, Thangaraja J. Effect of biodiesel, biodiesel binary blends, hydrogenated biodiesel and injection parameters on NOx and soot emissions in a turbocharged diesel engine. Fuel 2019;240:101–18. doi:https://doi.org/10.1016/j.fuel.2018.11.141.
[4] Hoekman SK, Robbins C. Review of the effects of biodiesel on NOx emissions. Fuel Process Technol 2012;96:237–49. doi:10.1016/j.fuproc.2011.12.036.
[5] Yuan W, Hansen AC. Computational investigation of the effect of biodiesel fuel properties on diesel engine NOx emissions. Int J Agric Biol Eng 2009;2:41–8.
[6] Kim D-S, Hanifzadeh M, Kumar A. Trend of biodiesel feedstock and its impact on biodiesel emission characteristics. Environ Prog \& Sustain Energy 2018;37:7–19.
[7] Hazar H, Sevinc H. Investigation of exhaust emissions and performance of a diesel engine fueled with preheated raw grape seed oil/propanol blends. Chem Eng Process - Process Intensif 2023;188:109378. doi:https://doi.org/10.1016/j.cep.2023.109378.
[8] Giakoumis EG, Rakopoulos CD, Dimaratos AM, Rakopoulos DC. Exhaust emissions of diesel engines operating under transient conditions with biodiesel fuel blends. Prog Energy Combust Sci 2012;38:691–715. doi:10.1016/j.pecs.2012.05.002.
[9] Xue J, Grift TE, Hansen AC. Effect of biodiesel on engine performances and emissions. Renew Sustain Energy Rev 2011;15:1098–116. doi:https://doi.org/10.1016/j.rser.2010.11.016.
[10] Pulkrabek WW. Engineering Fundamentals of the Internal Combustion Engine. Second. Published by Pearson; 2004.
[11] Boningari T, Smirniotis PG. Impact of nitrogen oxides on the environment and human health: Mn-based materials for the NOx abatement. Curr Opin Chem Eng 2016;13:133–41. doi:https://doi.org/10.1016/j.coche.2016.09.004.
[12] Reşitoğlu İA, Altinişik K, Keskin A. The pollutant emissions from diesel-engine vehicles and exhaust aftertreatment systems. Clean Technol Environ Policy 2015;17:15–27. doi:10.1007/s10098-014-0793-9.
[13] Palash SM, Kalam MA, Masjuki HH, Masum BM, Rizwanul Fattah IM, Mofijur M. Impacts of biodiesel combustion on NOx emissions and their reduction approaches. Renew Sustain Energy Rev 2013;23:473–90. doi:https://doi.org/10.1016/j.rser.2013.03.003.
[14] Çakmak A. Improvement of exhaust emissions in a diesel engine with the addition of an oxygenated additive to diesel-biodiesel blends. Energetika 2022;68:79–90. doi:https://doi.org/10.6001/energetika.v68i1.4859.
[15] Krishnamoorthi M, Malayalamurthi R, He Z, Kandasamy S. A review on low temperature combustion engines: Performance, combustion and emission characteristics. Renew Sustain Energy Rev 2019;116:109404. doi:https://doi.org/10.1016/j.rser.2019.109404.
[16] Fathi M, Jahanian O, Shahbakhti M. Modeling and controller design architecture for cycle-by-cycle combustion control of homogeneous charge compression ignition (HCCI) engines – A comprehensive review. Energy Convers Manag 2017;139:1–19. doi:https://doi.org/10.1016/j.enconman.2017.02.038.
[17] Holman JP. Experimental methods for engineers. 7th editio. New York: McGraw-Hill Series in Mechanical Engineering; 2001.
[18] Kapusuz M, Cakmak A, Ozcan H. Emissions analysis of an SI engine with humidified air induction. Energy Procedia 2018;147:235–41. doi:10.1016/j.egypro.2018.07.087.
[19] Tauzia X, Maiboom A, Shah SR. Experimental study of inlet manifold water injection on combustion and emissions of an automotive direct injection Diesel engine. Energy 2010;35:3628–39. doi:https://doi.org/10.1016/j.energy.2010.05.007.
[20] Chen B, Zhang L, Han J. An investigation on the effect of intake air humidification on the thermal balance of a turbocharged gasoline direct injection engine. Case Stud Therm Eng 2020;21:100719. doi:https://doi.org/10.1016/j.csite.2020.100719.
[21] Wang K, Zhao C, Cai Y. Effect of Intake Air Humidification and EGR on Combustion and Emission Characteristics of Marine Diesel Engine at Advanced Injection Timing. J Therm Sci 2021;30:1174–86. doi:10.1007/s11630-021-1460-1.
[22] Heywood JB. Internal combustion engine fundamentals. New York: McGraw-Hill; 1988.
[23] Kapusuz M, Çakmak A, Özcan H. Application of oxygen enrichment and adiabatic humidification to suction air for reducing exhaust emissions in a gasoline engine. Energy Sources, Part A Recover Util Environ Eff 2023;45:194–211.

[24] Mehra KS, Pal J, Goel V. A comprehensive review on the atomization and spray characteristics of renewable biofuels. Sustain Energy Technol Assessments 2023;56:103106. doi:https://doi.org/10.1016/j.seta.2023.103106.
[25] Boggavarapu P, Ravikrishna R V. A Review on Atomization and Sprays of Biofuels for IC Engine Applications. Int J Spray Combust Dyn 2013;5:85–121. doi:10.1260/1756-8277.5.2.85.
[26] Ebrahimi P, Kumar A, Khraisheh M. A review of recent advances in water-gas shift catalysis for hydrogen production. Emergent Mater 2020;3:881–917. doi:10.1007/s42247-020-00116-y.

International Conference on Advances and Innovations in Engineering

Influence of welding tool advance speed on weld tensile strength in friction stir lap welding of 7075-T651 aluminum alloy plates

Omer EKİNCİ[1], Zulkuf BALALAN[2]

[1]Department of Astronautical Engineering, Faculty of Aviation and Space Sciences, Sivas University of Science and Technology, Sivas, Turkey.
[2]Department of Mechanical Engineering, Faculty of Engineering and Architecture, Bingol University, Bingol, Turkey.
[1]omerekinci@sivas.edu.tr, [2]zbalalan@bingol.edu.tr

[1](ORCID: 0000-0002-0179-6456), [2](ORCID: 0000-0001-5808-6263)

Abstract

High-strength 7075-T651 aluminum alloy is widely used as a structural material in aircraft. It is not possible to reliably weld this alloy with conventional fusion welding methods. Therefore, friction stir welding, a solid-state welding method, was developed. Since the materials are welded without melting by this welding method, defects related to melting do not appear, so it is effective in welding aluminum alloys. In this study, 2 mm thick 7075-T651 aluminum alloy plates were combined with friction stir lap welding after being placed on top of each other. According to the results obtained, a stronger weld was produced when the welding tool advance speed, that is, the welding speed, was increased. The weld having the highest tensile load of 6167 N was made with the highest tool advance speed of 51 mm/min.

Keywords: aluminum alloy, tool advance speed, tensile strength

1. Introduction

7075 aluminum alloy is a high-strength metal and crucial, particularly for the aerospace industry structural applications, and is usually utilized as stringers structural components in aircraft fuselage panels and wings [1]. However, welding this alloy is very hard by traditional fusion welding methods. Because it has some amount of copper leading to cracks in the weld and liquation cracks in the heat-affected zone and thus impairing the joint mechanical characteristics [2,3]. Hence, rivets have become the main joining elements for aircraft structures. On the other hand, a solid-state welding technique of friction stir welding (FSW) is assessed as a substitute for riveting [4]. The maximum temperature in the FSW operation is below the melting point of the metals being welded. Thus, the FSW does not produce the problems of solidification cracking and gas porosity particularly prevalent in fusion welding methods. The FSW process comes forward when welding light metals like aluminum alloys, magnesium alloys compared to fusion welding and mechanically joining items [5,6]. Besides, there are no mechanical joining elements such as rivets in the FSW, and thus structures and components can be produced in shorter times and at lower weights [7]. The most crucial variables in the FSW process are the welding tool's rotational and feed rate speeds [8]. Choosing the right combination of these parameters provides ideal heat input for materials to be softened, flowed, and mixed, resulting in high-strength joints. It has been demonstrated that FSW works well for butt-joining aluminum alloys such as 2024-T3 [9,10], and 7075-T6 [9,11]. Aircraft structural components are generally lap joined with rivets [12, 13]. The FSW is used for producing butt and lap joints, but it has been utilized mostly for creating butt joints so far [14]. Babu et al. [15] investigated the microstructure and mechanical properties of the lap joints of AA2014 aluminum alloy sheets made by the FSLW and rivet. It is found that the joints made with the FSLW performed much better tensile lap shear strength compared to the joints made with rivets. Tashkandi [16] studied the lap joining of the 6061 Al Alloy sheets with FSW using 900 and 1120 rpm tool rotation speeds and 60 and 90 mm/min advancing speeds. They obtained the joint with the highest strength at 1120 rpm and 90 mm/min. Yazdanian et al. [17] studied

[1]Corresponding author

the lap joining of AA6060-T5 Al Alloy sheets with FSW applying tool rotation speed varied from 500 to 2000 rpm and advancing speed varied from 112 to 630 mm/min. According to the results, the weld strength decreased with an increase in the rotation speed.

2. Material and Method

A 2 mm thick, 100 mm long and 100 mm wide 7075-T651 aluminum alloy plate was put on another 7075-T651 aluminum alloy plate on a region of 50x100 mm2. After that, they were firmly attached to the table on the Falco model universal milling machine with the help of the clamping apparatus and then joined via the friction stir lap welding (FSLW) method as seen in the schematic illustration in Figure 1. Plates were welded under conditions of a constant 1-degree clockwise tool tilt angle, the tool rotation speed of 980 rpm, and 3.8 mm tool immersion depth by applying three different welding tool feed rates (22, 37, and 51 mm/min). The triangle tip welding tool used in the welding process was produced from H13 hot work tool steel. The welding tool is given in Figure 2. The Welded plates are presented in Figure 3. 25 mm wide and 150 mm long specimens for tensile testing cut from the welded plates are given in Figure 4. Tensile specimens were pulled on a SHIMADZU tensile machine with a tensile rate of 1 mm/min. The cross-sectional area samples of the welds were etched for 15 seconds with Keller's solution (2.5 ml nitric acid, 1.5 ml hydrochloric acid, 1 ml hydrofluoric acid and 100 ml distilled water) after sanding to 1500 grit sandpaper.

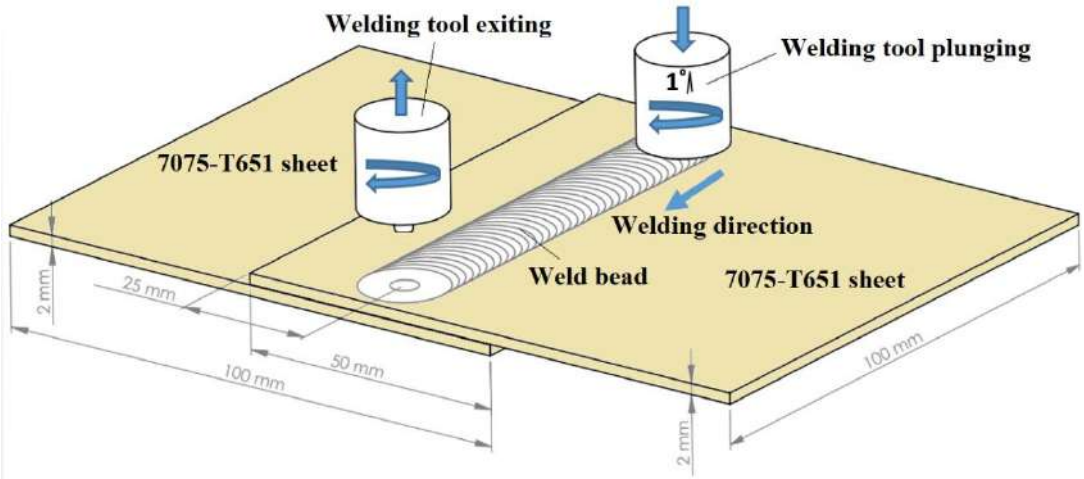

Figure 1. FSLW process schematic illustration

Figure 2. Welding tool employed in the FSLW operation

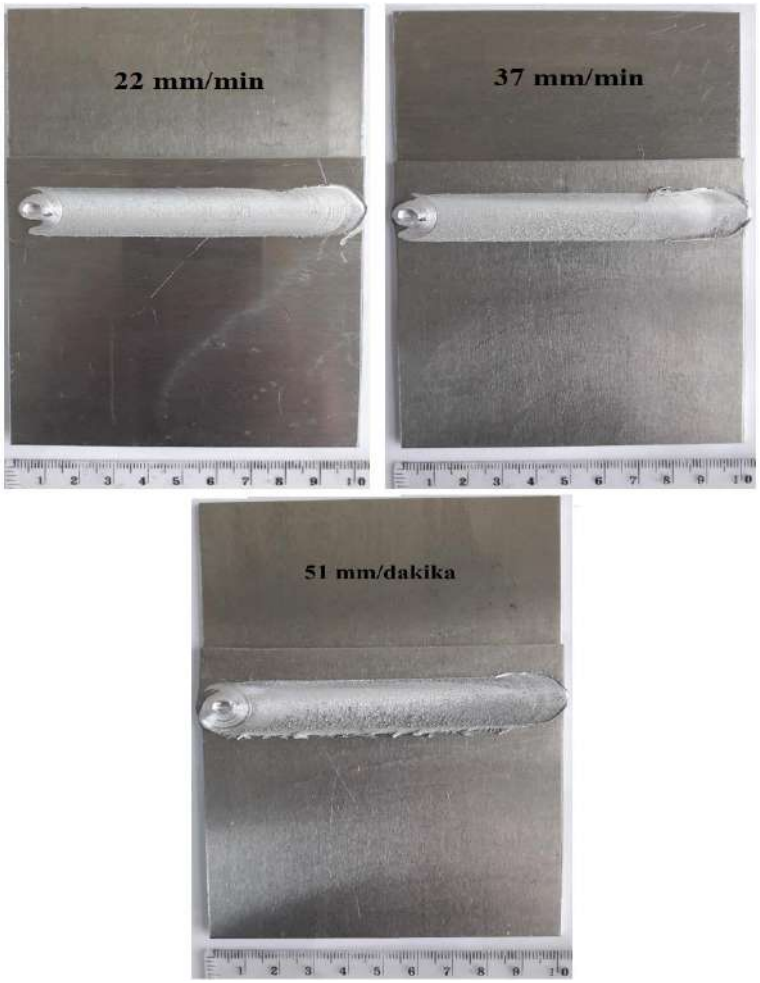

Figure 3. Sheets combined with the FSLW at various welding tool feed rates

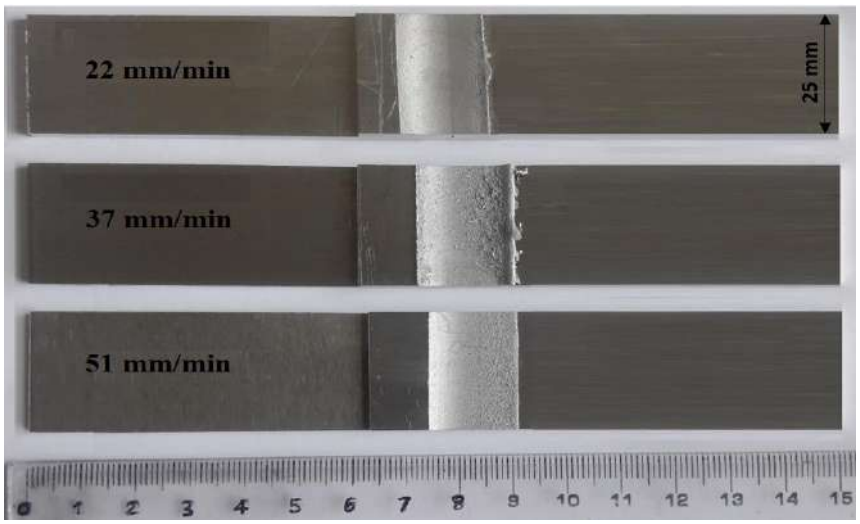

Figure 4. Tensile specimens of FSLW joints produced at different tool feed rates

3. Results and discussion

Top views of the weld beads of the produced joints are given in Figure 5. It is seen that there is a cavity formation at the tool exiting region in the welds made at tool feed rates of 22 and 37 mm/min. However, no cavity formation was observed in the weld made at 51 mm/min. The lines formed by the tool shoulder at the top of the weld bead decreased by turning into small particles with an increase in the tool feed rate.

Figure 5. Top view of the FSLW joints produced at different tool feed rates

Macro Cross-section views of the welds are given in Figure 6. It is evident that there is occurrence of the tunnel defect in the welds created at 22 and 37 mm/min tool feed rates. In addition, the tunnel defect got slightly smaller when increasing from 22 to 37 mm/min. However, there was no tunnel defect formation in the weld created by 51 mm/min.

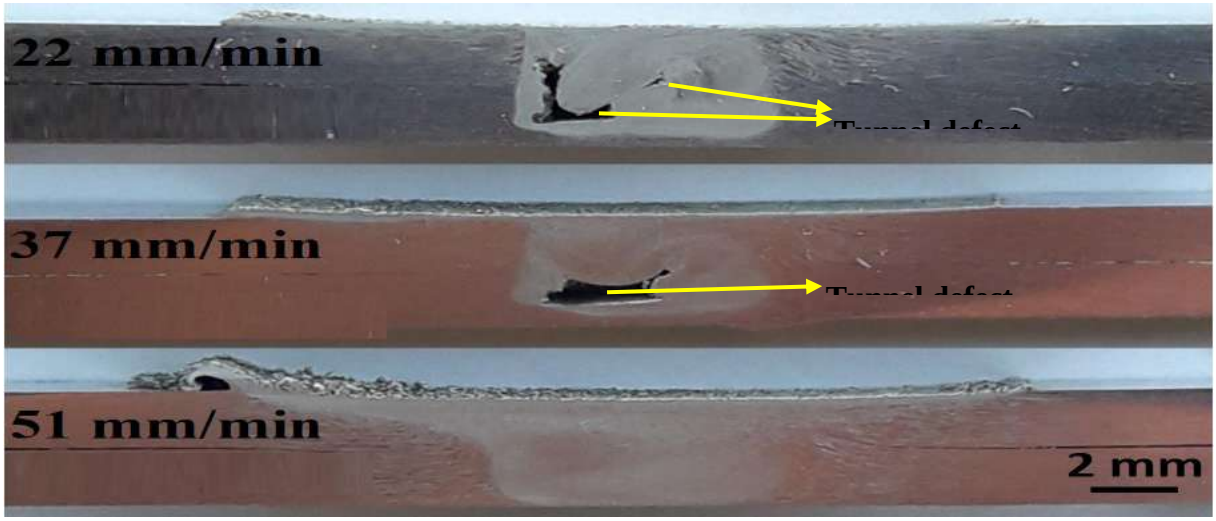

Figure 6. The cross-sectional appearance of FSLW joints produced at different tool feed rates

Tensile shear loads of the fabricated welds are given in Figure 7. As can be seen, there was a significant increase in the strength of the weld when the welding speed (tool advancing speed) was improved from 22 to 51 mm/min. The increase in the weld strength is considerably higher when the tool feed rate was improved from 22 to 37 mm/min compared with enhancing the tool feed rate from 37 to 51 mm/min. In other words, the increase in the amount of the weld strength decreased significantly with enhancing the tool feed rate from 22 to 37 mm/min and then to 51 mm/min.

This means that the weld strength could slightly increase with increasing the tool feed rate from 51 to a certain point under the other constant welding conditions used in this study. The weld having maximum tensile shear load of 5637 N made at 51 mm/min while the weld with minimum load produced at 22 mm/min. The weld made at 51 mm/min is the strongest as it does not possess cavity and tunnel defect as shown on the weld bead and in the weld cross-section in Figures 5 and 6, respectively. The joint of 37 mm/min is stronger than that of 22 mm/min because of having a smaller tunnel defect (larger bonding area) as seen in Figure 6. Lee et al. [18] studied FSLW of dissimilar 5052 and 6061 Al alloys and they stated that higher tool welding speed produced stronger joints. Dubourg et al. [19] also reported that increasing the tool welding rate generates better joints in the FSLW of AA7075-T6 and AA2024-T3 alloys.

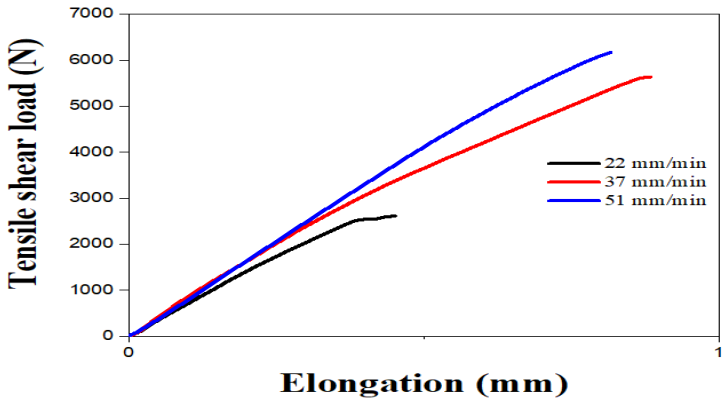

Figure 7. Tensile strength results for the FSLW joints

Figure 8 illustrates the fracture surface of the joint made at 51 mm/min tool welding speed. Dimples of different sizes were observed on the fracture surface, which is an indication of ductile-type fracture.

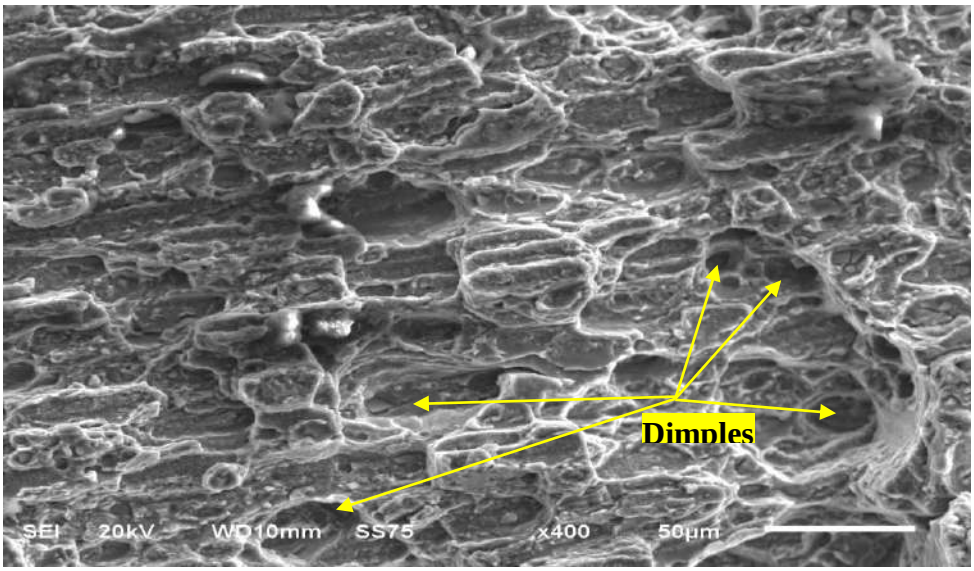

Figure 8. Fracture surface SEM image of the joint produced at 51 mm/min tool feed rate

4. Conclusions

The cavity and tunnel defects took place in the welds made at 22 and 37 mm/min speeds. However, these defects disappeared with increasing the tool feed rate to 51 mm/min. Therefore, the weld of the 51 mm/min had the greatest strength. The weld strength improved with improving tool feed rate from 22 to 51 mm/min thanks to getting smaller and then disappearing of the tunnel defect. Maximum tensile shear load of 5637 N was reached in the joint created at 51 mm/min. However, it is possible to obtain stronger welds with a rising tool feed rate above 51 mm/min.

5. References

[1] Christner B, Mc Coury J, Higgins S. Development and testing of friction stir welding as a joining method for primary aircraft structure. In: 4th International symposium on friction stir welding, Park City, UT, USA, Session 4A, May 14–16, TWI Ltd., Abington, Cambridge CB1 6AL, UK; 2003.

[2] Fu RD, Sun ZQ, Sun RC, Li Y, Liu HJ, Liu L. Improvement of weld temperature distribution and mechanical properties of 7050 aluminum alloy butt joints by submerged friction stir welding. Mater Des 2011;32:4825–31.

[3] Rajakumar S, Muralidharan C, Balasubramanian V. Influence of friction stir welding process and tool parameters on strength properties of AA7075-T6 aluminum alloy joints. Mater Des 2011;32:535–49.

[4] L. Dubourg, A. Merati, M. Jahazi, Process optimisation and mechanical properties of friction stir lap welds of 7075-T6 stringers on 2024-T3 skin, Materials and Design 31 (2010) 3324–3330,

[5] Abdollah-Zadeh A, Saeid T, Sazgari B. Microstructural and mechanical properties of friction stir welded aluminum/copper lap joints. J Alloy Compd 2008;460:535–8.

[6] Leal RM, Loureiro A. Effect of overlapping friction stir welding passes in the quality of welds of aluminium alloys. Mater Des 2008;29:982–91.

[7] Leal RM, Loureiro A. Effect of overlapping friction stir welding passes in the quality of welds of aluminium alloys. Mater Des 2008;29:982–91.

[8] M. Grujicic, G. Arakere, C.-F. Yen, and B.A. Cheesema, "Computational Investigation of Hardness Evolution During Friction-Stir Welding of AA5083 and AA2139 Aluminum Alloys," (English), Journal of Materials Engineering and Performance, vol. 20, no. 7, pp. 1097–1108, 2011

[9] Russell SG, Tester M, Nichols E, Cleaver A, Maynor J. Static, fatigue and crack growth behavior of friction stir welded 7075-T6 and 2024-T3 aluminum alloys. In: Friction stir welding and processing, Indianapolis, IN, USA, 93-104, TMS (The Minerals, Metals & Materials Society); 2001.

[10] Murphy A, Price M, Wang P. The integration of strength and process modeling of friction-stir-welded fuselage panels. In: 46th AIAA/ASME/ASCE/AHS/ASC structures, structural dynamics, and materials conference, Austin, TX, USA, April 18–21; 2005. p. 1–15.

[11] Su J-Q, Nelson TW, Sterling CJ. Microstructure evolution during FSW/FSP of high strength aluminum alloys. Mater Sci Eng A 2005;405(1–2):277–86.

[12] Christner B, Mc Coury J, Higgins S. Development and testing of friction stir welding as a joining method for primary aircraft structure. In: 4th international symposium on friction stir welding, Park City, UT, USA, Session 4A, May 14–16. Cambridge CB1 6AL, UK: TWI Ltd., Abington; 2003.

[13] Dracup BJ, Arbegast WJ. Friction stir welding as a rivet replacement technology. In: Automated fastening conference & exposition, Nashville, TN, USA; October, 1999

[14] Chang-Yong Lee, Won-Bae Lee, Jong-Woong Kim, Don-Hyun Choi, Yun-Mo Yeon, Seung-Boo Jung, Lap joint properties of FSWed dissimilar formed 5052 Al and 6061 Al alloys with different thickness, J Mater Sci (2008) 43:3296–3304 DOI 10.1007/s10853-008-2525-1

[15] S. Babu, G.D. Janaki Ram, P.V. Venkitakrishnan, G. Madhusudhan Reddy and K. Prasad Rao, Microstructure and Mechanical Properties of Friction Stir Lap Welded Aluminum Alloy AA2014, J. Mater. Sci. Technol., 2012, 28(5), 414–426.

[16] M. A. Tashkandi, Lap Joints of 6061 Al Alloys by Friction Stir Welding, Materials Science and Engineering 205 (2017) 012005 doi:10.1088/1757-899X/205/1/012005

[17] Yazdanian S., Chen Z. W., Littlefair G. Effects of friction stir lap welding parameters on weld features on advancing side and fracture strength of AA6060-T5 welds, J Mater Sci (2012) 47:1251–1261, DOI 10.1007/s10853-011-5747-6.

[18] Chang-Yong Lee, Won-Bae Lee, Jong-Woong Kim, Don-Hyun Choi, Yun-Mo Yeon, Seung-Boo Jung, Lap joint properties of FSWed dissimilar formed 5052 Al and 6061 Al alloys with different thickness, J Mater Sci (2008) 43:3296–3304, DOI 10.1007/s10853-008-2525-1

[19] Dubourg L, Merati A, Jahazi M. Process optimisation and mechanical properties of friction stir lap welds of 7075-T6 stringers on 2024-T3 skin. Mater Des 2010;31:3324–30.

International Conference on Advances and Innovations in Engineering

Development Of Hybrid (Metal & Plastic) Brake Pedal For Manual And Automatic Transmissions Vehicles

Salih KARAKAŞ[1] , Neslişah HAMZAÇELEBİOĞLU[2], Hüseyin KARABULUT [3]

[1,2,3]ORAU Orhan Otomotiv Kontrol Sistemleri, Ar-Ge Merkezi, Bursa, TÜRKİYE.
[1]salih.karakas@orau.com.tr, [2]neslisah.hamzacelebioglu@orau.com.tr, [3]huseyin.karabulut@orau.com.tr

Abstract

In this study, development steps of brake pedal and its structure is investigated which is used manual and automatic transmission vehicles. Brake pedal is part of brake system which is provide activation to all counter parts like brake booster. All other components of brake system like brake caliper, master cylinder (brake booster), hydraulic block (dynamic stability control), brake discs, brake caliper and all tubes for hydraulic fluids activated by pedal mechanism. Also, sensor which is provide stop lamb activation is linked to pedal system.

This study is based on development of brake pedal mechanism in innovative way and take advantages from its design and materials. Considering latest trends in automotive industry which is very competitive and competition level and challenges is increasing day by day with new regulations and news targets like to find environmentally friendly engineering solutions, low weight cars and less fuel consumption. Main goal of this study is combining this new trend requirements and main functions must be fulfil to safety and efficient activation of brake system.

According to these criteria's design limits is determined and virtually is analyzed via Abaqus CAE program and after physical confirmations are performed by laboratory tests. During virtual validation part of this study Digimat® program is used to analyze for get more accurate results. Digimat is providing to transfer mold flow analysis to Abaqus its advantage is simulating fiber orientation on the mold like physical injection of part and calculate risk of defects like welding line. This study is investigating all development steps of brake pedal mechanism Theorical studies optimized design solution and it is well defined, after that theorical validation, practical studies like laboratory tests all theorical studies are validated.

Keywords: Brake pedal, Hybrid design solution, Environmental-friendly, Brake system

1. Introduction

In parallel rapid increasement of number of vehicles in the world, high growth of industries and the reason of these growth is huge demand and consumption is causing excessive release of carbon monoxide (CO). Nature is getting more polluted and the natural balance of nature is being destroyed. This contamination has reached serious dimensions that threaten human health and life. Studies are being carried out and decisions are taken in many parts of the world on this subject. Automotive industry is supporting engineering solutions which are taking advantages for less CO emission and aiming to protect nature and human health and life. In these challenges also automotive industry has big competition especially cost effective and light components are best solution. Hybrid brake pedal mechanism is allowing to produce pedal mechanism with less weight compared conventional steel brake pedals and due to less carbon ingredient of plastic raw material it is beneficial. In this study replacing steel brake pedal mechanism (especially support of brake pedal and pedal arm) (1) with plastic support and over-molded pedal arm and validation steps of the development is described. When literature is checked that there are many works on pedal development including the design and testing of the brake pedal from metal to polymers. [1,2,3,4,5,6,7,8]

[1]Corresponding author

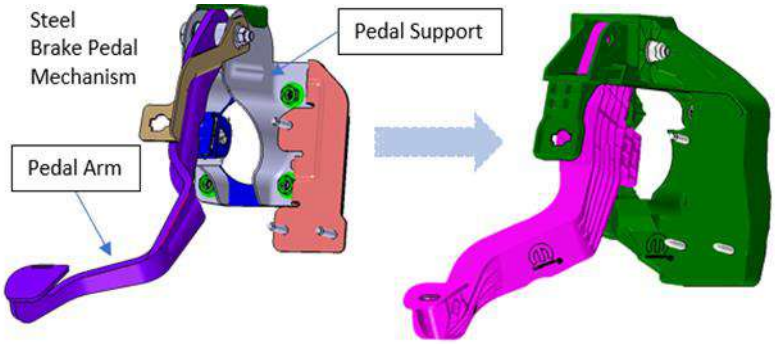

Figure1. View of steel pedal mechanism and hybrid pedal mechanism

2. Methodology

2.1 Building Kinematic & Ratio

First study as always for all mechanism is build efficient and most precise kinematic and well define distances to other parts surrounding of brake pedal. Considering minimum clearance between steering column in all strokes and calculate necessary stroke to brake booster push rod. According to kinematic study (2) stroke ratio (1) is calculate and average value is compared with pure geometric ratio (3).

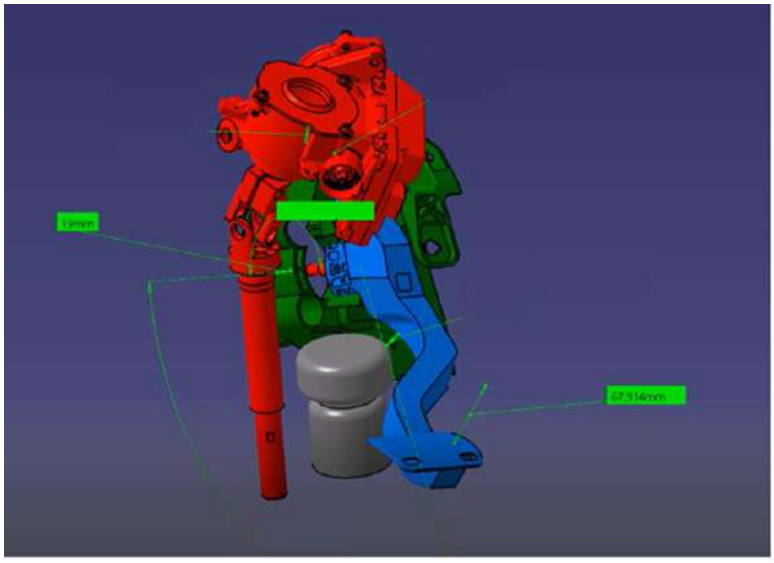

Figure2. View of kinematic study on CATIA

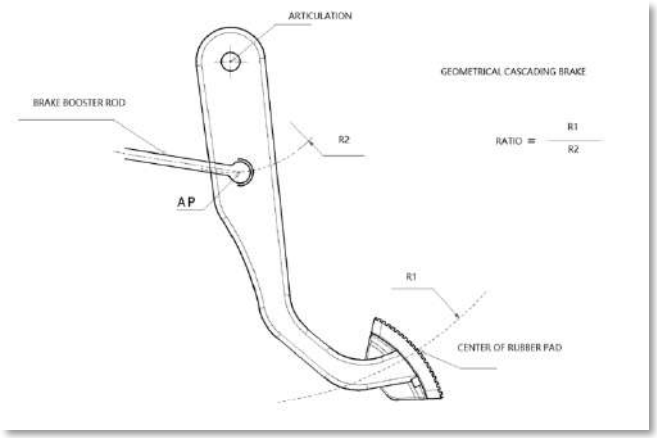

Figure3. Sketch of pure geometrical ratio (R1/R2)

Table 1. Stroke Ratio Calculation Table according to kinematic analysis

R2	R1	RATIO
0	0	0
2.24	8.19	3.67
4.47	16.33	3.65
6.71	24.42	3.64
8.94	32.46	3.63
…	…	…
…	…	…
…	…	…
38	131.84	3.47
		3.57 (average)

2.2. Finite Element Analysis

Design is built according to criteria which is required to provide convenient stroke to brake booster push rod and with exact ratio to transfer required load to brake system. After that maximum severity condition is virtually analyzed. Most critical load cases between 200 daN and 250 daN from foot pad area load application point is simulated with different thermal and moisture condition. (23 °C and 80°C + HR). Digimat material card for plastic raw material and Mold-flow analysis results (4) transferred to Abaqus program to have more accuracy results.

2.2.1 Mold Flow Analysis Data Used as Input For FEA

FEA simulation which is performed without Digimat cannot check effect of injection process. There is no data for check the influence of fiber orientation, welding lines on part etc. Digimat has advantage to check these details during simulation and giving chance to get more realistic results.

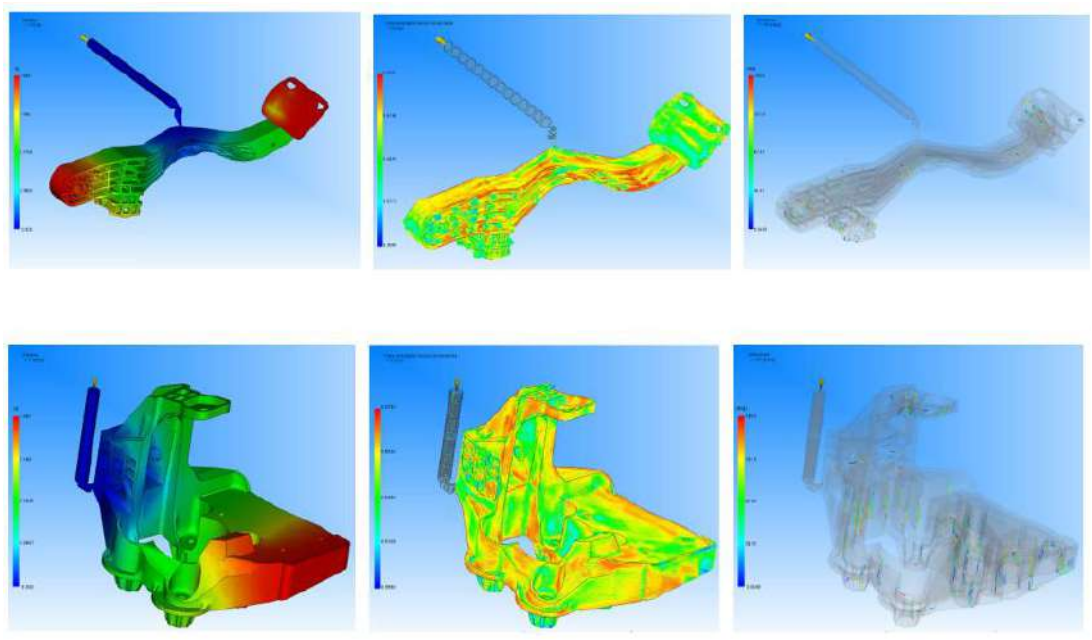

Figure 4. View of mold flow data's used as well for FEA simulation input (filling time, fiber orientation, welding line)

2.2.2 Raw Material Card Integrated to FEA Simulation

Plastic raw materials mechanical properties highly influenced from temperature and humidity. Digimat is allowing to transfer exact properties depending on thermal condition by preparation of material card.

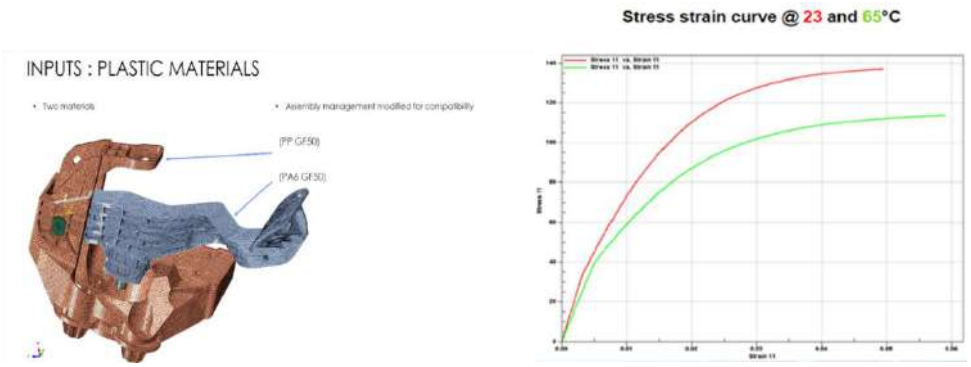

Figure 5. Material card for different temperature and moisture condition is integrated to FEA simulation.

2.2.3. FEA Simulation Results

FEA simulation is performed different load cases with different cycle, brake pedal fixed, load applied according to vehicle configuration (6), max stress values (7) and failure risk factor(7) is checked.

Figure 6. Input data view of FEA simulation

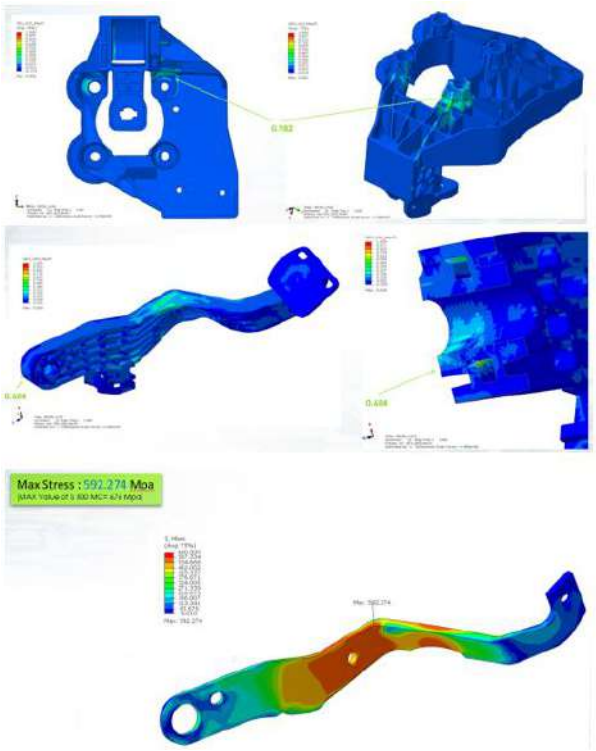

Figure 7. Digimat failure indicator and max stress values example.

2.3 Laboratory Tests

Validate and prove theoretical study tests performed by ORAU Orhan Automotive R&D center by using pedal characterization test machine (8). Brake pedal is assembled to rigid plate according to vehicle configuration, servo piston is positioned perpendicular to load application point and single load, load cycles applied with different conditioning of brake pedal unit. Thermal cabin (9) is used to pre-conditioning of the part and part is exposed to high temperature and humidity. During test plastic and elastic deformation values (10) are recorded. After the test functionality of parts are checked, any crack or breakage is cause failure of the test.

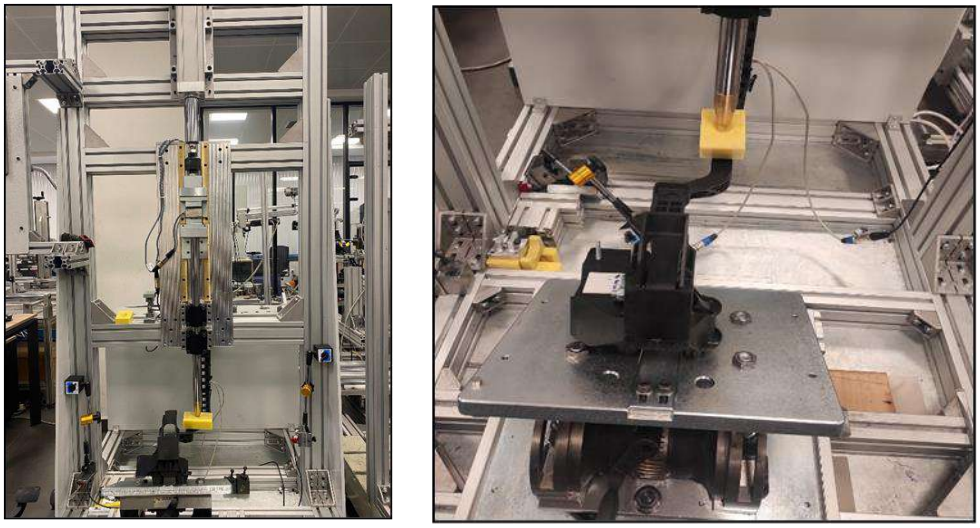

Figure 8. Brake pedal characterisation test bench view.

Figure 9. Thermal cabin view.

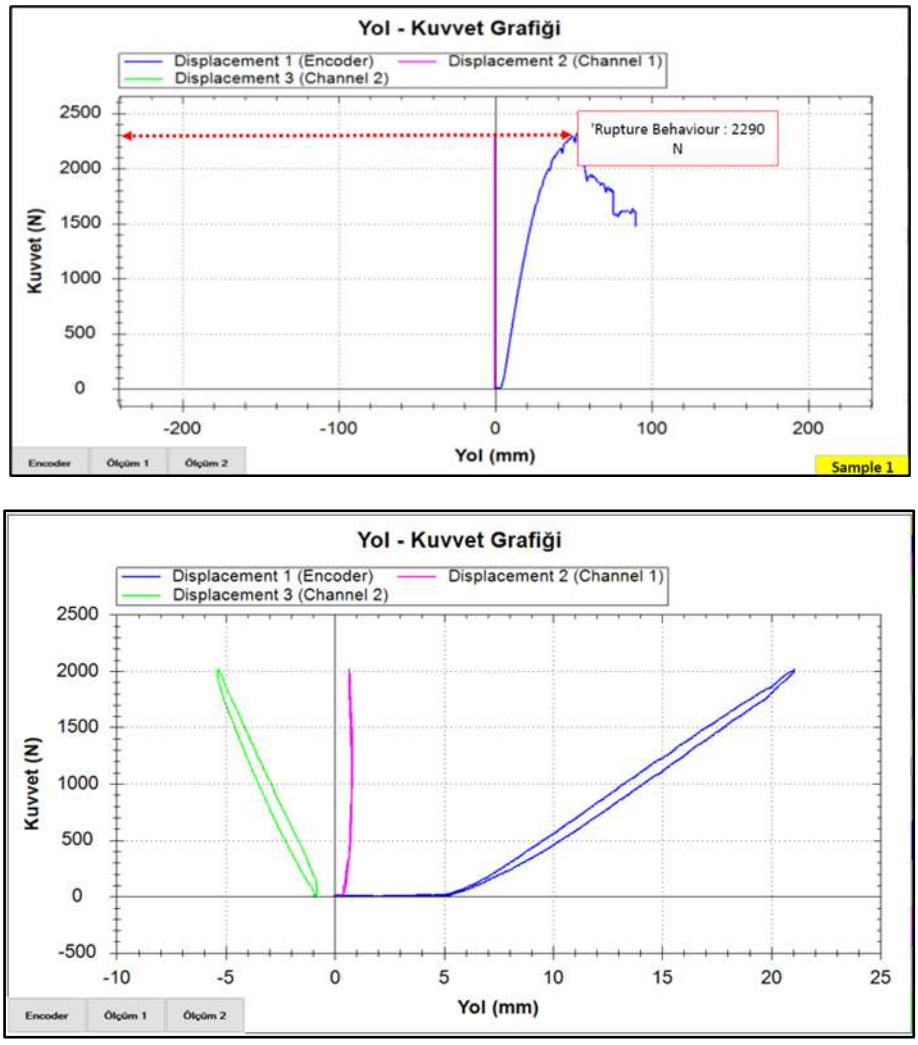

Figure 10. Data which is received during execution of tests.

Figure 11. Tested part visuals. No breakage or crack observed.

3. Results

Main functions of brake pedal unit is validated in theoretical methods and also after theoretical confirmation is completed, physical test performed to check alignment of the results. FEA simulations performed with consideration of injection defects like fiber orientation and plastic raw material behaviour in different thermal condition, as an advantage theoretical study and practical study match perfectly. FEA results and validation test results match with high accuracy like 97%.

As a result of all study conventional metal brake pedals and hybrid (plastic brake pedal with metal insert) could achieve same function and could resist same effort under same conditions. Hybrid brake pedal has significant advantages and there is no performance loss by achieving these advantages.

4. References

[1] Sapuan, S.M., (2005). A Conceptual Design of the Con-current Engineering Design System for Polymeric-Based Composite Automotive Pedals, *American Journal of Applied Sciences* 2(2): 514-525,

[2] Lee,S.H.,Park, T.W., Jung, I.H., Seo, J.H., (2004). Development of Automotive Braking Performance Analysis Program Considering Dynamic Characteristics, *Trans. KSAE,* Vol. 12, No. 2, pp. 175-181.

[3] Kim, J. D., (2004). A Study on Load Analysis and Durability Test Condition Evaluation of Automotive Brake Pedal, M. S. Thesis, Changwan National University.

[4] Martinho Soares, (2016). Hybrid Brake Pedal, *Metal Morphosis, Final Even*t, BWI.

[5] Megan Scheitlin, (2011). Pedal Box Design for Formula SAE, *Renewable Energy Vehicle Project*,

[6] K.K. Dhande, PN.I. Jamadar, Sandeep Ghatge, (2014). Conceptual Design and Analysis of Brake Pedal Profile, *Int. Journal of Innovative Research in Science, Engineering and Technology* Vol.3, 11, pp.17432-17441.

[7] K K Dhande, N I Jamadar and Sandeep Ghatge, (2014). Design and Analysis of Composite Brake Pedal: An Ergo-nomic Approach" *Int. J. Mech. Eng. & Rob. Res*, Vol. 3, No. 3.

[8] Dincel S., (2022). "OPTIMUM DESIGN OF VEHICLE BRAKE PEDAL FROM POLYMER COMPOSITE MATERIAL FOR ADDITIVE MANUFACTURING METHOD AND PRODUCTION AS SERIAL PART REPLACEMENT*"*

[9] Orau Orhan Otomotiv Internal Product Specifications

[10] Reduced Weight Automotive Brake Pedal Test & Analysis, *International Journal of Automotıve Scıence And Technology* 2017, VOL. 1, NO:2, 8-13

International Conference on Advances and Innovations in Engineering

Investigation of Heat Storage Capacities of Organic and Inorganic Phase Change Materials in a Heat Exchanger

Mustafa KILIÇ[1], Mahir ŞAHİN[2]

[1,2]Mechanical Engineering, Faculty of Engineering, Adana Alparslan Turkes Science and Technology University, Adana, Turkey.
[1]mkilic@atu.edu.tr, [2]msahin@atu.edu.tr

[1](ORCID: 0000-0002-8006-149X), [2](ORCID: 0000-0002-9565-9160)

Abstract

Increasing energy demand and limited resources have led to the search for innovative solutions in the field of energy saving and energy storage. Phase-change materials play a crucial role for energy conservation with their features such as high energy storage capacities, chemical stability, and sensitivity to low operation temperatures. In this study, the heat storage capacities of different types of organic (RT31, RT50) and inorganic (SP31, SP50) phase change materials were numerically investigated for different Reynolds numbers (Re=500, 1000, 1500, 2000) under laminar conditions in a heat exchanger. In the regenerative double-pipe heat exchanger, pure water as hot and cold fluid with different inlet temperature is formed in a counter-flow arrangement, and phase change material is placed in annular tube between two fluids. In order to investigate the effect of Re number on heat storage capacity of phase change material, Re number depending on the hot fluid velocity was increased gradually in the heat exchanger. As a result, SP31 yielded 42% more heat storage capacity than RT31 and SP31 yielded 50% more heat storage capacity than RT31. Increasing Re number led to increase in heat storage capacity and heat transfer rate for all type of phase change materials. Inorganic phase change materials showed better heat transfer performance than organic phase change materials. It has been evaluated that with the results obtained from this study, energy-effective and cost-efficient heat storage and transfer systems can be designed.

Keywords: "Phase change material, heat transfer, heat storage, Reynolds number"

1. Introduction

Thermal energy storage (TES) systems play crucial role in heat transfer thermal control systems in terms of both energy efficiency and energy supply. The use of phase change materials (PCMs) in these systems can provide great convenience and effective solutions [1]. PCMs have an important place in the design of thermal systems due to sensitivity for low temperature changes, chemical stability, and high energy storage capacity. PCMs have the ability to store and to release heat energy by changing its phase as melting and solidification caused by the temperature difference of one or more materials [2], [3]. Researching passive methods in regenerative heat exchangers gains importance in order to develop energy efficiency and cost-effective heat transfer systems [4]–[6]. In the literature, passive methods such as surface modifications, vortex generators, different geometrical structures, baffles, and nanoparticles that affect the flow dynamics and heat transfer in the heat exchanger can significantly increase the performance of the heat exchanger [7]–[9]. In addition to these passive methods, PCMs can significantly improve the performance in a heat exchanger as a passive method. Nomura et al. [10] investigated numerically the heat storage capacity of the heat exchanger using erythritol as the phase change material. Increasing inlet temperature and increasing flow rate has enhanced the average heat storage rate of the phase change material. Lin et al. [11] investigated experimentally the thermal energy storage capacity of the pillow type plate heat exchanger by using sodium acetate trihydrate as the phase changing medium and distilled water as the working fluid. It was determined that the pillow type plate heat exchanger exhibits better thermal performance than plate type heat exchanger and provides a high heat transfer rate. Sardari et al. [12] investigated the heat storage and heat transfer performance of porous metal structures in a phase change medium in a heat exchanger. Porous metal structure showed a better

[1]Corresponding author

temperature distribution than the plain type of heat exchanger. Liu et al. [13] studied PCMs as respect to the preparation methods, application fields and heat transfer properties of different types of phase change materials. Bugaje [14] found that adding aluminum nanoparticles to paraffin wax significantly reduces the melting and solidification time. Elgafy and Lafdi [15] researched carbon nanofibers into PCM material to increase the thermal performance of the phase change material. It was determined that increasing the mass ratio of carbon nanofiber in PCM significantly increases the cooling rate during the solidification process. Chen et al. [16] investigated energy storage capacity of paraffin integrated with metal foam porous structure. The numerical results showed that the heat transfer rate of solar plate collector can be considerably increased by using the aluminum foams filled with paraffin. In this study, the heat storage capacities of different types of organic (RT31, RT50) and inorganic (SP31, SP50) phase change materials were numerically investigated for different Reynolds numbers (Re=500, 1000, 1500, 2000) under laminar conditions in a regenerative heat exchanger.

2. Materials and Methods

The regenerative heat exchanger numerical model was created in ANSYS Fluent. The diameters of the three concentric pipes are 50 mm, 70 mm and 100 mm, from the inside out, respectively, and the pipe lengths are 1000 mm. Working fluids modeled as hot pure water in the inner tube, cold pure water in the outer tube, and PCM material modeled in the annular tube between inner and outer tubes. 2D and 3D views of the model are shown in Figure 1.

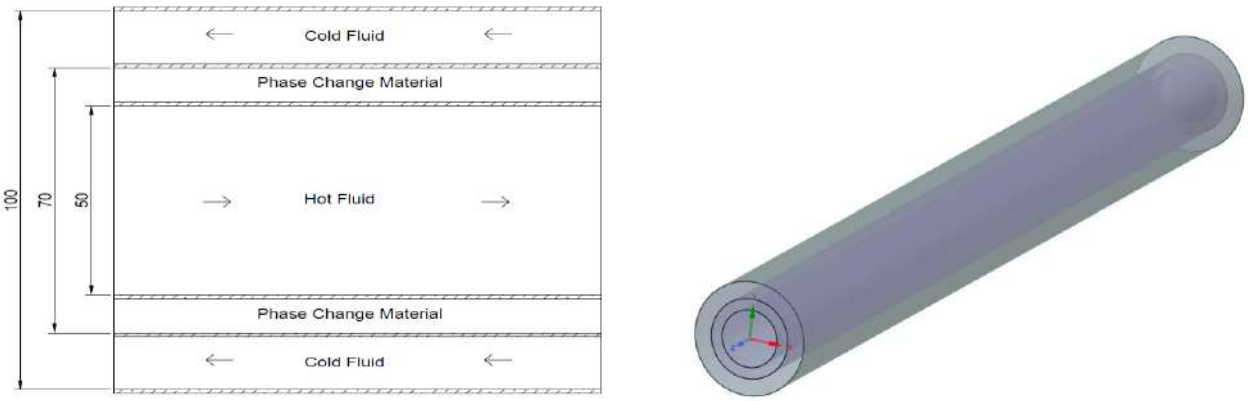

Figure 1. The geometry of the regenerative heat exchanger

Hot and cold fluids were formed as counter-flow arrangement in laminar condition. Mesh structure of the model is presented in Figure 2.

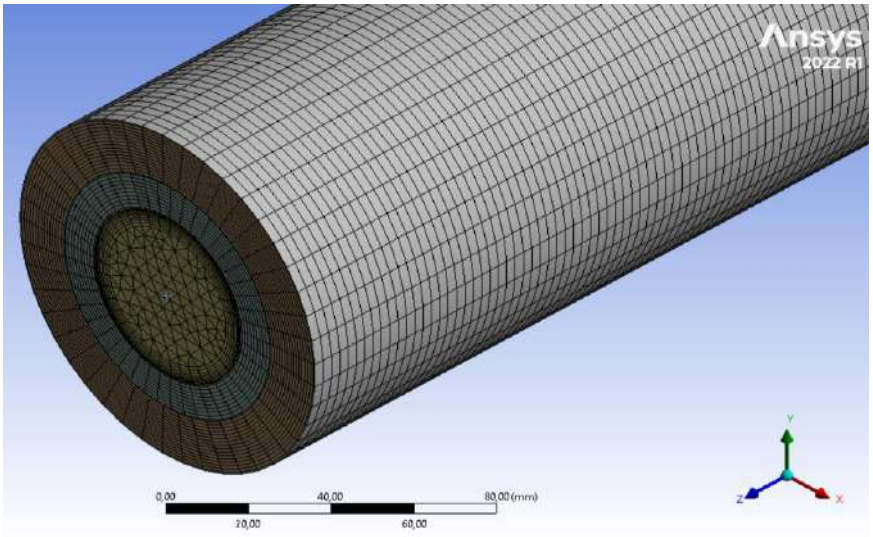

Figure 2. Mesh structure of the numerical model

2.1 Mesh Independence Study

Mesh number of the model was intensified at boundary layer between solid-liquid interface. Convergence study was conducted according to average temperature of the hot fluid by creating 5 different numerical model in respect to mesh number. It was evaluated that after 800000 cell there was no significant change on avetage temperature of the hot fluid. Therefore, in numerical calculation, the model with 800000 cell number was used to run calculation. The variation of the hot fluid average temperature according to the cell number is presented in Figure 3.

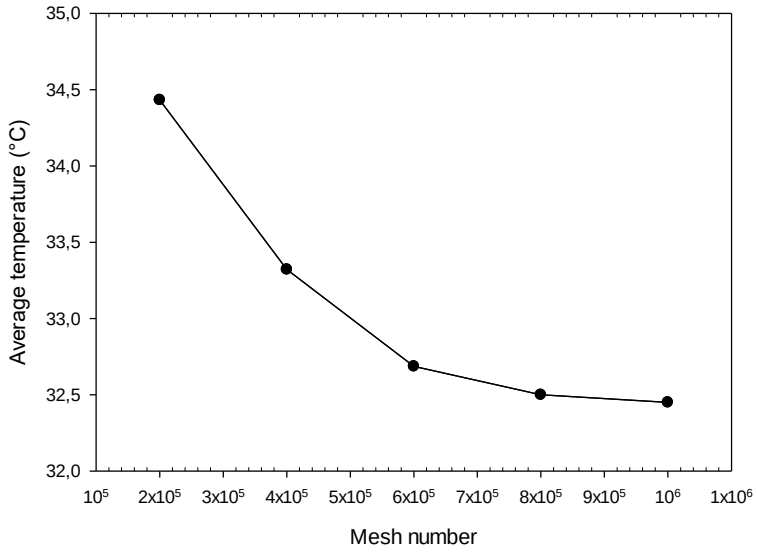

Figure 3. Convergence of the model as respect to average fluid temperature

2.2 Validation of the Numerical Model

In order to validate the numerical model, the data obtained from the experimental study [17] in which pure water was used as hot and cold fluid in the double-pipe heat exchanger were compared with the numerical model data. The maximum error between experimental and numerical data was determined as 11%. It was determined that the numerical study was good agree with experimental study. Comparison of numerical data with experimental data is presented in Figure 4.

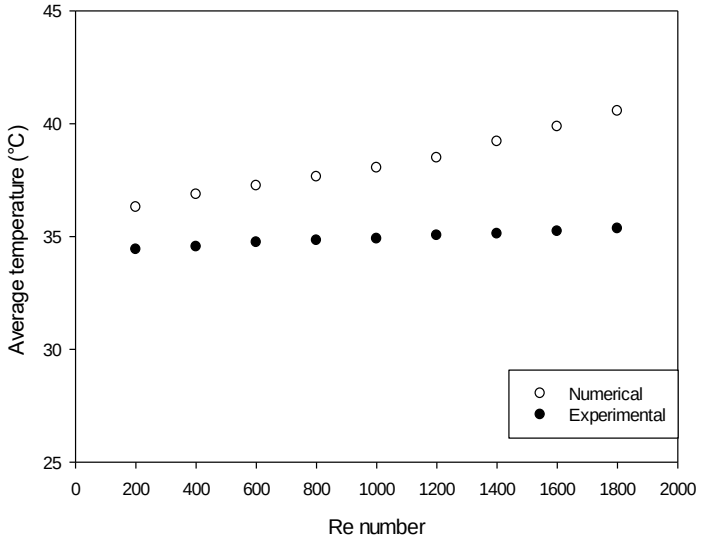

Figure 4. Comparison of numerical and experimental data

2.3 Phase Change Materials

In the study, as organic material RT31 and RT50, as inorganic material SP31 and SP50 were selected in order to compare the heat transfer performances of organic and inorganic phase change materials according to the same temperature ranges. These PCMs have high heat storage capacity between 30-50°C temperature range. Thermophysical properties of the PCMs are presented in Table 1.

Table 1. Thermophysical properties of organic and inorganic phase change materials.

Thermophysical properties	RT31	SP31	RT50	SP50	Unit
Melting range	29-34	31-33	45-51	50-51	°C
Congealing range	34-29	28-30	51-46	47-48	°C
Heat storage capacity	165	210	160	220	kJ/kg
Specific heat capacity	2	2	2	2	kJ/kg·K
Density (solid)	0.88	1.35	0.88	1.50	kg/L
Density (liquid)	0.76	1.25	0.76	1.4	kg/L
Thermal conductivity	0.2	0.5	0.2	0.6	W/m·K
Volume expansion	12.5	5	12.5	8	%
Max. operation temperature	50	50	70	80	°C

2.4 Mathematical Formulation and Boundary Conditions

The formulas and continuity, momentum and energy equations used to calculate the heat transfer rate of the generated numerical model are presented below.

Continuity equation:

$$\frac{1}{r}\frac{\partial(ru_r)}{\partial r}+\frac{1}{r}\frac{\partial(u_\theta)}{\partial \theta}+\frac{\partial(u_z)}{\partial z}=0 \quad (1)$$

Momentum equation:
In the r-direction:

$$p\left(\frac{\partial(u_r)}{\partial t}+u_r\frac{\partial(u_r)}{\partial r}+\frac{u_\theta}{r}\frac{\partial(u_r)}{\partial \theta}-{u_\theta}^2+u_z\frac{\partial(u_r)}{\partial z}\right)=-\frac{\partial P}{\partial r}+pg_r+\mu\left[\frac{1}{r}\frac{\partial}{\partial r}\left(r\frac{\partial u_r}{\partial r}\right)-\frac{u_r}{r^2}+\frac{1}{r^2}\frac{\partial^2 u_r}{\partial \theta}-\frac{2}{r^2}\frac{\partial u_\theta}{\partial \theta}+\frac{\partial^2 u_r}{\partial z^2}\right] \quad (2)$$

In the -θ direction:

$$p\left(\frac{\partial u_\theta}{\partial t}+u_r\frac{\partial u_\theta}{\partial r}+\frac{u_\theta}{r}\frac{\partial u_\theta}{\partial \theta}+\frac{u_\theta u_r}{r}+u_z\frac{\partial u_\theta}{\partial z}\right)=-\frac{1}{r}\frac{\partial P}{\partial \theta}+pg_\theta+\mu\left[\frac{1}{r}\frac{\partial}{\partial r}\left(r\frac{\partial u_\theta}{\partial r}\right)-\frac{u_\theta}{r^2}+\frac{1}{r^2}\frac{\partial^2 u_\theta}{\partial \theta^2}+\frac{2}{r^2}\frac{\partial u_r}{\partial \theta}+\frac{\partial^2 u_\theta}{\partial z^2}\right] \quad (3)$$

In the z-direction:

$$p\left(\frac{\partial u_z}{\partial t}+u_r\frac{\partial u_z}{\partial r}+\frac{u_\theta}{r}\frac{\partial u_z}{\partial \theta}+u_z\frac{\partial u_z}{\partial z}\right)=-\frac{\partial P}{\partial z}+pg_z+\mu\left[\frac{1}{r}\frac{\partial}{\partial r}\left(r\frac{\partial u_z}{\partial r}\right)+\frac{1}{r^2}\frac{\partial^2 u_z}{\partial \theta^2}+\frac{\partial^2 u_z}{\partial z^2}\right] \quad (4)$$

Energy equation:

$$\boldsymbol{\frac{\partial T}{\partial t}+u_r\frac{\partial T}{\partial r}+\frac{u_\theta}{r}\frac{\partial T}{\partial \theta}+u_z\frac{\partial T}{\partial z}=\frac{\dot{q}_g}{c_p}+\alpha\left[\frac{1}{r}\frac{\partial}{\partial r}\left(r\frac{\partial T}{\partial r}\right)+\frac{1}{r^2}\ \frac{\partial^2 T}{\partial \theta^2}+\frac{\partial^2 T}{\partial z^2}\right]+\frac{\varphi}{pc_p}} \quad (5)$$

Boundary conditions of the numerical model are expressed in Table 2.

Table 2. Boundary conditions of the numerical model

Boundaries	U (m/s)	V (m/s)	W (m/s)	T (K)
Hot fluid inlet	$U=U_{inlet}$	V=0	W=0	$T=T_{hot,in}$
Cold Fluid inlet	U=0	$V=V_{in}$	W=0	$T=T_{cold,in}$
Hot fluid outlet	$\frac{\partial U}{\partial x}=0$	$\frac{\partial V}{\partial x}=0$	$\frac{\partial W}{\partial x}=0$	$\frac{\partial T}{\partial x}=0$
Cold fluid outlet	$\frac{\partial U}{\partial x}=0$	$\frac{\partial V}{\partial x}=0$	$\frac{\partial W}{\partial x}=0$	$\frac{\partial T}{\partial z}=0$
Body	U=0	V=0	W=0	$\frac{\partial T}{\partial z}=0$

The logarithmic mean temperature difference is expressed in the equations below in order to calculate heat transfer rate and heat transfer effectiveness.

$$\Delta T_1=T_{h,in}-T_{c,out} \quad (6.1)$$

$$\Delta T_2=T_{h,out}-T_{c,in} \quad (6.2)$$

$$\Delta T_{lm}=\frac{\Delta T_1-\Delta T_2}{\ln(\Delta T_1/\Delta T_2)} \quad (6.3)$$

Heat transfer rate in the heat exchanger is calculated as:

$$\dot{Q}=UA_s\Delta T_{lm} \quad (7)$$

A_s and U are the heat transfer surface area and the overall heat transfer coefficient, respectively.

$$C_c=\dot{m}_c c_{pc} \quad (8.1)$$

$$C_h=\dot{m}_h c_{ph} \quad (8.2)$$

$$\Delta T_{max}=T_{h,in}-T_{c,in} \quad (8.3)$$

$$\dot{Q}_{max}=C_{min}\Delta T_{max} \quad (8.4)$$

$$\varepsilon = \frac{\dot{Q}_{act}}{\dot{Q}_{max}} = \frac{Gerçek\ ısı\ transfer\ hızı}{Maksimum\ ısı\ transfer\ hızı} \tag{8.5}$$

3. Results and Discussions

In this study, the heat storage capacities of different types of organic (RT31, RT50) and inorganic (SP31, SP50) phase change materials were numerically investigated for different Reynolds numbers under laminar conditions in a regenerative heat exchanger with counter-flow arrangement. Inlet temperature of the hot fluid was determined as 31°C for RT31 and SP31 materials, and 50°C for RT50 and SP70 materials while inlet temperature of the cold fluid was constant at 20°C for all run calculations. In order to investigate the effect of Re number on heat storage capacity of phase change material, Re number depending on the hot fluid velocity was increased gradually (Re=500, 1000, 1500, 2000) in the heat exchanger.

For RT31 material, increasing Re number between Re=500-1000 has led an increase by 45.45% in heat storage capacity. For Re=1000-1500 has led an increase by 21.34%, for Re=1500-2000 has led an increase by 13.35%. For SP31 material, increasing Re number between Re=500-1000 has led an increase by 44.31% in heat storage capacity. For Re=1000-1500 has led an increase by 20.70%, for Re=1500-2000 has led an increase by 13.20%. Temperature contours of RT31 and SP31 materials for Re=500-2000 are presented in Figure 5.

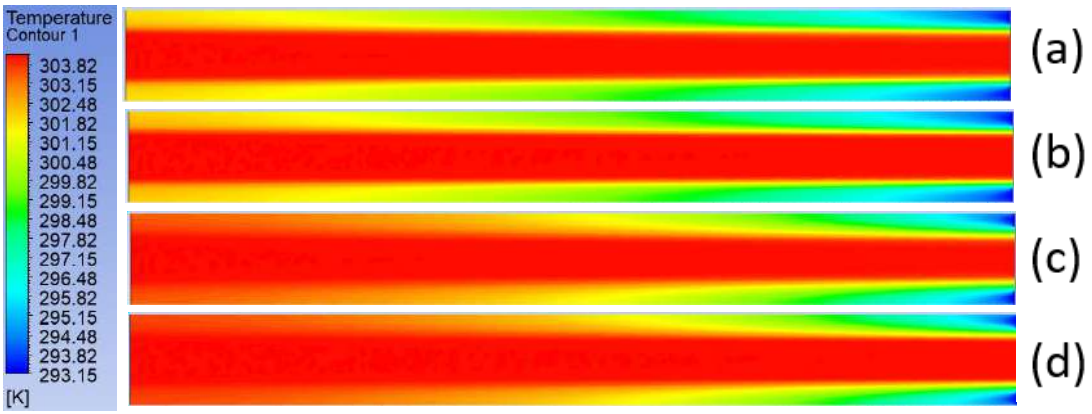

Figure 5. Temperature contours of RT31 Re=500 (a), RT31 Re=1000 (b), SP31 Re=500 (c), SP31 Re=1000 (d)

Effect of increasing Re number on heat storage capacity of RT31 and SP31 materials are presented in Figure 6.

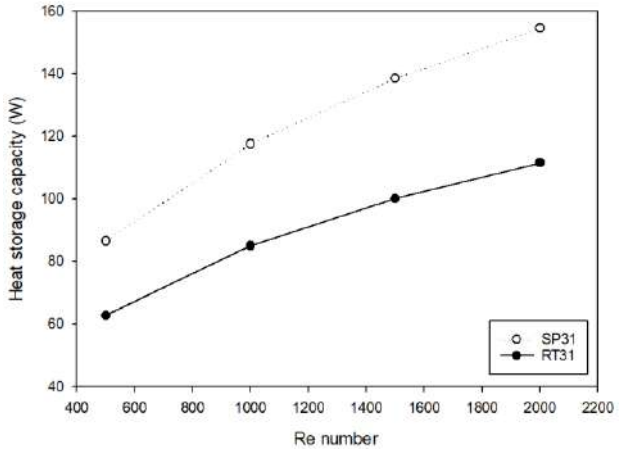

Figure 6. Effect of increasing Re number on heat storage capacity for RT31 and SP31

For RT50 material, increasing Re number between Re=500-1000 has led an increase by 45.46% in heat storage capacity. For Re=1000-1500 has led an increase by 21.21%, for Re=1500-2000 has led an increase by 13.40%. For SP50 material, increasing Re number between Re=500-1000 has led an increase by 44.03% in heat storage capacity. For Re=1000-1500 has led an increase by 20.80%, for Re=1500-2000 has led an increase by 13.22%. Temperature contours of RT50, SP50 materials for Re=500-2000 are presented in Figure 7.

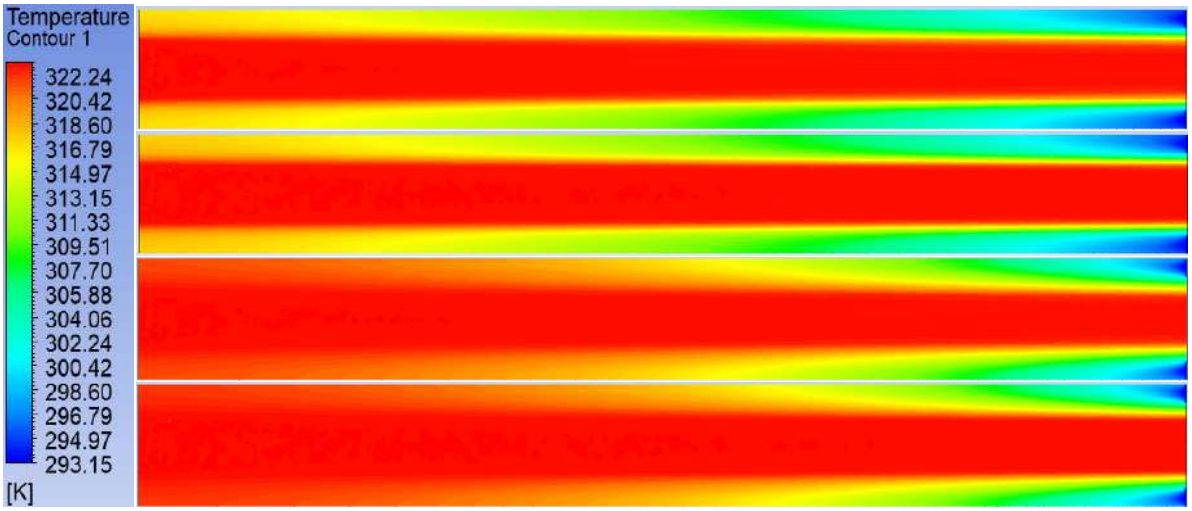

Figure 7. Temperature contours of RT31 Re=500 (a), RT31 Re=1000 (b), SP31 Re=500 (c), SP31 Re=1000 (d)

Effect of increasing Re number on heat storage capacity of RT50 and SP50 materials are presented in Figure 8.

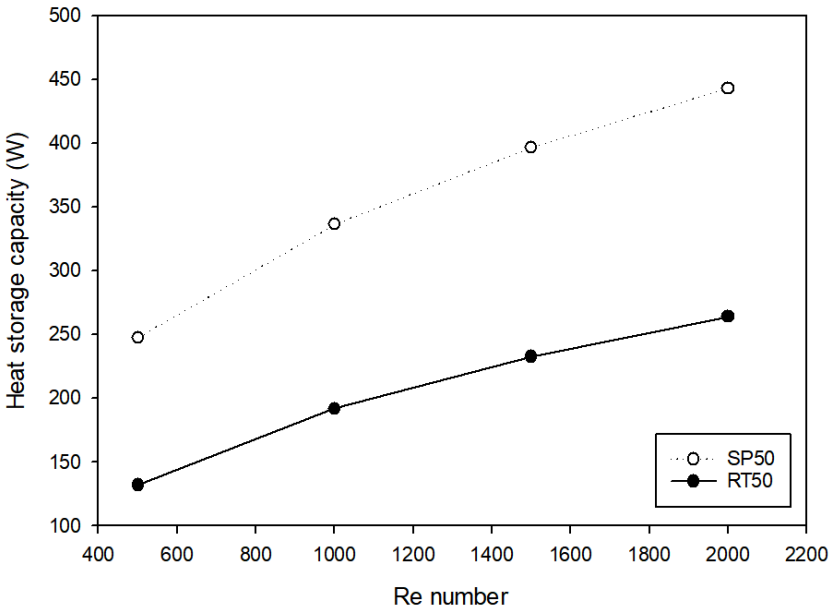

Figure 8. Effect of increasing Re number on heat storage capacity for RT50 and SP50

4. Conclusion Remarks

In this study, heat transfer performance of organic (RT31, RT50) and inorganic (SP31, SP50) phase change materials were investigated in a regenerative heat exchanger as respect to Reynolds number in laminar conditions. Each run calculation has been performed in ANSYS Fluent for range of Re=500, 1000, 1500, 2000. As a result;

1. Heat storage capacity of all types of organic and inorganic phase change materials increased by increasing Re number.
2. Effect of increasing Re number in range of Re=500-2000 has same impact for same types of phase change materials.
3. Inorganic phase change materials SP31 and SP50 have better heat transfer performance than organic materials RT31 and RT50, respectively.

For future research, it was evaluated that it would be useful to investigate phase change materials with porous metal structures, nanoparticles, and nanofluids in heat exchangers in order to increase heat transfer performance.

5. References

[1] G. Hed and R. Bellander, "Mathematical modelling of PCM air heat exchanger," *Energy Build*, vol. 38, no. 2, pp. 82–89, Feb. 2006, doi: 10.1016/j.enbuild.2005.04.002.

[2] M. Al-Maghalseh and K. Mahkamov, "Methods of heat transfer intensification in PCM thermal storage systems: Review paper," *Renewable and Sustainable Energy Reviews*, vol. 92. Elsevier Ltd, pp. 62–94, Sep. 01, 2018. doi: 10.1016/j.rser.2018.04.064.

[3] M. Rahimi, A. A. Ranjbar, D. D. Ganji, K. Sedighi, M. J. Hosseini, and R. Bahrampoury, "Analysis of geometrical and operational parameters of PCM in a fin and tube heat exchanger," *International Communications in Heat and Mass Transfer*, vol. 53, pp. 109–115, 2014, doi: 10.1016/j.icheatmasstransfer.2014.02.025.

[4] M. Medrano, M. O. Yilmaz, M. Nogués, I. Martorell, J. Roca, and L. F. Cabeza, "Experimental evaluation of commercial heat exchangers for use as PCM thermal storage systems," *Appl Energy*, vol. 86, no. 10, pp. 2047–2055, 2009, doi: 10.1016/j.apenergy.2009.01.014.

[5] N. Stathopoulos, M. El Mankibi, R. Issoglio, P. Michel, and F. Haghighat, "Air-PCM heat exchanger for peak load management: Experimental and simulation," *Solar Energy*, vol. 132, pp. 453–466, Jul. 2016, doi: 10.1016/j.solener.2016.03.030.

[6] Y. Hu and P. K. Heiselberg, "A new ventilated window with PCM heat exchanger—Performance analysis and design optimization," *Energy Build*, vol. 169, pp. 185–194, Jun. 2018, doi: 10.1016/j.enbuild.2018.03.060.

[7] M. J. Hosseini, M. Rahimi, and R. Bahrampoury, "Experimental and computational evolution of a shell and tube heat exchanger as a PCM thermal storage system," *International Communications in Heat and Mass Transfer*, vol. 50, pp. 128–136, 2014, doi: 10.1016/j.icheatmasstransfer.2013.11.008.

[8] C. J. Ho, S. T. Hsu, S. Rashidi, and W. M. Yan, "Water-based nano-PCM emulsion flow and heat transfer in divergent mini-channel heat sink—An experimental investigation," *Int J Heat Mass Transf*, vol. 148, Feb. 2020, doi: 10.1016/j.ijheatmasstransfer.2019.119086.

[9] L. Kalapala and J. K. Devanuri, "Influence of operational and design parameters on the performance of a PCM based heat exchanger for thermal energy storage – A review," *Journal of Energy Storage*, vol. 20. Elsevier Ltd, pp. 497–519, Dec. 01, 2018. doi: 10.1016/j.est.2018.10.024.

[10] T. Nomura, M. Tsubota, T. Oya, N. Okinaka, and T. Akiyama, "Heat storage in direct-contact heat exchanger with phase change material," in *Applied Thermal Engineering*, 2013, pp. 26–34. doi: 10.1016/j.applthermaleng.2012.04.062.

[11] W. Lin, W. Zhang, Z. Ling, X. Fang, and Z. Zhang, "Experimental study of the thermal performance of a novel plate type heat exchanger with phase change material," *Appl Therm Eng*, vol. 178, Sep. 2020, doi: 10.1016/j.applthermaleng.2020.115630.

[12] P. T. Sardari, D. Giddings, D. Grant, M. Gillott, and G. S. Walker, "Discharge of a composite metal foam/phase change material to air heat exchanger for a domestic thermal storage unit," *Renew Energy*, vol. 148, pp. 987–1001, Apr. 2020, doi: 10.1016/j.renene.2019.10.084.

[13] C. Liu, Z. Rao, J. Zhao, Y. Huo, and Y. Li, "Review on nanoencapsulated phase change materials: Preparation, characterization and heat transfer enhancement," *Nano Energy*, vol. 13. Elsevier Ltd, pp. 814–826, Apr. 01, 2015. doi: 10.1016/j.nanoen.2015.02.016.

[14] I. M. Bugaje, "Enhancing the thermal response of latent heat storage systems," *Int J Energy Res*, vol. 21, no. 9, pp. 759–766, 1997, doi: 10.1002/(SICI)1099-114X(199707)21:9<759::AID-ER254>3.0.CO;2-7.

[15] A. Elgafy and K. Lafdi, “Effect of carbon nanofiber additives on thermal behavior of phase change materials,” *Carbon N Y*, vol. 43, no. 15, pp. 3067–3074, Dec. 2005, doi: 10.1016/j.carbon.2005.06.042.
[16] Z. Chen, M. Gu, and D. Peng, “Heat transfer performance analysis of a solar flat-plate collector with an integrated metal foam porous structure filled with paraffin,” *Appl Therm Eng*, vol. 30, no. 14–15, pp. 1967–1973, Oct. 2010, doi: 10.1016/j.applthermaleng.2010.04.031.
[17] Congress Id Congress Tıtle 3. Internatıonal Dğcle Scıentıfic Research And Innovatıon Congress Date And Place 26-27 November 2022 Dğyarbakır-Turkey/Turkey Onlıne Presentatıons Organızatıon Isarc Internatıonal Scıence And Art Research Center. 2022. [Online]. Available: Www.İksadyayinevi.Com

International Conference on Advances and Innovations in Engineering

Investigation of the Effect of Nozzle Diameter and Collision Distance on Resultant Momentum in an Active Protection System

Hüseyin Aydın EKER[1], Mahir ŞAHİN[2], Mustafa KILIÇ[3]

[1,2,3]Mechanical Engineering, Faculty of Engineering, Adana Alparslan Turkes Science and Technology University, Adana, Turkey.
[1]haydin.eker@gmail.com, [2]msahin@atu.edu.tr, [3]mkilic@atu.edu.tr

[1](ORCID: 0000-0002-8988-5153), [2](ORCID: 0000-0002-9565-9160), [3](ORCID: 0000-0002-8006-149X)

Abstract

Strengthening armor has a negative effect on armored vehicles in respect to size/weight and maneuverability. Active protection systems eliminate the threat by detecting missiles and destroying them with high pressured water jet before collision without any damage on vehicles. In this study, the effect of different parameters of high-pressured water jet system was investigated. The effects of water jet velocity and collision distance parameters were examined numerically on ANSYS LS-Dyna Computational Fluid Dynamics software. In order to analyze the effects of collision distance, water jet velocity was determined as constant at 500 m/s. For 4 mm and 6 mm nozzle diameters, increasing collision distance from 300 mm to 600 mm has led to increase in resultant momentum by 25.3% and 140.6% respectively. In order to analyze the effects of water jet velocity, collision distance was determined as constant at 300 mm. For 4 mm nozzle diameters, increasing water jet velocity in range of 150-500 m/s caused decrease in resultant momentum by 7%, for 6 mm nozzle diameters, increasing water jet velocity in range of 150-500 m/s yielded an increase in resultant momentum by 144%. It has been evaluated that obtained results from this study, active protection systems with high pressured water jet can be improved and can be designed cost effective armored vehicles.

Keywords: "Computational fluid dynamics, water jet, active protection system, armored vehicle"

1. Introduction

The release of hot gas and large amounts of energy within milliseconds as a result of a chemical reaction is called an explosion [1]. The hot gas formed as a result of the explosion makes a wave-type expansion that expanding spherically in the surrounding environment [2]–[5]. The pressure magnitude and the propagation speed of the shock wave develop inversely with the distance from the center of the explosion [6]. Jacinto et al. [7] investigated the accuracy of experimental and numerical methods to study the effects of the explosion on the plates. Linear dynamic loading analyzes were obtained using Abaqus program. The numerical and experimental results were compared, and it was determined that different vibration modes cause significant differences on the pressure distribution. Karlos et al. [8] investigated the wave behavior under sudden pressure change conditions. Spherical and hemispherical explosion effects are examined according to the distance from the structure. For the maximum pressure approximation, different pressure models are compared. Li and Hong [9] studied the aerodynamic properties of anti-tank missile. Lift coefficients and static pressure contours of the missile are examined. It was determined that missiles which have higher lift to drag coefficients are practicing more stable flight and much more fatal against armored vehicles. Song et al. [10] examined the working range of an APS which should be capable of detecting the main properties such as size and speed of the approaching threat. The system should also be able to track the threat and identify the position of impact then send the obtained info to the computer in order to counter-attack. Drawbacks of this system is the radar which use millimeter wave can only counterattack to typical anti-tank missiles and cannot detect high speed missiles. In order to overcome this issue and increase reliability of the detection service multi-sensor and data fusion technique is advised which also decrease the false alarm possibility. Tatekura et al. [11] studied the pressure effects of generated between solid and liquid interface during an instant impact. Leach et al. [12]

[1]Corresponding author

investigated the effect of nozzle shape on reducing the kinetic energy of a target. Relation between distance and pressure value was examined. Heymann [13] reviewed characteristics of a high-speed effect between compressible liquid and solid surface. The study presented that the relationship between the instantaneous impact pressure and the critical pressure was determined as approximately 2.8. Damage mechanism and repeated impact is investigated as well. Hashish [14] investigated high speed water jet on impact solid surfaces and developed an equation in order to describe cutting behavior of materials. Ohlsson et al. [15] investigated the forces that enforced on aluminum and mild steel surfaces. The parameters which measured are pressure, thickness, water flow rate, and nozzle diameter. Numerical data obtained from the study are valuable in terms of comparison with experimental values. Rajaratnam et al. [16] studied the behavior and interaction of high velocity water jet. The equations were examined for velocity of water jet as respect to target distance ratio and nozzle diameter. Velocity profile and decay was created with respect to distance and initial velocity at the nozzle exit.

In literature, pressurized water jet was investigated on plate for different parameters such as sudden pressure changes, different explosion effects, aerodynamic characteristics, and solid-liquid interactions. In this study, high pressurized water jet was investigated in respect to effect of water jet velocity and collision distance to anti-tank missile on resultant momentum.

2. Materials and Methods

2.1. ANSYS-LS Dyna Mathematical Model

The numerical model depends on explicit analysis due to the high-speed and high-energy for a very short time interval. The missile is modelled in finite element method and water jet in Smooth Particle Hydrodynamics. SPH is preferred to solve mesh structure in extreme deformation conditions [6].
By using Johnson and Cook Plasticity Model in Ls-Dyna, solid missile and fluid water interaction can be calculated. The flow stress is presented below.

$$\sigma_y = (A+B\epsilon^{-p^n})(1+c\ln\dot{\epsilon})(1-T^m) \quad (1)$$

A, B, C, and n are $1.67\text{x}10^8$ $5.96\text{x}10^8$, 0.001 and 0.051 respectively. Effect of temperature and m value are neglected.

$\boldsymbol{\epsilon^{-p}}$ = effective plastic strain (2)

$$\dot{\boldsymbol{\epsilon}}=\frac{\dot{\epsilon}^{-p}}{\dot{\epsilon}_0} \quad (3)$$

Effective plastic strain rate for $\dot{\epsilon}_0$ in units of 1/time.

$$T = \frac{T-Tenv}{Tmelt-Tenv} \quad (4)$$

Temperature difference is neglected.

$$\boldsymbol{\epsilon^f = [D_1 + D_2 \exp(D_3\sigma)][1 + D_4 ln\epsilon][1 + D_5 T]} \quad (5)$$

D_i= 1,..,5 are 0.0261, 0.0263, -0.349, 0.247 and 16.799 respectively. σ is the ratio of pressure divided by effective stress.

$$\boldsymbol{\sigma = \frac{p}{\sigma_{eff}}} \quad (6)$$

$$\boldsymbol{D_p = \Sigma \frac{\Delta\epsilon^{-p}}{\epsilon^f}} \quad (7)$$

Equation of pressure for compressed materials is presented with Gruniesen in LS-Dyna.

$$p = \frac{\rho_0 c^2 \mu[1+(1-\frac{\gamma_0}{2})\mu-\frac{a}{2}\mu^2]}{[1-(S_1-1)\mu-S_2\frac{\mu^2}{\mu+1}-S_3\frac{\mu^3}{(\mu+1)^2}]^2} + (\gamma_0 + a\mu)E_v \quad (8)$$

E is internal energy per volume, C is the intercept of the μs-μp curve, S_1, S_2 and S_3 are the coefficients of the slope of the μs-μp curve, Y_0 is the Gruniesen gamma, and a is the first order volume correction to Y_0. Constants C, S_1, S_2, S_3, Y_0 and a are input parameters defined as 1647, 1.921, -0.096, 0 and 0.35 respectively [6].
During the simulation, to update the stresses and the right-hand side force vector solutions are looped through the elemets. Taking the minimum value over all elements a new time step is determined with:

$$\Delta tn+1 = a \cdot \min\{\Delta t_1, \Delta t_2, \Delta t_3, \ldots, \Delta t_N\} \quad (9)$$

where N is the number of elements which is 18561.
For stability, the scale factor a is typically set to a value of 0.9 (default) or some smaller value. In this study 0.45 is set for scale factor.

2.2. Water Jet Properties

Water jet flow is assumed steady and not pulsative; therefore, erosion and fatigue are neglected. Pressure exceeding the yield strength of missile material, force to divert or detonate the missile is investigated by this point of view. In order to get the same results using high pressure water jets. Numerical model of the geometry is presented in Figure 1.

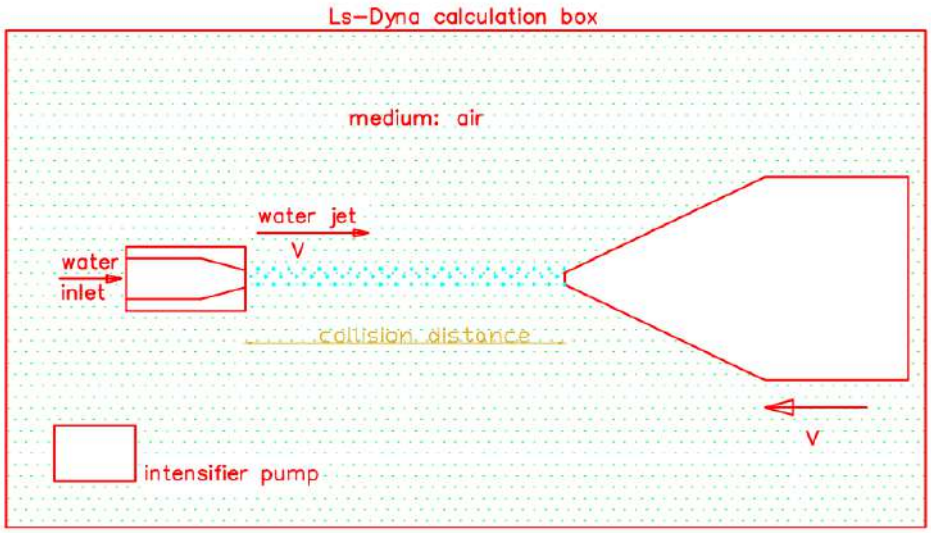

Figure 1. Numerical model of the geometry [6]

Aluminum missile warhead model and mesh structure was created in LS-Prepost. Air and water media is first prepared as planar surfaces. Then using LS-Prepost surface of both media planar mesh size was identified. In the next step, using element generation planar surfaces are extruded and 3D forms were given.
Using Smooth Partical Hydrodynamics (SPH) 3D form of air and water are transferred into fluid particles with appropriate density.

Nozzle diameter, water jet speed, air length and the distance of collision LS-Prepost keyword files are formed. Simulation parameters depend on water jet velocity, nozzle diameter, and collision distance from jet spray. Water and air interaction are shown in Figure 2.

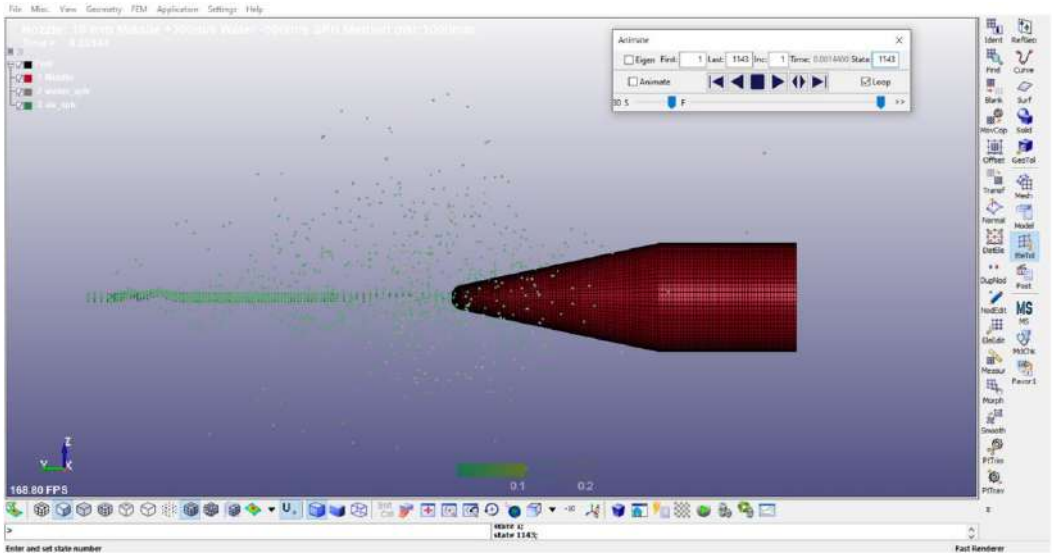

Figure 2. Water and air interaction [6]

3. Results and Discussions

In this study, the effect of different parameters of high-pressured water jet system was investigated. The effects of water jet velocity and collision distance parameters were examined numerically on ANSYS LS-Dyna Computational Fluid Dynamics software.

3.1 Effect of Collision Distance

In order to analyze the effects of collision distance, water jet velocity was determined as constant at 500 m/s. For 4 mm nozzle diameters, increasing collision distance from 300 mm to 600 mm has led to increase in resultant momentum by 25.3% totally. The effect of increasing collision distance on resultant momentum for 4 mm nozzle diameter is presented graphically in Figure 3.

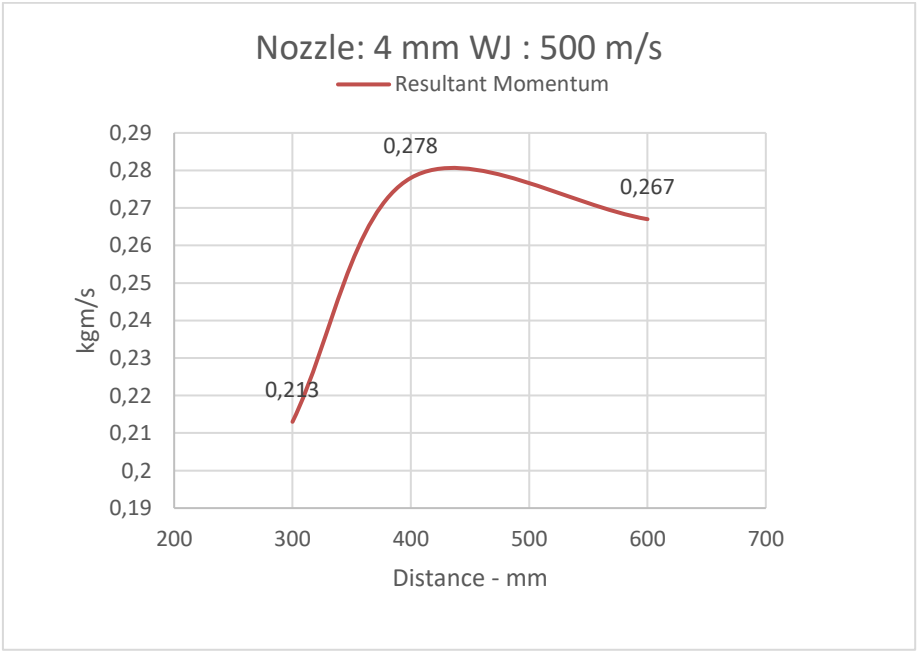

Figure 3. The effect of increasing collision distance on resultant momentum for 4 mm nozzle

For 6 mm nozzle diameters, increasing collision distance from 300 mm to 600 mm has led to increase in resultant momentum by 140.6% totally. The effect of increasing collision distance on resultant momentum for 6 mm nozzle diameter is presented graphically in Figure 3.

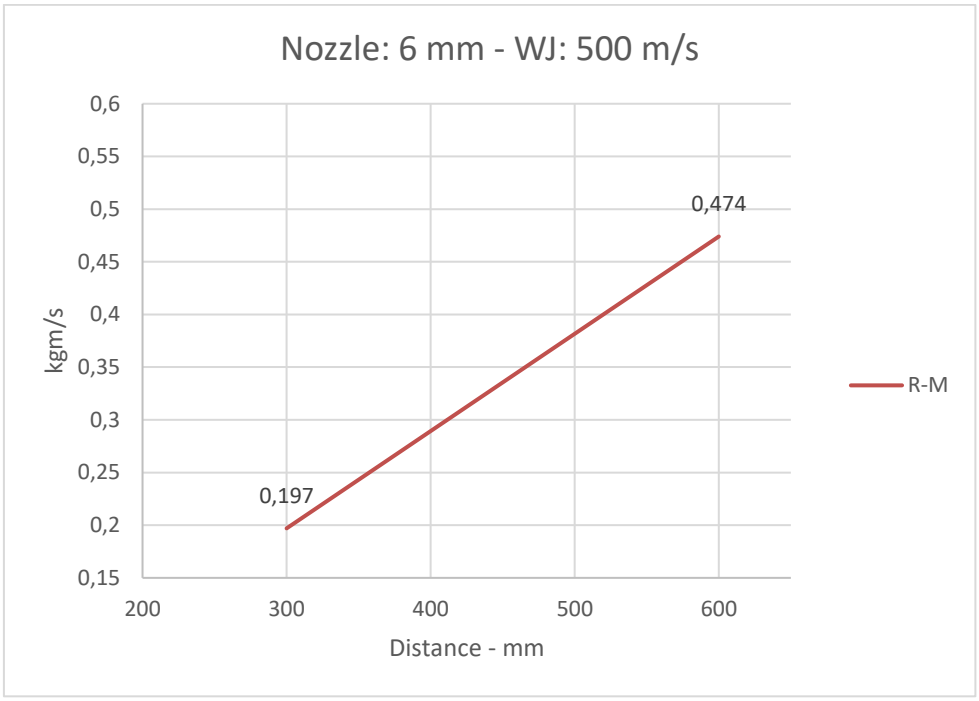

Figure 4. The effect of increasing collision distance on resultant momentum for 6 mm nozzle

3.2 Effect of Water Jet Velocity

In order to analyze the effects of water jet velocity, collision distance was determined as constant at 300 mm. For 4 mm nozzle diameter, increasing water jet velocity in range of 150-500 m/s caused decrease in resultant momentum by 7% totally. The effect of increasing water jet velocity on resultant momentum is presented graphically in Figure 5.

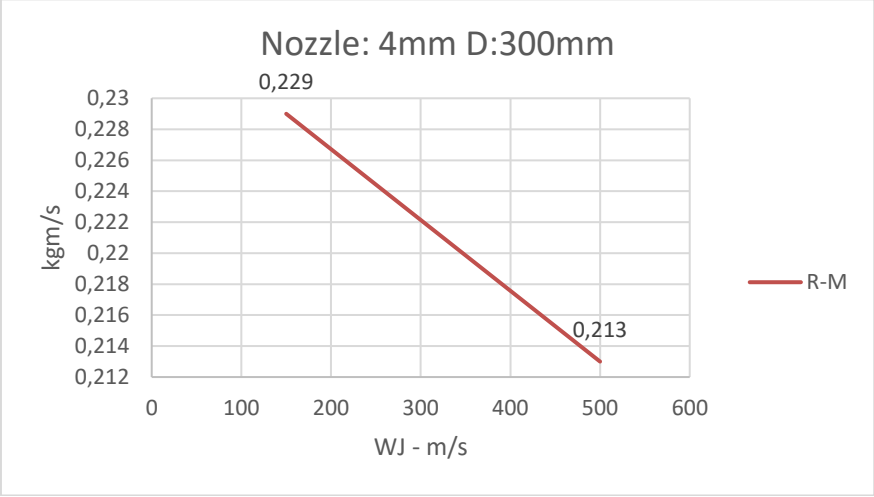

Figure 5. The effect of increasing water jet velocity on resultant momentum for 4 mm nozzle

For 6 mm nozzle diameter, increasing water jet velocity in range of 150-500 m/s caused decrease in resultant momentum by 144% totally. The effect of increasing water jet velocity on resultant momentum is presented graphically in Figure 6.

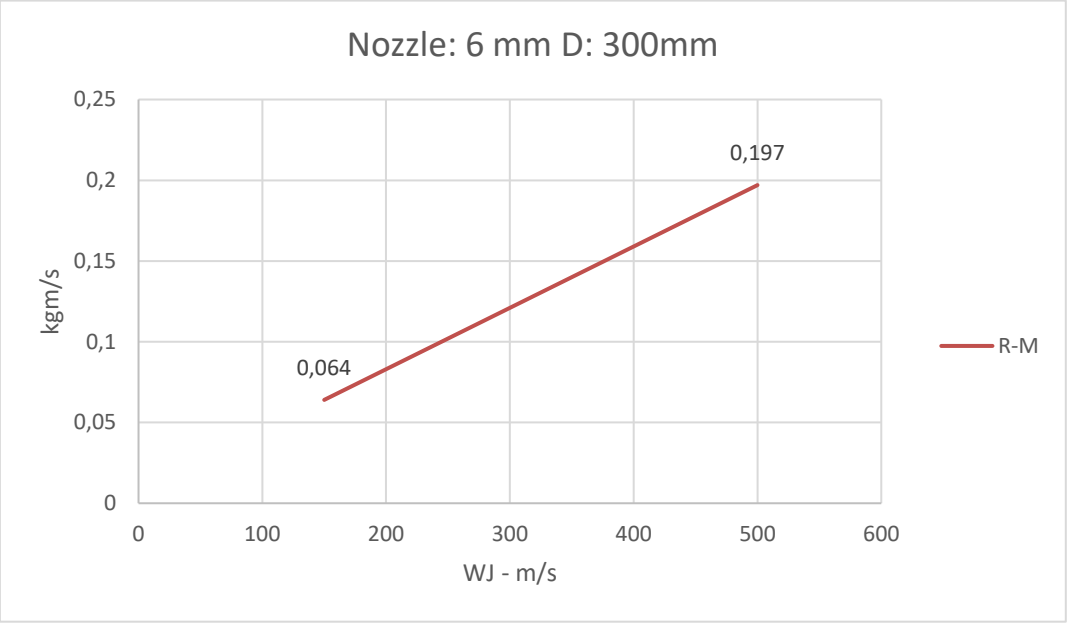

Figure 6. The effect of increasing water jet velocity on resultant momentum for 6 mm nozzle

4. Conclusion Remarks

The effects of water jet velocity and collision distance parameters of high-pressured water jet system were investigated. As a result;

1. Increasing collision distance from 300 mm to 600 mm has led to increase in resultant momentum by 25.3% for 4 mm and 140.6% for 6 mm nozzle diameter.
2. Increasing water jet velocity in range of 150-500 m/s caused decrease in resultant momentum by 7% for 4 mm and 144% for 6 mm nozzle diameter.

It was evaluated that obtained results from this study, active protection systems with high pressured water jet can be improved and can be designed cost effective armored vehicles.

5. References

[1] T. Baykara, V. Günay, and A. Demirural, "Structural Evolution and Microstructural Features of the Hydrodynamically Penetrating Copper Jet of a Shaped Charge," *J Mater Eng Perform*, vol. 30, no. 3, pp. 1862–1871, Mar. 2021, doi: 10.1007/s11665-021-05514-9.

[2] S. J. Leach, G. L. Walker, A. V Smith, I. W. Farmer, and G. Taylor, "Some Aspects of Rock Cutting by High Speed Water Jets [and Discussion] Discussion on Deformation of Solids by the Impact of Liquids, and its Relation to Rain Damage in Aircraft and Missiles, to Blade Erosion in Steam Turbines, and to Cavitation Erosion [295] F. THE APPLICATION OF HIGH SPEED LIQUID JETS TO CUTTING XXVI. Some aspects of rock cutting by high speed water jets," 1966.

[3] B. Moylan, B. Landrum, and G. Russell, "Investigation of the physical phenomena associated with rain impacts on supersonic and hypersonic flight vehicles," in *Procedia Engineering*, Elsevier Ltd, 2013, pp. 223–231. doi: 10.1016/j.proeng.2013.05.026.

[4] P. Wey, V. Fleck, and P.-Y. Chanteret, "ANALYSIS OF ACTIVE PROTECTION SYSTEMS: WHEN ATHENA MEETS ARENA," 2001.

[5] N. Medan and E. Nicolae MEDAN, "Evaluation of Nozzle Coefficients for Water Jet Used in Sewer Cleaning." [Online]. Available: https://www.researchgate.net/publication/311739152

[6] H. Aydin Eker, “REPUBLIC OF TURKEY ADANA ALPARSLAN TÜRKEŞ SCIENCE AND TECHNOLOGY UNIVERSITY GRADUATE SCHOOL OF NATURAL AND APPLIED SCIENCES DEPARTMENT OF MECHANICAL ENGINEERING ACTIVE PROTECTION OF ARMORED LAND VEHICLES USING WATER JET MASTER OF SCIENCE ADANA 2022.”
[7] A. Carlos Jacinto, R. Daniel Ambrosini, and R. Francisco Danesi, “Experimental and computational analysis of plates under air blast loading,” 2001.
[8] Vasilis. Karlos, George. Solomos, Bernard. Viaccoz, and European Commission. Joint Research Centre. Institute for the Protection and the Security of the Citizen., *Calculation of blast loads for application to structural components.* Publications Office, 2013.
[9] “A Study of Aerodynamic Characteristics of an Anti-tank Missile,” Universal Researchers, Jan. 2017. doi: 10.17758/eirai.f0217101.
[10] C. Song, L. Yao, and Z. Xiao, “Data-fusion-based detect equipment of tank initiative defense system,” in *MATEC Web of Conferences*, EDP Sciences, Nov. 2018. doi: 10.1051/matecconf/201822801008.
[11] Y. Tatekura, M. Watanabe, K. Kobayashi, and T. Sanada, “Pressure generated at the instant of impact between a liquid droplet and solid surface,” *R Soc Open Sci*, vol. 5, no. 12, Dec. 2018, doi: 10.1098/rsos.181101.
[12] S. J. Leach, G. L. Walker, A. V Smith, I. W. Farmer, and G. Taylor, “Some Aspects of Rock Cutting by High Speed Water Jets [and Discussion] Discussion on Deformation of Solids by the Impact of Liquids, and its Relation to Rain Damage in Aircraft and Missiles, to Blade Erosion in Steam Turbines, and to Cavitation Erosion [295] F. THE APPLICATION OF HIGH SPEED LIQUID JETS TO CUTTING XXVI. Some aspects of rock cutting by high speed water jets,” 1966.
[13] F. J. Heymann, “High-speed impact between a liquid drop and a solid surface,” *J Appl Phys*, vol. 40, no. 13, pp. 5113–5122, 1969, doi: 10.1063/1.1657361.
[14] M. P. Cfupiessis Professor, “M. Hashish Doctoral Student,” 1978. [Online]. Available: http://www.asme.org/about-asme/terms-of-use
[15] L. Ohlsson, “The Theory and Practice of Abrasive Water Jet Cutting,” 1995.
[16] N. Rajaratnam, S. A. H. Rizvi, P. M. Steffler, and P. R. Smy, “An experimental study of very high velocity circular water jets in air: Etude expérimental de jets d’eau circulaires à trés grande vitesse émis dans l’air,” *Journal of Hydraulic Research*, vol. 32, no. 3, pp. 461–470, 1994, doi: 10.1080/00221689409498746.

International Conference on Advances and Innovations in Engineering

Experimental analysis of impinging circular jet on a moving plate

Celal KISTAK[1], Ali TAŞKIRAN[2], Nevin ÇELİK[3]

[1,2,3] Mechanical Engineering Department, Engineering Faculty, Firat University, Elazig, Türkiye.
[1]ckistak@firat.edu.tr ,[2]ataskiran@firat.edu.tr, [3]nevincelik@firat.edu.tr

[1](ORCID: 0000-0003-4621-5405), [2](ORCID: 0000-0001-6810-7291),[3](ORCID: 0000-0003-2456-5316)

Abstract

Various geometries, design parameters, and thermal boundary conditions have led to advancements in heat transfer techniques. An extensive evaluation of these parameters, analysis of their interrelationships, and subsequent identification of the optimal heat transfer technique has undoubtedly posed a significant engineering challenge.
Upon examination of high cooling rate heat management techniques in industrial settings, jet cooling was found to be the most effective. Heat transfer is achieved on solid surfaces utilizing fluid jets in this method. Jet cooling systems have been implemented in gas turbines for an extensive period and have widespread industrial applications, including the tempering of glass plates, dyeing and drying of paper and textile products, cooling of electronic circuitry, as well as the cooling of turbine blades which heat up due to combustion gases, in modern aircraft with air-breathing engines.
The present study experimentally investigates the impact of an air jet on the local and average heat transfer on a moving target plate. The experimental setup incorporates a stepper motor guiding the plate's movement upon fluid impingement. The experiments were conducted using a circular jet at a Reynolds number of 6000, with temperatures being acquired via a thermal camera. Subsequently, the acquired data was utilized to produce Nusselt graphs.

Keywords: Heat transfer, Impinging jet, Moving surface, Thermal imaging

1. Introduction

Effective heat transfer is a crucial element of numerous industrial processes, ranging from the cooling of electronics to the management of thermal energy conversion systems. The drive towards improved heat transfer rates, compact designs and cost-effective solutions has prompted researchers to seek out innovative methods. One such method is the use of impinging jets, a technique that has been extensively studied and recorded in the literature.

Subba and Schlünder [1] presented a pioneering experimental study of the impact of a jet on a moving wall. The experiments entailed directing a single jet of air at a heated, continuously moving belt, with the jet impinging perpendicularly to the belt's movement. The attained maximum heat transfer coefficients were 1.5 to 2 times higher than those obtained for a stationary plate.

Active methods of enhancing heat transfer often involve the utilization of a jet to alter the flow and cool a surface via impingement. This technique has various advantages over conventional heat transfer methods, including greater heat transfer coefficients, uniform distribution of surface temperature, and reduced usage of materials. Extensive experimental and numerical research on this approach is available in the existing literature, including pioneering works by Chou et al. [2] and Beitelmal et al [3].

Chung et al. [4], Chattopadhyay et al. [5], Sagot et al. [6], Trávníček et al. [7], and Afroz et al. [8] present relevant research on the topic. Recently, Pakhomov et al. [9] conducted a numerical investigation to analyze the flow structures and heat transfer properties of turbulent air-driven jets.

[1]Corresponding author

Although there are advantages and extensive research regarding impinging jets interacting with stationary surfaces, little attention has been given to exploring the potential benefits and challenges of impinging jets on moving surfaces.

Therefore, it is crucial to investigate the effects of impinging jets on moving surfaces in dynamic systems. Such systems can experience continuous surface temperature fluctuations or necessitate heat source transportation while upholding effective heat transfer. These situations are prevalent in diverse engineering settings, including chemical reactors, manufacturing processes, and power generation systems.

The objective of this paper is to close this research gap by conducting a comprehensive investigation into the relationship between a moving heated surface and an air impinging jet.

The study aims to investigate heat transfer enhancement, fluid dynamics, and their interrelation through experimentation. This will involve designing and constructing a bespoke testing apparatus to simulate actual operating conditions.

2. Material and Method

The experimental setup comprises crucial elements, including a;

- Heated copper plate: Its selection is based on high thermal conductivity for uniform heat distribution on the surface during the experiments. Additionally, it is coated with dark black paint for optimal thermal camera results. Technical terms are explained adequately when first used, and the language is objective and formal in line with academic writing conventions. Careful attention is given to precise word choice, balanced statements, and grammatical correctness, adhering to style guides consistently. The text flows logically, with causal connections between statements, ensuring comprehension.

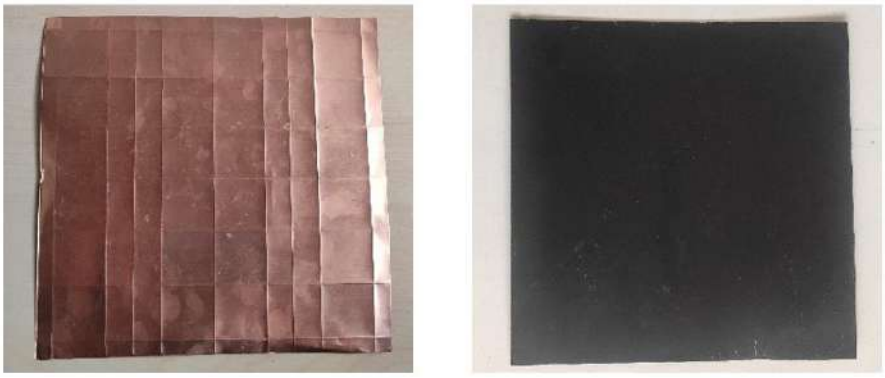

Figure 1. a) copper plate b) thermal painted copper plate

- Belt drive system: A belt drive system controlled by a stepper motor is used to move the heated copper plate. The stepper motor allows the speed of the moving plate to be precisely controlled, allowing the effects of different surface speeds on the heat transfer properties to be studied.

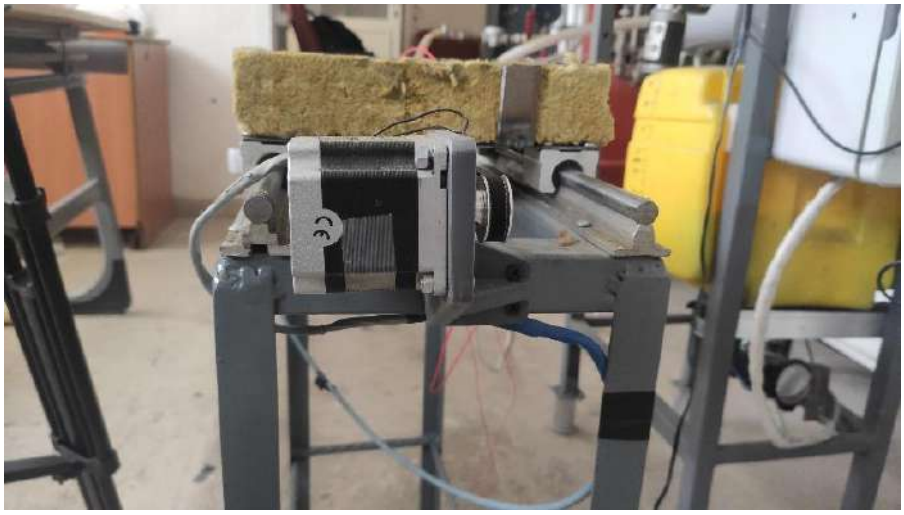

Figure 2. Belt drive system

- Supply air fan: A supply air fan is used to create an impinging jet of air. The fan speed is adjustable, allowing the jet speed to be varied for different experimental runs.

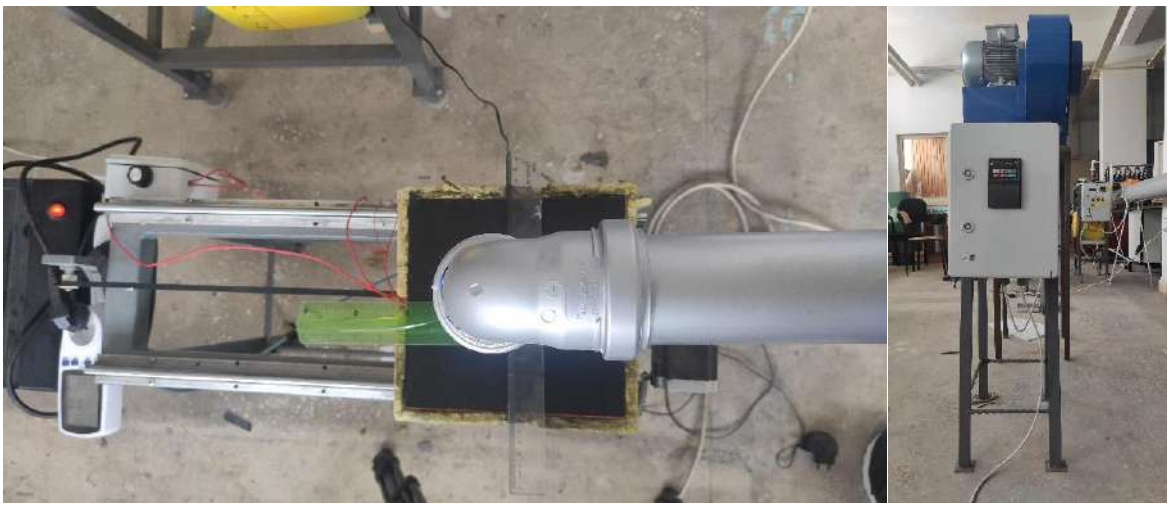

Figure 3. Air supply fan

- Data Recording Software: Specialized data acquisition software is used to collect and store data from the thermal camera. This software also allows real-time monitoring and post-processing analysis of the experimental data.

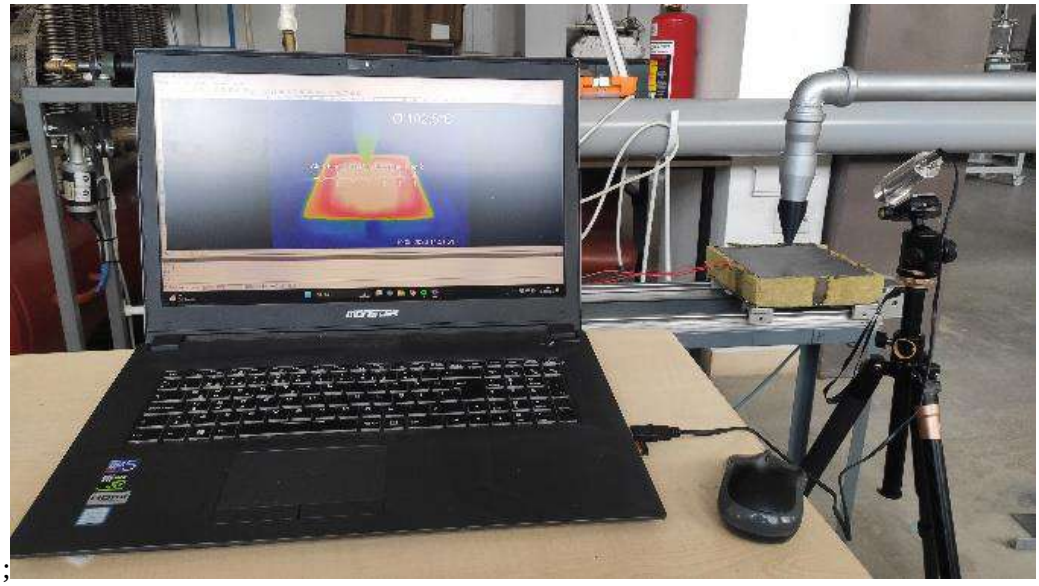
;

Figure 4. Data recording software

- Thermal camera: A thermal camera is used to measure the temperature distribution on the moving heated surface. The thermal camera captures real-time thermal images of the copper surface as it interacts with the impinging beam, providing detailed temporal and spatial temperature analysis.

Figure 5. Thermal camera

- Experimental Method:

The experimental procedure is as follows:

- The copper plate is uniformly heated to a predetermined initial temperature.
- The step motor initiates the motion of the heated copper plate at a specified speed.

- The air supply fan is activated, generating an air jet that impinges on the moving heated copper surface. The fan speed is adjusted to achieve the desired jet velocity.
- The thermal camera continuously records the temperature distribution on the copper surface during the experiment. The recorded data are saved using the data recording software for subsequent analysis.
- The experiment is repeated for various plate speeds and air jet velocities to investigate the effects of these parameters on the heat transfer from the impinging jet to the moving heated surface.

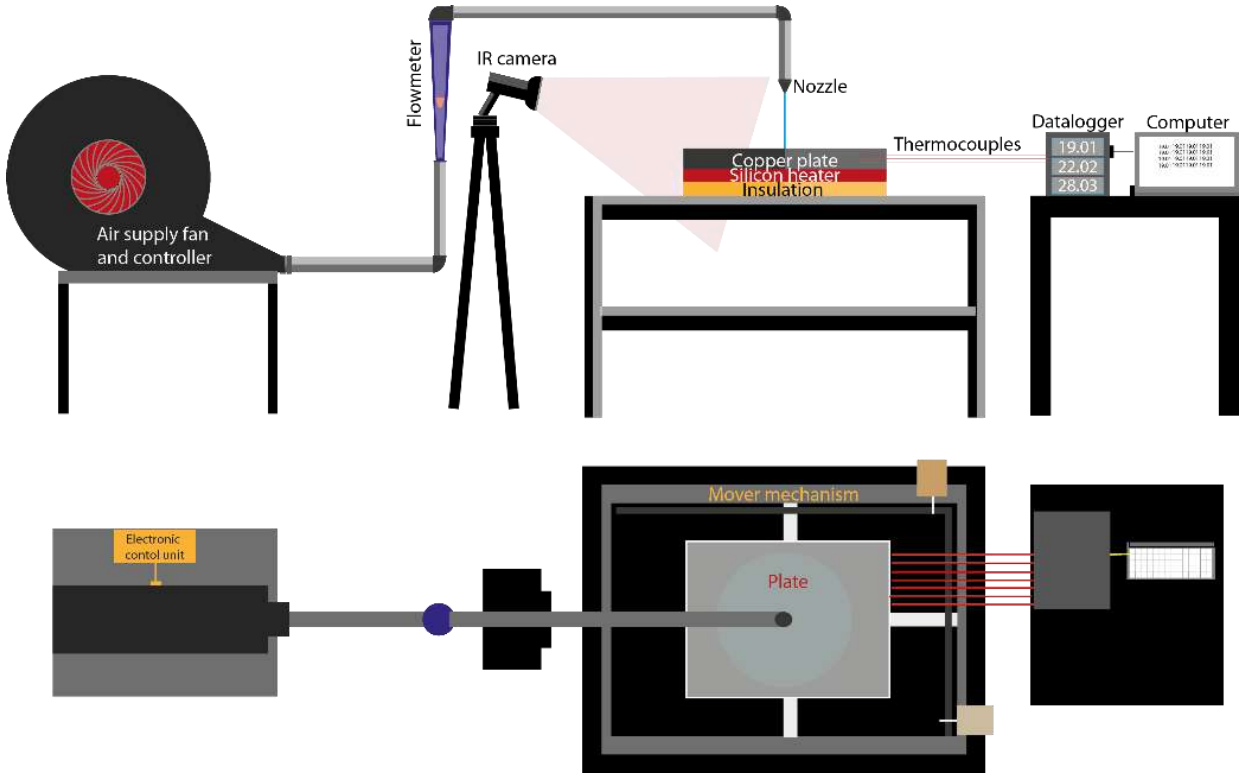

Figure 6. Schematic view of experimental setup

Nusselt numbers are computed and depicted through the utilisation of temperature distribution data obtained from both internal camera and software, in conjunction with the following formulas. Consequently, the study analyses the impact of motion using the acquired data.

$$h = Q / (A \times T_w\text{-}T_j) \quad (1)$$

$$Nu = h \times D_n / k) \quad (2)$$

3. Results

This section presents the results of the research study conducted through two different scenarios. The first scenario comprised of a jet impacting a stationary heated plate, whereas the second scenario involved an impacting jet on a moving heated plate. Technical term abbreviations have been appropriately defined upon first use. The writing style follows a conventional structure, emphasising clear and objective language, while avoiding emotional or figurative expressions. In both scenarios, the plate received a steady heat flux of 35 W. The plate-to-jet height ratio (h/d) was maintained at 4, and the impinging jets' Reynolds number was 6000. The language used is formal British English. The jets were heated to a temperature of 25 degrees Celsius. In the second scenario, the speed of the moving plate was set to 4 cm per second, and the stroke distance was set to 5 cm.

Data were collected from the thermal camera in the first stationary plate scenario to determine the impinging jet's heat transfer characteristics. The analysis of the spatial and temporal temperature distributions on the plate surface was undertaken to evaluate the impinging jet's effects.

An initial rise in the surface temperature was observed when the impinging jet was initiated, attributed to the 35 W heat flux, indicating the start of heat transfer from the jet to the plate.

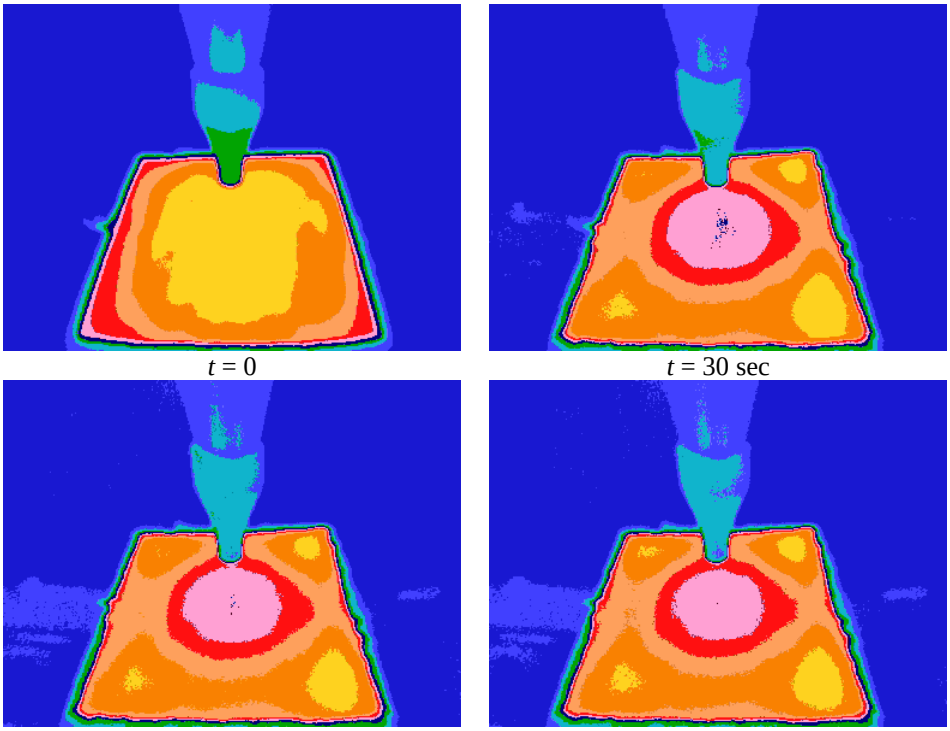

Figure 7. Fixed plate thermal images

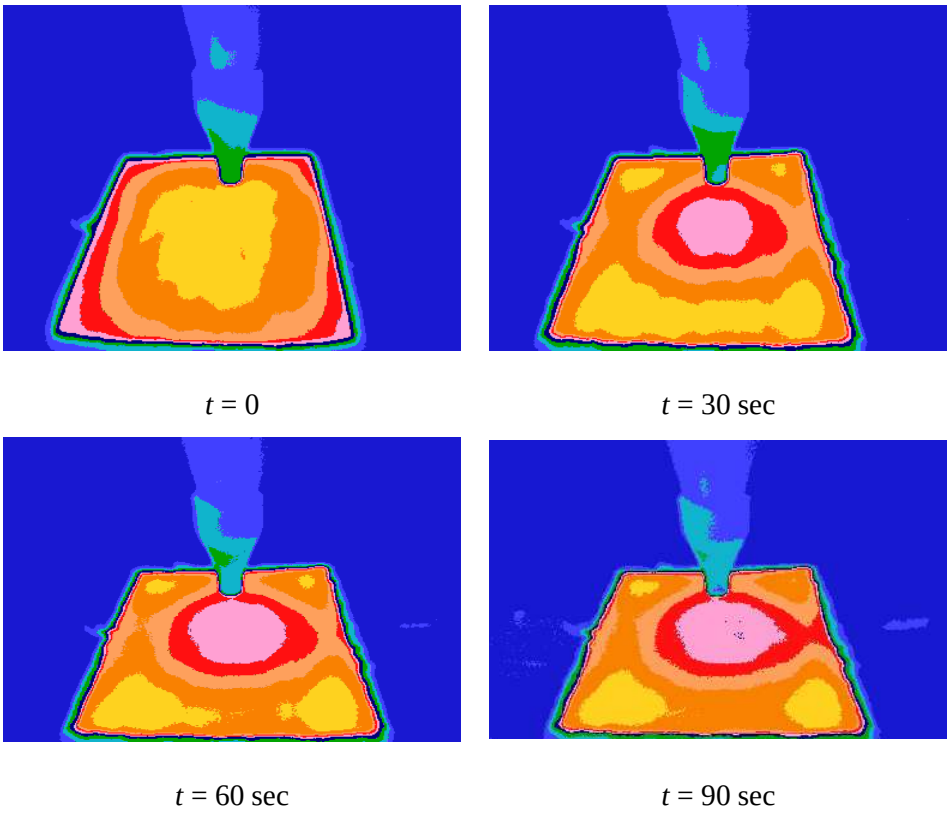

Figure 8. Moving plate thermal images

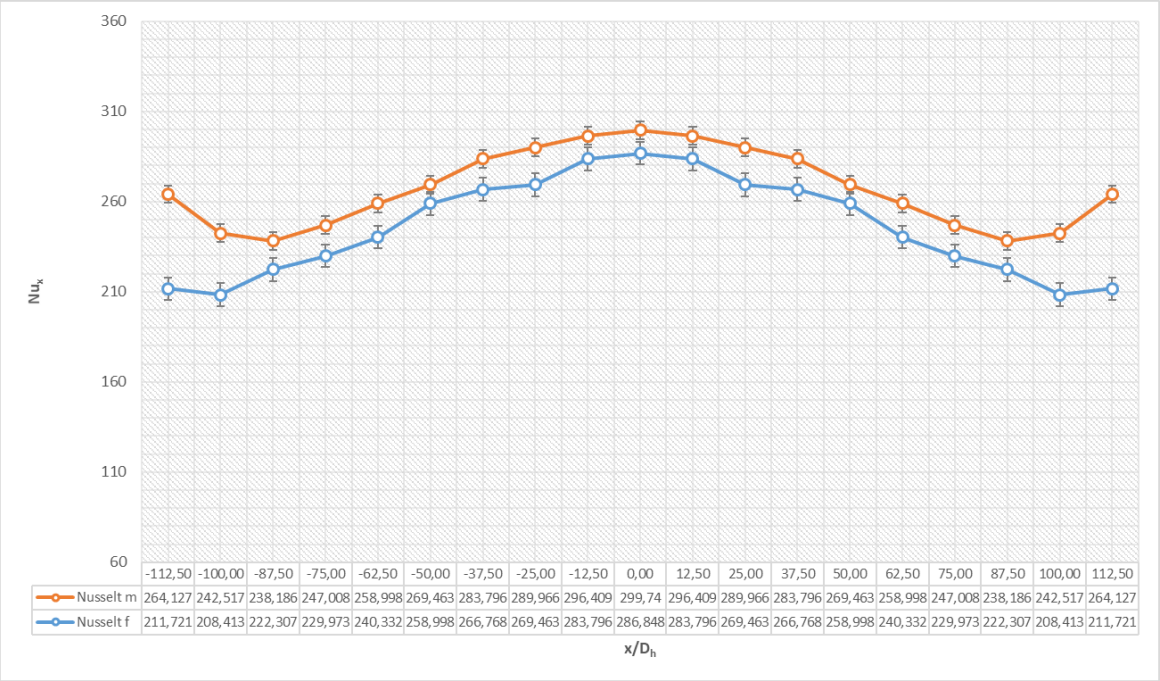

Figure 9. Local Nusselt Numbers

4. Conclusion

This investigation aimed to experimentally examine the impact of an air jet impinging heated copper plates (fixed and moving) under constant heat flux conditions. The focus was on comprehending modifications in heat transfer properties, which are essential for enhancing the performance of thermal management systems.

Our analysis produced Nusselt number data based on the average temperature alterations on the copper plate. A noteworthy augmentation in heat transfer occurs when the plate is in motion as opposed to stationary. Specifically, the moving plate scenario generated a rise of up to 24,75% in the Nusselt number, signifying an escalation in convective heat transfer, attributing it to the plate's movement.

Furthermore, based on the average alteration observed in all experimental runs, the moving plate demonstrated better performance, exhibiting an 9,27% rise in the Nusselt number in comparison to the fixed plate state. This enhancement resulted from the supplementary convective influence produced by the plate's motion, which supplements the heat transfer caused by the air jet impingement.

The results unequivocally illustrate that the motion of the heated plate can appreciably augment the heat transfer from the impinging air jet, consequently enhancing the cooling efficacy in thermal management systems. The present investigation is a noteworthy addition to the current research on impinging jets and their implementations by providing fundamental insights for devising more efficient thermal systems.

However, it is crucial to acknowledge that the ideal speed at which plates travel and the parameters of the jet may rely on numerous factors, such as specific heat flux, jet Reynolds number, and geometrical configurations. Therefore, additional research is necessary to examine these aspects in greater detail and produce more accurate guidelines for practical applications in the real world. However, the considerable rise in the Nusselt number identified in this study provides a strong indication of the potential advantages of integrating plate movement when devising cooling systems that employ impinging jets.

5. References

[1] Raju KS, Schlünder EU. “Heat transfer between an impinging jet and a continuously moving flat surface”. Wärme-und Stoffübertragung, 10 (2), (1977).

[2] Afroz F, Sharif MAR. “Numerical Study of Heat Transfer from an Isothermally Heated Flat Surface Due to Turbulent Twin Oblique Confined Slot-Jet Impingement”. International Journal of Thermal Sciences, 74:1–13 2013.

[3] Beitelmal AH, Saad MA, Patel CD. “The Effect of Inclination on the Heat Transfer between a Flat Surface and an Impinging Two-Dimensional Air Jet”. International Journal of Heat and Fluid Flow 21(2):156–63, 2000.

[4] Chattopadhyay H, Biswas G, Mitra N. “Heat Transfer From a Moving Surface Due to Impinging Slot Jets”. Journal of Heat Transfer. 124 (3), 433-440, 2002.

[5] Chou YJ, Hung YH. “Impingement Cooling of an Isothermally Heated Surface With a Confined Slot Jet”. Journal of Heat Transfer 116(2), 479–482, 1994.

[6] Chung YM, Luo KH, Sandham ND. “Numerical Study of Momentum and Heat Transfer in Unsteady Impinging Jets”. International Journal of Heat and Fluid Flow, 23(5), 592–600, 2002.

[7] Pakhomov MA, Terekhov VI. "Numerical Study of Fluid Flow and Heat Transfer Characteristics in an Intermittent Turbulent Impinging Round Jet". International Journal of Thermal Sciences, 87:85–93, 2015.

[8] Sagot B, Antonini G, Christgen A, Buron F. "Jet Impingement Heat Transfer on a Flat Plate at a Constant Wall Temperature". International Journal of Thermal Sciences, 47(12), 1610–1619, 2008.

[9] Trávníček Z, Dančová P, Kordík J, Vít T, Pavelka M. "Heat and Mass Transfer Caused by a Laminar Channel Flow Equipped With a Synthetic Jet Array". Journal of Thermal Science and Engineering Applications, 2(4), 2011.

International Conference on Advances and Innovations in Engineering

The tensile properties of three- dimensional (3D) textile reinforced composites

Mehmet KORKMAZ[1] , Halis KANDAŞ[2]

[1]Textile Engineering Department, Engineering Faculty, Dokuz Eylül University, İzmir, Türkiye.
[2] The Graduate School of Natural and Applied Sciences, Dokuz Eylül University, İzmir, Türkiye.
[1]mehmet.korkmaz@deu.edu.tr, [2]haliskandas1@gmail.com

[1](ORCID: 0000-0001-7000-0653), [2](ORCID: 0000-0002-7556-6979)

Abstract

The three- dimensional (3D) textile reinforced composites have extraordinary mechanical properties in their third direction thanks to the separated yarn or fiber group, which is placed at the thickness direction. Therefore, the 3D composites have been demanded by various industries for decades such as aviation, space, defense, automotive, etc. The 3D textiles can be obtained by the weaving, knitting, sewing, tufting, braiding or non- woven production methods. The different production methods gain specific structural and mechanical properties to the 3D composites. Although number of research studies were carried out to mechanically characterize the 3D composites, the mechanical properties of 3D composites were comparatively examined according to the production methods in the few studies.
In this study, the 3D carbon woven, 3D multi- axis carbon knitted, and 3D stitched carbon woven composites were produced, and their tensile properties were investigated. As regards the tensile strength and stiffness values, the significant differences were determined among the 3D composites.

Keywords: 3D woven composite, 3D multi- axis warp knitted composite, 3D stitched woven composite, carbon fiber, tensile test

1. Introduction

The three- dimensional (3D) textiles are advanced fabric systems, which include the fiber or yarn group in their three main axes. The 3D textiles can be produced by the weaving, knitting, braiding, tufting, stitching or non- woven production methods. Different production methods gain specific properties to the 3D textiles.

In the 3D textiles, the Z group yarn is oriented in the thickness direction. Therefore, the 3D textiles improve the out-of- plane mechanical properties of composite. On the other hand, this phenomenon may cause to reduce the in-plane mechanical properties of 3D composites. Number of studies focused to characterize the mechanical properties of 3D textile and their composites [1]–[4]. However, the mechanical behavior of 3D textiles was comparatively investigated in the few studies [5], [6].

In this study, the 3D carbon woven, 3D multi- axis carbon warp knitted, 3D stitched carbon woven fabric reinforced composites were produced, and their tensile properties were investigated. In addition, a traditional carbon woven laminated composite was produced and tested to make comparison. As result, the significant differences could be obtained according to the tensile strength and stiffness values of 3D composites.

[1]Corresponding author

2. Material and Method

2.1. 3D Textiles

The 3D carbon woven, 3D multi-axis carbon warp knitted, and 3D stitched carbon woven fabrics were used as reinforcements. All 3D textiles have four layers and similar areal density values, which are almost 800 g/m². The surface appearances of 3D textiles are presented in Figure 1.

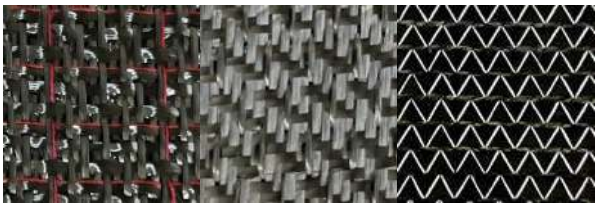

Figure 1. The 3D textiles. (a) 3D carbon woven, (b) 3D stitched carbon woven fabric, (c) 3D carbon multi- axis warp knitted fabric

2.2. Composite Production

The composites were produced with the vacuum infusion resin transfer method (VARIM). In addition to 3D composites, a traditional laminated composite, which include four carbon woven layers, was produced to make comparison. The epoxy resin was preferred as matrix material and resin to hardener ratio was settled at 3:1. The matrix had been cured at 80°C for eight hours. The produced carbon composites are presented in Figure 2.

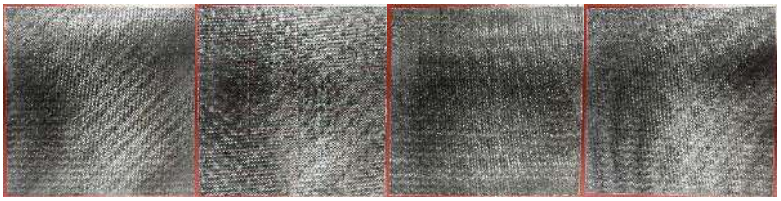

Figure 2. The produced composites. (a) traditional laminated composite (LC), (b) 3D woven composite (3WC), (c) 3D multi-axis warp knitted composite (MAC), (d) 3D stitched woven composite (SWC)

2.3. Tensile Test of Composites

The composites were tested with the Shimadzu Autograph AG-X 100 kN test machine according to the ASTM-D3039/D3039M-14 test standard. The five test specimens were tested for every type of composite and the tests were applied for both directions. The test specimens were prepared at 250 × 15 mm and 175 × 25 mm dimensions for the warp and weft directions, respectively. The tensile test specimens of 3D stitched woven composite is presented in Figure 3.

Figure 3. The tensile test specimens of 3D stitched woven composite

3. Results and Discussion

The tensile strength and elastic modules values of composites were determined for their both sides in the tensile test. The maximum tensile stress values of composites are presented in Figure 4. While the blue columns represent the warp directions of composites (1. direction), the orange columns present the weft directions (2. direction). The strength values of composites have almost the same values in their both directions. The traditional laminated composite has the highest tensile strength in its warp direction among all tested composites. As the carbon yarns are

oriented at four different directions in the 3D multi- axis warp knitted composite, it has the lowest tensile strength value.

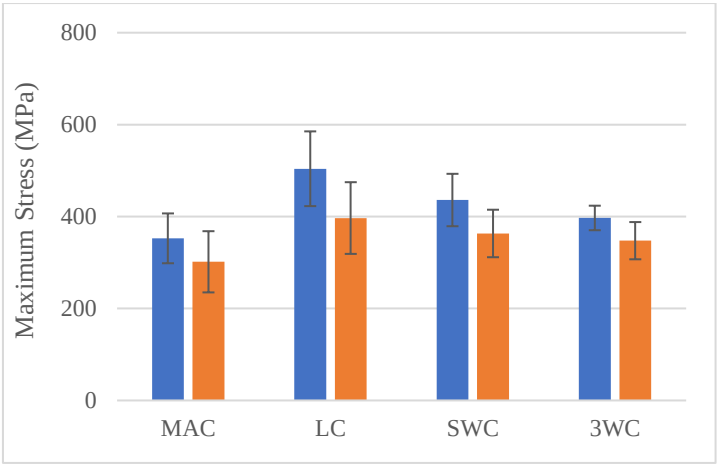

Figure 4. The maximum tensile stress values of composites

The elastic module values of composites are showed in Figure 5. The blue and orange columns represent the warp and weft directions of composites, respectively. While 3D multi- axis warp knitted and laminated composites have the same elastic module values in their both directions, the 3D stitched, and 3D woven composites have higher elastic modules in the weft direction than warp direction.

The stitching process was applied through the warp direction of fabric. Although the elastic module was not affected by the process in the weft direction of 3D stitched composite, the module was decreased in the warp direction. This phenomenon can be explained by the stitching process. The stitching can damage the carbon fiber, which are placed in- plane direction. Furthermore, the process can change the orientation of yarn in the fabric plane.

In the 3D woven composite, the binding warp yarns are placed in the third direction and connect the weft layers. Therefore, the binding warp yarns have highest crimp among all yarn groups. Contrary, the weft yarn group straightly laid at perpendicular to the stuffer warp yarns in the 3D woven composite. Thus, the weft yarns can better transfer the strength from yarn to the composite. As result, the 3D woven composite has higher elastic module value in the weft direction than warp direction.

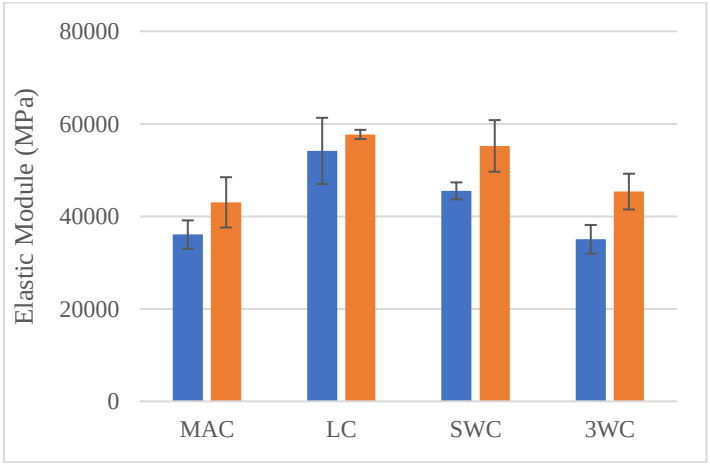

Figure 5. The elastic module values of composites

4. Conclusion

The 3D textiles have been demanded by the various industries thanks to their superior mechanical properties. Number of studies focus to characterize their mechanical behavior. On the other hand, different production methods gain

specific mechanical properties to the 3D textiles and their composites. The mechanical properties of 3D textile reinforced composites were comparatively investigated in the few studies and need to be elucidated.
The 3D carbon woven, 3D multi- axis carbon warp knitted, and 3D stitched carbon woven reinforced composites were produced and their tensile properties were investigated in the study. In addition, a traditional laminated carbon woven composite was produced to make a comparison.

The 3D weaving and 3D stitching methods reduced the tensile strength of composite but did not create statistically significant differences. A meaningful difference was occurred between the laminated and 3D multi- axis warp knitted composites in their warp direction. This result could be explained with the four axes yarn orientations of 3D multi-axis warp knitted composite.

According to the elastic module values, the 3D weaving and 3D multi- axis warp knitting methods cause to reduce the elastic module of composite in both directions. Contrary, the 3D stitching did not affect the elastic module of composite in the weft direction. However, the process reduced the module in the warp direction, which is the stitching direction. The out- of- plane mechanical properties of 3D composites will be investigated as further study.

5. References

[1] Korkmaz M, Okur A, Labanieh AR, and Boussu F, "Investigation of the mechanical and forming behaviour of 3D warp interlock carbon woven fabrics for complex shape of composite material," *Journal of Industrial Textiles*, vol. 51, no. 3S, pp. 5427S-5465S, 2022.

[2] Xiao S, Wang P, Soulat D, and Gao H, "An exploration of the deformability behaviours dominated by braiding angle during the forming of the triaxial carbon fibre braids," *Compos Part A Appl Sci Manuf*, vol. 133, no. December 2019.

[3] Hui C, Wang P, and Legrand X, "Improvement of tufting mechanism during the advanced 3-dimensional tufted composites manufacturing: To the optimisation of tufting threads degradation," *Compos Struct*, vol. 220, no. April, pp. 423–430, 2019.

[4] Mouritz AP, Leong KH, and Herszberg I, "A review of the effect of stitching on the in-plane mechanical properties of fibre-reinforced polymer composites," *Compos Part A Appl Sci Manuf*, vol. 28, no. 12, pp. 979–991, 1997.

[5] Mouritz AP and Cox BN, "A mechanistic interpretation of the comparative in-plane mechanical properties of 3D woven, stitched and pinned composites," *Compos Part A Appl Sci Manuf*, vol. 41, no. 6, pp. 709–728, 2010.

[6] Wang Y and Zhao D, "Effect of fabric structures on the mechanical properties of 3-D textile composites," *Journal of Industrial Textiles*, vol. 35, no. 3, pp. 239–256, Jan 2006.

International Conference on Advances and Innovations in Engineering

Numerical Analysis of A Pulsating Nanofluid Impinging Jet

Ali TASKIRAN[1] , Celal KISTAK [2], Ihsan DAGTEKIN [3] and Nevin CELIK[4]

[1,2,3,4] Firat University, Department of Mechanical Engineering, 23119, Elazig, Turkey.
[1]taskiranalii@gmail.com [2]ckistak@firat.edu.tr [3]idagtekin@firat.edu.tr, [4]nevincelik23@gmail.com

[1](ORCID: 0000-0001-6810-7291), [2](ORCID: 0000-0003-4621-5405), [3](ORCID: 0000-0003-0128-7149), [4](ORCID: 0000-0003-2456-5316)

Abstract

In this study, heat transfer and flow characteristics of an impinging pulsating nanofluid (water-based Al_2O_3) jet were investigated numerically. The pure water jet was also solved for comparison. As the analysis conditions; the volumetric concentration ratio of the nanofluid was kept 5%, both laminar and turbulent flow regimes were handled as Re = 1000 and Re = 15000, dimensionless jet-to-plate distance was considered to be H/D = 4, pulsation wave type was triangular, frequency was 10 Hz and amplitude value was 0.3 m/s.
From the numerical analysis of nanofluid jet, the adoption of triangular pulsations at H/D = 4, Re = 1000, f = 10 Hz, and A = 0.3 m/s led to a remarkable 22% increase in heat transfer efficiency comparatively to water jet. Briefly, nanoparticle-added jets increased the heat transfer. In addition, the heat transfer increased with the turbulent jet case with respect to the laminar case as expected. The addition of triangular pulsation wave with constant frequency and amplitude have also significant effect on heat transfer
Keywords: pulsating jet flow, single jet, ansys, heat transfer, numerical analysis

1. Introduction

Jet flow, found in aerodynamics, stands as one of the most foundational and crucial subjects with a wide array of engineering applications. Jets are extensively employed in various industrial sectors to enhance both heat and mass transfer. For instance, water jets are frequently harnessed within high-temperature gas turbines, paper and textile manufacturing, glass production, metal heat treatment processes, as well as electrical and electronic circuitry. Impinging jets result from the ejection of fluids with varying nozzle geometries striking a surface. In the case of impinging jets, the boundary layer thickness diminishes within the impact region, leading to an augmented heat transfer coefficient. Consequently, this ensures efficient heat transfer on the surface subjected to the jet's impact. The primary objective behind employing impinging jets is to achieve a heightened heat transfer rate while minimizing fluid usage.

Enhancing heat transfer is actively achieved by incorporating a jet into the flow and cooling the surface through impingement. Numerous experimental and numerical studies on this topic can be found in the existing literature [1–6]. In a numerical investigation, the flow patterns and heat transfer characteristics of turbulent impinging jets driven by air were thoroughly analyzed [7].

They conducted an analysis employing the Reynolds stress model as the turbulence model to examine the alterations in flow behavior in relation to the distance between the jet and the target surface, as well as variations in the Reynolds number.

Additionally, [8] explored the cooling of a heated cube through impingement by employing the Large-Eddy simulation technique to study heat transfer and flow in channel flow. Another experimental investigation was

[1]Corresponding author

conducted to examine the flow field characteristics of twin slot jets, both unconfined and confined, impacting an inclined surface [9].
A pulsating jet is characterized by a fluid flow pattern in which the fluid is periodically discharged at consistent intervals, creating intermittent bursts of fluid jet with specific speeds and time intervals. These pulsating jets find widespread application in various industrial settings and laboratory investigations. Additionally, researchers have extensively explored the aerodynamic, hydrodynamic, and acoustic properties of pulsating jets in numerous studies. In contemporary industrial and medical contexts, the precise control of jet flow holds significant significance. In pursuit of this objective, pulsating impinging jets have emerged as an innovative approach to manipulate fluid flow patterns. The utilization of pulsating impinging jets has attracted considerable attention, primarily owing to their perceived effectiveness in addressing challenges related to heat transfer enhancement. Consequently, this has led to a multitude of research endeavors in the scientific literature aimed at further understanding and optimizing this approach. [10–15].

Mladin and Zumbrunnen [16], conducted detailed boundary layer analysis to numerically explore the behavior of pulsating impinging jets around a planar stopping point, considering various pulsation waveform, frequency, and amplitude parameters. This investigation centered on examining heat and mass transfer characteristics in a two-dimensional turbulent slot air impinging jet subjected to intermittent pulsation, encompassing both cooling and heating scenarios. The study also investigated the influence of jet Reynolds numbers, pulsation frequency, time ratio (on/off ratio) of intermittent pulsation, temperature differentials, and geometrical configurations on heat transfer [17].

Allauddin et al. [18] investigated the numerical heat transfer of an impinging jet using nanofluid. The target surface exposed to a constant heat flux was cooled by the impinging jet. As a result of the research, they investigated heat transfer using pure water and Al_2O_3 - water nanofluid.

Akcay and Demiral [19], the convective heat transfer of CuO-water-based nanofluids was numerically studied in a triangular wavy channel under pulsating inlet flow conditions, considering different Reynolds numbers ($200 \leq Re \leq 700$) and a nanoparticle volume fraction of 5%. The study analyzed the effects of Reynolds number, pulsating frequency, and amplitude on heat transfer performance. Lastly, a numerical study assessed the impact of porosity on heat transfer characteristics in a confined impinging jet utilizing an Al_2O_3/water nanofluid within a metal foam for various porosity levels.

Bianco et al. [20], outcomes encompass temperature and stream function fields, along with temperature profiles along the symmetry axis. Additionally, the study provides insights into both average and local Nusselt numbers computed for the heated wall, considering different nanoparticle volume concentration values.

Zeitoun et al. [21], investigated the jet flow impinging on a circular surface with Al_2O_3 - water nanofluid. The study shows that the increase in Nusselt number for turbulent flow can reach 40% and 75% at concentrations of 6.6% and 10%, respectively. Zao and Cheng [22], conducted a study to experimentally and numerically investigate laminar pulsating forced convection in a long pipe heated by uniform heat flux and subjected to reciprocal air flow.

Selimefendigil and Öztop [23], numerically investigated pulsating rectangular jets of nanofluids. The effects of various parameters such as pulsation frequency, Reynolds number, nanoparticle volume concentration ratio on the fluid and heat transfer properties are numerically investigated.

The primary objective of this study is to assess the influence of impinging pulsating nanofluid jets on heat transfer and flow characteristics. The numerical investigation was conducted using the ANSYS-FLUENT commercial software.

2. Mathematical Model and Numerical Method

In order to replicate the turbulent flow characteristics, this study relies on numerical solutions for the turbulent two-dimensional Navier–Stokes and energy equations, employing a finite-difference scheme. These equations are coupled with the continuity equation. The turbulence effects are accounted for using an eddy viscosity model. The assumptions made include a steady, incompressible, and two-dimensional flow, with the neglect of buoyancy and

radiation heat transfer effects. The governing equations for mass, momentum, turbulent kinetic energy, turbulent energy dissipation rate, and energy within the steady turbulent main flow are described using the standard k–e model, as detailed in [24];

Continuity equation

$$\frac{\partial \rho u_i}{\partial x_i} = 0 \tag{1}$$

Momentum equation

$$\rho u_j \frac{\partial u_i}{\partial x_j} = -\frac{\partial P}{\partial x_i} + \frac{\partial}{\partial x_j}\left[\mu_t \left(\frac{\partial u_i}{\partial x_j} + \frac{\partial u_j}{\partial x_i}\right)\right] \tag{2}$$

Energy equation

$$\rho u_j \frac{\partial T}{\partial x_j} = \frac{\partial}{\partial x_j}\left[\left(\frac{\mu_L}{\sigma_L} + \frac{\mu_t}{\sigma_t}\right)\frac{\partial T}{\partial x_j}\right] \tag{3}$$

Transport equation for k

$$\rho u_j \frac{\partial k}{\partial x_j} = \frac{\partial}{\partial x_j}\left(\frac{\mu_t}{\sigma_k}\frac{\partial k}{\partial x_j}\right) + \mu_t \left(\frac{\partial u_i}{\partial x_j} + \frac{\partial u_j}{\partial x_i}\right)\frac{\partial u_i}{\partial x_j} - \rho \varepsilon \tag{4}$$

Transport equation for ε

$$\rho u_j \frac{\partial \varepsilon}{\partial x_j} = \frac{\partial}{\partial x_j}\left(\frac{\mu_t}{\sigma_\varepsilon}\frac{\partial \varepsilon}{\partial x_j}\right) + c_1 \mu_t \frac{\varepsilon}{k}\left(\frac{\partial u_i}{\partial x_j} + \frac{\partial u_j}{\partial x_i}\right)\frac{\partial u_i}{\partial x_j} - c_2 \rho \frac{\varepsilon^2}{k} \tag{5}$$

The empirical constants appear in the above equations are given by the following values [24],

$$c_1 = 1.44, c_2 = 1.92, c_\mu = 0.09, \sigma_k = 1, \sigma_\varepsilon = 1.3, \sigma_t = 0.7$$

For turbulence models to get good results, the mesh elements should be as small as possible. However, the fact that the elements are too small increases the time in the solution. Therefore, it is very important to choose suitable sized elements here. The geometry and mesh were created after several trials (Figure 1). The convergence criteria for continuity, momentum and energy equations are set to 10^8. The time dependent parts are solved with implicit scheme. Second order implicit time integration is chosen for the temporal discretization. For the unsteady calculations, steady state solutions are used as the initial condition. The computational domain consists of rectangular elements.

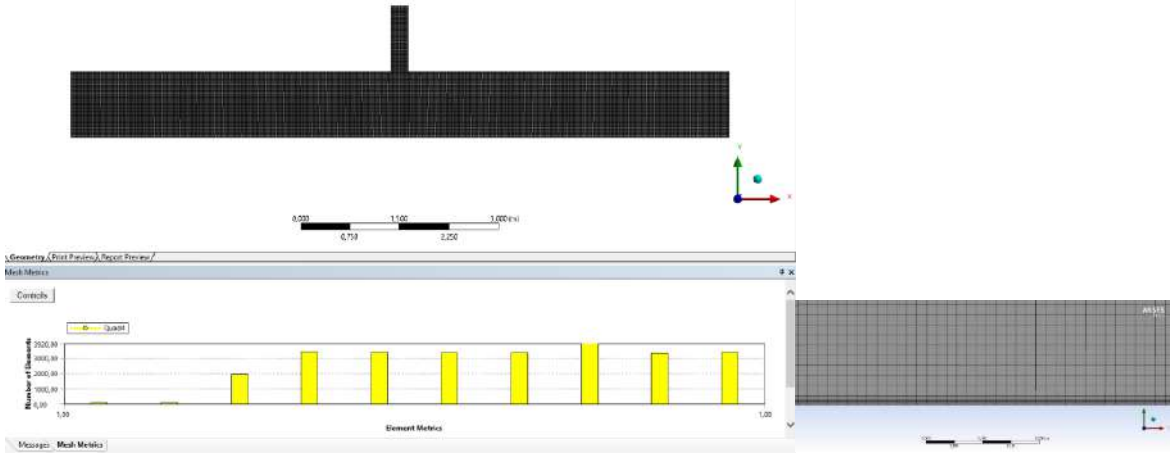

Figure 1. Mesh structure of model.

This study focuses on a computational domain described schematically in Figure 1. The two-dimensional model of the physical problem has two plates separated with a distance H and length L. A jet from the rectangular slot on the top plate impinges on the bottom plate. The width of slot is W. The jet has a uniform velocity with a triangular time dependent part $u_{jet} = 2u_0 \frac{sin^{-1}[-Asin(ft)]}{sin^{-1}(-A)}$, for amplitude A and frequency f of the pulsating jet inlet velocity (Figure 2) and a uniform temperature T_c = 298 K. In this configuration, the bottom plate is maintained at a temperature T_h = 350 K, while the top plate is considered adiabatic. The study assumes that the thermo-physical properties of the fluid remain independent of temperature. Additionally, the flow is assumed to be two-dimensional, Newtonian, incompressible, and within the turbulent flow regime, with a specific emphasis on Newtonian flow. Gravitational forces in both the x-axis and y-axis directions are neglected. Transient simulations are conducted with time steps

resolved for both 30 and 60 seconds. The k-ε turbulence model is modified to be realizable. For the fluid, a nanofluid consisting of water and 5% Aluminum oxide (Al_2O_3) nanoparticles is used. A single-phase or homogeneous model was applied, assuming that the liquid phase and nanoparticles are in thermal equilibrium and move at the same velocity. Regarding boundary conditions, the inlet, the wall where the jet impacts the plate (heat wall), and the area where the jet spreads were designated as openings, while the other sections were defined as adiabatic.

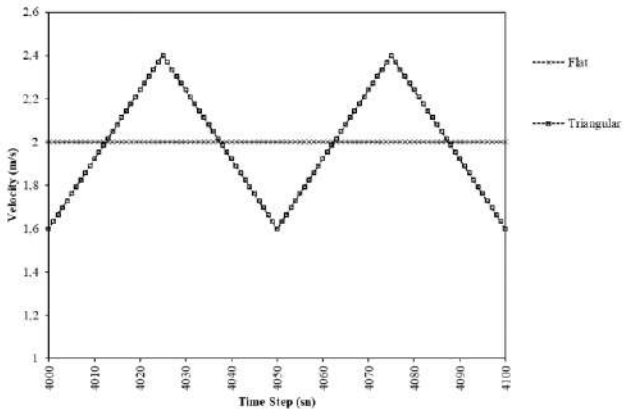

Figure 2. Comparison of time-dependent pulsating and velocity flow.

Figure 3 provides a representation of the boundary conditions applicable to the specified two-dimensional geometry in the study. Within this geometry, the velocity of the jet is defined as a function within the FLUENT software, encompassing both a uniform velocity profile and the generation of triangular pulsations. At the inlet of the jet, the temperature is consistently maintained at 298 K. The surface where the jet impinges, referred to as the impactor surface, is assumed to maintain a constant temperature of 350 K. Notably, the exit of the jet is left open to the surrounding environment, establishing free flow conditions. In contrast, all other surfaces within the system are designated as adiabatic, indicating that no heat transfer occurs across these surfaces. Additionally, the turbulence intensity at the inlet is specified at 1%.

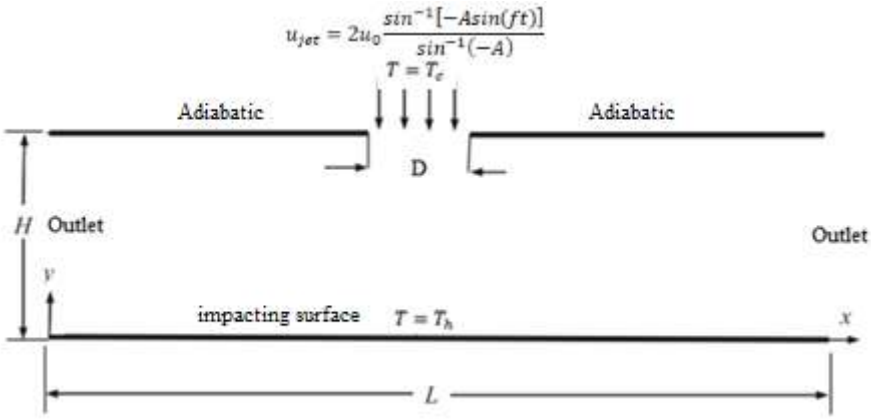

Figure 3. Boundary conditions

3. Results and Discussions

In order to see the flow characteristics in more detail, the time-dependent velocity vectors for the first 10 s are shown in Figure 4 for the impinging event triangular vibration at H/D = 4, Re = 1000, f = 10 Hz and A = 0.3 m/s. It confirms the vortex states obtained for the vectorial velocity contours. It is concluded that the vortices increase as time progresses due to the effect of the thermal boundary layer, especially in the impact zone. The intensity of the streamlines increases with increasing velocity. Thus, a significant increase in heat transfer is observed in this region [25].

In Figure 5, streamlines are depicted during the time interval t = 50 - 55 s, considering parameters of H/D = 4, Re = 1000, f = 10 Hz, and A = 0.3 m/s. Upon impact with the hot bottom surface, the jet generates two counter-rotating vortices due to the constraining effect of the upper adiabatic plate. This results in a symmetric flow pattern relative to the stagnation point for both flow and thermal fields. The intensity of these vortices experiences variations, although the vector lines exhibit slight changes over different time frames. Within the wall jet region, the thickness of the normal component increases as its velocity decreases.

The tested nanoparticle volumetric concentration ratio leads to a rise in the effective thermal conductivity of the nanofluid. This, in turn, results in a reduction in temperature due to the multiplier effect, promoting a more uniform temperature distribution and contributing to enhanced heat transfer.

Additionally, the pulsation applied to the inlet velocity amplifies the density of streamlines, driven by the influence of frequency and amplitude. With higher velocity, streamlines become denser, consequently leading to a significant augmentation in heat transfer within this region [25].

In Figure 6, concerning H/D = 4, we observe bidirectional rotational velocity and reversible vortices at the point of impact caused by the jet. It's essential to highlight that at the surface where the jet strikes, the velocity of the jet reaches zero. Subsequently, an inflow vortex expands and grows in the y-axis direction, resulting in the formation of a small vortex near the target surface and another vortex downstream. Nonetheless, it's noteworthy that the jet velocity does not reach zero throughout the entire flow duration, leading to the formation of only small vortices near the adiabatic wall and the heated surface [26].

In Figure 7, velocity contours are depicted at time intervals t = 0 - 30 s, considering parameters of H/D = 4, Re = 15000, f = 10 Hz, and A = 0.3 m/s. Upon impact with the hot bottom surface, the jet generates two counter-rotating vortices due to the constraining effect of the upper adiabatic plate. This results in a symmetric flow pattern relative to the stagnation point for both flow and thermal fields. While there are slight variations in the vector plots across different time intervals, the intensity of the vortices is notably influenced. Within the wall jet region, the thickness of the normal component increases as its velocity decreases.

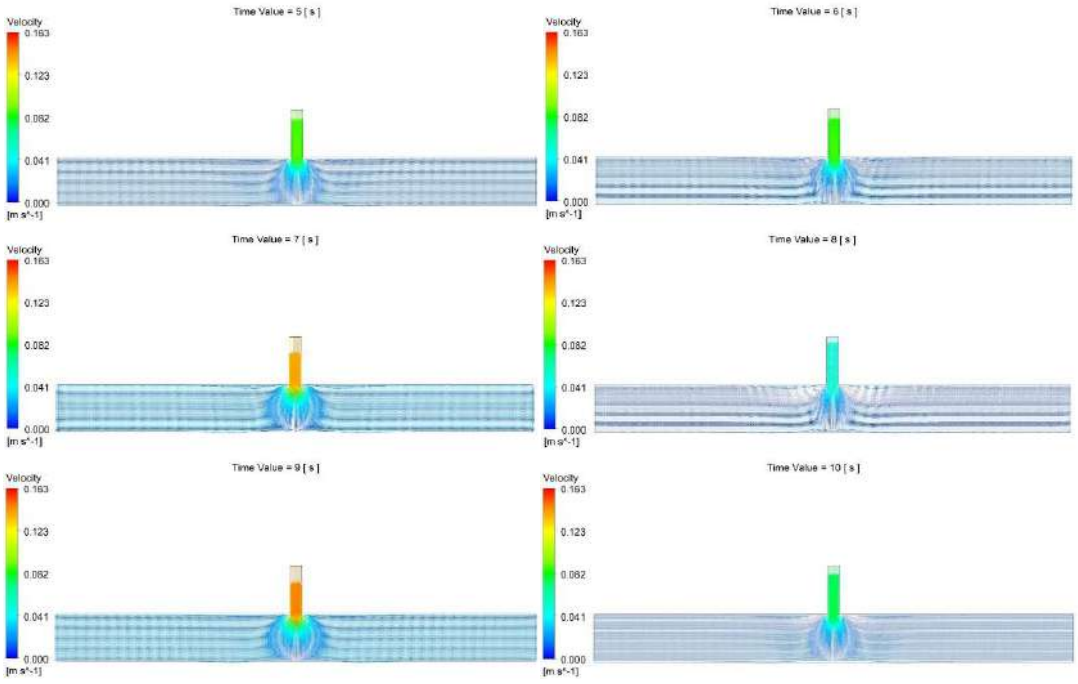

Figure 4. Time-dependent velocity vectors of the impinging nanofluid jet in the range H/D = 4, Re = 1000, t = 0-10 s

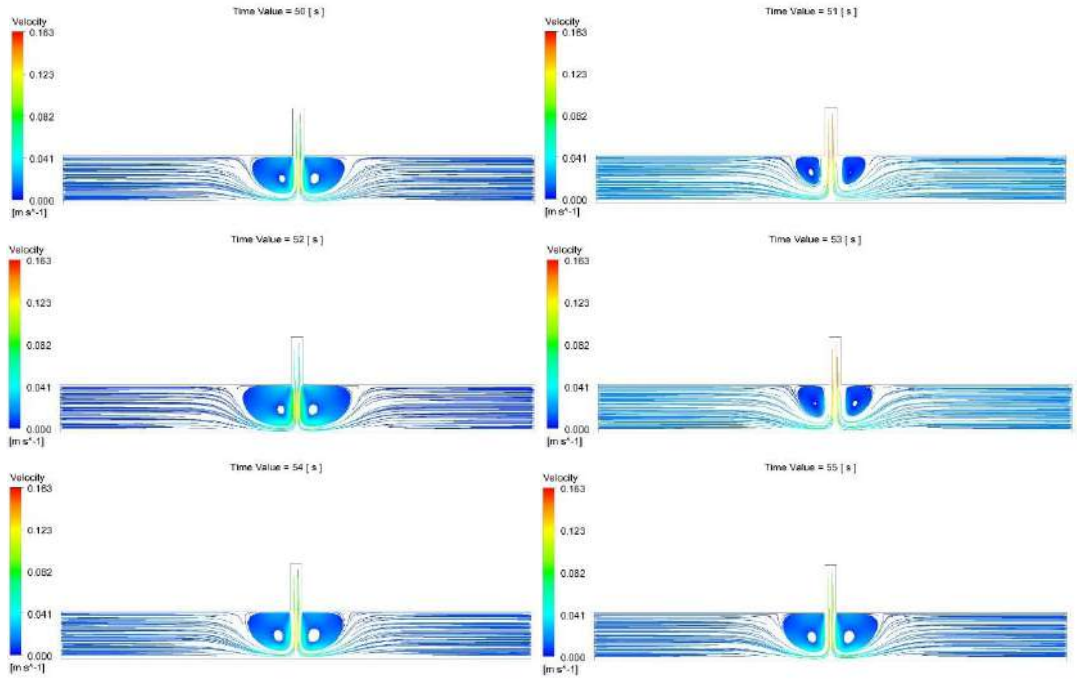

Figure 5. Time-dependent streamlines of the impinging nanofluid jet in the range t = 50 - 55 s for H/D = 4, Re = 1000

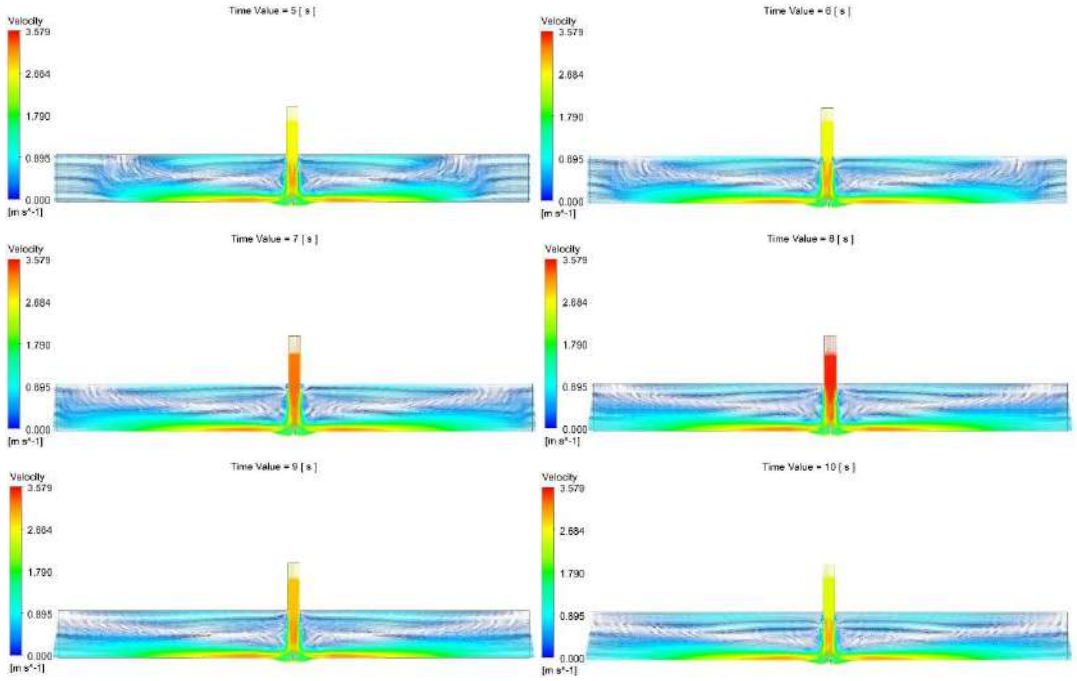

Figure 6. Time-dependent streamlines of the impinging nanofluid jet in the range t = 0 - 10 s for H/D = 4, Re = 15000

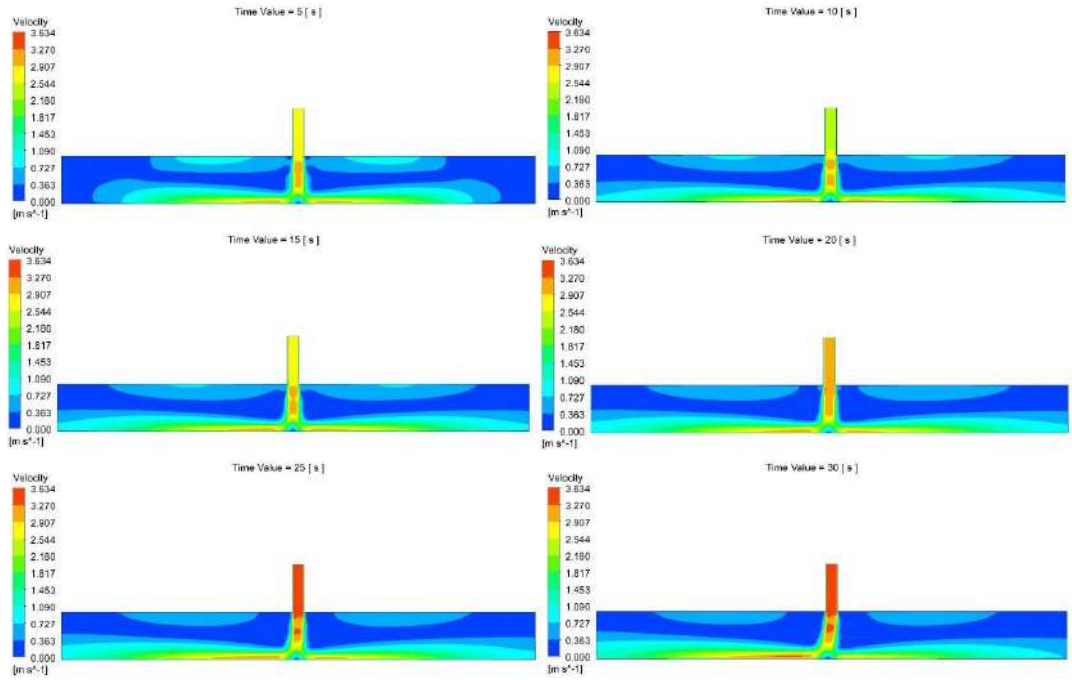

Figure 7. Time-dependent velocity contours of the impinging nanofluid jet in the range t = 0 - 30 s for H/D = 4, Re = 15000

Up to this point, our focus has been on providing a detailed analysis of flow characteristics within wide (0 - 60 s) and narrow (0 - 10 s) time intervals, particularly for H/D = 4. Now, it's essential to shift our attention to the realm of heat transfer. In Figure 8, we observe the distribution of local Nusselt numbers along the impinging surface for various nanoparticle volumetric concentration ratios, with parameters set at H/D = 4, triangular pulsation, Re = 1000, f = 10 Hz, and A = 0.3 m/s. Notably, the highest Nusselt number is clearly evident at the point of impingement. This is attributed to the reduction in the thermal boundary layer thickness in this region, resulting in an increased Nusselt number. Additionally, it's worth noting that an increase in volumetric concentration leads to a corresponding rise in the Nusselt number. Specifically, at a volumetric concentration of ϕ = 5%, heat transfer shows a 22% improvement compared to the case without nanoparticles namely water (ϕ = 0).

Figure 9 shows the variation in local Nusselt numbers concerning nanoparticle volumetric concentration ratio ϕ = 5% across different Reynolds numbers. As the Reynolds number increases from Re = 1000 to Re = 15000, a corresponding increase in the local Nusselt number is observed. In the impingement region, there is a slight decrease in the local Nusselt number, as expected, owing to the reduction in velocity. At the initial stages of the wall jet region, the local Nusselt number reaches its peak due to the influence of velocity resulting from momentum transfer. However, within the wall jet region, the local Nusselt number decreases due to surface friction. The variations in local Nusselt numbers exhibit similarities among different Reynolds numbers, with the most significant disparity occurring during pulsation and diminishing within the wall jet region.

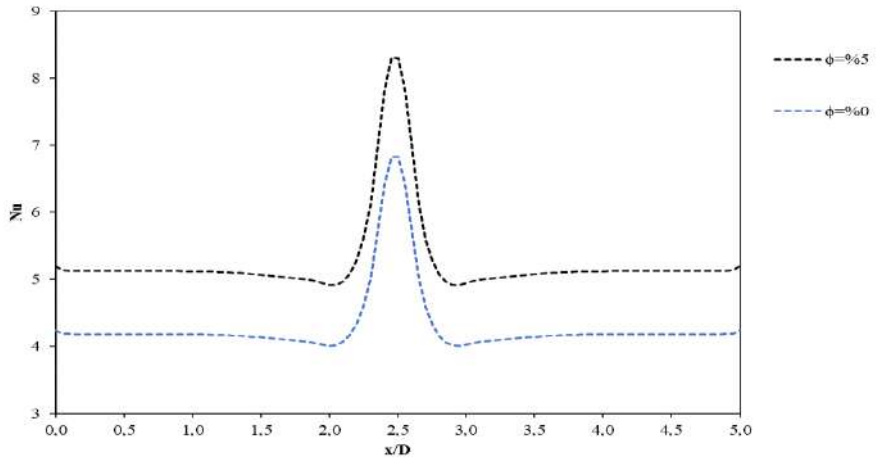

Figure 8. Local Nusselt variation for different nanoparticle volume concentration ratios for H/D = 4, Re = 1000

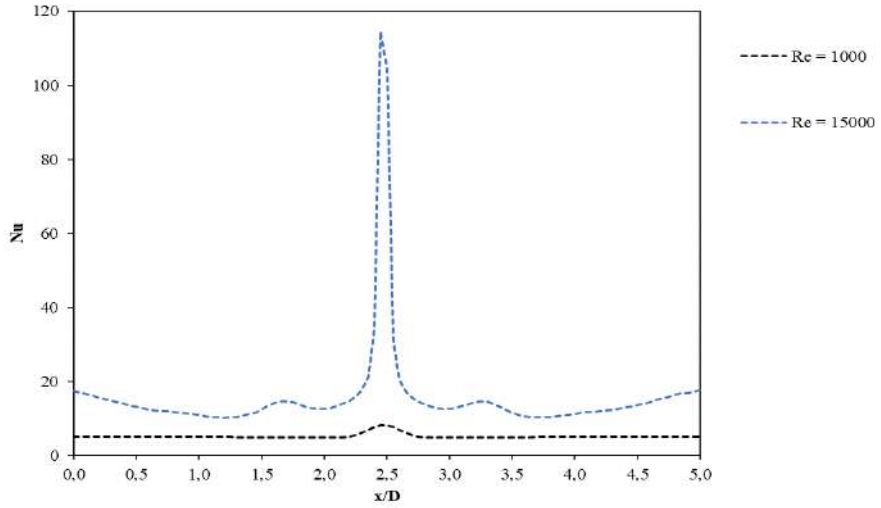

Figure 9. Local Nusselt variation for different Reynolds number ϕ = 5% nanoparticle volume concentration ratios

4. Conclusions

In this study, we examined the impact of single impinging pulsating nanofluid jets on heat transfer and flow characteristics. The analysis aimed to identify analysis conditions across various parameters, including volumetric concentration ratio (5%), Reynolds numbers (Re = 1000 and 15000), dimensionless jet-to-plate distance (H/D = 4), pulsation wave type (triangular), frequency (10 Hz), along with amplitude value (0.3 m/s) for water and water-based Al_2O_3 nanofluid.

The numerical analysis of the nanofluid impinging jet demonstrated a remarkable 22% increase in heat transfer when utilizing triangular pulsations under the mentioned conditions comparatively to the pure water impinging jet conditions. In conclusion, nanoparticle-enhanced jets exhibited significantly improved heat transfer performance, particularly. In addition the pulsation with even constant parameters yield a higher heat transfer.

5. References

[1] Chou YJ, Hung YH. “Impingement cooling of an isothermally heated surface with a confined slot jet”. Journal of Heat Transfer, 116 (2), 479–482, 1994.

[2] Beitelmal AH, Saad MA, Patel CD. “The effect of inclination on the heat transfer between a flat surface and an impinging two-dimensional air jet”. International Journal of Heat and Fluid Flow, 21 (2), 156–163, 2000.

[3] Chung YM, Luo KH, Sandham ND. “Numerical study of momentum and heat transfer in unsteady impinging

jets". International Journal of Heat and Fluid Flow, 23 (5), 592–600, 2002.
[4] Sagot B, Antonini G, Christgen A, Buron F. "Jet impingement heat transfer on a flat plate at a constant wall temperature". International Journal of Thermal Sciences, 47 (12), 1610–1619, 2008.
[5] Trávníček Z, Dančová P, Kordík J, Vít T, Pavelka M. "Heat and mass transfer caused by a laminar channel flow equipped with a synthetic jet array". Journal of Thermal Science and Engineering Applications, 2 (4), 041006-14, 2010.
[6] Afroz F. Sharif MAR. "Numerical study of heat transfer from an isothermally heated flat surface due to turbulent twin oblique confined slot-jet impingement". International Journal of Thermal Sciences, 74, 1–13, 2013.
[7] Pakhomov MA, Terekhov VI. "Numerical study of fluid flow and heat transfer characteristics in an intermittent turbulent impinging round jet". International Journal of Thermal Sciences, 87, 85–93, 2015.
[8] Rundström D, Moshfegh B. "Investigation of Flow and Heat Transfer of an Impinging Jet in a Cross-Flow For Cooling of a Heated Cube". Journal of Electronic Packaging, 128 (2), 150–156, 2005.
[9] Özmen Y. "Eğik Bir Yüzeye Çarpan İkili Slot Hava Jetlerinde Basınç Dağılımlarının Deneysel İncelenmesi". J. of Thermal Science and Technology, 36, 29–36, 2016.
[10] Poh HJ, Kumar K, Mujumdar AS. "Heat transfer from a pulsed laminar impinging jet". International Communications in Heat and Mass Transfer, 32 (10), 1317–1324, 2005.
[11] Gillespie MB, Black WZ, Rinehart C, Glezer A. "Local Convective Heat Transfer From a Constant Heat Flux Flat Plate Cooled by Synthetic Air Jets". Journal of Heat Transfer, 128 (10), 990–1000, 2006.
[12] Hofmann HM, Kaiser R, Kind M, Martin H. "Calculations of steady and pulsating impinging jets - An assessment of 13 widely used turbulence models". Numerical Heat Transfer, Part B: Fundamentals, 51 (6), 565–583, 2007.
[13] Utturkar Y, Arik M, Seeley CE, Gursoy M. "An experimental and computational heat transfer study of pulsating Jets". Journal of Heat Transfer, 130 (6), 062201-11, 2008.
[14] Xu P, Qiu S, Yu MZ, Qiao X, Mujumdar AS. "A study on the heat and mass transfer properties of multiple pulsating impinging jets". International Communications in Heat and Mass Transfer, 39 (3), 378–382, 2012.
[15] Jiang Y, Xu P, Mujumdar AS, Qiu S, Jiang Z. "A Numerical Study on the Convective Heat Transfer Characteristics of Pulsed Impingement Drying". Drying Technology, 30 (10), 1056–1061, 2012.
[16] Mladin EC, Zumbrunnen DA. "Local convective heat transfer to submerged pulsating jets". International Journal of Heat and Mass Transfer, 40 (14), 3305–3321, 1997.
[17] Xu P, Yu B, Qiu S, Poh HJ, Mujumdar AS. "Turbulent impinging jet heat transfer enhancement due to intermittent pulsation". International Journal of Thermal Sciences, 49 (7), 1247–1252, 2010.
[18] Allauddin U, Mahrukh M, Rehman NU, Haque ME, Uddin N. "Numerical investigation of heat transfer by an impinging jet using alumina–water nanofluid". Numerical Heat Transfer, Part A: Applications, 74 (8), 1486–1502, 2018.
[19] Akdag U, Akcay S, Demiral D. "Heat Transfer In a triangular wavy channel with CuO-water nanofluids under pulsating flow". Thermal Science, 23 (1), 191–205, 2019.
[20] Bianco V, Buonomo B, di Pasqua A, Manca O. "Heat transfer enhancement of laminar impinging slot jets by nanofluids and metal foams". Thermal Science and Engineering Progress, 22, 100860, 2021.
[21] Zeitoun O, Ali M. "Nanofluid impingement jet heat transfer". Nanoscale Research Letters, 7, 1–13, 2012.
[22] Zhao TS, Cheng P. "Oscillatory Heat Transfer in a Pipe Subjected to a Laminar Reciprocating Flow". Journal of Heat Transfer, 118 (3), 592–597, 1996.
[23] Selimefendigil F, Öztop HF. "Pulsating nanofluids jet impingement cooling of a heated horizontal surface". International Journal of Heat and Mass Transfer, 69, 54–65, 2014.
[24] Alawadhi EM. Meshing guide. Finite Element Simulations Using ANSYS. 15317 (November), 407–424, 2020.
[25] Farahani SD, Kowsary F. "Heat Transfer from Pulsating Laminar Impingement Slot Jet on a Flat Surface with Inlet Velocity: Sinusoidal and Square Wave". Heat Transfer Engineering, 39 (10), 901–913, 2018.
[26] Li P, Guo D, Liu R. "Mechanism analysis of heat transfer and flow structure of periodic pulsating nanofluids slot-jet impingement with different waveforms". Applied Thermal Engineering, 152, 937–945, 2019.

International Conference on Advances and Innovations in Engineering

2ICAIE

Energy Efficiency in Public Buildings

Sinan KAPAN[1], Hacı Mehmet KULOĞLU [2], Nevin ÇELİK [3]

[1,3]Mechanical Engineering Department, Engineering Faculty, Firat University, Elazig, Türkiye.
[2]Ministry of Education, Ankara, Türkiye.
[1]skapan@firat.edu.tr, [2]e-mail address, [3]ncelik@firat.edu.tr

[1](ORCID: 0000-0001-5690-1041), [2](ORCID: 0000-0000-0000-YYYY),[3](ORCID: 0000-0003-2456-5316)

Abstract

There are 55,311 school buildings affiliated to the Ministry of National Education and approximately 140,000 buildings connected to it, and approximately 30 thousand of these schools were built before 2000. The said educational buildings do not provide the desired level of efficiency in terms of energy performance as of the year of construction.
The National Energy Efficiency Action Plan 2017-2023 was announced and the ratio of imported energy resources in primary energy supply was 75.9% in 2015, and our country is among the countries with high foreign dependency in energy. It aims to increase efficiency in all processes from production to final consumption of energy throughout the country, especially in public buildings.
As a result of the studies to be done, it is aimed to study the studies on energy efficiency in both project design and maintenance and repair works in educational buildings, and to give an idea both in terms of cost and benefit.

Keywords: Energy, efficiency, buildings

1. Introduction

Turkey's current energy resources cannot produce enough energy to meet its own needs. In particular, due to the rapidly increasing technological developments in our country, as well as factors such as the increasing population and welfare level, the amount of energy consumption and Turkey's foreign dependency on this axis is gradually increasing. This situation emerges as the main factor that needs to be emphasized in terms of national economy and environmental sustainability. Although various supply-demand policies have been developed in terms of energy economy in Turkey, foreign dependency could not be prevented. The first application to be made in countries like Turkey, which is foreign-dependent in energy supply and where energy losses are high, is to determine the amount of energy savings in all areas and processes and to implement investments to increase energy efficiency by supporting related studies within the scope of government policies.

New energy supply systems to meet excess consumption in areas where energy efficiency practices cannot be implemented properly; it will create high costs for the country's economy and energy losses will continue. For this reason, considering our limited natural resources, strategies and policies for the effective use of energy in every field should be determined and practices should be put into use.

Many studies have been conducted in the literature on the energy efficiency of buildings [1-2]. Some of them are presented below. Kazanasmaz [3] evaluated the natural lighting performance of buildings. Illuminance levels and luminosity values were measured in the relevant spaces, and relevant standards and design norms were investigated. Öztürk et al. [4] examined natural and forced ventilation systems in residences and formulated heating loads for mechanical ventilation to create air flow and wind pressures for natural ventilation. As a result, the building should be positioned to receive maximum wind. Sarıman [5] examined the concept of sustainability and ecology, which has

[1]Corresponding author

become important with the developing technology and human needs, and the environmental science definitions, the transition to the building scale in sustainability, and the roof systems related to ecology, which is an important element of the shell. Zağpus and Günaydın [6] examined the building automation systems implemented in Turkey, the smart building design process and their quality. Yılmaz and Gürdal [7] designed and implemented a computer-controlled building automation system. In this study, a computer-based automation system for a building was designed and implemented.

Within the scope of this study, the current situation and future projections of Turkey on energy efficiency and energy efficiency performance in buildings were examined, and evaluations were made on the basis of important sectors in energy consumption.

2. Case Study: Kırıkkale Mehmet Akif Ersoy Anatolian High School Building Improvement Works

In this part of the study, a study we have done is presented. The Ministry of National Education participated in the project as a stakeholder with pilot implementation and project studies within the scope of the Energy Efficiency in Public Buildings Project in Turkey carried out by the German International Cooperation Agency (GIZ) and the Ministry of Environment and Urbanization and Climate Change.

Within the scope of the project, Mehmet Akif Ersoy Anatolian High School in Kırıkkale was determined as a pilot school for energy survey and other renovation works by the Ministry of National Education. In Figure 1, the location of the school is shown on the map.

Figure 9. Location of the building

The school building is a 1986-built building, the facade of which is shown in Figure 2.

- The current number of students is 512;
- The total number of classrooms is 25, including one computer room and 2 laboratories;
- Total construction area is 3,748 m2;
- The building consists of 4 floors (including the ground floor) with two main sections each connected by a small middle section with only a staircase;

The typical floor plan of the building is given in Figure 3, and the typical sectional example is given in Figure 4.

Figure 10. Front view of the building

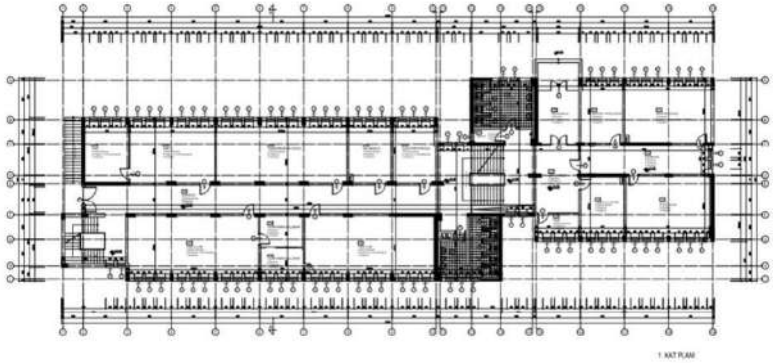

Figure 11. General floor plan

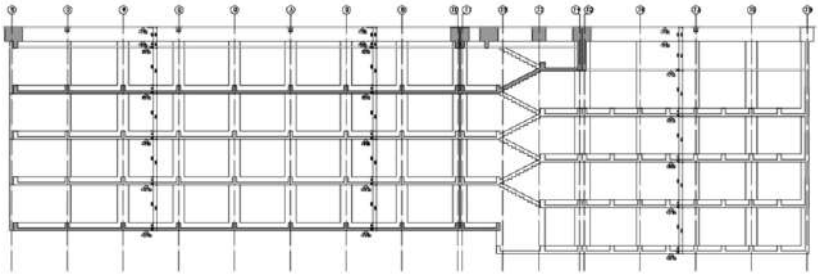

Figure 12. Section view of the building

3. Energy consumptions of the building

The electricity and natural gas consumption values of the building in 2017 are given in Table 1. Accordingly, a total of 2.1939 TOE of electricity and 21,942 TOE of natural gas were spent in 2017.

Table 4. Energy consumption values of the building

Consumption				
Months	Electric		Natural Gas	
	kWh	TOE	Sm^3	TOE
January	2571,45	0,2211	12648	10,435
February	2550,96	0,2194	7683	6,338
March	2217,64	0,1907	5461	4,505
April	2777,36	0,2389	4382	3,615
May	2063,98	0,1775	2226	1,836
June	860,52	0,0740	0	0
July	721	0,0620	0	0
August	716,17	0,0616	0	0
September	1620,63	0,1394	0	0
October	2710,63	0,2331	0	0
November	3203,84	0,2755	2198	1,813
December	3496,03	0,3007	4649	3,835
Total	25510,21	2,1939	39247	21,942

The CO emission values from electricity and natural gas expenditures are calculated in tons and are given in Table 2.

Table 2. CO Emission Values (tonnes)

Energy type	2017
Electric	0,012003
Natural Gas	0,068187

4. Improvement Operations in the Building

The energy consumption and CO emission values resulting from the renovation and repair works to be carried out in the building and the measures to increase the energy performance will be determined. The determined values will be compared with the values of the building before the renovation. Improvements made in the building are listed as follows:

- Building energy analysis
- Compliance with current earthquake regulations
- Creation of new designs that will increase energy performance
- Improvement of building comfort conditions
- Improvement of the physical structure of the building
- Making return and cost calculations

To reduce the energy consumption of the educational building and its annexes:

- Facade thermal performance improvements (joinings, glazing and insulation works)
- Renovation of the heating system (condensing boiler, radiator thermostatic valve, frequency controlled pump, etc.)
- Programmable (weekly, hourly) heating systems,
- High efficiency heat recovery ventilation systems in classrooms and laboratories,
- Solar panel etc. for hot water needs. systems,
- Roof type fan systems activated by presence sensors and lighting lamps to ensure regular and energy efficient ventilation of toilets,
- Photocell batteries for clean water use
- LED lighting systems,
- To obtain energy by installing a Solar Energy System on the roof of the building.

After the renovation works carried out in the building, energy costs were checked in order to measure the improvement. Electricity and natural gas bills were examined as energy expenses. Electricity and natural gas bill of Kırıkkale Mehmet Akif Ersoy Anatolian High School for 2022 is as shown in Table 3. In Table 4 the CO emission values calculated as a result of the improvement works of Kırıkkale Mehmet Akif Ersoy Anatolian High School are given in tons.

As a result of the energy efficiency studies; The consumption, which was at the level of 34,000 cm^3 in the 2017 natural gas consumption scenario, was realized as 20,000 cm^3 excluding November-December 2022. In this case, the minimum savings rate is expected to be 25%.

Table 3. Energy consumption values of the building after renewal

Consumption				
Months	Electric		Natural Gas	
	kWh	TOE	Sm^3	TOE
January	477,21	0,0410	6790	5,602
February	2104,23	0,1810	11650	9,611
March	986,3	0,0848	0	0
April	1631,01	0,1403	601	0,496
May	839,54	0,0722	0	0
June	950,71	0,0818	0	0
July	1274,09	0,1096	0	0
August	1540,56	0,1325	0	0
September	1857,92	0,1598	0	0
October	2616,91	0,2251	1237	1,021
November	0	0	0	0
December	0	0	0	0
Total	14278,48	1,2281	20278	11,128

Table 5. CO emission values after renewal (tonnes)

	2017
Electric	0,012003
Natural Gas	0,068187

The school started to generate electricity as of June 2021 with the Solar Energy System with a power of 48.5 kW installed on the roof of the school building. Although the annual electricity consumption was 22,000 kWh in 2017, with the additional electricity provided by the Solar Energy System, the electricity consumption is predicted to be 16.000 kWh for 2022, and in this case, 25% electricity savings are expected.

5. Conclusions

Various legal regulations, standards and regulations on the use of renewable energy sources have been implemented in Turkey since 2005 on the effective and efficient use of energy in buildings within the framework of the harmonization process with the European Union. The projects examined in the study; It was carried out within the framework of the activities to be carried out by the public, private sector and local governments in order to create sufficient awareness about energy efficiency and to draw attention to the importance of energy [8]. Accordingly, the results that will be beneficial in practice when the projects are evaluated are as follows:

- Developing energy policies at the national level, strengthening the institutional and legal structure,
- Increasing the energy performance of buildings and energy conservation,
- Use of renewable energy sources,
- Integrated design approach,

- Revision of relevant standards,
- Development of energy performance calculation programs,
- The importance of the functioning of control and audit mechanisms,
- Raising awareness and training of the public on energy consumption and energy efficiency
- Eliminating the lack of knowledge and expertise

6. References

[1] Mendoza R C, Hernandez J M R, Martinez F J R, "Industrial Decarbonization by A New Energy-Baseline Methodology—Case Study" Sustainability (12) 1960 (2020).

[2] Grillone B, Mor G, Danov S, Cipriano J, Lazzari F, Sumper A, "Baseline Energy Use Modeling and Characterization in Tertiary Buildings Using an Interpretable Bayesian Linear Regression Methodology" Energies (14) 5556 (2021).

[3] Uygun, İ, Aral, D, Kazanasmaz, T, "Eğitim Yapılarının Doğal Aydınlatma Performansı Açısından İncelenmesi" Megaron (6). 39-51 (2011).

[4] Öztürk, H K., Yılancı, A. Ve Atalay Ö, "Konutlarda Doğal ve Zorlanmış Havalandırma Sistemleri" Tesisat Mühendisliği Dergisi (89) 21-26 (2005).

[5] Sarıman E, "Yüksek Binalarda Enerji Etkin Çatı ve Cephe Sistemlerinin Önemi" 5. Ulusal Çatı&Cephe Sempozyumu (2010).

[6] Günaydın H M, Zağpus S, "Türkiye'de Bina Otomasyon Sistemlerinin Mimarlar Tarafından Algılanması, Akıllı Bina Tasarım Süreci ve Kalitesi" VI. Ulusal Tesisat Mühendisliği Kongresi,1-9 (2003).

[7] Yılmaz, C, Gürdal, O "Bilgisayar Kontrollü Bir Bina Otomasyonunun Tasarımı ve Uygulaması" Politeknik Dergisi , 9 (4) , 241-246, (2006).

[8] AYDIN, Binalarda Enerji Verimliliği Kapsamında Yapılan Projelerin Değerlendirilmesi: Türkiye Örneği, Mimarlık ve Yaşam Dergisi, Journal of Architecture and Life, 4(1), 55-68, (2019).

International Conference on Advances and Innovations in Engineering

Modeling the Hourly Distillation Volume of a Distillation Machine with a Parabolic Dish-Type Collector Using a Support Vector Machine

Erdem ALIÇ[1]

Andırın Vocational High School Department, Kahramanmaraş Sütcü İmam University, Kahramanmaraş, Türkiye.
ealic@ksu.edu.tr
(ORCID: 0000-0002-2852-0353)

Abstract
Increasing energy costs and depletion of traditional energy sources increase the importance of renewable energy sources. This study investigated a distillation machine that uses concentrated solar energy, one of the renewable energy sources. The system generally consists of parabolic dish-type collectors (PDC), solar tracking systems, a receiver, an evaporator, and a condenser. In order to optimize the amount of pure water produced by the system, parameters such as solar radiation, outdoor temperature, velocity of the wind, and average surface temperature of the receiver should be improved. It may be preferable to use computational intelligence algorithms to model the distillation amount of such a complex system. For this, the pure water production amount of the system was realized by using the support vector machine regression (SVMreg) algorithm, which is one of the artificial intelligence algorithms. Two different kernels, PolyKernel and Puk, were used for SVMreg analysis. Root Mean Square Error (RMSE) and mean absolute error (MAE) criteria were used to evaluate the performance of the model. The RMSE and MAE of Puk kernels were 0.013 and 0.0078, respectively.

Keywords: Dish collector, Distillation, Machine learning, Support Vector Machine,

1. Introduction

Concentrated solar energy systems are one of the methods that have emerged to meet the increasing energy demand. The most important difference between these systems from other systems is that they can reach high temperatures[1]. The need for high temperatures in many areas of industry is a well-known situation. PDCs come to the fore for systems operating at high temperatures. PDCs, one of the concentrator solar energy systems, are very popular with researchers. Much research has been and continues to be done on PDCs[2–4]. Artificial intelligence methods are uses in many studies in the literature to model experimental data [5–7]. In this section, a current literature review presents PDCs, pure water production, and artificial intelligence algorithms, which are related to the subject of the manuscript.

Starke et al. studied using Genetic Algorithm (GA) hybrid concentrated solar power (CSP), photovoltaic (PV) system optimization was performed. They made a case study, taking into account the characteristics of a place in northern Chile. They evaluated the performance of a hybrid CSP+PV plant with the methodology they developed and created a useful model for decision-makers despite the market constraints[8]. Khosravi et al., studied a case of the PDC/Stirling system. They are investigates four hybrid methods including, ANFIS-GA, ANFIS-PSO, MLP-GA, and, MLP-PSO are improved for energy modeling of a CSP Stirling system in Natal-RN, Brazil. They predicted with ANFIS-PSO the behavior of the global efficiency under different configurations with RMSE=0.025, R=0.9527, and R^2=0.9076[9].

Allouhi et al. multi-objective optimization is carried out to design the most energy and cost-effective Solar Dish Stirling (SDS) power plant. They have considered meteorological data from two (Morocco-Spain) sites to simulate the technical and economic performances. In their papers, Pareto Frontiers were established using a Genetic Algorithm, and TOPSIS was used to derive the ultimate, optimal solutions. They proposed a surrogate model of two cities in Morocco and Spain with high R-square values derived from 0.995 and 0.9964, respectively[10]. In order to forecast the energetic performance of a solar dish collector, Zayed et al., studied a hybrid adaptive neuro-fuzzy inference system integrated with an equilibrium optimizer algorithm. ANFIS and ANFIS integrated with equilibrium

[1]Corresponding author

optimizer (EO) have been used. The three models were tested in order to compare and forecast the temperature difference of the working fluid, heat gain, and energy efficiency of the cylindrical receiver for the SPDC operating with two different solar working fluids: multi-wall carbon nanotubes/thermal oil (MWCNT) nanofluid and thermal oil. The results of the paper show that the RMSE for the predicted energy efficiency of SPDC can be reduced by the ANFIS-EO model to a value of 0.00095, which is lower than those of ANN and ANFIS by 91.86% (0.01169) and 87.09% (0.00736), respectively[11].

Saurabh Jaywant Mohite and K.S. Reddy studied thermal and optical analysis of solar PDC receiver systems for hydrogen production adopting artificial intelligence of deep learning. The authors coupled the RNG k-Ɛ turbulence model, the Energy and Discrete Ordinates (DO) radiation model, the Arrhenius reaction rate chemical reaction of ZnO dissociation, and the Eulerian multiphase model for ZnO particle dynamics to analyze the 3D numerical model. They were directed at an artificial neural network (ANN) model used to forecast PDC's heat flux and uniformity factor values. In the last section of the paper, the authors R^2, RMSE, and Mean Absolute Percentage Error (MAPE) error metrics were used to figure out the model's performance. The paper's best prediction is the ANN model MAPE, RMSE, and, R^2 values of 0.984870%, 0.624409, and 0.92529396, respectively[12].

Two situations were assessed when the studies in the literature were looked at. First, AI models are generally based on ANN and GA. Other artificial intelligence algorithms have not been little studied. Secondly, the models have been studied on the overall performance of the PDC or the economic analysis of the system. Little work has been done on developing an artificial intelligence model based on the amount of product produced. This study, it is aimed to model the pure water production amount of a remotely followed and fully autonomous PDC distillation system with artificial intelligence. For this, SVMreg is preferred. The model analysis of two different kernels of SVMreg is compared. Artificial intelligence prediction results were also compared with experimental results.

2. Distillation System With PDC

PDC: By following the sun on two axes, they constantly concentrate the sun on the focusing area. The thermal energy can be taken from the focusing area with a suitable working fluid and sent to a thermodynamic circulation or it can be converted into electrical energy with the help of a Stirling engine mounted in the focus area.

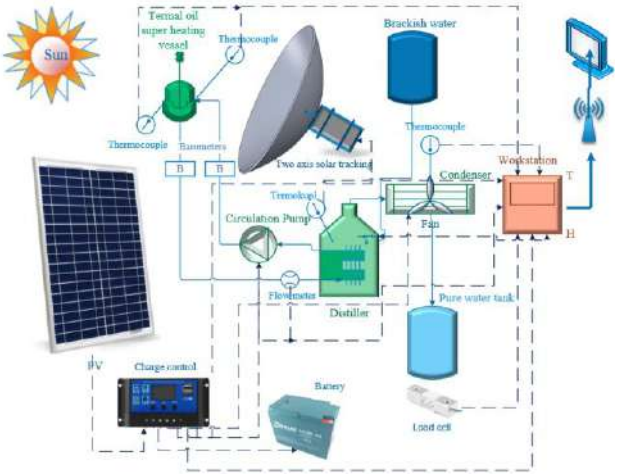

Figure 1. Experimental photography of the PDC distiller system

Figure 1 shows the experimental photo of a pure water distillation machine with remotely monitored autonomous solar PDCs. The system electrical energy is provided by 1 kW PV panels. Oil flow circulation has a single DC pump and flow meter. The system has a single boiler for distilling pure water. High temperature oil enters the distillation vessel and leaves at the water's saturation temperature. Water is transformed into the vapor phase at the boiler and then goes to the condenser. The condenser is accompanied by a DC fan. The thermocouple inside the still alerts the DC fan, which then turns on. Then, pure vapor is transformed into pure water. Under the tank holding the pure water, there is one 5000 g load sensor. This sensor allowed for immediate monitoring of the pure water accumulation in the

pure water tank. The instruments used for the measurements performed in the experiments and the precision values of the instruments are shown in Table 1.

Table 1. Measurement precision table

Parameter	Measurement Tool	Model	Precision
Oil Temperature	Temperature	K-Type thermocouple	±0.1°C
Volume flow rate	Oil flow meter		±0.1 l/min
Mass rate	Load cell	HX711	±0.5 gr/s
Solar radiation	Solar power meter	CEM DT-1307	±10 W/m^2
Air velocity	Anemometer	BENETECH, Model	±0.1 m/s
Air Temperature	Thermometer	GM8901	±0.1°C

Calculation of the energy to be transferred to the water; Here, Q_p stands for total energy, Q_v for evaporation energy, and Q_w is the energy needed for the well water to reach its saturation temperature. In equation 1, m_w denotes the rate at which liquid enters the system up until it evaporates, c_p denotes the liquid's specific heat, T_{sat} denotes the liquid's saturation temperature, and T_{avg} denotes the average temperature of the liquid entering the system. The amount of liquid evaporated is given in Eq. 2 m_v (where m_w=m_v) and the enthalpy of evaporation is given in Eq. 2.[4].

$$Q_p = Q_w + Q_v \quad (1)$$

$$Q_w = m_w . c_{pw} . (T_{sat} - T_{avg}) \quad (2)$$

$$Q_v = m_v . h_{fg} \quad (3)$$

The energy gained from the sun and the efficiency of PDC have been calculated in the literature[4].

2.1. Support Vector Machine Regression

The support vector algorithm is used in regression even though it was developed as a classification algorithm. Some data issues are resolved as a result of these two models. For the data we have, linear models are not always applicable. In these situations, we use other algorithms to try to make sense of the data we have. Support vector algorithms are one of them. Two models are used for regression and classification, to put it briefly.

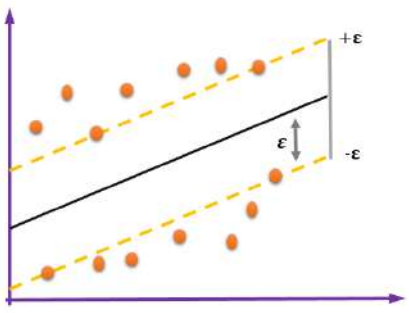

Figure 2. Simple SVMreg graph

Support Vector regression can be used for both linear and nonlinear regressions. In Figure 2 epsilon (Ɛ) is the distance around the hyperplanes. Points inside the epsilon are considered correct predictions. Thus, the epsilon can be adjusted to increase performance. Some SVMreg kernels are listed in Table 2[13].

Table 2. Kernels of SVMreg

Kernel's Name	Equation
Poly	$K(x,y) = \left((x^T y) + c\right)^d$
Normalize Poly	$K(m,n) = \frac{k(m.n)}{\sqrt{k(m.m), k(n.m)}}$
Pearson Universal (PUK)	$f(x) = \frac{H}{\left[1 + \left(\frac{2(x - x_0)\sqrt{2^{1/\omega} - 1}}{\sigma}\right)^2\right]^{\omega}}$
Radial Basis Function (RBF)	$k(x, x') = exp\left(-\frac{\|x - x'\|}{2\sigma^2}\right)$

To determine the accuracy of the predictive model, root mean square error (RMSE), mean absolute error (MAE), and, relative absolute error (RAE) analyses were performed. Error analysis equations are RMSE eq.4, MAE eq.5 and RAE eq.6. Where D_P is the estimated value, D_A is the actual value, and N is the total number of error values[14].

$$\boldsymbol{RMSE} = \sqrt{\frac{1}{N}\sum_{i=0}^{N}\left(\boldsymbol{D_A^i} - \boldsymbol{D_P^i}\right)^2} \quad (4)$$

$$\boldsymbol{MAE} = \frac{1}{N}\sum_{i=0}^{N}\left|\boldsymbol{D_P^i} - \boldsymbol{D_A^i}\right| \quad (5)$$

$$\boldsymbol{RAE} = \left|\frac{\boldsymbol{D_A^i} - \boldsymbol{D_P^i}}{\boldsymbol{D_P^i}}\right| \times \mathbf{100} \quad (6)$$

3. Result and Discussion

In this study, artificial intelligence modeling of pure water production and production potential of a pure water producer with PDC in Kahramanmaraş province in May, June, July, August, and September was carried out. Before evaluating the pure water production capacity of the system, some climate data of Kahramanmaras would be examined. These climate data were obtained from the website of Enerji.gov.tr by taking the averages of 1991-2020. Figure 3 shows the monthly average temperature distribution of Kahramanmaraş city center. Figure 4 shows the daily sunshine duration times[15].

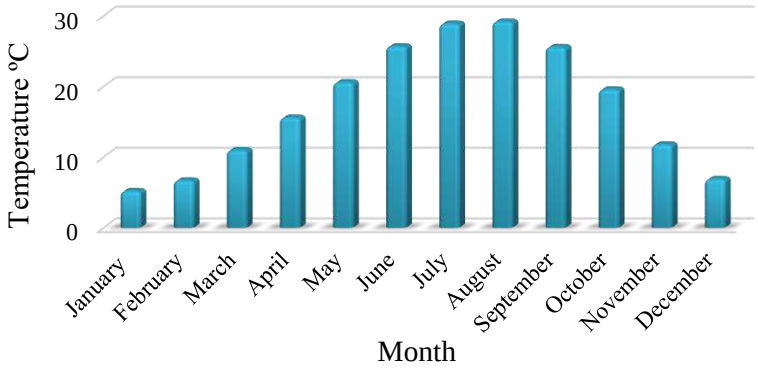

Figure 3. Monthly average temperature distribution in Kahramanmaraş

According to Figure 3, the hottest months are July and August. The longest sunshine duration is seen in Figure 4 in July. The sunshine duration in September is longer than in May. In such a case, the production in September is higher than in May. The daily sunshine duration times of Kahramanmaraş shows in Figure 4.

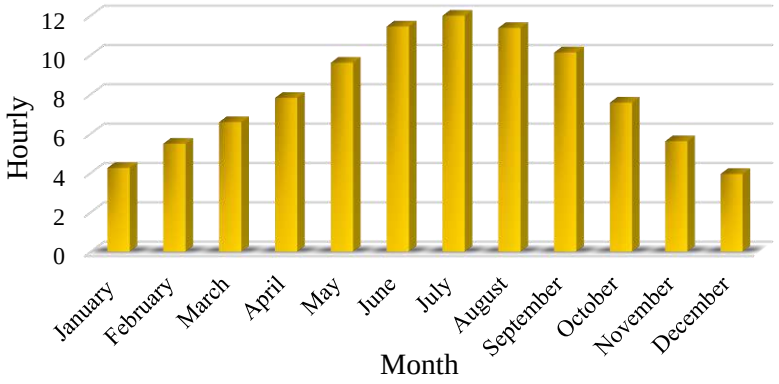

Figure 4. Daily sunshine duration of Kahramanmaraş

Figure 5 shows the experimental July hourly pure water production graph. In general, the pure water production of the system increased until noon. Pure water production decreases in the afternoon hours. It is considered that the slight decrease seen at 11.30 in the graph is related to wind and humidity.

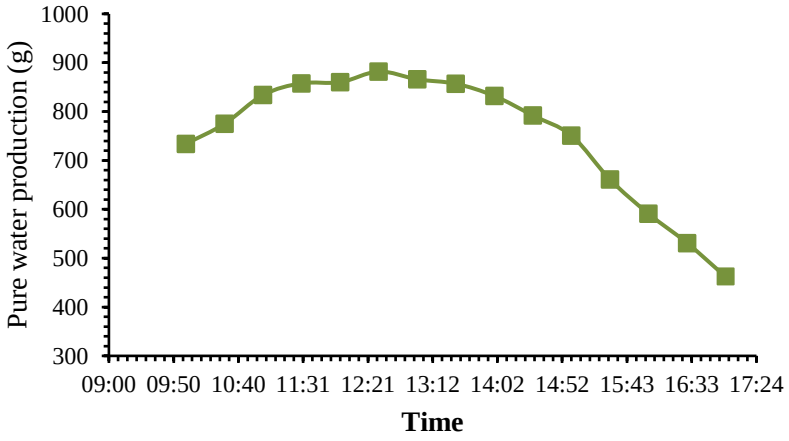

Figure 5. Average pure water production hourly in July

Within the scope of the experiment, the monthly average purification capacity of the system was investigated. For this purpose, experiments were carried out for 3 consecutive days in each week. The results obtained were averaged. In the figure, the average daily purification amount of the system was given every month. The highest purification rate was reached in August. The reason for this is that the highest outdoor temperature is in August, and the amount of solar radiation was the highest in July and August.

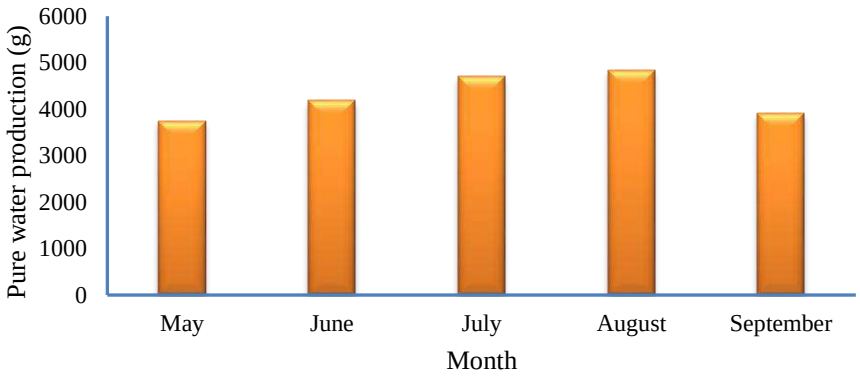

Figure 6. Average pure water production a day for a month

In Figure 7, the daily average pure water production of the system is modeled with artificial intelligence, taking into account the environmental conditions. SVMreg was used for this. SVMreg was modeled with two different kernels. For the Puk kernel, ω=4.0 and σ=3.0. For the Poly kernel, ε=1.0e-^{12} and $\varepsilon_{paramater}$=0.001 are taken. Other variables are defined the same. The learning and test distribution were defined as 85% - 15%, respectively.

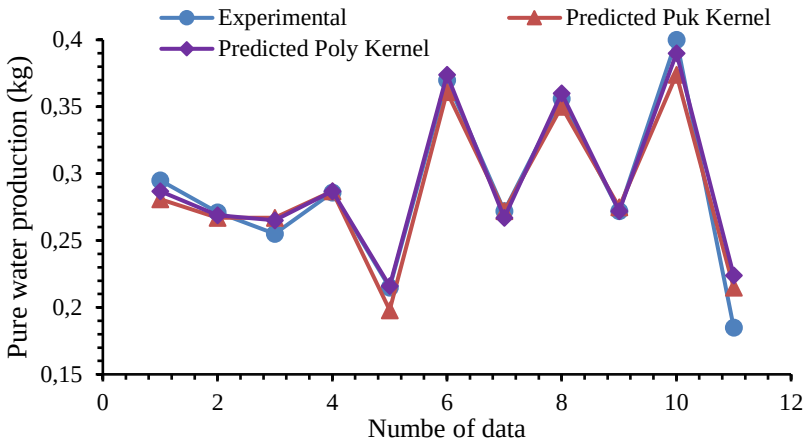

Figure 7. Average pure water production a day for a month

Under these conditions, the Puk kernel give better error results than the Poly kernel. The results obtained are presented in Table 3. Accordingly, the Puk kernel has MAE=0.013, RMSE=0.0078, and RAE(%)= 15.72. In many studies in the literature evaluated, it has been stated that error values similar to those in this study are acceptable[16,17].

Table 3. Results of kernels

Kernel's Name	MAE	RMSE	RAE (%)
Poly	0.011	0.0145	22.25
Puk	0.0078	0.013	15.72

In addition to this work in the future, other kernels of SVMreg can be worked on. Different models can be obtained by changing the artificial intelligence learning/test ratio. It is thought that as artificial intelligence algorithms develop, they can make better simulations.

4. Conclusion

In this study, the pure water production potential of a pure water producer with PDC was experimentally investigated and modeled with artificial intelligence algorithms. Poly kernel and Puk kernel were used in SVMreg regression. The experiments were carried out in Kahramanmaras in May, June, July, August, and September 2022. The mean daily purification capacity of the experimental system was determined. According to the artificial intelligence model results in Table 3, the lowest error was obtained with the MAE error analysis method. Puk kernel's lowest the MAE error value is 0.078. Figure 7. showed the experimental and estimated amounts of pure water production, which were fairly close to one another. The pure water production amount was successfully modeled according to the MAE error analysis method. For this study, models can be performed with different artificial intelligence algorithms in order to obtain more precise results in the future. A customized artificial intelligence algorithm can be developed for the experimental system.

5. Acknowledgements

This study was supported by "Kahramanmaras Sutcu Imam University Scientific Research Projects Coordination Unit
(Project Numbers: 2021/3-29 M)

6. References

[1] V.P. Stefanovic, S.R. Pavlovic, E. Bellos, C. Tzivanidis, A detailed parametric analysis of a solar dish collector, Sustainable Energy Technologies and Assessments. 25 (2018) 99–110. https://doi.org/10.1016/j.seta.2017.12.005.

[2] R. Pitz-Paal, Concentrating solar power, Future Energy: Improved, Sustainable and Clean Options for Our Planet. (2020) 413–430. https://doi.org/10.1016/B978-0-08-102886-5.00019-0.

[3] H. Sadat, A simple analytical thermal model of solar cavity receivers, Thermal Science and Engineering Progress. 29 (2022) 101223. https://doi.org/10.1016/j.tsep.2022.101223.

[4] E. Alic, Experimental and numerical performance assessment of a hybrid parabolic dish collector with photovoltaic for a distiller, Energy Sources, Part A: Recovery, Utilization, and Environmental Effects. 45 (2023) 3994–4016. https://doi.org/10.1080/15567036.2023.2200737.

[5] M. Das, E. Alic, E.K. Akpinar, Detailed analysis of mass transfer in solar food dryer with different methods, International Communications in Heat and Mass Transfer. 128 (2021) 105600. https://doi.org/10.1016/j.icheatmasstransfer.2021.105600.

[6] E. Alic, M. Das, O. Kaska, Heat Flux Estimation at Pool Boiling Processes with Computational Intelligence Methods, Processes. 7 (2019) 293. https://doi.org/10.3390/pr7050293.

[7] O.E. Akay, M. Das, Modeling the total heat transfer coefficient of a nuclear research reactor cooling system by different methods, Case Studies in Thermal Engineering. 25 (2021) 100914. https://doi.org/10.1016/j.csite.2021.100914.

[8] A.R. Starke, J.M. Cardemil, R. Escobar, S. Colle, Multi-objective optimization of hybrid CSP+PV system using genetic algorithm, Energy. 147 (2018) 490–503. https://doi.org/10.1016/j.energy.2017.12.116.

[9] A. Khosravi, S. Syri, J.J.G. Pabon, O.R. Sandoval, B.C. Caetano, M.H. Barrientos, Energy modeling of a solar dish/Stirling by artificial intelligence approach, Energy Conversion and Management. 199 (2019) 112021. https://doi.org/10.1016/j.enconman.2019.112021.

[10] H. Allouhi, A. Allouhi, A. Jamil, Multi-objective optimization of a CSP-based dish Stirling field layout using Genetic Algorithm and TOPSIS method: Case studies in Ouarzazate and Madrid, Energy Conversion and Management. 254 (2022) 115220. https://doi.org/10.1016/j.enconman.2022.115220.

[11] M.E. Zayed, J. Zhao, W. Li, A.H. Elsheikh, M.A. Elaziz, A hybrid adaptive neuro-fuzzy inference system integrated with equilibrium optimizer algorithm for predicting the energetic performance of solar dish collector, Energy. 235 (2021) 121289. https://doi.org/10.1016/j.energy.2021.121289.

[12] S.J. Mohite, K.S. Reddy, Optical and thermal analysis of solar parabolic dish cavity receiver system for hydrogen production using deep learning, Energy Conversion and Management. 292 (2023) 117415.

https://doi.org/10.1016/j.enconman.2023.117415.
[13] C.B. Pande, N.L. Kushwaha, I.R. Orimoloye, R. Kumar, H.G. Abdo, A.D. Tolche, A. Elbeltagi, Comparative Assessment of Improved SVM Method under Different Kernel Functions for Predicting Multi-scale Drought Index, Springer Netherlands, 2023. https://doi.org/10.1007/s11269-023-03440-0.
[14] Q.B. Pham, M. Kumar, F. Di Nunno, A. Elbeltagi, F. Granata, A.R.M.T. Islam, S. Talukdar, X.C. Nguyen, A.N. Ahmed, D.T. Anh, Groundwater level prediction using machine learning algorithms in a drought-prone area, Neural Computing and Applications. 34 (2022) 10751–10773. https://doi.org/10.1007/s00521-022-07009-7.
[15] G.E.P. Atlası, T.C. Enerji ve Tabii Kaynaklar Bakanlığı, (n.d.). https://gepa.enerji.gov.tr/MyCalculator/pages/46.aspx (02.08.2023).
[16] S. Nazari, M. Najafzadeh, R. Daghigh, Techno-economic estimation of a non-cover box solar still with thermoelectric and antiseptic nanofluid using machine learning models, Applied Thermal Engineering. 212 (2022) 118584. https://doi.org/10.1016/j.applthermaleng.2022.118584.
[17] M. Das, E.K. Akpinar, Investigation of pear drying performance by different methods and regression of convective heat transfer coefficient with support vector machine, Applied Sciences (Switzerland). 8 (2018). https://doi.org/10.3390/app8020215.

International Conference on Advances and Innovations in Engineering

Receptance Based Dynamic Structural Modification of an Unmanned Combat Aerial Vehicle (UCAV) Model

Murat ŞEN[1], Mesut HÜSEYİNOĞLU[2], Orhan ÇAKAR[3]

[1,3] Mechanical Engineering, Engineering Faculty, Fırat University, Elazig, Türkiye.
[2] Mechanical Engineering, Engineering Faculty, Dicle University, Diyarbakır, Türkiye.
[1]msen@firat.edu.tr, [2] mesuth@dicle.edu.tr, [3]cakaro@firat.edu.tr

[1](ORCID: 0000-0002-3063-5635), [2](ORCID: 0000-0002-6130-6658),[3](ORCID: 0000-0001-6947-3875)

Abstract

Unmanned Combat Aerial Vehicles (UCAVs) are preferred and used effectively in military purposes as combat vehicles due to many advantages they provide. In any model updating applications to be carried out on these aircrafts equipped with various weapons or bombs they carry, their dynamic properties directly change. It is very important to know how the dynamic characteristics of these aircrafts will change after these model updating applications, in order for the system to work stably. In addition, in order for UCAVs to operate safely under many dynamic effects, it may be desirable to shift some resonance frequencies of the system to safe frequency ranges. In order to achieve this, it is necessary to calculate the required modifications to be made on the system.
In this study, a dynamic structural modification method based on frequency response functions (FRFs) is presented to make dynamic structural modifications on UCAVs. The presented method directly uses the FRFs of the active coordinates (response, excitation and modification) of the system. With this method, it can be calculated how the resonance frequencies will change as a result of some model updating studies on UCAVs and in order to shift some resonance frequencies of the system to safe frequency ranges, the required modification values (mass or stiffness) can be calculated. The proposed method is verified with some numerical simulation studies and remarkable results have been obtained.

Keywords: Resonance, frequency assignment, frequency response function, unmanned combat aerial Vehicle (UCAV) model

1. Introduction

UCAV systems are military-purpose aircraft used with different types of arms and bombs. When these aircraft are equipped with arms and bombs, their dynamic behavior changes completely according to the unarmed situation. It is very important to know in advance how the dynamic behavior of the system (resonance frequencies, anti-resonance frequencies, damping and vibration mode shapes) will change as a result of model updating studies, especially by adding a new ammunition to the system [1]. This is the subject of the direct structural modification study area in structural dynamics. In direct structural modification, it is determined how the dynamic properties of the system will change as a result of some changes made on a system [2, 3]. In addition, it is an important problem to determine some physical changes that need to be made on the system in order to shift some resonance frequencies that have changed as a result of a new arms to be added to the UCAV system, to safe frequency ranges. This is the subject of the inverse structural modification study area. In inverse structural modification, the changes that need to be made on the system in order for the system to have some desired dynamic properties are determined [3-6]. In this context, researchers and design engineers frequently benefit from structural modification in the design, production, development and model updating stages of engineering systems [7-10].

Structural modification is of great importance in engineering studies and studies in this field have been increasing recently. In these studies, methods using the physical properties, modal properties, sensitivity properties of mechanical systems or FRFs of the system are used [11-15]. Methods based on the use of FRFs directly are very

[1]Corresponding author

convenient for practical applications, since the physical or modal properties of the system under study are not needed. In addition, the required FRFs can be measured experimentally on the examined structure [16-18].
In this study, a FRFs based dynamic structural modification method using Sherman-Morrison formula [19] is presented to make dynamic structural modifications on UCAVs. The presented method directly uses the FRFs of only the active coordinates. This means, only the FRFs belong to the response (the coordinate from which the response of the system is measured), the excitation (the coordinate from which the system is excited), and the modification (the coordinate on which the modification is applied) coordinates are used. There is no need to calculate a matrix inversion that provides a fast solution for inverse structural modification applications. With proposed method, it is possible to predict the FRFs of a modified UCAV system after some physical changes or model updating studies. Also, in order to shift some resonance frequencies of the system to safe frequency ranges, the required modification values (mass or spring) can be calculated. The proposed method is verified with some numerical simulation studies and remarkable results have been obtained.

In the following sections, the theory of the study, numerical applications and results are given respectively.

2. Method and Formulations of Structural Modification

The receptance type FRFs of a structurally modified system can be calculated with the SM formula using the FRFs of the original system and the modifications with Equation 1 [3, 12].

$$\left[\alpha^{*}\right]=[\alpha]-\frac{([\alpha]\{u\})\left(\{v^{T}\}[\alpha]\right)}{1+\{v^{T}\}[\alpha]\{u\}} \tag{1}$$

Where, α and α^{*} represents the FRFs of the original and the modified system respectively. {u} and {v} are the vectors with all zero elements except the element corresponding to the modification coordinate. These vectors for a mass modification in any coordinate r and a stiffness modification between 2 coordinates i and j can be given with Equation 2-a,b respectively [3, 17].

$$\{u\}=\{...1...\}^{T},\ \{v\}=\{...-\omega^{2}m_{r}...\}^{T};\qquad \{u\}=\{...1..-1...\}^{T},\{v\}=\{...k_{r}..-k_{r}...\}^{T} \tag{2-a, b}$$

The FRF matrix [α] in Equation 1 contains all the FRFs of the structure. However, in practice, measuring all FRFs of the structure is a very laborious and time-consuming process. In real life applications, a limited number of FRF measurements are made on the structure. In most practical applications, FRFs consisting of a row or a column of the receptance matrix are measured. Therefore, Equation 1 can also be written for active coordinates (response, excitation and modification). Also, in case of multiple modifications, Equation 1 can be applied sequentially. If the modifications to be made are denoted by δd, Equation 1 for n successive direct structural modifications can be written as follows for active coordinates [1, 17].

$$\boldsymbol{\alpha}_{a}^{i}=\boldsymbol{\alpha}_{a}^{i-1}-\frac{\delta d_{i}\left(\boldsymbol{\alpha}_{a}^{i-1}\mathbf{u}_{i}\right)\left(\mathbf{u}_{i}^{T}\boldsymbol{\alpha}_{a}^{i-1}\right)}{1+\delta d_{i}\left(\mathbf{v}_{i}^{T}\boldsymbol{\alpha}_{a}^{i-1}\mathbf{u}_{i}\right)},\ i=1,2,..,n \tag{3}$$

Here, the matrix and vectors are in bold and the subscript a denotes the active coordinates. Equation 3 can be used for multi-rank forward structural modifications effectively. For inverse structural modifications Equation 3 can be rewritten as [1-17]:

$$\boldsymbol{\alpha}_{a}^{i}=\frac{\boldsymbol{\alpha}_{a}^{i-1}+\delta d_{i}\left[\boldsymbol{\alpha}_{a}^{i-1}\left(\mathbf{v}_{i}^{T}\boldsymbol{\alpha}_{a}^{i-1}\mathbf{u}_{i}\right)-\left(\boldsymbol{\alpha}_{a}^{i-1}\mathbf{u}_{i}\right)\left(\mathbf{v}_{i}^{T}\boldsymbol{\alpha}_{a}^{i-1}\right)\right]}{1+\delta d_{i}\left(\mathbf{v}_{i}^{T}\boldsymbol{\alpha}_{a}^{i-1}\mathbf{u}_{i}\right)} \tag{4}$$

It is possible to shift some resonance frequencies of a system to prescribed values by equating the denominator of Equation 4 to zero due to natural frequencies express the poles of the structure.

In the case of one mass modification in coordinate r or one stiffness modification between i and j coordinates for a desired resonance frequency ω_s, one can write the following equations, respectively by equaling the denominator of Equation 4 to zero [2, 3].

$$1-\omega_s^2 m_r \alpha_{rr}(\omega_s)=0 \qquad 1+k_r\left[\alpha_{ii}(\omega_s)-2\alpha_{ij}(\omega_s)+\alpha_{jj}(\omega_s)\right]=0 \tag{5-a, b}$$

Using Equation 5-a, b, one can calculate the required modification value (mass or stiffness) to obtain a prescribed resonance frequency. For shifting n number of resonance frequencies to some prescribed values ω_{s1}, ω_{s2}, …, ω_{sn} and by using the p (response), q (excitation) with r for mass and r_1, r_2 for stiffness (modification) coordinates, Equation 4 can be applied sequentially, for all equating the denominators to zero. For this case, nonlinear equation sets can be obtained to be solved for n number of mass modifications Equation 6-a and for n number of stiffness modifications Equation 6-b [2, 3].

$$\begin{aligned}
&F_1(m^i)=1-\omega_{s1}^2 m^n \alpha_{qq}^{n-1}(\omega_{s1})=0 && F_1(k^i)=1+k^n\left[\alpha_{r1r1}^{n-1}(\omega_{s1})-2\alpha_{r1r2}^{n-1}(\omega_{s1})+\alpha_{r2r2}^{n-1}(\omega_{s1})\right]=0\\
&F_2(m^i)=1-\omega_{s2}^2 m^n \alpha_{qq}^{n-1}(\omega_{s2})=0 && F_2(k^i)=1+k^n\left[\alpha_{r1r1}^{n-1}(\omega_{s2})-2\alpha_{r1r2}^{n-1}(\omega_{s2})+\alpha_{r2r2}^{n-1}(\omega_{s2})\right]=0\\
&\text{.....;} && \text{.....}\\
&F_n(m^i)=1-\omega_{sn}^2 m^n \alpha_{qq}^{n-1}(\omega_{sn})=0 && F_n(k^i)=1+k^n\left[\alpha_{r1r1}^{n-1}(\omega_{s3})-2_{r1r2}^{n-1}(\omega_{s3})+\alpha_{r2r2}^{n-1}(\omega_{s3})\right]=0
\end{aligned} \tag{6-a, b}$$

3. Numerical Simulations

In this section, some numerical simulation studies on the UCAV model created in Matlab are given. The UCAV model created is a Baykar Bayraktar Akıncı [20] type aircraft in approximate dimensions. In the created model, there are 2 engines with 130 kg each and it is assumed that 9 bombs with different properties can be placed under the wings in case of full equipment. Here, within the scope of forward structural modification, it will be determined how the resonance frequencies of the system will change after the bombs are placed on the UCAV model. In addition, within the scope of the inverse structural modification, some of the natural frequencies of the system will be shifted to prescribed values by mass and stiffness modifications to be made in some coordinates determined on the system. The length of the model is 12 m and the wing span is 20 m. The height is 4.1 m. The total mass of the model is assumed to be 1325 kg without bombs. The wingspan of the model is portioned into 14 elements and 15 nodal points are created on the model as seen in Figure 1. The FE model is created with Euler-Bernoulli beam approach.

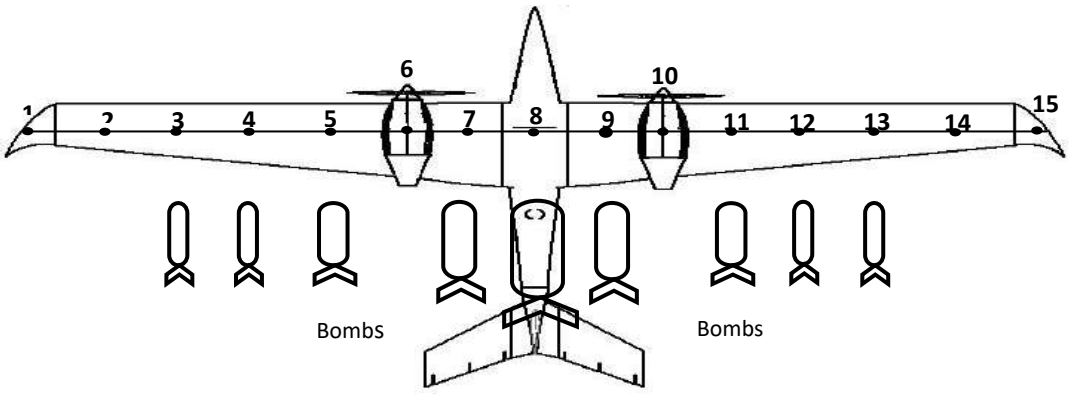

Figure 1. Portioned UCAV FE model with bombs to be placed on the nodal points

Direct Structural Modification

For direct structural modification studies, first, the FRFs of the unarmed UCAV model are obtained and the resonance frequencies are calculated using the obtained eigenvalue problem. These frequencies are named original. Second, different bomb types are placed on the UCAV, the FRFs of this new system are obtained and the resonance

frequencies are calculated. These frequencies are named modified. The bombs are assumed to be as Bomb 1 (140 kg), Bomb 2 (94 kg), Bomb 3 (22 kg) and Bomb 4 (6.5 kg). Third, the FRFs and the resonance frequencies of the modified system are calculated using the presented method. The obtained resonance frequencies are given in Table 1 and the FRFs are given with Figures 2-4 comparatively.

Table 1. The natural frequencies of the system after modifications (attaching bombs)

Modification Coordinates (r)	Bomb Type	Natural Frequencies of Modified System (Hz)									
		Original	2.7	7.7	13.3	26.7	31.4	61.0	72.1	84.2	128.5
7, 9	Bomb 2	Modified	2.6	7.4	13.3	24.8	30.8	50.7	65.9	80.7	93.6
		Calculated	2.6	7.4	13.3	24.8	30.8	50.7	65.9	80.7	93.6
8 7, 9	Bomb 1 Bomb 2	Modified	2.6	7.4	13.1	24.8	50.7	65.6	80.7	93.3	127.7
		Calculated	2.6	7.4	13.1	24.8	50.7	65.6	80.7	93.3	127.7
7, 9 5, 11	Bomb 2 Bomb 3	Modified	2.6	7.2	12.7	24.5	30.7	49.1	62.1	78.1	93.2
		Calculated	2.6	7.2	12.7	24.5	30.7	49.1	62.1	78.1	93.2
8 7, 9 5, 11	Bomb 1 Bomb 2 Bomb 3	Modified	2.6	7.2	12.5	24.5	30.5	49.1	61.8	78.1	92.9
		Calculated	2.6	7.2	12.5	24.5	30.5	49.1	61.8	78.1	92.9
7, 9 5, 11 4,12	Bomb 2 Bomb 3 Bomb 4	Modified	2.6	7.2	12.6	24.0	30.3	49.1	62.0	77.3	92.1
		Calculated	2.6	7.2	12.6	24.0	30.3	49.1	62.0	77.3	92.1
8 7, 9 5, 11 3, 4, 12, 13	Bomb 1 Bomb 2 Bomb 3 Bomb 4	Modified	2.5	7.2	12.4	23.8	29.7	48.4	60.8	76.7	91.6
		Calculated	2.5	7.2	12.4	23.8	29.7	48.4	60.8	76.7	91.6

The FRFs are obtained in 0-100 Hz frequency bandwidth with 0.1 Hz intervals. As seen in FRF graphs and Table1 the resonance frequencies can be obtained without any error.

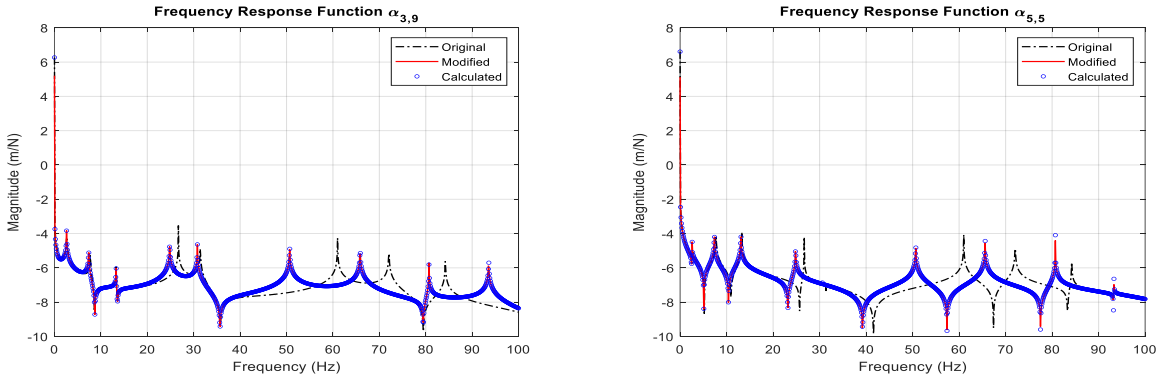

a) b)

Figure 2. Simulation applications for a) 2 modifications, b) 3 modifications

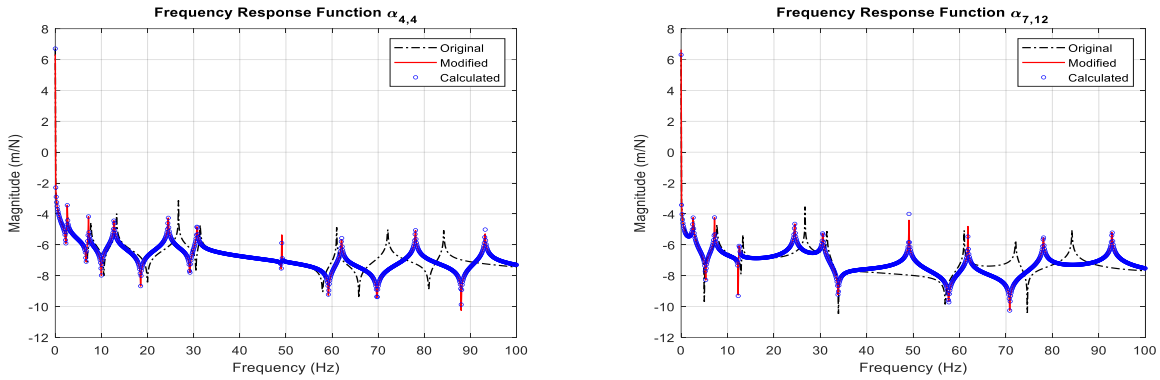

a) b)

Figure 3. Simulation applications for a) 4 modifications, b) 5 modifications

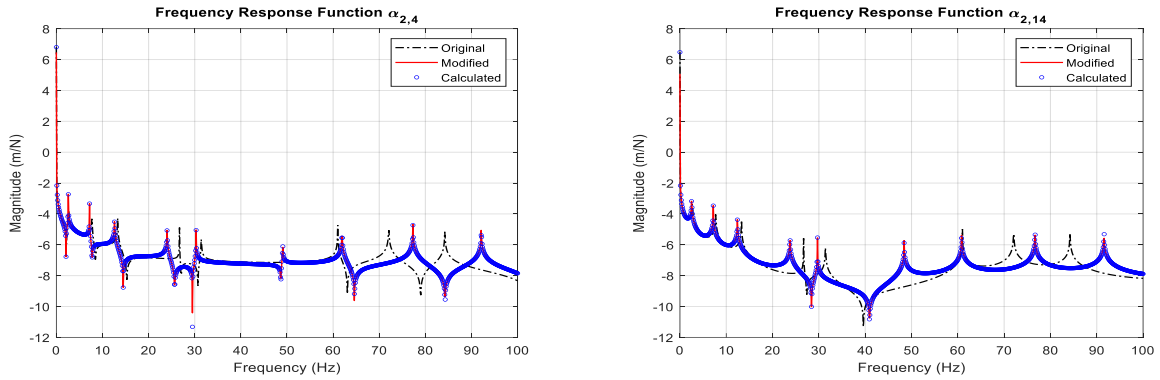

a) b)

Figure 4. Simulation applications for a) 6 modifications, b) 9 modifications

Inverse Structural Modification

For inverse structural modification applications, some target resonance frequencies are selected in 0-100 Hz frequency bandwidth. By using the presented method, the required mass or stiffness modification values that have to be applied to the system are determined to obtain these selected target frequencies. Then, after applying the determined modifications to the UCAV system the resonance frequencies are obtained solving the eigenvalue problem. The obtained results are given in Table 2 and Figures 5-8.

Table 2. The natural frequencies of the system after mass modifications

Modification Type (m, k)	Target Frequency (Hz)	Modification Coordinates (r)	Calculated Modification (kg, N/m)	Natural Frequencies (Hz)							
				Original	2.7	7.7	13.3	26.7	31.4	61.0	72.1	84.2
m	13.0	5	8.4	Modified	2.6	7.7	13.0	26.0	30.6	60.1	70.7	82.7
m	26.0	12	18.9									
m	26.0	4	12.2	Modified	2.6	7.7	13.1	26.0	31.0	60.7	71.0	83.2
m	31.0	12	2.6									
m	71.0	13	1.3									
m	13.0	3	7.4	Modified	2.6	7.6	13.0	26.0	31.5	60.0	70.0	83.2
m	26.0	4	8.0									
m	60.0	11	14.3									
m	70.0	13	-7.2									
m	13.0	4	9.9	Modified	2.7	7.6	13.0	26.0	31.0	59.4	72.0	84.0
m	26.0	5	17.6									
m	31.0	11	-8.4									
m	72.0	12	10.5									
m	84.0	13	-6.9									
k	14.0	4-5	683.6	Modified	3.4	9.4	14.0	28.0	32.5	62.2	72.8	84.5
k	28.0	8-9	2545.2									
k	14.0	3-4	317.4	Modified	3.2	7.5	14.0	28.2	32.0	62.0	71.0	83.6
k	32.0	7-8	4061.6									
k	62.0	12-13	-1590.3									
k	14.0	3-4	560.0	Modified	4.3	8.8	14.0	27.3	32.0	62.0	74.0	85.4
k	32.0	5-6	172.5									
k	62.0	10-11	663.1									
k	74.0	12-13	375.0									
k	3.0	2-3	2385.4	Modified	3.0	5.9	15.7	27.0	32.0	61.8	73.0	85.0
k	27.0	4-5	-6522.5									
k	32.0	9-10	4679.2									
k	73.0	11-12	2826.4									
k	85.0	13-14	-615.4									

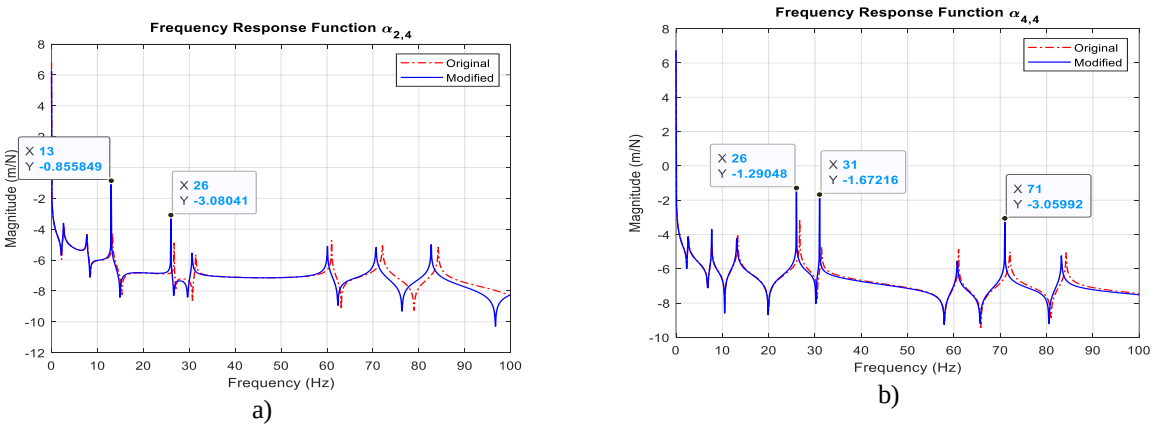

Figure 5. Simulation applications for mass modifications a) 2 modifications, b) 3 modifications

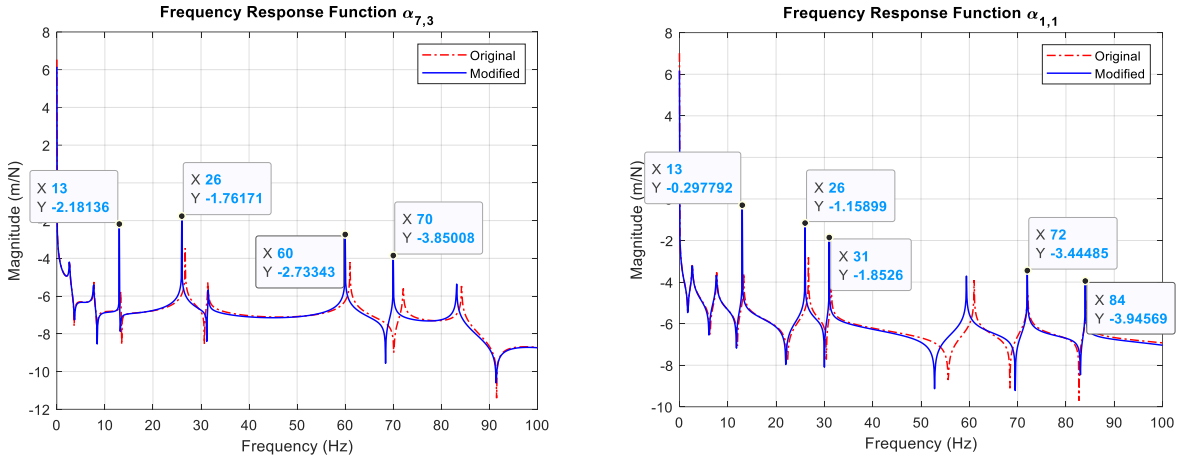

Figure 6. Simulation applications for a) 4 modifications, b) 5 modifications

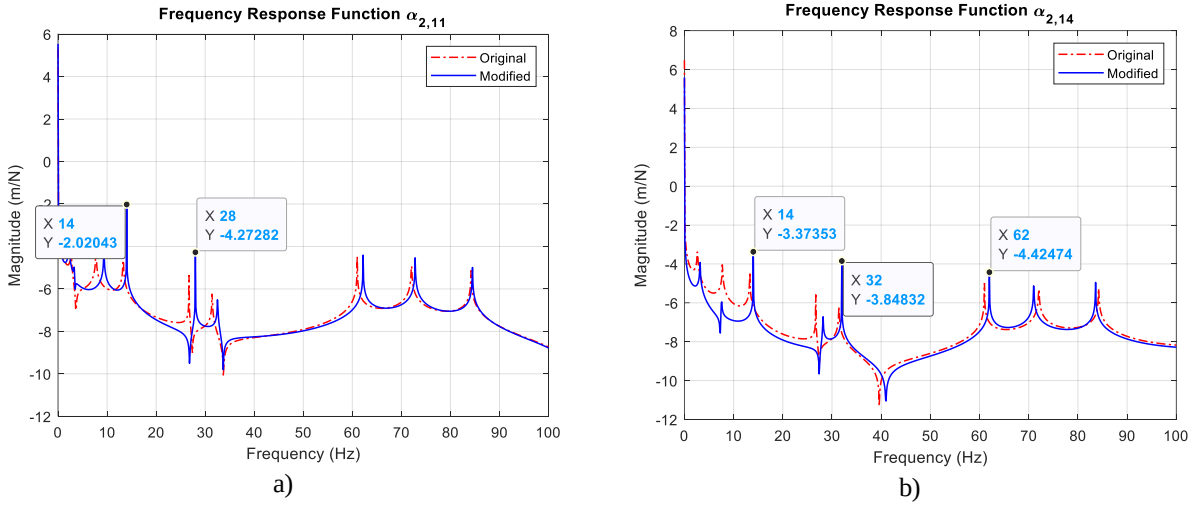

Figure 7. Simulation applications for stiffness modifications a) 2 modifications, b) 3 modifications

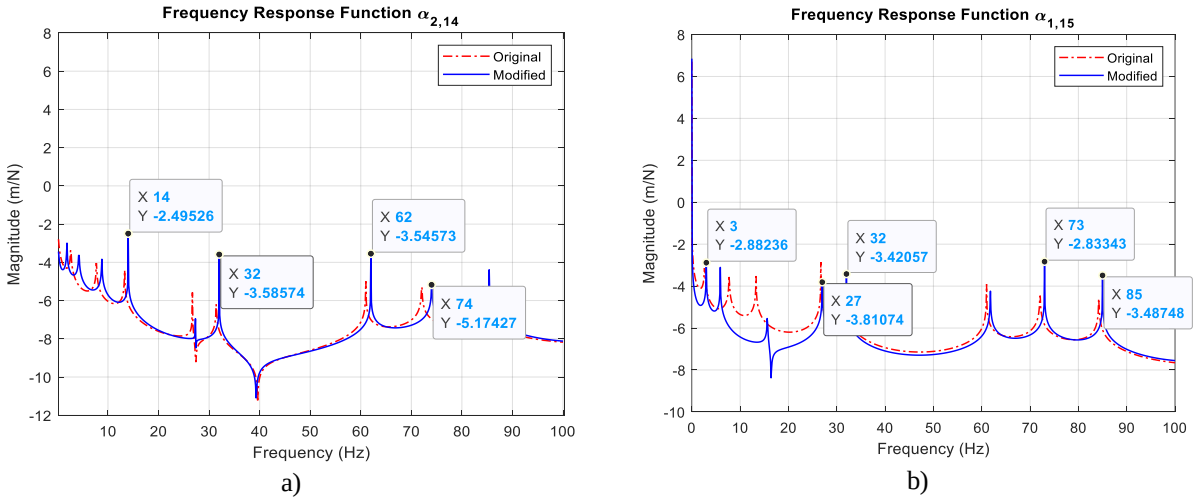

Figure 8. Simulation applications for stiffness modifications a) 4 modifications, b) 5 modifications

The obtained target frequencies after using the calculated modifications are shown on the FRF graphs in Figures 5-8. These frequencies are in agreement with selected target frequencies without any error.

4. Conclusions

In this study, a structural modification method using FRFs is presented to perform structural modification studies in UCAV systems. The presented method uses the Sherman-Morrison formula and does not need to calculate any matrix inverses. In this respect, it provides a very practical solution. The method is very convenient for real engineering applications as it directly uses FRFs of only the active coordinates of the system, that is, the coordinates affected by the modifications. The validity of the presented method has been verified by applying direct and inverse structural modifications on a Baykar Bayraktar Akıncı type UCAV model using Matlab, whose physical properties are approximate and estimated. Within the scope of direct structural modification, the changing resonance frequencies of the system as a result of placing bombs with different mass properties on the UCAV are determined using the proposed method. The results obtained are compared with the FRF graphics of the original system before and after the modifications. In the scope of inverse structural modification, the mass or stiffness values required for shifting some resonance frequencies to the determined values on the unarmed UCAV model are determined. The FRFs and resonance frequencies obtained by adding the calculated modification values to the system are presented in comparison with the FRFs and resonance frequencies of the original system before the modification.

With the obtained results, it has been shown that the proposed method can be used in direct and inverse structural modification studies on UCAV systems.

5. References

[1] Şen M, Çakar O. "Creating vibration-insensitive points by mass modifications in beams with different boundary conditions", 20th Ulusal Makina Teorisi Sempozyumu (UMTS 2021) Diyarbakır, Türkiye, 2021.

[2] Şen M, Çakar O. "Shifting resonance and anti-resonance frequencies of a shaft-disc-bearing rotor system to desired values by using frequency response functions", 12th International Conference on Mathematics, Engineering, Natural and Medical Sciences, Paris, France, 2021.

[3] Hüseyinoğlu M. "Updating and verification of the finite element models for structural dynamic analysis using frequency response functions", PhD Thesis, Fırat University, 2017.

[4] Kyprianou A, Mottershead JE, Ouyang H. "Assignment of natural frequencies by an added mass and one or more springs", Mech. Syst. Signal Process., 18(2), 263–289, 2004.

[5] Bucher I, Braun S. "The Structural modification inverse problem: An exact solution", Mechanical Systems and Signal Processing, 7(3), 217-238, 1993.

[6] Şen M, Çakar O. "Shifting the anti-resonance frequencies of a system to desired values by adding masses". 20th Ulusal Makina Teorisi Sempozyumu (UMTS 2021), Diyarbakır, Türkiye, 2021.

[7] Özgüven HN. "Structural modifications using frequency response functions", Mechanical Systems and Signal Processing, 4(1), 53-63, 1990.

[8] Ram YM. "Dynamic Structural Modification", The Shock and Vibration Digest, 32(1): 11-17, (1996).

[9] Park YH, Park YS. "Structural modification based on measured frequency response functions: an exact eigenproperties reallocation", J. Sound Vib., 237(3), 411–426, 2000.

[10] Braun SG, Ram YM. "Modal modification of vibrating systems: some problems and their solutions", Mech. Syst. Signal Process, 15(1), 101–119, 2001.

[11] Mottershead JE, Mares C, Friswell MI. "An inverse method for the assignment of vibration nodes", Mechanical Systems and Signal Processing, 15(1), 87-100, 2001.

[12] Sanliturk KY. “An Efficient Method for Linear and Nonlinear Structural Modifications“, Proceedings of ESDA 2002: 6th Biennial Conference on Engineering Systems Design and Analysis, ESDA 2002/APM-028, İstanbul, Turkey, 2002.

[13] Kyprianou A, Mottershead JE, Ouyang H. “Structural modification. Part 2: Assignment of natural frequencies and antiresonances by an added beam”, J. Sound Vib., 284(1–2), 267–281, 2005.

[14] Zhu J, Mottershead JE, Kyprianou A. “An inverse method to assign receptances by using classical vibration absorbers”, JVC/Journal Vib. Control, 15(1), 53–84, 2009.

[15] Liu Zhu Z, Li W, Ouyang H, Wang D. “Eigenstructure assignment in vibrating systems based on receptances”, Arch. Appl. Mech., 85(6), 713–724, 2015.

[16] Ouyang H, Richiedei D, Trevisani A, Zanardo G. “A convex-constrained modification method based on receptances”, Mechanical Systems and Signal Processing, 27, 397–409, 2012.

[17] Huseyinoglu M, Çakar O. “Determination of stiffness modifications to keep certain natural frequencies of a system unchanged after mass modifications”, Arch. Appl. Mech., 87(10), 1629–1640, 2017.

[18] Şen M, Çakar O. “An efficient method for structural coupling of mechanical systems by using frequency response functions”, Journal of Vibration and Control, First published online January 17, 2023. https://doi.org/10.1177/10775463231152069

[19] Sherman J, Morrison WJ. “Adjustment of an inverse matrix corresponding to a change in one element of a given matrix”, Annals of Mathematical Statistics, 21(1), 124–127, 1950.

[20] Vikipedi, https://tr.wikipedia.org/wiki/Baykar_Bayraktar_Ak%C4%B1nc%C4%B1, (30.08.2023).

International Conference on Advances and Innovations in Engineering

Investigation of the effects on support amounts of changing the coefficients in the YEKDEM formulation

Murat ERDEM[73], Mert GÜRTÜRK[2]

[1]Technical Vocational School, Fırat University, 23119, Elazig, Turkey
[2]Department of Energy Systems Engineering, Technology Faculty, Fırat University, 23100 Elazig, Turkey
[1]muratrdm01@gmail.com, [2]m.gurturk@gmail.com

[1](ORCID: 0000-0003-0287-1881), [2](ORCID: 0000-0003-0380-5704)

Abstract

In this study, an analysis was carried out on the Renewable Energy Support Mechanisms (YEKDEM) implemented in Turkey. In the study, since January 2019, calculations were made according to the formula in YEKDEM 2021. The calculation is valid for solar power plants. The starting price of 32 Turkish Liras–penny/kWh price valid in YEKDEM-2021 was also applied for 2019. Here, at first, calculations were made according to YEKDEM-2021 and the compatibility of these values with the applied upper limit was investigated. Then, the coefficients put into practice in the YEKDEM-2023 formula were applied to the formula in YEKDEM-2021 and the effects of the support given to the investor were examined. It was concluded that the findings obtained are not suitable for the upper limit of YEKDEM-2021, which is 5.10 USD-cents/kWh, but it is more appropriate for the YEKDEM-2023 lower and upper limit price of 4.95 and 6.05 USD-cents/kWh.

Keywords: Solar energy, Solar power plant, Renewable energy, YEKDEM

1. Introduction

One of the most crucial challenges in the global order is the development of technology, industrial growth, and the quest for new energy sources in various nations. Fossil fuels, which are the main source of energy today, are utilized to generate electricity [1]. Burning fossil fuels releases heat and dangerous gases into the environment as well as energy. This circumstance highlights issues like the greenhouse effect, sea level rise, and global warming. Even though humans are the only living species that use fossil fuels, they are the ones most harmed by the consequences [2]. Fossil fuels have significant and transient environmental drawbacks. More fossil fuels must be burned to meet the rising demand for energy. In addition, it takes a long time for fossil fuels to be recovered after usage [3,4]. Only today can fossil fuels be utilised, as they are a byproduct of the infrastructure built hundreds of years ago. Although it is well known that the best energy management preserves nature, rising population, dependence on technology, and the quick change in modern lifestyles boost demand even further [5,6].

The following are examples of renewable energy sources: solar, geothermal, hydro, wind, and wave. One of nature's greatest gifts to humans that doesn't cost anything is the sun. The fact that solar panels do not harm the environment is one of their most notable benefits while producing energy. Compared to fossil fuels, they produce no emissions and have a very small carbon footprint [6,7]. Calculations on solar energy were done due to Turkey's strong solar energy potential for this study [8]. In order to incentive both solar energy and other renewable energy sources, some incentives have been implemented in many countries. Some of these are USA [9], China [10], France [11], Spain [12] and India [13]. These incentives generally consist of tax reductions, accelerated loans, increasing incentive periods, giving more incentives to regions with high radiation, controlling premiums according to inflation, and tariff guarantees.

[1]Corresponding author

In Turkey, recently, it offers incentives with the help of an independent formula based on producer price index (PPI), consumer price index (CPI), US Dollar and EURO. This incentive program is called YEKDEM. Recently, Gürtürk et al. [14] in their analysis on YEKDEM-2021 for the years 2015-2020, they reported that the amount of incentives given was insufficient considering the cost of Solar Power Plants (SPPs). The aim of this study is to make some suggestions by analyzing YEKDEM-2021 and YEKDEM-2023 formulas.

2. Material and Methods

YEKDEM is the institution that carries out the Renewable Energy Resources Support Mechanisms in Turkey (Wind, Biomass, sun etc.). The establishment purpose of YEKDEM is to increase the use of our unlimited and clean domestic-national energy resources and to increase the number of production facilities thanks to incentives. As it is known, increasing renewable energy sources will significantly reduce the dependence on non-renewable energy sources (coal, oil, natural gas, etc.). This will make our universe more livable, especially for the next generations. YEKDEM was first established in 2005 and continues its activities with the latest update in 2023. For this purpose, a new formula was announced in 2021 [15] and this formula was updated again in 2023 [16]. However, in the decision number 7189 of the Official Gazette of the Republic of Turkey dated April 30, 2023, this law article was by making changed again YEKDEM-2021 was canceled, and YEKDEM-2023 was put into practice. The following paragraph contains the explanation about YEKDEM-2021.

In the Republic of Turkey, a decision regarding the prices and periods to be applied for electricity generation facilities based on renewable energy sources with Renewable Energy Resources (YEK) certificate, which will be put into operation from 01.07.2021 to 31.12.2025, has been put into effect. (Decision number: 3453, Law number and articles: 5346; 6 th - 6/B) [15]. The formulas of the announced YEKDEM-2021 Eq. (1) and 2023 Eq. (2) are given below:

$$YEKDEM_{GD} = YEKDEM_{\ddot{O}GD} x[\left(\frac{26}{100} x \frac{PPI_{A-2}}{PPI_{A-5}}\right) + \left(\frac{26}{100} x \frac{CPI_{A-2}}{CPI_{A-5}}\right) + \left(\frac{24}{100} x \frac{EXC.RATE_{D-A}}{EXC.RATE_{D-B}}\right) + \left(\frac{24}{100} x \frac{EXC.RATE_{E-A}}{EXC.RATE_{E-B}}\right)] \quad (1)$$

When the relations are examined, it is seen that the coefficients are completely changed, but some denominators are partially changed.

$$\frac{YEKDEM_{GD}}{YKF_{GD}} = \frac{YEKDEM_{\ddot{O}GD}}{YKF_{GD}} x[\left(\frac{25}{100} x \frac{PPI_{A-2}}{PPI_{A-3}}\right) + \left(\frac{15}{100} x \frac{CPI_{A-2}}{CPI_{A-3}}\right) + \left(\frac{30}{100} x \frac{EXC.RATE_{D-1}}{EXC.RATE_{D-2}}\right) + \left(\frac{30}{100} x \frac{EXC.RATE_{E-1}}{EXC.RATE_{E-2}}\right)] \quad (2)$$

Here, YKF; domestic contribution prices, PPI; producer price index, CPI; consumer price index, $EXC.RATE_D$; monthly average dollar rate and EXC.RATEE average monthly EURO rate. Number indices also represent the month it belongs to. The coefficients have been changed, that is, YEKDEM-2023 formulas have been applied to YEKDEM-2021, and the final form of the equation is shown below. Calculations related to modification were performed according to this formula (Eq. 3). The results found for these formulas are the amounts given in TL-penny per kWh.

$$\boldsymbol{YEKDEM_{GD} = YEKDEM_{\ddot{O}GD} x[\left(\frac{25}{100} x \frac{PPI_{A-2}}{PPI_{A-5}}\right) + \left(\frac{15}{100} x \frac{CPI_{A-2}}{CPI_{A-5}}\right) + \left(\frac{30}{100} x \frac{EXC.RATE_{D-A}}{EXC.RATE_{D-B}}\right) + \left(\frac{30}{100} x \frac{EXC.RATE_{E-A}}{EXC.RATE_{E-B}}\right)]} \quad (3)$$

3. Results and Discussion

In the scope of this study, an analysis was made according to YEKDEM-2021 for the years 2019-2023 and an evaluation was carried out on the incentive amounts by considering the limit values by applying the coefficients of the last updated YEKDEM to the previous one. The obtained findings are presented in the form of Tables. Support amounts are provided for US$/kWh, US Dollar-cents/kWh and accepted ranges of limit values.

Table 1 shows the amount of incentives given in US dollars. While the values for January varied between 0.04 - 0.07 US$/kWh, all values were calculated as 0.06 US$/kWh in April. In July, except for 2023, all values were 0.06 US$/kWh. The value for 2023 is 0.05 US$/kWh. In October, 2020 value was found as 0.05 US$/kWh and other values as 0.06 US$/kWh. Since YEKDEM stated that two numbers should be taken into account after the comma, two numbers were taken into account in the calculations. It is seen that there is no stability between the amount of incentives in US Dollars. Considering the calculations in US Dollar-cents/kWh, it was determined that the incentive amounts varied between 4.47 - 6.67 US$-cent/kWh in January, 5.51 - 6.21 US$-cent/kWh in April, 4.78 - 6.39 US$-cent/kWh in July and 5.40 - 6.26 US$-cent/kWh in October (Table 2). However, all data with the exception of 4.78 US$-cent/kWh will be given as 5.10 US$-cent/kWh, in which all values except 4.78 US$-cent/kWh are attached to the upper limit of 5.10 US$-cent/kWh set by the government. If the support starting price was 2019 and the first YEKDEM support mechanism price was 32.00 US$-cent/kWh, the amounts to be obtained would be like this. As mentioned above, such a form of support would not be appropriate since these values are attached to the upper limit. Table 3 shows the values that would be appropriate according to the calculation if the lower limit and upper limit prices valid in YEKDEM-2023 were in the range of 4.95 - 6.05 US$-cent/kWh. These values are shown in yellow. When Table 2 and Table 3 are compared, it is clear that the YEKDEM-2023 limit ranges are much more suitable for calculations. According to the YEKDEM-2023 limit ranges, only six values shown in gray were outside the acceptable limits.

Table 1. Results obtained in US$/kWh according toYEKDEM-2021

SUPPORT AMAOUNTS (US$/kWh)			
JANUARY	**APRIL**	**JULY**	**OCTOBER**
0.07	0.06	0.06	0.06
0.06	0.06	0.06	0.05
0.06	0.06	0.06	0.06
0.04	0.06	0.06	0.06
0.06	0.06	0.05	

Table 2. Results obtained in US$-cent/kWh according to YEKDEM-2021

SUPPORT AMAOUNTS (US$-Cent)			
JANUARY	**APRIL**	**JULY**	**OCTOBER**
6.67	5.93	6.39	6.26
6.17	5.51	5.91	5.40
6.35	5.81	5.95	5.98
4.47	5.74	5.59	5.60
5.99	6.21	4.78	

Table 3. Limited results obtained in US$-cent/kWh according to YEKDEM-2021

LIMITED SUPPORT AMAOUNTS (US$-Cent/kWh)			
JANUARY	**APRIL**	**JULY**	**OCTOBER**
6.67	5.93	6.39	6.26
6.17	5.51	5.91	5.40
6.35	5.81	5.95	5.98
4.47	5.74	5.59	5.60
5.99	6.21	4.78	

Table 4 is again calculated according to YEKDEM-2021, but instead of YEKDEM-2021 - PPI, CPI, US Dollar and EURO coefficients, the coefficients in YEKDEM 2023 are applied. Here, it is aimed to see the effects of the aforementioned coefficient changes on the amount of incentives given. Within the scope of five years, incentive amounts were found between 0.05 - 0.07 US$/kWh in January, 0.05 - 0.06 US$/kWh in April, 0.05 - 0.06 US$/kWh in July and 0.05 - 0.06 US$/kWh in October. In the coefficient change, it is seen that the values in July and October are equal in US$/kWh. In the coefficient change, it is seen that the values in July and October are equal in US$/kWh. In January, one of these values increased, but in April, one value decreased. Therefore, it is difficult to say anything about advantages-disadvantages here. The values in the coefficient change are presented in Table 5 in US$-cent/kWh. The values in the coefficient change are presented in Table 5 in US$-cent/kWh. Only two values in this Table are below the upper limit of YEKDEM-2021, which is 5.10 US$-cent/kWh. They are painted yellow (4.52 and 4.90 US$-cent/kWh). Since all other values are above 5.10 US$-cent/kWh, they will be applied as 5.10 US$-cent/kWh. When YEKDEM-2023 is examined according to the lower and upper limits of 4.95 and 6.05 US$-cent/kWh, respectively, it is understood that many values are between these limits (Table 6). They are painted yellow. Two values that are painted green are below the lower limit of values, and those that are shown in gray are above the upper limit. The lower ones will be increased to the lower limit, while the higher ones will be reduced to the upper limit. Therefore, based on the start date and the initial YEKDEM application fee, it can be concluded that the YEKDEM-2023 boundary ranges are much more appropriate compared to 2021 in the calculation made according to YEKDEM-2021. When all Tables are examined, there is an increase or decrease in the values obtained from January to October. When Table 2 and Table 5 are compared, it can be concluded that the application of YEKDEM 2023 coefficients causes an increase in the amount of incentives compared to the YEKDEM-2021 coefficients, that is, it is more suitable for Solar Power Plant (SPP) investors.

Table 4. Results with modified coefficient of YEKDEM-2021 in US$/kWh

SUPPORT AMAOUNTS (US$/kWh)			
JANUARY	**APRIL**	**JULY**	**OCTOBER**
0.07	0.06	0.06	0.06
0.06	0.05	0.06	0.05
0.06	0.06	0.06	0.06
0.05	0.06	0.06	0.06
0.06	0.06	0.05	

Table 5. Results with modified coefficient of YEKDEM-2021 in US$-cent/kWh

SUPPORT AMAOUNTS (US$-Cent)			
JANUARY	**APRIL**	**JULY**	**OCTOBER**
6.73	5.90	6.39	6.23
6.12	5.48	5.93	5.45
6.46	5.85	6.02	6.05
4.52	5.86	5.65	5.82
6.18	6.38	4.90	

Table 6. Limited results with modified coefficient of YEKDEM-2021 in US$-cent/kWh

LIMITED SUPPORT AMAOUNTS (US$-Cent/kWh)			
JANUARY	**APRIL**	**JULY**	**OCTOBER**
6.73	5.90	6.39	6.23
6.12	5.48	5.93	5.45
6.46	5.85	6.02	6.05
4.52	5.86	5.65	5.82
6.18	6.38	4.90	

4. Conclusion

In present study, an analysis was made out on the Renewable Energy Support Mechanisms (YEKDEM) implemented in Turkey for the years 2019 – 2020. The results were found for YEKDEM-2021 and as the application of the coefficients in 2023 to 2021. The results and recommendations are presented below.

- Incentive amounts in US$/kWh are 0.04 - 0.07 according to the current situation (YEKDEM-2021).
- According to the current situation (YEKDEM-2021), the amount of incentives in US$-cent/kWh is 4.78 – 6.67.
- In the current situation (YEKDEM-2021), only one value remained below the 5.10 US$-cent/kWh limit, while 13 values remained in the range of 4.95 - 6.05 US$-cent/kWh. This revealed that the YEKDEM-2023 range is more suitable.
- Values found according to the modified formula are in the range of 0.05 -0.07 in US$/kWh.
- The values found according to the modified formula are in the range of 4.52 - 6.73 in US$-cent/kWh.
- According to the modified formula, the YEKDEM-2023 range is more suitable in terms of the suitability of the mathematical relation. Because more values remained in this range.
- In general, the amount of support provided by the modified formula was higher than the current situation.

References

[1] Rahman MN, Wahid MA. "Renewable-based zero-carbon fuels for the use of power generation: A case study in Malaysia supported by updated developments worldwide". Energy Reports, 7, 1986–2020, 2021.

[2] Perera F, Nadeau K. "Climate Change, Fossil-Fuel Pollution, and Children's Health". New England Journal of Medicine 386, 2303–14, 2022.

[3] Mete G, Karanja W, Njenga N. Fossil Fuels and Transitions: The UK Maximising Economic Recovery Strategy and Low-Carbon Energy Transitions BT - The Palgrave Handbook of Managing Fossil Fuels and Energy Transitions. In: Wood G, Baker K, editors., Cham: Springer International Publishing; p. 167–94, 2020.

[4] Williams LO." Fossil fuels". Applied Energy, 47, 1994.

[5] Wolniak R, Skotnicka-Zasadzień B. "Development of Photovoltaic Energy in EU Countries as an Alternative to Fossil Fuels". Energies, 15, 2022.

[6] Yılmaz H, Şahin M. "Solar panel energy production forecasting by machine learning methods and contribution of lifespan to sustainability". Int J Environ Sci Technol, 2023.

[7] Yu J, Saydaliev HB, Liu Z, Nazar R, Ali S. "The asymmetric nexus of solar energy and environmental quality: Evidence from Top-10 solar energy-consuming countries". Energy, 247, 123381, 2022.

[8] GEPA. https://gepa.enerji.gov.tr/MyCalculator/], 2021.

[9] Ding L, Kinnucan HW. "This document is discoverable and free to researchers across the globe due to the work of AgEcon Search . Help ensure our sustainability". J Gender, Agric Food Secur, 1, 1–22, 2011.

[10] China Institute, China's renewable energy & Clean-Tech Market, Sum-mary Report, (March) U of A. No Title, 2016.

[11] Celik AN, Özgür E. "Review of Turkey's photovoltaic energy status: Legal structure, existing installed power and comparative analysis". Renewable and Sustainable Energy Reviews, 134, 2020.

[12] Mir-Artigues P, Cerdá E, Del Río P. "Analyzing the impact of cost-containment mechanisms on the

profitability of solar PV plants in Spain". Renewable and Sustainable Energy Reviews, 46, 166–77, 2015.
[13] De La Flor FJS, Cebolla RO, Félix JLM, Domínguez SÁ. "Solar radiation calculation methodology for building exterior surfaces". Solar Energy, 79, 513–22, 2005.
[14] Gürtürk M, Ucar F, Erdem M. "A novel approach to investigate the effects of global warming and exchange rate on the solar power plants". Energy, 239, 122344, 2022.
[15] Gazette of republic of Turkey. Turkish Gov Leg Gaz Repub Turkey, 2021. https://www.resmigazete.gov.tr/eskiler/2021/01/20210130-9.pdf.
[16] Gazette of republic of Turkey. Turkish Gov Leg Gaz Repub Turkey, 2023, https://www.resmigazete.gov.tr/eskiler/2023/05/20230501-7.pdf.

International Conference on Advances and Innovations in Engineering

Design of Spin Coating Unit and Parameters Affecting the System

Mehmet Erbil ÖZCAN[1]

[1]Department of Mechanical Engineering, Engineering Faculty, Firat University, Elazig.

[1]meozcan@firat.edu.tr

[1](ORCID: 0000-0003-1641-8279)

Abstract

In our time, there are many ways to obtain thin films used in many different industries. One of the existing methods is a type of coating called Spin Coating. Spin coating is a method used to prepare smooth and homogeneous thin films on the substrate using the concept of centripetal force and surface tension of the solution. In this process, a small amount of coating material is dripped into the center of the substrate. The substrate is then rotated at high speed for a certain period of time so that the coating material is evenly spread on the substrates.
The spin coating method, which is the subject of many research and development activities and is frequently preferred and used in optical mirrors, lenses, compact discs, is also frequently used in the production of combined circuits, color television screens, optical mirrors, nanoscale devices, solar panels, DVD and CD ROM production, and gas sensors.
In this study, the design of the spin coating device to obtain thin film coatings with the spin coating method, the points to be considered during the design and the control of the coating parameters were examined. During the design, system parts that directly affect the coating such as engine, chassis and control unit were selected and designed. In addition, an evaluation was made by making a cost analysis of the spin coating method, which has a lower installation cost compared to other coating methods.

Keywords: coating, spin coating, material, design

1. Introduction

Technological developments increase the demand for new materials in different applications day by day. Of course, it is not possible to find new material every day. For this reason, it is tried to be solved by improving the properties of the materials that are needed. There are many methods used to improve material properties in different applications. The spin coating method is also a method that is frequently used to improve the properties of materials. When the studies on the coating of materials with the rotational coating method are examined: Jeong et al. [1] synthesized a coatable W03 NP dispersed ink to aimed to develop an appropriate design strategy for achieving optimal physicochemical properties of the inks. Polyvinyl alcohol (PVA) was added to the W03 NP ink to improve its adhesion to indium tin oxide-coated glass substrates. The W03 NP fi lms exhibited an excellent transmittance change of 77 % at 633 nm and a coloration efficiency of 35 cm2/C. Song et al. [2] constructed the foldable and stretchable proton exchange membranes (PEMs) based on Kevlar nanofibers and polystyrene-block-poly-block-polystyrene (SEBS) through spin coating technology. The membranes did not show high proton conductivity and strength properties. Yu et al. [3] prepared delafossite CuAl02/ AlN thin films by a spin coating method. In this study, CuAIO2 was formed by hot annealing CuO on AIN film by spin coating method. The CuAl02/AlN film was examined in a scanning electron microscope. The thickness of the CuAl02 and AlN film were 346 nm and 625 nm, respectively. Huo et al. [4] prepared thick-film ceramics based on Co2.77Mn1.71Fe1.10Zn0.42O8 (CMFZ) using a slurry spin coating technique. They found that the microstructure and electrical properties of films are sensitive to the solid content in pastes. Sekiguchi et al. [5] investigated the effects of varying particle sizes and concentrations in

[1]Corresponding author

silica nanoparticle (SN) on the AAO substrates. They found that the particle loading densities varied and had the maximum value around a particle size/pore size ratio of 1.5. Wang et al. [6] made a spin coating method as use of Al-doped ZnO (AZO) and F, Al co-doped ZnO (FAZO) films. They researched on the AZO and FAZO thin film structures for different temperatures. The results showed that for the AZO film, the intensity of the diffraction peak (DP) first increases and then decreases with temperature, while the intensity of the DP of the FAZO film gradually increases with temperature. Devi et al. [7] produced TiO2 thin films by spin coating using the Sol-Gel method. These films were then annealed at temperatures ranging from 400 ºC to 550 ºC. Then their surface morphology, were analysed using X-Ray diffraction, Raman spectroscopy, UV–Vis spectroscopy, FESEM and AFM. Kishor et al. [8] produced p-CuI/n-ZnO heterojunction using spin coating technique. The structural properties of the produced Cul and ZnO thin films were analyzed by XRD, FESEM. The ZnO thin films were grown by spin coating show hexagonal wurtzite structure from the XRD studies. Chatterjee et al [9] prepared pure Zinc oxide (ZnO), Copper oxide (CuO) nanoparticles (NPs) and their (ZnO/CuO) nanocomposites (NCs) in 1:1 M ratio by co-precipitation method. The structural properties of the synthesized samples were investigated by scanning electron microscopy (SEM) and X-ray spectroscopy (EDX) techniques. According to Sopcak et al. [10] Ti6Al4V substrate was coated with thin bredigite-type coatings with the aid of sol-gel spin coating. Coatings were analyzed by Scanning Electron Microscopy (SEM/FIB), Atomic Force Microscopy (AFM), differential thermal analysis (DTA-TG), X-ray diffraction (XRD) methods. All the films obtained are 25-50 nm, smooth and porous. Boron addition increased the coating thickness as a result of the interaction of borate ions and PVA. Lee et al. [11] applied the static and dynamic spin coating method in the production of CsFAMAPbIBr film with two-step ambient air. When the PbI2-CsI layer was coated with organic materials (FAI/MABr/MACl) with different reaction times by static and dynamic spin coating method, different composition and morphology were obtained. Tajima et al. [12] produced WO3 thin film using humidity-controlled spin coating technique.WO3 films obtained by this technique exhibited favorable electrochromic properties.Thus, controlling the humidity in systems containing volatile solvents allowed the film deposition process. Tiwari et al. [13] have coated variable Ga/Co doped ZnO film layers on quartz substrates by spin coating method. Coatings were analyzed by X-ray diffraction (XRD) and all films were obtained with ZnO 8-24 nm thickness. Olivares et al. [14] developed a new method for accelerated indoor testing. Dusts were collected from Atmaca desert to investigate the effects of pollution on the performance of solar cells. The spin coating method was used to deposit dirt on the photovoltaic glass. As a result, it has been shown that the X-ray diffraction of dusty samples artificially deposited indoors and naturally outdoors is similar. Jain et al. [15] V2O5 film was deposited by spin coating method. The coatings were annealed at 250, 350 and 450 oC to examine the effect of temperature. By performing XRD analysis of the coatings, an increase in coating quality was obtained with an increase in temperature. According to Garmim et al. [16] SnS film was produced by spin coating method. The Taguchi method was used to optimize the annealing temperature, time and concentration parameters. According to the results obtained, the most effective parameter in film preparation is concentration. Nwanna et al. [17] Nb2O5 film was produced by using sol-gel spin coating method at variable temperatures.The produced films were analyzed by Scanning Electron Microscopy (SEM) and X-ray diffraction (XRD).In addition, it has been confirmed that the films are good semiconductors by conductivity tests. Ahmoum et al. [18] have coated different layers of Cu2ZnSnS4 on soda-limestone by spin coating method.With X-ray diffraction (XRD) analysis, it has been observed that increasing the number of layers increases the crystal size.When 4 layers were deposited, minimum surface roughness was obtained. When the studies in the literature are examined, it is seen that there are many studies on the subject and the method is quite popular. In this study, the design of the spin coating device to obtain thin film coatings with the spin coating method, the points to be considered during the design and the control of the coating parameters were examined. It is planned to continue the experiments and studies related to the spin coating method in the continuation of the study, which is produced at a very low cost in terms of cost and as a result, the desired coating properties can be obtained.

The spin coating process generally consists of two basic parts. The first of these parts is called the static and dynamic distribution phases. At this stage, the solution is to spread on the surface of the material to be coated, and the second stage is to dry this solution-covered material (Figure 1). In the static dispersion process, the coating agent is dripped onto the surface of the material to be coated by means of a 1cc – 10cc syringe or dropper material, depending on the viscosity of the material.

In materials that are resistant to flow, the speed is increased and the amount of coating material is increased in order to cover the surface part more smoothly. During the dynamic spreading phase, it is often rotated at 500 rpm, the

reason for which is to provide less solution consumption by losing the solution on the substrate. The steps of the spin coating method are listed below.

Figure 1. Stages of spin coating method [19]

2. Stages of the spin coating method

1. Deposition of the precursor solution of the desired material on the substrate.
2. Rotate the substrate for a few seconds at a certain constant speed.
3. Twist off the substrate.
4. Dry the film layer by evaporating the solvent.
5. Repeat (1)–(4) above to obtain the desired thickness film.

3. Design

The most important issue to be considered while sizing the design was the power of the engine along with its size. The profile suitable for the size of the engine and facilitating its operation was selected and the design of the project was realized. The brushed universal motor, which supports 220 V 50-60 Hz frequency according to the small size of the rotated material and the rotation speed, was preferred as the main motor and connected to the bench (Figure 2 and Figure 3).

In the spin coating process, the number of revolutions is one of the most important factors affecting the coating. For this reason, during the coating, the speed of the previously selected engine should be adjusted. In order to adjust the speed of the engine used, the apparatus called the engine control unit was also selected. A control unit was selected according to the appropriate voltage and motor capacity and integrated into the system (Figure 2).

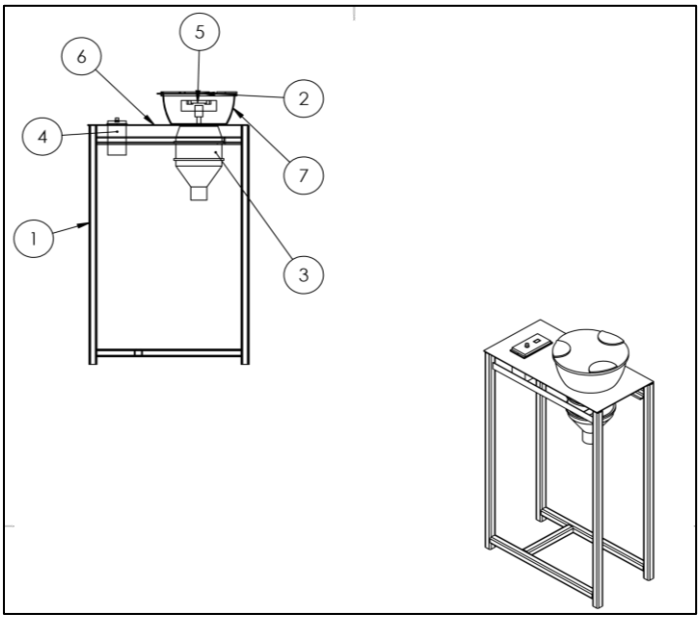

Figure 2. Assembly drawing (1.body, 2.cover, 3.motor, 4.motor control unit, 5. Sample holder, 6.desk, 7.tank)

Figure 3. Photos of coating unit

After selecting the motor and control unit, the sample holder and holder cover (Figure 4 and Figure 5) to which the coating sample will be attached were designed. The point to be considered here is to prevent the coating liquid from spreading around during rotation. To prevent this, a plastic material protector was designed around the sample holder and a cover was added to this protector. In this way, the sample will be connected to the holder and the cover will be closed and the coating will be completed without scattering.

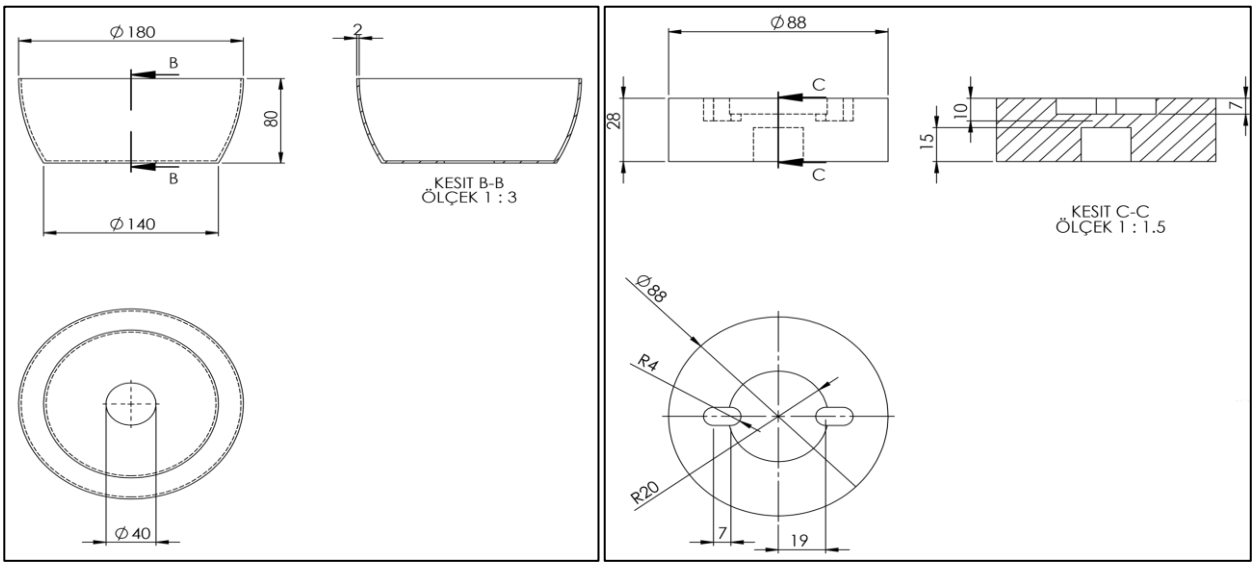

Figure 4. Chamber and sample holder cover

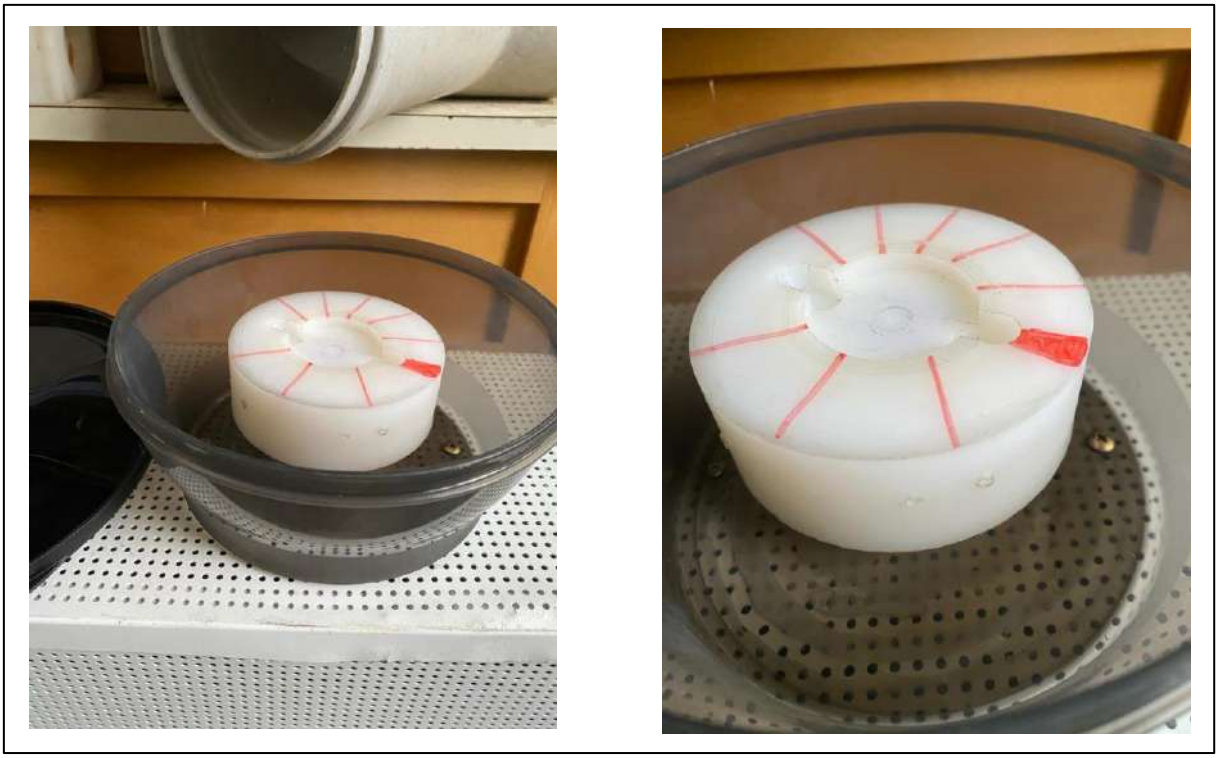

Figure 5. Photos of chamber and sample holder

4. Cost analysis

The price of a product; Cost also indicates the quality function, as well as an indication of buyer demand due to its superior competitive design. In this case, it reveals that the progress of cost analysis should be observed from a wide range.

In the study, the importance of cost analysis, which is the method of cost reduction, was emphasized in terms of revealing current values (May 2022) with the increase in the competitive environment.

Table 1. Cost analysis

Part Name/ Unit	Engine Power(V)	Frequency (Hz)	Size (mm)	Unit price	Price	TOTAL
Brush Universal Engine	220	50-60	250x125	500	500	500 TL
Polyamide			28x88	0.3		60 TL
Profile			630x380 x180	180	180	180 TL
Smart Screw			2	20	20	20 TL
Container			80x140	30	30	30 TL
Glue				25	25	25 TL
Engine Control unit			90x46x8 0	268	268	268 TL
Workmanship	80				50	130 TL
Grand total						**1213 TL**

5. Conclusions and Recommendations

In this study, necessary calculations were made for the coating of materials with a maximum diameter of 40 mm with the spin coating device and the production of the coating unit was completed. At the end of the studies, the following results were obtained.

- The coating unit made is suitable for materials to be coated with a maximum diameter of 40 mm. The substrate material holders are sized according to this value. The solution dripped onto the material to be coated distributes homogeneously and provides equal thickness solution distribution. Thanks to the bearing that opens to the holder made of polyamide material, it is aimed to prevent the material to be covered from scattering and to minimize the scattering of the excess solution around. Thanks to this process, loss of solution is prevented. Notches have been made on the sides of the opened bearing to be deeper, the reason for this is to easily remove the material to be covered after it is covered.
- While sizing the coating unit, it was dimensioned for the purpose of more comfortable working, and the external appearance was aimed to exhibit a more aesthetic stance. Considering the height of the engine that we placed on the profile, it was preferred to be higher in terms of more ergonomic working. In addition, it was preferred that the outdoor unit be made of perforated sheet in order for the engine to operate more efficiently. With the speed control unit, the number of revolutions, which is one of the coating parameters, was kept at the desired value.
- When compared in terms of cost, it has been determined that our device is cost-effective compared to normal spin coating devices (while a spin coating device was 5500 TL in May 2022, our device cost 1250 TL).
- Considering the disadvantages, the diameter of the material to be coated with the coating unit is limited. The workbench we manufacture is lower in size and lower in cost than normal rotating veneer benches. One of the reasons for the low cost is that instead of the vacuum system, an apparatus that will hold the base material is built and integrated into the system.
- After this study, an adjustable sample holder will be manufactured for the spin coating process, and a speed control device that can digitally display the engine speed and can be changed instantly with a timer will be integrated into the system, so that the cycle can be seen without the need for calculation.
- After the design of the coating unit and the sample experiments, it was envisaged to continue the scientific studies by continuing the experiments.

6. References

[1] C. Y. Jeong, H. Watanabe, and K. Tajima, "Adhesive electrochromic WO3 thin films fabricated using a WO3 nanoparticle-based ink," *Electrochim. Acta*, vol. 389, pp. 0–7, 2021, doi: 10.1016/j.electacta.2021.138764.

[2] D. Song, K. Liu, T. Zuo, J. Jia, N. Wang, and Q. Che, "Constructing foldable and stretchable proton exchange membranes through spin coating technology," *J. Mol. Liq.*, vol. 360, 2022, doi: 10.1016/j.molliq.2022.119421.

[3] C. Yu *et al.*, "CuA102/ AlN double-layer thin film prepared by the spin coating approach," vol. 753, no. December 2021, 2022.

[4] P. Huo *et al.*, "Effect of solid contents on the electrical properties of Co2.77Mn1.71Fe1.10Zn0.42O8 ceramic prepared by slurry spin coating technique," vol. 332, 2021.

[5] K. Sekiguchi, K. ichi Katsumata, H. Segawa, T. Nakanishi, and A. Yasumori, "Effects of particle size, concentration and pore size on the loading density of silica nanoparticle monolayer arrays on anodic aluminum oxide substrates prepared by the spin-coating method," *Mater. Chem. Phys.*, vol. 277, no. November 2021, 2022, doi: 10.1016/j.matchemphys.2021.125465.

[6] Y. Wang *et al.*, "Fabrication of AZO and FAZO films using low-cost spin-coating method," *Opt. Mater. (Amst).*, vol. 126, no. February, 2022, doi: 10.1016/j.optmat.2022.112204.

[7] K. Priyalakshmi Devi, P. Goswami, and H. Chaturvedi, "Fabrication of nanocrystalline TiO2 thin films using Sol-Gel spin coating technology and investigation of its structural, morphology and optical characteristics," *Appl. Surf. Sci.*, vol. 591, no. December 2021, 2022, doi: 10.1016/j.apsusc.2022.153226.

[8] C. H. R. Kishor, T. Sreelakshmy, A. Das, and P. M. Aneesh, “Fabrication of transparent p-CuI/n-ZnO heterojunctions using solution-processed spin coating technique,” *Phys. B Condens. Matter*, vol. 639, no. January, 2022, doi: 10.1016/j.physb.2022.414020.
[9] A. Chatterjee, A. V. Ravindra, G. Kiran Kumar, and C. Rajesh, “Improvement in the light conversion efficiency of silicon solar cell by spin coating of CuO, ZnO nanoparticles and CuO/ZnO mixed metal nanocomposite material,” *J. Indian Chem. Soc.*, vol. 99, no. 9, 2022, doi: 10.1016/j.jics.2022.100653.
[10] T. Sopcak *et al.*, “Influence of boron addition on the phase transformation, microstructure, mechanical and in-vitro cellular properties of bredigite-type coatings deposited by a spin coating technique,” *Mater. Chem. Phys.*, vol. 283, no. March, 2022, doi: 10.1016/j.matchemphys.2022.126049.
[11] J.-H. Lee, K. Jung, and M.-J. Lee, “Influence of spin-coating methods on the properties of planar solar cells based on ambient-air-processed triple-cation mixed-halide perovskites,” *J. Alloys Compd.*, vol. 404–406, no. SPEC. ISS., p. 1, 2005, doi: 10.1016/j.jallcom.2005.05.002.
[12] K. Tajima, T. Kubota, and C. Y. Jeong, “Preparation of electrochromic thin films by humidity-controlled spin coating,” *Thin Solid Films*, vol. 758, no. November 2021, 2022, doi: 10.1016/j.tsf.2022.139412.
[13] A. Tiwari and P. P. Sahay, “Structural and optical behavior of gallium and cobalt co-doped ZnO thin films fabricated by a sol-gel spin coating technique,” *Mater. Today Proc.*, no. xxxx, 2022, doi: 10.1016/j.matpr.2022.07.261.
[14] D. Olivares *et al.*, “Study of the effects of soiling on PV devices using the spin-coating technique in accelerated indoor exposures,” *Sol. Energy*, vol. 231, no. November 2021, pp. 317–327, 2022, doi: 10.1016/j.solener.2021.11.036.
[15] V. Jain, D. Shah, and K. Patel, “Study of vanadium pentoxide thin film prepared by spin coating method,” *Mater. Today Proc.*, vol. 48, pp. 706–708, 2019, doi: 10.1016/j.matpr.2021.09.559.
[16] T. Garmim *et al.*, “Synthesis and optimization of SnS absorber layer by spin-coating process and Taguchi approach,” *Bioresour. Technol. Reports*, p. 100310, 2019, doi: 10.1016/j.msea.2022.143695.
[17] E. C. Nwanna, P. E. Imoisili, and T. C. Jen, “Synthesis of niobium pentoxide from bis(cyclopentadienyl) niobium(IV) dichloride using the spin coating process,” *Polyhedron*, vol. 220, 2022, doi: 10.1016/j.poly.2022.115828.
[18] H. Ahmoum *et al.*, “The impact of precursor thickness and surface roughness on the power factor of Cu2ZnSnS4 (CZTS) at near room temperature: Spin-coating deposition,” *Superlattices Microstruct.*, vol. 160, no. November, 2021, doi: 10.1016/j.spmi.2021.107091.
[19] S. Nandy and K. H. Chae, “Chemical synthesis of ferrite thin films,” *Ferrite Nanostructured Magn. Mater. Technol. Appl.*, pp. 309–334, 2023, doi: 10.1016/B978-0-12-823717-5.00021-8.

International Conference on Advances and Innovations in Engineering

Numerical Analysis of Battery Thermal Management System Include Phase Change Material at Temperatures Lower than Normal Conditions

Halil İbrahim YAMAÇ[1]

[1]Mechatronics Engineering, Technology Faculty, Fırat University, Elazığ, Türkiye.
[1]halilymc@gmail.com

[1](ORCID: 0000-0002-4628-0971)

Abstract

In the realm of electrical storage devices, lithium-ion (Li-ion) batteries have emerged as a promising contender due to their advantageous traits. However, their performance is significantly affected by temperature fluctuations, leading to heat generation during charge-discharge cycles. The study employs ANSYS Fluent to model an air-phase change material (PCM) hybrid battery thermal management system (BTMS). The simulation investigates the behavior of Li-ion batteries and PCM during charging-discharging processes, shedding light on PCM's heat transfer capabilities and potential benefits for efficient thermal management. RT15HC is employed as PCM, Li-ion batteries have 625 kW/m^3 heat generation for 5C are investigated in transient numerical analysis. In the model designed in the numerical simulation study, the solidification time of even half of the PCM is almost the same with a complete melting time of PCM. When the batteries-on mode, their temperature does not exceed 40 ºC at the end of 2 hours. When the batteries-off mode, their temperature does not drop below 15 ºC at the end of 2 hours.

Keywords: Battery Thermal Management System, Computational Fluid Dynamics, Phase Change Material

1. Introduction

In recent times, one of the most promising electrical storage devices has emerged: lithium-ion (Li-ion) batteries [1]. The following are some benefits that Li-ion batteries offer over other rechargeable batteries: reduced mass density, increased energy density, absence of effects of memory, and low rates of self-discharge [2]. According to research, a Li-ion battery's performance is significantly impacted by temperature changes [3]. Due to the intrinsic electrochemical exothermic process and joule thermal effect, Li-ion batteries produce a significant quantity of heat while being charged and discharged. The temperature of the battery increase if the heat cannot be dispersed in a timely manner. The capacity and cycle performance deteriorate as a result of the excessive temperature [4].

Power output, safety, energy capacity, charge-discharge efficiency, longevity, and reliability of multiple battery processes are all directly influenced by the temperature of operation of the battery. The highest electrical capacity that the accumulator can store and supply is one crucial characteristic. It is constrained by the reversibility requirements of electrochemical reactions and diminished by electrode or electrolyte depletion [5-7]. Lithium electroplating during high-speed charge-discharge drastically lowers battery capacity and shortens battery life if the temperature is low. When the temperature is high, the battery's deterioration and side reactions are sped up to the point of thermal runaway. Additionally, the constancy of the battery is decreased by an uneven temperature distribution within the battery pack. Local deterioration is a result of the varying rates at which various batteries charge and discharge [8-11].

Temperature can affect Li-ion batteries negatively. Li-ion batteries perform best in a temperature range of 15 to 40 °C, and there should be no more than a 5 °C variation in temperature between any two battery components. A number of issues will arise in the Li-ion battery if the incorrect temperature range and temperature difference range persist for an extended period of time [12,13]. Additionally, fluctuations in internal cell temperature would lead to variations

[1]Corresponding author

in chemical reaction rates, which would become more pronounced with an increase in the number of cycles [14]. The Li-ion battery's capacity and charging and discharging voltage substantially alter in colder environments. A Li-ion battery's power capacity is reduced when lithium plating occurs on it at low temperatures, which severely degrades the battery [15]. To ensure that power batteries are kept in the range of ideal temperature zones, an efficient battery thermal management system (BTMS) must be developed [16].

In the course of the electrical charging-discharging processes of batteries, Phase Change Material (PCM) can collect and release a lot of latent heat during the process of solidification and melting while their temperature nearly remains constant [17]. When compared to the conventional thermal management technique, PCM uses no energy and doesn't call for any extra parts [18].

There are a lot of numerical studies on PCM employed in BTMS. The variations as geometrical application of PCM, materials used in BTMS, type and placement of battery ex. in these modellings of numerical studies [19-24].

In this numerical study, Li-ion batteries and PCM are modelled in ANSYS Fluent to see behavior of the air-PCM hybrid BTMS in the scenarios of charging-discharging processes of batteries.

2. Materials and Methods

Numerical analyzes are performed in the ANSYS Fluent module on a two-dimensional (2D) simulation created with four identical Li-ion batteries, ventilation channels and phase-change material. RT15HC is chosen as the phase change material. While creating the geometric model, it is assumed that there is a three-dimensional (3D) battery box cross-sectional area. Compared to 3D analysis, of course, there may be differences in the melting solidification processes of PCM related to natural convection (due to gravitational acceleration). It is thought that 2D work is valuable in terms of providing preliminary ideas. The designed geometry of BTMS is shown in the Fig. 1.

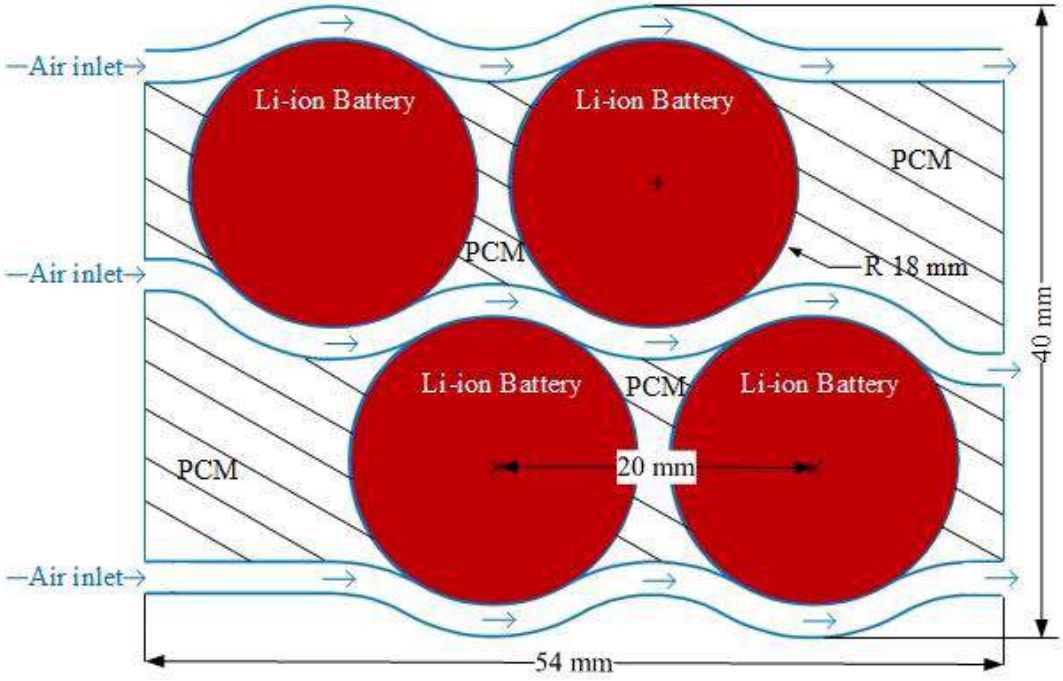

Figure 1. Geometry of BTMS

The air duct cross-section is 2 mm, the diameter of the circular coil section is 18 mm, the distance between the coils is 2 mm. Battery box dimensions are x plane 54 mm, y plane 40 mm. RT15HC is available in all areas except battery and air ducts. The numerical simulation is created in order to visualize the melting and freezing processes.

Fluent is used in numerical simulation with the SIMPLE solver. The continuity, momentum, and energy equations are shown in Equations 1-2, respectively [25].

$$\rho\frac{\partial u}{\partial t}+\rho u\frac{\partial u}{\partial x}+\rho v\frac{\partial u}{\partial y}=\nabla(\mu\nabla u)-\frac{\partial P}{\partial x} \quad (1)$$

$$\rho\frac{\partial v}{\partial t}+\rho u\frac{\partial v}{\partial x}+\rho v\frac{\partial v}{\partial y}=\nabla(\mu\nabla v)-\frac{\partial P}{\partial y} \quad (2)$$

Where, in PCM solid region $\mu=\mu_s, \rho=\rho_s,$ in PCM liquid region $\mu=\mu_L, \rho=\rho_L.$ Therefore, the coefficient of thermal expansion is β, the reference density is ρ_0, the solidification or melting temperature is T_m. The equation of energy is:

$$\frac{\partial}{\partial t}(\rho cT)+\frac{\partial}{\partial x}(\rho ucT)+\frac{\partial}{\partial y}(\rho vcT)=\nabla(k\nabla T) \quad (3)$$

Given that a phase transition takes place at a certain temperature, the temperature field can be defined as follows:

$$T=\begin{cases}\dfrac{E}{c_L} & T<T_m\ (solid\ phase)\\ T_m & 0<E<H, \quad T<T_m\ (melt\ zone)\\ T_m+\dfrac{E-H}{c_L} & E\geq H, \quad T>T_m\ (liquid\ phase)\end{cases} \quad (4)$$

Therefore, latent heat capacity is H, specific heat capacity is c_L and energy is E. The thermophysical parameters of RT15HC as PCM specifications can be seen in Table 1.

Table 1. RT15HC specifications [26].

Property	**Unit**	**RT15 HC**
Solidus temperature	K	283.15
Liquidus temperature	K	300.15
Latent heat of fusion	kJ/kg	155.00
Density (solid)	kg/m^3	880.00
Density (liquid)	kg/m^3	770.00
Volumetric thermal expansion coefficient	1/K	1x10^{-3}
Specific heat capacity (solid)	kJ/(kg K)	2.00
Specific heat capacity (liquid	kJ/(kg K)	2.00
Thermal conductivity (solid)	W/(m K)	0.20
Thermal conductivity (liquid)	W/(m K)	0.20
Dynamic viscosity	mPa s	3.10

In the solution, models as laminar, energy, solidification and melting are used. The discrete equations used for mass fraction matching are solved using the finite volume approach and the SIMPLE algorithm.

The batteries produce 625 kW/m^3 of heat generation at a power consumption of 5C [27]. While modeling the process in which the batteries work, the air inlet velocity of wavy channels is determined as 0.5 m/s. The air inlet and the initial temperatures of each zone are chosen as 10 °C. The domain boundaries are adiabatic (the effect of heat transfer with the outside environment is neglected because the effect of heat transfer with the air passing through the air channels is much lower). The numerically simulated scenario is to see the PCM melting behavior around the batteries, in general, all temperatures depending on time while the batteries are running. While modeling the process in which the batteries do not work, the domain boundaries are determined as 10 ºC under the constant temperature boundary condition without air entry. The initial temperature of all parts of the domain is chosen as 17 °C.

The numerically simulated scenario is to see the PCM solidification behavior around the batteries, in general, all temperatures depending on time, while the batteries are not working.
The mesh structure can be seen in Fig.2. The mesh properties are shown in Table 2.

Table 2. Mesh properties

Node Number	Element Number	Mesh Skewness			Orthogonal Quality		
		Max.	Min.	Ave.	Max.	Min.	Ave.
212140	211723	0.98	$1.3e^{-10}$	0.05	1.00	$2.0e^{-2}$	0.99

The mesh skewness and orthogonal quality values are in the range where the numerical study gives consistent results within itself.

3. Results

The numerical results can be investigated on the melting process of PCM (batteries-on mode) first, then the solidification process of PCM (batteries-off mode). As a result of the batteries-on mode, Fig. 2 shows the transient results of temperature contours.

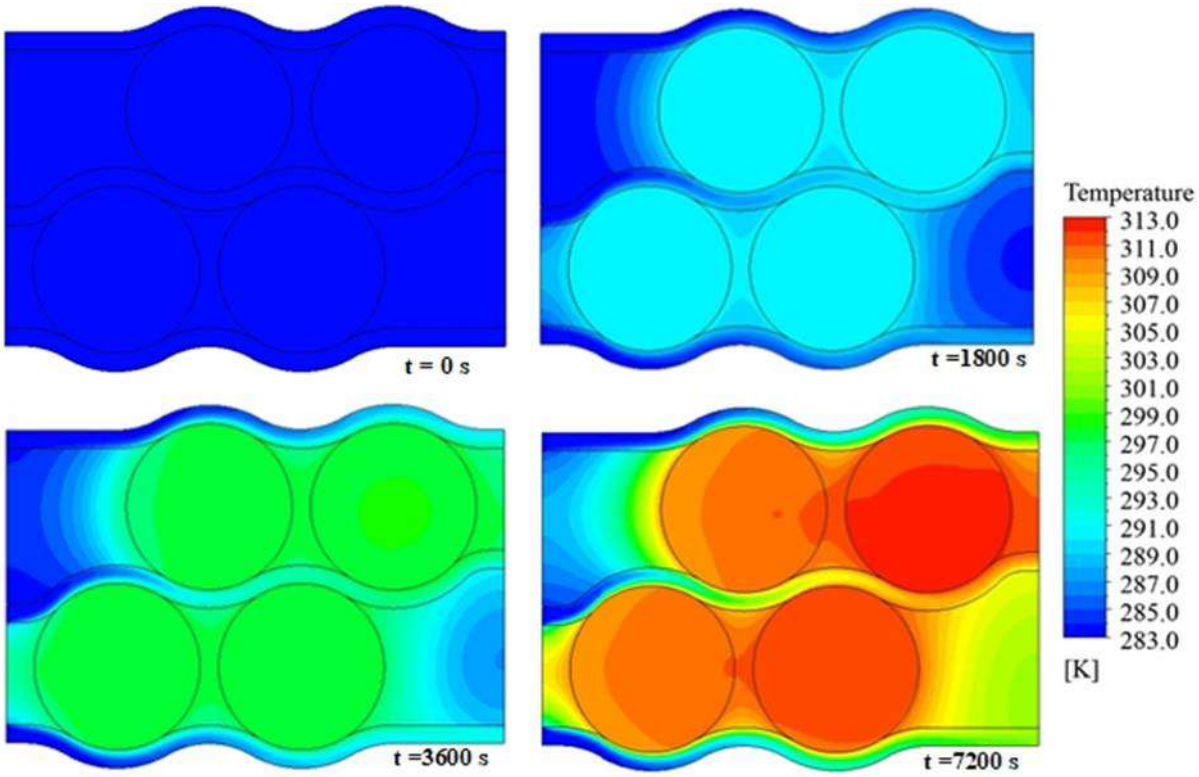

Figure 2. Temperature contours of batteries-on mode

The contours of 0, 1800, 3600 and 7200 seconds can be seen in Fig. 2. At the end of half an hour, the temperature of the batteries is around 18 ºC, at the end of one hour, the temperature of the batteries is around 28 ºC. The maximum temperature is occurred in batteries at the end of 2 hours around 40 ºC. The graph in Fig. 3 shows the temperature of batteries separately (batteries-on mode).

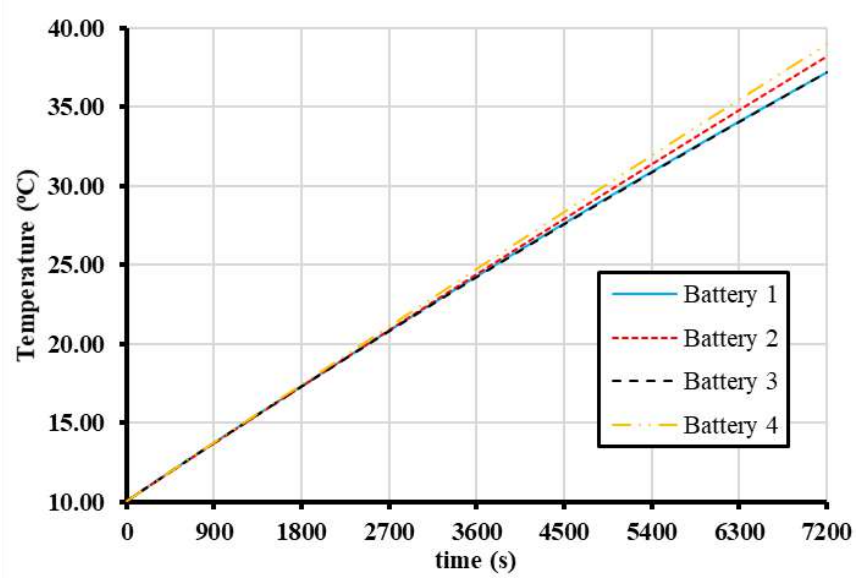

Figure 3. Temperature of batteries vs. time chart (batteries-on mode)

As expected, the battery temperatures close to the air inlet are slightly lower than the others. The important point is that all battery temperatures are kept below 40 ºC at the end of two hours. The maximum temperature indicates that the batteries are within the acceptable thermal operating range. Another point to be examined is the melting behavior of the PCM.

Fig. 4 shows the transient mass fraction counters of PCM. Fig. 5 shows the mass fraction vs. time chart of PCM.

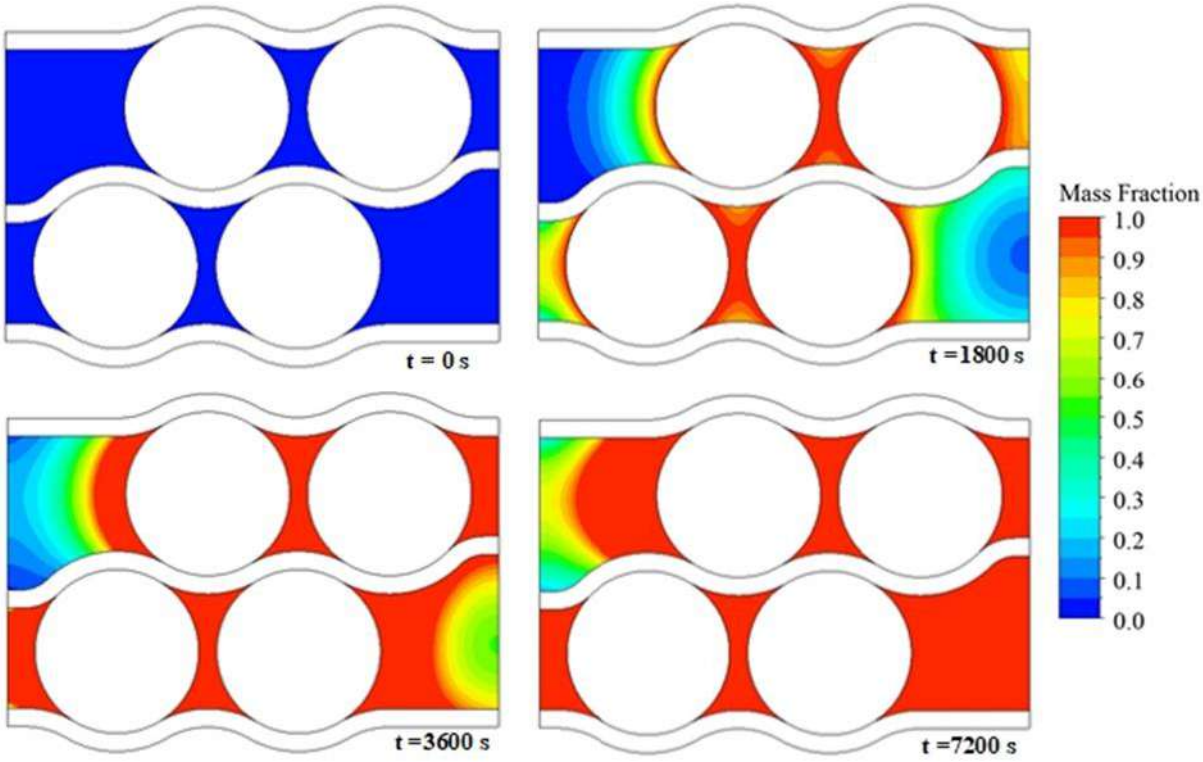

Figure 4. Mass fraction contours of batteries-on mode

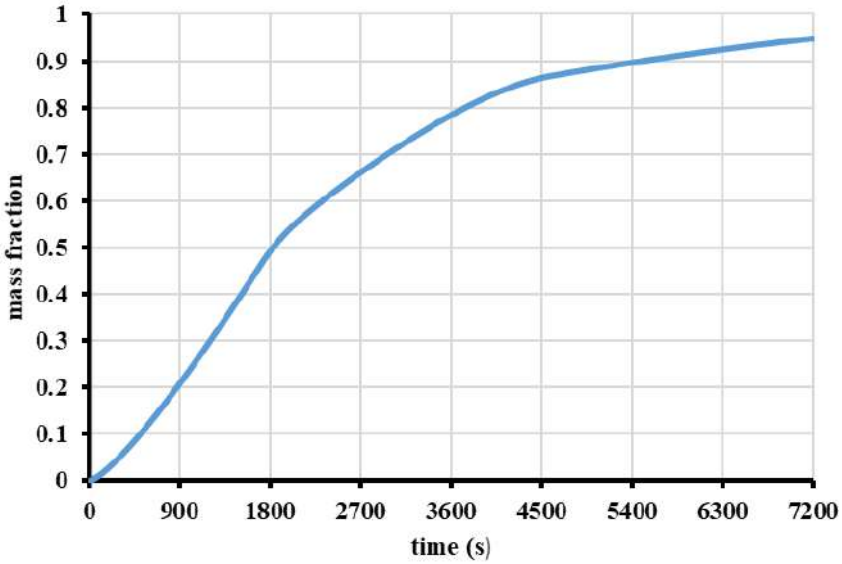

Figure 5. Mass fraction of PCM vs. time chart (batteries-on mode)

The PCM, which was initially completely in the solid phase (colored blue), almost completely transitioned to the liquid phase (colored red) after two hours. Looking at the half-hour and one-hour results, it is seen that the phase change spreads starting from the battery circles, which are the heat source. The parts close to the air inlet area show the melting behavior last due to the cooling effect. (Mass fraction = 0 means completely solid, Mass fraction = 1 means completely fluid.)

As a result of the batteries-off mode, Fig. 6 shows the transient results of temperature contours. The contours of 0, 3600, 7200 and 14400 seconds can be seen in Fig. 6.

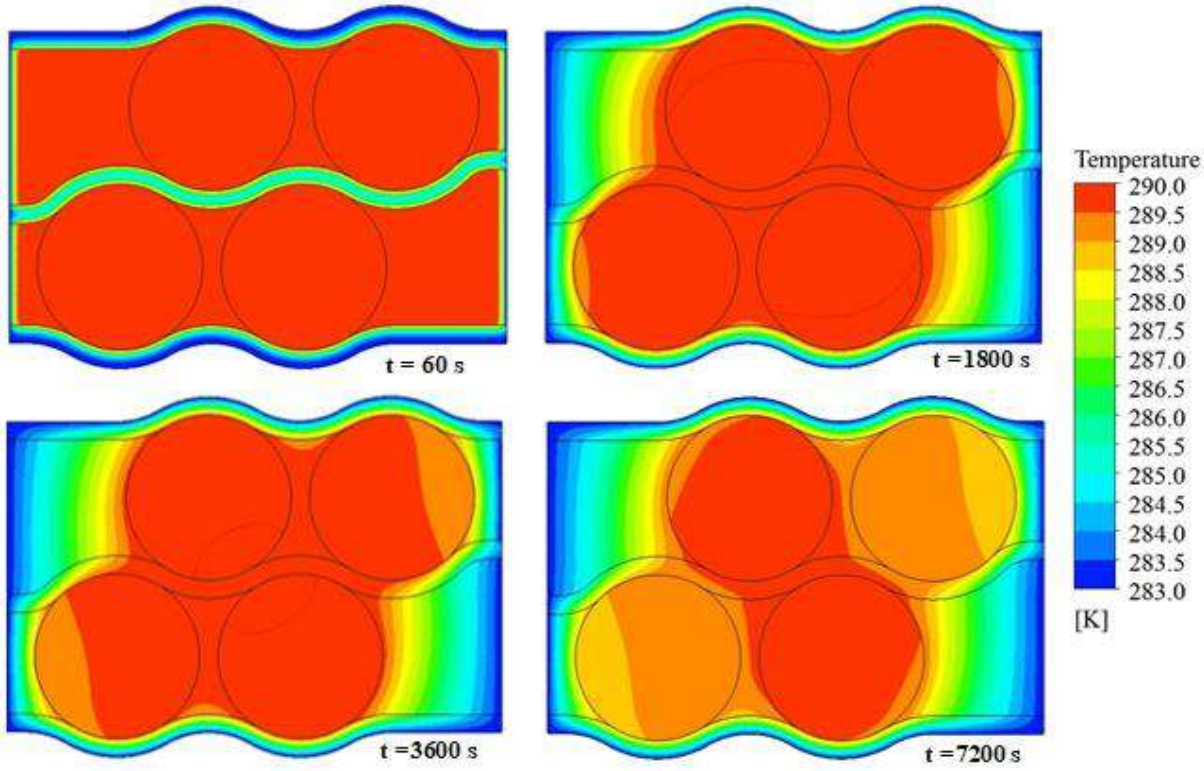

Figure 6. Temperature contours of batteries-on mode

At the end of an hour, the temperature of the batteries is around 16 ºC, at the end of two hours, the temperature of the batteries is around at least 16.5-17 ºC.

The minimum temperature is occurred in batteries at the end of 2 hours around 16 ºC. The graph in Fig. 7 shows the temperature of batteries separately (batteries-off mode).

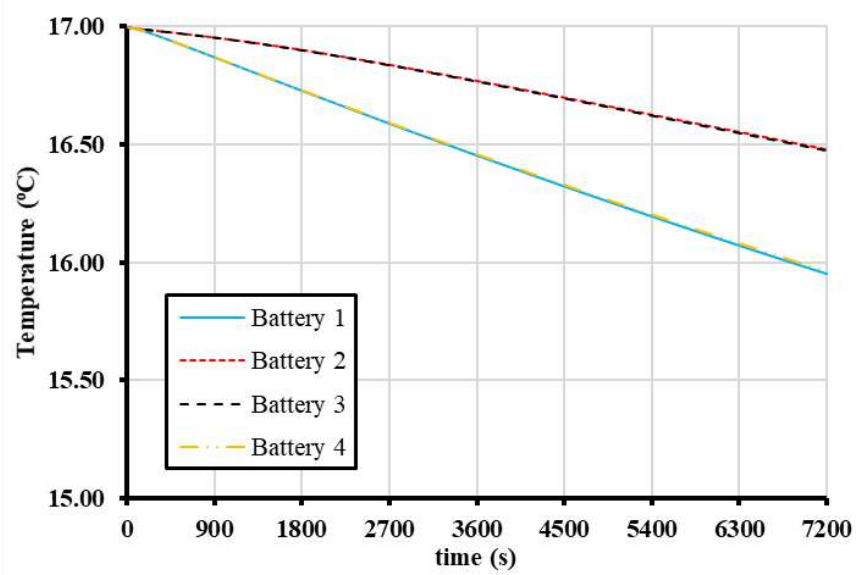

Figure 7. Temperature of batteries vs. time chart (batteries-off mode)

The important point is that all battery temperatures are kept over 15 ºC at the end of two hours. The minimum temperature indicates that the batteries are within the acceptable thermal operating range. Another point to be examined is the solidification behavior of the PCM. Fig. 8 shows the transient mass fraction counters of PCM. Fig. 9 shows the mass fraction vs. time chart of PCM.

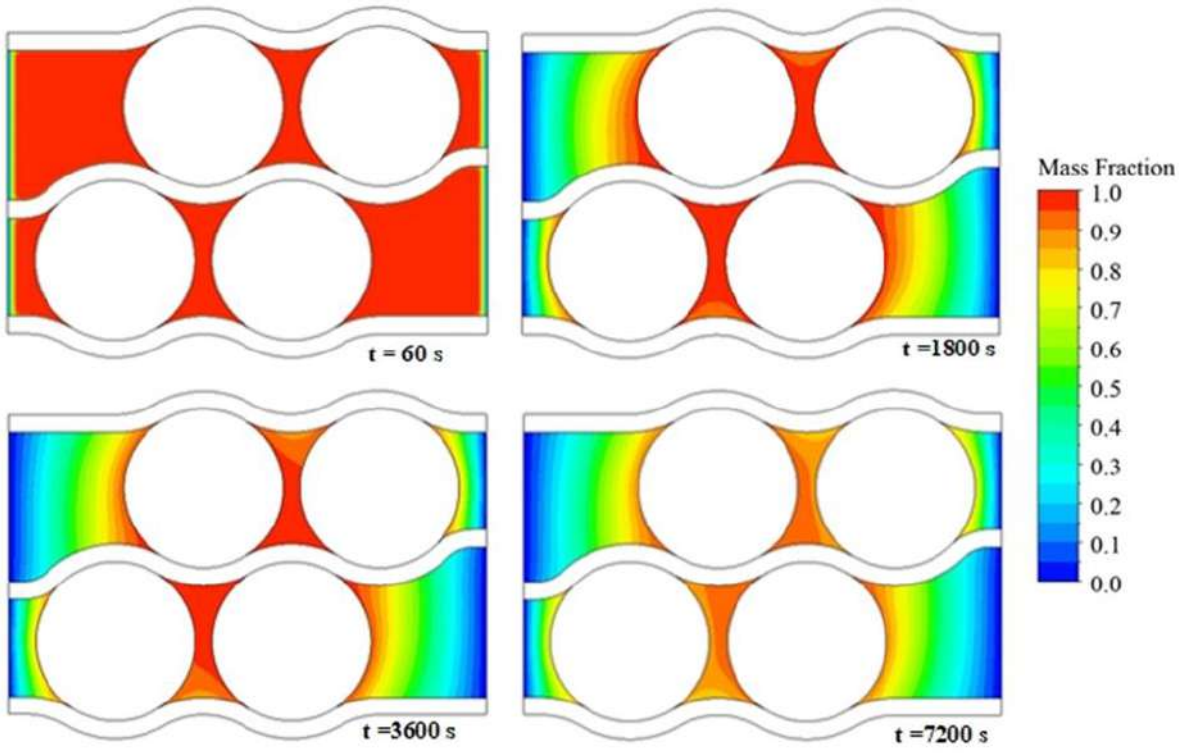

Figure 8. Mass fraction contours of batteries-on mode

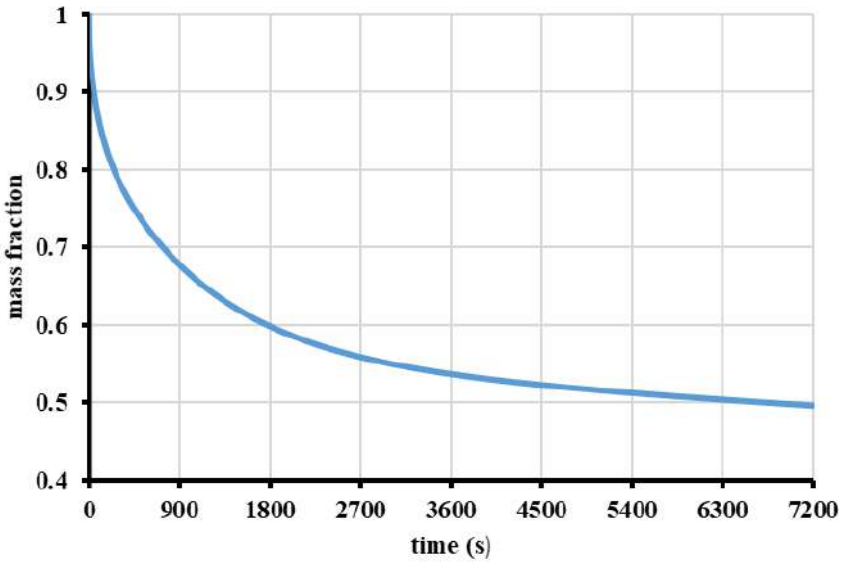

Figure 9. Mass fraction of PCM vs. time chart (batteries-on mode)

PCM, which is initially completely in the fluid phase (colored red), almost half of the PCM completely transitions to the solid phase (colored blue) at the end of two hours. Looking at the half and one-hour, it is seen that the phase change spreads from the outside of the model (from constant temperature boundary conditions).

4. Conclusions

In the model designed in the numerical simulation study the solidification time of even half of the PCM (when the initial temperature of the PCM and batteries is 17 ºC and the environmental boundary condition temperature is 10 ºC) is the same with complete melting time of PCM (when the initial temperature of the PCM and batteries is 17 ºC and the environmental boundary condition temperature is 10 ºC, there is heat generation of batteries and cooling air inlet).

Analysis results show that at the end of the solidification time taken, the time needed for the PCM to solidify completely will be even more. When the batteries-on mode, their temperature does not exceed 40 ºC at the end of 2 hours. When the batteries-off mode, their temperature does not drop below 15 ºC at the end of 2 hours.

The situations modeled in the numerical study show that the design, materials and operating conditions keep the batteries in the desired operating thermal range. In future work, numerical data must be validated with experimental results. The temperature of boundary conditions, batteries' heat generation, geometrical distributions, the thermal behavior of the PCM used, the air inlet temperature and velocity can be variable parameters after validation. Also, 3D numerical analysis in this field with this method can be more reliable.

5. References

[1] R. Zhao, S. Zhang, J. Liu, and J. Gu, "A review of thermal performance improving methods of lithium ion battery: Electrode modification and thermal management system," *J. Power Sources*, vol. 299, pp. 557–577, 2015, doi: 10.1016/j.jpowsour.2015.09.001.

[2] C. Zhao, W. Cao, T. Dong, and F. Jiang, "Thermal behavior study of discharging/charging cylindrical lithium-ion battery module cooled by channeled liquid flow," *Int. J. Heat Mass Transf.*, vol. 120, pp. 751–762, 2018, doi: 10.1016/j.ijheatmasstransfer.2017.12.083.

[3] J. Xu, C. Lan, Y. Qiao, and Y. Ma, "Prevent thermal runaway of lithium-ion batteries with minichannel cooling," *Appl. Therm. Eng.*, vol. 110, pp. 883–890, 2017, doi: 10.1016/j.applthermaleng.2016.08.151.

[4] L. Song, "Thermal Performance Analysis of the Battery Thermal Management Using Phase Change Material," *OALib*, vol. 05, no. 12, pp. 1–5, 2018, doi: 10.4236/oalib.1105127.

[5] J. Sarkar and S. Bhattacharyya, "Application of graphene and graphene-based materials in clean energy-

related devices Minghui," *Arch. Thermodyn.*, vol. 33, no. 4, pp. 23–40, 2012, doi: 10.1002/er.
[6] L. Ianniciello, P. H. Biwolé, and P. Achard, "Electric vehicles batteries thermal management systems employing phase change materials," *J. Power Sources*, vol. 378, no. January, pp. 383–403, 2018, doi: 10.1016/j.jpowsour.2017.12.071.
[7] A. Jarrett and I. Y. Kim, "Design optimization of electric vehicle battery cooling plates for thermal performance," *J. Power Sources*, vol. 196, no. 23, pp. 10359–10368, 2011, doi: 10.1016/j.jpowsour.2011.06.090.
[8] S. Arora, A. Kapoor, and W. Shen, "A novel thermal management system for improving discharge/charge performance of Li-ion battery packs under abuse," *J. Power Sources*, vol. 378, no. November 2017, pp. 759–775, 2018, doi: 10.1016/j.jpowsour.2017.12.030.
[9] M. Lu, X. Zhang, J. Ji, X. Xu, and Y. Zhang, "Research progress on power battery cooling technology for electric vehicles," *J. Energy Storage*, vol. 27, no. November 2019, p. 101155, 2020, doi: 10.1016/j.est.2019.101155.
[10] X. Feng, L. Lu, M. Ouyang, J. Li, and X. He, "A 3D thermal runaway propagation model for a large format lithium ion battery module," *Energy*, vol. 115, pp. 194–208, 2016, doi: 10.1016/j.energy.2016.08.094.
[11] B. Wu, V. Yufit, M. Marinescu, G. J. Offer, R. F. Martinez-Botas, and N. P. Brandon, "Coupled thermal-electrochemical modelling of uneven heat generation in lithium-ion battery packs," *J. Power Sources*, vol. 243, pp. 544–554, 2013, doi: 10.1016/j.jpowsour.2013.05.164.
[12] L. H. Saw, Y. Ye, and A. A. O. Tay, "Integration issues of lithium-ion battery into electric vehicles battery pack," *J. Clean. Prod.*, vol. 113, pp. 1032–1045, 2016, doi: 10.1016/j.jclepro.2015.11.011.
[13] H. Jouhara *et al.*, "Applications and thermal management of rechargeable batteries for industrial applications," *Energy*, vol. 170, pp. 849–861, 2019, doi: 10.1016/j.energy.2018.12.218.
[14] V. Powar and R. Singh, "Stand-alone direct current power network based on photovoltaics and lithium-ion batteries for reverse osmosis desalination plant," *Energies*, vol. 14, no. 10, 2021, doi: 10.3390/en14102772.
[15] M. Farag, H. Sweity, M. Fleckenstein, and S. Habibi, "Combined electrochemical, heat generation, and thermal model for large prismatic lithium-ion batteries in real-time applications," *J. Power Sources*, vol. 360, pp. 618–633, 2017, doi: 10.1016/j.jpowsour.2017.06.031.
[16] Z. Ling *et al.*, "Review on thermal management systems using phase change materials for electronic components, Li-ion batteries and photovoltaic modules," *Renew. Sustain. Energy Rev.*, vol. 31, pp. 427–438, 2014, doi: 10.1016/j.rser.2013.12.017.
[17] W. Wu, X. Yang, G. Zhang, K. Chen, and S. Wang, "Experimental investigation on the thermal performance of heat pipe-assisted phase change material based battery thermal management system," *Energy Convers. Manag.*, vol. 138, pp. 486–492, 2017, doi: 10.1016/j.enconman.2017.02.022.
[18] A. Verma, S. Shashidhara, and D. Rakshit, "A comparative study on battery thermal management using phase change material (PCM)," *Therm. Sci. Eng. Prog.*, vol. 11, no. March, pp. 74–83, 2019, doi: 10.1016/j.tsep.2019.03.003.
[19] A. R. Mazhar, A. Shukla, and S. Liu, "Numerical analysis of rectangular fins in a PCM for low-grade heat harnessing," *Int. J. Therm. Sci.*, vol. 152, p. 106306, 2020, doi: 10.1016/j.ijthermalsci.2020.106306.
[20] M. Safdari, R. Ahmadi, and S. Sadeghzadeh, "Numerical investigation on PCM encapsulation shape used in the passive-active battery thermal management," *Energy*, vol. 193, p. 116840, 2020, doi: 10.1016/j.energy.2019.116840.
[21] Z. An, X. Chen, L. Zhao, and Z. Gao, "Numerical investigation on integrated thermal management for a lithium-ion battery module with a composite phase change material and liquid cooling," *Appl. Therm. Eng.*, vol. 163, no. 66, p. 114345, 2019, doi: 10.1016/j.applthermaleng.2019.114345.
[22] S. Mousavi, M. Siavashi, and M. M. Heyhat, "Numerical melting performance analysis of a cylindrical thermal energy storage unit using nano-enhanced PCM and multiple horizontal fins," *Numer. Heat Transf. Part A Appl.*, vol. 75, no. 8, pp. 560–577, 2019, doi: 10.1080/10407782.2019.1606634.
[23] V. G. Choudhari, A. S. Dhoble, and S. Panchal, "Numerical analysis of different fin structures in phase change material module for battery thermal management system and its optimization," *Int. J. Heat Mass Transf.*, vol. 163, p. 120434, 2020, doi: 10.1016/j.ijheatmasstransfer.2020.120434.
[24] M. Pan and Y. Zhong, "Experimental and numerical investigation of a thermal management system for a Li-ion battery pack using cutting copper fiber sintered skeleton/paraffin composite phase change materials," *Int. J. Heat Mass Transf.*, vol. 126, pp. 531–543, 2018, doi: 10.1016/j.ijheatmasstransfer.2018.06.014.
[25] *ANSYS Fluent Theory Guide 15.0*. ANSYS, Inc.

[26] “RT15 Data Sheet,” 2020. https://www.rubitherm.eu/en/productcategory/organische-pcm-rt.
[27] Y. Wang, T. Gao, L. Zhou, J. Gong, and J. Li, “A parametric study of a hybrid battery thermal management system that couples PCM with wavy microchannel cold plate,” *Appl. Therm. Eng.*, vol. 219, no. PC, p. 119625, 2023, doi: 10.1016/j.applthermaleng.2022.119625.

International Conference on Advances and Innovations in Engineering

Retrogression and Reaging of a Flow Formed 7075 Aluminum Alloy

Eda URAL[1], Erdem BALCI[2], Mertcan KABA[3], Aptullah KARAKAŞ[4], Murat BAYDOĞAN[5]

[1,2,3,5]Department of Metallurgical and Materials Engineering, Istanbul Technical University, Istanbul, Türkiye.
[4]Repkon Machine and Tool Industry, Istanbul, Türkiye.
[1]edaural2@gmail.com, [2]balcier@itu.edu.tr, [3]mertcankaba@itu.edu.tr, [4]aptullah.karakas@repkon.com.tr, [5]baydogan@itu.edu.tr

[1](ORCID: 0000-0002-9683-0898), [2](ORCID: 0000-0002-9032-0467), [3](ORCID: 0000-0001-8565-0421), [4](ORCID: 0000-0003-0773-5483), [5](ORCID: 0000-0002-3683-8476)

Abstract

In this study, retrogression and reaging (RRA) heat treatments were applied to a flow formed AA7075 alloy, and variation of hardness and electrical conductivity with respect to the retrogression time was evaluated. Because there is a well-known correlation between the electrical conductivity of aged aluminum alloys and their corrosion resistance, increased electrical conductivity was taken as an indicator of a higher corrosion resistance. The flow forming was applied in three thickness reductions such as 40%, 55%, and 75%. Retrogression was applied from 5 s to 20 min in a salt bath at 220 □C, followed by reaging at 120 □C for 24 h. The hardness was measured by Vickers hardness test, and electrical conductivity was measured by a conductivity meter in the unit of %IACS (International Annealed Copper Standard). The results showed that the electrical conductivity continuously increased with the increase of retrogression times. The highest electrical conductivity (44% IACS) was obtained in the sample, which was flow formed by 55%, retrogressed for 20 min, and then reaged. In contrast to increase in the electrical conductivity, there was no increment in hardness upon reaging for the flow formed samples. The results suggest that RRA heat treatment is beneficial to increase electrical conductivity of a flow formed aluminum alloy, and thus has a potentiality to be considered to improve the corrosion resistance of the flow formed alloys.

Keywords: Al 7075, electrical conductivity, flow forming, retrogression and reaging, RRA.

1. Introduction

The process of flow forming enables forming of tubular steel and aluminum products by controlling material flow and deformation. Because it is conducted at room temperature, it contributes to hardness and strength by strain hardening mechanism [1].

Retrogression and reaging (RRA) heat treatment is applied to alloys in the T6 temper condition. The retrogression process is carried out by heating the alloy to a temperature between solution annealing and aging temperatures and holding it at that temperature for a time, and quenched afterwards. During this process, precipitate phases within the matrix dissolve, and the precipitates at the grain boundaries get coarsen. In the reaging stage, where the retrogressed alloy is reaged at the same temperature and time of T6 temper, the formation of precipitate phases within the matrix is promoted again. Following the retrogression and reaging (RRA) process, a more stable structure is obtained with a greater number and larger size of precipitate phases compared to the T6 temper condition [2]. While preserving mechanical properties through the RRA process at a level of close to T6 temper, an increase in electrical conductivity and corrosion resistance is also obtained. Although the RRA heat treatment for AA7075 alloy has been extensively studied in the literature up to date, it has not been investigated for a flow formed AA7075 alloy. It is therefore this study aims to investigate the potentiality of the RRA process for a flow formed AA7075 alloy, which are used in aerospace and automotive industries.

[1]Corresponding author

2. Experiments

AA7075 alloy was received in O-temper (annealed) condition. Its hardness and electrical conductivity were 82 HV1 and 41 % IACS, respectively. AA7075-O alloy tubes (preform samples) were first solution annealed at 470 □C for 1 h, quenched in PA8 containing water, flow formed at room temperature by a thickness reduction ratio of 40%, 55% and 75%, and then aged at 121 □C for 24 h. These samples were designated as T8 temper because the flow forming was applied between the solution annealing and artificial aging. Some samples were not given such an intermediate flow forming, and they were designated as T6 temper. The samples in T8 temper condition were retrogressed at 220 □C for various times between 5 s and 20 min in a salt bath containing AS135 annealing salt. The retrogression temperature and time were determined from the previous works in the literature [3,4]. The salt bath was stirred prior to the retrogression to ensure uniform temperature distribution throughout each region, and its temperature was continuously monitored using a Ni-NiCr thermocouple (Type K). After the retrogression process, the samples were removed from the salt bath, quenched in water at the room temperature, and reaged at 121 □C for 24 h.

Hardness measurements of the samples were performed by using a Wilson Hardness tester with a diamond pyramid indenter under a 1 kg load (HV1). Five measurements were taken for each sample, and the results were averaged. Electrical conductivity measurements were conducted using the Hocking Electrical Conductivity Meter Auto Sigma 3000 DL instrument operating according to the eddy current principle. A 500 kHz probe was used for conductivity measurements, and average of 5 measurements was taken as the conductivity of the samples.

3. Results

Figure 1 shows hardness variation of R and RRA samples with retrogression times after being flow formed 40%, 55%, and 75% (Figures 1a to c), and that of T6 sample without flow forming (Figure 1d). For the R and RRA samples, the hardness continuously decreased below T6 temper level (182 HV1) regardless of the flow forming ratio. Also, there was no clear difference among the hardness depending on the flow forming ratio. This leads to an important conclusion that the flow forming prevents the activation of the retrogression and reaging process for AA7075 alloy. On the other hand, as seen in Figure 1d, the samples without flow forming responded well to R and RRA heat treatments, i.e. the hardness gives a minimum with increasing retrogression time after retrogression due to dissolution of coherent phases (GP zones, η' precipitates) within the matrix, and it increases again after reaging due to the formation of the matrix precipitates [5].

Considering that the horizontal dashed lines in Figure 1a to c represent the values of the flow formed and aged samples (T8 temper condition), and the dashed line in Figure 1d represents the hardness of T6 sample, it is seen that T6 sample has a hardness of 182 HV1. Application of the flow forming by 40% decreases the hardness to about 160 HV1. Increase the flow forming ratio to 55% slightly increases the hardness to 168 HV1, and further increment in the flow forming ratio to 75% decreases the hardness again to 162 HV1. It is seen from these results that moderate level of flow forming, i.e. 55% in this study, might be beneficial to increase hardness. However higher ratio of flow forming reduces it.

Figure 2 shows the variation of electrical conductivity of R and RRA samples with retrogression times after being flow formed 40%, 55%, and 75% (Figures 2a to c), and that of T6 sample without flow forming (Figure 2d). R and RRA heat treatments increase the electrical conductivity of flow formed alloys with the increase in retrogression time up to 20 min. However, it was noted a small decrease in the electrical conductivity for short retrogression times for R samples followed by a continuous increase up to 20 min of retrogression time. This is attributed to dissolution of microstructural components at short retrogression times, and formation of the precipitates afterwards. For the RRA samples, there was a continuous increment in the electrical conductivity up to 20 min depending on the formation of precipitates within the grains. Among the R and RRA samples, there was no marked change in the electrical conductivity depending on the flow forming ratio for a given retrogression times, except that the highest electrical conductivity (44% IACS) was achieved with the flow forming of 55% for a retrogression time of 20 min.

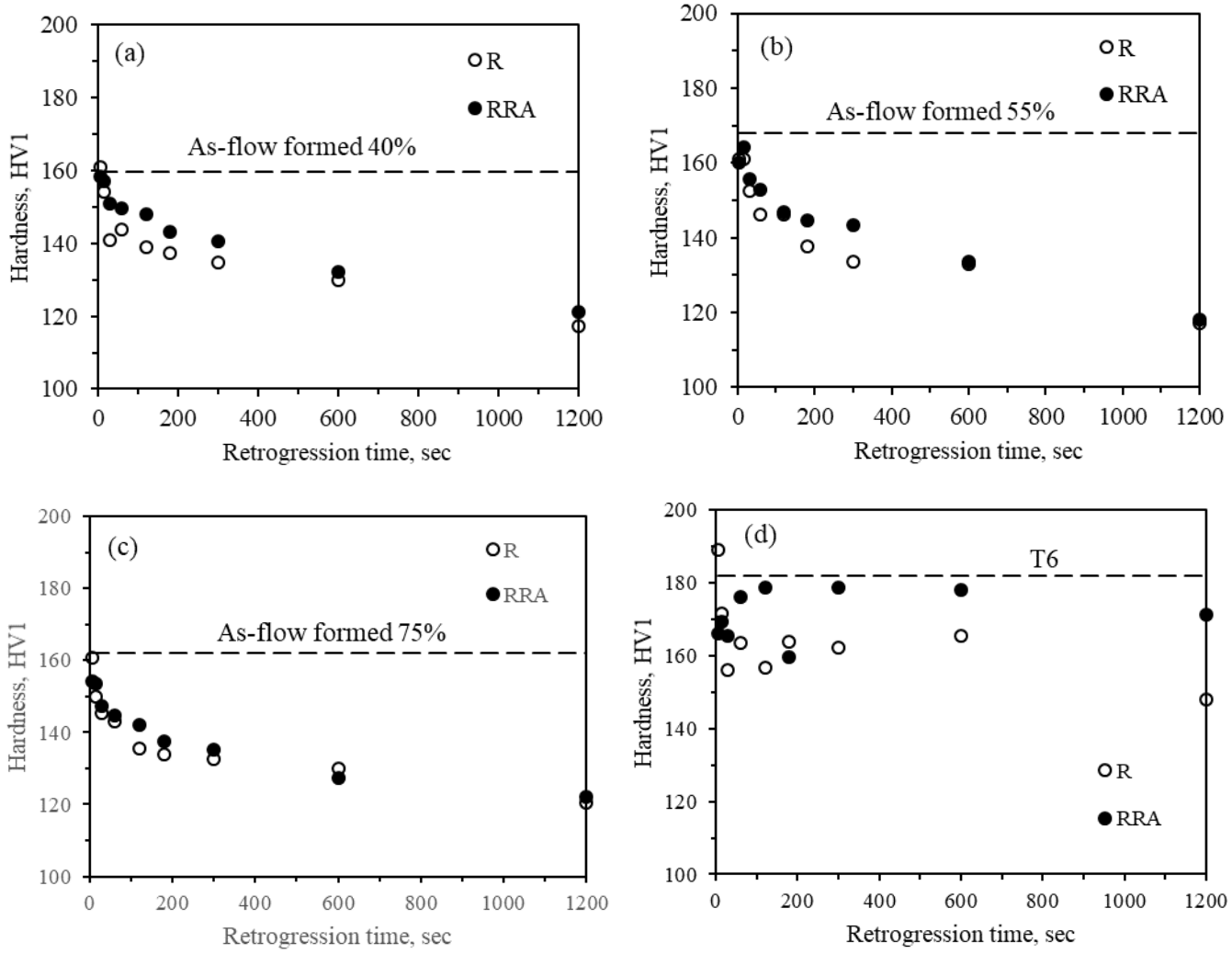

Figure 1. Variation in hardness with retrogression time after R and RRA heat treatments for (a) 40%, (b) 55%, (c) 75% flow formed samples, and (d) T6 sample without flow forming.

The horizontal dashed lines in Figure 2a to c represent the values of the flow formed and aged samples (T8 temper condition), while the dashed line in Figure 2d represents the electrical conductivity of T6 sample. The electrical conductivity of the preform sample is 41 % IACS. It decreases to 31 % IACS for T6 temper. By the application of flow forming, electrical conductivity was measured as 36% IACS for 40% and 55% flow formed samples, and to 37.4% IACS for the 75% flow formed sample. It shows that electrical conductivity of AA 7075 Al alloy in O temper decreases upon aging to T6 temper condition, and the flow forming increases the electrical conductivity with respect to that of T6 temper condition. It also shows that the highest electrical conductivity was obtained from the sample subjected to the highest ratio of flow forming.

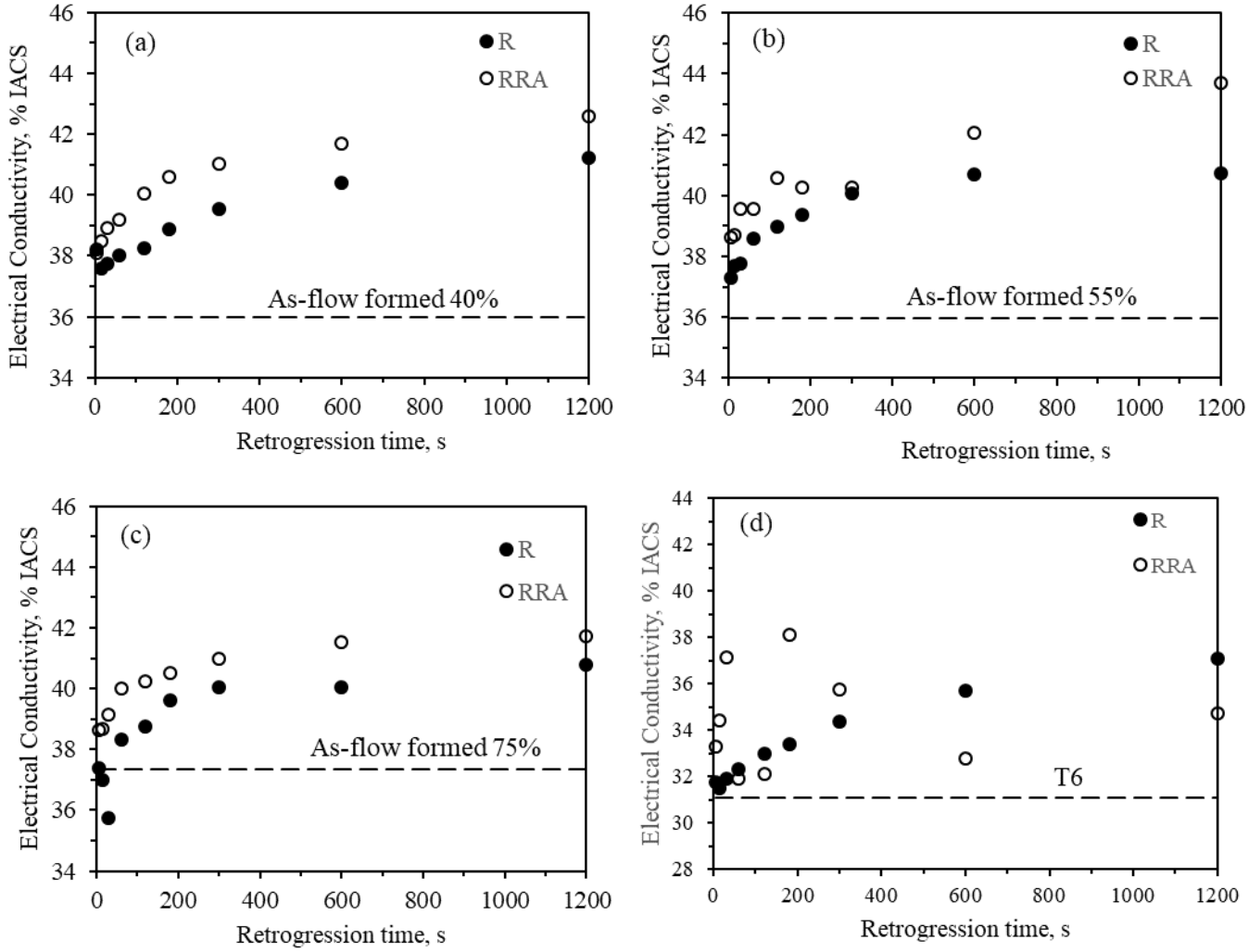

Figure 2. Variation in electrical conductivity with retrogression time after R and RRA heat treatments for (a) 40%, (b) 55%, (c) 75% flow formed samples, and (d) T6 sample without flow forming.

4. Conclusions

The following conclusion can be drawn from the present study:

1. AA 7075-O tubes have a hardness of 82 HV1 and an electrical conductivity of 41 % IACS. Upon aging to T6 temper, hardness increases to 182 HV1 with a corresponding decrease of electrical conductivity to 31 % IACS. This corresponds to a hardness increment of 122%, and an electrical conductivity decrement of 24 % upon aging.
2. 7075-T6 samples, when retrogressed and reaged, the maximum hardness was obtained at a retrogression time of 5 min as 178 HV1, which is close to that of T6 temper condition (182 HV1), and the electrical conductivity of this sample was 35% IACS, which was 13% higher than that of T6 level.
3. The hardness values of the flow formed samples were 160 HV1, 168 HV1, and 162 HV1 for 40%, 55%, and 75% flow formed samples, respectively. It shows that the highest hardness was obtained by the moderate level of flow forming (55%).
4. When the flow formed samples were retrogressed and reaged, the hardness was continuously decreased with the increase in retrogression time, and no hardness increment was observed. The maximum decrement in hardness was 32-34% with a corresponding increase in electrical conductivity about 35-37%. This indicates that the flow formed samples did not respond to RRA heat treatment in contrast to T6 sample.

5. Acknowledgements

The authors would like to express their sincere thanks to Repkon Machine and Tool Industry and Trade Inc. for their support on the main subject of the study and supply of the samples.

6. References

[1] Y. Zhang, F. Wang, J. Dong, L. Jin, C. Liu, W. Ding. "Grain refinement and orientation of AZ31B magnesium alloy in jot flow forming under different thichness reductions". Journal of Material Science & Technology, 34, 1091-1102, 2018.

[2] Baydoğan, M. Investigation of Mechanical and Corrosion Properties of Retrogressed and Reaged 2014 and 7075 quality Aluminium Alloys. PhD Thesis, Istanbul Technical University, Istanbul, Turkey, 2003.

[3] Rajan, K., Wallace, W., Beddoes, J.C. "Microstructural Study of a High Strength Stress Corrosion Resistant 7075 Aluminum Alloy". Journal of Materials Science, 17, 2817-2824, 1982

[4] Park, J.K. "Influence of Retrogression and Reaging Treatments on the Strength and Stress Corrosion Resistance of Aluminum Alloy 7075-T6". Materials Science and Engineering A103, 223-231, 1988.

[5] Park, J.K. and Ardell. "Effect of Retrogression and Reaging Treatments on the Microstructure of Al-7075-T651". Metallurgical Transactions A, 15, 8, 1531-1543, 1984.

International Conference on Advances and Innovations in Engineering

Confocal Raman Studies on mafic volcanics north of Fahribey (Elazığ)

Mutlu Ercan ÇELİK[1] , Melek URAL [2]

[1,2]Department of Geology, Engineering Faculty, Firat University, Elazığ, Turkey.
[1]mutluercancelik@gmail.com, [2]melekural@firat.edu.tr

[1](ORCID: 0000-0002-4034-8613), [2](ORCID: 0000-0002-4174-6058)

Abstract

Mafic volcanogenic rocks outcropping in the north of Fahribey village in the east of Elazığ province, located on the Eastern Taurides and Bitlis suture belt, are mainly composed of plagioclase, pyroxene, opaque minerals, and are intergranular, subophytic, which is the typical texture of the rocks. All observations and determinations define the rocks in this area as dolerite and basalt. Within the scope of detailed mineralogical studies, plagioclase, pyroxene, opaque minerals were examined for the first time from the mafic volcanic rocks around the north-northeast of Fahribey village in the east of Elazığ with the help of the Confocal Raman Spectrometer instrument, which helps to examine minerals and rocks with a non-destructive method, and their augite, albite, labrarite, and albiteite minerals were examined for the first time. Secondary mineral formations such as epidote have been detected together with other type minerals.

Keywords: Fahribey, Raman spectroscopy, mafic volcanic rocks.

1. Introduction and Geology

Petrographic studies are essentially the study of minerals in thin sections; Imaging Raman spectroscopy is particularly well suited for this task, given that it interprets the identity of each mineral in a rock, making inferences about the rock's formation, history, alteration history, and can be used not only to identify minerals but also to map their appearance (Fries and Steele, 2010).

In order to accurately distinguish the composition and distribution of chemical phases in an inorganic material, many tools are available in the analytical toolkit: XRD, EPMA, TEM, SEM-EDXS, IR, which have specific requirements for their use and hence cost (operational and capital) Raman imaging, which gives successful results even on rough surfaces without requiring any operation, is a very successful and preferable method when compared with aspects such as time (scanning time, analysis time), ease of use (Polavaram and Garg, 2021).

For this purpose, with the help of Confocal Raman Spectrometer studies, plagioclase and pyroxene minerals from the mafic volcanic rocks (Figure 2, 3) around the north-northeast of Fahribey village in the east of Elazığ province (Figure 1) were examined.

[1]Corresponding author

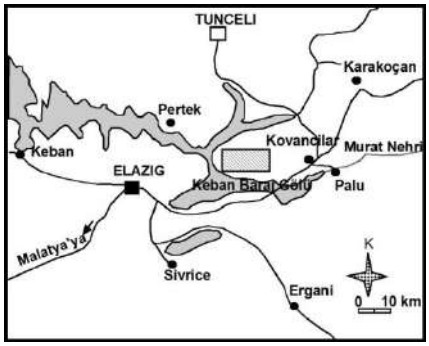

Figure 1. Location map of the study area

Figure 2. Pillow lavas intercalated with volcaniclastics. North of Fahribey village. ÇAB-5

Figure 3. Volcanogenic mudstones overlying the spilitic lavas. North of Fahribey village. ÇAB-5

2. Material and Method

This study was carried out to reveal the mineralogical properties of mafic rock samples with detailed petrographic and Confocal Raman spectroscopy, and suitable samples for this purpose were prepared in advance with the help of Horiba Jobin Yvon Labram HR model Raman Confocal Spectrometer device at Ankara University YEBİM Mineralogy-Petrography Research Laboratories. and analyzed on spots on polished glass material.

3. Petrography

The mafic volcanogenic rocks outcropping in the north of Fahribey village are dominated by plagioclase (45-60%), pyroxene (20-45%), opaque minerals (5-10%), and doleritic textured sections (both in the inner parts of the pillows and In the massive vascular stocks, quite abundant and sufficiently coarse plagioclase laths and pyroxenes are observed as intertwined subophytic or intergranular textures (Figure 4).Poikilitic texture is also observed in both plagioclase and pyroxenes. Euhedral or subhedral crystals are pink, blue, orange in colors in the recognizable and abundant sections. They attract attention with their vivid interference colors in the 2nd row. In these sections, zoning and karlspar twins are observed in the pyroxenes in a usual way, as well as the abundance of opaque mineral formation. Opaque minerals are observed especially in euhedral and subhedral doleritic or subophytic sections. In some sections, pyroxenes are pseudomorph and they are filled with materials in the form of opacification + carbonation. While dense calcite and chlorite fillings are observed both in the cavities in the amygdaloidal sections and in spilitic rocks filled with fractures, chloritization and opacification type alterations are observed from the dough and or glass. The doleritic texture formed by swallowtail elongated plagioclases and accompanying pyroxenes is typical, and the pyroxenes in these rock sections show alterations in the type of epidotization. All observations and determinations define the rocks in this area as dolerite and basalt.

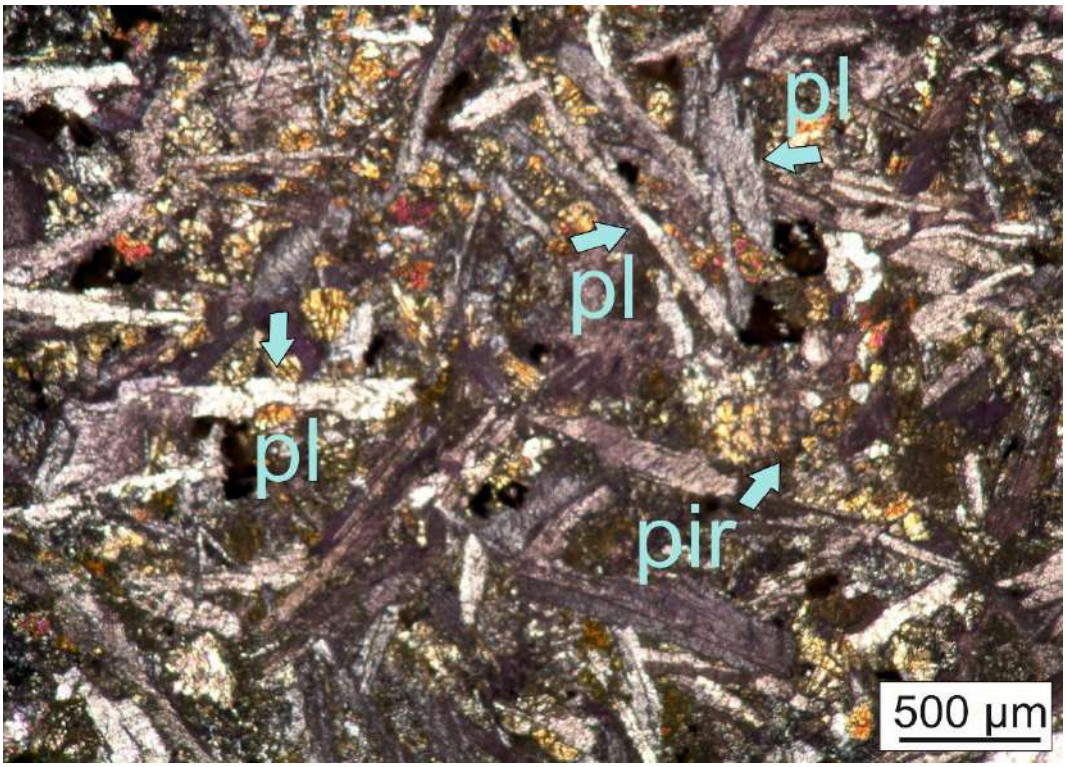

Figure 4. Subophytic and intergranular basalt. North of Fahribey. Locally zoned plagioclases with swallowtail appearance, epidotized pyroxenes in places. Pir: pyroxene, pl: plagioclase.

4. Confocal Raman Studies

Based on Confocal Raman Spectrometer studies, analysis view of the plagioclase mineral in the basaltic pillow lava ÇAB-7 outcropping in the north of Fahribey village (Figure 4, 5), measured Raman peaks (Figure 6), Raman spectrum (Figure 7), measured from small to large peak. values 117.64, 156.03, 175.84, 190.70, 214.23, 258.80, 276.14, 295.33, 334.96, 422.25, 462.50, 484.17, 513.27, 551.65, 538.85, 646.38, 679.19, 768.35, 819.12, 983.18, 6, 116.92 (Figure 7). comes out. 'Albite', a tectosilicate group mineral with $NaAlSi_3O_8$ composition, is the obtained composition.

Within the scope of Confocal Raman Spectrometer studies, plagioclase, pyroxene and opaque mineral measurements in samples no. ÇAB-5 from the mafic volcanic rocks in the north of Fahribey village were also carried out. With the help of Raman peaks obtained as a result of the measurement, the minerals obtained respectively are labradorite, augite and magnetite.

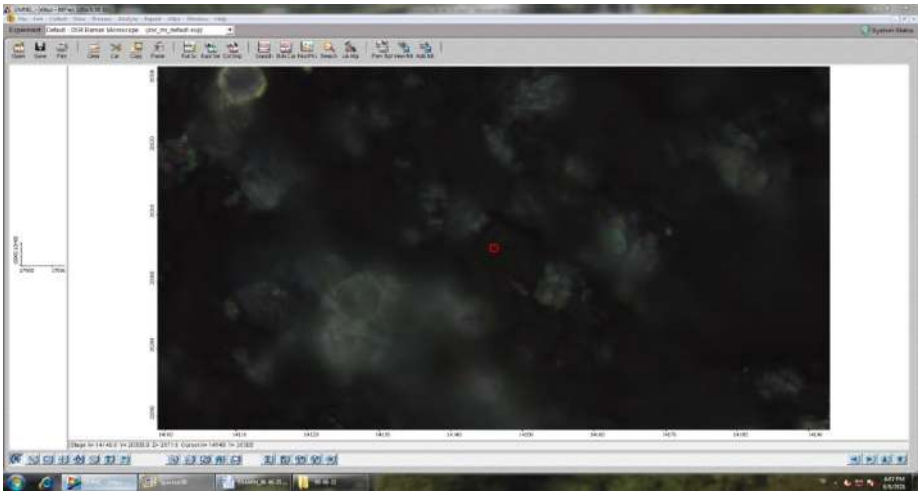

Figure 5. The appearance of the albite (plagioclase) mineral in the basalts in the north of Fahribey village in the Confocal Raman Spectrometer and the analyzed point views. Sample No: ÇAB-7.

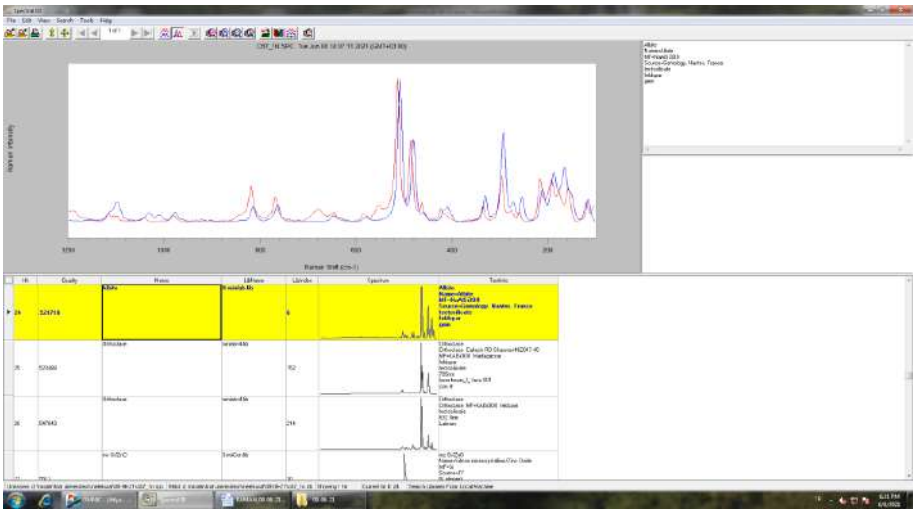

Figure 6a,b. Measured peak graphs of albite (plagioclase) mineral in basalts north of Fahribey village. The blue line is the reference peak, the red line is the measured peak. Sample No: ÇAB-7

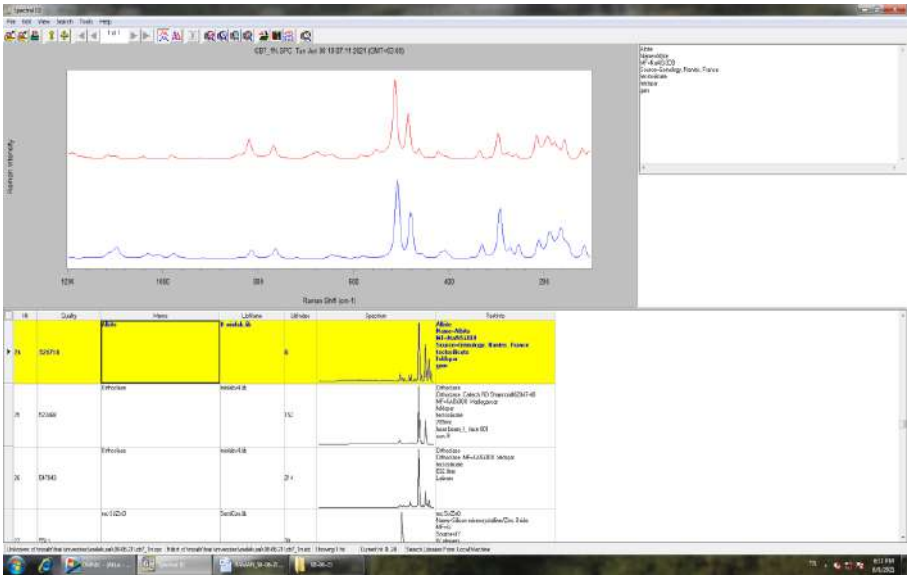

Figure 6a,b. Measured peak graphs of albite (plagioclase) mineral in basalts north of Fahribey village. The blue line is the reference peak, the red line is the measured peak. Sample No: ÇAB-7 (Continue)

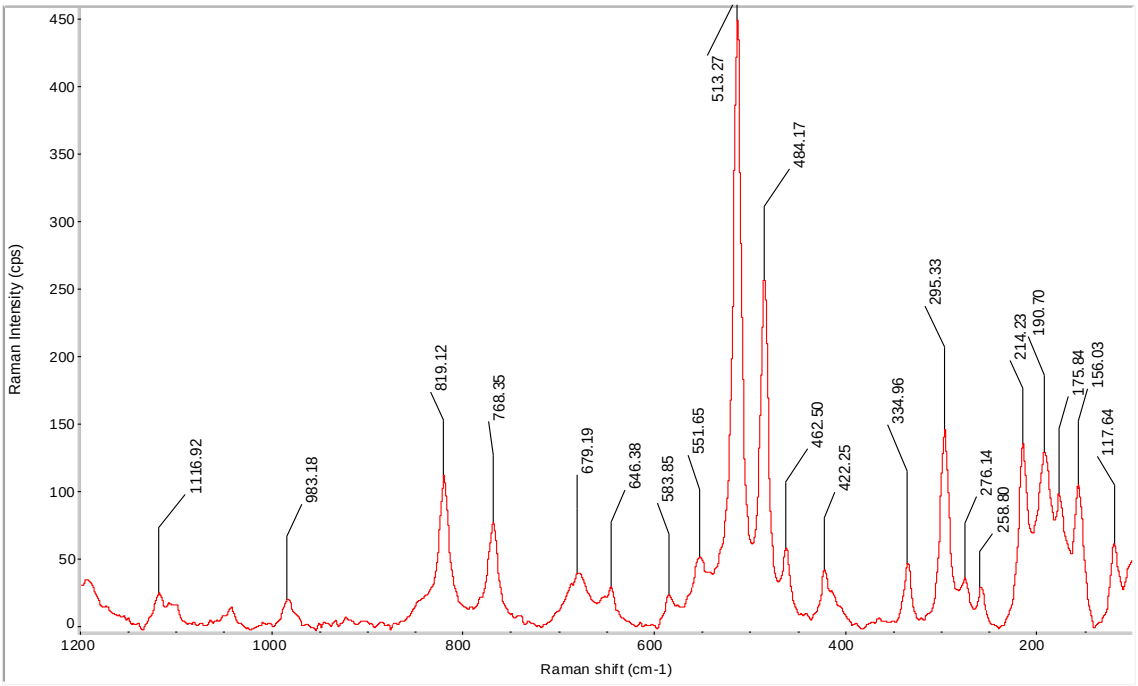

Figure 7. Raman peak spectrum of albite (plagioclase) mineral in basalts north of Fahribey village. Sample no: ÇAB-7

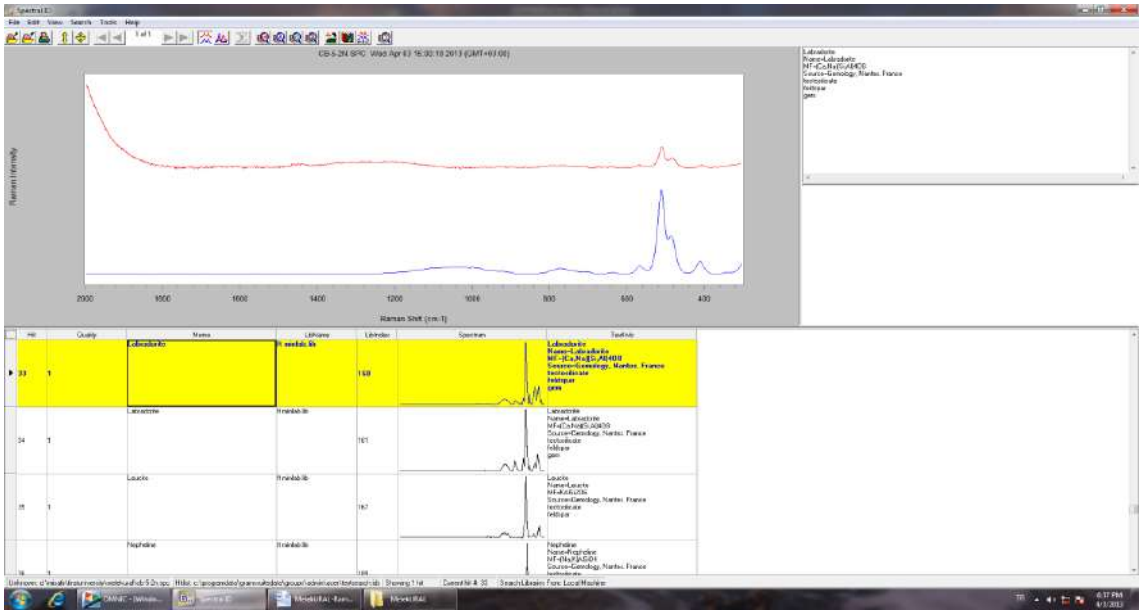

Figure 8. Peak measurement graph on labradorite (plagioclase) mineral in basalts north of Fahribey village. The blue line is the reference peak, the red line is the measured peak

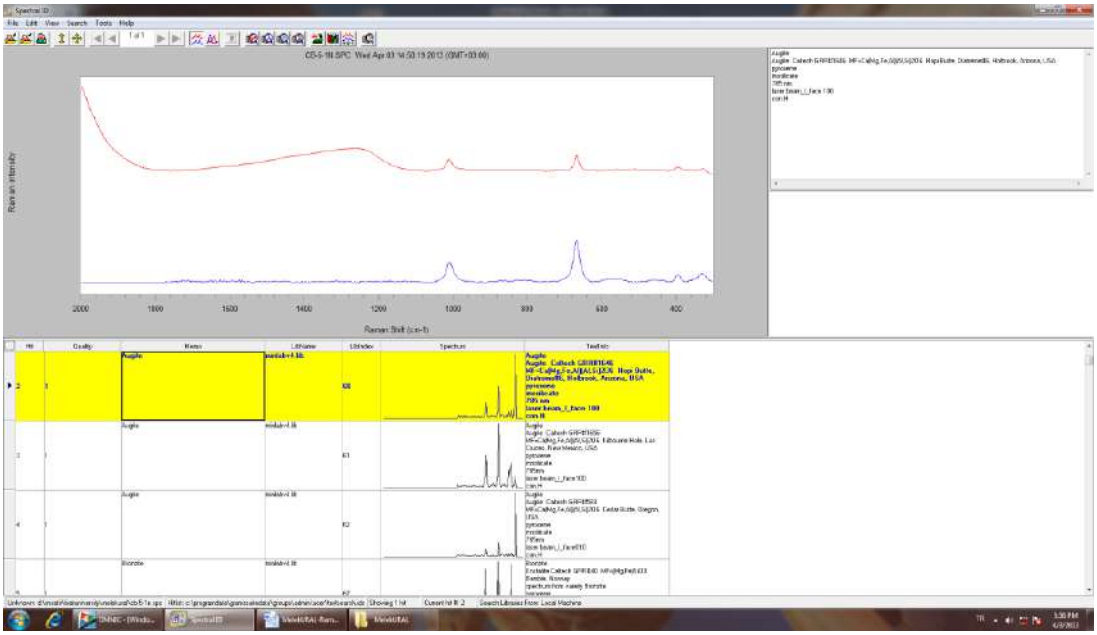

Figure 9. Peak measurement graph on augite (pyroxene) mineral in basalts north of Fahribey village. The blue line is the reference peak, the red line is the measured peak

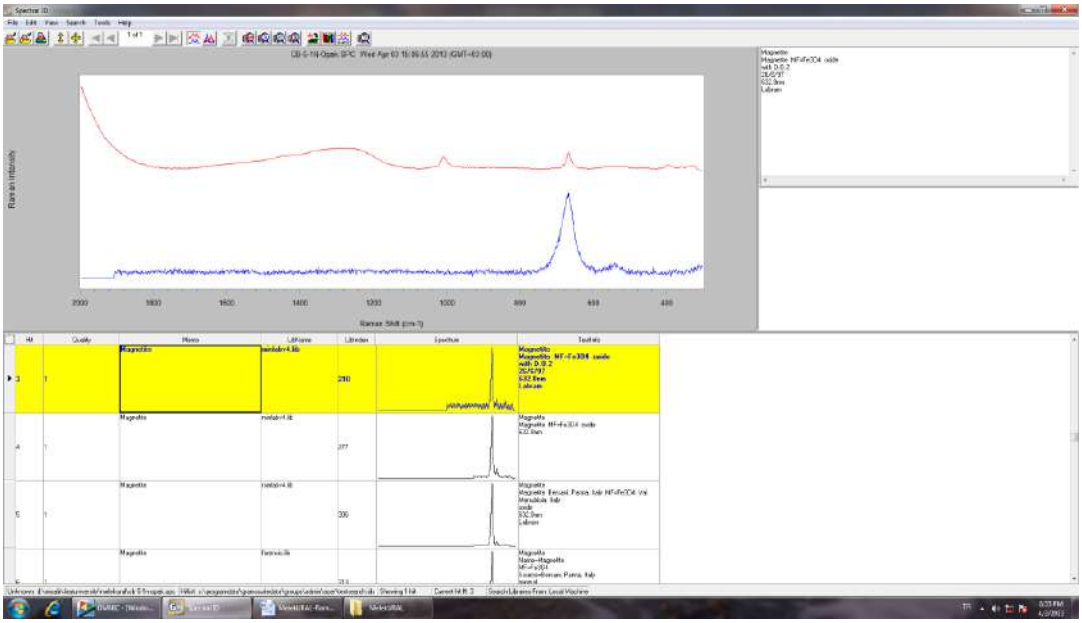

Figure 10. Peak measurement graph on magnetite (opaque) mineral in basalts north of Fahribey village. The blue line is the reference peak, the red line is the measured peak.

Within the scope of Confocal Raman Spectrometer studies, the Raman peaks obtained as a result of the pyroxene mineral measurement in the mafic volcanic rock sample ÇAB-21 in the north of Fahribeyköy belong to the augite mineral in Figure 11.

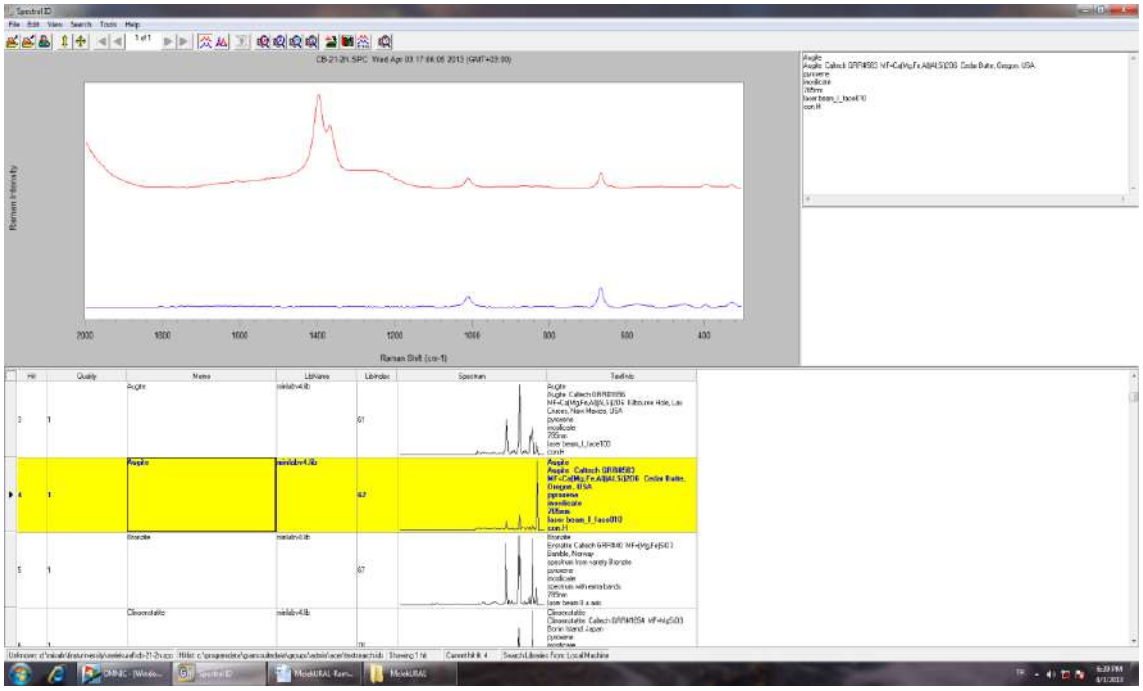

Figure 11. Peak measurement graph on augite (pyroxene) mineral in basalts north of Fahribey village. The blue line is the reference peak, the red line is the measured peak.

5. Discussion and Results

Plagioclase minerals in basaltic pillow lavas cropping out in the north of Fahribey village were determined as albite, labradorite, pyroxene and opaque minerals as augite and magnetite. The Raman peaks obtained as a result of the pyroxene mineral measurement in the mafic volcanic rock sample in the north of Fahribey village belong to the augite mineral.

6. References

[1] Fries, M. & Steele, A. (2011). Raman Spectroscopy and Confocal Raman Imaging in Mineralogy and Petrography. In T. Dieing, O. Hollricher, & J. Toporski, J. (Eds). Confocal Raman Microscopy (pp. 111–135). Springer-Verlag, Berlin, Heidelberg.

[2] Polavaram, K.C. & Garg, N., (2021). Enabling phase quantification of anhydrous cements via Raman imaging. Cem Concr Res. 150.

International Conference on Advances and Innovations in Engineering

Production and Characterization of Graphene Nanohseets+Boron Nitride Nanosheets-doped CdS by Sol-Gel Method

Seval Hale GÜLER [1]

1, Rare Earth Elements Application and Research Center (MUNTEAM), Munzur University, Tunceli, Turkey.
[1]sevalhaleguler@munzur.edu.tr,

1(ORCID: 0000-0001-5888-9437),

Abstract

Due to the abundance of the solar spectrum in the universe, photocatalysts capable of responding to the visible conductive some semiconductor conductors to explode. Among them, CdS is one of the semiconductors under intense scrutiny due to its desired band gap of 2.4 eV and its high absorption rate in the solar spectrum. However, the photocatalytic realization of CdS is at its limit to ensure its real survival. The main reason for this operation is due to the rapid reunification of actively owned cargo ships. Graphene, honeycomb crystal structure, running sp^2 hybridization of C atoms forming the structure, guide as a material with zero band gap. Because of its excellent electrical conductivity, graphene accepts activated electrons in the semiconductor and transfers them efficiently if it is doped into a semiconductor. This in turn leads to times of recombination of holes and electrons and increased lifespan of freighters. As a result, the photocatalytic services of graphene-doped nanocomposites are greatly improved. Another missing point in CdS photocatalysts is; In case of excessive irradiation, they may undergo photocorrosion. Boron nitride nanosheets have been used to eliminate the corrosion resistance of various organic coatings used in semiconductors. For these reasons, CdS matrix Graphene nanosheets (GNS) and boron nitride nanosheets (BNNS) are co-doped with this assumption. Graphene nanolayers and boron nitride nanolayers, which are used as reinforcements, were produced by liquid phase exfoliation method. CdS, on the other hand, was produced with the sol-gel method, and GNS+BNNS supplements were produced with sol-gel. The obtained samples were subjected to analysis obtained by X-ray diffraction (XRD) and scanning electron microscopy (SEM). It has optical properties of samples obtained by UV-vis spectrometry.
GNS+BNNS-doped CdS was successfully synthesized and experienced difficulties in its homogeneous distribution with increasing doping ratio. In addition, with the increasing reinforcement ratio, a significant decrease in reflected values was detected in all of them. The band-gap values of the samples managed to decrease with the reinforcement ratio.

Keywords: Graphene, Boron Nitride nanosheet, Cadmium sulfide, sol-gel

1. Introduction

CdS is a photocatalyst that can be activated by visible light, with a bandgap of 2.4 eV and an n-type semiconductor property. It is one of the most prominent metal sulfides for photocatalytic degradation. CdS absorbs visible light at 516 nm and has an excellent carrier transport ability that allows it to efficiently transfer the electrons and holes generated by light, prolonging their lifetime and enhancing the photocatalytic performance [1-5]. CdS has two different crystal morphologies: hexagonal and cubic. The cubic crystal, also known as the zinc blende phase, has a tetrahedral shape, which belongs to the equiaxed type with facial configuration. The hexagonal crystal, also known as the wurtzite phase, has a hexagonal cone shape [5-7]. TiO_2 and ZnO are currently the most popular semiconductor photocatalysts because of their non-toxicity, low cost and photochemical stability [8]. However, they also have some drawbacks that limit their photocatalytic activity, such as the wide band gap and the recombination of the charge carriers. CdS and CdS-based catalysts also have some main disadvantages, such as low photocatalytic activity and poor photostability, caused by severe photocorrosion and fast charge carrier recombination [9, 10]. To overcome these disadvantages, 2D nanomaterials can be doped into CdS.

[1]Corresponding author

Graphene, an allotrope of carbon, boasts remarkable electronic, optical, thermal, and mechanical properties that find applications across a spectrum of fields. Its unique attributes have led to substantial research interest, making it a significant area of exploration [11]. Discovered in 2004, graphene represents a novel form of carbon nanomaterial, captivating attention due to its monolayer-thick, two-dimensional configuration, where carbon atoms are intricately bonded through sp^2 bonds [12, 13]. Remarkably, graphene stands as the thinnest nanomaterial, possessing a tensile strength of 125 GPa, an elasticity modulus of 1.1 TPa, and a two-dimensional in-plane rupture strength of 42 $N.m^{-2}$. Despite its impressive electron mobility of 2 x 105 cm^2 (V^{-1} s^{-1}), graphene remains primarily influenced by impurities and defects. Its thermal conductivity reaches up to 5.5x103 W ($m^{-1}K^{-1}$). These unparalleled physical attributes position graphene for a diverse array of applications, including nanoelectronic devices, energy storage, thermally conductive materials, optoelectronic devices, and sensors [14, 15].

A single planar nanosheet of boron nitride (BN) consists of a few atomic layers, with alternating boron (B) and nitrogen (N) atoms forming a distinctive honeycomb network of B3-N3 hexagons through sp^2 bonding [16, 17]. Covalent bonds hold the B and N atoms together, while weak van der Waals forces maintain the layer cohesion, resulting in an interplanar spacing of 0.334 nm. These nanosheets share a similar lattice parameter and crystalline structure with graphene. Therefore, they possess significant potential for use in comparable or complementary electronic and composite devices.

For instance, BN nanosheets (BNNSs) are considered ideal dielectric and substrate materials for graphene-based nano-electronic devices due to their atomically smooth surface, which is relatively free from dangling bonds and charge traps [18]. Additionally, the material's excellent thermal and chemical stability, along with its remarkable resistance to oxidation, have quickly paved the way for new applications in high-performance nano-electronic devices.

In this study, graphene nanolayers and boron nitride nanolayers were doped together to see the effect of nanolayers on CdS. Graphene nanolayers and boron nitride nanolayers were synthesized by liquid phase exfoliation method.

2. Experımental Procedure

2.1. Production of nanosheets in graphene and boron nitride

In this study, liquid phase exfoliation method was used to synthesize graphene. This method is based on the separation of layers by placing solvent atoms between hexagonal graphite powders. In this study, hexagonal pure graphite (Merck, purity 99.5%) was used as the starting material. In order to increase the distance between the graphite layers and thus increase the possibility of the solvent atoms to settle, expanded graphite was first produced. For this, the graphite powder was mixed in an acid mixture consisting of H_2SO_4 and HNO_3 for 12 hours. Then it was separated from the acid mixture and washed with distilled water until the pH level of the powder reached equilibrium. The obtained powder was then annealed at 900°C. The resulting powder was then incorporated into N,N-dimethylformamide (DMF) for graphene production. The powder-DMF mixture was treated in an ultrasonic homogenizer for 1 hour and then the powder and DMF were separated from each other.

For the production of BNNSs, Hexagonal boron nitride powders (h-BN) (Merck, 99.5%) was used as the starting material. h-BN powders were dried in an oven at 75 °C for 2 h. Then, the dehumidified h-BN powders were ground in a Fritsch Pulverisette Premium line 7 brand device at 400 rpm for 50 hours using a single ball of 19 mm diameter. The powders obtained after the grinding process were mixed in a saturated acid mixture consisting of H_2SO_4 and HNO_3 for 12 hours in a magnetic stirrer to provide a homogeneous mixture. The powder mixture filtered from the acid mixture was washed with distilled water until the pH became neutral. The powder obtained from the acid treatment was heated to 950 °C. In order to obtain BNNSs layers, thermally treated powders were mixed in N,N-dimethylformamide (DMF) for 2 hours with the help of an ultrasonic homogenizer (Bandelin Sonoplus, model HD 3200, 200 W, at 50 % power). The suspension of 0.05 mg/ml concentration of BN powders with DMF was prepared. Then, the mixture was centrifuged at 5000 rpm for 8 hours to remove DMF. The powders were washed by ethanol and were dried under vacuum oven at 75°C for 4 h to remove the alcohol.

2.2. Production graphene nanohseets+boron nitride nanosheets-doped CdS by sol-gel method

First, 1.15 g of cadmium acetate was mixed in 50 ml of distilled water. Meanwhile, GNS+BNNS was added to 50 ml distilled water at the required rate and mixed in an ultrasonic homogenizer for 5 minutes. Immediately after, 0.182 g of Cetyltrimethylammonium Bromide (CTAB) was added and mixing was continued for 10 more minutes in the homogenizer. At the end of the process, Cadmium acetate + water mixture was slowly added to the Water + Supplement + CTAB mixture and stirred under magnetic stirring. 0.3 g of Na_2S + 50 ml of distilled water was added to this mixture. The entire mixture was stirred for 3 hours at 75 °C. After mixing, it was washed with distilled water + alcohol mixture and dried at 120 °C for 12 hours. The obtained samples were subjected to structural characterization processes with X-Ray diffraction (Rigaku model Smartlab), Scaning Electron Microscobe (SEM) (Zeiss model Supra 55). Optical measurements of the samples were performed using a Shimadzu UV-3600, PC, UV-Vis spectrophotometer.

GNS+BNNS reinforcement to CdS was made at the rates of 0.1%, 0.5% and 1% by weight. The rates of GNS and BNNS in the reinforcement are 50% - 50%. Sample codes and doped ratios are given in Table 1.

Table 1. The samples codes and weight percentages

Sample codes	Matrix type	Doped ratio Weight, (%)
S	Sol-Gel	Undoped CdS
H_1	Sol-Gel	0.1
H_2	Sol-Gel	0.5
H_3	Sol-Gel	1

3. Results And Dıscussıon

Although graphene and BNNS are two nanomaterials that are structurally and mechanically similar to each other, the electrical and optical properties of these two materials are very different from each other. It is a matter of curiosity, what kind of change will be caused in the properties of semiconductors by doped together with these two nanomaterials. A synergistic effect can occur by reinforcing both nanomaterials together. In this study, it was investigated what kind of change can occur in the properties of CdS by doped together with Graphene and BNNS.As supplements, Graphene nano sheets and BNNSs were produced by the liquid phase exfoliation method. Characterization results of these materials produced in this study are given. Detailed characterization results of these materials can be followed from our previous studies [19-21].

Figure 1 shows the powder XRD pattern of the S, H1, H2, H3 samples that were prepared. The pattern has clear peaks of the (111), (220), and (311) planes, which correspond to the cubic zinc blend structure of CdS, according to the JCPDS-10-0454 data. The peak (111) of the cubic structure can be confused with the peak (002) of the hexagonal structure, but the other peaks of the hexagonal CdS are absent. Therefore, the samples are likely to have a mainly cubic structure, as also reported by other studies [22, 23]. The XRD analysis revealed that the all samples product is a crystalline CdS with a cubic zinc blend crystal structure [24].

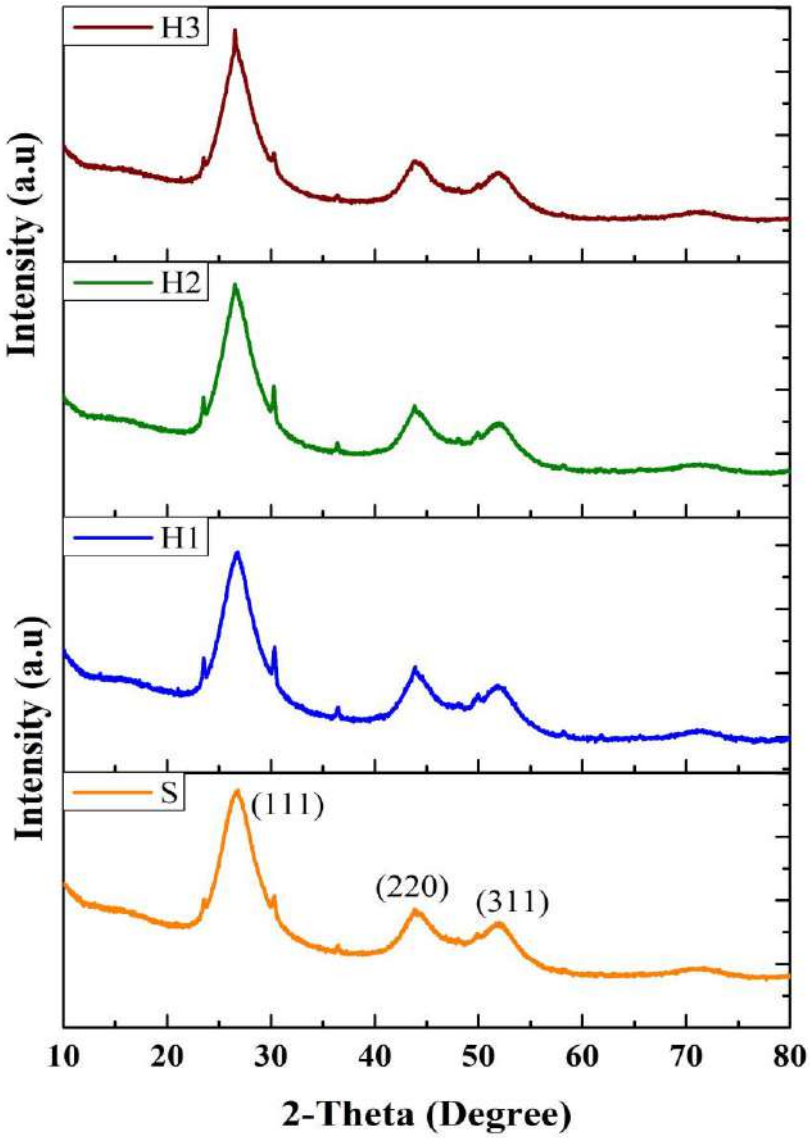

Figure 1. XRD spectra of synthesized samples

SEM images of the produced samples are given in Figure 2. Figure-2a shows the microstructure image of undoped CdS. The particle size in the S sample is below 50 nm and consists of homogeneously dispersed spherical shaped particles. Figure-2a, b, c show SEM images of H1, H2 and H3 samples, respectively. Shown with blue arrows are nanolayers doped into CdS. While the layers are thinner in the H1 sample, it is possible to see nanolayers in many different regions in the H3 sample. In general, it can be said that Graphene+BNNSs are homogeneously distributed in the structure.

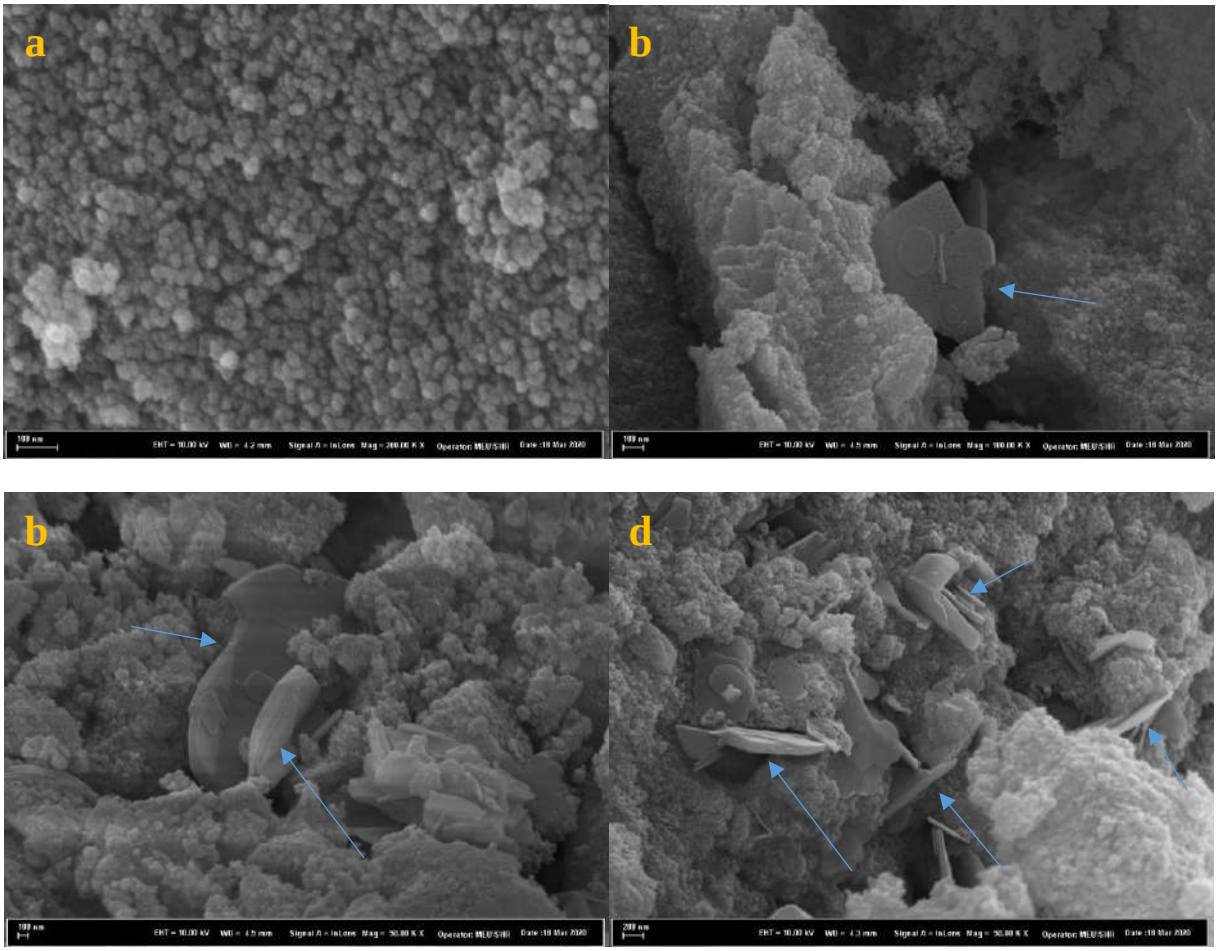

Figure 2. SEM images of synthesized samples, a) S, b) H1, c) H2, d) H3

In Figure-3, the diffused reflectance values obtained as a result of the UV-vis analysis of the samples are given. For undopped CdS the absorption band edge (λe) is about 606 nm, whereas H1, H2, H3 samples exhibit well-defined absorption features at 543, 579, and 561 nm, respectively.

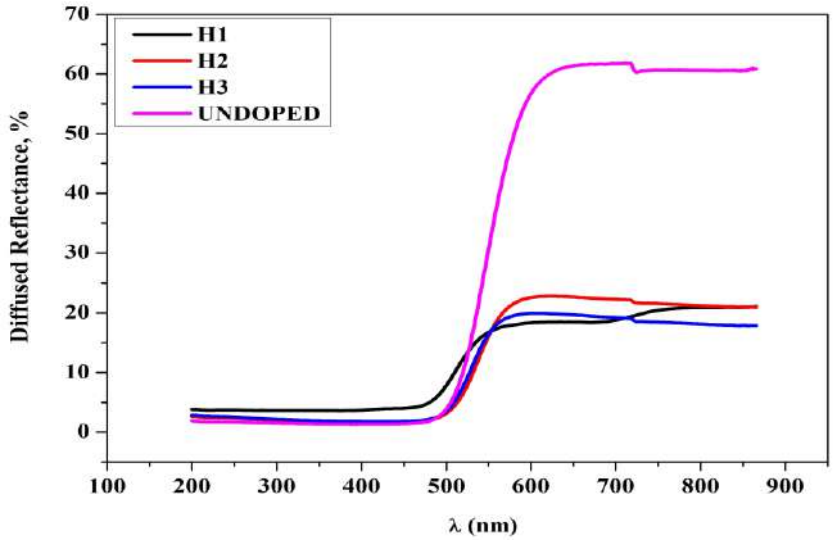

Figure 3. Reflection-wavelength spectrum of synthesized samples

To avoid the uncertainty about the band gap energy (E_g) values obtained from UV–Vis absorption spectroscopy of dispersed samples, diffuse reflectance measurements were performed with dry CdS powders. The band gap of al samples were determined by the following equation (Kubelka and Munk)[25] :

$$\alpha h\upsilon = C(h\upsilon - E_g)^{1/2}, \quad (1)$$

where C is a constant, α is absorbance coefficient, and $h\upsilon$ is the photon energy. The $(\alpha h\upsilon)^2$ graph against $h\upsilon$ is plotted with the aid of the absorption values measured using the optical absorption method and Eq. 1.

Figure.3 showed the graphs of $(\alpha h\upsilon)^2 \sim h\upsilon$ for all samples. As can be seen from the figure, the E_g of the S sample was found to be 2.46 Ev. Sample H1 is 2.48 eV, sample H2 is 2.42 eV, and sample H3 is 2.40 eV. With the increasing reinforcement ratio, the E_g value of the samples first increased and then decreased. The decrease in the E_g values of the semiconductor by making additives with nanolayers such as graphene or boron nitride has been reported in different studies before [26, 27].

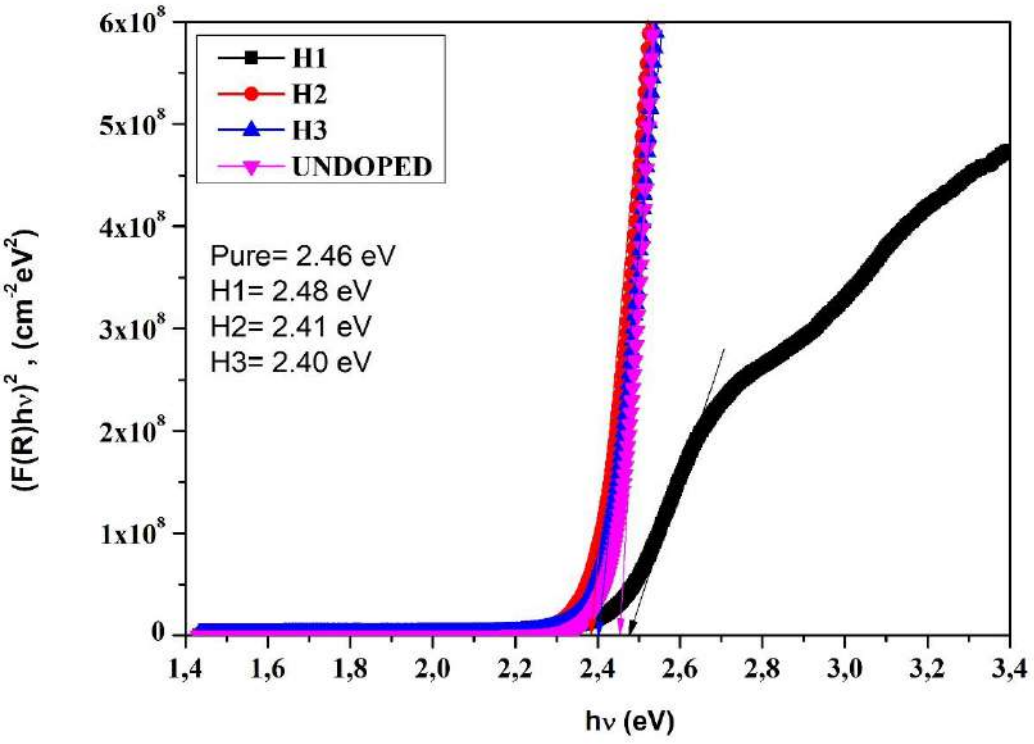

Figure 4. The plots of $(\alpha h\upsilon)^2 \sim h\upsilon$ for of all samples.

4. Conclusions

Graphene nanosheets and boron nitride nanosheets, which are used as reinforcement to CdS matrix, were produced successfully by liquid phase exfoliation method and they were reinforced to CdS at different rates by sol-gel process. Structural characterization of the obtained samples was done successfully. As a result of optical examinations, it was observed that the reflectance of CdS decreased with increasing reinforcement ratio. In addition, an increase and then a decrease in the Eg value of the samples was observed with increasing reinforcement ratio. In this study, the changes that occur in CdS with the addition of graphene and BNNSs to CdS were revealed. Further studies are needed to reveal the synergistic effects of graphene and BNNSs on CdS when supplemented together. In future studies, the

changes in CdS should be revealed by supplementing CdS by changing the ratio instead of 50%-50% Graphene-BNNS.

5. References

[1] V. Dutta, S. Sharma, P. Raizada, A. Hosseini-Bandegharaei, J. Kaushal, P. Singh, Fabrication of visible light active BiFeO3/CuS/SiO2 Z-scheme photocatalyst for efficient dye degradation. Materials Letters, 270 (2020) 127693.

[2] R.C. Pawar, C.S. Lee, Single-step sensitization of reduced graphene oxide sheets and CdS nanoparticles on ZnO nanorods as visible-light photocatalysts. Applied Catalysis B: Environmental, 144 (2014) 57-65.

[3] T. Simon, N. Bouchonville, M.J. Berr, A. Vaneski, A. Adrović, D. Volbers, R. Wyrwich, M. Döblinger, A.S. Susha, A.L. Rogach, Redox shuttle mechanism enhances photocatalytic H 2 generation on Ni-decorated CdS nanorods. Nature materials, 13 (2014) 1013-1018.

[4] C. Wang, L. Wang, J. Jin, J. Liu, Y. Li, M. Wu, L. Chen, B. Wang, X. Yang, B.-L. Su, Probing effective photocorrosion inhibition and highly improved photocatalytic hydrogen production on monodisperse PANI@ CdS core-shell nanospheres. Applied Catalysis B: Environmental, 188 (2016) 351-359.

[5] S. Sharma, V. Dutta, P. Raizada, A. Hosseini-Bandegharaei, P. Singh, V.-H. Nguyen, Tailoring cadmium sulfide-based photocatalytic nanomaterials for water decontamination: a review. Environmental Chemistry Letters, 19 (2021) 271-306.

[6] K. Iwashina, A. Iwase, Y.H. Ng, R. Amal, A. Kudo, Z-schematic water splitting into H2 and O2 using metal sulfide as a hydrogen-evolving photocatalyst and reduced graphene oxide as a solid-state electron mediator. Journal of the American Chemical Society, 137 (2015) 604-607.

[7] X. Xu, W. Liu, Y. Kim, J. Cho, Nanostructured transition metal sulfides for lithium ion batteries: progress and challenges. Nano Today, 9 (2014) 604-630.

[8] P. Akhter, S. Nawaz, I. Shafiq, A. Nazir, S. Shafique, F. Jamil, Y.-K. Park, M. Hussain, Efficient visible light assisted photocatalysis using ZnO/TiO2 nanocomposites. Molecular Catalysis, 535 (2023) 112896.

[9] Y. Zhao, Y. Lu, L. Chen, X. Wei, J. Zhu, Y. Zheng, Redox dual-cocatalyst-modified CdS double-heterojunction photocatalysts for efficient hydrogen production. ACS Applied Materials & Interfaces, 12 (2020) 46073-46083.

[10] S. Shenoy, K. Tarafder, Enhanced photocatalytic efficiency of layered CdS/CdSe heterostructures: Insights from first principles electronic structure calculations. Journal of Physics: Condensed Matter, 32 (2020) 275501.

[11] A. Hadi, J. Zahirifar, J. Karimi-Sabet, A. Dastbaz, Graphene nanosheets preparation using magnetic nanoparticle assisted liquid phase exfoliation of graphite: the coupled effect of ultrasound and wedging nanoparticles. Ultrasonics sonochemistry, 44 (2018) 204-214.

[12] E. Lotfi, M. Neek-Amal, Temperature distribution in graphene doped with nitrogen and graphene with grain boundary. Journal of Molecular Graphics and Modelling, 74 (2017) 100-104.

[13] X. Zou, F. Shang, S. Wang, Electrochemical luminescence determination of hyperin using a sol-gel@ graphene luminescent composite film modified electrode for solid phase microextraction. Spectrochimica Acta Part A: Molecular and Biomolecular Spectroscopy, 173 (2017) 843-848.

[14] J. Wang, F. Ma, M. Sun, Graphene, hexagonal boron nitride, and their heterostructures: properties and applications. RSC advances, 7 (2017) 16801-16822.

[15] P. Xu, J. Kang, J.-B. Choi, J. Suhr, J. Yu, F. Li, J.-H. Byun, B.-S. Kim, T.-W. Chou, Laminated ultrathin chemical vapor deposition graphene films based stretchable and transparent high-rate supercapacitor. ACS nano, 8 (2014) 9437-9445.

[16] D. Golberg, Y. Bando, Y. Huang, T. Terao, M. Mitome, C. Tang, C. Zhi, Boron nitride nanotubes and nanosheets. ACS nano, 4 (2010) 2979-2993.

[17] K. Watanabe, T. Taniguchi, H. Kanda, Direct-bandgap properties and evidence for ultraviolet lasing of hexagonal boron nitride single crystal. Nature materials, 3 (2004) 404-409.

[18] L.H. Li, E.J. Santos, T. Xing, E. Cappelluti, R. Roldán, Y. Chen, K. Watanabe, T. Taniguchi, Dielectric screening in atomically thin boron nitride nanosheets. Nano letters, 15 (2015) 218-223.

[19] Ö. Güler, S.H. Güler, V. Selen, M.G. Albayrak, E. Evin, Production of graphene layer by liquid-phase exfoliation with low sonication power and sonication time from synthesized expanded graphite. Fullerenes, Nanotubes and Carbon Nanostructures, 24 (2016) 123-127.
[20] Ö. Güler, S.H. Güler, Production of graphene–boron nitride hybrid nanosheets by liquid-phase exfoliation. Optik, 127 (2016) 4630-4634.
[21] Ö. Güler, S.H. Güler, M. Taşkin, The production of graphene–boron nitride nanosheet heterostructures via liquid phase exfoliation assisted by a milling process. Bulletin of Materials Science, 42 (2019) 1-8.
[22] S. Mahanty, D. Basak, F. Rueda, M. Leon, Optical properties of chemical bath deposited CdS thin films. Journal of Electronic Materials, 28 (1999) 559-562.
[23] O. Zelaya-Angel, J. Alvarado-Gil, R. Lozada-Morales, H. Vargas, A. Ferreira da Silva, Band-gap shift in CdS semiconductor by photoacoustic spectroscopy: Evidence of a cubic to hexagonal lattice transition. Applied Physics Letters, 64 (1994) 291-293.
[24] S.R. Dhage, H.A. Colorado, T. Hahn, Morphological variations in cadmium sulfide nanocrystals without phase transformation. Nanoscale research letters, 6 (2011) 1-5.
[25] P. Kubelka, Ein beitrag zur optik der farbanstriche. Z. tech. Phys, 12 (1931) 593-601.
[26] Ö. Güler, S.H. Güler, Ö. Başgöz, M.G. Albayrak, I. Yahia, Synthesis and characterization of ZnO-reinforced with graphene nanolayer nanocomposites: electrical conductivity and optical band gap analysis. Materials Research Express, 6 (2019) 095602.
[27] Ö. Güler, S.H. Güler, Ö. Başgöz, I. Yahia, The effect of graphene+ boron nitride/ZnO-based hybrid nanocomposites: synthesis, electrical, optical properties. Journal of the Australian Ceramic Society, 57 (2021) 1085-1095.

International Conference on Advances and Innovations in Engineering

The leaching behavior of copper slags in presence of hydrochloric acid and acetone

M. Deniz TURAN[1] , Zeynel Abidin SARI [2], Hasan NİZAMOĞLU [3], Tuğrulhan DEMİR[4]

[1,3,4] Department of Metallurgy and Materials Engineering, Engineering Faculty, Fırat University, Elazığ, Turkey.
[2] Department of Metallurgy, Iskenderun Vocational School of Higher Education, Iskenderun Technical University, Hatay, Turkey.
[1]mdturan@firat.edu.tr, [2]zeynel.sari@iste.edu.tr, [3]hsnizamoglu@gmail.com, [4]tugrul235723@gmail.com

[1](ORCID: 0000-0002-2136-1425), [2](ORCID: 0000-0001-5932-2141),[3](ORCID: 0000-0002-1801-7156), [4](ORCID: 0000-0001-9482-1624)

Abstract

Copper production from sulphide copper ores is mostly carried out by pyrometallurgical methods. Various slag phases occur in copper production made by pyrometallurgical methods. In parallel with the increasing world population, the increase in copper consumption causes a decrease in the amount of reserves in nature. For this reason, copper production from sources that can be considered as secondary sources such as slag is a good alternative today. Flash and converter slags are the leading slags that occur during pyrometallurgical copper production. The slag produced during the production of copper matte and blister copper has a significant copper content. Since the mineralogical structure of the slags changes and the copper content is low compared to the feed material, it cannot be fed directly into the furnace. Metal extraction from copper production slag via hydrometallurgical techniques has an increasing popularity in wide world because of above discussions.
The copper slag used in the experiments was obtained from the Karadeniz Copper Plant in Samsun, Turkey. The copper slag used in these experiments is from converter and flash furnace slag. The slag sample was crushed, ground, and sieved to minus 200 mesh. Leaching experiments were performed in presence of hydrochloric acid (HCl) and acetone (C_3H_6O). All experiments were carried out under atmospheric pressure and with magnetic stirrer with temperature control. Effect of experimental parameters such as hydrochloric acid concentration (1-4 M), leaching time (5-120 min) and leaching temperature (35-55 ℃) was investigated.
The optimum leaching conditions were determined as 4 M HCl, 1 M C_3H_6O, 55 ℃ of leaching temperature, 90 minutes of leaching time, 1:50 of solid–liquid ratio and 400 rpm of stirring speed. Dissolution of copper and iron from copper slag under these leaching conditions was achieved as 100 % and 94.8 % respectively.

Keywords: Copper slags, leaching, hydrochloric acid, acetone

1. Introduction

Today, the most important resources for the production of basic metals such as copper, zinc, lead, etc. are sulfide, oxide ores and concentrates obtained from them by flotation techniques. Of these ores and/or concentrates, those containing sulfur are processed pyrometallurgically at high temperatures. On the other hand, almost all of the oxidized ores and a small part of the sulphurous are processed hydrometallurgically. The gases released during these high temperature processes contain significant proportions of SOx (SO_2 and SO_3) [1]. Due to various environmental and economic reasons, studies on the development of new methods that can be an alternative to pyrometallurgical methods for the processing of sulfide ores and concentrates have been accelerated. Due to the environmental and economic advantages it provides, the most important alternative to pyrometallurgical production techniques is hydrometallurgical production methods based on leaching processes in aqueous medium. Although the leaching process in hydrometallurgical methods can be easily applied to oxide ores, difficulties arise for sulfide ores such as fine ore size, strong oxidizing medium requirements under atmospheric or pressure leaching conditions [2].

Metal solubility is very low in direct acid treatment of slags, which are sulfide ore and/or metal production residues. Therefore, various oxidizing leaching agents are used to increase metal solubility by oxidizing sulfur to metallic sulfur. When the literature data has been extensively searched, various processes are available for the

[1]Corresponding author

hydrometallurgical evaluation of sulfide ores and/or concentrates. In addition, direct leaching of these sulfide ore and/or slags, which are production residues, in an oxidizing environment under atmospheric conditions in an acid or basic environment was also investigated in order to increase the extraction efficiency. In acidic leaching processes, iron (III) chloride [3], iron (III) sulfate [4], sodium chloride, manganese dioxide [5] and potassium dichromate ($K_2Cr_2O_7$); On the other hand, the possibilities of using thiosulfate and ammonium sulfate [6] in basic ammonia leaching processes were investigated. Flash and converter slags, which have a partially sulfide structure, are the leading slags formed during pyrometallurgical copper production from copper ores. The slag produced during the production of copper matte and the slag formed during the production of blister copper have a significant copper content. Since the mineralogical structure of the slags changes and the copper content is low compared to the feed material, it cannot be fed directly into the furnace. For this, the mixture, which is first crushed and ground into fine particles, is sent to the flotation unit. However, the flotation efficiency in the flotation unit in the facility can be quite low.

In this study, the dissolution of copper from the copper production slags in the presence of hydrochloric acid and acetone was investigated.

2. Material and Methods

The copper slag used in the experiments was obtained from the Karadeniz Copper Plant in Samsun, Turkey. The slag is made up of the slag formed during the matte production in a flash-type copper melting furnace of chalcopyrite concentrate and the slag formed during blister copper production in a converter furnace. The slag sample was crushed, ground, and sieved to minus 200 mesh. Leaching experiments were performed in presence of hydrochloric acid (HCI) and acetone (C_3H_6O). All experiments were carried out under atmospheric pressure and with magnetic stirrer with temperature control. At the end of the leaching period, the contents were cooled and filtered. The filtered solutions were analyzed in terms metals using AAS (Atomic Absorption Spectrometer- Perkin Elmer, AAnalyst 400 Model). Chemical analyses of the slag were carried out by ICP-OES (Inductively Coupled Plasma Optical Emission Spectrometer- Perkin-Elmer, Optima 2000DV) in clear supernatant that was obtained by the microwave digestion process. The sample used in the leach tests contained averages of 6.74% Cu, 36.45% Fe, 4.34% Zn, 0.29% Al and 1.66% S. The XRD characterization of the copper slag were determined by XRD (X-Ray Diffraction- Bruker/D8 Advance) analysis. According to the results of the XRD analysis, the copper slag sample was mainly composed of $FeSiO_4$, Cu_9S_5, $ZnSiO_3$, $Cu_{67}Fe_{2.33}O_4$ and Fe_3O_4.

3. Results and Discussion

This experimental study has been revealed dissolution behavior of various metals (Cu, Fe) from the copper slag in conventional leaching conditions with hydrochloric acid and acetone. The parameters examined in the study are as follows: leaching temperature (35-55 ℃), hydrochloric acid concentration (1-4 M) and leaching time (5-120 min). A series of leaching temperature experiments were carried out by varying of leaching temperature and leaching time at 1 M HCI and 1 M C_3H_6O with a stirring speed of 400 rpm, an *S*/*L* ratio of 1:25. The results are shown in Fig. 1. In the leaching experiments, it was observed that the dissolved copper and iron ratios increased with increasing leaching time. In addition, it was determined that iron, which is richer in the solid in terms of initial concentration, dissolves more in the medium than copper. At the end of 120 minutes, which is the maximum leaching time at 55 ℃, the dissolved copper and iron ratios were determined to be approximately 85% and 73%. On the other hand, it was observed that the leaching temperature was not very effective on dissolution, and partial increases in copper and iron dissolution occurred with increasing temperature from 25 ℃ to 55 ℃.

Investigations of the hydrochloric acid concentration effect were carried out at 1-4 M HCI concentrations, at a constant C_3H_6O concentration of 1 M. The HCI concentration also plays a significant role in metal extraction. The results are shown in Fig. 2. Accordingly, it was determined that the ratio of dissolved copper and iron increased as the hydrochloric acid concentration and leaching time increased. When the experimental data were examined, it was determined that the ideal condition for metal extraction was 100% iron and 94.8% copper recovery obtained with 4 M HCl concentration and 90 minutes leaching time. In addition, in studies examining the concentration of 4 M HCl, it was calculated that around 50% of copper was dissolved in a very short time such as 5 minutes.

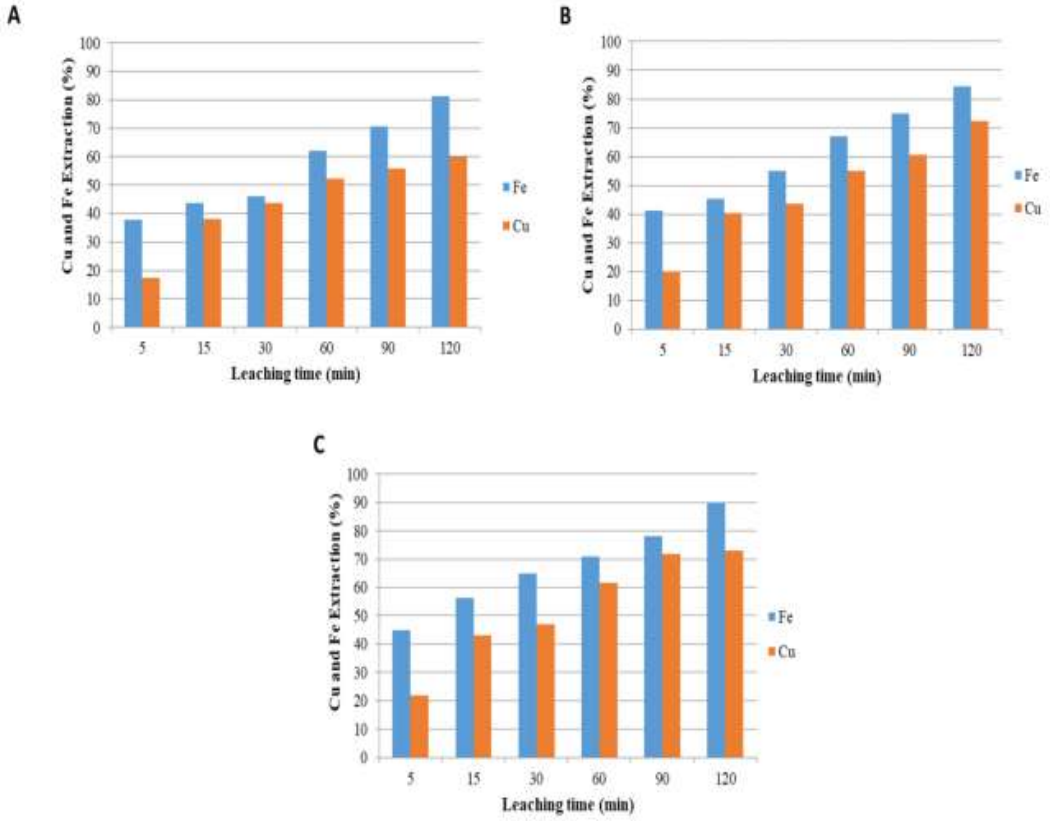

Figure 1. Effect of varying eaching time and temperature on metal extraction (Acetone concentration: 1 M, HCl concentration: 1 M, stirring speed: 400 rpm, Solid/liquid ratio: 1/50 g/ml, leaching temperature: (A): 35 °C, (B): 45°C, (C): 55°C.

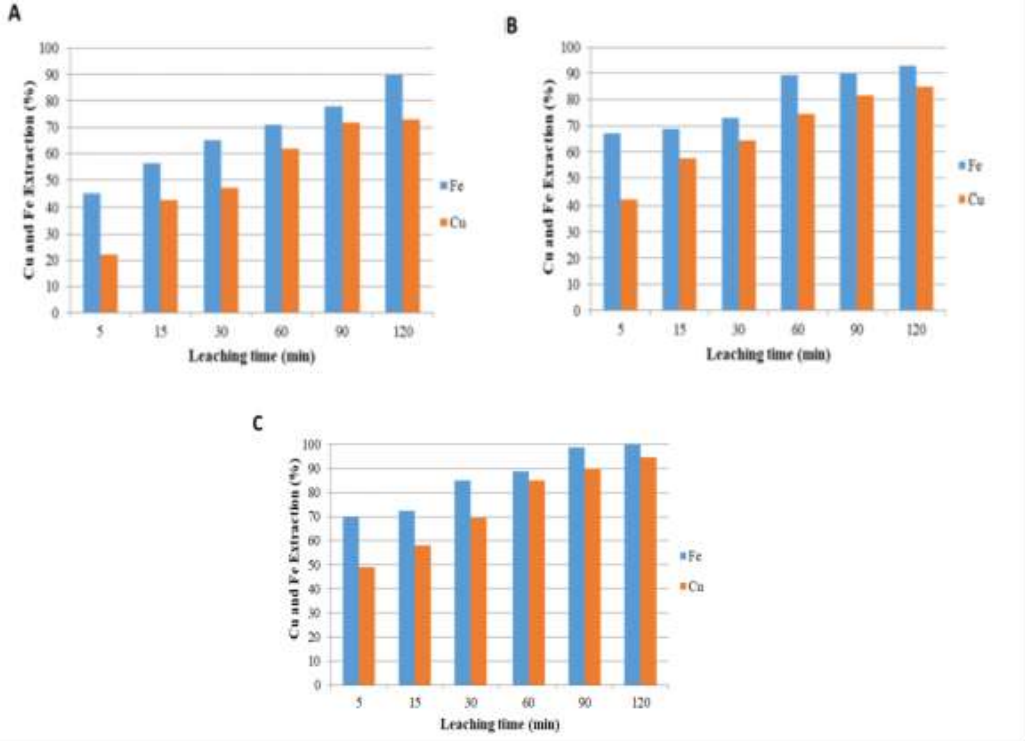

Figure 2. Effect of varying leaching time and HCl concentration on metal extraction (Acetone concentration: 1 M, leaching temperature: 55°C, stirring speed: 400 rpm, solid/liquid ratio: 1/50 g/ml, HCl concentration: (A): 1 M, (B): 3 M, (C): 4 M

4. Conclusion

In this study, the recovery of copper metal by leaching copper slags in the presence of hydrochloric acid and acetone was investigated. Based on this research, it can be concluded that:

- It was determined that copper dissolution increased with increasing HCl concentration and leaching temperature.
- The optimum leaching conditions were determined as 4 M HCI, 1 M C_3H_6O, 55 °C of leaching temperature, 90 minutes of leaching time, 1:50 of solid–liquid ratio and 400 rpm of stirring speed.
- Dissolution of copper and iron from copper slag under these leaching conditions was achieved as 100 % and 94.8 % respectively.

5. Acknowledgements

This study is a part of FÜPAB project (MF.21.08). The authors like to acknowledge the FÜBAP (FIRAT University Scientific Research Projects).

6. References

[1] Turan MD, Sarı ZA. "Demiraslan, A. "Ultrasound-assisted leaching and kinetic study of blended copper slag". Metall. Mater. Trans., B., 50, 1949–1956, 2019.

[2] Turan MD, Sarı ZA, Miller JD. "Leaching of blended copper slag in microwave oven". Transactions of Nonferrous Metals Society of China, 27(6), 1404-1410, 2017.

[3] Muravyov MI, Fomchenko NV, Usoltsev AV, Vasilyev AE, Kondrat'eva, TF. "Leaching of copper and zinc from copper converter slag flotation tailings using H_2SO_4 and biologically generated $Fe_2(SO_4)_3$". Hydrometallurgy, 119-120, 40–46, 2012.

[4] Dımıtrıjevıc MD, Urosevıc DM, Jankovıc ZD, Mılıc SM. "Recovery of copper from smelting slag by sulphation roasting and water leaching". Physicochem. Probl. Miner. Process. 52(1), 409−421, 2016.

[5] Li XIAO, Guan-zhou QIU, Zheng FANG, Jian-she LIU. "Dynamics in simultaneous electro-generative leaching for sphalerite-MnO_2". Trans. Nonferrous Met. Soc. China, 17, 1045-105, 2007.

[6] Babu MN, Sahu KK, Pandey BD. "Zinc recovery from sphalerite concentrate by direct oxidative leaching with ammonium, sodium and potassium persulphates". Hydrometallurgy, 64 (2), 119–129, 2002.

International Conference on Advances and Innovations in Engineering

Comparison of photoelectric conversion efficiencies of DSSCs sensitized with velvet red rose and ivy rose dye

Fehmi ASLAN[1]

[1] Department of Motor Vehicles and Transportation Technologies, Yesilyurt Vocational School, Malatya Turgut Ozal University, Malatya, Turkey.

[1]fehmi.aslan@ozal.edu.tr

[1](ORCID: 0000-0002-5304-0503)

Abstract

In this study, extracts from velvet red rose and ivy rose were used as sensitizers in dye-sensitized solar cells. XRD analyses confirmed the anatase structure of the TiO_2 thin film. SEM photographs showed that the nanospheres were in tight contact with each other, allowing for greater dye absorption on the TiO_2 surface. It was understood from the UV-vis analysis that the velvet red rose dye exhibited a wider absorption in the visible region. The I-V characterizations showed that DSSC sensitized with velvet red rose dye exhibited higher cell performance (η=0.12) than DSSC sensitized with ivy rose dye.

Keywords: Dye-sensitive solar cells, Natural dyes, Photovoltaic performance, Velvet red rose dye, İvy rose dye.

1. Introduction

Photovoltaic technology is attractive because it converts light energy directly into electrical energy [1]. The high cost and non-reversible nature of silicon-based solar cells have made it inevitable for new technologies to emerge in this field [2]. In this field, dye-sensitized solar cells (DSSCs)are very attractive due to their ease of manufacture and low cost [3]. A typical DSSC; consists of a photoanode layer, counter electrode, sensitizing dye, redox electrolyte, and counter electrode [4].

Sensitizing dyes produced from some natural plants exhibit remarkable absorption in the visible region. This feature positively affects the performance of DSSCs [5]. The highest cell yields for DSSCs were achieved with Ru-based dyes [6]. However, these dyes' high costs and toxic properties have accelerated the studies on alternative sensitizers [7]. In this context, dyes extracted from natural plants are promising for DSSCs. Especially natural dyes containing some flavonoid groups provided high power conversion efficiency in DSSCs [8].

In this study, it was investigated how sensitizers extracted from velvet red rose and ivy rose affected the performance of DSSCs.

2. Research Significance

In this study, the effect of dyes extracted from velvet red rose plant and ivy rose plant on DSSCs was investigated. The aim of this study is how sensitizers produced from different species of two plants of the same genus affect the power conversion efficiency. In this context, two different rose species were extracted using the soxhlet method. It was determined that there were significant changes in photovoltaic parameters of DSSCs produced using two different sensitizers. This is due to the fact that the sensitizing sizes have different phenolic contents. In particular, dyes with high anthionine content show better cell performance in DSSCs. The highlights of this study are given below.

[1]Corresponding author

Highlights:

- DSSC sensitized with velvet red rose dye showed superior cell performance.
- Velvet red rose dye exhibited a wider range of absorption in the visible region.
- The open circuit voltage (Voc=0.5V) of the cell sensitized with the velvet red rose dye is higher than that of the cell sensitized with the ivy rose dye (Voc=0.3V).

3. Experimental Method-Process

3.1. Materials

All materials were used in the experiments without the need for extra purification. In experiments; Titanium IV isopropoxide (TTIP, ≥97.0%, Sigma-Aldrich), ethyl alcohol (≥99.5%, Sigma-Aldrich), urea (Chemsolid), terpineol (Sigma-Aldrich), ethyl cellulose (Sigma-Aldrich), FTO conductive glass (RS < 15 Ω/Sq Sigma), counter electrode (Platinum: Solaronix), redox electrolyte solution (Solaronix) used.

3.2. Production of TiO_2 nanoparticles

In this study, the sol-gel method was used for the production of TiO_2 nanoparticles. 6 ml of TTIP was dissolved in 5 ml of isopropanol. 75 ml of distilled water and 2.5 ml of citric acid were added to this mixture and vigorously stirred at 80 °C for 4 h. After 4 h, the viscous solution formed was centrifuged and the precipitate formed was washed several times with pure and then sintered at 450 °C for 2 h. The white particles formed were crushed in an agate mortar and turned into powder.

3.3. Extraction of plant dyes

Velvet red rose and ivy rose leaves were washed several times with distilled water and dried in a vacuum oven in the dark for one day. The dried leaves were pulverized in a high-speed grinder. 5 g of each dye extract was taken and placed in soxhlet cartridges containing 100 ml of alcohol separately. It was waited until the systems siphoned 5 times, then waited for it to cool down. The cooled extracted dyes were stored in a dark environment at 4 °C until used in the experiments. The beaten rose leaves and the soxhlet system is shown in Fig. 1.

Figure 1. a) Ivy rose extract, b) Velvet red rose extract, c) Production of dyes with the Soxhlet system

3.4. Production of DSSCs

For TiO_2 paste making, 1.5 g TiO_2, some ethyl cellulose, and a few drops of terpineol were mixed in an agate mortar to obtain the appropriate paste consistency. TiO_2 paste was coated with the doctor blade method on the conductive surface of the FTO glasses, which were previously cleaned with alcohol and pure water. It was sintered at 450 °C for 45 min to form the photoanode layer. Photoanodes taken from the muffle furnace were immersed in the dye for 24 h after cooling. A few drops of electrolyte solution were dropped on the dye-sensitized photoanodes and closed with a Pt counter electrode. Then the measurement process was started. The photoanodes produced are given in Fig. 2.

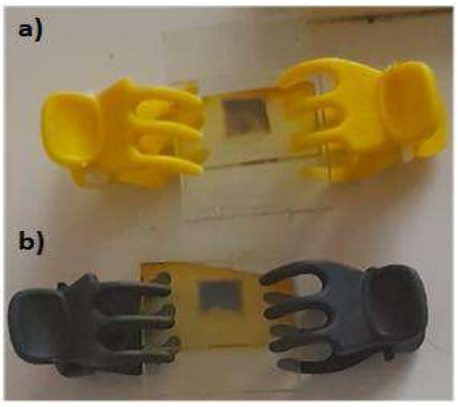

Figure 2. a) DSSC sensitized with ivy rose dye, b) DSSC sensitized with velvet red rose dye.

3.5 Characterization

X-ray diffraction (XRD) analyses were performed with Rigaku ManiFlex-600, Scanning electron microscope (SEM) images with Zeiss sigma 300, and UV measurements with UV-3600-Shimadzu-Japan. Electrochemical impedance spectroscopy (EIS) measurements were taken with the Fytronix Impedance Analysis System and I-V measurements were taken with the Fytronix Solar Simulator LSS 9000 I-V Characterization System.

4. Findings and Discussions

The structural analysis of TiO_2 particles produced by the sol-gel method is shown in Fig. 3. The crystal planes corresponding to the 2θ angles in the given figure show that TiO_2 is in anatase structure [9].

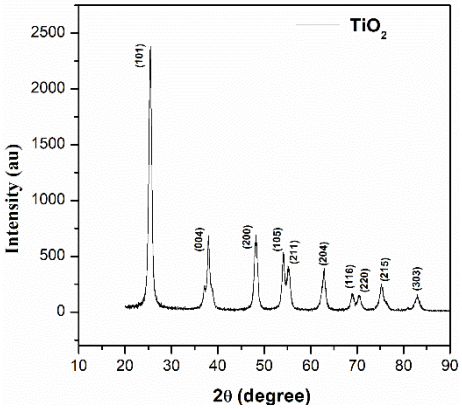

Figure 3. XRD diffraction pattern of produced TiO_2.

SEM images in Fig. 4 show the presence of spherical particles. The tight contact between these particles improves electron transport on the photoanode surface [10]. In addition, the presence of tightly packed nanospheres allows better dye absorption on the surface. On the other hand, the presence of such a morphological feature may facilitate charge transport at the interface.

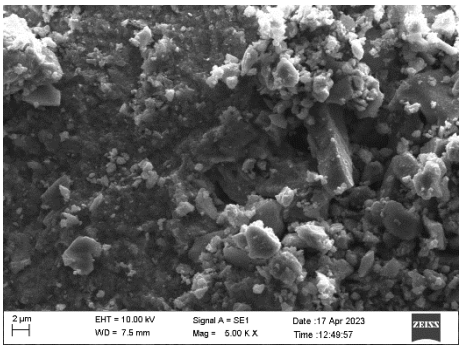

Figure 4. SEM image of TiO_2 particles.

Fig. 5 reflects the UV analysis of natural dyes extracted from two different rose varieties. The dyes obtained from both rose varieties exhibited absorption in a wide wavelength range at 300-700 nm. The dye of the velvet red rose has an extra absorption peak in the wavelength range of 500-600 nm. This absorption behavior can be explained by the higher cell performance of the velvet red rose (η=0.12).

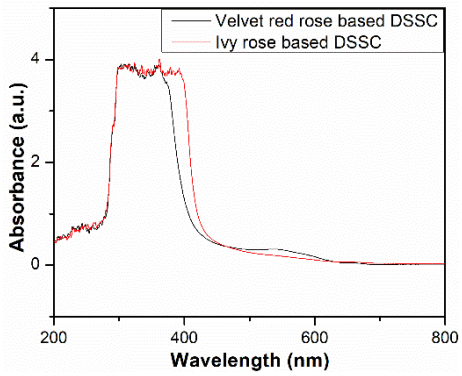

Figure 5. Absorption curves of extracted dyes.

The photovoltaic parameters of the produced DSSCs are given in Fig. 6 and summarized in Table 1. When Table 1 was examined, it was seen that the cell sensitized with velvet red rose dye had higher power conversion efficiency than the cell sensitized with ivy rose dye. This can be explained by the high interaction of carbonyl and hydroxyl groups with the TiO_2 surface and stronger absorption in the visible region in the velvet red rose dye [11].

Table 1. Photovoltaic parameters of the produced cells

Sample	J_{sc} (mA/cm^2)	V_{oc} (V)	FF	η (%)
Velvet red rose-based DSSC	0.55	0.5	0.46	0.12
Ivy rose-based DSSC	0.70	0.3	0.35	0.07

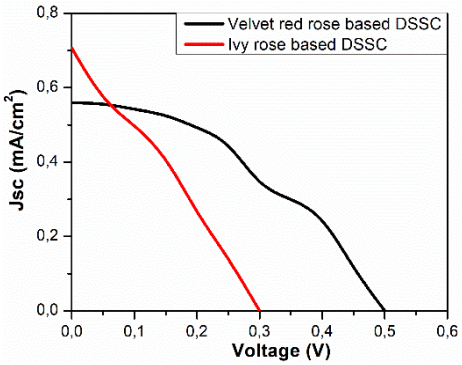

Figure 6. I-V curves of produced DSSCs.

The Nyquist curves in Fig. 7 show two semicircles. As the diameter of the semicircles increases, the impedance value of the DSSC increases and the cell efficiencies decrease [12]. The cell sensitized with ivy rose dye has a larger impedance value because it has a larger semicircular diameter. This could be explained by the lower cell performance of the cell sensitized with the ivy rose dye.

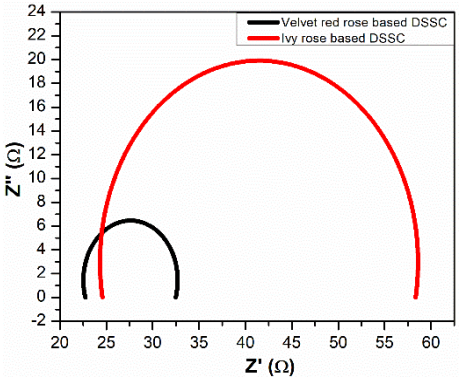

Figure 7. Nyquist curves of DSSCs sensitized with different dyes.

5. **Conclusion and Recommendations**

XRD analyses confirmed the crystal structure of anatase TiO_2. SEM images showed tight contact between the spherical particles, which facilitated electron transfer. UV analyses showed that dyes sensitized with velvet red rose dye exhibited stronger absorption in the visible region. This was explained by the high cell performance of DSSC sensitized with velvet red rose dye. I-V measurements showed that DSSc sensitized with velvet red rose dye exhibited higher power conversion efficiency. This was attributed to the high interaction of the carbonyl and hydroxyl groups found in the red velvet rose dye with the TiO_2 surface. EIS analyses showed that the cell sensitized with ivy rose dye had a greater impedance value. This was explained by the poor cell performance of DSSC sensitized with ivy rose dye.

6. Declaration of Competing Interest

The authors declare that they have no known competing financial interests or personal relationships that could have appeared to influence the work reported in this paper.

7. Credit Authorship Contribution Statement

Fehmi Aslan: Conceptualization, Data curation, Formal analysis, Investigation, Methodology, Validation, Visualization, Writing – original draft, Writing - review & editing.

8. References

[1] Kumar B.A, Vetrivelan V, Ramalingam G, Manikandan A, Viswanathan S, Boomi P, Ravi G. "Computational studies and experimental fabrication of DSSC device assembly on 2D-layered TiO_2 and MoS2@TiO_2 nanomaterials". Physica B: Condensed Matter, 633, 413770, 2022.

[2] Nnorom O.O, Onuegbu G.C, Etus C. "Photo-performance characteristics of Baphia nitida and rosella dye-sensitized solar cell". Results in Optics, 9, 100311, 2022.

[3] Zatirostami A. "A dramatic improvement in the efficiency of TiO_2-based DSSCs by simultaneous incorporation of Cu and Se into its lattice". Optical Materials, 117, 111110, 2021.

[4] Peiris D, Ekanayake P, Karunaratne B.A. "M.I. Petra, Improved Performance of DSSC Photoanodes After the Modification of TiO_2 with Reduced Graphene Oxide". Journal of Electronic Materials, 50, 1044–1053, 2021.

[5] Singh S, Maurya I.C, Sharma S, Kushwaha S, Srivastava P, Bahadur L. "Application of new natural dyes extracted from Nasturtium flowers (Tropaeolum majus) as a photosensitizer in dye-sensitized solar cells". Optik, 243 167331, 2021.

[6] Yoo K, Kim J.Y, Lee J.A, Kim J.S, Lee D.K, Kim K, Kim J.Y, Kim B, et al. "Completely transparent conducting oxide-free and flexible dye-sensitized solar cells fabricated on plastic substrates". ACS Nano, 9, 3760-3771, 2015.

[7] Lee C.P, Li C.T, Ho K.C. "Use of organic materials in dye-sensitized solar cells". Materials Today, 20, 267-283, 2017.

[8] Gao F, Wang Y, Shi D, Zhang J, Wang M, Jing X, Humphry-Baker R, Wang P, et al. "Enhance the optical absorptivity of nanocrystalline TiO_2 film with high molar extinction coefficient ruthenium sensitizers for high performance dye-sensitized solar cells". Journal of the American Chemical Society, 130, 10720-10728, 2008.

[9] Sethy P.P, Pani T.K, Rout S. "Structural and magnetic properties of Ni/C core–shell nanofibers prepared by one step co-axial electrospinning method". Journal of Materials Science: Materials in Electronics, 807, 1-15, 2023.

[10] Nelson J, Chandler R.E. "Random walk models of charge transfer and transport in dye-sensitized systems". Coordination Chemistry Reviews, 248, 1181-1194, 2004.

[11] Calogero G, Marco G, Caramori S, Cazzanti S, Argazzi R, Bignozzi C.A. "Natural dye sensitizers for photoelectrochemical cells". Energy and Environmental Science, 2, 1162-1172, 2009.

[12] Qi K, Liu S, Chen Y, Xia B, Li G.D. "A simple post-treatment with urea solution to enhance the photoelectric conversion efficiency for TiO_2 dye-sensitized solar cells". Solar Energy Materials and Solar Cells, 183, 193-199, 2018.

International Conference on Advances and Innovations in Engineering

Characterization of Activated Carbon Produced by Hydrothermal Carbonization Method Using Tea Plant Wastes

Mustafa Boyrazli[1], Mustafa Süner[1], Emrah Çelik[1], Aysegul Dere[2], Erdoğan Karip[1], Canan Aksu Canbay[3]

[1]Department of Metallurgical and Materials, Faculty of Engineering, Fırat University, Elazığ, Türkiye
[2]Department of Electricity, Vocational School of Technical Sciences, Fırat University, Elazığ, Türkiye
[3]Department of Physics, Faculty of Science, Fırat University, Elazığ, Türkiye

Abstract

In this study, characterization of activated carbon produced by hydrothermal carbonization(HTC) method using tea plant wastes was examined. Tea plant wastes used in the experiments, were supplied from Rize-ÇAYKUR tea production facilities. For the production of activated carbon, the samples were subjected to carbonization process in a hydrothermal device both with activator and without activator at different times and temperatures. SEM, EDX and BET analyses of the produced activated carbon samples were performed. According to the BET analyses results of the samples obtained from the experiments performed without using an activating agent, the surface area of the sample treated at 100°C for 8 hours was determined as 2.13 m^2/gr. The BET surface area of the samples activated after hydrothermal carbonization was determined as 887.41 m^2/gr and 874.77 m^2/gr depending on the KOH/Hydrochar ratio.

Keywords: Activated Carbon, Almond Shells, Hydrothermal Carbonization

1. Introduction

Increasing environmental pollution due to developing technology threatens the world population more and more day by day. Some of the technological wastes mix with drinking water and pollute it. In the context of wastewater treatment, many technologies and techniques have been researched and used (Sharma and Naushad, 2020). Currently, many technologies such as adsorption, membrane filtration, precipitation and ion exchange are used to remove metallic contaminants from aqueous solution (Chingombe et al, 2005; Karnib et al, 2014). Most of these systems have weaknesses such as high cost, difficulty in implementation, low efficiency, and possibility of co-pollutant generation (Yaashikaa et al., 2019). The adsorption process is a widely used technique to efficiently remove heavy metals, organic pollutants and inorganic substances from polluted water, and it has become one of the most preferred methods due to its high efficiency and low cost.

The most widely used adsorbent is activated carbon due to its high surface area and high adsorption capacity (Gercel et al., 2007; Tehrani-Bagha and Balchi, 2018). Activated carbon is a well-known adsorbent due to its unique and versatile properties that allow gas or liquid to reach the inner pore surface and high surface reactivity (Mohamad Nor et al., 2013). Activated carbon can attract molecules and ions in the solution through its pores to its inner surface. Although there is no chemical structure and formula expressing the structure of activated carbon, its high specific surface area, well-developed pore structure, high adsorption capacity and thermo-stability have enabled this material to be used as an important adsorbent in the removal of organic and inorganic pollutants (Huang et al., 2013 and Yasli, 2019). The high cost of activated carbon has led researchers to work on the production of activated carbon from different raw materials. In recent years, the production of activated carbon from agricultural wastes has gained

[1]Corresponding author

importance (Aslan, 2021). Also, producing activated carbon from biomass waste helps to minimize waste disposal costs and the negative impact on the environment (González-García, 2018).
HTC, also known as wet roasting, is an environmentally friendly method used to convert biomass into a carbon-rich solid product. The use of hydrothermal carbonization (HTC) to convert biomass wastes into valuable carbon materials has recently become attractive. During the HTC process, hydrocoal is the main product with a mass yield of about 35-80%. The biomass is placed in an autoclave and treated at specified times and temperatures. The reaction pressure is self-generated by the saturated vapor pressure of the water (subcritical water zone) corresponding to the reaction temperature. Compared to traditional thermal technologies such as pyrolysis and dry roasting, the HTC process eliminates the need for pre-drying, an energy costly step (Suarez et al., 2020).
In this study, activated carbon was produced from tea plant wastes obtained from Rize-ÇAYKUR production facilities by hydrothermal carbonization method. The obtained activated carbon was characterized by performing SEM, EDX and BET analyses.

2. Materials And Method

Tea plant wastes used in the experiments were obtained from RİZE-ÇAYKUR tea production facilities. KOH (Merck CAS NO: 1310-58-3), used as activator, was purchased and used in experiments.
HTC Experiments Without Using Activating Agent;

Tea plant wastes were first dried in an oven at 80 ºC for 24 hours in order to remove the moisture in their structure. The dried sample was ground in a ball mill for 15 minutes and sieved through a -212 µm sieve. The sieve material was mixed at the rate of tea plant wastes/pure water=1/10(5 g tea plant wastes/50 ml distilled water) and processed in a hydrothermal device at 100 ºC and 200 ºC for 4, 8, 12, 16 hours. Materials taken from HTC device were filtered. The solid hydrochar remaining on the filter paper was dried at 80 ºC for 24 hours. The final product was stored in ziplock bags for necessary analysis. The flow chart of the experiments without the use of activator was given in figure 1.

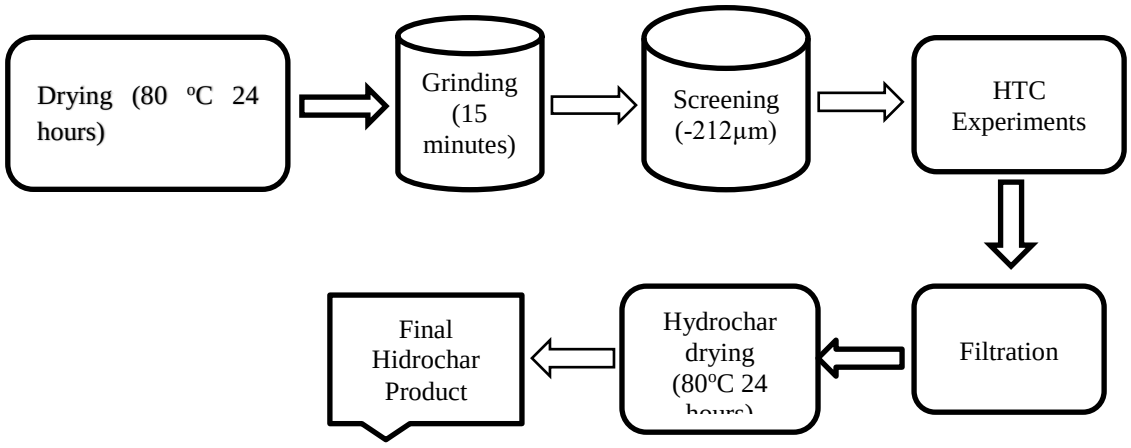

Figure 1. Flowchart of HTC experiments without activating agent

2.1. Experiments Using Activating Agent

Tea plant wastes, which were ground in a ball mill, were carbonized in a muffle furnace at 800 ºC for 24 hours. Then, the samples were prepared by mixing the carbonized product/pure water=1/10 (5gr carbonized product/50 ml distilled water). Afterwards, the prepared samples were processed in a Hydrothermal Carbonization Device (HTC) at 200 ºC for 12 hours. Carbonized samples obtained from hydrothermal were filtered on filter paper to make solid-liquid separation. The obtained Hidrochar was activated in a muffle furnace at 600ºC for 4 hours by blending KOH/Hydrochar=1/1 and 1/2. The activated product was shaken in a 3 M HCl solution for 1 hour in a vortex device,

with activated carbon/HCl solution =1/10, to remove impurities in its pores. After vortexing, the mixtures were filtered through filter paper, the sample remaining on the filter paper was washed repeatedly with distilled water until pH= 4.5-5 and filtered. The washed samples were dried in an oven at 80 oC for 24 hours and stored in ziplock bags for analysis. Figure 2 shows the flow chart of HTC experiments using the activating agent KOH.

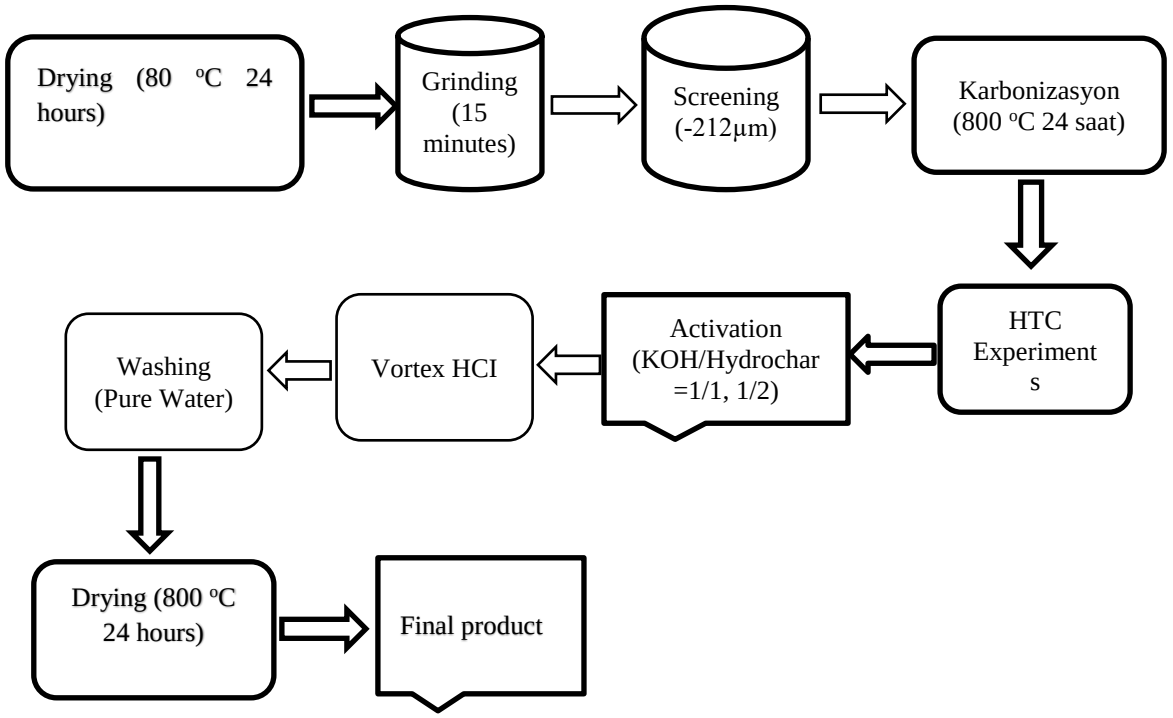

Figure 2. Flow chart of HTC experiments performed using activating agent KOH

Hydrothermal treatment of ground tea plant waste was carried out on the Fytronix brand HTC device shown in Figure 3. It consists of a temperature and time controlled control panel, a hydrothermal reactor and a magnetic stirrer. The hydrothermal reactor is made of stainless steel. The inside of the reactor is designed in such a way that a 80 ml teflon cup can enter. On the cover of the reactor, there are two valves and a digital pressure gauge to provide gas inlet and outlet. The mixing process takes place by rotating the magnetic fish placed in the Teflon container by the magnetic stirrer.

Figure 3. The hydrothermal device used in the experiments

3. Results and Discussion

3.1. Results of Experiments Performed Without Using Activating Agent

SEM image of untreated tea plant wastes is given in Figure 4. As seen in the SEM image, it is understood that there is no porous structure on the surface of the material and the surface is smooth. When SEM images of HTC treated samples are examined (Figures 5, 6, 7), it is seen that porous structures are formed and the surface is indented and protruding. In Figure 7, it is seen that the pores have mostly micro and mesopore structures.

The carbon content of the HTC treated samples increases with time and temperature (Figure 7). However, it has been observed that elements such as Ca, K and Cu also appear in structure. It is thought that these components were previously present as inorganic material in the structure of the tea plant waste, separated from the organic structure due to high pressure during the HTC process, but adhered to the surface of the material because it was in a closed container.

The carbonized products obtained after the hydrothermal carbonization process were subjected to surface area analysis by N_2-BET method. According to the BET analysis results, the surface area of the tea plant waste sample, which was HTC treated for 8 hours at 100ºC, was obtained as 2.13 m^2/gr.

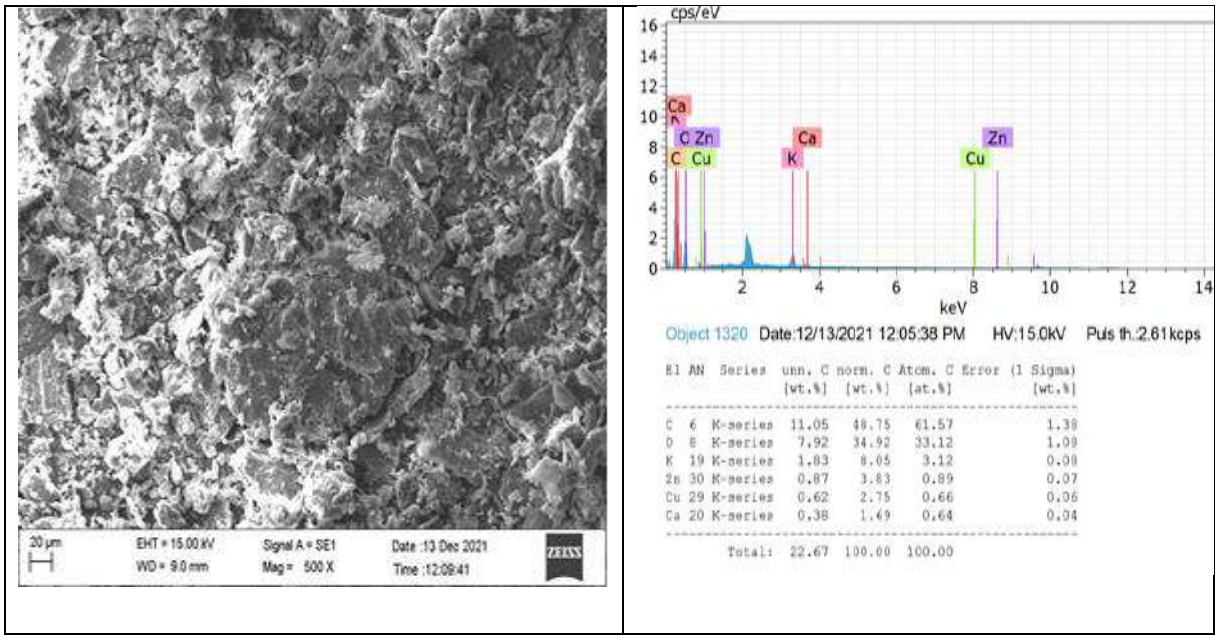

Figure 4. SEM image (500X) of HTC untreated sample and EDX analysis of the marked region

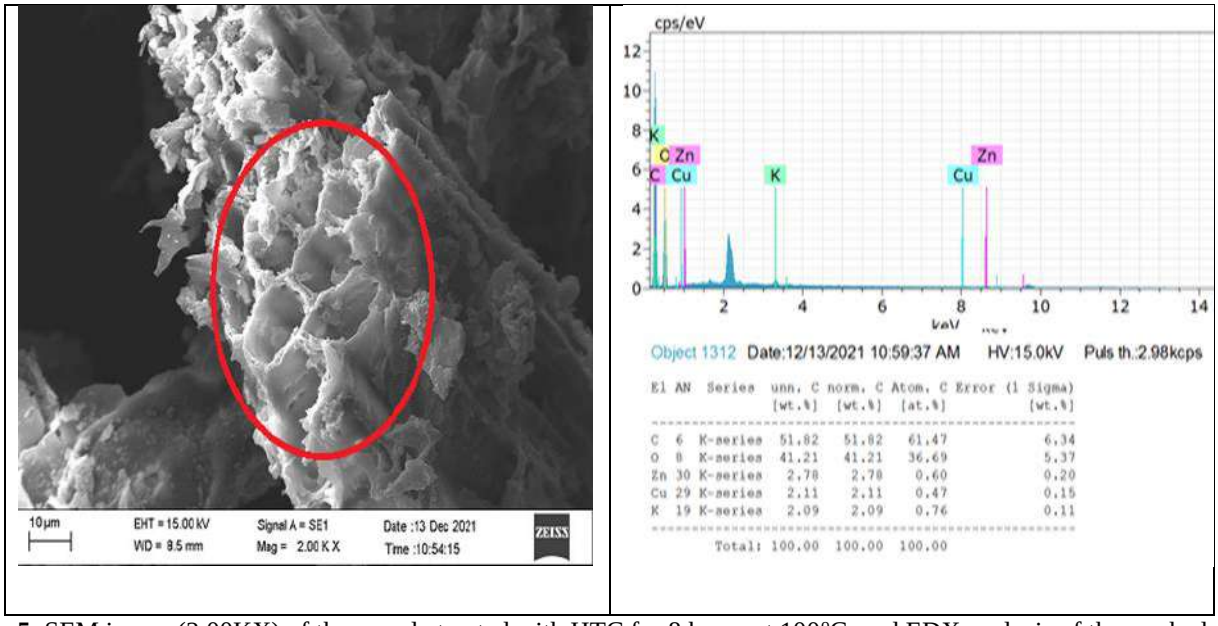

Figure 5. SEM image (2.00KX) of the sample treated with HTC for 8 hours at 100ºC, and EDX analysis of the marked region

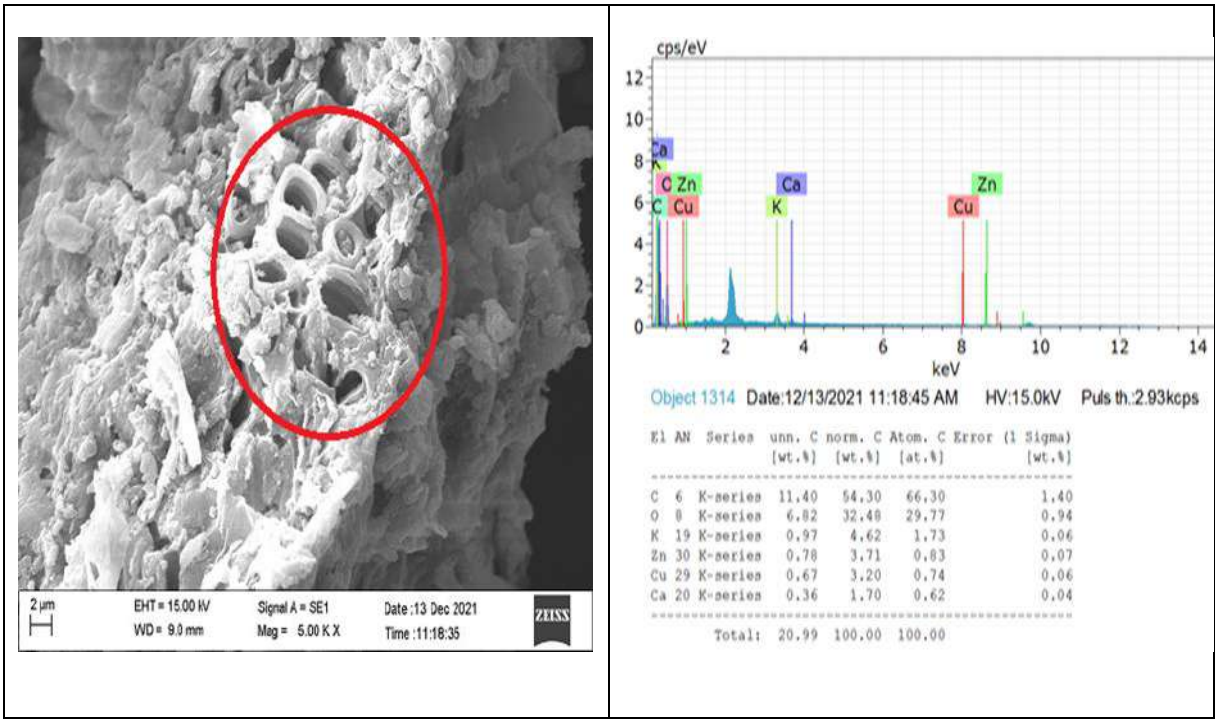

Figure 6. SEM image (5.00KX) of the sample treated with HTC for 16 hours at 100ºC, and EDX analysis of the marked region

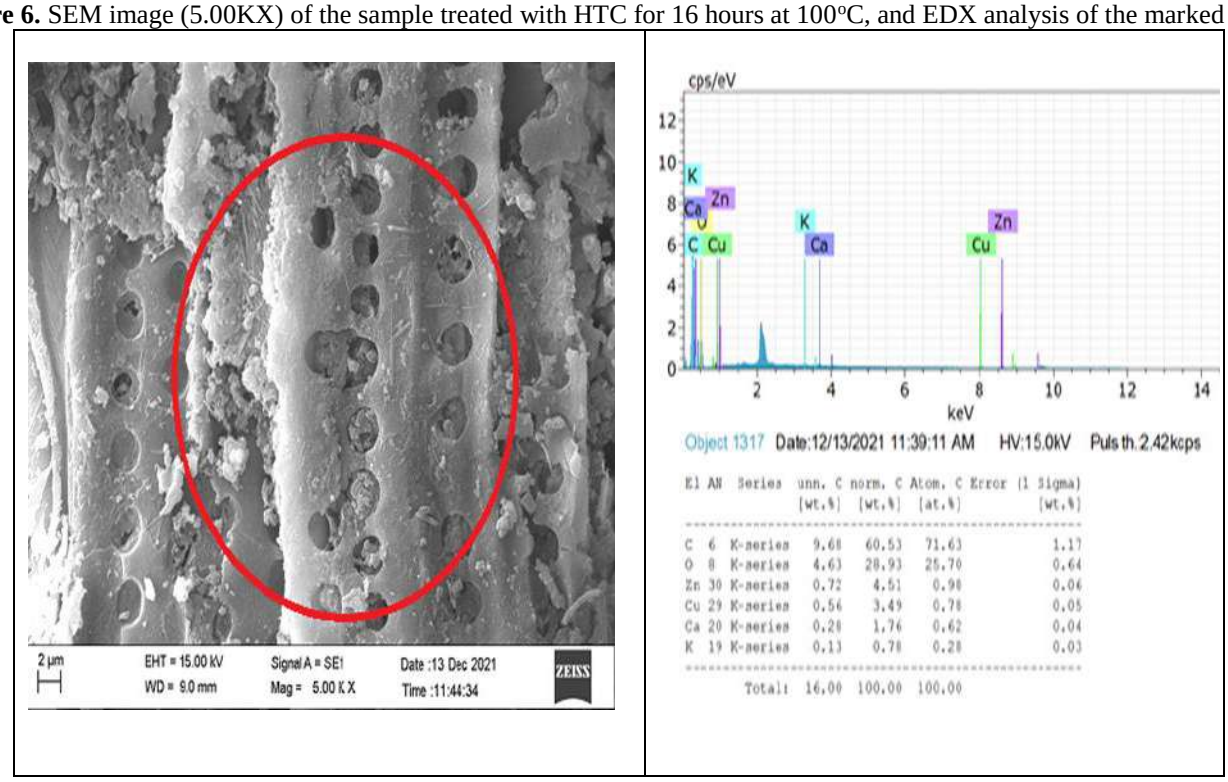

Figure 7. SEM image (5.00KX) of the sample treated with HTC for 8 hours at 200ºC, and EDX analysis of the marked region

3.2. Results of Experiments Performed Using Activating Agent

SEM images and EDX analysis results of samples activated with KOH after hydrothermal carbonization are given in Figure 8 and Figure 9. In the SEM images, it was determined that the chemical activation process applied after HTC was effective in the formation of the pores.

It is understood that KOH, which is used as an activator, accelerates the degradation of the structure of the raw material in the carbonization process. During carbonization, the structure of the product was largely degraded by

thermal decomposition, most of the functional groups were removed from the structure and a large part of the volatile substances were removed from the structure to obtain a porous structure. Carbonized products obtained from samples activated with KOH after hydrothermal carbonization were subjected to surface area analysis by N_2-BET method. Accordingly, the BET surface area of the sample mixed with KOH/Hydrochar=1/1 ratio was determined as 887.41 m^2/g, while the BET surface area of the sample mixed with KOH/Hydrochar=1/2 ratio was determined as 874.77 m^2/g. In the EDX analysis of the samples, 48.65% C by weight was found in the untreated tea plant waste, while this rate was 77.10% C after the activation process.

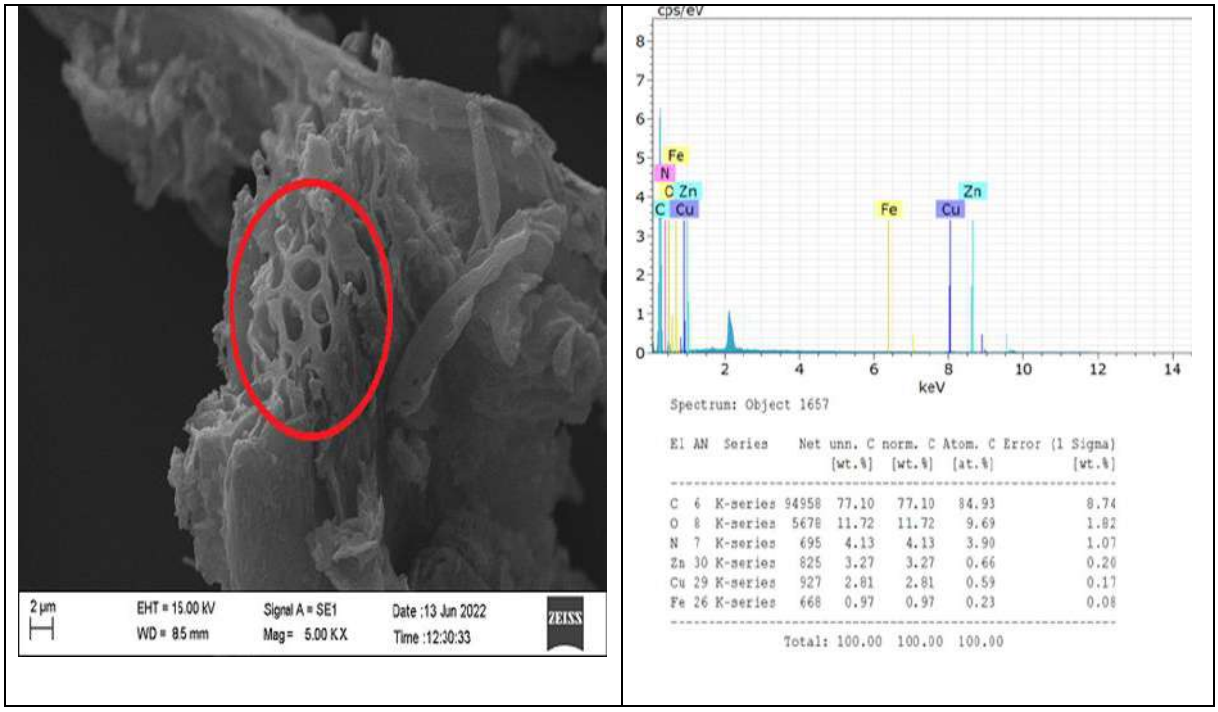

Figure 8. SEM image of the test sample with KOH/Hydrochar=1/1 (5.00KX), and EDX analysis of the marked region

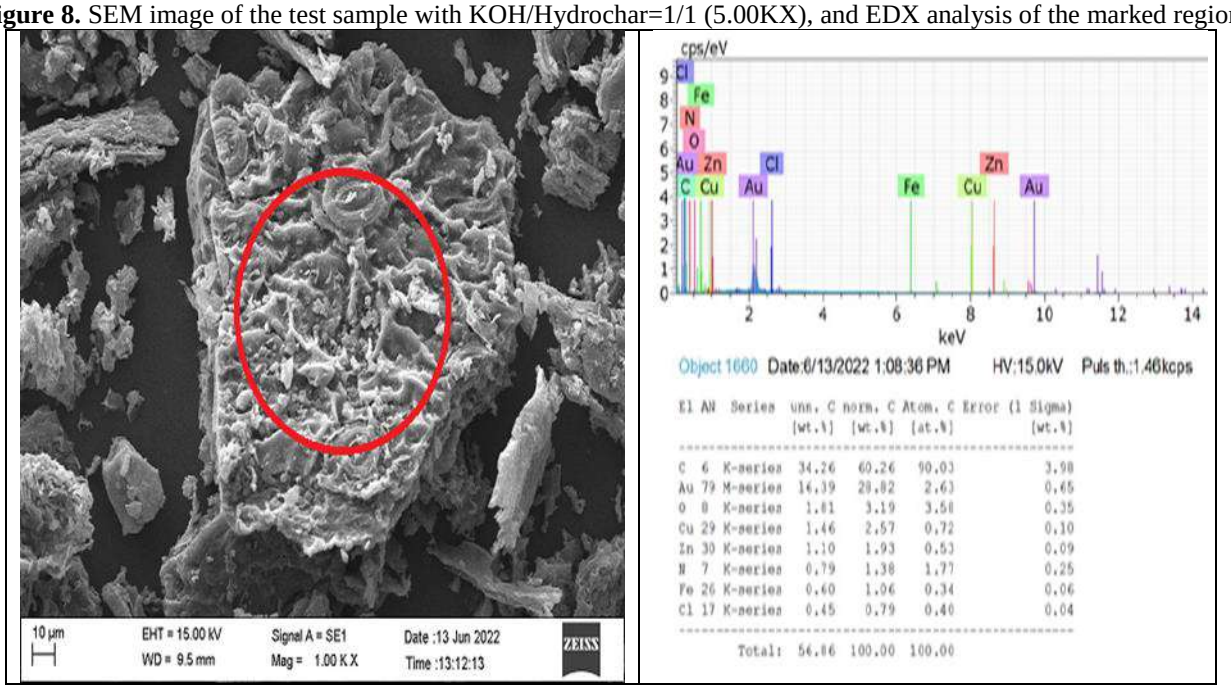

Figure 9. SEM image of the test sample with KOH/Hydrochar=1/2 (1.00KX), and EDX analysis of the marked region

3.3. Methylene Blue Adsorption Experiment Results.

The amount of chemical material used for activation is an important parameter in the activated carbon production process. In the interaction of lignocellulosic materials with potassium hydroxide, simultaneous reactions occur. These reactions, which start at low temperatures, can be listed as depolymerization of biomass, dehydration of biopolymers, formation of aromatic structures and separation of hydroxyl groups (Yaslı, 2019).

In order to understand the effect of different KOH ratios on the product properties in the production of activated carbon, experimental studies, the conditions of which are given in Table 1, were carried out, and the absorption property of the obtained activated carbon was examined. In the absorption studies performed with methylene blue, the extraction yields seen in Table 2 and Table 3 were obtained. As a result of the absorption experiments, it was observed that the absorption properties of activated carbon improved as the KOH ratio increased. Accordingly, in the experiments performed as KOH/Hydrochar=1/1 and 1/2, it was observed that the highest adsorption efficiency (KOH/Hydrochar:1/1) was 99.24% in the A1 sample.

Table 1. Experimental operating conditions with KOH

Sample Code	Sample Name	Step 1 (Carbonization)		Step 2(HTC)		Step 3 (Activation)		
		Temp. (°C)	Time (h)	Temp. (°C)	Time (h)	Temp. (°C)	Time (h)	KOH/Hydrochar
A1	Tea Plant Waste	800	24	200	12	600	4	(1/1)
A4		800	24	200	12	600	4	(1/2)

Table 2. Methylene blue absorption capacities (In solutions of 100 mg/L and 300 mg/L.) of the samples produced in the experiments performed with KOH

Sample Code	Initial Methylene Blue (ppm)	Remaining in solution MM (ppm)	Extraction Yield (%)	Initial Methylene blue (ppm)	Remaining in solution Methylene blue (ppm)	Extraction Yield (%)
A1	100	1,82	98,18	300	2,27	99,24
A4	100	1,90	98,10	300	5,10	98,30

When the data in Table 1 and Table 2 were examined, it was seen that the best result was obtained in the A1 coded sample in solutions containing 100 mg/L and 300 mg/L methylene blue, and the extraction efficiency of this sample was calculated as 99.24%.

4. Results

In the BET analyzes of the products obtained from the hydrothermal carbonization experiments, it was determined that the surface area of the product that was not activated after HTC treatment was 2.13 $m^{2/}$gr. When the SEM images of these samples were examined, it was seen that the surface on which the porous structures were formed was recessed and protruding, and rough surfaces were formed. While the surface area of the samples activated with KOH after

hydrothermal carbonization was determined as 887.41 m^2/g in the sample mixed with KOH/Hydrochar=1/1 ratio, it was determined as 874.77 m^2/g in the sample mixed with KOH/Hydrochar=1/2 ratio. It was determined that the chemical activation process applied after the HTC process was effective in the formation of the pores. It was understood that KOH, which is used as an activator, increases the rate of degradation of the raw material during the carbonization process. According to SEM images and BET analysis results, it was understood that the activation method applied with KOH was effective in pore formation.

5. Acknowledgements

This study was supported by the Fırat University Scientific Research Projects Coordination Unit, within the body of the Fırat University Rectorate, within the scope of the FÜBAP MF.22.02 code number 'Production of Activated Carbon from Tea Plant Wastes and Almond Shells by Hydrothermal Carbonization Method' project. We would like to thank Fırat University Scientific Research Projects Coordination Unit for its economic support in the project.

6. Resources

Aslan, S., (2021). Çörek otu posasının aktif karbon üretiminde değerlendirilmesi, Fırat Üniversitesi Müh. Bil. Dergisi 33(1), 193-201, 2021

Chingombe, P., Saha, B., Wakeman, R.J., (2005). Surface modification and characterisation of a coal-based activated carbon. *Carbon* N Y 43,3132–3143. Http://Dx.Doi.Org/10.1016/J.Carbon.2005.06.021.

Gerçel, Ö., Özcan, A., Özcan, A.S., Gerçel, H.F.,(2007). preparation of activated carbon from a renewable bio-plant of euphorbia rigida by H_2SO_4 activation and its adsorption behavior in aqueous solutions, *Appl. Surf. Sci*. 253, 4843–4852. Http://Dx.Doi.Org/10.1016/J.Apsusc.2006.10.053.

González-García, P. (2018). Activated carbon from lignocellulosics precursors: a review of the synthesis methods, characterization techniques and applications, *Renewable and Sustainable Energy Reviews*, 82(1), 1393-1414.

Huang, Q., Gao, L., Sun, Y., Gao, Y., Li, B.Q., Wang, Y.,(2013). Preparation, characterization and evaluation of adsorptive properties of leather waste based activated carbon via physical and chemical activation, *Chemical Engineering Journal*, 22, 62–71.

Karnib, M., Kabbani, A., Holail, H., Olama, Z.,(2014). Heavy metals removal using activated carbon, silica and silica activated carbon composite, *Energy Procedia* 50, 113–120. http://dx.doi.org/10.1016/j.egypro.2014.06.014.

Mohamad Nor, N., Lau, L.C., Lee, K.T., Mohamed, A.R., (2013). Synthesis of activated carbon from lignocellulosic biomass and its applications in air pollution control - A review, *J. Environ. Chem. Eng*. 1, 658–666. http://dx.doi.org/10.1016/j.jece.2013.09.017.

Sharma, G., Naushad, M., (2020). Adsorptive removal of noxious cadmium ions from aqueous medium using activated carbon/zirconium oxide composite: Isotherm and kinetic modelling, *J. Mol. Liq*. 310, 113025. http://dx.doi.org/10.1016/j.molliq.2020.113025.

Suarez, L., Benavente-Ferraces, I., Plaza, C., de Pascual-Teresa, S., Suarez-Ruiz, I., Centeno, T.A., (2020). hydrothermal carbonization as a sustainable strategy for integral valorisation of apple waste, *Bioresource Technology* 309, 123395.

Tehrani-Bagha, A.R., Balchi, T., (2018). Catalytic wet peroxide oxidation, adv. oxid process wastewater treat emerg. *Green Chem. Technol*,375–402. http://dx.doi.org/10.1016/B978-0-12-810499-6.00012-7.

Yaashikaa, P.R., Senthil Kumar, P., Varjani, S.J., Saravanan, A., (2019). Advances in production and application of biochar from lignocellulosic feedstocks for remediation of environmental pollutants, *Bioresour. Technol*, 292, 122030. http://dx.doi.org/10.1016/j.biortech.2019.122030.

Yaslı, M, A., (2019). Antep fıstığı kavlatma tesisi atıklarından hidrotermal yöntemle aktif karbon üretimi, Mehmet Ali Yaslı, Yüksek Lisans Tezi, Fırat Üniversitesi, Fen Bilimleri Enstitüsü.

International Conference on Advances and Innovations in Engineering

Design of Pellet Extrusion System for 3D Printers

Erdoğan KARİP[1], Mehtap MURATOĞLU [2], Emrah ÇELİK [3]

[1,2,3] Department of Metallurgical and Materials Engineering, Faculty of Engineering, Fırat University, Elazığ, Türkiye
[1]erdogankarip13@gmail.com, [2]mehtug@firat.edu.tr, [3]emrahcelik@firat.edu.tr,

[1](ORCID: 0000-0002-2679-1360), [2](ORCID: 0000-0002-8237-7869), [3](ORCID: 0000-0001-7443-0351)

Abstract

Three-dimensional (3D) printers, their ever-increasing use and successful examples in different sectors have made these printers more popular. Recently, the use of 3D printing has been spreading in areas such as industrial applications, bioprinting, medical applications and artistic applications. However, the extruder designs of the devices used in 3D printing are mostly suitable for materials in filament form. Although filament printing is not a problem per se, it creates problems in printing materials that do not exist as filaments (e.g., biopolymer and composite materials). Especially 3D printing of biopolymers developed at laboratory scale is an important problem. In this study, a prototype with a pellet extrusion system was designed for 3D printing of composite biopolymers. The plastic parts of the prototype are 3D printed. Other parts required for pellet extrusion (extruder, fan, thermistor, heating and DIY parts etc.) were procured through purchase. The utility of the designed pellet extrusion system has been tested by printing composite biopolymers. This design will bring a different perspective and speed to laboratory-scale studies.

Keywords: 3D printers, pellet extrusion system, composite, biopolymer.

1. Introduction

Three-dimensional printing (3D printer) technologies are widely used today [1]. Objects designed in a computer environment and meeting different needs can be printed with three-dimensional printers. The interest in 3D printers considering the ease of printing, unique design and economic aspects is increasing [2]. There are different material alternatives according to the function of the object to be printed in 3D printers. The most commonly used materials are acrylic nitrile butadiene styrene (ABS) and polylactic acid (PLA) materials [3, 4]. There has been an increase in filament types with different properties in recent years [5].

3D printing technology, defined as additive manufacturing, meets needs in many different areas [6-8]. Increasing usage areas day by day and obtaining many different products from 3D printers have increased the need for 3D printers indispensably. One of the biggest reasons for this is used the different printing technologies [9]. The most commonly used 3D printing technologies:

- Stereolithography (SLA),
- Fused deposition modelling (FDM),
- Selective Laser Sintering (SLS),
- Laminated object manufacturing (LOM),
- Digital Light Processing (DLP).

FDM, one of the 3D printing technologies, is the most frequently used printer technology for model or printing. Printing products obtained by melting thermoplastic filaments are created from the printer based on the layer-by-layer printing principle [10]. After the melt material sprayed in the layer principle is flowed, the 3D object is created by instant cooling with the fan air flow [9]. This extrusion method is simple and consistent. It can also be applied to

[1]Corresponding author

almost any material that can be pushed out of the mold and cured quickly [11]. Therefore, it offers superior application opportunity in composite biopolymer materials. FDM technology is used in many new materials such as nanocomposites [12], ceramics [13] and biopolymers [14]. However, preparing composite biopolymer as filament causes different problems (time, cost, design, etc.).

A filament extruder is a system where the material (usually polymer; PLA, ABS etc.) is rapidly heated from a solid state and pressed through the extrusion system. The heated polymer passes through the nozzle and is shaped in three dimensions. The printing process then deposits the material and builds it up in layers to create a 3D object. If the extruder does not perform properly, the 3D printer will not produce geometrically or mechanically correct parts [15, 16]. For this reason, a great amount of effort has been dedicated by many researchers, in the past, to improve the extruder designs and characterize their performance [17, 18]. But there are areas that need further improvement. One of these areas is the printing of composite biopolymers without turning them into filaments. Because the filament formation process adds at least one further heating step to the material. This heating step may cause deterioration in the structure of composite polymers. Also, some biomaterials are affected by this additional heating step. Therefore, it may be necessary to use a pellet extrusion system [19]. This is of particular interest in the printing of biopolymers for environmental biodegradability, mechanical, or esthetic reasons. Unfortunately, pellet 3D printers exist in very few numbers and either do not suit the intended small scale or do not provide the versatility and freedom to configure and develop [11].

In this study, a prototype with a pellet extrusion system was designed for 3D printing of composite biopolymers. The utility of the designed extruder was tested by printing composite biopolymers. This design will provide benefits especially for laboratory scale studies such as a different perspective, time, cost and ease of design.

2. Design of Pellet Extrusion System

A three-dimensional printer with fused deposition modelling (FDM) technology was used in experimental studies. There are two fundamental components of any FDM 3D printer: the extruder assembly and the mechanical scanning system. The extruder's ability to reliably and accurately output the correct quantity of material over varying distances is fundamental to the printing process. However, the accuracy of the extruded material is insignificant if the mechanical axis is inaccurate or has a limited capability. For this reason, several 3D printers that are available on the market at affordable prices, are non-proprietary, are open-coded and allow some changes to be made, were examined. In the examinations, it was observed that three-dimensional printers such as Creality Ender 3 3D pro, Creality Ender 3 V2, Easy Threed X2 were in a structure that allowed the changes suggested within the scope of the project. The Creality Ender 3 V2 model 3D printer was purchased within the scope of the FÜBAP (MF.21.64) project.

Creality Ender 3 V2 printer has been successfully installed in the laboratory. Then, optimization settings were made and samples were printed. Figure 1 shows the Creality Ender 3 V2 printer and the printed sample.

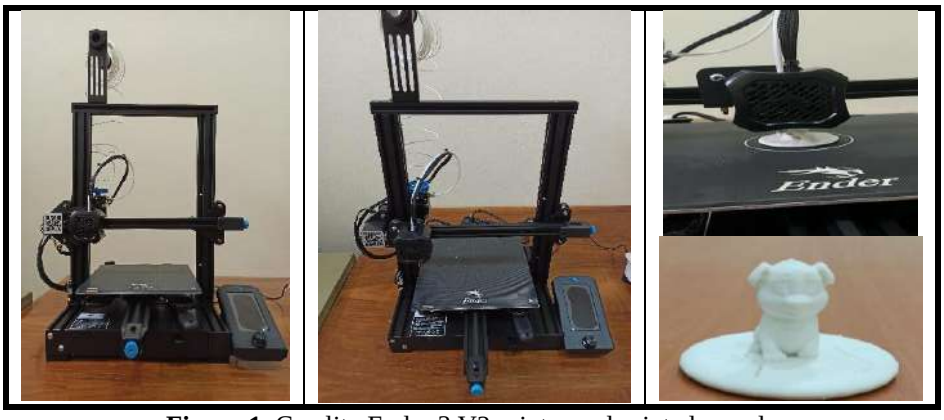

Figure 1. Creality Ender 3 V2 printer and printed sample

System parts supplied for use in the pellet extrusion system and also design plan are given in Figure 2.

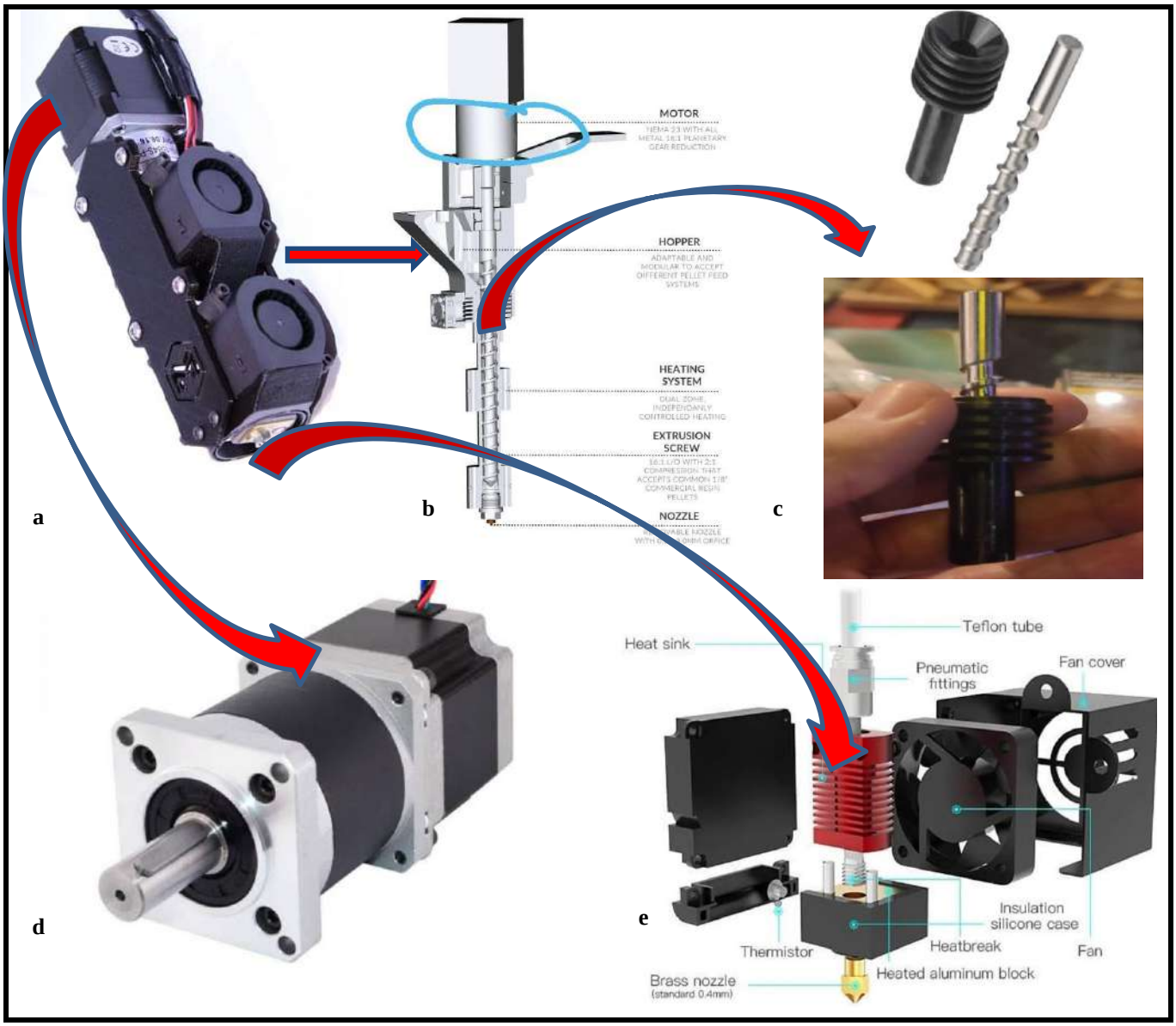

Figure 2. System parts supplied for use in the pellet extrusion system and design plan

Figure 2-a shows the designed pellet extruder system. Figure 2-b shows the internal structure of the pellet extrusion system. This section consists of the nema stepper motor, hopper section, heating system, extrusion screw and nozzle section. Figure 2-c shows the DIY section where the biopolymers will move and be pushed by the stepper motor in the heating system. Figure 2-d shows the nema stepper motor used in the pellet extrusion system. Nema 23 stepper motor has L=56 mm gear and ratio 15:1 high precision. Finally, figure 2-e includes the extruder head compatible with the standard Crealty Ender 3 V2 model printer used in pellet extrusion design.

Other system parts such as side valves and fan holders of the planned pellet extrusion system, namely plastic parts, were printed in three dimensions. These system parts are made ready for printing using the 3D slicing program. Simplify 3D files of the pellet extrusion system are given in Figure 3. Additionally, the pellet extrusion system parts printed on a three-dimensional printer are given in Figure 4.

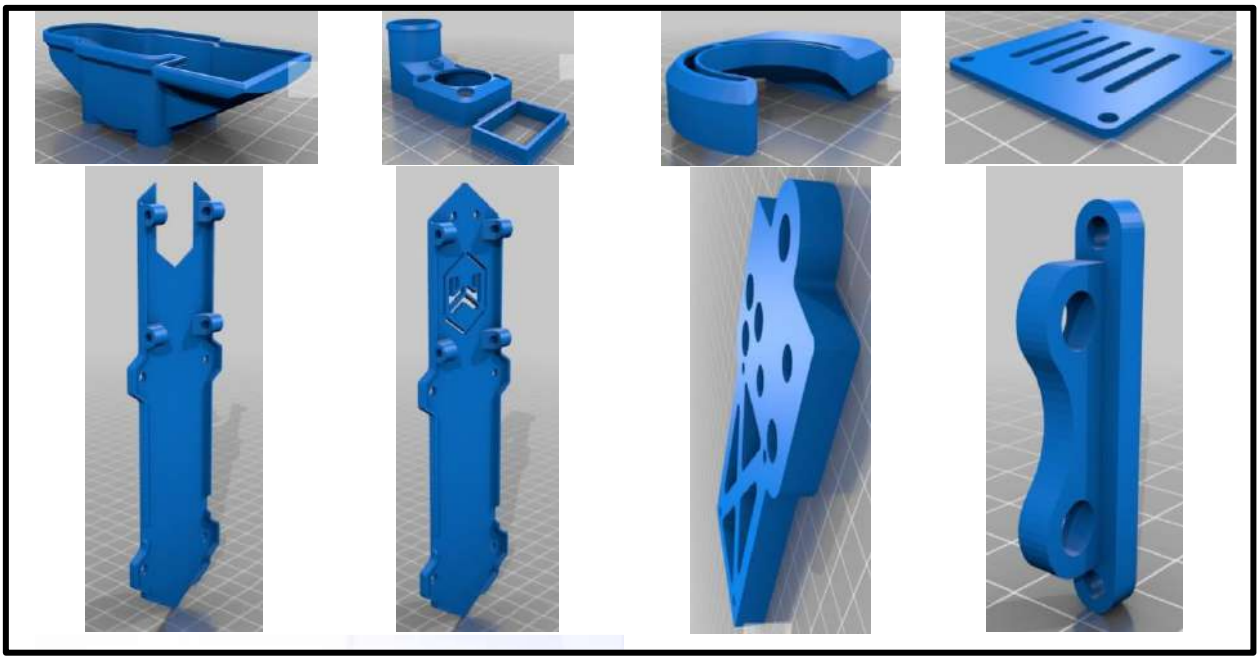

Figuer 3. simplify 3D files of pellet extrusion system

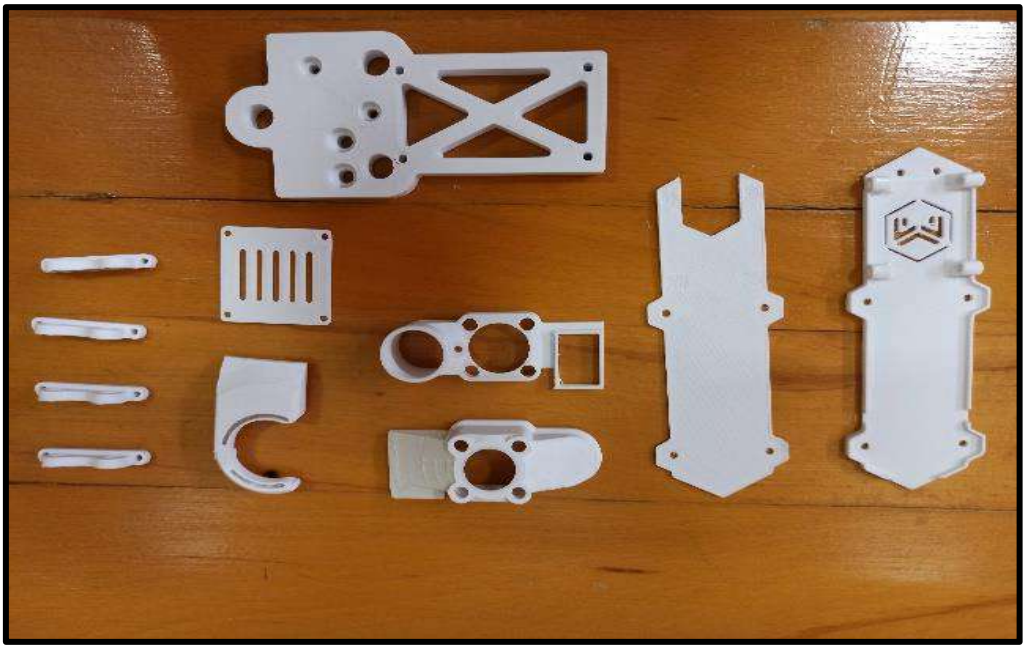

Figure 4. Pellet extrusion system parts printed on a three-dimensional printer

Then, the assembly process of the system parts (see Fig. 2) and the system parts printed on a 3D printer (see Fig. 3-4) was carried out. The final version of the pellet extrusion, the assembly process of which is completed, is given in Figure 5.

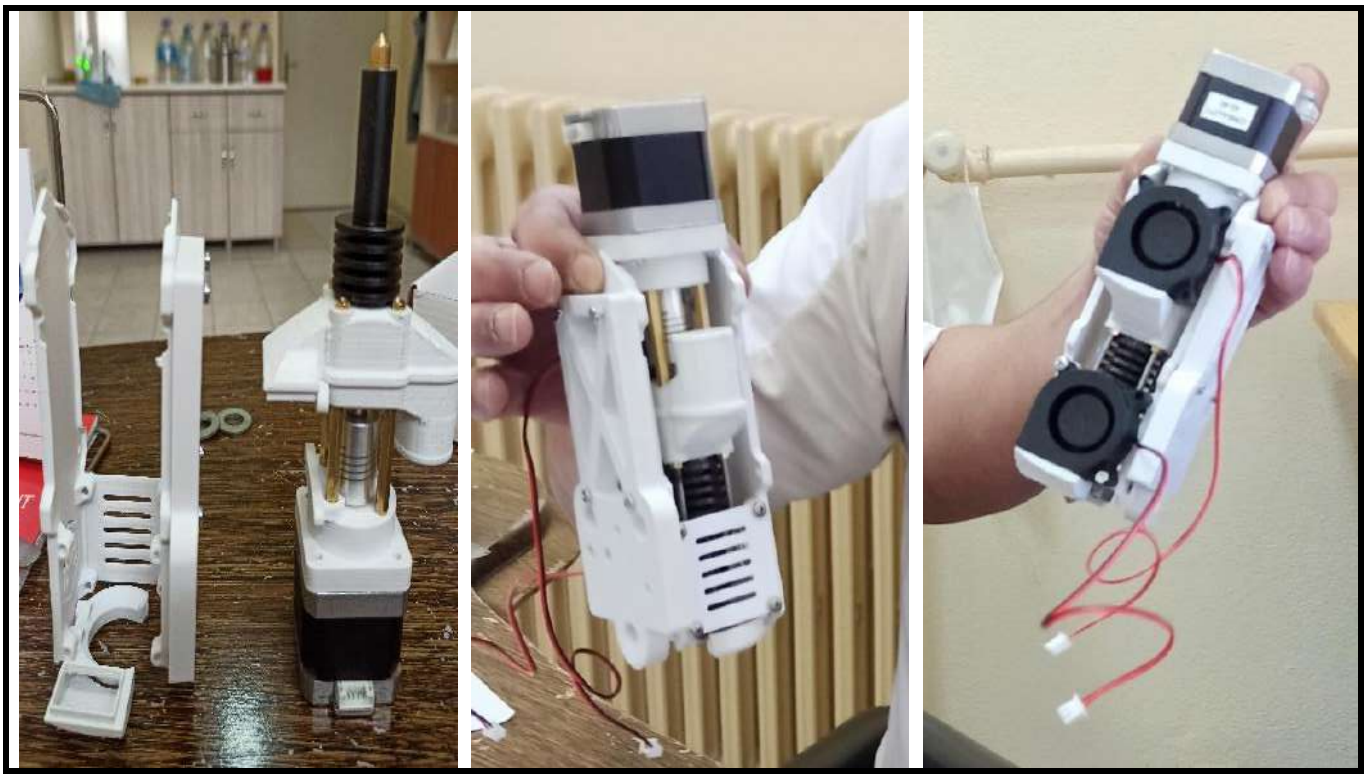

Figure 5. The final state of the pellet extrusion

After this stage, the pellet extrusion system was mounted on the Creality Ender 3 V2 3D printer. Installation images of the pellet extrusion system to the Creality Ender 3 V2 three-dimensional printer are given in Figure 6.

Although pellet extrusion has been around for a long period of time, studies on its application in 3D printing are limited. It is mostly due to the difficulty in obtaining a consistent extruded material from pellets. A simple reason is the material introduced to the extruder is hard to control in exact quantities. The pelleted material is held in a hopper in the form of granular-sized pellets for the screw to push through the system. Commonly, the material is gravity assisted and in some cases the hopper is assisted by an agitator or stirrer. This is to help prevent poor pellet flow characteristics and remove any material sticking to the wall. To reduce any conveying problems, the hopper has been designed to be cylindrical in shape as a square hopper's corners could cause feeding issues. As this design has the screw in line with the hopper, the hopper acts more as a guide for the polymer to flow into the throat of the extruder [11].

It is possible to use by converting them into filament of composite biopolymers prepared in laboratory studies. However, single screw or twin screw extruder is needed for this process. These extruders are both expensive and not very common. Moreover, in some studies, it may not be possible to turn into filament the prepared composite polymer. Another problem encountered in converting into filament of composite biopolymer is the need for a large amount of powder/granular sample. As a result, it causes problems such as prolonging the sample preparation phase, increasing the need for consumables and loss of time. The pellet extrusion system offers the opportunity to print the sample directly without the need for filament preparation. For this reason, it provides a great advantage, especially in laboratory-scale studies. In addition, it provides a great advantage in applications such as nanocomposite, ceramic reinforced polymer and preparation of different polymer mixtures. Another advantage of the pellet extrusion system is that it allows three-dimensional printing of polymer waste or plastic waste. It will also provide great convenience in the studies to be carried out by the researchers in this context.

Figure 6. Installation images of the pellet extrusion system on the Creality Ender 3 V2 three-dimensional printer

3. Results

We have successfully developed a pellet extrusion system that allows three-dimensional printing of composite polymers prepared in a laboratory.

The pellet extrusion system resulted in a design that can be mounted on an innovative, open-source three-dimensional printer and print PLA, ABS or composite biopolymer.

In addition, it was observed that better printing quality could be achieved by homogeneously mixing and heating the composite polymers to be three-dimensionally printed.

4. Acknowledgements

This study was financed by Fırat University Scientific Research Projects Coordination Office (FÜBAP) within the scope of project number MF.21.64. We would like to thank FÜBAP employees for their support.

5. References

[1] Wimmer, R., Steyrer, B., Woess, J., Koddenberg, T., Mundigler, N. "3D printing and wood". Pro Ligno, 11(4), 144-149, 2015.
[2] Conner, B, P., Manogharan, G, P., Martof A. N., Rodomsky, L. M., Rodomsky, C. M., Jordan, D. C., Limperos, J. W. "Making sense of 3-D printing: Creating a map of additive manufacturing products and services". Additive manufacturing, 1, 64-76, 2014.
[3] Bulanda, K., Oleksy, M., Oliwa, R., Budzik, G., Gontarz, M. "Biodegradable polymer composites based on polylactide used in selected 3D Technologies". Polimery, 65(7- 8), 557-562, 2020.
[4] Cengiz, Ö., Aktepe, Ş. "Evaluation of the Potentiality of Wood and Processing Dust as Sustainable Raw Materials for 3 Dimensional (3D) Printers". European Journal of Science and Technology, 38, 143-150, 2022.
[5] Hunt, E, J., Zhang, C., Anzalone, N., Pearce, J, M. "Polymer recycling codes for distributed manufacturing with 3-D printers". Resour Conserv Recycl 97, 24–30, 2015.
[6] Mpofu, T, P., Mawere, C., Mukosera, M. "The Impact and Application of 3D Printing Technology." International Journal of Science and Research (IJSR) ISSN (Online): 2319-706, 2014.
[7] http://www.chocedge.com 12/2018.
[8] Lee, J, Y., An, J., Chua, C, K., "Fundamentals and applications of 3D printing for novel materials, Applied Materials today." 7, 120-133, 2017.
[9] Gül, M. "Development of 3D Printer for Use in Biomedical Engineering". International Journal of 3D Printing Technologies and Digital Industry, 2(3), 85-92, 2018.
[10] Marcincinova, L, N., Kuric, I. "Basic and Advanced Materials for Fused Deposition Modelling Rapid Prototyping Technology." Manuf. and Ind. Eng., 11(1), 1338-6549, 2012.
[11] Whyman, S., Arif, K, M., Potgieter, J. "Design and development of an extrusion system for 3D printing biopolymer pellets" The International Journal of Advanced Manufacturing Technology, 96, 3417–3428, 2018.
[12] Dul, S., Fambri, L., Pegoretti, A. "Fused deposition modelling with ABS–graphene nanocomposites". Compos A: Appl Sci Manuf 85, 181–191, 2016.
[13] Salea, A., Prathumwan, R., Junpha, J., Subannajui, K. "Metal oxide semiconductor 3D printing: preparation of copper (ii) oxide by fused deposition modelling for multi-functional semiconducting applications". J Mater Chem C 5 (19), 4614–4620, 2017.
[14] Brooks, B, J., Arif, K, M., Dirven, S., Potgieter, J. "Robot-assisted 3D printing of biopolymer thin shells. Int J Adv Manuf Technol, 89 (1–4), 957–968, 2017.
[15] Durgun, I., Ertan, R. "Experimental investigation of FDM process for improvement of mechanical properties and production cost". Rapid Prototyp J, 20 (3), 228–235, 2014.
[16] Sun, Q., Rizvi, G., Bellehumeur, C., Gu, P. "Effect of processing conditions on the bonding quality of FDM polymer filaments". Rapid Prototyp J, 14 (2), 72–80, 2008.
[17] Agarwala, M, K., Jamalabad, V, R., Langrana, N, A., Safari, A., Whalen, P, J., Danforth, S, C., "Structural quality of parts processed by fused deposition". Rapid Prototyp J, 2 (4), 4–19, 1996.
[18] Ahn, D., Kweon, J, H., Kwon, S., Song, J., Lee, S. "Representation of surface roughness in fused deposition modeling". J Mater Process Technol, 209 (15-16), 5593–5600, 2009.
[19] Covas, J., Costa, P. "A miniature extrusion line for small scale processing studies". Polym Test, 23 (7), 763–773, 2004

International Conference on Advances and Innovations in Engineering

Synchronous Reluctance Motor Design for Washing Machine

Deniz Can Dursun[1] , Ahmet Yildiz [2], Mehmet Polat [3]

[1,2,3]Mechatronics Engineering, Faculty of Engineering, Firat University, Elazig, Turkey.
[1]denizcandursun.7@gmail.com, [2]ayildiz@firat.edu.tr, [3]mpolat@firat.edu.tr

[2](ORCID: 0000-0002-8062-2752),[3](ORCID: 0000-0001-6188-8726)

Abstract

In this study, a synchronous reluctance motor was designed for the washing machine. A four pole, three flux barrier, transversally laminated anisotropic rotor synchronous reluctance motor was designed for the washing machine. The designed synchronous reluctance motor for the washing machine was analyzed for wash cycle and spin cycle. Analyzes were carried out with a computer-aided software based on the finite element method. In line with the results obtained, it is observed that a suitable synchronous reluctance motor design was made for the washing machine.

Keywords: finite element method, synchronous reluctance motor, washing machine.

1. Introduction

With the changing energy regulations in the white goods sector, the efficiency of the electric motors used has become an important factor. With the obligations brought by the regulations, the transition from universal motors to brushless synchronous motors in washing machines has become inevitable. However, with the need for motor drivers brought by this transition, a cost disadvantage arises. In addition, fluctuations in the price of magnets in the magnet motors used and the price of magnets due to the fact that most of the raw material is in the Far East countries pose a great risk for mass production conditions. In this context, energy savings can be achieved by replacing the universal motors used in the washing machine with more efficient permanent magnet synchronous motors (PMSMs) or synchronous reluctance motors (SynRMs). However, it is known that PMSM is more expensive than universal motor and SynRM [1]. In addition, the dependence of these motors on the Far East countries in magnet production necessitates the offering of alternative motors to SMSMs. In this respect, SynRMs can be considered as a strong alternative to universal motors due to their high efficiency and low cost [2], [3]. Since there is no winding on the rotors of SynRMs, rotor losses and heating problems do not occur. Due to the absence of copper losses in the rotor of these motors, these machines are called “cold rotor” machines [4], [5]. The fact that it has a lower heating level compared to induction motor (IM) and PMSM is an advantage for these motors. These advantages extend the life and maintenance intervals of SynRM [6], [7]. The fact that SynRMs have a stator structure similar to an IM enables them to be produced on the same production line as the asynchronous machine and offers an advantage over other reluctance machines. The biggest disadvantages of these motors are that they require an external power electronic circuit and their torque ripple values are high [8]–[10]. Thanks to the developing and cheaper power electronics-based driver circuits, the advantages of SynRMs over universal motors have come to the fore and they have become the preferred motors. However, torque ripple in these motors is still an important disadvantage and maintains its importance in studies. There are studies in the literature on reducing torque ripple of SynRM. When SynRM studies are examined in the literature, it is observed that the studies are generally on rotor structure, since the stator structures of SynRMs are similar to other multi-phase alternating current motors. The studies on the rotor design of SynRM are summarized. In the study conducted in [11], a non-parametric model was used to optimize the rotor structure to reduce the torque ripple of SynRMs. An optimization method of rotor structure is proposed to reduce torque ripple using deep neural network. Sample data of the relationship between rotor structural parameters and torque ripple were obtained by the

[1]Corresponding author

finite element method (FEM). As a result of the optimization study, it has been observed that the parameters of the rotor can significantly reduce the torque ripple and increase the average torque. In [12], the effect of considering the current angle when designing the SynRM rotor on the final optimal geometry was investigated. For different ranges of current angles, they were examined and compared using FEM. The ideal current angle was determined for the design and the study was supported by the simulation results. In [13], a torque ripple minimization process for SynRM using the symmetric rotor flux barrier shape is presented. The 30 stator slot, 4-pole SynRM has been shown to be a viable option for high-performance applications. The results of the study were confirmed by Finite Element Analysis (FEA).

2. SynRM Design for Washing Machine

In this study, a preliminary design of a 12 stator slotted, 4-pole, distributed winding, transversally laminated anisotropic (TLA) rotor SynRM for washing machine has been done. The reason for choosing TLA type rotor is because it is simple and cheap to produce compared to axially laminated anisotropic (ALA) rotor SynRM. The reason TLA is simple is that the flux barriers of the rotor are obtained by laser cutting. In the ALA type, the parts of the rotor are cut one by one. TLA and ALA rotor structures are shown in Figure 1. For high performance SynRMs, the TLA rotor type will give the best efficiency and power factor. The torque, current and efficiency of SynRM were calculated according to the characteristics of the washing machine motor.

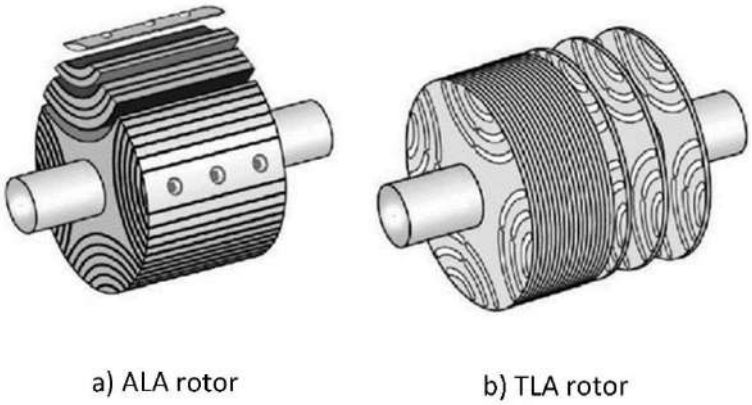

Figure 1. ALA and TLA rotor structures

The SynRM rotor has flux barriers. It has been observed that the increase in the number of flux barriers leads to better channeling of the flux in the rotor and thus an improvement in motor performance. Theoretically, the number of flux barriers should be as much as possible to increase torque performance. However, due to mechanical structure and manufacturing limitations, the number of flux barriers should have a limit according to the design to be made. Figure 2 shows SynRM rotors with different flux barrier numbers. In this study, SynRM with 3 flux barriers was designed.

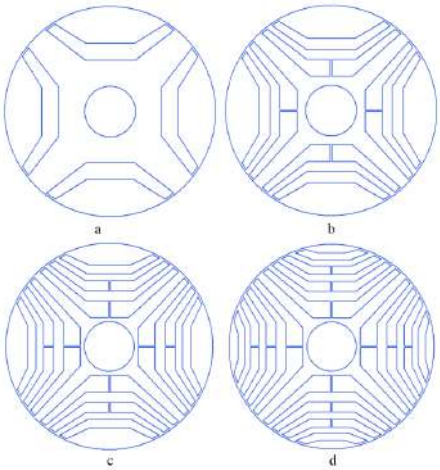

Figure 2. SynRM rotors with different number of flux barriers; a) one barrier b) two barrier c) three barrier d) four barrier

In Figure 3, the design parameters of SynRM are given. In the figure, B_0 is the flux barrier width, Y_0 is the segment width, W is the radial rib width, H is the tangential rib width, and R_b is the starting point distance from the center of the barrier.

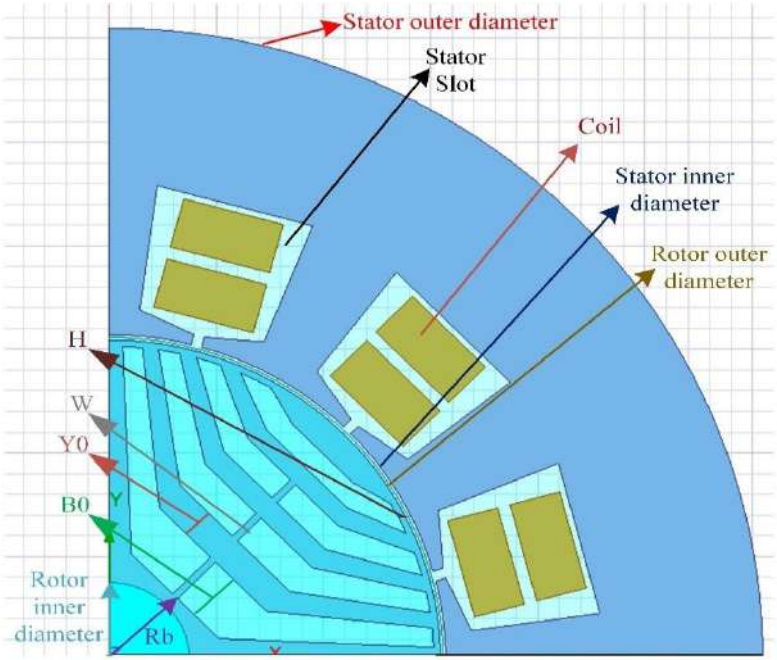

Figure 3. Design parameters of SynRM

The dimensional design parameters of SynRM are shown in Table 1. Distributed winding is used in the designed SynRM. Aluminum is preferred as the winding material. SynRM operates at 3480 rpm in wash mode and 8584 rpm in spin mode. Output parameters in Table 2 [14] were taken as reference when designing SynRM for the washing machine.

Table 9. Dimensional design parameters of SynRM

Stator Outer Diameter (mm)	Stator Inner Diameter (mm)	Rotor Outer Diameter (mm)	Rotor Inner Diameter (mm)	H (mm)	W (mm)	B_0 (mm)	Y_0	R_b (mm)
122	62.8	61.8	15	0.6	0.6	5	2.9	8.7

Table 2. Output parameters of SynRM [14]

Parameter	Wash Cycle	Spin Cycle
Power (W)	408	731
DC-Link Voltage (V)	310	310
Speed (rpm)	3480	8584

3. Finite Element Method Based Analysis of SynRM

In this section, finite element method-based analysis of the designed SynRM was carried out. Analysis studies were carried out separately for wash cycle and spin cycle.

3.1. Output Parameters of SynRM for Wash Cycle

In the wash cycle, the torque of the SynRM was observed to be 1.5 Nm and the current to be approximately 2.31 A, shown in Figure 4 and Figure 5, respectively.

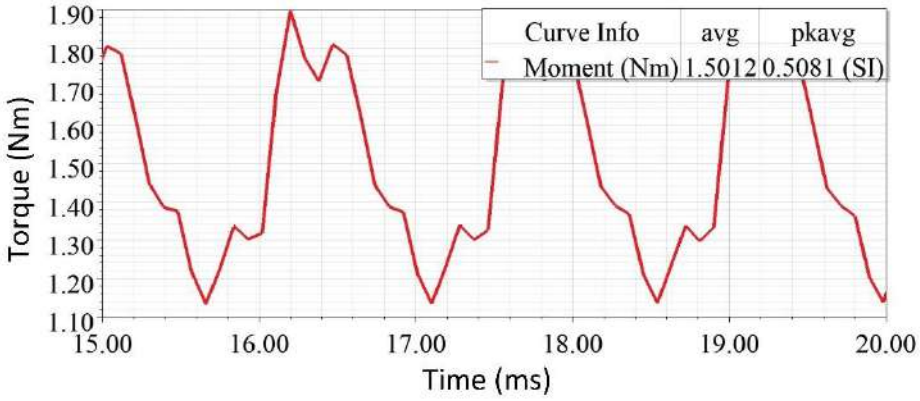

Figure 4. Output torque of SynRM for wash cycle

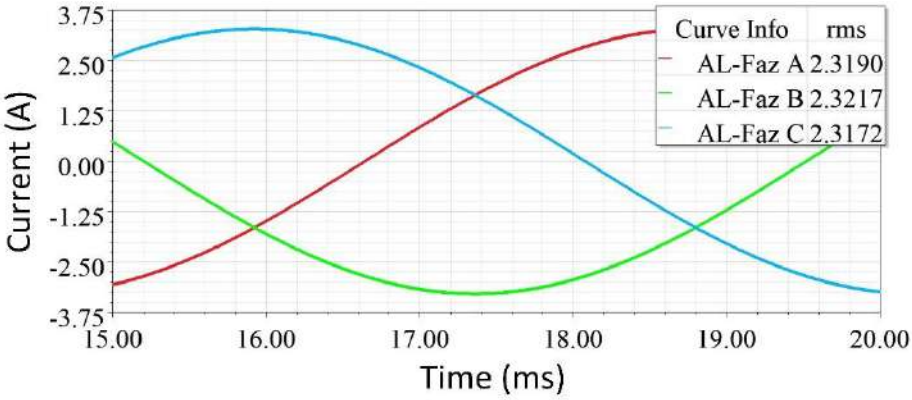

Figure 5. Phase currents of SynRM for wash cycle

As a result of the analysis, the inductance values for the d and q axis were observed to be approximately 149.66 and 62.54, respectively, and are shown in Figure 6.

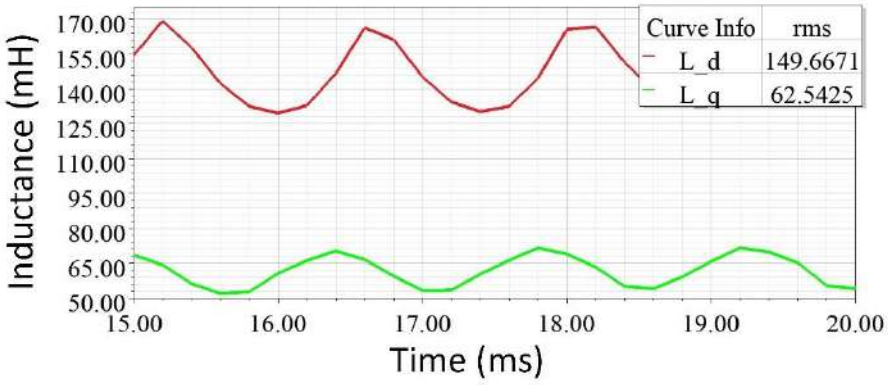

Figure 6. d and q axis inductance of SynRM for wash cycle

The flux distribution of SynRM is given in Figure 7. As can be seen from the results, there was no oversaturation in the motor. A flux density of 1.8 T was observed in the stator teeth. When the flux density distribution is examined,

partial saturations are noticeable. Particularly, there is partial saturation in the tangential rib regions of the rotor. The flux density value of this region is observed to be approximately 2 T.

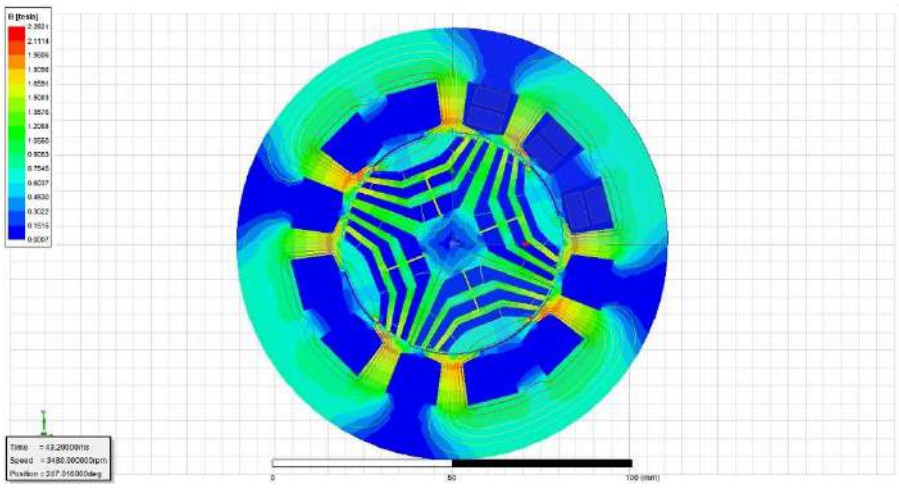

Figure 7. Magnetic flux distribution of SynRM for wash cycle

The output parameters obtained for the wash cycle are summarized in Table 3. In the Table 3, T_r is torque ripple, L_d is d axis inductance, L_q is q axis inductance, P_{out} output power, P_{in} input power and η is efficiency.

Table 3. Output parameters of SynRM for wash cycle

Torque (Nm)	T_r (%)	Current (A)	Back EMF (V)	L_d (mH)	L_q (mH)	η (%)
1.5	40.21	2.31	163	146.66	62.54	79.53

3.2. Output Parameters of SynRM for Spin Cycle

In the spin cycle, the torque of the SynRM was observed to be 0.39 Nm and the current to be approximately 0.97 A, shown in Figure 8 and Figure 9, respectively.

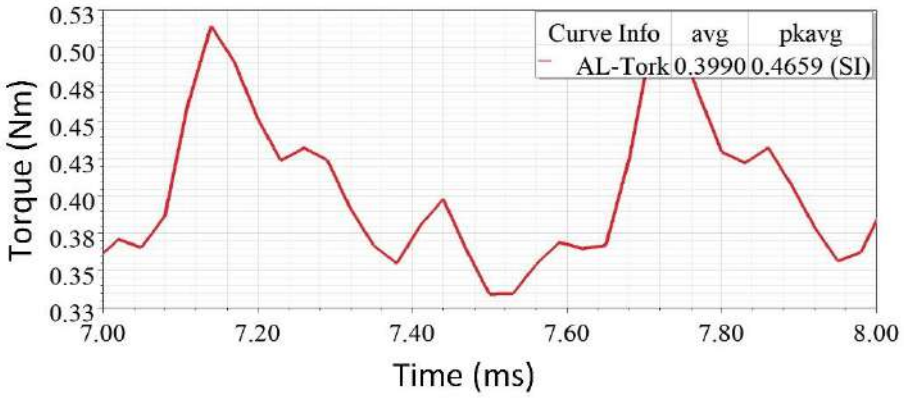

Figure 8. Output torque of SynRM for spin cycle

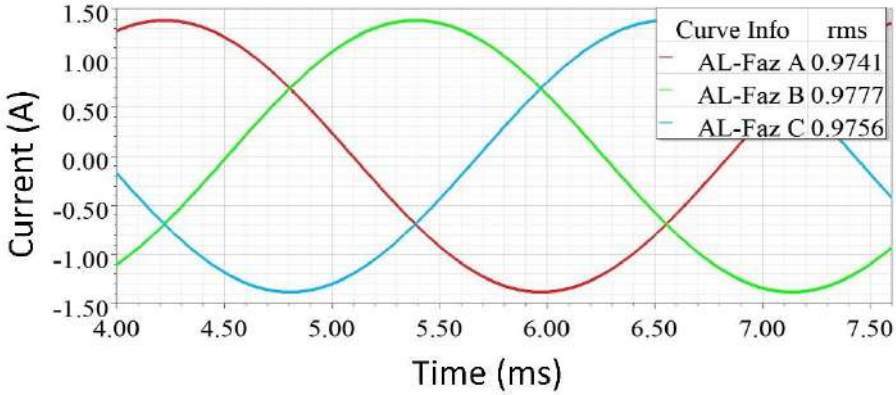

Figure 9. Phase currents of SynRM for spin cycle

As a result of the analysis, the inductance values for the d and q axis were observed to be approximately 230.59 and 73.41, respectively, and are shown in Figure 10.

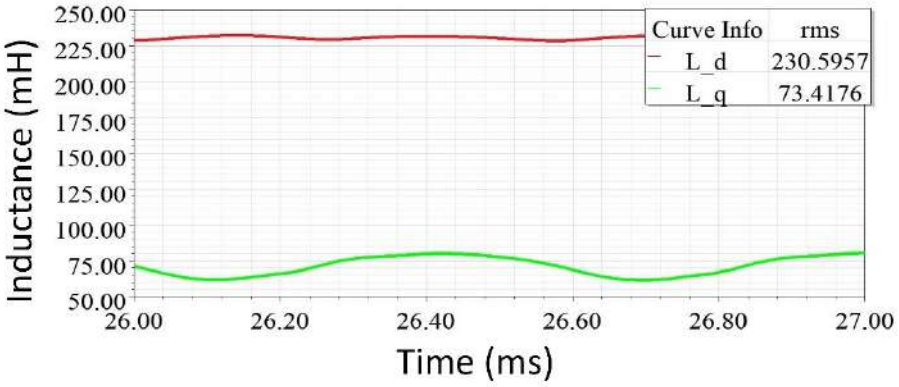

Figure 10. d and q axis inductance of SynRM for spin cycle

The flux distribution of SynRM is given in Figure 11. As can be seen from the results, there is no saturation in the motor. A flux density of 1.3 T was observed in the stator teeth. When the flux density distribution is examined, partial saturations are noticeable. Particularly, there is partial saturation in the tangential rib regions of the rotor. The flux density value of this region is observed to be approximately 1.85 T.

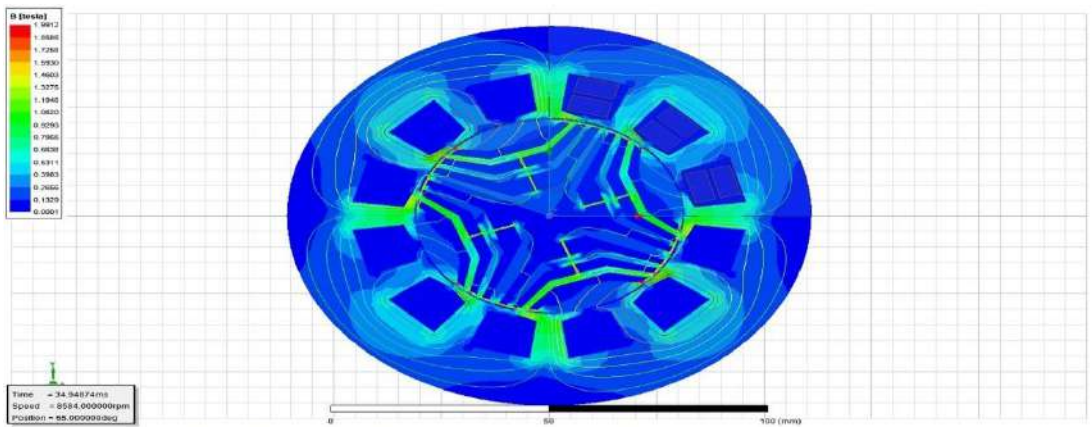

Figure 11. Magnetic flux distribution of SynRM for spin cycle

The output parameters obtained for the spin cycle are summarized in Table 4.

Table 4. Output parameters of SynRM for spin cycle

Torque (Nm)	T_r (%)	Current (A)	Back EMF (V)	L_d (mH)	L_q (mH)	η (%)
0.39	35.29	0.97	284	230.59	73.41	86.24

4. Conclusion

In this study, a four pole, three flux barrier, TLA rotor synchronous reluctance motor was designed for the washing machine. The SynRM design was analyzed with a computer-aided software based on the finite element method. As a result of the study, the output performance of SynRM, designed for the washing machine, was examined for wash cycle and spin cycle. In line with the results obtained, it is observed that a suitable SynRM design has been made for the washing machine. However, it is observed that the torque ripple of the designed SynRM is high. In future studies, it is planned to design SynRM with less torque ripple by optimizing the design parameters of SynRM. In addition, it is aimed to produce the designed SynRM and verify the study with experimental results.

5. References

[1] Lahne HC, Gerling D. "Comparison of state-of-the-art high-speed high-power machines: Research study including a design example of a 50000 rpm induction machine". IECON 2015 - 41st Annual Conference of the IEEE Industrial Electronics Society, November 2015. doi: 10.1109/IECON.2015.7392646.

[2] Mohammadi MH, Rahman T, Silva RCP, Wang B, Chang K, Lowther DA. "Effect of Acoustic Noise on Optimal SynRM Design Regions". IEEE Transactions on Magnetics, 54(3), 1–4, 2018. doi: 10.1109/TMAG.2017.2760859.

[3] Lin FJ, Chen SG, Hsu CW. "Intelligent Backstepping Control Using Recurrent Feature Selection Fuzzy Neural Network for Synchronous Reluctance Motor Position Servo Drive System". IEEE Transactions on Fuzzy Systems, 27(3), 413–427, 2019. doi: 10.1109/TFUZZ.2018.2858749.

[4] Murataliyev M, Degano M, Di Nardo M, Bianchi N, Gerada C. "Synchronous Reluctance Machines: A Comprehensive Review and Technology Comparison". Proceedings of the IEEE, 110(3), 382–399, 2022. doi: 10.1109/JPROC.2022.3145662.

[5] Accetta A, Cirrincione M, Pucci M, Sferlazza A. "A Saturation Model of the Synchronous Reluctance Motor and its Identification by Genetic Algorithms". 2018 IEEE Energy Conversion Congress and Exposition (ECCE), 4460–4465, September 2018. doi: 10.1109/ECCE.2018.8558250.

[6] Yildiz A, Polat M. "Analysis of Synchronous Reluctance Motor using ANSYS Maxwell". 2023 International Conference on Power, Instrumentation, Energy and Control (PIECON), 1–5, February 2023. doi: 10.1109/PIECON56912.2023.10085832.

[7] Özdıl A, Uzun Y. "Finite Element Analyses of a TLA-type Synchronus Reluctance Machine". 2022 International Conference on Electrical, Computer, Communications and Mechatronics Engineering (ICECCME), 1–5 November 2022. doi: 10.1109/ICECCME55909.2022.9988209.

[8] De Pancorbo SM, Ugalde G, Poza J, Egea A. "Comparative study between induction motor and Synchronous Reluctance Motor for electrical railway traction applications". 2015 5th International Electric Drives Production Conference (EDPC), 1–5 September 2015. doi: 10.1109/EDPC.2015.7323219.

[9] Akhila K, Selvajyothi K. "Torque Ripple Minimization in Synchronous Reluctance Motor by Magnetic Circuit Adjustment". 2021 24th International Conference on Electrical Machines and Systems (ICEMS), 472–476, October 2021. doi: 10.23919/ICEMS52562.2021.9634354.

[10] Truong PH, Flieller D, Nguyen NK, Mercklé J, Sturtzer G. "Torque ripple minimization in non-sinusoidal synchronous reluctance motors based on artificial neural networks". Electric Power Systems Research, 140, 37–45, 2016. doi: 10.1016/j.epsr.2016.06.045.

[11] Xu D, Bao X, Xu W, Xu Y. "Rotor topology optimization of a synchronous reluctance motor based on deep neural network model". International Journal of Applied Electromagnetics and Mechanics, 66(3), 445–459, 2021. doi: 10.3233/JAE-201577.

[12] Rezk H, Tawfiq KB, Sergeant P, Ibrahim MN. "Optimal Rotor Design of Synchronous Reluctance Machines Considering the Effect of Current Angle". Mathematics, 9(4), 2021. doi: 10.3390/math9040344.

[13] Chowdhury M, Tesfamicael A, Islam M, Husain I. "Design Optimization of a Synchronous Reluctance Machine for High-Performance Applications". IEEE Transactions on Industry Applications, 57(5), 4720–4732, 2021. doi: 10.1109/TIA.2021.3091416.

[14] Jang H, Cho S, Lee KS, Oh YJ, Lee J. "Design of Power Density Improvement by Applying Novel Shape of Slit and Notch to Outer Rib of Rotor of Spoke-type Permanent Magnet Synchronous Motor". The Open Electrical & Electronic Engineering Journal, 12(1), 2018. doi: 10.2174/1874129001812010075.

International Conference on Advances and Innovations in Engineering

Harnessing AI and NLP Techniques for Combatting Racism and Xenophobia on Online Platforms: A Comprehensive Analysis and Evaluation of Machine Learning Models

Sule KAYA[1] , Bilal ALATAS [2]

[1,2]Software Department, Engineering Faculty, Firat University, Elazig, Turkey.
[1]sule.kaya@firat.edu.tr, [2]balatas@firat.edu.tr

[1](ORCID: 0000-0001-5527-8913), [2](ORCID: 0000-0002-3513-0329)

Abstract

In the contemporary digital landscape, online platforms, while being a source of numerous benefits, unfortunately also serve as a breeding ground for societal issues such as hate speech and racism. These platforms, which facilitate interaction among users, sometimes become mediums where some individuals propagate racist narratives, potentially deepening societal divides and isolating marginalized groups further. The study at hand seeks to address this pressing issue by harnessing the capabilities of artificial intelligence and machine learning, specifically focusing on Natural Language Processing (NLP) techniques, to expedite the process of identifying and mitigating racist content online. Utilizing a unique dataset from Twitter, categorized to indicate the presence or absence of racism and xenophobia, the research applies various data preprocessing techniques to facilitate efficient text analysis. Feature engineering is conducted using the TF-IDF vectorization method, a pivotal tool in text mining. The study evaluates diverse machine learning models using metrics such as accuracy, precision, and recall, offering a comprehensive insight into their performance. The logistic regression and SVM models exhibited promising results, with accuracies of 72.3% and 72.8% respectively, showcasing proficiency in identifying true positive instances. Meanwhile, the decision tree model demonstrated moderate performance with a 63.4% accuracy rate. The research suggests a promising avenue for further optimizing these models, emphasizing the need to enhance accuracy and recall values, especially in detecting racist remarks. Future work should focus on refining the models and exploring additional feature engineering techniques to bolster performance.

Keywords: Racism, Xenophobia, Machine Learning, Artificial Intelligence

1. Introduction

In the digital era, online platforms not only offer numerous benefits but also serve as a breeding ground for societal issues such as hate speech and racism [1]. On these platforms, while users interact with each other, unfortunately, some adopt and propagate racist narratives [2]. This can potentially lead to a greater divide in society and further isolation of marginalized groups [3]. Consequently, the detection of racism has become critically important in identifying racist remarks and content on online platforms [4][5].

Artificial intelligence and machine learning present powerful tools capable of automatically detecting such racist content [6]. In particular, Natural Language Processing (NLP) techniques can be employed to identify racist remarks in text-based content [7]. These techniques facilitate a quicker and more efficient identification of racist content on online platforms, thereby enabling a swifter management and removal of such content [8].

In recent years, numerous researchers have developed various artificial intelligence models and algorithms to detect online hate speech and racism [9]. These models analyze text data using language processing techniques and pinpoint potentially racist content [10]. These studies have made significant strides in the field of racism detection, demonstrating the potential of these techniques in managing racist content on online platforms more effectively [11].

[1]Corresponding author

This article explores the current research and methodologies in the field of racism detection, investigating the potential of artificial intelligence and machine learning in this domain. Furthermore, it discusses how these techniques can be utilized more effectively in racism detection. This study aims to contribute to the development of strategies to prevent online racism.

2. Related Works

The digital world has facilitated the increase of hate speech on online platforms, particularly in the forms of racism and xenophobia [12]. This study focuses on developing strategies to detect and reduce such harmful language usage through Artificial Intelligence (AI) and NLP techniques, thereby making online spaces safer and more inclusive.

Previous research has explored various aspects of hate speech - such as cyberbullying and profane language. A detailed analysis of these terms can help us understand how these phenomena are interconnected. Racism, a significant portion of hate speech, often manifests through derogatory and aggressive language. This study aims to evaluate machine learning models to develop comprehensive strategies to reduce racism and xenophobia on online platforms.

In the study conducted by Dinakar et al. [13] the authors utilized the Hate Speech dataset to evaluate the proposed method. By employing a combination of lexical, syntactic, and semantic features, along with the Support Vector Machines (SVM) classifier, they achieved an F1 score of 0.76. However, the current studies face several limitations including small dataset sizes, a lack of representation of hate content ratio, and deficiencies in label definitions and annotator agreements. Therefore, future research should focus on the development of more robust and accurate models capable of addressing the complexity and variability of hate speech in different contexts.

In their recent study, Nicole Ma and Yu Sun [14] developed a sophisticated system named "TweetWatch" to address the escalating issue of hate speech on Twitter. Utilizing a binary classification Convolutional Neural Network (CNN) and a multi-class CNN, they managed to categorize hate speech tweets into five distinct groups using real-time Twitter data. Remarkably, the binary classification model achieved an AUC score of 98.95% and an F1 score of 97.88%, while the multi-class classification model reported an AUC score of 89.46%. These metrics signify a targeted increase of over 5% compared to previous models documented in various studies, thereby affirming the efficacy of the proposed solution. Furthermore, the study pioneered in developing the first real-time choropleth map for monitoring hate speech in the United States. However, the paper falls short in providing extensive details regarding the utilized dataset and methodology.

In the recent research spearheaded by Aulia Rayhan Syaifullah and Yuliant Sibaroni [15], a novel Hybrid Classifier technique was devised to categorize instances of hate speech prevalent on Twitter, frequently appearing as racial or gender biases, or politically motivated attacks directed at certain groups or individuals. Leveraging data from Twitter tweets pertaining to trending hashtags between November 2021 and June 2022, the researchers amalgamated the Muktiple Layer Perceptron (MLP), K-Nearest Neighbors (kNN), and Naïve Bayes (NB) methodologies within a Hybrid Classifier framework. This approach culminated in a 74% accuracy rate, notably exceeding the individual performance metrics of kNN (63%), NB (73%), and MLP (72%). Nonetheless, the study could benefit from a more comprehensive exploration of the utilized features and the intricacies of the hybrid method applied.

Using Natural Language Processing, a thorough analysis of the identification of hate speech was reported in the recent paper by Md Saroar Jahan and Mourad Oussalah [16]. The study meticulously reviews various machine learning and deep learning methods including Naive Bayes, Logistic Regression, and deep learning architectures such as Convolutional Neural Network (CNN) and Long Short-Term Memory (LSTM). Utilizing metrics like accuracy, precision, and F1 score, it was found that deep learning models generally surpassed traditional machine learning approaches, with Bidirectional Encoder Representations from Transformers (BERT) showcasing the highest performance. However, the study highlights the existing gaps in the research, emphasizing the need for more inclusive language datasets and a deeper exploration of model features and methodologies. The paper calls for further research to enhance the performance and comparability of hate speech detection models.

Kaya and Alatas aimed to develop a new hybrid prediction model capable of identifying racist, xenophobic, and sexist comments published on Twitter [17]. In the utilized dataset, 7.48% of the data were classified as such comments. The authors developed a new hybrid model based on LSTM Neural Network and Recurrent Neural Network (RNN), comparing it with popular supervised intelligent classification models such as Logistic Regression, SVM, NB, Random Forest (RF), and k-NN. The LSTM Neural Network model demonstrated the best performance with an accuracy rate of 95.20%, a recall value of 48.94%, a precision of 60.95%, and a F1 Score of 51.32%. However, it is believed that these deep learning models would produce much better results with a larger dataset.

3. Materials and Methods

This study employs a series of machine learning models to automatically identify racist remarks on online platforms. Below, the methods and materials utilized in this study are elaborated in detail:

Data Set

***Source and Structure of Data**:* This study utilizes a unique dataset comprising Turkish data retrieved from Twitter using Python Web Scraping techniques. The data collected and labeled from Twitter are bifurcated into two categories: 0 (not containing racism and xenophobia) and 1 (containing racism and xenophobia), with 1315 instances labeled as 0 and 1069 instances labeled as 1. The dataset consists of two main columns: 'label' and 'content'. The 'label' column indicates whether the text samples are racist, while the 'content' column contains the text data to be analyzed. Sample data from the dataset are presented in Table 1.

Table 1. Sample Data from The Racism Dataset

content	label
@Hadise Kimsenin amacı özgürlük falan değil hep kendini öne atma çabaları. Onca müslüman kardeşimiz ölürken sesiniz çıkıyor muydu? Türk soydaşlarımız katledilirken sesiniz çıkıyor muydu? Yapılan şey yanlış tabi ki doğru demiyorum fakat burda öyle kendizi üzgünmüş gibi göstermeyin komik**	1
Bu eskiden de bilinen bir şey idi, bu hamas denilen yapının Filistin topraklarına en az israil ve İran kadar zarar vermiştir. kimler kimler ile iş tutuyor, ancak kuran sünnet ile ayırt edebilirsiniz. https://t.co/hXp6xaR1t7	0
@lordsinov Valla putin inattır vazgeçmez ama ülkesi iyice bataklığa gider. Ya da rus halkı artık yeter der protestolar başlarsa belki işler değişebilir...	0
@ayliinustc @iesareyy masmaalesef daha çok bekleriz… benim prodüktör dolandırıcı çıktı..	0
Sığınmacılar bence de gitmeliler onu tartışmayacağım ama bu dünyadaki açlık sorununu nüfusa bağlamakla yani düpedüz yalan söylemekle aynı şey	1
@ajans_muhbir Araplar ve israilliler israeli yine Türkiye'ye Türk milletine kardeş olduğunu gösterdi birçok Arap ülkesi Ermeni soykırımına kabul etti https://t.co/RLgmSu3yIG	0
@Haber Bize zenci muzu yedirmek istiyorlar sanırım. 🤔	0
@sirgreenwod @vinijr Irkçı şerefsiz #Notoracism	1
@ayyildirim1 Birtek Suriyeliler değil afganlar,iranlilar dönmeli Yabancılara gayrimenkul satışı durdurulmalı toprak satışı yasaklanmalı Süreli oturma veya kullanma izni olmalı tapu verilmemeli Yoksa hiçbir anlamı yok	1

Data Preprocessing

Removal of Unnecessary Information: Unnecessary information in the texts (such as URLs, usernames, emojis, etc.) is removed. This step aims to reduce noise in the text data.

Text Cleaning: Special characters in the texts are removed, and all letters are converted to lowercase. This facilitates more efficient text processing by the model.

Tokenization and Stop Words Removal: Texts are tokenized into words, and common words in Turkish (stop words) are removed. This process allows the model to focus solely on significant words.
Stemming: The roots of the words are identified, enabling the model to process the text more effectively.

After all these preprocessing steps, the average data lengths after each step are given in Figure 1.

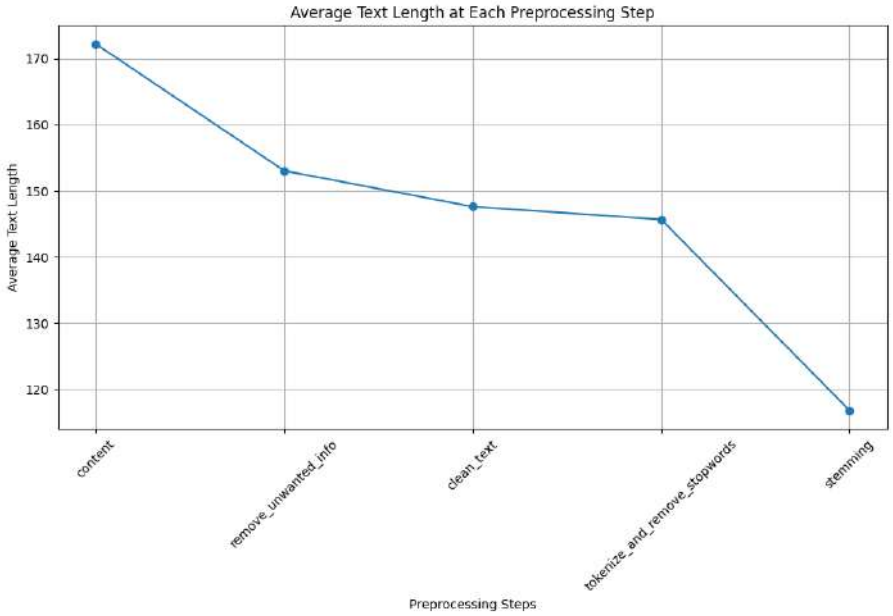

Figure 1. Average Text Length at Each Preprocessing Step

Figure 2. Word Cloud of Processed Text

Feature Engineering

TF-IDF Vectorization: Text data are transformed into numerical features using the TF-IDF (Term Frequency-Inverse Document Frequency) vectorization method. This method represents the relationship between a word's frequency in a document and its inverse frequency across the entire document set, playing a crucial role in text mining.

Modeling

This study employs a range of machine learning models. The suitability of each model for this kind of task and the hyperparameters used are described below:

- ***Logistic Regression (LR):*** This model establishes a linear relationship between features and labels using a logit function. Hyperparameters: { 'C': 1.0, 'penalty': 'l2' }. It is preferred for its quick training time and simplicity.
- **Decision Tree (DT)*:*** This model classifies data using a series of decision rules. Hyperparameters: { 'max_depth': None, 'min_samples_split': 2 }. The tree structure visually represents the importance of features and classification rules.
- ***RF:*** This model creates a more stable and accurate model by using a collection of decision trees. Hyperparameters: { 'n_estimators': 100, 'max_depth': None }. It reduces the risk of overfitting and generally provides high accuracy rates.
- ***SVM:*** This model finds the hyperplane that best separates the classes. Hyperparameters: { 'C': 1.0, 'kernel': 'rbf' }. It utilizes techniques such as the kernel trick and margin optimization.
- ***k-NN:*** This model determines the class of a sample based on the classes of its K nearest neighbors. Hyperparameters: { 'n_neighbors': 5 }. KNN is preferred for its simplicity and comprehensibility.
- ***NB:*** This model is based on Bayes' theorem and assumes independence between features. Hyperparameters: { 'alpha': 1.0 }. It is a popular choice for text mining.
- ***MLP:*** This model can model complex feature relationships using an artificial neural network. Hyperparameters: { 'hidden_layer_sizes': (100,), 'activation': 'relu' }. It employs deep learning techniques.
- ***Gradient Boosting (GB):*** This model creates a strong model by combining weak learners. Hyperparameters: { 'n_estimators': 100, 'learning_rate': 0.1 }. It utilizes boosting techniques.

Model Evaluation

Models are evaluated using various metrics:

- **Accuracy**: Indicates the rate at which the model makes correct classifications.
- **Precision**: Shows how many of the samples predicted as positive are actually positive.
- **Recall**: Indicates how many of all positive samples are correctly identified.
- **F1 Score**: Represents the harmonic mean of Precision and Recall.
- **ROC AUC**: Represents the area under the ROC curve, evaluating the classification performance of the model.
- **Precision-Recall Curve:** A plot that illustrates the relationship between the precision and the recall for different thresholds, providing a comprehensive view of the model's performance.

Optimization and Validation

Stratified K-Fold Cross-Validation: This method ensures a balanced division of the dataset and utilizes each fold for model training and testing. This enhances the model's generalization ability and reduces the risk of overfitting.

Visualization

At this stage, various visualization techniques are used to evaluate model performance, making the analysis more understandable and accessible.

Software and Libraries

This study is conducted in the Python programming language and utilizes libraries such as pandas, scikit-learn, matplotlib, seaborn, re, and snowballstemmer. These libraries provide the necessary tools for data analysis, machine learning modeling, and visualization.

4. Results

In this section, we present the performance evaluation of various machine learning models employed in the automatic detection of racist remarks in online platforms. The evaluation metrics encompass accuracy, precision, recall, and F1-score, which provide a comprehensive view of the models' performance. Here, we delve into the detailed analysis of each model based on the obtained results:

LR

The LR model exhibited a promising performance with an accuracy of 69%. It managed to achieve a precision of 68% and 73% for class 0 and class 1, respectively, indicating a relatively high proportion of true positive predictions. The recall values suggest that the model could correctly identify 84% of class 0 instances and 51% of class 1 instances, showcasing a better identification rate for non-racist remarks. The F1-score, which is the harmonic mean of precision and recall, stood at 75% and 60% for class 0 and class 1, respectively, indicating a balanced performance.

DT

The DT model demonstrated an accuracy of 61%, with a slightly lower performance compared to the logistic regression model. The precision and recall values for both classes hovered around the 60% mark, suggesting a moderate ability to correctly classify instances. The F1-score mirrored the precision and recall values, indicating a balanced but moderate performance.

RF

The RF model showcased an accuracy of 68%, slightly edging out the decision tree model. It exhibited a higher precision for class 1 (72%) compared to class 0 (66%), indicating a better true positive rate for identifying racist remarks. However, the recall value for class 1 was lower (47%), suggesting a need for improvement in correctly identifying positive instances.

SVM

The SVM model mirrored the performance of the random forest model with an accuracy of 68%. It demonstrated a slightly higher precision for class 1 (74%) compared to class 0 (66%), showcasing a proficient identification of true positive instances. The recall values indicate a better performance in identifying class 0 instances, with a score of 87%.

k-NN

The k-NN model exhibited a balanced performance with an accuracy of 62%. The precision, recall, and F1-score values for both classes were closely aligned, indicating a consistent but moderate performance across both classes.

NB

The NB model demonstrated an accuracy of 68%, with a higher precision for class 1 (73%) compared to class 0 (67%). The recall values, however, were higher for class 0 (86%), indicating a proficient identification of non-racist remarks.

MLP

The neural network model showcased a balanced performance with an accuracy of 64%. The precision and recall values for both classes were closely aligned, indicating a consistent ability to identify true positive instances across both classes.

GB

The GB model exhibited an accuracy of 68%, with a slightly higher precision for class 1 (70%) compared to class 0 (66%). The recall values were higher for class 0 (84%), suggesting a proficient identification of non-racist remarks.

In conclusion, the models exhibited a range of performances, with logistic regression and SVM models slightly outperforming others in terms of accuracy and precision. The results suggest a promising avenue for further optimization and enhancement of the models to achieve higher accuracy and recall values, particularly in the identification of racist remarks (class 1). Future work should focus on fine-tuning the models and exploring additional feature engineering techniques to further bolster the performance.

Upon scrutinizing the results delineated in the Table 2 provided, it is discernible that there exists a notable disparity in the performance metrics of various models.

The LR model, manifested in the 10th fold, exhibits a superior performance with an accuracy rate of 72.27% and a ROC AUC value of 80.74%. Its precision and recall stand at 74.22% and 72.27% respectively, with a commendable F1 score of 70.92%. The Precision-Recall Curve value of 72.98% further signifies its proficiency in making accurate classifications and in estimating the true positive rate of the predicted samples.

Conversely, the DT model, as evidenced in the 8th fold, portrays a relatively subdued performance, registering an accuracy rate of 63.45% and a ROC AUC value of 63.20%. The model also recorded precision and recall values of 63.55% and 63.45% respectively, with an F1 score of 63.49%. A Precision-Recall Curve value of 67.60% suggests a potential limitation in the model's classification efficacy and in determining the veracity of samples predicted as positive.

Furthermore, the RF and SVM models demonstrate substantial competence with respective accuracy rates of 71.13% and 72.80%. Their recorded ROC AUC values, standing at 75.76% and 76.18% respectively, underscore a robust classification performance, indicating their aptitude in this specific task. The RF model showcases a precision of 72.94% and a recall of 71.13%, with an F1 score of 69.65%. The SVM model, on the other hand, boasts a precision of 74.65% and a recall of 72.80%, accompanied by an F1 score of 71.52%. Their respective Precision-Recall Curve values of 71.33% and 73.95% further emphasize their competence.

Meanwhile, the k-NN, NB, MLP, and GB models showcase moderate performance, with accuracy rates oscillating between 67.65% and 70.59%. These models maintain a reasonable level of performance, as indicated by their respective precision, recall, and F1 score values, although they do not reach the pinnacle of efficacy exhibited by the LR and SVM models. Their Precision-Recall Curve values, ranging from 60.62% to 72.30%, imply a moderate level of performance in predicting the positive class correctly.

Overall, this analysis serves as a pivotal tool in discerning the relative performance of different models in classification tasks, thereby assisting in pinpointing the models that are more suited for this particular endeavor. It is imperative that further studies be conducted to corroborate these findings and potentially enhance the performance of the less efficacious models.

The graphical representations of the ROC AUC and Precision-Recall Curve analyses are elaborately delineated in Figure 3 and Figure 4.

Table 6. Best Results of Machine Learning Models

Model	Fold	Accuracy	Precision	Recall	F1 Score	ROC AUC	Precision-Recall Curve
LR	10	0,722689	0,74217	0,722689	0,709179	0,807448	0,729840834
DT	8	0,634454	0,635474	0,634454	0,634864	0,631983	0,676007563
RF	2	0,711297	0,729446	0,711297	0,696491	0,757647	0,713316565
SVM	3	0,728033	0,746459	0,728033	0,715231	0,761753	0,739491787
k-NN	10	0,701681	0,701439	0,701681	0,701548	0,730185	0,606153051
NB	10	0,705882	0,719876	0,705882	0,692758	0,785546	0,723040782
MLP	10	0,676471	0,675749	0,676471	0,676002	0,740458	0,659054902
GB	8	0,676471	0,693209	0,676471	0,657109	0,710423	0,717706885

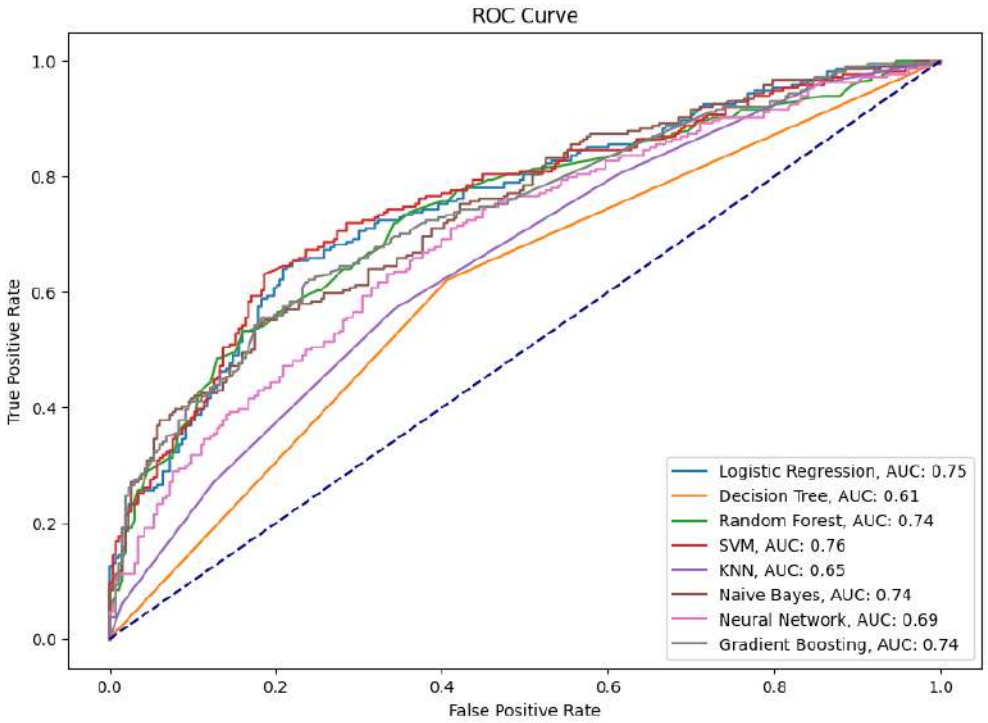

Figure 13. ROC Curve of Machine Learning Models

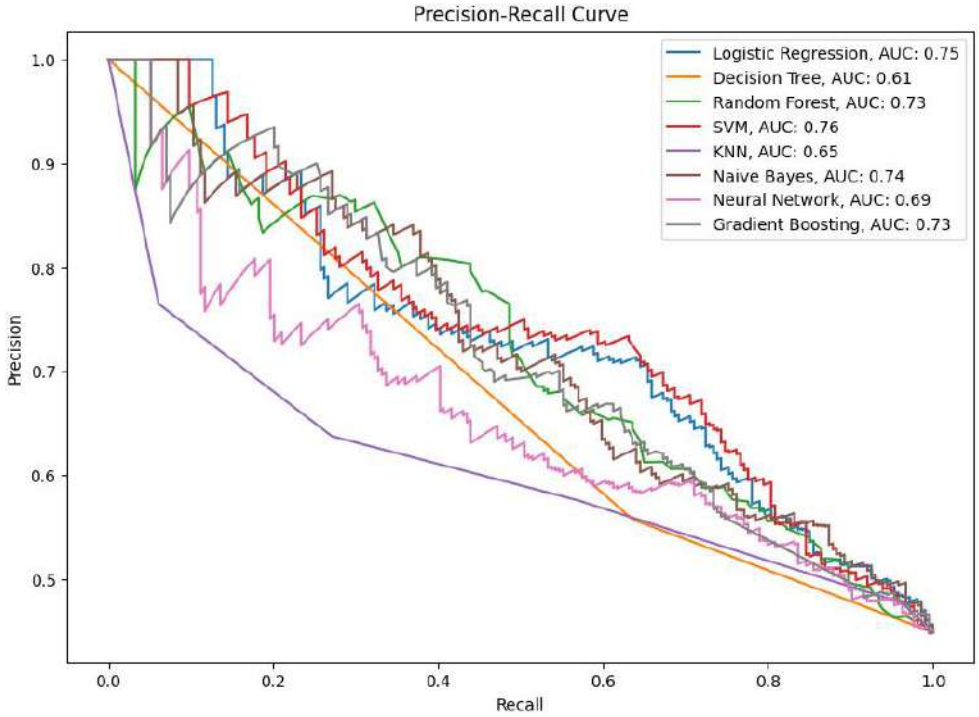

Figure 14. Precision-Recall Curve of Machine Learning Models

5. Conclusions

In the modern digital era, online platforms serve as both a boon and a bane, fostering connectivity while also becoming hotbeds for hate speech and racism. These platforms, unfortunately, have become arenas where some individuals adopt and disseminate racist narratives, potentially widening societal divides and isolating marginalized groups. This situation highlights the pressing need to detect and address racist remarks and content on online platforms.

AI and machine learning emerge as powerful allies in this fight, with NLP techniques spearheading the identification of racist remarks in text-based content. These methodologies have revolutionized the management and removal of such content, making the process faster and more efficient.

This study ventures into the current research and methodologies in the field of racism detection, aiming to contribute to the development of strategies to curb online racism. It focuses on crafting strategies through AI and NLP techniques to detect and mitigate harmful language usage, particularly racism and xenophobia, thereby aiming to create safer and more inclusive online spaces.

By evaluating a series of machine learning models, this study seeks to foster comprehensive strategies to reduce racism and xenophobia on online platforms. It aligns with the recent surge in research efforts to develop various artificial intelligence models and algorithms for detecting online hate speech and racism. These models, utilizing language processing techniques to analyze text data, have shown promising potential in managing racist content more effectively on online platforms.

In conclusion, this study marks a significant step towards developing more nuanced strategies to combat online racism, aiming to foster a more integrated and inclusive society. Future research should focus on refining these models, potentially facilitating more effective management of racist content on online platforms, thereby transforming these platforms into safer and more welcoming environments for all users.

6. References

[1] Mozafari M, Farahbakhsh R, Crespi N. “A BERT-Based Transfer Learning Approach for Hate Speech Detection in Online Social Media”, 2019.

[2] Founta A-M, Chatzakou D, Kourtellis N, Blackburn J, Vakali A, Leontiadis I. “A Unified Deep Learning Architecture for Abuse Detection”, 2018.

[3] Chiril P, Pamungkas EW, Benamara F, Moriceau V, Patti V. “Emotionally Informed Hate Speech Detection: A Multi-target Perspective”, 2021.

[4] Calderón CA, Amores JJ, Sánchez-Holgado P, Blanco-Herrero D. “Using Shallow and Deep Learning to Automatically Detect Hate Motivated by Gender and Sexual Orientation on Twitter in Spanish”, 2021.

[5] Thaher T, Saheb M, Turabieh H, Chantar H. “Intelligent Detection of False Information in Arabic Tweets Utilizing Hybrid Harris Hawks Based Feature Selection and Machine Learning Models”, 2021.

[6] Meesad P. “Thai Fake News Detection Based on Information Retrieval, Natural Language Processing and Machine Learning”, 2021.

[7] Raj C, Agarwal A, Bharathy G, Narayan B, Prasad M. “Cyberbullying Detection: Hybrid Models Based on Machine Learning and Natural Language Processing Techniques”, 2021.

[8] Nijhawan L, Soni U. “A Comprehensive Review on Text-Based Fake News Detection Using Machine Learning and Deep Learning Approaches”, 2021.

[9] Waseem Z, Hovy D. “Hateful Symbols or Hateful People? Predictive Features for Hate Speech Detection on Twitter”, 2016.

[10] Davidson T, Warmsley D, Macy M, Weber I. “Automated Hate Speech Detection and the Problem of Offensive Language”, 2017.

[11] Badjatiya P, Gupta S, Gupta M, Varma V. “Deep Learning for Hate Speech Detection in Tweets”, 2017.

[12] Schmitz M, Burghardt K, Muric G. “Quantifying How Hateful Communities Radicalize Online Users”. Proceedings of the IEEE/ACM International Conference on Advances in Social Networks Analysis and Mining (ASONAM), 2022.

[13] Dinakar K, Jones B, Havasi C, Lieberman H, Picard R. “Common sense reasoning for detection, prevention, and mitigation of cyberbullying”. ACM Transactions on Interactive Intelligent Systems (TiiS), 2, 1-30, 2012.

[14] Ma N, Sun Y. “A Novel System for Regional Twitter Hate Speech Analysis and Detection using Deep Learning Models and Web Scraping”. Computer Science & Information Technology, 13(02), 207-214, 2023. DOI:10.5121/csit.2023.130207

[15] Syaifullah AR, Sibaroni Y. “Hate Speech Hashtag Classification on Twitter Using the Hybrid Classifier Method”. JURIKOM (Jurnal Riset Komputer), 9(4), 828-833, 2022.

[16] Jahan MS, Oussalah M. “A systematic review of hate speech automatic detection using natural language processing”. arXiv preprint arXiv:2106.00742, 2021.

[17] Kaya S, Alatas B. “A New Hybrid LSTM-RNN Deep Learning Based Racism, Xenomy, and Genderism Detection Model in Online Social Network”. International Journal of Advanced Networking and Applications, 14(2), 5318-5328, 2022. [Online]. Available: https://www.ijana.in/papers/V14I2-1.pdf

International Conference on Advances and Innovations in Engineering

Classification of Alzheimer's disease using ADNI dataset with deep learning techniques

Esra YÜZGEÇ[1,2], Muhammed TALO[3]

[1]Software Engineering, Faculty of Engineering, Firat University, Elazig, Turkey.
[2]Computer Engineering, Faculty of Engineering and Architecture, Bingöl University, Bingöl, Turkey.
[3]Software Engineering, Faculty of Engineering, Firat University, Elazig, Turkey.
[1,2] eyuzgec@firat.edu.tr, [3]mtalo@firat.edu.tr

[1,2](ORCID: 0000-0003-2914-2603, [3](ORCID: 0000-0002-1595-5681)

Abstract

Alzheimer's disease is a type of disease that progresses over time and cannot be diagnosed at an early stage. The treatment of Alzheimer's disease, whose cause and initial process cannot be clearly identified, has not yet been found. In order to diagnose the disease, various clinical tests and blood tests are performed, as well as computer-assisted devices such as Magnetic Resonance (MR) and Computed Tomography (CT). Images taken from these devices; Deep learning models can be created by using it as an input image. In this study, MR images obtained from the ADNI dataset, which is an open source dataset, were used. Three different deep learning models were trained using the data received in DICOM format, Axial directional and T1 type. The models trained using the EfficientNet, ResNet-50 and ResNext-50 architectures achieved accuracy rates of 91.54%, 93.53% and 88.80%, respectively. ResNet-50 model, which gives the most successful results among the obtained models, is aimed to be used in the field of medicine to support the stages of disease diagnosis and treatment.

Keywords: Alzheimer's, Magnetic Resonance, Deep Learning

1. Introduction

Alzheimer's disease is a degenerative disease that progresses over time and leads to loss of mental function [1]. Alzheimer's disease occurs long before it is diagnosed and progresses. Early diagnosis of the disease is very difficult. Since it cannot be diagnosed early, it continues to progress for years and continues to progress until it prevents the fulfilment of basic vital functions in the brain.

A clear cause and treatment of Alzheimer's disease has not yet been defined. Since the time interval between the onset of the disease cannot be clearly determined, the physical or mental causes are not clearly known [2]. However, it is estimated that the disease may be caused by different genetic reasons, damage due to head concussion, external factors that may affect the brain such as hypertension [3]. In the definition of the disease, the loss/death of healthy brain cells over time is shown as the cause [4].

Alzheimer's disease is a disease whose initial cause and duration cannot be determined. However, it is known that the disease consists of four main stages. These stages are defined as pre-Alzheimer's stage, early stage, middle stage and advanced stage [5]. In the early stage, loss of basic functions such as learning and impairment of recent memory are recognised as early stage symptoms. In the middle stage, these symptoms are accompanied by difficulty in speaking and weakening of daily life skills such as reading and writing. In the advanced stage, near and far memory disorders and inability to fulfil the most basic vital functions such as eating occur. Alzheimer's disease results in death as a result of failure to treat the advanced disease [6].

Alzheimer's disease is clinically diagnosed by listening to the medical and trauma history of the patient and the patient's relatives. In addition, the patient's brain image is taken by means of computer-aided devices (Magnetic Resonance, Computed Tomography, etc.). Changes in the brain are observed through these images and are expected

[1]Corresponding author

to support the clinical diagnosis of the disease. It is very difficult to distinguish the changes on these images with the human eye, especially in Alzheimer's disease. With the developed deep learning models, it is expected to facilitate disease diagnosis.

Image analysis using Convolutional neural network, one of the deep learning models, is becoming increasingly widespread. Especially security systems, agricultural applications, biomedical applications and image analysis processes in the field of health have started to be used intensively [7]. In the field of health, it is increasingly used in fatal cancer types such as breast cancer, stomach cancer, lung cancer and in the diagnosis of diseases that cause death if not diagnosed early, such as brain hemorrhage, tumour, internal bleeding, Alzheimer's disease [8].

When the articles published in recent years are examined, Serkan Savaş, in an article published in 2021, performed the diagnosis of Alzheimer's stages using pre-trained deep learning architectures. In this article, Efficientnet B2 and B3 models were used and the highest success results were 94.42% and 97.28%, respectively [9]. One of the recent studies in the literature is Mosleh Hmoud Al-Adhaileh's Convolutional Neural Network based study for Alzheimer's disease detection. In this study, models trained using AlexNet and ResNet-50 architectures were used. The architecture trained with AlexNet showed better success than ResNet-50 with an accuracy rate of 94.53% [10].

In this study, it is aimed to create an auxiliary support for disease diagnosis with deep learning models developed using MR images obtained by computer-aided devices. Within the scope of the study, deep learning models were trained using data from the ADNI dataset, which is an internationally published open data set. In the trained models, EfficientNet, ResNet-50 and ResNext-50 models from deep learning architectures were trained and success rates of 91.54%, 93.53% and 88.80% were obtained respectively. By comparing the success rates and metrics, the model with the best success and accuracy rate was determined.

2. Material and Method

Deep learning is a sub-branch of artificial intelligence that has started to be used in almost every field in the world. Inspired by the learning structure of the human mind, deep learning is learning by experience [11]. In the history of programming, a command was expected to be entered for each operation expected from the computer. However, deep learning, as shown in Figure 1, goes beyond commands and follows the learning path by experiencing and making inferences from the data obtained.

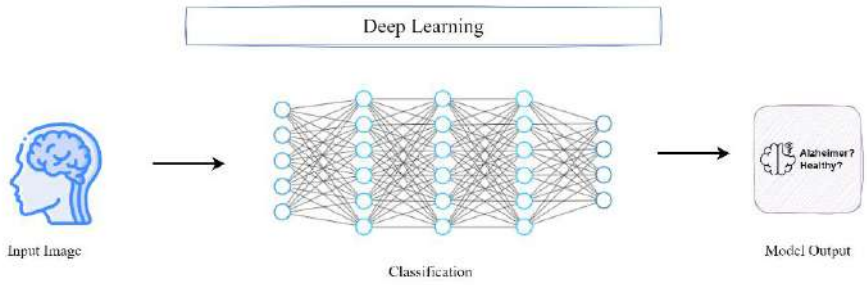

Figure 15. Deep learning method

Images taken from computerized imaging devices such as MRI and CT are data to be processed for deep learning methods. With the use of these data, it is aimed that deep learning methods will play a role in Alzheimer's diagnosis together with clinical memory tests and laboratory tests as shown in Figure 2.

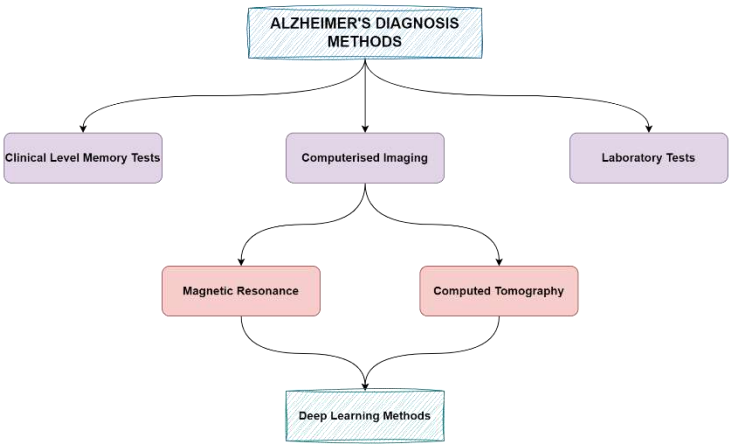

Figure 16. A representation of deep learning and Alzheimer's diagnosis

In this study, EfficientNet B0, ResNet-50, ResNext-50 models were used for the detection of Alzheimer's disease. EfficientNet was proposed by Mingxing Tan and Quoc V. Le from the Google team in 2019. This architecture, which aims to be computationally efficient, has achieved a high success rate in the ImageNet dataset [12]. This architecture uses inverse residual block and swish activation function. Swish activation function is the product of sigmoid and linear activation functions. The EfficientNet B0 architecture used in this study was trained with a total number of 12,277,288 parameters and 80 training rounds.

ResNet-50, one of the ResNet models developed using deep residual block logic, has one maximum pooling, one average pooling and 48 Convolution Layers [13]. Although it is expected that the success of the model will increase as the layers increase in the neural network, this situation may cause the success of the model to decrease after a certain layer level. ResNet-50, which emerged with the aim of creating a truly deep neural network with a residual layer understanding, was used in this study. In the trained ResNet-50 model, 100 training rounds were performed with a total of 25,615,424 parameters.

ResNext Architecture is an architecture prepared and introduced by UC San Diego and Facebook AI Research (FAIR) [14]. This architecture, which was developed based on ResNet models, achieved a great success with a loss rate of 3.03% in 2016 in the Large Scale Image Classification competition (ILSVRC) on the ImageNet dataset. In this study, ResNext-50 architecture was used as an up-to-date architecture. ResNext-50 architecture was trained for 100 epochs with 31,725,456 parameters and accuracy and loss rate results were obtained.

2.1 Datasets

In this study, the ADNI dataset collected by the Alzheimer's Disease Neuroimaging Initiative (ADNI) researchers and checked for accuracy was used to classify Alzheimer's disease and diagnose the time of progression. The dataset, which brings together the data of Alzheimer's patients with various imaging methods and parameters, is shared on the internet for public access [15].

In this study, the Magnetic Resonance images obtained from the ADNI dataset were selected as 3-plane-localiser type images obtained in T1 format. Based on these selection procedures, a special dataset was created using all images of the ADNI dataset. In this dataset, there are 213 Patients and 407 Normal, patient-based data. In the class labelled Patient, the average age is 76 years and consists of 104 female and 109 male patients. In the classes labelled Normal, the average age was calculated as 85 years and consisted of images taken in axial direction from 223 female and 184 male individuals.

Table 3. Dataset properties

Class/Features	Number of Women	Number of Men	Average Age	Total Number of Data
Normal	223	184	85	407
Patient	104	109	76	213

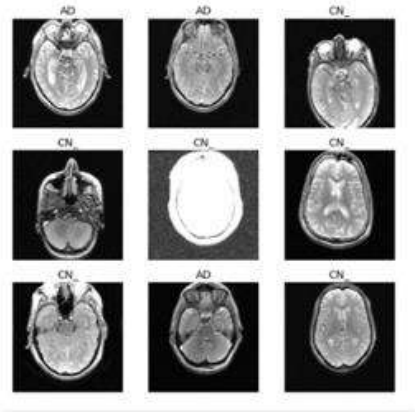

Figure 17. Images of Patient (AD) and Normal (CN) classes from the dataset.

3. Results

The models used in this study were trained using 3 different architectures. EfficientNet, ResNet-50 and ResNext-50 were used in these architectures with 91.54%, 93.53% and 88.80% success rates, respectively. The training of the models was performed using powerful graphics cards and processors. A complexity matrix output was also obtained to detail the success rates and error levels of the models. Figure 4 is given for comparison of the models.

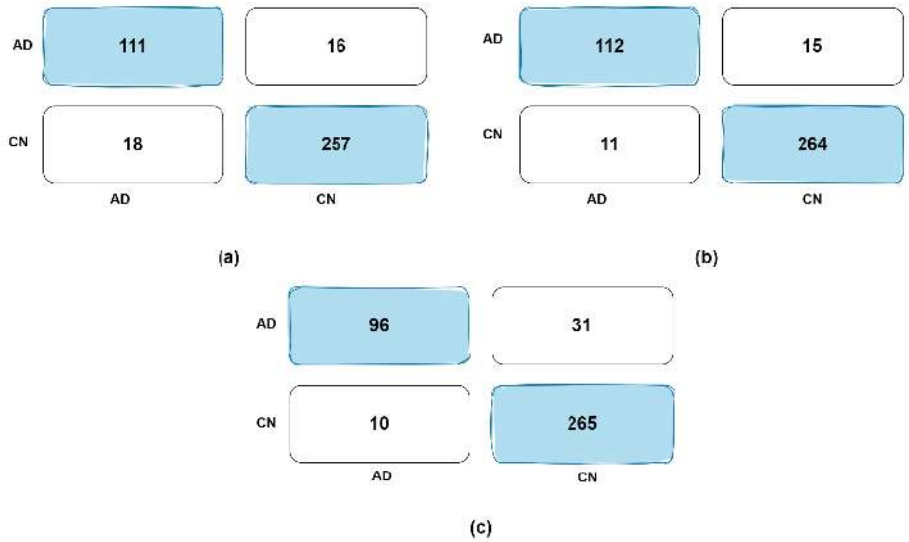

Figure 18. Confusion matrices of the trained models. (a) Confusion matrix of the EfficientNet model, (b) Confusion matrix of the ResNet-50 model, (c) Confusion matrix of the ResNext-50 model

A detailed observation was made on the model success by obtaining the loss graphs in the training and test sets, and the loss graphs of EfficientNet, ResNet-50 and ResNext-50 models are given in Figure 5, respectively.

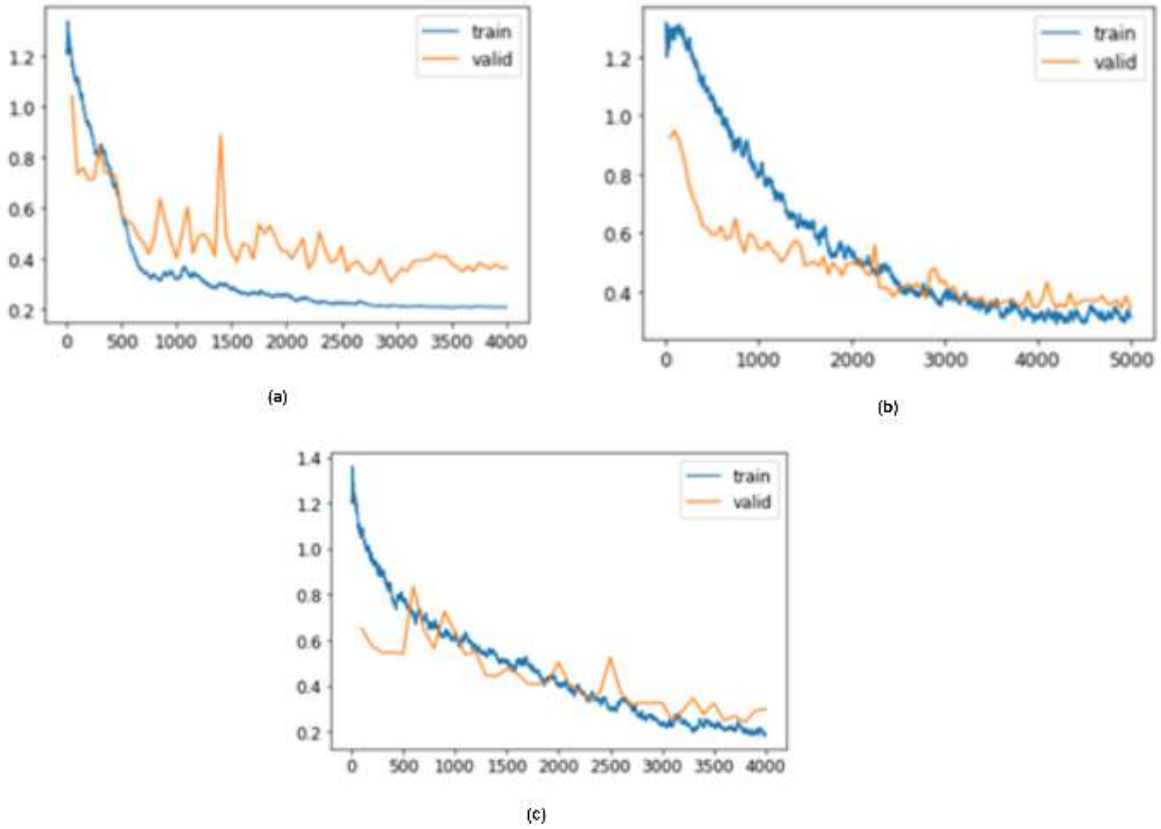

Figure 19. Lost graphs of models. (a) Loss graph of EfficientNet model, (b) Loss graph of ResNet-50 model, (c) Loss graph of ResNext-50 model

4. Discussion / Conclusion

In this study, two stages of Alzheimer's disease, normal and advanced, were classified using deep learning methods. Data for this study were derived from patient-based split MR images. Three different models were trained for the classification process. The model with the highest performance is trained with the ResNet-50 architecture. This model; The images are trained without any preprocessing steps. The proposed model reaches 93.53% accuracy without any preprocessing steps on the images taken from the patient for the diagnosis of Alzheimer's disease. As the next stage of the study, it is aimed to carry out training with the multi-class classifier as early, intermediate and advanced stages of Alzheimer's disease.

5. References

[1] Fung, Y. R., Guan, Z., Kumar, R., Wu, J. Y., & Fiterau, M. (2019). Alzheimer's disease brain mri classification: Challenges and insights. arXiv preprint arXiv:1906.04231.

[2] Jain, R., Jain, N., Aggarwal, A., & Hemanth, D. J. (2019). Convolutional neural network based Alzheimer's disease classification from magnetic resonance brain images. Cognitive Systems Research, 57, 147-159.

[3] Acharya, U. R., Fernandes, S. L., WeiKoh, J. E., Ciaccio, E. J., Fabell, M. K. M., Tanik, U. J., ... & Yeong, C. H. (2019). Automated detection of Alzheimer's disease using brain MRI images–a study with various feature extraction techniques. Journal of Medical Systems, 43(9), 1-14.

[4] Shanmugam, J. V., Duraisamy, B., Simon, B. C., & Bhaskaran, P. (2022). Alzheimer's disease classification using pre-trained deep networks. Biomedical Signal Processing and Control, 71, 103217.

[5] Farooq, A., Anwar, S., Awais, M., & Rehman, S. (2017, October). A deep CNN based multi-class classification of Alzheimer's disease using MRI. In 2017 IEEE International Conference on Imaging systems and techniques (IST) (pp. 1-6). IEEE.
[6] Acharya, U. R., Fernandes, S. L., WeiKoh, J. E., Ciaccio, E. J., Fabell, M. K. M., Tanik, U. J., ... & Yeong, C. H. (2019). Automated detection of Alzheimer's disease using brain MRI images–a study with various feature extraction techniques. Journal of Medical Systems, 43(9), 1-14.
[7] Al-Adhaileh, M. H. (2022). Diagnosis and classification of Alzheimer's disease by using a convolution neural network algorithm. Soft Computing, 1-12.
[8] Umut, K. A. Y. A., YILMAZ, A., & Dikmen, Y. (2019). Sağlık alanında kullanılan derin öğrenme yöntemleri. Avrupa Bilim ve Teknoloji Dergisi, (16), 792-808.
[9] Savaş, S. (2022). Detecting the Stages of Alzheimer's Disease with Pre-trained Deep Learning Architectures. Arabian Journal for Science and Engineering, 47(2), 2201-2218.
[10] Al-Adhaileh, M. H. (2021). Diagnosis and Classification of Alzheimer's Disease by Using a Convolution Neural Network Algorithm.
[11] Deep Learning - Kwang Gi Kim - PhD Biomedical Engineering Branch, Division of Precision Medicine and Cancer Informatics, National Cancer Center, Goyang, Korea
[12] Derin Öğrenme hangi alanlarda kullanılır? - https://www.webtures.com/tr/blog/deep-learning-derin-ogrenme-nedir/
[13] Tan, M., & Le, Q. (2019, May). Efficientnet: Rethinking model scaling for convolutional neural networks. In International conference on machine learning (pp. 6105-6114). PMLR.
[14] He, K., Zhang, X., Ren, S., & Sun, J. (2016). Deep residual learning for image recognition. In Proceedings of the IEEE conference on computer vision and pattern recognition (pp. 770-778).
[15] Alzheimer's Disease Neuroimaging Initiative (ADNI): https://adni.loni.usc.edu/

International Conference on Advances and Innovations in Engineering

Comparative Study of Deep Learning and Machine Learning Algorithms to Predict Hospitalization to Cardiology on Patients Who Applied Emergency Department with Chest Pain

Betül DAĞOĞLU HARK[1], Kübra Elif AKBAŞ[2], Meryem GÖRAL YILDIZLI[3], Duygu SIDDIKOĞLU[4*]

[1,2]Fırat University, Faculty of Medicine, Department of Biostatistics and Medical Informatics, Elazig, Turkey.
[3]Çukurova University Balcali Hospital Health Practice and Research Center, Adana, Turkey.
[4]Çanakkale Onsekiz Mart University, Faculty of Medicine, Department of Biostatistics and Medical Informatics, Çanakkale, Turkey.
[1]bdagoglu@firat.edu.tr, [2]keet@firat.edu.tr, [3]meryem@cu.edu.tr, [4]sduygu@comu.edu.tr

[1](ORCID: 0000-0002-5189-1929), [2](ORCID: 0000-0002-2804-000X),[3](ORCID: 0000-0001-9394-7030),
[4](ORCID: 0000-0002-5093-7948)

Abstract

Today, some of the patients who apply to the emergency department (ED) with chest pain are diagnosed with unexplained chest pain. This situation causes delaying the diagnosis or applying the wrong treatment method to patients who do not have cardiological disease. Accordingly, it is important to correctly classify the patients presenting to the ED with chest pain. Based on this reason, it is aimed to guide physicians in the diagnosis and treatment process by creating a patient profile with machine learning algorithms and deep learning (DL), which are widely used in data mining.
From the database of Çukurova University Balcalı Hospital Information Management System, 3360 patients admitted to the ED with chest pain in 2018-2020 were included in the analysis. This data set was modeled with six frequently used algorithms logistic regression (LR), support vector machine (SVM), decision tree (DT), random forest (RF), naïve bayes (NB) and DL and algorithm performances were evaluated according to performance criteria.
The algorithms with the highest performance according to the accuracy criterion are SVM (0.671±0,016), NB (0.658±0,009) and LR (0.655±0,004), respectively. The models with the highest performance according to the AUC criteria are RF (0.696±0.031), LR (0.692±0.023) and DL (0.682±0.022), respectively. The highest performing model for sensitivity criterion is SVM (0.182±0.040), while for specificity criterion DT (1.000±0.000). Thus, the hospitalization status of the patients in the cardiology service was classified correctly with an accuracy rate of 67%, 66% and 66% respectively, using SVM, NB and LR algorithms.
Considering all the performance criteria, it was found that the SVM algorithm was the best model for determining the hospitalization status of the patients admitted to the ED with chest pain. Also NB method was determined as the second method with high performance in terms of accuracy, classification error and sensitivity criteria.

Keywords: machine learning, deep learning, performance measures, chest pain

1. Introduction

Big data stored in databases turn into information through data processing processes. In order to find patterns and relationships in a big data set, data mining uses sophisticated data analytic techniques. These techniques include machine learning (ML), mathematical algorithms, and statistical models. In other words, data mining goes beyond just gathering and maintaining data to include analysis and predictions (1, 2).

One of the data mining techniques is ML, which has a wide range of applications and is one of the fastest developing fields in computer science. It refers about the automated recognition of significant data patterns. At the same time, ML tools are about giving programs the ability to learn and adapt (3). In particular, ML provides automated and highly flexible analyzes for identifying complex data structures (for example, nonlinear relationships, interactions, key dimensions or subgroups) in applied health research (4).

*Corresponding author

Today, numerous ML algorithms have been developed and updated. The most recent advancements in ML have made it an area that offers the capacity to automatically apply many sophisticated mathematical calculations to a big data set that generates answers much more quickly. Using algorithms along with statistics, probability and optimization methods, useful patterns are obtained from large, unstructured and complex data sets. ML algorithms are basically divided into three general groups as supervised, unsupervised and semi-supervised learning (5, 6). There are several uses for these algorithms. Automated text classification, spam filtering, credit card fraud detection, consumer purchase behavior detection, manufacturing process optimization, and illness modeling are a few of these domains (6). Classes are predetermined in supervised algorithms. These classes are created as a researcher-defined finite set, which practically means that a particular data segment will be labeled from these classifications. The primary components of supervised learning (SL) algorithms are regression models and classification models. However, unsupervised learning systems do not get classifications. Unsupervised learning's primary objective is the automated development of categorization labels. These algorithms search for similarity between datasets to categorize or form a group. These groups are called clusters, and clustering represents the entire family of ML techniques (5). Semi-supervised learning can be used to train a large amount of unlabeled data with a small amount of labeled data (7). Deep learning (DL) techniques are considered as an important part of ML methods based on artificial neural networks. DL is widely applied in analyzing, predicting, designing, filtering, processing, recognition and detection tasks (8).

Chest pain is pain that is usually described as sharp, dull, pressure, heaviness, or squeezing in the front of the chest. This type of pain may be accompanied by nausea, sweating, or shortness of breath, along with shoulder, arm, upper abdomen, or jaw pain (9, 10). More than half of the patients who apply to the ED with chest pain are diagnosed with unexplained chest pain (11, 12). The goal of this study was to compare the classification abilities of these methods in order to ascertain the hospitalization status of patients who presented with chest pain to the emergency department of the Balcali Training and Research Hospital, which receives nearly 76,000 patient visits annually and serves a city with a population of 2 million. The algorithms employed were Naive Bayes (NB), DL, Decision Tree (DT), Random Forest (RF), Logistic Regression (LR), Support Vector Machine (SVM), and Decision Tree (DT). These ML methods have numerous advantages such as being nonparametric and being free from any distribution assumptions (13).

2. Materials and Methods

2.1. Supervised Learning (SL)

SL is quite commonly used in classification. The purpose here is to teach an algorithm to a computer in order to get arecognition and classification learning (14). In supervised machine learning (SML) methods, the underlying algorithm is initially trained using a labeled training dataset. In order to categorize them into comparable categories, the trained algorithm is next evaluated on the unlabeled test dataset. Classification and regression issues are compatible with SL techniques (6).

The main purpose of SL techniques is to learn how to predict the random variable $\boldsymbol{Y} \in \boldsymbol{\mathcal{Y}}$ based on a set of explanatory random variables denoted by $\boldsymbol{X} \in \boldsymbol{\mathcal{X}}$. Generally, $\boldsymbol{X}$ is expressed as input and $\boldsymbol{Y}$ as output. The general aim in ML is to find the estimator selected from all function sets $\boldsymbol{\mathcal{F}} = \{\boldsymbol{f}: \boldsymbol{\mathcal{X}} \to \Upsilon\}$.

$$\boldsymbol{f}: \ \boldsymbol{\mathcal{X}} \to \Upsilon$$
$$\boldsymbol{X} \ \to \boldsymbol{f}(\boldsymbol{X})$$

To create a "good" estimator, performance criteria must be determined. That is, a loss function denoted by L which depends on $\boldsymbol{f}$ X and Y must be define and If $\boldsymbol{f}$ estimator is a better estimator than $\boldsymbol{g}$ estimator then $\boldsymbol{L}(\boldsymbol{f}, \boldsymbol{X}, \boldsymbol{Y}) < \boldsymbol{L}(\boldsymbol{g}, \boldsymbol{X}, \boldsymbol{Y})$.

The optimal estimator minimizing the loss function L is as follows (13).

$$\boldsymbol{f}^* = \underset{\boldsymbol{f} \in \boldsymbol{\mathcal{F}}}{\boldsymbol{argmin}}\, \boldsymbol{L}(\boldsymbol{f}, \boldsymbol{X}, \boldsymbol{Y}) \qquad (\mathbf{1})$$

It is not possible to minimize L over all possible set of functions $\boldsymbol{\mathcal{F}}$. But the $\boldsymbol{f}^{**}$ estimator is obtained over a given class of C estimators corresponding to a practically computable set of estimators.

$$f^{**} = \underset{f \in C}{argmin}\, L(f, X, Y) \quad (2)$$

The empirical estimator of f^{**} based on n-dimensional $\hat{L}_n$ sampling is as follows.

$$\hat{f}_n = \underset{f \in C}{argmin}\, \hat{L}_n(f, X, Y) \quad (3)$$

The difference of $L(f^*) - L(f^{**})$, is called approximation error or modeling error. If there is a large sample (i.e. n goes to infinity), the $\hat{f}_n$ estimator converges to the f^{**} estimator. The difference $L(f^{**}) - L(\hat{f}_n)$ is defined as the estimation error.

Optimal Model

The loss function used to estimate the f model depends on the output variable Y. The overall goal in regression modeling is to minimize the quadratic error.

$$L(f) = E\left[\left(Y - f(X)^2\right)\right] \quad (4)$$

In Equation 4, E is the expected value of the (X,Y) common distribution. Under this situation, the optimal model is the conditional expected value of Y with respect to X.

$$f^*(x) = \underset{f \in \mathcal{F}}{argmin}\, L(f) = E(Y|X = x) \quad (5)$$

The sample estimator is based on the solution of the following equation, which minimizes the empirical version of the quadratic error.

$$\hat{f}_n = \underset{f \in C}{argmin}\, \hat{L}_n(f, X, Y) = \underset{f \in C}{argmin} \frac{1}{n} \sum_{i=1}^{n} [Y_i - f(X_i)]^2 \quad (6)$$

In Equation 6, $(X_i, Y_i)_{i=1,\ldots,n}$ are n independent and identically distributed (iid) realizations of (X, Y) (13).

Estimating the Model Loss

The estimator of the f function $\hat{f}_n$, $S = \{(X_1, Y_1), \ldots, (X_n, Y_n)\}$ is based on the iid training sample. The performance of $\hat{f}_n$ is tested with a new sample $(X_1^v, Y_1^v), \ldots, (X_m^v, Y_m^v)$, called the evaluation sample. This evaluation example is independent of the training example and is another iid example. This method prevents overfitting.

The data is really split into two sub-samples at random: a training sample and an evaluation or test sample. The model is estimated using the training set, and the evaluation example is used to assess the model's performance. To lessen any bias brought on by the assessment sample's random selection, the loss is averaged over numerous random splits of the data (Figure 1).

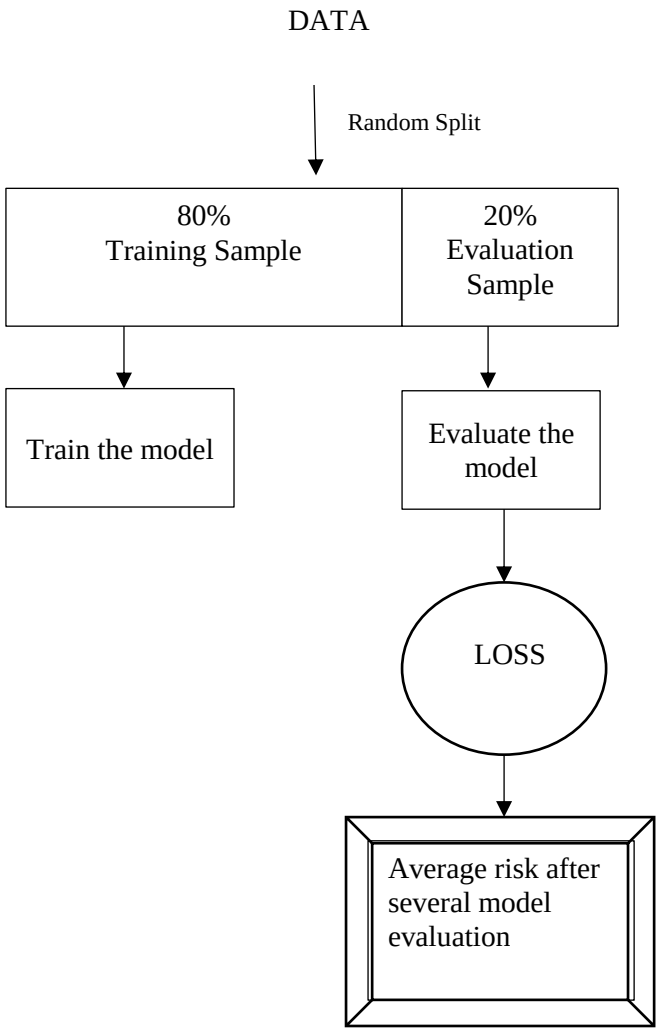

Figure 1. An example of random data splitting for model training and evaluation

Other performance estimates based on well-known processes, such as cross-validation, leave one-out, bootstrap, and other resampling approaches, can be utilized to provide realistically unbiased and computationally effective estimates (13).

2.1.1. Logistic Regression (LR)

LR is a powerful and well-performed method for supervised classification (15). In general, the purpose of a LR model is to calculate the class membership probability for one of two categories in the dataset.

$$\boldsymbol{p(y=1|x,\alpha)=\frac{1}{1+e^{-(\alpha x)}}} \quad (7)$$

The decision line between the two classes is the hyperplane of all points satisfying the equation $\boldsymbol{\alpha x=0}$; these are the points for $\boldsymbol{p(y=1|x,\alpha)=p(y=0|x,\alpha)=0.50}$ (16).

2.1.2. Support Vector Machine (SVM)

SVMs are frequently employed to train classification, regression, or ranking algorithms. Structural risk reduction and statistical learning theory are the foundations of SVM. Its goal is to identify decision boundaries, also known as hyperplanes, that result in the best class separation (1). Support vector points, or the data points at the hyperplane's edge, are used to describe the solution as a linear combination of these points. Other information is disregarded (17).

Practically, most data sets are not linearly separable, and any dividing line, no matter how narrow the margin, can cause misclassification (18). This problem may be solved by using a soft margin that accepts some misclassification of training samples (17, 19).
In a training data set with input variable $\mathbb{R}^d$ and binary output variable $Y \in \{-1, 1\}$, it is assumed that the data are linearly separable. Under this assumption, there is at least one hyperplane at $\mathbb{R}^d$ that perfectly separates the two subgroups corresponding to each level of Y. It is the main purpose of SVM to choose the hyperplane that best separates the classes and is as far away as possible from all states.
Considering a hyperplane H defined by f(x) = 0;

$$\boldsymbol{f(x) = \langle w, x \rangle + b} \quad (\mathbf{8})$$

In equation 8, $\boldsymbol{w} \in \mathbb{R}^d$ corresponds to the normal vector of the hyperplane. The observation margin i in the H hyperplane is defined as:

$$\boldsymbol{\gamma_i = y_i f(x_i)} \quad (\mathbf{9})$$

For observation i, $\boldsymbol{\gamma_i > 0}$ is possible if and only if this observation is well classified by H. Hyperplane margin according to the S sample; $\boldsymbol{\gamma_H = min_{i=1,\ldots,n} \gamma_i}$. It corresponds to the edge of the point closest to H.
SVM aims to find the margin-maximizing one among all hyperplanes in $\mathbb{R}^d$,

$$\boldsymbol{H^* = \underset{H}{argmax} \gamma_H} \quad (\mathbf{10})$$

The data is contained in a higher dimensional space that is provided via the Kernel function for the nonlinearly separable situation. The fundamental assumption is that it is simpler to differentiate classes in the higher dimension. Kernel describes how data transformations happen. Typically, a Gaussian Kernel is used:

$$\boldsymbol{K(x, y) = exp^{-\delta ||x-y||^2}} \quad (\mathbf{11})$$

In Equation 11, $\boldsymbol{\delta > 0}$ (13).

2.1.3. Decision Tree (DT)

One of the first and most used algorithms, DT is utilized in many industries, including ML and image processing. The DT is a sequential model that successfully and harmoniously integrates a number of test methods, each of which compares a numerical property with a threshold value. Additionally, DT is frequently used in data mining for categorization. There are nodes and branches in every tree. Each node represents a property in a classification category, and each subset specifies a value that the node may access. DT has found various uses because of its straightforward analysis and accuracy across a variety of data types. There are several DT methods, including Successor of ID3 (C4.5), Iterative Dichotomies 3 (ID3), Classification And Regression Tree (CART), Multivariate Adaptive Regression Splines (MARS), and others (20).

2.1.4. Random Forest (RF)

RF is based on using several classification trees together. For a new observation, the estimate given by the RF is based on the majority of the estimates given by the trees in the forest. Steps of the RF algorithm:
• The size of the training sample (how many boostrap samples) will be used to build each tree. This is done similarly to bagging.
• Every tree is developed to the fullest extent without the use of pruning.
• At each node of a tree, the best split is chosen from among all splits on only m < d randomly selected variables (13).

2.1.5. Naive Bayes (NB)

The NB Classifier (Probabilistic Learner), which is based on the Bayes theorem, is utilized when the inputs have a high degree of dimensionality. This approach makes the assumption that the value of a variable inside a specific class

is unrelated to the values of the other variables. Calculates the conditional probabilities of the given classes and selects the class with the highest posterior. NB classifiers can be productively employed in SL models, depending on the probability model.

Bayes rule used to calculate posterior probabilities;

$$\boldsymbol{p(y|x) = \frac{p(x,y)}{p(x)} = \frac{p(x|y)p(y)}{\sum_{y'=1}^{C} p(x|y')p(y')}} \quad (\mathbf{12})$$

Equation 12 is called a generative model because it specifies a way to generate the x vectors for every possible class of y.

In the NB approach, it is to learn a function called the discriminant function, which directly maps the inputs to the outputs, without moving from probabilities (21) .

$$\boldsymbol{f(x) = \hat{y}(x) = \underset{y}{argmax} p(y|x)}$$

2.2. Deep Learning (DL)

Artificial neural networks are the basis of DL. Learning algorithms are now available thanks to artificial neural networks, and by adding more data to training processes, training efficiency is boosted. Artificial neural networks have made it possible to use learning algorithms, and as data volumes rise, so does the effectiveness of the training procedures. The training process is referred to as deep since the neural network's level count rises. The training and inferring phases make up the DL process's operation. Large data's labeling and matching characteristics are chosen during the training phase. Inferring involves classifying new unaccounted-for data and making conclusions from previously acquired knowledge (22).

2.3. Classifier performance measures

Typically, the confusion matrix and the receiver operating characteristic (ROC) curve determine how well classifiers function. It is usual practice to evaluate the performance of classifiers using metrics like accuracy, F_1 score, precision, sensitivity (recall, true positive rate), specificity, and false positive rate based on the confusion matrix. Additionally, metrics like mean absolute error (MAE) and running mean square error (RMSE) are used to assess how well certain classifiers perform (5, 23).

$$\boldsymbol{Accuracy = \frac{TP + TN}{TP + TN + FP + FN}}$$

$$\boldsymbol{F_1\ score = \frac{2xTP}{2xTP + FN + FP}}$$

$$\boldsymbol{Precision = \frac{TP}{TP + FP}}$$

$$\boldsymbol{Sensitivity = \frac{TP}{TP + FN}}$$

$$\boldsymbol{Specificity = \frac{TN}{TN + FP}}$$

2.4. Data Application

In this retrospective study we enrolled 3395 patients who admitted to the ED with ICD (international statistical classification of diseases and related health problems) code R07.3 between 2018-2020 in the Cukurova University Balcali Hospital Information Management System (HIMS) database and some of most frequently performed diagnostic tests results. Gender, age, hospitalization, alanine aminotransferase (ALT), aspartate aminotransferase

(AST), creatine kinase-mb (CKMB), troponin I, lactate dehydrogenase (LDH), d-dimer (quantitative), myoglobin tests results were taken as input variables. The data were classified in two groups as cardiology clinic and other departments according to where the patients were hospitalized. The effect of factors on the admission to the cardiology clinic was examined.

2.4.1. Data Preprocessing

Data pre-processing was mainly carried out with the PLSQL query on HIMS database. The patients who were admitted to the emergency room and hospitalized with ICD diagnosis code R07.3 chest pain in 2018-2020 were determined. Gender and age were considered as demographic variables. Additionally, the first six blood test (ALT, AST, CKMB, d-dimer, troponin I, LDH) results are used to compare supervised ML algorithms. Thirty-five patients were excluded because they did not have laboratory test results. Missing data in 6 diagnostic tests were completed with multiple imputation method. Thus, the total number of data included in the analysis was 3360. The data set was standardized and classification algorithms were applied. The 80% of the dataset were used for training the models while the remaining 20% were used for testing the models. The preprocessing and data analysis were performed using R Statistical Software and Rapid Miner.

3. Result

We used variables extracted from the electronic medical records in Table 1.

Table 1. The detailed explanation of the variables in the dataset.

Abbreviation	Explanation	Type	Role
Gender	(1 – Male, 2 – Female)	Categorical	Input
Age	Age (year)	Continuous	Input
ALT	Alanine aminotransferase (IU)	Categorical	Input
AST	Aspartate aminotransferase (IU)	Categorical	Input
CKMB	Creatine kinase myocardial band (ng/ml)	Categorical	Input
troponin I	Troponin I (TnI, ng/ml)	Categorical	Input
LDH	Lactate dehydrogenase (U/L)	Categorical	Input
Hospitalization Status in Cardiology Department	(0—not hospitalized, 1—hospitalized)	Nominal	Output

Descriptive statistics according to the demographic information and blood test results was given in Table 2.

Table 2. Descriptive statistics of patients according to demographic information and blood test results

Variables		Hospitalization Status in Cardiology Department		p value
		Hospitalized (n=1185) n(%)	Not hospitalized (n=2175) n(%)	
Gender	Male	717(60.5)	1148(52.8)	<0.001
	Female	468(39.5)	1027(47.2)	
Age*		63.72±14.316	55.28±19.941	<0.001
ALT	-	950(79.9)	1662(75.3)	0.003
	+	239(20.1)	544(24.7)	
AST	-	835(70.2)	1460(66.2)	0.017
	+	354(29.8)	746(33.8)	
CKMB	-	773(65.0)	1348(61.1)	0.026
	+	416(35.0)	858((38.9)	
d-dimer	-	437(36.8)	528(23.9)	<0.001
	+	752(63.2)	1678(76.1)	

Troponin I	-	324(27.2)	690(31.3)	0.015
	+	865(72.8)	1516(68.7)	
LDH	-	564(47.4)	983(44.6)	0.112
	+	625(52.6)	1223(55.4)	

*mean±sd is used as descriptive statistics.

The percentage of male patients hospitalized (717 (60.5%)) was higher than the percentage of female patients (1148 (52.8%)), and the difference was statistically significant ($p<0.001$). The mean age was significantly higher in hospitalized patients (63.72±14.316)compared to not hospitalizedpatients (55.28±19.941 , $p<0.001$). The total number of patients hospitalized into cardiology service was n=1185 (35.3%), and the remainig (n=2175) was distributed as into emergency medicine service n=797 (23.7%), into internal medicine service n=529 (15.7%), into pulmonary disease service n=288 (8.6%), into general surgery service n=149 (4.4%) and into other departments n=412 (12.3%). When biochemical measurements are evaluated, it is seen that all measurements except the LDH variable had statistically significant differences. However, the LDH variable was considered clinically important and was added to the model as a adjusted variable. The frequency of negative ALT, AST and CKMB variables in patients admitted to cardiology for ALT, AST and CKMB variables is higher than patients not admitted to cardiology (p - values respectively 0.003, 0.017 and 0.026).

The performances of supervised ML algorithms given in Table 3. Six algorithms were evaluated according to the performance criteria such as accuracy, AUC, F1 score, precision, sensitivity and specificity.

Table 3. Results obtained according to classifier performance criteria of ML algorithms and DL

Algorithms	Classifier performance measures					
	Accuracy	AUC	F_1 score	Precision	Sensitivity	Specificity
LR	0.655±0.004	0.692±0.023	0.056±0.018	0.767±0.224	0.029±0.010	0.963±0.015
SVM	0.671±0.016	0.680±0.031	0.279±0.054	0.597±0.065	0.182±0.040	0.935±0.009
DT	0.649±0.000	0.585±0.023	-	-	0.000±0.000	1.000±0.000
RF	0.649±0.000	0.696±0.031	-	0.513±0.366	0.018±0.012	0.990±0.009
NB	0.658±0.009	0.676±0.027	0.157±0.009	0.590±0.106	0.091±0.007	0.963±0.015
DL	0.653±0.003	0.682±0.022	-	-	0.018±0.0012	0.990±0.009

*The algorithm with the highest value for accuracy, AUC, F1 score, precision, sensitivity, and specificity is the best algorithm.

According to Table 3, the algorithms with the highest performance according to the accuracy criterion are SVM(0.671±0,016), NB (0.658±0,009) and LR (0.655±0,004), respectively. The models with the highest performance according tothe AUC criteria are RF (0.696±0.031), LR (0.692±0.023) and DL (0.682±0.022), respectively. The highest performing model for sensitivity criterion is SVM (0.182±0.040), while for specificity criterion DT (1.000±0.000).Thus, the hospitalization status of the patients in the cardiology service was classified correctly with an accuracy rate of 67%,66% and 66% respectively, using SVM, NB and LR algorithms. In general, sensitivity values of model fitting algorithms were low. In other words, for this data set, the ratio of correctly classified positive samples (in case of cardiology service hospitalization) to the total number of positive samples was low. Instead we got higher values of specificity which means a higher value of true negatives and a lower false-positive rate.

4. Discussion

Accurate diagnosis and triage readily available in the initial assessment of patients who admittedto the emergency department (ED) with chest pain. It enables the stratification of patients into risk groups so that, when necessary, particular actions and levels of care may be provided. All patients who are admitted to the emergency room with chest discomfort and who may be experiencing acute coronary ischemia are often accepted by doctors. As a result, a lot of people are hospitalized to hospitals every year with non-cardiac chest discomfort (24, 25). These patients hospitalized in expensive intensive care beds, increasing costs significantly. In this study, we investigated the capabilities of ML and DL algorithms to determine whether patients with chest discomfort who were referred to the

ED should also be admitted to the cardiology department. These algorithms; LR, SVM, DT, RF, NB and DL. The classification success of the patients was evaluated with the classifications obtained using ML algorithms, and the diagnosis of the patients who present to the ED with chest pain was revealed by these algorithms by using eight independent variables. For the data set, the SVM algorithm was determined as the algorithm with the highest performance, while the DT and RF algorithms were determined as the algorithms with the lowest performance.

For scenarios where categorical variables are included in the algorithm comparison, the highest performance belongs to the NB algorithm, while the lowest performance belongs to the DT algorithm. When continuous measurements are taken into account, the methods with the highest performance are; DT, LR, NB and K-NN (26). In this study, all variables included in the model except the age variable are categorical and the models with the highest accuracy are SVM, NB and LR.

Muhammad et al. conducted a study in which categorical variables were included in to model. According to the findings, DT was determined as the methods with the highest accuracy, SVM with the highest sensitivity and NB with the highest specificity (27).

Kivrak et al. in their study used DL, RF, K-NN, extreme gradient boosting [XGBoost]). They used accuracy, precision sensitivity, specificity, Classification Error, and Kappa performance metrics to compare model performances. According to the performance metric results, the most successful method is the XGBoost (accuracy 99.7%) classification algorithm. The accuracy rate based on DL is 97.15%. Also in this study RF and K-NN, which are ML methods, have an accuracy rate of 92.15% and 93.4%, respectively. In this study, the accuracy value found for RF is 0.740, while the accuracy value found for K-NN is 0.609. According to Kivrak et al., the accuracy value of the RF algorithm was found to be higher than the K-NN algorithm. The reason for this is thought to be variable types, training and test data set ratio (28) .

5. Conclusion

For the purpose of this study, the classification performances of patients who present to the ED with chest pain were evaluated according to the factors affecting the hospitalization in to cardiology department. Considering all the performance criteria, it was found that the SVM algorithm was the best model for determining the hospitalization status of the patients admitted to the ED with chest pain. Also NB method was determined as the second method with high performance in terms of accuracy, classification error and sensitivity criteria.

6. References

1. Bhavsar H, Ganatra A. A comparative study of training algorithms for supervised machine learning. International Journal of Soft Computing and Engineering (IJSCE). 2012;2(4):2231-307.
2. Akbaş KE, Kivrak M, Arslan AK, Çolak C, editors. Assessment of association rules based on certainty factor: an application on heart data set. 2019 International artificial intelligence and data processing symposium (IDAP); 2019: IEEE.
3. Osisanwo F, Akinsola J, Awodele O, Hinmikaiye J, Olakanmi O, Akinjobi J. Supervised machine learning algorithms: classification and comparison. International Journal of Computer Trends and Technology (IJCTT). 2017;48(3):128-38.
4. Jiang T, Gradus JL, Rosellini AJ. Supervised machine learning: a brief primer. Behavior Therapy. 2020;51(5):675-87.
5. Uddin S, Khan A, Hossain ME, Moni MA. Comparing different supervised machine learning algorithms for disease prediction. BMC medical informatics and decision making. 2019;19(1):1-16.
6. Nasteski V. An overview of the supervised machine learning methods. Horizons b. 2017;4:51-62.
7. Li Q, Han Z, Wu X-M, editors. Deeper insights into graph convolutional networks for semi-supervised learning. Thirty-Second AAAI conference on artificial intelligence; 2018.
8. Ardabili S, Mosavi A, Dehghani M, Várkonyi-Kóczy AR, editors. Deep learning and machine learning in hydrological processes climate change and earth systems a systematic review. Engineering for Sustainable Future: Selected papers of the 18th International Conference on Global Research and Education Inter-Academia–2019 18; 2020: Springer.

9. Dooley-Hash S. Tintinalli's Emergency Medicine: A Comprehensive Study Guide. JAMA. 2011;306(1):100-.
10. Schey R, Villarreal A, Fass R. Noncardiac chest pain: current treatment. Gastroenterology & hepatology. 2007;3(4):255.
11. Jerlock M, Welin C, Rosengren A, Gaston-Johansson F. Pain Characteristics in Patients with Unexplained Chest Pain and Patients with Ischemic Heart Disease. European Journal of Cardiovascular Nursing. 2007;6(2):130-6.
12. Karlson BW, Kalin B, Karlsson T, Svensson L, Zehlertz E, Herlitz J. Use of medical resources, complications and long-term outcome in patients hospitalized with acute chest pain. A comparison between a city university hospital and a county hospital. International journal of cardiology. 2002;85(2-3):229-38.
13. Crisci C, Ghattas B, Perera G. A review of supervised machine learning algorithms and their applications to ecological data. Ecological Modelling. 2012;240:113-22.
14. Ayodele TO. Types of machine learning algorithms. New advances in machine learning. 2010;3:19-48.
15. Lemeshow S, Sturdivant RX, Hosmer Jr DW. Applied logistic regression: John Wiley & Sons; 2013.
16. Dreiseitl S, Ohno-Machado L. Logistic regression and artificial neural network classification models: a methodology review. Journal of biomedical informatics. 2002;35(5-6):352-9.
17. Maglogiannis IG. Emerging artificial intelligence applications in computer engineering: real word ai systems with applications in ehealth, hci, information retrieval and pervasive technologies: Ios Press; 2007.
18. Bzdok D, Krzywinski M, Altman N. Machine learning: supervised methods. Nature methods. 2018;15(1):5.
19. Burges CJ. A tutorial on support vector machines for pattern recognition. Data mining and knowledge discovery. 1998;2(2):121-67.
20. Charbuty B, Abdulazeez A. Classification based on decision tree algorithm for machine learning. Journal of Applied Science and Technology Trends. 2021;2(01):20-8.
21. Murphy KP. Naive bayes classifiers. University of British Columbia. 2006;18(60):1-8.
22. Dargan S, Kumar M, Ayyagari MR, Kumar G. A survey of deep learning and its applications: a new paradigm to machine learning. Archives of Computational Methods in Engineering. 2020;27:1071-92.
23. Arslan AK, Colak C, Sarihan ME. Different medical data mining approaches based prediction of ischemic stroke. Computer methods and programs in biomedicine. 2016;130:87-92.
24. Gibler WB, Runyon JP, Levy RC, Sayre MR, Kacich R, Hattemer CR, et al. A rapid diagnostic and treatment center for patients with chest pain in the emergency department. Annals of emergency medicine. 1995;25(1):1-8.
25. Lee TH, Cook EF, Weisberg M, Sargent RK, Wilson C, Goldman L. Acute chest pain in the emergency room: identification and examination of low-risk patients. Archives of Internal Medicine. 1985;145(1):65-9.
26. Kartal E, Balaban ME. Machine learning techniques in cardiac risk assessment. Turkish Journal of Thoracic and Cardiovascular Surgery. 2018;26(3):394.
27. Muhammad L, Algehyne EA, Usman SS, Ahmad A, Chakraborty C, Mohammed IA. Supervised machine learning models for prediction of COVID-19 infection using epidemiology dataset. SN computer science. 2021;2(1):1-13.
28. Kivrak M, Guldogan E, Colak C. Prediction of death status on the course of treatment in SARS-COV-2 patients with deep learning and machine learning methods. Computer methods and programs in biomedicine. 2021;201:105951.

International Conference on Advances and Innovations in Engineering

2ICAIE

A Cloud GIS Based Street Food Recommender Web App

Sevket BEDİROGLU[1] , Volkan YILDIRIM [2]

[1,]City and Regional Planning, Architecture, Gaziantep University, Gaziantep, Turkey.
[2]Geomatic Engineering, Engineering Faculty, Karadeniz Technical University, Trabzon, Turkey.

[1]sbediroglu@gantep.edu.tr, [2] yvolkan@gantep.edu.tr

[1](ORCID: 0000-0002-7216-6910), [2](0000-0002-5503-9522)

Abstract

Various tourist activities have raised in all over world in recent years. Turkey also hosts millions of tourists every year. One of the most important challenge tourists face while their tourism activity is finding compatible food with their needs. Geographical Information Systems and internet based Geographical Information Systems getting popular for tourism activities. With the help of these systems visitors can be informed about land, cultural places, accommodation places and foods. This study aims developing a web app containing street foods including, type, quality, prices etc. App is developed via using web based Geographical Information Systems, Arcgis Online and Javascript Programming language. Study area of study is located at Gaziantep City Center area where is popular with delicious food types.

Keywords: GIS, Tourism, Street Foods, Cloud GIS

1. Introduction

Through space and time, tourists travel and experience geographies, interact with the built and/ or natural environment, and often engage with other individuals. Tourists navigate street networks, explore public spaces, visit iconic buildings, and, more broadly, enjoy the multifaceted components of a city's urban life that they may not be accustomed to. As a result of this striking growth, urban tourism is acting as the primary catalyst of radical transformations in the social, economic, and cultural structures of many cities [1,2]. The concept of smart mobility and tourism has evolved from a technology-driven approach to one that focuses on sustainable solutions to address economic, social, and environmental issues [3].

GIS can handle a wide range of data from multiple geographical, temporal, and scale levels from various sources. It is a quick and low-cost tool for site identification, environmental impact assessment, spatial planning, and informed policy decisions for sustainable ecotourism development [4]. Application of GIS to the food environment is relatively new in public health nutrition. In this context, a major challenge lies in ensuring appropriate and effective use of GIS data and spatial analysis methods to measure the food environment [5]. Despite a lack of consensus on the definition of food deserts, efforts to identify areas of concerns with respect to limited accessibility to healthy foods are now regarded as critical to a targeted intervention program for promoting healthy food consumption [6,7]. A growing body of literature is devoted to how individuals interact with the food environment, including a focus on the relationship between neighborhood food availability and frequency of use of restaurants and food stores [8].

Cloud computing is the distribution of hardware and software systems from service provider data centers in the form of applications over the Internet [9, 10]. One of the important characteristics of cloud computing is that it seamlessly integrates the computational resources distributed in the physical space and provides them to its users, so that the

[1]Corresponding author

users are able to quickly access the required computational resources or services at any time and at any location [11]. In Cloud GIS, the time and monetary losses required for the initial setup and maintenance of the system can be avoided. This is very important because in a GIS project, the creation of basic components such as software licensing, application development, software and hardware in the initial setup of the system are processes that require high budgets. For such reasons, many companies do not use GIS even though they know that they need GIS-supported solutions. Thanks to the flexible structure of Spatial Cloud Computing, such problems will decrease to very low levels, especially the initial setup cost of the system.

Gaziantep has important and valuable resources for the development of gastronomy tourism. The city stands out with its rich culinary heritage. The region has original product, food preparation and consumption patterns. Reason for choosing Gaziantep city for study area lays behind the reasons cities rich cuisine culture. Purpose of study is presenting regional and street foods via cloud GIS and making dominant types of foods accessible from internet.

2. Methodology

Methodology of this study follows 3 stages after literature research. First is collecting GIS data from internet and approving collected data from internet. At this stage a geodatabase including food information was created at GIS software (Arcmap). Second stage is moving collected GIS dataset to cloud infrastructure and final stage is designing, creating and publishing web GIS apps. These apps have different functionalities such as searching in a given distance area, routing option, attribute query etc.

3. Case Study

3.1. Data Collection

The relevant data is collected in three steps. First is gathering data from Google Maps with My Maps section (Figure 1). Second step is verifying collected data at study area. Third step is entering attribute values at GIS software such as type, price and presentation alternatives (porsion, table ditch etc).

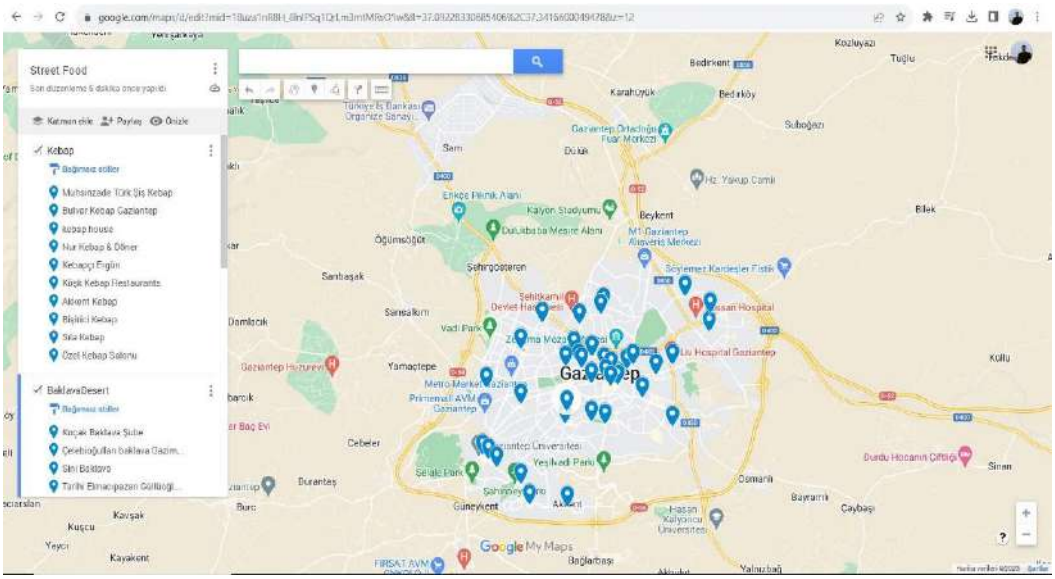

Figure 1. Gathering data from Google Maps with My Maps section

3.2. Migrating Geospatial Data to Cloud

All the collected data was zipped to .zip file. Then zipped file was uploaded to Arcgis Online platform which is a SaaS service for geospatial operations. A screenshot from Arcgis Online Map viewer before Symbology and labeling operations may be seen at Figure 2.

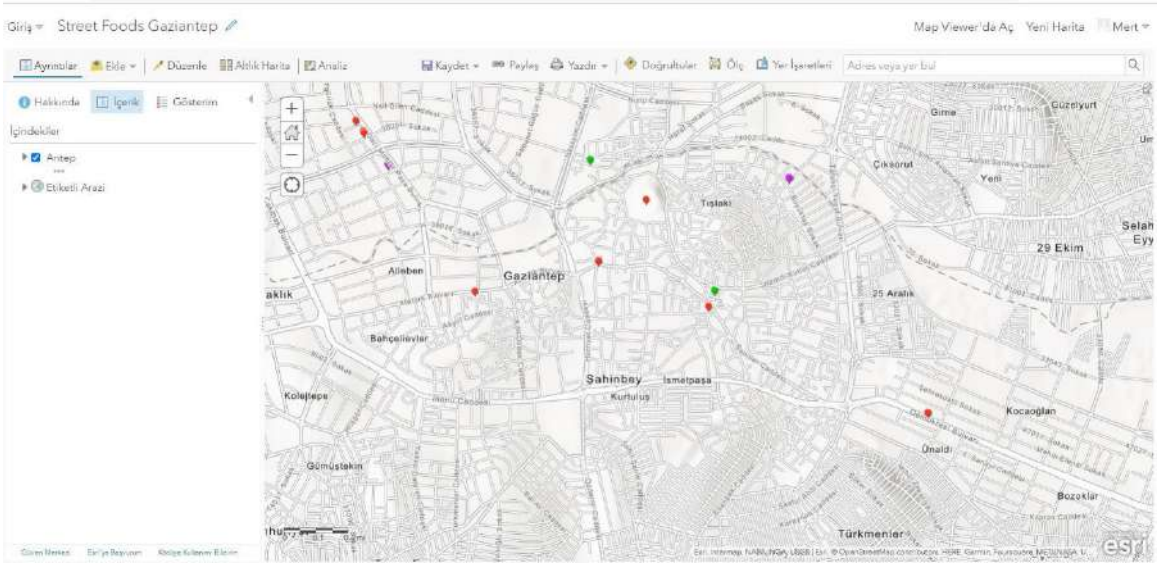

Figure 2. Migrating geospatial data to cloud, Arcgis Online Map viewer

3.3. Creating Cloud Based Web GIS applications

At this stage street food web application was created. App also includes various restaurants beside street foods. Figure 3 is initial welcome screen of web app and users can query related attribute information about food corners.

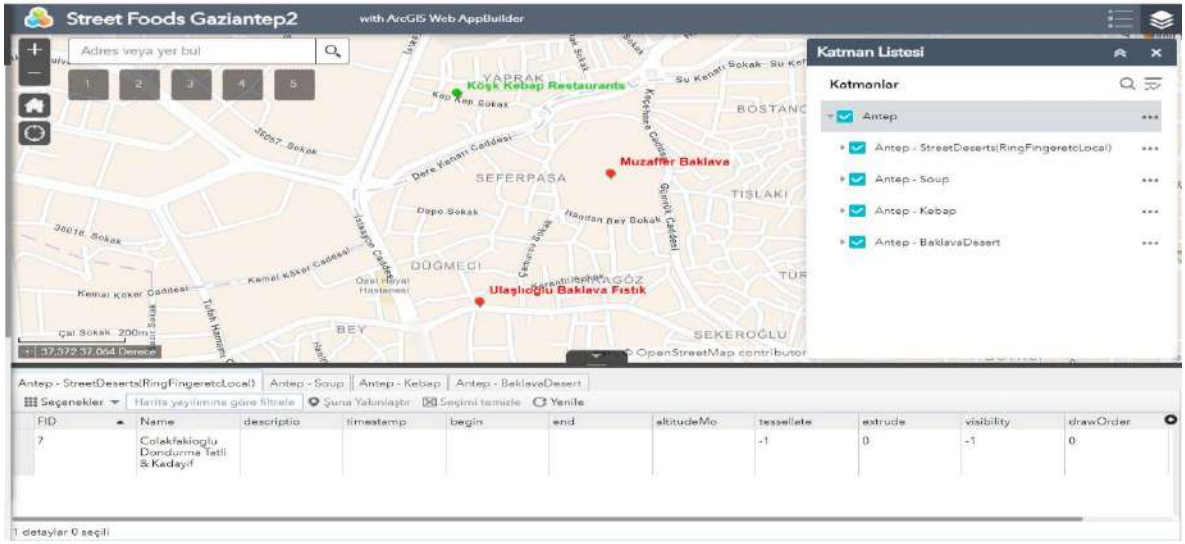

Figure 3. Welcome screen and attribute query

Figure 4 shows navigation and routing capability of web app. With using this function users can navigate to preferred street food location with car, walking or public transport.

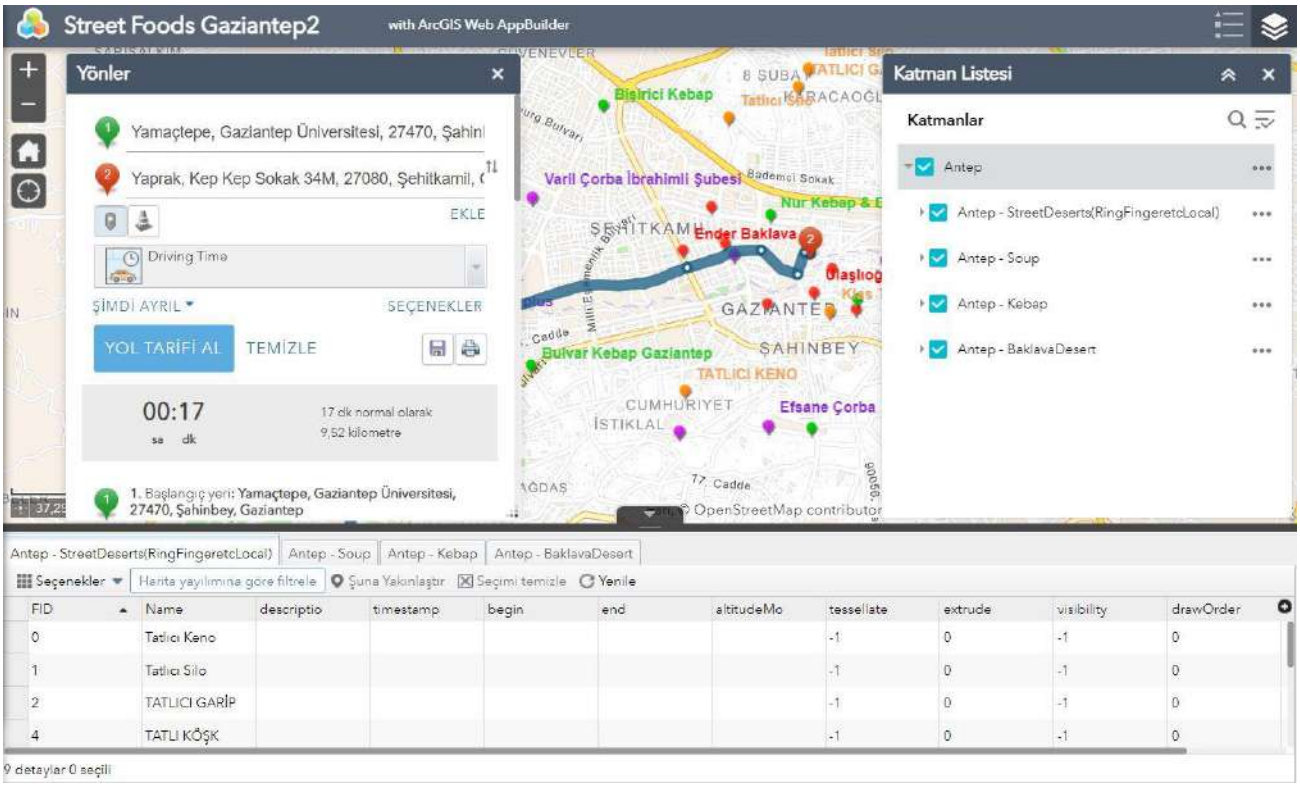

Figure 4. Routing and navigation function

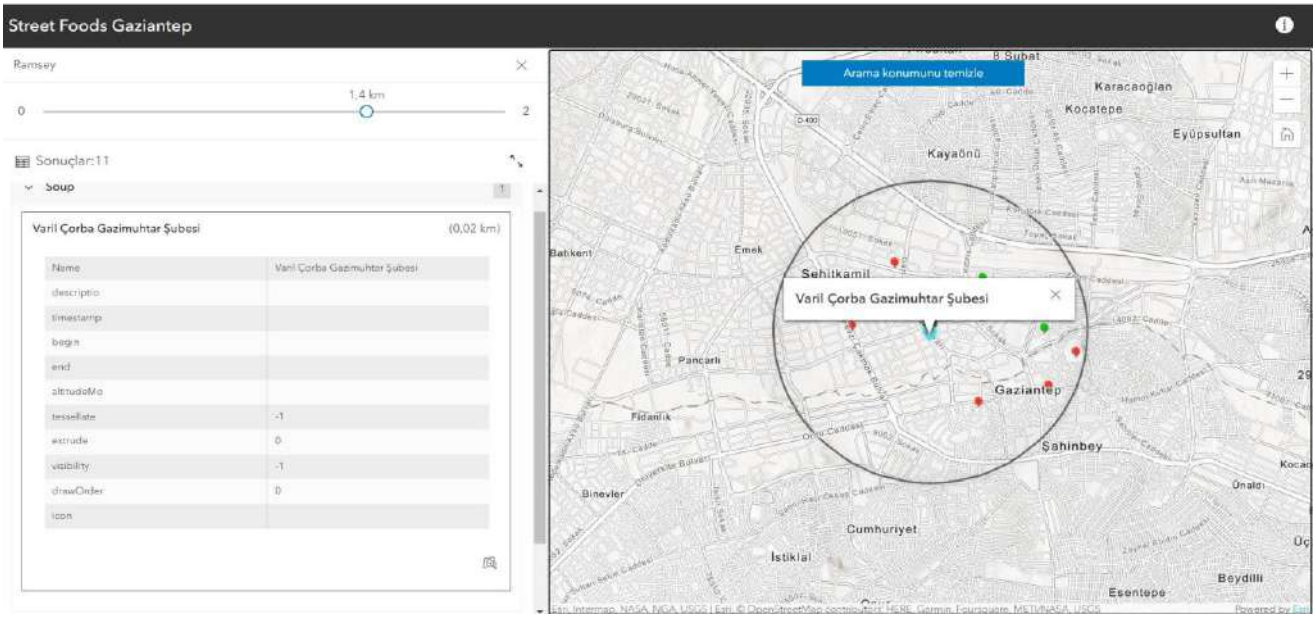

Figure 5. Searching street food alternatives within a given distance

Figure 5 shows search function of app. By this function users can query street foods in a given distance to their current location.

3. Results

This study shows sophisticated and subject-specific web-based apps are very useful for tourism activities. Tourists visiting exterior cities search for qualified and well-priced food alternatives for themselves. The apps developed by this study helps tourists in this manner. Study has shown that using digital sources such as Google Maps, OSM are beneficial for collecting geospatial data before working is field. Finally, cloud GIS based platforms presents good tools for publishing web maps and creating web apps. At this point Arcgis Online platform is a good alternative with having Javascript developer support. Cloud based platforms also support relating and streaming medias (photos, videos) besides attribute data in web GIS applications.

4. References

[1] Dunne, G., Flanagan, S., & Buckley, J. (2010). Towards an understanding of International City break travel: Towards an understanding of International City break travel.

[2] Ignaccolo C, Zheng Y, Williams S. "Tourism Morphometrics in Venice: Constructing a Tourism Services Index (TSI) to unmask the spatial interplay between tourism and urban form". Cities 140 (2023) 104369.

[3] Hussain S, Ahonen V, Karasu T, Leviakangas P. "Sustainability of smart rural mobility and tourism: A key performance indicators-based approach". Technology in Society 74 (2023) 102287

[4] Yassin KH, Woldemariam GW. "GIS-based ecotourism potentiality mapping in the East Hararghe Zone, Ethiopia". Heliyon. 9 (2023) e18567

[5] Charreire H, Casey R, Salze P, Simon C, Chaix B, Banos A, Badariotti D, Weber C, Oppert J. "Measuring the food environment using geographical information systems: a methodological review". Public Health Nutrition: 13(11), 1773–1785

[6] ennings A, Cassidy A, Winters T, Barnes S, Lipp A, Holland R, Welch A. Positive effect of a targeted intervention to improve access and availability of fruit and vegetables in an area of deprivation. Health Place 2012;18:1074-8.

[7] Kim D, Lee CK, Seo DY. "Food deserts in Korea? A GIS analysis of food consumption patterns at sub-district level in Seoul using the KNHANES 2008-2012 data". Nutrition Research and Practice 2016;10(5):530-536. 2016 The Korean Nutrition Society and the Korean Society of Community Nutrition

[8] Peng K, Rodríguez DA, Peterson M, Braun L, Howard AG, Lewis CE, Shikany JM, Gordon-Larsen P. "GIS-Based Home Neighborhood Food Outlet Counts, Street Connectivity, and Frequency of Use of Neighborhood Restaurants and Food Stores". GISJ Urban Health (2020) 97:213–225.https://doi.org/10.1007/s11524-019-00412-x

[9] Armbrust, M. et al., (2010). A View of Cloud Computing, 2010, Association for Computing Machinery

[10] Bediroğlu, Ş. (2013). Web haritalarının bulut bilişim ile yayımlanması: Trabzon ili örneği. Karadeniz Teknik Üniversitesi. Fen Bilimleri Enstitüsü.

[11] Wang, C. et al. (2018). Cloud Platform for the Management of Tourism Resources', in 2018 26th International Conference on Geoinformatics, pp. 1–9. doi: 10.1109/GEOINFORMATICS.2018.8557190.

Weather Analysis and Renewable Energy Sources

Serap ERÇEL[1], Sinem AKYOL[2]

[1,2]Software Engineering, Engineering Faculty, Fırat University, Elazığ, Türkiye.

[1]ercelserap@gmail.com, [2]sakyol@firat.edu.tr

[1](ORCID:0009-0004-2817-8588), [2](ORCID: 0000-0001-9308-3500)

Abstract

Energy is needed for the development of production, imports and exports as well as industrialisation. Depending on social and environmental factors, population growth and economic growth, the consumption of commonly used fossil fuels is accelerating. Due to the limited nature of these resources and the damages they cause to the environment, investments and developments in renewable energy alternatives are becoming widespread worldwide. Incentives and policies in many countries have led to more efficient use of renewable energy resources. There are challenges regarding the cost, efficiency and performance of renewable energy sources. Accurate analyses should be made in order to install the most suitable, low-cost and highly efficient system for geographical conditions. In this study, the correlation between energy consumption and various weather parameters such as solar radiation, temperature, pressure, humidity, humidity, wind speed and precipitation is evaluated. The most suitable among hydroelectric energy, wind energy and solar energy possibilities were determined by data analyses. It has been observed that hydroelectric energy cannot be preferred when rainfall is insufficient, and wind energy cannot reach the desired energy efficiency when there is no continuity in wind power. In this context, it was concluded that solar energy would be the best choice considering the intense sunlight.

Keywords: Renewable Energy, Hydroelectric Energy, Wind Energy, Solar Energy

1. Introduction

In history, people have needed energy sources and these sources have changed over time. Apart from the biological energy used by humans for food intake, various sources have been used almost everywhere. As the first source of energy instead of the tools we use energy now, people used the power of animals such as horses, donkeys and oxen as a source. They built farm vehicles and cars to use in agriculture and transport. People lived around water sources. They used water power for grinding by building water-driven mills, for weaving by building looms, and even for kneading dough. In ancient Egypt, they carried out agricultural activities with the water energy of the Nile River. Ancient Greece milled grain and weaved with hydraulic wheels. In Ancient Rome, they provided water to cities with systematised waterways and agricultural irrigation. In the Middle Ages, water mills became widespread in Europe for grain processing. When it came to the Industrial Revolution, it was used in industrial branches from iron production to textiles by making use of steam power [1, 2].

The discovery of steam power during the Industrial Revolution first popularised the use of coal from fossil fuels. With this process, oil and natural gas were discovered later. Especially since the beginning of the 20th century, oil, natural gas and nuclear energy sources have been the source of energy in electricity generation, especially in transport, in addition to industry.The fact that fossil fuels have limited resources and the need for cleaner energy sources has led to different searches. With the awareness of the information age, sensitivity and sensitivity have increased, and problems such as energy security and environmental damages have attracted attention worldwide. Energy efficiency is an important aspect to study the complex low carbon economic model and sustainable development. In the last hundred years, the world output has increased multifold, which causes a massive increase in Greenhouse gas (GHG) emissions. Since the industrial revolution, the CO2 concentration has increased by 47%, increasing the earth temperature by 1.9 Fahrenheit and sea level by 7 inches (IPCC, 2019). Such GHG emissions have imparted grave consequences for human life on earth (NASA, 2020). The global GHG emissions have reached such an unprecedented level that even if these emissions are halted today, the current level of already stowed emissions will continue to affect future generations. Increasing economic activities with mass production and excessive consumption have gained importance in terms of environmental safety and sustainability in the energy

[1]Corresponding author

market. Therefore, there are two alternatives. Natural gas as a clean energy source and relatively expensive and high-tech renewable energy sources have become widespread [3].

The cost of producing renewable energy is decreasing, making it a more viable option for reducing greenhouse gas emissions [4]. The Intergovernmental Panel on Climate Change (IPCC) has also emphasized the importance of renewable energy in mitigating climate change. The IPCC reports provide comprehensive information on the cost of mitigating climate change and highlight the potential of renewable energy sources [5]. These reports serve as valuable resources for understanding the impact of renewable energy on climate change mitigation. In addition to climate change mitigation, renewable energy sources offer other benefits. For example, biomass, a type of renewable energy source, has gained attention for its potential in waste valorization and biorefinery applications. The efficient valorization of energy sources, including renewable ones, has become a prominent research topic within the sustainable development sphere [6].

Renewable energy obtained from the resources offered and reproduced by nature can be diversified as solar energy, wind energy, hydroelectric energy, biomass energy, geothermal energy. Weather conditions such as sunshine duration, rainfall, wind speed, humidity and temperature should be determined. Considering the cost and efficiency, it is necessary to build the most suitable system for the conditions determined. For this reason, the conditions should be analysed in detail and choices should be made according to the inferences [7].

In this study, various weather parameters such as energy consumption, solar radiation, temperature, pressure, humidity, humidity, wind speed and precipitation will be observed and the energy change in a certain time period will be analysed. Through hourly and monthly evaluations, the relationship between renewable energy production and weather patterns will be examined with the time parameter.

The aim of the study is to determine the renewable energy source that will provide optimum efficiency according to the analysis of weather conditions. Weather data between 2017-2022 are supported by analyses and the relationships between each other are determined.

The analysis is prepared against the difficulties of using renewable energy sources and aims to be a reference for making the right choice for optimum efficiency. For example, wind energy and solar energy may not be a reliable source by not providing the expected production due to fluctuations in energy demand or changes in weather conditions. In case of insufficient rainfall and drought, hydroelectric energy may not be the right choice. As a result, considering the cost of these systems and the continuity of energy demand, it involves a critical evaluation.

The difference of the study against the renewable energy problems and solutions frequently encountered in the literature is that it analyses long-term data in both hour and month scales. A comprehensive evaluation of the relationship between different parameters has been made.

2. Materials And Methods

This dataset is designed to investigate the complex relationships between key weather parameters related to energy production and consumption and is available through the Kaggle platform. The hourly measured data covers weather conditions such as solar radiation, temperature, humidity, pressure, wind speed and precipitation. The "Energy delta [Wh]" column represents the change in energy consumption over a given time period, while the "GHI" column measures the amount of solar radiation received by a horizontal surface. In addition, the dataset provides information on the presence of sunlight ("isSun"), the duration of daylight ("dayLength") and the amount of time sunlight is available ("sunlightTime"). The "weather_type" column provides information on the general weather conditions during the time periods included in the dataset. The dataset is organised by hour and month, making it ideal for studying the relationship between long-term weather patterns and renewable energy production. This dataset can be used to predict renewable energy production and the impact of weather conditions, providing a valuable resource for anyone working in the renewable energy sector.

Time: Time information of the data saved in YYYY-MM-DD HH:MM:SS format.

Energy delta[Wh]: The difference in energy consumption in Watt-hours (Wh) from the previous timestamp to the current timestamp.
GHI (Global Horizontal Irradiance): The total intensity of solar radiation incident on a horizontal surface. It is the Global Horizontal Irradiance in Watts per square metre (W/m²) measured with a pyranometer.
Temp: The temperature in degrees centigrade (°C) measured with a pyranometer at the same height.
Pressure: Atmospheric pressure in hectopascals (hPa) measured at the same height with the pyranometer.
Humidity: Relative humidity in percent (%) measured at the same altitude as the pyranometer.
Wind_speed: Wind speed in metres per second (m/s) measured at the same height as the pyranometer.
Rain_1h: Precipitation in millimetres (mm) measured in the last hour.
Snow_1h: The amount of snowfall in millimetres.
Clouds_all: Cloud condition.

Table 10. Dataset Examples

Time	2017-01-01 00:00:00	2017-01-01 00:15:00	2017-01-01 00:30:00
Energy delta[Wh]	0	0	0
GHI	0.0	0.0	0.0
temp	01.06.2023	01.06.2023	01.06.2023
pressure	1021	1021	1021
humidity	100	100	100
wind_speed	04.09.2023	04.09.2023	04.09.2023
rain_1h	0.0	0.0	0.0
snow_1h	0.0	0.0	0.0
clouds_all	100	100	100
isSun	0	0	0
sunlightTime	0	0	0
dayLength	450	450	450
SunlightTime/daylength	0.0	0.0	0.0
weather_type	4	4	4
hour	0	0	0
month	1	1	1

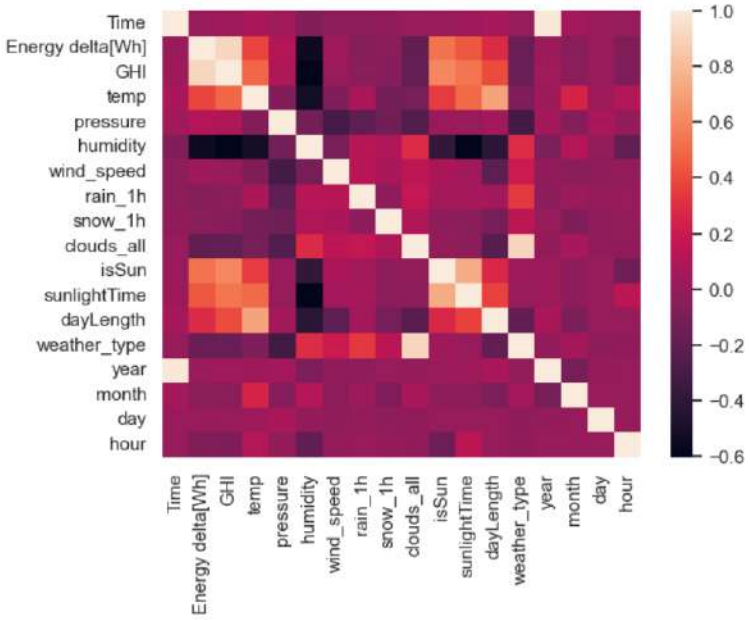

Figure 1. Correlation Matrix

Table 11. Dataset Properties

	conta	mean	std	min	%25,00	%50,00	%75,00	max
Energy delta[Wh]	196776.000000	573.008228	1044.824047	0.000000	0.000000	0.000000	577.000000	5020.000000
GHI	196776.000000	32.596538	52.172018	0.000000	0.000000	1.600000	46.800000	229.200000
temp	196776.000000	9.790521	7.995428	-16.600000	3.600000	9.300000	15.700000	35.800000
pressure	196776.000000	1015.292780	9.585773	977.000000	1010.000000	1016.000000	1021.000000	1047.000000
humidity	196776.000000	79.810566	15.604459	22.000000	70.000000	84.000000	92.000000	100.000000
wind_speed	196776.000000	3.937746	1.821694	0.000000	2.600000	3.700000	5.000000	14.300000
rain_1h	196776.000000	0.066035	0.278913	0.000000	0.000000	0.000000	0.000000	8.090000
snow_1h	196776.000000	0.007148	0.069710	0.000000	0.000000	0.000000	0.000000	2.820000
clouds_all	196776.000000	65.974387	36.628593	0.000000	34.000000	82.000000	100.000000	100.000000
isSun	196776.000000	0.519962	0.499603	0.000000	0.000000	1.000000	1.000000	1.000000
sunlightTime	196776.000000	211.721094	273.902186	0.000000	0.000000	30.000000	390.000000	1020.000000
dayLength	196776.000000	748.644347	194.870208	450.000000	570.000000	765.000000	930.000000	1020.000000
SunlightTime/daylength	196776.000000	0.265187	0.329023	0.000000	0.000000	0.050000	0.530000	1.000000
weather_type	196776.000000	3.198398	1.289939	1.000000	2.000000	4.000000	4.000000	5.000000
hour	196776.000000	11.498902	6.921887	0.000000	5.000000	11.000000	17.000000	23.000000
month	196776.000000	6.298329	3.376066	1.000000	3.000000	6.000000	9.000000	12.000000

For LSTM estimation, 80% of the dataset is allocated for training, 10% for validation and 10% for testing. The dataset was formatted for model training, which aims to separate the input features from the target variable, scale the data and group the samples by window size. Various scaling techniques were used, including fit-transform and transform using Python's MinMaxScaler.

A model consisting of a series of Keras layers was created. The first layer is the LSTM layer. LSTM stands for Long Short Term Memory and is of the RNN type. This layer is a good choice for sequential data. Because the LSTM structure keeps the incoming input with gates if it is important and forgets it if it is unimportant. Gate and Cell State determine what will be forgotten and what will be remembered.

Then there are three Dense layers. It is for learning the features in the input data. The first layer contains 128 neurons and ReLU activation function. ReLU is reduced to 0 if the input is negative and returns the input value when it is positive. The second Dense layer has 256 neurons and the last Dense layer has 512 neurons. The layers use the ReLU activation function.

The next layer is the Dropout layer. It closes randomly selected neurons and connections, allowing learning of different parts and generalisability. It is used to prevent overfitting. This is a regularisation technique.
Finally, we show that the model is prepared to solve a regression problem using a single neuron dense layer and a linear activation function.

```
Model: "sequential_1"
_________________________________________________________________
 Layer (type)                Output Shape              Param #
=================================================================
 lstm (LSTM)                 (None, 64)                20992

 dense_3 (Dense)             (None, 128)               8320

 dense_4 (Dense)             (None, 256)               33024

 dense_5 (Dense)             (None, 512)               131584

 dropout (Dropout)           (None, 512)               0

 dense_6 (Dense)             (None, 1)                 513

=================================================================
Total params: 194,433
Trainable params: 194,433
Non-trainable params: 0
_________________________________________________________________
```

Figure 2. Model Summary

MSE (Mean Squared Error) and MAE (Mean Absolute Error) values were measured. The SignificanceResult result from the Scipy library was calculated. MSE is expressed as Mean Squared Error. It is used to evaluate the performance of a machine learning model or predictor. It expresses in absolute value how much the predictions differ from the actual number. MAE is expressed as Mean Absolute Error. It is a more direct representation that takes the sum of the absolute error values of the machine learning model.

SignificanceResult gives the result of the test calculated by Spearmanr. The Spearman rank correlation coefficient measures the relationship between variables. The larger the value between -1 and 1, the greater the connection between the variables. This is useful when the data are not normally distributed. The value of the model was calculated as statistic=0.9352883880629038, which is very close to 1.

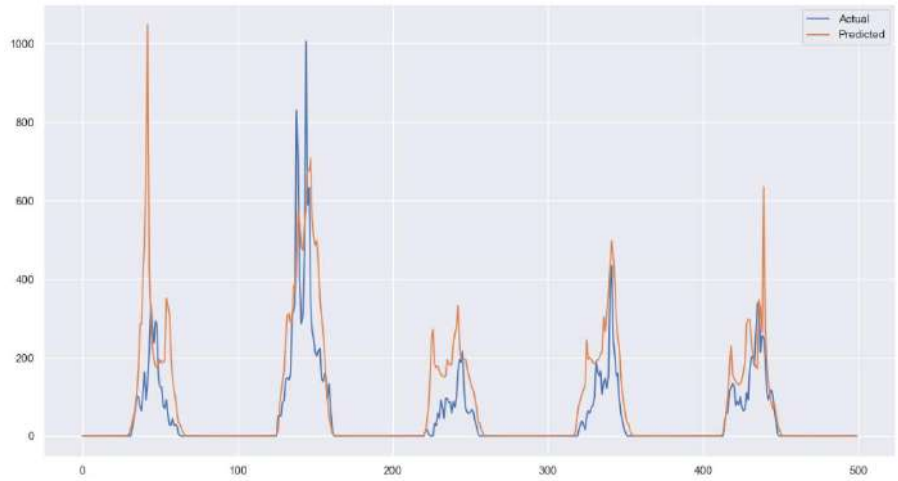

Figure 3. Model Performance Analysis

According to the output, it can be said that the predictions of the model are close to the actual values. According to SignificanceResult results, the correlation coefficient between model predictions and actual values is quite high.

3. Results

In terms of energy production by month, January, November and December exhibited the lowest production, indicating a seasonal effect with reduced production during the winter months. In contrast, June recorded the highest energy production, while April, May, July and August also showed significant production.

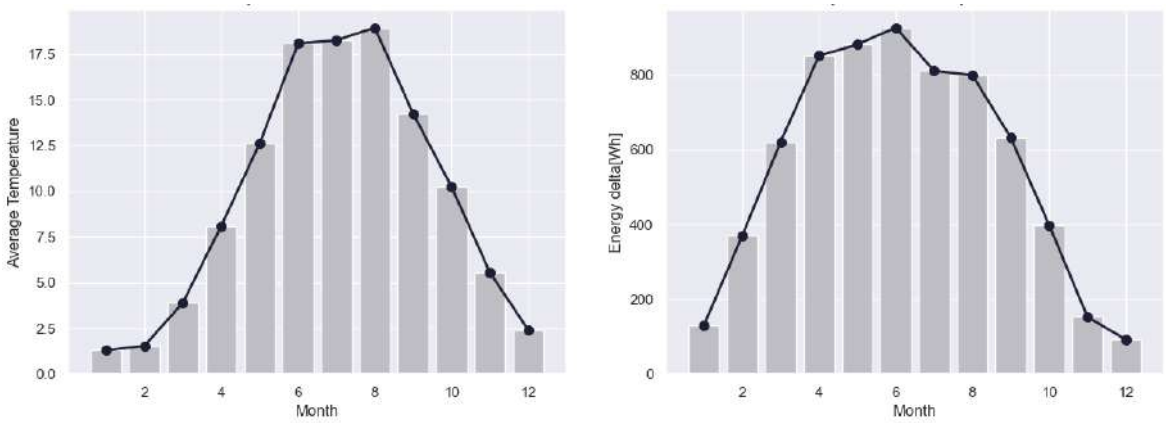

Figure 4. Comparison of Monthly Average Temperature and Energy Delta Graphs

Energy changes over the years showed a consistent pattern, with notable decreases in 2021 and 2022. The average temperature and energy consumption data showed a common pattern between energy consumption and temperature on a monthly basis.

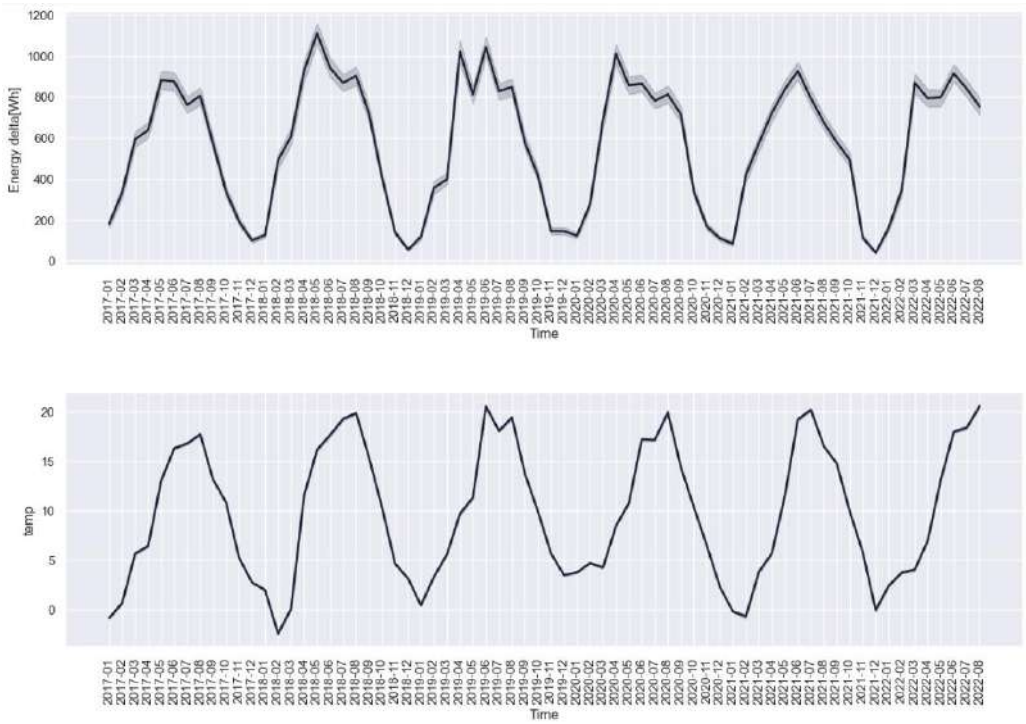

Figure 5. Energy Delta and Temperature Over the Years

The hourly analysis of energy consumption revealed significant fluctuations between 9:00 and 12:00, when solar radiation is most intense. A similar relationship was observed on a monthly basis.

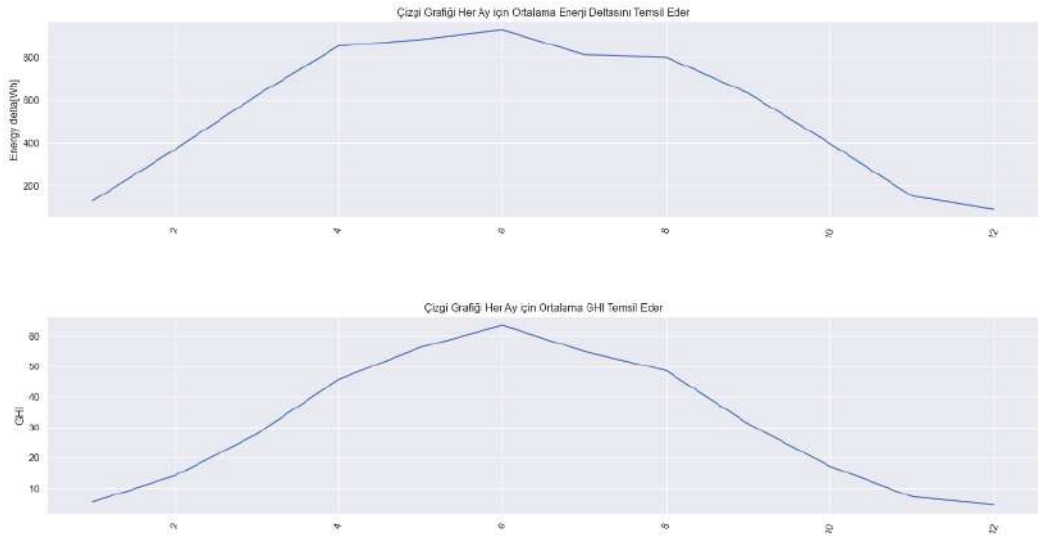

Figure 6. Energy Delta with GHI Average for Each Month

At 977 and 1047 pressure levels, no energy production was observed, indicating that there is no direct relationship with energy. Lower pressure was associated with less energy production, while the highest energy production occurred at pressure level 1038. Humidity showed a negative correlation with energy consumption.

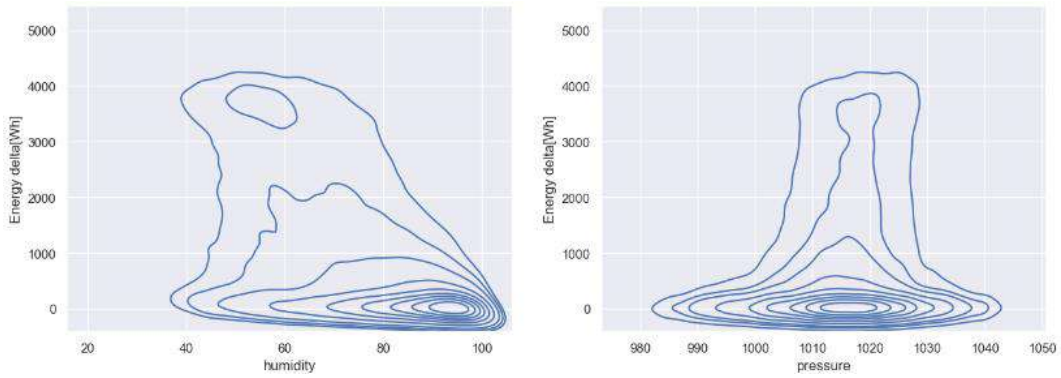

Figure 7. Pressure and Humidity

The average rainfall decreased throughout the year, making hydropower an impractical energy source for the region.

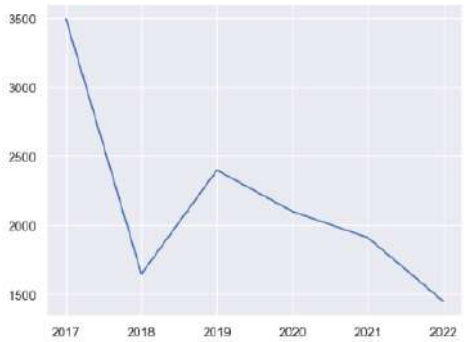

Figure 8. Average Rainfall

Wind speed for wind power generation was consistently below 5 m/s.

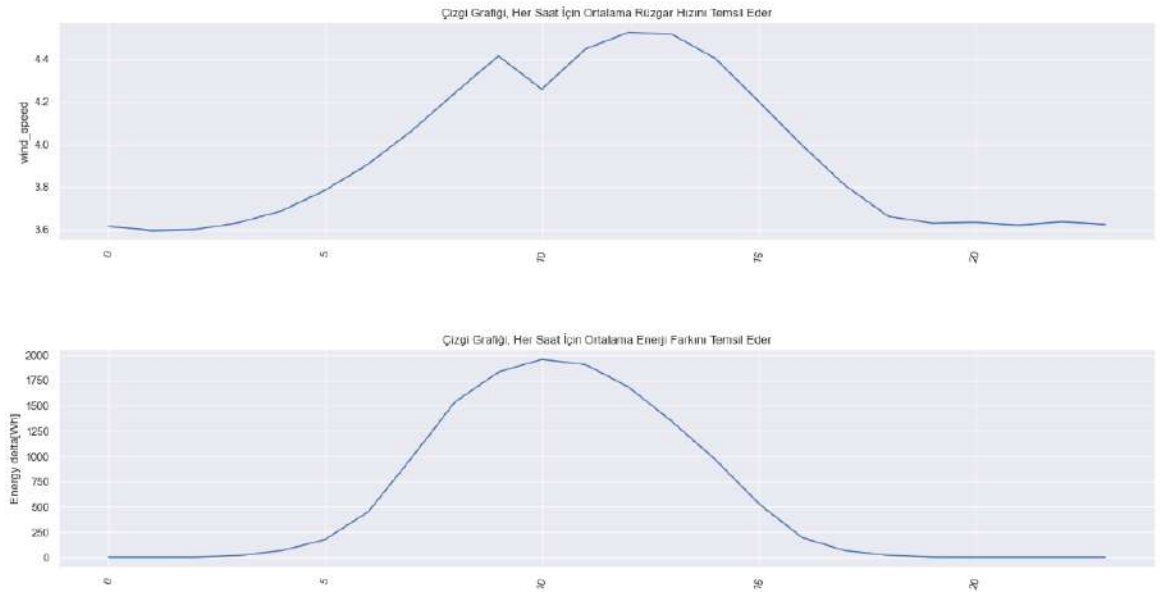

Figure 9. Relationship between Average Wind Speed and Hourly Energy Delta

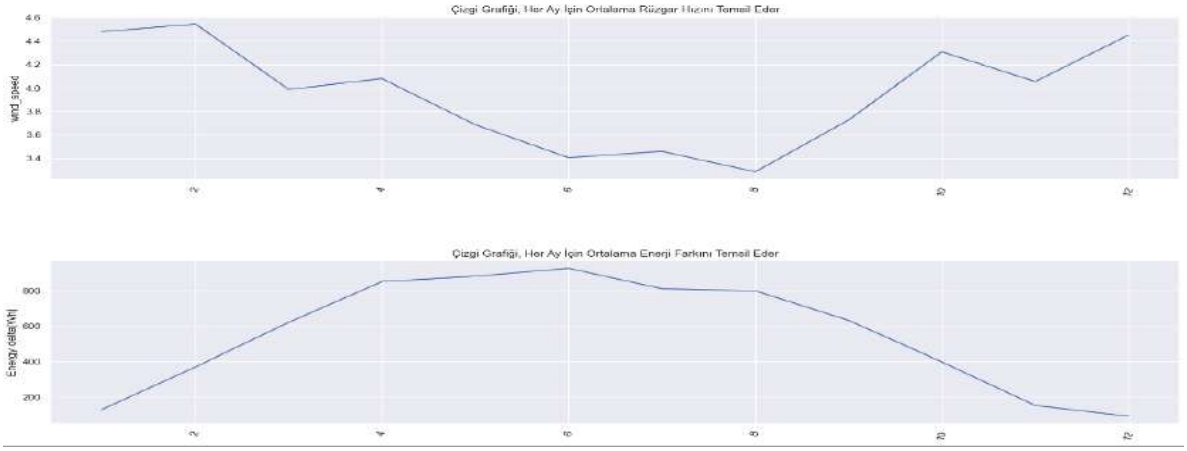

Figure 10. Relationship between Monthly Average Wind Speed and Energy Delta

4. Conclusions

In conclusion, this study illuminates the complex relationship between meteorological conditions and renewable energy sources and reveals that solar energy is the leading option for certain geographical regions. According to the results of the study, the region in question has advantages in energy production. The region's low snowfall and low cloud cover indicate that solar energy is the most favourable option. Solar Irradiance (GHI) data revealed that it is maximised during periods of increased energy demand. This means that solar energy can produce in direct proportion to energy demand. It is predicted that solar energy can play an important role in this region if energy demand increases in the future.

This study emphasises the importance of considering regional conditions in the selection of energy sources and contributes to strategic decisions to support sustainability in energy production.

Future studies can extend these analyses to different regions and time periods and contribute to the development of sustainable and environmentally friendly energy production and consumption practices. However, these results are subject to local conditions and fluctuations in energy demand. Therefore, it is vital to consider weather conditions and integrate various energy sources when planning energy strategies.

5. References

[1] ÇETİNBAKIŞ, Melike; KUTLU, Şeyma ŞAHİN. Türkiye'de yenilenebilir enerji tüketimi ve çevresel sürdürülebilirliğin ekonomik büyüme üzerine etkisi. Journal of Empirical Economics and Social Sciences, 2022, 4.1: 20-38.

[2] ÖZKAN, Arda; YETER, U. S. L. U.; GEDİKLİ, Erman. Türkiye'nin Yenilenebilir Enerji Potansiyelinde Rüzgâr Gücü ve Danimarka Örneği. Akdeniz İİBF Dergisi, 2022, 22.2: 26-35.

[3] CHEN, Huangxin; SHI, Yi; ZHAO, Xin. Investment in renewable energy resources, sustainable financial inclusion and energy efficiency: A case of US economy. Resources Policy, 2022, 77: 102680.

[4] Uğurlu, Ekin, et al. "Renewale energy sources and climate change mitigation". Energy Policy Advancement, 2021, p. 69-92.

[5] Başar, İbrahim, et al. "A review on key design and operational parameters to optimize and develop hydrothermal liquefaction of biomass for biorefinery applications". Green Chemistry, vol. 23, no. 4, 2021, p. 1404-1446.

[6] Hariri, Muhammad, et al. "Grid-connected pv generation system—components and challenges: a review". Energies, vol. 13, no. 17, 2020, p. 4279.

[7] KAYA, Zehra. Türkiye'de yenilenebilir enerji üretiminin döviz kuru ile ilişkisi ve dış ticaret dengesi üzerine etkileri. 2022. Master's Thesis. Alanya Alaaddin Keykubat Üniversitesi/Lisansüstü Eğitim Enstitüsü.

International Conference on Advances and Innovations in Engineering

A Novel Dynamometer Design for Bogie Suspension Balancement on Trams: Finite Elements and Statistical Approach

İbrahim Taha MALATYALIOĞLU[1], Ufuk KELLECİ[2], Erkan ÖZTÜRK[3*]

[1,2,3] Department of Mechanical Engineering, Faculty, Ondokuz Mayıs University, Samsun, Türkiye.
[1]ibrahimtahamalatyalioglu@gmail.com, [2]ufukkelleci58@gmail.com, [3]erkan.ozturk@omu.edu.tr

[1](ORCID: 0009-0005-9023-1930), [2](ORCID: 0009-0004-3717-6904),[3](ORCID: 0000-0002-7056-718X)

Abstract
Bogies are systems responsible for moving rail vehicles, carrying wagons and passengers. Equal loading on the wheels of the rail vehicles by balancing the suspension in bogie systems is necessary for wearing the wheels evenly, for driving safety, and to be used longer. For this reason, measuring the forces acting on the tram wheels and taking these forces into account as balancing is essential. In this study, a novel strain gauge-based dynamometer was designed for balancing the suspension of bogie systems used in trams. Dynamometer designs in different geometries, the strain gauge's positions, and the dimensions to be used have been investigated by the deformation values determined under a specific distributed load. Static Structural Analysis and Taguchi Method approaches were preferred in the dynamometer design optimization. As a result, dynamometer dimensions were optimized, and strain gauge locations and sizes were determined for optimum-sized dynamometer design. The optimum geometry for the dynamometer was defined as 31, 38, 240, 15, and 31 mm for the height (h), width (b), length (L), the diameter of the cavity geometry on the load cell (d), and the distance between their centers (l), respectively, according to the 1-1-3-3-3 optimum condition.

Keywords: bogie, dynamometer, finite element method, taguchi method

1. Introduction

Bogie can be defined as a system that provides movement in rail vehicles and carries wagons (**Figure 1.a**). Three primary purposes of bogies can be determined as (1) providing an easier transition of long rail vehicles over curved rails, (2) damping the vibrations that will occur in the vehicle between the wheel axle and the vehicle body, and (3) increasing driving comfort. In addition, bogies provide ride quality, cause less wear on the rails, and allow rail system vehicles to move more easily and quickly from curves (railroad bends) without derailment. The primary suspensions dampen the rails' vibrations, while the secondary suspensions ensure the flexible connection of the wagon and the bogie (**Figure 1.a**). In this way, passenger comfort is increased by transmitting less vibration to the passenger wagons.

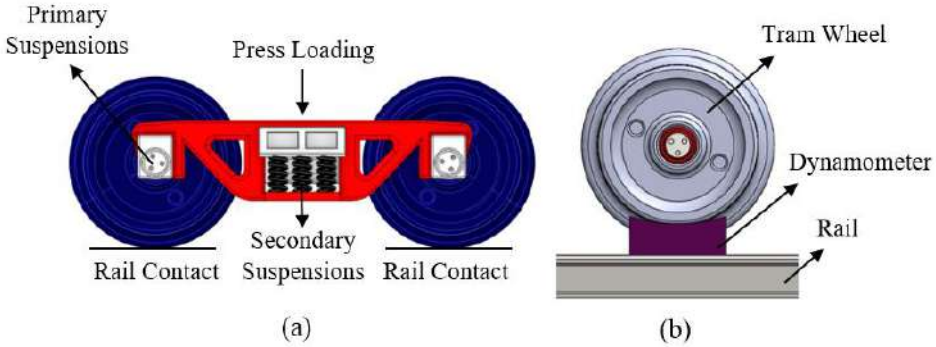

Figure 1. Schematic view of a bogie system (a) Symbolic view of the joint of load cell between tram wheel and rail (b)

The bogie press mimics the loads applied to the bogie by the wagons and rails, so it corrects the positions of the suspension. The primary purpose is to balance the suspension. Moreover, the bogies are tried to be balanced via the deformation distances on the wheels. To fully adjust suspension balancing, the force acting on the suspension must be considered during the pressing. For this reason, measuring the forces acting on the tram wheels and taking these forces into account is essential during the balancing. As passengers can stand or sit in different positions in tram transport, they can overload any wheel

*Corresponding author

on the bogie. In this case, it causes uneven wear of the tram wheels and more frequent maintenance and replacement of spare parts. In addition, unbalanced suspension triggers excessive noise in the rail bends. If the force values can be measured and balanced over their upper limits, the wear effects of the passenger positions on the bogie wheels can be minimized. The current load cells in the market are generally bending, shear, and S-type. Due to their geometric character, they can not be mounted directly on the tram wheel. Therefore, this problem can be solved with a load cell/dynamometer explicitly designed for the bogie wheels, as shown symbolically in **Figure 1.b**.

In the current literature, original dynamometer designs using strain gauges have been manufactured for different purposes, such as measuring cutting forces [1-5], the loads on vehicle engine mounts [6], designing high-capacity load cells [7], etc. Some of the related and recent literature can be realized in this section to emphasize the usage areas of the strain gauge-based dynamometers. For example, I. Korkut [1] designed a strain gauge-based dynamometer to measure three force components during milling. He performed machining experiments at different cutting parameters and proved that the dynamometer could be used to determine cutting forces. Yaldız et al.[2] designed a milling dynamometer using strain gauges and a piezoelectric accelerator to measure cutting forces and torque. They selected an octagonal ring for the strain gauges' positions and directions to a more sensitive dynamometer. Also, they reported that the dynamometer could be used effectively. Shahidi [6] designed and produced a novel load cell that can measure the three components of force and the three components of the moment for engine mounts. Strain gauges are conveniently placed in locations under the highest stress areas. The Finite Element Method (FEM) is used to characterize the mechanical behavior of the load cell and allows for a quick preliminary design focused on the provided technical requirements. After calibrating the load cell, they proposed it is suitable and successful for the engine mounts. Y. Turgut and I. Kokut designed [7], manufactured, and calibrated a high-capacity (up to 20 kN) three-component single-point load cell. This load cell consists of three Wheatstone Bridge modules based on strain gauges to measure the different direction force components. R. Jain et al. [3] designed a cutting for a dynamometer by positioning the strain gages on a cylindrical bar. The places of the strain gauge and alignment of the cylindrical bar were arranged to minimize cross-sensitivity and increase dynamometer measuring sensitivity. Lastly, the dynamometer was validated by turning for different cutting parameters. Y. Qin et al.[4] developed a high-performance torque sensor utilizing Piezoresistive MEMS Strain gages as Wheatstone Bridge Curciut application to measure the torque force during milling. Consequently, the authors cited that the dynamometer is stable and practical for monitoring the milling torques. A. Ashok Kumar et al. [8] performed an exciting study by improving an indicator measuring draft force and wheel slip for agricultural tractor implements. The indicator is a load cell-based dynamometer, and the load cells have Full Wheatstone Bridge Circuits.Y. Qin et al. [9] designed and manufactured a unique cutting force dynamometer for monitoring axial force and torque during milling. The dynamometer uses a semiconductor strain gauge to measure the deformation of a sensor element in the form of a lantern. Static calibration and a modal impact test were performed to assess the viability of the dynamometer. Then the dynamometer was mounted on a milling machine to evaluate performance under various cutting scenarios. The authors cited that the dynamometer is highly effective. H. Gökçe et al. [10] fabricated a load cell-based dynamometer to measure shear forces on drilling processes. The shear force values obtained from a commonly used and designed dynamometer were compared during the drilling 1040 material with HSS drills. E. Öztürk and K. Yıldızlı [11, 12] revealed a new static calibration methodology for strain gauge-based cutting force dynamometers to solve the cross interactions of the three cutting force components during the turning process. After the authors eliminated the cross-interaction of the three force components, they used their self-designed dynamometer to turn prismatic parts application in the following study. Furthermore form the cutting force dynamometers, M. Riddle et al. [13] presented an fascinated aspect of using strain gauges. A wearable strain gauge-based system by placing on the fingernails were produced and calibrated to measure tactile forces during the activities of daily living such as opening a jam bottle and grabing a knife. F. Meyer et al. [14] developed a new strain gauge-integrated dyanomometer for measuring the forces and torques at interface between the ski and the skier to analyze the skier's performance and injury risk. J. Pytka et al. [15] designed, developed, and applied practically a new wheel dynamometer for aircraft landing gear testing by measuring two force components acting along the longitudinal and vertical axes of the wheel. Lastly, O. Dahiree et al. [16] described a new design and analysis of a strain gauge-based load cell by shape optimization (using FEM) to measure axial forces for test benches.

Regarding the summary above, the load cell/dynamometer is said to be an essential component of various technical machines and industrial automation for detecting and sensing force and torque. A dynamometer design that can work effectively and compatibly with tram wheels is still needed. An innovative strain gauge-integrated dynamometer was created in this work to balance the suspension of the tram's bogie systems. The deformation values obtained under a particular distributed load (Totally 50000 N) have been utilized to investigate different designed dynamometer geometries,

effective strain gauge locations, and suitable strain gauge dimensions for the dynamometer. The Taguchi Method and Static Structural Analysis techniques were chosen for the dynamometer design optimization. As a consequence, the dimensions of the dynamometer were optimized, and the positions and sizes of the strain gauges were established for the best-sized dynamometer design.

2. Material and Methods

The design steps for a new strain gauge-based dynamometer for bogies' balancing are explained in detail, such title as; (1) general design criteria, (2) determination of strain gauge application, and (3) determination of the sizes and positions of the strain gauges via FEM and statistic.

2.1. General Design Criteria

The primary needs can be listed as; (1) Compact design, (2) Easy manufacturing and low cost, (3) Direct assembly to the tram wheel, and (4) A section that can stand 50000 N compressive load. As regards the four needs, the concept design of the dynamometer was set in a 3D CAD program. The geometry of the tram wheel consists of 2 stages. A half-moon fastener was designed to fit the wheel on the load cell. During the practical bogie press tests, a small chock was modeled to place the dynamometer on any platform. The assembly of the dynamometer, half-moon fastener, and chocks can be bolts and nuts, as presented in **Figure 2**.

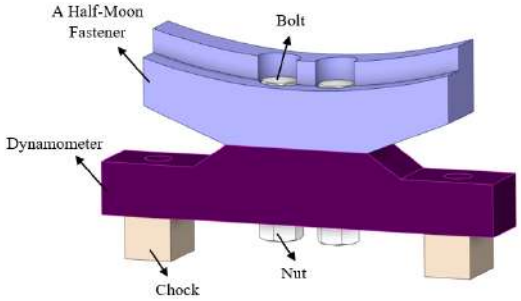

Figure 2. The assembly view of the dynamometer, half-monn fastener part, and chocks.

In the concept design, the sizes of the dynamometer were shown at level 2 in **Table 3**. Then, Static structural analysis was modeled under the 50000 N distributed load. The dynamometer material was chosen as structural steel due to its low cost and availability. The FEM was first used to determine the maximum deformation areas for the assumed dynamometer design without sockets (**Figure 3.a**). After that, three types of sockets were formed on the CAD design to increase the deformation by (1) cavity shape (**Figure 3.b**), (2) hole (**Figure 3.c**), and (3) hexagon (**Figure 3.d**). The suitable socket type was selected regarding the maximum deformation determined from FEM.

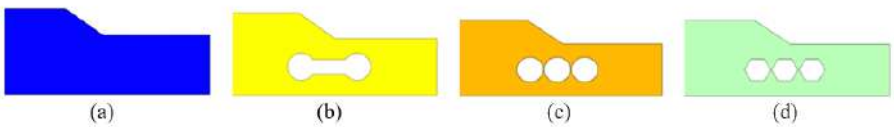

Figure 3. Assumed dimensions of the concept dynamometer (a) and cavity shape (b), hole (c), hexagon (d)

2.2. Determination of Strain Gauge Application

The change in resistance due to strain is minimal in a strain gauge. Thus, direct measuring strain with a strain gauge can be difficult. This problem can be solved with Wheatstone Bridge Circuits. An unknown resistance value is determined with the help of known resistors in the Wheatstone Bridge. A Full Whetstone Bridge is shown in **Figure 4.a**, consisting of four resistors. As connecting strain gauges instead of these resistors, strain can be measured. Wheatstone bridge types are formed with variables such as the connection places of strain gauges and their numbers. These variants are created by connecting full-bridge strain gauges to four corners, half-bridge strain gauges connecting to two corners, and quarter-bridge connecting only one corner of the Wheatstone Bridge. The basic usage areas of Wheatstone Bridge in engineering are shown in **Figure 4.b-e** in four categories. This study used the bending loading approach seen in **Figure 4.c**. Here, each strain gauge is the same. The strain values are the same for the upper and lower surfaces but with opposite signs. Having

values with opposite signs increases the accuracy of the result. In addition, there are parasitic effects on strain gauges due to temperature and cable resistance. Instead, these parasitic effects are eliminated by the Full Wheatstone Bridge Circuit [11].

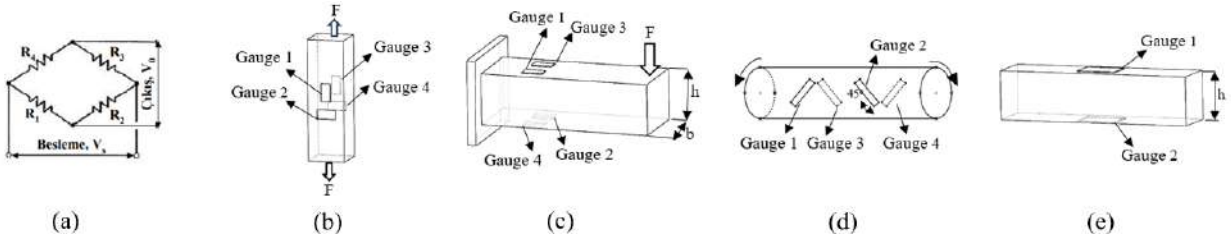

Figure 4. Full Wheatstone Bridge circuit (a) and its engineering applications for, namely, Tensile/compress condition (b), bending condition (c), Torsion condition (d), and both tensile and bending condition (e)

2.3. Determination of the Sizes and Positions of the Strain Gauges via Finite Element Method and Statistic

In the static structural analysis, the stresses and deformations on the part can be easily determined. The set FEM in this study was built regarding the following steps:

a. Importing the CAD model into Static Structural Analysis simulation
b. Defining the Materials
c. Forming the suitable mesh
d. Creating the forces and boundary conditions
e. Solve and evaluate the results.

Before starting the FEM analysis, the geometry was simplified using the dynamometer geometry without chocks and half-moon fastener. The dynamometer material was selected from the ANSYS library as structural steel (**Table 2**). After that, the mesh was created on the dynamometer CAD file. In the Static Structural analysis, the tutorial of ANSYS recommends checking the Skewness parameters of the created mesh regarding **Table 1**, and the skewness values must not be high [17]. The average skewness value of the created mesh in this study was determined as **0.2479**. Thus, the mesh is suitable for the analysis.

Table 1. The Skewness Parameters for meshing

Excellent	Good	Fair	Poor	Bad	Degenerate
0-0.25	0.25-0.50	0.50-0.75	0.75-0.9	0.9-<1	1.00

It is assumed that the force is applied to the upper surface of the dynamometer as a distributed load of 50000 N. The bolt-hole surfaces are considered to be fix-supported (**Figure 5**). In addition, the assumptions and boundary conditions for the model are given in detail in **Table 2**.

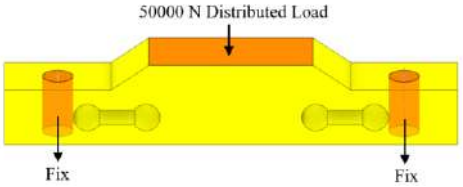

Figure 5. Boundary condition of the dynamometer

Table 2. Assumptions and Boundary Conditions for the FEM

Assumptions and Boundary Conditions	
Material Properties	Structural steel (selected from the ANSYS 2021 R2 library) Density: 7850 kg/m^3 Young's Modulus: 2x10^{11} Pa Poison Ratio: 0,3
Analysis Module	Time Independent/Static Structural Analysis
Mesh Structure	Element Size: 3 mm
Boundary Conditions	50000 N Distributed Load Support from Bolt Connection Surfaces
Solution	Directional Deformation – X Axis

The Taguchi Method is a design of experiments approach that considers more than one factor simultaneously and provides the optimum result with fewer experiments. So it was selected to optimize the dynamometer dimensions. Here, the dynamometer was designed regarding the factors, namely, the height (h), width (b), length (L), diameter (d) of the cavity geometry on the dynamometer, and the distance between the centers (l) that will directly affect the deformation (**Figure 6.a**). After that, the levels of these factors were determined. While examining the effects of these parameters at different levels, it was assumed that the dimensions of the created cavity geometry remained constant in each simulation from the upper and side edges of the dynamometer (**Figure 6.b**).

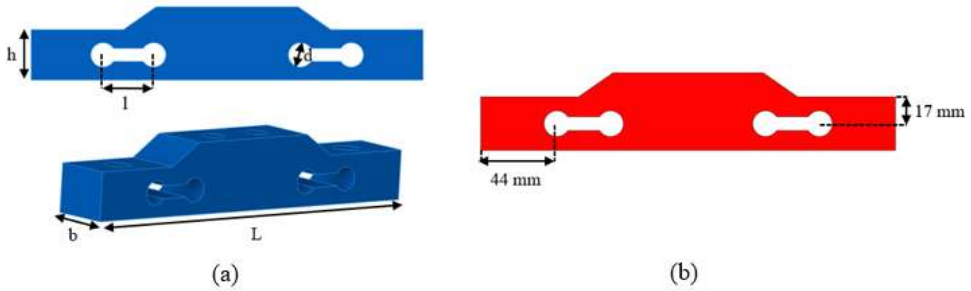

Figure 6. The factor affected the deformation (a) and constant variables for the simulations (b)

Three characteristic solving approaches are available in the Taguchi method [18, 19]. These are:

1. The smallest condition is the best.
   - $\frac{S}{N} = -10 \log\left(\frac{1}{n}\sum_{i=1}^{n} y_i^2\right)$ (1)
2. The highest condition is the best.
   - $\frac{S}{N} = -10 \log\left(\frac{1}{n}\sum_{i=1}^{n} \frac{1}{y_i^2}\right)$ (2)
3. The nominal condition is the best.
   - $\frac{S}{N} = -10 \log\left(\frac{1}{n}\sum_{i=1}^{n} \frac{y^{-2}}{S^2}\right)$ (3)

It is better for the dynamometer measurement capability that the deformation reaches as large values as possible. For this reason, "The highest condition is the best." was chosen, and the L27 orthogonal array for three levels and five factors was chosen for the simulations (**Table 5**). The factors and their levels are shown in **Table 3**.

Table 3. Factors and levels

FACTORS	LEVEL 1	LEVEL 2	LEVEL 3
H (MM)	31	34	37
B(MM)	38	41	44
L(MM)	200	220	240
D(MM)	11	13	15
L(MM)	25	28	31

After calculating S/N ratios in the Taguchi method, the ANOVA test can be performed to decide whether the results are significant. ANOVA test is a tool used to measure whether there is a statistically significant difference between the means of independent groups [18]. After the optimum condition was determined by Taguchi Method, it was verified with simulation results in the same situation.

3. Results

Firstly, the concept dynamometer design (**Figure 3.a**) was investigated by FEM to observe the absolute maximum deformation region regarding the X axis under a 50000 N distributed load. The absolute maximum deformation region was observed symmetrically bottom of the dynamometer, as shown in **Figure 7**. After that, three types of sockets were pocketed on the dynamometer by cavity shape, hole, and hexagon to increase the absolute deformation (**Figure 3. b-d**). Whereas each simulation for the sockets had a similar deformation distribution to the concept design, like in **Figure 7**, the

maximum deformation was determined for the cavity shape dynamometer design (**Table 4**). Thus the cavity shape dynamometer was selected for the optimization process.

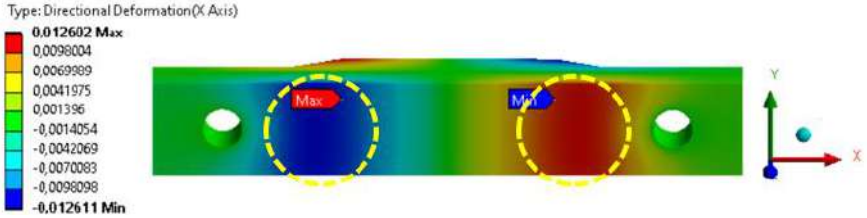

Figure 7. Deformation distribution for the concept design

Table 4. The maximum absolute deformation differences for the dynamometer considering three types of sockets

SOCKET TYPE	MAX. DEFORMATİON	MİN. DEFORMATİON	ABSOLUTE DEFORMATİON
WİTHOUT SOCKET	0,01044	-0,010439	0,02879
CAVİTY-SHAPED	**0,014688**	**-0,014690**	**0,02938**
HOLE	0,012876	-0,012876	0,02575
HEXAGON	0,014114	-0,014110	0,02822

Secondly, by referencing three levels, the cavity-shaped dynamometer (Figure 6.a) was modified considering the factors, namely, h, b, L, d, and l (Table 3). In Taguchi Method, the L27 orthogonal array for three levels and five factors was set for the simulations. Then, Signal to Noise (S/N) ratios were determined according to the absolute deformation difference in Table 5. As the responses and the ranks of the factors are presented in Table 6, the main effect plot of S/N ratios is shown in Figure 8. The optimum geometry for the dynamometer was calculated as h1b1L3d3I3 factors, as shown in red points in Figure 8. The ANOVA test was performed to decide whether the factors were significant by checking the significance level (p). Since all p values were calculated smaller than 0.05 significance level, all factors have significantly affected the deformation results. As a result, most influence factor was determined as L at 65.1% contribution ratio, and then the influence sequences of the factors were observed as L, h, d, b, I (Table 7).

Lastly, the optimum condition evaluated from the Taguchi Method should be verified by the same situation as the simulation. The design of simulations via the Taguchi Method predicted that the optimum absolute deformation was 0.042, whereas the simulation result was 0.046. Due to these values being close, the design of simulations can be acceptable. Therefore, the dynamometer with optimum geometry (11333 condition) can be used for evaluating the strain gauge positions and dimensions. Strain gauges can be adhered to regions with the greatest absolute deformation over a distance of approximately 25 mm (Figure 9). While two strain gauges on the left side of the dynamometer bottom shorten, two on the right side lengthen, as seen in Figure 9. In this case, it can be said that the maximum strain gauge length can be 25 mm. The shortening and elongating regions on the dynamometer are symmetrical. Strain gauges should be positioned at a distance of 45 mm from both edges of the dynamometer (Figure 9).

Table 5. L27 orthogonal Array, Simulation results, and S/N ratios

No	h	b	L	d	l	Absolute Deformation	S/N Ratio
1	1	1	1	1	1	0,023371	-32,62645
2	1	1	1	1	2	0,023438	-32,60159
3	1	1	1	1	3	0,023455	-32,59529
4	1	2	2	2	1	0,029909	-30,48396
5	1	2	2	2	2	0,030101	-30,42838
6	1	2	2	2	3	0,030222	-30,39354
7	1	3	3	3	1	0,040972	-27,75026
8	1	3	3	3	2	0,041053	-27,73310
9	1	3	3	3	3	0,041046	-27,73458
10	2	1	2	3	1	0,030576	-30,29239
11	2	1	2	3	2	0,030882	-30,20589
12	2	1	2	3	3	0,031101	-30,14451
13	2	2	3	1	1	0,030118	-30,42348
14	2	2	3	1	2	0,030815	-30,22476
15	2	2	3	1	3	0,031355	-30,07386
16	2	3	1	2	1	0,021392	-33,39497
17	2	3	1	2	2	0,021728	-33,25960
18	2	3	1	2	3	0,021928	-33,18002
19	3	1	3	2	1	0,030322	-30,36484
20	3	1	3	2	2	0,031098	-30,14535
21	3	1	3	2	3	0,031748	-29,96567
22	3	2	1	3	1	0,020228	-33,88094
23	3	2	1	3	2	0,020401	-33,80697
24	3	2	1	3	3	0,020474	-33,77595
25	3	3	2	1	1	0,020585	-33,72898
26	3	3	2	1	2	0,020949	-33,57673
27	3	3	2	1	3	0,021252	-33,45200

Table 6. Response Table

Level	h	b	L	d	l
1	**-30,26**	**-30,99**	-33,24	-32,14	-31,44
2	-31,24	-31,5	-31,41	-31,29	-31,33
3	-32,52	-31,53	**-29,38**	**-30,59**	**-31,26**
Delta	2,26	0,54	3,86	1,55	0,18
Rank	2	4	1	3	5

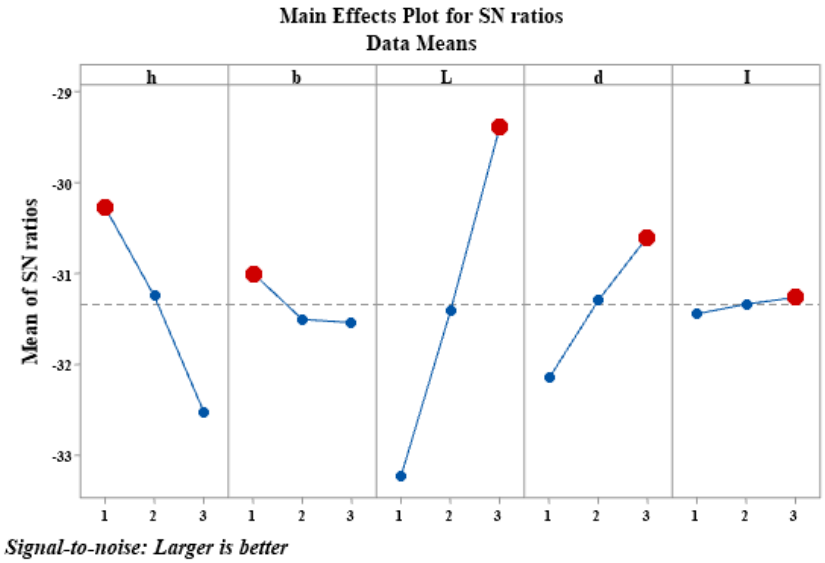

Figure 8. Main effects plot of the S/N ratios

Table 7. ANOVA Resulst for S/N ratios

Source	DF	Seq SS	Contribution	Adj SS	Adj MS	F-Value	P-Value
h	2	23,137	22,49%	23,1371	11,5685	2439,19	0
b	2	1,648	1,60%	1,6482	0,8241	173,76	0
L	2	66,982	65,10%	66,9817	33,4908	7061,44	0
d	2	10,892	10,59%	10,8916	5,4458	1148,23	0
l	2	0,149	0,15%	0,1494	0,0747	15,75	0
Error	16	0,076	0,07%	0,0759	0,0047		
Total	26	102,884	100,00%				

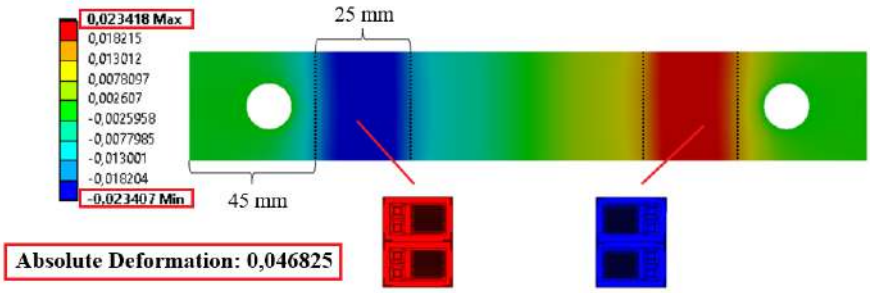

Figure 9. Strain gauge positions for the optimum dynamometer geometry

4. Conclusion

A unique strain gauge-based dynamometer was developed in this study in order to balance the suspension of bogie systems in trams. FEM has been used to determine the absolute deformation differences under a specific distributed load to reveal the optimum dynamometer geometry, strain gauge placements, and dimensions on the dynamometer. Thus, The static structural analysis and Taguchi Method techniques were performed in the dynamometer design optimization process. As a result, dynamometer dimensions were optimized, and strain gauge positions and sizes for optimal-sized dynamometer design were identified. According to the 1-1-3-3-3 optimum condition, the ideal geometry for the dynamometer was defined as 31, 38, 240, 15, and 31 mm for h, b, L, d, and l, respectively. Also, the maximum strain gage lengths were examined at 25 mm, and the strain gages must be positioned 45 mm away from the side edges on the bottom surface.

5. References

[1] Korkut, I., *A dynamometer design and its construction for milling operation.* Materials & Design, 2003. **24**(8): p. 631-637.

[2] Yaldiz, S. and F. Unsacar, *A dynamometer design for measurement the cutting forces on turning.* Measurement, 2006. **39**(1): p. 80-89.

[3] Jain, R., J.K. Rathore, and V.K. Gorana, *Design, Development and Testing of a Three Component Lathe Tool Dynamometer Using Resistance Strain Gauges.* Cad/Cam, Robotics and Factories of the Future, 2016: p. 13-21.

[4] Qin, Y.F., et al., *A High Performance Torque Sensor for Milling Based on a Piezoresistive MEMS Strain Gauge.* Sensors, 2016. **16**(4).

[5] Mohanraj, T., et al., *Design and analysis of a strain gauge based eight-shaped elliptical ring dynamometer for milling force measurement.* Proceedings of the Institution of Mechanical Engineers Part C-Journal of Mechanical Engineering Science, 2021. **235**(17): p. 3125-3134.

[6] Shahidi, K., *Design of Multi-Axial Load Cell to Measure the Forces and Moments Acting on Engine Mounts*, in *Mechanical Engineering*. 2014, Boğaziçi University. p. 107.

[7] Turgut, Y. and I. Korkut, *High capacity three-component dynamometer design, construction and its calibration.* Scientific Research and Essays, 2012. **7**(30).

[8] Kumar, A.A., V.K. Tewari, and B. Nare, *Embedded digital draft force and wheel slip indicator for tillage research.* Computers and Electronics in Agriculture, 2016. **127**: p. 38-49.
[9] Qin, Y.F., et al., *A novel dynamometer for monitoring milling process.* International Journal of Advanced Manufacturing Technology, 2017. **92**(5-8): p. 2535-2543.
[10] Gökçe, H., M. Yavuz, and M. Karayel, *Dynamometer Design and Manufacturing for Cutting Force Definition on Machining Process.* Gazi Journal of Engineering Sciences, 2017. **3**(2): p. 27-32.
[11] Ozturk, E. and K. Yildizli, *A new static calibration methodology for strain gage integrated dynamometers.* International Journal of Advanced Manufacturing Technology, 2017. **91**(5-8): p. 1823-1838.
[12] Ozturk, E. and K. Yildizli, *Measured Cutting Forces in the Turning of Prismatic Parts at Different Spindle Speeds and Side Cutting Edge Angles.* Arabian Journal for Science and Engineering, 2018. **43**(9): p. 4635-4647.
[13] Riddle, M., et al., *Wearable strain gauge-based technology measures manual tactile forces during the activities of daily living.* Journal of Rehabilitation and Assistive Technologies Engineering, 2018. **5**.
[14] Meyer, F., A. Prenleloup, and A. Schorderet, *Development of a New Embedded Dynamometer for the Measurement of Forces and Torques at the Ski-Binding Interface.* Sensors, 2019. **19**(19).
[15] Pytka, J., et al., *Wheel dynamometer system for aircraft landing gear testing.* Measurement, 2019. **148**.
[16] Al-Dahiree, O.S., et al., *Design and Shape Optimization of Strain Gauge Load Cell for Axial Force Measurement for Test Benches.* Sensors, 2022. **22**(19).
[17] ANSYS., *ANSYS Meshing User's Guide*. Vol. 13.0. 2010: ANSYS, Inc. 342.
[18] Ozturk, E. and K. Yildizli, *Comparison of Thermal Behavior of Self-Designed Internally Cooled Cutting Tool for Various Heat Transfer Fluids-Statistic and Computational Fluid Dynamics Approach.* Journal of Manufacturing Science and Engineering-Transactions of the Asme, 2022. **144**(10).
[19] Gologlu, C. and N. Sakarya, *The effects of cutter path strategies on surface roughness of pocket milling of 1.2738 steel based on Taguchi method.* Journal of Materials Processing Technology, 2008. **206**(1-3): p. 7

Effect of welding tool rotation speed on weld tensile strength in friction stir lap welding of 7075-T651 aluminum alloy sheets

Omer EKİNCİ[1], Zulkuf BALALAN[2]

[1]Department of Astronautical Engineering, Faculty of Aviation and Space Sciences, Sivas University of Science and Technology, Sivas, Turkey.
[2]Department of Mechanical Engineering, Faculty of Engineering and Architecture, Bingol University, Bingol, Turkey.
[1]omerekinci@sivas.edu.tr, [2]zbalalan@bingol.edu.tr

[1](ORCID: 0000-0002-0179-6456), [2](ORCID: 0000-0001-5808-6263)

Abstract

7075-T651 aluminum alloy is one of the aluminum alloys with the highest strength. This alloy is often utilized in the aerospace industry. Joining plays an important role in increasing the application areas of materials. When 7075-T651 aluminum alloy is combined by fusion welding methods, many defects occur in the weld area that causes poor weld formation. Therefore, these methods are not preferred for welding this alloy. On the other hand, friction stir welding, which is a solid-state welding method developed especially for joining aluminum alloys, has proven to be highly suitable for aluminum alloys. In this study, the effect of welding tool rotation speed, which is one of the most important welding parameters, on weld tensile strength was investigated in joining 2 mm thick 7075-T651 aluminum alloy sheets with friction stir lap welding. It has been observed that the weld strength decreases with the increase of the welding tool rotation speed. The weld with the highest tensile load of 3627 N was produced by the lowest tool rotation speed of 720 rpm.

Keywords: 7075-T651 aluminum alloy, tool rotation speed, tensile strength

1. Introduction

Today, automobile and aerospace industries use aluminum alloys extensively, especially for saving weight, which is extremely important for these sectors [1, 2, 3]. 7075 Aluminum alloy is one of the strongest aluminum alloys and has a high strength-to-weight ratio and natural aging properties. Therefore, it is generally used as structural parts in aircraft [4, 5]. But, it is highly hard to weld this alloy by traditional fusion welding methods because the copper it contains causes cracks in the weld and liquation cracks in the heat-affected zone, which seriously deteriorates the strength of the weld [6, 7]. This is one of the reasons that rivet has become the primary joining element in aircraft. On the other hand, the newly developed friction stir welding (FSW) is evaluated as an alternative to the rivet [8], and it is an environmentally friendly, energy-efficient, and versatile solid-state welding method compared to traditional fusion welding techniques [9]. Materials are welded without melting with FSW [10]. Thus, the negativities such as cracks and pores seen in fusion welding do not occur in FSW. Moreover, it has been proven that even 7XXX series aluminum alloys like 7075 that are nearly impossible to be welded via fusion welding can be reliably joined by the FSW [11, 12, 13].

2. Material and Method

A 7075-T651 aluminum alloy sheet with a thickness of 2 mm, a length of 100 mm, and a width of 100 mm was placed on a 50x100 mm2 area on another 7075-T651 aluminum alloy sheet with the same dimensions. After that, they were firmly clamped with the help of a clamping apparatus on a Falco FMH-4 brand universal milling machine table, and then they were combined by friction stir lap welding (FSLW) as schematic illustration in Figure 1. Sheets were combined under welding tool rotation speeds of 720, 980 and 1325 revolution per minute (rpm) while keeping the tool tilt angle of 2 degrees clockwise, tool immersion depth into the sheets placed on top of each other of 3.5 mm and tool feed rate of 22 mm/min constant. The triangle tip welding tool used in the welding process was fabricated from H13 hot work tool steel

[1]Corresponding author

and is shown in Figure 2 with its dimensions. Welded sheets are given in Figure 3. For the tensile shear test, 150 mm long and 25 mm wide welded samples in Figure 4 and specimens for the cross-sectional area examination of the welds in Figure 6 were cut from the welded sheet in Figure 3 with a KMY DG 280 model band saw machine. Tensile specimens were tested at room temperature on a SHIMADZU 250 kN tensile tester at a tensile velocity of 1 mm/min. Cross-sectional area samples of welds were etched for 6 seconds with Keller's reagent (2 ml hydrofluoric acid, 3 ml hydrochloric acid, 5 ml nitric acid and 190 ml water) after sanding from 200-grit to 1500-grit sandpaper. Etched cross-sectional areas were examined with an AOB inverted metal optical microscope.

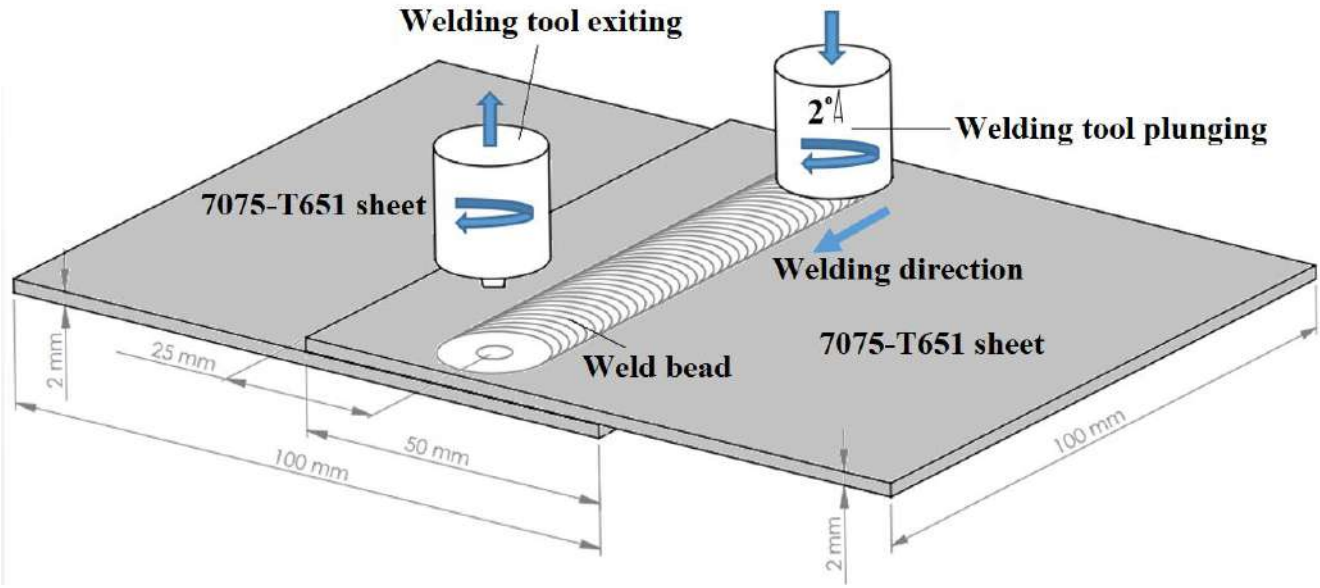

Figure 1. Schematic representation of the FSLW process

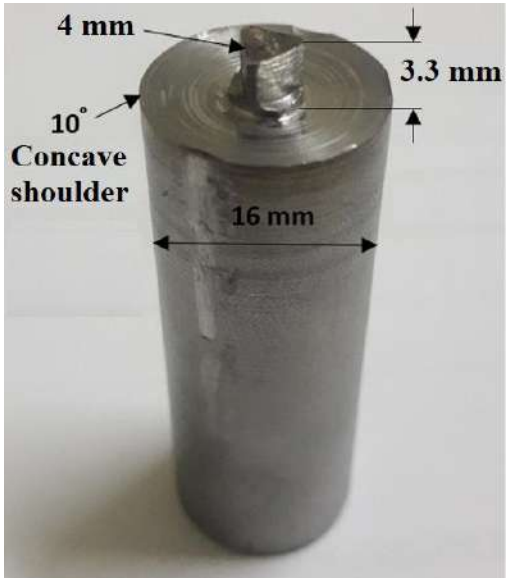

Figure 2. Welding tool used in the FSLW process

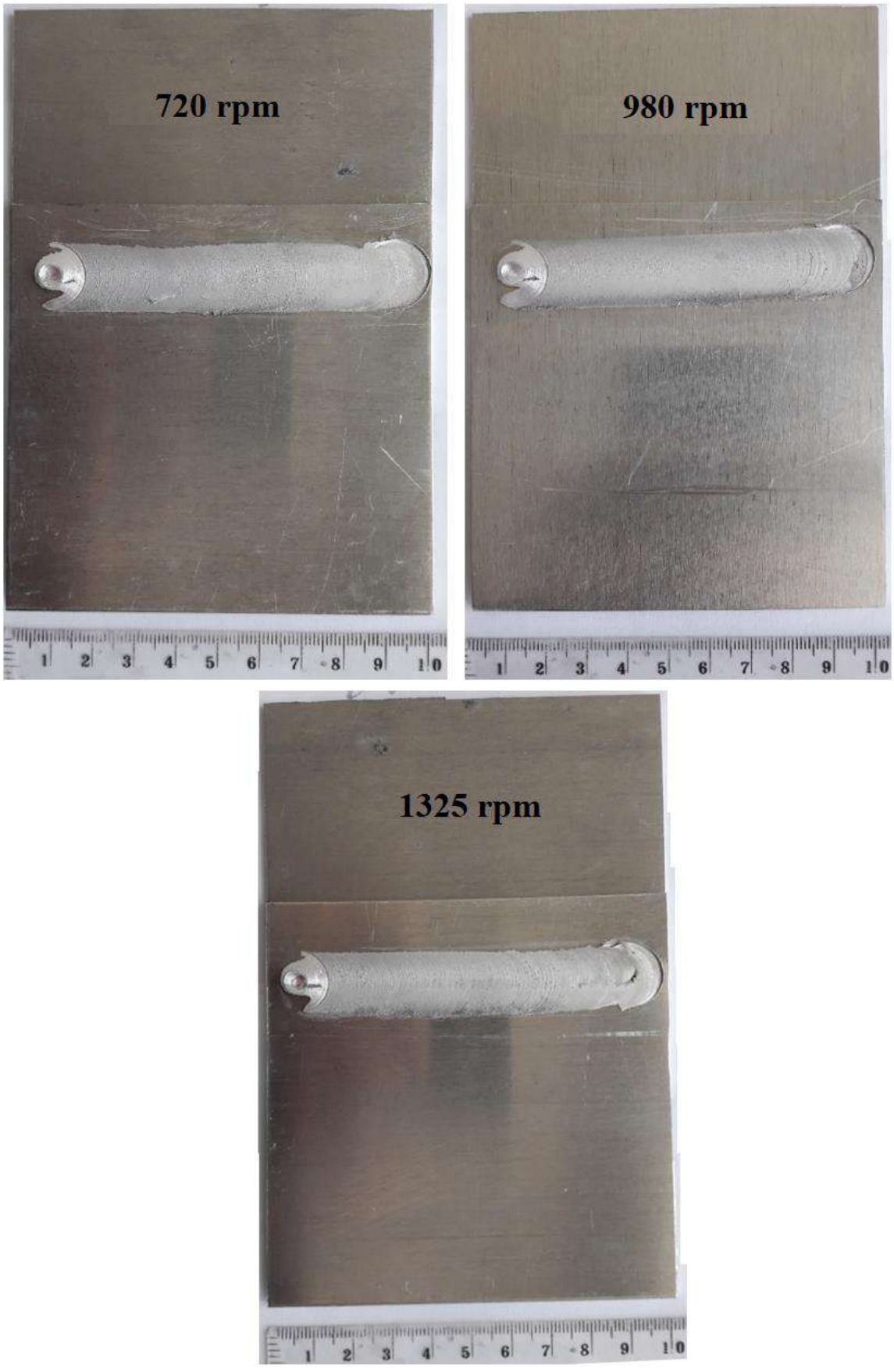

Figure 3. Sheets joined with the FSLW at different tool rotation speeds

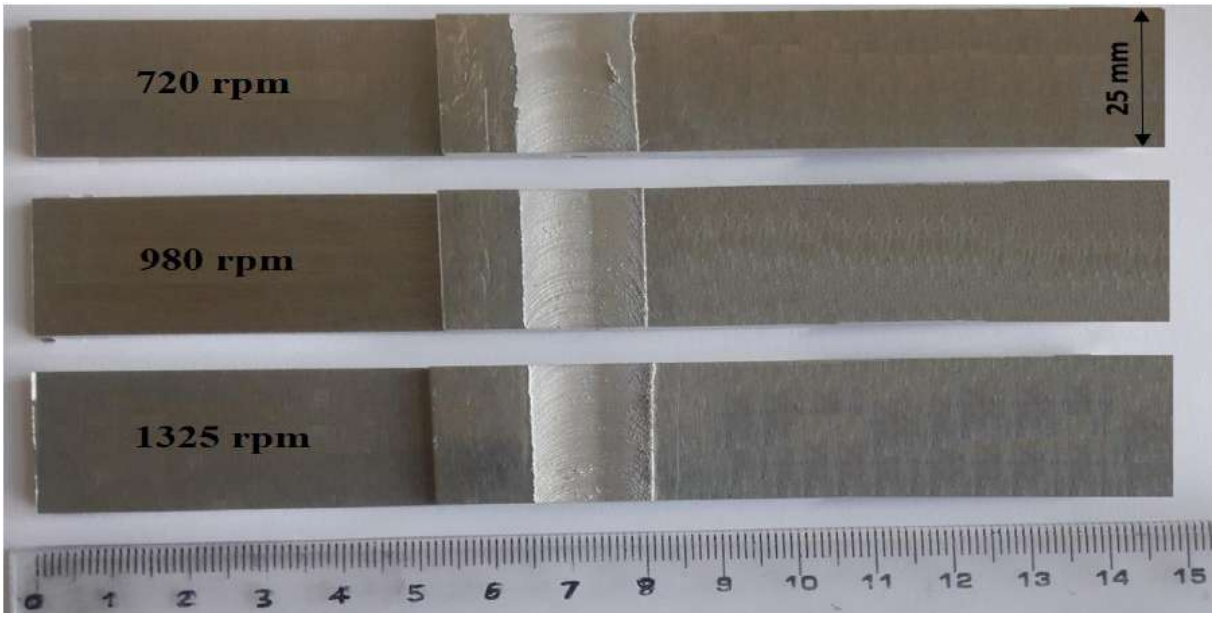

Figure 4. Tensile samples and dimensions of the FSLW welds produced at different tool rotation speeds

3. Results and discussion

Top views of the produced weld beads at various rotation speeds are provided in Figure 5. It is clear that all of the weld beads have cavity defect and it got slightly bigger and bigger with an increase in the rotation speed. It can be seen that there are two cavities formed at tool plunging and exiting regions on the top of the weld bead made at 1325 rpm.

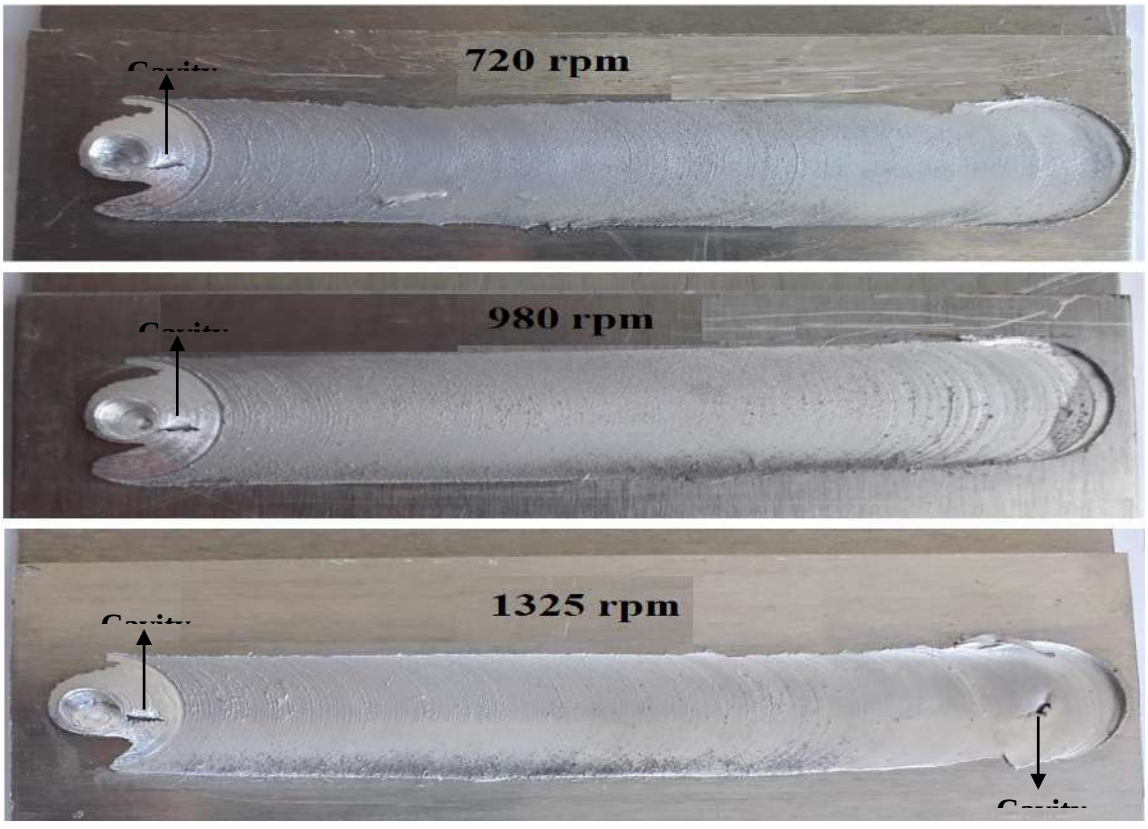

Figure 5. Top view of the FSLW welds produced at different tool rotation speeds

Macro weld cross-sections of the joints are given in Figure 6. As can be seen, a tunnel defect was formed in all the welds. Tunnel defect got bigger with a rise in the tool rotation speed. Also, it is evident that the tunnel defect gets bigger and bigger with a rise in the tool rotation speed.

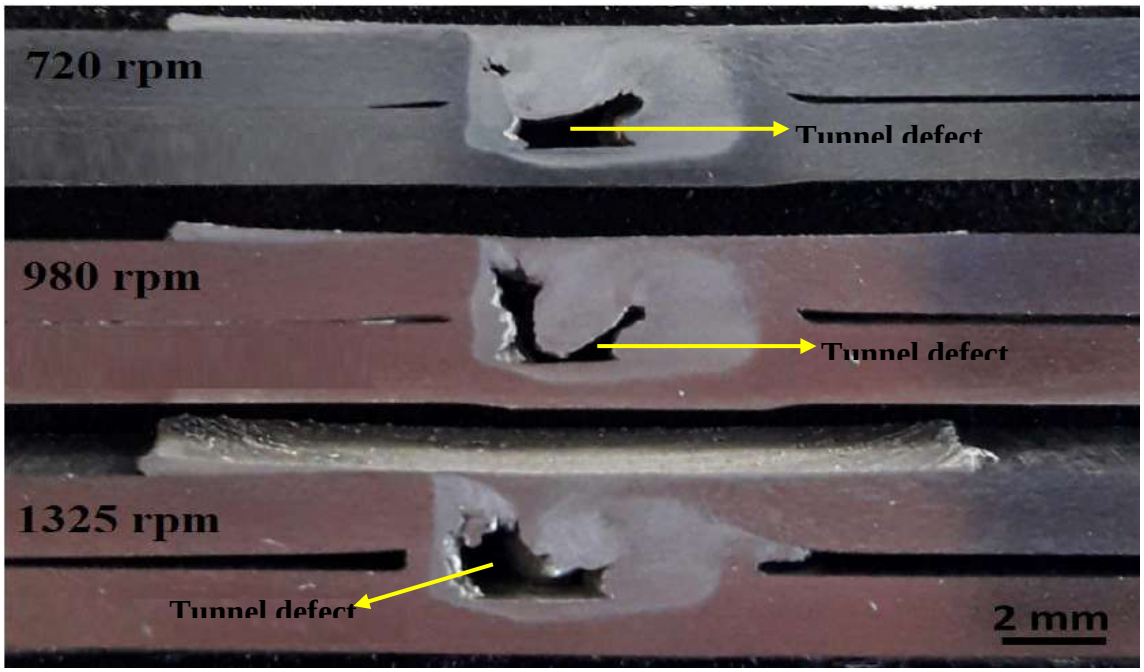

Figure 6. Cross-sectional view of the FSLW welds produced at different tool rotation speeds

Tensile shear load of the joints are presented in Figure 7. It is obvious that the tensile shear load dramatically decreased when the tool rotation speed was increased from 720 to 1325 rpm. The amount of reduction in the tensile shear load gradually decreased with an increase in the tool rotation speed. In other words, this reduction in the tensile shear load is greater by increasing the rotation speed from 720 to 980 rpm than that from 980 to 1325 rpm. As the rotation speed increased, the weld strength decreased because the unbonded tunnel defect throughout the weld bead in the weld region became larger and larger. This result showed that for the 22 mm/min tool feed rate, a high rotation speed of even 700 rpm by using a tool with a triangular pin is not suitable for properly stirring this material and obtaining a weld without tunnel defect. Lee et al. [14] obtained stronger welds by lower tool rotation speed in the FSLW of dissimilar Al alloys. Dubourg et al. [15] found similar results for FSLW of 7075 and 2024 Al alloys.

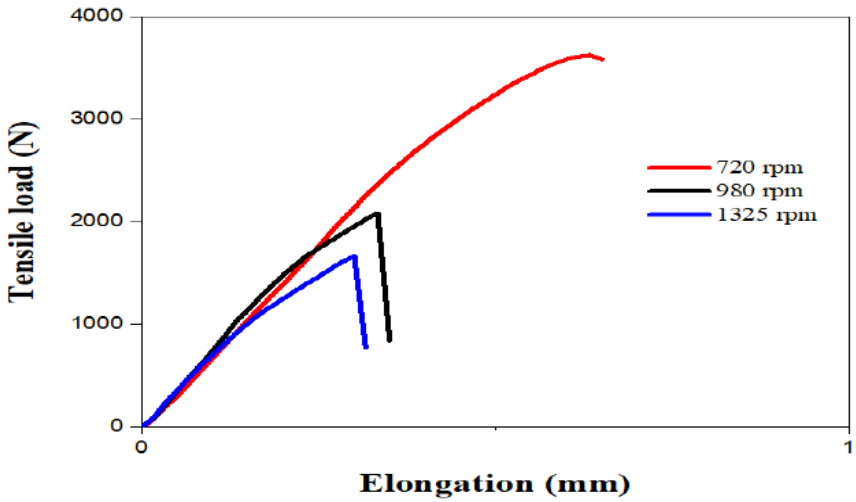

Figure 7. Tensile test results of the FSLW welds

4. Conclusions

2 mm thick 7075-T651 aluminum alloy sheets were joined at 720, 980 and 1325 rpm welding tool rotation speeds by the FSLW method. The tunnel flaw was observed in all the welds. However, the tunnel flaw in the weld bead became bigger and bigger with the rise in the tool rotation speed, resulting in a reduction in the weld bonding area and thus lowering the weld strength. The strongest weld with a tensile load of 3627 N was created at the rotational speed of 720 rpm, while the weakest weld with a load of 1667 N at 1325 rpm. The tunnel flaws can be eliminated and hence much stronger welds can be obtained by increasing the tool feed rate in coordination with the low tool rotation speed.

References

[1] Uematsu Y, Tokaji K. Comparison of fatigue behaviour between resistance spot and friction stir spot welded aluminium alloy sheets. Sci Technol Weld Join 2009;14:62–71.

[2] John Prakash S, Muthukumaran S. Refilling probe hole of friction spot joints by friction forming. Mater Manuf Process 2011;26:1539–45.

[3] Uematsu Y, Tokaji K, Tozaki Y, Kurita T, Murata S. Effect of re-filling probe hole on tensile failure and fatigue behavior of friction stir spot welded joints in Al– Mg–Si alloy. Int J Fract 2008;30:1956–66.

[4] Feng AH, Chen DL, Ma ZY. Microstructure and cyclic deformation behavior of a friction-stir-welded 7075 Al alloy. Metall Mater Trans A 2010;41:957–71.

[5] Fuller CB, Mahoney MW, Calabrese M, Micona L. Evolution of microstructure and mechanical properties in naturally aged 7050 and 7075 Al friction stir welds. Mater Sci Eng A 2010;527:2233–40.

[6] Fu RD, Sun ZQ, Sun RC, Li Y, Liu HJ, Liu L. Improvement of weld temperature distribution and mechanical properties of 7050 aluminum alloy butt joints by submerged friction stir welding. Mater Des 2011;32:4825–31.

[7] Rajakumar S, Muralidharan C, Balasubramanian V. Influence of friction stir welding process and tool parameters on strength properties of AA7075-T6 aluminum alloy joints. Mater Des 2011;32:535–49.

[8] L. Dubourg, A. Merati, M. Jahazi, Materials and Design 31 (2010) 3324–3330, rocess optimisation and mechanical properties of friction stir lap welds of 7075-T6 stringers on 2024-T3 skin.

[9] Thomas WM, Nicholas ED, Needham JC, Murch MG, Temple SP, Dawes CJ. Friction stir butt welding. International patent application No. PCT/GB92/ 02203; December 1991.

[10] Su JQ, Nelson TW, Mishra R, Mahoney M. Microstructural investigation of friction stir welded 7050–T651 aluminium. Acta Mater 2003;51:713–29.

[11] Jata KV, Sankaran KK, Ruschau J. Friction stir welding effects on microstructure and fatigue of aluminum alloy 7050–T7451. Metall Mater Trans A 2000;31:2181–92.

[12] Nandan R, DebRoy T, Bhadeshia H. Recent advances in friction-stir weldingprocess, weldment structure and properties. Prog Mater Sci 2008;53:980–5.

[13] Rhodes CG, Mahoney MW, Bingel WH. Effects of friction stir welding on microstructure of 7075 aluminium. Scripta Mater 1997;36:69–75.

[14] Chang-Yong Lee, Won-Bae Lee, Jong-Woong Kim, Don-Hyun Choi, Yun-Mo Yeon, Seung-Boo Jung, Lap joint properties of FSWed dissimilar formed 5052 Al and 6061 Al alloys with different thickness, J Mater Sci (2008) 43:3296–3304, DOI 10.1007/s10853-008-2525-1

[15] Dubourg L, Merati A, Jahazi M. Process optimisation and mechanical properties of friction stir lap welds of 7075-T6 stringers on 2024-T3 skin. Mater Des 2010;31:3324–30.

High Temperature Oxidation and Hot Corrosion Behavior of NiAl-34Cr Eutectic Alloys With Different Fe Contents

Nuri ERGİN[1], Cihan ÇEPER[2], Necati KOÇAK[3], Ahmet ŞİMŞEK[4], Özkan ÖZDEMİR[5]

[1,2,3,4,5]Sakarya University of Applied Sciences, Sakarya, Türkiye.
[1]nergin@subu.edu.tr, [3]ahmetsimsek@subu.edu.tr, [4]necatikocak@subu.edu.tr, [5]oozdemir@subu.edu.tr,

Abstract

NiAl-34Cr-xFe (x= at. 1, 3 and 5%) eutectic alloys were produced by electric current activated sintering method using elemental powders. Microstructure and phase analyzes of the produced samples were made with the help of scanning electron microscope (SEM-EDS) and x-ray diffraction (XRD) analysis.The cycle oxidation behaviors of alloys at 800 - 1000°C for 165 h in an open air atmosphere were investigated. The oxidation resistance of alloys was evaluated by the weight change measurements. The activation energy values calculated according to the Fe element content (at. 1, 3 and 5%) added to the NiAl-34Cr eutectic alloy were determined as 155.9 kJ/mol, 109.2 kJ/mol and 91.6 kJ/mol, respectively. The hot corrosion experiments were conducted cyclically for 165 hours in an environment consisting of a mixture of 75% Na_2SO_4 and 25% K_2SO_4 salts at temperatures ranging from 800°C to 1000°C. Activation energy values of NiAl-34Cr samples with 1% Fe, 3% Fe, and 5% Fe additives have been calculated as 114.1 kJ/mol, 105.3 kJ/mol, and 84.6 kJ/mol, respectively. The structures formed on the surface after cyclic oxidation and corrosion experiments were examined using SEM-EDS and XRD analyses.

Keywords: NiAl-34Cr eutectic alloy, Hot Corrosion, Oxidation, Electric Current Activated Sintering

1. Introduction

Intermetallic compounds based on the aluminides of transition metals such as titanium, nickel and iron are candidate materials for low and high temperature structural applications. Of these intermetallics, nickel aluminides based on the B2-ordered NiAl alloys exhibit excellent oxidation resistance, high melting point (1911 K), relative low density (5.86 g/cm^3), high thermal conductivity and good wear resistance [1-3]. These advantages have led to the identification of several potential uses, including furnace equipment, high-performance mold, aerospace and automotive industries [4]. NiAl intermetallic compounds are very important for technical applications used at high temperatures such as jet engines and gas turbines, as they have a high melting point, high thermal conductivity and excellent oxidation resistance[5]. However, the poor ductility and fracture toughness at ambient temperature and inadequate strength at high temperature hinders its practical application [6]. The methods that have been used in improving the room temperature ductility include second phase strengthening, grain refinement, micro and macro alloying. Especially recent research indicates that macro-alloying is a good way to improve these properties, like the addition of high Cr or Mo contents into NiAl results in the formation of NiAl-Cr, NiAl-Mo and NiAl-Cr(Mo) eutectic alloys. In addition, micro-alloying is carried out to improve the high temperature properties of NiAl-based eutectic alloys. [7,8].

Intermetallic compounds are produced by conventional powder metallurgy, mechanical alloying, self-propagating high-temperature synthesis, casting and directional solidification methods. In recent studies, powder metallurgy methods have been preferred for synthesizing intermetallic compounds due to their advantages such as production close to net shape [9-11]. Electric Current Activated Sintering (ECAS) technique, one of the alternative powder metallurgy methods, makes it possible to produce uniform material with theoretical density, owing to its fast heating speed and short waiting time at low sintering temperatures [12].

In this study, the NiAl-34Cr eutectic alloy was produced atomically with 1%, 3%, and 5% Fe ratios through an electric current-assisted sintering method, and the effect of the alloying element on the eutectic alloy was investigated.

[1] Corresponding author

The properties of the samples produced were investigated using various techniques including scanning electron microscopy (SEM), X-ray diffraction (XRD), hot corrosion and oxidation properties.

2. ExperimentalProcedure

Elemental powders of nickel (99.8% from Goodfellow; rough surface, sphericity particles with a mean size 3-7 μm), aluminum (99.95% from Alfa Easer; high sphericity particles with a mean size 7-15 μm), chromium (99.8% from Atlantic Equipment; sharp-edged particles with a volume mean diameter of 5 μm) and iron (99% from Goodfellow; flake form particles with a volume mean diameter of 7 μm) were ball milled for 12h at a ball to powder ratio of 2:1 in the stoichiometric ratio to form NiAl-34Cr-xFe (x= at. 1, 3 and 5%). Three powder mixed of compositions in atomic percentage 32,5Ni+32,5Al+34Cr+1Fe (mix A), 31,5Ni+31,5Al+34Cr+3Fe (mix B) and 30,5Ni+30,5Al+34Cr+5Fe (mix C) were made. Prior to sintering, powder mixes were cold pressed into a cylindrical compact in a metal die under a uniaxial pressure of 50 MPa. Cylindrical pellets with a diameter of 20 mm and a height of 5 mm were produced by electric current activated sintering in open air at 3500-4200A for 47 minute.
The synthesized specimens for microstructural and compositional analysis using a scanning electron microscope (SEM) /energy dispersive spectroscopy (EDS) were grounded to a 1200 grit SiC papers and then polished with a 0.3 μm diamond suspension. Phase analysis was carried out using X-ray diffraction. XRD analysis performed using Rigaku, D/MAX-B/2200/PC X-ray diffractometer with Cu Kα radiation (λ_{Cu}= 1.5418°A). Cyclic oxidation behavior of the samples was investigated by measuring the weight change. Before the oxidation test, the original surface area of each specimens was measured using the Solidworks, dried and weighed by an electronic scale with an accuracy of 0.0001 mg. The oxidation tests were performed in an open atmosphere electric furnace at 800, 900, and 1000°C with 15 cycles up to 165 h. Each cycle is a combination of 11 hour heating and 5 min air cooling to room temperature. After a waiting time of 5 min in cooling cycle, the specimen was again placed inside the furnace and the cycle continued. Weight of specimen was recorded at the end of each cooling cycle. Hot corrosion tests were carried out in molten-salt environment (75% Na_2SO_4 + 25% K_2SO_4) in a muffle furnace in an ambient atmosphere for 165 hour at 800, 900 and 1000 °C.

3. Results and Discussion

3.1 Material Characterization

The SEM microstructure images of the samples prepared with the stoichiometric composition ratio of the NiAl-34Cr eutectic alloy, to which 1%, 3%, and 5% Fe were added atomically using the ECAS technique, along with EDS analyses taken from various points, are provided in Figures 1-3. According to the analysis results, it can be observed that the matrix consists of Ni-Al, the light-colored regions contain Fe-Cr, and the protruding areas are rich in chromium. According to the Cr-Fe phase diagram, the maximum chromium solubility in α-Fe is about 100% atomic. In the Ni-Fe phase diagram, the maximum nickel solubility in α-Fe is about 5.8% atomic, and according to the Al-Fe phase diagram, the maximum aluminum solubility in α-Fe is about 28% atomic [12]. Based on the point EDS analysis results, the light-colored regions consist of approximately 36% Fe + 39% Cr + 18% Al + 7% Ni. Consistent with the literature, the lowest elemental solubility was found to be nickel.

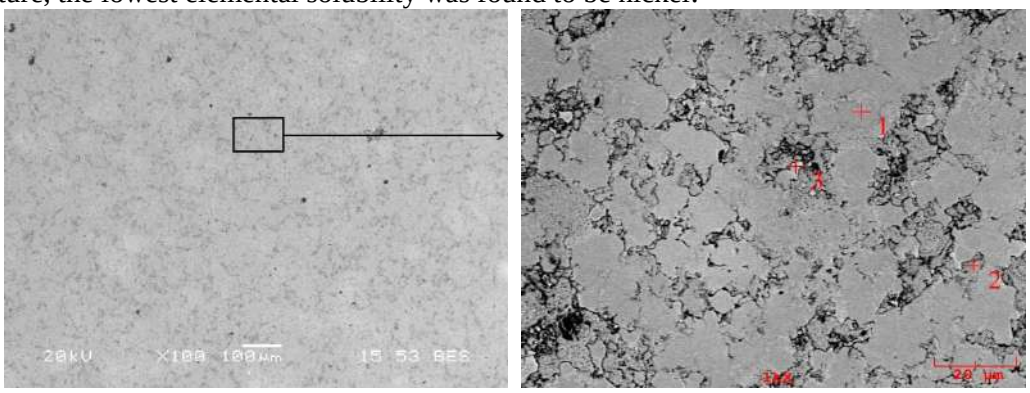

Figure 1. SEM-EDS analysis of NiAl-34Cr-1Fe alloy

Table 1. EDS analysis values of NiAl-34Cr-1Fe alloy (% at.)

Element	1	2	3
Al	54,40	5,76	44,44
Cr	6,01	89,48	10,26
Fe	0,12	0,13	0,33
Ni	39,47	4,63	44,97

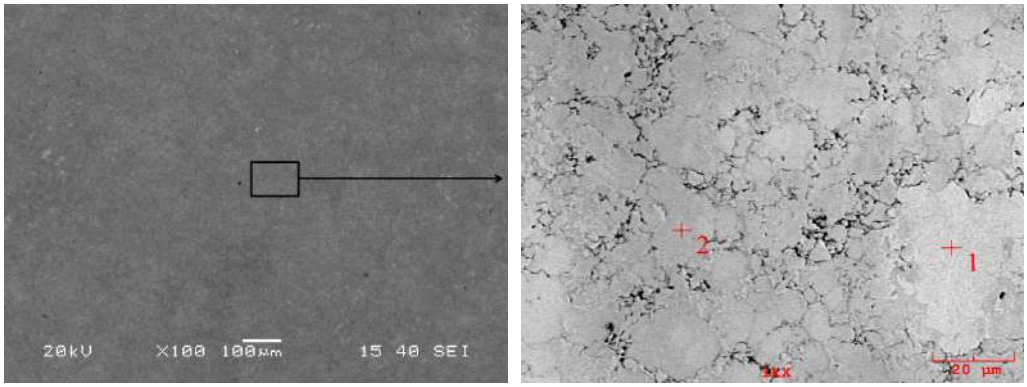

Figure 2. SEM-EDS analysis of NiAl-34Cr-3Fe alloy

Table 2. EDS analysis values of NiAl-34Cr-3Fe alloy (% at.)

Element	1	2
Al	14,33	53,53
Cr	32,81	3,36
Fe	47,41	0,02
Ni	5,45	43,09

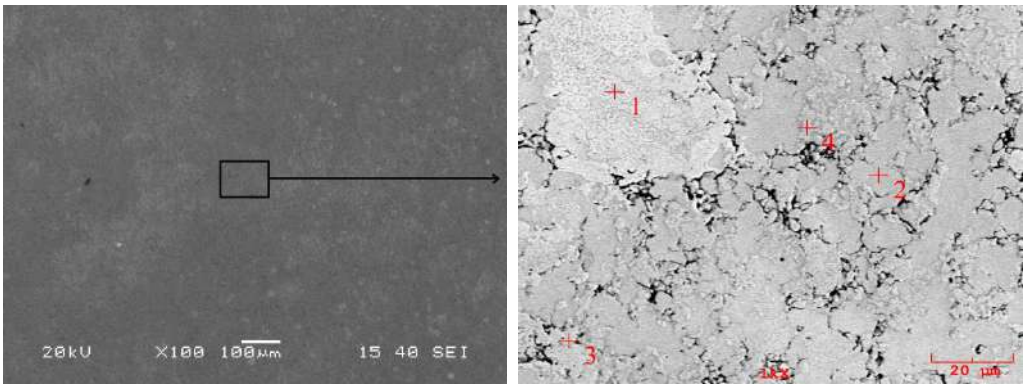

Figure 3. SEM-EDS analysis of NiAl-34Cr-5Fe alloy

Table 3. EDS analysis values of NiAl-34Cr-5Fe alloy (%At.)

Element	1	2	3	4
Al	17,82	56,32	10,11	51,63
Cr	39,53	3,11	80,54	9,02
Fe	35,62	0,54	7,51	0,48
Ni	7,03	40,03	1,84	38,87

To determine the phases formed in the produced Fe-doped eutectic NiAl-34Cr materials, X-ray diffraction analysis was employed, and the XRD patterns are provided in Figure 4. Consistent with the findings of many researchers,

XRD patterns of the NiAl-34Cr-X (x = Nb, Ti, Fe, etc.) eutectic alloy with alloying elements added reveal the NiAl (B2) and Cr (A2) phases, along with a minor phase associated with the added alloying element [14-16]. In this study, a similar phase structure was obtained, with a minor peak corresponding to Fe detected, and it was observed that the intensity of the peak increases with the higher content of the added element.

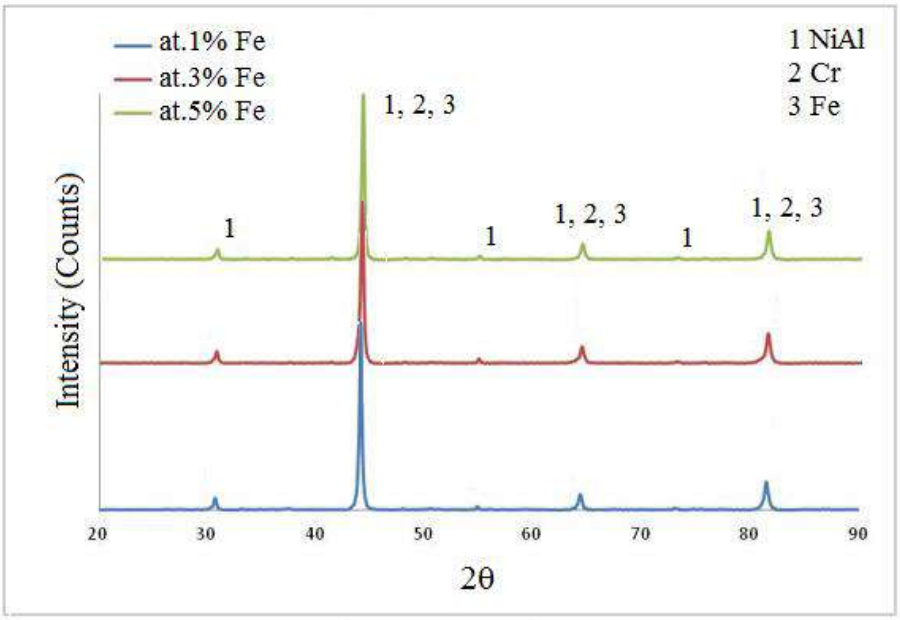

Şekil 4. Fe ilaveli NiAl-34Cr alaşımlarının XRD analizi

3.2 Oxidation Behaviors

In general, the oxidation of a metal exposed to high temperatures initiates with the absorption of oxygen and the nucleation of oxides on the surface. Subsequently, the formed oxide nuclei grow laterally to create a film layer. The thickening of this layer occurs as a result of oxygen ion diffusion from the environment to the oxide-metal matrix interface, or through the diffusion of metal ions along with free electrons towards the oxide-air interface. Often, due to the smaller size of metal ion radius compared to oxygen ions, the outward diffusion of metal ions occurs faster than the inward diffusion of oxygen.

Over time, as the oxide layer thickness, microcracks and pores begin to form on the surface. With increasing exposure time, the proportion of defective regions grows, and oxidation rapidly advances through these defects. Microcracks can develop into macrocracks, leading to delamination of the oxide layer. Depending on the nature of the oxide formed on the material's surface, oxide layers that melt or vaporize at lower temperatures can also develop. [17].
To determine the high-temperature oxidation behavior of the eutectic NiAl-34Cr intermetallic compound alloyed with 1%, 3%, and 5% Fe, samples were produced using the electric current-assisted sintering method. Oxidation experiments were conducted in an open atmosphere furnace at temperatures of 800°C, 900°C, and 1000°C for a total of 165 hours, consisting of 15 cycles with 11-hour intervals. The SEM microstructures of the samples after oxidation are provided in Figure 5. Based on SEM-EDS studies conducted after the oxidation of the two-phase (B2-cP2 and A2-cI2) substrate material, the increase in oxide structures on the surface is clearly visible. Furthermore, with increasing temperature, the quantity of the aluminum-rich phase also increases. Through the addition of iron as an alloying element, it was determined that iron is more present in the phase with higher chromium content. Upon oxidation at 800°C, the chromium-rich phase with a rough appearance contains approximately 5.6% Fe, while the aluminum-rich phase with a smooth surface contains about 0.19% Fe. In the microstructure taken from the sample at 1000°C, the white-colored chromium-rich oxide phase contains approximately 7.6% Fe. Okamoto and colleagues [13] emphasized that according to the Cr-Fe phase diagram, there is 100% solid solubility in the (α-Fe, Cr) phase. The increase in the aluminum-rich oxide, which appears in a dark shade, is clearly visible on the surface. Additionally, it was determined that the nickel content is quite low in these phases.

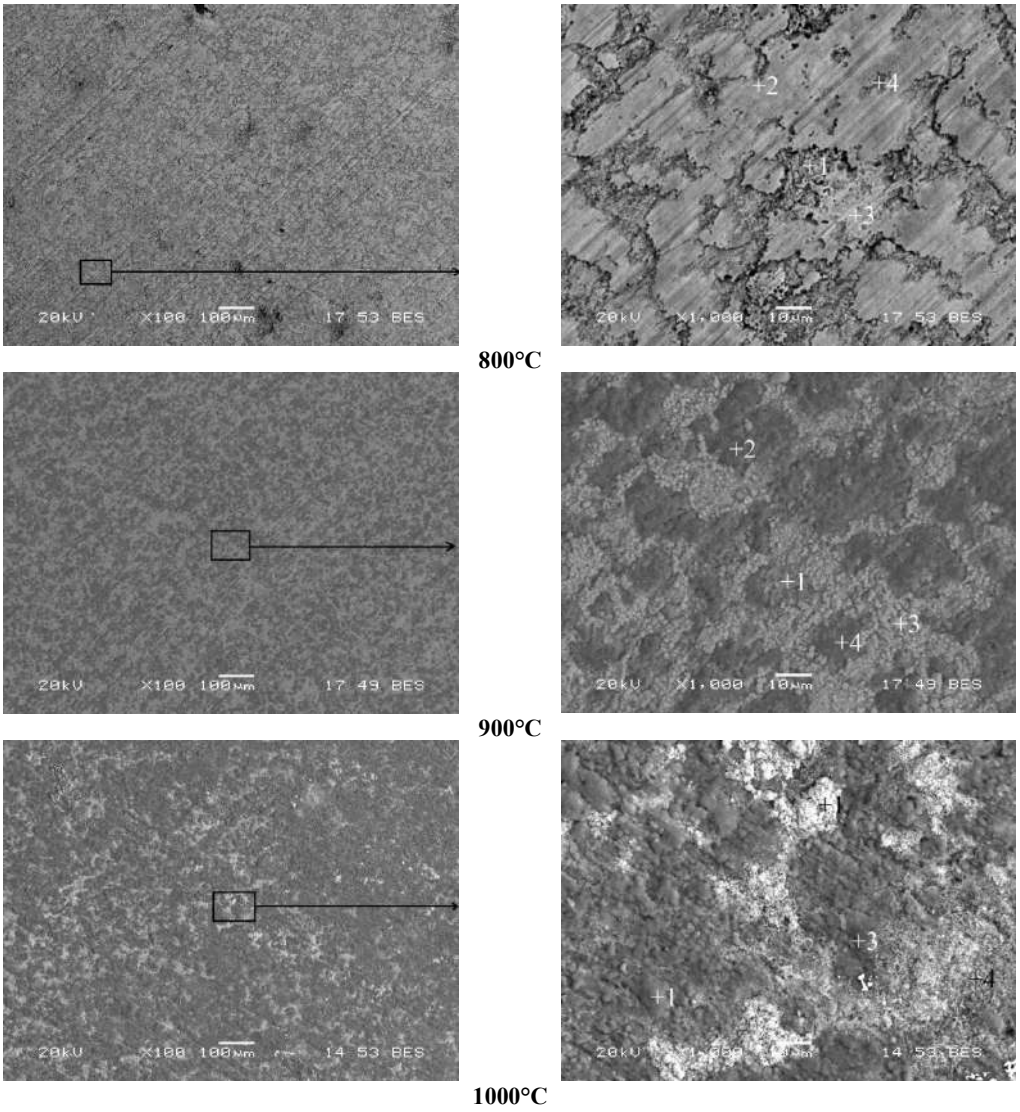

Figure 5. SEM-EDS analysis of oxidized NiAl-34Cr-1Fe alloy

Table 4. EDS analysis values of oxidized NiAl-34Cr-1Fe alloy (at. %)

Element	800°C				900°C				1000°C			
	1	2	3	4	1	2	3	4	1	2	3	4
O	59,42	41,37	36,69	43,39	54,97	51,11	64,75	54,28	65,04	56,32	49,30	51,91
Al	3,69	26,61	13,85	30,45	27,17	44,91	7,90	43,15	3,43	36,84	41,73	34,75
Cr	29,55	13,33	27,07	22,98	13,16	1,99	19,79	1,74	23,28	6,21	8,16	12,98
Fe	5,60	1,45	17,03	0,91	0,24	0,34	4,01	0,08	7,65	0,16	0,22	0,13
Ni	1,74	17,24	5,36	2,27	4,46	1,65	3,55	0,75	0,60	0,47	0,59	0,23

SEM-EDS analyses of the NiAl-34Cr3Fe alloy subjected to oxidation at different temperatures are provided in Figure 6 and Table 5. Accordingly, it has been observed that the alloying element, iron, promotes the oxidation of the chromium solid solution, which is one of the phases of the substrate material, and it preferentially occurs in chromium-rich oxides.

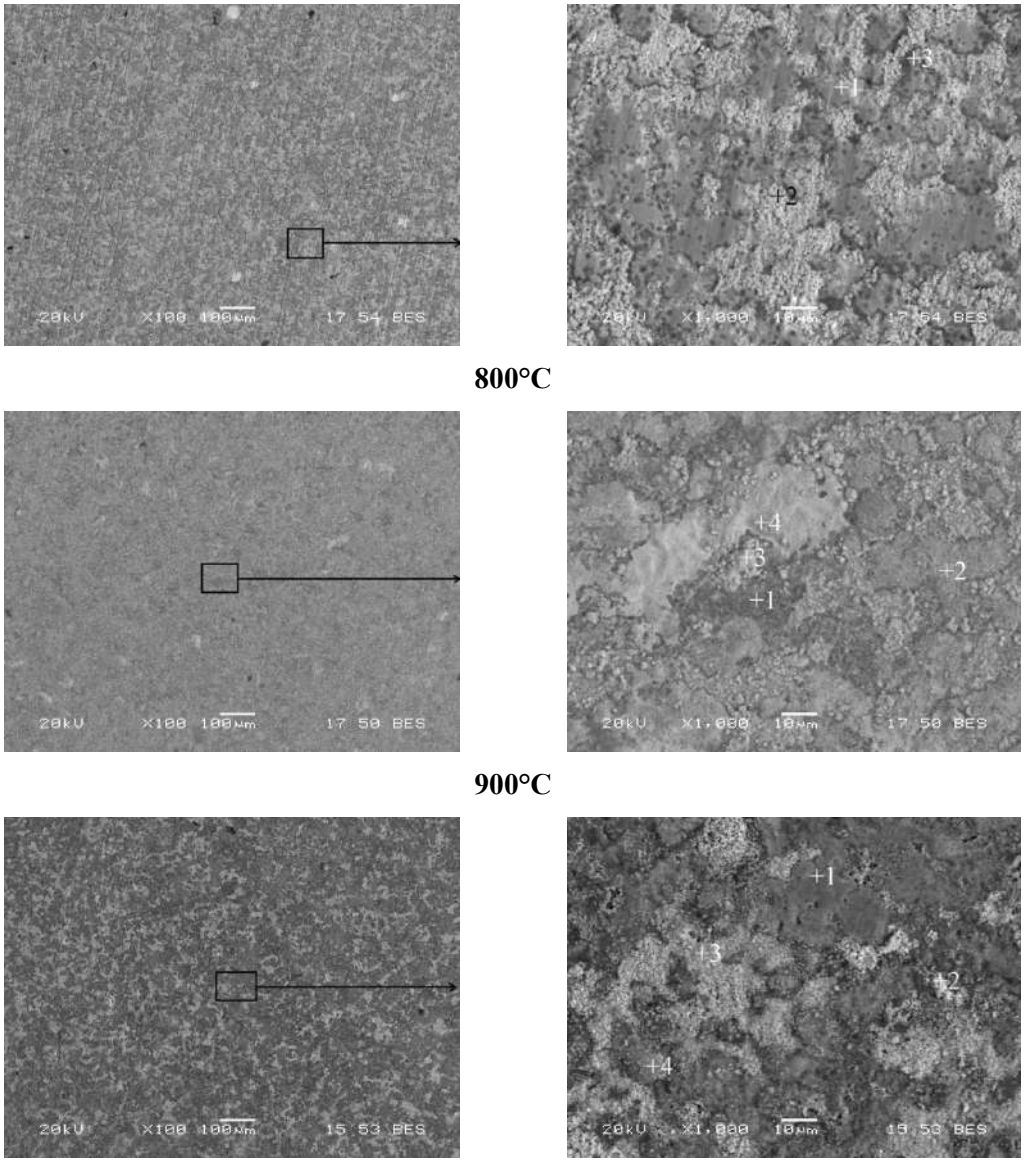

Figure 6. SEM-EDS analysis of oxidized NiAl-34Cr-3Fe alloy

Table 5. EDS analysis values of oxidized NiAl-34Cr-3Fe alloy (%at.)

	800°C			900°C				1000°C			
Element	1	2	3	1	2	3	4	1	2	3	4
O	41,45	41,23	45,89	57,57	51,33	64,15	54,03	32,00	34,28	33,12	31,56
Al	42,61	9,34	42,34	36,08	29,28	1,89	15,59	40,57	42,46	10,95	34,75
Cr	2,98	48,31	8,80	5,68	6,89	23,94	17,00	7,76	21,58	54,14	22,54
Fe	0,46	0,47	0,33	0,20	1,11	5,85	3,56	1,02	1,03	0,74	1,90
Ni	12,50	0,65	2,64	0,47	11,39	4,17	9,82	18,65	0,65	1,05	9,25

The SEM microstructure images of the surface and the EDS analysis results of the NiAl-34Cr-5Fe sample after oxidation are provided in Figure 7 and Table 6. When compared to samples with 1% and 3% Fe content, it can be observed that the chromium-rich phase oxidizes more intensively.

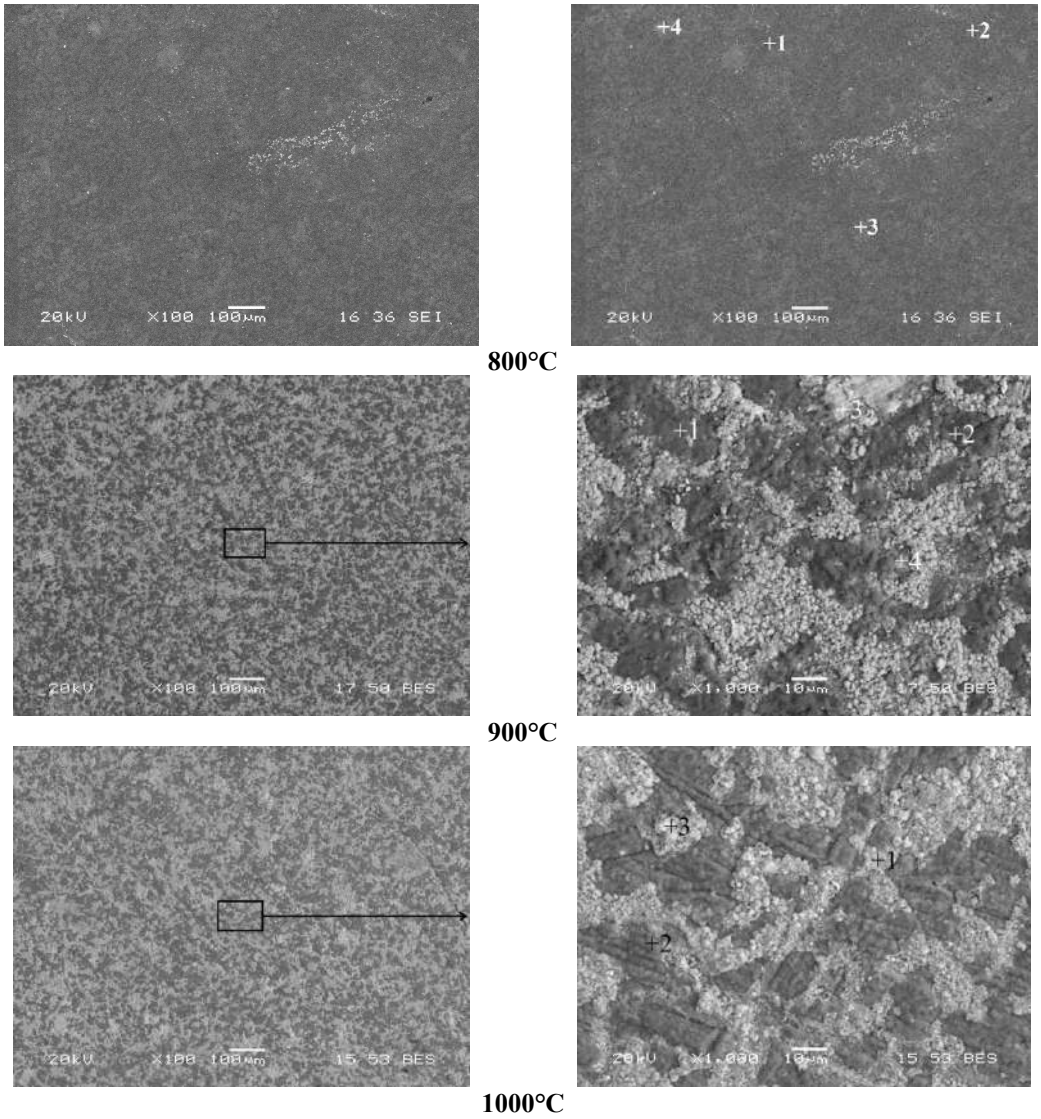

Figure 7. SEM-EDS analysis of oxidized NiAl-34Cr-5Fe alloy

Table 6. EDS analysis values of oxidized NiAl-34Cr-5Fe alloy (%at.)

Element	800°C				900°C				1000°C		
	1	2	3	4	1	2	3	4	1	2	3
O	39,43	45,36	52,33	41,80	48,47	53,36	39,87	42,60	55,22	60,23	65,80
Al	51,00	48,44	8,69	34,52	48,68	35,39	15,93	32,87	10,82	35,95	2,20
Cr	4,77	3,90	34,16	7,62	1,93	7,43	36,10	7,04	29,16	2,41	10,45
Fe	0,30	0,70	2,11	2,80	0,13	3,28	4,63	1,93	1,02	0,19	3,20
Ni	4,50	1,60	2,71	13,26	0,79	0,54	3,47	15,56	3,78	1,22	18,35

The XRD patterns of samples with Fe additions of at.% 1, 3, and 5 to the NiAl-34Cr alloy, subjected to oxidation at 800°C, 900°C, and 1000°C for 165 hours, are shown in Figure 8(a-c). At 800°C, the main matrix phase peaks (NiAl) are accompanied by minor phases of Cr_2O_3 and Al_2O_3. For samples oxidized at 900°C and 1000°C, in addition to these phases, NiO and $(Al_{0.9}Cr_{0.1})_2O_3$ phases are present. Furthermore, a Ni_3Al phase is also detected at 900°C and 1000°C. This phase was not observed after sintering and low-temperature oxidation, but was identified after high-temperature oxidation. This could be attributed to the growth of the Al-rich oxide layer on the surface with increasing oxidation temperature, leading to the formation of the Ni_3Al phase through the $2Ni + NiAl \rightarrow Ni_3Al$ reaction in an environment enriched in nickel.

In Figure 8(a), it can be seen that the Ni_3Al peaks, first detected at 900°C, intensify at 1000°C. Additionally, as the oxidation temperature increases, alongside the NiAl matrix phase, peaks of Ni1.1Al0.9 are observed. These peaks

weaken at 1000°C, while the Ni_3Al peaks strengthen. In the XRD analysis of the alloy containing 5% Fe (Figure 8(c)), the intensities of Ni_3Al and NiO peaks were found to increase

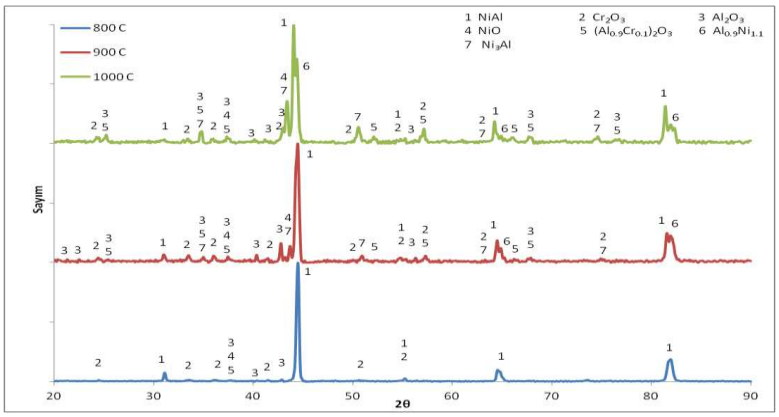

(a)

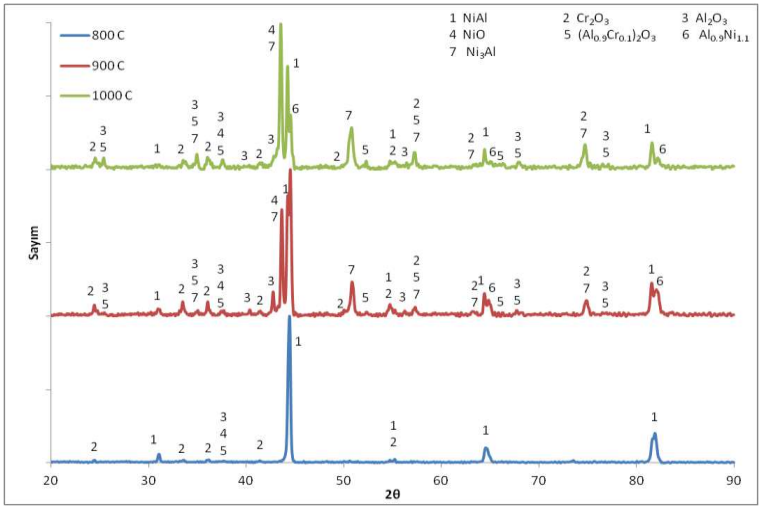

(b)

Figure 8. XRD analysis of NiAl-34Cr-xFe (at.%) alloy subjected to oxidation a) 1 Fe%, b) 3 Fe%, c) 5% Fe%.

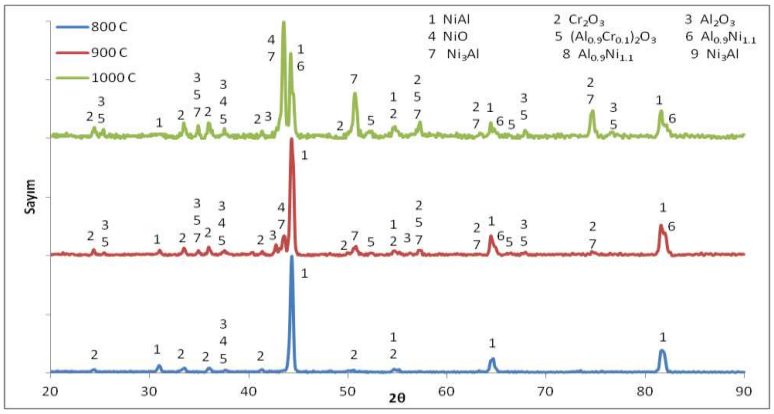

(c)

Figure 8. XRD analysis of NiAl-34Cr-xFe (at.%) alloy subjected to oxidation a) 1 Fe%, b) 3 Fe%, c) 5% Fe%.

The weight changes per unit area of NiAl-34Cr-xFe (at.%; x: 1, 3, 5) materials subjected to 165 hours of oxidation at various temperatures are presented in Figure 9a-c. It can be observed that the parabolic trend in the diagrams increases with rising temperature. The parabolic rate constants calculated from the slope of the diagram are listed in Table 7. Time-dependent graphs of the rate constant, plotted based on the Arrhenius equation, are provided in Figure 10, and the values of -Q/R and activation energy calculated from the slope are presented in Table 8.

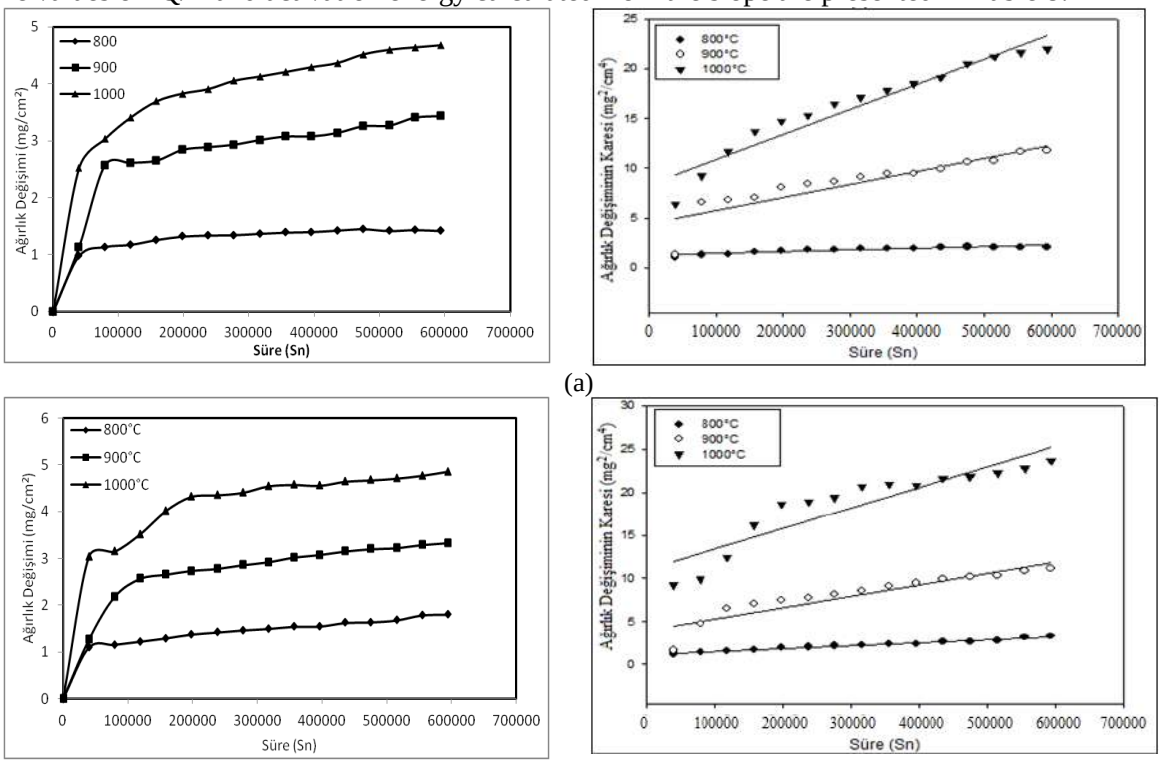

(a)

(b)

Figure 9. Weight change graphs of NiAl-34Cr-xFe (% at.) alloy exposed to oxidation depending on time and temperature a)1Fe, b)3Fe and c)5Fe

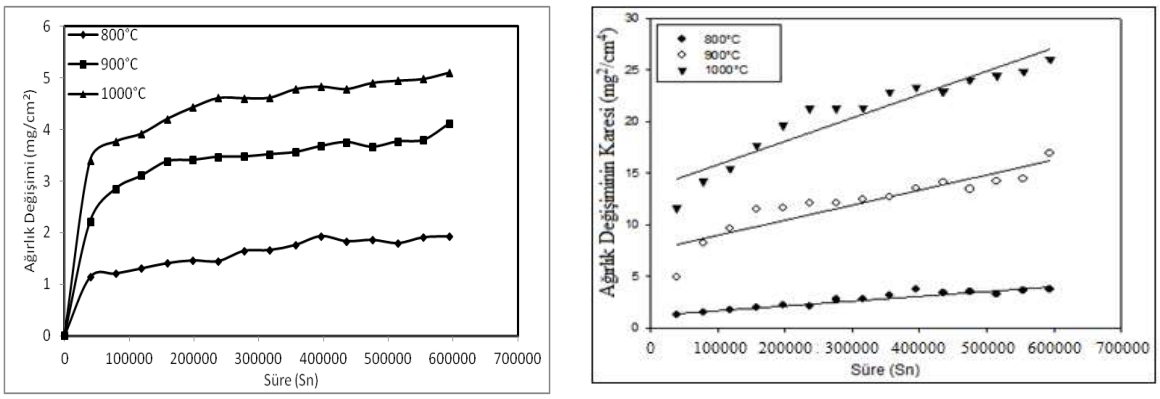

(c)

Figure 9. Weight change graphs of NiAl-34Cr-xFe (% at.) alloy exposed to oxidation depending on time and temperature a)1Fe, b)3Fe and c)5Fe

Table 7. Parabolic rate constants of NiAl-34Cr-xFe alloy subjected to oxidation with temperature.

Material	Parabolic rate constant, kp ($gr^2/cm^4.sn$) Temperature (°C)		
	800	900	1000
NiAl-34Cr-1Fe	$1,7x10^{-12}$	$1,3x10^{-11}$	$2,5x10^{-11}$
NiAl-34Cr-3Fe	$3,5x10^{-12}$	$1,3x10^{-11}$	$2,4x10^{-11}$
NiAl-34Cr-5Fe	$4,6x10^{-12}$	$1,5x10^{-11}$	$2,3x10^{-11}$

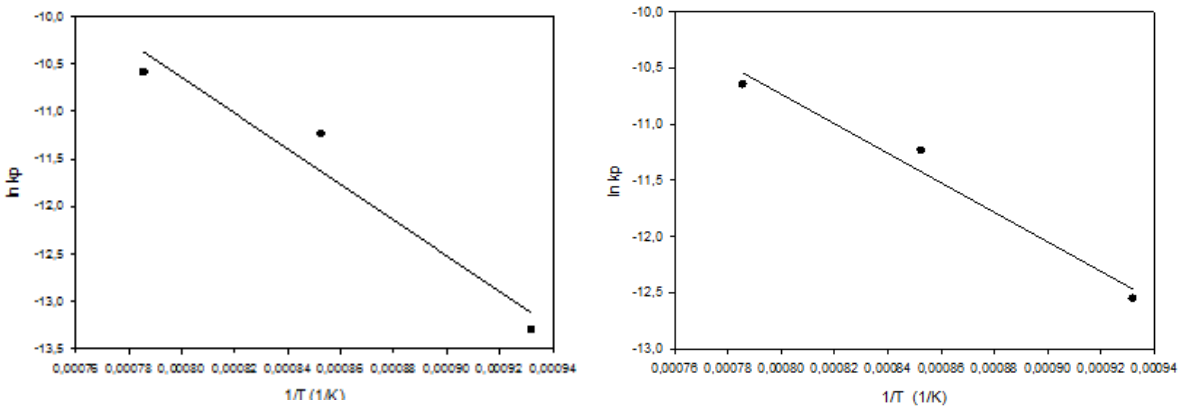

(a) (b)

Figure 10. Arrhenius curves drawn depending on Ln kp and 1/T of NiAl-34Cr-xFe (% at.) alloy exposed to oxidation a)1Fe, b)3Fe and c)5Fe

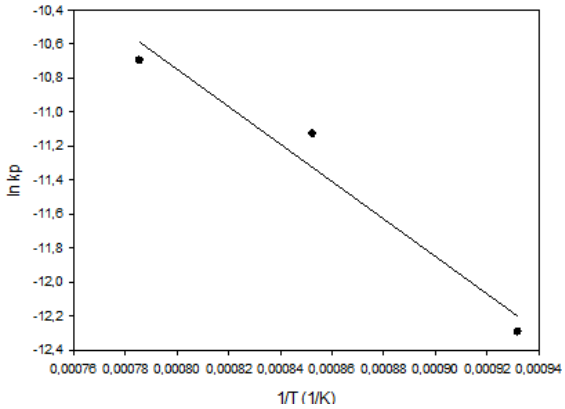

(c)

Figure 10. Arrhenius curves drawn depending on Ln kp and 1/T of NiAl-34Cr-xFe (% at.) alloy exposed to oxidation a)1Fe, b)3Fe and c)5Fe.

Table 8. –Q/R and activation energy values of NiAl-34Cr-xFe (% at.) alloy exposed to oxidation.

Material	-Q/R	Activation energy, Q kJ/mol
NiAl-34Cr-1Fe	18746,5	155,9
NiAl-34Cr-3Fe	13136,1	109,2
NiAl-34Cr-5Fe	11011,5	91,6

When comparing the calculated activation energy values of NiAl-34Cr-xFe (% at. x: 1, 3, and 5) alloys that underwent 165 hours of cyclic oxidation, it is evident that an increase in Fe content results in a decrease in activation energy. This suggests that the presence of iron as an alloying element promotes oxide formation.

3.3 Hot Corrosion Behaviors

The samples cyclic hot corrosion tests in an environment of 75% Na_2SO_4 + 25% K_2SO_4 at 800°C, 900°C, and 1000°C cyclically for 165 hours. The SEM-EDS microstructure images of the surface obtained from subjecting the NiAl-34Cr-1Fe alloy to cyclic hot corrosion at different temperatures for 165 hours, along with the analysis results, are presented in Figure 11 and Table 9. In the conducted studies, a generally observed oxide structure consists of two phases (NiAl and Cr) on the corrosion surface of the substrate material. It has been reported that the quantity of the chromium-rich oxide phase increases with the rise in temperature. [18]
Similarly, in this study, it was composed of Al2O3+Cr2O3 on the outside and the dominant Cr2O3 on the inside. Under more aggressive hot corrosion conditions compared to oxidation, at 1000°C, EDS analysis results from the

sample surface revealed the presence of only chromium oxide contents that also included alkali elements. It was determined that the alloying element added as Fe is present in the phase with higher chromium content. At 1000°C, within the chromium-rich oxide phase of the sample's structure, approximately 7.86% Fe was detected (Point 2).

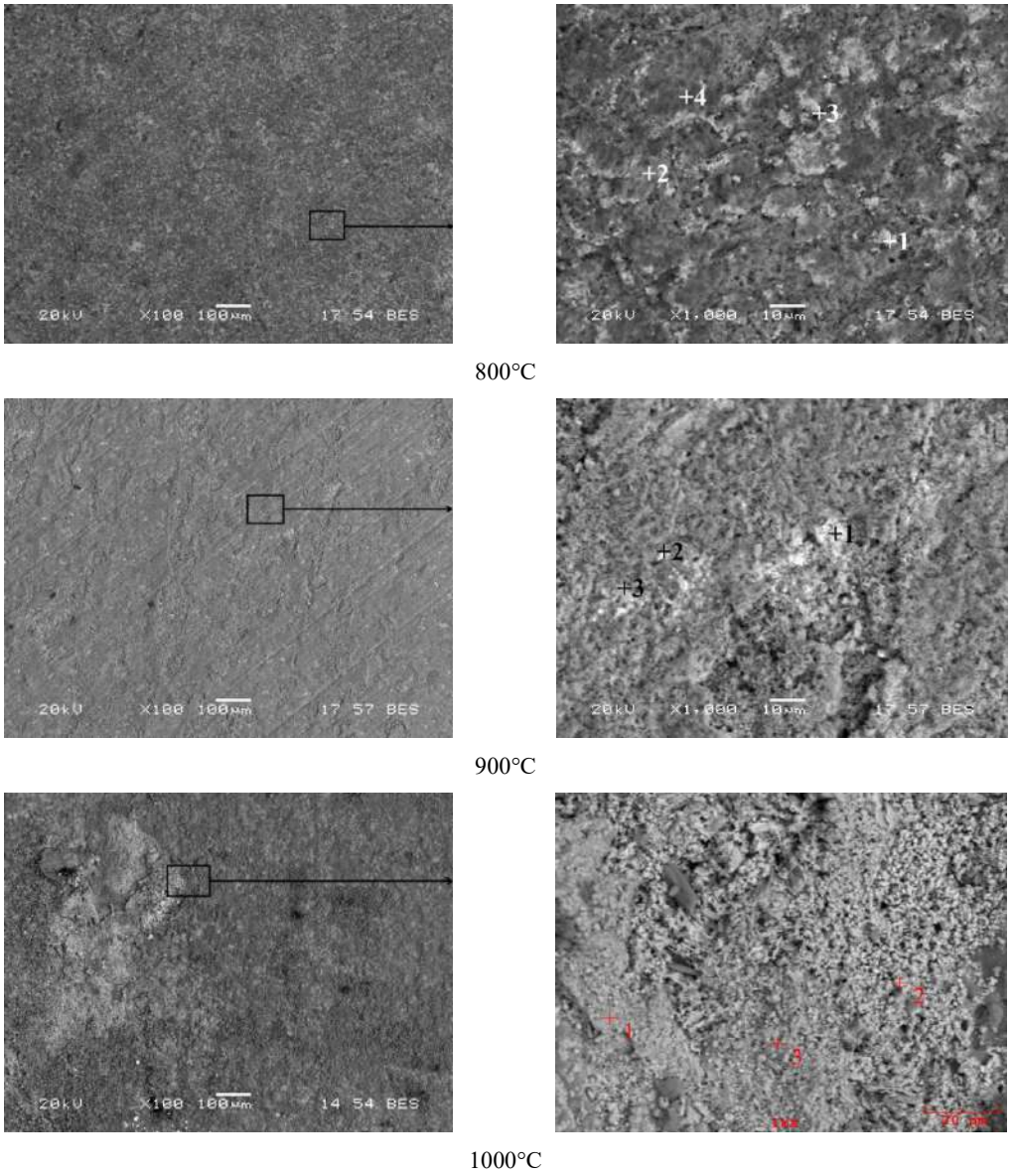

Figure 11. SEM images of NiAl-34Cr-1Fe alloy exposed to hot corrosion.

Table 9. EDS analysis values (at.%) of NiAl-34Cr-1Fe alloy exposed to hot corrosion.

Element	800°C				900°C			1000°C		
	1	2	3	4	1	2	3	1	2	3
O	29,6	48,8	43,7	49,2	63,1	59,9	43,1	67,4	66,4	53,9
Al	38,3	40,3	32,1	36,9	13,1	36,5	32,0	0,1	2,1	0,9
Cr	2,2	2,4	10,6	9,3	22,8	3,2	24,2	31,3	16,0	41,8
Fe	1,0	0,2	0,5	0,3	0,8	0,1	0,4	0,3	7,8	0,6
Ni	28,9	8,3	13,1	4,3	0,2	0,3	0,3	0,9	7,7	2,8

In the SEM images obtained after the 3% Fe added sample was exposed to hot corrosion for 165 hours, the biphasic oxide structure can be clearly distinguished at 800°C. Intense chromium oxide content was observed at 1000°C under the same conditions.

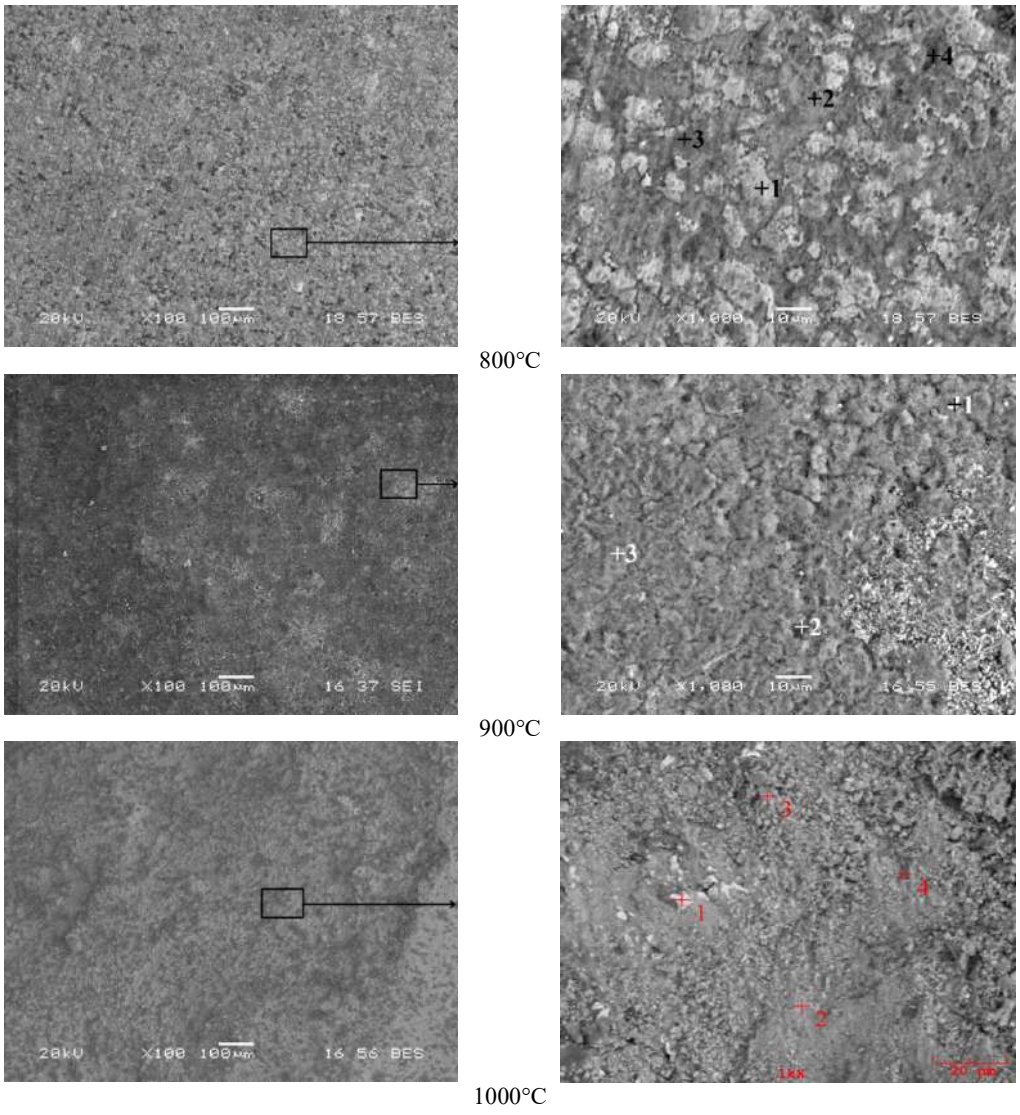

Figure 12. SEM images of NiAl-34Cr-3Fe alloy exposed to hot corrosion.

Table 10. EDS analysis values (at.%) of NiAl-34Cr-3Fe alloy exposed to hot corrosion.

Element	800°C				900°C			1000°C			
	1	2	3	4	1	2	3	1	2	3	4
O	28,0	63,9	56,4	39,7	59,1	47,8	50,2	5,2	63,0	69,4	20,0
Al	41,2	13,4	24,7	21,1	29,8	41,5	43,1	0,2	0,8	0,2	0,5
Cr	3,0	21,0	14,6	33,4	10,5	9,5	5,8	7,8	29,3	27,6	65,0
Fe	0,4	0,4	0,4	0,8	0,3	0,4	0,2	86,4	1,4	0,7	0,9
Ni	27,4	1,3	3,9	5,0	0,3	0,8	0,7	0,4	5,5	2,1	13,6

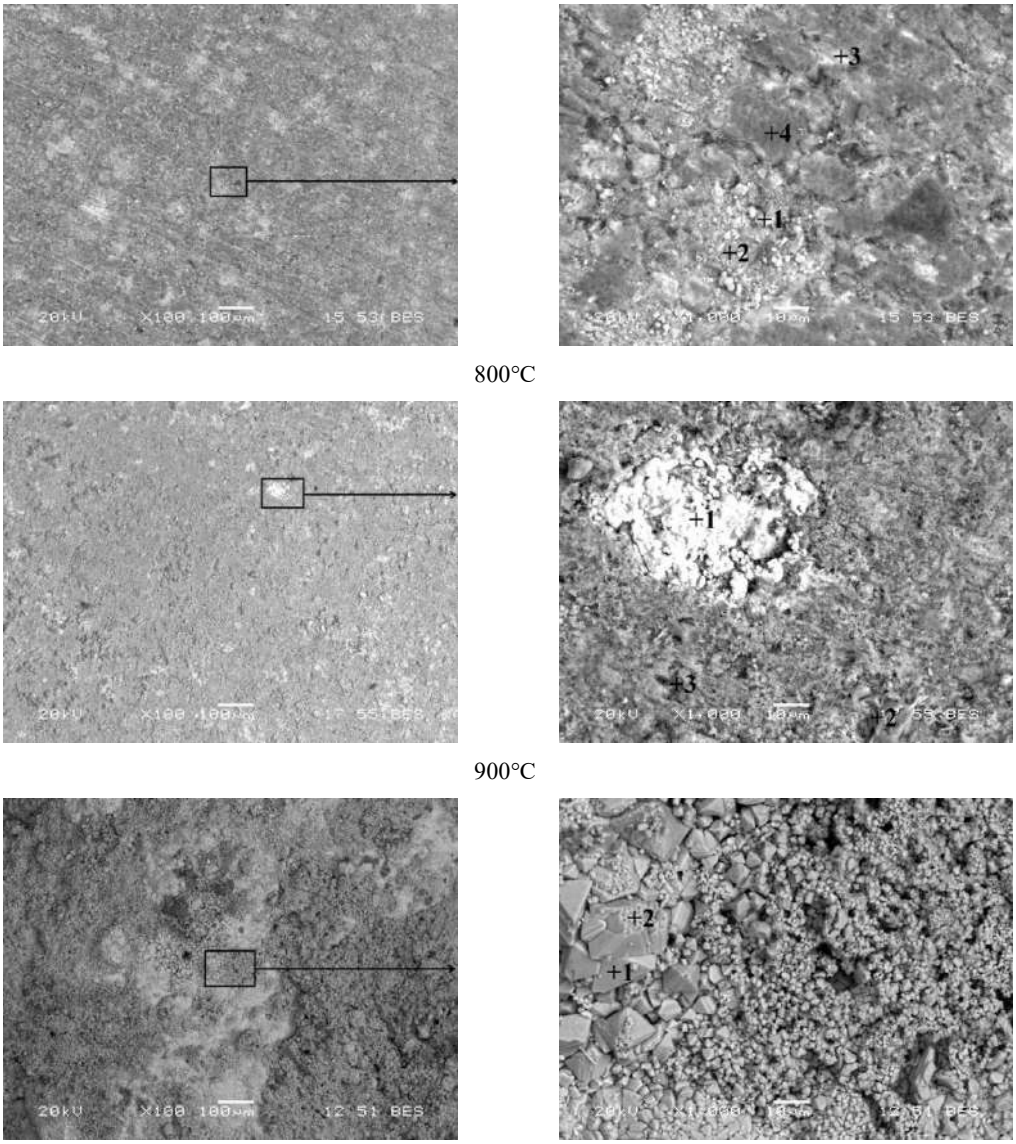

Figure 13. SEM-EDS analysis of NiAl-34Cr-5Fe alloy exposed to hot corrosion.

Table 11. EDS analysis values (at.%) of NiAl-34Cr-5Fe alloy exposed to hot corrosion.

Element	800°C				900°C			1000°C	
	1	2	3	4	1	2	3	1	2
O	65,9	53,9	22,5	51,7	43,2	62,1	41,8	47,1	62,5
Al	2,4	17,5	36,0	42,4	29,8	34,7	41,7	1,1	0,8
Cr	10,5	21,8	3,4	1,1	8,4	2,9	15,7	7,4	3,3
Fe	20,4	5,6	1,4	0,3	4,0	0,1	0,3	30,3	23,1
Ni	0,8	1,2	36,7	4,5	14,6	0,2	0,5	14,1	10,3

When comparing the NiAl-34Cr-5Fe alloy with NiAl-34Cr-1Fe and NiAl-34Cr-3Fe alloys, at 1000°C, sharp-edged particles are observed, and EDS analysis (at points 1 and 2) confirms that these particles are rich in Fe oxide.

The XRD patterns of the NiAl-34Cr-xFe (% at.) alloy samples exposed to corrosion in a mixture of 75% Na_2SO_4 and 25% K_2SO_4 salts at 800°C, 900°C, and 1000°C for 165 hours are presented in Figure 14. At 800°C, the main material peaks of NiAl are accompanied by minor phases of Cr_2O_3, Al_2O_3, NiO, and $(Al_{0.9}Cr_{0.1})O_3$. At 900°C and 1000°C, the presence of $Al_3Fe_5O_{12}$ phase is observed. Additionally, an $Al_{0.9}Ni_{1.1}$ phase is detected at 900°C, and a Ni_3Al phase is observed at 1000°C. This is attributed to the increase in the quantity of the Al-rich oxide phase, which leads to the

formation of the $Al_{0.9}Ni1.1$ and Ni_3Al phases in an environment enriched with nickel. Moreover, at 1000°C, the Ni_3Al phase is observed to have higher counts than the matrix material peak (NiAl)

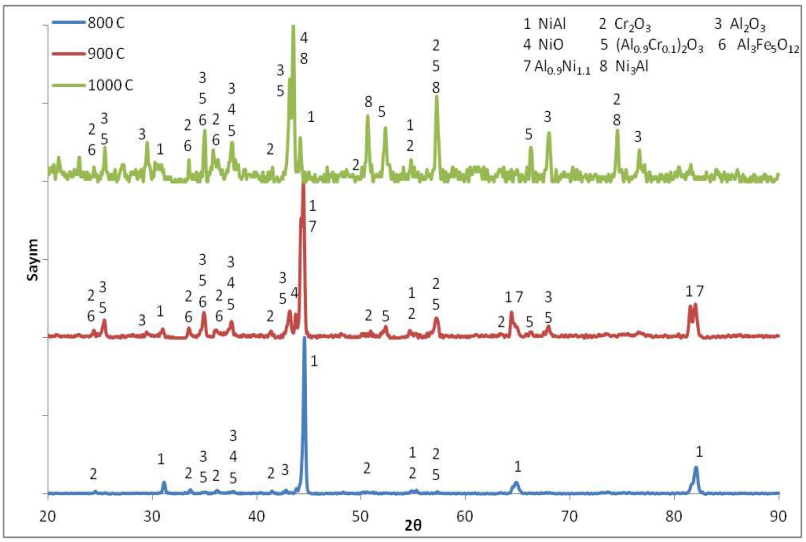

(a)

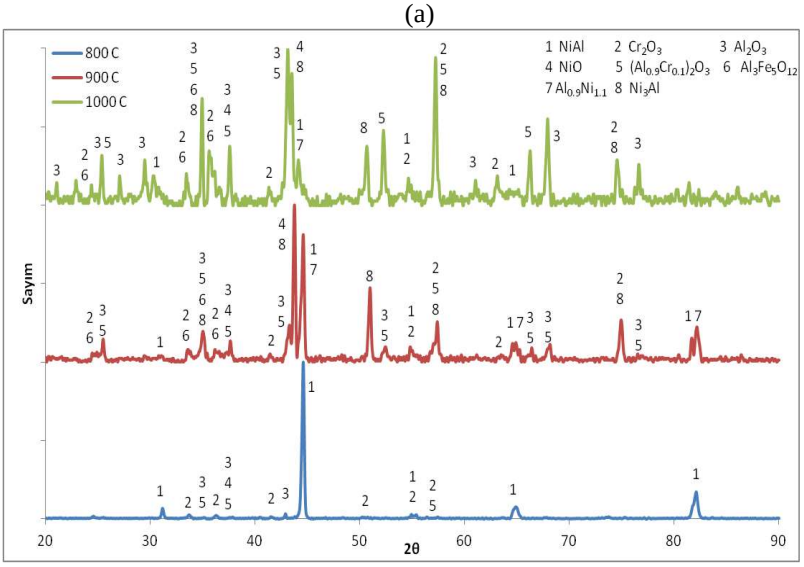

b

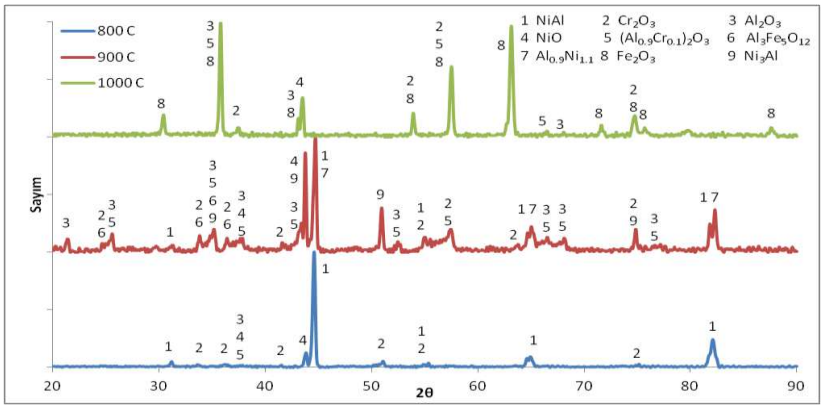

(c)

Figure 14. XRD analysis of NiAl-34Cr-xFe (% at.) alloy exposed to hot corrosion a)1Fe, b)3Fe, c)5Fe.

The weight change per unit area due to cyclic hot corrosion in a salt environment for 165 hours has been presented as a function of time and temperature for NiAl-34Cr-xFe alloys in Figure 15a-c. The calculated parabolic rate

constants are listed in Table 12, and the time-dependent graphs of the rate constant plotted based on the Arrhenius equation are provided in Figure 16(a-c). The values of -Q/R and activation energy calculated from the slope of the graphs are listed in Table 13.

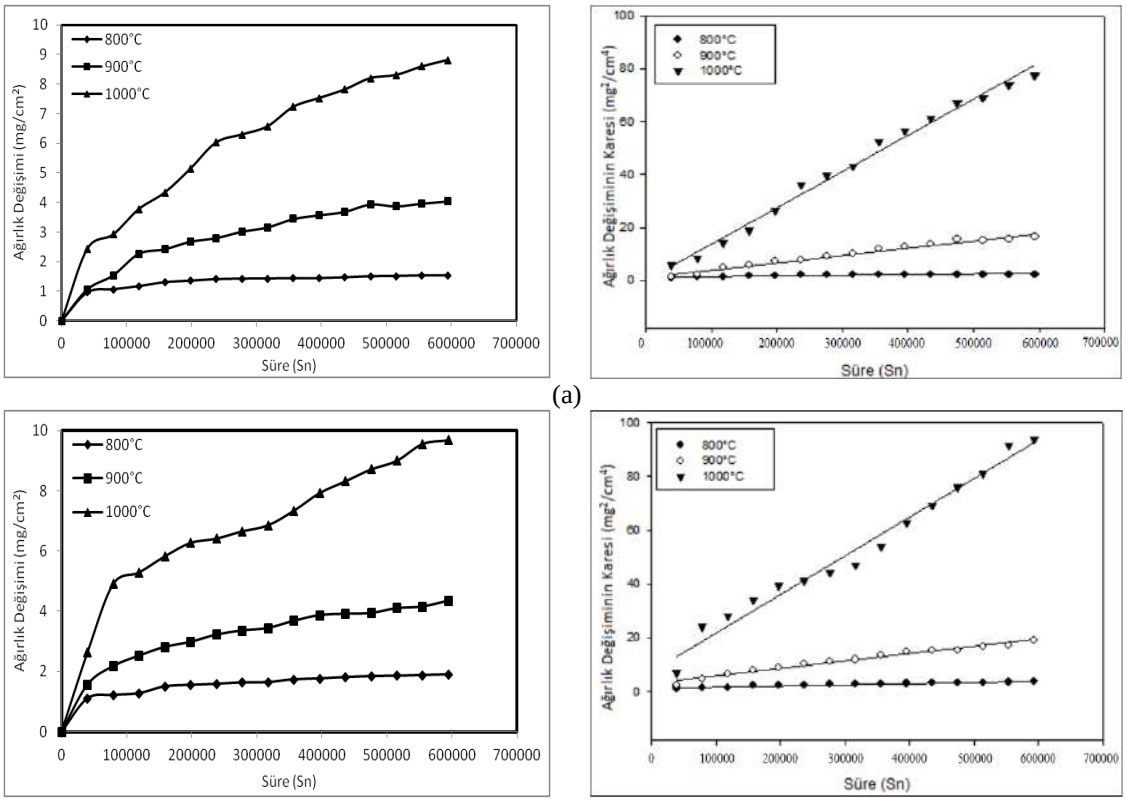

(a)

(b)

Figure 15. Weight change graphs of NiAl-34Cr-xFe (% at.) alloy exposed to hot corrosion, depending on time and temperature a)1Fe, b)3Fe and c)5Fe.

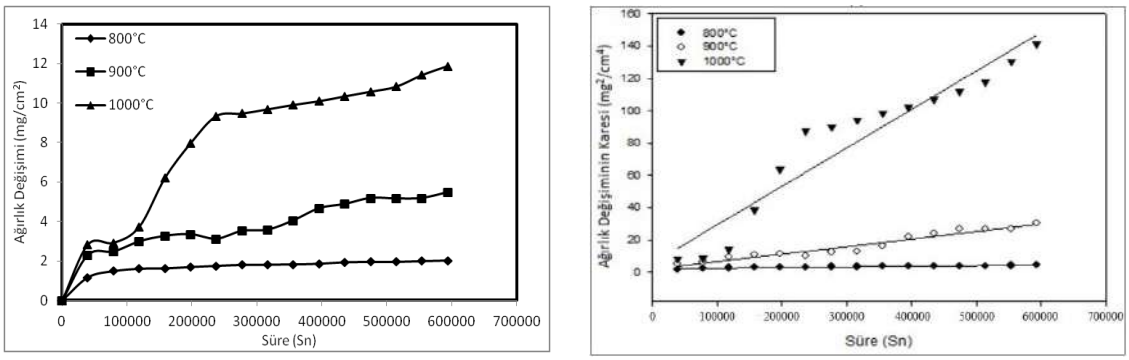

(c)

Figure 15. Weight change graphs of NiAl-34Cr-xFe (% at.) alloy exposed to hot corrosion, depending on time and temperature a)1Fe, b)3Fe and c)5Fe.

Table 12. Parabolic rate constants varying with temperature of NiAl-34Cr-xFe alloy exposed to hot corrosion.

Material	Parabolic rate constant, kp ($gr^2/cm^4.sn$) Temperature (°C)		
	800	900	1000
NiAl-34Cr-1Fe	$2,3x10^{-12}$	$2,8x10^{-11}$	$1,4x10^{-10}$
NiAl-34Cr-3Fe	$8,5x10^{-12}$	$3,6x10^{-11}$	$5,3x10^{-11}$
NiAl-34Cr-5Fe	$3,0x10^{-11}$	$7,9x10^{-11}$	$1,3x10^{-10}$

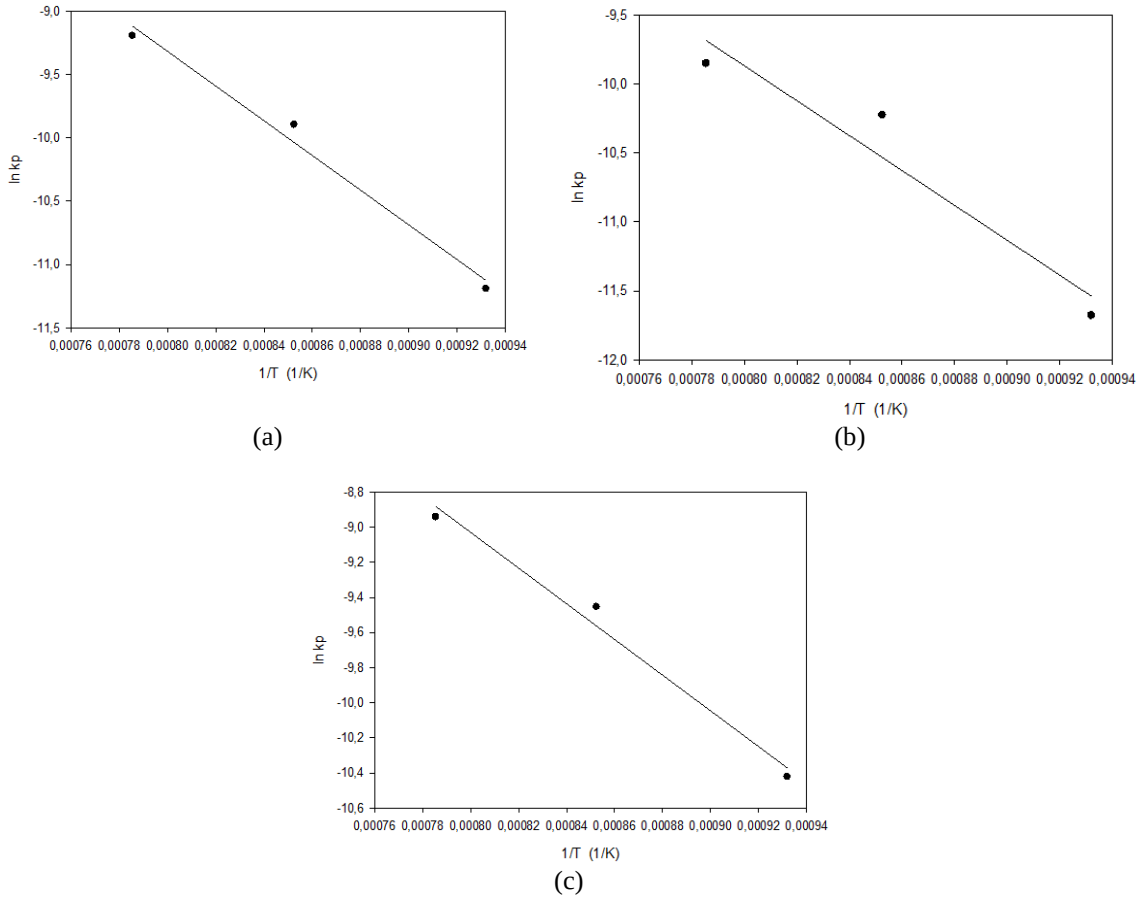

Figure 16. Arrhenius curves drawn depending on Ln kp and 1/T of NiAl-34Cr-xFe (% at.) alloy exposed to hot corrosion a)1Fe, b)3Fe, c)5Fe.

Table 13. –Q/R and activation energy values of NiAl-34Cr-xFe (% at.) alloy exposed to hot corrosion.

Material	-Q/R	Activation energy (Q), kJ/mol
NiAl-34Cr-1Fe	13720,1	114,1
NiAl-34Cr-3Fe	12664,5	105,3
NiAl-34Cr-5Ti	10177,5	84,6

4. Conclusions

In this study, the NiAl-34Cr eutectic alloy, alloyed with 1%, 3%, and 5% Fe, was produced using electric current-assisted sintering method in the range of 3500-4200A within 47 minutes. The effect of the alloying element on the eutectic alloy was investigated.

- The XRD patterns of the produced Fe-doped eutectic NiAl-34Cr materials revealed the presence of NiAl (B2) and Cr (A2) major phases, along with a minor phase represented by a peak corresponding to Fe. It was observed that the intensity of the Fe peak increases as the amount of added Fe increases.
- In order to assess the high-temperature oxidation behavior of the produced NiAl-34Cr-xFe (x= 1%, 2%, and 3%) eutectic alloy, oxidation experiments were conducted in an open atmosphere furnace at temperatures of 800°C, 900°C, and 1000°C. These experiments were performed cyclically in 15 cycles with 11-hour intervals, totaling 165 hours of exposure. After oxidation, the samples exhibited XRD patterns indicating that at 800°C, the main matrix phase peaks (NiAl) were accompanied by minor phases of Cr_2O_3 and Al_2O_3. In the samples that are oxidized at 900°C and 1000°C, there are NiO and $(Al_{0,9}Cr_{0,1})_2O_3$ phases in addition to these phases. Additionally, the presence of a Ni_3Al phase was identified in samples subjected to oxidation at both 900°C and 1000°C.

- The calculated activation energy values for alloys exposed to 165 hours of cyclic oxidation are determined as 155.9 kJ/mol for 1% Fe, 109.2 kJ/mol for 3% Fe, and 91.6 kJ/mol for 5% Fe-doped NiAl-34Cr alloy. Therefore, it is observed that as the Fe content increases, the activation energy decreases, suggesting that iron as an alloying element promotes oxide formation.
- The hot corrosion experiments were conducted cyclically for 165 hours in an environment of 75% Na_2SO_4 + 25% K_2SO_4 salts at temperatures of 800°C, 900°C, and 1000°C. At 800°C, the XRD patterns of the samples showed the main material peaks of NiAl accompanied by minor phases of Cr_2O_3, Al_2O_3, NiO, and $(Al_{0.9}Cr_{0.1})O_3$. At 900°C and 1000°C, the presence of $Al_3Fe_5O_{12}$ phase was observed. Additionally, an Al0.9Ni1.1 phase was detected at 900°C, and a Ni_3Al phase was identified at 1000°C.
- In the alloys subjected to 165 hours of corrosion, an increase in iron content has led to surface roughening, and the calculated activation energy values for 1% Fe, 3% Fe, and 5% Fe-doped NiAl-34Cr were determined as 114.1 kJ/mol, 105.3 kJ/mol, and 84.6 kJ/mol, respectively.

5. References

[1] S.O.Moussa, K.Morsi (2006). High-temperature oxidation of reactively processed nickel aluminide intermetallics, Journal of Alloys and Compounds, 426, pp.136-143.

[2] Y.B. Pithawalla, M.S. El Shall, S.C. Deevi (2000). Synthesis and characterization of nanocrystalline iron aluminide particles, Intermetallics, 8, pp.1225-1231.

[3] C. S. Bautistaa, A. Ferrierec, G. P. Rodríguez, M. López-Almodovar, A. Barba, C. Sierra, A. J. Vázquez (2006). NiAl intermetallic coatings elaborated by a solar assisted SHS process, Intermetallics, 14, pp.1270-1275.

[4] Y. Meng, J. Li, M. Gao, X. Zeng (2021). Microstructure characteristics of wire arc additive manufactured Ni–Al intermetallic compounds, Journal of Manufacturing Processes, 68, pp.932-939.

[5] C. Çeper (2019). NiAl-34Cr-X(Fe, Nb, Ti) *Alaşımının Elektrik Akım Destekli Sinterleme (Ecas) Yöntemiyle Üretimi Ve Karakterizasyonu,* (Yüksek Lisans Tezi). https://tez.yok.gov.tr/UlusalTezMerkezi/.

[6] O. O. Ayodele, M. A. Awotunde, A. O. Adegbenjo, M. B. Shongwe, B. A. Obadele, P. A. Olubambi (2020). Synthesis and heating rate effect on the mechanical properties of NiAl intermetallic compound, Materials Today: Proceedings 28, pp.785–788.

[7] L. Wanga, C. Yaoa, J. Shenb, Y. Zhanga, T. Wanga, H. Xua, L. Gaoa, G. Zhanga (2019). Microstructures and compressive properties of NiAl-Cr(Mo) and NiAl-Cr eutectic alloys with different Fe contents, Materials Science & Engineering A 744, pp.593–603.

[8] C. S. Tiwary, P. Pandey, S. Sarkar, R. Das, S. Samal, K. Biswas, K. Chattopadhyay (2022). Five decades of research on the development of eutectic as engineering materials, Progress in Materials Science 123, pp.1-33.

[9] J.Rodriguez, S.O. Moussa, J. Wall, K. Morsi (2003). Low-energy forging of aluminide intermetallics, Scripta Materialia, 48, pp.707-712.

[10] E.Godlewska, S. Szczepanik, R. Mania, J. Krawiarz, S. Koziński (2003). FeAl materials from intermetallic powders, Intermetallics, 11, pp. 307-312.

[11] J. Peng, F. Zhang, Y. Huang, J. Liu, K. Li, Y. Zhou, Y. Long, C. Wang, S. Wu, H. Tang (2021). Comparative study on NiAl and FeAl intermetallic-bonded diamond tools and grinding performance for Si_3N_4 ceramic, Ceramics International, 47, pp. 32736-32746.

[12] R. Orrù, R. Licheri, A. M. Locci, A. Cincotti, G. Cao (2009). Consolidation/synthesis of materials by electric current activated/assisted sintering, Materials Science and Engineering: R: Reports, 63, pp.127-287.

[13] Okamoto, H., Schlesinger, M.E., Mueller, E.M. (2016). ASM Handbook Volume 3: Alloy Phase Diagrams.

[14] B. Tang, D. A. Cogswell, G. Xu,, S. Milenkovic, Y. Cui (2016). The formation mechanism of eutectic microstructures in NiAl-Cr composites, Physical Chemistry Chemical Physics, 18 (29), pp. 19773–19786.

[15] M. Kellner, I. Sprenger, P. Steinmetz, J. Hötzer, B. Nestler, M. Heilmaier (2017). Phase-field simulation of the microstructure evolution in the eutectic NiAl-34Cr system" Computational Materials Science, 128, pp. 379–387.

[16] D. R. Johnson, X. F. Chen, , B. F. Oliver, R. D. Noebe, J. D. Whittenberger (1995). Processing and mechanical properties of in-situ composites from the NiAlCr and the NiAl(Cr,Mo) eutectic systems, Intermetallics, 3(2), pp.99–113.

[17] N. Solak (2002). Nitrür Esaslı Sert Seramik İnce Film Kaplamaların Oksidasyon Davranışları (Yüksek Lisans Tezi). https://tez.yok.gov.tr/UlusalTezMerkezi/.

[18] Ulu, R. (2013). *Alaşım Elementlerinin NiAl Alaşımlarının Mikroyapı ve Mekanik Özelliklerine Etkisi* (Yüksek Lisans Tezi). https://tez.yok.gov.tr/UlusalTezMerkezi/.

Investigation of Short Column Damages After 6 February 2023 Kahramanmaraş Earthquakes

Ozan İNCE[1] , Muhammed ATAR[2]

[1,2]Department of Civil Engineering, Faculty of Engineering, Firat University, Elazig, Türkiye.
[1]o.ince@firat.edu.tr, [2]m.atar@firat.edu.tr

[1](ORCID: 0000-0002-6319-1129), [2](ORCID: 0000-0001-7812-0086)

Abstract

On February 6, 2023, Kahramanmaraş, Turkey, experienced two powerful earthquakes with magnitudes of 7.7 and 7.6, occurring approximately 9 hours apart and having epicenters located 90 kilometers apart. Following these seismic events, numerous reinforced concrete buildings suffered varying degrees of damage, including some that completely collapsed. While reinforced concrete structures are typically expected to exhibit ductile behavior during earthquakes, observations have shown that brittle damage is frequently encountered. This research focuses on investigating the phenomenon known as the "short column effect," which is responsible for causing brittle damage in reinforced concrete buildings. The study identifies the factors contributing to the short column effect and illustrates the damages sustained during the earthquake through the virtual inspection and figures.

Keywords: Earthquake damages, short column, brittle failure, reinforced concrete buildings

1. Introduction

Reinforced concrete buildings are designed to show ductile behavior to provide high energy absorption capacity during earthquakes. However, brittle damages are commonly encountered in earthquakes. One of the most common brittle damage is caused by short column effect. In design of reinforced concrete structures it is assumed that columns can displace freely. However, if the displacement of the columns is limited to a certain height, the stiffness of this column increase and this column is exposed to more shear forces during the earthquake. This situation, called the short column effect, is usually seen in band windows or basements.

On 6 February 2023, two destructive earthquakes (Mw: 7.7 and Mw: 7.6) occurred in Kahramanmaraş, Türkiye. These earthquakes occurred with 9 hour apart and the distance between the epicenters of these earthquakes is nearly 90 km [1]. These earthquakes affected many provinces and caused severe damages to structures. After Kahramanmaraş earthquakes, many studies are made about structural damages [2-5]

Reinforced concrete buildings that main building stocks in Türkiye are severely damaged after Kahramanmaraş earthquakes. There are many damage reasons such as poor material quality, design mistakes, mistakes in reinforcement details or insufficient information about soil. In field observation it was seen that most of reinforced concrete buildings are designed according to Türkiye Earthquake Codes 1975 or later published codes. Türkiye Earthquakes Codes were updated in 1998, 2007 and 2018 [6-9].

In this study, after Kahramanmaraş earthquakes (Pazarcık and Elbistan) reinforced concrete buildings are investigated. Short column damages are commonly observed in field investigations. Reason of short column damages were examined and presented with figures.

[1]Corresponding author

2. Short column effect and damages

TBEC-2018 do not prohibit short column condition, but increases shear force for transverse reinforcement in short column condition. As effective length of column decrease, shear force become more for transverse reinforcement. Short column effect could happened by infill wall constructed certain height of column (Figure 1). Also short column affect could happened in basement.

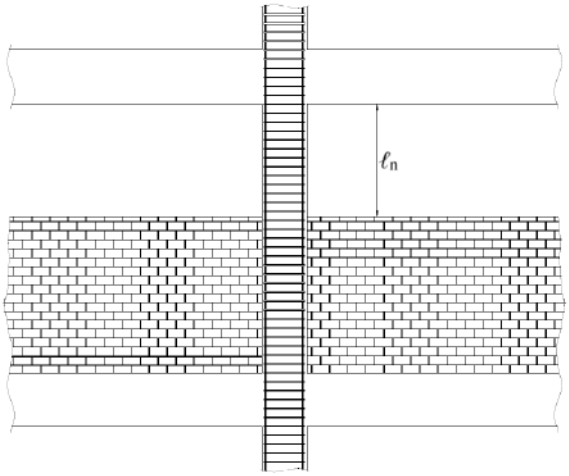

Figure 1. Short column effect by infill wall (TBEC-2018)

In field observation brittle short column damages commonly observes. In figure 2, a circular column is damaged because of infill wall with band window. Damaged columns because of basement are seen in figure 3. Although column height are decreased nearly 1 m, the columns are seriously damaged. In figure 4, a column is damaged due to basement wall and garden wall.

Figure 2. Short column damage due to infill wall

Figure 3. Short column damages because of basement

Figure 4. Short column damages due to basement and garden wall

3. Conclusions

Reinforced concrete buildings are designed with the assumption that they will exhibit ductile behavior. To achieve their maximum load-bearing capacity, these concrete elements need to form bending hinges without experiencing shear damage. However, the short column effect disrupts this ideal behavior, leading to brittle damage in the reinforced concrete elements and compromising the overall performance of the building.

One approach to mitigate the short column effect, especially when it arises due to infill walls, is to introduce flexible joints between these walls and the load-bearing structural elements. Nevertheless, prudent precautions are required to prevent the infill wall from collapsing out of its intended plane. To address the impact of short columns on the

basement floor, one effective strategy is to extend the reinforced concrete walls of the basement for a certain distance from the column face.

Furthermore, the significance of transverse reinforcement becomes more pronounced as the shear forces in vertical load-bearing elements increase, posing a risk of short columns. To ensure the effectiveness of transverse reinforcement, close attention should be paid to both the angle (135°) and the lengths of the hooks used in the reinforcement process.

4. References

[1] Disaster and Emergency Management Presidency (DEMA), 06 February 2023 Pazarcık-Elbistan (Kahramanmaraş) Mw: 7.7 – Mw: 7.6 Earthquakes Report, 2023.

[2] Ozturk, Murat, Musa Hakan Arslan, and Hasan Hüsnü Korkmaz. "Effect on RC buildings of 6 February 2023 Turkey earthquake doublets and new doctrines for seismic design." Engineering Failure Analysis 153 (2023): 107521.

[3] Sagbas, Gulsah, et al. "Field reconnaissance on seismic performance and functionality of Turkish industrial facilities affected by the 2023 Kahramanmaras earthquake sequence." Bulletin of Earthquake Engineering (2023): 1-28.

[4] Kocaman, İrfan. "The effect of the Kahramanmaraş earthquakes (Mw 7.7 and Mw 7.6) on historical masonry mosques and minarets." Engineering Failure Analysis 149 (2023): 107225.

[5] Mertol, Halit Cenan, et al. "Investigation of RC Buildings after 6 February 2023, Kahramanmaraş, Türkiye Earthquakes." Buildings 13.7 (2023): 1789.

[6] TEC-1975, Ministry of Construction and Settlement, Specifications on Structures Constructed in Disaster Area, Ankara, Türkiye,1975.

[7] TEC-1998, Ministry of Construction and Settlement, Specifications on Structures Constructed in Disaster Areas, Ankara, Türkiye,1998.

[8] TEC-2007, Ministry of Construction and Settlement, Specifications on Buildings Constructed in Dısaster Areas, Ankara, Türkiye, 2007.

[9] TBEC-2018, Türkiye Building Earthquake Specifications, Disaster and Emergency Management Authority, Ankara, Türkiye, 2018.